Transactions of the ASME®

Technical Editor, **LEWIS T. WHEELER**

Department of Mechanical Engineering,
University of Houston,
Houston, TX 77204-4792

Transactions of the ASME, Journal of Applied Mechanics (ISSN 0021-8936) is published quarterly (Mar., June, Sept., Dec.) for $240.00 per year by The American Society of Mechanical Engineers, Three Park Avenue, New York, NY 10016.

Periodicals postage paid at New York, NY and additional mailing office. POSTMASTER: Send address changes to Transactions of the ASME, Journal of Applied Mechanics, c/o THE AMERICAN SOCIETY OF MECHANICAL ENGINEERS, 22 Law Drive, Box 2300, Fairfield, NJ 07007-2300.

CHANGES OF ADDRESS must be received at Society headquarters seven weeks before they are to be effective. Please send old label and new address. **PRICES:** To members, $40.00; to nonmembers, $240.00; single issue, $96.00. Add $40.00 (airmail $60.00) for postage to countries outside the United States and Canada.

INDEXED by Applied Mechanics Reviews and Engineering Information, Inc. Canadian Goods & Services Tax Registration #126148048.

Journal of Applied Mechanics

Published Quarterly by The American Society of Mechanical Engineers

VOLUME 66 • NUMBER 2 • JUNE 1999

TECHNICAL PAPERS

(Contents continued on outside back cover)

This journal is printed on acid-free paper, which exceeds the ANSI Z39.48-1992 specification for permanence of paper and library materials. ♾™
♻ 85% recycled content, including 10% post-consumer fibers.

CONTENTS (CONTINUED)

BRIEF NOTES

(Contents continued on inside back cover)

CONTENTS (CONTINUED)

DISCUSSION

BOOK REVIEW

ANNOUNCEMENTS AND SPECIAL NOTICES

Plastic Yielding as a Phase Transition

M. Ortiz
Graduate Aeronautical Laboratories,
California Institute of Technology,
Pasadena, CA 91125
Mem. ASME

A statistical mechanical theory of forest hardening is developed in which yielding arises as a phase transition. For simplicity, we consider the case of a single dislocation loop moving on a slip plane through randomly distributed forest dislocations, which we treat as point obstacles. The occurrence of slip at the sites occupied by these obstacles is assumed to require the expenditure of a certain amount of work commensurate with the strength of the obstacle. The case of obstacles of infinite strength is treated in detail. We show that the behavior of the dislocation loop as it sweeps the slip plane under the action of a resolved shear stress is identical to that of a lattice gas, or, equivalently, to that of the two-dimensional spin-$\frac{1}{2}$ Ising model. In particular, there exists a critical temperature T_c below which the system exhibits a yield point, i.e., the slip strain increases sharply when the applied resolved shear stress attains a critical value. Above the critical temperature the yield point disappears and the slip strain depends continuously on the applied stress. The critical exponents, which describe the behavior of the system near the critical temperature, coincide with those of the two-dimensional spin-$\frac{1}{2}$ Ising model.

1 Introduction

The aim of this paper is to show that yielding in crystals may be understood as a phase transition, and to establish conceptual links between theories of crystalline slip and the theory of critical phenomena.

A phase transition occurs in a system when there is a singularity in its free energy or one of its derivatives. Phase transitions manifest themselves as sharp changes in the properties of the system. Examples of phase transitions are the evaporation of a liquid into gas, the transition from a normal conductor to a superconductor, or from paramagnet to ferromagnet. The theory of critical phenomena is a well-developed discipline which delves on the commonalities in the behavior of seemingly disparate physical systems near their critical points. The theory has been successfully applied to a wide variety of systems and has led to the identification of universality classes obeying well-defined scaling laws (see, e.g., Stanley (1971), Binney et al. (1992), and Chaikin and Lubensky (1995)).

By contrast, the full potential of the theory of critical phenomena as regards the formulation of macroscopic constitutive theories for solids, and particularly to the understanding of crystal plasticity, is far from realized at present. The classical KTHNY theory on the statistical mechanics of ensembles of linear elastic dislocations in crystals (Kosterlitz and Thouless, 1972, 1973; Nelson and Halperin, 1979; Young, 1979; Chaikin and Lubensky, 1995) was mainly intended as a theory of defect-mediated melting and did not address issues related to the macroscopic plasticity of crystals. In particular, the KTHNY model of a dislocated crystal, which may be understood as a vectorial extension of the Coulomb gas model (Kosterlitz and Thouless, 1972, 1973), is not appropriate for the study of yielding, plastic flow, and hardening of crystals, as these phenomena are macroscopic manifestations of the motion of dislocations and their interaction with obstacles. More recently, Chrzan and Mills (1993, 1994) have argued for a connection between rates of hardening and critical exponents in $L1_2$ intermetallic compounds, and for the kind of scale invariance which accompanies criticality in the dislocation pinning-depinning transition in those materials. Chrzan and Mills pioneering work provides compelling evidence for a link between plastic yielding and criticality.

The work presented in this paper endeavors to demonstrate this link for the classical forest-hardening mechanism (e.g., Kovács, 1967; Kovács and Zsoldos, 1973; Cuitiño and Ortiz, 1992). In the forest-dislocation theory of hardening, the motion of dislocations, which are the agents of plastic deformation in crystals, is impeded by secondary—or "forest"—dislocations piercing through the slip plane. As the moving and forest dislocations intersect, they form junctions of varying strengths which may be idealized as point obstacles. The strength of some of these obstacles has recently been computed by Baskes et al. (1997) and Phillips and Shenoy (1998) using atomistic models. Moving dislocations are pinned down by the forest dislocations and require a certain elevation of the applied resolved shear stress in order to bow out and bypass the pinning obstacles. The net effect of this mechanism is a steady increase in the critical resolved shear stress required for macroscopic slip to operate, a phenomenon known as "hardening."

The simplest analytical treatments of the forest-hardening mechanism are based on a line-tension approximation. Thus, in these approaches long-range interactions between dislocation are entirely neglected. Despite its apparent coarseness, this approximation may be closer to reality than other formulations which painstakingly account for the interaction energy between dislocations, but fail to account for the formation of low-energy microstructures. Begin by recalling that the net Burgers vector—or net "charge"—of a dislocation ensemble must be zero. For instance, in multipolar arrangements this condition implies that there is an equal number of positive and negative dislocations in the ensemble. In addition, dislocations often tend to attain low-energy configurations (Hansen and Kuhlmann-Wilsdorff, 1986; Kuhlmann-Wilsdorf, 1989). These are arrangements in which the long-range stress field of the dislocations vanishes. Roughly speaking, this is accomplished by surrounding each dislocation segment with segments of the opposite sign, i.e., by *screening* the segment; or by arranging dislocations as low-angle grain boundaries, dipolar walls, and other configurations for which the attendant plastic strains are compatible (Ortiz and Repetto, 1998). Under these circumstances, the remaining energy of the dislocations, or "self-energy," is proportional to the dislocation length, as presumed in the line-tension approximation.

One of the most successful analytical treatments of the forest-hardening mechanism was advanced by Kocks (1964) (see also

Contributed by the Applied Mechanics Division of THE AMERICAN SOCIETY OF MECHANICAL ENGINEERS for publication in the ASME JOURNAL OF APPLIED MECHANICS.
Discussion on the paper should be addressed to the Technical Editor, Professor Lewis T. Wheeler, Department of Mechanical Engineering, University of Houston, Houston, TX 77204-4792, and will be accepted until four months after final publication of the paper itself in the ASME JOURNAL OF APPLIED MECHANICS.
Manuscript received by the ASME Applied Mechanics Division, Aug. 14, 1998; final revision, Nov. 20, 1998. Associate Technical Editor: L. T. Wheeler.

Ortiz and Popov (1982) and Cuitiño and Ortiz (1992)), and is sometimes referred to as Kock's percolation model. In this approach, the applied resolved shear stress is equilibrated by the line tension of the dislocations. The critical stress τ_c required for a dislocation segment to bypass a pair of pinning point obstacles is proportional to the line tension and inversely proportional to the distance between the obstacles. If the point obstacles are assumed to be randomly distributed over the slip plane, it follows that τ_c itself is a random variable with a well-characterized probability density function $f(\tau_c)$ (Grosskreutz and Mughrabi, 1975; Mughrabi, 1975). As the resolved shear stress is raised from τ to $\tau + \Delta\tau$, all dislocation segments with τ_c in the interval $[\tau, \tau + \Delta\tau]$ become unstable and effect random flights. The length of these flights, and the attendant slip-strain increment, was estimated by Kocks (1964) by imagining that the dislocation segments move over a *one-dimensional* "obstacle course" consisting of obstacles of random heights distributed as $f(\tau_c)$. In particular, the segments arrest when they reach obstacles of strength greater than $\tau + \Delta\tau$.

It is clear that the one-dimensional character of this analysis represents a sweeping simplification as regards the geometry and topology of moving dislocation loops. For instance, an expanding dislocation loop may become *pinched,* with the result that the number of connected components of the loop is increased by one. Conversely, loops can shrink to a point or be left behind as debris surrounding point obstacles, or Orowan loops. Evidently, these intricacies are not accounted for in one-dimensional renditions of the forest-hardening mechanism. More detailed analyses of forest-hardening have invariably been based on numerical methods (Foreman and Makin, 1966, 1967). Despite these limitations, Kock's percolation model, or subsequent extensions thereof (Ortiz and Popov, 1982; Cuitiño and Ortiz, 1992; Kocks et al., 1991) has provided an effective basis for describing the hardening of materials such as fcc metals (Cuitiño and Ortiz, 1993; Cuitiño, 1996), $L1_2$ intermetallic compounds (Cuitiño and Ortiz, 1993), and others.

The theory developed in this paper overcomes the topological restrictions inherent to one-dimensional treatments of the forest-hardening mechanism, and establishes a clear link between yielding and criticality. In order to establish this link in the simplest possible terms, we restrict our attention to the motion of a single dislocation loop through a slip plane containing a random array of point obstacles. As discussed above, we assume that the dislocations are well screened and hence their energy is ostensibly proportional to their length. In the spirit of level-set methods, the dislocation loop is described by a scalar field ξ which takes the value of 1 inside the loop and 0 outside the loop. The transition between these two extreme values occurs over the dislocation line. In this manner, no restrictions are placed on the evolving geometry and topology of the loop. In order to simplify the analysis, however, we discretize the field ξ on a square lattice spanning the slip plane. The motion of the loop is impeded by forest dislocations piercing the slip plane, which we treat as point obstacles. The occurrence of slip at the sites occupied by these obstacles is assumed to require the expenditure of a certain amount of work commensurate with the strength of the obstacle.

The equilibrium properties of the dislocation loop/obstacle system may be described within the framework of Gibbsian statistical mechanics. We show that, once the effect of the point obstacles is taken into account, the effective Hamiltonian of the system is identical to that of a lattice gas, or, by a simple change of variables, to the two-dimensional spin-$\frac{1}{2}$ Ising model (see, e.g., Yeomans (1992)). In the parlance of the theory of critical phenomena, crystals whose plasticity is well described by the forest-hardening mechanism belong to the universality class of the two-dimensional spin-$\frac{1}{2}$ Ising model. In particular, the behavior and scaling properties of all such crystals should be identical near the critical point, and be described by a few material-independent critical exponents. For zero applied field, the spin-$\frac{1}{2}$ Ising model was solved by Onsager (Baxter, 1982), and to date furnishes one of the rare few examples of nontrivial model systems which can be solved exactly. In particular, the critical exponents are known exactly for the two-dimensional spin-$\frac{1}{2}$ Ising model and, by extension, for the forest-hardening model developed in this paper.

Systems which can be described by the two-dimensional spin-$\frac{1}{2}$ Ising model exhibit a phase transition at a critical temperature T_c. In the particular case of the dislocation loop/obstacle system, below the critical temperature this transition is signalled by a sudden increase in the slip strain. For sufficiently low temperatures, the system jumps from a state characterized by a slip strain close to zero to a state characterized by generalized slip over most of the slip plane. The critical resolved shear stress at which yielding occurs follows from the theory as a function of temperature, the obstacle density and material constants. The size of the slip-strain jump at yielding decreases to zero as the critical temperature is approached from below, and disappears altogether above the critical temperature. In this latter regime, therefore, the slip strain depends continuously on the applied resolved shear stress and no yield point is in evidence. However, examination of model materials, such as copper, suggests that T_c is close to the melting temperature. Therefore, yielding in these materials is predicted to persist up to very high temperatures, in keeping with observation.

Unfortunately, no exact solution is presently known for the two-dimensional spin-$\frac{1}{2}$ Ising model in the presence of an applied field. A simple approximate solution may be obtained by recourse to mean-field theory. Mean-field theory reveals compelling geometrical insights into the equilibrium properties of the system. In addition, it suggests the rudiments of a kinetic theory which accounts for hysteresis. This rudimentary kinetics is in analogy to that which is envisioned in theories of hysteresis proposed for wires or bars which undergo martensitic transformations (Abeyaratne and Knowles, 1988). It should be emphasized, however, that the resulting kinetic model represents an extension of equilibrium statistical mechanics, in as much as it requires additional assumptions regarding the *accessibility* of states in phase space. These restrictions on accessibility clearly violate ergodicity and place the model outside the realm of equilibrium statistical mechanics.

The paper is organized as follows. In Section 2 the Hamiltonian of the dislocation loop/obstacle system is formulated. This Hamiltonian includes terms which account for the self-energy of the dislocations, computed from the line-tension approximation, the applied resolved shear stress, and the point obstacles introduced in the slip plane by forest dislocations. In particular, a chemical potential is introduced as a device for controlling the density of point obstacles. In Section 3 the equilibrium properties of the system are established within the framework of Gibbsian statistical mechanics. These developments lead to he computation of the internal and free energies of the system, and the attendant relations between slip strain, applied resolved shear stress, temperature, and obstacle density. In Section 4, the nature of the phase transition and its relation to yielding is uncovered with the aid of mean-field theory. In Section 5, a simple kinetic theory is developed which accounts for hysteresis and plastic dissipation. Possible extensions of the theory and suggestions for further work are discussed in Section 6.

2 Forest Hardening

The aim next is to formulate a simple model of forest-hardening mechanism which captures the essential physics of the mechanism while lending itself to a full analytical treatment within the framework of equilibrium statistical mechanics. In the interest of simplicity, we focus on the motion of a single dislocation loop through a random array of point obstacles corresponding to the intersections between the slip plane and forest dislocations.

We begin by discretizing the slip plane into a square lattice of parameter a (Fig. 1). In order to avoid infinite sums, we consider a square subdomain containing N sites, e.g., with periodic boundary conditions enforced on its boundary. The thermodynamic limit

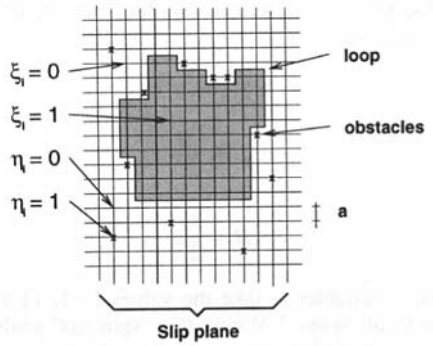

Fig. 1 Schematic of the dislocation/obstacle system

of interest may then be attained by letting $N \to \infty$ and is independent of the precise nature of the boundary conditions. Each point $i = 1, \ldots, N$ in the lattice is assigned a variable ξ_i of value 1 if the point is within the dislocation loop and 0 if it is without (Fig. 1). Thus ξ_i is the characteristic lattice function of the area covered by the dislocation loop. The lattice function ξ_i may also be regarded as a two-state field describing the configuration of the loop. The dislocation line may be identified with the collection of segments which join lattice sites in different states, i.e., unslipped lattice sites, $\xi_i = 0$, with slipped lattice sites, $\xi_i = 1$.

We shall assume that the dislocation loop is well screened, so that the main contribution to its energy arises from its self-energy. For simplicity, we shall assume that the self-energy Γ per unit dislocation length, or line tension, is isotropic, i.e., does not depend on the local orientation of the dislocation segments. An estimate for the line tension is (e.g., Hirth and Lothe (1968))

$$\Gamma = CGb^2 \tag{1}$$

where G is the elastic shear modulus, b is the Burgers vector length, and C is a constant of order unity. It should be noted that G is strongly temperature-dependent in general and may be expected to reduce to zero at the melting temperature.

With these assumptions, the self-energy of the dislocation loop represented by the field ξ_i is

$$E = \sum_{\langle i,j \rangle} \Gamma a(\xi_i - \xi_j)^2 \tag{2}$$

where the sum is restricted to nearest-neighbor pairs, and Γa may be regarded as an "exchange" energy. Indeed, for a straight dislocation aligned with the lattice, it is readily verified that Eq. (2) gives an energy per unit length equal to Γ. If, in addition, the slip plane is under the action of a resolved shear stress τ, then the total energy becomes

$$E = \sum_{\langle i,j \rangle} \Gamma a(\xi_i - \xi_j)^2 - \tau b a^2 \sum_{i=1}^{N} \xi_i \tag{3}$$

where b is the Burgers vector length and $\tau b a^2$ plays the role of an applied field. The energy (2) is direct analogy to that of a lattice gas (Stanley, 1971; Yeomans, 1992).

Next we wish to model the effect of forest dislocations piercing the slip plane and hindering the motion of the loop. We shall restrict the intersection points to coincide with the lattice sites. A pinned mobile dislocation is assumed to drag the point obstacle when the force exerted by the dislocation on the obstacle attains a critical value f, which may be regarded as the strength of the obstacle. As the dislocation drags the obstacle one lattice distance, it does work in the amount fa. Heidenreich and Shockley (Nabarro, 1967) were the first to make a quantitative estimate of the work required to cause two dislocations to cross. They showed that, when two dislocations cut, each acquires a jog with an energy which they estimated as Gb^3. Nabarro (1967) later refined this estimate to $Gb^3/4\pi$ for each jog or $Gb^3/2\pi$ in all. Using Nabarro's formula with $a = b$ the strength of a forest obstacle is computed to be

$$f = Gb^2/2\pi. \tag{4}$$

Since the strength of the obstacles is proportional to the shear modulus, it may be expected to reduce to zero at the melting temperature, which accounts for the observed thermal softening of crystals. For simplicity, we restrict our attention to the case of one species of point obstacles of uniform strength. Under these assumptions, the total energy of the system becomes

$$E = \sum_{\langle i,j \rangle} \Gamma a(\xi_i - \xi_j)^2 - \tau b a^2 \sum_{i=1}^{N} \xi_i + fa \sum_{i=1}^{N} \xi_i \eta_i \tag{5}$$

where η_i is 1 if site i contains a point obstacle, and 0 otherwise, Fig. 1. The four possible states at a site i are, therefore,

1 $\xi_i = 0$, $\eta_i = 0$: the site has not slipped and is not occupied by a point obstacle; the work done against obstacles is zero.

2 $\xi_i = 1$, $\eta_i = 0$: the site has slipped and is not occupied by a point obstacle; the work done against obstacles is zero.

3 $\xi_i = 0$, $\eta_i = 1$: the site has not slipped and is occupied by a point obstacle; the work done against obstacles is zero.

4 $\xi_i = 1$, $\eta_i = 1$: the site has slipped and is occupied by a point obstacle; the work done against the obstacle is fa.

Evidently, the effect of the last term in (5) is to introduce an energetic barrier to slip across obstacles. This barrier effectively pins the dislocations and forces the dislocation loops to bow out between obstacles, which is the desired effect.

Finally, we wish to have control on the number of point obstacles

$$n = \sum_{i=1}^{N} \eta_i \tag{6}$$

populating the slip plane. A conventional means of accomplishing this control is to introduce a chemical potential μ, whereupon the total energy becomes

$$E = \sum_{\langle i,j \rangle} \Gamma a(\xi_i - \xi_j)^2 - \tau b a^2 \sum_{i=1}^{N} \xi_i + fa \sum_{i=1}^{N} \xi_i \eta_i - \mu \sum_{i=1}^{N} \eta_i. \tag{7}$$

This energy constitutes the basis for all subsequent developments, and is the centerpiece of the present theory.

3 Equilibrium Thermodynamic Behavior

We proceed to explore the equilibrium properties of the dislocation loop/obstacle model introduced in the foregoing. According to the fundamental principle of equilibrium statistical mechanics (Feynman, 1972), the probability that a system in equilibrium be in a state $\boldsymbol{\xi} = \{\xi_1, \ldots, \xi_N\}$ and $\boldsymbol{\eta} = \{\eta_1, \ldots, \eta_N\}$ is

$$p(\boldsymbol{\xi}, \boldsymbol{\eta}) = \frac{1}{Z} e^{-\beta E(\boldsymbol{\xi}, \boldsymbol{\eta})} \tag{8}$$

where

$$\beta = \frac{1}{kT}. \tag{9}$$

k is Boltzmann's constant, T is the absolute temperature, and

$$Z = \sum_{\xi_1 \in \{0,1\}} \cdots \sum_{\xi_N \in \{0,1\}} \sum_{\eta_1 \in \{0,1\}} \cdots \sum_{\eta_N \in \{0,1\}} e^{-\beta E(\xi,\eta)} \quad (10)$$

is the partition function. The thermodynamic properties of interest follow directly from Z. For instance, the internal energy per unit volume is

$$U = \frac{1}{a^2 l} \lim_{N\to\infty} \frac{1}{N} \left\{ -\frac{\partial \log Z}{\partial \beta} \right\} \quad (11)$$

whereas the free energy per unit volume is

$$F = \frac{1}{a^2 l} \lim_{N\to\infty} \frac{1}{N} \left\{ -\frac{\log Z}{\beta} \right\}. \quad (12)$$

Here l is the distance between slip planes. The expected number of point obstacles per unit area follows as

$$c = \frac{1}{a^2} \lim_{N\to\infty} \frac{1}{N} \langle \sum_{i=1}^{N} \eta_i \rangle = -l \frac{\partial F}{\partial \mu} \quad (13)$$

and the slip strain is

$$\gamma = \frac{b}{l} \lim_{N\to\infty} \frac{1}{N} \langle \sum_{i=1}^{N} \xi_i \rangle = -\frac{\partial F}{\partial \tau}. \quad (14)$$

In addition, the mobile dislocation length ρ on the slip plane per unit volume of the crystal is given by

$$\rho = \frac{1}{al} \lim_{N\to\infty} \frac{1}{N} \langle \sum_{\langle i,j \rangle} (\xi_i - \xi_j)^2 \rangle = \frac{\partial F}{\partial \Gamma}. \quad (15)$$

As may be seen, this dislocation density is closely related to the two-point correlation function of the slip distribution.

The partition function corresponding to energy (7) may be evaluated as follows. The sum over the obstacle occupancy field $\boldsymbol{\eta}$ is trivial and gives

$$Z = \sum_{\xi_1 \in \{0,1\}} \cdots \sum_{\xi_N \in \{0,1\}} e^{-\beta E(\xi)} \prod_{i=1}^{N} [1 + e^{-\beta(fa\xi_i - \mu)}] \quad (16)$$

where $E(\boldsymbol{\xi})$ is given by (3). Alternatively, (16) may be recast in the form

$$Z = \sum_{\xi_1 \in \{0,1\}} \cdots \sum_{\xi_N \in \{0,1\}} \exp\left\{ -\beta \left[E(\boldsymbol{\xi}) - \frac{1}{\beta} \sum_{i=1}^{N} \log (1 + e^{-\beta(fa\xi_i - \mu)}) \right] \right\}. \quad (17)$$

But, since ξ_i takes the values 0 and 1 only, we can write

$$\log (1 + e^{-\beta(fa\xi_i - \mu)}) = \log (1 + e^{-\beta(fa-\mu)})\xi_i + \log (1 + e^{\beta\mu})(1 - \xi_i), \quad \xi_i \in \{0, 1\}. \quad (18)$$

Inserting this identity into (17) gives

$$Z = (1 + e^{\beta\mu})^N \sum_{\xi_i \in \{0,1\}} \cdots \sum_{\xi_N \in \{0,1\}} \exp\{-\beta[\sum_{\langle i,j \rangle} \Gamma a(\xi_i - \xi_j)^2 - \epsilon \sum_{i=1}^{N} \xi_i]\} \quad (19)$$

where

$$\epsilon = \tau b a^2 + \frac{1}{\beta} \log \left(\frac{1 + e^{-\beta(fa-\mu)}}{1 + e^{\beta\mu}} \right). \quad (20)$$

It is possible to reduce (19) to a familiar form by the following change of variables:

$$s_i = 2\xi_i - 1 \quad (21)$$

$$J = \frac{\Gamma a}{2} \quad (22)$$

$$H = \frac{\epsilon}{2}. \quad (23)$$

The new state variables s_i take the values $\{-1, 1\}$ and may be regarded as local "spins'." Within this "spin gas" analogy, J may be regarded as an exchange energy, $\langle \xi \rangle$ as the magnetization, and H as an applied field. Inserting these definitions into (19) gives

$$Z = (1 + e^{\beta\mu})^N e^{-\beta(J-H)N} Z^{\text{ising}}(K, h) \quad (24)$$

where

$$K = \beta J \quad (25)$$

$$h = \beta H \quad (26)$$

and

$$Z^{\text{ising}} = \sum_{s_1 = \pm 1} \cdots \sum_{s_N = \pm 1} e^{-\beta E^{\text{ising}}(\mathbf{s})} \quad (27)$$

$$E^{\text{ising}}(\mathbf{s}) = -K \sum_{\langle i,j \rangle} s_i s_j - h \sum_{i=1}^{N} s_i \quad (28)$$

are the partition function and energy of the two-dimensional spin-$\frac{1}{2}$ Ising model. Substitution of (24) into (12) gives the free-energy density of the loop/obstacle system as

$$F = \frac{1}{a^2 l} \left\{ -\frac{1}{\beta} \log (1 + e^{\beta\mu}) + J - H \right\} + F^{\text{ising}}(K, h). \quad (29)$$

Thus, the equilibrium properties of the loop/obstacle system are closely related to those of the two-dimensional spin-$\frac{1}{2}$ Ising model, which are well understood at present (e.g., Baxter (1982)).

Subsequent calculations may be simplified by the introduction of the following dimensionless variables:

$$t = \beta \tau b a^2 \quad (30)$$

$$m = \beta\mu \quad (31)$$

$$\varphi = \beta F a^2 l \quad (32)$$

We also note the identities

$$\langle \xi \rangle = \lim_{N\to\infty} \frac{1}{N} \langle \sum_{i=1}^{N} \xi_i \rangle = \frac{\gamma}{\gamma^{\text{sat}}} \quad (33)$$

$$r \equiv \lim_{N\to\infty} \frac{1}{N} \langle \sum_{\langle i,j \rangle} (\xi_i - \xi_j)^2 \rangle = \frac{\rho}{\rho^{\text{sat}}} \quad (34)$$

$$\langle \eta \rangle = \lim_{N\to\infty} \frac{1}{N} \langle \sum_{i=1}^{N} \eta_i \rangle = \frac{c}{c^{\text{sat}}} \quad (35)$$

which follow from (13), (14), and (15) with

$$\gamma^{\text{sat}} = \frac{b}{l} \quad (36)$$

$$\rho^{\text{sat}} = \frac{1}{al} \quad (37)$$

$$c^{\text{sat}} = \frac{1}{a^2}. \tag{38}$$

Evidently, these are: the saturation slip strain which is attained when the loop sweeps the entire slip plane; the saturation dislocation density which is obtained, e.g., when the dislocation population consists of parallel straight dislocations at a distance a; and the saturation obstacle density, which is obtained when the forest dislocations intersect the slip plane through every lattice site. We also note that $\langle \xi \rangle$ plays the role of a normalized slip strain, r the role of a normalized dislocation density, and $\langle \eta \rangle$ the role of a normalized obstacle density, all ranging from 0 to 1. In terms of these variables (29) becomes

$$\varphi = -\log(1 + e^m) + K - h + \varphi^{\text{ising}}(K, h) \tag{39}$$

with

$$h = \frac{t}{2} - \frac{1}{2}\log(1 + e^m) \tag{40}$$

whereas (13), (14), and (15) simplify to

$$\langle \xi \rangle = -\frac{\partial \varphi}{\partial t} \tag{41}$$

$$r = \frac{1}{4}\frac{\partial \varphi}{\partial K} \tag{42}$$

$$\langle \eta \rangle = -\frac{\partial \varphi}{\partial m}. \tag{43}$$

This last relation may be inverted to determine the chemical potential m as a function of the obstacle density $\langle \eta \rangle$.

4 Criticality and Yielding

Criticality underlies and unifies a number of important physical phenomena such as the transitions from liquid to gas, from a normal conductor to a superconductor, and from paramagnetic to ferromagnetic behavior (e.g., Stanley (1971), Feynman (1972), Yeomans (1992), Binney et al. (1992), and Chaikin and Lubensky (1995)). As is well known, the phase diagram of the two-dimensional spin-$\frac{1}{2}$ Ising model exhibits a phase transition (e.g., Yeomans (1992)). In the present theory, this phase transition provides a model for the yield phenomenon in crystals.

Unfortunately, the two-dimensional spin-$\frac{1}{2}$ Ising model with nonzero field has not been solved analytically. The numerical calculation of F^{ising} offers no particularly difficulties and is extensively discussed in the literature (e.g., Binder, ed. (1986, 1987) and Koonin and Meredith (1990)). Here, however, in order to obtain explicit results we shall resort to a mean-field approximation (Yeomans, 1992; Chaikin and Lubensky, 1992). We begin by introducing an effective or mean-field energy of the form

$$E_0 = -H_0 \sum_{i=1}^{N} s_i \tag{44}$$

and we seek to optimize the value of the effective field H_0. To this end, we recall Bogoliubov's inequality

$$F \le F_0 + \lim_{N\to\infty} \frac{1}{N}\frac{1}{a^2 l}\langle E - E_0 \rangle_0 \tag{45}$$

where F is the free energy per unit volume, Eq. (12), corresponding to the original energy E, the average $\langle \cdot \rangle_0$ is taken with respect to the mean-field probability,

$$p_0(\mathbf{s}) = \frac{1}{Z_0} e^{-\beta E_0(\mathbf{s})} \tag{46}$$

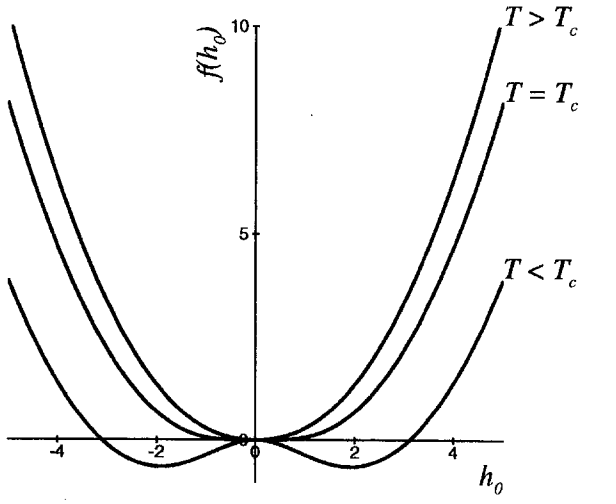

Fig. 2 Bogoliubov's function $f(h_0)$ shown in the zero applied field case, $h = 0$

$$Z_0 = \sum_{s_1=\pm 1} \cdots \sum_{s_N=\pm 1} e^{-\beta E_0(\mathbf{s})} \tag{47}$$

and F_0 is the free energy per unit volume corresponding to the mean-field energy E_0. Inequality (45) holds for any choice of energy E_0 (e.g., Feynman (1972)), with the equality sign attained for $E_0 = E$. Inserting (28) and (44) and using normalization (32) and (26), the bound in (45) becomes

$$f(h_0) = \tfrac{1}{2}h_0^2 - \kappa \log(\cosh h_0) - hh_0. \tag{48}$$

The optimum value of the effective field h_0 is identified with the absolute minimizer of $f(h_0)$. The resulting mean-field free energy for the two-dimensional spin-$\frac{1}{2}$ Ising model with nonzero applied field is (cf. Yeomans (1992)):

$$\varphi^{\text{ising}} \approx \min_{h_0} f(h_0) = -\log(2\cosh h_0) + \tfrac{1}{2}Kz\tanh^2 h_0 \tag{49}$$

where z is the coordination number of the lattice, e.g., $z = 4$ for the square lattice. A trite but straightforward calculation of (41), (42), and (43) using (49) gives

$$\langle \xi \rangle = \tfrac{1}{2}(1 + \tanh h_0) \tag{50}$$

$$r = \frac{z}{8}(1 - \tanh^2 h_0) \tag{51}$$

$$\langle \eta \rangle = \tfrac{1}{2}(1 - \tanh h_0)\frac{e^m}{1 + e^m}. \tag{52}$$

Equations (50) and (51) yield the normalized shear strain and dislocation density, respectively, whereas (52) can be used to eliminate the chemical potential m in favor of the obstacle density $\langle \eta \rangle$.

The function $f(h_0)$, Eq. (48), is shown in Fig. 2 for the zero applied field case, $h = 0$. It is seen from this figure that $f(h_0)$ is convex in the *supercritical* regime $K < K_c$, where

$$K_c = \frac{1}{z} \tag{53}$$

defines a critical value of K. By contrast, in the *subcritical* regime, $K > K_c$, $f(h_0)$ is nonconvex and exhibits two minima, or *wells*, separated by a maximum. It is therefore expected that the behavior of the system will differ sharply in the two regimes, and that the condition $K = K_c$ signals the onset of a phase transition. The corresponding critical temperature is

$$T_c = K_c^{-1}\frac{J}{k} = K_c^{-1}\frac{\Gamma a}{2k} = K_c^{-1}\frac{CGb^2 a}{2k} \tag{54}$$

and, thus, the subcritical and supercritical regimes correspond to the temperature ranges $T < T_c$ and $T > T_c$, respectively.

As a check on the accuracy of the mean field approximation it may be noted that the exact critical point of the Ising model on a square lattice ($z = 4$) at zero applied field is $K_c = \frac{1}{2}\log(1 + \sqrt{2}) \approx 0.44069$, whereas the mean-field critical point is $K_c = \frac{1}{4}$, which is somewhat lower than the exact value. The mean-field critical exponents also differ from those obtained from an exact treatment of the Ising model. Despite these discrepancies, the mean-field theory does furnish a simple and analytically tractable model which exhibits a phase transition, and thus suffices to demonstrate the connection between criticality and yielding pursued here.

The extrema of the function $f(h_0)$, Eq. (48), are the solutions of the secular equation

$$h = h_0 - \kappa \tanh h_0. \tag{55}$$

Here and subsequently we write

$$\kappa = Kz = \frac{K}{K_c}. \tag{56}$$

The solutions of Eq. (55) in turn correspond to the intersections of the function $h_0 - \kappa \tanh h_0$ with the horizontal line of height h (Figs. 3(*a*) and 3(*b*)). It is clear from these figures that $f(h_0)$ has a single minimum h_0 in the *supercritical* case $T > T_c$ (Fig. 3(*a*), point *A*), and that h_0 depends continuously on h. In view of (50), (51), (52), and (40) it follows that the slip strain and the dislocation density are continuous functions of the applied resolved shear stress and no yielding occurs in the supercritical regime.

The subcritical or low-temperature equilibrium behavior of the loop/obstacle system is more eventful and may be characterized as follows. The function $h_0 - \kappa \tanh h_0$ attains the maximum

$$h_c = \operatorname{acosh}\sqrt{\kappa} - \sqrt{\kappa(\kappa - 1)} \tag{57}$$

at $h_0 = \operatorname{acosh}\sqrt{\kappa}$. In the range $h < -h_c$, which by virtue of Eq. (40) corresponds to a low applied shear stress t, Eq. (55) has a unique solution h_0 (Fig. 3(*b*), point *A*). An increase in h, e.g., due to an elevation in the applied resolved shear stress t, results in a corresponding increase in h_0 and $\langle\xi\rangle$. In the range $-h_c < h < h_c$, the horizontal line at h intersects the function $h_0 - \kappa \tanh h_0$ at three points, Fig. 3(*b*), corresponding to three extrema of $f(h_0)$. Of these extrema, the central point is a maximum and the remaining points are minima. Of these two minima, the left point $h_0 < 0$ is the absolute minimizer in the range $h < 0$ (Fig. 3(*b*), point *B*), and the right point $h_0 > 0$ is the absolute minimizer in the range $h > 0$ (Fig. 3(*b*), point *C*). The point of exchange of stability is, therefore, $h = 0$, at which point the effective field h_0 jumps discontinuously to a larger value. This jump is accompanied by a sudden increase in slip activity and may, therefore, be identified with the yield point of the system. In the range $h > h_c$, corresponding to a high applied shear stress t, Eq. (55) has again a unique solution h_0 (Fig. 3(*b*), point *D*).

It may be noted that, at zero temperature, the yield transition just described is in analogy to solid-solid phase transitions in bars and wires, and the applied field $h = 0$ plays a role analogous to the Maxwell stress (Ericksen, 1975; James, 1979). This analogy will be exploited further in Section 5 with a view to formulating a simple kinetic theory which accounts for hysteresis and plastic dissipation.

The critical resolved shear stress corresponding to the yield point $h = 0$ follows from Eq. (40) as

$$t_c = \log(1 + e^m). \tag{58}$$

Equivalently, t_c may be rewritten in terms of the obstacle density using (52), with the result

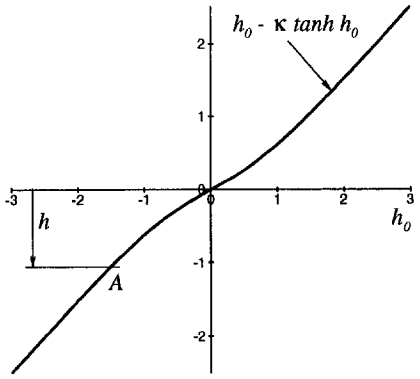

(a)

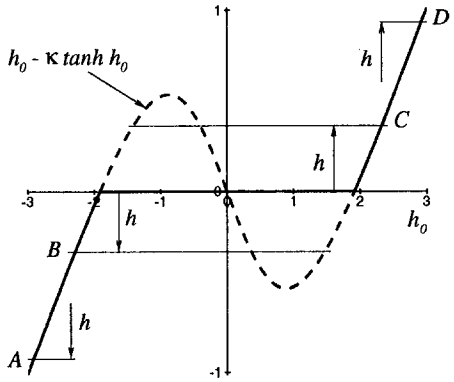

(b)

Fig. 3 Mean-field construction for the determination of the effective field h_0 from the applied field h. (*a*) Supercritical case $\kappa = \frac{1}{2}$; (*b*) subcritical case $\kappa = 2$.

$$t_c = -\log\left(1 - \frac{2\langle\eta\rangle}{1 + \tanh h_{0c}}\right) \tag{59}$$

where h_{0c} is the positive root of the equation

$$h_0 - \kappa \tanh h_0 = 0. \tag{60}$$

It follows from this relation that the critical resolved shear stress vanishes in the absence of point obstacles, $\langle\eta\rangle = 0$, and diverges to infinity at the "percolation limit"

$$\langle\eta\rangle = \frac{1 + \tanh h_{0c}}{2}. \tag{61}$$

As the critical temperature is approached from below, one has that $h_{0c} \to 0$ and the percolation limit is attained when one-half of the lattice sites are occupied by obstacles. In the opposite extreme of zero temperature, the root h_{0c} diverges to infinity and the percolation limit is attained when all lattice sites are occupied by obstacles.

Figure 4 displays the equilibrium properties of the system in the subcritical regime $T < T_c$. The evolution of the slip strain $\langle\xi\rangle$ with applied resolved shear stress t is shown in Fig. 4(*a*) for three values of the obstacle density $\langle\eta\rangle$. As expected, the critical resolved shear stress hardening rate increase with obstacle density. Figure 4(*b*) shows the dependence of the chemical potential m on the slip

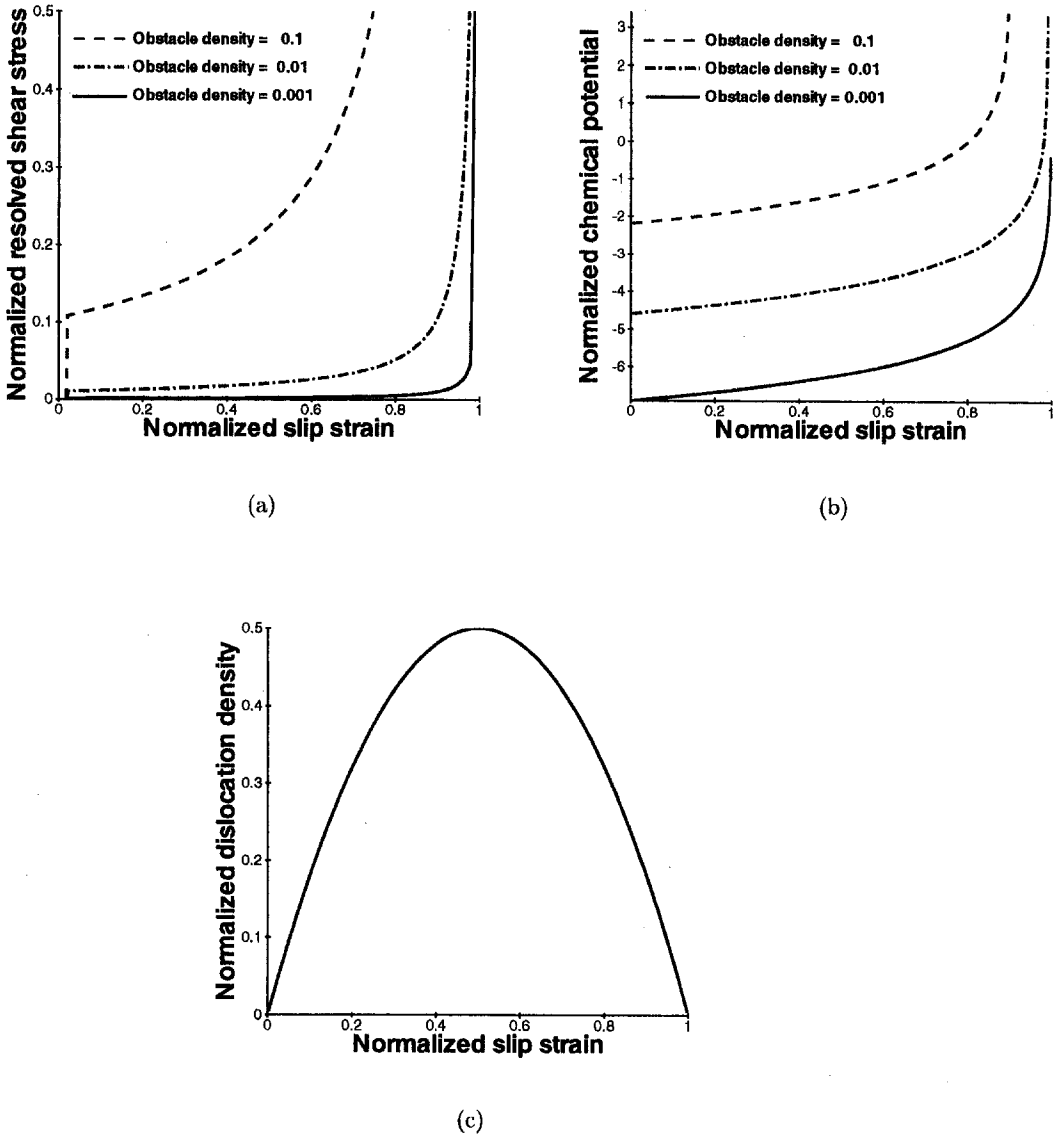

Fig. 4 (*a*) Normalized resolved shear stress $t = \beta\tau ba^2$; (*b*) normalized chemical potential $m = \beta\mu$; and (*c*) normalized dislocation density $r = \rho a^2$ versus the normalized slip strain $\langle\xi\rangle = \gamma/(b/l)$ for three values of the normalized obstacle density $\langle\eta\rangle = ca^2$ in the subcritical regime, $\kappa = 2$

strain and obstacle density. It is seen from the figure that the chemical pontential is an increasing function of the obstacle density. It is also interesting to note how, as the slip strain and, consequently, the energy of interaction between the dislocation loop and the obstacles increases, it becomes necessary to compensate by raising the chemical potential in order to maintain the number of obstacles constant. The variation of the dislocation density with slip is also noteworthy (Fig. 4(*c*)). During the early stages of loading, the dislocation density r is close to zero. In this stage, the mobile dislocation population consists of small loops covering a small area fraction of the slip plane. Physically, these loops emanate from dislocation sources, which we assume to be plentiful and easy to operate. In the neighborhood of the yield point, the mobile dislocation density explodes to accommodate the rapidly increasing slip strain, attains the maximum $z/8$, and subsequently decreases monotonically to zero as dislocation dipoles annihilate. As the slip strain nears its saturation value, the dislocation population consists of small debris, or Orowan, loops surrounding the forest obstacles, slip having occurred everywhere outside the loops.

If follows from the preceding discussion that the critical point $T = T_c$ is marked by divergences in the zero-field specific heat

$$C_H = \left(\frac{\partial U}{\partial T}\right)_H \tag{62}$$

and the plastic compliance

$$\chi_T = \left(\frac{\partial \gamma}{\partial \tau}\right)_T. \tag{63}$$

The precise understanding of these divergences, and more generally of the behavior of the system near the critical point, has been one of the principal objectives of the theory of critical phenomena. Near the critical point, it is convenient to introduce the variable

$$\theta = \frac{T - T_c}{T_c} \tag{64}$$

which measures the deviation in temperature from T_c. Then one has (Yeomans, 1992)

$$C_H \sim |\theta|^{\bar{\alpha}}, \quad (H = 0) \tag{65}$$

$$\gamma \sim (-\theta)^{\bar{\beta}}, \quad (H = 0) \tag{66}$$

Table 1 Exact critical exponents for the two-dimensional spin-$\frac{1}{2}$ Ising model and mean-field approximation

Exponent	$\bar{\alpha}$	$\bar{\beta}$	$\bar{\gamma}$	$\bar{\delta}$
Ising	0 (log)	1/8	7/4	15
Mean field	0	1/2	1	3

$$\chi_T \sim |\theta|^{\bar{\gamma}}, \quad (H = 0) \tag{67}$$

$$H \sim |\gamma|^{\bar{\delta}} \operatorname{sgn}(\gamma), \quad (T = T_c) \tag{68}$$

for some *critical exponents* $\bar{\alpha}$, $\bar{\beta}$, $\bar{\gamma}$, and $\bar{\delta}$. As noted earlier, the rate of growth of the dislocation density ρ also diverges at yield. It may be shown (Yeomans, 1992) that the sum of the correlation function over site pairs involved in Eq. (15) is proportional to the plastic compliance χ_T. It therefore follows that the characteristic exponent for ρ coincides with the characteristic exponent for χ_T, namely $\bar{\gamma}$. The characteristic exponents obtained by an exact treatment of the Ising model and from the mean-field approximation are collected in Table 1. It should be noted that the mean-field exponents generally differ from the exact values.

Critical exponents are important because they afford a classification of critical phenomena into universality classes. They also define scaling relations between various thermodynamic quantities near the critical point. Striking evidence of universality was provided by Guggenheim (1945), who showed that the coexistence curves for eight different fluids near the critical point, when plotted in terms of reduced variables, collapse into a universal curve which can be described by a characteristic exponent. In a similar manner, whereas T_c and other aspects of the hardening of single crystals may vary widely between materials, the characteristic exponents should be universal and therefore define material-independent scaling relations between quantities of interest, such as the critical resolved shear stress and the obstacle density.

5 A Simple Kinetic Theory

The equilibrium properties of the dislocation loop/obstacle system described in the foregoing rest critically on an assumption of ergodicity, i.e., the assumption that the system is free to explore the entire phase space and that all states are accessible from all other states regardless of any intervening energy barriers. Under these assumptions, the behavior of the system is reversible. Whereas instances of reversible dislocation motion exist, e.g., the "flip-flop" of Taylor lattices in fatigue crystals (Kuhlmann-Wilsdorf, 1979), the plasticity of single crystals is most commonly observed to be irreversible and to be accompanied by hysteresis and dissipation.

The mean-field approximation developed above, in conjunction with its analogy to solid-solid phase transitions (e.g., Ericksen (1975)), affords the following simple model of hysteresis. Consider a loop/obstacle system below the critical temperature. As in the equilibrium case, the effective field h_0 is assumed to minimize the Bogoliubov function $f(h_0)$, Eq. (48). In the range $h < -h_c$ the minimizer is unique (Fig. 5, point A). Imagine now increasing the applied field h monotonically above the point $h = -h_c$ (Fig. 5, point B). In the range $-h_c < h < h_c$, the function $f(h_0)$ has two minima. Of these, the leftmost point, $h_0 < 0$, is the absolute minimizer in the range $h < 0$. As noted earlier, the absolute minimum shifts to the positive axis, $h_0 > 0$, for $h > 0$. However, we may argue that this exchange of stability is impeded by the intervening maximum of the function $f(h_0)$, which plays the role of an energy barrier, and that, in consequence, the leftmost minimizer $h_0 < 0$ is the only state accessible to the system (Fig. 5, point B). In the range $h > h_c$ the function $f(h_0)$ has a unique minimizer $h_0 > 0$ (Fig. 5, point E). Therefore, it follows that h_0 must jump discontinuously at the critical point $h = h_c$ (Fig. 5, points C and D), which therefore sets the yield point in the kinetic theory. The corresponding critical resolved shear stress, or yield stress, then follows from (40) as

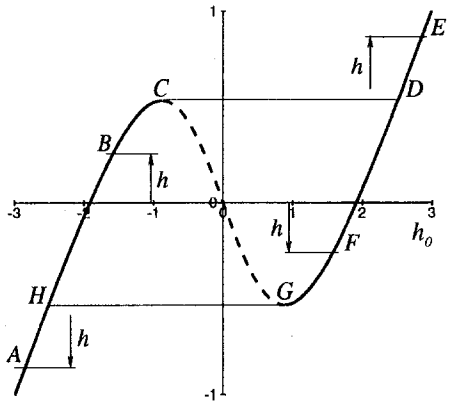

Fig. 5 Mean-field construction including hysteresis and plastic dissipation. Subcritical case $\kappa = 2$.

$$t_c = 2 \operatorname{acosh} \sqrt{\kappa} - 2\sqrt{\kappa(\kappa - 1)} + \log(1 + e^m). \tag{69}$$

This critical resolved shear stress may be rewritten directly in terms of the obstacle density $\langle \eta \rangle$ by the elimination of the chemical potential m with the aid of Eq. (52), with the result

$$t_c = 2 \operatorname{acosh} \sqrt{\kappa} - 2\sqrt{\kappa(\kappa - 1)} + \log\left(1 + \frac{2\langle \eta \rangle}{1 - \sqrt{1 - 1/\kappa - 2\langle \eta \rangle}}\right). \tag{70}$$

Imagine that the process of loading just described, in which the applied field h is increased monotonically from A to E in Fig. 5, is followed by unloading, i.e., the applied field is subsequently decreased monotonically from E. The fundamental assumption is that, upon unloading the loading path $ABCDE$ is not traversed in reverse. Indeed, during unloading the point D defines the absolute minimum of $f(h_0)$ and, therefore, the jump from D to E is not energetically favorable. Instead, the unloading path is postulated to be $EDGHA$, Fig. 5, and involves reverse yielding at $h = -h_c$. Indeed, at the yield point the effective field h_0 jumps discontinuously. The net result is a hysteresis loop $ABCDEDGHA$ and the dissipation of energy as plastic work.

It should be carefully noted that both the hysteresis model and the *accessibility* criteria invoked to select minimizers constitute physical postulates that are formulated in addition to the strict principles of equilibrium statistical mechanics. In particular, postulates are introduced regarding what subset of the phase space is *accessible* from a given state, with the result that the system is no longer ergodic. These additional postulates form the rudiments of a kinetic theory, as attested to by the irreversible and dissipative character of the predicted behavior.

6 Summary and Concluding Remarks

We have developed a statistical mechanical theory of forest hardening in which yielding arises naturally as a phase transition. Our focus in this paper has been to identify the simplest possible model of slip which clearly demonstrates the connection between yielding and criticality. With this objective in mind, we have focused on the motion of a single dislocation loop on a slip plane. We have assumed that the dislocations are well screened so that their energy is proportional to their length. The motion of the loop is impeded by forest dislocations piercing the slip plane, which we treat as point obstacles. The occurrence of slip at the sites occupied by these obstacles requires the expenditure of a certain amount of work commensurate with the strength of the obstacle. The case of obstacles of infinite strength has been treated in detail.

We have shown that the behavior of the dislocation loop as it

sweeps the slip plane under the action of a resolved shear stress is identical to that of a lattice gas and, equivalently, to the two-dimensional spin-$\frac{1}{2}$ Ising model. In particular, there exists a critical temperature T_c below which the system exhibits a yield point: The slip strain increases abruptly when the applied resolved shear stress attains a critical value. Above the critical temperature the yield point disappears and the slip strain depends continuously on the applied stress. The critical exponents, which describe the behavior of the system near the critical temperature, coincide with those of the two-dimensional spin-$\frac{1}{2}$ Ising model.

It is revealing to compute the transition temperature T_c for specific materials. For the sake of argument let us simply assume that the shear modulus decreases linearly with temperature and vanishes at the melting temperature T_m, i.e.,

$$G = G_0 \left(1 - \frac{T}{T_m} \right) \tag{71}$$

where G_0 is the shear modulus at zero temperature. Inserting this relation into the expression (54) for the critical temperature yields

$$T_c = \left(\frac{1}{T_0} + \frac{1}{T_m} \right)^{-1} \tag{72}$$

where

$$T_0 = K_c^{-1} \frac{C G_0 b^2 a}{2k}. \tag{73}$$

Taking copper by way of example, one has $G_0 \approx 40$ GPa, $b = 2.556$Å, $a \approx b$, $k = 1.380 \times 10^{-23}$ J K^{-1}, $C \approx 0.3$, and $T_m = 1{,}343$ K. With these constants, (73) gives $T_0 = 16{,}474$ K and (72) $T_c = 1{,}241$ K, or 92 percent of the melting temperature. This example suggests that metals remain within the subcritical regime and, consequently, exhibit a yield point, up to temperatures very close to the melting temperature, although the sharpness of yielding should be blunted with increasing temperature. These general conclusions are indeed in keeping with observation.

Unfortunately, the full effect of temperature on the behavior of the system cannot be ascertained without knowing the dependence of the elastic moduli on temperature. Thus, linear elastic estimates predict the line tension, Eq. (1), and the obstacle strength, Eq. (4), to be proportional to the shear modulus G, which is itself a strong function of temperature. Under these conditions, as the crystal approaches melting G tends to zero and, correspondingly, both the line tension and the obstacle strength should decrease to zero. This in turn accounts for the thermal softening observed to occur in many ductile crystals with increasing temperature.

As stated above, the system defined by a single dislocation loop moving through forest dislocations has the virtue of exhibiting the connection between criticality and yielding in the simplest possible terms. However, in this model the slip displacement is restricted to be either 0 or b and the maximum slip strain which can be born by a slip system is (36). By way of contrast, the unconstrained plastic flow characteristic of the macroscopic behavior of single crystals requires the simultaneous operation of many dislocation loops on each slip plane. An extension of the Hamiltonian (7) which accounts for this effect may be obtained by allowing the slip ξ_i at site i to take any nonnegative integer value. The resulting Hamiltonian, however, cannot be solved analytically but should yield to approximation techniques such are mean-field theory based, e.g., on a mean-field energy of the form (44).

Also in the interest of simplicity, we have given special attention to obstacles of infinite strength. The treatment of obstacles of finite strength does not offer any particular difficulties. A more challenging extension concerns the combined hardening effect of obstacles of different strengths, e.g., such as are introduced by the activation of more than one secondary system. Foreman and Makin (Foreman, 1955; Foreman and Makin, 1966) have investigated this problem numerically, and have characterized the effective strength of the obstacles. Here again, an extension of the Hamiltonian (7) which accounts for more than one obstacle species is

$$E = \sum_{\langle i,j \rangle} \frac{\Gamma a}{2} (\xi_i - \xi_j)^2 - \tau b a^2 \sum_{i=1}^{N} \xi_i + \sum_{s=1}^{S} \{ f^{(s)} a \sum_{i=1}^{N} \xi_i \eta_i^{(s)} - \mu^{(s)} \sum_{i=1}^{N} \eta_i^{(s)} \}. \tag{74}$$

Here the sum over s extends to the S species of forest dislocations contributed by different secondary systems; the variable $\eta_i^{(s)}$ is 1 if site i is occupied by an obstacle of type s and is 0 otherwise; $f^{(s)}$ is the strength of the obstacles of type s; and $\mu^{(s)}$ is a chemical potential to be determined on the condition that the density of obstacles of type s match a prescribed value. It should be noted that, in this model, a site i may be occupied by several obstacles of different species. As in the case $S = 1$ considered in this paper, Eq. (16), the sums over the obstacle occupancy fields $\eta_i^{(s)}$ are trivial. The resulting model should provide a precise characterization of how obstacles of different strengths cooperate to determine the hardening characteristics of a crystal.

Other worthwhile extensions of the basic Hamiltonian (7) might account for the energy required to activate dislocation sources, e.g., of the Frank-Read type; the Peierls stress required to overcome the resistance of the atomic lattice to dislocation slip, specially in materials other than elemental metals where such barrier is not negligible; the inertia attendant to the motion of dislocations; the anisotropy of the elastic moduli and of the line tension; and other effects. Evidently, while these extensions enhance the predictive character of the theory, they are also introduced at a certain expense as regards the complexity of the theory. In any case, the statistical mechanical framework sketched out in this paper may open the way for a physics-based description of crystalline slip which benefits from the tools and principles of the theory of critical phenomena.

Acknowledgments

The support of the DOE through Caltech's ASCI Center for the Simulation of the Dynamic Response of Materials is gratefully acknowledged.

References

Abeyaratne, R., and Knowles, J. K., 1988, "On the dissipative response due to discontinuous strains in bars of unstable elastic material," *International Journal of Solids and Structures,* Vol. 24, No. 10, pp. 1021–1044.

Baskes, M. I., Hoagland, R. G., and Tsuji, T., 1997, "An atomistic study of the strength of an extended dislocation barrier."

Baxter, R. J., *Exactly Solved Models in Statistical Mechanics,* Academic Press, London.

Binder, K., ed., 1986, *Monte Carlo Methods in Statistical Physics,* 2nd Ed., Springer-Verlag, New York.

Binder, K., ed., 1987, *Applications of the Monte Carlo Method in Statistical Physics,* 2nd Ed., Springer-Verlag, New York.

Binney, J. J., Dowrick, N. J., Fisher, A. J., and Newman, M. E. J., 1992, *The Modern Theory of Critical Phenomena,* Clarendon Press, Oxford.

Chaikin, P. M., and Lubensky, T. C., 1995, *Principles of condensed matter physics,* Cambridge University Press, Cambridge, UK.

Chrzan, D. C., and Mills, M. J., 1993, "Collective behavior and superdislocation motion in Il_2 alloys," *Materials Science and Engineering A,* Vol. 164, No. 1–2, pp. 82–92.

Chrzan, D. C., and Mills, M. J., 1994, "Criticality in the plastic deformation of Il_2 intermetallic compounds," *Physical Review B,* Vol. 50, No. 1, pp. 30–42.

Cuitiño, A. M., 1996, "Effect of temperature and stacking fault energy on the hardening of fcc crystals," *Materials Science and Engineering,* Vol. A216, pp. 104–116.

Cuitiño, A. M., and Ortiz, M., 1992, "Computational Modelling of Single Crystals," *Modelling and Simulation in Materials Science and Engineering,* Vol. 1, pp. 255–263.

Cuitiño, A. M., and Ortiz, M., 1993, "Constitutive Modeling of $L1_2$ Intermetallic Crystals," *Materials Science and Engineering,* Vol. A170, pp. 111–123.

Ericksen, J. L., 1975, "Equilibrium of bars," *Journal of Elasticity,* Vol. 5, pp. 191–201.

Feynman, R. P., 1972, *Statistical Mechanics,* Addison-Wesley, Reading, MA.

Foreman, A. J., 1995, "Dislocation energies in anisotropic crystals," *Acta Metallurgica,* Vol. 3, pp. 322–330.

Foreman, A. J. E., and Makin, M. J., 1966, "Dislocation Movement through Random Arrays of Obstacles," *Philosophical Magazine,* Vol. 14, p. 911.

Foreman, A. J. E., and Makin, M. J., 1967, "Dislocation movement through random arrays of obstacles," *Canadian J. Phys.,* Vol. 45, p. 273.

Grosskreutz, J. C., and Mughrabi, H., 1975, "Description of the work-hardened structure at low temperature in cyclic deformation," *Constitutive Equations in Plasticity,* A. S. Argon, ed., M.I.T. Press, Cambridge, MA, pp. 251–326.

Guggenheim, E. A., 1945, "The Principle of Corresponding States" *Journal of Chemical Physics,* Vol. 13, pp. 253–261.

Hansen, N., and Kuhlmann-Wilsdorff, D., 1986, "Low Energy Dislocation Structures due to Unidirectional Deformation at Low Temperatures," *Materials Science and Engineering,* Vol. 81, pp. 141–161.

Hirth, J. P., and Lothe, J., 1968, *Theory of Dislocations,* McGraw-Hill, New York.

James, R. D., 1979, "Co-exitent phases in the one-dimensional theory of elastic bars," *Archive for Rational Mechanics and Analysis,* Vol. 72, pp. 99–140.

Kocks, U. F., 1964, "Latent hardening and secondary slip in aluminum and silver," *Transactions of the Metallurgical Society of the AIME,* Vol. 230, p. 1160.

Kocks, U. F., Franciosi, P., and Kawai, M., 1991, "A forest model of latent hardening and its applications to polycrystal deformation," *Textures and Microstructures,* Vol. 14–18, pp. 1103–1114.

Koonin, S. E., and Meredith, D. C., 1990, *Computational Physics,* Addison-Wesley, Reading, MA.

Kosterlitz, J. M., and Thouless, D. J., 1972, "Long Range Order and Metastability in Two Dimensional Solids and Superfluids," *Journal of Physics C,* Vol. 5, pp. L124–L126.

Kosterlitz, J. M., and Thouless, D. J., 1973, "Ordering, Metastability and Phase Transitions in Two-Dimensional Systems" *Journal of Physics C,* Vol. 6, pp. 1181–1203.

Kovacs, I., 1967, "The Mechanism of the Work-Harderning in F.C.C. Metals," *Acta Metallurgica,* pp. 1731–1736.

Kovács, I., and Zsoldos, L., 1973, *Dislocation and plastic deformation,* Pergamon Press, Oxford, UK.

Kuhlmann-Wilsdorf, D., 1979, "Dislocation behavior in fatigue. IV. Quantitative interpretation of friction stress and back stress derived from hysteresis loops," *Materials Science and Engineering,* Vol. 39, pp. 231–245.

Kuhlmann-Wilsdorf, D., 1989, "Theory of plastic deformation: properties of low energy dislocation structures," *Materials Science and Engineering,* Vol. A113, p. 1.

Mughrabi, H., 1975, "Description of the Dislocation Structure after Unidirectional Deformation at Low Temperatures," *Constitutive Equations in Plasticity,* A. S. Argon, ed., M.I.T. Press, Cambridge, MA, pp. 199–250.

Nabarro, F. R. N., 1967, *Theory of crystal dislocations,* Oxford University Press, Oxford, UK.

Nelson, D. R., and Halperin, B. I., 1979, "Dislocation-Mediated Melting in Two Dimensions," *Physical Review B,* Vol. 19, pp. 2457–2484.

Ortiz, M., and Popov, E. P., 1962, "A Statistical Theory of Polycrystalline Plasticity," *Proceedings of the Royal Society of London,* Vol. A379, pp. 439–458.

Ortiz, M., and Repetto, E. A., 1998, "Nonconvex energy minimization and dislocation structures in ductile single crystals," *Journal of the Mechanics and Physics of Solids,* in press.

Phillips, R., and Shenoy, V., 1998, manuscript in preparation.

Stanley, H. E., 1971, *Introduction to Phase Transitions and Critical Phenomena,* Oxford University Press, Oxford, UK.

Yeomans, J. M., 1992, *Statistical Mechanics of Phase Transitions,* Clarendon Press, Oxford, UK.

Young, A. P., 1979, "Melting and the Vector Coulomb Gas in two Directions," *Physical Review B,* Vol. 19, pp. 1855–1866.

Contributions to Understanding the Behavior of Axially Compressed Cylinders

Seishi Yamada
Associate Professor,
Toyohashi University of Technology,
Toyohashi 441-8580, Japan

J. G. A. Croll
Professor,
Head of Department,
Department of Civil Engineering,
University College London,
London WC1E 6BT, UK

An elastic nonlinear Ritz analysis is used to investigate the behavior of axially loaded imperfect cylindrical shells. It is shown how the initially positive contributions arising from the shells membrane energy are eroded with increasing levels of both deformations and imperfections. This loss of membrane energy is shown to be responsible for the notoriously imperfection sensitive buckling of the shell. Extensive parameter studies demonstrate the existence of a well-defined lower bound to buckling loads and the dominance of characteristic incremental deformation modes as this lower bound is approached. For the first time the physically based hypotheses of the reduced stiffness method are theoretically demonstrated. Furthermore, it is shown how a slightly modified form of the reduced stiffness method provides very close predictions of the lower bounds to buckling loads.

1 Introduction

Partly due to the major discrepancies between observed buckling loads and the predictions from classical theory, the buckling of axially compressed cylindrical shells has excited extraordinary interest over the past 75 years. Indeed, the list of contributions to the understanding of the behavior of axially loaded cylinders almost reads as a Pantheon of the 20th century's leading mechanicians. It was early realized that small changes in imperfections, combined with the highly unstable forms of post-buckling behavior, were largely responsible for the immense scatter of buckling loads and at times severe reductions from the classical linear theory. There was a growing appreciation that this sensitivity to small changes in geometric form was the converse, and indeed the consequence, of the cylinder providing such a strong optimal form for axial load carrying capacity. However, despite the immense effort put into its understanding, added to the growth in our ability to undertake sophisticated nonlinear calculations, most cylindrical shell design still relies more upon empirical evidence than it does upon the fruits of the many ingenious theoretical solutions. The present paper is directed towards the reconciliation of the two dominant, but at times competing approaches to the theoretical analysis of axially loaded cylindrical shell buckling.

Broadly, the theory of shell buckling, including that of the axially loaded cylinder, has been presented using one of two theoretical approaches. With its earlier successful application to the buckling of slender columns, classical eigenvalue analysis was also applied to shells. To reconcile the lack of agreement with tests, this classical theory was extended to include the effects of nonlinear post-buckling, with many clever methods developed to relate the imperfection sensitive buckling loads to the initial post-buckling characteristics of the perfect or idealized shell response. Although this approach has achieved considerable success when buckling is dominated by very small imperfections, it has for cases like the axially loaded cylinder, failed to provide reliable estimates of buckling loads for shells containing imperfection levels reminiscent of those found in engineering practice. Hence, the continuing reliance upon accumulated test results, or the growing tendency towards the second theoretical approach.

With our capacity to now undertake immensely complicated nonlinear calculations, the second theoretical approach has been based upon large-scale numerical analysis. Although there must remain uncertainty as to the reliability of some of the many numerical solutions available, the best of them have recently been shown capable of reproducing in the minutist of detail the nonlinear paths observed in carefully conducted test programs (Yamada and Yamada, 1983). However, without very great care, and possibly having to run very large numbers of costly parameter studies, there are still severe problems in the use of numerical analysis in design other than final design checking. Its adoption as a method for choosing the "best" choice of stiffeners in, say, rib stiffened shells or on the "optimum" levels, distributions, and orientations of fiber reinforcement in composite shells, and yet capturing the worst possible effects from a wide ranges of potential imperfect shapes and amplitudes, is far from settled.

Our present study seeks to bring together the potential advantages from each of these approaches. It uses the reduced stiffness method, first proposed (Croll and Chilver, 1971) as on extension to classical theory in the early 1970s, as a means for guiding careful nonlinear numerical studies. The reduced stiffness method is based upon the observation that it is components of the initial membrane stiffness, or energy, that are lost in the unstable post-buckling of shells. With imperfections acting as catalysts for this loss of membrane energy it was reasoned that a lower bound to the imperfection sensitive buckling into a particular mode will be provided by a linear eigenvalue analysis from which this at risk membrane energy has been eliminated. A more recent summary of some of the main features of the reduced stiffness method has been presented by Croll (1995). By comparing its predictions with accumulated physical test data, it has been shown that the reduced stiffness method provides realistically safe, lower bounds, to the scatter of imperfection sensitive shell buckling loads for a wide range of shell geometries and loading cases. However, it was early recognized that nonlinear analytical confirmation would be needed before the method could be confidently used as a basis for design. It was not until the early 1980s that numerical simulation of the highly nonlinear buckling responses for shell problems reached a level of reliability that the complex observations from physical tests could be reproduced in detail (Yamada and Yamada, 1983). This made it possible to carry out systematic numerical studies as a means of validating the me-

Contributed by the Applied Mechanics Division of THE AMERICAN SOCIETY OF MECHANICAL ENGINEERS for publication in the ASME JOURNAL OF APPLIED MECHANICS.
Discussion on the paper should be addressed to the Technical Editor, Professor Lewis T. Wheeler, Department of Mechanical Engineering, University of Houston, Houston, TX 77204-4792, and will be accepted until four months after final publication of the paper itself in the ASME JOURNAL OF APPLIED MECHANICS.
Manuscript received by the ASME Applied Mechanics Division, Apr. 23, 1998; final revision, Oct. 17, 1998. Associate Technical Editor: S. Kyriakides.

chanics of, and predictions from, the reduced stiffness method. Under these circumstances, an international research collaboration was initiated in late 1985. As a first example, the case of pressure-loaded cylindrical barrel vaults was considered (Yamada and Croll, 1989). This showed that with very small total imperfections the buckling loads relate closely to the classical critical loads. However, at large total imperfections the buckling loads were shown to converge to the reduced stiffness buckling loads. In many ways the barrel vault proved more difficult than the second example to be considered, as a consequence of the constraints along the longitudinal boundaries introducing a form of loading imperfection which contributed to the total imperfections. Hence, the second example of pressure buckling of complete cylinders (Yamada and Croll, 1993) proved to be rather more straightforward, and demonstrated even more convincingly that with large imperfections, shells exhibit buckling loads that closely relate to reduced stiffness theory. By looking at the incremental energies this study also indicated how the positive linear components of membrane energy are eventually eroded by the development of nonlinear negative components arising from modal interactions stimulated by the presence of imperfections.

The present work extends this same approach to the case of axially loaded cylinders. With this case being perhaps the most imperfection sensitive of all shell buckling problems, it provides perhaps the ultimate test of the reduced stiffness method.

2 Theoretical Background

Because it provides a systematic framework for the interpretation of behavior, and also represents a convenient and compact basis for analytical modeling, the principle of stationary total potential energy will be used to formulate the equations of equilibrium.

2.1 Total Potential Energy. For an imperfect thin-walled circular cylinder of longitudinal length L, wall thickness t, and radius R, shown in Fig. 1, the change in the total potential energy, consequent upon the application of a uniform axial compression stress of σ, may be written as

$$\Pi = U_B + U_M + V_\lambda \tag{1}$$

where the bending and membrane strain energy (U_B, U_M) and the increase in load potential (V_λ) for an axial compressive stress of σ, are given as

$$U_B = \tfrac{1}{2}\int_0^{2\pi R}\int_0^{L}(m_x\kappa_x + m_y\kappa_y + 2m_{xy}\kappa_{xy})dxdy \tag{2a}$$

$$U_M = \tfrac{1}{2}\int_0^{2\pi R}\int_0^{L}(n_x\epsilon_x + n_y\epsilon_y + 2n_{xy}\epsilon_{xy})dxdy \tag{2b}$$

$$V_\lambda = -\sigma t\int_0^{2\pi R}\int_0^{L}\left(-\frac{\partial u}{\partial x}\right)dxdy. \tag{2c}$$

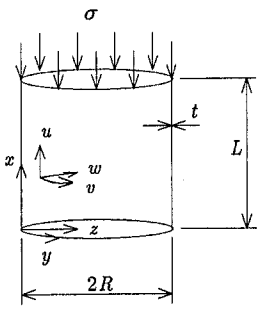

Fig. 1 Notation and convention adopted for geometry

In these expressions, (m_x, m_y, m_{xy}) and (n_x, n_y, n_{xy}) are the total bending and membrane stress resultants, and (κ_x, κ_y, κ_{xy}) and (ϵ_x, ϵ_y, ϵ_{xy}) are the corresponding strains associated with total displacements (u, v, w) from an imperfect but stress-free unloaded state. The compressive stress may be written in terms of the nondimensional load parameter λ as

$$\sigma \equiv \lambda\sigma_{cl} \tag{3}$$

where σ_{cl} is the well-known classical buckling load,

$$\sigma_{cl} = \frac{E}{\sqrt{3(1-\mu^2)}}\frac{t}{R}.$$

The bending and membrane stress resultants are related to strains through the constitutive equations

$$m_x = D(\kappa_x + \mu\kappa_y), \quad m_y = D(\mu\kappa_x + \kappa_y),$$
$$m_{xy} = D(1-\mu)\kappa_{xy} \tag{4a}$$

$$n_x = K(\epsilon_x + \mu\epsilon_y), \quad n_y = K(\mu\epsilon_x + \epsilon_y),$$
$$n_{xy} = K(1-\mu)\epsilon_{xy} \tag{4b}$$

where $D = Et^3/\{12(1-\mu^2)\}$, $K = Et/(1-\mu^2)$, E = modulus of elasticity, and μ = Poisson's ratio.

The strain-displacement relations associated with deformation from an initial imperfection w^0, are taken as

$$\kappa_x = -\frac{\partial^2 w}{\partial x^2}, \quad \kappa_y = -\frac{\partial^2 w}{\partial y^2}, \quad \kappa_{xy} = -\frac{\partial^2 w}{\partial x\partial y} \tag{5a}$$

$$\epsilon_x = \frac{\partial u}{\partial x} + \frac{\partial w^0}{\partial x}\frac{\partial w}{\partial x} + \frac{1}{2}\left(\frac{\partial w}{\partial x}\right)^2 \tag{5b}$$

$$\epsilon_y = \frac{\partial v}{\partial y} - \frac{w}{R} + \frac{\partial w^0}{\partial y}\frac{\partial w}{\partial y} + \frac{1}{2}\left(\frac{\partial w}{\partial y}\right)^2 \tag{5c}$$

$$\epsilon_{xy} = \frac{1}{2}\left(\frac{\partial u}{\partial y} + \frac{\partial v}{\partial x} + \frac{\partial w^0}{\partial x}\frac{\partial w}{\partial y} + \frac{\partial w^0}{\partial y}\frac{\partial w}{\partial x} + \frac{\partial w}{\partial x}\frac{\partial w}{\partial y}\right). \tag{5d}$$

2.2 Boundary Conditions and Modal Approximation. The end boundary is assumed to be supported in such a way as to conform with the classical simple support, corresponding with the conditions

$$w = \frac{\partial^2 w}{\partial x^2} = \frac{\partial u}{\partial x} = v = 0, \quad \text{at } x = 0, L. \tag{6}$$

By taking displacement functions u, v, and w as linear combinations of the harmonic expressions,

$$u = \frac{Lt}{R}\sum_i\sum_j^{J_i^u}\bar{u}_{i,j}\cos(iy/R)\cos(j\pi x/L) \tag{7a}$$

$$v = \frac{Lt}{R}\sum_i\sum_j^{J_i^v}\bar{v}_{i,j}\sin(iy/R)\sin(j\pi x/L) \tag{7b}$$

$$w = t\sum_i\sum_j^{J_i^w}\bar{w}_{i,j}\cos(iy/R)\sin(j\pi x/L). \tag{7c}$$

These boundary conditions will be exactly satisfied since each separate component satisfies the boundary conditions of Eq. (6). In these expressions, i and j are the circumferential full-wave and the longitudinal half-wave numbers; $\bar{u}_{i,j}$, $\bar{v}_{i,j}$, and $\bar{w}_{i,j}$ are the nondimensional amplitudes of each harmonic function.

The initial geometric imperfection is expressed as

$$w^0 = t \sum_i \sum_j^{J_i^0} \bar{w}_{i,j}^0 \cos(iy/R) \sin(j\pi x/L). \quad (8)$$

2.3 Equilibrium Equation by the Ritz Method. By substituting Eqs. (4), (5), (7), and (8) into Eq. (2), the energy components associated with the unknown coefficients $\bar{u}_{i,j}$, $\bar{v}_{i,j}$, and $\bar{w}_{i,j}$ can be expressed as

$$U_B = (24\pi DL/R) \sum_{r'}^{N^w} \sum_{m'}^{N^w} \bar{w}_{r'} \bar{w}_{m'} \alpha_{m'r'}^{B33} \quad (9a)$$

$$U_M = (24\pi DL/R)\{\sum_{r'}^{N^u} \bar{u}_{r'} (\sum_{m'}^{N^u} \bar{u}_{m'} \alpha_{m'r'}^{11} + \sum_{m'}^{N^v} \bar{v}_{m'} \alpha_{m'r'}^{21}$$
$$+ \sum_{m'}^{N^w} \bar{w}_{m'} \alpha_{m'r'}^{31}) + \sum_{r'}^{N^v} \bar{v}_{r'} (\sum_{m'}^{N^v} \bar{v}_{m'} \alpha_{m'r'}^{22} + \sum_{m'}^{N^w} \bar{w}_{m'} \alpha_{m'r'}^{32})$$
$$+ \sum_{r'}^{N^w} \sum_{m'}^{N^w} \bar{w}_{r'} \bar{w}_{m'} \alpha_{m'r'}^{33} + \sum_{r'}^{N^u} \sum_{m'}^{N^w} \sum_{k'}^{N^w} \bar{u}_{r'} \bar{w}_{m'} \bar{w}_{k'} \alpha_{k'm'r'}^{331}$$
$$+ \sum_{r'}^{N^v} \sum_{m'}^{N^w} \sum_{m'}^{N^w} \bar{v}_{r'} \bar{w}_{m'} \bar{w}_{k'} \alpha_{k'm'r'}^{332}$$
$$+ \sum_{r'}^{N^w} \sum_{m'}^{N^w} \sum_{k'}^{N^w} \bar{w}_{r'} \bar{w}_{m'} \bar{w}_{k'} \alpha_{k'm'r'}^{333}$$
$$+ \sum_{r'}^{N^w} \sum_{m'}^{N^w} \sum_{k'}^{N^w} \sum_{i'}^{N^w} \bar{w}_{r'} \bar{w}_{m'} \bar{w}_{k'} \bar{w}_{i'} \alpha_{i'k'm'r'}^{3333}\} \quad (9b)$$

$$V_\lambda = (24\pi DL/R)\lambda \sum_{r'}^{N^u} \bar{u}_{r'} \alpha_{r'}^{1} \quad (9c)$$

where

$$\alpha_{r'}^{1} = -\sqrt{\frac{4(1-\mu^2)}{3}}; \quad \text{for } i = 0 \text{ and } j = \text{odd}$$

$$\alpha_{r'}^{1} = 0; \quad \text{for } i \neq 0 \text{ or } j = \text{even}.$$

$(\bar{u}_{r'}, \bar{v}_{r'}, \bar{w}_{r'})$ is a set of generalized coordinates equivalent to $(\bar{u}_{i,j}, \bar{v}_{i,j}, \bar{w}_{i,j})$ and the constants $\alpha_{m'r'}^{B33}$, $\alpha_{m'r'}^{11}$, $\alpha_{m'r'}^{21}$, ..., $\alpha_{i'k'm'r'}^{3333}$ obtained from the integrations of Eq. (2) are exactly the same as those for pressurized cylinders (see the appendix of Yamada and Croll, 1993); it is noteworthy that only the constant $\alpha_{r'}^{1}$ depends on the loading condition.

The Ritz method is used to obtain approximate solutions, by requiring the total potential energy to be stationary with respect to all the independent degrees-of-freedom, so that

$$\frac{\partial \Pi}{\partial \bar{u}_{r'}} = \frac{\partial \Pi}{\partial \bar{v}_{r'}} = \frac{\partial \Pi}{\partial \bar{w}_{r'}} = 0. \quad (10)$$

A total of $(N^u + N^v + N^w)$ nonlinear algebraic equations expressing the unknown coefficient $\bar{u}_{r'}$, $\bar{v}_{r'}$, $\bar{w}_{r'}$, in terms of the load parameter λ are obtained; these nondimensionalized forms can be represented as

$$\lambda \alpha_{r'}^{1} + \sum_{m'}^{N^u} \bar{u}_{m'} (\alpha_{m'r'}^{11} + \alpha_{r'm'}^{11}) + \sum_{m'}^{N^v} \bar{v}_{m'} \alpha_{m'r'}^{21} + \sum_{m'}^{N^w} \bar{w}_{m'} \alpha_{m'r'}^{31}$$
$$+ \sum_{m'}^{N^w} \sum_{k'}^{N^w} \bar{w}_{m'} \bar{w}_{k'} \alpha_{k'm'r'}^{331} = 0, \quad r' = 1, 2, \ldots, N^u \quad (11a)$$

$$\sum_{m'}^{N^u} \bar{u}_{m'} \alpha_{r'm'}^{21} + \sum_{m'}^{N^v} \bar{v}_{m'} (\alpha_{m'r'}^{22} + \alpha_{r'm'}^{22}) + \sum_{m'}^{N^w} \bar{w}_{m'} \alpha_{m'r'}^{32}$$
$$+ \sum_{m'}^{N^w} \sum_{k'}^{N^w} \bar{w}_{m'} \bar{w}_{k'} \alpha_{k'm'r'}^{332} = 0, \quad r' = 1, 2, \ldots, N^v \quad (11b)$$

$$\sum_{m'}^{N^u} \bar{u}_{m'} \alpha_{r'm'}^{31} + \sum_{m'}^{N^v} \bar{v}_{m'} \alpha_{r'm'}^{32} + \sum_{m'}^{N^w} \bar{w}_{m'} (\alpha_{m'r'}^{B33} + \alpha_{r'm'}^{B33}$$
$$+ \alpha_{m'r'}^{33} + \alpha_{r'm'}^{33}) + \sum_{m'}^{N^w} \sum_{k'}^{N^u} \bar{w}_{m'} \bar{u}_{k'} (\alpha_{r'm'k'}^{331} + \alpha_{m'r'k'}^{331})$$
$$+ \sum_{m'}^{N^w} \sum_{k'}^{N^v} \bar{w}_{m'} \bar{v}_{k'} (\alpha_{r'm'k'}^{332} + \alpha_{m'r'k'}^{332})$$
$$+ \sum_{m'}^{N^w} \sum_{k'}^{N^w} \bar{w}_{m'} \bar{w}_{k'} (\alpha_{k'm'r'}^{333} + \alpha_{m'r'k'}^{333} + \alpha_{r'k'm'}^{333})$$
$$+ \sum_{m'}^{N^w} \sum_{k'}^{N^w} \sum_{i'}^{N^w} \bar{w}_{m'} \bar{w}_{k'} \bar{w}_{i'} (\alpha_{i'k'm'r'}^{3333} + \alpha_{k'm'r'i'}^{3333}$$
$$+ \alpha_{m'r'i'k'}^{3333} + \alpha_{r'i'k'm'}^{3333}) = 0, \quad r' = 1, 2, \ldots, N^w. \quad (11c)$$

2.4 Incremental Strain Energy Analysis. The sets of nonlinear equation (Eq. (11)) can be solved using a step-by-step process in which either load or displacement is used as a control parameter. At each step a Newton-Raphson iteration is used to provide convergence to an acceptable level of precision. This incremental analytical procedure makes it convenient to compute, at any stage along the equilibrium path, the nature of the incremental strain energy components. A sufficiently small amplitude $(0.001 \times t)$ of a displacement control parameter provides a very close approximation to the tangent vectors (u^d, v^d, w^d) in the form of differences between the two close equilibrium states (u^E, v^E, w^E) and $(u^E + u^d, v^E + v^d, w^E + w^d)$. The total strain components at a point (x, y) after the small incremental deformations about the equilibrium state may be written

$$\kappa_x = \kappa_x^E + \kappa_x^d, \quad \kappa_y = \kappa_y^E + \kappa_y^d, \quad \kappa_{xy} = \kappa_{xy}^E + \kappa_{xy}^d \quad (12)$$

$$\epsilon_x = \epsilon_x^E + \epsilon_x^d + \epsilon_x^{Ed} + \epsilon_x^{dd}, \quad \epsilon_y = \epsilon_y^E + \epsilon_y^d + \epsilon_y^{Ed} + \epsilon_y^{dd},$$
$$\epsilon_{xy} = \epsilon_{xy}^E + \epsilon_{xy}^d + \epsilon_{xy}^{Ed} + \epsilon_{xy}^{dd} \quad (13)$$

where

$$\kappa_x^E = -\frac{\partial^2 w^E}{\partial x^2}, \quad \kappa_y^E = -\frac{\partial^2 w^E}{\partial y^2}, \quad \kappa_{xy}^E = -\frac{\partial^2 w^E}{\partial x \partial y} \quad (14a)$$

$$\kappa_x^d = -\frac{\partial^2 w^d}{\partial x^2}, \quad \kappa_y^d = -\frac{\partial^2 w^d}{\partial y^2}, \quad \kappa_{xy}^d = -\frac{\partial^2 w^d}{\partial x \partial y} \quad (14b)$$

$$\epsilon_x^E = \frac{\partial u^E}{\partial x} + \frac{\partial w^0}{\partial x}\frac{\partial w^E}{\partial x} + \frac{1}{2}\left(\frac{\partial w^E}{\partial x}\right)^2 \quad (15a)$$

$$\epsilon_y^E = \frac{\partial v^E}{\partial y} - \frac{w^E}{R} + \frac{\partial w^0}{\partial y}\frac{\partial w^E}{\partial y} + \frac{1}{2}\left(\frac{\partial w^E}{\partial y}\right)^2 \quad (15b)$$

$$\epsilon_{xy}^E = \frac{1}{2}\left(\frac{\partial u^E}{\partial y} + \frac{\partial v^E}{\partial x} + \frac{\partial w^0}{\partial x}\frac{\partial w^E}{\partial y} + \frac{\partial w^0}{\partial y}\frac{\partial w^E}{\partial x} + \frac{\partial w^E}{\partial x}\frac{\partial w^E}{\partial y}\right) \quad (15c)$$

$$\epsilon_x^d = \frac{\partial u^d}{\partial x}, \quad \epsilon_y^d = \frac{\partial v^d}{\partial y} - \frac{w^d}{R}, \quad \epsilon_{xy}^d = \frac{1}{2}\left(\frac{\partial u^d}{\partial y} + \frac{\partial v^d}{\partial x}\right) \quad (16)$$

$$\epsilon_x^{Ed} = \frac{\partial(w^0 + w^E)}{\partial x}\frac{\partial w^d}{\partial x}, \quad \epsilon_y^{Ed} = \frac{1}{2}\left(\frac{\partial(w^0 + w^E)}{\partial y}\frac{\partial w^d}{\partial y}\right) \tag{17a}$$

$$\epsilon_{xy}^{Ed} = \frac{1}{2}\left\{\frac{\partial(w^0 + w^E)}{\partial x}\frac{\partial w^d}{\partial y} + \frac{\partial(w^0 + w^E)}{\partial y}\frac{\partial w^d}{\partial x}\right\} \tag{17b}$$

$$\epsilon_x^{dd} = \frac{1}{2}\left(\frac{\partial w^d}{\partial x}\right)^2, \quad \epsilon_y^{dd} = \frac{1}{2}\left(\frac{\partial w^d}{\partial y}\right)^2,$$

$$\epsilon_{xy}^{dd} = \frac{1}{2}\frac{\partial w^d}{\partial x}\frac{\partial w^d}{\partial y}. \tag{18}$$

The corresponding stress components are

$$m_x^\gamma = D(\kappa_x^\gamma + \mu\kappa_y^\gamma), \quad m_y^\gamma = D(\mu\kappa_x^\gamma + \kappa_y^\gamma),$$
$$m_{xy}^\gamma = D(1-\mu)\kappa_{xy}^\gamma \tag{19a}$$

$$n_x^\gamma = K(\epsilon_x^\gamma + \mu\epsilon_y^\gamma), \quad n_y^\gamma = K(\mu\epsilon_x^\gamma + \epsilon_y^\gamma),$$
$$n_{xy}^\gamma = K(1-\mu)\epsilon_{xy}^\gamma \tag{19b}$$

where γ takes the values E, d, Ed, and dd.

To fully understand the changing nature of the resistance to incremental deformations as buckling progresses, it is necessary to break the quadratic form for the incremental energy into its component parts. These component parts of the quadratic form of the incremental energy may be written as

$$\Pi_2 = \Pi_{2B} + \Pi_{2M} \tag{20}$$

where the contributions from bending Π_{2B} are

$$\Pi_{2B} = U_{2B}$$

$$= \tfrac{1}{2}\int_0^{2\pi R}\int_0^L (m_x^d\kappa_x^d + m_y^d\kappa_y^d + 2m_{xy}^d\kappa_{xy}^d)dxdy, \tag{21}$$

and these from membrane strain energy Π_{2M} may be further broken down as

$$\Pi_{2M} = U_{2M} + V_{2M} + W_{2M}. \tag{22}$$

In Eq. (22) the membrane contributions arising from the linear incremental strains may be written

$$U_{2M} = U_{2M}^x + U_{2M}^y + U_{2M}^{xy} \tag{23a}$$

where

$$U_{2M}^x = \tfrac{1}{2}\int_0^{2\pi R}\int_0^L n_x^d\epsilon_x^d dxdy \tag{23b}$$

$$U_{2M}^y = \tfrac{1}{2}\int_0^{2\pi R}\int_0^L n_y^d\epsilon_y^d dxdy \tag{23c}$$

$$U_{2M}^{xy} = \int_0^{2\pi R}\int_0^L n_{xy}^d\epsilon_{xy}^d dxdy, \tag{23d}$$

while those resulting from the nonlinear incremental strains are

$$V_{2M} = V_{2M}^x + V_{2M}^y + V_{2M}^{xy} \tag{24a}$$

where

$$V_{2M}^x = \tfrac{1}{2}\int_0^{2\pi R}\int_0^L (n_x^{dd}\epsilon_x^E + n_x^E\epsilon_x^{dd})dxdy \tag{24b}$$

$$V_{2M}^y = \tfrac{1}{2}\int_0^{2\pi R}\int_0^L (n_y^{dd}\epsilon_y^E + n_y^E\epsilon_y^{dd})dxdy \tag{24c}$$

$$V_{2M}^{xy} = \int_0^{2\pi R}\int_0^L (n_{xy}^{dd}\epsilon_{xy}^E + n_{xy}^E\epsilon_{xy}^{dd})dxdy. \tag{24d}$$

The additional interaction between the incremental linear response and the current total nonlinearities can be written

$$W_{2M} = W_{2M}^x + W_{2M}^y + W_{2M}^{xy} \tag{25a}$$

where

$$W_{2M}^x = \tfrac{1}{2}\int_0^{2\pi R}\int_0^L (n_x^d\epsilon_x^{Ed} + n_x^{Ed}\epsilon_x^d + n_x^{Ed}\epsilon_x^{Ed})dxdy \tag{25b}$$

$$W_{2M}^y = \tfrac{1}{2}\int_0^{2\pi R}\int_0^L (n_y^d\epsilon_y^{Ed} + n_y^{Ed}\epsilon_y^d + n_y^{Ed}\epsilon_y^{Ed})dxdy \tag{25c}$$

$$W_{2M}^{xy} = \int_0^{2\pi R}\int_0^L (n_{xy}^d\epsilon_{xy}^{Ed} + n_{xy}^{Ed}\epsilon_{xy}^d + n_{xy}^{Ed}\epsilon_{xy}^{Ed})dxdy. \tag{25d}$$

Since it is the membrane resistance that is undergoing the significant change as buckling progresses, the membrane strain energy, Π_{2M}, has been broken down into its component parts associated with axial, hoop, and in-plane shear action. Because it derives from the linear incremental strains, the term U_{2M} may be referred to as the linear membrane strain energy. The term V_{2M} represents the interaction between the nonlinear incremental membrane action and the current membrane equilibrium state. The term W_{2M} results from the interaction between the linear incremental membrane actions and the current total deflections including the effects of imperfections; these terms do not appear in the classical bifurcation analysis.

3 Nature of Buckling

To illustrate the behavior of a typical cylinder under axial compression and to use this behavior to exemplify the mechanics of post-buckling, a sample of the shells tested by Yamaki (1984) is considered. Direct comparisons with the test results cannot be made since the present simply supported boundaries differ from the clamped ends used in the experiments. However, the geometries are ones that in the past have been the subject of extensive numerical studies and against which the present solutions have been validated. Shell geometry is defined by $R = 100$ mm and $t = 0.247$ mm so that $R/t = 405$. By varying the length L, the geometric parameter L/R, and the well-known Batdorf parameter, $Z = \sqrt{1-\mu^2}\,L^2/(Rt)$ are chosen as

L mm	L/R	Z
36.0	0.360	50
50.9	0.509	100
72.0	0.720	200.

For this and all subsequent examples the material is taken to have $\mu = 0.3$.

3.1 Classical Bifurcation Analysis. An *idealized* classical bifurcation analysis (see, for example, Koiter, 1963) can easily allow derivation of the nondimensional classical load spectrum (Brush and Almroth, 1975), in the form

$$\lambda^c = \frac{\xi}{4} + \frac{1}{\xi} \tag{26}$$

where

$$\xi = \frac{\pi^2(\beta_i^2 + j^2)^2}{\sqrt{3}\,Zj^2}, \quad \beta_i = i\,\frac{L}{\pi R}. \tag{27}$$

The classical critical load λ^c is the minimum occurring when $\xi = 2$, resulting in the so-called Koiter *circle* (Koiter, 1963; Arbocz and Sechler, 1974; Hunt et al., 1986) represented as

$$\beta_i^2 + j^2 = 2Bj \tag{28}$$

and shown in Fig. 2, where

$$B = \left(\frac{\sqrt{3}\,Z}{2\pi^2}\right)^{1/2}. \tag{29}$$

As is well known, this means that several different buckling modes $i = b$ have critical loads close to the minimum classical critical load $\lambda^c = 1$. For the present shell model having $R/t = 405$, the parameters of this Koiter circle are

Z	$i_{\max}$	$j_{\max} = 2B$
50	18.3	4.19
100	18.3	5.92
200	18.3	8.38

Through nonlinear post-buckling analysis, solution convergence has been found to reach acceptable limits by using in Eq. (7)

$$u = \frac{Lt}{R}\sum_{j=1}^{21}\bar{u}_{0,j}\cos\frac{j\pi x}{L} + \frac{Lt}{R}\sum_{j=1}^{15}\bar{u}_{b,j}\cos\frac{by}{R}\cos\frac{j\pi x}{L}$$
$$+ \frac{Lt}{R}\sum_{j=1}^{11}\bar{u}_{2b,j}\cos\frac{2by}{R}\cos\frac{j\pi x}{L}$$
$$+ \frac{Lt}{R}\sum_{j=1}^{5}\bar{u}_{3b,j}\cos\frac{2by}{R}\cos\frac{j\pi x}{L} \tag{30a}$$

$$v = \frac{Lt}{R}\sum_{j=1}^{15}\bar{v}_{b,j}\sin\frac{by}{R}\sin\frac{j\pi x}{L} + \frac{Lt}{R}\sum_{j=1}^{11}\bar{v}_{2b,j}\sin\frac{2by}{R}\sin\frac{j\pi x}{L}$$
$$+ \frac{Lt}{R}\sum_{j=1}^{5}\bar{v}_{3b,j}\sin\frac{3by}{R}\sin\frac{j\pi x}{L} \tag{30b}$$

$$w = t\sum_{j=1}^{15}\bar{w}_{0,j}\sin\frac{j\pi x}{L} + t\sum_{j=1}^{11}\bar{w}_{b,j}\cos\frac{by}{R}\sin\frac{j\pi x}{L}$$
$$+ t\sum_{j=1}^{9}\bar{w}_{2b,j}\cos\frac{2by}{R}\sin\frac{j\pi x}{L}. \tag{30c}$$

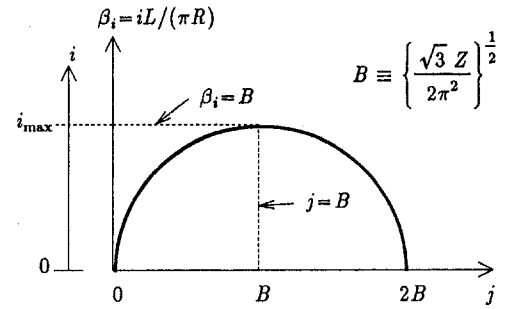

Fig. 2 Koiter circle described by Eq. (28)

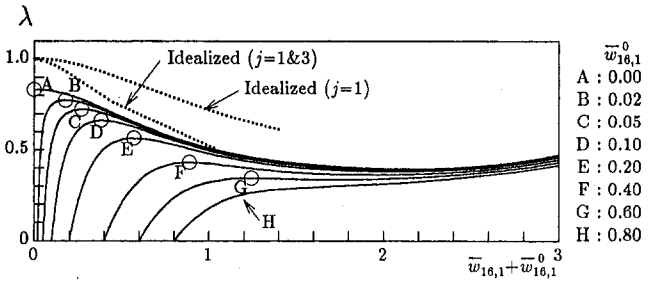

Fig. 3(*a*) Nondimensional load versus total deflection in harmonic $i = b = 16$ and $j = 1$

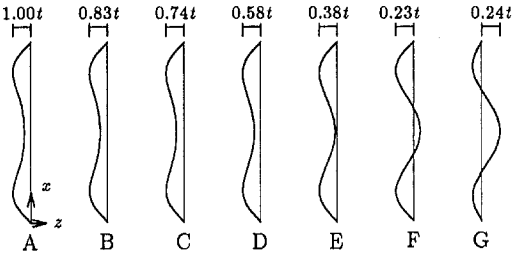

Fig. 3(*b*) Axial shapes of the total axisymmetric out-of-plane displacement component at the buckling load

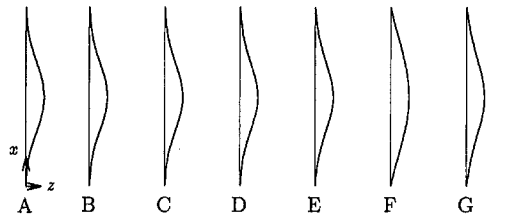

Fig. 3(*c*) Axial shapes (at $y = 2k\pi R/16$: $k = 0, 1, 2, \ldots, 16$) of the incremental asymmetric out-of-plane displacement component at the buckling load

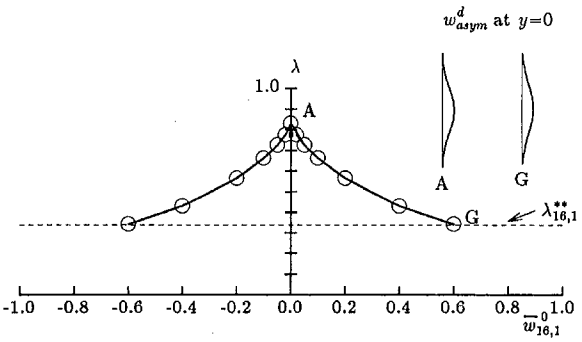

Fig. 3(*d*) Imperfection sensitivity

Fig. 3 Effects of initial imperfections (a single asymmetric mode $\bar{w}^0_{16,1}$) for shells ($Z = 50$, $R/t = 405$, $L/R = 0.360$, $b = 16$)

Post-buckling from this classical critical bifurcation state is illustrated in Fig. 3(*a*). Two cases of perfect shell bifurcation are shown. *Idealized* bifurcation models, shown dotted, are based upon the assumption that prior to buckling the effects of bending are ignored and the internal shell stress and strain take the form of a uniform membrane state, for which

$$n_x^F = -\sigma t, \quad n_y^F = n_{xy}^F = 0,$$
$$\epsilon_x^F = -\sigma/E, \quad \epsilon_y^F = \mu\sigma/E, \quad \epsilon_{xy}^F = 0. \tag{31}$$

The two idealized bifurcation curves relate to two very close critical loads having modes with $i = 16$ and either $j = 1$ or $j =$

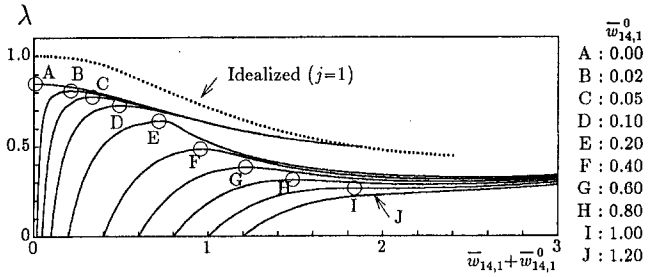

Fig. 4(*a*) Nondimensional load versus total deflection in harmonic $i = b = 14$ and $j = 1$

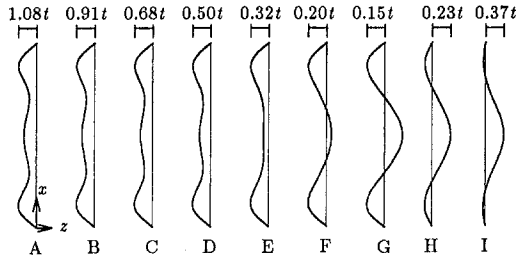

Fig. 4(*b*) Axial shapes of the total axisymmetric out-of-plane displacement component at the buckling load

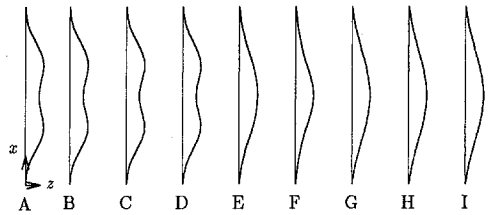

Fig. 4(*c*) Axial shapes (at $y = 2k\pi R/14$: $k = 0, 1, 2, \ldots, 14$) of the incremental asymmetric out-of-plane displacement component at the buckling load

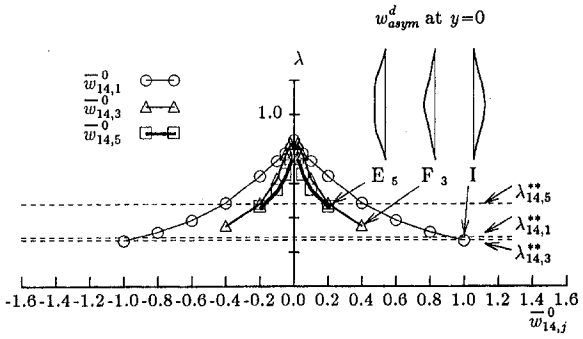

Fig. 4(*d*) Imperfection sensitivity for single asymmetric modes, $\bar{w}^0_{14,1}$, $\bar{w}^0_{14,3}$, and $\bar{w}^0_{14,5}$

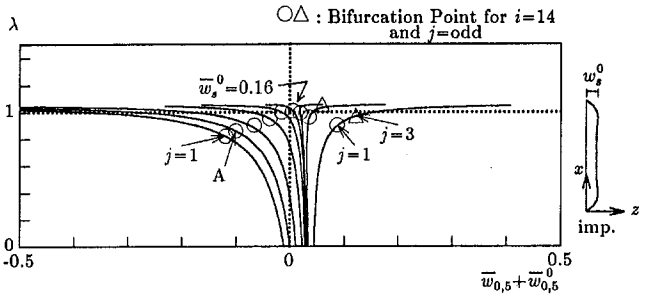

Fig. 4(*e*) Effects of axisymmetric initial imperfections

Fig. 4 Effects of initial imperfections for shells ($Z = 100$, $R/t = 405$, $L/R = 0.509$, $b = 14$)

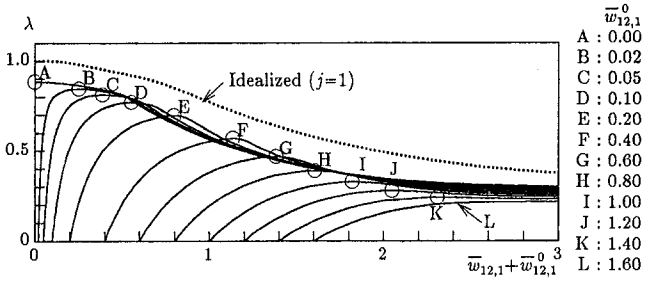

Fig. 5(*a*) Nondimensional load versus total deflection in harmonic $i = b = 12$ and $j = 1$

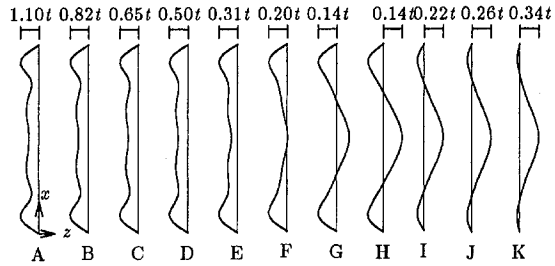

Fig. 5(*b*) Axial shapes of the total axisymmetric out-of-plane displacement component at the buckling load

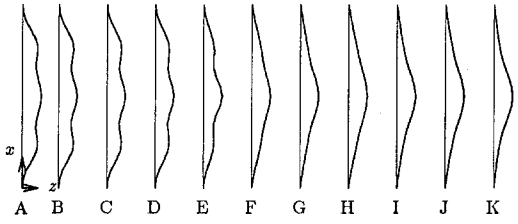

Fig. 5(*c*) Axial shapes (at $y = 2k\pi R/12$: $k = 0, 1, 2, \ldots, 12$) of the incremental asymmetric out-of-plane displacement component at the buckling load

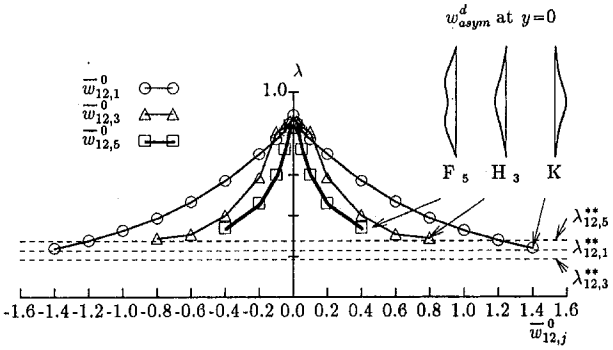

Fig. 5(*d*) Imperfection sensitivity for single asymmetric modes, $\bar{w}^0_{12,1}$, $\bar{w}^0_{12,3}$, and $\bar{w}^0_{12,5}$

Fig. 5 Effects of initial imperfections for shells ($Z = 200$, $R/t = 405$, $L/R = 0.720$, $b = 12$)

3; the near coincidence of the critical loads is seen in Fig. 8(*a*). These idealized post-buckling curves are obtained using the incremental method with respect to the displacement coefficients $\bar{w}_{16,1}$ and $\bar{w}_{16,3}$ for the upper and lower curves, respectively. A second bifurcation model, indicated by curve "A," is based upon the assumption that the effects of bending in a fundamental prebuckling nonlinear axisymmetric deformation state are taken into account. Due largely to the additional axisymmetric hoop compressions arising from the end boundary constraints, this more exact bifurcation analysis predicts lower critical loads. As is evident from Figs. 3 to 5, there remains on average an about 15 percent

difference.

3.2 Imperfect Shell Response. Included in Figs. 3(*a*), 4(*a*), and 5(*a*) are representative imperfect curves, where the horizontal axis $\bar{w}_{b,1}$ represents the nondimensional total displacement component having a circumferential full-wave number $i = b$ and a single half-wave in the axial direction, $j = 1$.

Previous experiments, not only by Arbocz and Babcock (1969), but also by Batista and Croll (1979), have shown that at the last load level prior to buckling the shell displays a dominant mode with only a one-half axial wave covering the entire length of the shell, even though the advanced post-buckled pattern is characterized by the well-known diamond pattern in which the axial and circumferential wavelengths appear to be approximately the same. Furthermore, Croll and Batista (1981) have indicated that a solution for the lower bound to imperfection-sensitive critical load has a single axial half-wave. In view of these earlier findings the initial imperfection function Eq. (8) is taken to be a single mode having the single axial half-wave $j = 1$; that is the asymmetric imperfection takes the form

$$w^0 = \bar{w}^0_{b,1} t \cos (by/R) \sin (\pi x/L). \tag{32}$$

Recalling that the imperfection amplitude $\bar{w}^0_{b,1}$ has been nondimensionalized with respect to the shell thickness, it can be seen that the sensitivity of buckling load to changes in imperfection is most severe when the imperfection has a very small amplitude. In Fig. 3 for $Z = 50$, an imperfection in the single axial half-wave mode of just two percent the shells thickness will reduce the buckling load by around eight percent of the bifurcation load of the perfect shell. With an imperfection of around 60 percent the shell's thickness, the maximum load has all but disappeared with the behavior approaching that which is more reminiscent of column buckling; the buckling load in this case has been reduced by some 58 percent compared with the bifurcation load of the perfect shell and 65 percent compared with the classical critical load. This imperfection sensitivity is more clearly illustrated in Fig. 3(*d*). As the shell slenderness increases so also does the potential reduction in buckling load due to imperfections. This is illustrated in Figs. 4(*a*) and 5(*a*) where for, respectively, $Z = 100$ and 200; the lowest buckling loads are reduced by 75 percent and nearly 80 percent of the classical critical load.

Figures 3(*b,c*), 4(*b,c*), and 5(*b,c*) show the axial distributions of deformation on meridians at $y = 2k\pi R/i$ ($k = 0, 1, 2, \ldots, i$), where the periodic buckling modes take on their extreme values, at the maximum or buckling loads. Figures 3(*b*), 4(*b*), and 5(*b*) show the axisymmetric components in the total deformations, while the incremental modes in Figs. 3(*c*), 4(*c*), and 5(*c*) are of the periodic buckling components associated with an increment of $0.001 \times t$ in the control parameter neglecting the incremental axisymmetric components. As the level of imperfection $\bar{w}^0_{b,1}$ is increased there is a gradual change in the incremental mode shape at the buckling load; this is shown in profiles "B," "C," . . . in Fig. 4(*c*). For small imperfection the mode $\bar{w}_{14,5}$ can be seen to dominate, while at large imperfections the incremental mode at buckling consists almost entirely of mode $\bar{w}_{14,1}$. The total axisymmetric deformation at the buckling loads are seen in Fig. 4(*b*) to also undergo major changes. Whereas at low imperfections, $\bar{w}^0_{b,1}$, the axisymmetric deformation "B" takes the form of a constrained axisymmetric bulging; at high imperfection the axisymmetric deformation at the buckling contains a major component of $\bar{w}_{0,3}$. It is this axisymmetric mode $\bar{w}_{0,3}$ that plays such a vital role in eroding the nonlinear membrane energy associated with buckling into mode $\bar{w}_{b,1}$; this Donnell coupling is discussed more fully in Batista and Croll (1979).

In Fig. 4(*e*), the initial imperfection function Eq. (8) is taken to be an axisymmetric mode having the inverse form to the linear bending mode; that is for $Z = 100$ the axisymmetric imperfection takes the form

$$w^0 = \bar{w}^0_s t \Big\{ 1.1200 \times \sin \frac{\pi x}{L} + 0.3938 \times \sin \frac{3\pi x}{L} + 0.1888 \times \sin \frac{5\pi x}{L} + 0.0650 \times \sin \frac{7\pi x}{L} + 0.0200 \times \sin \frac{9\pi x}{L} + 0.0063 \times \sin \frac{11\pi x}{L} + 0.0025 \times \sin \frac{13\pi x}{L} + 0.0006 \times \sin \frac{15\pi x}{L} \Big\} \tag{33}$$

It becomes evident that when an inward geometric imperfection of $\bar{w}^0_s$ ($\equiv w^0_{\max}/t$) = 0.16 is chosen, the outward loading-induced imperfection caused by the end constraint is being almost exactly counterbalanced by the inward geometric imperfection. The axisymmetric response can be seen to develop a major component in mode $\bar{w}_{0,5}$, which corresponds with the lowest of the axisymmetric critical loads. It is the additional circumferential membrane stress associated with this axisymmetric deformation that causes the additional destabilization which in turn is responsible for reducing the bifurcation, at "A" in Fig. 4(*a*) and 4(*e*), from the classical load $\lambda^c = 1$.

As Z increases the number of axial half-waves $j_{\max}$, associated with the lowest axisymmetric critical load, also increase. For $Z = 50$, 100, and 200, for example, it follows from the substitution of $i = 0$ into Eq. (28) that $j_{\max}$ are 4.19, 5.92 and 8.38, respectively. It is for this reason that in Fig. 3(*b*) the deformation at the bifurcation load "A" has a major component of $j = 3$, while that in Figs. 4(*b*) and 5(*b*) are dominanted by $j = 5$ and $j = 7$, respectively. Since these nonlinear axisymmetric deformations arise from the effects of the end restraints on the Poisson bulging, resulting in a form of loading imperfections (see Croll, 1984), it is the odd components $j = 1, 3, 5, \ldots$ that provide the dominant components in the nonlinear prebuckling response.

It is noticeable in the case of $Z = 50$ that the nonsymmetric buckling mode shapes shown in Fig. 3(*c*) change very little as the amplitude of the initial imperfection increases; for all imperfection levels it is mode $\bar{w}_{16,1}$, with a smaller contribution from $\bar{w}_{16,3}$, which dominates. For larger values of Z there are distinct changes in axial mode participation as the critical imperfections $\bar{w}^0_{b,1}$ increase. As Fig. 4(*c*) shows, there is a significant change in the form of nonsymmetric buckling mode between cases "D" and "E." Similarly, Fig. 5(*c*) displays changes in the axial mode shape between "E" and "F." These shifts in dominant buckling mode are reflected in the forms of imperfection sensitivity and post-buckling curves. This feature is most clearly seen in the changes to post-buckling lower bounds between "D" and "E" in Fig. 4(*a*), and less so in the similar mode shifts that occur in Fig. 5(*a*). Whereas Fig. 3(*a*) exhibits a smooth drop-off in buckling loads and associated mode shapes with increasing $\bar{w}^0_{b,1}$, this is not the case for the shell of Fig. 4(*a*) and 5(*a*) having higher Z values.

With the preference of the $Z = 100$ shell to develop incremental modes dominated by $\bar{w}_{b,5}$ when imperfection $\bar{w}^0_{b,1}$ is small, as shown in Fig. 4(*c*), it might be anticipated that imperfections having short axial wavelengths would produce even more extreme imperfection sensitivity. This is shown to be the case in the two further studies are summarized in Fig. 4(*d*). These show that for small imperfection amplitudes, the shorter axial wavelengths have asymptotically more extreme imperfection sensitivities. For larger amplitudes, however, these shorter axial wavelength imperfections cease to exhibit a (maximum) buckling load; it is for this reason that there is no buckling load shown for $\bar{w}^0_{14,3} > 0.4$ and $\bar{w}^0_{14,5} > 0.2$. A similar situation is evident in the studies of varying the axial shape of imperfections in Fig. 5(*d*). Although not shown, there is a tendency as the amplitudes of these shorter axial wavelength imperfections are increased, for the axial mode shape to become dominated by $\bar{w}_{b,1}$.

3.3 Incremental Energy Characteristics Along Nonlinear Paths. To identify which of the shells components of initial resistance to buckling are lost in the unstable post-buckling process, it is instructive to look at the changes in incremental energy.

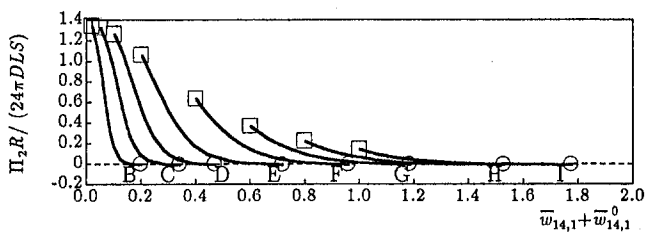

Fig. 6(*a*) Total energy Π_2

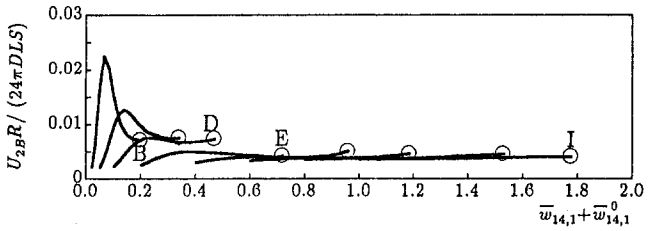

Fig. 6(*b*) Bending energy $\Pi_{2B} = U_{2B}$

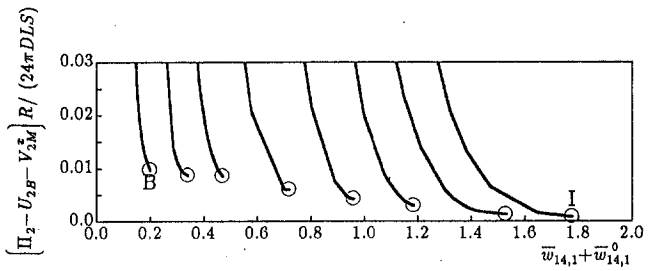

Fig. 6(*c*) Stabilizing membrane energy $\Pi_2 - U_{2B} - V^x_{2M}$

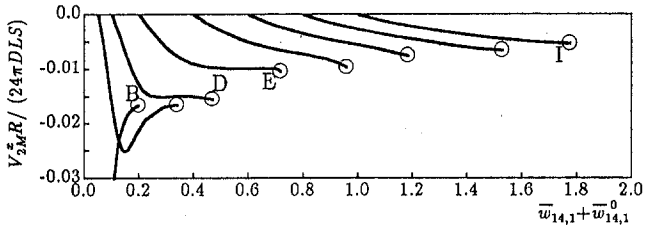

Fig. 6(*d*) Destabilizing membrane energy V^x_{2M}

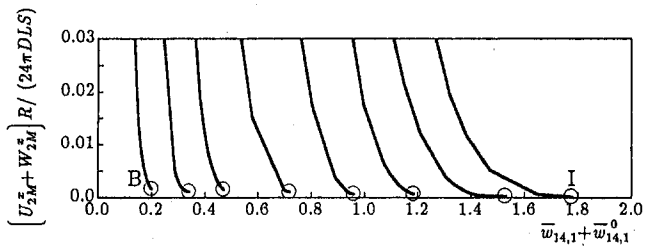

Fig. 6(*e*) $U^x_{2M} + W^x_{2M}$

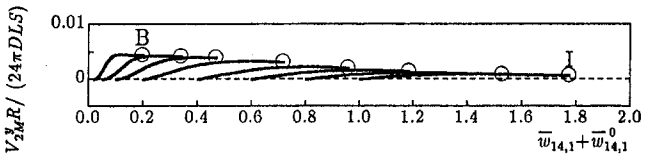

Fig. 6(*f*) V^y_{2M}

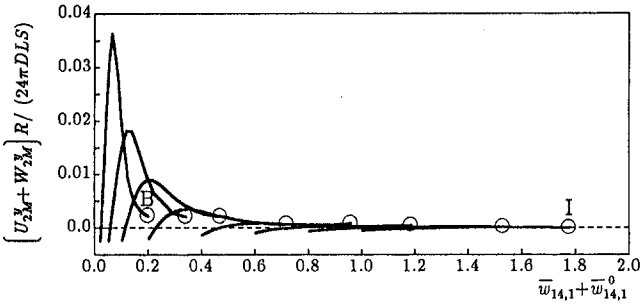

Fig. 6(*g*) $U^y_{2M} + W^y_{2M}$

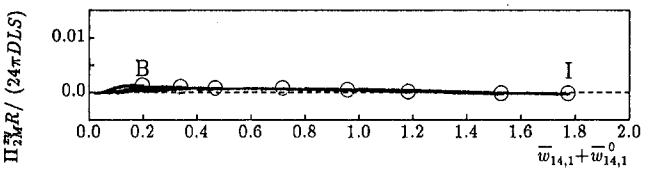

Fig. 6(*h*) Π^{xy}_{2M}

Fig. 6 Variations of quadratic energies ($Z = 100$, $R/t = 405$, $L/R = 0.509$, $b = 14$, see Fig. 4)

Figure 6(*a*) shows the variation of the incremental quadratic components of total potential energy, Π_2, defined in Eq. (20). Rectangles represent the initial stiffness; circles indicate the zero resistance at the maximum buckling loads. All results show the extreme sensitivity of the shell initial resistance to incremental buckling deformations as imperfection levels are increased. They also show that Π_2 of the prebuckling paths undergoes rapid decreases as the load approaches the buckling point; at the buckling point Π_2 becomes zero. For the results shown in Fig. 6(*a*), and in subsequent discussions of the energy, the quadratic incremental energies are normalized with respect to the summation of the squares of the incremental (non-dimensional) displacement components, S, given as

$$S = \sum_i \sum_j^{J_i^u} (\bar{u}^d_{ij})^2 + \sum_i \sum_j^{J_i^v} (\bar{v}^d_{ij})^2 + \sum_i \sum_j^{J_i^w} (\bar{w}^d_{ij})^2. \quad (34)$$

It has been suggested that the nonlinearity of the shell buckling is all to do with changes in the initial membrane resistance; this is certainly a central hypothesis of the reduced stiffness method. To emphasize this, Figs. 6(*b*)–(*h*) show the contributions to the incremental quadratic form of total potential energy from its bending components $\Pi_{2B} = U_{2B}$ and the various membrane components. As the level of the imperfection increases, the originally positive contribution from membrane energy, $\Pi_2 - U_{2B} - V^x_{2M}$ in Fig. 6(*c*), is rapidly reduced, eventually becoming almost zero at the buckling load (as in case "I"). At large deformations the total destabilizing membrane V^x_{2M} energy reaches a fairly consistent negative asymptote, which can be seen to exactly counteract the almost invariant positive contribution from bending energy as imperfections and deformation increase as shown in Fig. 6(*b*).

By breaking down the membrane energy into the linearized axial membrane energy V^x_{2M}, see Eq. (24*b*), and the rest, it becomes even clearer how the resistance of the axially loaded cylinder is eroded with increasing deformation and/or imperfections. It is clear that the destabilization is provided by the axial linearized component V^x_{2M}. When it is considered from Eq. (24*b*) that the uniform axial stress n^E_x and its associated strain ϵ^E_x are necessarily negative, while incremental strain ϵ^{dd}_x and its associated stress n^{dd}_x must be positive, it becomes clear why V^x_{2M} provides the negative or destabilizing contribution. What is noteworthy is the important positive stabilizing contribution from V^y_{2M}. This arises from the first term in Eq. (24*c*), for which the positive Poisson bulging

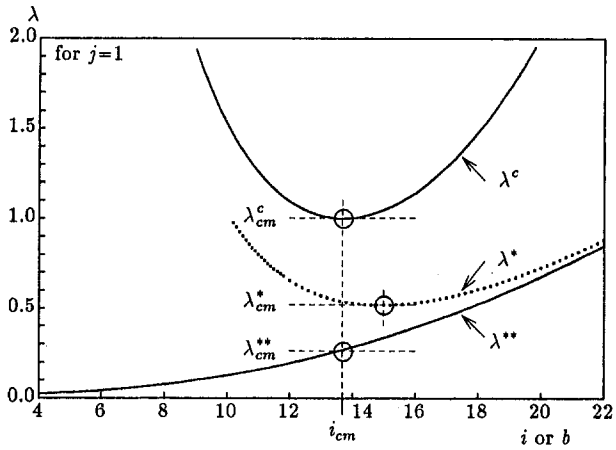

Fig. 7(*a*) Critical load spectra

strain ϵ_y^E and the necessarily positive definite incremental hoop stress n_y^{dd} (positive definite as a result of the nonlinear strain ϵ_x^{dd} of Eq. (18) also of necessity being everywhere positive) give rise to a positive energy term V_{2M}^y. However, what Fig. 6(*f*) shows is that this initially important stabilizing contribution from V_{2M}^y together with the contribution from the membrane strain energy $U_{2M}^y + W_{2M}^y$ as shown in Fig. 6(*g*), are both lost with increasing deformation into the buckling mode and increasing imperfection. For sufficiently large imperfections, these stabilizing membrane terms have been eroded at the maximum buckling loads. These observations support the physically based reasoning underpinning the reduced stiffness method (Croll, 1975; Batista and Croll, 1979).

4 Nonlinear Behavior and the Reduced Stiffness Method

Although it has been described elsewhere (see, for example, Batista and Croll, 1979), it will be instructive to summarize in the present context the major features of the reduced stiffness method.

4.1 Reduced Stiffness Method. The classical bifurcation analysis of Eq. (26) for a prospective buckling deformation (u^d, v^d, w^d) from a uniform prebuckling stress and strain state, Eq. (31), could be represented in terms of energy as

$$U_{2B} + U_{2M} + \lambda^c\left(\frac{\partial V_{2M}^{Fx}}{\partial \lambda} + \frac{\partial V_{2M}^{Fy}}{\partial \lambda}\right) = 0. \tag{35}$$

In this equation, U_{2B} is the linear[1] bending energy (Eq. (21)), U_{2M} is the linear[1] membrane energy (Eq. (23)), and V_{2M}^{Fx} is the linearized membrane component associated with axial direction, while V_{2M}^{Fy} is associated with circumferential direction, that is

$$V_{2M}^{Fx} = \tfrac{1}{2}\int_0^{2\pi R}\int_0^L (n_x^{dd}\epsilon_x^F + n_x^F\epsilon_x^{dd})dxdy \tag{36}$$

$$V_{2M}^{Fy} = \tfrac{1}{2}\int_0^{2\pi R}\int_0^L (n_y^{dd}\epsilon_y^F + n_y^F\epsilon_y^{dd})dxdy. \tag{37}$$

For the shell having $Z = 100$ and critical modes with a single axial half-wave, Fig. 7(*b*) shows the breakdown of the total potential energy. It can be seen that V_{2M}^{Fx} provides the negative destabilizing contributions to the critical loads λ^c shown in Fig. 7(*a*). Both the linear bending U_{2B} and membrane U_{2M} energies contribute to the stabilization, as does the linearized circumferential component V_{2M}^{Fy} (this linearized circumferential energy V_{2M}^{Fy} is closely related to the incremental component V_{2M}^y discussed in Section 3.3 and shown to be eventually eliminated at buckling in Fig. 6(*f*)). Batista and Croll (1979) (following Donnell, 1934) have reasoned how V_{2M}^{Fy} would be lost due to the occurrence of mode coupling. They have obtained a reduced stiffness critical load, λ^*, by solving the following eigenvalue problem:

$$U_{2B} + U_{2M} + \lambda^* \frac{\partial V_{2M}^{Fx}}{\partial \lambda} = 0. \tag{38}$$

However, Yamada and Croll (1993) have shown, for the related case of pressure buckling, that the linear membrane energy U_{2M} is also eliminated. Based upon the elimination of both V_{2M}^{Fy} and U_{2M}, an alternative critical load equation λ^{**} may be proposed as

$$U_{2B} + \lambda^{**} \frac{\partial V_{2M}^{Fx}}{\partial \lambda} = 0. \tag{39}$$

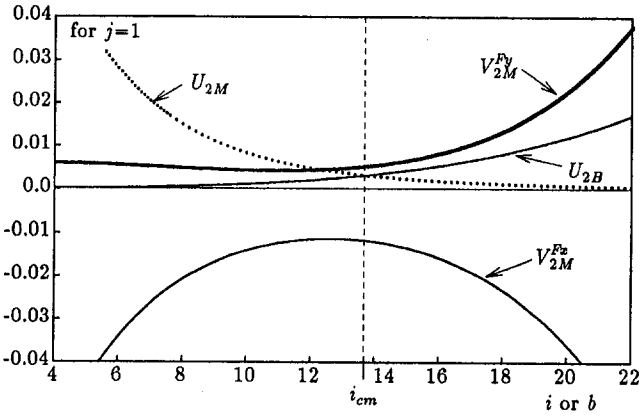

Fig. 7(*b*) Contributions of energy components in critical mode

Fig. 7 Bifurcation analytical results (Z = 100, R/t = 405, L/R = 0.509)

Based upon this reduced energy a modified reduced stiffness load is given by

$$\lambda_{i,j}^{**} = \frac{1-\mu^2}{2\sqrt{3Z}}\,\frac{\{(j\pi)^2 + (iL/R)^2\}^2}{\{(2-\mu^2)(j\pi)^2 + \mu(iL/R)^2\}}. \tag{40}$$

This alternative has the advantage of being consistent with the reduced stiffness philosophy applied to other loading cases and more importantly the observations of Fig. 6(*c*) and Fig. 6(*e*) to 6(*h*). Lower-bound buckling would be given by the value of λ^{**} corresponding with a mode having a single half-wave in the axial direction $j = 1$ and at a circumferential full-wave number i_{cm} associated with the lowest classical critical load. Defining i_{cm} from Eq. (28), with $j = 1$, Eq. (40) leads to the modified expression

$$\lambda_{cm}^{**} = \frac{1-\mu^2}{2-\mu^2-\mu+\dfrac{\mu}{\pi}(2\sqrt{3}Z)^{1/2}} \tag{41}$$

for the reduced stiffness lower bound to elastic buckling. As noted in previous discussion of the reduced stiffness method, lower bounds to axial loaded cylinder buckling have both a dependence upon Z and Poisson's ratio μ (see Croll and Batista, 1981). But how does this modified reduced stiffness load relate to the results of nonlinear buckling studies?

4.2 Parameter Studies and Lower Bound Buckling. Figure 8(*a*) shows the various critical load spectra for the shell Z = 50. To provide additional confirmation of the lower boundedness of the modified reduced stiffness critical load λ_{cm}^{**} a number of imperfection sensitivity studies like that shown in Fig. 3(*a*) have

[1] Linear in the sense of being related to the linear strain-displacement relationships in the incremental critical buckling deformations.

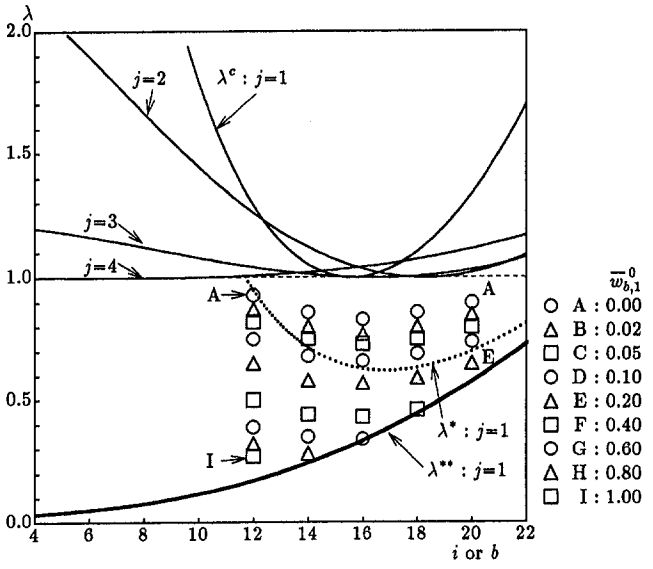

Fig. 8(*a*) $Z = 50$

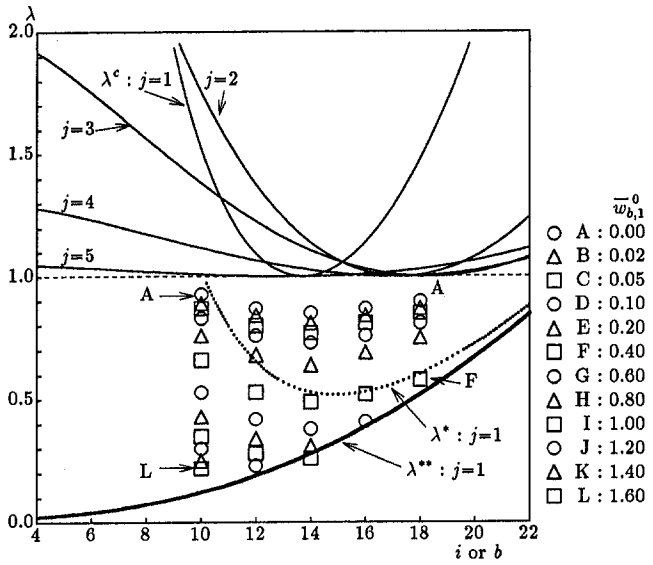

Fig. 8(*b*) $Z = 100$

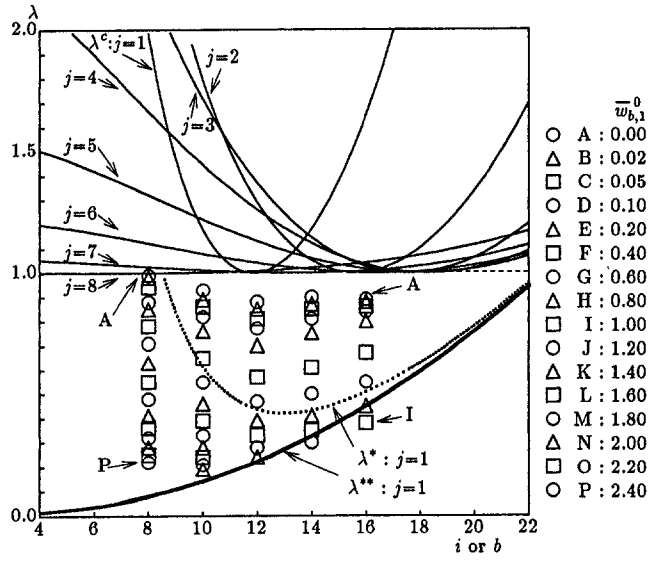

Fig. 8(*c*) $Z = 200$

Fig. 8 Summary of buckling loads from nonlinear analysis for imperfect shells and comparison with linear classical and reduced stiffness analyses

been undertaken. The many dots in Fig. 8(*a*) show the buckling loads for imperfections in modes $12 \leq b \leq 20$. Those shown for $b = 16$ relate to the results described in Fig. 3(*a*). For this shell the integer mode nearest to that resulting in the minimum critical load λ_{cm} is $b = 16$. It is evident that the imperfection sensitivity in this mode is at its highest; an imperfection of 60 percent the shell thickness is enough to almost reach the reduced stiffness load λ^{**}_{cm}. For this same amplitude of imperfection in modes $b < 16$ the buckling load is a little higher, while for $b > 16$ the snap buckling no longer occurs and nonlinear responses approach $\lambda^{**}_{b,1}$ in Eq. (40) monotonically from below. It is for this reason that no buckling loads are shown for some imperfections in modes $b > i_{cm}$ and also why in mode $b = 16$ there are no buckling loads shown for $\bar{w}^0 > 0.6$. With the lower imperfection sensitivity in modes $b < i_{cm}$ it takes rather larger imperfections to reach their lower bounds. It is again significant that the lower bounds are effectively constant and equal to λ^{**}_{cm}.

Figures 8(*b*) and 8(*c*) show the related behaviors for shell having $Z = 100$ and 200, respectively. For each case, and others not shown, the characteristics are effectively the same. Maximum imperfection sensitivity is experienced in the classical critical mode $(i_{cm}, 1)$, with the reduced stiffness critical load λ^{**}_{cm} providing very close approximation of the lower bounds to imperfection sensitivity. Table 1 summarizes the relationships between λ^{**}_{cm} and the lower bounds to nonlinear buckling loads $\lambda^{N}_{\min}$.

Before leaving the parameter studies of Fig. 8(*a*) to 8(*c*) it is relevant to note that as the imperfections in mode $b < i_{cm}$ are increased there is a gradual shift in the incremental buckling mode from that of the imperfection to that of i_{cm}. This is illustrated in Fig. 9 for the case of $Z = 200$. Imperfections in mode $(i, j) = (8, 1)$ result in the nonlinear responses shown in Fig. 9(*a*); these relate to the buckling loads shown in Fig. 8(*c*) for mode $i = b = 8$. With small imperfections, exemplified by "B," the incremental deflection mode at buckling is seen in Fig. 9(*b*) to be essentially associated with the imperfection $i = b = 8$. For large imperfections, case "P," the dominant wavelength of the incremental deflection modes has shortened to conform closely with the critical wavelength $i_{cm} = 12$. It is these mode shifts resulting from mode coupling at large deformations and for larger levels of imperfection that eventually make the reduced stiffness λ^{**}_{cm} relevant even for initial imperfections having very different wavelengths.

5 Conclusions

An elastic nonlinear Ritz analysis has been developed to allow investigation of the imperfect behavior of axially compressed cylindrical shells. This has allowed a number of important observations. First, as deformations increase along the nonlinear equilibrium path for a particular imperfection, the originally positive (stabilizing) contributions from membrane energy are rapidly reduced, eventually becoming effectively zero at moderate levels at post-buckling deformation. Second, as the imperfection levels are increased, the significance of incremental membrane energy at the buckling (maximum) load

Table 1 Comparison between the present lower bound of buckling loads by nonlinear numerical analysis ($\lambda^{N}_{\min}$) and the modified reduced stiffness loads (λ_{cm}) for $j = 1$

Z	$i_{cm}(j=1)$	$\lambda^{N}_{\min}(i)$	λ^{**}_{cm}
50	15.6	0.34(16)	0.317
100	13.7	0.26(14)	0.269
200	11.9	0.24(12)	0.221

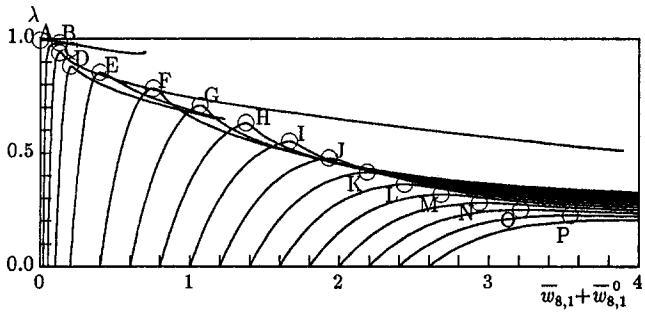

Fig. 9(*a*) Nondimensional load versus total deflection in harmonic $i = b = 8$ and $j = 1$

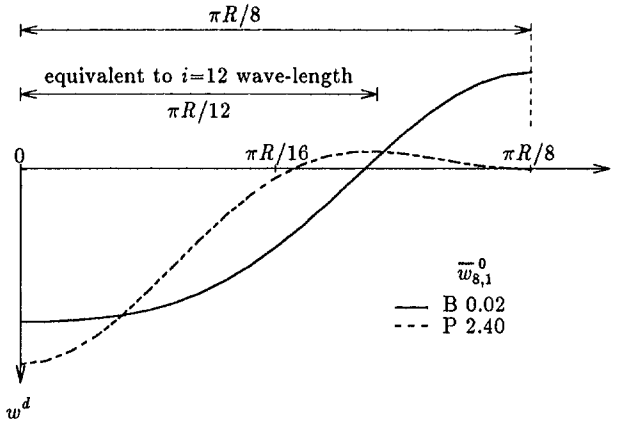

Fig. 9(*b*) Circumferential shapes (at $x = L/2$) of the incremental out-of-plane displacement component at the buckling load

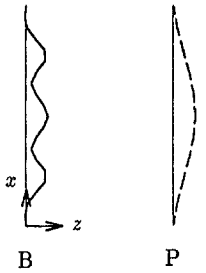

Fig. 9(*c*) Axial shapes (at $y = 2k\pi R/8$: $k = 0, 1, 2, \ldots, 8$) of the incremental asymmetric out-of-plane displacement component at the buckling load

Fig. 9 Effects of initial imperfections (a single asymmetric mode $\bar{w}^0_{8,1}$) for a shell ($Z = 200$, $R/t = 405$, $L/R = 0.720$, $b = 8$)

is also reduced, becoming effectively zero when buckling loads reach their minimum levels. Third, although for extremely small imperfections the incremental deformation modes at buckling show considerable variability, there is a particular incremental mode that dominates buckling when imperfections reach moderate levels. This dominant buckling mode, having a single axial half-wave and a characteristic circumferential full-wave number, is shown to conform closely with that predicted from a reduced stiffness analysis. Furthermore, the lowest recorded nonlinear buckling loads are demonstrated to be accurately predicted by a modified form of the reduced stiffness critical load.

In terms of the specific problem considered it is concluded that this modified form of the reduced stiffness method, which is a straightforward extension of classical linear buckling theory, provides a simple but safe basis for the design of axially compressed cylinders. At a wider level the paper shows how a synthesis of classical and numerical nonlinear analysis can lead to an understanding of greater significance than if either were considered alone.

References

Arbocz, J., and Babcock, C. D., 1969, "The Effect of General Imperfections on the Buckling of Cylindrical Shells," ASME JOURNAL OF APPLIED MECHANICS, Vol.36, pp.28–38.

Arbocz, J., and Sechler, E. E., 1974, "On the Buckling of Axially Compressed Imperfect Cylindrical Shells," ASME JOURNAL OF APPLIED MECHANICS, Vol.41, pp.737–743.

Batista, R. C., and Croll, J. G. A., 1979, "A design approach for axially compressed unstiffened cylinders," *Stability Problems in Engineering Structures and Components,* T. H. Richards and P. Stanley, eds., Applied Science, London, pp.377–399.

Brush, D. O., and Almroth, B. O., 1975, *Buckling of Bars, Plates, and Shells,* McGraw-Hill, New York, p.168.

Croll, J. G. A., 1984, "Axisymmetric elastic-plastic buckling of axial and pressure loaded cylinders," *Proc. Instn Mechanical Engrs,* Vol.198c, No.16, pp.243–254.

Croll, J. G. A., 1995, "Towards a rationally based elastic-plastic shell buckling design methodology," *Thin-Walled Structures,* Vol.23, pp.67–84.

Croll, J. G. A., and Batista, R. C., 1981, "Explicit lower bounds for the buckling of axially loaded cylinders," *Int. J. Mech. Science,* Vol.23, pp.331–343.

Croll, J. G. A., and Chilver, A. H., 1971, "Approximate estimation of the stability of cooling towers under wind loading," *Proc. IASS Recommendations for the Structural Design of Hyperbolic or Other Similarly Shaped Cooling Towers,* Brussels.

Donnell, L. H., 1934, "A New Theory for the Buckling of Thin Cylinders Under Axial Compression and Bending," *Transactions of the ASME,* Vol.56, pp.795–806.

Hunt, G. W., Williams, K. A. J., and Cowell, R. G., 1986, "Hidden symmetry concepts in the elastic buckling of axially-loaded cylinders," *Int. J. Solid Structures,* Vol.22, pp.1501–1515.

Koiter, W. T., 1963, "The effect of axisymmetric imperfections on the buckling of cylindrical shells under axial compression," *Koninkl. Ned. Akad. Weterschap., Proceedings,* Series B, Vol.66, pp.265–279.

Yamada, S., and Croll, J. G. A., 1989, "Buckling behavior of pressure loaded cylindrical panels," *Journal of Engineering Mechanics, ASCE,* Vol.115, No.2, pp.327–344.

Yamada, S., and Croll, J. G. A., 1993, "Buckling and Post-buckling Characteristics of Pressure Loaded Cylinders," ASME JOURNAL OF APPLIED MECHANICS, Vol.60, pp.290–299.

Yamada, M., and Yamada, S., 1983, "Agreement between theory and experiment on large-deflection behaviour of clamped shallow spherical shells under external pressure," *Collapse, Proc. IUTAM Symp. on Collapse,* Cambridge Univ. Press, London, pp.431–441.

Yamaki, N., 1984, *Elastic Stability of Circular Cylindrical Shells,* North-Holland, Amsterdam.

V. M. Harik[1]
Department of Mechanical Engineering,
The Johns Hopkins University,
315 Latrobe Hall
3400 N. Charles Street
Baltimore, MD 21218
e-mail: harik@ccm.udel.edu
Mem. ASME

R. A. Cairncross
Chemical Engineering Department,
Drexel University,
Philadelphia, PA 19104

Evolution of Interfacial Voids Around a Cylindrical Inclusion

The formation and evolution of interfacial cavities is predicted for compression flows of a viscous solid around a rigid cylindrical inclusion. The resulting free-boundary problem is solved by the finite element method with boundary-fitted mesh motion. The matrix-inclusion interface is perfectly weak and separates at a dynamic contact line. For a fixed set of geometric parameters, increasing the external pressure causes smaller interfacial voids and slower growth rates. The size of the stagnant voids found is affected by the applied pressure. The profiles of interfacial voids change from convex to convex-concave as the strain increases. This can lead to unstable cusps at low enough external pressures. The numerical predictions compare well with the experiments of Kao and Kuhn (1990) for void size as a function of strain in viscoplastic model materials.

1 Introduction

Imperfect interfaces in two-phase materials are often criticized when manufactured structures demonstrate unexpectedly poor mechanical properties. Interfacial debonding, sliding, and separation are among interfacial problems which may occur during processing and can later lead to premature failure (see, e.g., Mura (1987) and Achenbach and Zhu (1989)). Recently these interfacial problems have been studied by a number of researchers (e.g., Xia et al. (1994), Budiansky et al. (1995) Chao and Laws (1997), Jasiuk et al. (1997), and Ru (1998)). When such materials are subjected to compressive or extensional loads, interfacial voids may occur by further decohesion of the matrix material from the inclusions (Hashin, 1991). Evolution of large interfacial voids around cylindrical inclusions in two-phase materials is the focus of this paper.

Budiansky, Hutchinson, and Slutsky (1982) investigated the evolution of isolated spherical voids in an infinite linear viscous solid subjected to various biaxial stresses. The effect of outside pressure on the final shape of such voids was extensively analyzed. Deformation of spherical cavities has been also studied by Rice et al. (1978) for a class of fluid-infiltrated elastic materials. For viscous materials, Budiansky et al. (1982) showed that tension or transverse compression loads lead to elongated ellipsoidal voids. In this work, we show that similar tendencies develop in plane compression flows around cylindrical inclusions, although the deformation of cavities is no longer homogeneous. Taya and Patterson (1982) pointed out that the viscous solid model can effectively predict interfacial voids around debonded rigid inclusions in a ductile two-phase material. The ductile matrix was modeled as a linear viscous solid (Nadai, 1950). This assumption is based on the mechanical behavior of ductile metals, such as copper or aluminum, which can be described by

$$\sigma_0 = a + b\dot{\epsilon}, \tag{1}$$

where σ_0 is the flow stress and a and b are constants for a certain range of strain rates $\dot{\epsilon}$ and flow temperatures. Note that the debonded particles have interfacial mechanical properties which are similar to a perfectly weak interface. Such interfaces represents an important limit for weak interfaces. Recently Jasiuk et al. (1997) examined perfectly strong and weak interfaces for a class of elastic matrices and an inclusion in a half-space. In this work, we demonstrate how perfectly weak interfaces separate, undergo large nonlinear deformation, evolve in time, and that they may be prone to interfacial instabilities.

Needleman (1987) studied formation of interfacial separation and evolution of interfacial voids in a periodic array of rigid spherical inclusions in an elastic-viscoplastic matrix. A rectangular unit cell was subjected to the external tensile loads, which lead to monotonically increasing separation and the complete voids associated with complete debonding along the entire interface. In particular, it was noted that the shear stiffness parameter of the phenomenologically described interface had insignificant effect on the voids studied. In the case of compression flows around cylindrical particles with perfectly weak interfaces, we also show that the interfacial sliding has rather small influence on the voids as they are formed by predominantly normal interfacial separation.

In this paper we investigate the temporal evolution of interfacial voids around a cylindrical inclusion in a thick plate subjected to biaxial compressive loads. The influence of external pressure on the development and shape of voids at rigid inclusions is examined. The biaxial loads considered lead to the formation of interfacial voids with variable rate of growth, voids with convex and convex-concave profiles, and cusps. The numerical simulations are compared with physical modeling experiments of Kao and Kuhn (1990).

2 Formulation of the Problem

This paper analyzes two-dimensional symmetric compression flows around a cylindrical inclusion (as shown in Fig. 1). These flows represent physical situations of practical importance: for example, extensional flows around cylindrical obstacles and forging of two-phase specimens with cylindrical inclusions (e.g., Kao and Kuhn, 1990). The physical domain contains a thick plate with a single cylindrical inclusion, which is subjected to biaxial compressive loads. The computational cell considered is a rectangle of dimensions $2L \times 2H$ which is centered around the inclusion. Both dimensions of the cell are smaller than those of the plate (see Section 2.1). We assume that the matrix is an incompressible viscous solid. The total stress $\boldsymbol{\sigma}$ is

$$\boldsymbol{\sigma} = -p\mathbf{I} + \mu(\nabla\mathbf{V} + (\nabla\mathbf{V})^T), \tag{2}$$

where p is pressure, $\mathbf{I}$ is the identity tensor, μ is the dynamic shear viscosity, and $\mathbf{V}$ is the fluid velocity. We shall demonstrate that for certain cases this constitutive model can simulate material deformation of low Deborah numbers. It also ensures numerical stability of the simulations. For incompressible materials, the equation of mass conservation is

[1] Currently at the Army Research Laboratory and the Center for Composite Materials, University of Delaware, Newark, DE 19716.

Contributed by the Applied Mechanics Division of THE AMERICAN SOCIETY OF MECHANICAL ENGINEERS for publication in the ASME JOURNAL OF APPLIED MECHANICS.

Discussion on the paper should be addressed to the Technical Editor, Professor Lewis T. Wheeler, Department of Mechanical Engineering, University of Houston, Houston, TX 77204-4792, and will be accepted until four months after final publication of the paper itself in the ASME JOURNAL OF APPLIED MECHANICS.

Manuscript received by the ASME Applied Mechanics Division, June 30, 1998; final revision, Oct. 27, 1998. Associate Technical Editor: R. C. Becker.

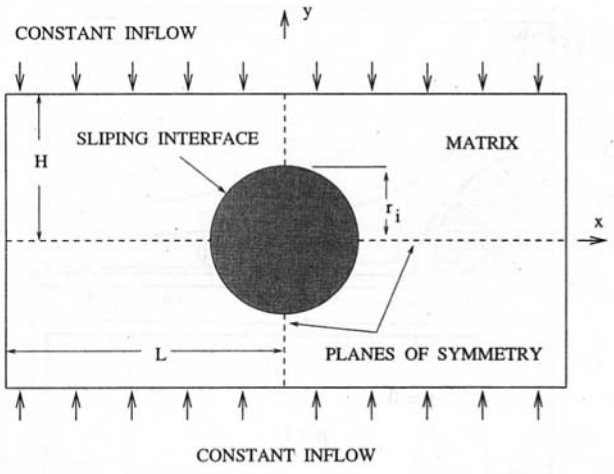

Fig. 1 Schematic of the compression flow region near a rigid cylindrical inclusion in a viscous two-dimensional column

$$\nabla \cdot \mathbf{V} = \frac{\partial u}{\partial x} + \frac{\partial v}{\partial y} = 0, \tag{3}$$

where u and v are two components of the material velocity vector.

In the case of quasi-static deformation of a viscous solid, the Reynolds number $\mathrm{Re} = \rho V_0 H/\mu$ is small and the momentum balance is described by the Stokes equation for creeping flows:

$$\nabla p = \nabla \cdot \tau \quad \text{or} \quad \nabla p = \mu \nabla^2 \mathbf{V}. \tag{4}$$

Here, ρ is density, V_0 is the compression velocity, and $2H$ is height of the specimen. Typical values of these parameters are $V_0 \approx 3 \times 10^{-4}$ m/s, $H \approx 0.1$ m, ρ and μ are 2,600 kg/m^3 and 11×10^{11} kg/m · s for a glass at the temperature 575(°C), and 1800 kg/m^3 and 4.7×10^5 kg/m · s for a wax at the temperature 8(°C) (Weast, 1988). Thus, $\mathrm{Re} \ll 1$ for a number of highly viscous Newtonian solids. Note that the time-dependence of the flow-field is caused solely by interfacial boundary motion.

2.1 Boundary Conditions. By symmetry, only a quarter of the solution domain needs to be analyzed (Fig. 2). Following Needleman (1987), we replace the constant strain rate at infinity by a constant velocity along a side of a rectangular computational cell. As a result, boundary conditions on the top shear-free boundary of the cell are

$$v(x, y = H) = -V_0, \quad \mathbf{t} \cdot \boldsymbol{\sigma}\,(x, y = H) = 0, \tag{5}$$

for $x \in [0, L]$, where V_0 is the inflow velocity, $2H$ is the height of the cell, and $2L$ is the width of the cell. The symmetry lines $x = 0$ and $y = 0$ are also shear-free with no penetration

$$u\,(x = 0, y) = 0, \quad \mathbf{t} \cdot \boldsymbol{\sigma}\,(x = 0, y) = 0, \tag{6}$$

for $y \in [r_i, H]$, and

$$v\,(x, y = 0) = 0, \quad \mathbf{t} \cdot \boldsymbol{\sigma}\,(x, y = 0) = 0, \tag{7}$$

for $x \in [r_i, L]$, where r_i is the radius of a cylindrical inclusion. The cell boundary at $x = L$ is subjected to a constant pressure P and zero shear stress:

$$\mathbf{n} \cdot \boldsymbol{\sigma}\,(x = L, y) = -P, \quad \mathbf{t} \cdot \boldsymbol{\sigma}\,(x = L, y) = 0. \tag{8}$$

The perfectly weak interface may slip and even separate from the inclusion if the processing pressure is low enough. The sliding interface should satisfy the following conditions for free slip and no penetration:

$$\sigma_{r\theta}\,(r = r_i, \theta) = 0, \quad \mathbf{V}\,(r = r_i, \theta) \cdot \mathbf{n} = 0, \tag{9}$$

for $\theta \in [0, \pi/2]$, where $\mathbf{n}$ is the normal vector, r and θ are polar coordinates with the origin at $(x = 0, y = 0)$, and r_i is the inclusion radius. The sliding part of interface should satisfy conditions (9) for $\theta \in [\theta_0, \pi/2]$, where the angle θ_0 defines the contact line at $(r = r_i, \theta = \theta_0)$. The unknown angle θ_0 may change with time. When interfacial boundary slips or separates from the inclusion, it is also required to satisfy the kinematic boundary conditions

$$(\mathbf{V} - \mathbf{V}_s) \cdot \mathbf{n} = 0, \tag{10}$$

where $\mathbf{V}_s$ is the surface velocity vector. The free interfacial boundary at $r = r_i$ and $\theta \in [0, \theta_0]$ is assumed to be subjected to zero radial stress and zero shear stress,

$$\sigma_{rr}\,(r = r_i, \theta) = 0, \quad \sigma_{r\theta}\,(r = r_i, \theta) = 0. \tag{11}$$

This part of the interface is free to move, deform, and take any kinematically admissible location and shape.

Note that two different sets of boundary conditions are required for the sliding part of the interface and the "freely" evolving part of the boundary. The position and the shape of interfacial free boundary and the location of the contact line joining the two parts of interface together is not known before hand. The numerical aspects of such nonlinear problems are thoroughly discussed by Christodoulou et al. (1996). We show that the dynamic contact line problem involved can be resolved by introducing an equivalent set of interfacial conditions for the resulting system of equations.

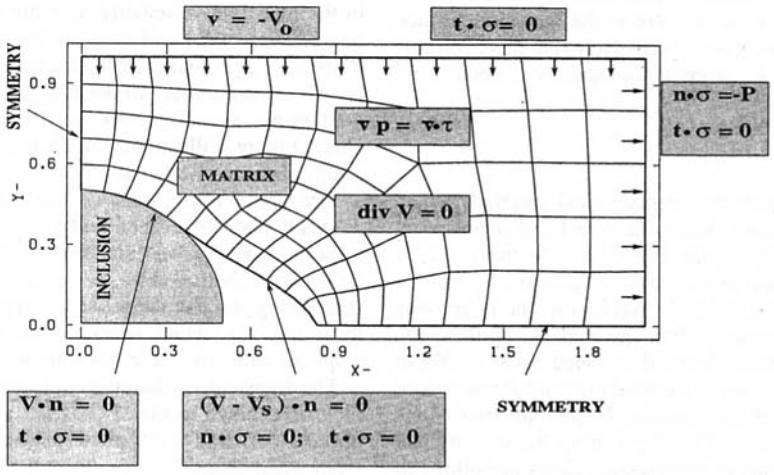

Fig. 2 Schematic of the computational domain with the boundary conditions and the governing equations used

3 Numerical Simulations

The plane compression flows around a cylindrical inclusion are investigated in a quarter of the solution domain (Fig. 2). The Galerkin finite element method is implemented for the computational cell which is discretized with nine-node quadrilateral finite elements. The mesh was tested for convergence under refinement. The resulting system of nonlinear algebraic equations is solved by a fully coupled Newton-Raphson iterative scheme with boundary-fitted mesh motion (Christodoulou et al., 1996). The finite element analysis is performed by using the code developed in cooperation with Sandia National Laboratories (Schunk et al., 1995). There are several commercial computational mechanics packages which can address similar problems for elastoplastic solids (e.g., ABAQUS and ANSYS) or viscoplastic materials (e.g., DEFORM and DYNA). The present code offers additional flexibility in defining a phenomenological weak interface by introducing a repulsion potential along the ill-defined interfacial surface with a dynamic contact line (Harik, 1997). This code also avoids additional iterations by utilizing a fully coupled scheme for the mesh motion and the momentum equations. Such approach increases accuracy of the free surface modeling, which is especially important at the onset of the cusp instability.

In the numerical calculations presented, the initial inclusion volume fraction is 9.8 percent, for the inclusions of normalized radius 0.5. The x and y-coordinates and the velocity vector components are nondimensionalized as $x^* = x/H$, $y^* = y/H$, $u^* = u/V_0$ and $v^* = v/V_0$. The nondimensionalized pressure p^* is given by $p^* = p/(\mu V_0/H)$. The external pressure P applied to the outer surface of the cell at $x = L$ is varied. The location of the top cell boundary is set at $y = H = 1$. The normalized vertical velocity along this cell boundary is set to be -1. The location of the outflow boundary is set at $x = L = 2$. Geometry of inclusion and the matrix material viscosity remain fixed, $\mu = 1$, for all numerical calculations.

In order to enforce two sets of interfacial boundary conditions and allow slip along the sliding interface together with unrestricted evolution on the free interfacial surface, phenomenological repulsion is introduced (Harik, 1997). The corresponding boundary condition is defined for the entire surface of the interface:

$$p(r, \theta) = p_a + \frac{b_\epsilon}{(r - r_0)^4}, \tag{12}$$

where $p(r, \theta)$ is the repulsion pressure, p_a is the ambient pressure parameter, b_ϵ is the sensitivity coefficient for the repulsion potential, and r_0 defines a circular surface along which the repulsion potential is infinite. Note that r_0 is smaller than the radius of inclusion r_i, $r_i - r_0 < 0.001$. To simulate zero pressure on the free interface boundary the ambient pressure parameter p_a is set to be zero. The sensitivity coefficient b_ϵ is chosen so that the repulsion potential balances the flow pressure at the inclusion surface and simulates the presence of a rigid body. Note that this approach is similar to the modeling of a phenomenologically defined interface by Needleman (1987).

4 Analysis of Results

In two-phase materials with the perfectly weak interface, interfacial separation starts on both sides of a cylindrical inclusion at the line of symmetry ($y = 0$; see Fig. 3(a)). At the place of separation, there is a small region of zero pressure, which is preserved for some time (Fig. 3(b)). In that region, the matrix has a "dead zone" of the deformation-free material. A similar zone near interfacial voids has been observed by Needleman (1987) in an extensional flow. High values of external pressure P can reduce the growth and the size of microvoids. Interfacial microvoids rapidly grow into finite cavities. Development of finite interfacial voids at cylindrical inclusions in compression flows goes through a sequence of convex profiles for small strains and low external pressures (Fig. 3(a, b)). Figure 3(a) shows a set of instantaneous

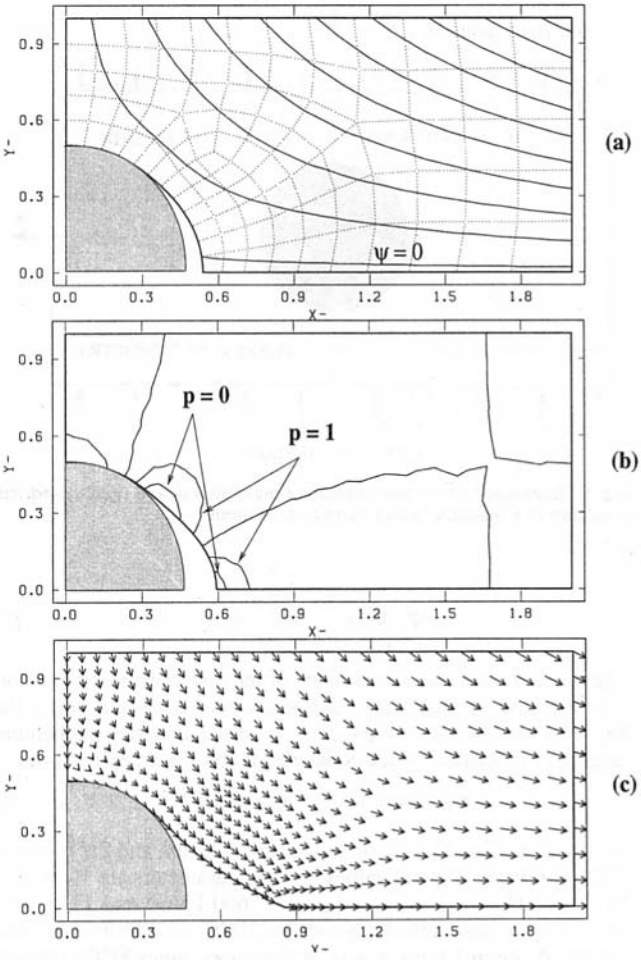

Fig. 3 Transient evolution of an interfacial void at a cylindrical inclusion at zero external pressure P. (a) Stream lines of the deformation flow at $t^* = t/(H/V_0) = 0.053$, (b) pressure contours at $t^* = 0.126$, and (c) velocity vector field at $t^* = 0.422$.

flow stream lines which is characteristic for all stages in void growth. The zero line moves upward as the strain increases and the length of void δ grows.

Under low external pressure, the sequence of convex interfacial cavities breaks down when a cusp develops in the interfacial free surface at the symmetry line (Fig. 3(c)). This marks a highly unstable stage in the evolution of free interfacial surfaces subjected to low external pressures. It is characterized by a sudden increase in the matrix flow velocity near the interface at the line of symmetry. High values of external pressure P reduce not only the growth of voids and their final size (Fig. 4) but also suppress their interfacial instability. Under high enough pressure, an interfacial void grows monotonically until its size reaches a steady-state value. Figure 4 illustrates the changes in the time-dependent evolution of finite interfacial voids caused by the outside pressure.

The rate of void growth decreases as the applied pressure rises. A steady state is reached under higher external pressures, which limit the cavity growth and the interfacial instability. The limiting void size is controlled by the external pressure for a range of large strains (Fig. 4). The shape of the stagnant void is determined by the local flow-field which resembles the Bingham plastic flow around a sphere with solid stagnation regions (see Beris et al., 1985).

The transient evolution of an interfacial void at a cylindrical inclusion shown in Fig. 3 provides a good qualitative description of the experiments performed by Kao and Kuhn (1990). In fact, all topological characteristics of the convex interfacial cavities are in agreement (see Figs. 3 and 6 in Kao and Kuhn (1990)). That is, similarities extend even to the break up of the sequence of convex

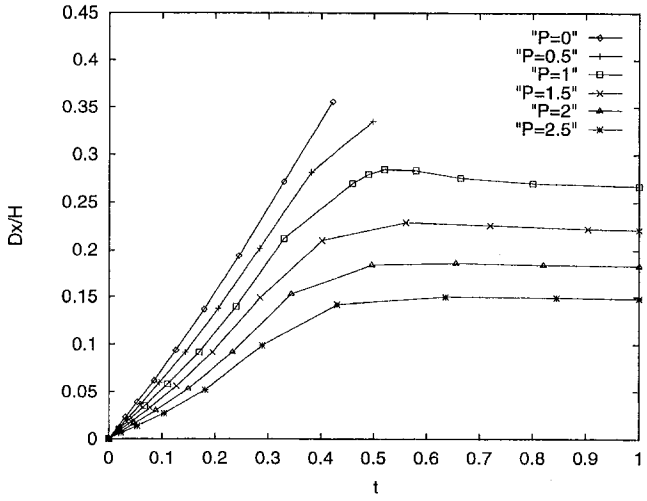

Fig. 4 The time-dependence of the interfacial separation δ (δ = Dx/H) at y = 0 around a cylindrical inclusion of normalized radius 0.5 for different outside pressures P ($P = \Delta p/(\mu V_0/H)$)

profiles by unstable transition to the cusp in the evolving interfacial surface. The velocity vector fields obtained from the experiments and the finite element modeling are quite similar as well (see Fig. 3(*c*) and Fig. 6 in Kao and Kuhn (1990)). Figure 5 illustrates a quantitative agreement between the physical modeling of void growth and finite element simulations.

Similarity between the flow of a viscoplastic paste-type model material and the finite element simulations based on the viscous solid model is the result of low rates of deformation and low Deborah number of the paste flow. Lipscomb and Denn (1984) demonstrated that the Bingham plastic flow around a sphere can be approximated by a linear viscous flow when the yield stress and the rate of deformation are small. Duvaut and Lions (1976) proved that a unique solution for the creeping flow of Bingham plastics exists and it approaches the Newtonian limit as the yield stress approaches zero. In the physical modeling experiments, the shear thinning near the particle surface creates rheological conditions resembling weak interfaces.

5 Conclusions

This paper presents finite element modeling of time-dependent evolution of interfacial voids at a cylindrical inclusion in plane compression flows. In particular, the influence of applied external pressure on the development of voids at the inclusion surrounded by a highly viscous matrix is examined for a variety of cases. For a fixed set of geometric parameters, increasing the normalized pressure drop between the free surface and the inclusion $\Delta p/(\mu V_0/H)$ reduces the interfacial void size. The profiles of interfacial voids change from convex to convex-concave (with smaller area) as the applied pressure and strain increases.

The external pressure affects the initiation of interfacial separation and all stages in the void development. The presence of an inclusion leads to complex deformation of interfacial free surface. As a result, the topology of deformed voids is more complicated than that of elongated voids without inclusions. It is especially true in the case of biaxial compressive loads which lead to interaction between the interfacial free surface and the rigid inclusion. The compression velocity and the matrix viscosity also affect the void formation as they change the time scale. The initial convex profile of the nucleated voids simulated by Needleman (1987) is similar to the shape of interfacial voids simulated at cylindrical inclusions. The formation of "dead zones" at both lines of symmetry of inclusions is observed as well. However, the difference in loading leads to distinct evolution patterns.

Analysis and examples of the transient deformation of interfacial voids at a cylindrical inclusion illustrate how such voids evolve under various external pressures. The sequence of void profiles shown in Fig. 3 provides a good qualitative description of the experiments performed by Kao and Kuhn (1990). Altogether, this demonstrates that advanced finite element codes involving the boundary-fitted mesh motion (Schunk et al., 1995) or other schemes for moving boundaries (Hu et al., 1992; Tezduyar et al., 1992) can successfully simulate highly nonlinear deformation of free or moving boundaries.

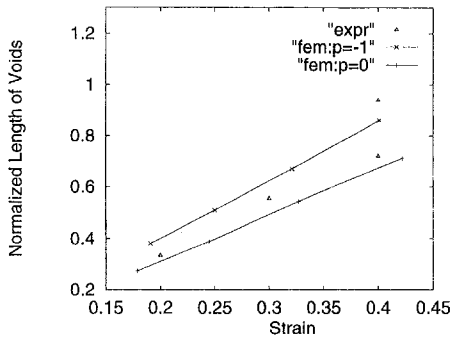

Fig. 5 The dependence of interfacial separation (Dx/r_i) on the compressive strain (V_0t/H). The experimental data is shown for zero outside pressure (Kao and Kuhn, 1990). The data reflect the unstable development of an interfacial cusp. The two sets of data obtained by finite element modeling are shown for $P = \Delta p/(\mu V_0/H) = 0$ and $\Delta p/(\mu V_0/H) = -1$. The final strains mark the onset of interfacial instability.

Acknowledgments

The authors gratefully acknowledge the computing support of the Sandia National Laboratories and Dr. P. R. Schunk, in particular, and useful discussions with Profs. V. N. Kaliakin, J. Lambros, and L. W. Schwartz (University of Delaware). Helpful remarks of Dr. R. C. Becker (Alcoa Technical Center) are also appreciated.

References

Achenbach, J. D., and Zhu, H., 1989, "Effects of interfacial zone on mechanical behavior and failure of fiber-reinforced composites," *Journal of Mechanics and Physics of Solids,* Vol. 37, pp. 381–393.

Beris, A. N., Tsamopoulos, J. A., Armstrong, R. C., and Brown, R. A., 1985, "Creeping motion of a sphere through a Bingham plastic," *Journal of Fluid Mechanics,* Vol. 158, pp. 219–244.

Budiansky, B., Evans, A. G., and Hutchinson, J. W., 1995, "Fiber-matrix debonding effects on cracking in aligned fiber ceramic composites," *International Journal of Solids and Structures,* Vol. 32, pp. 315–328.

Budiansky, B., Hutchinson, J. W., and Slutsky, S., 1982, "Void growth and collapse in viscous solids," *Mechanics of Solids* H. Hopkins and M. Sewell, eds., Pergamon Press, Oxford, pp. 13–45.

Chao, R., and Laws, N., 1997, "The Fiber-Matrix Interface Crack," ASME JOURNAL OF APPLIED MECHANICS, Vol. 64, pp. 992–999.

Christodoulou, K. N., Kistler, S. F., and Schunk, P. R., 1996, "Advances in computational methods," *Liquid Film Coating* S. F. Kistler and S. M. Schweizer, eds., Chapman and Hall, New York, pp. 299–366.

Duvaut, G., and Lions, J. L., 1976, *Inequalities in Mechanics and Physics,* Springer, Berlin.

Harik, V. M., 1997, "Experimental and theoretical studies of interfacial effects in multiphase media," Ph. D. dissertation, University of Delaware.

Hashin, Z., 1991, "The Spherical Inclusion With Imperfect Interface," ASME JOURNAL OF APPLIED MECHANICS, Vol. 53, pp. 444–449.

Hu, H. H., Joseph, D. D., and Crochet, M. J., 1992, "Direct simulation of fluid particle motions," *Theoretical Computational Fluid Dynamics,* Vol. 2, pp. 285–306.

Jasiuk, I., Sheng, P. Y., and Tsuchida, E., 1997, "A Spherical Inclusion in an Elastic Half-Space Under Shear," ASME JOURNAL OF APPLIED MECHANICS, Vol. 64, pp. 471–479.

Kao, A. S., and Kuhn, H. A., 1990, "Physical Modeling of Ductile Fracture During Metal-Forming Process," ASME *Journal of Engineering Materials and Technology,* Vol. 112, pp. 302–308.

Lipscomb, G. G., and Denn, M. M., 1984, "Flow of Bingham fluids in complex geometries," *Journal of Non-Newtonian Fluid Mechanics,* Vol. 14, pp. 337–346.

Mura, T., 1987, *Micromechanics of Defects in Solids,* 2nd Ed., Martinus Nijhoff, Dordrecht, The Netherlands.

Nadai, A., 1950, *Theory of flow and fracture of solids,* McGraw-Hill, New York.

Needleman, A., 1987, "A Continuum Model for Void Nucleation by Inclusion Debonding," ASME JOURNAL OF APPLIED MECHANICS, Vol. 54, pp. 525–531.

Rice, J. R., Rudnicki, J. W., and Simons, D. A., 1978, "Deformation of spherical cavities and inclusions in fluid-infiltrated elastic materials," *International Journal of Solids and Structures,* Vol. 14, pp. 289–303.

Ru, C. Q., 1998, "A Circular Inclusion With Circumferentially Inhomogeneous Sliding Interface in Plane Elastostatics," ASME JOURNAL OF APPLIED MECHANICS, Vol. 65, pp. 30–38.

Schunk, P. R., Sackinger, P. A., Rao, R. R., Chen, K. S., and Cairncross, R. A., 1995, "GOMA—A Full-Newton Finite Element Program for Free and Moving Boundary Problems with Coupled Fluid/Solid Momentum, Energy, Mass, and Chemical Species Transport: User's Guide," Report SAND95-2937 · UC-905, Sandia National Laboratories, Albuquerque, NM.

Taya, M., and Patterson, W. G., 1982, "Growth of debonded void at a rigid secondary particle in a viscous metal," *Journal of Materials Science,* Vol. 17, pp. 115–120.

Tezduyar, T. E., Liou, J., Behr, M., and Mittal, S., 1992, "A new strategy for finite element computations involving moving boundaries and interfaces—the DSD/ST procedure: II. Computation of free-surface flows, two-liquid flows and flows with drafting cylinders," *Computational Methods in Applied Mechanics and Engineering,* Vol. 94, pp. 353–371.

Weast, R. C., ed., 1988, *Handbook of Chemistry and Physics,* CRC Press, New York.

Xia, Z. C., Hutchinson, J. W., Evans, A. G., and Budiansky, B., 1994, "On large scale sliding in fiber-reinforced composites," *Journal of Mechanics and Physics of Solids,* Vol. 42, No. 7, pp. 1139–1158.

Analytic Solution for Eshelby's Problem of an Inclusion of Arbitrary Shape in a Plane or Half-Plane

C. Q. Ru
Department of Mechanical Engineering,
University of Alberta,
Edmonton, Alberta T6G 2G8, Canada

Despite extensive study of the Eshelby's problem for inclusions of simple shape, little effort has been made to inclusions of arbitrary shape. In this paper, with aid of the techniques of analytical continuation and conformal mapping, a novel method is presented to obtain analytic solution for the Eshelby's problem of an inclusion of arbitrary shape in a plane or a half-plane. The boundary of the inclusion is characterized by a conformal mapping which maps the exterior of the inclusion onto the exterior of the unit circle. However, the boundary value problem is studied in the physical plane rather than in the image plane. The conformal mapping is used to construct an auxiliary function with which the technique of analytic continuation can be applied to the inclusion of arbitrary shape. The solution obtained by the present method is exact, provided that the expansion of the mapping function includes only a finite number of terms. On the other hand, if the exact mapping function includes infinite terms, a truncated polynomial mapping function should be used and then the method gives an approximate solution. In particular, this method leads to simple elementary expressions for the internal stresses within the inclusion in an entire plane. Several examples of practical interest are discussed to illustrate the method and its efficiency. Compared to other existing approaches for the two-dimensional Eshelby's problem, the present method is remarked by its elementary characters and applicability to inclusions of arbitrary shape in a plane or a half-plane.

1 Introduction

Stress analysis of an infinite homogeneous elastic body that contains a subdomain undergoing a uniform stress-free strain (Eshelby's problem) is a classic topic. Among various physical phenomena which lead to the Eshelby's problem, thermal stresses and intrinsic stresses, caused by thermal or lattice mismatch between dissimilar materials, are of particular significance. The examples of current interest include passivated interconnect lines and trench isolations in large-scale integrated circuits (see Hu, 1991; Okabayashi, 1993; Burges et al., 1996), and strained semiconductor laser devices (see Gosling and Willis, 1995; Faux et al., 1996, 1997; Downes et al., 1997), where residual stresses induced by thermal or lattice mismatch between buried active components and surrounding materials crucially affect electronic performance of devices and, in some cases, are identified as the major cause of degradation and failure. For these problems, a common simplification made by many researchers is that the thermal or lattice mismatch plays the dominant role and the difference in elastic constants between dissimilar constituents can be ignored. For example, Niwa et al. (1990) have modeled the passivated metallic line as an elliptic thermal inclusion surrounded by an infinite elastic medium of the same elastic constants (called "thermal inclusions," see Hu, 1991). Their results show that the solution based on this simplified model is in reasonably good agreement with accurate numerical solutions.

Various methods have been developed for the Eshelby's problem. Among others, Green's function (see, e.g., Seo and Mura, 1979; Chui, 1980; Hu, 1989; Yu and Sanday, 1991; Muller et al., 1994; Wu and Du, 1995, 1996; Faux et al., 1996; Nozaki and Taya, 1997) is the most widely used method. However, because Green's function involves nontrivial integrations, it cannot be used to obtain an analytic solution for a stress field, especially when the shape of the inclusion is not simple. This explains why, until very recently, most works have focussed on the inclusions of special shape (in addition to those mentioned above, see also Rodin (1996)). To our knowledge, no simpler analytical method is available for inclusions of any shape. Here it should be stated that although the method of the singular integral equation (see e.g. Sherman 1959, Theocaris and Ioakiidis 1977) can be applied to inclusions of any shape, its solution requires substantial numerical effort, making it difficult to apply the solution to complex practical problems. Hence, from a practical viewpoint (see Niwa et al., 1990; Hu, 1991; Faux et al., 1996), a simple method that gives an analytical solution for inclusions of any shape, even only for a two-dimensional case and with a certain degree of approximation, is of great interest. The present work is triggered by such a desire.

It is known that the technique of conformal mapping provides a powerful method for stress analysis of two-dimensional elastic body containing a hole or rigid inclusion of any shape (see Savin, 1961; Cherepanov, 1974). However, it should be clearly recognized that, due to the lack of a conformal mapping which maps, simultaneously, the exterior and interior of the inclusion onto a plane with a simple interface, this technique cannot be directly applied to elastic inclusions of any shape (see, e.g., Jaswon and Bhargava, 1960; List and Silberstein, 1966; Sendeckyj, 1970). In the present paper, combining the techniques of analytical continuation with conformal mapping, a novel procedure is presented to obtain the analytic solution for the Eshelby's problem of an arbitrary shaped inclusion in a plane or a half-plane. One remarkable advantage of this method is that simple elementary expressions can

Contributed by the Applied Mechanics Division of THE AMERICAN SOCIETY OF MECHANICAL ENGINEERS for publication in the ASME JOURNAL OF APPLIED MECHANICS.
Discussion on the paper should be addressed to the Technical Editor, Professor Lewis T. Wheeler, Department of Mechanical Engineering, University of Houston, Houston, TX 77204-4792, and will be accepted until four months after final publication of the paper itself in the ASME JOURNAL OF APPLIED MECHANICS.
Manuscript received by the ASME Applied Mechanics Division, July 7, 1998; final revision, Nov. 17, 1998. Associate Technical Editor: J. R. Barber.

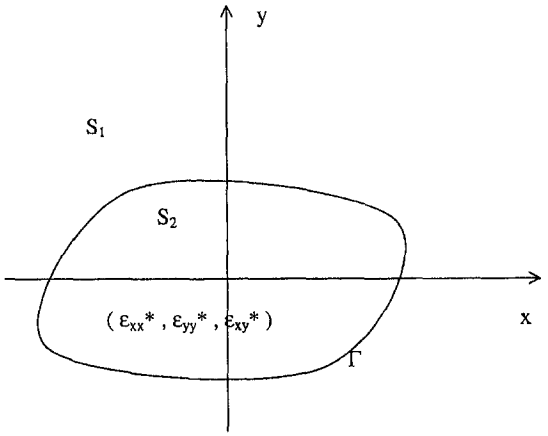

Fig. 1 An inclusion of arbitrary shape in an entire plane

be obtained for the internal stresses within the inclusion in an entire plane.

2 An Inclusion in an Entire Plane

Consider an infinite homogeneous elastic plane containing a subdomain which undergoes uniform stress-free eigenstrains (ϵ^*_{xx}, ϵ^*_{xy}, ϵ^*_{yy}). Let S_2 and S_1 denote the subdomain and its supplement to the elastic plane, respectively, and Γ the interface separating S_2 and S_1. Throughout the paper, the subscripts 1 and 2 are used to identify the respective quantities in S_1 and S_2 (see Fig. 1).

For plane problems, the stresses and the associated displacements can be given in terms of two complex potentials, $\varphi(z)$ and $\psi(z)$, as follows (Muskhelishvili, 1963; England, 1971):

$$2\mu(u + iv) = \kappa\varphi(z) - z\overline{\varphi'(z)} - \overline{\psi(z)},$$

$$\sigma_{xx} + \sigma_{yy} = 2[\varphi'(z) + \overline{\varphi'(z)}],$$

$$\sigma_{xx} - i\sigma_{xy} = \varphi'(z) + \overline{\varphi'(z)} - \bar{z}\varphi''(z) - \psi'(z) \qquad (2.1)$$

where $\kappa = 3 - 4\nu$ for plane strain and $\kappa = (3 - \nu)/(1 + \nu)$ for plane stress, and μ and ν are the shear modulus and Poisson's ratio. In addition, the resultant force acting on the left of an arbitrary arc AB is

$$-i[\varphi(z) + z\overline{\varphi'(z)} + \overline{\psi(z)}]^B_A. \qquad (2.2)$$

Thus, the boundary value problem of the Eshelby's problem has the form

$$\kappa\varphi_1(z) - z\overline{\varphi_1'(z)} - \overline{\psi_1(z)}$$
$$= \kappa\varphi_2(z) - z\overline{\varphi_2'(z)} - \overline{\psi_2(z)} + 2\mu[\delta_1 z + (\delta_2 + i\delta_3)\bar{z}],$$

$$\varphi_1(z) + z\overline{\varphi_1'(z)} + \overline{\psi_1(z)} = \varphi_2(z) + z\overline{\varphi_2'(z)} + \overline{\psi_2(z)}, \quad z \in \Gamma;$$

$$\varphi_1(z) \cong o(1), \quad \psi_1(z) \cong o(1), \quad |z| \to \infty \qquad (2.3)$$

where the two conditions at the interface indicate the continuity of tractions and displacements; the last one represents the zero-stress condition at infinity, and

$$\delta_1 = \frac{\epsilon^*_{xx} + \epsilon^*_{yy}}{2}, \quad \delta_2 = \frac{\epsilon^*_{xx} - \epsilon^*_{yy}}{2}, \quad \delta_3 = \epsilon^*_{xy}. \qquad (2.4)$$

For an arbitrary simply connected inclusion enclosed by a simple curve, it is known (see Kantorovich and Krylov (1958) and Savin (1961)) that there exists a conformal mapping, $z = \omega(\xi)$ that maps the exterior of the inclusion onto the exterior of the unit circle in the ξ-plane. The conformal mapping can be generally expressed by an infinite series in $(1/\xi)$ (see A1) of the Appendix). For many practical problems, the infinite series can be truncated and replaced, with good accuracy, by a *polynomial in* $(1/\xi)$ *which includes only a small number of terms.* Various methods for the construction of an accurate or approximate polynomial mapping function have been extensively developed, and there are plentiful known solutions in the literature. Hence, without loss of generality, we assume that such a polynomial mapping function, $\omega(\xi)$, exists for the inclusion of arbitrary shape. Consequently, it is shown (see (A4) of the Appendix) that there exists a function $D(z)$ which satisfies the condition

$$\bar{z} = D(z), \quad z \in \Gamma \qquad (2.5)$$

and, moreover, is *analytic in the exterior of the inclusion except infinity where it has a pole of finite degree* determined by its asymptotic behavior

$$D(z) \to P(z) + o(1), \quad |z| \to \infty, \qquad (2.6)$$

where $P(z)$ is a polynomial in z of finite degree. A simple procedure for the construction of $D(z)$, in terms of the polynomial mapping function $\omega(\xi)$, is given in the Appendix. In particular, the polynomial $P(z)$ can be easily determined without the details of $D(z)$. Here it should be stated that a condition similar to (2.5) has been used, in a different way, by some authors (see, e.g., Jaswon and Silberstein (1960) and Varley and Cumberbatch (1980)) to elliptic hole or elliptic inclusion. In the present paper, based on the relation (2.5) for inclusions of any shape, the technique of analytical continuation is used to obtain an analytic solution of the Eshelby's problem for an inclusion of any shape. Since the solution of the Eshelby's problem for multiple inclusions can be obtained by simply adding the solutions for individual inclusions, our discussion is confined to the single inclusion.

Throughout the paper, it is assumed that the function $D(z)$, defined by (2.5), (2.6), exists. Thus, the interface conditions in (2.3) along Γ can be written into an equivalent form

$$\varphi_1(z) = \varphi_2(z) + \frac{2\mu}{\kappa + 1}[\delta_1 z + (\delta_2 + i\delta_3)\bar{z}],$$

$$\psi_1(z) + \bar{z}[\varphi_1'(z) - \varphi_2'(z)]$$
$$= \psi_2(z) - \frac{2\mu}{\kappa + 1}[\delta_1\bar{z} + (\delta_2 - i\delta_3)z], \quad z \in \Gamma. \qquad (2.7)$$

Using (2.5), the first condition of (2.7) can be written as

$$\varphi_1(z) - \frac{2\mu}{\kappa + 1}[\delta_1 z + (\delta_2 + i\delta_3)D(z)] = \varphi_2(z), \quad z \in \Gamma. \qquad (2.8)$$

Since the left and the right of (2.8) are analytic functions on two sides of Γ, respectively, the continuity condition (2.8) implies that any one of them can be extended analytically to the other across Γ. Thus, their derivatives are also continuous across the interface Γ, and

$$\varphi_1'(z) - \frac{2\mu}{\kappa + 1}[\delta_1 + (\delta_2 + i\delta_3)D'(z)] = \varphi_2'(z), \quad z \in \Gamma. \qquad (2.9)$$

Using (2.5) and (2.9), the second condition of (2.7) along Γ can be written as

$$\psi_1(z) + \frac{2\mu}{\kappa + 1}[2\delta_1 D(z) + (\delta_2 + i\delta_3)D(z)D'(z)$$
$$+ (\delta_2 - i\delta_3)z] = \psi_2(z), \quad z \in \Gamma. \qquad (2.10)$$

Evidently, the left sides of the interface conditions (2.8) and (2.10) are analytic outside the inclusion, except infinity, where they have the poles of finite degree, while the right sides are analytic inside the inclusion. Thus, one can define two new functions as

$$\Phi(z) = \begin{cases} \varphi_1(z) - \dfrac{2\mu}{\kappa+1}[\delta_1 z + (\delta_2 + i\delta_3)D(z)], & z \in S_1 \\ \varphi_2(z), & z \in S_2 \end{cases} \tag{2.11}$$

$$\Psi(z) = \begin{cases} \psi_1(z) + \dfrac{2\mu}{\kappa+1}[2\delta_1 D(z) + (\delta_2 + i\delta_3)D(z)D'(z) \\ \quad + (\delta_2 - i\delta_3)z], & z \in S_1 \\ \psi_2(z), & z \in S_2 \end{cases} \tag{2.12}$$

both of which are analytical in S_1 and S_2, respectively. It is seen from (2.8), (2.10) that $\Phi(z)$ and $\Psi(z)$ are continuous across Γ and then analytic in the whole plane, except infinity, where they have the poles of finite degree, described by

$$\Phi(z) \Rightarrow -\frac{2\mu}{\kappa+1}[\delta_1 z + (\delta_2 + i\delta_3)P(z)],$$

$$\Psi(z) \Rightarrow \frac{2\mu}{\kappa+1}[2\delta_1 P(z) + (\delta_2 + i\delta_3)Q(z) + (\delta_2 - i\delta_3)z], \quad z \to \infty \tag{2.13}$$

where $Q(z)$, a polynomial in z, is the principle part of the product $D(Z)D'(z)$ at infinity, namely

$$D(z)D'(z) = Q(z) + o(1), \quad |z| \to \infty. \tag{2.14}$$

This simply implies that

$$\Phi(z) = -\frac{2\mu}{\kappa+1}[\delta_1 z + (\delta_2 + i\delta_3)P(z)],$$

$$\Psi(z) = \frac{2\mu}{\kappa+1}[2\delta_1 P(z) + (\delta_2 + i\delta_3)Q(z) + (\delta_2 - i\delta_3)z] \tag{2.15}$$

in the whole z-plane. Once $\Phi(z)$ and $\Psi(z)$ are known, the original complex potentials $\varphi_k(z)$ and $\psi_k(z)$ $(k = 1, 2)$ can be easily obtained from (2.11), (2.12) and then the full-field stresses can be calculated through (2.1). In particular, within the inclusion S_2, we have

$$\psi_2(z) = \frac{2\mu}{\kappa+1}[2\delta_1 P(z) + (\delta_2 + i\delta_3)Q(z) + (\delta_2 - i\delta_3)z]$$

$$\varphi_2(z) = -\frac{2\mu}{\kappa+1}[\delta_1 z + (\delta_2 + i\delta_3)P(z)], \quad z \in S_2. \tag{2.16}$$

The formulas (2.16) give the explicit solution for the internal stress field inside the inclusion in an entire plane. It is emphasized that the expressions (2.16) depend only on the polynomials $P(z)$ and $Q(z)$, but not on $D(z)$ itself. This fact is of great value because $P(z)$ and $Q(z)$ can be easily determined, whereas $D(z)$ involves the inverse of $\omega(\xi)$ and then is relatively troublesome (see the Appendix).

On the other hand, the simple expressions for $\varphi_1(z)$ and $\psi_1(z)$ in S_1 are given by

$$\psi_1(z) = \frac{2\mu}{\kappa+1}[2\delta_1[P(z) - D(z)] + (\delta_2 + i\delta_3)[Q(z) - D(z)D'(z)]],$$

$$\varphi_1(z) = \frac{2\mu}{\kappa+1}(\delta_2 + i\delta_3)(D(z) - P(z)), \quad z \in S_1. \tag{2.17}$$

The function $D(z)$ is given by (A4) in terms of the inverse of the polynomial mapping function $\omega(\xi)$. Evidently, the right of (2.17) depends on $D(z)$, not only on $P(z)$ and $Q(z)$. Hence, the calculation of external stresses is more complicated than the internal stresses. However, the internal stresses are of major interest for many practical problems, such as those related to thermal stress-induced failure of passivated interconnect lines in integrated circuits (see Hu (1991) and Okabayashi (1993)). Therefore, in Section 4, detailed discussion will mainly focus on the internal stress field within the inclusion.

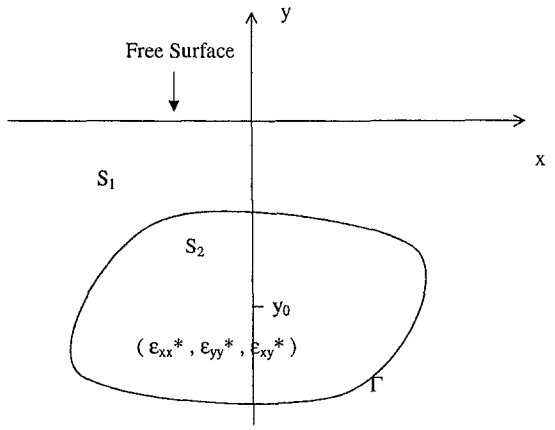

Fig. 2 An inclusion of arbitrary shape in a half-plane

For a thermal inclusion of arbitrary shape, we have $\epsilon_{xx}^* = \epsilon_{yy}^*$, $\epsilon_{xy}^* = 0$ and then $\delta_2 = \delta_3 = 0$. It follows from (2.16), (2.17) that

$$\varphi_2(z) = -\frac{2\mu}{\kappa+1}\delta_1 z, \quad \psi_2(z) = \frac{4\mu}{\kappa+1}\delta_1 P(z), \quad z \in S_2 \tag{2.18}$$

inside the inclusion, and

$$\varphi_1(z) \equiv 0, \quad \psi_1(z) = \frac{4\mu\delta_1}{\kappa+1}[P(z) - D(z)], \quad z \in S_1 \tag{2.19}$$

outside the inclusion. In particular, since the mean stress $(\sigma_{xx} + \sigma_{yy})$ is determined by the first derivative of $\varphi(z)$ (see (2.1)), it follows from (2.18), (2.19) that the mean stress remains constant inside the thermal inclusion and vanishes outside, regardless of the shape of the inclusion. This result has been stated in some earlier works (see, e.g., Gosling and Willis, 1995) for several special cross sections.

3 An Inclusion in a Half-Plane

The Eshelby's problem for an inclusion in a half-plane is of practical importance. For example, for interconnect lines of integrated circuits, because the passivation layer is usually much thinner than the underlying substrate, the passivated metallic line which lies between the passivation and the substrate, can be modeled, more realistically, by a thermal inclusion in a half-plane rather than in an entire plane. Similar circumstance occurs for trench insulations in electronic packaging (see Hu, 1989, 1990). In general, due to the presence of a free surface, the analysis of the Eshelby's problem for a half-plane is significantly complicated. Despite this, the present method can be extended to the inclusion of arbitrary shape in a half-plane.

Assume that the elastic half-plane occupies the lower half-plane, $y < 0$, and contains an internal subdomain that undergoes uniform stress-free eigenstrains $(\epsilon_{xx}^*, \epsilon_{xy}^*, \epsilon_{yy}^*)$. Let S_2 and S_1 denote the subdomain and the remainder of the lower half-plane, respectively, and Γ the interface separating S_2 and S_1 (see Fig. 2). Thus, the boundary value problem for two pairs of analytical functions, $\varphi_k(z)$ and $\psi_k(z)$ $(k = 1, 2)$, defined in S_1 and S_2, respectively, is of the form

$$\kappa\varphi_1(z) - z\overline{\varphi_1'(z)} - \overline{\psi_1(z)} = \kappa\varphi_2(z) - z\overline{\varphi_2'(z)} - \overline{\psi_2(z)} + 2\mu[\delta_1 z + (\delta_2 + i\delta_3)\bar{z}],$$

$$\varphi_1(z) + z\overline{\varphi_1'(z)} + \overline{\psi_1(z)} = \varphi_2(z) + z\overline{\varphi_2'(z)} + \overline{\psi_2(z)}, \quad z \in \Gamma;$$

$$\varphi_1(z) + z\overline{\varphi_1'(z)} + \overline{\psi_1(z)} = 0, \quad y = 0^-$$

$$\varphi_1(z) \cong o(1), \quad \psi_1(z) \cong o(1), \quad |z|_{y\le 0} \to \infty. \tag{3.1}$$

In a manner similar to that described in Section 2, the interface conditions on Γ can be written in the forms of (2.8) and (2.10), where $D(z)$ satisfies the condition (2.5) on Γ and is analytic in the entire plane exterior to the inclusion except infinity where it has a pole of finite degree. Further, one can define two new functions $\Phi(z)$ and $\Psi(z)$ in the lower half-plane, in a way similar to (2.11), (2.12). Thus, it follows that $\Phi(z)$ and $\Psi(z)$ are analytic in the lower half-plane except infinity where they have poles of finite degree, determined by

$$\Psi(z) \Rightarrow \frac{2\mu}{\kappa+1}[2\delta_1 P(z) + (\delta_2 + i\delta_3)Q(z) + (\delta_2 - i\delta_3)z],$$

$$\Phi(z) \Rightarrow -\frac{2\mu}{\kappa+1}[\delta_1 z + (\delta_2 + i\delta_3)P(z)], \quad |z|_{y\le 0} \to \infty \tag{3.2}$$

where $Q(z)$ is a polynomial defined in a manner similar to (2.14). Now, the free-surface condition of (3.1) can be given in terms of $\Phi(z)$ and $\Psi(z)$ as

$$\Phi(z) + \frac{2\mu}{\kappa+1}[2\delta_1 z + (\delta_2 + i\delta_3)D(z) + (\delta_2 - i\delta_3)z\overline{D'(z)}]$$

$$+ \overline{\Psi(z)} + z\overline{\Phi'(z)} - \frac{2\mu}{\kappa+1}[2\delta_1\overline{D(z)} + (\delta_2 - i\delta_3)\overline{D(z)D'(z)}$$

$$+ (\delta_2 + i\delta_3)\bar{z}] = 0, \quad y = 0. \tag{3.3}$$

Since $D(z)$ and its derivative are analytic in the upper half-plane including the real axis, the functions

$$\bar{D}(z), \quad \overline{D'}(z)$$

are analytic in the lower half-plane including the real axis. Thus, the condition (3.3) can be written into the form

$$\Phi(z) - \frac{2\mu}{\kappa+1}[2\delta_1[\bar{D}(z) - z] + (\delta_2 - i\delta_3)\overline{D'}(z)[\bar{D}(z) - z]]$$

$$= \frac{2\mu}{\kappa+1}(\delta_2 + i\delta_3)[z - D(z)] - \bar{\Psi}(z) - z\overline{\Phi'}(z),$$

$$y = 0. \tag{3.4}$$

Evidently, the right and the left of (3.4) are analytic in the lower and the upper half-planes, respectively, except infinity, where they have the same principle part as follows:

$$\frac{2\mu}{\kappa+1}[\delta_1[z - 2\bar{P}(z)] - (\delta_2 + i\delta_3)P(z)$$

$$+ (\delta_2 - i\delta_3)[z\overline{P'}(z) - \bar{Q}(z)]]. \tag{3.5}$$

This implies that the right and the left sides of (3.4) are equal to the polynomial (3.5) in the upper and the lower half-planes, respectively. Thus, we have

$$\Phi(z) = \frac{2\mu}{\kappa+1}[\delta_1[2\bar{D}(z) - 2\bar{P}(z) - z]$$

$$+ (\delta_2 - i\delta_3)\overline{D'}(z)[\bar{D}(z) - z] - (\delta_2 + i\delta_3)P(z)$$

$$+ (\delta_2 - i\delta_3)[z\overline{P'}(z) - \bar{Q}(z)]], \quad y \le 0 \tag{3.6}$$

in the lower half-plane, and

$$\frac{2\mu}{\kappa+1}[\delta_1[z - 2\bar{P}(z)] - (\delta_2 + i\delta_3)P(z) + (\delta_2 - i\delta_3)$$

$$\times [z\overline{P'}(z) - \bar{Q}(z)]] = \frac{2\mu}{\kappa+1}(\delta_2 + i\delta_3)[z - D(z)]$$

$$- \bar{\Psi}(z) - z\overline{\Phi'}(z), \quad y \ge 0 \tag{3.7}$$

in the upper half-plane. In particular, the relation (3.7) implies that

$$\Psi(z) = -z\Phi'(z) - \frac{2\mu}{\kappa+1}[\delta_1[z - 2P(z)]$$

$$- (\delta_2 - i\delta_3)[z - \bar{D}(z) + \bar{P}(z)]$$

$$+ (\delta_2 + i\delta_3)[zP'(z) - Q(z)]], \quad y \le 0. \tag{3.8}$$

Hence, the equations (3.6), (3.8) give the explicit expressions for $\Phi(z)$ and $\Psi(z)$ in the lower half-plane. Consequently, within the inclusion S_2, we have

$$\varphi_2(z) = \frac{2\mu}{\kappa+1}[\delta_1[2\bar{D}(z) - 2\bar{P}(z) - z]$$

$$+ (\delta_2 - i\delta_3)\overline{D'}(z)[\bar{D}(z) - z] - (\delta_2 + i\delta_3)P(z)$$

$$+ (\delta_2 - i\delta_3)[z\overline{P'}(z) - \bar{Q}(z)]], \quad z \in S_2 \tag{3.9}$$

$$\psi_2(z) = -z\varphi_2'(z) - \frac{2\mu}{\kappa+1}[\delta_1[z - 2P(z)]$$

$$- (\delta_2 - i\delta_3)[z - \bar{D}(z) + \bar{P}(z)]$$

$$+ (\delta_2 + i\delta_3)[zP'(z) - Q(z)]], \quad z \in S_2. \tag{3.10}$$

On the other hand, in the lower half-plane exterior to the inclusion, we have

$$\varphi_1(z) = \frac{2\mu}{\kappa+1}[2\delta_1[\bar{D}(z) - \bar{P}(z)] + (\delta_2 - i\delta_3)\overline{D'}(z)$$

$$\times [\bar{D}(z) - z] + (\delta_2 + i\delta_3)[D(z) - P(z)]$$

$$+ (\delta_2 - i\delta_3)[z\overline{P'}(z) - \bar{Q}(z)]], \quad z \in S_1 \tag{3.11}$$

$$\psi_1(z) = -z\varphi_1'(z) - \frac{2\mu}{\kappa+1}[2\delta_1[D(z) - P(z)] + (\delta_2 - i\delta_3)$$

$$\times [\bar{D}(z) - \bar{P}(z)] + (\delta_2 + i\delta_3)[D(z)D'(z)$$

$$+ zP'(z) - zD'(z) - Q(z)]], \quad z \in S_1. \tag{3.12}$$

The expressions (3.9), (3.10) and (3.11), (3.12) give the analytic solution for the Eshelby's problem of an inclusion of arbitrary shape in a half-plane. The solutions are expressed through the function $D(z)$ and the associated polynomials $P(z)$ and $Q(z)$. As shown by the formula (A4) in the Appendix, $D(z)$ is given explicitly in terms of the inverse of the polynomial conformal function. Here, similar to all methods based on conformal mapping (see Muskhelishveli (1963), England (1971), and Savin (1961)), the inverse of the polynomial conformal mapping is treated as the known, although its explicit elementary expression is not always available especially for the inclusions of complex shape.

For a thermal inclusion of any shape in a half-plane, we have $\epsilon^*_{xx} = \epsilon^*_{yy}$, $\epsilon^*_{xy} = 0$ and then $\delta_2 = \delta_3 = 0$. It follows from (3.9)–(3.12) that

$$\varphi_2(z) = \frac{2\mu\delta_1}{\kappa+1}[2\bar{D}(z) - 2\bar{P}(z) - z]$$

$$\psi_2(z) = -\frac{4\mu\delta_1}{\kappa+1}[z\overline{D'}(z) - z\overline{P'}(z) - P(z)], \quad z \in S_2 \tag{3.13}$$

inside the inclusion, and

$$\varphi_1(z) = \frac{4\mu\delta_1}{\kappa+1}[\bar{D}(z) - \bar{P}(z)]$$

$$\psi_1(z) = -\frac{4\mu\delta_1}{\kappa+1}[z[\overline{D'}(z) - \overline{P'}(z)] + [D(z) - P(z)]], \quad z \in S_1 \quad (3.14)$$

outside the inclusion. It will be seen that, due to the appearance of a free surface, the internal stresses are no longer uniform even for an elliptical thermal inclusion embedded in a half-plane.

4 Examples

4.1 An Elliptic Inclusion in an Entire Plane. For an elliptic inclusion, the explicit expressions for $D(z)$ and $P(z)$ are given by (A9) and (A10) of the Appendix, respectively. If the inclusion is in an entire plane, we choose $y_0 = 0$ and then the complex potentials within the inclusion are given by

$$\psi_2(z) = \frac{2\mu}{\kappa+1}\left[\frac{2\delta_1}{R^2} + \frac{(\delta_2 + i\delta_3)}{R^4} + (\delta_2 - i\delta_3)\right]z$$

$$\varphi_2(z) = -\frac{2\mu}{\kappa+1}\left[\delta_1 + \frac{(\delta_2 + i\delta_3)}{R^2}\right]z, \quad z \in S_2. \quad (4.1)$$

On the other hand, the complex potentials in the exterior of the inclusion is given by

$$\psi_1(z) = \frac{2\mu}{\kappa+1}\left[\frac{2\delta_1(1-R^4)}{R^2}[z - dR\xi] + (\delta_2 + i\delta_3)\left[\frac{z}{R^4} - \left[R^2 z + \frac{d}{R}(1-R^4)\xi\right]\left[R^2 + \frac{d}{R}(1-R^4)\frac{\xi}{2dR\xi - z}\right]\right]\right],$$

$$\varphi_1(z) = \frac{2\mu}{\kappa+1}\frac{(\delta_2 + i\delta_3)(1-R^4)}{R^2}(dR\xi - z), \quad z \in S_1 \quad (4.2)$$

where $\xi = \omega^{-1}(z)$ is the inverse of the conformal transformation, given by (A7). It can be verified that these results agree with the known solution (see, e.g., Jaswon and Bhargava, 1961).

4.2 An Elliptic Thermal Inclusion in a Half-Plane. Now, let us consider the internal stresses within an elliptic *thermal* inclusion embedded in a half-plane (see Fig. 2). In this case, the internal stresses are determined by (3.13) with

$$\bar{D}(z) = R^2(z + iy_0) + \frac{d}{R}(1-R^4)\overline{\omega^{-1}}(z) + iy_0,$$

$$\bar{P}(z) = \frac{z}{R^2} + iy_0\frac{R^2+1}{R^2} \quad (4.3)$$

where

$$\overline{\omega^{-1}}(z) = \frac{z + iy_0}{2dR}\left[1 + \sqrt{1 - \left[\frac{2d}{z + iy_0}\right]^2}\right]. \quad (4.4)$$

If the depth of the inclusion is much larger than its size, then for $z \in S_2$, we have

$$\overline{\omega^{-1}}(z) = \frac{z + iy_0}{dR} + O\left(\frac{d^2}{|y_0|^2}\right), \quad |y_0| \gg dR. \quad (4.5)$$

Thus, as expected, the results (3.13) with (4.3), (4.4) reduce to (4.1) (except a constant which does not influence the stress field). In general case, however, the uniformity of internal stresses is diminished even for an elliptic thermal inclusion in a half-plane.

It is known (see Niwa et al. (1990) and Okabayashi (1993)) that voiding of interconnect lines is governed largely by the internal mean stress. It is found from (3.13), (4.3), and (4.4) that the mean stress field within the inclusion is

$$\sigma_{xx} + \sigma_{yy} = \frac{-8\mu\delta_1}{(\kappa+1)}\left[1 + \frac{1-R^4}{R^2}\mathrm{Re}\left[1 - \frac{1}{\sqrt{1 - \left(\frac{2d}{z + iy_0}\right)^2}}\right]\right], \quad z \in S_2. \quad (4.6)$$

Hence, to reduce the level of the mean stress within the inclusion, the simple formula (4.6) could provide useful insight into the design of the top passivation layer and the aspect ratio of the interconnect lines. For an elliptic thermal inclusion embedded in an entire plane, the internal mean stress is uniform. For an elliptic thermal inclusion in a half-plane, due to the effect of the free surface, the internal mean stress is no longer uniform. For instance, along the minor principal axis (with $x = 0$), the internal mean stress is

$$\sigma_{xx} + \sigma_{yy} = \frac{-8\mu\delta_1}{(\kappa+1)}\left[1 - \frac{R^4-1}{R^2}\left[1 - \frac{1}{\sqrt{1 + \frac{4d^2}{(y + y_0)^2}}}\right]\right]. \quad (4.7)$$

Evidently, in qualitative agreement with the three-dimensional results of Seo and Mura (1979), the effect of the free surface decreases with the depth of the inclusion. The formula (4.7) indicates that for some combination of the depth and the aspect ratio, the mean stress along the minor axis could change the sign at an interior point y^*, if any, determined by

$$\sqrt{1 + \left(\frac{2d}{y^* + y_0}\right)^2} = \frac{R^4 - 1}{R^4 - 1 - R^2}. \quad (4.8)$$

For example, when the aspect ratio is 2, the condition (4.8) gives

$$\frac{|y^* + y_0|}{\sqrt{a^2 - 4d^2}} = \sqrt{\frac{75}{39}} \approx 1.4.$$

Thus, such an interior point y^* exists, provided the depth y_0 is less than 1.2 the semiminor axis. These results show that the free surface has a significant effect on the internal stresses, especially when the inclusion depth is small.

4.3 Hypotrochoidal Inclusions. Next, we consider hypotrochoidal inclusions (see the Appendix). These inclusions are of practical interest because, with suitable combination of the parameters (say, $m = 2/[n(n+1)]$, see Fig. 3, and Savin (1961), and England (1971)), they provide good approximations to regular polygonal inclusions. For instance, the hypotrochoid with $n = 2$ and $m = \frac{1}{3}$ resembles a triangle with rounded corners, and the hypotrochoid with $n = 3$ and $m = \frac{1}{6}$ resembles a square with rounded corners. Although the hypotrochoidal hole and rigid inclusion have been studied by some authors (see, e.g., Milne-Thomson (1968) and England (1971)), it seems that the explicit solutions for the Eshelby's problem of hypotrochoidal inclusions are not available in the literature.

Consider a hypotrochoid thermal inclusion in an entire plane. In this case, the complex potentials within the inclusion are given by (see (2.18) and (A14) of the Appendix)

$$\varphi_2(z) = -\frac{2\mu}{\kappa+1}\delta_1 z, \quad \psi_2(z) = \frac{4\mu\delta_1 m}{\rho^{n-1}(\kappa+1)}z^n, \quad z \in S_2. \quad (4.9)$$

Thus, the exact internal stresses are given by

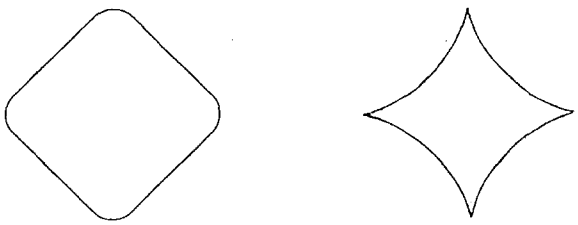

Hypotrochoid with rounded corners (mn(n+1)=2)

Hypotrochoid with cusps (mn =1)

Fig. 3 Hypotrochoidal inclusions

$$z = re^{i\theta}, \quad \sigma_{xx} = \frac{-4\mu\delta}{(\kappa+1)}\left(1 + \frac{nmr^{n-1}\cos[(n-1)\theta]}{\rho^{n-1}}\right),$$

$$\sigma_{yy} = \frac{-4\mu\delta}{(\kappa+1)}\left(1 - \frac{nmr^{n-1}\cos[(n-1)\theta]}{\rho^{n-1}}\right),$$

$$\sigma_{xy} = \frac{4\mu\delta}{\kappa+1}\frac{nmr^{n-1}\sin[(n-1)\theta]}{\rho^{n-1}}, \quad z \in S_2. \quad (4.10)$$

Since the hypotrochoidal inclusions provide approximations to regular polygons, it is of interest to compare the above formulas with, say, recent numerical results of Nozaki and Taya (1997) for regular polygonal inclusions. First, at the center of the inclusion ($x = y = 0$), the stresses given by (4.10) are identical to the Eshelby's solution for a circular inclusion. This is in agreement with Nozaki and Taya's conclusion. On the other hand, different from the logarithmic singularity appearing at the sharp corners of a polygon, the internal stresses given by (4.10) for hypotrochoids remain bounded for any combination of the parameters m and n, even when $mn = 1$ and then the hypotrochoidal inclusion has $(n + 1)$ cusps (see Fig. 3). This is due to that fact that the internal angle between two neighboring boundary curves reduces to zero as the tip of the cusp is approached.

For a more detailed comparison, let us consider strain distribution along the positive x-axis ($\theta = 0$) under the conditions of plane strain. The present formulas (4.10) give

$$\frac{\epsilon_{xx} + \delta}{\delta} = \frac{1}{2(1-\nu)}\left[1 - mn\left(\frac{x}{\rho}\right)^{n-1}\right]$$

$$\frac{\epsilon_{yy} + \delta}{\delta} = \frac{1}{2(1-\nu)}\left[1 + mn\left(\frac{x}{\rho}\right)^{n-1}\right],$$

$$0 \le x \le (1+m)\rho. \quad (4.11)$$

First, the results (4.11) with $m = 2/[n(n + 1)]$ (it gives the lowest-order approximation to regular polygons, see England (1971)) are compared to the numerical solutions of Nozaki and Taya (see their Figs. 3 and 4, where $\nu = 0.3$). A good agreement is found in the major part of the interval considered (say, when $0 \le x \le 0.8(1 + m)\rho$). However, a large error occurs in the neighborhood of the corners where, as stated previously, the solution for polygons exhibits logarithmic singularity whereas the results (4.10), (4.11) for the hypotrochoids remain bounded. This discrepancy is apparently due to the fact that the hypotrochoidal inclusion with $m = 2/[n(n + 1)]$ has rounded corners and cannot resemble local geometry of a polygon at its sharp corners.

Since the hypotrochoids with $mn = 1$ have $(n + 1)$ cusps, it could resemble, more accurately, a polygon near its sharp corners provided n is not large. In fact, the formulas (4.11) with $mn = 1$ give

$$\frac{\epsilon_{xx} + \delta}{\delta} = \frac{1}{2(1-\nu)}\left[1 - \left(1 + \frac{1}{n}\right)^{n-1}\right]$$

$$\frac{\epsilon_{yy} + \delta}{\delta} = \frac{1}{2(1-\nu)}\left[1 + \left(1 + \frac{1}{n}\right)^{n-1}\right],$$

$$x = (1+m)\rho \quad (4.12)$$

at the cusps. Note that

$$\frac{3}{2} \le \left(1 + \frac{1}{n}\right)^{n-1} < e, \quad n \ge 2$$

a comparison of (4.12) with Nozaki and Taya's Figs. 3 and 4 indicates that (4.12) provides a good estimate for local strains near the sharp corners of a regular polygon provided, say, $n < 5$. Hence, despite their elementary forms, the formulas (4.10) can be used, with a good accuracy, to estimate the internal stresses within a regular polygonal inclusion.

4.4 Rectangular Inclusion. An important geometrical shape of thermal inclusions in many practical problems (e.g., electronic packaging) is the rectangle (see, e.g., Hu (1989, 1990)). Based on a truncated polynomial mapping function (see (A15) of the Appendix), it follows from (2.18) and (A.17) that $\varphi_2(z)$ and $\psi_2(z)$ inside the rectangular thermal inclusion, centered at the origin and with the sides parallel to the coordinate axes, can be approximated by

$$\varphi_2(z) = -\frac{2\mu}{\kappa+1}\delta_1 z$$

$$\psi_2(z) = \frac{4\mu\delta_1}{\kappa+1}\left[\frac{(P-\bar{P})^2}{24c^2}z^3 + \frac{P+\bar{P}}{2}\left[1 - \frac{(P-\bar{P})^2}{8}\right]z\right],$$

$$z \in S_2 \quad (4.13)$$

where c and P are two geometrical parameters determined by the size and aspect ratio of the rectangular inclusion, respectively (see the Appendix). Thus, the internal stresses within the inclusion are given by

$$\sigma_{xx} = -\frac{4\mu}{\kappa+1}\delta_1 - \frac{4\mu\delta_1}{\kappa+1}\left[\frac{(P-\bar{P})^2}{8c^2}r^2\cos 2\theta + \frac{P+\bar{P}}{2}\left[1 - \frac{(P-\bar{P})^2}{8}\right]\right]$$

$$\sigma_{yy} = -\frac{4\mu}{\kappa+1}\delta_1 + \frac{4\mu\delta_1}{\kappa+1}\left[\frac{(P-\bar{P})^2}{8c^2}r^2\cos 2\theta + \frac{P+\bar{P}}{2}\left[1 - \frac{(P-\bar{P})^2}{8}\right]\right]$$

$$\sigma_{xy} = \frac{4\mu\delta_1}{\kappa+1}\frac{(P-\bar{P})^2}{8c^2}r^2\sin 2\theta. \quad (4.14)$$

It can be verified that (4.14) reduces to (4.10) with $n = 3$ and $m = \frac{1}{6}$ when $k = \frac{1}{4}$ (the rectangle becomes a square, see the Appendix). Further, it follows from (4.14) that the internal deviatoric stress is

$$\sigma_{xx} - \sigma_{yy} = -\frac{8\mu\delta_1}{\kappa+1}\left[\frac{(P-\bar{P})^2}{8c^2}r^2\cos 2\theta + \frac{P+\bar{P}}{2}\left[1 - \frac{(P-\bar{P})^2}{8}\right]\right] \quad (4.15)$$

which vanishes at the center only if the rectangle is a square.

When the aspect ratio of the rectangle is very large, the number k approaches zero and then the limit values of (4.14) for the case of plane strain (then $\epsilon_{zz} = 0$) read

$$\sigma_{xx} = -\frac{2\mu}{1-\nu}\delta_1, \quad \sigma_{zz} = \frac{-2\mu\delta_1}{1-\nu}(1 + \nu - \nu^2),$$

$$\sigma_{yy} = \sigma_{xy} = 0 \tag{4.16}$$

where the direction z is perpendicular to the x-y plane. Hence, the internal stress field is in a bi-axial stress state in the x-z plane. These results are in good agreement with those obtained by Niwa et al. (1990) for a thin-film conductor of elliptic cross section.

5 Conclusions

A general method is presented to obtain an analytic solution for the Eshelby's problem of inclusions of any shape in a plane or in a half-plane. The method is based on the auxiliary function $D(z)$, which can be constructed, accurately or approximately, from the associated polynomial mapping function. With aid of the function $D(z)$, the technique of analytic continuation can be applied to the inclusion of arbitrary shape in a plane or a half-plane. It is emphasized that the problem is studied in the original physical plane rather than in the image plane. The solution obtained by the present method is exact, provided that the mapping function includes only a finite number of terms. On the other hand, if the exact mapping function includes an infinite number of terms, a truncated polynomial mapping function should be used and then the method gives an approximate solution. In particular, this method gives simple elementary expressions for the internal stresses within the inclusion in an entire plane, even without the need of determining $D(z)$. This fact makes the present method particularly useful for internal stress analysis and optimal design of the shapes of inclusions in some practical problems, such as those mentioned in the Introduction. Several example are discussed to illustrate the method and its efficiency. It is believed that the method provides an effective approach to obtain an analytical solution for the Eshelby's problem of an inclusion of arbitrary shape in a plane or a half-plane.

Acknowledgment

The author is grateful to Dr. P. Schiavone and Dr. A. Mioduchowski for useful discussions. The financial support of the Natural Science and Engineering Research Council of Canada is gratefully acknowledged.

References

Burges, U., Eppler, I., Schiling, W., Schroeder, H., and Trinkaus, H., 1996, "Analysis of stresses in passivated metal lines," *Stress-Induced Phenomena in Metalization* ed. P. S. Ho, J. Bravman, C. Y. Li and J. Sanchez, eds., AIP Conference Proceedings 373, AIP, New York.

Cherepanov, G. P., 1974, "Inverse problem of the plane theory of elasticity," *J. Mech. Appl. Math. (PMM),* Vol. 38, pp. 963–979.

Chiu, Y. P., 1980, "On the Internal Stresses in a Half-Plane and a Layer Containing Localized Inelastic Strains or Inclusions," ASME JOURNAL OF APPLIED MECHANICS, Vol. 47, pp. 313–318.

Downes, J. R., Faux, D. A., and O'Reilly, E. P., 1997, "A simple method for calculating strain distribution in quantum dot structures," *J. Appl. Phys.,* Vol. 81, pp. 6700–6702.

England, A. H., 1971, *Complex Variable Methods in Elasticity,* Wiley-Interscience, London.

Faux, D. A., Downes, J. R., and O'Reilly, E. P., 1996, "A simple method for calculating strain distribution in quantum-wire structures," *J. Appl. Phys.,* Vol. 80, pp. 2515–2517.

Faux, D. A., Downes, J. R., and O'Reilly, E. P., 1997, "Analytic solutions for strain distribution in quantum-wire structures," *J. Appl. Phys.,* Vol. 82, pp. 3754–3762.

Gosling, T. J., and Willis, J. R., 1995, "Mechanical stability and electronic properties of buried strained quantum wire arrays," *J. Appl. Phys.,* Vol. 77, pp. 5601–5610.

Hu, S. M., 1989, "Stress from a parallelepipedic thermal inclusion in a semispace," *J. Appl. Phys.,* Vol. 66, pp. 2741–2743.

Hu, S. M., 1990, "Stress from isolation trenches in silicone substrates," *J. Appl. Phys.,* Vol. 67, pp. 1092–1101.

Hu, S. M., 1991, "Stress-related problems in silicon technology," *J. Appl. Phys.,* Vol. 70, pp. R53–R80.

Jaswon, M. A., and Bhargava, R. D., 1961, "Two-dimensional elastic inclusion problems," *Proc. Camb. Phil. Soc. Math. Phys. Sci.,* Vol. 57, pp. 669–679.

Kantorovich, L. V., and Krylov, V. I., 1958, *Approximate methods of higher analysis,* Wiley Interscience, London.

List, R. D., and Silberstein, J. P. O., 1966, "Two-dimensional elastic inclusion problems," *Proc. Camb. Phil. Soc. Math. Phys. Sci.,* Vol. 62, pp. 303–311.

Milne-Thomson, L. M., 1968, *Plane Elastic Systems,* Springer-Verlag, Berlin.

Muller, W. H., Harris, D. O., and Dedhia, D., 1994, "Stress Intensity Factors of Two-Dimensional and Three-Dimensional Cracks Next to a Thermally Mismatch Inclusion," ASME JOURNAL OF APPLIED MECHANICS, Vol. 61, pp. 731–735.

Muskhelishvili, N. I., 1963, "Some basic problems of the mathematical theory of elasticity," P. Noordhoff Ltd., The Netherlands.

Niwa, H., Yagi, H., Tsuchikawa, H., and Kato, M., 1990, "Stress distribution in an aluminum interconnect of very large scale integration," *J. Appl. Phys.* Vol. 68, pp. 328–333.

Nozaki, H., and Taya, M., 1997, "Elastic Fields in a Polygon-Shaped Inclusion With Uniform Eigenstrains," ASME JOURNAL OF APPLIED MECHANICS, Vol. 64, pp. 495–501.

Okabayashi, H., 1993, "Stress-induced void formation in metallization for integrated circuits," *Materials Science and Engineering,* Vol. R, pp. 191–241.

Rodin, G. J., 1996, "Eshelby's inclusion problem for polygons and polyhedra," *J. Mech. Phys. Solids,* Vol. 44, pp. 1977–1995.

Ru, C. Q., and Schiavone, P., 1996, "On the elliptical inclusion in anti-plane shear," *Math. Mech. Solids,* Vol. 1, pp. 327–333.

Savin, G. N., 1961, *Stress Concentration Around Holes,* Pergamon Press, London.

Sendeckyj, G. P., 1970, "Elastic inclusion problems in plane elastostatics," *Int. J. Solids & Struct.,* Vol. 6, pp. 1535–1543.

Seo, K., and Mura, T., 1979, "The Elastic Field in a Half-Space due to Ellipsoidal Inclusion With Uniform Dilatational Eigenstrains," ASME JOURNAL OF APPLIED MECHANICS, Vol. 46, pp. 568–572.

Sherman, D. I., 1959, "On the problem of plane strain in non-homogeneous media," *Nonhomogeneity in Elasticity and Plasticity,* Pergamon Press, London, pp. 3–20.

Theocaris, P. S., and Ioakimidis, N. I., 1977, "The inclusion problem in plane elasticity," *Quart. J. Mech. Appl. Math.,* Vol. 30, pp. 437–448.

Varley, E., and Cumberbatch, E., 1980, "Finite deformation of elastic materials surrounding cylindrical holes," *J. Elasticity,* Vol. 10, pp. 341–405.

Wu, L., and Du, S. Y., 1995, "The Elastic Field Caused by a Circular Cylindrical Inclusion. Part I and Part II," ASME JOURNAL OF APPLIED MECHANICS, Vol. 62, pp. 579–584 and 585–589.

Wu, L., and Du, S. Y., 1996, "The Elastic Field in a Half-Space With a Circular Cylindrical Inclusion," ASME JOURNAL OF APPLIED MECHANICS, Vol. 63, pp. 925–932.

Yu, H. Y., and Sanday, S. C., 1991, "Elastic field in jointed semi-infinite solids with an inclusion," *Proc. Royal. Soc. London,* Vol. 434, pp. 521–530.

APPENDIX

Here, a simple method is described to construct the auxiliary function $D(z)$, which is analytic in the exterior of the inclusion and satisfies the condition (2.5) along the boundary of the inclusion. First, according to the conformal mapping theory (see, e.g., Kantorovich & Krylov, 1958), the exterior of the inclusion can be mapped onto the exterior of the unit circle in the ξ-plane by an analytical function of the form

$$z = \omega(\xi) = \lambda\xi + \sum_{k=0}^{\infty} c_k \xi^{-k} \tag{A1}$$

where λ is a real number and c_k ($k = 0, 1, \ldots$) are some complex constants. Various methods for accurate or approximate determination of the expansion (A1) are described in the literature (see Savin, (1961) and Kantorovich and Krylov (1958)). For many simple boundary curves, the mapping function (A1) includes only a finite number of terms. On the other hand, for many practical problems, the truncation of the infinite series (A1) to finite (say, N) terms offers a good approximation to (A1). In fact, almost all existing methods of conformal mapping are based on an expansion with only a finite number of terms. Hence, under fairly general conditions, one can reasonably assume that the conformal mapping (A1) is a finite polynomial in $(1/\xi)$ as follows:

$$z = \omega(\xi) = \lambda\xi + \sum_{k=0}^{N} c_k \xi^{-k}. \tag{A2}$$

In this case, at the boundary Γ (or equivalently, along the unit circle of the ξ-plane), we have

$$\bar{z} = \bar{\omega}\left(\frac{1}{\xi}\right) = \frac{\lambda}{\xi} + \sum_{k=0}^{N} \bar{c}_k \xi^k, \quad z \in \Gamma, \quad |\xi| = 1. \tag{A3}$$

Thus, the desired function $D(z)$ can be defined by

$$D(z) = \bar{\omega}\left(\frac{1}{\omega^{-1}(z)}\right) = \frac{\lambda}{\omega^{-1}(z)} + \sum_{k=0}^{N} \overline{c_k}[\omega^{-1}(z)]^k \quad \text{(A4)}$$

where $\omega^{-1}(z)$ is the inverse function of (A2). Because $\omega^{-1}(z)$ is analytic in the exterior of the inclusion (except at infinity where it has a simple pole) and the right of (A3) is analytic in the exterior of the unit circle in the ξ-plane (except at infinity where it has a pole of the degree N) $D(z)$ is analytic in the exterior of the inclusion (except at the point at infinity where it has a pole of the degree N). Therefore, the auxiliary function $D(z)$ complying with the condition (2.5) and (2.6) exists.

To determine the asymptotic expansion of $D(z)$ at infinity, let us assume that

$$D(z) = \sum_{k=-\infty}^{N} b_k z^k, \quad |z| \to \infty \quad \text{(A5)}$$

where b_k ($k = N, N-1, \ldots$) are some complex constants. Combining (A2), (A3) with (A4) yields

$$\frac{\lambda}{\xi} + \sum_{k=0}^{N} \overline{c_k}\xi^k = \sum_{k=-\infty}^{N} b_k\left[\lambda\xi + \sum_{n=0}^{N} c_n\xi^{-n}\right]^k. \quad \text{(A6)}$$

The coefficients b_k ($k = N, N-1, \ldots$) can be determined by equating the coefficients for like terms of ξ. In particular, the polynomial $P(z)$ is related to only $(N+1)$ coefficients b_k ($k = N, N-1, \ldots 0$) and then can be determined easily. In what follows, some examples serve to illustrate the details.

Elliptic Inclusion

Let the ellipse have the semimajor axes a and the foci $2d$ ($2d < a$). Assume that the center of the ellipse is located at $y = y_0$ (with $x = 0$) and its principal axes are parallel to the coordinate axes. Thus, the required conformal mapping and its inverse can be given by (see Muskhelishvili (1963) and Ru and Schiavone (1996))

$$z = \omega(\xi) \equiv d\left(R\xi + \frac{1}{R\xi}\right) + iy_0,$$

$$\xi = \omega^{-1}(z) = \frac{z - iy_0}{2dR}\left[1 + \sqrt{1 - \left[\frac{2d}{z - iy_0}\right]^2}\right] \quad \text{(A7)}$$

where

$$R = \frac{a + \sqrt{a^2 - 4d^2}}{2d} > 1. \quad \text{(A8)}$$

Thus, using (A4) and (A7), the function $D(z)$ is of the form

$$D(z) = R^2(z - iy_0) + \frac{d}{R}(1 - R^4)\omega^{-1}(z) - iy_0 \quad \text{(A9)}$$

where $\omega^{-1}(z)$ is given by (A7). Obviously, from (A6), (A9), $P(z)$ is easily obtained as

$$P(z) = \frac{z}{R^2} - iy_0\frac{R^2 + 1}{R^2}. \quad \text{(A10)}$$

Hypotrochoidal Inclusions

Next, let us consider the hypotrochoids defined by

$$z = \omega(\xi) = \rho\left(\xi + \frac{m}{\xi^n}\right) + iy_0, \quad \rho > 0, \quad 0 \le m \le \frac{1}{n} \quad \text{(A11)}$$

with $|\xi| = 1$. It is known that the mapping (A11) maps the outside of the hypotrochoid onto the exterior of the unit circle (see Muskhelishvili (1963) and England (1971)). Further, for the hypotrochoids (A11), we have

$$\bar{z} = \rho\left(\frac{1}{\xi} + m\xi^n\right) - iy_0, \quad z \in \Gamma, \quad |\xi| = 1.$$

Thus, the function $D(z)$ is given by

$$D(z) = \rho\left(\frac{1}{\omega^{-1}(z)} + \frac{m^2\rho}{z - iy_0 - \rho\omega^{-1}(z)}\right) - iy_0 \quad \text{(A12)}$$

where the inverse $\omega^{-1}(z)$ should be determined by (A11). The asymptotic expansion of $D(z)$ can be obtained through (A6). For example, when $y_0 = 0$, it is easy to verify that

$$b_0 = b_1 = \ldots = b_{N-1} = 0, \quad b_N = \frac{m}{\rho^{N-1}} \quad \text{(A13)}$$

then

$$P(z) = \frac{mz^n}{\rho^{n-1}}. \quad \text{(A14)}$$

Rectangular Inclusion

Finally, let us consider the rectangle, centered at the origin and with the sides parallel to the coordinate axes. In this case, the exact mapping function $\omega(\xi)$ includes infinite terms and, therefore, a truncated polynomial mapping function should be used. To the lowest-order approximation, the exterior of a rectangle can be mapped onto the exterior of the unit circle by the mapping function (see the formula (1.26) of Savin (1961))

$$z = \omega(\xi) = c\left[\xi + \frac{P + \bar{P}}{2}\frac{1}{\xi} + \frac{(P - \bar{P})^2}{24}\frac{1}{\xi^3}\right],$$

$$c > 0, \quad P \equiv e^{2ik\pi} \quad \text{(A15)}$$

with $|\xi| = 1$, where c and k are two real numbers determined by the size and aspect ratio of the rectangle, respectively. In particular, the corner in the first quadrant is identified by $e^{ik\pi}$. Thus, the rectangle becomes a square when $k = \frac{1}{4}$. In this case, the mapping function (A15) reduces to (A11) with $n = 3$ and $m = \frac{1}{6}$ through a rotation of the coordinate system.

It is seen from (A4) and (A15) that

$$D(z) = c\left[\frac{1}{\omega^{-1}(z)} + \frac{P + \bar{P}}{2}\omega^{-1}(z) + \frac{(P - \bar{P})^2}{24}[\omega^{-1}(z)]^3\right] \quad \text{(A16)}$$

where $\omega^{-1}(z)$ is the inverse of (A15). Further, it can be verified from (A6) that

$$P(z) = \frac{(P - \bar{P})^2}{24c^2}z^3 + \frac{P + \bar{P}}{2}\left[1 - \frac{(P - \bar{P})^2}{8}\right]z. \quad \text{(A17)}$$

M. E. Levenston[1]
Assoc. Mem. ASME

E. H. Frank

A. J. Grodzinsky
Mem. ASME

Continuum Electromechanics Group,
Department of Electrical Engineering
and Computer Science,
Center for Biomedical Engineering,
Massachusetts Institute of Technology,
Cambridge, MA 02139

Electrokinetic and Poroelastic Coupling During Finite Deformations of Charged Porous Media

Due to microstructural interactions between the charged solid matrix and ionic interstitial fluid, hydrated biological tissues and other porous media may exhibit macroscopic coupling between solid deformation, fluid, and electrical flows. In the present manuscript, we develop a variationally motivated finite deformation continuum theory for describing such coupled phenomena. The theoretical formulation combines descriptions of poroelastic and electroquasistatic subsystems along with a continuum electromechanical coupling law, and leads to a five-field finite element formulation. Several axisymmetric problems are presented as examples of mechanical-to-electrical and electrical-to-mechanical transduction phenomena in common experimental configurations.

1 Introduction

Models for saturated porous media are often used to describe the mechanical response of hydrated biological tissues, including articular cartilage (Mow et al., 1980; Eisenberg and Grodzinsky, 1987), blood vessels (Kenyon, 1979; Simon and Gaballa, 1988), corneal stroma (Friedman, 1971; Eisenberg and Grodzinsky, 1987), intervertebral disk (Simon et al., 1985), and skin (Oomens et al., 1987). In such continuum formulations, microstructural fluid-solid interactions are represented by macroscopic coupling between tissue deformation, fluid pressurization, and fluid flow. Although this approach accurately represents tissue behavior over a wide range of physical situations, other microstructural interactions of electrical or chemical origin may produce additional macroscopic behaviors beyond the scope of such theories.

The solid matrix of articular cartilage, which occupies approximately 20 percent of the total tissue volume, is composed of a complex network of biological macromolecules, primarily collagen and aggregated proteoglycans (Fig. 1). The proteoglycans contain a large number of sulfated glycosaminoglycan side chains which are negatively charged at physiological pH. Principally due to these molecules, the solid matrix contains a high negative fixed (or immobile) charge density on the order of 0.2 M (Maroudas, 1979). Conversely, the interstitial fluid contains an excess of positively charged dissociated ions in order to maintain tissue electroneutrality at a macrocontinuum length scale. Microstructurally, these ions form electrical dipole layers (double layers) with the fixed charge groups of the solid matrix. Because the microstructural arrangements of solid, fluid, and ionic constituents must satisfy both microscopic and macroscopic balance laws, the macroscopic mechanical, electrical, and chemical fluxes are all coupled. Manifestations of such coupling mechanisms include the phenomena of streaming potential and streaming current, (mechanical-to-electrical) electroosmosis (electrical-to-mechanical), and osmotically induced swelling (chemical-to-mechanical) (Dukhin and Derjaguin, 1974).

A number of continuum theories have been proposed to describe these macroscopic couplings in porous membranes and biological tissues, including single continuum (Helfferich, 1962; Eisenberg and Grodzinsky, 1987; Frank and Grodzinsky, 1987b; Simon et al., 1996) and multiple continuum mixture theory (Swenson, 1979; Lai et al., 1991; Snijders et al., 1992; Gu et al., 1993; Huyghe and Janssen, 1997) approaches. Although analytical solutions are possible for simple geometries and material property distributions, treatment of more complex physical situations requires a numerical implementation. To date, the majority of such implementations have been restricted to situations where boundary conditions are primarily mechanical or chemical in nature and macroscopic electric fields are assumed to have negligible impact (Snijders et al., 1995; Simon et al., 1996). In the present study, we address a different class of problems in which boundary conditions are primarily mechanical or electrical in nature and macroscopic chemical concentration gradients are assumed to have negligible impact on the electromechanical phenomena of interest. Analytical (Neev and Yeatts, 1989) and finite element (Lewis and Garner, 1972; Massé and Berthier, 1996) approaches have been introduced for modeling electrokinetic coupling in geomechanics, but these methods have been primarily restricted to rigid or infinitesimally deformed solids and deformation-independent material properties. In contrast, consideration of the effects of finite deformation and deformation-dependent material properties is required for many practical problems in the mechanics of gels and biological tissues.

In the present study, we derive a finite deformation theory for analysis of coupled fluid and electrokinetic flows in deformable porous media. In Section 2, we develop the continuum theory within the variational framework of the principal of virtual power by combining descriptions of finite deformation poroelasticity, electroquasistatics of deformable media, and continuum electromechanical coupling. In Section 3, we then discuss numerical implementation of the theory using the finite element method, resulting in a five-field mixed finite element formulation. Finally, in Section 4 we utilize the model to examine several case studies of electromechanical coupling in a sample of articular cartilage during commonly used experimental configurations.

[1] To whom correspondence should be addressed. Current address: George W. Woodruff School of Mechanical Engineeering, Georgia Institute of Technology, Atlanta, GA 30332-0405.

Contributed by the Applied Mechanics Division of THE AMERICAN SOCIETY OF MECHANICAL ENGINEERS for publication in the ASME JOURNAL OF APPLIED MECHANICS.

Discussion on the paper should be addressed to the Technical Editor, Professor Lewis T. Wheeler, Department of Mechanical Engineering, University of Houston, Houston, TX 77204-4792, and will be accepted until four months after final publication of the paper itself in the ASME JOURNAL OF APPLIED MECHANICS.

Manuscript received by the ASME Applied Mechanics Division, May 29, 1997; final revision, Apr. 17, 1998. Associate Technical Editor: M. K. Liu.

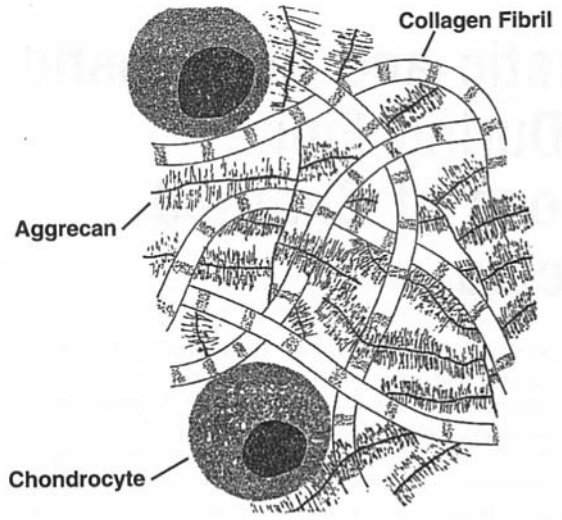

Fig. 1 Microstructural makeup of articular cartilage. The aggrecan molecules contain a large number of sulfated glycosaminoglycan subunits, which contribute to the highly negative fixed charge density of the solid matrix.

2 Theory

2.1 Continuum Mechanics Preliminaries. In the following treatment, we consider a porous medium to be a single continuum defined by the boundaries of the solid matrix. As a preliminary, we state some standard definitions from continuum mechanics (Eringen, 1967; Marsden and Hughes, 1994).

Let the volume $\Omega_o \subset \Re^3$ bounded by the surface Γ_o be the Lagrangian reference configuration for the solid matrix and let $\mathbf{X}$ indicate the material coordinates of a particle in Ω_o (Fig. 2). Let $\boldsymbol{\varphi}(\mathbf{X}, t) : \Omega_o \times [0, t] \rightarrow \Re^3$ represent the invertible deformation map from Ω_o to the present Eulerian configuration Ω_t. The spatial position of a particle in Ω_t is given by

$$\mathbf{x}(\mathbf{X}, t) = \boldsymbol{\varphi}(\mathbf{X}, t) = \mathbf{X} + \mathbf{u}(\mathbf{X}, t) \tag{1}$$

where $\boldsymbol{\varphi}$ is a continuously differentiable, invertible mapping and $\mathbf{u}$ is the solid displacement. The invertible deformation gradient $\mathbf{F}$ and its Jacobian J are defined as

$$\mathbf{F} = \frac{\partial \boldsymbol{\varphi}}{\partial \mathbf{X}} \tag{2}$$

$$J = \det \mathbf{F} \tag{3}$$

where det is the determinant operator. The Jacobian J must be strictly positive to prohibit self-penetration of the continuum. The right Cauchy-Green tensor $\mathbf{C}$ and its inverse, the Piola deformation tensor $\mathbf{B}$ are defined as

$$\mathbf{C} = \mathbf{F}^T\mathbf{F} \tag{4}$$

$$\mathbf{B} = \mathbf{F}^{-1}\mathbf{F}^{-T} \tag{5}$$

where the superscript T indicates transposition.

A vector $\mathbf{a}$ and its divergence $\nabla \cdot \mathbf{a}$ defined on Ω_t are related to their respective Lagrangian "images" on Ω_o by the Piola transformation and Piola identity,

$$\mathbf{A} = J\mathbf{F}^{-1} \cdot \mathbf{a}, \tag{6}$$

$$\text{Div } \mathbf{A} = J\nabla \cdot \mathbf{a}, \tag{7}$$

where $\nabla \cdot$ and Div are the Eulerian and Lagrangian divergence operators, respectively. Likewise, the Eulerian and Lagrangian gradients of a scalar b are related by

$$\text{Grad } b = \mathbf{F}^T \cdot \nabla b, \tag{8}$$

where ∇ and Grad are the Eulerian and Lagrangian gradient operators, respectively.

The spatial time derivative is defined as the partial time derivative holding the spatial position $\mathbf{x}$ fixed,

$$\frac{\partial}{\partial t} = \frac{\partial}{\partial t}\bigg|_{\mathbf{x}}. \tag{9}$$

Likewise, the material time derivative is defined as the partial time derivative holding the particle $\mathbf{X}$ fixed,

$$\dot{(\,)} = \frac{d}{dt} = \frac{\partial}{\partial t}\bigg|_{\mathbf{X}} = \frac{\partial}{\partial t} + \mathbf{v} \cdot \nabla, \tag{10}$$

where the solid velocity $\mathbf{v} = d\mathbf{x}/dt$ is the material time derivative of the spatial position. Finally, the convective time derivative of $\mathbf{a}$ is defined as

$$\overset{*}{\mathbf{a}} = \frac{\partial \mathbf{a}}{\partial t} + \mathbf{v} \cdot (\nabla \mathbf{a}) + \mathbf{a}\nabla \cdot \mathbf{v} - \mathbf{a} \cdot (\nabla \mathbf{v}). \tag{11}$$

If $\mathbf{a}$ is an objective vector field, then $\overset{*}{\mathbf{a}}$ is an objective rate.

2.2 Variational Framework. In the subsequent sections, we motivate our theoretical formulation within the variational framework of the principle of virtual power (PVP) (Penfield and Haus, 1967; Maugin and Eringen, 1977). We first define a power balance functional Ψ for the medium

$$\Psi(\mathbf{d}, \dot{\mathbf{d}}) = \frac{d}{dt} E^{\text{int}} + P^{\text{diss}} - P^{\text{ext}} \tag{12}$$

where E^{int} is the internal energy in the medium, P^{diss} is the dissipative power, and P^{ext} is the external power supplied across the boundary. In a quasi-static formulation, Ψ depends on the independent variables $\mathbf{d}$ and their time derivatives (or generalized velocities) $\dot{\mathbf{d}}$. In addition to the requirement that Ψ itself be identically zero (as implied by the first law of thermodynamics), we require the first variation of Ψ in a generalized virtual velocity field to vanish,

$$\delta\Psi = \frac{\partial}{\partial \eta} \Psi(\mathbf{d}, \dot{\mathbf{d}} + \eta\delta\dot{\mathbf{d}})|_{\eta=0} = 0, \tag{13}$$

where the virtual velocities $\delta\dot{\mathbf{d}}$ represent arbitrary admissible variations in $\dot{\mathbf{d}}$ and η is an arbitrarily small parameter. For a nonequilibrium open system, this condition is analogous to requiring the first variation of the Gibbs free energy to vanish for thermodynamic equilibrium of a closed system. Enforcement of Eq. (13) will directly imply the local governing equations for the physical system of interest.

To apply this formalism to the electromechanically coupled porous medium, we must identify appropriate forms of E^{int}, P^{diss}, and P^{ext}, as well as a consistent set of independent variables $\mathbf{d}$. In the present study, this will be achieved by uniting descriptions of

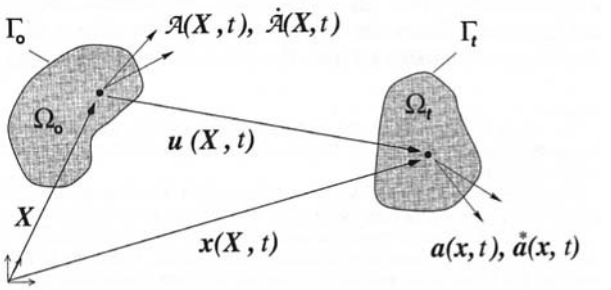

Fig. 2 Kinematic relationship between the Lagrangian reference configuration Ω_o and the Eulerian present configuration Ω_t

interacting poroelastic and electroquasistatic "subsystems" such that

$$\Psi = \Psi_{pe} + \Psi_{eqs}. \tag{14}$$

Additionally, we will introduce a continuum electromechanical coupling law describing interactions (energy transfer) between the subsystems.

2.3 Poroelastic Subsystem. Kinematic descriptions of porous media are often posed within the framework of continuum mixture theory, where the porous medium is treated as the superposition of two interacting continua simultaneously occupying the same physical space (Bowen, 1980; Kwan et al., 1990; Thomas, 1991). In the present treatment, we adopt an alternate approach (Biot, 1972), viewing the porous medium mechanically as a single continuum defined by the boundaries of the solid material and considering area-averaged fluid flow (or volumetric flux) relative to the solid. Under assumptions about the mixture commonly invoked for biological tissues (e.g., immiscible, nonreactive, isothermal, quasi-static), the two finite deformation formulations are mathematically equivalent (Simon, 1992; Levenston et al., 1998).

We previously utilized the PVP to generate a three-field mixed poroelastic formulation appropriate for finite deformation analysis (Levenston et al., 1998) when electrokinetic phenomena have minimal influence on the mechanical response. In that formulation, we modeled quasi-static deformations of an isothermal,[2] saturated porous medium in which both the solid and fluid constituents are treated as intrinsically incompressible. The combination of the saturation condition (i.e., the sum of the solid and fluid volume fractions must be 1) with intrinsic constituent incompressibility produces a constraint on the relationship between solid and fluid dilatations,

$$J - 1 - \xi = 0, \tag{15}$$

where ξ is defined as the change in fluid volume content,

$$\xi = -\text{DIV}\,\mathbf{W}, \tag{16}$$

and we have introduced $\mathbf{W}$ as a Lagrangian fluid "displacement" relative to the solid. Physically, $\mathbf{W}$ represents the net volume of fluid that has passed through a unit area since the medium "left" the reference state. Consequently, $\dot{\mathbf{W}}$ is the Lagrangian relative fluid velocity (or volumetric flux).

Thus, Eq. (15) states that any change $(J - 1)$ in the volume occupied by an initially undeformed continuum region must be accompanied by an equal change (ξ) in the fluid volume content. This constraint implies the mass continuity equation for the porous medium,

$$\nabla \cdot (\mathbf{v} + \overset{*}{\mathbf{w}}) = 0, \tag{17}$$

where the relative fluid velocity $\overset{*}{\mathbf{w}}$ is the convective time derivative of $\mathbf{w}$, the Eulerian relative fluid displacement. Note that $\overset{*}{\mathbf{w}}$, representing the fluid volumetric flux relative to the solid, is objective.

By introducing the scalar fluid pressure p and treating it as a Lagrange multiplier enforcing Eq. (15), we formulated the internal energy of the porous medium as

$$E_{pe}^{\text{int}} = \int_{\Omega_o} [U(\mathbf{C}) - p(J - 1 - \xi)]d\Omega. \tag{18}$$

The (Lagrangian) hyperelastic stored energy density $U(\mathbf{C})$ represents the energy stored through deformation of the solid matrix irrespective of any fluid pressurization.[3] Likewise, we wrote the dissipative[4] and external powers as

$$P_{pe}^{\text{diss}} = -\int_{\Omega_o} \text{GRAD}\, p \cdot \dot{\mathbf{W}} d\Omega \tag{19}$$

$$P_{pe}^{\text{ext}} = \int_{\Gamma_o} (\mathbf{f} \cdot \mathbf{v} - p\dot{\mathbf{W}} \cdot \mathbf{N}) d\Gamma \tag{20}$$

where $\mathbf{f}$ and $\mathbf{N}$ are, respectively, the traction and surface normal vectors defined on the Lagrangian boundary Γ_o.

Were we to consider this subsystem in isolation, we would close the poroelastic formulation by combining Eqs. (12), (18), (19), and (20) and explicitly introducing Darcy's law (defined in the Eulerian configuration) relating fluid flow to the gradient in fluid pressure,

$$\overset{*}{\mathbf{w}} = -\mathbf{k}_d(\mathbf{u}) \cdot \nabla p, \tag{21}$$

where $\mathbf{k}_d$ is the deformation-dependent rank-two permeability tensor. For a total Lagrangian formulation, we considered $(\mathbf{u}, \mathbf{W}, p)$ to be the set of independent variables, with $(\delta\mathbf{v}, \delta\dot{\mathbf{W}}, \delta\dot{p})$ as the corresponding generalized virtual velocities.

2.4 Electroquasistatic Subsystem. We consider the electroquasistatic (EQS) subsystem to be governed by the electroquasistatic form of Maxwell's equations for an electrically linear dielectric medium (Haus and Melcher, 1989):

$$\nabla \times \mathbf{E} = \mathbf{0}; \quad \mathbf{E} = -\nabla\Phi \quad \text{(Faraday's law)} \tag{22}$$

$$\nabla \cdot \epsilon\mathbf{E} = \rho_u \quad \text{(Gauss's law)} \tag{23}$$

$$\nabla \times \mathbf{H} = \mathbf{j}_u + \frac{\partial}{\partial t}\epsilon\mathbf{E} + \nabla \times (\mathbf{P} \times \mathbf{v}) \quad \text{(Ampére's law)} \tag{24}$$

where Φ is the scalar electrical potential, $\mathbf{E}$ is the electric field intensity, ρ_u is the net macroscopic density of unpaired charges, ϵ is the dielectric permittivity for the medium, $\mathbf{H}$ is the magnetic field intensity, $\mathbf{j}_u$ is the unpaired current density (not associated with polarization), and $\mathbf{P}$ is the polarization density.

The EQS energy balance (or Poynting's theorem) for such a system may be written in a fixed (or "laboratory") spatial frame as (Haus and Melcher, 1989; Penfield and Haus, 1967)

$$\int_{\Omega_t} \left\{ \frac{\partial}{\partial t}\left(\frac{1}{2}\epsilon\mathbf{E} \cdot \mathbf{E}\right) + \mathbf{E} \cdot [\mathbf{j}_u + \nabla \times (\mathbf{P} \times \mathbf{v})] \right\} d\Omega + \int_{\Gamma_t} (\mathbf{E} \times \mathbf{H}) \cdot \mathbf{n} d\Gamma = 0, \tag{25}$$

where $\mathbf{n}$ is the surface normal vector on Γ_t. In this laboratory frame, $\frac{1}{2}\epsilon\mathbf{E} \cdot \mathbf{E}$ represents the spatial density of energy stored in the electric field, $\mathbf{E} \cdot [\mathbf{j}_u + \nabla \times (\mathbf{P} \times \mathbf{v})]$ represents the spatial density of electrical dissipation, and $\mathbf{E} \times \mathbf{H}$ (the Poynting vector) represents the flux of power into the spatial region.

Utilizing Eqs. (22)–(24), Stokes's theorem and the divergence theorem, Eq. (25) can be rewritten as

[2] We assume that the rate of dissipation is small with respect to the characteristic thermal conduction rate and that the medium resides in an infinite bath of constant temperature (typically, ≈37°C for biological systems). Thus, we do not explicitly model the heat conduction "subsystem," and instead assume that the system remains isothermal.

[3] For a porous medium with compressible constituents, the "total" energy density would be the sum of $U(\mathbf{C})$ and a term describing the energy stored through dilatation of the individual constituents by the fluid pressure. Because we treat both the solid and fluid constituents as incompressible, this second term becomes $p(J - 1 - \xi)$, an energy of constraint which is identically zero. See Simon (1992) or Levenston et al. (1998) for a more thorough discussion of this point.

[4] The "dissipative" power P_i^{diss} for a given subsystem actually represents the total rate of energy transfer out of the subsystem, not merely the dissipative power. Consequently, P_i^{diss} for any given subsystem may be negative. However, the net dissipation for the system (obtained by summing the contributions from all subsystems except the heat transfer subsystem) must be non-negative.

$$\int_{\Omega_t} \left(\Phi \frac{\partial \rho_u}{\partial t} - \nabla\Phi \cdot \mathbf{j_u} \right) d\Omega + \int_{\Gamma_t} \Phi \mathbf{j_u} \cdot \mathbf{n} d\Gamma = 0. \quad (26)$$

In this form, $\Phi(\partial \rho_u/\partial t)$ represents the rate of capacitive energy (density) storage in the dielectric medium. We next consider a pointwise Galilean transformation from the laboratory frame to a frame moving with the solid medium at a velocity $\mathbf{v}$. Under this transformation, Eq. (26) becomes

$$\int_{\Omega_t} (\Phi \overset{*}{\rho}_u - \nabla\Phi \cdot \mathbf{j}) d\Omega + \int_{\Gamma_t} \Phi \mathbf{j} \cdot \mathbf{n} d\Gamma = 0, \quad (27)$$

where the scalar convective time derivative $\overset{*}{\rho}_u$ and the free current density relative to the solid $\mathbf{j}$ are defined as

$$\overset{*}{\rho}_u = \dot{\rho}_u + \rho_u(\nabla \cdot \mathbf{v}) \quad (28)$$

$$\mathbf{j} = \mathbf{j_u} - \rho_u \mathbf{v}. \quad (29)$$

Note that the relative current density $\mathbf{j}$, representing the net charge flux relative to the solid, is objective.

We now define $\mathbf{g}$ (with Lagrangian image $\mathbf{G}$) representing the net "displacement density" of charge relative to the solid, such that

$$\rho_u = -\nabla \cdot \mathbf{g}; \quad \hat{\rho}_u = -\text{Div } \mathbf{G} \quad (30)$$

$$\mathbf{j} = \overset{*}{\mathbf{g}}; \quad \mathbf{J} = \dot{\mathbf{G}} \quad (31)$$

where $\hat{\rho}_u$ and $\mathbf{J}$ are the Lagrangian charge density and relative current density, respectively. The charge displacement density vector $\mathbf{g}$ can be interpreted as describing the net amount of charge that has passed through a unit surface since the medium "left" the reference state. Equations (28)–(31) imply three equivalent statements of charge continuity:

$$\nabla \cdot \mathbf{j_u} + \frac{\partial \rho_u}{\partial t} = 0 \quad \text{(total current, spatial frame)} \quad (32)$$

$$\nabla \cdot \mathbf{j} + \overset{*}{\rho}_u = 0 \quad \text{(relative current, spatial frame)} \quad (33)$$

$$\text{Div } \mathbf{J} + \dot{\hat{\rho}}_u = 0 \quad \text{(relative current, material frame)}. \quad (34)$$

Strictly speaking, we now view ρ_u as the *change* in charge density relative to the undeformed reference state. If we stipulate macroscopic electroneutrality as an initial condition, then ρ_u is also the present charge density. The Lagrangian form of the energy balance can now be written as

$$\int_{\Omega_o} \Phi \dot{\hat{\rho}}_u d\Omega + \int_{\Omega_o} -\text{Div } \Phi \cdot \mathbf{J} d\Omega - \int_{\Gamma_o} (-\Phi \mathbf{J}) \cdot \mathbf{N} d\Gamma = 0. \quad (35)$$

Finally, we consider the limiting case of a medium with no macroscopic capacitive energy storage. In this situation, the electric potential becomes mathematically decoupled from the charge density,[5] and we can write the energy balance for the EQS subsystem as

$$\Psi_{eqs} = \frac{d}{dt} \int_{\Omega_o} \Phi \hat{\rho}_u d\Omega + \int_{\Omega_o} (-\text{Div } \Phi \cdot \mathbf{J}) d\Omega - \int_{\Gamma_o} (-\Phi \mathbf{J}) \cdot \mathbf{N} d\Gamma = 0 \quad (36)$$

where Φ now functions as a Lagrange multiplier enforcing continuum electroneutrality as a constraint,

$$\hat{\rho}_u = 0. \quad (37)$$

The three integrals in Eq. (36) represent the rate of energy storage, dissipative power, and external power supply, respectively, for the EQS subsystem. Were we to consider this subsystem in isolation, we would close the formulation by introducing a constitutive law (e.g., Ohm's law) relating the current density to the potential gradient. We consider $(\mathbf{G}, \Phi)$ to be the independent variables for this subsystem, with $(\delta\mathbf{J}, \delta\Phi)$ as the corresponding generalized virtual velocities.

REMARK 1. *A distinction should be noted between our macroscopic notions of electroneutrality and zero capacitive energy storage and the underlying microstructural picture. Clearly, electroneutrality will be violated microscopically within the double-layer region of the fluid adjacent to a charged region of the solid. With Eq. (37), we require that the charge in the double layer exactly balance the solid charge, so the net charge at a continuum length scale is identically zero.*

Likewise, maintenance of this charge distribution requires that energy be stored in the double layer. Deformation of the solid matrix alters the spatial density of matrix fixed charge, and consequently alters the double-layer charge distribution and the double-layer energy. In the present treatment, we view these phenomena as functions of the solid deformation, and incorporate this energy storage into the hyperelastic stored energy function for the solid (see Eq. (18)). Thus, microscopic double-layer interactions are manifest as contributions to the macroscopic solid elasticity. By considering the medium to be noncapacitive at the continuum level, we adopt the view that the establishment of a macroscopic electric field within the material will negligibly alter the microscopic double-layer energy. As the microscopic electric fields are typically in the range of eight orders of magnitude higher than the macroscopic fields associated with streaming potentials, this assumption is reasonable.

2.5 Electromechanical Coupling. The two subsystems have now been formulated in such a way that the pairs $(\overset{*}{\mathbf{w}}, \nabla p)$ and $(\mathbf{j}, \nabla\Phi)$ are sets of conjugate fluxes and thermodynamic "forces." To close the formulation, we introduce a phenomenological coupling law relating the fluxes $\overset{*}{\mathbf{w}}$ and $\mathbf{j}$ to the forces ∇p and $\nabla\Phi$ (DeGroot and Mazur, 1969; Frank and Grodzinsky, 1987b):

$$\begin{Bmatrix} \overset{*}{\mathbf{w}} \\ \mathbf{j} \end{Bmatrix} = \begin{bmatrix} -\mathbf{k}_{11}(\mathbf{C}) & \mathbf{k}_{12}(\mathbf{C}) \\ \mathbf{k}_{21}(\mathbf{C}) & -\mathbf{k}_{22}(\mathbf{C}) \end{bmatrix} \begin{Bmatrix} \nabla p \\ \nabla\Phi \end{Bmatrix}, \quad (38)$$

where the $\mathbf{k}_{ij}$ are deformation-dependent rank-two coupling tensors. This coupling law plays the role that Darcy's law plays in the poroelastic formulation,[6] with the first line representing a generalized Darcy's law and the second line representing a generalized Ohm's law. The tensors $\mathbf{k}_{11}$ and $\mathbf{k}_{22}$ represent the "short circuit" permeability and the effective electrical conductivity at zero pressure gradient, respectively, and the off-diagonal tensors represent electrokinetic coupling. Statistical thermodynamic arguments using the property of "time reversal invariance" lead to Onsager's reciprocity theorem (DeGroot and Mazur, 1969), a basic theorem of nonequilibrium thermodynamics implying that the macroscopic coupling matrix in Eq. (38) is symmetric. Consequently, $\mathbf{k}_{11}$ and $\mathbf{k}_{22}$ are symmetric tensors, and $\mathbf{k}_{21} = \mathbf{k}_{12}^T$. Additional relationships between the macroscopic coupling tensors can be derived from microstructural models or from macroscopic constitutive models (see Section 4).

[5] This is analogous to the decoupling of the pressure and the volumetric deformation when incompressible elasticity is viewed as a limit of compressible elasticity.

[6] Under open circuit conditions ($\mathbf{j} = 0$), an "effective" Darcy permeability can be derived for use in Eq. (21):

$$\mathbf{k}_d = \mathbf{k}_{11} - (\mathbf{k}_{12}\mathbf{k}_{22}^{-1}\mathbf{k}_{21}). \quad (39)$$

Table 1 Local equations implied by the global variational equation (Eq. (46)) for an electromechanically coupled poroelastic medium. Note that $\tilde{p}$ and $\tilde{\Phi}$ are values prescribed on portions of the boundary and the total first Piola-Kirchoff stress T is defined in the text (Eq. (48)). The reference configuration must be defined such that the mass and charge conservation constraints are initially satisfied.

Linear momentum balance	$\text{DIV}\,\boldsymbol{T}$	=	0	in Ω_o
Mass conservation	$J-1-\xi$	=	0	in Ω_o
Charge conservation	$\hat{\rho}_u$	=	0	in Ω_o
Generalized Darcy's law	$\text{GRAD}\,p+\boldsymbol{r}_{11}\cdot\dot{\boldsymbol{\mathcal{W}}}+\boldsymbol{r}_{12}\cdot\mathrm{j}_u$	=	0	in Ω_o
Generalized Ohm's law	$\text{GRAD}\,\Phi+\boldsymbol{r}_{21}\cdot\dot{\boldsymbol{\mathcal{W}}}+\boldsymbol{r}_{22}\cdot\mathrm{j}_u$	=	0	in Ω_o
Traction boundary condition	$\boldsymbol{N}\cdot\boldsymbol{T}-\boldsymbol{f}$	=	0	on Γ_{o_f}
Pressure boundary condition	$p-\tilde{p}$	=	0	on Γ_{o_p}
Potential boundary condition	$\Phi-\tilde{\Phi}$	=	0	on Γ_{o_Φ}

The coupling relationship can be posed in an equivalent Lagrangian form as

$$\begin{Bmatrix}\dot{\mathbf{W}}\\ \mathbf{J}\end{Bmatrix}=\begin{bmatrix}-\mathbf{K}_{11} & \mathbf{K}_{12}\\ \mathbf{K}_{21} & -\mathbf{K}_{22}\end{bmatrix}\begin{Bmatrix}\text{GRAD}\,p\\ \text{GRAD}\,\Phi\end{Bmatrix}, \tag{40}$$

where the Lagrangian forms of the coupling tensors are given by

$$\mathbf{K}_{ij}=J\mathbf{F}^{-1}\mathbf{k}_{ij}\mathbf{F}^{-T}. \tag{41}$$

Inversion of Eq. (40) leads to expressions for the Lagrangian gradients of pressure and potential,

$$\begin{Bmatrix}\text{GRAD}\,p\\ \text{GRAD}\,\Phi\end{Bmatrix}=\begin{bmatrix}-\mathbf{R}_{11} & -\mathbf{R}_{12}\\ -\mathbf{R}_{21} & -\mathbf{R}_{22}\end{bmatrix}\begin{Bmatrix}\dot{\mathbf{W}}\\ \mathbf{J}\end{Bmatrix}, \tag{42}$$

where the inverse coupling tensors $\mathbf{R}_{ij}$ are functions of the $\mathbf{K}_{ij}$,

$$\begin{aligned}\mathbf{R}_{11}&=(\mathbf{K}_{11}-\mathbf{K}_{12}\mathbf{K}_{22}^{-1}\mathbf{K}_{21})^{-1}\\ \mathbf{R}_{22}&=(\mathbf{K}_{22}-\mathbf{K}_{21}\mathbf{K}_{11}^{-1}\mathbf{K}_{12})^{-1}\\ \mathbf{R}_{12}&=\mathbf{R}_{11}\mathbf{K}_{12}\mathbf{K}_{22}^{-1}\\ \mathbf{R}_{21}&=\mathbf{R}_{22}\mathbf{K}_{21}\mathbf{K}_{22}^{-1}=\mathbf{R}_{12}.\end{aligned} \tag{43}$$

2.6 Variational Formulation for a Coupled Medium. The power balance for the electromechanically coupled porous medium can now be stated as

$$\begin{aligned}\Psi=&\frac{d}{dt}\int_{\Omega_o}[U(\mathbf{C})-p(J-1-\xi)+\Phi\hat{\rho}_u]d\Omega\\ &-\int_{\Omega_o}(\text{GRAD}\,p\cdot\dot{\mathbf{W}}+\text{GRAD}\,\Phi\cdot\mathbf{J})d\Omega\\ &-\int_{\Gamma_o}(\mathbf{f}\cdot\mathbf{v}-p\dot{\mathbf{W}}\cdot\mathbf{N}-\Phi\mathbf{J}\cdot\mathbf{N})d\Gamma=0.\end{aligned} \tag{44}$$

We require the first variation of Ψ with respect to the generalized virtual velocities to vanish:

$$\begin{aligned}\frac{\partial}{\partial\eta}\Psi(&\mathbf{u},\mathbf{W},\mathbf{G},p,\Phi,\mathbf{v}+\eta\delta\mathbf{v},\dot{\mathbf{W}}+\eta\delta\dot{\mathbf{W}},\mathbf{J}+\eta\delta\mathbf{J},\\ &\dot{p}+\eta\delta\dot{p},\dot{\Phi}+\eta\delta\dot{\Phi})|_{\eta=0}=0.\end{aligned} \tag{45}$$

After explicit introduction of the electromechanical coupling law, we obtain the following variational equation:

$$\begin{aligned}\int_{\Omega_o}&[\tfrac{1}{2}(\mathbf{S}^e-pJ\mathbf{B}):\delta\dot{\mathbf{C}}+p\delta\dot{\xi}+(\dot{\mathbf{W}}\cdot\mathbf{R}_{11}^t+\mathbf{J}\cdot\mathbf{R}_{12}^t)\cdot\delta\dot{\mathbf{W}}\\ &+\phi\delta\dot{\hat{\rho}}_u+(\dot{\mathbf{W}}\cdot\mathbf{R}_{21}^t+\mathbf{J}\cdot\mathbf{R}_{22}^t)\cdot\delta\mathbf{J}\\ &-\delta\dot{p}(J-1-\xi)+\delta\dot{\Phi}\hat{\rho}_u]d\Omega\\ &-\int_{\Gamma_o}(\mathbf{t}\cdot\delta\mathbf{v}-p\mathbf{N}\cdot\delta\dot{\mathbf{W}}-\Phi\mathbf{N}\cdot\delta\mathbf{J})d\Gamma=0,\end{aligned} \tag{46}$$

where $\delta\dot{\mathbf{C}}$, $\delta\dot{\xi}$, and $\delta\dot{\hat{\rho}}_u$ are defined consistently with $\delta\mathbf{v}$, $\delta\dot{\mathbf{W}}$ and $\delta\mathbf{J}$, respectively, and $\mathbf{S}^e$ is the elastic (or "extra") second Piola-Kirchoff stress tensor, defined by

$$\mathbf{S}^e=2\,\frac{\partial U(\mathbf{C})}{\partial\mathbf{C}}. \tag{47}$$

As the virtual velocities are arbitrary and independent, Eq. (46) implies the local equations shown in Table 1. Note that we have defined the total first Piola-Kirchoff stress $\mathbf{T}$ as

$$\mathbf{T}=(\mathbf{S}^e-pJ\mathbf{B})\cdot\mathbf{F}^T=\mathbf{T}^e-pJ\mathbf{F}^{-1}, \tag{48}$$

indicating that the total stress on the medium is carried by a combination of solid matrix deformation and fluid pressurization. Thus, the variational formulation implies the appropriate governing equations for our coupled medium, and requires only the specification of the geometry, boundary conditions, and constitutive relations for a fully posed problem.

REMARK 2. *A discussion of boundary conditions is appropriate at this point. In this formulation, we must specify boundary conditions on Γ_o for the porous medium as a whole. Thus, we must prescribe either the solid displacement* $\mathbf{u}$ *and corresponding velocity* $\mathbf{v}$ *on Γ_{o_u} or the traction* $\mathbf{f}$ *on Γ_{o_f}, where Γ_{o_u} and Γ_{o_f} are complementary portions of Γ_o:*

$$\Gamma_o=\Gamma_{o_u}\cup\Gamma_{o_f},\quad \Gamma_{o_u}\cap\Gamma_{o_f}=\varnothing. \tag{49}$$

Likewise, we must prescribe either the relative fluid displacement $\mathbf{W}$ *and corresponding relative fluid velocity* $\dot{\mathbf{W}}$ *on Γ_{o_w} or the pressure p on Γ_{o_p}, where Γ_{o_w} and Γ_{o_p} are also complementary portions of Γ_o:*

$$\Gamma_o=\Gamma_{o_w}\cup\Gamma_{o_p},\quad \Gamma_{o_w}\cap\Gamma_{o_p}=\varnothing. \tag{50}$$

Finally, we must prescribe either the relative charge displacement density $\mathbf{G}$ *and corresponding relative current density* $\mathbf{J}$ *on Γ_{o_g} or the electric potential Φ on Γ_{o_Φ}, where Γ_{o_g} and Γ_{o_Φ} too are complementary portions of Γ_o:*

$$\Gamma_o = \Gamma_{o_g} \cup \Gamma_{o\Phi}, \quad \Gamma_{o_g} \cap \Gamma_{o\Phi} = \varnothing. \tag{51}$$

In general, the solid, fluid, and electrical boundary partitions need not coincide.

3 Finite Element Implementation

Finite element matrix equations for a total Lagrangian implementation are derived from the variational formulation in the usual manner. We approximate the reference domain Ω_o as the union of n_{el} nonintersecting elements Ω_o^e, and spatially discretize the primary variables and their real and virtual velocities. Within an element

$$\begin{aligned}
&\mathbf{u}^h = \mathbf{N}^{u^T} u_e \quad \mathbf{v}^h = \mathbf{N}^{u^T} v_e \quad \delta\mathbf{v}^h = \mathbf{N}^{u^T}\delta v_e \\
&\mathbf{W}^h = \mathbf{N}^{w^T} W_e \quad \dot{W}^h = \mathbf{N}^{w^T}\dot{W}_e \quad \delta\dot{\mathbf{W}}^h = \mathbf{N}^{w^T}\delta\dot{W}_e \\
&\mathbf{G}^h = \mathbf{N}^{g^T} G_e \quad \mathbf{J}^h = \mathbf{N}^{g^T} J_e \quad \delta\mathbf{J}^h = \mathbf{N}^{g^T}\delta J_e \\
&p^h = \mathbf{N}^{p^T} p_e \quad \dot{p}^h = \mathbf{N}^{p^T}\dot{p}_e \quad \delta\dot{p}^h = \mathbf{N}^{p^T}\delta\dot{p}_e \\
&\Phi^h = \mathbf{N}^{\Phi^T}\Phi_e \quad \dot{\Phi}^h = \mathbf{N}^{\Phi^T}\dot{\Phi}_e \quad \delta\dot{\Phi}^h = \mathbf{N}^{\Phi^T}\delta\dot{\Phi}_e
\end{aligned} \tag{52}$$

where $(\ )^h$ indicates a discretized approximation to the corresponding variable; $(\ )_e$ indicates a vector of nodal values; and $\mathbf{N}^u$, $\mathbf{N}^w$, $\mathbf{N}^g$, $\mathbf{N}^p$, and $\mathbf{N}^\Phi$ are the element shape functions for the solid, fluid, current density, pressure and potential, respectively. As is typical of mixed finite element formulations, the pressure interpolation will generally be of lower order than the solid and fluid interpolations, and the potential interpolation will generally be of lower order than the current density interpolation. We require C_0 interelement continuity for the vector interpolations, but the scalar interpolations (pressure and potential) may be discontinuous. Additionally, the solid displacement is isoparametric with the element coordinates

$$\mathbf{X}^h = \mathbf{N}^{u^T} X_e. \tag{53}$$

Introduction of the discretizations into Eq. (46) produces a semi-discretized nonlinear system of equations that must be solved via an iterative method (e.g., modified Newton-Raphson). Appropriate linearization produces the following matrix equation for iteration (i) of the present loading increment:

$$\begin{bmatrix} \mathbf{K}^{uu} & \mathbf{0} & \mathbf{0} & \mathbf{K}^{up} & \mathbf{0} \\ \mathbf{0} & \mathbf{0} & \mathbf{0} & \mathbf{K}^{wp} & \mathbf{0} \\ \mathbf{0} & \mathbf{0} & \mathbf{0} & \mathbf{0} & \mathbf{K}^{g\Phi} \\ \mathbf{K}^{up^T} & \mathbf{K}^{wp^T} & \mathbf{0} & \mathbf{0} & \mathbf{0} \\ \mathbf{0} & \mathbf{0} & \mathbf{K}^{g\Phi^T} & \mathbf{0} & \mathbf{0} \end{bmatrix}^{(i)} \begin{Bmatrix} \Delta\bar{u} \\ \Delta\bar{W} \\ \Delta\bar{G} \\ \Delta\bar{p} \\ \Delta\bar{\Phi} \end{Bmatrix}^{(i)} + \begin{bmatrix} \mathbf{0} & \mathbf{0} & \mathbf{0} & \mathbf{0} & \mathbf{0} \\ \mathbf{0} & \mathbf{C}^{ww} & \mathbf{C}^{wg} & \mathbf{0} & \mathbf{0} \\ \mathbf{0} & \mathbf{C}^{wg^T} & \mathbf{C}^{gg} & \mathbf{0} & \mathbf{0} \\ \mathbf{0} & \mathbf{0} & \mathbf{0} & \mathbf{0} & \mathbf{0} \\ \mathbf{0} & \mathbf{0} & \mathbf{0} & \mathbf{0} & \mathbf{0} \end{bmatrix}^{(i)} \begin{Bmatrix} \Delta\bar{v} \\ \Delta\dot{\bar{W}} \\ \Delta\bar{J} \\ \Delta\dot{\bar{p}} \\ \Delta\dot{\bar{\Phi}} \end{Bmatrix}^{(i)} = -\begin{Bmatrix} \mathbf{R}^u \\ \mathbf{R}^w \\ \mathbf{R}^g \\ \mathbf{R}^p \\ \mathbf{R}^\Phi \end{Bmatrix}^{(i)} \tag{54}$$

where $\Delta(\bar{\ })$ and $\Delta(\dot{\bar{\ }})$ indicate iterative updates to the corresponding vector of nodal variables and their respective velocities. The stiffness terms $\mathbf{K}$ are derived from the internal energy expression, the damping terms $\mathbf{C}$ are derived from the dissipative power expression, and the force terms $\mathbf{R}$ are derived from the power supply expression. All global submatrices and vectors are defined in Appendix A.

In the present study, we discretized the linearized system in time using the backwards Euler algorithm. This produced a fully discretized linear system:

$$\begin{bmatrix} \Delta t\mathbf{K}^{uu} & \mathbf{0} & \mathbf{0} & \Delta t\mathbf{K}^{up} & \mathbf{0} \\ \mathbf{0} & \mathbf{C}^{ww} & \mathbf{C}^{wg} & \Delta t\mathbf{K}^{wp} & \mathbf{0} \\ \mathbf{0} & \mathbf{C}^{wg^T} & \mathbf{C}^{gg} & \mathbf{0} & \Delta t\mathbf{K}^{g\Phi} \\ \Delta t\mathbf{K}^{up^T} & \Delta t\mathbf{K}^{wp^T} & \mathbf{0} & \mathbf{0} & \mathbf{0} \\ \mathbf{0} & \mathbf{0} & \Delta t\mathbf{K}^{g\Phi^T} & \mathbf{0} & \mathbf{0} \end{bmatrix}^{(i)} \begin{Bmatrix} \Delta\bar{v} \\ \Delta\dot{\bar{W}} \\ \Delta\bar{J} \\ \Delta\dot{\bar{p}} \\ \Delta\dot{\bar{\Phi}} \end{Bmatrix}^{(i)} = -\begin{Bmatrix} \mathbf{R}^u \\ \mathbf{R}^w \\ \mathbf{R}^g \\ \mathbf{R}^p \\ \mathbf{R}^\Phi \end{Bmatrix}^{(i)} \tag{55}$$

where Δt is the time-step and the iterative updates to the generalized displacements are computed as

$$\begin{Bmatrix} \Delta\bar{u} \\ \Delta\bar{W} \\ \Delta\bar{G} \\ \Delta\bar{p} \\ \Delta\bar{\Phi} \end{Bmatrix}^{(i)} = \Delta t \begin{Bmatrix} \Delta\bar{v} \\ \Delta\dot{\bar{W}} \\ \Delta\bar{J} \\ \Delta\dot{\bar{p}} \\ \Delta\dot{\bar{\Phi}} \end{Bmatrix}^{(i)}. \tag{56}$$

For each time increment, iteration continued until the norm of the residual vector fell below a specified tolerance. We utilized modified Newton-Raphson iteration in the current study, retaining the initial stiffness and damping matrices for each time increment.

As with any mixed method, care must be taken to choose element configurations that are numerically well behaved. Because the saturation/incompressibility constraint acts on two vector fields ($\mathbf{u}$ and $\mathbf{W}$) while the electroneutrality constraint acts on only one vector field ($\mathbf{G}$), an interpolation scheme that satisfies the inf-sup (or Babuška-Brezzi) condition (Brezzi and Fortin, 1991) for one constraint may not be suitable for the other.

In the following examples, we utilize a simple Q1/P0 element formulation that does not satisfy the inf-sup condition, yet still performs adequately for a large class of problems. Specifically, we utilized axisymmetric, quadrilateral elements with bilinear interpolations of solid, fluid, and current variables and constant (within an element) values of the pressure and electrical potential, for a total of 26 degrees-of-freedom per element. A simple constraint count (Hughes, 1987) indicates that the inf-sup condition is not satisfied for the EQS subsystem, and this element may be prone to the development of spurious electrical potential modes analogous to pressure modes in the incompressible elements. Exploration of alternate interpolation strategies or enhanced-strain-like approaches may lead to more generally optimal element formulations. As a practical matter, the axisymmetric Q1/P0 elements appear to perform adequately in our example problems.

4 Numerical Examples

4.1 Constitutive Models. Although the formulation is amenable to the use of anisotropic material models, in the present study we restrict our analysis to isotropic (on Ω_t) constitutive laws with material parameters chosen to be representative of articular cartilage (Maroudas et al., 1973; Armstrong and Mow, 1982; Frank and Grodzinsky, 1987b). We consider homogeneous samples of tissue with an initial solid volume fraction $\phi_o^s = 0.2$ and corresponding initial fluid volume fraction $\phi_o^f = 0.8$. The initial matrix fixed charge density (expressed as matrix charge per unit fluid volume) was chosen as $\rho_{m_o} = -16$ MC/m^3 ($\sim$0.17 M). Note that the constraint of continuum electroneutrality implies that $\rho_m = -\rho_i$, where ρ_i is the charge density in the ionic fluid (expressed as the net ionic charge per unit fluid volume). Due to the intrinsic constituent incompressibility, the solid and fluid volume fractions and the matrix fixed charge density vary as functions of the volumetric deformation:

$$\phi^s = \frac{\phi_o^s}{J} \tag{57}$$

$$\phi^f = 1 - \phi^s = \frac{J - 1 + \phi_o^f}{J} \tag{58}$$

$$\rho_m = \left(\frac{\phi_o^f}{\phi^f}\right)\rho_{m_o} = \left(\frac{J\phi_o^f}{J - 1 + \phi_o^f}\right)\rho_{m_o}. \tag{59}$$

For the present study, we utilized the following hyperelastic energy density function for the solid matrix (Holmes and Mow, 1990):

$$U(\mathbf{C}) = \beta \frac{\exp[\alpha_1(I_1 - 3) + \alpha_2(I_2 - 3)]}{I_3^{(\alpha_1 + 2\alpha_2)}}, \tag{60}$$

where the three principal invariants of $\mathbf{C}$ are defined as

$$I_1 = \text{tr}\,\mathbf{C}, \tag{61}$$

$$I_2 = \det \mathbf{C}\ \text{tr}\,\mathbf{C}^{-1}, \tag{62}$$

$$I_3 = \det \mathbf{C} = J^2, \tag{63}$$

where tr is the trace operator. The positive constants α_1, α_2, and β were assigned values of 0.2333, 0.0333, and 0.4261, respectively, corresponding to a reference state linearized Young's modulus of 0.5 MPa and a Poisson's ratio of 0.1. This function produces an experimentally observed stiffening at large compressive deformations (greater than ~20 percent) and maintains monotonicity in the nominal stress-deformation relationship for large compressive strain magnitudes.

Relationships between the macroscopic coupling tensors of Eq. (38) can be derived if we consider the free current density to be the sum of Ohmic and convective currents:

$$\mathbf{j} = -\boldsymbol{\sigma} \cdot \nabla\Phi + \rho_i \overset{*}{\mathbf{w}}, \tag{64}$$

where $\boldsymbol{\sigma}$ is the rank-two conductivity tensor for the medium. Combining Equations (38) and (64) yields

$$\mathbf{k}_{12} = \mathbf{k}_{21} = -\rho_i \mathbf{k}_{11}. \tag{65}$$

$$\mathbf{k}_{22} = \boldsymbol{\sigma} + \rho_i^2 \mathbf{k}_{11}. \tag{66}$$

We modeled the deformation dependence of the isotropic short-circuit permeability $\mathbf{k}_{11}$ using an approximation to a unit-cell-based microstructural model (Happel, 1959; Eisenberg and Grodzinsky, 1988). Over a reasonable range of volumetric deformations, this model can be approximated quite well by a two-parameter quadratic function in J:

$$\mathbf{k}_{11}(\mathbf{C}) = k_o \frac{(J - \phi_o^s)(\gamma + J - \phi_o^s)}{(1 - \phi_o^s)(\gamma + 1 - \phi_o^s)}\mathbf{1} \tag{67}$$

where k_o is the permeability in the undeformed state, γ is a unitless constant, and $\mathbf{1}$ is the rank-two identity tensor. Note that $\mathbf{k}_{11}$ vanishes as the fluid volume fraction goes to zero (Eq. (58)). For the present study, the fit parameters had values of $k_o = 5 \times 10^{-15}$ $m^4/N - s$ and $\gamma = 1.08$.

Macroscopically, we can view the conductivity of the medium as proportional to the effective mobility of the ionic solutes, which in turn depend on the volumetric deformation through a "tortuosity" factor (Mackie and Meares, 1955; Helfferich, 1962). Consequently, the deformation-dependent isotropic conductivity can be modeled as

$$\boldsymbol{\sigma}(\mathbf{C}) = \sigma_o\left[\frac{\phi^f(2 - \phi_o^f)}{\phi_o^f(2 - \phi^f)}\right]^2 \mathbf{1}$$

$$= \sigma_o\left[\frac{(J - \phi_o^s)(1 + \phi_o^s)}{(J + \phi_o^s)(1 - \phi_o^s)}\right]^2 \mathbf{1}. \tag{68}$$

where σ_o is the conductivity in the undeformed state, taken to be 1 S/m for the present study. Note that the solid matrix itself is considered to be nonconducting, with all conduction taking place in the ionic interstitial fluid. The remaining coupling coefficients were determined using Eqs. (65), (66), (59), (67), and (68).

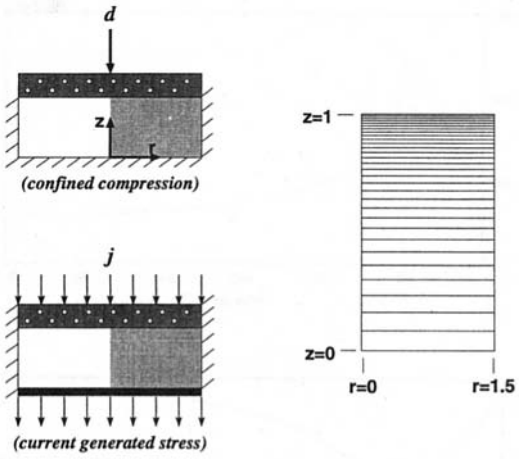

Fig. 3 Geometry and finite element mesh for confined compression and current generated stress. In the confined compression configuration, the chamber walls and base are rigid, impermeable and nonconducting, and a displacement d is applied via the rigid porous platen. In the current generated stress configuration, the chamber base and platen are conducting and the porous platen is held in position while an imposed current density j is applied through the tissue. The finite element mesh (not shown to scale) contained 30 quadrilateral elements, with mesh spacing biased towards the porous platen.

4.2 Example Problems. We first examined two one-dimensional test configurations that have been used to assess material properties of articular cartilage and other biological tissues (Frank and Grodzinsky, 1987a). The first, "confined compression," demonstrates mechanical-to-electrical transduction under finite deformations. The second, "current generated stress," demonstrates electrical-to-mechanical transduction, with large internal deformations. We then examined the two-dimensional example of "unconfined compression," which has been utilized in experiments investigating the effects of mechanical stimulation on the biological activity of live tissue samples (Sah et al., 1989).

4.2.1 Confined Compression. In the confined compression configuration, we modeled a disk of cartilage (3-mm diameter, 1 mm thick) placed in a confining chamber with rigid, impermeable, nonconducting walls and compressed by a rigid, highly permeable porous platen (Fig. 3). The pressure and electrical potential were taken to be zero (ambient) at the top surface, allowing free flow of fluid through the platen. Note that these boundary conditions ensure that no net current flow will occur in this configuration. A 30 element mesh was utilized, with mesh spacing biased towards the loaded surface where the highest strains are expected. A 50 μm compressive displacement (or five percent nominal strain) was applied at the platen in a 60 s constant velocity ramp, followed by a 300 s hold (or relaxation) period. A uniform time-step of 1 s was used during the ramp, and a variable time-step from 0.01 s to 10 s was used during the relaxation.

Application of the constant velocity displacement required a monotonically increasing compressive stress at the platen (Fig. 4(*a*)). At the end of the ramp, the matrix deformation and fluid velocity profiles were highly nonuniform, with the greatest deformation (over 20 percent compression) and fluid flow occurring beneath the platen (Fig. 4(*b*)). In regions with little matrix deformation, the majority of the load was carried by fluid pressurization (Fig. 4(*c*)). During the hold period, the total stress decayed to a lower steady-state value (Fig. 4(*a*)). As no further fluid exudation occurred during the hold period (because the total sample volume was constant), this relaxation period represents gradual internal redistribution of fluid (and matrix deformation) and a correspond-

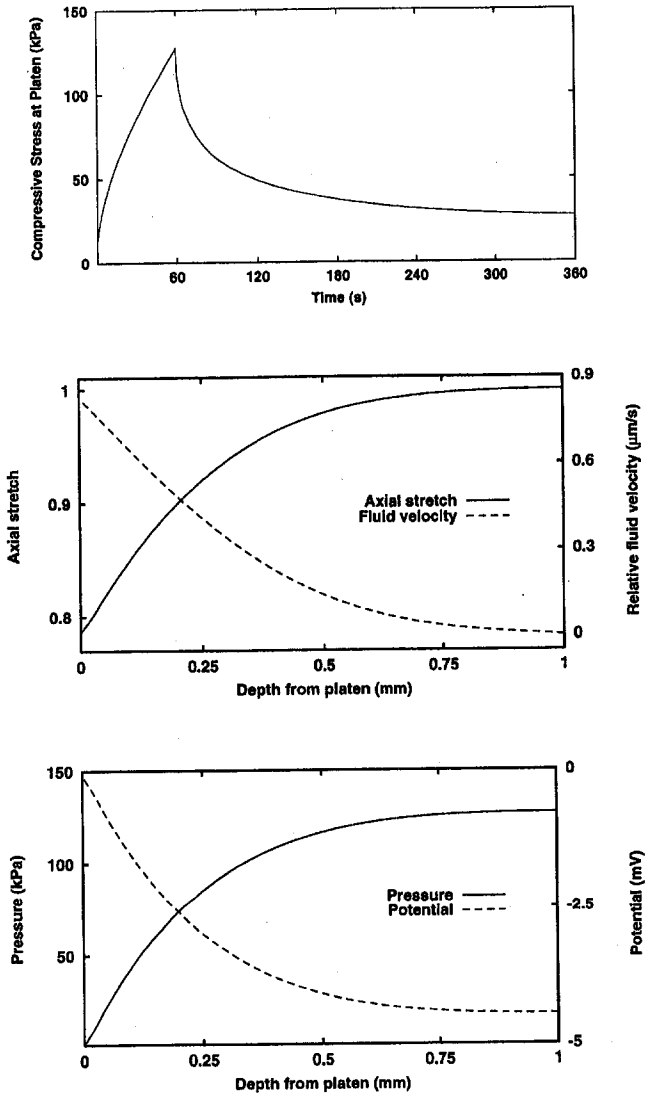

Fig. 4 Simulation results for the confined compression example: (*a*) total stress at the platen as a function of time during the 60 s ramp and 300 s hold, (*b*) axial deformation gradient and fluid velocity profiles at the end of the ramp displacement, and (*c*) fluid pressure and electrical potential profiles at the end of the ramp displacement

ing decay of the fluid pressure. At steady-state, the fluid carried no pressure and the entire load was equilibrated by uniform matrix deformation. This predicted mechanical behavior is typical of porous media, but additional electrokinetic effects are predicted by our model. Because the fluid carries a net positive charge, convection would tend to create a net charge imbalance within the tissue. To oppose this, an induced electrical potential (and associated internal electrical field) was generated within the tissue (Fig. 4(*c*)). Like the pressure, this induced electrical potential decayed to zero at steady-state. The large variations in matrix deformation (Fig. 4(*b*)) produced corresponding variations in the strain-dependent material properties. Consequently, the temporally evolving relaxation phenomena predicted by our model were more complicated than those predicted by previous linear or noncoupled models.

4.2.2 Current Generated Stress. The current generated stress configuration is similar to that of confined compression, with different mechanical and electrical boundary conditions. Although the walls of the confining chamber were still modeled as rigid, impermeable, and nonconducting, the base of the chamber was modeled as a conducting electrode used to drive current through the sample. The porous platen (also conducting) was held in a fixed position, and a constant amplitude current density (2 mA/cm^2) was applied through the tissue (from the platen towards the base). The same mesh was used as in the previous example, and a constant time-step of 10 s was utilized.

The electrical-mechanical coupling in this configuration can be seen by examining the stress required to hold the platen in its original position (Fig. 5(*a*)). Application of the current density immediately required the application of a compressive stress, which increased in magnitude with time and eventually reached a steady-state value. In the absence of this restraining stress, the specimen would tend to expand under this applied current. An examination of the tissue sample at steady-state reveals the mechanisms responsible for this transduction phenomenon.

To impose this current density, it was necessary to induce an electrical potential gradient across the tissue (Fig. 5(*c*)). If the boundaries at both ends of the sample were permeable, this current flow would have induced an electroosmotic fluid flow due to drag between the ions and the solvent fluid. Because the base was impermeable and the specimen volume was fixed, however, no fluid flow could take place across the porous platen. Consequently, a fluid pressure gradient was induced

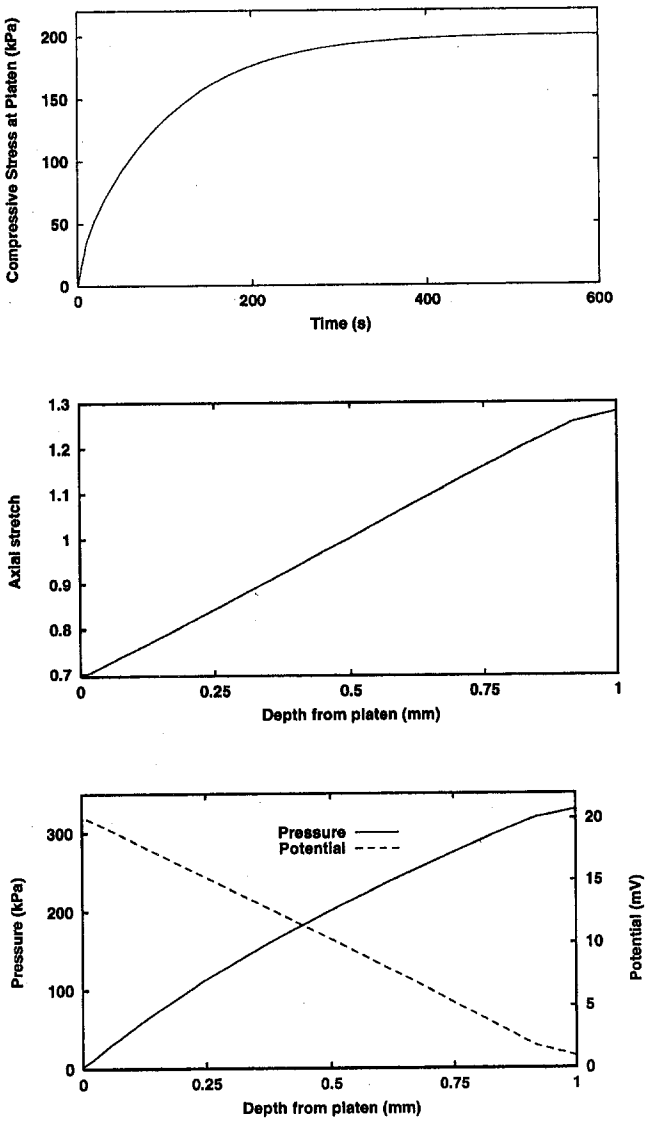

Fig. 5 Simulation results for the current generated stress example: (*a*) total stress required to hold the platen in its original position as a function of time, (*b*) axial deformation gradient profile at t = 600 s, and (*c*) fluid pressure and electrical potential profiles at t = 600 s

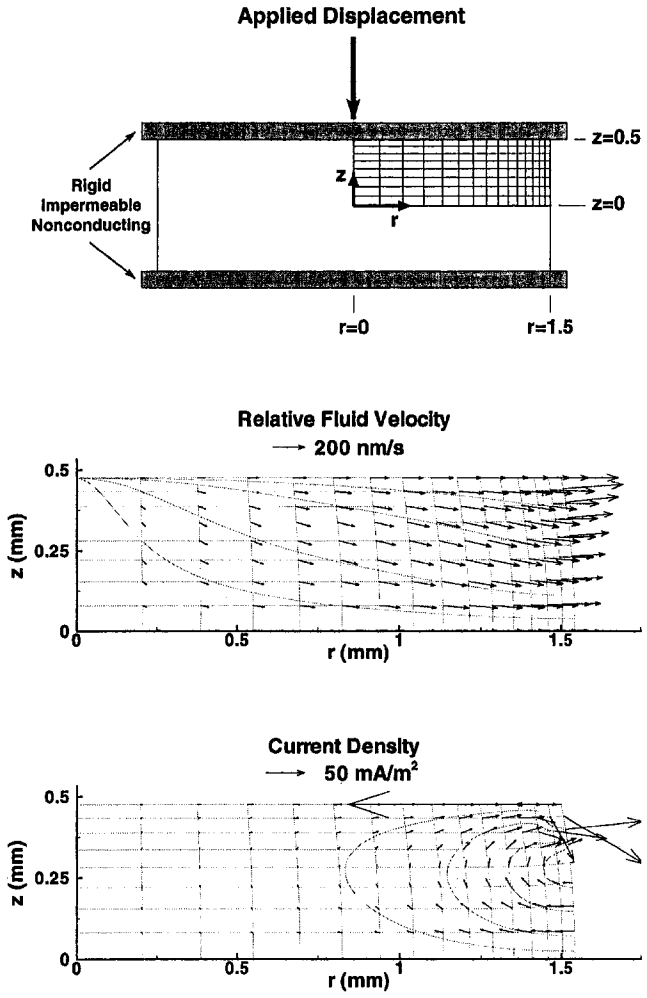

Fig. 6 Unconfined compression example. (*a*) Geometry and finite element mesh. Because of symmetry, only one quadrant of the plug was modeled. The mesh contained 120 quadrilateral elements, with mesh spacing biased towards the loading platen and the radial edge. (*b*) Relative fluid velocity. (*c*) Electrical current density distributions at the end of the ramp displacement. Streamlines have been included to aid in flow visualization, and results are displayed only for the meshed quadrant of the plug.

within the tissue to prevent any net fluid flow (Fig. 5(*c*)). This in turn required a gradient in stress supported by the solid matrix (so that the total stress was a constant), producing a nonuniform deformation field within the sample (Fig. 5(*b*)). This matrix deformation varied from approximately 30 percent compression at the porous platen to approximately 30 percent tension near the specimen base. Thus, imposition of the current flow through the tissue produced deformations (and corresponding changes in strain-dependent material properties) beyond the range of a linear model.

4.2.3 Unconfined Compression. To examine electromechanical interactions in a two-dimensional setting, we considered "radially unconfined compression" of a disk of cartilage (3-mm diameter, 1 mm thick) between two rigid, impermeable platens (Fig. 6(*a*)). To approximate the effects of boundary friction, we considered the bounding case of perfectly adhesive platens (no radial displacement at the platens). The fluid pressure and electrical potential were taken to be zero (ambient) on the radial surface, allowing free flow of fluid and current along this boundary. For the analogous purely mechanical problem, linear analytical (Kim et al., 1995) and nonlinear numerical solutions (Spilker et al., 1990; Levenston et al., 1998) are available, allowing verification of the mechanical predictions of the model. Taking advantage of geometric and material symmetry about the midplane, we modeled only the upper quadrant of the sample with a mesh of 120 quadrilateral elements. A 25 μm compressive displacement was applied at the platen (50 μm total compression) in a 60 s constant velocity ramp. A uniform time step of 3 s was utilized during the ramp.

As would be expected for any poroelastic medium, a monotonically increasing compressive stress was required to apply the constant velocity platen displacement. Because very little fluid exudation could occur during the displacement ramp, the material effectively responded as a nearly incompressible hyperelastic solid. Due to the physical restraint imposed by the adhesive platen, a two-dimensional deformation field was produced within the specimen. Consequently, two-dimensional profiles developed in all of the mechanical and electrical phenomena. At the end of the ramp, the predominant pattern of fluid flow was radial, with maximal flow near the radial edge (Fig. 6(*b*)). Superimposed on this, however, was an axial flow distribution, with fluid flowing from the relatively constrained material beneath the platen to the relatively unconstrained material near the midplane. Similarly, the pressure field (not shown) developed two-dimensionally, with both radial and axial pressure gradients. The pressure was maximal in the center of the sample beneath the loading platen, and dropped off to ambient at the free radial edge. The electrical potential distribution (not shown) was qualitatively similar to the pressure distribution, with the lowest electrical potential coinciding with the highest fluid pressure.

Interestingly, while the total current across the specimen boundary was zero, the current density was not zero at every point in the sample (Fig. 6(*c*)). Relatively high current densities were produced beneath the loading platen at the radial edge (where the largest deformation occurred),[7] and were equilibrated by lower, more distributed current densities towards the midplane. This produced an overall circulating pattern of current flow. We note that this solution satisfied the requirements of a divergence-free current density (Eqs. (34) and (37)) and a curl-free electric field (Eq. (22)).

Examination of the electromechanical coupling relationship (Eq. (38)) provides some insights into the induced current density field. In this example, the physical restraint at the platen gave rise to two-dimensionally varying deformation field. Because the various coupling coefficients depended on the deformation through different relationships, the induced gradients in pressure and potential were themselves no longer collinear. Consequently, the resulting convective and migration current densities were no longer collinear, and a nonzero net current arose. Utilizing Eq. (38), the curl of the current density can be written (for isotropic $\mathbf{k}_{ij}$) as

$$\nabla \times \mathbf{j} = (\nabla \cdot \mathbf{k}_{21} \times \nabla p - \nabla \cdot \mathbf{k}_{22} \times \nabla \Phi) + (\mathbf{k}_{21} \cdot \nabla \times \nabla p - \mathbf{k}_{22} \cdot \nabla \times \nabla \Phi). \quad (69)$$

The second grouping in this equation vanishes, and the first vanishes if the coupling coefficients are spatially uniform. The first grouping also vanishes if the divergences of $\mathbf{k}_{21}$ and $\mathbf{k}_{22}$ are collinear with the pressure and potential gradients, respectively. This was the case in the confined compression example, where all variations were purely axial. In this unconfined compression example, however, the deformation-induced inhomogeneities were not collinear with the pressure and potential gradients. Consequently, the induced current density distribution was not curl-free. We note that the same analysis applies to baseline inhomogeneities in the undeformed material properties. For example, if the material properties varied with radial position in the confined compression example, we would also expect induced current patterns to arise. This may be of biological relevance to adult articular cartilage, which is known to have a highly inhomogeneous composition and material properties (Maroudas, 1979).

Overall, the mechanical predictions of this model were consis-

[7] If the purpose of this example were to accurately predict the current patterns near the platen edge, we would need a much finer mesh (or alternate formulation) to capture the boundary layer behavior.

tent with previous purely mechanical analyses (Spilker et al., 1990; Kim et al., 1995; Levenston et al., 1998). None of these previous models, however, could represent the induced current patterns found in the present study. We note that other physical situations where the forced boundary conditions are primarily electrical (i.e., electroosmotic flow or the current generated stress example discussed earlier) fall entirely outside of the realm of the previous mechanical models.

5 Summary

In the present study, we developed a variational theory for quasistatic analysis of coupled electrokinetic and fluid flow in porous media with intrinsically incompressible constituents. Utilizing the principle of virtual power, we combined mathematical descriptions of poroelastic mechanical behavior, electroquasistatics, and continuum electromechanical coupling. This produced a five-field mixed finite element formulation, with the fluid pressure and electrical potential acting as Lagrange multipliers enforcing the mechanical saturation/incompressibility constraint and the bulk electroneutrality constraint, respectively. As examples, several experimental configurations involving finite deformations and electromechanical coupling were considered.

For a restricted class of problems with specific combinations of boundary conditions and material homogeneities, this formulation is equivalent to purely mechanical theories (with appropriate post-processing for electrical potential distributions). The confined compression example (with homogeneous properties) is one such problem, and the model predictions agree with those of previous poroelastic analyses. However, for general problems with complicated boundary conditions and/or inhomogeneity patterns, the new formulation predicts additional coupling phenomena that earlier approaches could not represent. In the current generated stress configuration, an imposed current flow through the tissue induced large tensile and compressive deformations within the sample despite the fact that the overall specimen size was held fixed. In the unconfined compression example, inhomogeneities induced by the spatially varying deformation field led to the development of circulating current distributions, although the boundary conditions ensured that the total current into the specimen was zero. The phenomena described in the latter two examples are beyond the scope of earlier formulations, and can only be predicted by a model that includes electromechanical coupling while accounting for finite deformations and deformation-dependent material properties. This new formulation may be of use in analyzing geometrically and materially complex problems in charged porous media in the fields of biomechanics, membrane physics, and geomechanics.

Acknowledgments

Supported by the Public Health Service and the Arthritis Foundation through postdoctoral research grants to M. Levenston, and by the National Institutes of Health through Grant AR33236.

References

Armstrong, C. G., and Mow, V. C., 1982, "Variations in the Intrinsic Mechanical Properties of Human Articular Cartilage with Age, Degeneration and Water Content," *The Journal of Bone and Joint Surgery,* Vol. 64-A, pp. 88–94.

Biot, M. A., 1972, "Theory of Finite Deformations of Porous Solids," *Indiana University Mathematics Journal,* Vol. 21, pp. 597–620.

Bowen, R. M., 1980, "Incompressible Porous Media Models by Use of the Theory of Mixtures," *International Journal of Engineering Science,* Vol. 18, pp. 1129–1148.

Brezzi, F., and Fortin, M., 1991, *Mixed and Hybrid Finite Element Methods,* Springer-Verlag, New York.

DeGroot, S. R., and Mazur, P., 1969, *Nonequilibrium Thermodynamics,* North Holland, Amsterdam.

Dukhin, S. S., and Derjaguin, B. V., 1974, *Electrokinetic Phenomena,* E. Matijević, ed. (Vol. 7 of Surface and Colloid Science), John Wiley and Sons, New York.

Eisenberg, S. R., and Grodzinsky, A. J., 1987, "The Kinetics of Chemically Induced Nonequilibrium Swelling of Articular Cartilage and Corneal Stroma," ASME *Journal of Biomechanical Engineering,* Vol. 109, pp. 79–89.

Eisenberg, S. R., and Grodzinsky, A. J., 1988, "Electrokinetic Micromodel of Extracellular Matrix and Other Polyelectrolyte Networks," *PhysicoChemical Hydrodynamics,* Vol. 10, pp. 517–539.

Eringen, A. C., 1967, *Mechanics of Continua,* John Wiley and Sons, New York.

Frank, E. H., and Grodzinsky, A. J., 1987a, "Cartilage Electromechanics—I. Electrokinetic Transduction and the Effects of Electrolyte pH and Ionic Strength," *Journal of Biomechanics,* Vol. 20, pp. 615–627.

Frank, E. H., and Grodzinsky, A. J., 1987b, "Cartilage Electromechanics—II. A Continuum Model of Cartilage Electrokinetics and Correlation With Experiments," *Journal of Biomechanics,* Vol. 20, pp. 629–639.

Friedman, M. H., 1971, "General theory of tissue swelling with application to the corneal stroma," *Journal of Theoretical Biology,* Vol. 30, pp. 93–109.

Gu, W. Y., Lai, W. M., and Mow, V. C., 1993, "Transport of fluid and ions through a porous-permeable charged-hydrated tissue, and streaming potential data on normal bovine articular cartilage," *Journal of Biomechanics,* Vol. 26, pp. 709–723.

Happel, J., 1959, "Viscous Flow Relative to Arrays of Cylinders," *AIChE Journal,* Vol. 5, pp. 174–177.

Haus, H. A., and Melcher, J. R., 1989, *Electromagnetic Fields and Energy,* Prentice-Hall, Englewood Cliffs, NJ.

Helfferich, F., 1962, *Ion Exchange,* McGraw-Hill, New York.

Holmes, M. H., and Mow, V. C., 1990, "The Nonlinear Characteristics of Soft Gels and Hydrated Connective Tissues in Ultrafiltration," *Journal of Biomechanics,* Vol. 23, pp. 1145–1156.

Hughes, T. J. R., 1987, *The Finite Element Method,* Prentice-Hall, Englewood Cliffs, NJ.

Huyghe, J. M., and Janssen, J. D., 1997, "Quadriphasic mechanics of swelling incompressible porous media," *International Journal of Engineering Science,* Vol. 35, pp. 793–802.

Kenyon, D. E., 1979, "A mathematical model of water flux through aortic tissue," *Bulletin of Mathematical Biology,* Vol. 41, pp. 79–90.

Kim, Y. J., Bonassar, L. J., and Grodzinsky, A. J., 1995, "The Role of Cartilage Streaming Potential, Fluid Flow and Pressure in the Stimulation of Chondrocyte Biosynthesis During Dynamic Compression," *Journal of Biomechanics,* Vol. 28, pp. 1055–1066.

Kwan, M. K., Lai, W. M., and Mow, V. C., 1990, "A Finite Deformation Theory for Cartilage and Other Soft Hydrated Connective Tissues—I. Equilibrium Results," *Journal of Biomechanics,* Vol. 23, pp. 145–155.

Lai, W. M., Hou, J. S., and Mow, V. C., 1991, "A Triphasic Theory for the Swelling and Deformation Behaviors of Articular Cartilage," ASME *Journal of Biomechanical Engineering,* Vol. 113, pp. 245–258.

Levenston, M. E., Frank, E. H., and Grodzinsky, A. J., 1998, "Variationally derived 3-field finite element formulations for quasistatic poroelastic analysis of hydrated biological tissues," *Computer Methods in Applied Mechanics and Engineering,* Vol. 156, pp. 231–246.

Lewis, R. W., and Garner, R. W., 1972, "A Finite Element Solution of Coupled Electrokinetic and Hydrodynamic Flow in Porous Media," *International Journal for Numerical Methods in Engineering,* Vol. 5, pp. 41–55.

Mackie, J. S., and Meares, P., 1955, "The Diffusion of Electrolytes in a Cation-Exchange Resin. I. Theoretical," *Proceedings of the Royal Society (London),* Vol. A232, pp. 498–509.

Maroudas, A., 1979, "Physicochemical properties of articular cartilage," *Adult Articular Cartilage,* M. A. R. Freeman, ed., 2nd Ed., Pitman Medical, Kent, UK, pp. 215–290.

Maroudas, A., Evans, H., and Almeida, L., 1973, "Cartilage of the Hip Joint. Topographical Variation of Glycosamioglycan Content in Normal and Fibrillated Tissue," *Annals of the Rheumatic Diseases,* Vol. 32, pp. 1–9.

Marsden, J. E., and Hughes, T. J. R., 1994, *Mathematical Foundations of Elasticity,* Dover Publications, New York.

Massé, P., and Berthier, J., 1996, "Three Dimensional Finite Element Modeling of Streaming Potential and Associated Magnetic Field in Porous Media," *IEEE Transactions on Magnetics,* Vol. 32, pp. 994–997.

Maugin, G. A., and Eringen, A. C., 1977, "On the Equations of the Electrodynamics of Deformable Bodies of Finite Extent," *Journal de Mécanique,* Vol. 16, pp. 101–147.

Mow, V. C., Kuei, S. C., Lai, W. M., and Armstrong, C. G., 1980, "Biphasic Creep and Stress Relaxation of Articular Cartilage in Compression: Theory and Experiments," ASME *Journal of Biomechanical Engineering,* Vol. 102, pp. 73–103.

Neev, J., and Yeatts, F. R., 1989, "Electrokinetic Effects in Fluid-Saturated Poroelastic Media," *Physical Review B,* Vol. 40, pp. 9135–9141.

Oomens, C. W., van Campen, D. H., and Grootenboer, H. J., 1987, "A mixture approach to the mechanics of skin," *Journal of Biomechanics,* Vol. 20, pp. 877–885.

Penfield, Jr., P., and Haus, H. A., 1967, *Electrodynamics of Moving Media,* M.I.T. Press, Cambridge, MA.

Sah, R. L., Kim, Y. J., Doong, J. Y., Grodzinsky, A. J., Plaas, A. H., and Sandy, J. D., 1989, "Biosynthetic response of cartilage explants to dynamic compression," *Journal of Orthopaedic Research,* Vol. 7, pp. 619–636.

Simon, B. R., 1992, "Multiphase Poroelastic Finite Element Models for Soft Tissue Structures," ASME *Applied Mechanics Reviews,* Vol. 56, pp. 191–218.

Simon, B. R., and Gaballa, M. A., 1988, "Finite strain, poroelastic finite element models for large arterial cross sections," *Computational Methods in Bioengineering,* R. L. Spilker and B. R. Simon, eds. ASME, New York, pp. 325–334.

Simon, B. R., Laible, J. P., Pflaster, D., Yuan, Y., and Krag, M. H., 1996, "A Poroelastic Finite Element Formulation Including Transport and Swelling in Soft Tissue Structures," ASME *Journal of Biomechanical Engineering,* Vol. 118, pp. 1–9.

Simon, B. R., Wu, J. S.-S., Carlton, M. W., Evans, J. H., and Kazarian, L. E., 1985, "Structural Models for Human Spinal Motion Segments Based on a Poroelastic View

of the Intervertebral Disk," ASME *Journal of Biomechanical Engineering,* Vol. 107, pp. 327–335.

Snijders, H., Huyghe, J., Willems, P., Drost, M., Janssen, J., and Huson, A., 1992, "A Mixture Approach to the Mechanics of the Human Intervertebral Disc," *Mechanics of Swelling,* T. K. Karalis, ed. (Vol. H 64 of NATO ASI Series), Springer-Verlag, Berlin, pp. 545–558.

Snijders, H., Huyghe, J. M., and Janssen, J. D., 1995, "Triphasic Finite Element Model for Swelling Porous Media," *International Journal for Numerical Methods in Fluids,* Vol. 20, pp. 1039–1046.

Spilker, R. L., Suh, J. K., and Mow, V. C., 1990, "Effects of Friction on the Unconfined Compressive Response of Articular Cartilage: A Finite Element Analysis," ASME *Journal of Biomechanical Engineering,* Vol. 112, pp. 138–146.

Swenson, Jr., L. W., 1979, "Mechanics of Human Articular Cartilage," Ph.D. thesis, Stanford University, Stanford, CA.

Thomas, J. P., 1991, "The Modeling of Open Mass Continuum Mixtures," *International Journal of Engineering Science,* Vol. 29, pp. 1451–1469.

APPENDIX

The following are general definitions of the global vectors and matrices in the incrementally linearized matrix equation (Eq. (54)), which are assembled from the corresponding element vectors and matrices in the usual manner. These definitions are applied using the appropriate compacted matrix forms, depending on the spatial order of the particular implementation. Following Einsteinian indicial notation, repeated subscripts imply summation. Uppercase subscripts indicate material coordinates, lowercase subscripts indicate spatial coordinates, and Greek superscripts indicate a global node number. Components of the consistent tangent elasticity tensor for the solid are represented by D_{IKLM}, and components of the rank-two identity tensor are represented by δ_{st}.

$$K_{st}^{uu\,\alpha\epsilon} = \int_{\Omega_o^h} \frac{\partial N^{u\,\alpha}}{\partial X_K} \{(S_{KL}^e - pJB_{KL})\delta_{st} + F_{si}[D_{IKLM} - pJ(B_{IK}B_{LM} - B_{KL}B_{IM} - B_{IL}B_{KM})]F_{tM}^{-1}\} \frac{\partial N^{u\,\epsilon}}{\partial X_L} d\Omega \quad (70)$$

$$K_s^{up\,\alpha\tau} = -\int_{\Omega_o^h} \frac{\partial N^{u\,\alpha}}{\partial X_K} JF_{Ks}^{-1} N^{p\,\tau} d\Omega \quad (71)$$

$$K_L^{wp\,\beta\tau} = -\int_{\Omega_o^h} \frac{\partial N^{w\,\beta}}{\partial X_L} N^{p\,\tau} d\Omega \quad (72)$$

$$K_L^{g\Phi\,\gamma\xi} = -\int_{\Omega_o^h} \frac{\partial N^{g\,\gamma}}{\partial X_L} N^{\Phi\,\xi} d\Omega \quad (73)$$

$$C_{LM}^{ww\,\beta\eta} = \int_{\Omega_o^h} N^{w\,\beta} r_{11_{LM}} N^{w\,\eta} d\Omega \quad (74)$$

$$C_{LM}^{wg\,\beta\xi} = \int_{\Omega_o^h} N^{w\,\beta} r_{12_{LM}} N^{g\,\xi} d\Omega \quad (75)$$

$$C_{LM}^{gg\,\mu\xi} = \int_{\Omega_o^h} N^{g\,\mu} r_{22_{LM}} N^{g\,\xi} d\Omega \quad (76)$$

$$R_s^{u\,\alpha} = \int_{\Omega_o^h} \frac{\partial N^{u\,\alpha}}{\partial X_K} (T_{sK}^e - pJF_{Ks}^{-1}) d\Omega - \int_{\Gamma_{o_t}^h} N^{u\,\alpha} f_s d\Gamma \quad (77)$$

$$R_L^{w\,\beta} = \int_{\Omega_o^h} \left[-\frac{\partial N^{w\,\beta}}{\partial X_L} p + N^{w\,\beta}(r_{11_{LM}} \dot{W}_M + r_{12_{LM}} J_M) \right] d\Omega + \int_{\Gamma_{o_p}^h} N^{w\,\beta} \tilde{p} n_L d\Gamma \quad (78)$$

$$R_L^{g\,\gamma} = \int_{\Omega_o^h} \left[-\frac{\partial N^{g\,\gamma}}{\partial X_L} \Phi + N^{g\,\gamma}(r_{21_{LM}} \dot{W}_M + r_{22_{LM}} J_M) \right] d\Omega + \int_{\Gamma_{o_\Phi}^h} N^{g\,\gamma} \tilde{\Phi} n_L d\Gamma \quad (79)$$

$$R^{p\,\lambda} = \int_{\Omega_o^h} N^{p\,\lambda}(1 - J + \xi) d\Omega \quad (80)$$

$$R^{\Phi\,\mu} = \int_{\Omega_o^h} N^{\Phi\,\mu} \hat{\rho}_u d\Omega \quad (81)$$

A Steady-State Thermomechanical Solution of Continuously Quenched Axisymmetric Bodies

Y. Ruan
Alcoa Technical Center,
Aluminum Company of America,
100 Technical Drive,
Alcoa Center, PA 15069
Assoc. Mem. ASME

A finite element methodology to solve steady-state thermochemical problems is presented in this paper, where axisymmetric geometry is considered, and small strain and small rotation are assumed for the mechanical problem. Both thermal and mechanical problems are formulated in the Eulerian frame with the finite element method. The heat transfer problem is solved with the Petrov-Galerkin method due to the convection-diffusion nature of the governing equation, and the virtual work principle is applied to the equation of motion to obtain the finite element formulation. To determine the inelastic deformation, an additional system of equations is formed by applying the Petrov-Galerkin method to the material derivatives of the inelastic strain rates. Studies in this paper focus on continuous axisymmetric problems with quenching examples. Generally, the computational time with the steady-state (Eulerian) method presented in this paper is significantly less than that with transient (Lagrangian) approaches.

1 Introduction

Many industrial processes involve continuously heating and cooling in a product line, where the product experiences various mechanical deformation such as that in the continuous rod and tube quenching processes. During the quenching process, a certain level of cooling rate must be maintained in order to obtain proper material properties. The cooling is generally performed in a cooling chamber or cooling region, and the quenched body continuously passes through the cooling region. Because of the nature of the cooling process, the temperature in the quenched body is not uniform, consequently, high thermal stresses may result. The stresses in the body after the quenching process (residual stresses) are undesirable because they may cause a finished product to have excess distortion. In addition, the residual stresses may have a deleterious effect on fracture and corrosion performance. Therefore, it is important to understand the stress evolution in order to control the stresses and have quality products.

Thermomechanical analysis of the quenching process can be performed with a transient (Lagrangian) approach by including a large computation domain to ensure that steady-state conditions are reached. Examples for transient (Lagrangian) analyses of non-continuous quenching problems can be found in the references by Fletcher and Lewis (1985), Zabaras et al. (1987), and Becker et al. (1994).

The transient approaches may not be desirable to simulate the continuous quenching process because a significant amount of computational time is required. To overcome the drawback of the transient approaches, a steady-state method is developed in this paper to perform the thermomechanical analysis of continuous processes such as the continuous quenching process.

Contributed by the Applied Mechanics Division of THE AMERICAN SOCIETY OF MECHANICAL ENGINEERS for publication in the ASME JOURNAL OF APPLIED MECHANICS.
Discussion on the paper should be addressed to the Technical Editor, Professor Lewis T. Wheeler, Department of Mechanical Engineering, University of Houston, Houston, TX 77204-4792, and will be accepted until four months after final publication of the paper itself in the ASME JOURNAL OF APPLIED MECHANICS.
Manuscript received by the ASME Applied Mechanics Division, June 1, 1995; final revision, Oct. 2, 1998. Associate Technical Editor: M. Taya.

2 The Heat Transfer Problem

The heat transfer for the steady-state quenching problem is governed by the advection-diffusion equation, that is

$$\rho c \mathbf{V} \cdot \nabla T = \nabla \cdot k \nabla T \quad r,z \in A \tag{1}$$

where ρ, c, and k are the density, specific heat, and conductivity, respectively; r and z are the radial and axial coordinates (Fig. 1); the gradient operator and the velocity vector are $\nabla = \mathbf{r}\partial/\partial r + \mathbf{z}\partial/\partial r$ and $\mathbf{V} = \mathbf{r}V_r + \mathbf{z}V_z$, respectively, where $\mathbf{r}$, and $\mathbf{z}$ are the unit base vectors in the cylindrical coordinate system and V_r and V_z are the steady-state radial and axial velocity components, respectively; and A is the control volume. In this paper, the component related to $\partial/\partial\theta$ is dropped because only axisymmetric problems are considered.

Generally, the quenched material is solution heat treated at a uniform temperature, T_u, to allow solute elements to defuse into the solid solution. Then the material is quickly cooled to retain the solute in the solid solution. Therefore, at the upstream of the control volume, the temperature is

$$T(r, z) = T_u \quad r, z \in \partial A_u \tag{2}$$

and the convection and radiation boundary conditions can be used to represent the cooling effect at the surface of the axisymmetry body, i.e.,

$$-k\ \partial T/\partial n = h(T - T_\infty) + R\ (T^4 - T_\infty^4) \quad r, z \in \partial A_c \tag{3}$$

where h and R are the convection and radiation heat transfer coefficient, respectively; and T_∞ is the environmental temperature (the temperature of the cooling medium). Here ∂A_c represents the surface of the body where it is cooled and ∂A_u denotes the upstream boundary of the control volume.

3 The Mechanical Problem

The equations that governs the mechanical deformation for the axisymmetric problem are as follows:

$$-\frac{1}{r}\frac{\partial(r\sigma_r)}{\partial r} - \frac{\partial \sigma_{rz}}{\partial z} + \frac{\sigma_\vartheta}{r} = \rho b_r - \rho \frac{DV_r}{Dt} \tag{4}$$

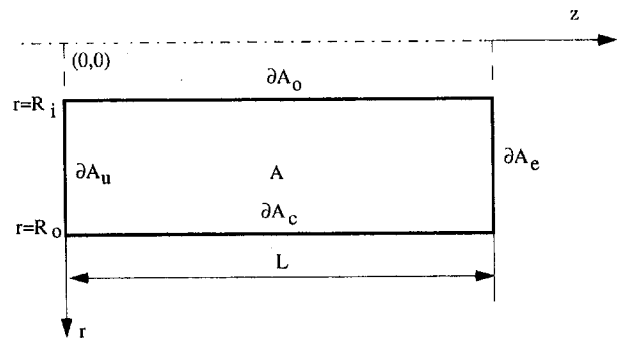

Fig. 1 Schematic diagram of the quenched axisymmetric body

$$-\frac{1}{r}\frac{\partial(r\sigma_{rz})}{\partial r}-\frac{\partial\sigma_z}{\partial z}=\rho b_z-\rho\frac{DV_z}{Dt} \tag{5}$$

where σ_r, σ_z, σ_{rz}, and σ_θ are the components of the vector form of the Cauchy stress tensor.

The relationship between the stress and elastic strain is governed by Hook's law, that is,

$$\sigma=\mathbf{D}(T)\epsilon^E \tag{6}$$

where σ is the Cauchy stress tensor with the vector form, $\sigma=(\sigma_r\ \sigma_z\ \sigma_{rz}\ \sigma_\theta)^T$, ϵ^E is the elastic strain sensor, $\mathbf{D}(T)$ is the temperature-dependent elastic constant tensor and the matrix form of $\mathbf{D}(T)$ is given as

$$\mathbf{D}=\frac{E(T)}{(1+\nu)(1-2\nu)}\begin{pmatrix}1-\nu & \nu & 0 & \nu\\ \nu & 1-\nu & 0 & \nu\\ 0 & 0 & \dfrac{(1-2\nu)}{2} & 0\\ \nu & \nu & 0 & 1-\nu\end{pmatrix} \tag{7}$$

where $E(T)$ is the Young's modulus and ν is the Poisson's ratio.

Because small strain and rotation problems are studied here, we can assume that the total strain tensor ϵ can be additively decomposed into the elastic, ϵ^E, the thermal, ϵ^T, and the inelastic, ϵ^N, part, respectively, that is

$$\epsilon=\epsilon^E+\epsilon^T+\epsilon^N \tag{8}$$

where ϵ is total strain tensor, whose vector form is $\epsilon=(\epsilon_r\ \epsilon_z\ \epsilon_{rz}\ \epsilon_\theta)^T$, and ϵ^N have the same form as ϵ does. The total strain tensor can be calculated through the displacement field as $\epsilon_r=\partial u_r/\partial r$, $\epsilon_z=\partial u_z/\partial z$, $\epsilon_\theta=u_r/r$, $\epsilon_{rz}=0.5\ \gamma_{rz}=0.5\ (\partial u_r/\partial z+\partial u_z/\partial r)$.

The thermal strains are dilatational and can be expressed as

$$\epsilon_r^T(T)=\epsilon_z^T(T)=\epsilon_\theta^T(T)=\int_{T_R}^{T}a(\nu)d\nu,\quad \epsilon_{rz}^T(T)=0 \tag{9}$$

where $a(T)$ is the temperature dependent thermal expansion coefficient and T_R is the reference temperature at which the thermal strains are zero.

The inelastic deformation can be represented by the following generalized constitutive equation;

$$\dot{\epsilon}^N=\mathbf{f}(\sigma,\ \epsilon^N,\ T,\ \dots) \tag{10}$$

where $\dot{\epsilon}^N$ is the inelastic strain rate tensor.

4 Finite Element Formulation of the Heat Transfer Problem

Since standard Galerkin method may lead to unstable solutions for convection-diffusion problems with high Peclet numbers, the Petrov-Galerkin approach is used for the heat transfer analysis. With the trial and test functions, T, $\bar{T}\in V=\{v\in H_o^1\}$, where H_o^1 is a Soblev space, the following variational statement can be derived from the governing equation for the heat transfer problem, Eq. (1):

$$\int_A\rho c\mathbf{V}\cdot\nabla T(\bar{T}+\delta\cdot\nabla\bar{T})dA+\int_A k\nabla T\cdot\nabla\bar{T}dA-\int_A\nabla\cdot k\nabla T\ \delta\cdot\nabla\bar{T}dA-\int_{\partial A}k\nabla T\cdot n\bar{T}\,d\Gamma=0 \tag{11}$$

where δ is the function of the element size and velocity, $dA=rdrdz$ and $d\Gamma=rds$ ($ds^2=dx^2+dy^2$).

The control volume A can be divided into E elements and N nodes, and the temperature in the domain is represented with interpolation functions. The interpolation function for the temperature can be expressed as $T=\Sigma T_a\Phi_a$, $(a=1,2,\dots,M)$, where T_a is the nodal temperature, and Φ_a is the isoparametric finite element shape function. The function $\bar{T}$ can also be expressed with the finite element shape function as $\bar{T}=\Sigma\bar{T}_a\Phi_a$, where $\bar{T}_a$ is the nodal value of $\bar{T}$. Based on the element size and steady-state velocity, the function δ in Eq. (11) can be defined as $\delta=0.5(\coth\text{Pe}-1/\text{Pe})s\mathbf{V}/|\mathbf{V}|$, where s is the element size and $\text{Pe}=0.5|\mathbf{V}|s/k$ (Zienkiewicz and Taylor, 1991). After the finite element discretization, the following system of equations can be obtained:

$$\mathbf{KT}=\mathbf{F} \tag{12}$$

where $\mathbf{K}$ and $\mathbf{F}$ are the stiffness matrix and load vector, respectively; and $\mathbf{T}$ is the vector of temperatures at nodal points. The components of $\mathbf{K}$ and $\mathbf{F}$ are

$$K_{ab}=\int_A\rho c(\Phi_a+\delta\cdot\nabla\Phi_a)\mathbf{V}\cdot\nabla\Phi_b dA+\int_A k\nabla\Phi_a\cdot\nabla\Phi_b dA-\int_A\nabla\cdot k\nabla\Phi_b\delta\cdot\nabla\Phi_a dA+\int_{\partial A_c}(h+a_r(T,T_\infty))\Phi_a\Phi_b d\Gamma \tag{13}$$

$$F_a=\int_{A_c}(T_\infty+a_r(T,T_\infty)T_\infty)\Phi_a d\Gamma \tag{14}$$

where $a_r(T,T_\infty)=R\,(T^2+T_\infty^2)(T-T_\infty)$. Notice that when k is constant, some of the high-order terms in Eq. (13) will vanish when the linear or bilinear elements are used. More discussions on the calculation of the high-order term can be found in the book by Johnson (1987).

5 Virtual Work and Finite Element Formulation for the Stress Problem

Applying the virtual work principle to Eqs. (4) and (5), we can derive the following weak formulation:

$$\int_A\sigma(\mathbf{u}):\epsilon(\bar{\mathbf{u}})dA=\int_{\partial A}\tau\cdot\bar{\mathbf{u}}d\Gamma+\int_A\rho(\mathbf{b}+D\mathbf{V}/Dt)\cdot\bar{\mathbf{u}}dA \tag{15}$$

where $\mathbf{u}$ ($\mathbf{u}=(u_r\ u_z)^T$) is the displacement field and $\bar{\mathbf{u}}$ is virtual displacement field, $d\Gamma=rds$, and $dA=rdrdz$. The body force and the acceleration term in Eq. (15) can be neglected when their contribution to the mechanical deformation is negligible.

Although the finite element analysis of the stress problem can be performed with the same discretization as that used for the heat transfer analysis, we consider a general case with a different finite element discretization for the stress problem. Assuming that the control volume is discretized with N nodes and E elements, we can express the displacement field with isoparametric shape functions $\mathbf{N}$ as $\mathbf{d} = \mathbf{Nu}$. The corresponding strain and stress field are $\epsilon = \mathbf{Bu}$ and $\sigma = \mathbf{DBu}$, respectively, where $\mathbf{B}$ is derived through differentiation of the shape function $\mathbf{N}$. After the discretization and using Eqs. (6) and (8), we can derive the following system of equations from Eq. (15):

$$\mathbf{AU}=\mathbf{P} \tag{16}$$

where $\mathbf{A}$ is the stiffness matrix, $\mathbf{U}$ is the vector of the nodal displacement field, and $\mathbf{P}$ is the load vector. The components of $\mathbf{A}$ and $\mathbf{P}$ are

$$\mathbf{A} = \int_A \mathbf{B}^T\mathbf{D}\mathbf{B}dA \tag{17}$$

$$\mathbf{P} = \int_{\partial A} \mathbf{N}^T\tau\, d\Gamma + \int_A \mathbf{B}^T\mathbf{D}(\epsilon^T + \epsilon^N)dA + \int_A \mathbf{N}^T\rho(\mathbf{b} + D\mathbf{V}/Dt)dA \tag{18}$$

6 Calculation of the Inelastic Strains

To obtain the inelastic strain, we employ the concept of the material derivative. The material derivative of the inelastic strain can be expressed as follows:

$$\dot{\epsilon}^N = \partial\epsilon^N/\partial t + \mathbf{V}\cdot\nabla\epsilon^N. \tag{19}$$

Substituting Eq. (19) into Eq. (10), we can derive the following equation:

$$\partial\epsilon^N/\partial t + \mathbf{V}\cdot\nabla\epsilon^N = \mathbf{f}(\sigma, \epsilon^N, T, \ldots) \quad r, z \in A. \tag{20}$$

For the problem considered here, Eq. (20) involves four independent scalar equations corresponding to the inelastic strain components, ϵ_r^N, ϵ_z^N, ϵ_{rz}^N, ϵ_θ^N, and represents the evolution of inelastic strain with time. For a steady-state process, to an observer in the Eulerian frame, $\partial\epsilon^N/\partial t = 0$. In this analysis, the term $\partial\epsilon^N/\partial t$ is kept for the purpose of iteration.

Before the quenched body enters the quenching chamber, it has a uniform temperature. At this stage, there is no deformation in the body. Therefore, the value of the total inelastic strains at the upstream of the control volume A is

$$\epsilon^N = 0 \quad r, z \in \partial A_u. \tag{21}$$

To obtain the inelastic strains, a weak formulation is applied to Eq. (20) on the control volume A. The Petrov-Galerkin method is also used here to stabilize the algorithm. The variational statement of Eq. (20) employing the Petrov-Galerkin method is as follows:

$$\int_A \partial\epsilon^N/\partial t(w + \gamma\xi\mathbf{V}\cdot\nabla w)dA + \int_A \mathbf{V}\cdot\nabla\epsilon^N(w + \gamma\xi\mathbf{V}\cdot\nabla w)dA = \int_A \mathbf{f}(\sigma, \epsilon^N, T, \ldots)(w + \gamma\xi\mathbf{V}\cdot\nabla w)dA \tag{22}$$

where $w \in V = \{v \in H_o^1\}$ (H_o^1 is a Soblev space), γ is a constant, and ξ is the element parameter which represents the element size. Equation (22) can be considered as the summation of two equations with the standard Galerkin method for two different test functions, i.e., w and $(\gamma\xi\mathbf{V}\cdot\nabla w)$.

Equation (22) can be discretized with the finite element interpolation functions for the inelastic strains, ϵ^N, and the function w as $\epsilon^N = \Sigma\epsilon_\beta^N\Psi_\beta$, $w = \Sigma w_\beta\Psi_\beta$ ($\beta = 1, 2, \ldots, L$), respectively, where L is the number of nodes, ϵ_β^N is the nodal value of the inelastic strain tensor, and Ψ_β is shape function which may be the same as, or different from those used for temperature and displacement interpolations. Generally, integration of the inelastic strains can be performed with the mesh used for thermal or stress analysis. With the finite element interpolation functions, the following equation can be derived:

$$\int_A (\Psi_\alpha + \gamma\xi\mathbf{V}\cdot\nabla\Psi_\alpha)\Psi_\beta dA\,\partial\epsilon_\beta^N/\partial t + \int_A (\Psi_\alpha + \gamma\xi\mathbf{V}\cdot\nabla\Psi_\alpha)\mathbf{V}\cdot\nabla\Psi_\beta dA\,\epsilon_\beta^N = \int_A (\Psi_\alpha + \gamma\xi\mathbf{V}\cdot\nabla\Psi_\alpha)\mathbf{f}(\sigma, \epsilon^N, T, \ldots)dA. \tag{23}$$

Equation (23) can be written in the following compact form:

$$\mathbf{C}\dot{\mathbf{e}} + \mathbf{Q}\mathbf{e} = \mathbf{g} \tag{24}$$

where the vector $\mathbf{e}$ contains inelastic strains, the components of the matrix $\mathbf{C}$ and $\mathbf{Q}$ are

$$C_{\alpha\beta} = \int_A (\Psi_\alpha + \gamma\xi\mathbf{V}\cdot\nabla\Psi_\alpha)\Psi_\beta dA \tag{25}$$

$$Q_{\alpha\beta} = \int_A (\Psi_\alpha + \gamma\xi\mathbf{V}\cdot\nabla\Psi_\alpha)\mathbf{V}\cdot\nabla\Psi_\beta dA \tag{26}$$

and the components of the vector $\mathbf{g}$ is

$$g_\alpha = \int_A (\Psi_\alpha + \gamma\xi\mathbf{V}\cdot\nabla\Psi_\alpha)\mathbf{f}(\sigma, \epsilon^N, T, \ldots)dA. \tag{27}$$

Equation (24) can be integrated with the backward Euler scheme as

$$\left(\frac{\mathbf{C}}{\Delta t} + \mathbf{Q}\right)\mathbf{e}^n = \mathbf{g} + \frac{\mathbf{C}}{\Delta t}\mathbf{e}^{n-1} \tag{28}$$

where n represents the current step number.

The term $\mathbf{Ce}^{n-1}$ in Eq. (24) is the inelastic strains at the previous step. When the term $\mathbf{Ce}^{n-1}$ is combined with the load vector $\mathbf{g}$ to form a modified load vector $\mathbf{g}^*$, the following equation can be obtained:

$$\left(\frac{\mathbf{C}}{\Delta t} + \mathbf{Q}\right)\mathbf{e}^n = \mathbf{g}^* \tag{29}$$

where the components of $\mathbf{g}^*$ are

$$g_\alpha^* = \int_A \{(\Psi_\alpha + \gamma\xi\mathbf{V}\cdot\nabla\Psi_\alpha)(\mathbf{f}(\sigma, \epsilon^N, T, \ldots) + (\epsilon^N)^{n-1}/\Delta t\}dA. \tag{30}$$

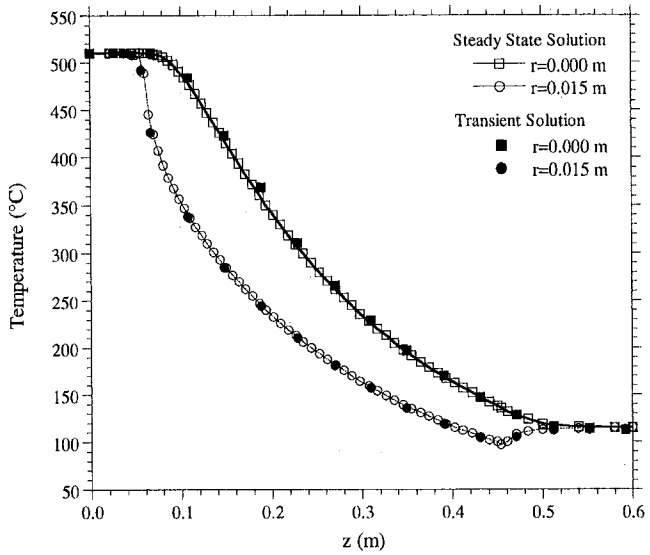

Fig. 2 Temperature variation along the moving direction of the quenched rod

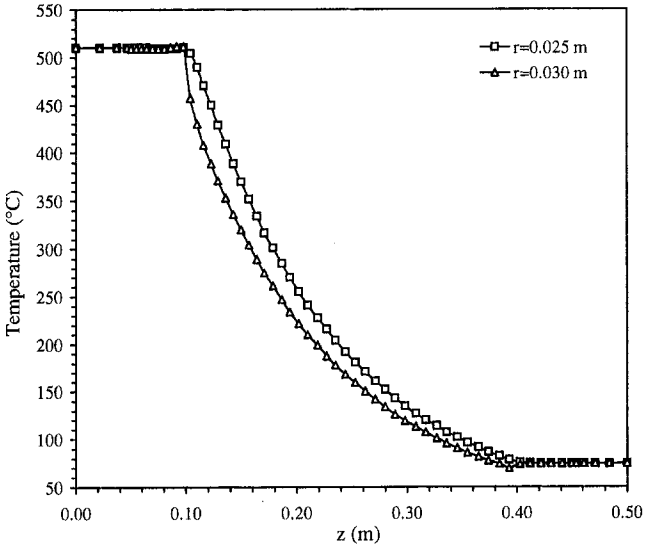

Fig. 4 Surface temperature variation along the moving direction of the quenched tube

Matrix **Q** and **C** are independent of the inelastic strains. When Δt is constant, the stiffness matrix will be constant. In this case, matrix forward elimination during iterations may not be needed.

7 Implementation Procedure

The methodology presented in this paper can be implemented with the following steps:

A. Solve the system of Eq. (12) to obtain the temperature filed.
B. Apply thermal loading.
   B.1. Divide the thermal loading into m increments so that $\Delta\epsilon^T = \epsilon^T/m$.
   B.2. Apply the thermal loading incrementally, i.e., $(\epsilon^T)_i = (\epsilon^T)_{i-1} + \Delta\epsilon^T$ with $(\epsilon^T)_o = 0$, where i is the increment number. If the full thermal loading is applied to the system (i.e., $i = m$), go to step C; otherwise, go to step B.3.
   B.3. Solve the system of Eq. (16) by substituting $(\epsilon^T)_i$ for ϵ^T to update the stress field.
   B.4. Solve the system of Eq. (29) to update the inelastic strains with the updated stress field, then go to step B.2.
C. Iteration.
   C.1. Solve Eq. (16) to update the stress field with the full thermal loading.
   C.2. Solve Eq. (29) to update the inelastic strains with the updated stress field.
   C.3. Check convergence. If convergence is achieved, i.e., $\partial\bar{\epsilon}^N/\partial t \approx 0$, stop iteration; if not, go to step C.1 with the updated inelastic strain obtained from step C.2.

Generally, the step B is necessary when a process, such as the quenching process studied here, involves a fast evolution of inelastic strains. Generally, the convergence tolerance should be small. In this paper, it is 10^{-7}, that is, iterations stop when $\partial\bar{\epsilon}^N/\partial t < 10^{-7}$, where $\bar{\epsilon}^N$ is the effective inelastic strain and is defined as $\bar{\epsilon}^N = \sqrt{\frac{2}{3}\epsilon_{ij}^N\epsilon_{ij}^N}$.

8 Results

The material considered here is an aluminum alloy. The thermal conductivity of the material is $k = 222$ W/m-°C, the specific heat

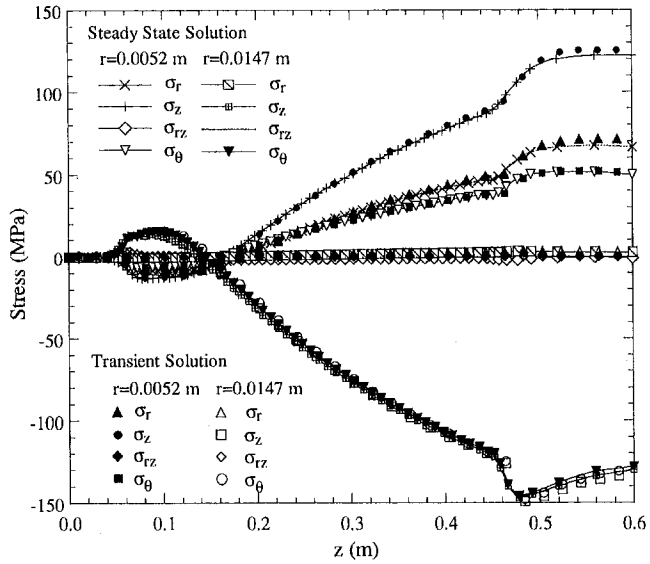

Fig. 3 Stress distribution along the moving direction of the quenched rod

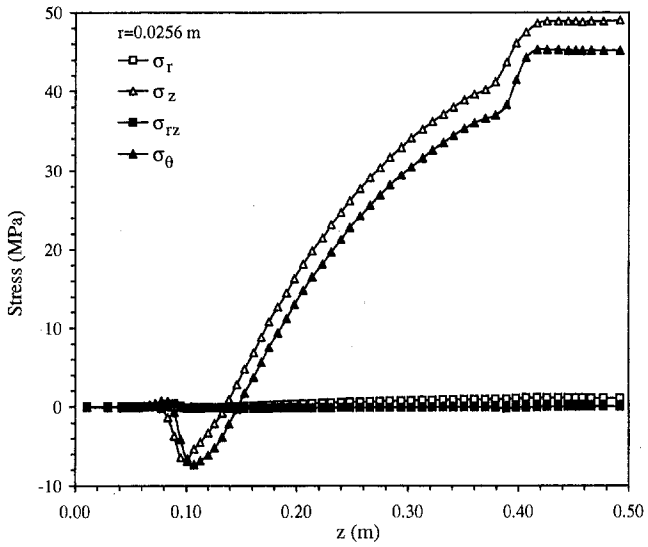

Fig. 5 Stress variation along the moving direction of the quenched tube in the surface of $r = 0.0256$ m

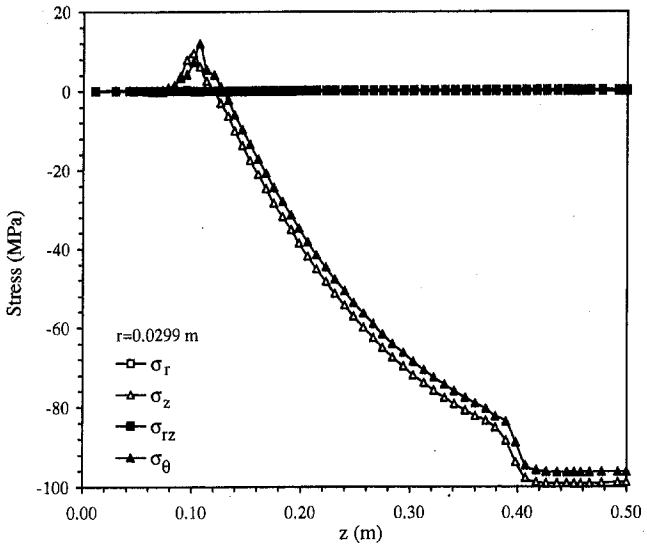

Fig. 6 Stress variation along the moving direction of the quenched tube in the surface of $r = 0.0299$ m

is $c = 904$ J/kg-°C, and the density is $\rho = 2650$ kg/m^3. The Young's modulus of the material varies with temperature, that is, $E(T) = 7310\text{-}48.6T$ MPa if $T \leq 340$°C and $E(T) = 103000\text{-}139T$ MPa if 340°C $< T \leq 540$°C; the Poison's ratio is $\nu = 0.37$. The thermal expansion coefficient of the material is $\alpha(T) = 25.5$ μm/m.

The inelastic deformation of the material obeys the following hyperbolic sine law:

$$\dot{\epsilon}_{ij}^{N} = f_{ij}(\sigma, \epsilon^{N}, T, \ldots) = \frac{3}{2} A e^{-C/(T+273)} [\sinh B\bar{\sigma}]^{n} \frac{s_{ij}}{\bar{\sigma}} \quad (31)$$

where A, B, C and n are the material constants, $\bar{\sigma}$ is the effective stress defined as $\bar{\sigma} = \sqrt{\frac{3}{2} s_{ij} s_{ij}}$. ($s_{ij}$ are the deviatoric stresses and $s_{ij} = \sigma_{ij} - \frac{1}{3}\sigma_{kk}\delta_{ij}$.) The temperature T is in degrees Celsius. The parameters of the hyperbolic-sine law are $A = 8.557 \times 10^{12}$ sec^{-1}, $B = 0.03223$ MPa^{-1}, $C = 21320$°K, and $n = 4.75$ (Becker et al., 1994).

To verify the methodology presented in this paper, a steady-state rod quenching problem is studied and the results are compared with a transient solution. The diameter of the rod is 0.03 m. The control volume is as shown in Fig. 1, where $R_o = 0.015$ m and $R_i = 0.0$ m, and the length of the control volume is $L = 0.7$ m. The rod moves at a steady-state velocity, $\mathbf{V} = (0, 0.15)$ m/sec and is water cooled from $z = 0.06$ m to $z = 0.46$ m with the cooling heat transfer coefficient $h = 14200$ W/m^2-°C. When the rod is outside of the cooling region, it is cooled by the surrounding air with $h = 30$ W/m^2-°C. The temperature of the water and air is $T_\infty = 25$°C. Before the rod is quenched, it has a uniform temperature, $T_u = 510$°C. With the assumption of uniform cooling around the rod surface, axisymmetric conditions can be applied to the rod. In addition, traction-free conditions are applied to the rod surface and ends with the point at (0, 0) fixed to eliminate rigid-body motion.

In the quenching problem studied here, the mechanical deformation is induced mainly by temperature gradient in the quenched body and the velocity due to mechanical deformation is negligible compared to the rigid-body velocity (steady-state moving velocity of the quenched body). Therefore, the rigid-body velocity can be used in Eqs. (12), (24), and (29).

With the steady-state methodology, the control volume is descretized with 455 elements (seven elements in the radial direction). Stress elements are quadrilateral with eight nodes and four integration points and thermal elements have four nodes and four integration points. The computational time is about 1.5 CPU hours on an HP 750 machine.

With the transient (Lagrangian) method, the rod 1 m long is selected to ensure that the solution can reach steady-state and end effects can be eliminated. Nine hundred ninety-five quadrilateral elements are used to descretize the domain with five elements in the radial direction. The stress elements have eight nodes and four integration points and the thermal elements have four nodes and four integration points. In addition, the elements are carefully generated to minimize the level of computation. To simulate the process, the cooling zone is fixed and the quenched body is moving. The transient analysis is performed with the commercial program ABAQUS (1995). The run time for this problem is about 30 CPU hours on the same HP 750 machine.

The steady-state and transient solution for the rod quenching problem are given in Figs. 2 and 3. Figure 2 shows the comparison

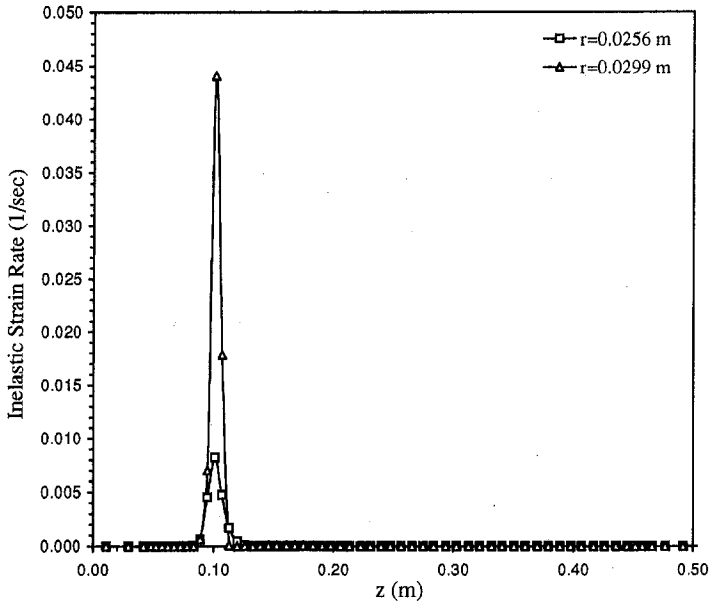

Fig. 7 Variation of the inelastic strain rate along the moving direction of the quenched tube

of temperatures of the quenched rod. Figure 3 shows the stress variation at two locations, i.e., $r = 0.0052$ m (close to the rod center) and $r = 0.0147$ m (close to the rod surface). The agreement between the results obtained from the two methodologies are good. But the computational time is significantly less with the steady-state approach.

A tube quenching problem is also solved with the steady-state method presented in this paper. The same aluminum material is also used. The inner diameter of the tube is 0.05 m and the outer diameter is 0.06 m with 0.005 thick wall (i.e., $R_o = 0.030$ m and $R_i = 0.025$ m). The length of the control volume is also 0.7 m. The tube moves at a constant velocity, $\mathbf{V} = (0, 0.15)$ m/sec and is water cooled from $z = 0.1$ m to $z = 0.4$ m with the cooling heat transfer coefficient $h = 14200$ W/m^2-°C. Outside the quenching area it is cooled by the surrounding air with $h = 30$ W/m^2-°C. The the water and air temperatures are $T_\infty = 25$°C. Before the tube is quenched, it has a uniform temperature, $T_u = 510$°C.

Figure 4 shows the surface temperature variation along the tube. Figures 5 and 6 show the stress evolution along the tube at $r = 0.0256$ m and $r = 0.0299$ m, respectively. Figure 7 illustrates the variation of the inelastic strain rate at $r = 0.0256$ m and $r = 0.0299$ m, respectively. Figures 8 and 9 show the variations of the inelastic strains along the tube at $r = 0.0256$ m and $r = 0.0299$ m, respectively.

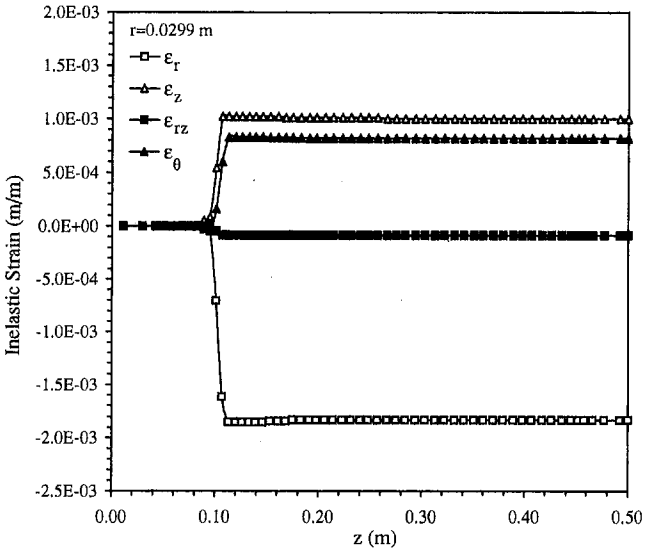

Fig. 9 Inelastic strain variation along the moving direction of the quenched tube in the surface of $r = 0.0299$ m

9 Conclusion

The steady-state method presented in this paper is effective and efficient to analyze the stress evolution involved for a continuous thermomechanical process. Test problems have shown that the results obtained with the steady-state (Eulerian) approach agree well with those obtained with the transient (Lagrangian) method. With the steady-state methodology, a significant amount of computation time can be saved. It is advantageous when repeated computation is required such as in an optimization procedure.

Generally, inelastic deformation occurs in a short period of time and it requires a fine mesh and small time steps to integrate the inelastic strain rate. With the transient method, the time step must be kept sufficiently small through the entire simulation and the fine mesh is needed in the entire domain. But with the steady-state approach, a fine mesh is only needed in the region where the inelastic deformation occurs.

The control volume should be selected larger than the region where the stresses need to be determined. According to the Saint Venant principle, the boundary conditions at the upstream and downstream of a control volume will only affect the local stress distribution. Once the computation region is large enough, the end influence to the stresses and deformation can be neglected.

In the examples studied here, the magnitude of the inelastic strain increases quickly at the beginning of the quenching process, then stays at almost constant level during the rest of cooling process. Axial and Hoop stresses in the region close to the outer surface are tensile at the beginning of the quenching process, and change from tensile to compressive at the early stage of the process and stay compressive. In the center area or near the inner surface, axial and Hoop stresses are compressive at the beginning and are tensile later on.

The inelastic deformation contributes significantly to the residual stresses of the end product. Therefore, the region where the high inelastic strain rate occurs must be studied carefully in order to minimize the residual stresses.

The methodology presented in this paper can also be applied to other steady-state processes with small deformations, i.e., small strains and small rotations.

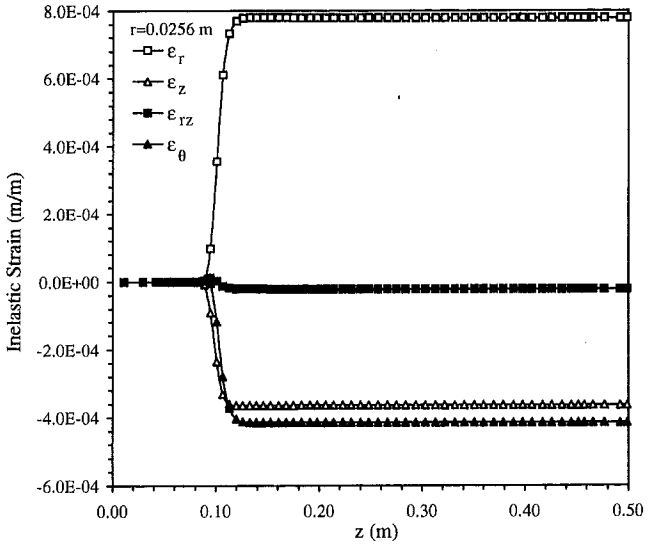

Fig. 8 Inelastic strain variation along the moving direction of the quenched tube in the surface of $r = 0.0256$ m

References

ABAQUS, 1995, Hibbitt, Karlsson & Sorensen, Pawtucket, RI.

Becker, R., Karabin, M. E., Liu, J. C., and Smelser, R. E., 1994, "Experimental Validation of Predicted Distortion and Residual Stresses in Quenched Bars," ASME Winter Meeting, Chicago, IL.

Fletcher, A. H. and Lewis, C., 1985, "Effect of Free Edge on Thermal Stresses in Quenched Plates," *Material Science and Technology,* Vol. 1, pp. 780–785.

Johnson, C., 1987, *Numerical Solution of Partial Differential Equations by the Finite Element Method,* Cambridge University Press, Cambridge, UK.

Kikuchi, N., 1986, *Finite Element Methods in Mechanics,* Cambridge University Press, Cambridge, UK.

Owen, D. R. J., and Hinton, E., 1980, *Finite elements in plasticity: Theory and Practice,* Pineridge Press, Swansea, UK.

Zabaras, N., Mukherjee, S., and Arthur, W. R., 1987, "A Numerical and Experimental Study of Quenching of Circular Cylinders," *J. Thermal Stress,* Vol. 10, pp. 177–191.

Zienkiewicz, O. C. and Taylor, R. L., 1991, *The Finite Element Method,* 4th Ed., McGraw-Hill, New York.

Application of the Hybrid Method to the Transient Thermal Stresses Response in Isotropic Annular Fins

L.-T. Yu
Department of Mechanical Engineering,
ChengShiu Junior College of
Technology & Commerce,
Neau-Song, Kaohsiung, Taiwan 83305
R.O.C.

C.-K. Chen
Department of Mechanical Engineering,
National Cheng Kung University,
Tainan, Taiwan 701, R.O.C.

This paper presents the transient stress distribution in a perfectly elastic isotropic annular fin. The nonlinear transient conduction-convection-radiation heat transfer annular fin equation is solved by the hybrid method of the Taylor transformation and the finite difference approximation. The temperature distribution curve is employed by the natural cubic spline fitting. The stress distribution is directly integrated to obtain the transient thermal stress distribution.

1 Introduction

Fins are employed to enhance the heat transfer between the primary surface and its convective, radiative, or convective-radiative environment. Annular fins (thin annular disk) are extensively used in various industrial applications (Kern et al., 1972). For proper prediction and control of the performance of a fin, it is necessary to know the dynamic response of it when an expected or unpredictable change occurs. Naturally, the plane-stress thermoelasticity problems of radial heating of annular fins are important in engineering practice (Boresi et al., 1974).

In this paper, the nonlinear conduction-convection-radiation heat transfer equation is solved by the hybrid method, which combines the Taylor transformation and the finite difference approximation. For the transient temperature distribution curve, we use the natural cubic spline fitting. Since a spline is a flexible strip, according to the law of beam flexture, it passes through each of the given points and moves smoothly from one interval to another. It is particularly advantageous when we want to find derivatives to the data. In the stress field of the annular fin, the ratio of the thickness, W, to the outer radius, r_e, is even smaller compared with unity. Therefore, we can make a statement that the annular fin is plane-stress field and the end faces are free of traction (Misra et al., 1983). We use the direct integration method to obtain the transient thermal stress distribution.

2 Analysis

Transient Heat Transfer Problem. We consider one-dimensional conduction of an annular fin with base radius, r_b, tip radius, r_e, and uniform thickness, W. The heat transfer coefficient, h, along the peripheral surfaces and at the tip surface of the fin is constant and uniform. The fin is a homogeneous, isotropic constant property material with thermal conductivity, k. Thermal generation is not considered. We assume that the heat dissipates from the fin surfaces with convection and radiation to the surrounding area. The fin initially is uniform in thermal equilibrium with the surrounding at temperature T_a. At time $t = 0$, the fin base temperature is suddenly changed to T_b and kept constant thereafter. Referring to the Fig. 1, the energy equation with the aforesaid initial and boundary conditions of the fin is

$$\frac{\partial^2\theta}{\partial r^2} + \frac{1}{r}\frac{\partial\theta}{\partial r} - m(\theta - 1) - n(\epsilon\theta^4 - \alpha\theta_e^4) = \frac{1}{\alpha^*}\frac{\partial\theta}{\partial t}, \quad t > 0, \quad r_b < r < r_e, \quad \theta = \theta(r, t), \tag{1}$$

$$\theta = 1, \quad t = 0, \quad r_b \le r \le r_e,$$

$$\theta = \theta_b, \quad t > 0, \quad r = r_b,$$

$$-\frac{\partial\theta}{\partial r} = P(\theta - 1) + U(\epsilon\theta^4 - \alpha\theta_e^4), \quad t > 0, \quad r = r_e, \tag{2}$$

where $m = 2h/kW$, $n = 2\sigma T_a^3/kW$, $P = h/k$, $U = \sigma T_a^3/k$, $\alpha^* = k/\rho c_p$, $\theta = T/T_a$, $\theta_e = T_e/T_a$, $\theta_b = T_b/T_a$, and r is the radius of the fin, t is the time, ρ is the density of material, and c_p is the constant pressure specific heat. T is the temperature of the fin, T_e is the effective temperature of the radiative surface except for the fin, α is the absorptivity of the fin, ϵ is the emissivity of the fin, and σ is the Stefan-Boltzmann constant. In order to consider the effect of possible differences in the emitting and absorbing spectra, the emissivity ϵ, and the absorptivity α, are not taken to be equal.

After taking the Taylor transformation (Chen et al., 1996; Yu et al., 1997) with respect to time domain t, Eqs. (1) and (2) become

$$\frac{d^2\Theta(r, k)}{dr^2} + \frac{1}{r}\frac{d\Theta(r, k)}{dr} - m(\Theta(r, k) - \delta(k)) - n\Big(\epsilon\sum_{\ell=0}^{k}\Theta(r, k-\ell)\sum_{s=0}^{\ell}\Theta(r, \ell - s) \times \sum_{q}^{s}\Theta(r, s-q)\Theta(r, q) - \alpha\theta_e^4\delta(k)\Big) = \frac{1}{\alpha^*}\frac{k+1}{H}\Theta(r, k+1), \tag{3}$$

$$\Theta(r, 0) = 1, \tag{4}$$

$$\Theta(r_b, k) = \theta_b\delta(k), \tag{5}$$

Contributed by the Applied Mechanics Division of THE AMERICAN SOCIETY OF MECHANICAL ENGINEERS for publication in the ASME JOURNAL OF APPLIED MECHANICS.
Discussion on the paper should be addressed to the Technical Editor, Professor Lewis T. Wheeler, Department of Mechanical Engineering, University of Houston, Houston, TX 77204-4792, and will be accepted until four months after final publication of the paper itself in the ASME JOURNAL OF APPLIED MECHANICS.
Manuscript received by the ASME Applied Mechanics Division, Apr. 1, 1997; final revision, Oct. 2, 1998. Associate Technical Editor: M. Taya.

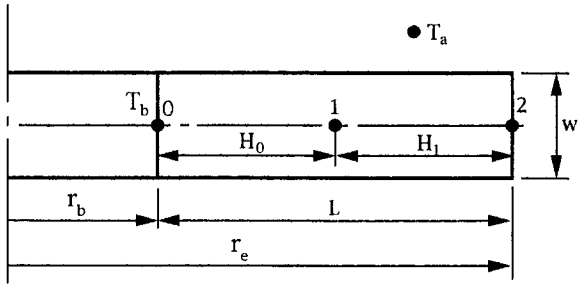

Fig. 1 Rectangular profile annular fins

$$-\frac{d\Theta(r_e, k)}{dr} = P(\Theta(r_e, k) - \delta(k)) + U(\epsilon \sum_{\ell=0}^{k} \Theta(r_e, k-\ell) \sum_{s=0}^{\ell} \Theta(r_e, \ell - s) \times \sum_{q=0}^{s} \Theta(r_e, s-q)\Theta(r_e, q) - \alpha\theta_e^4\delta(k)), \quad (6)$$

where

$$\delta(k) = \begin{cases} 1 & \text{for } k = 0 \\ 0 & \text{otherwise,} \end{cases}$$

and Θ is the Taylor spectra of θ, H is the time interval, and k is the transformation parameter. The fundamental properties of the Taylor transformation are given in the Appendix.

For the finite difference approximation with respect to r in Eqs. (3)–(6), in this paper the region $r_b \le r \le r_e$ (Fig. 1) is divided into two equal subregions and each of the thickness, δ, is given by

$$\delta = \frac{r_e - r_b}{2}. \quad (7)$$

Equations (3)–(6) are discretized by using the second-order accurate central difference formula for both the second and first derivatives (Özisik, 1994). We obtain

$$\frac{\Theta_{i-1}(k) - 2\Theta_i(k) + \Theta_{i+1}(k)}{\delta^2} + \frac{1}{r_b + i\delta}\frac{\Theta_{i+1}(k) - \Theta_{i-1}(k)}{2\delta} - m(\Theta_i(k) - \delta(k)) - n\epsilon \sum_{\ell=0}^{k} \Theta_i(k-\ell) \sum_{s=0}^{\ell} \Theta_i(\ell - s) \times \sum_{q=0}^{s} \Theta_i(s-q)\Theta_i(q) + n\alpha\theta_e^4\delta(k) = \frac{k+1}{\alpha^* H}\Theta_i(k+1), \quad i = 1, \quad (8)$$

$$\Theta_i(0) = 1, \quad i = 1, 2, \quad (9)$$

$$\Theta_0(k) = \theta_b\delta(k), \quad (10)$$

$$-\frac{\Theta_3(k) - \Theta_1(k)}{2\delta} = P(\Theta_2(k) - \delta(k)) + U\epsilon \sum_{\ell=0}^{k} \Theta_2(k-\ell) \times \sum_{s=0}^{\ell} \Theta_2(\ell - s) \sum_{q=0}^{s} \Theta_2(s-q)\Theta_2(q) - U\alpha\theta_e^4\delta(k). \quad (11)$$

Now, to eliminate the fictitious spectrum $\Theta_3(k)$ by utilizing the expressions obtained from Eq. (8) with $i = 2$ and Eq. (11), we obtain

$$\frac{k+1}{\alpha^* H}\Theta_2(k+1) = \frac{2}{\delta}(P(\Theta_2(k) - \delta(k)) + U\epsilon \sum_{\ell=0}^{k} \Theta_2(k-\ell) \times \sum_{s=0}^{\ell} \Theta_2(\ell - s) \sum_{q=0}^{s} \Theta_2(s-q)\Theta_2(q) - U\alpha\theta_e^4\delta(k)) + \frac{2(\Theta_1(k) - \Theta_2(k))}{\delta^2} + \frac{1}{r_b + 2\delta}(P(\Theta_2(k) - \delta(k)) + U\epsilon \sum_{\ell=0}^{k} \Theta_2(k-\ell) \sum_{s=0}^{\ell} \Theta_2(\ell - s) \sum_{q=0}^{s} \Theta_2(s-q)\Theta_2(q) - U\alpha\theta_e^4\delta(k)) - m(\Theta_2(k) - \delta(k)) - n\epsilon \sum_{\ell=0}^{k} \Theta_2(k-\ell) \times \sum_{s=0}^{\ell} \Theta_2(\ell - s) \sum_{q=0}^{s} \Theta_2(s-q)\Theta_2(q) + n\alpha\theta_e^4\delta(k), \quad (12)$$

where H is the time interval. Take $k = 0, 1, 2, \ldots, 5$, and $i = 0, 1, 2$; we may obtain $\Theta_i(k)$ as follows:

$$\Theta_0(0) = \theta_b, \quad (13)$$

$$\Theta_1(0) = 1, \quad (14)$$

$$\Theta_2(0) = 1, \quad (15)$$

$$\Theta_0(1) = 0, \quad (16)$$

$$\Theta_1(1) = \alpha^* H\left(\frac{\Theta_0(0) - 2\Theta_1(0) + \Theta_2(0)}{\delta^2} + \frac{\Theta_2(0) - \Theta_0(0)}{2\delta(r_b + \delta)} - m(\Theta_1(0) - 1) - n\epsilon\Theta_1^4(0) + n\alpha\theta_e^4\right), \quad (17)$$

$$\Theta_2(1) = \alpha^* H\left(\left(\frac{2P}{\delta} + \frac{P}{r_b + 2\delta} - m\right)(\Theta_2(0) - 1) - \left(\frac{2U\epsilon}{\delta} + \frac{U\epsilon}{r_b + 2\delta} + n\epsilon\right)\Theta_2^4(0) + \frac{2(\Theta_1(0) - \Theta_2(0))}{\delta^2} + \left(\frac{2U\alpha}{\delta} + \frac{U\alpha}{r_b + 2\delta} + n\alpha\right)\theta_e^4\right), \quad (18)$$

$$\Theta_0(2) = 0, \quad (19)$$

$$\Theta_1(2) = \frac{\alpha^* H}{2}\left(\frac{\Theta_0(1) - 2\Theta_1(1) + \Theta_2(1)}{\delta^2} + \frac{\Theta_2(1) - \Theta_0(1)}{2\delta(r_b + \delta)} - m\Theta_1(1) - 4n\epsilon\Theta_1(1)\Theta_1^3(0)\right), \quad (20)$$

$$\Theta_2(2) = \frac{\alpha^* H}{2}\left(\left(\frac{2P}{\delta} + \frac{P}{r_b + 2\delta} - m\right)\Theta_2(1) - 4\left(\frac{2U\epsilon}{\delta} + \frac{U\epsilon}{r_b + 2\delta} + n\epsilon\right)\Theta_1(1)\Theta_1^3(0) + \frac{2(\Theta_1(1) - \Theta_2(1))}{\delta^2}\right), \quad (21)$$

$$\Theta_0(3) = 0, \quad (22)$$

$$\Theta_1(3) = \frac{\alpha^* H}{3}\left(\frac{\Theta_0(2) - 2\Theta_1(2) + \Theta_2(2)}{\delta^2} + \frac{\Theta_2(2) - \Theta_0(2)}{2\delta(r_b + \delta)} - m\Theta_1(2) - n\epsilon(4\Theta_1(2)\Theta_1^3(0) + 6\Theta_1^2(1)\Theta_1^2(0))\right), \quad (23)$$

Table 1 Nodes temperature of convection and radiation

time (s)	T_0^* (K)	T_1^* (K)	T_2^* (K)
10	600	469.30	436.56
20	600	525.41	507.72
30	600	547.72	536.02
40	600	556.51	547.16
steady state	600	561.31	553.24

Table 2 Nodes temperature of pure convection

time (s)	T_0^* (K)	T_1^* (K)	T_2^* (K)
10	600	470.53	437.91
20	600	529.09	512.18
30	600	553.65	543.37
40	600	563.96	556.46
steady state	600	570.10	564.26

Table 3 Nodes temperature of pure radiation

time (s)	T_0^* (K)	T_1^* (K)	T_2^* (K)
10	600	475.50	442.84
20	600	539.31	523.44
30	600	566.90	558.29
40	600	578.69	573.16
steady state	600	585.81	582.14

$$\Theta_2(3) = \frac{\alpha^* H}{3}\left(\left(\frac{2P}{\delta} + \frac{P}{r_b + 2\delta} - m\right)\Theta_2(2) - \left(\frac{2U\epsilon}{\delta} + \frac{U\epsilon}{r_b + 2\delta} + n\epsilon\right)\cdot(4\Theta_1(2)\Theta_1^3(0) + 6\Theta_1^2(1)\Theta_1^2(0)) + \frac{2(\Theta_1(2) - \Theta_2(2))}{\delta^2}\right), \quad (24)$$

$$\Theta_0(4) = 0, \quad (25)$$

$$\Theta_1(4) = \frac{\alpha^* H}{4}\left(\frac{\Theta_0(3) - 2\Theta_1(3) + \Theta_2(3)}{\delta^2} + \frac{\Theta_2(3) - \Theta_0(3)}{2\delta(r_b + \delta)} - m\Theta_1(3) - n\epsilon(4\Theta_1(3)\Theta_1^3(0) + 12\Theta_1(2)\Theta_1(1)\Theta_1^2(0) + 4\Theta_1^3(1)\Theta_1(0))\right), \quad (26)$$

$$\Theta_2(4) = \frac{\alpha^* H}{4}\left(\left(\frac{2P}{\delta} + \frac{P}{r_b + 2\delta} - m\right)\Theta_2(3) - \left(\frac{2U\epsilon}{\delta} + \frac{U\epsilon}{r_b + 2\delta} + n\epsilon\right)\cdot(4\Theta_1(3)\Theta_1^3(0) + 12\Theta_1(2)\Theta_1(1)\Theta_1^2(0) + 4\Theta_1^3(1)\Theta_1(0)) + \frac{2(\Theta_1(3) - \Theta_2(3))}{\delta^2}, \quad (27)$$

$$\Theta_0(5) = 0, \quad (28)$$

$$\Theta_1(5) = \frac{\alpha^* H}{5}\left(\frac{\Theta_0(4) - 2\Theta_1(4) + \Theta_2(4)}{\delta^2} + \frac{\Theta_2(4) - \Theta_0(4)}{2\delta(r_b + \delta)} - m\Theta_1(4) - n\epsilon(4\Theta_1(4)\Theta_1^3(0) + 6\Theta_1^2(2)\Theta_1^2(0) + 12\Theta_1(3)\Theta_1(1)\Theta_1^2(0) + 12\Theta_1(2)\Theta_1^2(1)\Theta_1(0) + \Theta_1^4(1))\right), \quad (29)$$

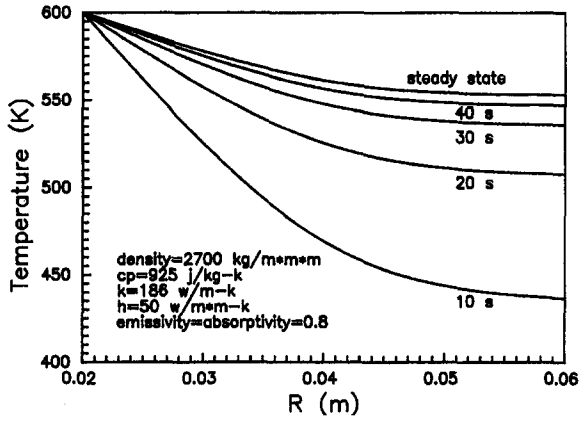

Fig. 2 The transient temperature response of annular fins with convection and radiation boundary conditions

$$\Theta_2(5) = \frac{\alpha^* H}{5}\left(\left(\frac{2P}{\delta} + \frac{P}{r_b + 2\delta} - m\right)\Theta_2(4) - \left(\frac{2U\epsilon}{\delta} + \frac{U\epsilon}{r_b + 2\delta} + n\epsilon\right)\cdot(4\Theta_1(4)\Theta_1^3(0) + 6\Theta_1^2(2)\Theta_1^2(0) + 12\Theta_1(3)\Theta_1(1)\Theta_1^2(0) + 12\Theta_1(2)\Theta_1^2(1)\Theta_1(0) + \Theta_1^4(1)) + \frac{2(\Theta_1(4) - \Theta_2(4))}{\delta^2}\right). \quad (30)$$

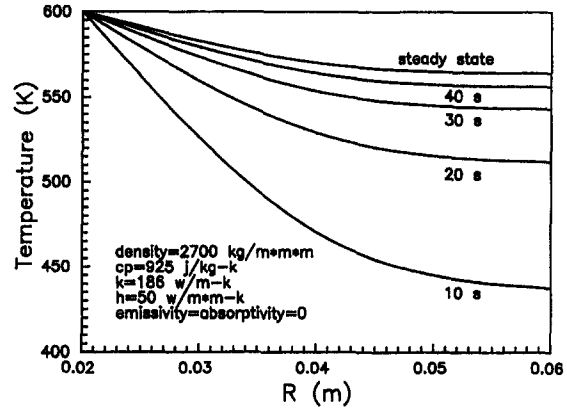

Fig. 3 The transient temperature response of annular fins with pure convection boundary condition

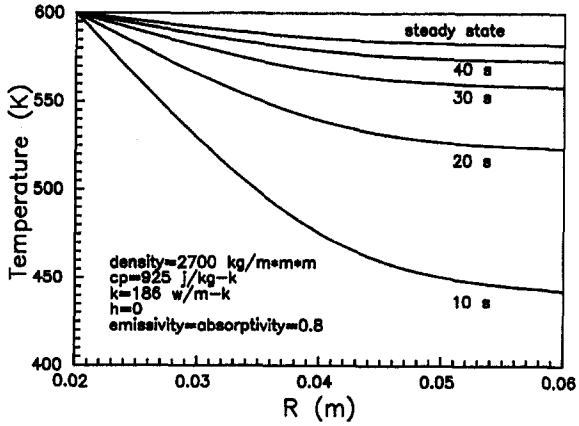

Fig. 4 The transient temperature response of annular fins with pure radiation boundary condition

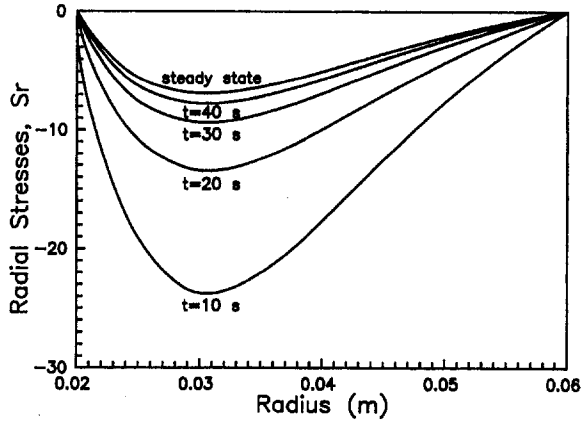

Fig. 5 The transient radial thermal and radiation heat transfer

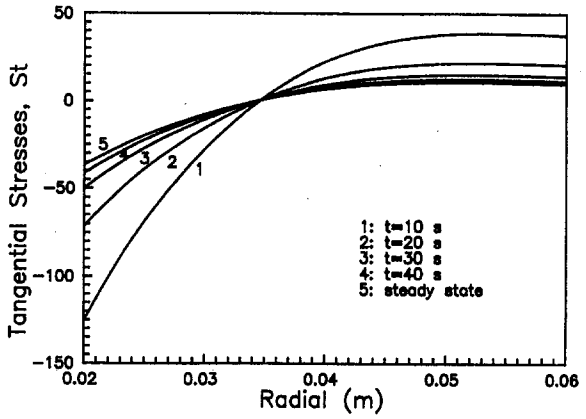

Fig. 6 The transient tangential thermal stresses of annular fin for convection and radiation heat transfer

From Eqs. (13)–(30), we may obtain $\Theta_i(k)$; $i = 0, 1, 2$, $k = 0, 1, 2, 3, 4, 5$, for each time interval.

Now, from the inverse Taylor transformation formula (Chen et al., 1996), the temperature of the ith node and the jth time interval $\theta_{ij}(t)$ is

$$\theta_{1j}(t) = \sum_{k=0}^{5} \left(\frac{t}{H_j}\right)^k \Theta_{1j}(k), \quad H_{j-1} \le t \le H_j, \tag{31}$$

$$\theta_{2j}(t) = \sum_{k=0}^{5} \left(\frac{t}{H_j}\right)^k \Theta_{2j}(k), \quad H_{j-1} \le t \le H_j, \tag{32}$$

and

$$\theta_{1j}(0) = \sum_{k=0}^{5} \Theta_{1j-1}(k), \tag{33}$$

$$\theta_{2j}(0) = \sum_{k=0}^{5} \Theta_{2j-1}(k). \tag{34}$$

Thermal Stress Analysis. The stress associated with a radial temperature field, $T(r, t)$, is independent of the axial dimension. Also, the temperature is symmetrical about the center. For the thin annular disk, the temperature does not vary over the thickness of the disk. We may assume that the stress and displacement due to the heating also do not vary over the thickness. For thin annular disk/fins ($W/r_e \ll 1$, Fig. 1), it is an axisymmetrically plane stress problem (Timoshenko et al., 1970).

In the absence of body forces, the equation of equilibrium is

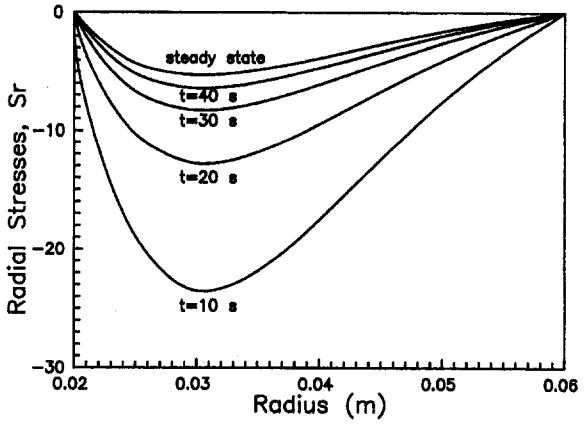

Fig. 7 The transient radial thermal stresses of annular fin for pure convection heat transfer

$$\frac{d\sigma_r(r, t)}{dr} + \frac{\sigma_r(r, t) - \sigma_\theta(r, t)}{r} = 0 \tag{35}$$

and the strain-displacement relations are

$$\epsilon_r(r, t) = \frac{du(r, t)}{dr}$$

$$\epsilon_\theta(r, t) = \frac{u(r, t)}{r}$$

$$\gamma_{r\theta}(r, t) = 0 \tag{36}$$

where σ_r is the radial stress of the fin, σ_θ is the circumferential stress, ϵ_r is the radial strain, ϵ_θ is the circumferential strain, $\gamma_{r\theta}$ is the shear strain, and u is the radial displacement.

In this case of plane stress, the applicable equations of stress and strain are as follows:

$$\sigma_r(r, t) = \frac{E}{1 - \nu^2}(\epsilon_r(r, t) + \nu\epsilon_\theta(r, t) - (1 + \nu)\alpha^{**}T(r, t)) \tag{37}$$

$$\sigma_\theta(r, t) = \frac{E}{1 - \nu^2}(\epsilon_\theta(r, t) + \nu\epsilon_r(r, t) - (1 + \nu)\alpha^{**}T(r, t)) \tag{38}$$

where ν is the Poisson's ratio, α^{**} is the coefficient of linear thermal expansion, and E is the modulus of elasticity.

The equation of equilibrium, Eq. (35) is now

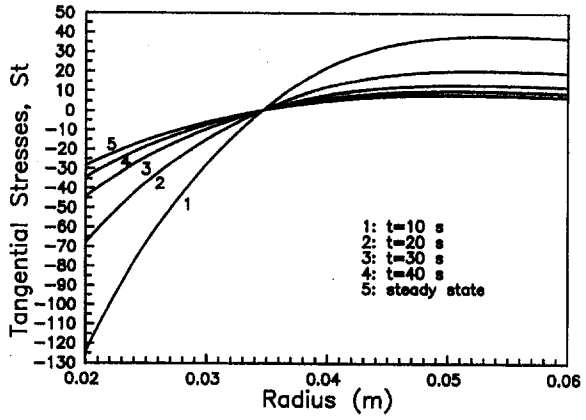

Fig. 8 The transient tangential thermal stresses of annular fin for pure convection heat transfer

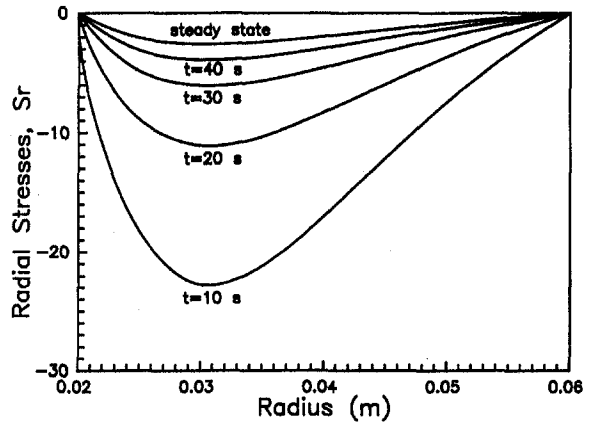

Fig. 9 The transient radial thermal stresses of annular fin for pure radiation heat transfer

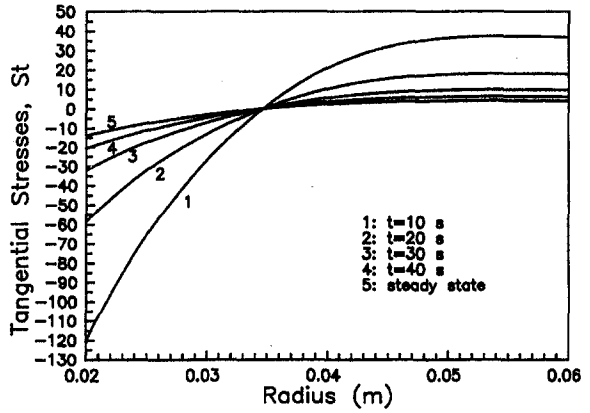

Fig. 10 The transient tangential thermal stresses of annular fin for pure radiation heat transfer

$$r\frac{d}{dr}(\epsilon_r(r,t)+\nu\epsilon_\theta(r,t))+(1-\nu)(\epsilon_r(r,t)-\epsilon_\theta(r,t))=(1+\nu)\alpha^{**}r\frac{dT(r,t)}{dr}. \quad (39)$$

Introducing Equations (36) into Eq. (39), we obtain

$$\frac{d^2u(r,t)}{dr^2}+\frac{1}{r}\frac{du(r,t)}{dr}-\frac{u(r,t)}{r^2}=(1+\nu)\alpha^{**}\frac{dT(r,t)}{dr}$$

which may be written as

$$\frac{d}{dr}\left(\frac{1}{r}\frac{d(ru(r,t))}{dr}\right)=(1+\nu)\alpha^{**}\frac{dT(r,t)}{dr}. \quad (40)$$

Integration of this equation yields

$$u(r,t)=(1+\nu)\alpha^{**}\frac{1}{r}\int_{r_b}^{r}rT(r,t)dr+c_1r+\frac{c_2}{r} \quad (41)$$

where r_b is the inner radius of the annular fin.

The stress components are now found by using the solution (41) in Eqs. (36) and substituting the results into Eqs. (37)–(38). Then

$$\sigma_r(r,t)=-\alpha^{**}E\frac{1}{r^2}\int_{r_b}^{r}T(r,t)rdr+\frac{E}{1-\nu^2}\left(c_1(1+\nu)-c_2(1-\nu)\frac{1}{r^2}\right) \quad (42)$$

$$\sigma_\theta(r,t)=\alpha^{**}E\frac{1}{r^2}\int_{r_b}^{r}T(r,t)rdr-\alpha^{**}ET(r,t)+\frac{E}{1-\nu^2}\left(c_1(1+\nu)+c_2(1-\nu)\frac{1}{r^2}\right). \quad (43)$$

In this article, the constants c_1 and c_2 are determined on the basis of the boundary conditions $(\sigma_r)_{r_b,t}=0$, and $(\sigma_r)_{r_e,t}=0$. Equation (42) thus gives

$$c_1=\frac{(1-\nu)\alpha^{**}}{r_e^2-r_b^2}\int_{r_b}^{r_e}rT(r,t)dr$$

$$c_2=\frac{(1+\nu)\alpha^{**}r_b^2}{r_e^2-r_b^2}\int_{r_b}^{r_e}rT(r,t)dr.$$

From Eqs. (42), (43), the stresses are therefore

$$\sigma_r(r,t)=\alpha^{**}E\left(-\frac{1}{r^2}\int_{r_b}^{r}rT(r,t)dr+\frac{r^2-r_b^2}{r^2(r_e^2-r_b^2)}\int_{r_b}^{r_e}rT(r,t)dr\right), \quad (44)$$

$$\sigma_\theta(r,t)=\alpha^{**}E\left(-T(r,t)+\frac{1}{r^2}\int_{r_b}^{r}rT(r,t)dr+\frac{r^2+r_b^2}{r^2(r_e^2-r_b^2)}\int_{r_b}^{r_e}rT(r,t)dr\right). \quad (45)$$

Now, let $S_r(r,t)=\sigma_r(r,t)/\alpha^{**}E$, $S_t(r,t)=\sigma_\theta(r,t)/\alpha^{**}E$; then, for radius interval $[r_b, r_i=r_b+\delta]$, the two kinds of stress distribution are, respectively, given below

$$S_r(r,t)=-\frac{1}{r^2}\int_{r_b}^{r}rT_0(r,t)dr+\frac{r^2-r_b^2}{r^2(r_e^2-r_b^2)}\left(\int_{r_b}^{r_i}rT_0(r,t)dr+\int_{r_i}^{r_e}rT_1(r,t)dr\right), \quad r_b\le r\le r_i, \quad (46)$$

$$S_t(r,t)=-T_0(r,t)+\frac{1}{r^2}\int_{r_b}^{r}rT_0(r,t)dr+\frac{r^2+r_b^2}{r^2(r_e^2-r_b^2)}\left(\int_{r_b}^{r_i}rT_0(r,t)dr+\int_{r_i}^{r_e}rT_1(r,t)dr\right), \quad r_b\le r\le r_i. \quad (47)$$

The radius interval $[r_i=r_b+\delta, r_e]$, and the stress distribution are as follows:

$$S_r(r,t)=-\frac{1}{r^2}\left(\int_{r_b}^{r_i}rT_0(r,t)dr+\int_{r_i}^{r}rT_1(r,t)dr\right)+\frac{r^2-r_b^2}{r^2(r_e^2-r_b^2)}\left(\int_{r_b}^{r_i}rT_0(r,t)dr+\int_{r_i}^{r_e}rT_1(r,t)dr\right), \quad r_i\le r\le r_e, \quad (48)$$

$$S_r(r, t) = -T_1(r, t) + \frac{1}{r^2}\left(\int_{r_b}^{r_i} rT_0(r, t)dr + \int_{r_i}^{r} rT_1(r, t)dr\right) + \frac{r^2 - r_b^2}{r^2(r_e^2 - r_b^2)}\left(\int_{r_b}^{r_i} rT_0(r, t)dr + \int_{r_i}^{r_e} rT_1(r, t)dr\right), \quad r_i \le r \le r_e, \quad (49)$$

where T_0 is the temperature distribution between nodes 0 and 1, and T_1 is between the nodes 1 and 2. From Eqs. (46)–(49), we may obtain the radial and circumferential stress distribution.

3 Numerical Results and Discussion

In order to illustrate the foregoing analysis, numerical calculations have been carried out. We take the following values, for example.

Material properties:

$$\rho = 2700 \text{ kg/m}^3, \quad c_p = 925 \text{ J/kgK}, \quad k = 186 \text{ W/mK},$$

$$\alpha = 0.8, \quad \epsilon = 0.8.$$

Dimension of annular fin:

$$r_b = 0.02 \text{ m}, \quad r_e = 0.06 \text{ m}, \quad W = 0.004 \text{ m}.$$

Convection condition:

$$h = 50 \text{ W/m}^2\text{K}.$$

Given temperatures:

$$T_a = 300 \text{ K}, \quad T_e = 300 \text{ K}, \quad T_b = 600 \text{ K}.$$

Time-step interval:

$$H_j = 1 \text{ s}, \quad t = 1 \text{ s}.$$

Radiation parameter:

$$\sigma = 5.67 \times 10^{-8} \text{ W/m}^2\text{K}^4.$$

The different nodes of temperatures after calculation as shown in Tables 1, 2, and 3 (T_0^*: node 0, T_1^*: node 1, T_2^*: node 2). The transient temperature response for convection-radiation is shown in Fig. 2, pure convection in Fig. 3, and pure radiation in Fig. 4. From Eqs. (46)–(49), the transient thermal stress for convection and radiation is presented in Figs. 5 and 6, pure convection is presented in Figs. 7 and 8, pure radiation is presented in Figs. 9 and 10.

It appears that the hybrid method, which combines the Taylor transformation and finite difference approximation, is one of the most useful methods for solving nonlinear heat transfer equations for annular fins with nonlinear boundary conditions. Although the temperature distribution solution requires numerical calculations, the solution is a closed-form series (See Eqs. (31), (32)).

4 Conclusions

We have described the hybrid method for the transient annular fin heat transfer problem with homogeneous isotropic material in constant thermal properties, and also formulated the transient linearly elastic thermal stress distributions for the traction-free annular fin.

From the results of the analysis, it appears that the present method is a useful and practical method, and the solutions can predict quite accurately the dynamic performance of an annular fin in a transient state.

Acknowledgment

This research was supported by the National Science Council of Taiwan, Republic of China, under Grant No. NCS 88-2212-E-006-018.

References

Boresi, A. P., and Lynn, P. P., 1974, *Elasticity in Engineering Mechanics*, Prentice-Hall, Englewood Cliffs, NJ.

Chen, C. L., Lin, S. H., and Chen, C. K., 1996, "Application of Taylor Transformation to Nonlinear Predictive Control Problem," *Appl. Math. Modelling*, Vol. 20, Sept., pp. 609–710.

Kern, D. Q., and Kraus, A. D., 1972, *Extended Surface Heat Transfer*, McGraw-Hill, New York.

Misra, J. C., and Achari, R. M., 1983, "Thermal Stresses in Orthotropic Disk due to Rotating Heat Source," *J. Thermal Stresses*, Vol. 6, pp. 115–123.

Özisik, M. N., 1994, *Finite Difference Methods in Heat Transfer*, CRC Press, Ann Arbor, MI.

Timoshenko, S. P., and Goodier, J. N., 1970, *Theory of Elasticity*, McGraw-Hill, New York.

Yu, L. T., and Chen, C. K., 1997, "On the solution of the Blasius equation by the differential transformation method," *Mathematical and Computer Modelling*, in press.

APPENDIX

If $x(t)$ is analytic in the T domain, then the spectrum of $x(t)$ at $t = t_i$ in the K domain can be represented as

$$X(k) = \phi(t_i, k) = \left[\frac{\partial^k x(t)}{\partial t^k}\right]_{t=t_i}, \quad \forall k \in K. \quad (A1)$$

If $x(t)$ can be expressed by the Taylor series, then $x(t)$ can be represented as

$$x(t) = \sum_{k=0}^{\infty} \frac{(t - t_i)^k}{k!} X(k). \quad (A2)$$

Table 4 shows the Taylor transformation. The symbol "∧" denotes the differential operator, and "*" denotes the convolution operation in the K domain.

The operation properties of Taylor transform are as follows.

If $f(t)$ and $g(t)$ are two uncorrelated functions of t, and $F(k)$, $G(k)$ are the corresponding Taylor transformations, respectively, then the basic properties of the Taylor transform are shown as follows (T denotes Taylor transformation):

1 Linearity:

If $F(k) = T[f(t)]$, $G(k) = T[g(t)]$, and c_1 and c_2 are independent of t and k, then $T[c_1 f(t) + c_2 g(t)] = c_1 F(k) + c_2 G(k)$.

2 Convolution:

If $z(t) = f(t)\,g(t)$, $f(t) = T^{-1}[F(k)]$ and $g(t) = T^{-1}[G(k)]$ then

Table 4 Operation in K domain

Spectrum $X(k)$	$X(k) = \frac{H^k}{k!}\left(\frac{\partial^k x(t)}{\partial t^k}\right)_{t=0}$
function $x(t)$	$x(t) = \sum_{k=0}^{\infty}\left(\frac{t}{H}\right)^k X(k)$
Convolution	$X(k) * Y(k) = \sum_{\ell=0}^{k} X(\ell)Y(k - \ell)$
Derivative	$\wedge \times (k) = \frac{k+1}{H} X(k+1)$

$$T[z(t)] = T[f(t)g(t)]$$
$$= F(k) * G(k)$$
$$= \sum_{\ell=0}^{k} F(\ell)G(k-\ell)$$
$$= \sum_{\ell=0}^{k} F(k-\ell)G(\ell) \quad \text{(A3)}$$

Therefore, the Taylor transform of $f^m(t)$, where m is a positive integer, can be obtained as

$$T[f^m(t)] = F_W^m(k)$$
$$= F_W^{m-1}(k) * F(k)$$
$$= \sum_{\ell=0}^{k} F_W^{m-1}(\ell)F(k-\ell). \quad \text{(A4)}$$

3 Derivative:

If $f(t)$ and its derivatives $f'(t), f''(t), \ldots, f^{(n)}(t)$ are continuous functions for interval $[0, H]$, then

$$T\left[\frac{d^n f(t)}{dt^n}\right] = \wedge^n F(k)$$
$$= \frac{(k+1)(k+2)\ldots(k+n)}{H^n} F(k+n). \quad \text{(A5)}$$

Convection Effects for Rapidly Moving Mechanical Sources on a Half-Space Governed by Fully Coupled Thermoelasticity

L. M. Brock
Department of Mechanical Engineering,
University of Kentucky,
Lexington, KY 40506
Fellow ASME

H. G. Georgiadis
Mechanics Division,
National Technical University of Athens,
One Konitsis Street,
Zographou 15773, Greece

The two-dimensional steady-state analysis of rapidly moving mechanical sources over the insulated surface of a thermoelastic half-space is extended by allowing surface heat convection. An exact transform solution based on the fully coupled (dynamic) equations of thermoelasticity is obtained, and robust asymptotic expressions for the surface displacements and temperature change are extracted. Convection is manifest in these expressions in terms of a positive dimensionless parameter of small magnitude, and results in a surface response that is more complicated than that for the insulated surface. In particular, surface temperature changes decay less with distance from the source, and convection effects can dominate all surface responses at low and near-critical speeds.

Introduction

The study of rapidly moving forces over the surface of an elastic half-space sheds light on processes of contact, tribology, and impact. Isothermal steady-state analyses can be found in work by Cole and Huth (1958) and Georgiadis and Barber (1993). When thermal effects are included, analyses generally use un- or partly coupled thermoelasticity theory (Boley and Weiner, 1985), minimize inertial (dynamic) effects, and treat the motion of heat sources alone over the surface (e.g., Ling and Mow, 1965; Mow and Cheng, 1967; Barber, 1984; Bryant, 1988).

Brock and Georgiadis (1997), therefore, considered the steady-state motion of a line mechanical/heat source over the surface of a half-space governed by fully coupled (dynamic) thermoelasticity (Biot, 1956; Chadwick, 1960). A two-dimensional plane-strain model was assumed, and exact bilateral Laplace transform solutions obtained. Asymptotic forms of the solutions, valid when the distance from the moving line surface source was large in comparison with a thermoelastic characteristic length, were then inverted analytically, and evaluated on the half-space surface. Because, however, the length is of order $O(10^{-4})$ μm, the results were robust. They showed, in fact, that thermoelastic coupling influences the surface displacement and change in temperature, especially when source speeds are high.

However, that work treated an insulated half-space surface, i.e., no surface heat flux occurred except at the heat source itself. Such models are common, e.g., in contact problems (Brock, 1996a), but neglect heat exchange with the medium surrounding the solid. Moreover, even if such heat exchange is negligible, manufacturing processes give surfaces that may differ in microstructural detail (Bayer, 1994) from the material underneath. Such a de facto surface layer might not affect the elastic properties of the solid, but any surface layer with a significant Biot number can give rise to surface heat flux by convection (Boley and Weiner, 1985).

As a first step, therefore, in examining the effects of surface heat convection in the response to dynamic loads of a solid that obeys the laws of fully coupled thermoelasticity, this article extends the work of Brock and Georgiadis (1997) by treating the steady-state motion of mechanical line sources over a half-space surface which now allows a surface heat flux. This effect is represented (Chadwick, 1960; Boley and Weiner, 1985) by a proportionality law between the heat flux and the temperature change at surface points. To highlight the effect, no heat source is included, and only subcritical source speeds are considered. As in the earlier work, robust asymptotic expressions for the surface displacements and temperature change are obtained. It will be seen that convection modifies the solution response observed by Brock and Georgiadis (1997). This first-step approach allows a clear comparison of an insulated and a convective surface in terms of basic Green's function solutions.

Problem Formulation

Consider a thermoelastic half-space defined in terms of the Cartesian coordinates (x, y, z) as $y > 0$. The half-space is initially at rest at a uniform (absolute) temperature $T_o > 0$ when normal and tangential line loads of magnitude (P, S) are applied to the surface. These loads are then moved across the surface in the positive x-direction at a constant subcritical speed v, so that a steady-state situation is eventually attained.

This process is two dimensional, so that z-dependence can be ignored, and Fig. 1 used as a schematic representation. As depicted there, it is convenient to fix the xy-axes to the sources, i.e., $(x, y) = 0$ always locates them. The boundary conditions for $y = 0$ can then be written as

$$\sigma_{xy} = -S\delta(x), \quad \sigma_y = -P\delta(x), \quad \frac{\partial \theta}{\partial y} - \frac{\theta}{h_c} = 0. \quad (1a\text{–}c)$$

In (1), $\delta(\,)$ is the Dirac function, θ is the change in absolute temperature from T_o, and $h_c > 0$ is a characteristic length (Chadwick, 1960; Boley and Weiner, 1985), while the line loads (P, S) have the same meaning in the work by Brock and Georgiadis (1997). The convection law (1c) allows h_c to characterize either the effects of heat exchange with the surrounding medium or, in terms of the dimensionless Biot number

$$B_l = \frac{l}{h_c} \quad (2)$$

the effects of heat flux through a de facto effective surface layer, where l—here assumed to be of microscale order—is the layer thickness.

Contributed by the Applied Mechanics Division of THE AMERICAN SOCIETY OF MECHANICAL ENGINEERS for publication in the ASME JOURNAL OF APPLIED MECHANICS.
Discussion on the paper should be addressed to the Technical Editor, Professor Lewis T. Wheeler, Department of Mechanical Engineering, University of Houston, Houston, TX 77204-4792, and will be accepted until four months after final publication of the paper itself in the ASME JOURNAL OF APPLIED MECHANICS.
Manuscript received by the ASME Applied Mechanics Division, July 7, 1998; final revision, Nov. 17, 1998. Associate Technical Editor: M.-J. Pindera.

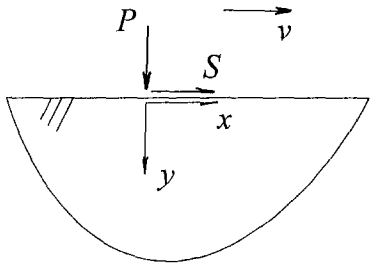

Fig. 1 Line sources moving at constant speed on a thermoelastic half-space

The two-dimensional steady-state problem involves only θ, displacement components (u_x, u_y), and tractions $(\sigma_x, \sigma_y, \sigma_{xy})$. Furthermore, these field quantities depend only on (x, y), and time derivatives in the absolute (inertial) frame reduce to the form $-v\partial(\,)/\partial x$. Thus, from Chadwick (1960) and Brock (1996b), the governing field equations of fully coupled thermoelasticity for $y > 0$ are

$$\left(\nabla^2 - m^2c^2\frac{\partial^2}{\partial x^2}\right)(u_x, u_y) + \left(\frac{\partial}{\partial x}, \frac{\partial}{\partial y}\right)[(m^2 - 1)\Delta + \chi\theta] = 0 \quad (3a)$$

$$h\nabla^2\theta + c\frac{\partial}{\partial x}\left(\theta - \frac{m^2\epsilon}{\chi}\Delta\right) = 0 \quad (3b)$$

$$\frac{1}{\mu}\sigma_{xy} = \frac{\partial u_x}{\partial y} + \frac{\partial u_y}{\partial x},$$

$$\frac{1}{\mu}(\sigma_x, \sigma_y) = (m^2 - 2)\Delta + \chi\theta + 2\left(\frac{\partial u_x}{\partial x}, \frac{\partial u_y}{\partial y}\right). \quad (3c)$$

In (3), (∇^2, Δ) are the two-dimensional Laplacian and dilatation, and

$$\chi = \chi_o(4 - 3m^2), \quad \epsilon = \frac{T_o}{c_v}\left(\frac{\chi v_r}{m}\right)^2, \quad h = \frac{kv_r}{\mu m c_v},$$

$$m = \frac{v_d}{v_r}, \quad c = \frac{v}{v_d} \quad (4)$$

where (χ_o, c_v, k, μ) are the thermal expansion, coefficient, specific heat, thermal conductivity, and shear modulus. The parameters (v_r, v_d) are the rotational and isothermal dilatational wave speeds while (ϵ, h) are the dimensionless thermoelastic coupling constant and thermoelastic characteristic length. It can be shown (Chadwick, 1960; Brock, 1992) that for many materials

$$\epsilon \approx O(10^{-2}), \quad h \approx O(10^{-4})\ \mu\text{m}, \quad m > \sqrt{2}. \quad (5)$$

In addition, we expect $(\sigma_x, \sigma_y, \sigma_{xy}, \theta)$ to vanish as $\sqrt{x^2 + y^2} \to \infty$, $y > 0$, and for these fields to be nonsingular everywhere except perhaps at $y = 0$, $x = 0$.

At this point we define subcritical source speed to be that which does not exceed v_r, i.e., $0 < c < 1/m$.

Exact Transform Solution

To consider this problem, the bilateral Laplace transform operator pair (van der Pol and Bremmer, 1950)

$$g^* = L(g) = \int_{-\infty}^{\infty} g(x)e^{-px}dx,$$

$$g(x) = L^{-1}(g^*) = \frac{1}{2\pi i}\int g^*e^{px}dp \quad (6a,b)$$

is introduced, where p is generally complex and integration in (6b) is along the Bromwich contour. Application of (6a) to (3) in view of the boundedness conditions noted above gives the transform solution set

$$\begin{bmatrix} u_x^* \\ \frac{1}{p^2}\theta^* \\ \frac{1}{\mu p}\sigma_y^* \end{bmatrix} = \begin{bmatrix} -p & -p & 1 \\ \omega_+ & \omega_- & 0 \\ -Kp & -Kp & -2 \end{bmatrix}\begin{bmatrix} A_+e^{-\alpha+y} \\ A_-e^{-\alpha-y} \\ \mathrm{B}e^{-\beta y} \end{bmatrix} \quad (7a)$$

$$\begin{bmatrix} u_y^* \\ \frac{1}{p^2}\frac{\partial\theta^*}{\partial y} \\ \frac{1}{\mu p}\sigma_{xy}^* \end{bmatrix} = \begin{bmatrix} -1 & -1 & -p \\ \omega_+ & \omega_- & 0 \\ -2 & -2 & Kp \end{bmatrix}\begin{bmatrix} -\alpha_+A_+e^{-\alpha+y} \\ -\alpha_-A_-e^{-\alpha-y} \\ -\frac{p}{\beta}\mathrm{B}e^{-\beta y} \end{bmatrix} \quad (7b)$$

for $y > 0$. Here the coefficients $(A_\pm, B)$ are as yet undetermined functions of p, while

$$\alpha_\pm = a_\pm\sqrt{-p}\sqrt{p}, \quad \beta = b\sqrt{-p}\sqrt{p},$$

$$\omega_\pm = \frac{m^2}{\chi}(1 - c^2 - a_\pm^2) \quad (8a)$$

$$a_\pm = \sqrt{1 + \frac{c}{p}(\tau_+ \pm \tau_-)^2}, \quad b = \sqrt{1 - m^2c^2},$$

$$K = m^2c^2 - 2 \quad (8b)$$

$$2\tau_\pm = \sqrt{\left(\sqrt{-cp} \pm \frac{1}{\sqrt{h}}\right)^2 + \frac{\epsilon}{h}}, \quad \omega_+\omega_- = \frac{m^4c^3\epsilon}{\chi^2 ph} \quad (8c)$$

where branch cuts must be chosen so that $\mathrm{Re}(\alpha_\pm, \beta) \geq 0$ in the cut complex p-plane.

Operation on (1) with (6a) and use of (7) then gives the equations necessary to find

$$\mu p R_\epsilon A_+ = \omega_-\left(\alpha_- + \frac{1}{h_c}\right)(2\beta S - KpP) \quad (9a)$$

$$\mu p R_\epsilon A_- = \omega_+\left(\alpha_+ + \frac{1}{h_c}\right)(KpP - 2\beta S) \quad (9b)$$

$$\mu p\frac{R_\epsilon}{\beta}B = \omega_+\left(\alpha_+ + \frac{1}{h_c}\right)(KpS + 2\alpha_-P) - \omega_-\left(\alpha_- + \frac{1}{h_c}\right)(KpS + 2\alpha_+P) \quad (9c)$$

where R_ϵ is the thermoelastic Rayleigh function defined by

$$R_\epsilon = \omega_+\left(\alpha_+ + \frac{1}{h_c}\right)R_- - \omega_-\left(\alpha_- + \frac{1}{h_c}\right)R_+,$$

$$R_\pm = 4\alpha_\pm\beta + K^2p^2. \quad (10)$$

It should be noted that letting $h_c \to \infty$ in (9) gives forms that, appropriately, agree with those obtained by Brock and Georgiadis (1997) for the insulated surface case.

With (7)–(10) available, the problem solution is complete, and inversion of (7) can be performed by means of (6b). As noted at the outset, however, the inversion process will be carried out for

robust asymptotic forms of (7)–(10), and the results evaluated on the half-space surface $y = 0$. This will result in more tractable expressions and, more importantly, allow a direct comparison with the results of Brock and Georgiadis (1997) in order to discern the effects of convection.

Development of Asymptotic Forms

Brock and Georgiadis (1997) used the fact (van der Pol and Bremmer, 1950) that the asymptotic form of a bilateral Laplace transform valid for small $|hp|$ gives an inversion that is valid for large $|x/h|$. The results were solutions in the form of analytic functions that were, as demonstrated by the behavior of h in (5), in fact, robust. The same basic approach is adopted here: When $y = 0$, (7) and (9) show that the expressions for (u_x^*, u_y^*, θ^*) are essentially ratios of functions of p, where R_ϵ is the common denominator. Expansion of each numerator and R_ϵ as Taylor series in the dimensionless variable hp, where $|hp| \ll 1$, produces the asymptotic forms

$$\mu \frac{R}{h} u_x^* = \frac{1}{hpD}\left(NP - m^2c^2bS\frac{\sqrt{-hp}}{\sqrt{hp}}\right) \times \left(1 + \frac{\lambda}{\sqrt{c(1+\epsilon)}}\frac{1}{\sqrt{-hp}}\right) + \frac{2\lambda bc\epsilon}{(1+\epsilon)^2}\frac{P}{hpD}\frac{\sqrt{-hp}}{\sqrt{hp}} + O(|hp|^{-1/2}) \quad (11a)$$

$$\mu \frac{R}{h} u_y^* = \frac{-1}{hpD}\left(NS + m^2c^2aP\frac{\sqrt{-hp}}{\sqrt{hp}}\right) \times \left(1 + \frac{\lambda}{\sqrt{c(1+\epsilon)}}\frac{1}{\sqrt{-hp}}\right) + \frac{\lambda c\epsilon}{(1+\epsilon)^2}\frac{1}{hpD}\left[(K+2b)P - 2bS\frac{\sqrt{-hp}}{\sqrt{hp}}\right] + O(|hp|^{-1/2}) \quad (11b)$$

$$\mu R\theta^* = \frac{m^2c^2\epsilon}{\chi(1+\epsilon)}\frac{1}{D}\left(KP - 2bS\frac{\sqrt{-hp}}{\sqrt{hp}}\right) + O(|hp|) \quad (11c)$$

whose inversions will be valid for $y = 0$, $|x/h| \gg 1$. In (11) the dimensionless quantities (λ, R, N, a) and the transform function D are given by

$$\lambda = \frac{h}{h_c}, \quad a = \sqrt{1 - \frac{c^2}{1+\epsilon}},$$
$$R = 4ab - K^2, \quad N = 2ab + K \quad (12a)$$

$$D = 1 + \frac{\lambda}{\sqrt{c(1+\epsilon)}}\frac{1}{\sqrt{-hp}} + \frac{4\lambda bc\epsilon}{(1+\epsilon)^2R}\frac{\sqrt{-hp}}{\sqrt{hp}} \quad (12b)$$

where λ is the dimensionless convection parameter, the positive real constant a is a manifestation of the asymptotic thermoelastic (adiabatic) dilatational wave speed $v_d\sqrt{1+\epsilon}$, and $R = R(c)$ is the asymptotic thermoelastic Rayleigh function. It can be shown (Brock, 1997) that R has zeros at $c = (0, \pm c_R)$ in the cut c-plane, where $0 < c_R < 1/m$. The zero c_R, which is the asymptotic thermoelastic Rayleigh speed nondimensionalized with respect to v_d, can be obtained as

$$c_R = \sqrt{2\left(m^2 - \frac{1}{1+\epsilon}\right)}\frac{1}{m^2G_o},$$
$$\ln G_o = \frac{1}{\pi}\int_{1/m}^{\sqrt{1+\epsilon}} \frac{\Psi dt}{t} \quad (13a)$$

$$\Psi = \tan^{-1}\frac{4\sqrt{1+\epsilon-t^2}\sqrt{m^2t^2-1}}{\sqrt{1+\epsilon}\,(m^2t^2-2)^2}. \quad (13b)$$

To avoid singular behavior, we now define, finally, the subcritical range of source speeds to be

$$0 < c < c_R. \quad (14)$$

The forms of (11) demonstrate that, despite the Taylor series expansions in hp, the existence of two characteristic lengths (h, h_c) allows in effect two sets of lowest-order terms that differ by $O(|hp|^{1/2})$. In the insulated surface limit $(h_c \to \infty, \lambda \to 0)$, the lower of these two orders disappears.

Transform Inversions

In view of (8a), (11) and the requirements on $(\alpha_\pm, \beta)$ in the cut p-plane, the radicals $(\sqrt{p}, \sqrt{-p})$ must exhibit branch cuts along, respectively, the lines $\mathrm{Im}(p) = 0$, $\mathrm{Re}(p) < 0$ and $\mathrm{Im}(p) = 0$, $\mathrm{Re}(p) > 0$. Because $D = 1$ in the insulated surface limit, it is worthwhile to obtain the inverses of (11) as convolutions of the inverses of $(1/D, 1/hpD)$ with those terms that multiply them. A glance at (11) indicates that these factors are of the four types

$$1, \quad \frac{\sqrt{-p}}{\sqrt{p}}, \quad \frac{1}{\sqrt{p}}, \quad \frac{1}{\sqrt{-p}}. \quad (15)$$

Substitution of each element of (15) into (6b) and use of Cauchy theory to simplify the resulting integrations leads to, respectively, the inversions

$$\delta(x), \quad \frac{1}{\pi x}, \quad \frac{H(x)}{\sqrt{\pi x}}, \quad \frac{H(-x)}{\sqrt{-\pi x}} \quad (16)$$

where $H(\,)$ is the Heaviside function. In view of (16); the inversion of (11a), for example, takes the form

$$\mu \frac{R}{h} u_x = NPG(x) + \left[m^2c^2bS - \frac{2\lambda bc\epsilon}{(1+\epsilon)^2}P\right]\frac{1}{\pi}\int_{-\infty}^{\infty}\frac{G(t)}{t-x}dt + \frac{\lambda}{\sqrt{c(1+\epsilon)}}\left[NP\int_x^\infty \frac{G(t)dt}{\sqrt{\pi h(t-x)}} - m^2c^2bS\int_{-\infty}^{x}\frac{G(t)dt}{\sqrt{\pi h(x-t)}}\right] \quad (17)$$

where f denotes Cauchy principal value integration and

$$G(x) = L^{-1}\left(\frac{1}{hpD}\right). \quad (18)$$

A direct substitution of (18) into (6b) and use of the $\mathrm{Im}(p)$-axis as the Bromwich contour yields the formal result

$$hG(x) = \frac{1}{\pi}\mathrm{Im}\int_0^\infty \frac{e^{iqx}dq}{\sqrt{q}S(q)},$$
$$S(q) = \left[1 - \frac{i4\lambda bc\epsilon}{(1+\epsilon)^2R}\right]\sqrt{q} + \frac{\lambda e^{i\pi/4}}{\sqrt{c(1+\epsilon)}} \quad (19)$$

where q is real. Assuming that the order of the (q, t)-integrations in (17) can be interchanged, use of Cauchy theory and standard tables (Gradshteyn and Ryzhik, 1980) gives the relations

$$\int_{-\infty}^{\infty} \frac{e^{iqt}dt}{t-x} = i\pi e^{iqx} \tag{20a}$$

$$\int_{x}^{\infty} \frac{e^{iqt}dt}{\sqrt{t-x}} = \sqrt{\frac{\pi}{q}}\, e^{i(qx+(\pi/4))},$$

$$\int_{-\infty}^{x} \frac{e^{iqt}dt}{\sqrt{x-t}} = \sqrt{\frac{\pi}{q}}\, e^{i(qx-(\pi/4))}. \tag{20b}$$

In view of (19) and (20), each of the terms in (17) can be written as real integrals with respect to q. Because $S(q)$ has no zeros in the cut q-plane, these integrals can be simplified by use of the Cauchy theory. Upon introducing the dimensionless variables

$$\xi = \frac{x}{h}, \quad \bar{P} = \frac{P}{\mu h}, \quad \bar{S} = \frac{S}{\mu h}, \tag{21}$$

it can then be shown, finally, that (17) and its counterparts for (u_y, θ) give the forms

$$\pi \frac{R}{h} u_x = N\bar{P} g(\xi) + \left[m^2 c^2 b \bar{S} - \frac{2\lambda bc\epsilon}{(1+\epsilon)^2} \bar{P} \right] g_p(\xi) \times \frac{\lambda}{\sqrt{c(1+\epsilon)}} [N\bar{P} g_+(\xi) - m^2 c^2 b \bar{S} g_-(\xi)] \tag{22a}$$

$$\pi \frac{R}{h} u_y = \left[\frac{\lambda c\epsilon}{(1+\epsilon)^2} (K+2b) - N \right] \bar{P} g(\xi) + \left[m^2 c^2 a \bar{P} + \frac{2\lambda bc\epsilon}{(1+\epsilon)^2} \bar{S} \right] g_p(\xi) - \frac{\lambda}{\sqrt{c(1+\epsilon)}} [N\bar{S} g_+(\xi) + m^2 c^2 a \bar{P} g_-(\xi)] \tag{22b}$$

$$\pi R\theta = \frac{m^2 c^2 \epsilon}{\chi(1+\epsilon)} [K\bar{P} f(\xi) + 2b\bar{S} f_p(\xi)] \tag{22c}$$

for $y = 0$, $|\xi| \gg 1$. When $\xi > 0$ the dimensionless functions in (22) are given by

$$[f(\xi), g(\xi)] = \frac{4\lambda bc\epsilon}{(1+\epsilon)^2 R} \int_0^{\infty} \frac{e^{-u}}{S_+} \left[\frac{-u}{\xi}, 1 \right] du \tag{23a}$$

$$[f_p(\xi), g_p(\xi)] = \int_0^{\infty} \left(1 + \frac{\lambda}{\sqrt{c(1+\epsilon)}} \sqrt{\frac{\xi}{u}} \right) \frac{e^{-u}}{S_+} \left[\frac{-u}{\xi}, 1 \right] du \tag{23b}$$

$$[g_+(\xi), g_-(\xi)] = \sqrt{\xi} \int_0^{\infty} \frac{1-e^{-u}}{\sqrt{u} S_+} \times \left[\frac{-4\lambda bc\epsilon}{(1+\epsilon)^2 R}, \quad 1 + \frac{\lambda}{\sqrt{c(1+\epsilon)}} \sqrt{\frac{\xi}{u}} \right] du \tag{23c}$$

while for $\xi < 0$ the forms

$$[f(\xi), g(\xi)] = \lambda \int_0^{\infty} \frac{e^{-u}}{S_-} \left(\frac{4bc\epsilon}{(1+\epsilon)^2 R} - \frac{1}{\sqrt{c(1+\epsilon)}} \sqrt{\frac{-\xi}{u}} \right) \times \left[\frac{-u}{\xi}, 1 \right] du \tag{24a}$$

$$[f_p(\xi), g_p(\xi)] = \int_0^{\infty} \frac{e^{-u}}{S_-} \left[\frac{-u}{\xi}, 1 \right] du \tag{24b}$$

$$[g_+(\xi), g_-(\xi)] = \sqrt{-\xi} \int_0^{\infty} \frac{1-e^{-u}}{\sqrt{u} S_-} \times \left[1, \frac{4\lambda bc\epsilon}{(1+\epsilon)^2 R} - \frac{\lambda}{\sqrt{c(1+\epsilon)}} \sqrt{\frac{-\xi}{u}} \right] du \tag{24c}$$

govern, where in the integrands we have

$$S_+ = \left[\frac{4\lambda bc\epsilon}{(1+\epsilon)^2 R} \right]^2 u + \left[\sqrt{u} + \frac{\lambda\sqrt{\xi}}{\sqrt{c(1+\epsilon)}} \right]^2 \quad (\xi > 0) \tag{25a}$$

$$S_- = u + \lambda^2 \left[\frac{4bc\epsilon\sqrt{u}}{(1+\epsilon)^2 R} - \frac{\sqrt{-\xi}}{\sqrt{c(1+\epsilon)}} \right]^2 \quad (\xi < 0). \tag{25b}$$

It should be noted that (12a) exhibits the behavior

$$c \to 0: \quad R \approx 2\left(m^2 - \frac{1}{1+\epsilon} \right) c^2 \tag{26a}$$

$$c \to c_R^-: \quad R \approx 2m^4 c_R^3 G_R (c_R - c),$$

$$\ln G_R = \frac{2}{\pi} \int_{1/m}^{\sqrt{1+\epsilon}} \frac{t\Psi dt}{t^2 - c_R^2} \tag{26b}$$

where (c_R, Ψ) are given in (13). In view of this result and (22)–(25), it can be shown that (u_x, u_y, θ) become unbounded at line surface source speeds near the critical (Rayleigh) value.

Effects of Convection

The Eqs. (22) correspond to the formulas numbered as (36)–(38) in the paper by Brock and Georgiadis (1997) when their heat flux term $Q = 0$. The latter results are in terms of analytic functions, while (22) involve simple quadratures. Despite the differing formats, the present results (22) show clearly the contributions due to convection. Indeed, appearance of the convection parameter λ in both (22) and the expressions (23) and (24) indicates that convection is manifest, for $y = 0$, $|x/h| \gg 1$ at least, both as first and second-order effects.

In view of (5) and (12a) it is reasonable to assume that $\lambda \ll 1$. This assumption allows a more direct comparison of (22) and the results of Brock and Georgiadis (1997): By manipulating the numerators of the integrands in (23) and (24), expansions to the first order in λ can be obtained that do not exhibit the denominator terms $S_\pm$. Such expansions can be integrated exactly, and the results are that, for $y = 0$, $|x/h| \gg 1 (\lambda \ll 1)$,

$$\frac{R}{h} u_x = \frac{N}{2} \bar{P} sgn(\xi) - \frac{m^2 c^2 b}{\pi} \left[\bar{S} + \frac{2\lambda c\epsilon}{(1+\epsilon)^2} \frac{K}{R} \bar{P} \right] \ln|\xi| + O(\lambda^2) \tag{27a}$$

$$\frac{R}{h} u_y = \frac{1}{2} \left[-N\bar{S} + \frac{\lambda m^2 c^3 \epsilon}{(1+\epsilon)^2} \bar{P} \right] \text{sgn}(\xi) + \frac{m^2 c^2}{\pi} \left[-a\bar{P} + \frac{2\lambda c\epsilon}{(1+\epsilon)^2} \frac{bK}{R} \bar{S} \right] \ln|\xi| + O(\lambda^2) \tag{27b}$$

$$R\theta = \frac{m^2 c^2 \epsilon}{\chi(1+\epsilon)} \times K\bar{P}\delta(\xi) - \frac{2b}{\pi} \left[\bar{S} + \frac{2\lambda c\epsilon}{(1+\epsilon)^2} \frac{K}{R} \bar{P} \right] \frac{1}{\xi} + \frac{\lambda c\epsilon}{(1+\epsilon)^2} \left[2b\bar{S} \frac{H(\xi)}{\sqrt{\pi\xi}} - K\bar{P} \frac{H(-\xi)}{\sqrt{-\pi\xi}} \right] + O(\lambda^2). \tag{27c}$$

When $\lambda = 0$, (27) agrees with the results of Brock and Georgiadis (1997), save that the S-terms in their formulas (36) and (38) exhibit, through typographical error, the wrong sign. In (27), the result $2H(\xi) = 1 + \text{sgn}(\xi)$ has been used, and it is noted that (27*a, b*) are correct only to within an arbitrary rigid-body motion.

The expressions (27*a, b*) also show that convection does not alter the functional response of the surface displacements, but does couple the moving source components (P, S) more fully into that response. Equation (27*c*) for the temperature change induced on the surface, however, indicates that the nature of the functional response is altered. In particular, the last two terms in (27*c*), which are convection effects, show less decay at large distances from the moving line surface source. That is, allowing convection produces a temperature change field that is more prominent far from the source than for an insulated surface. Equation (27*c*) also shows, however, that this effect depends on the loading and whether or not an observer is located ahead or in the wake of the moving source.

It is seen that the convection parameter λ in (27) always forms the product $\lambda\epsilon$. This demonstrates that, to the first order, convection effects are proportional to thermoelastic coupling and, because $\lambda \ll 1$ and (5) holds, suggests that the effects are small. However, (26) and the coefficients of the $\ln|\xi|$-terms in (27*a, b*) and the $1/\xi$-term in (27*c*) demonstrate that the effects can actually dominate solution response at low ($c \approx 0$) and nearly critical ($c \approx c_R$) source speeds.

Some Closing Comments

This study extended the work of Brock and Georgiadis (1997) on rapidly moving sources over the insulated surface of a thermoelastic half-space by allowing surface heat convection. An exact transform solution for the associated two-dimensional steady-state problem based on the fully coupled (dynamic) equations of thermoelasticity was obtained and, following the procedure of the earlier work, robust asymptotic forms extracted. Inversion of these forms for the displacements and temperature change engendered on the half-space surface gave expressions as simple quadratures.

Comparison of these with corresponding results by Brock and Georgiadis (1997) indicated that convection is manifest in terms of a positive dimensionless parameter that can reasonably be taken as much less than unity, and that it results in a more complicated surface response. A first-order expansion of the expressions in terms of this convection parameter produced analytic results that, upon comparison with those of Brock and Georgiadis (1997), showed that the convection effects are proportional to the well-known (Chadwick, 1960) thermoelastic coupling constant, and more fully couple the components of the applied surface line loads into the solution response. More importantly, convection effects produce a surface temperature change that decays less rapidly with distance from the moving loads than in the insulated surface case. The small magnitudes of the radiation parameter and coupling constant suggested that the convection effects may numerically be small. However, it was found that at both low and nearly critical line load speeds, the effects can actually dominate solution response.

As noted at the outset, the Biot number given in (2) is a characterization of surface convection due to an effective surface layer. Clearly, the model used here of a layer which does not affect elastic properties of the solid requires a small effective layer thickness l, while some conclusions about convection effects were drawn on the basis of the dimensionless convection parameter λ being small. If, for example, $l \approx O(10^{-1})$ μm and $\lambda \approx O(10^{-2})$, then (2), (5), and (12*a*) lead to the result that $B_l \approx O(10)$, which is a typical (Boley and Weiner, 1985) value.

Brock and Georgiadis (1997) considered a combined mechanical/heat source, and super-critical source speeds, while the present first-step analysis, in order to focus on convection effects, treated only line forces, i.e., mechanical loads, and subcritical source speeds. Work is proceeding which will extend the present results to the more general cases. Moreover, studies that illustrate surface convection effects in the mechanical treatment of surfaces and in fracture are under way. While the problem treated here exhibited unmixed boundary conditions, the studies under way involve both mixed thermal and mechanical boundary conditions. Nevertheless, their Green's function solution nature make the present results useful in formulating the newer problems, and the comparisons made here with the insulated results of Brock and Georgiadis (1997) demonstrate that convection effects should indeed be noticeable.

Acknowledgment

The authors acknowledge the support of NATO Grant CRG 972116.

References

Barber, J. R., 1984, "Thermoelastic Displacements and Stresses due to a Heat Source Moving Over the Surface of a Half-Plane," ASME JOURNAL OF APPLIED MECHANICS, Vol. 51, pp. 636–640.

Bayer, R. G., 1994, *Mechanical Wear Prediction and Prevention*, Marcel Dekker, New York.

Biot, M. A., 1956, "Thermoelasticity and irreversible thermodynamics," *Journal of Applied Physics*, Vol. 27, pp. 240–253.

Boley, B. A., and Weiner, J. H., 1985, *Theory of Thermal Stresses*, Krieger, Malabar, FL.

Brock, L. M., 1992, "Transient thermal effects in edge dislocation generation near a crack edge," *International Journal of Solids and Structures*, Vol. 29, pp. 2217–2234.

Brock, L. M., 1996a, "Some analytical results for heating due to irregular sliding contact of thermoelastic solids," *Indian Journal of Pure and Applied Mathematics*, Vol. 27, pp. 1257–1278.

Brock, L. M., 1996b, "Effects of thermoelasticity and a von Mises criterion in rapid steady-state quasi-brittle fracture," *International Journal of Solids and Structures*, Vol. 33, pp. 4131–4142.

Brock, L. M., 1997, "Some results for Rayleigh and Stoneley signal effects in thermoelastic solids," *Indian Journal of Pure and Applied Mathematics*, Vol. 28, pp. 835–850.

Brock, L. M., and Georgiadis, H. G., 1997, "Steady-State Motion of a Line Mechanical/Heat Source Over a Half-Space: A Thermoelastodynamic Solution," ASME JOURNAL OF APPLIED MECHANICS, Vol. 64, pp. 562–567.

Bryant, M. D., 1988, "Thermoelastic Solutions for Thermal Distributions Moving Over Half-Space Surfaces and Applications to the Moving Heat Source," ASME JOURNAL OF APPLIED MECHANICS, Vol. 55, pp. 87–92.

Chadwick, P., 1960, "Thermoelasticity: The dynamical theory," *Progress in Solid Mechanics*, Vol. 1, I. N. Sneddon and R. Hill, eds., North-Holland, Amsterdam, pp. 263–328.

Cole, J., and Huth, J., 1958, "Stresses Produced in a Half-Plane by Moving Loads," ASME JOURNAL OF APPLIED MECHANICS, Vol. 25, pp. 433–436.

Georgiadis, H. G., and Barber, J., 1993, "Steady-State Transonic Motion of a Line Load Over an Elastic Half-Space: The Corrected Cole-Huth Solution," ASME JOURNAL OF APPLIED MECHANICS, Vol. 60, pp. 772–774.

Gradshteyn, I. S., and Ryzhik, I. M., 1980, *Tables of Integrals, Series and Products*, Academic Press, New York.

Ling, F. F., and Mow, V. C., 1965, "Surface Displacements of a Convective Elastic Half-Space Under an Arbitrarily Distributed Fast-Moving Heat Source," ASME *Journal of Basic Engineering*, Vol. 87, pp. 729–734.

Mow, V. C., and Cheng, H. S., 1967, "Thermal stresses in an elastic half-space associated with an arbitrarily distributed moving heat source," *Journal of Applied Mathematics and Physics (ZAMP)*, Vol. 18, pp. 500–507.

van der Pol, B., and Bremmer, H., 1950, *Operational Calculus Based on the Two-Sided Laplace Integral*, Cambridge University Press, Cambridge, UK.

Local and Global Bifurcation Analyses of a Spatial Cable Elastica

O. Gottlieb
Mem. ASME
Faculty of Mechanical Engineering,
Technion—Israel Institute of Technology,
Haifa 32000, Israel

N. C. Perkins
Mem. ASME
Department of Mechanical Engineering and
Applied Mechanics,
University of Michigan,
Ann Arbor, MI 48109-2125

This paper focuses on a boundary value problem governing the equilibrium of a slender cable subject to thrust, torsion, and gravity. In the absence of field (gravity) loading, this boundary value problem is integrable and admits periodic solutions describing planar and spatial equilibrium forms. A bifurcation analysis of the integrable problem reveals the conditions controlling local stability of periodic solutions and the existence of two limiting (bounding) homoclinic solutions. The addition of field (gravity) loading renders the boundary value problem nonintegrable. This effect is first investigated through perturbation of the limiting homoclinic solutions for weak gravity loading. Approximate existence conditions for aperiodic and spatially complex forms are determined using Melnikov's method. The effect of field loading is then re-evaluated through numerical solution of the original problem. Spatially complex solutions are determined that might mimic the loops and tangles sometimes found in underwater cables.

1 Introduction

A large variety of biological, chemical, and structural systems may be described by the mechanics of rod elements. Here, the term rod follows that used by Antman (1972), and describes a one-dimensional solid whose deformation depends on time and a single spatial variable. A comprehensive review of rational rod theories is described in Antman (1972, 1995) including the original contributions by Clebsch and Kirchhoff. Their efforts led to the 'classical' rod theory (Love, 1944) in which the three-dimensional deformation of a rod is described by the differential geometry of a space curve with superimposed twist. As reviewed below, the classical theory has enjoyed substantial utility in diverse applications ranging from the fields of structural mechanics to biochemistry. As discussed by Antman (1972), such "technical" theories form special cases of more general theories for one-dimensional continua. More general, higher-order theories have subsequently followed from modern treatments of the subject (see, for example, Green et al., 1967; Green and Naghdi, 1970; Antman, 1972; Green et al., 1974, Coleman et al., 1993; Rubin, 1996).

Of primary interest here are the potentially complex deformations realized by rod-like elements under steady loading conditions. Within the field of structural mechanics, such deformations may characterize the response of slender structural elements such as pipelines and marine risers (Bernitsas, 1982) and mechanical (Zajac, 1962) and electromechanical (Liu, 1975) cables. The curved and three-dimensional geometries realized in these structures may bear remarkable similarity to those observed in certain biological tissues. Consider, for example, the spiralling collagen bundles forming tendons (Woo and Buckwalter, 1988) and superhelical DNA molecules which, following Benhan (1987, 1989), may be modeled as hyperelastic symmetric rods. The use of Kirchhoff's theory of elastic rods has recently been employed to investigate the structure of looped DNA segments (Coleman et al., 1994, Tobias et al., 1995). The complex writhing forms of DNA molecules also motivated a recent study by (Thompson and Champneys, 1996) who note that such forms follow from a dynamic jump from spatially localized forms. Spatially complex forms may also characterize the response of marine cables and particularly under low-tension conditions. Low-tension conditions naturally arise in cable laying operations where the tension is reduced as the cable is supported by the sea bed. Prior analysis of cable laying (e.g., submarine cables, instrumentation cables and fiber optic cables) have focused on how loops (often referred to as "hockles") form under low tension; refer to (Zajac, 1962; Rosenthal, 1976; Yubata, 1984, Coyne, 1990; Tan and Witz, 1993; Lu and Perkins, 1994). Recent experiments by Welch and Tulin (1995) suggest that spatially complex forms are created for rapid cable payout rates.

Models of low-tension cables have been proposed starting with the classical theory of the elastica. The "kinetic analogy" between the temporal response of the classical pendulum and the (static) spatial response of the elastica was known to Kirchhoff in 1859 (see Love, 1944). Recognizing this, global/local bifurcation techniques developed for time-dependent ordinary differential equations (Guckenheimer and Holmes, 1983; Ioos and Joseph, 1980; Wiggins, 1992) may also be brought to bear in evaluating the spatial bifurcations of the elastica. To this end, Mielke and Holmes (1988) determined the existence of spatially chaotic planar equilibrium states for nonlinear hyperelastic rods using Melnikov's method. This analytical study is complemented by numerical investigations of spatial chaos and localization phenomena of (linearly) elastic rods undergoing large deformations (Thompson and Virgin, 1988). Further numerical studies include chaotic soliton models of elastic chains (El Naschie and Kapitaniak, 1990) and spatial chaos forming in long elasticas having (spatially) periodic changes in cross section (Davies and Moon, 1993). Recently Champneys and Thompson (1996) demonstrated that the loss of integrability of an infinitely long noncircular rod subject to end tension and moment implies a multiplicity of localized buckling modes. These studies have important implications for the study of marine cable hockling for which only periodic solution forms have been analyzed to date.

The purpose of this paper is to extend prior analyses of cable hockling to include spatially complex forms that may also be three dimensional. The existence of spatially complex forms is already known from the limiting case of planar deformations (Mielke and Holmes, 1988). For marine cable applications, the addition of torsion may very well lead to three-dimensional solutions exhibiting spatial complexity. These complex forms may provide further

Contributed by the Applied Mechanics Division of THE AMERICAN SOCIETY OF MECHANICAL ENGINEERS for publication in the ASME JOURNAL OF APPLIED MECHANICS.
Discussion on the paper should be addressed to the Technical Editor, Professor Lewis T. Wheeler, Department of Mechanical Engineering, University of Houston, Houston, TX 77204-4792, and will be accepted until four months after final publication of the paper itself in the ASME JOURNAL OF APPLIED MECHANICS.
Manuscript received by the ASME Applied Mechanics Division, Aug. 13, 1998; final revision, Feb. 2, 1999. Associate Technical Editor: L. T. Wheeler.

insight into the loading required to induce marine cable hockling and tangling.

This manuscript is organized as follows. Section 2 reviews the equilibrium boundary value problem of Lu and Perkins (1994) which governs the globally large static response of a cable subject to boundary and field loading. Section 3 examines an integrable form of the boundary value problem describing a cable subjected to uniaxial torque (m_0) and thrust (f_0). Analysis of this unperturbed problem reveals the bifurcation structure governing planar and spatial periodic solution forms. Evaluation of the fixed points of the spatial system for this integrable case further reveals coexisting elliptic and (hyperbolic) saddle solutions for various combinations of boundary loads described by the torque/thrust pair (m_0, f_0). Two limiting cases are identified which are governed by a homoclinic bifurcation: (1) a planar system ($m_0 = 0$), and (2) a spatial system where the geometric torsion is proportional to half the internal torque. Section 4 considers a nonintegrable form of the boundary value problem realized through the addition of (small) field loading as an approximation to the cable weight. Approximate existence conditions for aperiodic and spatially complex forms for the perturbed problem are determined via Melnikov's method. Numerical solutions of the original boundary value problem with field loading are presented in Section 5 and support the analytical findings of Section 4.

2 Equilibrium Boundary Value Problem

We start with the (nondimensional) equilibrium boundary value problem derived in Lu and Perkins (1994) which describes the two-axis flexure and torsion of a slender cable of circular cross section employing classical Kirchhoff assumptions for rod deformation. The resulting equilibrium equations, describing globally large three-dimensional equilibrium forms, govern the principle curvature $\kappa(s)$ and geometric torsion $\tau(s)$ of the cable centerline as well as the resultant cable tension $p(s)$ and internal torque $h(s)$:

$$p' = -\kappa\kappa' - \bar{q}\cdot\hat{l}_1$$

$$\kappa'' = (p + \tau^2 - h\tau)\kappa + \bar{q}\cdot\hat{l}_2$$

$$\kappa\tau' = (\kappa h)' - 2\kappa'\tau + \bar{q}\cdot\hat{l}_3$$

$$h' = 0. \tag{1}$$

Here, $(')$ denotes differentiation with respect to the independent arc length variable s measured along the equilibrium cable centerline, $\bar{q}$ denotes any steady external force/length and $(\hat{l}_1, \hat{l}_2, \hat{l}_3)$ denote the Serret-Frenet triad defined by the equilibrium centerline; refer to Fig. 1. The relationship between the Serret-Frenet triad and the Cartesian triad $(\hat{e}_1, \hat{e}_2, \hat{e}_3)$ of Fig. 1 is determined via the Euler angle transformation matrix (cf. Greenwood, 1988).

$$\begin{pmatrix} \hat{l}_1 \\ \hat{l}_2 \\ \hat{l}_3 \end{pmatrix} = [D]\begin{pmatrix} \hat{e}_1 \\ \hat{e}_2 \\ \hat{e}_3 \end{pmatrix} \tag{2}$$

where

$$[D] = \begin{pmatrix} c\psi c\theta & -s\psi c\theta & s\theta \\ s\psi c\phi + c\psi s\theta s\phi & c\psi c\phi - s\psi s\theta s\phi & -c\theta s\phi \\ s\psi s\phi - c\psi s\theta c\phi & c\psi s\phi + s\psi s\theta c\phi & c\theta c\phi \end{pmatrix} \tag{3}$$

and c and s denote sine and cosine, respectively, of the Euler angles defined in Fig. 1.

Two forms of the equilibrium boundary value problem are subsequently evaluated. The first of these is the integrable form for which $\bar{q} = 0$ which defines the unperturbed problem of Section 3. The second of these is the nonintegrable form for which $\bar{q} \neq 0$ which defines the perturbed problem of Section 4. The perturbation considered represents the addition of cable self-weight, thus

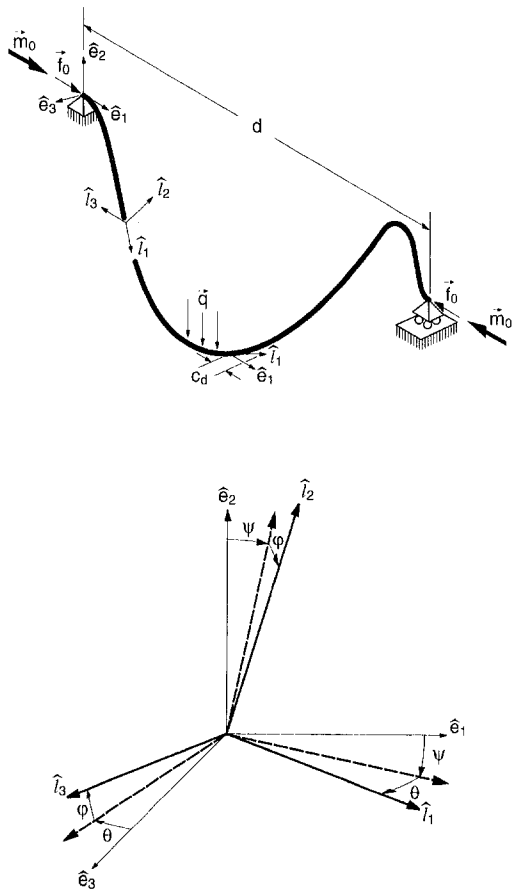

Fig. 1 Definition sketches

$$\bar{q} = -\gamma\hat{e}_2, \quad \gamma = \frac{\rho g A L}{EI/L^2} \tag{4}$$

where γ represents the cable weight/length (refer to Appendix A for nondimensional scaling).

2.1 Equilibrium for Three-Dimensional (Spatial) Forms. We recast the equilibrium Eqs. (1) with (2) and (4) in state-space form:

$$p' = -\kappa\mu + \gamma g_1(\psi, \theta, \phi)$$

$$\kappa' = \mu$$

$$\mu' = (p + \tau^2 - \bar{h}\tau)\kappa - \gamma g_2(\psi, \theta, \phi)$$

$$\tau' = \frac{\mu}{\kappa}(\bar{h} - 2\tau) - \gamma\frac{g_3(\psi, \theta, \phi)}{\kappa} \tag{5}$$

where $\bar{h}$ is the constant internal torque ($h' = 0$ in (1)) and

$$g_1 = -\sin\psi\cos\theta$$

$$g_2 = \cos\psi\cos\phi - \sin\psi\sin\theta\sin\phi$$

$$g_3 = \cos\psi\sin\phi + \sin\psi\sin\theta\cos\phi \tag{6}$$

are the components of $\hat{e}_2$ resolved along the Serret-Frenet triad.

We complete the state-space formulation with the Euler angle evolution equations (Greenwood, 1988):

$$\psi' = -\kappa\cos\phi\sec\theta$$

$$\theta' = -\kappa\sin\phi$$

$$\phi' = -\tau + \kappa \cos \phi \tan \theta. \tag{7}$$

The boundary conditions considered here are those considered by Rosenthal (1976) and Lu and Perkins (1994) and describe the response of a cable subject to uniaxial torque m_0 and thrust f_0 directed along the $\hat{e}_1$-axis in Fig. 1. From Lu and Perkins (1994), the boundary conditions at $s = 0$ are

$$\kappa(0) = m_0 \sin \psi(0), \quad \mu(0) = 0$$

$$p(0) = f_0 \cos \psi(0), \quad \tau(0) = m_0 \cos \psi(0) - f_0/m_0 \tag{8}$$

from which the constant internal torque becomes $\bar{h} = h(0) = m_0 \cos \psi(0)$. The same boundary conditions hold at $s = 1$ by symmetry.

2.2 Equilibrium for Two-Dimensional (Planar) Forms. Planar forms result from the special case of $\tau = 0$ (vanishing geometric torsion) and $\theta' = \phi' = 0$. Consequently, θ and ϕ are constants and ψ is related to the principle curvature through $\psi' = -\kappa$. Thus, (5)–(7) reduce to

$$p' = -\kappa\mu - \gamma \sin \psi$$

$$\kappa' = \mu$$

$$\mu' = p\kappa + \gamma \cos \psi$$

$$\psi' = -\kappa. \tag{9}$$

The boundary conditions at $s = 0$ for the planar forms ($\tau = h = 0$) are

$$\kappa(0) = 0, \quad p(0) = f_0 \cos \psi(0). \tag{10}$$

3 Solutions of the Unperturbed System

In the absence of domain loading, ($\gamma = 0$), the system (5) can be integrated (incorporating boundary conditions) and reduced to a second-order equation governing the curvature $\kappa(s)$ (see Lu and Perkins, 1994, Eq. (14) or Coleman et al., 1993, Eq. (4.9)). Following Lu and Perkins (1994), this is achieved by

(i) integration of $p' = -\kappa\kappa'$ to yield $p = -\kappa^2/2 + d_1$ where $d_1 = p(0) + \kappa^2(0)/2$;
(ii) multiplication of $\kappa\tau' = \kappa'(\bar{h} - 2\tau)$ by κ and integration to yield $\tau = \bar{h}/2 + d_2/\kappa^2$ where $d_2 = \kappa^2(0)[\tau(0) - \bar{h}/2]$; and
(iii) substitution of p and τ into $\kappa'' = (p + \tau^2 - \bar{h}\tau)\kappa$.

Thus, the integrable structure of the unperturbed boundary value problem is revealed to be that of a nonlinear autonomous Hamiltonian system:

$$\kappa' = \mu = \frac{\partial H}{\partial \mu}$$

$$\mu' = -\left(\frac{\kappa^3}{2} - \alpha\kappa - \frac{\beta}{\kappa^3}\right) = -\frac{\partial H}{\partial \kappa} \tag{11}$$

where

$$H(\kappa, \mu) = \frac{\mu^2}{2} + \frac{\kappa^4}{8} - \frac{\alpha\kappa^2}{2} + \frac{\beta}{2\kappa^2} \tag{12}$$

and (α, β) are parameters obtained from the boundary conditions defined by the uniaxial torque/thrust pair (f_0, m_0)

$$\alpha = p(0) + \frac{\kappa^2(0)}{2} - \left(\frac{\bar{h}}{2}\right)^2 \tag{13}$$

and

$$\beta = \left[\tau(0) - \frac{\bar{h}}{2}\right]^2 \kappa^4(0) \geq 0. \tag{14}$$

Note that for $\beta = 0$, the system returns the (spatial form of the) classical Hamiltonian Duffing equation that has either a unique center (at the origin of the μ-κ phase plane) for $\alpha \leq 0$ or a saddle at the origin coexisting with a center at $(\kappa, \mu) = ((2\alpha)^{1/2}, 0)$ for $\alpha > 0$. Two limiting forms lead to the Duffing equation: (i) all planar forms (for which the torque $m_0 = 0$), and (ii) a special spatial form for which $\tau(0) = \bar{h}/2$. In either of these limits, (11)–(12) reduces to

$$\kappa'' - \alpha\kappa + \frac{\kappa^3}{2} = 0 \tag{15}$$

where the parameter α for either planar or spatial forms is obtained from (13). For the planar forms, $\kappa(0) = \kappa(1) = 0$ and $\tau(s) = 0$. Consequently,

$$\alpha = p(0) = f_0 \cos \psi(0). \tag{16}$$

For the limiting spatial form, $\mu(0) = \mu(1) = 0$, $\tau(s) = \bar{h}/2$, and $\bar{h} = 2f_0/m_0$. Recall that $\bar{h} = m_0 \cos \psi(0)$. Thus, $\cos \psi(0) = 2f_0/m_0^2$ and from (8), $p(0) = 2(f_0/m_0)^2$. Consequently, the initial curvature is $\kappa(0) = m_0 \sin \psi(0) = (m_0^2 - (2f_0/m_0)^2)^{1/2}$ and

$$\alpha = \left(\frac{\bar{h}}{2}\right)^2 + \frac{\kappa^2(0)}{2} = \frac{m_0^2}{2} - \left(\frac{f_0}{m_0}\right)^2 > 0. \tag{17}$$

We consider further these two limiting forms and provide closed-form periodic solutions and an associated homoclinic solution that serves as a lower bound to the planar form and an upper bound to the limiting spatial form.

3.1 Planar Forms. The solution of (15) with α from (16) is found in terms of the following Jacobi elliptic function

$$\kappa(s) = \kappa_m cn[\mathbf{K}(1 - 2s)], \quad \kappa_m = 4\sqrt{m}\mathbf{K} \tag{18}$$

where m and $\mathbf{K} = \mathbf{K}(m)$ are the parameter and quarter-period of the Jacobi elliptic function (Abramowitz and Stegun, 1970). Consequently, the derivative of the curvature ($\mu(s)$) can be determined as well as the internal axial force $p(s) = \mu'(s)/\kappa(s)$ employing (9). The value of the parameter α (and corresponding applied thrust f_0) can be determined from $p(0)$ or by integrating $\kappa(s)$ from $\kappa(0) = 0$ to $\kappa(\frac{1}{2}) = \kappa_m$. Thus,

$$\alpha = 4(2m - 1)\mathbf{K}^2, \quad f_0 = 4\mathbf{K}^2. \tag{19}$$

Note that apriori knowledge of $\mu(0)$ enables solution of (15) as an initial value problem as opposed to the boundary value problem evaluated by numerical shooting in previous studies (cf. Rosenthal, 1976).

$$\mu(0) = 8[m(1 - m)]^{1/2}\mathbf{K}^2. \tag{20}$$

The μ-κ phase plane of (15) with α (19) and initial conditions $\kappa(0) = 0$ and $\mu(0)$ (20) is illustrated in Fig. 2 (for $m = 0.99$: $f_0 = 54.63$). Note that above the bifurcation threshold $\alpha = 0$ (corresponding to $m = \frac{1}{2}$), the planar solutions are bounded from below ($m \to 1$) by the homoclinic solution (separatrix) of (15).

Integration of $\kappa(s)$ enables the determination of $\psi(s)$ for later use in the perturbed problem of Section 4; namely,

$$\psi(s) = 2 \cos^{-1}\{dn[\mathbf{K}(1 - 2s)]\}. \tag{21}$$

We define the projection of the tangent ($\hat{l}_1$) at midspan ($s = \frac{1}{2}$) onto the loading axis ($\hat{e}_1$) as $c_d = (\hat{l}_1 \cdot \hat{e}_1)_{1/2} = \cos \psi(\frac{1}{2}) \cos \theta(\frac{1}{2})$ as illustrated in Fig. 1, and note that for planar forms $c_d = 1$. Thus, using the value of $\cos \psi(\frac{1}{2}) = 1$ from (21) results in $\cos \theta(\frac{1}{2}) = 1$. However, the angles $\theta(s)$ and $\phi(s)$ are constant for the planar forms with their values determined by (7) from $\cos \theta(s) = 1$ and $\cos \phi(s) = 1$.

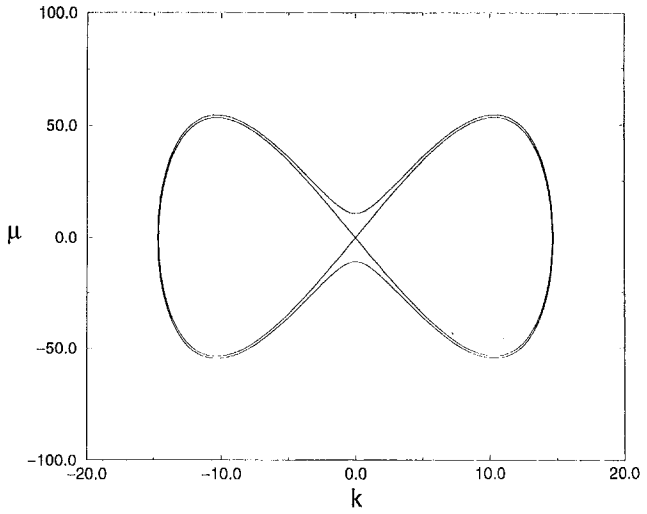

Fig. 2 Phase plane for unperturbed planar solution ($f_0 = 54.631$, $m_0 = 0$)

Substitution of the curvature and its derivative into the Hamiltonian energy function yields the following relationship:

$$E = \int_0^1 \left(\frac{\mu^2}{2} + \frac{\kappa^4}{8} - \alpha \frac{\kappa^2}{2} \right) ds = 32m(1 - m)\mathbf{K}^4. \quad (22)$$

Note that $E = \mu^2(0)/2$. Consequently, solution stability can be determined by calculation of extreme values in the $\mu(0)$-f_0 parameter plane. Furthermore, as f_0 increases monotonically with m, we differentiate $\mu(0)$ with respect to m (cf. Lawden, 1989 for $d\mathbf{K}/dm$) and determine that $\mu(0)$ achieves a maxima for the following criterion:

$$\frac{d\mu(0)}{dm} = \frac{8\mathbf{K}}{\sqrt{1 - m}} (2\mathbf{E} - \mathbf{K}) = 0 \quad (23)$$

Solving $\mathbf{E}(m^*)/\mathbf{K}(m^*) = 2$ for m^* results in $m^* \approx 0.82611$, which provides an upper bound for the system energy corresponding to a critical thrust value $f_0^* = 4\mathbf{K}^2(m^*) \approx 21.549$. This result coincides with the stability findings obtained using variational (Maddocks, 1984) and numerical (Lu and Perkins, 1994) methods and describes a configuration where the two ends of the cable meet; that is $d = 0$, where d denotes the separation of the ends as depicted in Fig. 1.

3.2 Limiting Spatial Form ($\tau = \bar{h}/2$). The solution of (15) with α from (17) for $\mu(0) = \mu(1) = 0$ is found in terms of the following Jacobi elliptic function:

$$\kappa(s) = \kappa_0 nd(2\mathbf{K}s), \quad \kappa_0 = 4\sqrt{1 - m}\mathbf{K}. \quad (24)$$

As before, the derivative of the curvature (μ), the internal axial force (p), and the geometric torsion (τ) can again be determined. The value of the parameter α and corresponding applied thrust f_0 and torque m_0 are determined by integrating $\kappa(s)$ from $\kappa(0) = \kappa_0$ to $\kappa(\frac{1}{2}) = \kappa_m$ which yields

$$\alpha = 4(2 - m)\mathbf{K}^2, \quad f_0 = 8\sqrt{m}\mathbf{K}^2, \quad m_0 = 4\mathbf{K}. \quad (25)$$

The equilibrium problem (15) can again be solved as an initial value problem with $\kappa(0) = \kappa_0$ and $\mu(0) = 0$. This solution coincides with the stability limit for periodic spatial forms found by Lu and Perkins (1994). The stability limit describes spatial forms for which the tangent at the midspan is orthogonal to the loading axis; i.e., $c_d = (\hat{l}_1 \cdot \hat{e}_1)_{1/2} = \cos \psi(\frac{1}{2}) \cos \theta(\frac{1}{2}) = 0$. Moreover, this stability limit is asymptotic to $f_0 = m_0^2/2$. The phase plane of (15) with α (25) and initial conditions $\kappa(0) = \kappa_0$ and $\mu(0)$ is illustrated in Fig. 3. Note that the spatial solutions are bounded from above ($m \to 1$) by the homoclinic solution (separatrix) of (15).

The Euler angles for the spatial forms can not be determined explicitly but are determined implicitly as follows. Observe that the solution $\phi(s)$ to (7) (for $\tau = \bar{h}/2$) may be decomposed as

$$\phi(s) = \phi_L(s) + \phi_N(s), \quad \phi_L(s) = -\frac{\bar{h}}{2} s + B \quad (26)$$

with

$$\phi_N'(s) = \kappa \cos \phi \tan \theta. \quad (27)$$

Consequently, $\theta(s)$ and $\psi(s)$ are obtained as functions of κ and ϕ_N':

$$\theta(s) = \tan^{-1} \left(\frac{\phi_N'}{\kappa \cos \phi} \right) \quad (28)$$

and

$$\psi(s) = -\int_0^s \sqrt{(\kappa \cos \phi)^2 + (\phi_N')^2} ds. \quad (29)$$

The arbitrary constant B in (26) can then be determined using the condition $c_d = \cos \psi(\frac{1}{2}) \cos \theta(\frac{1}{2}) = 0$. In order to determine ϕ_N', we differentiate θ from (28) and equate the resulting expression with the second Euler angle Eq. (7), namely $\theta' = -\kappa \sin \phi$. The result is the nonlinear second-order differential equation for ϕ_N':

$$\phi_N'' + (2 \tan \phi)(\phi_N')^2 - \left(\frac{\bar{h}}{2} \tan \phi + \frac{\mu}{\kappa} \right) \phi_N' + \kappa^2 \sin \phi \cos \phi = 0 \quad (30)$$

where $\bar{h} = 4\sqrt{m}\mathbf{K}$ and $\phi = \phi_L + \phi_N$ with ϕ_L given by (26).

As with the planar limit, substitution of the curvature and its derivative into the Hamiltonian energy function yields the following relationship:

$$E = 32(1 - m)\mathbf{K}^4. \quad (31)$$

Consequently, solution stability can be determined by differentiation of E with respect to m:

$$\frac{dE}{dm} = \frac{64\mathbf{K}^3}{\sqrt{m}} [2\mathbf{E} - (2 - m)\mathbf{K}] = 0. \quad (32)$$

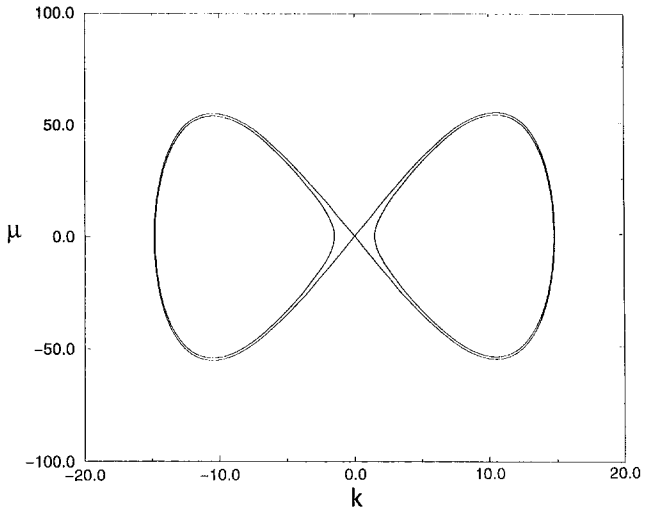

Fig. 3 Phase-plane for unperturbed spatial solution ($f_0 = 108.714$, $m_0 = 14.783$)

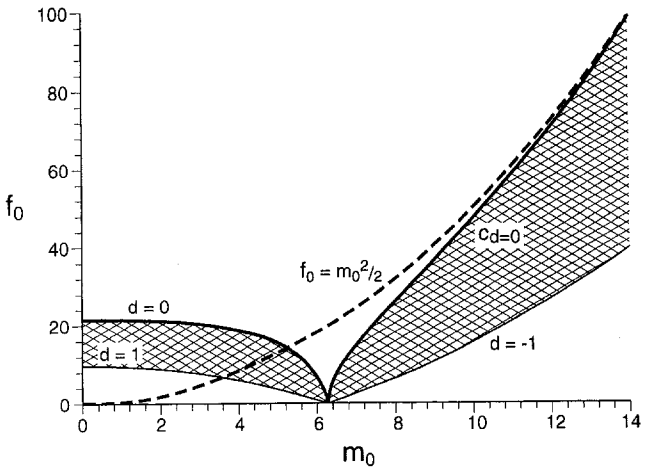

Fig. 4 Stability diagram for unperturbed periodic forms: $d = 1, -1$ solution by Greenhill (Timoshenko and Gere, 1961); $c_d = 0$ solution given by Eq. (25); asymptotic limit to $c_d = 0$ given by $f_0 = m_0^2/2$; shaded areas denote regions of stable periodic spatial forms

Solving $\mathbf{E}(m^*)/\mathbf{K}(m^*) + m^*/2 = 1$ for m^* reveals that a critical value for the energy is achieved only for $m^* = 0$ which corresponds to $f_0 = 0$ and $m_0 = 2\pi$ using (25). We summarize these results in the stability diagram of Fig. 4. Stable periodic spatial forms exist in the two regions that are shaded:

(i) one is the region for $m_0 > 2\pi$, bounded from above by the condition $c_d = 0$ and from below by the fundamental (linear) buckling condition $(d = -1)\, f_0 = (m_0/2)^{1/2} - \pi$ obtained by Greenhill (1883);

(ii) another is the region for $0 < m_0 < 2\pi$, bounded from above by the condition $d = 0$ (Lu and Perkins, 1994) and from below by the same fundamental buckling load ($d = 1$). Note that the region for stable periodic planar forms ($m_0 = 0$) is bounded by the condition $d = 0$ ($f_0 = 21.549$) and the Euler buckling load ($f_0 = \pi^2$).

3.3 A Limiting Homoclinic Solution. Solution of the spatial Hamiltonian Duffing Eq. (15) for an orbit including the saddle at the origin, results in the classical homoclinic orbit (cf. Guckenheimer and Holmes, 1983)

$$\kappa^0(s) = \pm 2\sqrt{\alpha}\ \mathrm{sech}\,[\sqrt{\alpha}(s - s_0)]$$

$$\mu^0(s) = \mp 2\alpha\ \mathrm{sech}\,[\sqrt{\alpha}(s - s_0)]\ \tanh\,[\sqrt{\alpha}(s - s_0)] \quad (33)$$

where α is given by (16) and (17) for the planar and limiting spatial ($\tau = \bar{h}/2$) forms, respectively. We note that this solution is valid for the integrable boundary value problem on an infinite domain; that is for $-\infty < s < \infty$ and describes a saddle orbit originating from and returning to the origin in the μ-κ plane. This homoclinic solution serves as both (i) a lower bound for the periodic solution (18) obtained for the planar forms (Fig. 2), and (ii) an upper bound for the periodic solution (24) obtained for the limiting spatial form (Fig. 3).

4 Global Bifurcation of the Perturbed System

Having established an integrable structure for the unperturbed system, we now integrate the spatial system (5) including the steady field loading terms $\gamma g_i(s)$. This is achieved by

(i) integration of $p' = -\kappa\kappa' + \gamma g_1(s)$ to yield $p = -\kappa^2/2 + \gamma G_1(s) + d_1$ where $G_1(s) = \int g_1(s)ds$ and $d_1 = p(0) + \kappa^2(0)/2 - \gamma G_1(0)$;

(ii) multiplying $\kappa\tau' = \kappa'(\bar{h} - 2\tau) - \gamma g_3(s)$ by κ and integrating to yield $\tau = \bar{h}/2 - \gamma G_3(s)/\kappa^2 + d_2/\kappa^2$ where $G_3(s) = \int \kappa(s) g_3(s) ds$ and $d_2 = \kappa^2(0)[\tau(0) - \bar{h}/2] + \gamma G_3(0)$; and

(iii) substituting p and τ into $\kappa'' = (p + \tau^2 - \bar{h}\tau)\kappa - \gamma g_2(s)$.

These steps lead to the following parametrically and externally forced differential equation:

$$\kappa' = \mu$$

$$\mu' = -R(\kappa) + \gamma F_1(\kappa, s) + \gamma^2 F_2(\kappa, s) \quad (34)$$

where

$$R = \frac{\kappa^3}{2} - \alpha\kappa - \frac{\beta}{\kappa^3}$$

$$F_1 = [G_1(s) - G_1(0)]\kappa - g_2(s) - 2\sqrt{\beta}\,\frac{[G_3(s) - G_3(0)]}{\kappa^3}$$

$$F_2 = \frac{[G_3(s) - G_3(0)]^2}{\kappa^3} \quad (35)$$

with $g_i(s)$ given by (6) and with

$$G_1(s) = \int g_1(s)ds, \quad G_3(s) = \int \kappa(s) g_3(s) ds. \quad (36)$$

Next, we consider the case of weak field loading ($\gamma \ll 1$) and neglect the second-order term ($\gamma^2 F_2$) in (34). Furthermore, we cast the spatial system as a perturbation of the two limiting cases evaluated in the Section 3. Thus, the (nonintegrable) spatial structure of the perturbed boundary value problem is governed by a nonlinear nonautonomous Hamiltonian system

$$\kappa' = \mu = \frac{\partial H_0}{\partial \mu}$$

$$\mu' = -\left(\frac{\kappa^3}{2} - \alpha\kappa\right) + \gamma\left[F_1(\kappa, s) + \frac{\bar{\beta}}{\kappa^3}\right]$$

$$= -\frac{\partial H_0}{\partial \kappa} - \gamma\frac{\partial H_1}{\partial \kappa} \quad (37)$$

where $\beta = \gamma\bar{\beta} \ll 1$, and

$$H_0(\kappa, \mu) = \frac{\mu^2}{2} + \frac{\kappa^4}{8} - \alpha\frac{\kappa^2}{2} \quad (38)$$

$$H_1(\kappa, s) = [G_1(0) - G_1(s)]\frac{\kappa^2}{2} + g_2(s)\kappa + \frac{\bar{\beta} + 2\sqrt{\beta}[G_3(0) - G_3(s)]}{2\kappa^2}. \quad (39)$$

The spatial system (37) consists of a (spatially dependent) Hamiltonian perturbation ($\gamma[F_1(\kappa, s) + \bar{\beta}/\kappa^3]$) of the (spatially independent) Hamiltonian ($\kappa^3/2 - \alpha\kappa$) which has a homoclinic orbit to a hyperbolic saddle (see Section 3.3). We investigate the boundary value problem where weak field loading ($\gamma \ll 1$) may break the global unperturbed bifurcation structure. We formulate the Melnikov function for the system via integration of the Poisson bracket $\{H_0, H_1\}$ utilizing the unperturbed homoclinic orbit of Section 3 (cf. Guckenheimer and Holmes, 1986).

$$M(s_0) = \int_{-\infty}^{\infty} \{H_0, H_1\} ds$$

$$= \int_{-\infty}^{\infty} \mu^0(x)\left[F_1(\kappa^0(x); x + s_0) + \frac{\bar{\beta}}{(\kappa^0(x))^3}\right] dx \quad (40)$$

where $x = (s - s_0)$ and (κ^0, μ^0) denote the homoclinic solution (33). Simple zeros of $M(s_0)$ imply transverse intersections of the separatrix manifolds leading to spatially complex solutions of the boundary value problem for boundary conditions near the unperturbed separatrix.

In order to obtain an analytic formulation for the weak perturbation, we estimate the forcing terms (F_1) for the two limiting cases evaluated in Section 3. In the following we consider: (i) planar perturbations of the planar solution (eg., $m_0 = 0$); (ii) spatial perturbations of the planar solution (eg., m_0 small); and (iii) spatial perturbations of the limiting spatial solution $(\tau = \bar{h}/2)$ (eg., perturbations from the stability limit $c_d = 0$).

4.1 Planar Perturbation of Planar Solutions. In this case consider planar perturbations of the planar solutions near the separatrix. Recall that for the unperturbed planar system, $\theta(s) = 0$ and $\phi(s) = \pi$. Consequently, $G_3(s) = 0$ and the perturbation $(F_1(\kappa, s))$ reduces to

$$F_1 = [G_1(s) - G_1(0)]\kappa - g_2(s);$$

$$G_1 = -\int \sin \psi(s) ds, \quad g_2 = \cos \psi(s). \quad (41)$$

Substitution of $\psi(s)$ from (21) yields

$$G_1 = -\frac{\sqrt{m}}{\mathbf{K}} cn[\mathbf{K}(1 - 2s)],$$

$$g_2 = 2dn^2[\mathbf{K}(1 - 2s)] - 1 \quad (42)$$

The Melnikov function can then be determined by substitution of (41) and (42) into (40).

$$M(s_0) = -\int_{-\infty}^{+\infty} \mu^0(x)\left[\frac{\sqrt{m}}{\mathbf{K}} \kappa^0(x) cn(\delta - 2\mathbf{K}x) + 2mcn^2(\delta - 2\mathbf{K}x) + (1 - 2m)\right] dx \quad (43)$$

where $\delta = \mathbf{K}(1 - 2s_0)$ and (κ^0, μ^0) are given by (33). The Jacobi elliptic functions in the integrand can be approximated by a series representation in terms of the nome $(q = \exp[-\pi\mathbf{K}'/\mathbf{K}])$ and the argument (πx) (Abramowitz and Stegun, 1972). The integrals of the first two terms can then be evaluated using the method of residues and the integral of the third term vanishes as μ^0 is odd. The resulting Melnikov function

$$M(s_0) = Q_n \sin\left[\frac{\pi}{2}(1 - 2s_0)\right] \quad (44)$$

is obtained where Q_n is an infinite series (see Appendix B for details). Hence, $M(s_0)$ has simple zeros implying that perturbation of a planar solution with boundary conditions near the separatrix (33) results in transverse intersections for a sufficiently small gravity field perturbation.

4.2 Spatial Perturbation of a Planar Solution. We consider next spatial perturbations of planar solutions for small torque ($\beta \ll 1$ for m_0 small). The planar solution enables estimation of the forcing $F_1(\kappa, s)$ that is identical in form to that of Section 4.1 with the value of α given by (16). However, as we allow deviation from the plane, the perturbation (37) consists of $\gamma[F_1(\kappa, s) + \bar{\beta}/\kappa^3]$. Thus,

$$M(s_0) = \int_{-\infty}^{\infty} \mu^0(x)\left[F_1(\kappa^0(x); x + s_0) + \frac{\bar{\beta}}{(\kappa^0(x))^3}\right] dx \quad (45)$$

where the integrals of the first three terms are identical to those of (43). Moreover, the integral of the fourth term vanishes (integrand is odd). Consequently, the result (44) remains valid for three-dimensional perturbations from the plane for small m_0.

4.3 Spatial Perturbation of a Limiting Spatial Solution $(\tau = \bar{h}/2)$. This last case considers perturbations of the limiting spatial solutions $(\tau = \bar{h}/2)$ near the separatrix (33) with α given by (17). To this end, we require the Euler angles for the unperturbed problem which, as discussed in Section 3.2, cannot be determined explicitly; refer to (26)–(30). Thus, we resort to approximations of $\phi(s)$ (which is antisymmetric about $s = \frac{1}{2}$). A candidate form is $\phi(s) = \phi_L + \phi_N = B - (\bar{h}/2)s - \tan^{-1}(J(2\mathbf{K}s))$ where $(\bar{h}/2) = 2\mathbf{K}\sqrt{m}$ and J is a combination of elliptic functions. This approximation enables estimation of the remaining Euler angles $\theta(s)$ and $\psi(s)$ (which are symmetric and antisymmetric about $s = \frac{1}{2}$, respectively) from (28) and (29). Substitution of the angles into the forcing components (6) and subsequently into the perturbation (35) and (36) yields the Melnikov function

$$M(s_0) = \int_{-\infty}^{+\infty} \mu^0(x)\left\{[\hat{G}_1(x; \delta) - \hat{G}_{10}]\kappa^0(x) - \hat{g}_2(x; \delta) - \frac{2\sqrt{\beta}[\hat{G}_3(x; \delta) - \hat{G}_{30}]}{(\kappa^0(x))^3} + \frac{\bar{\beta}}{(\kappa^0(x))^3}\right\} dx \quad (46)$$

where $\hat{G}_{1,3}(x, \delta)$, $\hat{g}_2(x, \delta)$ can be approximated by a series representation and $\delta = (2Ks_0)$. The integrals of the first, third, and fourth terms can be evaluated using the method of residues whereas the integrals of the second, fifth and sixth terms vanish as $\hat{G}_{10,30}$ are constants and μ^0 is odd. We verify that the result (44) remains valid by numerical simulation. Here, as in the previous cases, $M(s_0)$ has simple zeros implying that the perturbation of the limiting spatial solution $(\tau = \bar{h}/2)$ with boundary conditions near the separatrix, results in transverse intersections for sufficiently small gravity perturbation.

5 Numerical Results

Numerical results are presented to highlight the major conclusions of Section 4. These results are obtained by numerical approximation of the spatial system (5)–(7) and the planar system (9) when subject to weak field gravity loading. The initial conditions $(s = 0)$ remain close to those of the limiting unperturbed problems of Section 3 and are chosen so that the numerical solution satisfies the symmetric end conditions $(s = 1)$ required for this boundary value problem. Integration of the spatial system is achieved via a sixth-order Runge-Kutta method where an adaptive step size is determined (to accuracy imposed for the end conditions) by simultaneous solution of the unperturbed system and monitoring its (constant) Hamiltonian function. In order to discern whether a solution is periodic or aperiodic (e.g., quasi-periodic or a stochastic layer), the simulation is continued in space enabling construction of a Poincaré section (sampled at $s = 1$). Results are depicted in the (μ, κ) plane where a finite set of points on the perturbed phase plane defines a periodic solution and an infinite set of points defining a closed curve represents a quasi-periodic solution. The emergence of a stochastic (or resonance) layer occurs for boundary conditions near the unperturbed separatrix as the strength of the perturbation (γ) increases (cf. Lichtenberg and Liberman, 1992).

5.1 Planar Perturbation of Planar Forms. Figure 5 illustrates the evolution of a perturbed planar solution confined to the plane (for example, $f_0 = 143.6$) from a quasi-periodic solution for $\gamma = 0.01$ (Fig. 5(*a*)), to a confined stochastic layer for $\gamma = 0.1$ (Fig. 5(*b*)) and to a fully developed layer for $\gamma = 1$ (Fig. 5(*c*)). Note that the Poincaré points of the stochastic layer are immediately outside the unperturbed separatrix which remains as a lower bound for determining planar solutions in keeping with the analysis of Section 3.

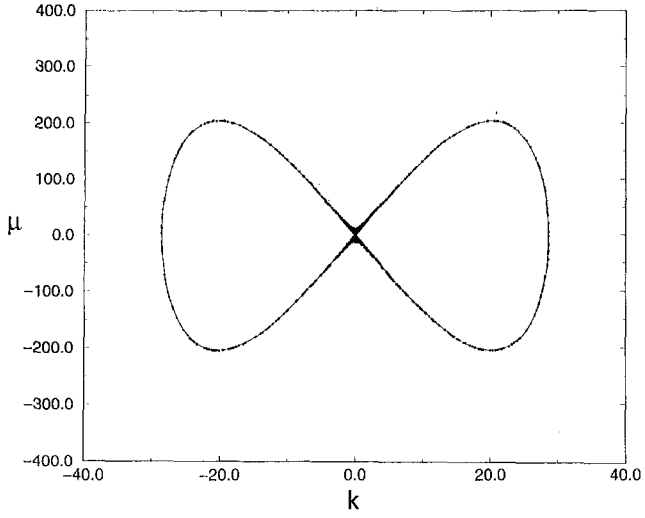

Fig. 5(*a*)

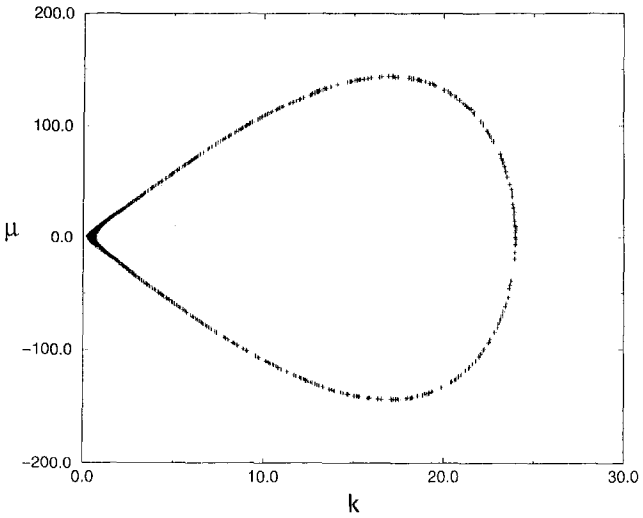

Fig. 6(*a*)

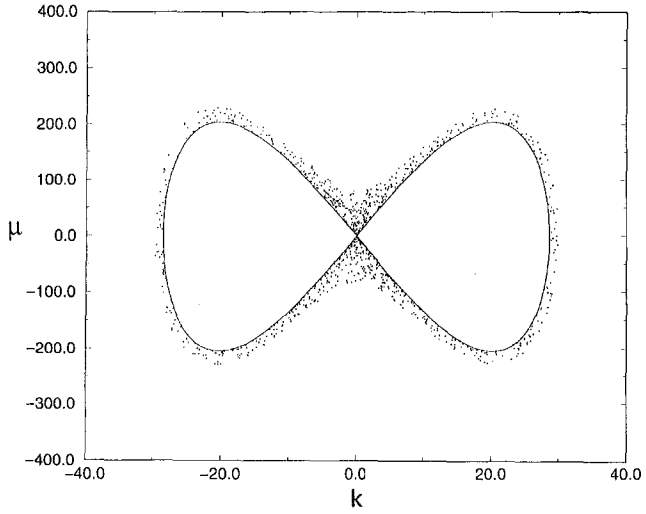

Fig. 5(*b*)

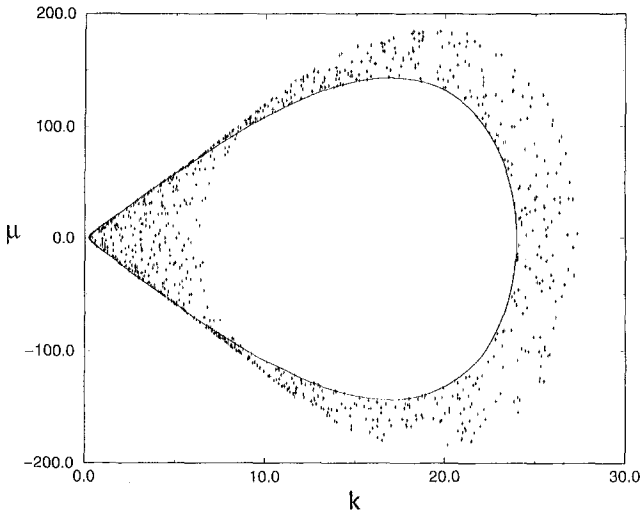

Fig. 6(*b*)

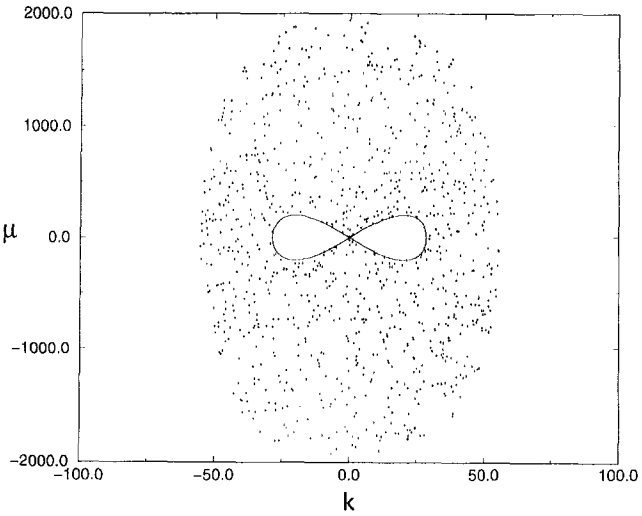

Fig. 5(*c*)

Fig. 5 Poincaré maps (γ = 0.01, 0.1, 1) for perturbed planar forms (f_0 = 143.596, m_0 = 0)

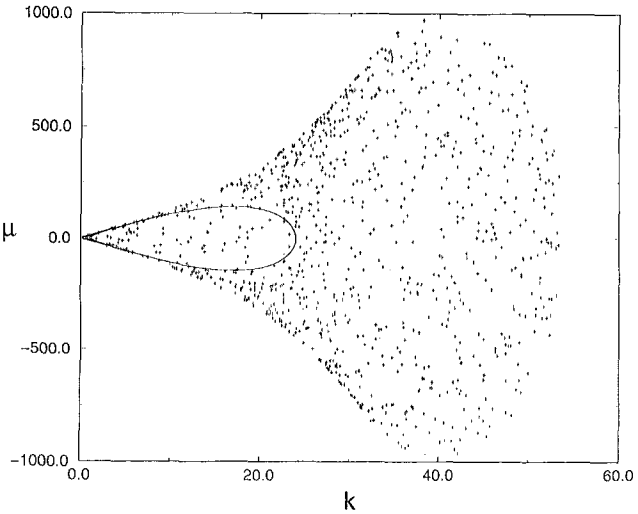

Fig. 6(*c*)

Fig. 6 Poincaré maps (γ = 0.01, 0.1, 1) for perturbed spatial forms (f_0 = 287.18, m_0 = 23

5.2 Spatial Perturbation of a Limiting Spatial Form. Figure 6 depicts the evolution of a perturbed spatial solution with modified boundary conditions near the limiting case of $\tau = \bar{h}/2$ (for example, $f_0 = 287.18$, $m_0 = 23.97$). As in the planar case, a quasi-periodic solution for $\gamma = 0.01$ evolves to a fully developed layer for $\gamma = 1$. Note that the Poincaré points of the stochastic

layer are not confined to the interior of the unperturbed separatrix defining the limiting spatial case ($\beta = 0$).

6 Closing Remarks

An equilibrium boundary-value problem for a nonlinear cable elastica with pure boundary loading and perturbed by steady field loading (gravity) is formulated as a spatial dynamical system with parameters defined by boundary conditions. Local and global bifurcation analyses of the boundary value problem, complemented by numerical solutions, are applied to investigate periodic solutions in the absence of field loading and spatially complex solutions in the presence of (small) field loading. Two limiting (homoclinic) solutions of the unperturbed (vanishing field loading) boundary value problem are found and identified: (i) a lower bound to periodic planar forms, and (ii) an upper bound to a periodic spatial form where the geometric torsion is proportional to half the internal torque. Perturbations of these limits via weak gravity field loading are performed via Melnikov's method to reveal the existence of transverse homoclinic intersections. Subsequent numerical solutions of the original boundary value problem illustrate spatially complex solution forms and the evolution of a stochastic layer. Thus, the emergence of spatial complexity in this boundary value problem arises from steady field loads in contrast to other generating mechanisms (e.g., initial imperfections, asymmetric cross sections, periodic boundary conditions) evaluated in Mielke and Holmes (1988), Davies and Moon (1993); and Champneys and Thompson (1996). We close by noting that sensitivity to (finite) boundary conditions implies difficulties in repetition of numerical (and experimental) results.

Acknowledgment

This work was supported in part by the Technion V.P.R. Fund and in part by the U.S. Office of Naval Research.

References

Abramowitz, M., and Stegun, I. A., 1972, *Handbook of Mathematical Functions,* Dover, New York.

Antman, S. S., 1972, "The Theory of Rods," *Handbuch der Physik,* VIa/2, Springer-Verlag, Berlin, pp. 641–703.

Antman, S. S., 1995, *Nonlinear Problems of Elasticity,* Springer-Verlag, New York.

Benham, C. J., 1987, "The role of stress resultant in determining mechanical equilibria of superhelical DNA," *Biopolymers,* Vol. 26, pp. 9–15.

Benham, C. J. 1989, "Onset of writhing in circular elastic polymers," *Physical Rev. A,* Vol. 39, pp. 2582–2586.

Bernitsas, M. M., 1982, "A three dimensional nonlinear large deflection model for dynamic behavior of risers, pipelines and cables," *J. Ship Res.,* Vol. 26, pp. 59–64.

Champneys, A. R., and Thompson, J. M. T., 1996, "A multiplicity of localized buckling modes for twisted rod equations," *Proc. R. Soc. Lond.,* Vol. A452, pp. 2467–2491.

Coleman, B. D., Dill, E. H., Lembo, M., Lu, Z., and Tobias, I., 1993, "On the dynamics of rods in the theory of Kirchhoff and Clebsch," *Arch. Rat. Mech. Anal.,* Vol. 121, pp. 339–359.

Coleman, B. D., Tobias, I., and Swigon, D., 1995, "Theory of the influence of end conditions on self-contact in DNA loops," *J. Chem. Phys.,* Vol. 103, pp. 9101–9109.

Coyne, J., 1990, "Analysis of the formation and elimination of loops in twisted cables," *IEEE J. Oceanic Eng.,* Vol. 15, pp. 72–83.

Davies, M. A., and Moon, F. C., 1993, "3D spatial chaos in the elastica and the spinning top: Kirchhoff Analog," *Chaos,* Vol. 3, pp. 93–99.

El Naschie, M. S., and Kapitaniak, T., 1990, "Soliton models for mechanical and biological elastic chains," *Phys. Lett. A,* Vol. 147, pp. 275–281.

Green, A. E., Laws, N., and Naghdi, P. M., 1967, "A linear theory of straight elastic rods," *Arch. Rat. Mech. Anal.,* Vol. 25, pp. 285–298.

Green, A. E., and Naghdi, P. M., 1970, "Non-isothermal theory of rods, plates and shells," *Int. J. Solids and Structures,* Vol. 6, pp. 209–244.

Greenwood, D. T., 1988, *Principles of Dynamics,* Prentice-Hall, Englewood Cliffs, NJ.

Guckenheimer, J., and Holmes, P. J., 1983, *Nonlinear Oscillations, Dynamical Systems and Bifurcations of Vector Fields,* Springer-Verlag, New York.

Ioos, G., and Joseph, D. D., 1980, *Elementary Stability and Bifurcation Theory,* Springer-Verlag, New York.

Lawden, D. F., 1989, *Elliptic Functions and Applications,* Springer-Verlag, New York.

Lichtenberg, A. J., and Liberman, M. A., 1992, *Regular and Chaotic Dynamics,* Springer-Verlag, New York.

Liu, F. C., 1975, "Kink formation and rotational response of single and multistrand electromechanical cables," Technical Note N-1403, Civil Engineering Laboratory, Naval Construction Battalion Center, Port Hueneme, CA.

Love, A. E. H., 1944, *A Treatise on the Mathematical Theory of Elasticity,* 4th Ed., Dover, New York.

Lu, C.-L., and Perkins, N. C., 1994, "Nonlinear Spatial Equilibria and Stability of Cable Under Uni-Axial Torque and Thrust," ASME JOURNAL OF APPLIED MECHANICS, Vol. 61, pp. 879–886.

Lu, C.-L., and Perkins, N. C., 1995, "Complex spatial equilibria of U-joint supported cables under torque, thrust and self-weight," *Int. J. Nonlinear Mech.,* Vol. 49, pp. 584–588.

Maddocks, J. H., 1984, "Stability of nonlinearly elastic rods," *Arch. Rat. Mech. Anal.,* Vol. 85, pp. 311–354.

Mielke, A., and Holmes, P. J., 1988, "Spatially complex equilibria of buckled rods," *Arch. Rat. Mech. Anal.,* Vol. 101, pp. 319–348.

Rosenthal, F., 1976, "The Application of Greenhill's Formulae to Cable Hockling," ASME JOURNAL OF APPLIED MECHANICS, Vol. 43, pp. 681–683.

Rubin, M. B., 1997, "An intrinsic formulation nonlinear elastic rods," *Int. J. Solids Structures,* Vol. 34, pp. 4191–4212.

Tan, Z., and Witz, J. A., 1993, "On the Flexural-Torsional Behavior of a Straight Elastic Beam Subject to Thermal Moments," ASME JOURNAL OF APPLIED MECHANICS, Vol. 60, pp. 498–505.

Timoshenko, S. P., and Gere, J. M., 1961, *Theory of Elastic Stability,* 2nd Ed., McGraw-Hill, New York, pp. 76.

Thompson, J. M. T., and Champneys, A. R., 1996, "From helix to localized writhing in torsional post-buckling of elastic rods," *Proc. R. Soc. Lond.,* A Vol. A452, pp. 117–138.

Thompson, J. M. T., and Virgin, L., 1988, "Spatial chaos and localization phenomena in nonlinear elasticity," *Phys. Lett. A,* Vol. 126, pp. 491–496.

Tobias, I., Coleman, B. D., and Olson, W. K., 1994, "The dependence of DNA tertiary structure on end-conditions: Theory and implications for topological transitions," *J. Chem. Phys.,* Vol. 101, pp. 10,990–10,996.

Welch, S. M., and Tulin, M. P., 1995, "Analysis of laboratory cable deployment experiments for payout rates in the vicinity of the buckling rate," *Proc. Int. Symp. Cable Dynamics,* Liege, Belgium, pp. 331–342.

Wiggins, S., 1990, *Introduction to Applied Nonlinear Dynamical Systems and Chaos,* Springer-Verlag, New York.

Woo, S. L.-Y., and Buckwalter, J. A., eds., 1988, "Symposium on Injury and repair of the musculoskeletal soft tissues," American Academy of Orthopaedic Surgeons, Savannah, GA.

Yabuta, T., 1984, "Submarine cable kink analysis," *Bull. JSME,* Vol. 29, pp. 1821–1828.

Yabuta, T., Yoshizaawa, N., and Kojima, N., 1982, "Cable Kink Analysis: Cable Loop Stability Under Tension," ASME JOURNAL OF APPLIED MECHANICS, Vol. 49, pp. 584–588.

Zajac, E. E., 1962, "Stability of Two Planar Loop Elasticas," ASME JOURNAL OF APPLIED MECHANICS, Vol. 29, pp. 136–142.

APPENDIX A

Nondimensional Parameters

The following nondimensional parameters are used (Lu and Perkins, 1994): $s = S/L$, $d = D/L$, $\mathbf{q} = \mathbf{Q}L^3/EI$, $f_0 = F_0L^2/EI$, $m_0 = M_0L/EI$, $p = F'L^2/EI$, $h = M_1L/EI$, $\kappa = K'L$, $\tau = \Gamma'L$.

APPENDIX B

Evaluation of Melnikov Integrals

Evaluation of the Melnikov function for a planar perturbation of the planar solution (43) is achieved via the method of residues with use of a series representation of the Jacobi elliptic function (Abramowitz and Stegun 1972): $cn(u|m) = (2\pi/m^{1/2}\mathbf{K}) \sum A_n \cos [(2n + 1)\pi u/2\mathbf{K}]$; $n = 0, \ldots, \infty$. The integral of the first term in (43) is

$$I_1 = \int_{-\infty}^{+\infty} \frac{\sqrt{m}}{\mathbf{K}} \mu^0(x)\kappa^0(x)cn(\delta - 2\mathbf{K}x)dx$$

$$= \frac{-8\alpha\pi}{\mathbf{K}^2} \sum_{n=0}^{\infty} A_n \sin(\phi_{1n})$$

$$\times \int_{-\infty}^{+\infty} \operatorname{sech}^2(\eta) \tanh(\eta) \sin(\Omega_{1n}\eta)d\eta$$

$$= \frac{-4\pi^4}{\mathbf{K}^2} \sum_{n=0}^{\infty} (2n + 1)^2 A_n \operatorname{csch}\left[\frac{(2n + 1)\pi^2}{2\sqrt{\alpha}}\right] \sin(\phi_{1n}) \tag{B1}$$

where

$$A_n = \frac{q^{n+1/2}}{1+q^{2n+1}}, \quad q = \exp\left(-\pi \frac{\mathbf{K}'}{\mathbf{K}}\right),$$

$$\phi_{1n} = \frac{\pi}{2}(2n+1)(1-2s_0), \quad \Omega_{1n} = \frac{\pi}{\sqrt{\alpha}}(2n+1). \quad \text{(B2)}$$

The integral of the second term in (43) is

$$I_2 = \int_{-\infty}^{\infty} 2m\mu^0(x)cn^2(\delta - 2\mathbf{K}x)dx$$

$$= \frac{-16\alpha\pi^2}{\mathbf{K}^2} \sum_{n=0}^{\infty} A_n \sum_{l=0}^{\infty} A_l \int_{-\infty}^{\infty} \text{sech}\,(\sqrt{\alpha}x)\,\tanh\,(\sqrt{\alpha}x)$$

$$\times \cos\,[\phi_{2n} - (2n+1)\pi x]\cos\,[\phi_{2l} - (2l+1)\pi x]dx$$

$$= \frac{-16\pi^4}{\mathbf{K}^2} \sum_{n=0}^{\infty} A_n \sum_{l=0}^{\infty} A_l \Bigg\{ (n-l)$$

$$\times \text{sech}\left[\frac{(n-l)\pi^2}{\sqrt{\alpha}}\right] \sin\,(\Phi_{21})$$

$$+ (n+l-1)\,\text{sech}\left[\frac{(n+l-1)\pi^2}{\sqrt{\alpha}}\right] \sin\,(\Phi_{22})\Bigg\} \quad \text{(B3)}$$

where

$$\Phi_{21} = \pi(n-l)(1-2s_0),$$
$$\Phi_{22} = \pi(n+l-1)(1-2s_0). \quad \text{(B4)}$$

Consequently, as the third integral vanishes, the Melnikov function becomes

$$M(s_0) = Q_n \sin\left[\frac{\pi}{2}(1-2s_0)\right]$$
$$= \left[\frac{4\pi^4}{\mathbf{K}^2}(R_n + S_n)\right] \sin\left[\frac{\pi}{2}(1-2s_0)\right] \quad \text{(B5)}$$

where

$$R_n = \sum_{n=0}^{\infty} (2n+1)^2 A_n\,\text{csch}\left(\frac{N_1\pi^2}{2\sqrt{\alpha}}\right) F_1(N_1)$$

$$S_n = 4\sum_{n=0}^{\infty} A_n \sum_{l=0}^{\infty} A_l \Bigg[\frac{N_2}{2}\,\text{sech}\left(\frac{N_2\pi^2}{2\sqrt{\alpha}}\right) F_2(N_2)$$
$$+ \frac{N_3}{2}\,\text{sech}\left(\frac{N_2\pi^2}{2\sqrt{\alpha}}\right) F_3(N_3)\Bigg] \quad \text{(B6)}$$

and

$$F_j(N_j) = (2\cos\omega)^{N_j-1} - \binom{N_j-2}{1}(2\cos\omega)^{N_j-3}$$
$$+ \binom{N_j-3}{2}(2\cos\omega)^{N_j-5} + \ldots$$

$$\omega = \frac{\pi}{2}(1-2s_0), \quad N_1 = 2n+1,$$
$$N_2 = 2(n-l), \quad N_3 = 2(n+l-1). \quad \text{(B7)}$$

Buckling of an Elastic Ring Forced by a Periodic Array of Compressive Loads

A. F. Vakakis
Associate Professor,
Department of Mechanical and Industrial Engineering,
University of Illinois at Urbana-Champaign,
Urbana, IL 61801
Mem. ASME

T. M. Atanackovic
Professor,
University of Novi Sad,
Novi Sad, Yugoslavia

We use an analytical technique based on nonsmooth coordinate transformations to study discreteness effects in the post-buckling state of a circular ring loaded by a periodic array of compressive point loads. The method relies on eliminating singularities due to the point loads in the governing equations, at the expense of increasing the dimensionality of the problem. As a result, the original nonsmooth governing equations are transformed to a larger set of equations with no singularities, together with a set of "smoothening" boundary conditions. The transformed equations are solved by expressing the variables in regular perturbation expansions, and studying an hierarchy of boundary value problems at successive orders of approximation; these problems can be asymptotically solved using techniques from the theory of smooth nonlinear or parametrically varying dynamical systems. As a result, we model analytically discreteness effects in the post-buckling states of the ring, and estimate the effect of the discrete load distribution on the critical buckling loads. This effect is found to be of very low order, in agreement with numerical results reported in an earlier work.

1 Introduction

We analytically study the buckling of a circular ring that is loaded by a discrete periodic array of concentrated compressive forces. The singularities due to the discrete loads in the governing equations are eliminated by a nonsmooth change of variables, at the expense of increasing the dimensionality of the problem. The resulting transformed equations are free of singularities and can be analyzed using techniques from the theory of smooth nonlinear or parametrically varying dynamical systems. The method used in this work enables the *analytic* computation of discreteness effects in the post-buckling state of the ring due to the discrete array of compressive loads, as well as, the estimation of the effect on the critical buckling load of the discreteness of the load distribution.

The method of nonsmooth transformations employed herein was first developed by Pilipchuk (1985, 1988), and subsequently used by Pilipchuk and co-workers to analyze strongly nonlinear subharmonic motions of a forced pendulum (Pilipchuk et al., 1997), as well as discreteness effects in free periodic oscillations of a discretely nonlinearly supported string (Pilipchuk and Vakakis, 1998). Forced oscillations of this later system employing nonsmooth transformations were studied by Salenger and Vakakis (1998).

The problem of the stability of a circular ring under *uniform hydrostatic pressure* has been formulated and examined in numerous previous works; see, for example, (Seide and Albano, 1973) where the bifurcations of circular rings under concentrated loads are examined by employing transfer matrices and solving a linear eigenvalue problem, and (Kabanov and Astrakharchuk, 1983). In addition, we mention the recent works by Troger and Steindl (1991), Chaskalovic and Naili (1995) on rings obeying Bernulli-Euler theory, the works by Kämmel (1967) and Atanackovic (1998) on rings with constitutive laws accounting for axial compressibility, and the work by Schmidt (1979) on rings with shear deformation and axial compressibility. Fu and Waas (1995) studied the effect of ring thickness on the postbuckling behavior. A review of numerical methods for studying buckling in thin shells is given by Riks and Rankin (1997).

2 Governing Equations and Nonsmooth Transformations

Considering a circular ring with material obeying Bernulli-Euler beam theory and forced by a periodic array of N compressive loads, the normalized internal force, moment, displacement, and rotation distributions are governed by the following set of ordinary differential equations (Atanackovic, 1998):

$$\left.\begin{aligned} \dot{q}(t) &= -\frac{\tilde{\lambda}2\pi}{N}\sum_{k=0}^{N-1}\delta\left(2t-\frac{2\pi(2k+1)}{N}\right) \\ &\quad - n(t)[1+m(t)] \\ \dot{n}(t) &= q(t)[1+m(t)] \\ \dot{m}(t) &= -q(t) \end{aligned}\right\} \tag{1a}$$

$$\left.\begin{aligned} \dot{u}(t) &= \cos\vartheta(t) \\ \dot{v}(t) &= \sin\vartheta(t) \\ \dot{\vartheta}(t) &= 1+m(t) \end{aligned}\right\}. \tag{1b}$$

Complementing (1) there exist the following periodicity conditions:

$$q(0)=q(2\pi),\quad n(0)=n(2\pi),\quad m(0)=m(2\pi)$$
$$u(0)=u(2\pi),\quad v(0)=v(2\pi),\quad \vartheta(0)=\vartheta(2\pi)+2\pi. \tag{2}$$

In the equations above, $\delta(\cdot)$ represents Dirac's generalized function, and the normalized variables are defined as follows: $t=S/R$, where S denotes the arc-length of the undeformed ring axis, and R is the radius of the undeformed ring; $q=QR^2/EI$, where Q is the shear force, E the modulus of elasticity, and I

Contributed by the Applied Mechanics Division of THE AMERICAN SOCIETY OF MECHANICAL ENGINEERS for publication in the ASME JOURNAL OF APPLIED MECHANICS.

Discussion on the paper should be addressed to the Technical Editor, Professor Lewis T. Wheeler, Department of Mechanical Engineering, University of Houston, Houston, TX 77204-4792, and will be accepted until four months after final publication of the paper itself in the ASME JOURNAL OF APPLIED MECHANICS.

Manuscript received by the ASME Applied Mechanics Division, Apr. 28, 1998; final revision, Sept. 12, 1998. Associate Technical Editor: S. Kyriakides.

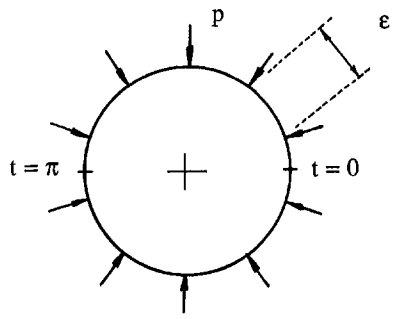

Fig. 1 The circular ring with discrete load distribution

the moment of inertia of the cross section of the ring; $n = NR^2/EI$, where N is the axial force; $m = MR/EI$, where M is the bending moment; $\tilde{\lambda} = [2p/(2\pi R/N)](R^3/EI) = NpR^2/(\pi EI)$, where p is the magnitude of each of the compressive loads; $u = x/R$ and $v = y/R$, where x and y are the horizontal and vertical deformations, respectively, of an arbitrary point of the deformed ring; and ϑ is the angle between the axial force N and the horizontal axis in the deformed ring. The discrete forcing distribution of the ring is depicted in Fig. 1, and the discrete array of loads are normally oriented to the ring.

The singularities in the first of Eqs. (1a) prevent a direct analytical treatment of the system. To circumvent this problem we assume at this point that the discrete forces are densely placed by requiring that the distance between adjacent forces is small:

$$\frac{2\pi}{N} = \epsilon \ll 1.$$

For ϵ sufficiently small, we anticipate that the solution of (1–2) possesses two spatial scales, a *long* scale t, and a *short* one t/ϵ. Hence the solution is expressed as, $w = w(t, t/\epsilon)$, where $w = q, n, m, u, v$ or ϑ. We now introduce the following nonsmooth transformations of the long scale as follows (cf. Fig. 2):

$$\tau(t/\epsilon) = \frac{1}{\pi}\arcsin\left[\sin\left(\frac{\pi t}{\epsilon}\right)\right],$$

$$e(t/\epsilon) = \operatorname{sgn}\left[\cos\left(\frac{\pi t}{\epsilon}\right)\right] = \tau'(t/\epsilon), \tag{3}$$

and express the dependent variables of the problem in the following way:

$$\begin{aligned} q(t, t/\epsilon) &= Q_1(t, \tau) + eQ_2(t, \tau) \\ n(t, t/\epsilon) &= N_1(t, \tau) + eN_2(t, \tau) \\ m(t, t/\epsilon) &= M_1(t, \tau) + eM_2(t, \tau) \\ u(t, t/\epsilon) &= U_1(t, \tau) + eU_2(t, \tau) \\ v(t, t/\epsilon) &= V_1(t, \tau) + eV_2(t, \tau) \\ \vartheta(t, t/\epsilon) &= \Theta_1(t, \tau) + e\Theta_2(t, \tau). \end{aligned} \tag{4}$$

Substituting (4) into (1–2), using the chain rule to express differentiation with respect to t in terms of the short and long variables, and eliminating singular terms by setting their coefficients equal to zero, we obtain an alternative system of governing equations *that does not contain any singular terms.*

To demonstrate this procedure, consider the first of relations (1a). Taking into account expressions (4), the first derivative of $q = q(t, t/\epsilon)$ is expressed as follows:

$$\frac{dq}{dt} = \frac{1}{\epsilon}\frac{\partial Q_1}{\partial \tau}e + \frac{\partial Q_1}{\partial t} + \frac{1}{\epsilon}Q_2\tau'' + \frac{1}{\epsilon}\frac{\partial Q_2}{\partial \tau} + \frac{\partial Q_2}{\partial t}e, \tag{5}$$

where the identity $(\tau')^2 = e^2 = 1$ was imposed. In the relation above the term τ'' is singular since it is a series of Dirac's functions,

$$\tau'' = -2\ \operatorname{sgn}(\tau)\sum_{k=-\infty}^{\infty}\delta\left(\frac{2t}{\epsilon} - 1 - 2k\right). \tag{6}$$

A comparison of (6) with the summation of the singular terms in (1a) reveals that these terms are identical in the domain of interest (cf. above definition of ϵ),

$$\sum_{k=0}^{N-1}\delta\left(2t - \frac{2\pi(2k+1)}{N}\right) = \frac{1}{\epsilon}\sum_{k=0}^{N-1}\delta\left(\frac{2t}{\epsilon} - 1 - 2k\right)$$

$$= \frac{1}{\epsilon}\sum_{k=-\infty}^{\infty}\delta\left(\frac{2t}{\epsilon} - 1 - 2k\right) \quad \text{for} \quad 0 \le t \le 2\pi,$$

and, hence, *the singularities in* (1a) *can be eliminated by canceling them with the corresponding terms in* (5). Indeed, substituting (4) and (5) into the first of Eqs. (1a), setting the coefficients of terms not depending and depending on e separately equal to zero, and eliminating the singular terms depending on τ'', we obtain the following set of equations:

$$\begin{aligned} \frac{\partial Q_1}{\partial \tau} &= -\epsilon\frac{\partial Q_2}{\partial t} - \epsilon[N_1M_2 + N_2(1 + M_1)], \\ Q_1(0, \tau) &= Q_1(2\pi, \tau) \\ \frac{\partial Q_2}{\partial \tau} &= -\epsilon\frac{\partial Q_1}{\partial t} - \epsilon[N_2M_2 + N_1(1 + M_1)], \\ Q_2(0, \tau) &= Q_2(2\pi, \tau) \\ Q_2|_{\tau=\pm1} &= \mp\epsilon\lambda, \end{aligned} \tag{7a}$$

where $\lambda = -\tilde{\lambda}/2$. The last relation in (7a) is the *smoothening condition* that eliminates singular terms from the equations; the terms in this relation are coefficients of τ'' in the transformed governing equation, and the requirement that they vanish at $\tau = \pm 1$ eliminates the singular effects due to τ'' which also appear

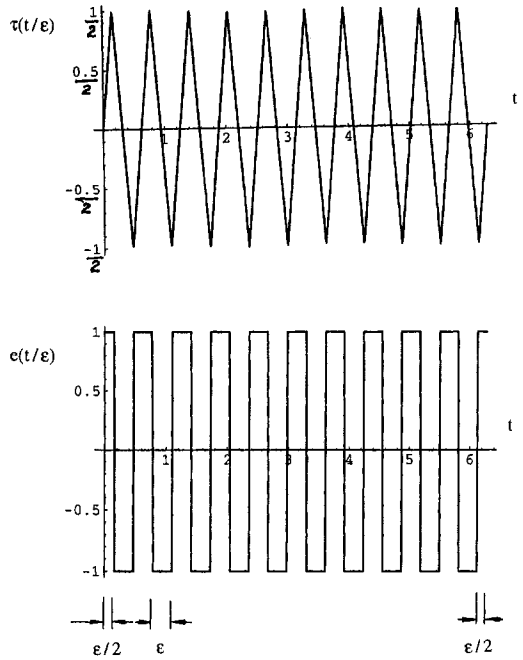

Fig. 2 The nonsmooth coordinate transformations $\tau(t/\epsilon)$ and $e(t/\epsilon)$

at these values of τ (cf. Eq. (3) and (6)). The justification for setting separately terms depending or not on e equal to zero, is that by replacing the scale t/ϵ by the two nonsmooth variables τ and e, quantities in the first of Eqs. ($1a$) that originally depended on t/ϵ are now partitioned into two independent components: One depending only on τ, and the other depending both on τ and e (Vakakis et al., 1996). As a result, there is a need to balance separately these two types of terms in the transformed equations of motion, a requirement that leads to the two Eqs. ($7a$). In essence, we "smoothen" the first of equations ($1a$) by replacing it with two smoothened equations; we also note that, whereas the first of Eqs. ($1a$) possesses *two* independent variables, t and t/ϵ, the transformed set ($7a$) possesses *three,* namely, t, τ, and e; hence, the appearance of partial derivatives in ($7a$). Finally, as pointed out by a reviewer of this work, the last smoothening condition in ($7a$) appears to impose symmetry restrictions on the variable Q_2. This, however, does not reflect to the physical buckling state which, as shown later, can be asymmetric.

Working similarly, we transform the rest of equations in (1–2) and obtain the following new expressions:

$$\frac{\partial N_1}{\partial \tau} = -\epsilon \frac{\partial N_2}{\partial t} - \epsilon[Q_1 M_2 + Q_2(1 + M_1)],$$

$$N_1(0, \tau) = N_1(2\pi, \tau)$$

$$\frac{\partial N_2}{\partial \tau} = -\epsilon \frac{\partial N_1}{\partial t} - \epsilon[Q_2 M_2 + Q_1(1 + M_1)],$$

$$N_2(0, \tau) = N_2(2\pi, \tau) \qquad (7b)$$

$$N_2|_{\tau=\pm 1} = 0$$

$$\frac{\partial M_1}{\partial \tau} = -\epsilon \frac{\partial M_2}{\partial t} - \epsilon Q_2, \quad M_1(0, \tau) = M_1(2\pi, \tau)$$

$$\frac{\partial M_2}{\partial \tau} = -\epsilon \frac{\partial M_1}{\partial t} - \epsilon Q_1, \quad M_2(0, \tau) = M_2(2\pi, \tau) \quad (7c)$$

$$M_2|_{\tau=\pm 1} = 0$$

$$\frac{\partial U_1}{\partial \tau} = -\epsilon \frac{\partial U_2}{\partial t} + \epsilon I_c, \quad U_1(0, \tau) = U_1(2\pi, \tau)$$

$$\frac{\partial U_2}{\partial \tau} = -\epsilon \frac{\partial U_1}{\partial t} + \epsilon R_c, \quad U_2(0, \tau) = U_2(2\pi, \tau) \quad (7d)$$

$$U_2|_{\tau=\pm 1} = 0$$

$$\frac{\partial V_1}{\partial \tau} = -\epsilon \frac{\partial V_2}{\partial t} + \epsilon I_s, \quad V_1(0, \tau) = V_1(2\pi, \tau)$$

$$\frac{\partial V_2}{\partial \tau} = -\epsilon \frac{\partial V_1}{\partial t} + \epsilon R_s, \quad V_2(0, \tau) = V_2(2\pi, \tau) \quad (7e)$$

$$V_2|_{\tau=\pm 1} = 0$$

$$\frac{\partial \Theta_1}{\partial \tau} = -\epsilon \frac{\partial \Theta_2}{\partial t} + \epsilon M_2, \quad \Theta_1(0, \tau) = \Theta_1(2\pi, \tau) + 2\pi$$

$$\frac{\partial \Theta_2}{\partial \tau} = -\epsilon \frac{\partial \Theta_1}{\partial t} + \epsilon(1 + M_1), \quad \Theta_2(0, \tau) = \Theta_2(2\pi, \tau) \quad (7g)$$

$$\Theta_2|_{\tau=\pm 1} = 0$$

where (Pilipchuk et al., 1997)

$$R_c = (1/2)[\cos(\Theta_1 + \Theta_2) + \cos(\Theta_1 - \Theta_2)],$$

$$I_c = (1/2)[\cos(\Theta_1 + \Theta_2) - \cos(\Theta_1 - \Theta_2)]$$

$$R_s = (1/2)[\sin(\Theta_1 + \Theta_2) + \sin(\Theta_1 - \Theta_2)],$$

$$I_s = (1/2)[\sin(\Theta_1 + \Theta_2) - \sin(\Theta_1 - \Theta_2)].$$

Comparing the sets (1–2) and ($7a$–g) we note that by *using the nonsmooth transformations* (3) *we were able to eliminate the singular terms from the governing equations.* The transformed (smoothened) problem consists of a set of smooth nonlinear boundary value problems (NLBVPs) in terms of the short variable τ, which can be studied using perturbation methods from the theory of smooth dynamical systems. At the same time, *the elimination of the singularities was at the expense of expanding the dimensionality of the problem,* with two new dependent variables replacing each of the old ones. Once the solutions of the transformed problems are derived, the solutions of the original problem are obtained using relations (4), and *discreteness effects arising due to the applied point loads are analytically incorporated in the final expressions.* In addition, we note that the solutions for problems ($7d$–g) can be derived by direct integrations once the solutions of problems ($7a$–c) are computed. Hence, in the following analysis we will focus mainly on the solution of the later problems; however, problem ($7g$) must be taken into consideration at certain stages of the following analysis in order to obtain compatibility conditions necessary for the solution.

Using ϵ as a perturbation parameter, we seek solutions of the problems ($7a$–c) and ($7g$) in the following regular perturbation expansions:

$$Q_{1,2}(t, \tau) = Q^{(0)}_{1,2}(t, \tau) + \epsilon Q^{(1)}_{1,2}(t, \tau) + \epsilon^2 Q^{(2)}_{1,2}(t, \tau) + \cdots$$

$$N_{1,2}(t, \tau) = N^{(0)}_{1,2}(t, \tau) + \epsilon N^{(1)}_{1,2}(t, \tau) + \epsilon^2 N^{(2)}_{1,2}(t, \tau) + \cdots$$

$$M_{1,2}(t, \tau) = M^{(0)}_{1,2}(t, \tau) + \epsilon M^{(1)}_{1,2}(t, \tau) + \epsilon^2 M^{(2)}_{1,2}(t, \tau) + \cdots$$

$$\Theta_{1,2}(t, \tau) = \Theta^{(0)}_{1,2}(t, \tau) + \epsilon \Theta^{(1)}_{1,2}(t, \tau) + \epsilon^2 \Theta^{(2)}_{1,2}(t, \tau) + \cdots$$

$$\lambda = \lambda_0 + \epsilon\lambda_1 + \epsilon^2\lambda_2 + \ldots. \qquad (8)$$

Substituting (8) into ($7a$–c) and matching the coefficients of equal powers of ϵ we obtain a series of subproblems governing each of the successive approximations of the solution. In what follows we discuss the leading-order subproblems separately.

$O(1)$ Subproblem. Considering terms of $O(\epsilon^0)$, we obtain the following leading-order approximations for the variables under consideration:

$$Q^{(0)}_1(t, \tau) = A_0(t), \quad A_0(0) = A_0(2\pi), \quad Q^{(0)}_2(t, \tau) = 0$$

$$N^{(0)}_1(t, \tau) = B_0(t), \quad B_0(0) = B_0(2\pi), \quad N^{(0)}_2(t, \tau) = 0$$

$$M^{(0)}_1(t, \tau) = C_0(t), \quad C_0(0) = C_0(2\pi), \quad M^{(0)}_2(t, \tau) = 0$$

$$\Theta^{(0)}_1(t, \tau) = \gamma_0(t), \ \gamma_0(0) = \gamma_0(2\pi) + 2\pi, \ \Theta^{(0)}_2(t, \tau) = 0. \qquad (9)$$

The t-dependent functions in (9) result as constants of integration with respect to τ, and are determined by considering higher-order subproblems. Moreover, at this order of approximation no information regarding the variable (nonlinear eigenvalue) λ is extracted.

$O(\epsilon)$ Subproblem. Solving the $O(\epsilon^1)$ subproblem we obtain

$$Q^{(1)}_1(t, \tau) = A_1(t), \quad A_1(0) = A_1(2\pi), \quad Q^{(1)}_2(t, \tau) = -\lambda_0\tau$$

$$N^{(1)}_1(t, \tau) = B_1(t), \quad B_1(0) = B_1(2\pi), \quad N^{(1)}_2(t, \tau) = 0$$

$$M^{(1)}_1(t, \tau) = C_1(t), \quad C_1(0) = C_1(2\pi), \quad M^{(1)}_2(t, \tau) = 0$$

$$\Theta^{(1)}_1(t, \tau) = \gamma_1(t), \ \gamma_1(0) = \gamma_1(2\pi), \ \Theta^{(1)}_2(t, \tau) = 0 \quad (10)$$

as well as the following expressions governing the yet undetermined coefficients of the previous order of approximation,

$$\dot{A}_0(t) = -B_0(t)[1 + C_0(t)] + \lambda_0$$

$$\dot{B}_0(t) = -A_0(t)[1 + C_0(t)]$$

$$\dot{C}_0(t) = -A_0(t)$$

$$\dot{\gamma}_0(t) = 1 + C_0(t), \tag{11}$$

with the periodicity conditions in (9) enforced. Note that the last of the above equations can be decoupled from the first three ones which constitute a NBVP with λ_0 as the eigenvalue. The solution of this problem is discussed in Section 3, but at this point we remark that the NLBVP (11) *governs the buckling problem with uniform (hydrostatic) forcing and no discreteness effects.* Indeed, (9) and (11) provide the $O(1)$ smooth approximation to the solution and nonsmooth discreteness effects start appearing only at higher orders (for example, see the expression for $Q_2^{(1)}(t, \tau)$ in (10)). These discreteness effects will be more evident in higher order approximations and will be manifested by the presence of the nonsmooth variables $\tau(t/\epsilon)$ and $e(t/\epsilon)$ in the solutions. In essence, problem (11) governs the dependence of the solution on the long variable t, whereas discreteness effects depend on the short spatial scale t/ϵ.

$O(\epsilon^2)$ Subproblem. Proceeding to the next order of the asymptotic analysis, we derive the expressions

$$Q_1^{(2)}(t, \tau) = A_2(t), \quad A_2(0) = A_2(2\pi), \quad Q_2^{(2)}(t, \tau) = -\lambda_1 \tau$$

$$N_1^{(2)}(t, \tau) = -\lambda_0[1 + C_0(t)]\frac{\tau^2}{2} + B_2(t),$$

$$B_2(0) = B_2(2\pi), \quad N_2^{(2)}(t, \tau) = 0$$

$$M_1^{(2)}(t, \tau) = \lambda_0 \frac{\tau^2}{2} + C_2(t),$$

$$C_2(0) = C_2(2\pi), \quad M_2^{(2)}(t, \tau) = 0$$

$$\Theta_1^{(2)}(t, \tau) = \gamma_2(t), \ \gamma_2(0) = \gamma_2(2\pi), \ \gamma_2^{(2)}(t, \tau) = 0 \tag{12}$$

and the complementary equations for the coefficients of the previous order of approximation:

$$\dot{A}_1(t) = -B_0(t)C_1(t) - B_1(t)[1 + C_0(t)] + \lambda_1$$

$$\dot{B}_1(t) = -A_0(t)C_1(t) + A_1(t)[1 + C_0]$$

$$\dot{C}_1(t) = -A_1(t)$$

$$\dot{\gamma}_1(t) = C_1(t), \tag{13}$$

with the periodicity conditions in (10) enforced. Note the discreteness effects in terms $Q_2^{(2)}(t, \tau)$, $N_1^{(2)}(t, \tau)$, and $M_1^{(2)}(t, \tau)$, and the absence of discreteness effects in the remaining terms. Similarly to (11), the first three equations in (13) form a parametrically varying linear boundary value problem (LBVP) with λ_1 as the eigenvalue which will be discussed in the next section. The last of Eqs. (13) provides compatibility conditions for the solutions of the boundary value problems. Relations (13) govern the dependence of the $O(\epsilon)$ approximation on the long spatial scale, whereas (12) computes $O(\epsilon^2)$ discreteness effects in the solution. The unknown t-dependent coefficients in (12) represent constants of integration and for their determination it is necessary to consider $O(\epsilon^3)$ terms.

$O(\epsilon^3)$ Subproblem. The solutions of this order of approximation are given by

$$Q_1^{(3)}(t, \tau) = A_3(t), \quad A_3(0) = A_3(2\pi),$$

$$Q_2^{(3)}(t, \tau) = \left\{B_0(t)\frac{\lambda_0}{6} - \lambda_0[1 + C_0(t)]^2 - \lambda_2\right\}\tau - \{B_0(t) - [1 + C_0(t)]^2\}\lambda_0 \frac{\tau^3}{6}$$

$$N_1^{(3)}(t, \tau) = B_3(t), \quad B_3(0) = B_3(2\pi), \quad N_2^{(3)}(t, \tau) = 0$$

$$M_1^{(3)}(t, \tau) = C_3(t), \quad C_3(0) = C_3(2\pi), \quad M_2^{(3)}(t, \tau) = 0$$

$$\Theta_1^{(3)}(t, \tau) = \gamma_3(t), \quad \gamma_3(0) = \gamma_3(2\pi),$$

$$\Theta_2^{(3)}(t, \tau) = -\frac{\lambda_0}{6}(\tau - \tau^3), \tag{14}$$

and the undetermined coefficients in the previous order of approximation are governed by the following linear nonhomogeneous parametrically varying LBVP:

$$\dot{A}_2(t) = -B_0(t)C_2(t) - B_2(t)[1 + C_0(t)] - \frac{\lambda_0}{6}B_0(t) + \lambda_0[1 + C_0(t)]^2 + \lambda_2$$

$$\dot{B}_2(t) = -A_0(t)C_2(t) + A_2(t)[1 + C_0(t)]$$

$$\dot{C}_2(t) = -A_2(t)$$

$$\dot{\gamma}_2(t) = C_2(t) + \frac{\lambda_0}{6}, \tag{15}$$

with the periodicity conditions in (12) enforced.

The unknown parameters in (14) are similarly computed by considering the equations of the subproblem at the next order of approximation, but this task will not be pursued further herein. Instead we will now focus on the boundary value problems (11), (13), and (15) whose solution is required for studying the discreteness effects in the buckling behavior of the ring. We also note that by computing the eigenvalues λ_1 and λ_2 we obtain an estimate of the effect of the discreteness of the load distribution on the critical buckling loads of the ring.

3 Study of the Boundary Value Problems (11), (13), and (15)

We first consider the NLBVP (11) which as mentioned previously governs the buckling problem with no discreteness effects. The base (unbuckled) state of the ring is obtained by setting the derivatives in the first three equations equal to zero; this provides the relation $\hat{B}_0[1 + \hat{C}_0] = \lambda_0$. We then solve the last of Eqs. (11) and enforce its boundary conditions. This determines uniquely the base state in the following form:

$$\hat{A}_0 = 0, \quad \hat{B}_0 = \lambda_0, \quad \hat{C}_0 = 0, \quad \hat{\gamma}_0(t) = t. \tag{16}$$

To analytically study the bifurcation leading to buckling we introduce the following coordinate transformation in the neighborhood of the base state,

$$\begin{Bmatrix} A_0(t) \\ B_0(t) \\ C_0(t) \\ \gamma_0(t) \end{Bmatrix} = \begin{Bmatrix} 0 \\ \lambda_0 \\ 0 \\ t \end{Bmatrix} + \mu \begin{Bmatrix} x_1(t) \\ x_2(t) \\ x_3(t) \\ x_4(t) \end{Bmatrix}, \quad |\mu| \ll 1, \tag{17}$$

where μ is a second perturbation parameter independent from ϵ, denoting the closeness of the buckled state from the unbuckled (trivial) one. Substituting (17) into (11) we obtain the following local NLBVP in the neighborhood of the unbuckled state:

$$\dot{x}_1 = -\lambda_0 x_3 - x_2(1 + \mu x_3)$$

$$\dot{x}_2 = x_1(1 + \mu x_3)$$

$$\dot{x}_3 = -x_1$$

$$\dot{x}_4 = x_3$$

$$x_i(0) = x_i(2\pi), \quad i = 1, 2, 3, 4. \tag{18}$$

Seeking a solution in the form

$$x_i(t) = x_i^{(0)}(t) + \mu x_i^{(1)}(t) + \mu^2 x_i^{(2)}(t) + \ldots, \ i = 1, 2, 3, 4$$

$$\text{and} \quad \lambda_0 = \lambda_0^{(0)} + \mu\lambda_0^{(1)} + \ldots, \tag{19}$$

substituting into (18), and matching coefficients of corresponding powers of μ, we obtain a series of linear, constant-parameter boundary value problems that can be conveniently solved using standard linear analysis. Omitting the details of the analysis, and combining the perturbation solution of (18) with (17) we obtain the following asymptotic solution to problem (11):

$$\begin{Bmatrix} A_0(t) \\ B_0(t) \\ C_0(t) \\ \gamma_0(t) \end{Bmatrix} = \begin{Bmatrix} 0 \\ \lambda_0 \\ 0 \\ t \end{Bmatrix} + \delta \begin{Bmatrix} \sin jt \\ -(1/j)\cos jt \\ (1/j)\cos jt \\ -(1/j^2)\sin jt \end{Bmatrix} + \delta^2 \begin{Bmatrix} (1/2j^3)\sin 2jt \\ (1/4j^4)[2j^2 - (1+j^2)\cos 2jt] \\ (1/4j^4)\cos 2jt \\ (1/8j^5)\sin 2jt \end{Bmatrix} + O(\delta^3) \quad (20)$$

where δ is a small parameter defined as in terms of the buckling load as

$$\delta = \pm\left[\frac{8j^4(\lambda_0 - 1 + j^2)}{3(1-j^2)}\right]^{1/2}, \qquad j = 2, 3, \ldots \text{ and } |\delta| \ll 1. \quad (21)$$

The new perturbation parameter δ was obtained by expressing μ in terms of λ_0 from the last of expansions (19), and substituting into the perturbation solutions for $A_0(t)$, $B_0(t)$, $C_0(t)$, and $\gamma_0(t)$. The plus and minus signs in δ correspond to the two bifurcating states of the ring, which at this order are identical. When we consider higher-order terms below, we show that the discrete loading gives rise to asymmetries in the buckled states. We also point out that the periodicity requirements of the last of Eqs. (18) provides compatibility conditions that are necessary to uniquely determine the solutions of the first three equations.

Observing the solution (20–21) we remark that the critical buckling loads for the $O(1)$ NLBVP (11) are given by $\lambda_{0c} = -j^2 + 1, j = 2, 3, \ldots$, a result that is consistent with previous ones dealing with buckling of *hydrostatically loaded* circular rings. The solution with $j = 2$ corresponds to the first buckling mode, and will be examined more closely in the next section. We note that, by construction, the above asymptotic results are valid only close to points of bifurcation (buckling), i.e., only for $0 < \lambda_0 - 1 + j^2 \ll 1, j = 2, 3, \ldots$.

Proceeding to problem (13) we realize that it admits the trivial solution,

$$A_1(t) = B_1(t) = C_1(t) = \gamma_1(t) = \lambda_1 = 0, \quad (22)$$

indicating that there are no $O(\epsilon)$ t-dependent coefficients in the solution. Hence, we focus on the $O(\epsilon^2)$ LBVP (15) which does not admit the trivial solution. Taking into account solution (20), this nonhomogeneous, parametrically varying LBVP is expressed as

$$\begin{Bmatrix} \dot{A}_2(t) \\ \dot{B}_2(t) \\ \dot{C}_2(t) \end{Bmatrix} + \begin{bmatrix} 0 & 1 + \delta(1/j)\cos jt & 1 - j^2 - \delta(1/j)\cos jt \\ -1 - \delta(1/j)\cos jt & 0 & -\delta \sin jt \\ 1 & 0 & 0 \end{bmatrix} \begin{Bmatrix} A_2(t) \\ B_2(t) \\ C_2(t) \end{Bmatrix}$$

$$= \begin{Bmatrix} -[(1-j^2)/6][1 - j^2 + \delta(1/j)\cos jt] + [(1-j^2)/6][1 + 2\delta(1/j)\cos jt] + \lambda_2 \\ 0 \\ 0 \end{Bmatrix} + O(\delta^2) \quad (23)$$

$$\dot{\gamma}_2(t) = C_2(t) + \lambda_0/6,$$

with the periodicity conditions (12) imposed. We note that although $O(\delta^2)$ are not shown explicitly in (23), these were taken into account in the perturbation analysis in order to compute the $O(\delta)$ approximation for λ_2.

To obtain the solution of the LBVP (23), we express the dependent variables and the eigenvalue in formal series in terms of the small parameter δ (for example, $A_2(t) = A_2^{(0)}(t) + \delta A_2^{(1)}(t) + \ldots$, $\lambda_2 = \lambda_2^{(0)} + \delta\lambda_2^{(1)} + \ldots$), substitute into (23), and solve the resulting series of LBVPs with constant parameters at each successive order of δ. We then derive the following asymptotic solutions:

$$A_2(t) = 0 + O(\delta^2),$$

$$B_2(t) = \frac{(1-j^2)}{6} + \delta\frac{(1-j^2)}{6}\cos jt + O(\delta^2),$$

$$C_2(t) = -\frac{(1-j^2)}{6} + O(\delta^2),$$

$$\gamma_2(t) = 0 + O(\delta^2),\ \lambda_2 = 0 + O(\delta^2)\ \ j = 2, 3, \ldots. \quad (24)$$

From these results we note that the correction to the critical buckling load due to discreteness effects is at least of $O(\epsilon^2\delta^2, \epsilon^3)$, and, thus, small. This is in agreement with the numerical results reported in (Seide and Albano, 1973), where it was found that for dense discrete loading distribution the first critical buckling load is almost identical (actually, is slightly smaller) compared to that of the uniformly loaded case. In fact, they proved that for $N = 2, 4$ discrete loads, the discreteness of the loading distribution increases the critical buckling load; however, for $N \geq 5$ the discreteness effects result in a slight decrease of the critical buckling load. The result for $N = 4$ was obtained also by (Kabanov and Astrakharchuk, 1983).

In addition, from the expression of $B_2(t)$ we note that the post-buckled state of the discretely loaded ring depends on the sign of δ; as a result, the two bifurcating states of the ring corresponding to the positive or negative values of δ are not identical (as in the case of hydrostatic loading), and asymmetries develop in the buckled shapes. Again, this finding is in agreement with the numerical results of (Seide and Albano, 1973).

Summarizing, the post-buckling state of the discretely forced circular ring is approximated as follows:

$$q(t, t/\epsilon) = [A_0(t) + O(\delta^3, \epsilon^2\delta^2, \epsilon^3)] + e\Big[-\epsilon\lambda_0\tau + \epsilon^3\Big\{\Big[B_0(t)\frac{\lambda_0}{6} - \lambda_0[1 + C_0(t)]^2 - \lambda_2\Big]\tau - \frac{\lambda_0\tau^3}{6}[B_0(t) - [1 + C_0(t)]^2]\Big\} + O(\epsilon^3\delta^3, \epsilon^4)\Big]$$

$$n(t, t/\epsilon) = \Big[B_0(t) + \epsilon^2\Big\{-\lambda_0[1 + C_0(t)]\frac{\tau^2}{2} + B_2(t)\Big\} + O(\delta^3, \epsilon^2\delta^2, \epsilon^3)\Big] + e[O(\epsilon^4)]$$

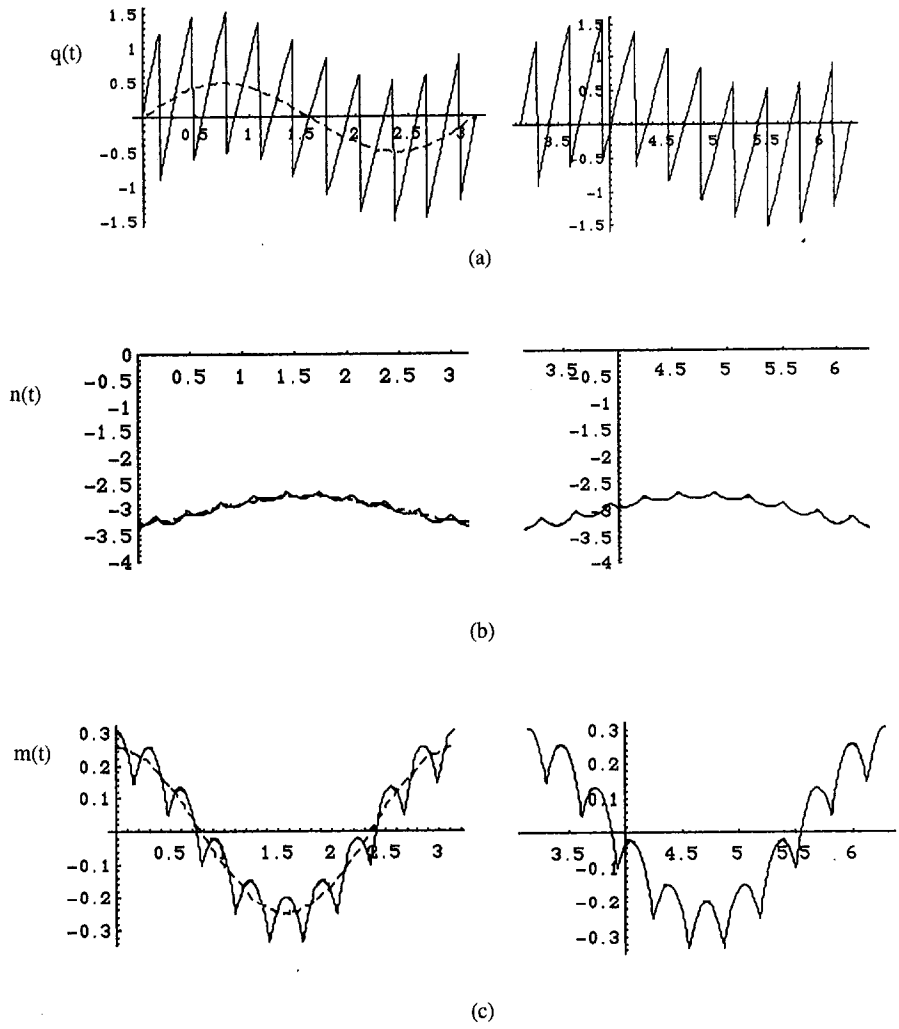

Fig. 3 Numerical results for $t \in [0, \pi]$ and $t \in [\pi, 2\pi]$: Normalized (*a*) shear force, (*b*) axial force, and (*c*) bending moment; —— discrete, --- uniform load distribution

$$m(t, t/\epsilon) = \left[C_0(t) + \epsilon^2 \left\{ \lambda_0 \frac{\tau^2}{2} + C_2(t) \right\} + O(\delta^3, \epsilon^2\delta^2, \epsilon^3) \right] + e[O(\epsilon^4)]$$

$$\tilde{\lambda} = -2\lambda_0 + O(\epsilon^2\delta^2, \epsilon^3), \quad j = 2, 3, \ldots . \tag{25}$$

with $\tau = \tau(t/\epsilon)$ and $e = e(t/\epsilon)$ defined by (3) and the small parameter δ by (21). The remaining variables in (4) can be determined similarly, taking into account the above solutions. The nonsmooth effects in the solution due to the point load distribution are analytically evaluated in (25) by the terms containing the nonsmooth variables τ and e.

Finally, we observe that in contrast to the normalized shear force q, the normalized axial force n, and bending moment m in (25) do not possess any e-dependent terms; as shown in the next section this result is compatible with the presence of C^0-discontinuities in the shear force, but only C^p-discontinuities, $p \geq 1$ in the internal axial force and bending moment due to the applied point loads.

4 Numerical Application

The solutions (25) are depicted in Fig. 3 for $j = 2$, $\epsilon = 2\pi/20 = 0.3146$ and $\delta = 0.5$. These parameters correspond to the first buckling mode of the ring, and a discrete distribution of 20 point loads, each of normalized magnitude $\lambda = -3.0176$. For comparison purposes we also show the results for $\epsilon = 0$, corresponding to a hydrostatically loaded buckled ring with identical magnitude of load distribution and no discreteness effects. Note the C^0-discontinuities in the shear force distribution due to the applied point loads and the C^1-discontinuities in the distributions of the axial force and bending moment.

5 Conclusions

In this work we employed an analytical technique based on non-smooth transformations of the short spatial scale of the problem to study discreteness effects in the post-buckling state of a circular ring loaded by a periodic array of point loads. The novelty of this technique is that it eliminates singularities in the governing equations due to the point loads, at the expense of increasing the dimensionality of the problem. As a result, the three nonsmooth governing equations were replaced by six smoothed ones, together with a set of smoothing conditions. The transformed equations were solved by expressing the dependent variables in regular perturbation series, and analyzing an hierarchy of boundary value problems at successive orders of approximation. These problems were asymptotically solved using techniques from the theory of smooth nonlinear or parametrically varying dynamical systems.

The technique presented herein can be applied to the study of a more general class of buckling problems, such as the ones

of circular rings or cylindrical shells obeying more general constitutive laws (for example, allowing ring axis compressibility (Atanackovic, 1998)) under compressive point loads. Also, nonlinear effects can be handled conveniently with only slight modifications of the NLBVPs. Finally, this technique can be used to validate the results of other buckling studies of such systems that rely on purely numerical methods.

References

Atanackovic, T.M., 1998, "Buckling of a compressible elastic ring," *Acta Mechanica,* Vol. 127, pp. 121–134.

Chaskalovic, J., and Naili, S., 1995, "Bifurcation theory applied to buckling states of a cylindrical shell," *ZAMP,* Vol. 46, pp. 149–155.

Fu, L., and Waas, A.M., 1995, "Initial Post-buckling Behavior of Thick Rings Under Uniform External Hydrostatic Pressure," ASME JOURNAL OF APPLIED MECHANICS, Vol. 62, pp. 338–345.

Kabanov, V.V., and Astrakharchuck, S.V., 1983, "Algorithm of stability analysis for variable-thickness rings under nonuniform loads," *Prikladnaya Mekhanika,* Vol. 19, No. 6, pp. 75–79.

Kämmel, G., 1967, "Der einfluß der längsdehnung auf die elastische stabilität geschlossener kreisringe," *Acta Mechanica,* Vol. 4, pp. 34–42.

Pilipchuk, V.N., 1985, "The calculation of strongly nonlinear systems close to vibration-impact systems," *Prikladneya Matematica i Mekhanika,* Vol. 49, No. 6, pp. 572–578.

Pilipchuk, V.N., 1988, "A transformation for vibrating systems based on a nonsmooth periodic pair of functions," *Doklady AN Ukr. SSR, Ser, A,* Vol. 4, pp. 37–40 (in Russian).

Pilipchuk, V.N., Vakakis, A.F., and Azeez, M.A.F., 1997, "Study of a class of subharmonic motions using a non-smooth temporal transformation," *Physica D,* Vol. 100, pp. 145–164.

Pilipchuk, V.N., and Vakakis, A.F., 1998, "Study of the oscillations of a nonlinearly supported string using nonsmooth transformations," *J. Vibr. Acoustics,* in press.

Riks, R., and Rankin, C.C., 1997, "Computer simulation of the buckling behavior of thin shells under quasi-static loads," *Arch. Comp. Meth. Eng.,* Vol. 4, No. 4, pp. 325–351.

Salenger, G., and Vakakis, A.F., 1998, "Discreteness effects in the forced dynamics of a string on a periodic array of nonlinear supports," *Int. J. Nonlinear Mech.,* Vol. 33, No. 4, pp. 659–673.

Schmidt, R., 1979, "A critical study of postbuckling behavior of thick rings under uniform external hydrostatic pressure," *ZAMM,* Vol. 59, pp. 581–582.

Seide, P., and Albano, E.D., 1973, "Bifurcation of Circular Rings Under Normal Concentrated Loads," ASME JOURNAL OF APPLIED MECHANICS, 40, 233–238.

Troger, H., and Steindl, A., 1991, *Nonlinear Stability and Bifurcation Theory,* Springer-Verlag, Wien.

Vakakis, A.F., Manevitch, L.I., Mikhlin, Yu, Pilipchuk, V.N., and Zevin, A.A., 1996, *Normal Modes and Localization in Nonlinear Systems,* John Wiley and Sons, New York.

Elasticity Interior Solution for Orthotropic Strips and the Accuracy of Beam Theories

N. Tullini

M. Savoia

DISTART–Structural Engineering,
Faculty of Engineering,
University of Bologna,
Viale Risorgimento 2,
40136 Bologna, Italy

The interior problem of an orthotropic strip subject to any given continuous distribution of normal and shear loads is solved by means of a polynomial expansion for the Airy stress function. The polynomial functions defined in the transverse direction are determined recursively by solving a Fredholm equation of second kind. Explicit formulas for displacements are given. A sufficient condition for the convergence of the series expansion is derived. This solution is used to evaluate the error in Timoshenko and higher-order theories. A new beam theory is finally proposed, whose error has the same asymptotic form as second-order theories but approaches zero for strips made of strongly orthotropic material.

1 Introduction

The solution of two-dimensional problems for long rectangular strips in the form of polynomial series is a classical result in the theory of elasticity. Usually, the Airy stress function is represented by a double series expansion in powers of axial and transverse coordinates, and the corresponding coefficients are obtained from the field equations and boundary conditions. This technique is used in Timoshenko and Goodier (1970), Silverman (1964), and Hashin (1967) for isotropic, orthotropic, and anisotropic strips, respectively. The main drawback of these methods is that the computation becomes rather involved if the degree of the polynomial load prescribed on the long sides increases.

A different type of solution can be obtained by a series expansion for the Airy stress function in terms of polynomials in the transverse coordinate multiplying the top and bottom loading functions. In this case, the first term of the series represents classical beam theory, and the next terms are corrections involving higher derivatives of loading functions. This technique has been proposed by Donnell (1952, 1976) for an isotropic beams in plane bending, and extended in Boley (1956) and Boley and Tolins (1956) to distributed shear forces and thermal loading. Stress fields for orthotropic strips subjected to uniform and linearly varying transverse loads can be also found in Tsai and Soler (1970), Rehfield and Murthy (1982), and Rychter (1988). Duva and Simmonds (1990) developed a formal asymptotic expansion in term of the slenderness ratio, so generating approximate strain and stress fields of "any accuracy" for orthotropic strips subjected to equal distributed transverse loads acting on the top and bottom faces.

In summary, the referenced solutions provide for closed-form solutions for power loading functions, series solutions for arbitrary continuous loads, or, in some cases, simple improvements on classical beam theory. However, the problem of convergence of such series is almost never undertaken. The only attempt has been made by Duva and Simmonds (1990), who showed that convergence of polynomial series may fail for strips weak in shear.

Polynomial solutions typically refer to long strips, neglecting pointwise self-equilibrated stress distributions or displacement constraints at the end sections (interior problem). Nevertheless, it is well established that Saint-Venant's principle must be invoked with prudence when strongly orthotropic materials are concerned, because the decay length of end effects can be much greater than the strip height (Choi and Horgan, 1977; Horgan and Simmonds, 1994; Miller and Horgan, 1995). The solution of elasticity problems can be decomposed into the interior solution, satisfying average end conditions, and the boundary solution, which reestablishes the pointwise prescriptions at the beam ends. For the boundary problem several techniques have been proposed, e.g., see the papers referenced in Kim and Steele (1990), Lin and Wan (1990), Savoia and Tullini (1996).

In the present paper, a polynomial expansion for the Airy stress function is derived for the interior problem of orthotropic strips subjected to any given continuous distribution of both normal and shear loads. The first term of the polynomial expansions satisfies the boundary conditions and coincides with classical beam theory, whereas the other terms are defined in order to satisfy the compatibility equation with homogeneous boundary conditions. The polynomial functions defined in the transverse direction are determined recursively by solving a Fredholm equation of second kind. Making use of Cauchy's criterion, a sufficient condition for the convergence of the series expansion is derived for both symmetric and antisymmetric loading conditions. *It is shown that for a typical composite strip the slenderness required for the convergence of the solution may be more than three times larger than for isotropic strips.*

In the second part of the paper, the strip solution obtained is used as a benchmark to evaluate the accuracy of Timoshenko-like beam theories and higher-order theories (Hashin, 1967; Tsai and Soler, 1970; Rehfield and Murthy, 1982; Rychter, 1988). Higher-order theories can be obtained from the present solution by retaining the first terms only in the polynomial expansion. As $H/l \to 0$, the actual error (i.e., with respect to the exact solution) is found to be of $O(H^2/l^2)$ and $O(H^{2N}/l^{2N})$ for first-order (Euler-Bernoulli) and Nth-order theories, l being a measure of the loading wavelength (Duva and Simmonds, 1990; Savoia, 1996). Finally, a new beam theory is proposed, whose error has the same asymptotic form as second-order theories but approaches zero for strips made of strongly orthotropic material.

2 Governing Equations

Consider a rectangular strip of length L and height $H = 2h$ and let $0x_1x_2$ be a Cartesian reference frame where x_1 coincides with the centroidal axis and x_2 is chosen in the transverse direction. The strip is made of homogeneous, orthotropic, linearly elastic material, with orthotropy axes coinciding with the

Contributed by the Applied Mechanics Division of THE AMERICAN SOCIETY OF MECHANICAL ENGINEERS for publication in the ASME JOURNAL OF APPLIED MECHANICS.

Discussion on the paper should be addressed to the Technical Editor, Professor Lewis T. Wheeler, Department of Mechanical Engineering, University of Houston, Houston, TX 77204-4792, and will be accepted until four months after final publication of the paper itself in the ASME JOURNAL OF APPLIED MECHANICS.

Manuscript received by the ASME Applied Mechanics Division, Jan. 3, 1996; final revision, Oct. 2, 1998. Associate Technical Editor: M. Taya.

reference axes; the strip is subject to smoothly varying tractions (for a unit width) $\mathbf{q}_t \equiv (q_{1t}, q_{2t})$ and $\mathbf{q}_b \equiv (q_{1b}, q_{2b})$ at the top and bottom faces and forces and couples $\bar{F}_1^0, \bar{F}_2^0, \bar{M}^0, \bar{F}_1^L, \bar{F}_2^L, \bar{M}^L$ at the end sections $x_1 = 0, L$ (interior problem). Accordingly, the boundary conditions are ($\alpha = 1, 2$)

$$\sigma_{\alpha 2}(x_1, h) = q_{\alpha b}, \quad \sigma_{\alpha 2}(x_1, -h) = -q_{\alpha t} \quad \text{at } x_2 = h, -h \tag{1}$$

$$\{N, Q, M\} = \{\bar{F}_1, \bar{F}_2, \bar{M}\} \quad \text{at } x_1 = 0, L \tag{2}$$

where $\sigma_{\alpha\beta}$ are the components of the stress tensor and N, Q, M are, for a unit width, the axial resultant, shear resultant, and the bending moment written in term of stresses. The equilibrium equations with null body forces are satisfied by the classical Airy stress function $F(x_1, x_2)$:

$$\sigma_{11} = F_{,22}, \quad \sigma_{22} = F_{,11}, \quad \sigma_{12} = -F_{,12} \tag{3}$$

where subscripts α preceded by a comma denotes partial differentiation with respect to x_α. The compatibility equation yields the governing differential equation (Lekhnitskii, 1981)

$$F_{,2222} + \bar{E}F_{,1122} + \epsilon^2\bar{E}^2F_{,1111} = 0 \tag{4}$$

where

$$\bar{E} = \frac{R_{66} + 2R_{12}}{R_{11}}, \quad \epsilon^2\bar{E}^2 = \frac{R_{22}}{R_{11}} \tag{5}$$

and constants R_{ij} are the usual reduced elastic coefficients. For instance, Eqs. (5) reduce to

$$\bar{E} = \frac{E_1}{G_{12}} - 2\nu_{12}, \quad \epsilon^2\bar{E}^2 = \frac{E_1}{E_2} \tag{6}$$

for plane stress and E_α, G_{12}, ν_{12} denote Young's moduli, shear modulus, and Poisson's ratio.

Introducing the dimensionless variables $x = x_1/L$, $y = x_2/h$ and making use of Eqs. (3), the field Eq. (4) and boundary conditions (1), (2) can be rewritten as

$$F_{,yyyy} + \rho F_{,xxyy} + \epsilon^2\rho^2F_{,xxxx} = 0 \tag{7}$$

$$F_{,xx}(x, \pm 1) = (\pm q_2 + p_2)L^2/2, \quad F_{,xy}(x, \pm 1) = (\mp q_1 - p_1)hL/2 \quad \text{at } y = \pm 1 \tag{8}$$

$$[\{F_{,y}, F_{,x}, yF_{,y} - F\}]_{y=-1}^{y=1} = \{\bar{F}_1 h, -\bar{F}_2 L, \bar{M}\} \quad \text{at } x = 0, 1 \tag{9}$$

where $\rho = \bar{E}h^2/L^2$, $q_\alpha = q_{\alpha b} + q_{\alpha t}$, $p_\alpha = q_{\alpha b} - q_{\alpha t}$. Equations (7)–(9) can be conveniently solved by considering the antisymmetric and symmetric parts of boundary conditions (8), corresponding to loads q_2 (case I), p_1 (II) and p_2 (III), q_1 (IV), respectively (Fig. 1).

3 Two-Dimensional Elasticity Interior Solution

For isotropic strips, Donnell (1952, 1976) solved cases I and III of Eqs. (7)–(9) by means of a series expansion involving derivatives of even order of the bending moment $M(x)$ and polynomial functions of y; Boley and Tolins (1956) solved all the four isotropic cases. Duva and Simmonds (1990) modified these series solutions for an orthotropic strip under transverse load q_2 (case I).

In the present section, the solution for an orthotropic strip subject to the four loading conditions is given. To this end, the stress functions is cast in the form

$$F_C(x, y) = -\Phi_C(x)P_0^C(y) - \sum_{n=1}^{\infty} \rho^n\Phi_C^{(2n)}(x)P_n^C(y) \qquad C = \text{I, II, III, IV} \tag{10}$$

where $(\cdot)^{(n)}$ denotes the nth derivative with respect to the axial coordinate x and index C stands for the case considered. Function

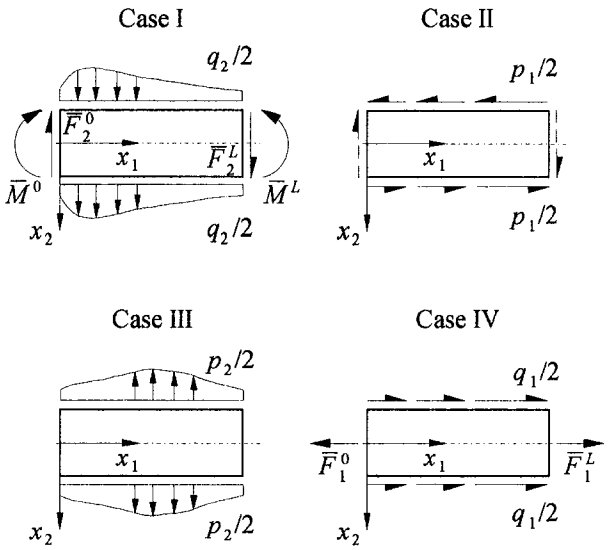

Fig. 1 Nomenclature for the four loading conditions

Φ_C and polynomials P_n^C are defined in such a way the first term in Eq. (10) satisfies boundary conditions (8), (9) and corresponds to the classical theory, whereas the summation at the R.H.S. fulfils the field Eq. (7) with homogeneous boundary conditions. These requirements are verified by the following sets of functions:

$$\{\Phi_{\text{I}}, \Phi_{\text{II}}, \Phi_{\text{III}}, \Phi_{\text{IV}}\} = \left\{M(x), hL\int_x^1 p_1(t)dt, L^2\int_x^1 (x-t)p_2(t)dt, hN(x)\right\} \tag{11}$$

$$\{P_0^{\text{I}}, P_0^{\text{II}}, P_0^{\text{III}}, P_0^{\text{IV}}\} = \left\{\frac{3y - y^3}{4}, \frac{y - y^3}{4}, \frac{1}{2}, \frac{1 - y^2}{4}\right\} \tag{12}$$

where

$$N(x) = \bar{F}_1^L + L\int_x^1 q_1(t)dt,$$

$$M(x) = \bar{M}^L - \bar{F}_2^L L(1 - x) + L^2\int_x^1 (x - t)q_2(t)dt \tag{13}$$

are the axial resultant and the bending moment in terms of loading functions. Moreover, $P_n^C(y)$ are polynomials functions which can be obtained from the following recursive formulas:

$$\frac{d^4P_1^C}{dy^4} = -\frac{d^2P_0^C}{dy^2} \ (n = 1), \quad \frac{d^4P_n^C}{dy^4} = -\frac{d^2P_{n-1}^C}{dy^2} - \epsilon^2P_{n-2}^C \quad \text{for } n \geq 2 \tag{14}$$

subjected to the following conditions:

$$P_n^C(\pm 1) = \frac{dP_n^C(\pm 1)}{dy} = 0 \quad \text{for } n \geq 1. \tag{15}$$

Explicit expressions for the polynomials P_n^C will be given in the following section. The solution (10)–(15) can be readily verified by direct substitution into Eqs. (7)–(9).

According to Eq. (14), for isotropic strips ($\epsilon = \frac{1}{2}$) the polynomials P_n^C are independent of the elastic constants. Moreover, although four elastic constants characterise an orthotropic strip, the polynomials P_n^C depend on the combined elastic parameter ϵ only.

With reference to the boundary problem, an analogous conclusion was drawn by Horgan and Simmonds (1991) for the strip eigenfunctions and corresponding eigenconditions.

Finally, displacement components can be derived from the stress function, as usual, through the integration of stress-strain relations, so obtaining

$$u_1(x, y) = u_0(x) - \frac{h}{L} v_0'(x)y - \frac{R_{66}}{L} \sum_{n=0}^{\infty} \rho^n \Phi_C^{(2n+1)}(x) U_n^C(y) \quad (16)$$

$$u_2(x, y) = v_0(x) + \frac{R_{66}}{h} \sum_{n=0}^{\infty} \rho^n \Phi_C^{(2n)}(x) V_n^C(y) \quad (17)$$

where

$$u_0'(x) = R_{11} \frac{N(x)L}{A},$$

$$v_0''(x) = -\frac{R_{11}L^2}{I} \left(M(x) + hL \int_x^1 p_1(t)dt \right) \quad (18)$$

$$U_n^C(y) = \left(1 + \frac{2R_{12}}{R_{66}} \right) \frac{d^2 P_{n+1}^C(y)}{dy^2} + \frac{R_{12}}{R_{66}} P_n^C(y) \quad (19)$$

$$V_n^C(y) = \frac{dP_n^C(y)}{dy} + \frac{dU_n^C(y)}{dy} \quad (20)$$

and $A = 2h$, $I = 2/3h^3$ are cross-sectional area and second area moment, respectively. Equations (18) coincide with the basic equation of classical beam theory, whereas $U_n^C(y)$ and $V_n^C(y)$ represent axial and transverse warpings given by polynomial functions of higher order of y.

Equations (18) must be integrated making use of an appropriate set of boundary conditions. The boundary conditions necessary to give a residual solution (both in terms of stresses and displacements) decaying exponentially to zero can be found in Lin and Wan (1990); this approach provides for the correct value of displacements far from the beam extremities, without requiring the solution of the boundary problem; nevertheless, it has been proposed for strips under tip loads, and higher-order moments of residual stresses than those tabulated in Lin and Wan (1990) should be calculated for more complex loadings. To avoid this problem, simpler boundary conditions in terms of average transverse deflection and mean rotation (see Section 6) can be prescribed; in this case, the associated boundary problem gives rise to decaying residual stresses together with an additional (small) term correcting the displacement field (Horgan and Simmonds, 1991; Savoia and Tullini, 1996).

4 Polynomial Functions $P_n^C(y)$

Making use of boundary conditions (15), the following solutions of the differential Eqs. (14) are obtained (Smirnov, 1964, Vol. IV):

$$\{P_1^{\mathrm{I}}, P_1^{\mathrm{II}}, P_1^{\mathrm{III}}, P_1^{\mathrm{IV}}\} = \left\{ \frac{y(1-y^2)^2}{80}, \frac{y(1-y^2)^2}{80}, 0, \frac{(1-y^2)^2}{48} \right\} \quad (21)$$

$$P_n^C(y) = \int_0^1 [K_1(y, t)P_{n-1}^C(t) - \epsilon^2 K_2(y, t)P_{n-2}^C(t)]dt \quad \text{for } n \geq 2. \quad (22)$$

Equation (22) is a Fredholm equation of second kind whose kernels $K_\alpha(y, t)$ for strips subjected to odd and even conditions (cases I, II and III, IV, respectively) are defined as

$$K_1^o(y, t) = \begin{cases} -yt(3 - y^2)/2 + t, & t \leq y \\ -yt(3 - y^2)/2 + y, & t \geq y \end{cases},$$

$$K_2^o(y, t) = \begin{cases} t(1 - y)^2(3y - 2t^2 - yt^2)/12, & t \leq y \\ y(1 - t)^2(3t - 2y^2 - y^2t)/12, & t \geq y \end{cases}$$

$$K_1^e(y, t) = \begin{cases} (1 + y^2)/2 - y, & t \leq y \\ (1 + y^2)/2 - t, & t \geq y \end{cases},$$

$$K_2^e(y, t) = \begin{cases} (1 - y)^2(1 + 2y - 3t^2)/12, & t \leq y \\ (1 - t)^2(1 + 2t - 3y^2)/12, & t \geq y \end{cases}. \quad (23)$$

These kernels are continuous in $[0, 1] \times [0, 1]$; hence existence and continuity of functions

$$A^2(y) = \int_0^1 |K_1(y, t)|^2 dt, \quad B^2(y) = \int_0^1 |K_2(y, t)|^2 dt \quad (24)$$

is guaranteed. The corresponding L^2-norm in $[0, 1]$, denoted by $\| \cdot \|_0$, gives

$$\|A^o\|_0^2 = \frac{1}{210}, \quad \|B^o\|_0^2 = \frac{13}{727650},$$

$$\|A^e\|_0^2 = \frac{1}{30}, \quad \|B^e\|_0^2 = \frac{29}{28350} \quad (25)$$

for the four kernels in Eqs. (23).

In order to obtain conditions for the convergence of polynomial representations of the interior problem solution (see the next section), an upper bound for the absolute value of polynomials P_n^C must be given. Making use of the Cauchy-Schwarz inequality, Eq. (22) yields the following upper bounds for the absolute value and the norm of the polynomials P_n^C:

$$|P_n^C(y)| \leq A(y)\|P_{n-1}^C\|_0 + \epsilon^2 B(y)\|P_{n-2}^C\|_0 \quad \text{for } n \geq 2 \quad (26)$$

$$\|P_n^C\|_0 \leq \|A\|_0\|P_{n-1}^C\|_0 + \epsilon^2\|B\|_0\|P_{n-2}^C\|_0 \quad \text{for } n \geq 2. \quad (27)$$

Therefore, it can be proved that (see the Appendix)

$$\|P_n^C\|_0 \leq \|A\|_0^n (1 + \epsilon^2)^{n-1}\|P_0^C\|_0 \quad \text{for } n \geq 2. \quad (28)$$

Finally, making use of inequality (28), inequality (26) reduces to

$$|P_n^C(y)| \leq \|A\|_0^{n-1}(1 + \epsilon^2)^{n-2}\|P_0^C\|_0 \times \left[A(y) + \frac{\epsilon^2}{1 + \epsilon^2} \frac{B(y)}{\|A\|_0} \right]. \quad (29)$$

The function in brackets at the R.H.S. is less than a constant c, for it is continuous for all ϵ in $[0, 1]$; hence, the following upper bound for the absolute value of polynomials P_n^C is obtained:

$$|P_n^C(y)| \leq c\|A\|_0^{n-1}(1 + \epsilon^2)^{n-2}\|P_0^C\|_0 \quad \text{for } n \geq 2. \quad (30)$$

5 Sufficient Condition for Convergence of Polynomial Series

A sufficient condition to establish the convergence of the polynomial series appearing in Eq. (10) can be obtained by analysing the absolute convergence; this can be done making use of Eq. (30) and Cauchy's criterion (Smirnov, 1964, Vol. I). The convergence condition strongly depends on the kind of loading applied and degree of orthotropy of the strip. For instance, consider the case of a stress function F_C where Φ_C is bounded together with all its even derivatives $\Phi_C^{(2n)}$. In this case, the following inequality is to be satisfied:

$$\rho\|A\|_0(1 + \epsilon^2) < 1. \quad (31)$$

Substituting Eqs. (25*a, b*) in (31), the polynomial representation turns out to be absolutely convergent when $\rho < 14.49/(1 + \epsilon^2)$

(cases I and II) or $\rho < 5.48/(1 + \epsilon^2)$ (III and IV) for antisymmetric and symmetric loading conditions, respectively.

It is worth noting that, for $\epsilon = 0$, making use of eigenfunction expansion of the corresponding kernels Savoia and Tullini (1996) established a wider range, i.e., $\rho < 20.19$ and $\rho < 9.87$, for odd and even polynomials, respectively. Unfortunately, due to nonorthogonality of eigenfunctions for orthotropic strips, the same procedure cannot be applied to the present case.

With reference to a general loading condition, the series reported in Eq. (10) is absolutely convergent if, starting from a given value n, the following inequality holds:

$$\rho\|A\|_0(1 + \epsilon^2)^n \sqrt[n]{|\Phi_C^{(2n)}|} < 1 \quad \forall x \in [0, 1]. \tag{32}$$

If the applied load varies along the beam according to a trigonometric or an exponential law [$\Phi_C = \cos(\alpha x)$, $\exp(\alpha x)$, etc.], it can be verified that $|\Phi_C^{(2n)}| = \alpha^{2n}|\Phi_C|$; consequently, Eq. (32) gives

$$\rho < \frac{1}{\alpha^2\|A\|_0(1 + \epsilon^2)} \Rightarrow \frac{L^2}{H^2} > \frac{\alpha^2\|A\|_0}{4}\bar{E}(1 + \epsilon^2). \tag{33}$$

In the isotropic case ($\bar{E} = 2$, $\epsilon = \frac{1}{2}$), inequality (33*b*) shows that a sufficient condition for convergence is established if $L/H > 0.21\alpha$ and $L/H > 0.34\alpha$ for antisymmetric and symmetric loadings; for a typical composite materials ($\bar{E} = 25$, $\epsilon \cong 0$), $L/H > 0.66\alpha$ and $L/H > 1.07\alpha$.

Finally, it is worth noting that the estimates presented in this section hold for the elasticity solution written in the form (10) as well as for every polynomial representation of the interior problem.

6 Accuracy of Beam Theories

Timoshenko-Like Beam Theories. In Timoshenko-like beam theories, two kinematic measures for displacements are usually employed. Following Cowper (1966), the dimensionless averaged transverse deflection η and the mean rotation φ of the cross section are introduced according to the following definition:

$$\eta(x) = \frac{1}{AL}\int_{-h}^{h} u_2 dx_2, \quad \varphi(x) = -\frac{1}{I}\int_{-h}^{h} u_1 x_2 dx_2. \tag{34}$$

Substituting Eqs. (16), (17) in (34), the following constitutive relations are obtained (C = I, II):

$$\varphi' = -\frac{R_{11}L}{I}\left[\Phi_C - \frac{R_{12}h^2}{R_{11}L^2}\sum_{n=0}^{\infty}\rho^n a_n^C \Phi_C^{(2n+2)}\right],$$

$$\eta' - \varphi = \frac{\Phi_C'/L}{k_0^C G_{12}A} + \sum_{n=1}^{\infty}\frac{\Phi_C^{(2n+1)}/L}{k_n^C G_{12}A} \tag{35}$$

where functions Φ_C are reported in Eq. (11), and $\Phi_I'/L = Q$ and $\Phi_{II}'/L = -p_1 h$ (see Eq. (35*b*)) represent the shear force and distributed moment; moreover,

$$a_n^C = \int_{-1}^{1} P_n^C(y) y dy,$$

$$\frac{1}{k_n^C} = 2\rho^n\left[P_n^C(1) + U_n^C(1) - \frac{3R_{12}}{2R_{66}}a_n^C\right] \tag{36}$$

are the first moment of polynomials P_n^C and the set of shear correction factors. For instance, the first correction factor k_0, is equal to

$$\frac{1}{k_0^{\mathrm{I}}} = \frac{6 + R_{12}/R_{66}}{5}, \quad \frac{1}{k_0^{\mathrm{II}}} = \frac{1 + R_{12}/R_{66}}{5}. \tag{37}$$

For isotropic and orthotropic strips, Eq. (37*a*) gives the shear coefficients obtained by Cowper (1966) and Dharmarajan and McCutchen (1973) for a constant or linear shear resultant, whereas, for strongly orthotropic beams in plane stress, the term $R_{12}/R_{66} = -\nu_{12}G_{12}/E_1$ is negligible and $k_0^{\mathrm{I}} = \frac{5}{6}$, $k_0^{\mathrm{II}} = 5$. For case I, the first terms in Eqs. (35) represent the classical Timoshenko constitutive equations. The summations contain higher-order correction terms, where the shear factors k_n^C defined in Eq. (36*b*) multiply the even derivatives of Q and p_1 and are required for nonuniform loads. Hence, Eqs. (35) are useful to establish the range of validity of Timoshenko classical theory. The dependence of the shear correction factor on the loading condition has been already pointed out by Berdichevsky and Kvashnina (1976) in their asymptotically exact beam theory and by Savoia et al. (1993) for multilayered beams.

It is worth remembering that only for slender beams the interior problem alone is meaningful and global parameter of deformability can be evaluated with Timoshenko's beam theory; on the contrary, for deep beams the end effects may become more important than higher-order interior refinements. Therefore, even though Eqs. (35) suggest the possibility of obtaining a refinement of Timoshenko's beam theory, no cross-sectional warping can be described using two kinematic variables only and, consequently, no boundary problem can be taken into account in a second step of analysis.

Higher-Order Beam Theories. A simple way to reobtain higher-order beam theories is to retain a finite numbers of terms in the series appearing in Eq. (10). For example, the stress field $\boldsymbol{\sigma}^{2\mathrm{nd}}$ corresponding to a second-order beam theory for plane bending (cases I, III) (Hashin, 1967; Tsai and Soler, 1970; Rehfield and Murthy, 1982; Rychter, 1988) can be obtained directly from the first two terms in Eq. (10):

$$\sigma_{11}^{2\mathrm{nd}} = \frac{Mhy}{I} - \bar{E}q_2\frac{3y - 5y^3}{20} \tag{38}$$

$$\sigma_{12}^{2\mathrm{nd}} = \frac{1}{A}\left[\frac{3M'}{2L}(1 - y^2) - \rho q_2' L\frac{1 - 6y^2 + 5y^4}{40}\right] \tag{39}$$

$$\sigma_{22}^{2\mathrm{nd}} = \frac{1}{2}p_2 + q_2\frac{3y - y^3}{4} + \rho q_2''\frac{y - 2y^3 + y^5}{80}. \tag{40}$$

The error of the stress field $\boldsymbol{\sigma}^{N\mathrm{th}}$ of the Nth-order beam theory with respect to the exact interior solution $\boldsymbol{\sigma}^{2D}$ derived in Section 3 can be evaluated as

$$e^{N\mathrm{th}} = \frac{\|\boldsymbol{\sigma}^{N\mathrm{th}} - \boldsymbol{\sigma}^{2D}\|}{\|\boldsymbol{\sigma}^{2D}\|} \tag{41}$$

where $\|\cdot\|$ is the norm for the stress tensor based on the complementary elastic energy,

$$\|\boldsymbol{\sigma}\|^2 = hL\int_0^1\int_{-1}^{1}(R_{11}\sigma_{11}^2 + R_{22}\sigma_{22}^2 + 2R_{12}\sigma_{11}\sigma_{22} + R_{66}\sigma_{12}^2)dxdy. \tag{42}$$

With reference to case I, for sufficiently slender beams (i.e., for values of the slenderness which allow for the Maclaurin's expansion of Eq. (41) in terms of powers of H/L), the dominant term in the complementary elastic energy is the axial normal stress σ_{11}. In fact, by direct inspection of stress field (38)–(40), stress components σ_{11}, σ_{12}, σ_{22} can be found to be of $O(L^2/H^2)$, $O(L/H)$, $O(1)$, respectively. Therefore, if the sufficient condition for the convergence of polynomial series representation is fulfilled, the error (41) can be given the following asymptotic form:

$$e^{N\mathrm{th}} \cong \rho^N\frac{\|M^{(2N)}\|_0}{\|M\|_0}\frac{\|d^2P_N^{\mathrm{I}}/dy^2\|_0}{\|d^2P_0^{\mathrm{I}}/dy^2\|_0} \quad \text{as } H/L \to 0 \tag{43}$$

where, as before, $\|\cdot\|_0$ stands for the L^2-norm on [0, 1] or, equivalently,

$$e^{N\text{th}} \cong \frac{\bar{E}^N}{4^N} \frac{\|d^2P_N^I/dy^2\|_0}{\|d^2P_0^I/dy^2\|_0} \left(\frac{H}{l_N}\right)^{2N} \quad \text{as } H/L \to 0 \qquad (44)$$

where l_N is the characteristic wavelength of the loading, defined as $(l_N/L)^{2N} = \|M\|_0/\|M^{(2N)}\|_0$.

Equation (44) shows that the error related to the Nth-order beam theory is of order $(H/l_N)^{2N}$. A similar result was obtained by Duva and Simmonds (1990) for the computable error obtained through the Synge-Prager hypercircle method by using kinematically admissible and statically-admissible strain fields. In addition, Eq. (43) gives the actual error with respect to the interior two-dimensional solution, together with the explicit computation of the coefficient multiplying $(H/l_N)^{2N}$. For instance, for the first-order (Euler-Bernoulli) beam theory and the second-order beam theory (Eqs. (38)–(40)), the following error estimates can be obtained:

$$e^{1\text{st}} \cong \frac{\bar{E}}{20\sqrt{21}} \left(\frac{H}{l_1}\right)^2, \quad e^{2\text{nd}} \cong \bar{E}^2 f_0^{2\text{nd}}(\epsilon) \left(\frac{H}{l_2}\right)^4 \quad \text{as } H/L \to 0 \qquad (45)$$

where

$$f_0^{2\text{nd}}(\epsilon) = \frac{(37 - 690\epsilon^2 + 3425\epsilon^4)^{1/2}}{8400\sqrt{33}}. \qquad (46)$$

Strongly Orthotropic Beam Theory. For composite materials with fiber reinforcement in the beam axis direction, the coefficient ϵ of Eq. (6*b*) approaches zero. Hence, a simple one-dimensional solution can be obtained setting $\epsilon = 0$ in Eq. (14*b*) defining the higher-order polynomials. This theory is particularly attractive, since both interior and boundary solutions turn out to be particularly simple. For instance, the boundary problem can be easily solved making use of the eigenfunction expansion proposed by Horgan and Simmonds (1991) and applied by Savoia and Tullini (1996) to beams with prescribed displacements and stresses at the beam ends. For case I, error estimate (41) assumes the following asymptotic form:

$$e^{(\epsilon\approx 0)} \cong \rho^4 \frac{\|M^{(4)}\|_0}{\|M\|_0} \frac{\|d^2P_2^I/dy^2|_{\epsilon=0} - d^2P_2^I/dy^2\|_0}{\|d^2P_0^I/dy^2\|_0} \quad \text{as } H/L \to 0 \qquad (47)$$

which can be rewritten in the same form of Eq. (45*b*), where Eq. (46) is replaced by

$$f_0^{(\epsilon\approx 0)}(\epsilon) = \frac{\epsilon^2}{1680}\sqrt{\frac{137}{33}}. \qquad (48)$$

By comparing Eqs. (46)–(48) it can be concluded that the orthotropy coefficient ϵ strongly influences the accuracy of beam theories considered here. For isotropic beams ($\epsilon = 0.5$), the second-order beam theory is more accurate than the strongly orthotropic beam theory, whereas for $\epsilon < 0.23$ (that is for typical orthotropic materials) the situation is completely reversed. For instance, for $\epsilon \to 0$ the error of strongly orthotropic beam theory approaches zero, whereas this is not the case for second-order beam theory.

7 Final Remarks

Figure 2 shows the actual mean square error of stress field given by first-order beam theory, second-order beam theory and strongly orthotropic beam theory for a cantilever orthotropic strip under a transverse load varying with a parabolic law. In this case, the asymptotic formulas ((45*a*, (45*b*), (47)) hold for $L/H > 4.7$, that is for this range of slenderness a Maclaurin's expansion in terms of power of H/L is possible for the denominator of Eq. (41). First of all, the asymptotic behavior as $L/H \to \infty$ for the three theories is confirmed, and the error for the strongly orthotropic beam theory is 9.2 times lower than for second-order theory. For very short strips ($L/H < 1$), the dominant term in the complementary elastic energy (42) is the transverse normal stress σ_{22} and the error approaches a constant value for all the theories. Nevertheless, the strongly orthotropic beam theory is still sufficiently accurate ($e^{(\epsilon\approx 0)} \approx 0.1$), whereas first-order and second-order theories are completely inadequate ($e^{1\text{st}} = e^{2\text{nd}} \approx 1$).

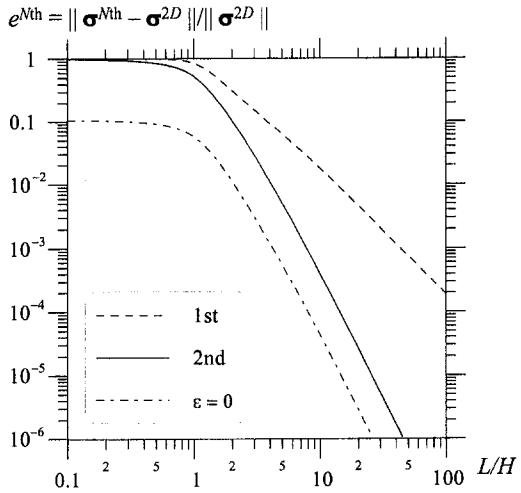

Fig. 2 Mean square error of stress fields given by the first-order (Euler-Bernoulli) theory, the second-order theory and the strongly orthotropic beam theory, for a cantilever orthotropic strip ($E_1/G_{12} = 50$, $E_1/E_2 = 25$, $\nu_{12} = 0.25$) under a transverse load varying with the parabolic law $q_2 = q_L x^2$.

Acknowledgment

The financial support of the (Italian) Ministry of University and Scientific and Technological Research (MURST, ex 60%) is gratefully acknowledged.

References

Berdichevsky, V. L., and Kvashnina, S. S., 1976, "On equations describing the transverse vibrations of elastic bars," *PMM*, Vol. 40, pp. 120–135.

Boley, B. A., 1956, "The determination of temperature, stresses and deflections in two-dimensional thermo-elastic problems," *J. Aero. Sci.*, Vol. 23, pp. 67–75.

Boley, B. A., and Tolins, I. S., 1956, "On the Stresses and Deflections of Rectangular Beams," ASME JOURNAL OF APPLIED MECHANICS, Vol. 23, pp. 339–342.

Choi, I., and Horgan, C. O., 1977, "Saint-Venant's Principle and End Effects in Anisotropic Elasticity," ASME JOURNAL OF APPLIED MECHANICS, Vol. 44, pp. 424–430.

Cowper, G. R., 1966, "The Shear Coefficient in Timoshenko's Beam Theory," ASME JOURNAL OF APPLIED MECHANICS, Vol. 33, pp. 335–340.

Dharmarajan, S., and McCutchen Jr, H., 1973, "Shear coefficients for orthotropic beams," *J. Composite Materials*, Vol. 7, pp. 530–535.

Donnell, L. H., 1952, "Bending of Rectangular Beams," ASME JOURNAL OF APPLIED MECHANICS, Vol. 19, p. 123.

Donnell, L. H., 1976, *Beams, Plates and Shells*, McGraw-Hill, New York.

Duva, J. M., and Simmonds, J. G., 1990, "Elementary, Static Beam Theory is as Accurate as You Please," ASME JOURNAL OF APPLIED MECHANICS, Vol. 57, pp. 134–137.

Hashin, Z., 1967, "Plane Anisotropic Beams," ASME JOURNAL OF APPLIED MECHANICS, Vol. 34, pp. 257–262.

Horgan, C. O., and Simmonds, J. G., 1991, "Asymptotic analysis of an end-loaded transversely isotropic, elastic, semi-infinite strip weak in shear," *Int. J. Solids Struct.*, Vol. 27, pp. 1895–1914.

Horgan, C. O., and Simmonds, J. G., 1994, "Saint-Venant end effects in composite structures," *Compos. Engineering*, Vol. 4, pp. 279–286.

Kim, Y. Y., and Steele, C. R., 1990, "Modifications of Series Expansions for General End Conditions and Corner Singularities on the Semi-Infinite Strip," ASME JOURNAL OF APPLIED MECHANICS, Vol. 57, pp. 581–588.

Lekhnitskii, S. G., 1981, *Theory of Elasticity of an Anisotropic Body*, Mir Publ., Moscow.

Lin, Y. H., and Wan, F. Y. M., 1990, "Bending and flexure of semi-infinite cantilevered orthotropic strips," *Comput. Struct.*, Vol. 35, pp. 349–359.

Miller, K. L., and Horgan, C. O., 1995, "End effects for plane deformations of an elastic anisotropic semi-infinite strip," *J. Elasticity,* Vol. 38, pp. 261–316.

Rehfield, L. W., and Murthy, P. L. N., 1982, "Toward a new engineering theory of bending: Fundamentals," *AIAA J.,* Vol. 20, pp. 693–699.

Rychter, Z., 1988, "A simple and accurate beam theory," *Acta Mech.,* Vol. 75, pp. 57–62.

Savoia, M., 1996, "On the accuracy of one-dimensional models for multilayered composite beams," *Int. J. Solids Struct.,* Vol. 33, pp. 521–544.

Savoia, M., and Tullini, N., 1996, "Beam theory for strongly orthotropic materials," *Int. J. Solids Struct.,* Vol. 33, pp. 2459–2484.

Savoia, M., Laudiero, F., and Tralli, A., 1993, "A refined theory for laminated beams: Part I—A new high order approach," *Meccanica,* Vol. 28, pp. 39–51.

Silverman, I. K., 1964, "Orthotropic beams under polynomial loads," *ASCE J. Eng. Mech.,* Vol. 90, pp. 223–319.

Smirnov, V. I., 1964, *A Course of Higher Mathematics,* Pergamon Press, New York.

Timoshenko, S. P., and Goodier, J. N., 1970, *Theory of Elasticity,* 3rd Ed., McGraw-Hill, New York.

Tsai, H., and Soler, A. I., 1970, "Approximate theory for locally loaded plane orthotropic beams," *Int. J. Solids Struct.,* Vol. 6, pp. 1055–1068.

APPENDIX

Equation (28) can be proved from Eq. (27) by using mathematical induction. Since $\|P_1^C\|_0 \leq \|A\|_0 \|P_0^C\|_0$, Eq. (27) for $n = 2$ reads as

$$\|P_2^C\|_0 \leq \|A\|_0^2 (1 + \epsilon^2 \|B\|_0 / \|A\|_0^2) \|P_0^C\|. \tag{A1}$$

Further, by direct computation from Eqs. (25), it can be verified that $\|B\|_0 / \|A\|_0^2 < 1$, then inequality (28) holds for $n = 2$. By assuming Eq. (28) to hold for n, Eq. (27) reduces to

$$\|P_{n+1}^C\|_0 \leq \|A\|_0^{n+1} (1 + \epsilon^2)^{n-2} \left[1 + \epsilon^2 + \frac{\epsilon^2 \|B\|_0}{\|A\|_0^2} \right] \|P_0^C\|_0 \tag{A2}$$

for $n + 1$. Since the term in brackets is less than $(1 + \epsilon^2)^2$, then Eq. (28) holds also for $n + 1$; thus, by mathematical induction, it is valid for all n.

Plastic Buckling of Circular Cylindrical Shells Under Nonuniform Axial Loads

D. Durban

E. Ore

Faculty of Aerospace Engineering,
Technion,
Haifa 32000, Israel

Elastoplastic buckling of circular cylindrical shells subjected to piecewise-uniform circumferentially varying axial loads is studied within the framework of linear stability analysis in conjunction with small strain plasticity. Both J_2 flow and deformation theories with arbitrary hardening are used to model material behavior. Donnell-type equations are solved separately for each loaded segment with the interfacial continuity conditions providing the eigenvalue equation for the buckling parameter. Sample results are presented for pure bending and for uniform compression over a finite axial band. In all cases, deformation theory predicts buckling loads smaller than those obtained from flow theory. Loading nonuniformity becomes appreciable as the applied stresses concentrate over a narrow axial band. In that context we discuss the possibility of plastic buckling under the action of concentrated forces. The analysis is restricted to a membrane prebuckling state of stress and hence applicable to relatively short shells.

1 Introduction

Elastic buckling of circular cylindrical shells under nonuniform (circumferentially varying) axial loads is practically independent of the load profile (Libai and Durban, 1973). Unless highly oscillatory loads are applied (Libai and Durban, 1977), or the shell is very short (Durban and Libai, 1974) or relatively thick (Durban and Libai, 1976), buckling will occur when the highest axial stress along the circumference attains the corresponding critical stress value of a uniformly compressed circular cylindrical shell. These observations follow from a detailed analysis, using the eigenfunction expansion method, and are valid within the framework of linear elastic buckling theory with a membrane prebuckling state of stress. Earlier studies by Abir and Nardo (1958), Bijlaard and Gallagher (1959) and Seide and Weingarten (1961) arrived at essentially the same conclusions.

A particularly interesting work by Hoff et al. (1964) examines the problem of buckling under axial compression (due to heating) distributed uniformly over an axial band of finite width. No appreciable increase of the critical stress, as compared with uniform loading over the entire circumference, has been found unless the width of the compressed band becomes very small.

Much less is known on plastic buckling of circular cylindrical shells under nonuniform axial loads. While plastic buckling under uniform compression has been studied in detail (Tvergaard, 1983a; 1983b; Ore and Durban, 1992), most available studies on plastic buckling under nonuniform loads deal with the important problem of pure bending. Reddy (1979a) performed tests on plastic buckling in pure bending of steel and aluminum tubes. The experimental data for the maximum compressive stress at buckling correlated to within ±5 percent with J_2 deformation theory predictions for buckling of uniformly compressed shells. In a companion paper Reddy (1979b) presented an approximate bifurcation analysis for pure bending, using the J_2 flow theory. An increase of up to about 35 percent in the buckling stress as compared to uniform compression was reported. The importance of considering nonlinear effects in the plastic bending behaviour and buckling of long cylindrical shells has been emphasized by Gellin (1980) and by Calladine (1983). The latter paper presents an original engineering-wise treatment of plastic buckling of tubes in pure bending. Fabian (1981) enhanced earlier studies on plastic buckling by examining the collapse of long tubes under combined bending and pressure load. A comprehensive investigation on elastoplastic instabilities in bending of long circular cylindrical shells is given in (Kyriakides and Ju, 1992; Ju and Kyriadides, 1992). These studies emphasize the importance of nonlinear prebuckling deformation and examine the details of various bifurcation modes with the J_2 deformation theory, though the primary path has been evaluated with the J_2 flow theory. For long shells made of Al 6061 T6 the authors identify experimentally and numerically three distinct regimes of plastic structural instability which depend on the radius to thickness ratio.

In this work we report the results of an investigation into the plastic analogue of the problem studied by Hoff et al. (1964) for elastic buckling. The basic setting is that of a circular cylindrical shell subjected to nonuniform axial compression by stresses that admit a piecewise-uniform circumferential profile. Thus, the elastoplastic instantaneous moduli are load dependent but remain constant within each separate segment. Assuming a membrane prebuckling state of stress it becomes possible to solve the governing buckling equations within each segment by separation of variables representation of the eigenmodes. Appropriate continuity conditions along the interfaces between the loaded segments provide the eigenvalue equation for critical stresses. The analysis is with both J_2 flow and deformation theories and accounts for arbitrary hardening. Sample calculations are presented, for pure bending and for uniform compression along a finite axial strip, for a number of metals. As expected, deformation theory predicts buckling loads which are always smaller than flow theory results. As in the elastic case, loading nonuniformity becomes important when the applied stresses concentrate over a narrow zone. Also discussed is the possible limit, when the loaded band becomes extremely narrow, of plastic buckling under concentrated axial forces. While neglecting the effect of prebuckling deformation the present paper highlights the influence of load nonuniformity, material

Contributed by the Applied Mechanics Division of THE AMERICAN SOCIETY OF MECHANICAL ENGINEERS for publication in the ASME JOURNAL OF APPLIED MECHANICS.

Discussion on the paper should be addressed to the Technical Editor, Professor Lewis T. Wheeler, Department of Mechanical Engineering, University of Houston, Houston, TX 77204-4792, and will be accepted until four months after final publication of the paper itself in the ASME JOURNAL OF APPLIED MECHANICS.

Manuscript received by the ASME Applied Mechanics Division, Sept. 23, 1997; final revision, June 30, 1998. Associate Technical Editor: S. Kyriakides.

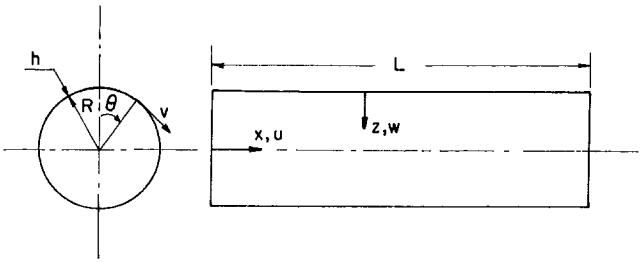

Fig. 1 Notation for circular cylindrical shells

nonlinearity and plasticity theory model. The validity of the present analysis is limited to relatively short shells that buckle in the classical sense of bifurcation theory, but excludes the Euler type column buckling.

2 Formulation of the Problem

A circular cylindrical shell is subjected to circumferentially varying edge loads given by the axial stress resultant

$$N_{xo} = \sigma_{xo}h = -\frac{Eh}{g^2}\rho S(\theta) \tag{2.1}$$

where, with the notation of Fig. 1, σ_{xo} is the axial stress, h is the thickness, E is the elastic modulus, ρ is the loading parameter (eigenvalue), $S(\theta)$—the piecewise-uniform circumferential profile of the load suitably normalized by $S_{\max} = S(\theta = 0) = 1$ and

$$g^2 = \sqrt{3(1-\nu^2)}\,\frac{R}{h} \tag{2.2}$$

with ν standing for Poisson's ratio, and R being the shell radius. Notice that in (2.1) $\sigma_{xo}^{\max} = \rho\sigma_c$ where $\sigma_c = Eh/g^2$ is the classical elastic bifurcation load in uniform axial compression.

Assuming a simple prebuckling membrane state of stress, where the only active component is (2.1), we wish to find the smallest value of ρ for which buckling is possible. To this end we employ the elastoplastic version of the Donnell type equations (Ore and Durban, 1992)

$$E_{xx}u_{,xx} + G_{x\theta}u_{,\theta\theta} + (E_{x\theta} + G_{x\theta})v_{,x\theta} - E_{x\theta}w_{,x} = 0 \tag{2.3a}$$

$$(E_{x\theta} + G_{x\theta})u_{,x\theta} + G_{x\theta}v_{,xx} + E_{\theta\theta}v_{,\theta\theta} - E_{\theta\theta}w_{,\theta} = 0 \tag{2.3b}$$

$$E_{xx}w_{,xxxx} + 2(E_{x\theta} + 2G_{x\theta})w_{,xx\theta\theta} + E_{\theta\theta}w_{,\theta\theta\theta\theta} - 12\left(\frac{R}{h}\right)^2[E_{x\theta}u_{,x} + E_{\theta\theta}(v_{,\theta} - w)] + 4E_o g^2\rho S(\theta)w_{,xx} = 0 \tag{2.3c}$$

Here (u, v, w) are the mid-surface velocities (Fig. 1) at buckling (normalized with respect to R). The instantaneous moduli (E_{xx}, $E_{x\theta}$, $E_{\theta\theta}$, $G_{x\theta}$) are determined by the in-surface constitutive relations

$$\dot\sigma_x = E_{xx}\dot\epsilon_x + E_{x\theta}\dot\epsilon_\theta \tag{2.4a}$$

$$\dot\sigma_\theta = E_{x\theta}\dot\epsilon_x + E_{\theta\theta}\dot\epsilon_\theta \tag{2.4b}$$

$$\dot\tau_{x\theta} = 2G_{x\theta}\dot\epsilon_{x\theta} \tag{2.4c}$$

where $(\dot\sigma_x, \dot\sigma_\theta, \dot\tau_{x\theta})$ and $(\dot\epsilon_x, \dot\epsilon_\theta, \dot\epsilon_{x\theta})$ are the usual in-surface stress rates and strain rates, respectively, x is the axial coordinate (Fig. 1) nondimensionalized with respect to R, and

$$E_0 = \frac{E}{1-\nu^2} \tag{2.5}$$

Note that all three velocity components depend on (x, θ).

The boundary conditions that supplement Eqs. (2.3) are those of simply supported ends, namely

$$u_{,x} = 0 \quad v = 0 \quad w = 0 \quad w_{,xx} = 0 \quad \text{at} \quad x = 0$$

$$\text{and} \quad x = \frac{L}{R} \tag{2.6}$$

Material behavior is modelled by the two small strain J_2 theories of plasticity. For the flow theory we have, with the standard notation,

$$\dot\sigma_{ij} = 2G\dot\epsilon_{ij} + \lambda\delta_{ij}\dot\epsilon_{kk} - 3(G - G_t)\frac{S_{ij}S_{kl}\dot\epsilon_{kl}}{\sigma_e^2} \tag{2.7}$$

where (G, λ) are the Lamé constants, G_t is the tangent shear modulus defined by

$$\frac{1}{G_t} = \frac{1}{G} + 3\left(\frac{1}{E_t} - \frac{1}{E}\right) \tag{2.8}$$

with E_t denoting the uniaxial tangent modulus, S_{ij} is the stress deviator, and σ_e is the effective stress

$$\sigma_e^2 = \tfrac{3}{2}S_{ij}S_{ij} \tag{2.9}$$

Specializing (2.7) for the uniaxial prebuckling state (2.1) we get the instantaneous moduli

$$E_{xx} = H_t\frac{\eta_t + 3}{4} \quad E_{\theta\theta} = H_t\eta_t$$

$$E_{x\theta} = H_t\frac{\eta_t + 2\nu - 1}{2} \quad G_{x\theta} = G \tag{2.10}$$

where

$$H_t = \frac{4E}{(5-4\nu)\eta_t - (1-2\nu)^2} \quad \eta_t = \frac{E}{E_t} \tag{2.11}$$

The rate form of the deformation theory reads

$$\dot\sigma_{ij} = 2G_s\dot\epsilon_{ij} + \lambda_s\delta_{ij}\dot\epsilon_{kk} - 3(G_s - G_t)\frac{S_{ij}S_{kl}\dot\epsilon_{kl}}{\sigma_e^2} \tag{2.12}$$

where (G_s, λ_s) are the secant Lamé-like moduli

$$G_s = \frac{E_s}{2(1+\nu_s)} \quad \lambda_s = \frac{\nu_s E_s}{(1+\nu_s)(1-2\nu_s)} \tag{2.13}$$

E_s is the uniaxial secant modulus, and the plastic Poisson ratio is defined by

$$\nu_s = \frac{1}{2} - \left(\frac{1}{2} - \nu\right)\frac{E_s}{E} \tag{2.14}$$

The instantaneous moduli associated with (2.12) are

$$E_{xx} = H_s\frac{\eta_t + 3\eta_s}{4} \quad E_{\theta\theta} = H_s\eta_t$$

$$E_{x\theta} = H_s\frac{\eta_t + 2\nu - 1}{2} \quad G_{x\theta} = G_s \tag{2.15}$$

where

$$H_s = \frac{4E}{(3\eta_s + 2 - 4\nu)\eta_t - (1-2\nu)^2} \quad \eta_s = \frac{E}{E_s} \tag{2.16}$$

The instantaneous moduli depend on the level of the effective stress which for our problem is given, via (2.1), by

$$\frac{\sigma_e}{E} = \frac{\rho}{g^2}\,|S(\theta)| \tag{2.17}$$

Thus, the eigenvalue ρ enters the coefficients of the partial differential Eqs. (2.3). For example, with the Ramberg-Osgood characteristic

$$\epsilon = \frac{\sigma_e}{E} + K\left(\frac{\sigma_e}{E}\right)^n \tag{2.18}$$

where ϵ is the total strain and (n, K) are material parameters, we find

$$\eta_t = 1 + nK\left(\frac{\rho}{g^2}\,|S(\theta)|\right)^{n-1} \tag{2.19}$$

$$\eta_s = 1 + K\left(\frac{\rho}{g^2}\,|S(\theta)|\right)^{n-1} \tag{2.20}$$

The problem lies in finding an eigensolution of Eqs. (2.3), along with the boundary data (2.6), which is associated with the minimal eigenvalue ρ. The difficulty in arriving at that solution arises from the circumferential variation (θ-dependence) of the instantaneous moduli in (2.3). However, as we shall see in the next section, when the load profile $S(\theta)$ is piecewise-uniform it becomes possible to obtain a piecewise separation of variables solution of the governing eigenvalue system.

3 The Eigenmodes

Consider the two segment loading

$$S(\theta) = \begin{cases} 1 & -\theta_0 \le \theta \le \theta_0 \\ -\xi & \theta_0 < \theta \le 2\pi - \theta_0 \end{cases} \tag{3.1}$$

With $\xi = 1$ the distribution (3.1) describes pure bending, and when $\xi = 0$ we have the case of a uniformly compressed axial strip of width $b = 2R\theta_0$.

Since $S(\theta)$ is piecewise uniform, Eqs. (2.3) admit separation of variables solutions of the form

$$u = A\cos(k\beta x)e^{p\theta} \tag{3.2a}$$

$$v = B\sin(k\beta x)e^{p\theta} \tag{3.2b}$$

$$w = C\sin(k\beta x)e^{p\theta} \tag{3.2c}$$

where (A, B, C) are constants, k is an integer, $\beta = \pi R/L$, and p is to be determined separately for each segment. The field (3.2) satisfies the boundary conditions (2.6). When substituted in (2.3) we arrive at the algebraic system

$$[-(k\beta)^2E_{xx} + p^2G_{x\theta}]A + (k\beta)p(E_{x\theta} + G_{x\theta})B - (k\beta)E_{x\theta}C = 0 \tag{3.3a}$$

$$-(k\beta)p(E_{x\theta} + G_{x\theta})A + [-(k\beta)^2G_{x\theta} + p^2E_{\theta\theta}]B - pE_{\theta\theta}C = 0 \tag{3.3b}$$

$$12(k\beta)\left(\frac{R}{h}\right)^2 E_{x\theta}A - 12p\left(\frac{R}{h}\right)^2 E_{\theta\theta}B + \left[(k\beta)^4E_{xx} - 2(k\beta)^2p^2(E_{x\theta} + 2G_{x\theta}) + p^4E_{\theta\theta} + 12\left(\frac{R}{h}\right)^2 E_{\theta\theta} - 4(k\beta)^2E_0g^2\rho S(\theta)\right]C = 0 \tag{3.3c}$$

For a nontrivial solution it is required that the determinant of the system (3.3) should vanish. This leads to the characteristic equation for the roots p

$$[E_{\theta\theta}p^4 - 2(E_{x\theta} + 2G_{x\theta})(k\beta)^2p^2 + E_{xx}(k\beta)^4 - 4(k\beta)^2E_0g^2\rho S(\theta)] \times \left[E_{\theta\theta}p^4 - \left(\frac{EE_0}{G_{x\theta}}\rho_{cl}^2 - 2E_{x\theta}\right)(k\beta)^2p^2 + E_{xx}(k\beta)^4\right] + 4(k\beta)^4E_0^2g^4\rho_{cl}^2 = 0 \tag{3.4}$$

where

$$\rho_{cl}^2 = \frac{1-\nu^2}{E^2}(E_{xx}E_{\theta\theta} - E_{x\theta}^2) \tag{3.5}$$

The classical buckling load for an axially compressed isotropic elastic shell, with $S(\theta) = 1$, is $\rho = \rho_{cl} = 1$. Here, however, it is convenient to use (3.5) as a nominal reference which depends on the eigenvalue ρ itself through the instantaneous moduli.

Equation (3.4) has 8 complex roots which will be labelled as $\pm p_i$ $(i = 1, \ldots, 4)$ where $p_3 = \bar{p}_1$ and $p_4 = \bar{p}_2$. The corresponding eigenmodes are either symmetric or antisymmetric with respect to $\theta = 0$. For symmetric buckling

$$u = \cos(k\beta x)\sum_{i=1}^{4} C_ia_i\cosh p_i\theta \tag{3.6a}$$

$$v = \sin(k\beta x)\sum_{i=1}^{4} C_ib_i\sinh p_i\theta \tag{3.6b}$$

$$w = \sin(k\beta x)\sum_{i=1}^{4} C_i\cosh p_i\theta \tag{3.6c}$$

where

$$a_i = -\frac{(k\beta)}{P_i}[E_{\theta\theta}p_i^2 + E_{x\theta}(k\beta)^2] \quad i = 1, \ldots, 4 \tag{3.7a}$$

$$b_i = -\frac{p_ia_i}{(k\beta)} - \left(\frac{p_i}{P_i}\right)\frac{EE_0}{G_{x\theta}}\rho_{cl}^2(k\beta)^2 \quad i = 1, \ldots, 4 \tag{3.7b}$$

and

$$P = E_{\theta\theta}p^4 - \left(\frac{EE_0}{G_{x\theta}}\rho_{cl}^2 - 2E_{x\theta}\right)(k\beta)^2p^2 + E_{xx}(k\beta)^4 \tag{3.8}$$

with $P_i = P(p = p_i)$ $i = 1, \ldots, 4$.

It is important to note that the roots p_i depend on the shell geometric parameters R/h and $L/\sqrt{Rh}$, on the material properties, the eigenvalue ρ, the axial half waves number k, and the load parameter ξ defined in (3.1). Thus, a different velocity field (3.6) will apply to each segment. For antisymmetric buckling we can use (3.6) with the transformations $\sinh p_i\theta \to \cosh p_i\theta$ and $\cosh p_i\theta \to \sinh p_i\theta$.

The equation for the eigenvalues ρ is provided by appropriate continuity conditions at the interfaces $\theta = \pm\theta_0$. Obviously, the velocity w and its derivative $w_{,\theta}$ should remain continuous. Also, the resultants rates $\dot{N}_\theta$ and $\dot{N}_{x\theta}$ cannot suffer a jump at the interfaces. So both quantities

$$\dot{N}_\theta = E_{x\theta}u_{,x} + E_{\theta\theta}(v_{,\theta} - w) \tag{3.9}$$

and

$$\dot{N}_{x\theta} = G_{x\theta}(u_{,\theta} + v_{,x}) \tag{3.10}$$

should be the same on both sides of the generators $\theta = \pm\theta_0$ when evaluated for each segment. An interesting phenomenon here is—with the exception of $G_{x\theta} = G$ in (2.10) and the case of the flow theory with linear hardening—the associated jump,

along the interfaces, in the instantaneous moduli (E_{xx}, $E_{x\theta}$, $E_{\theta\theta}$, $G_{x\theta}$) as determined by the loading (3.1). It is also required that the effective shear resultant rate (Hoff, 1954)

$$\dot{Q}_\theta^{\text{eff}} = \frac{1}{R}(\dot{M}_{\theta,\theta} - \dot{M}_{x\theta,x}) + \frac{1}{R}\dot{M}_{\theta x,x} = \frac{1}{R}(\dot{M}_{\theta,\theta} - 2\dot{M}_{x\theta,x}) \tag{3.11}$$

remains continuous. Thus

$$-(E_{x\theta}w_{,xx\theta} + E_{\theta\theta}w_{,\theta\theta\theta}) - 4G_{x\theta}w_{,xx\theta} \tag{3.12}$$

is continuous. (Recall that $\dot{M}_{\theta x} = -\dot{M}_{x\theta}$.)

Finally, the moment rate $\dot{M}_\theta$ and the velocities (u, v) provide three additional continuity conditions. For $\dot{M}_\theta$ the relevant quantity which should remain continuous at $\theta = \pm\theta_0$ is

$$E_{xx}w_{,xx} + E_{\theta\theta}w_{,\theta\theta} \tag{3.13}$$

Since the eigenmodes (3.6) are not periodic in the circumferential direction there is no guarantee that the appropriate smoothness conditions at $\theta = \pm\pi$ will be met. For example, symmetric buckling modes (3.6) should give $w_{,\theta} = 0$ at $\theta = \pm\pi$, while antisymmetric patterns should give $w = 0$ at $\theta = \pm\pi$. Solutions of the type (3.6), or its antisymmetric counterpart, clearly do not satisfy those conditions and in order to overcome that difficulty we introduce a new coordinate $\bar{\theta}$ defined as

$$\bar{\theta} = \theta - \pi \tag{3.14}$$

so that at $\theta = \pm\theta_0$ we have $\bar{\theta} = \mp(\pi - \theta_0) = \mp\bar{\theta}_0$. The symmetric solution in the segment $\theta_0 < \theta < 2\pi - \theta_0$ is now written as

$$u = \cos(k\beta x)\sum_{i=1}^{4} C_i^* a_i^* \cosh p_i^*\bar{\theta} \tag{3.15a}$$

$$v = \sin(k\beta x)\sum_{i=1}^{4} C_i^* b_i^* \sinh p_i^*\bar{\theta} \tag{3.15b}$$

$$w = \sin(k\beta x)\sum_{i=1}^{4} C_i^* \cosh p_i^*\bar{\theta} \tag{3.15c}$$

where the symbol $(\ )^*$ indicates quantities evaluated at that segment. Antisymmetric modes are obtained from (3.15) with the exchanges of $\sinh p_i^*\bar{\theta}$ to $\cosh p_i^*\bar{\theta}$ and of $\cosh p_i^*\bar{\theta}$ to $\sinh p_i^*\bar{\theta}$.

Compliance with the continuity conditions along the interfaces at $\theta = \pm\theta_0$ (or $\bar{\theta} = \mp\bar{\theta}_0$) leads to an algebraic eigenvalue equation for ρ. Thus, for symmetric buckling modes, we have at ($\theta = \pm\theta_0$, $\bar{\theta} = \mp\bar{\theta}_0$) the following eight continuity conditions: (i) continuity of u, v, w and $w_{,\theta}$, from (3.6) and (3.15),

$$\sum_{i=1}^{4} C_i a_i \cosh p_i\theta_0 - \sum_{i=1}^{4} C_i^* a_i^* \cosh p_i^*\bar{\theta}_0 = 0 \tag{3.16}$$

$$\sum_{i=1}^{4} C_i b_i \sinh p_i\theta_0 + \sum_{i=1}^{4} C_i^* b_i^* \sinh p_i^*\bar{\theta}_0 = 0 \tag{3.17}$$

$$\sum_{i=1}^{4} C_i \cosh p_i\theta_0 - \sum_{i=1}^{4} C_i^* \cosh p_i^*\bar{\theta}_0 = 0 \tag{3.18}$$

$$\sum_{i=1}^{4} C_i p_i \sinh p_i\theta_0 + \sum_{i=1}^{4} C_i^* p_i^* \sinh p_i^*\bar{\theta}_0 = 0 \tag{3.19}$$

(ii) continuity of $\dot{N}_\theta$, $\dot{N}_{x\theta}$, $\dot{Q}_\theta^{\text{eff}}$ and $\dot{M}_\theta$, from (3.9)–(3.10) and (3.12)–(3.13),

$$\sum_{i=1}^{4} C_i[-E_{x\theta}(k\beta)a_i + E_{\theta\theta}(b_i p_i - 1)]\cosh p_i\theta_0 - \sum_{i=1}^{4} C_i^*[-E_{x\theta}^*(k\beta)a_i^* + E_{\theta\theta}^*(b_i^* p_i^* - 1)]\cosh p_i^*\bar{\theta}_0 = 0 \tag{3.20}$$

$$\sum_{i=1}^{4} C_i G_{x\theta}[a_i p_i + (k\beta)b_i]\sinh p_i\theta_0 + \sum_{i=1}^{4} C_i^* G_{x\theta}^*[a_i^* p_i^* + (k\beta)b_i^*]\sinh p_i^*\bar{\theta}_0 = 0 \tag{3.21}$$

$$\sum_{i=1}^{4} C_i[(E_{x\theta} + 4G_{x\theta})(k\beta)^2 p_i - E_{\theta\theta}p_i^3]\sinh p_i\bar{\theta}_0 + \sum_{i=1}^{4} C_i^*[(E_{x\theta}^* + 4G_{x\theta}^*)(k\beta)^2 p_i^* - E_{\theta\theta}^* p_i^{*3}]\sinh p_i^*\bar{\theta}_0 = 0 \tag{3.22}$$

$$\sum_{i=1}^{4} C_i[-E_{xx}(k\beta)^2 + E_{\theta\theta}p_i^2]\cosh p_i\theta_0 - \sum_{i=1}^{4} C_i^*[-E_{xx}^*(k\beta)^2 + E_{\theta\theta}^* p_i^{*2}]\cosh p_i^*\bar{\theta}_0 = 0 \tag{3.23}$$

Here, moduli (E_{xx}^*, $E_{x\theta}^*$, $E_{\theta\theta}^*$, $G_{x\theta}^*$) are evaluated in the segment $\bar{\theta} < |\pi - \theta_0|$ and p_i^* ($i = 1, \ldots, 4$) are the corresponding roots of (3.4) in that segment.

For a nontrivial solution of (3.16)–(3.23) we require that the 8×8 determinant of that system vanish. This generates a transcendental equation which can be solved numerically for the smallest eigenvalue ρ. Repeating the analysis for antisymmetric modes we arrive at a similar system but with the (cosh, sinh) functions replaced by (sinh, cosh) in all equations.

4 Numerical Examples and Discussion

Consider first the simple case of pure bending where the load profile in (3.1) is described with $\theta_0 = \pi/2$ and $\xi = 1$. Thus, half of the circumference is under compressive loads (2.1) while the other half is in tension of the same magnitude. For given material properties, loading and geometric parameters the solution begins by assuming a value for the axial wave number k and guessing an initial value for the buckling eigenvalue ρ. Next, we calculate the instantaneous moduli from (2.10), or (2.15), and determine the corresponding roots of (3.4) in each of the loaded segments. Once the roots p_i and p_i^* have been found it is possible to evaluate (a_i, b_i) and (a_i^*, b_i^*) from (3.7)–(3.8) and finally calculate the determinant of the system (3.17)–(3.23) along with its antisymmetric counterpart. The procedure is then repeated iteratively with a new guess of the eigenvalue ρ until the governing 8×8 determinant vanishes. The method has to allow for all competing modes to be considered by employing a search procedure among different values of k to trace the smallest possible eigenvalue ρ within the entire space of symmetric and antisymmetric eigenmodes. The essence of this procedure lies in tracing the smallest root of the 8×8 determinant and satisfactory convergence was achieved to three significant figures in the value of ρ.

Calculations were performed with three materials characterized by the following Ramberg-Osgood parameters:

Commercial AL	$E = 6.87 \cdot 10^4$ MPa	$\nu = 0.3$	$K = 1.27 \cdot 10^{10}$	$n = 3.72$
AL 2014 T6	$E = 6.9 \cdot 10^4$ MPa	$\nu = 0.33$	$K = 6.08 \cdot 10^{31}$	$n = 15.62$
ST AISI 4340	$E = 2.01 \cdot 10^5$ MPa	$\nu = 0.28$	$K = 7.61 \cdot 10^{54}$	$n = 27.6$

Table 1 Critical eigenvalues in bending and in uniform compression. In all cases the axial wave number is $k = 2$.

Material	Flow Theory		Deformation Theory	
	Bending	Uniform	Bending	Uniform
Commercial AL	0.073	0.069	0.042	0.041
AL 2014 T6	0.502	0.490	0.487	0.485
ST AISI 4340	0.664	0.642	0.660	0.641

Results for a representative shell with $L/R = 1$ and $R/h = 50$, shown in Table 1, reveal that deformation theory predictions are consistently below flow theory results and that critical values of ρ in bending are only slightly higher than in uniform compression. Recall, by comparison, that in elastic buckling $\rho = 1$ for both uniform compression and pure bending. These findings are similar to the results obtained by Reddy (1979a, 1979b).

Our next example is the case of axial compression over a finite strip $\theta < |\theta_0|$ with the other zone remaining stress free (Fig. 2). Here we have in (3.1) that $\xi = 0$ but the solution procedure detailed earlier remains essentially unchanged. Figure 3 displays the critical eigenvalues, over a range of loaded band widths, for shells with $L/R = 1$ and $R/h = 50$. Also shown in Fig. 3 are the buckling values of ρ for an elastic shell with $\nu = 0.3$. That curve is in complete agreement with the results obtained by Hoff et al. (1964).

As expected, flow theory predictions in Fig. 3 are higher than deformation theory results for critical loads. The difference between the buckling loads obtained from the two plasticity models increases as the width of the loaded strip becomes smaller. For wide strips, however, the critical eigenvalue approaches, with both theories, its corresponding uniform load value. The difference between the predictions of flow and deformation theories increases with decreasing θ_0 and with decreasing hardening exponent n.

It is reasonable to expect that when θ_0 becomes very small the resultant compressive load should approach at buckling an asymptotic value. A convenient measure for elastic buckling of circular cylindrical shells under concentrated axial loads (Libai and Durban, 1977) is the parameter k defined by (not to be confused with the axial wave number in (3.2))

$$P = k\frac{EhR}{g^3} \tag{4.1}$$

where P is the buckling force. Libai and Durban (1977) estimated a lower bound on the value of k, in elastic buckling, to be $k = 1.337$. Comparing (4.1) with the resultant axial force in our problem, namely

$$P = 2\theta_0\rho\frac{EhR}{g^2} \tag{4.2}$$

we find the relation

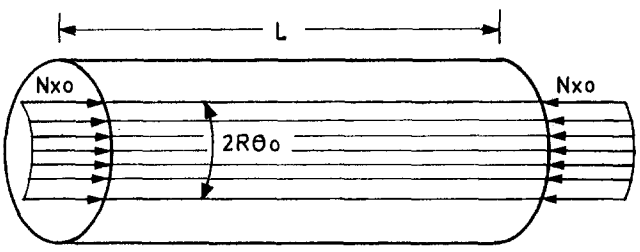

Fig. 2 Uniform axial compression over a finite strip $\theta < |\theta_0|$

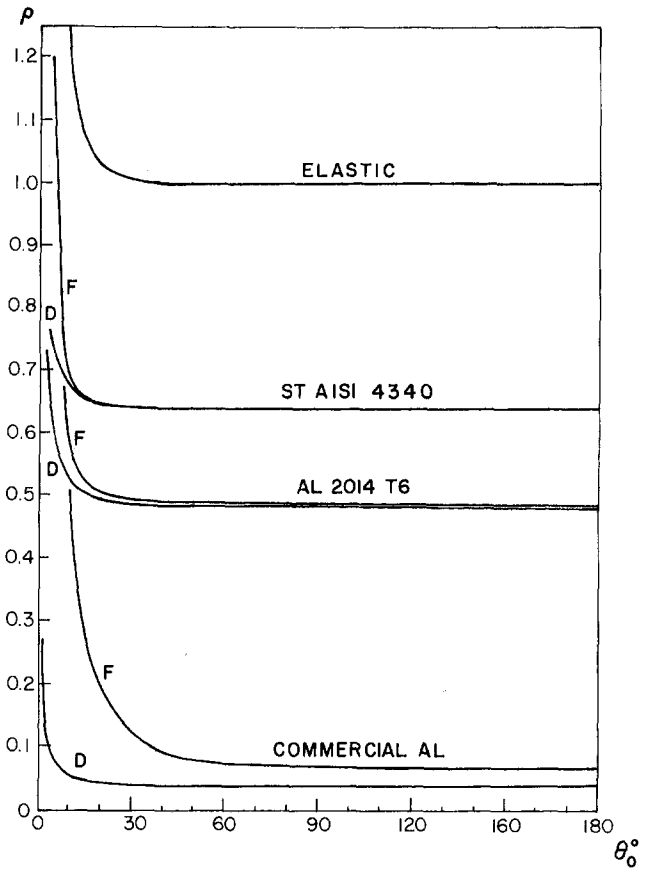

Fig. 3 Critical eigenvalues for axial loading along a finite axial strip. $R/L = 1$, $R/h = 50$. Elastic curve is for $\nu = 0.3$. F–flow theory, D–deformation theory.

$$k = 2g\theta_0\rho \tag{4.3}$$

The limit of (4.3) as $\theta_0 \to 0$ has been evaluated from previous calculations for the elastic shell, with $L/R = 1$ $R/h = 50$ and $\nu = 0.3$. Calculations with values of θ_0 up to 10^{-4} (degrees) have confirmed the limit of $k = 1.99$ which is about 49% higher than the estimate of Libai and Durban (1977). Values close to $k = 1.99$ have been obtained over a range of shell geometries by varying L/R and R/h and so we can put (4.1) in the form, with $\nu = 0.3$,

$$P \approx 0.94\frac{Eh^3}{\sqrt{Rh}} \tag{4.4}$$

for the elastic buckling of the shell under concentrated forces.

The dependence of k on θ_0 is traced in Fig. 4 for the same examples shown earlier in Fig. 3. Flow theory curves approach approximately the common limit of $k \approx 1.9$ for all three metals as $\theta_0 \to 0$. This behaviour can be explained by considering the asymptotic values of the flow theory instantaneous moduli (2.10)–(2.11) in the deep plastic range. Indeed, when η_t becomes very large we find the asymptotic expressions

$$E_{xx} \to \frac{E}{5-4\nu} \quad E_{x\theta} \to \frac{2E}{5-4\nu}$$

$$E_{\theta\theta} \to \frac{4E}{5-4\nu} \quad G_{x\theta} = G \tag{4.5}$$

which are in fact constants independent of plastic properties. By comparison, the initial elastic values of the instantaneous moduli are

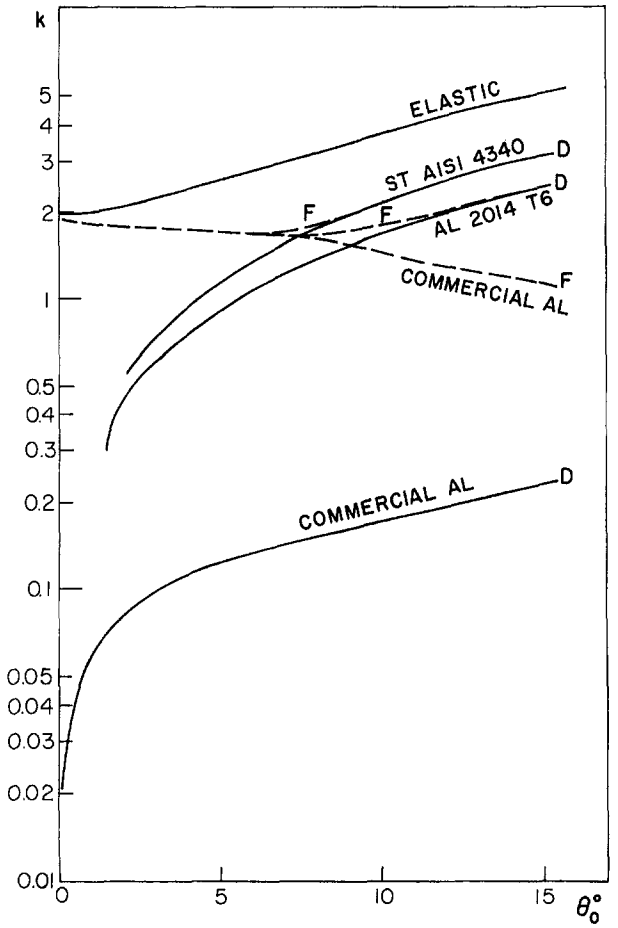

Fig. 4 Concentrated load parameter k for various values of θ_0. Solid lines (D) are for deformation theory, broken line (F) are for flow theory. Also shown in the elastic curve. Notice that all flow theory curves converge to approximately the same value of k.

$$E_{xx} = \frac{E}{1-\nu^2} \quad E_{x\theta} = \frac{\nu E}{1-\nu^2}$$

$$E_{\theta\theta} = \frac{E}{1-\nu^2} \quad G_{x\theta} = G \tag{4.6}$$

However, since the eigenvalue ρ depends only on (plastic/elastic) moduli ratio (e.g. $E_{x\theta}/E$)—as is apparent from the characteristic Eq. (3.4) and the buckling determinant (3.16)–(3.23)—flow theory curves in Fig. 4 should approach approximately a common limit, as $\theta_0 \to 0$, with only slight differences due to variations in Poisson's ratio. Moduli (4.5) represent a limiting state of an anisotropic elastic solid with constant moduli. By contrast, no definite limit for k has been detected with deformation theory analysis (Fig. 4) even for fairly small values of θ_0. The deformation theory instantaneous moduli (2.15)–(2.16) decrease monotonously with advancing plasticity and accordingly parameter k in Fig. 4 does not appear to converge to a finite limit when $\theta_0 \to 0$. However, Fig. 4 amplifies the constitutive sensitivity associated with predicting plastic buckling under concentrated loads, suggesting, in particular, that a nonlinear stability analysis is required to investigate problems of that nature.

Acknowledgment

This research was supported by the fund for promotion of research at the Technion.

References

Abir, D., and Nardo, S.V., 1958, "Thermal Buckling of Circular Cylindrical Shells Under Circumferential Temperature Gradients," *J. Aerospace Sciences*, Vol. 26, No. 12, pp. 803–808.

Bijlaard, P.P., and Gallagher, R.H., 1959, "Elastic Instability of a Cylindrical Shell Under Arbitrary Circumferential Variation of Axial Stresses," *J. Aerospace Sciences*, Vol. 27, No. 11, pp. 854–858, 866.

Calladine, C.R., 1983, "Plastic Buckling of Tubes in Pure Bending," *Collapse*, Thompson, J.M.T. and Hunt, G.W., eds., Cambridge Univ. Press.

Durban, D., and Libai, A., 1974, "Buckling of Short Cylindrical Shells Under Axial Compression," *AIAA J.*, Vol. 12, No. 7, pp. 909–914.

Durban, D., and Libai, A., 1976, "Influence of Thickness on the Stability of Circular Cylindrical Shells Subjected to Nonuniform Axial Compression," *Israel J. Tech.*, Vol. 14, No. 1–2, pp. 9–17.

Fabian, O., 1981, "Elastic-Plastic Collapse of Long Tubes Under Combined Bending and Pressure Load," *Ocean Engng.*, Vol. 8, pp. 295–330.

Gellin, S., 1980, "The Plastic Buckling of Long Cylindrical Shells Under Pure Bending," *Int. J. Solids Struct.*, Vol. 16, pp. 397–407.

Hoff, N.J., 1954, "Boundary-Value Problems of the Thin-Walled Circular Cylinder," ASME *Journal of Applied Mechanics*, Vol. 21, pp. 343–350.

Hoff, N.J., Chao, C.C., and Madsen, W.A., 1964, "Buckling of a Thin-Walled Circular Cylindrical Shell Heated Along an Axial Strip," ASME *Journal of Applied Mechanics*, Vol. 31, pp. 253–258.

Ju, G.T., and Kyriakides, S., 1992, "Bifurcation and Localization Instabilities in Cylindrical Shells under Bending—II. Predictions," *Int. J. Solids Struct.*, Vol. 29, pp. 1143–1171.

Kyriakides, S., and Ju, G.T., 1992, "Bifurcation and Localization Instabilities in Cylindrical Shells under Bending—I. Experiments," *Int. J. Solids Struct.*, Vol. 29, pp. 1117–1142.

Libai, A., and Durban, D., 1973, "A Method for Approximate Stability Analysis and its Application to Circular Cylindrical Shells Under Circumferentially Varying Edge Loads," ASME JOURNAL OF APPLIED MECHANICS, Vol. 40, pp. 971–976.

Libai, A., and Durban, D., 1977, "Buckling of Cylindrical Shells Subjected to Nonuniform Axial Loads," ASME JOURNAL OF APPLIED MECHANICS, Vol. 44, pp. 714–720.

Ore, E., and Durban, D., 1992, "Elastoplastic Buckling of Axially Compressed Circular Cylindrical Shells," *Int. J. Mech. Sci.*, Vol. 34, pp. 727–742.

Reddy, B.D., 1979a, "An Experimental Study of the Plastic Buckling of Circular Cylinders in Pure Bending," *Int. J. Solids Struct.*, Vol. 15, pp. 669–683.

Reddy, B.D., 1979b, "Plastic Buckling of a Cylindrical Shell in Pure Bending," *Int. J. Mech. Sci.*, Vol. 21, pp. 671–679.

Seide, P., and Weingarten, V.I., 1961, "On the Buckling of Circular Cylindrical Shells Under Pure Bending," ASME JOURNAL OF APPLIED MECHANICS, Vol. 28, pp. 112–116.

Tvergaard, V., 1983a, "Plastic Buckling of Axially Compressed Circular Cylindrical Shells," *Thin-Walled Struct.*, Vol. 1, pp. 139–163.

Tvergaard, V., 1983b, "On the Transition from a Diamond Mode to an Axisymmetric Mode of Collapse in Cylindrical Shells," *Int. J. Solids Struct.*, Vol. 19, pp. 845–856.

A Method for Exact Series Solutions in Structural Mechanics

J. T.-S. Wang[1]
School of Civil and Environmental Engineering,
Georgia Institute of Technology,
Atlanta, GA 30332

C.-C. Lin
Department of Applied Mathematics,
National Chung-Hsing University,
Taichung, Taiwan 402, R.O.C.

A systematic analysis method for solving boundary value problems in structural mechanics is presented. Euler-Lagrange differential equations are transformed into integral form with respect to sinusoidal weighting functions. General solutions are represented by complete sets of functions without being concerned with boundary conditions in advance while all boundary conditions are satisfied in the process. The convergence of results is assured, and the procedure leads to pointwise exact solutions. A number of simple structural mechanics problems of stress, buckling, and vibration analyses are presented for illustrative purposes. All results have verified the exactness of solutions, and indicate that this unified method is simple to use and effective.

Introduction

Structural mechanics problems of beams, plates, and shells are generally concerned with ordinary and two-dimensional differential equations with associated boundary conditions for stress, buckling, and vibration analyses. These equations, derived from variational principles, are Euler-Lagrange equations. Well-established theories for these structural components used satisfactorily in practical applications can be found in an uncountable number of books such as those in Timoshenko and Woinowsky-Kreiger (1959), Washizu (1968), Boresi and Sidebottom (1985), Ross (1996), and Hjelmstad (1997). Various numerical methods in structural mechanics may be found in Bittar and Sejnoha (1965). While finite element and boundary element methods are powerful tools for analyzing large structural systems, analytical methods are more desirable for investigating fundamental behaviors and characteristics of structural components. Although the Fourier series has probably been used the most in boundary value problems, its conventional applications in structural mechanics have often been restricted to specific classes of boundary conditions. The present method broadens the use of the Fourier series. While the Ritz-Galerkin and other energy-based methods provide effective procedures for approximate solutions, functions reasonably representing structural response or the trial functions must be selected for each case individually. Consequently, the selection or generation of trial functions may become difficult because of boundary conditions, especially for structures with moving or elastic end supports. Another disadvantage of these approximate methods is that their procedures often involve inconvenient or cumbersome integrations and differentiations of functions in the process. Also, as solutions of these approximate methods converge at best in energy, they do not assure pointwise accuracy. Hence, they are generally used for buckling and free-vibration analyses but not for stress analysis. In this paper, a unified procedure leading to exact solutions of structural mechanics problems with all types of boundary conditions, and a number of simple structural mechanics problems involving ordinary differential equations in stress, buckling, and vibration analyses for illustrative purposes are presented.

General Concept and Basic Relations

For the convenience of discussion, problems involving ordinary differential equations with all types of boundary conditions are considered. The general concept of the method of analysis is to require the governing Euler-Lagrange equations for structural mechanics problems be satisfied with respect to a complete set of sinusoidal weighting functions, and the general solution of the dependent variable is represented by a complete set of functions. While any type of complete set of functions can be used without being concerned with the boundary conditions in advance, only Fourier and power series are used in this study. The governing differential equations for boundary value problems in structural mechanics may be given in the following general form:

$$H(W) - Q = 0 \tag{1}$$

in which the linear differential operator H may have variable coefficients which are assumed to be in the form of x^j with x being the spatial coordinate and j being an integer in this study; the dependent variable W may represent displacement or stress in the structure, and Q may be the loading. Equation (1), representing Euler-Lagrange equations, along with boundary conditions, is derived from the variational principle in structural mechanics. The procedure of the analysis method is to multiply Eq. (1) by $\sin \alpha_m x$ or $\cos \alpha_m x$ for $m = 0$ to ∞ first, and then integrate through the interval of the region from $x = 0$ to L for each m as follows:

$$\int_0^L [H(W) - Q](\sin \alpha_m x \quad \text{or} \quad \cos \alpha_m x)dx = 0 \tag{2}$$

where $\alpha_m = m\pi/L$. Integrating Eq. (2) by parts successively, and defining

$$(\hat{W}^s_{jm} \text{ or } \hat{W}^c_{jm}) = \int_0^L x^j W(\sin \alpha_m x \text{ or } \cos \alpha_m x)dx$$

$$(\bar{W}_m \text{ or } W^*_m) = \int_0^L W(\sin \alpha_m x \text{ or } \cos \alpha_m x)dx \tag{3}$$

in which the overhat denotes transformed quantities and x^j is related to the coefficients of the differential operator H, one arrives at the following transformed equation in general form:

$$f(W_0, W_1, W_0', W_1', W_0'', W_1'' \ldots, \bar{Q}_m, Q^*_m) + g(\hat{W}^s_{jm}, \hat{W}^c_{jm}) = 0 \tag{4}$$

[1] To whom correspondence should be addressed: 2879 Greenbrook Way, N.E., Atlanta, GA 30345. e-mail: ewang01@emory.edu.

Contributed by the Applied Mechanics Division of THE AMERICAN SOCIETY OF MECHANICAL ENGINEERS for publication in the ASME JOURNAL OF APPLIED MECHANICS.

Discussion on the paper should be addressed to the Technical Editor, Professor Lewis T. Wheeler, Department of Mechanical Engineering, University of Houston, Houston, TX 77204-4792, and will be accepted until four months after final publication of the paper itself in the ASME JOURNAL OF APPLIED MECHANICS.

Manuscript received by the ASME Applied Mechanics Division, Feb. 10, 1998; final revision, Feb. 2, 1999. Associate Technical Editor: W. K. Liu.

where subscripts 0 and 1 of physical quantities denote the corresponding quantities at $x = 0$ and L, respectively, and primes denote differentiations with respect to x. Hence, the governing differential Eq. (1) is transformed to Eq. (4) in integral form of W. Some of the quantities in the function f in Eq. (4) may be given values while others are not. For those which are not specified quantities, they are determined eventually when the boundary conditions associated with Eq. (1) are used. Since the linear differential operator H may involve a combination of derivatives of various orders, derivatives of W up to fourth degree transformed with respect to $\sin \alpha_m x$ for potential applications are listed as follows:

$$\int_0^L \frac{dW}{dx} \sin \alpha_m x dx = -\alpha_m W_m^*$$

$$\int_0^L \frac{d^2W}{dx^2} \sin \alpha_m x dx = -\alpha_m[(-1)^m W_1 - W_0] - \alpha_m^2 \bar{W}_m$$

$$\int_0^L \frac{d^3W}{dx^3} \sin \alpha_m x dx = -\alpha_m[(-1)^m W_1' - W_0'] + \alpha_m^3 W_m^*$$

$$\int_0^L \frac{d^4W}{dx^4} \sin \alpha_m x dx = -\alpha_m[(-1)^m W_1'' - W_0''] + \alpha_m^3[(-1)^m W_1 - W_0] + \alpha_m^4 \bar{W}_m. \quad (5)$$

On the other hand, when $\cos \alpha_m x$ as weighting functions are used, the corresponding list becomes

$$\int_0^L W dx = W_0^*$$

$$\int_0^L \frac{d^r W}{dx^r} dx = \frac{d^{(r-1)}W}{dx^{(r-1)}}(L) - \frac{d^{(r-1)}W}{dx^{(r-1)}}(0) \quad (6)$$

for $m = 0$,

$$\int_0^L \frac{dW}{dx} \cos \alpha_m x dx = [(-1)^m W_1 - W_0] + \alpha_m \bar{W}_m$$

$$\int_0^L \frac{d^2W}{dx^2} \cos \alpha_m x dx = [(-1)^m W_1' - W_0'] - \alpha_m^2 W_m^*$$

$$\int_0^L \frac{d^3W}{dx^3} \cos \alpha_m x dx = [(-1)^m W_1'' - W_0''] - [(-1)^m W_1 - W_0] - \alpha_m^3 \bar{W}_m$$

$$\int_0^L \frac{d^4W}{dx^4} \cos \alpha_m x dx = [(-1)^m W_1''' - W_0'''] - \alpha_m^2[(-1)^m W_1' - W_0'] + \alpha_m^4 W_m^* \quad (7)$$

for $m > 0$. For the function Q,

$$\int_0^L Q(x) \sin \alpha_m x dx = \bar{Q}_m, \quad \int_0^L Q(x) \cos \alpha_m x dx = Q_m^* \quad (8)$$

for $m \geq 0$ with $\bar{Q}_0 = 0$. The associated boundary conditions at $x = 0$ and L are

$$B_k(W) = 0 \quad (9)$$

and the range of k depends on the order of H. At this stage, it is seen from Eq. (4) that there is the unknown function W in the function g, and some known and unknown quantities involved in the function f. Representing W by a complete set of functions having unknown coefficients A_n without concerning the boundary conditions, one arrives at a system of linear algebraic equations from Eq. (4) for the unknown coefficients A_n and quantities in f. It may be noted here that when the governing differential equation has constant coefficients and Fourier series is used to represent the dependent variables, A_n for each n may be explicitly expressed in terms of the quantities in the function f because of orthogonal properties of sinusoidal functions. After satisfying all boundary conditions, one arrives at the final solution in Fourier series form. Otherwise, one needs to solve a sufficiently large system of equations to arrive at solutions with desired accuracy. Since a complete set of functions is used to represent the general solution and all boundary conditions are enforced during the process, convergence of solutions is assured and the final solutions are exact implicitly. In this study, only Fourier and power series representations of the general solutions are considered. While Fourier series used for general solutions may take the advantage of orthogonality properties, other types of functions may potentially give more direct solutions. When power series is used to represent the general solution, the following quantities may be involved in the procedure:

$$S_{mn} = \int_0^L x^n \sin \alpha_m x dx, \quad C_{mn} = \int_0^L x^n \cos \alpha_m x dx \quad (10)$$

which can be readily generated. For $n = 0$ and 1 with $m \geq 1$,

$$S_{m0} = \frac{1}{\alpha_m}[1 - (-1)^m], \quad S_{m1} = -(-1)^m \frac{L}{\alpha_m} \quad (11)$$

$$C_{00} = L, \quad C_{m0} = 0, \quad C_{01} = \frac{L^2}{2},$$

$$C_{m1} = [(-1)^m - 1]\frac{1}{\alpha_m^2}. \quad (12)$$

The remaining ones, for $m \geq 1$ and $n \geq 2$, can be determined from the following recurrence relations:

$$S_{mn} = -(-1)^m \frac{L^n}{\alpha_m} - \frac{n(n-1)}{\alpha_m^2} S_{m(n-2)} \quad (13)$$

$$S_{m(n+1)} = -(-1)^m \frac{L^{n+1}}{\alpha_m} + \frac{n+1}{\alpha_m} C_{mn} \quad (14)$$

$$C_{mn} = (-1)^m \frac{n}{\alpha_m^2} L^{n-1} - \frac{n(n-1)}{\alpha_m^2} C_{m(n-2)} \quad (15)$$

$$C_{m(n+1)} = -\frac{n+1}{\alpha_m} S_{mn}. \quad (16)$$

In what follows, several simple examples are presented solely for illustrating the procedure and verifying the exactness of solutions. In particular, more detailed discussions involving Fourier series and polynomial representations of general solutions as well as analysis procedures are given in the first example which is the simplest class of structural mechanics problems where explicit exact solutions are readily available. Other examples involve various types of boundary conditions, including elastic support, and differential equations with constant and variable coefficients.

Illustrative Examples

Example 1. A uniform bar, fixed at $x = 0$ and free at $x = L$, under an axial force P at $x = L$ is considered. The differential equation governing the internal axial force N is

$$\frac{dN}{dx} = 0 \tag{17}$$

with $N = P$ at $x = L$ as the boundary condition. Clearly, the exact solution is $N = P$ throughout. For the present procedure, Eq. (17) is first multiplied by either $\sin \alpha_m x$ or $\cos \alpha_m x$, and then integrated by parts through the length of the bar. The general solution represented by Fourier cosine, Fourier sine and power series are presented as Schemes 1, 2, and 3 here for illustrating the procedure.

Scheme 1: When $\sin \alpha_m x$ as weighting functions are used, Eq. (10) is multiplied by $\sin \alpha_m x$ and then integrated from $x = 0$ to L, resulting in the following transformed equation:

$$\int_0^L N \cos \alpha_m x dx = 0 \quad \text{for} \quad m = 1, 2, 3, \ldots . \tag{18}$$

Representing the general solution of N by a Fourier cosine series,

$$N = A_0 + \sum_{n=1}^{\infty} A_n \cos \alpha_n x \tag{19}$$

and substituting Eq. (19) into Eq. (18), one finds $A_n = 0$. Hence, $N = A_0$. By using the boundary condition that $N = P$ at $x = L$, one obtains the exact solution $N = P$ throughout the bar.

Scheme 2: When $\cos \alpha_m x$ are used as weighting functions, Eq. (17) is multiplied by $\cos \alpha_m x$ and then integrated from 0 to L. As a result, $N_0 = N_1$ when m is taken to be 0. For $m > 0$, the transformed $\bar{N}$ becomes

$$\bar{N} = \int_0^L N \sin \alpha_m x dx = \frac{1}{\alpha_m}[N_0 - (-1)^m N_1]. \tag{20}$$

Using the Fourier sine series for N,

$$N = \sum_{n=1}^{\infty} A_n \sin \alpha_n x \tag{21}$$

and substituting Eq. (21) into Eq. (20), one obtains for each m,

$$\frac{L}{2} A_n \delta_{mn} = \frac{1}{\alpha_m}[N_0 - (-1)^m N_1]. \tag{16}$$

Using the result $N_0 = N_1$ for $m = 0$ and the boundary condition that $N = N_1 = P$ at $x = L$ in Eq. (22), we obtain

$$A_n = \frac{2}{n\pi}[1 - (-1)^n]P. \tag{23}$$

Using Eq. (23), the solution given in Eq. (21) becomes

$$N = P \sum_{n=1}^{\infty} \frac{2}{n\pi}[1 - (-1)^n] \sin \alpha_n x. \tag{24}$$

Knowing the following series identity,

$$\sum_{n=1}^{\infty} \frac{2}{n\pi}[1 - (-1)^n] \sin \alpha_n x = 1, \tag{25}$$

the exact solution of $N = P$ is recovered from Eq. (24) in conjunction with Eq. (25). While the series identity such as the one given in Eq. (25) is obvious for this simple problem, series involved in other complex problems may not be easily identified. However, it should be noted that the solution, though in series form, is implicitly exact.

While either sine or cosine functions can be used as weighting functions to give the exact solution, the use of sine functions in Scheme 1 is obviously more direct than the use of cosine functions in Scheme 2 for this problem. Inasmuch as solutions of certain structural mechanics problems are or may be implicitly exact in polynomial forms, it may be more effective to represent the general solutions by power series. The subsequent Scheme 3 is presented for illustrating the use of polynomials.

Scheme 3: Representing N by the following power series with $\sin \alpha_m x$ as weighting functions,

$$N = \sum_{0}^{\infty} A_n x^n, \tag{26}$$

and substituting Eq. (26) in Eq. (18) with $\sin \alpha_m x$ as weighting functions in conjunction with Eq. (10), one arrives at

$$\sum_{n=1}^{\infty} C_{mn} A_n = 0 \tag{27}$$

for $m = 1, 2, 3, \ldots \infty$ which represents a set of homogeneous algebraic equations. As a result, $A_n = 0$ for $n = 1$ to ∞ except A_0. Hence

$$N = A_0 = P \tag{28}$$

when the boundary condition at $x = L$ is used. This is the exact solution of the problem. On the other hand, if $\cos \alpha_m x$ are used as weighting functions, Eq. (20) becomes the transformed equation to be solved for N. Substituting Eq. (26) into Eq. (20) for $m = 1, 2, 3, \ldots \infty$, one arrives at the following system of algebraic equations:

$$\frac{1}{\alpha_m}[1 - (-1)^m]A_0 + \sum_{n=1}^{\infty} S_{mn} A_n = \frac{1}{\alpha_m}[1 - (-1)^m]P \tag{29}$$

which may be written as

$$\frac{1}{\alpha_m}[1 - (-1)^m]A_0^* + \sum_{n=1}^{\infty} S_{mn} A_n = 0 \tag{30}$$

for $m = 1, 2, 3, \ldots \infty$, where $A_0^* = A_0 - P$. Equation (30) represents a system of homogeneous algebraic equations. Hence $A_n = 0$ for $n = 1$ to ∞ as well as $A_0^* = 0$ from which one obtains

$$A_0 = P \tag{31}$$

and the exact solution $N = A_0 = P$ is recovered again according to Eq. (26).

For this simplest example, all of the various schemes presented give the exact solution explicitly. This should be considered as an exception rather than a rule, and the solutions would generally be implicitly exact in series form. However, the detailed steps presented in this example have provided an illustration for the concept of the present analysis method. Presentations of these various schemes show that either sine or cosine weighting functions in conjunction with Fourier or power series solutions may be used without being concerned with boundary conditions in advance while all boundary conditions are satisfied in the process. In principle, there is no restriction in representing general solutions in other potentially more convenient forms which would naturally depend on the nature of problems concerned. On the other hand,

one may use one type of series solution such as the Fourier series for all structural mechanics problems with any supporting conditions. Hence, the present procedure providing assured exact solutions is simpler and has broader applicability than other approximate methods such as the Ritz-Galerkin procedure.

To further illustrate the procedure and to demonstrate its effectiveness and exactness of solutions on higher-order differential equations, Fourier series representations of general solutions are used in the remaining examples 2–5 which involve second to fourth-order differential equations of constant coefficients. Power series solutions are used in Example 6 for differential equations with variable coefficients.

Example 2. Same problem as Example 1, except the objective is to determine the longitudinal deformation of the bar from a displacement formulation. The differential equation governing the longitudinal displacement U of the bar is

$$\frac{d^2U}{dx^2} = 0. \tag{32}$$

The boundary conditions are

$$U = 0 \quad \text{at} \quad x = 0 \tag{33}$$

$$EA\frac{dU}{dx} = P \quad \text{at} \quad x = L \tag{34}$$

where EA is the extensional stiffness of the bar. The exact solution of this problem is

$$U = \frac{Px}{EA}. \tag{35}$$

If $\sin \alpha_m x$ are used as the weighting functions in the present procedure, Eq. (32) is transformed into the following equation for each m:

$$\alpha_m[(-1)^m U_1 - U_0] - \alpha_m^2 \bar{U}_m = 0 \tag{36}$$

where subscripts 0 and 1 correspond to $x = 0$ and L, respectively, and an overbar denotes the transformed U with respect to $\sin \alpha_m x$ as weighting functions. Knowing that $U_0 = 0$, and representing U by the following Fourier sine series,

$$U = \sum_{n=1}^{\infty} A_n \sin \alpha_n x \tag{37}$$

one obtains from Eq. (36)

$$A_n = -(-1)^n \frac{2}{n\pi} U_1. \tag{38}$$

The derivative of U given in Eq. (37) accounting for the end quantities is

$$\frac{dU}{dx} = \frac{U_1 - U_0}{L} + \sum_{n=1}^{\infty} D_n^* \cos \alpha_n x \tag{39}$$

$$D_n^* = \frac{2}{L}[(-1)^n U_1 - U_0] + \alpha_n A_n. \tag{40}$$

Discussions on the differentiation of Fourier series for a function defined on end points can be found in Bromwich (1965) and Tolstov (1965). By satisfying the boundary condition (34) using Eq. (39) in conjunction with Eqs. (38)–(40), and $U_0 = 0$ given in Eq. (33), one arrives at $D_n^* = 0$, and

$$U_1 = \frac{PL}{EA}. \tag{41}$$

Using Eq. (38) in conjunction with Eq. (41), the general solution given in Eq. (37) becomes

$$U = -\frac{P}{EA}\sum_{n=1}^{\infty}(-1)^n \frac{2}{\alpha_n} \sin \alpha_n x. \tag{42}$$

Knowing the following series identity,

$$-\sum_{n=1}^{\infty}(-1)^n \frac{2}{\alpha_n} \sin \alpha_n x = x, \tag{43}$$

the exact solution $U = Px/EA$ is recovered from Eq. (42) when Eq. (43) is used.

Example 3. Elastic Buckling of Bars: The governing differential equation is

$$EI\frac{d^4W}{dx^4} + P\frac{d^2W}{dx^2} = 0 \tag{44}$$

where W is the transverse deflection, EI is the flexural rigidity, and P is the axial load. The critical load parameter

$$\lambda = \frac{PL^2}{\pi^2 EI} \tag{45}$$

depends on supporting conditions. For this example, $\sin \alpha_m x$ are used as weighting functions for demonstration, though one may use $\cos \alpha_m x$ as weighting functions as well. Equation (44) is transformed in the following equation for each m after it is multiplied by $\sin \alpha_m x$ and then integrated by parts from $x = 0$ to L, successively:

$$\alpha_m^2\left(\frac{\pi}{L}\right)^2 (m^2 - \lambda)\bar{W}_m = \alpha_m[(-1)^m W_1'' - W_0''] + \left[\lambda\left(\frac{\pi}{L}\right)^2 \alpha_m - \alpha_m^3\right][(-1)^m W_1 - W_0]. \tag{46}$$

A bar having fixed-hinge supports as a representative case is considered for illustrating the procedure. For such a case, $W_0 = W_1 = W_1'' = 0$, one obtains from Eq. (46)

$$\bar{W}_m = \int_0^L W \sin \alpha_m x dx = -\frac{L^3}{\pi^3 m(m^2 - \lambda)} W_0''. \tag{47}$$

Representing

$$W = \sum_{n=1}^{\infty} A_n \sin \alpha_n x \tag{48}$$

one obtains A_n by substituting Eq. (48) into Eq. (47) as follows:

$$A_n = -\frac{2L^2}{\pi^3 n(n^2 - \lambda)} W_0''. \tag{49}$$

By requiring zero slope boundary condition at $x = 0$ using Eq. (48) in conjunction with Eq. (49) and zero displacement at both ends, one arrives at

$$-\frac{2L^2}{\pi^3} W_0'' B^* = 0 \tag{50}$$

in which

$$B^* = \sum_{n=1}^{\infty} \frac{1}{n(n^2 - \lambda)} = 0 \tag{51}$$

becomes the buckling equation of the problem. The critical load parameter is found to be

$$\lambda_{cr} = 2.0499 \tag{52}$$

which should be considered as the exact solution as the standard value of $\lambda_{cr} \doteq 2.05$ is given in almost all text books on mechanics of solids.

For bars having other types of boundary conditions, the buckling load can be determined following the same procedure through Eqs. (46) and (48) using the same series representation of W. It may be noted that for Ritz-Galerkin procedure, different types of trial functions must be individually generated or selected for the bar with different boundary conditions.

Example 4. Flexural Vibration of Beams: The amplitude W of the harmonic motion of a beam is governed by

$$\frac{d^4W}{dx^4} - \beta^4 W = 0 \tag{53}$$

where $\beta^4 = \rho\omega^2/EI$, ρ is the mass density, and ω is the circular frequency. If $\cos \alpha_m x$ for $m = 0, 1, 2, \ldots \infty$ are used as weighting functions, Eq. (53) is multiplied by the weighting functions and then integrated successively from $x = 0$ to L, one arrives at

$$[(-1)^m W_1''' - W_0'''] - \alpha_m^2[(-1)^m W_1' - W_0'] + (\alpha_m^4 - \beta^4) W_m^* = 0 \tag{54}$$

for $m = 0, 1, 2, \ldots \infty$. Representing

$$W = \frac{A_0}{2} + \sum_{n=1}^{\infty} A_n \cos \alpha_n x \tag{55}$$

and substituting Eq. (55) into Eq. (54), one obtains A_n using the definition of the transformed quantity W_m^* given in Eq. (3). The general solution of W is found to be

$$W = \frac{1}{\beta^4 L}[W_1''' - W_0'''] - \frac{2}{L}\sum_{n=1}^{\infty}\{[(-1)^n W_1''' - W_0''']$$

$$- \alpha_n^2[(-1)^n W_1' - W_0']\}\frac{1}{\alpha_n^4 - \beta^4}\cos \alpha_n x. \tag{56}$$

The detailed expression for A_0 and A_n can be readily identified by comparing Eqs. (55) and (56).

Case 1. Free-Free Beams: According to the boundary conditions for this case, $W_1''' = W_0''' = 0$, and $W_0' = -W_1'$ and W_1' for symmetric and antisymmetric modes of deformation, respectively. From Eq. (56), one arrives at

$$W = \frac{2}{L} W_1' \sum_{n=1}^{\infty} [(-1)^n + c]\frac{\alpha_n^2}{\alpha_n^4 - \beta^4}\cos \alpha_n x \tag{57}$$

where $c = 1$ and -1 correspond to symmetric and antisymmetric modes of deformation, respectively. While the general solution given in Eq. (57) satisfies zero shear force at both ends, zero moment corresponding to the second derivative of W with respect to x must be satisfied at $x = 0$ and L. Second derivative of W with respect to x accounting for the quantities at end points results in

$$\frac{d^2W}{dx^2} = \frac{2}{L} W_1'\left\{a - \beta^4 \sum_{n=1}^{\infty}[(-1)^n + c]\frac{1}{\alpha_n^4 - \beta^4}\right\}. \tag{58}$$

The frequency equations corresponding to symmetric and antisymmetric modes of deformation by setting Eq. (58) to zero for $a = 1$ and 0, respectively, are as follows:

$$1 - 2p^4 \sum_{n=1}^{\infty} \frac{1}{(2n)^4 - p^4} = 0 \tag{59}$$

$$2p^4 \sum_{n=1}^{\infty} \frac{1}{(2n-1)^4 - p^4} = 0 \tag{60}$$

in which

$$p = \frac{\beta L}{\pi}. \tag{61}$$

The first four frequencies for p are found from Eqs. (59) and (60). They are 1.5057, 2.4998, 3.5001, and 4.5000, respectively. These results, which agree with solutions given in textbooks such as Tse et al. (1978) should be considered as exact solutions.

Case 2. Cantilever Beams: The beam is considered to be fixed at $x = 0$ and free at $x = L$. Since $W_0' = W_1''' = 0$ for the cantilevered beam, Eq. (56) reduces to

$$W = -\frac{1}{\beta^4 L} W_0''' + \frac{2}{L}\sum_{n=1}^{\infty}[W_0''' + (-1)^n \alpha_n^2 W_1']\frac{1}{\alpha_m^4 - \beta^4}\cos \alpha_m x. \tag{62}$$

While W given in Eq. (62) satisfies the zero slope boundary condition at $x = 0$ and zero shear condition at $x = L$, it must further satisfy the following boundary conditions:

$$W = 0 \quad \text{at} \quad x = 0, \quad \frac{d^2W}{dx^2} = 0 \quad \text{at} \quad x = L. \tag{63}$$

Substituting Eq. (62) into the conditions given in Eq. (63), one obtains the following two homogeneous algebraic equations:

$$R_{11}Y + R_{12}W_1' = 0 \tag{64}$$

$$R_{21}Y + R_{22}W_1' = 0 \tag{65}$$

in which

$$Y = \left(\frac{L}{\pi}\right)^2 W_0''', \quad R_{11} = -\frac{1}{p^4} + \sum_{n=1}^{\infty}\frac{2}{n^4 - p^4}$$

$$R_{12} = R_{21} = \sum_{n=1}^{\infty}(-1)^n \frac{2n^2}{n^4 - p^4}, \quad R_{22} = -1 + \sum_{n=1}^{\infty}\frac{2p^4}{n^4 - p^4}.$$

For nontrivial solutions, one requires

$$R_{11}R_{22} - R_{12}R_{21} = 0 \tag{66}$$

which is the frequency equation for cantilever beams. The first four values of the frequency parameter, p, are found to be 0.5969, 1.4942, 2.5003, and 3.5000. They should be considered as exact solutions as they agree with solutions given in textbooks on vibration such as Tse et al. (1978).

Case 3. Fixed-Hinged With Rotational Restraint Beams: The fixed end at $x = 0$ is considered for this case. If one continues to follow Eq. (56) on the basis of using $\cos \alpha_m x$ as weighting functions and Fourier cosine series for W for which $W_0' = 0$, one needs to satisfy three additional conditions that $W = 0$ at $x = 0$ and L, and

$$EI\frac{d^2w}{dx^2} = -K\frac{dw}{dx} \quad \text{at} \quad x = L$$

to solve the problem, where K is the coefficient of the end restraint. On the other hand, if $\sin \alpha_m x$ are used as weighting functions and Fourier sine series is used for W, the general solution, with $W_0 = W_1 = 0$ for this case becomes

$$W = \sum_{n=1}^{\infty} \frac{2n^4}{p^4 - m^4} [W_0'' - (-1)^m W_1''] \sin \alpha_m x \tag{67}$$

and one only needs to satisfy two additional conditions. They are

$$\frac{dW}{dx} = 0 \quad \text{at} \quad x = 0 \tag{68}$$

$$K \frac{dW}{dx} = -EIW_1'' \quad \text{at} \quad x = L \tag{69}$$

which lead to

$$c_{11} W_0'' + c_{12} W_1'' = 0 \tag{70}$$

$$c_{21} W_0'' + c_{22} W_1'' = 0 \tag{71}$$

in which

$$c_{11} = -\sum_{n=1}^{\infty} D_n, \quad c_{12} = \sum_{n=1}^{\infty} (-1)^n D_n$$

$$c_{21} = \bar{K} c_{12}, \quad c_{22} = \frac{\pi^4}{2} - \bar{K} \sum_{n=1}^{\infty} D_n$$

$$EI\pi^2 \bar{K} = KL, \quad D_n = \frac{n^2}{p^4 - n^4} \tag{72}$$

and the frequency equation becomes

$$c_{11} c_{22} - c_{12} c_{21} = 0. \tag{73}$$

The first four values of the frequency parameter $p = \beta L/\pi$ for fixed-hinged beams according to results given in Tse et al. (1978) are 1.25, 2.25, 3.25, 4.25. The present results, corresponding to a very small coefficient of end restraint $\bar{K} = 1$, are found to be 1.255, 2.255, 3.255, 4.255. For a large value of $\bar{K} = 2000$, the first four values of p are found to be 1.501, 2.493, 3.491, 4.488 which approach 1.506, 2.50, 3.50, 4.50 for fixed-fixed beams based on the results given in Tse et al. (1978). For $\bar{K} = 50$, the first eight values of p are found to be 1.369, 2.333, 3.315, 4.304, 5.297, 6.293, 7.289, 8.287 which should be considered as exact solutions. They may be used as benchmark solutions for future reference. It may also be noted that because of the elastic end constraining condition involved in this case, it is not convenient to use some of the approximate methods such as the Ritz-Galerkin procedure.

Example 5. Beams on Elastic Foundation Under Transverse Load: This example demonstrates the exactness of the solution of the present method for problems requiring pointwise accurate results whereas most of approximate methods such as Ritz-Galerkin are generally not adequate. The differential equation governing the transverse displacement W of a finite beam of length L on an elastic foundation of stiffness k is

$$\frac{d^4 W}{dx^4} + 4\beta^4 W = q \tag{74}$$

where q is the loading function, and $4\beta^4 = k/EI$ and EI is the flexural rigidity of the beam. For the beam, which is free at both ends, and is subjected to a concentrated load P at the midsection of beam, i.e., $q = P\delta(x - L/2)$ where $\delta(x - L/2)$ is the Dirac delta function, the exact expression for the end deflection given in Ugural and Fenster (1975) is

$$v_E = \frac{2P\beta}{k} \frac{\cos(\beta L/2) \cosh(\beta L/2)}{\sin \beta L + \sinh \beta L}$$

$$\frac{2P\beta}{k} = \frac{1}{2\beta^3 L^3} \frac{PL^3}{EI}. \tag{75}$$

If $\sin \alpha_m x$ are used as the weighting functions, Eq. (74) is transformed into the following equation:

$$\alpha_m [W_0'' - (-1)^m W_1''] + \alpha_m^3 [(-1)^m W_1 - W_0] + (\alpha_m^4 + 4\beta^4) \int_0^L W \sin \alpha_m x dx = \frac{P}{EI} \sin \alpha_m a \tag{76}$$

in which $a = L/2$ for the problem under consideration, $W_1'' = W_0'' = 0$ because of zero moments at the free ends, and $W_1 = W_0$ because of symmetry in deformation. Representing

$$W = \sum_{n=1}^{\infty} A_n \sin \alpha_n x \tag{77}$$

and substituting Eq. (77) in Eq. (76), one obtains

$$A_n = \frac{2}{L} \left\{ [1 - (-1)^n] \frac{\alpha_n^3}{\alpha_n^4 + 4\beta^4} W_0 + \frac{P}{EI} \frac{1}{\alpha_n^4 + 4\beta^4} \sin \alpha_n a \right\}. \tag{78}$$

With the conditions of zero moment at both ends and symmetrical deformation about the midsection already satisfied, we further require the following zero shear force condition at $x = 0$ be satisfied:

$$\frac{L}{2} \frac{d^3 W}{dx^3} = W_0 \sum_{n=1}^{\infty} [(-1)^n - 1] \alpha_m^2 \left[\frac{\alpha_m^4}{\alpha_m^4 + 4\beta^4} - 1 \right] - \frac{P}{EI} \sum_{m=1}^{\infty} \frac{\alpha_m^3 \sin \alpha_m a}{\alpha_m^4 + 4\beta^4} \tag{79}$$

from which one obtains the end deflection at $x = 0$ as follows:

$$W_e = \frac{EI}{PL^3} W_0 = \frac{\pi}{4\beta^4 L^4} \frac{\bar{D}}{D} \tag{80}$$

in which

$$\bar{D} = \sum_{n=1}^{\infty} \frac{m^3 \sin \alpha_m a}{m^4 + 4p^4}, \quad D = [1 - (-1)^m] \frac{m^2}{m^4 + 4p^4},$$

$$p = \frac{\beta L}{\pi}.$$

Once W_0 is found from Eq. (80), A_n can be determined from Eq. (78), the displacement W for $0 \le x \le L$ is determined from Eq. (77), and the displacement at the end points of $x = 0$ and L is equal to W_0. In Ugural and Fenster (1975), beams are classified as short for $\beta L < 1$, intermediate for $1 < \beta L < 3$, and long for $\beta L > 3$. The deflection at the end point becomes very small when βL is near 3, and changes from positive to negative between $\beta L = 3.1$ and 3.2. The end deflection W_e for a (short, intermediate, long) beam with corresponding $\beta L = (0.1, 2, 5)$ are found to be (2499, 0.01148, −0.00027), respectively. The ratio of the present results to the exact expression given in Eq. (75) on the end deflection for

these three cases are (0.9997, 0.9991, 1.0069), respectively. These results show that although the present solutions are in series form, they give pointwise exact solutions implicitly.

Example 6. When structural components with nonuniform cross sections or thicknesses, and other situations, their governing differential equations contain variable coefficients. Such differential equations are generally considered to be exceedingly difficult to solve for their exact solutions explicitly. We consider the following Legendre's equation, which is involved in many mechanics problems such as the axisymmetric stress and deformation in a solid of revolution discussed in Timoshenko and Goodier (1970), to illustrate the present procedure and to verify the exactness of the method:

$$(1 - x^2)\frac{d^2W}{dx^2} - 2x\frac{dW}{dx} + BW = 0 \tag{81}$$

for the interval from $x = 0$ to 1, and consider $W = W_0$ at $x = 0$ and $W = 1$ at $x = 1$ as boundary conditions. Clearly, Eq. (81) is the Legendre's equation when $B = r(r + 1)$ for any integer of r. For these values of B, exact solutions of Legendre polynomials P_r can be found in textbooks such as Churchill (1963). For $r = 0$ to 5, they are given in Churchill (1963) as follows:

$$P_0(x) = 1, \quad P_1(x) = x, \quad P_2(x) = \tfrac{1}{2}(3x^2 - 1)$$
$$P_3(x) = \tfrac{1}{2}(5x^3 - 3x), \quad P_4(x) = \tfrac{1}{8}(35x^4 - 30x^2 + 3)$$
$$P_5(x) = \tfrac{1}{8}(63x^5 - 70x^3 + 15x) \tag{82}$$

which are used for verifying results of the present method later. If $\sin \alpha_m x$ are used as the weighting functions in the present procedure, Eq. (81) is transformed into the following integral equation:

$$\alpha_m W_0 + (B - \alpha_m^2)\int_0^1 W \sin \alpha_m x dx - 2\alpha_m \int_0^1 xW \cos \alpha_m x dx + \alpha_m^2 \int_0^L x^2 W \sin \alpha_m x dx = 0. \tag{83}$$

Representing

$$W = A_0 + \sum_{n=1}^{\infty} A_n x^n \tag{84}$$

and substituting Eq. (84) in Eq. (83), we arrive at the following equation for each m:

$$\alpha_m W_0 + \sum_{n=0}^{\infty} [B - n(n + 1)]S_{mn}A_n - \sum_{n=0}^{\infty} [\alpha_m^2 S_{mn} + (-1)^m \alpha_m]A_n = 0 \tag{85}$$

where S_{mn} is defined in Eq. (10). Also, from the boundary conditions, we have

$$A_0 = W_0, \quad \sum_{n=0}^{\infty} A_n = 1. \tag{86}$$

For a general value of B, the result of W converges to the exact solution implicitly when a sufficiently large number of A_n are solved from the system of equations given in Eq. (85) in conjunction with Eqs. (86). If $B = r(r + 1)$, Eq. (85) becomes

$$\sum_{n=0}^{\infty} a_{rmn}A_n = 0 \tag{87}$$

for each m, where

$$a_{rm0} = \alpha_m + [r(r + 1) - \alpha_m^2]S_{m0} - (-1)^m \frac{1}{\alpha_m} \tag{88}$$

$$a_{rmn} = [r(r + 1) - n(n + 1) - \alpha_m^2]S_{mn} - (-1)^m \alpha_m \quad \text{for } n > 0. \tag{89}$$

When $r = 0$, we find that $a_{0m0} = 0$ for all values of m while all others are not. Hence, from Eqs. (89), $A_n = 0$ for all integers of n except A_0. Using the boundary condition at $x = 0$ that $W = W_0 = 1$, we obtain $A_0 = 1$, and the solution is $W(x) = 1 = P_0$, which is the exact solution given in Eq. (82).

When $r = 1$, only a_{1m1} is zero for all values of m. By the same reasoning as the last case, we conclude that $W(x) = A_1 x$. Using the boundary condition $W = 1$ at $x = 1$, we obtain the solution $W(x) = x = P_1(x)$, which is the exact solution.

When $r = 2$, $a_{2m0} = 6S_{m0}$ and $a_{2m2} = 2S_{m0}$. Hence, from Eq. (87), $A_n = 0$ except for $n = 0$ and 3 because $S_{m0}(6A_0 + 2A_2) = 0$ for all values of m. As a result, $6A_0 + 2A_2 = 0$ together with the boundary condition $W(1) = A_0 + A_2 = 1$ give $A_0 = -\frac{1}{2}$ and $A_2 = \frac{3}{2}$. We obtain the solution of $W(x) = P_2(x)$, which is the exact solution.

When $r = 3$, $a_{3m1} = 10S_{m1}$ and $a_{3m3} = 6S_{m1}$. As in the last case, we obtain $A_1 = -\frac{3}{2}$ and $A_3 = \frac{5}{2}$, and $W(x) = P_3(x)$, which is the exact solution.

When $r = 4$, we find $a_{4m0} = 20S_{m0}$, $a_{4m2} = 2S_{m0} + 14S_{m2}$, and $a_{4m4} = 12S_{m2}$. Hence $A_n = 0$ for all n except for $n = 0$, 2, 4; $20A_0 + 2A_2 = 0$ and $14A_2 + 12A_4 = 0$ for all values of m. The last two equations together with the second boundary condition in Eq. (86) give the results of A_0, A_2, and A_4, and the solution of $W(x)$ is the exact solution of $P_4(x)$.

When $r = 5$, we find $a_{5m1} = 28S_{m1}$, $a_{5m3} = 6S_{m1} + 18S_{m3}$, and $a_{5m5} = 20S_{m3}$. They lead to $28A_1 + 6A_3 = 0$ and $18A_3 + 20A_5 = 0$. Solving the last two equations along with the boundary condition at $x = 1$, one obtains $A_1 = 15/8$, $A_3 = -70/8$ and $A_5 = 63/8$. Hence, the solution of $W(x)$ matches the exact solution of P_5 given in Eq. (82).

In a similar manner, one can verify that the solutions of the problem using the present method are all exact for higher values of r.

Concluding Remarks

The method presented in this study is simple in concept and systematic in operation. The procedure can be used routinely by representing general solutions in any complete set of functions without being concerned with the boundary conditions in advance, but all boundary conditions are satisfied in the process. This method greatly broadens the applicability of various series solutions for structural mechanics problems and simplifies analysis procedures. The method is more convenient to use than other approximate methods such as the Ritz-Galerkin procedure because the same series representation of general solution may be used in the present method for a class of structures with any boundary conditions. For the Ritz-Galerkin procedure, however, different types of trial functions must be generated individually according to different boundary conditions. Since complete sets of functions are used, and all boundary conditions are enforced in the process, the present method gives implicitly exact solutions in general. This has been verified by all example problems considered in the study. Although the presented examples belong to a simple class of one-dimensional structural mechanics problems solely for the purpose of illustrating the procedure of the method and verifying the exactness of solutions, the method can be used for investigating more complex problems in structural mechanics.

Acknowledgments

The major part of the study was carried out during the first author's visit to the National Chung-Hsing University when he was invited by Prof. Chien-Chang Lin to collaborate in research with him through the National Science Council (NSC) in Taiwan of the Republic of China as the Visiting Research Chair Professor. The financial support of NSC is gratefully acknowledged.

References

Bittar, Z., and Sejnoha, J., 1996, *Numerical Methods in Structural Mechanics,* ASCE, Reston, VA.

Boresi, A. P., and Sidebottom, O. M., 1985, *Advanced Mechanics of Materials,* 4th Ed., John Wiley and Sons, New York.

Bromwich, T. J. I.'A., 1965, *An Introduction of the Theory of Infinite Series,* Macmillan, London.

Churchill, R. V., 1963, *Fourier Series and Boundary Value Problems,* 2nd Ed., McGraw-Hill, New York.

Hjelmstad, K. D., 1997, *Fundamentals of Structural Mechanics,* Prentice-Hall, Englewood Cliffs, NJ.

Ross, C. T. F., 1996, *Mechanics of Solids,* Prentice-Hall, Englewood Cliffs, NJ.

Timoshenko, S. P., and Goodier, J. N., 1970, *Theory of Elasticity,* 3rd Ed., McGraw-Hill, New York.

Timoshenko, S., and Woinowsky-Kreiger, S., 1959, *Theory of Plates and Shells,* 2nd Ed., McGraw-Hill, New York.

Tolstov, G. P., 1965, *Fourier Series,* Prentice-Hall, Englewood Cliffs, NJ.

Tse, F. S., Morse, I. E., and Hindle, R. T., 1978, *Mechanical Vibrations,* 2nd Ed., Allyn and Bacon, Boston.

Urural, A. C., and Fenster, S. K., 1975, *Advanced Strength and Applied Elasticity,* Elsevier, New York, p. 292.

Washizu, K., 1968, *Variational Methods in Elasticity and Plasticity,* Pergamon Press, Oxford.

Optimal Buckling Loads of Nonuniform Composite Plates With Thermal Residual Stresses

A. R. de Faria
Ph.D. Student

J. S. Hansen
Professor

Institute for Aerospace Studies,
UTIAS,
4925 Dufferin Street,
Toronto, ON M3H 5T6,
Canada

Optimal elastic buckling loads of spatially heterogeneous plates formed from a series of composite patches is considered. Reissner-Mindlin laminated composite plate theory including thermal effects is adopted for the analysis and the problem is solved using the finite element method based on a bi-cubic Lagrange C^0 element formulation. The thermal residual stresses considered are those that result during elevated temperature processing because of the different laminates forming the patches of the plate. In the optimization, the fiber angles in each patch are the design variables and three symmetric laminated plate configurations are investigated. The results illustrate that thermal residual effects can lead to optimal buckling loads which are as much as two times greater than the corresponding optimal buckling loads in which these manufacturing effects are ignored. The work demonstrates the importance of spatial heterogeneity as well as the significance of manufacturing-induced residual stresses in optimal design studies of composite structures.

1 Introduction

Due to their attractive properties, composite laminates have been used extensively in aerospace applications. It has been shown that moisture and thermal residual stresses impair the behavior of composite structures by reducing stiffness and strength and by bringing the buckling loads to undesirably low levels.

Models for the accurate description of hygrothermal effects on the static instability of symmetric and antisymmetric laminated composite plates were implemented and revealed, quantitatively, the degree of damage caused by elevated moisture concentrations and thermal residual stresses (Ram and Sinha, 1992).

Attempts to avoid or even take advantage of the thermal residual effects have been made. Almeida and Hansen (1997) showed that it is possible to increase buckling loads of composite plates when they are favorably tailored in order to take advantage of the inherent thermal residual stresses resulting from the high-temperature processing. Stiffeners are placed on the plate's edges and, due to the nonuniform design, residual stresses develop throughout the structure. Results indicate that this procedure increased the buckling load significantly. In their work, the stiffener location and stacking sequence were chosen on a logic basis. This means that the plate configurations adopted did not followed well-defined criteria; rather, the design was a choice based on common sense and previous experience. Further investigations suggest that some optimality criteria would be recommended in order to achieve even higher buckling loads.

The objective of the present work is to optimize nonuniform laminated plates composed of subregions. In these subregions or subdomains, the total thickness and number of layers is kept constant and the lamina orientations are allowed to vary. Therefore the structure under consideration consists of subdomains with piecewise continuous material properties. One of the most important assumptions made is the requirement of continuity of the displacement field; ultimately it means that the subdomains will not separate.

A finite element formulation is chosen to analyze the problem numerically. Reissner-Mindlin plate theory is applied along with bi-cubic 16-node Lagrangian elements. A general prebuckling state is adopted. Three symmetrically laminated plate configurations are investigated: one ply, three ply, and five ply.

2 Problem Formulation

The objective function of the problem is the critical buckling load, that is, the numerical procedure is committed to maximize the buckling load of plates where the fiber orientations are taken as the design variables. The evaluation of the objective function for a particular design involves three main steps: the thermal problem, the prebuckling problem, and the buckling problem. Figure 1 presents a sketch of the plate showing the prescribed displacements and boundary conditions.

The problem is analyzed using the Reissner-Mindlin plate theory. The thermal and prebuckling problems are considered to be linear and in-plane while in the buckling problem nonlinear strain-displacement relations are assumed. The assumptions made are reasonable for symmetric laminates because in this case there is no laminate induced membrane-bending coupling. Thus, no out-of-plane displacements result from the thermal processing and the plate produced is perfectly flat.

2.1 Thermal Problem. In this section the thermal problem is solved and afterward the displacement field and thermal loads are used to calculate the residual stresses.

The cure or consolidation process of composite laminates is usually carried out at elevated temperatures; 120°C to 180°C are typical for epoxy-based composites while 380°C is used for PEEK-based systems. It is assumed that the laminate is stress free at the processing temperature and thermal residual stresses develop during the cool down to room temperature due to the nonuniformity of the plate. Residual stresses develop and the stress resultants are nonzero because of the plate heterogeneity.

It is known that the thermal expansion coefficients depend on the temperature (Adams, Bowles, and Herakovich, 1988). This dependence is not taken into account in the present work. Moreover, the plate is assumed to be subjected to a uniform temperature distribution. Additional assumptions are: the constitutive and strain-displacement relations are linear and the plate is totally

Contributed by the Applied Mechanics Division of THE AMERICAN SOCIETY OF MECHANICAL ENGINEERS for publication in the ASME JOURNAL OF APPLIED MECHANICS.
Discussion on the paper should be addressed to the Technical Editor, Professor Lewis T. Wheeler, Department of Mechanical Engineering, University of Houston, Houston, TX 77204-4792, and will be accepted until four months after final publication of the paper itself in the ASME JOURNAL OF APPLIED MECHANICS.
Manuscript received by the ASME Applied Mechanics Division, Feb. 2, 1998; final revision, Oct. 22, 1998. Associate Technical Editor: J. N. Reddy.

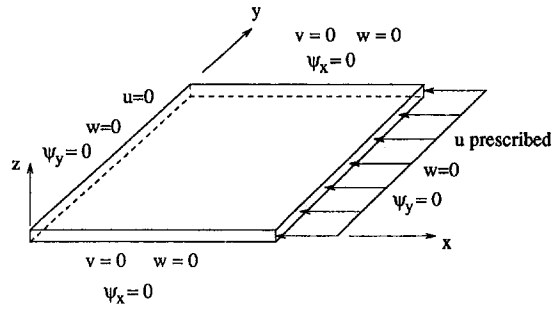

Fig. 1 Plate subjected to prescribed displacements and boundary conditions

unconstrained. The stress-strain relation, including thermal effects, is given in structural coordinates by (Jones, 1975)

$$\begin{Bmatrix} \sigma_x \\ \sigma_y \\ \tau_{xy} \end{Bmatrix} = [\bar{Q}]\left(\begin{Bmatrix} \epsilon_x \\ \epsilon_y \\ \gamma_{xy} \end{Bmatrix} - \Delta T \begin{Bmatrix} \alpha_x \\ \alpha_y \\ \alpha_{xy} \end{Bmatrix} \right),$$

$$\begin{Bmatrix} \tau_{xz} \\ \tau_{yz} \end{Bmatrix} = [\bar{Q}_S] \begin{Bmatrix} \gamma_{xz} \\ \gamma_{yz} \end{Bmatrix} \tag{1}$$

where σ_x, σ_y, τ_{xy} are the in-plane stress components; $[\bar{Q}]$ is the in-plane constitutive matrix; ϵ_x, ϵ_y, γ_{xy} are the strain components; ΔT is the temperature increment; α_x, α_y, α_{xy} are the thermal expansion coefficients in structural coordinates; τ_{xz}, τ_{yz} are the shear stress components; $[\bar{Q}_S]$ is the shear constitutive matrix; and γ_{xz}, γ_{yz} are shear strain components. The total potential energy for the thermal problem can be written as

$$\Pi_R = \tfrac{1}{2} \int_V \left(\begin{Bmatrix} \epsilon_x \\ \epsilon_y \\ \gamma_{xy} \end{Bmatrix}^T - \Delta T \begin{Bmatrix} \alpha_x \\ \alpha_y \\ \alpha_{xy} \end{Bmatrix}^T \right) [\bar{Q}] \left(\begin{Bmatrix} \epsilon_x \\ \epsilon_y \\ \gamma_{xy} \end{Bmatrix} - \Delta T \begin{Bmatrix} \alpha_x \\ \alpha_y \\ \alpha_{xy} \end{Bmatrix} \right) dV + \tfrac{1}{2} \int_V \begin{Bmatrix} \gamma_{xz} \\ \gamma_{yz} \end{Bmatrix}^T [\bar{Q}_S] \begin{Bmatrix} \gamma_{xz} \\ \gamma_{yz} \end{Bmatrix} dV. \tag{2}$$

It is to be noted that the thermal problem involves no application of mechanical loads and therefore there is no work term. Also, as noted above, the strain-displacement relation is taken to be linear. Thus, it is useful to define the vectors $\{\epsilon_0\}$, $\{\kappa\}$, $\{\gamma_0\}$, and $\{\bar{\alpha}\}$ as

$$\{\epsilon_0\} = \{u_{,x} \quad v_{,y} \quad u_{,y} + v_{,x}\}^T \quad \{\kappa\} = \{\psi_{x,x} \quad \psi_{y,y} \quad \psi_{x,y} + \psi_{y,x}\}^T$$

$$\{\gamma_0\} = \{w_{,x} + \psi_x \quad w_{,y} + \psi_y\}^T \quad \{\bar{\alpha}\} = \{\alpha_x \quad \alpha_y \quad \alpha_{xy}\}^T. \tag{3}$$

After Substitution of Eq. (3) into Eq. (2), the first variation of the total potential energy is obtained as

$$\delta\Pi_R = \int_S \begin{Bmatrix} \delta\epsilon_0 \\ \delta\kappa \\ \delta\gamma_0 \end{Bmatrix}^T \begin{bmatrix} [A] & [B] & [0] \\ [B] & [D] & [0] \\ [0] & [0] & [A^*] \end{bmatrix} \begin{Bmatrix} \epsilon_0 \\ \kappa \\ \gamma_0 \end{Bmatrix} dS - \int_S \begin{Bmatrix} \delta\epsilon_0 \\ \delta\kappa \end{Bmatrix}^T \begin{Bmatrix} \{N_t\} \\ \{M_t\} \end{Bmatrix} \Delta T dS \tag{4}$$

where $[A]$, $[B]$, $[D]$, and $[A^*]$ are the usual laminate stiffness matrices and $\{N_t\}$ and $\{M_t\}$ are thermal load vectors defined as $(\{N_t\}, \{M_t\}) = \int_{-t/2}^{t/2} (1, z)[\bar{Q}]\{\bar{\alpha}\}dz$.

Taking $\delta\Pi_R = 0$ in Eq. (4) yields the equilibrium equations which are solved for displacements and, subsequently, the thermal residual strains are evaluated using the strain-displacement relations. The residual strains obtained are used to recover the thermal residual stresses as follows:

$$\begin{Bmatrix} \sigma_x^R \\ \sigma_y^R \\ \tau_{xy}^R \end{Bmatrix} = [\bar{Q}]\left(\begin{Bmatrix} \epsilon_x^R \\ \epsilon_y^R \\ \gamma_{xy}^R \end{Bmatrix} - \Delta T \begin{Bmatrix} \alpha_x \\ \alpha_y \\ \alpha_{xy} \end{Bmatrix} \right), \quad \begin{Bmatrix} \tau_{xz}^R \\ \tau_{yz}^R \end{Bmatrix} = [\bar{Q}_S] \begin{Bmatrix} \gamma_{xz}^R \\ \gamma_{yz}^R \end{Bmatrix} \tag{5}$$

where the superscript R signifies residual.

2.2 Prebuckling Problem. In the prebuckling problem and the buckling problem the plate is assumed to be constrained by simple support boundary conditions on all four edges. No loads are induced when the boundary conditions are imposed. Also, the load, which causes the plate to buckle, is applied by imposing a uniform displacement on the loaded edge. A uniform displacement is applied rather than a uniform load because of the plate heterogeneity; for such a plate a uniform load is not physically realistic. It is assumed that during the load application the temperature is fixed. The first variation of the total potential energy is zero in the equilibrium state. Thus,

$$\delta\Pi_P = \int_S \begin{Bmatrix} \delta\epsilon_0 \\ \delta\kappa \\ \delta\gamma_0 \end{Bmatrix}^T \begin{bmatrix} [A] & [B] & [0] \\ [B] & [D] & [0] \\ [0] & [0] & [A^*] \end{bmatrix} \begin{Bmatrix} \epsilon_0 \\ \kappa \\ \gamma_0 \end{Bmatrix} dS = 0. \tag{6}$$

Along with the prescribed displacements and boundary conditions of Fig. 1, the solution for the mechanical prebuckling strains is obtained and used to generate the mechanical prebuckling stresses,

$$\begin{Bmatrix} \sigma_x^P \\ \sigma_y^P \\ \tau_{xy}^P \end{Bmatrix} = [\bar{Q}] \begin{Bmatrix} \epsilon_x^P \\ \epsilon_y^P \\ \gamma_{xy}^P \end{Bmatrix}, \quad \begin{Bmatrix} \tau_{xz}^P \\ \tau_{yz}^P \end{Bmatrix} = [\bar{Q}_S] \begin{Bmatrix} \gamma_{xz}^P \\ \gamma_{yz}^P \end{Bmatrix} \tag{7}$$

where the superscript P refers to prebuckling state.

2.3 Buckling Problem. The third step is the buckling state calculation. Here the full nonlinear strains are used. The constitutive equations must include the mechanical prebuckling and thermal residual effects. Thus,

$$\begin{Bmatrix} \sigma_x \\ \sigma_y \\ \tau_{xy} \end{Bmatrix} = [\bar{Q}] \begin{Bmatrix} \epsilon_x \\ \epsilon_y \\ \gamma_{xy} \end{Bmatrix} + \begin{Bmatrix} \sigma_x^R \\ \sigma_y^R \\ \tau_{xy}^R \end{Bmatrix} + \begin{Bmatrix} \sigma_x^P \\ \sigma_y^P \\ \tau_{xy}^P \end{Bmatrix}$$

$$\begin{Bmatrix} \tau_{xz} \\ \tau_{yz} \end{Bmatrix} = [\bar{Q}_S] \begin{Bmatrix} \gamma_{xz} \\ \gamma_{yz} \end{Bmatrix} + \begin{Bmatrix} \tau_{xz}^R \\ \tau_{yz}^R \end{Bmatrix} + \begin{Bmatrix} \tau_{xz}^P \\ \tau_{yz}^P \end{Bmatrix} \tag{8}$$

where ϵ_x, ϵ_y, γ_{xy}, γ_{xz}, and γ_{yz} contain both the linear and nonlinear parts of the strains as given by Almeida and Hansen (1997). The total potential energy of the plate is now written as

$$\Pi_B = \tfrac{1}{2} \int_V \begin{Bmatrix} \epsilon_x \\ \epsilon_y \\ \gamma_{xy} \end{Bmatrix}^T [\bar{Q}] \begin{Bmatrix} \epsilon_x \\ \epsilon_y \\ \gamma_{xy} \end{Bmatrix} dV + \int_V \begin{Bmatrix} \epsilon_x \\ \epsilon_y \\ \gamma_{xy} \end{Bmatrix}^T \left(\begin{Bmatrix} \sigma_x^R \\ \sigma_y^R \\ \tau_{xy}^R \end{Bmatrix} + \begin{Bmatrix} \sigma_x^P \\ \sigma_y^P \\ \tau_{xy}^P \end{Bmatrix} \right) dV + \tfrac{1}{2} \int_V \begin{Bmatrix} \gamma_{xz} \\ \gamma_{yz} \end{Bmatrix}^T [\bar{Q}_S] \begin{Bmatrix} \gamma_{xz} \\ \gamma_{yz} \end{Bmatrix} dV + \int_V \begin{Bmatrix} \gamma_{xz} \\ \gamma_{yz} \end{Bmatrix}^T \left(\begin{Bmatrix} \tau_{xz}^R \\ \tau_{yz}^R \end{Bmatrix} + \begin{Bmatrix} \tau_{xz}^P \\ \tau_{yz}^P \end{Bmatrix} \right) dV. \tag{9}$$

Before proceeding, it is worthwhile considering the laminate symmetry and the in-plane characteristics of both the thermal and prebuckling problems. Since the laminate is symmetric, no membrane-bending coupling occurs and, because all the loads are applied in-plane, $\{\sigma^P\}$ and $\{\sigma^R\}$ have a symmetric distribution about $z = 0$ and $\{\tau^P\} = \{\tau^R\} = \{0\}$. This means that simplifications can be introduced to Eq. (9) when integrating through the

thickness. For this purpose define stress moments $\{N\}$, $\{M\}$, $\{L\}$, $\{Q\}$, and $\{T\}$ as

$$\left(\begin{Bmatrix} N_x^S \\ N_y^S \\ N_{xy}^S \end{Bmatrix}, \begin{Bmatrix} M_x^S \\ M_y^S \\ M_{xy}^S \end{Bmatrix}, \begin{Bmatrix} L_x^S \\ L_y^S \\ L_{xy}^S \end{Bmatrix}\right) = \int_{-t/2}^{t/2} (1, z, z^2) \begin{Bmatrix} \sigma_x^S \\ \sigma_y^S \\ \tau_{xy}^S \end{Bmatrix} dz$$

$$\left(\begin{Bmatrix} Q_x^S \\ Q_y^S \end{Bmatrix}, \begin{Bmatrix} T_x^S \\ T_y^S \end{Bmatrix}\right) = \int_{-t/2}^{t/2} (1, z) \begin{Bmatrix} \tau_{xz}^S \\ \tau_{yz}^S \end{Bmatrix} dz \quad (10)$$

where $S = R, P$. Hence, dropping higher-order terms, recalling that the thermal residual stresses and prebuckling mechanical stresses represent linear states of equilibrium and recognizing that $\{M\}$, $\{Q\}$, and $\{T\}$ are identically zero yields, after integrating through the thickness,

$$\delta\Pi_B = \int_S \{\delta\epsilon_0\}^T [A] \{\epsilon_0\} dS + \int_S \{\delta\kappa\}^T [D] \{\kappa\} dS + \int_S \{\delta\gamma_0\}^T [A^*] \{\gamma_0\} dS + \int_S \left(\begin{Bmatrix} \delta u_{,x} \\ \delta u_{,y} \end{Bmatrix}^T \begin{bmatrix} N_x^{RP} & N_{xy}^{RP} \\ N_{xy}^{RP} & N_y^{RP} \end{bmatrix} \begin{Bmatrix} u_{,x} \\ u_{,y} \end{Bmatrix} + \begin{Bmatrix} \delta v_{,x} \\ \delta v_{,y} \end{Bmatrix}^T \begin{bmatrix} N_x^{RP} & N_{xy}^{RP} \\ N_{xy}^{RP} & N_y^{RP} \end{bmatrix} \begin{Bmatrix} v_{,x} \\ v_{,y} \end{Bmatrix} + \begin{Bmatrix} \delta w_{,x} \\ \delta w_{,y} \end{Bmatrix}^T \begin{bmatrix} N_x^{RP} & N_{xy}^{RP} \\ N_{xy}^{RP} & N_y^{RP} \end{bmatrix} \begin{Bmatrix} w_{,x} \\ w_{,y} \end{Bmatrix} + \begin{Bmatrix} \delta\psi_{x,x} \\ \delta\psi_{x,y} \end{Bmatrix}^T \begin{bmatrix} L_x^{RP} & L_{xy}^{RP} \\ L_{xy}^{RP} & L_y^{RP} \end{bmatrix} \begin{Bmatrix} \psi_{x,x} \\ \psi_{x,y} \end{Bmatrix} + \begin{Bmatrix} \delta\psi_{y,x} \\ \delta\psi_{y,y} \end{Bmatrix}^T \begin{bmatrix} L_x^{RP} & L_{xy}^{RP} \\ L_{xy}^{RP} & L_y^{RP} \end{bmatrix} \begin{Bmatrix} \psi_{y,x} \\ \psi_{y,y} \end{Bmatrix} \right) dS = 0 \quad (11)$$

where $(N_i^{RP}, L_i^{RP}) = (N_i^R + N_i^P, L_i^R + L_i^P)$, $i = x, y, xy$.

A buckling parameter, λ, is introduced to provide a measure of the prebuckling load. Without loss of generality, unit displacements are prescribed and, since the prebuckling problem is linear, multiplication of the moments N_i^P and L_i^P by λ gives the actual load level.

3 Finite Element Formulation

The finite element method was chosen to solve the thermal, prebuckling, and buckling problems described by Eqs. (4), (6), and (11), respectively. Isoparametric bi-cubic Lagrangian elements with 16 nodes are used (Heppler and Hansen, 1986). These elements are known to eliminate shear locking effects. The displacements and rotations can be written in terms of nodal variables and interpolation functions as

$$a = [\Phi]\{a_1 \quad a_2 \quad \ldots \quad a_{16}\}^T \quad (12)$$

where a stands for u, v, w, ψ_x, or ψ_y. It is observed that, in all three problems, the same stiffness matrix is present. Thus, with the aid of Eq. (12), it is possible to write the expression for the element stiffness matrix $[K]_e$:

$$[K]_e = \int_{S_e} \begin{bmatrix} [B_1]_{3\times32} & [0]_{3\times48} \\ [0]_{3\times48} & [B_1]_{3\times32} \\ [0]_{2\times32} & [B_2]_{2\times48} \end{bmatrix}^T \begin{bmatrix} [A] & [B] & [0] \\ [B] & [D] & [0] \\ [0] & [0] & [A^*] \end{bmatrix}_e \times \begin{bmatrix} [B_1]_{3\times32} & [0]_{3\times48} \\ [0]_{3\times48} & [B_1]_{3\times32} \\ [0]_{2\times32} & [B_2]_{2\times48} \end{bmatrix} dS \quad (13)$$

where

$$[B_1] = \begin{bmatrix} [\Phi_{,x}] & [0] \\ [0] & [\Phi_{,y}] \\ [\Phi_{,y}] & [\Phi_{,x}] \end{bmatrix}_{3\times32} \qquad [B_2] = \begin{bmatrix} [\Phi_{,x}] & [\Phi] & [0] \\ [\Phi_{,y}] & [0] & [\Phi] \end{bmatrix}_{2\times48}.$$

In addition to $[K]_e$, the load vector must be obtained for the thermal problem. Thus, the element thermal load vector $\{f_T\}_e$ is

$$\{f_T\}_e = \int_{S_e} \begin{bmatrix} [B_1]_{3\times32} & [0]_{3\times48} \\ [0]_{3\times48} & [B_1]_{3\times32} \\ [0]_{2\times32} & [B_1]_{2\times48} \end{bmatrix}^T \begin{Bmatrix} N_t \\ M_t \end{Bmatrix} dS. \quad (14)$$

At this point it is possible to write the matrix equations for the thermal and prebuckling problems. After assembling the element matrices and vectors, the linear systems describing, respectively, the thermal and prebuckling steps are

$$[K]\{q_T\} = \{f_T\}, \quad [K]\{q_P\} = \{f_P\} \quad (15)$$

where the load vector $\{f_P\}$ comes from the application of the prescribed displacements.

The calculation of the geometric stiffness matrices for the buckling problem is more elaborate since the stress moments $\{N\}$ and $\{L\}$ are present. These moments come from the previous problem steps. In general both $\{N\}$ and $\{L\}$ will vary within each element so numerical integration must be used to build up the geometric stiffness matrices taking into account this spatial variation. Defining matrix $[B_3]$ as

$$[B_3]^T = \begin{bmatrix} [\Phi_{,x}]^T & [\Phi_{,y}]^T & [0] & [0] & [0] & [0] & [0] & [0] & [0] & [0] \\ [0] & [0] & [\Phi_{,x}]^T & [\Phi_{,y}]^T & [0] & [0] & [0] & [0] & [0] & [0] \\ [0] & [0] & [0] & [0] & [\Phi_{,x}]^T & [\Phi_{,y}]^T & [0] & [0] & [0] & [0] \\ [0] & [0] & [0] & [0] & [0] & [0] & [\Phi_{,x}]^T & [\Phi_{,y}]^T & [0] & [0] \\ [0] & [0] & [0] & [0] & [0] & [0] & [0] & [0] & [\Phi_{,x}]^T & [\Phi_{,y}]^T \end{bmatrix}$$

allows the element geometric stiffness matrix, $[K_G]_e$, to be written as

$$[K_G^S]_e = \int_{S_e} [B_3]^T \begin{bmatrix} N_x^S & N_{xy}^S & 0 & 0 & 0 & 0 & 0 & 0 & 0 & 0 \\ N_{xy}^S & N_y^S & 0 & 0 & 0 & 0 & 0 & 0 & 0 & 0 \\ 0 & 0 & N_x^S & N_{xy}^S & 0 & 0 & 0 & 0 & 0 & 0 \\ 0 & 0 & N_{xy}^S & N_y^S & 0 & 0 & 0 & 0 & 0 & 0 \\ 0 & 0 & 0 & 0 & N_x^S & N_{xy}^S & 0 & 0 & 0 & 0 \\ 0 & 0 & 0 & 0 & N_{xy}^S & N_y^S & 0 & 0 & 0 & 0 \\ 0 & 0 & 0 & 0 & 0 & 0 & L_x^S & L_{xy}^S & 0 & 0 \\ 0 & 0 & 0 & 0 & 0 & 0 & L_{xy}^S & L_y^S & 0 & 0 \\ 0 & 0 & 0 & 0 & 0 & 0 & 0 & 0 & L_x^S & L_{xy}^S \\ 0 & 0 & 0 & 0 & 0 & 0 & 0 & 0 & L_{xy}^S & L_y^S \end{bmatrix} [B_3] dS \quad (16)$$

where S indicates either the thermal residual state R or the prebuckling state P. The global matrices for the eigenvalue problem related to the buckling calculation are then written as

$$([K] + [K_G^R] - \lambda[K_G^P])\{q_B\} = \{0\} \quad (17)$$

where matrix $[K_G^P]$ is obtained from the application of unit displacements and λ is the buckling parameter.

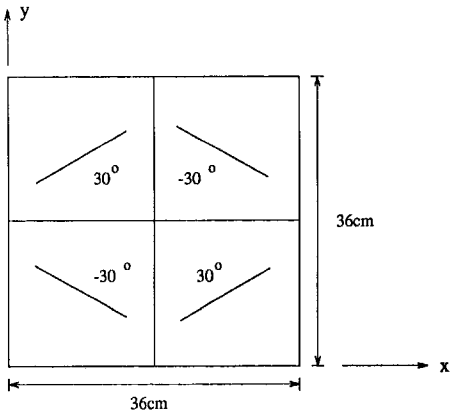

Fig. 2 Plate configuration for the validation tests

4 Preliminary Results

Before going on to the optimization procedures, a few tests are conducted in order to assess the accuracy of the implemented program. The model developed should furnish precise results while maintaining simplicity so as to minimize the numerical optimization effort.

The plate chosen for validation is square with 360 mm sides and 0.6 mm total thickness. The plate has four subregions oriented as shown in Fig. 2. The laminate has only one layer, hence it is symmetric. The material chosen for the simulations is graphite/epoxy T300-5208; its properties are given in Table 1.

Two models based on Eqs. (15) and (17) were implemented: one considering that the displacements u and v make a negligible contribution to the eigenvalue problem and the other considering the complete model, i.e., u, v, w, ψ_x, and ψ_y may be nonzero. This means that the eigenvector associated with the simplified model contains components related to w, ψ_x, and ψ_y only. The results for a temperature difference of $\Delta T = -15°C$ are in Table 2. Observe that the temperature difference is negative since processing is carried out at elevated temperatures while the operating temperature is lower.

The solution of the eigenproblem as in Eq. (17) provides an eigenvalue which is the prescribed displacement. In order to clarify the presentation, an equivalent force, P, is introduced. This equivalent force is the summation of the point forces required to impose the prescribed displacement on one edge of the plate. Notice the small percentage difference existing (<0.5 percent) between the λ's. This fact led to the adoption of the simplified model for the optimization procedures.

This preliminary example illustrates the potential enhancement of the critical buckling load of plates when thermal residual stresses are considered. Results are presented in Table 2 where λ_1 is the least eigenvalue, λ_2 the second least eigenvalue, P_1 the equivalent force associated with λ_1 and P_2 the equivalent force associated with λ_1. Notice that $P_1/\lambda_1 = P_2/\lambda_2$ because the pre-buckling problem is considered to be linear. Second eigenvalues are presented in Table 2 in order to illustrate the fact that the accuracy of the simplified model is extended to eigenvalues other than the first.

Table 1 Material properties of T300/5208 graphite/epoxy

property	value
Principal modulus of elasticity, E_1	154.5 GPa
Principal modulus of elasticity, E_2	11.13 GPa
In-plane poisson's ratio, ν_{12}	0.304
In-plane shear modulus, G_{12}	6.98 GPa
Transverse shear modulus, G_{13}	6.98 GPa
Transverse shear modulus, G_{23}	3.36 GPa
Principal thermal expansion coefficient, α_1	$-0.17\ 10^{-6}\,°C^{-1}$
Principal thermal expansion coefficient, α_2	$23.1\ 10^{-6}\,°C^{-1}$

Table 2 Comparison between reduced and full models

FE	complete model				simplified model				diff. (%)	
Mesh	λ_1	λ_2	P_1	P_2	λ_1	λ_2	P_1	P_2	1	2
2 × 2	8.540	12.09	258.1	365.3	8.562	12.12	257.9	365.0	0.26	0.25
4 × 4	7.744	9.324	215.6	259.6	7.755	9.335	251.5	259.4	0.14	0.12
6 × 6	7.679	9.248	210.0	252.4	7.704	9.255	210.0	252.3	0.09	0.07

a. λ_i in μm and P_i in N

The simulations in Table 2 were made for $\Delta T = -15°C$ but, if $\Delta T = 0°C$, the 6 × 6 mesh gives, for the same configuration, $\lambda_1 = 4.592\ \mu m$ and $P_1 = 125.3$ N. So, it can be noticed that, by simply considering the thermal effects, an increase of 66 percent is achieved.

5 Optimization Procedure

The eigenproblem described by Eq. (17) is solved by subspace iteration along with the Jacobi method to solve the projected problem (Bathe and Wilson, 1976). The least of the eigenvalues is referred to as the critical buckling load. The objective of this work is to maximize λ_{MIN} in Eq. (17). Previous studies have demonstrated that optimization disregarding the thermal stress ($\Delta T = 0°C$) of the simplified eigenproblem $|[K] - \lambda[K_G^P]| = 0$, where the geometric stiffness matrix is constant for the pure membrane prebuckling state, is possible and successfully increased the buckling loads of plates. A more general approach, intended to exploit the thermal stresses, allowing the matrix $[K_G^P]$ to vary is implemented in this work.

It is known that optimization procedures, where the fiber orientation is taken as the design variable, have multiple optima and near-optimal designs (Le Riche and Haftka, 1993). This peculiar feature suggests that care must be taken when selecting the optimization technique. Continuous optimization methods are often victims of convergence to local optima since they "climb the hill" where the search begins, irrespective of whether it contains the global optimum. To overcome these difficulties, structural designers have been using probabilistic methods where, during the optimization search, decisions are taken by drawing pseudo-random numbers and applying some acceptance rule to them. The strategy adopted here is a combination of deterministic and probabilistic approaches. First, a genetic algorithm (GA) (Holland, 1975) is used to obtain a design reasonably close to the global optimum. In the second-stage Powell's method (Vanderplaats, 1984), is used to improve the solution accuracy bringing it to the actual optimum.

6 Numerical Results

In order to assess the effectiveness of the proposed strategy, plates with one, three, and five plies and with four subregions (see Fig. 3) were investigated. Table 3 shows the fiber orientations in each case, where θ_i is the fiber orientation of the central ply of subregion i.

All plates analyzed are square with 360 mm sides, total thickness of 0.6 mm, free of initial imperfections, and laminate symmetry is maintained. For the thermal problem the plates are totally unconstrained; for the prebuckling and buckling problems the boundary conditions are shown in Fig. 1. Prescribed displacements, u, are applied to one side of the plate.

The thermal coefficients of expansion were chosen according to Adams, Bowles, and Herakovich (1988). As mentioned, these coefficients vary with temperature; however, for the present cal-

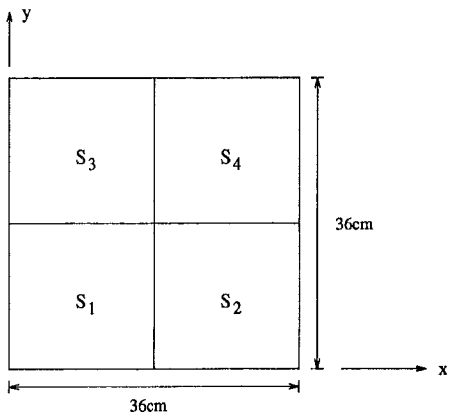

Fig. 3 Plate subregions

culations, the values shown in Table 1 were adopted and they correspond to a service temperature of 21°C.

6.1 Case 1—Single-Ply Plate. In this case, the plate has four subregions in which independent fiber orientation is allowed. Since there is only one layer per region, the number of design variables is four. Simulations for five different temperature decrements, ΔT, were conducted.

The first approximation to the optimal design was obtained with the genetic algorithm. The search parameters were chosen experimentally and are presented in Table 4.

Each design is encoded as a string (chromosome) of four genes, each of them representing the fiber orientation of a subregion. The alleles are the values that a gene can be assigned; in this case it ranges from −90 deg to +90 deg. The reproduction process, or crossover, can be implemented in several ways. The strategy chosen here is one of the most commonly adopted and consists in breaking the chromosomial string of two parents into substrings and, later, exchanging the substrings to generate the offspring.

A stochastic mutation operator is also introduced. This operator is required to avoid premature convergence. In fact, as the generations evolve, the individuals tend to become uniform implying a loss of genetic diversity. Mutation maintains the genetic diversity by introducing new information into the newly formed generations; it randomly modifies genes of the newborn child. In this work the probability of mutation is 50 percent per chromosome. This means that a child has a 50 percent chance of being modified by mutation. The mutation is carried out by choosing one of the four genes and assigning it a random orientation between −90 deg and +90 deg.

The elitist strategy is also used. It consists in actually cloning the best design of a given generation into the next generation. The elitist strategy provides a useful convergence criteria for the genetic algorithm. In the simulations made, the search is assumed to have converged when the best individual of a population remains unchanged for seven generations. In this work, 2 × 2, and sometimes 4 × 4, finite element meshes are implemented in all optimization calculations using the genetic algorithm method. A typical run of the GA takes from 10 to 15 generations to converge. Thus, about 500 function evaluations (buckling load calculations) are required.

After having found the first approximation by the GA, a more accurate optimization is conducted using Powell's method. The finite element mesh is refined and a continuous search is performed. In all cases, a convergence check is made by refining the mesh for the optimal design found. It was determined that a 6 × 6 mesh is required to ensure three percent precision of the first eigenvalue. Typically 150 objective function evaluations are needed for convergence. Notice, however, that Powell's method is often used with finer finite element meshes and, thus, more computational effort is required. At the end, the GA and Powell's method require approximately the same processing time.

In Table 5 the results for the optimized single-ply plates are presented. The angles θ_1, θ_2, θ_3, and θ_4 are those of subdomains 1, 2, 3, and 4, respectively, according to Fig. 3. P_1^r and P_2^r are the equivalent forces obtained using a finer finite element mesh. The optimization procedure is assumed to have converged when the difference between P_1 and P_1^r is no more than three percent.

The optimal design obtained for $\Delta T = -75$°C can be better understood if the symmetries of the problem are considered. Observe that, under the assumptions adopted, boundary conditions considered and load imposed, the laminate whose subdomains are oriented as $\theta_1' = -\theta_3$, $\theta_2' = -\theta_4$, $\theta_3' = -\theta_1$ and $\theta_4' = -\theta_2$ possesses the same buckling loads as that with θ_1, θ_2, θ_3, and θ_4 orientations.

An interesting question that arises is how the thermal residual stresses actually increase the critical buckling load of flat plates. It is readily observed in Table 5 that the buckling load roughly doubled when ΔT changed from 0°C to −25°C. A plot of the thermal residual stress levels is shown in Figs. 4(*a*), 4(*b*), and 4(*c*) for the optimal design at −25°C. Also, it is important to mention that the eigenvector of the optimal designs for $\Delta T =$, −25°C, −50°C, −75°C and −100°C present symmetry about the plate diagonals, as opposed to the usual symmetry about the plate center lines.

Figures 4(*a*), 4(*b*), and 4(*c*) suggest that the optimal plate is tailored in such a way that the thermal residual stresses tend to concentrate around the interfaces of the different subregions, specially near the plate edge. These stresses would try to imitate the

Table 3 Plate configurations

plate class	*i*-th subregion orientation
1	$[\theta_i]$
2	$[0°/\theta_i/0°]$
3	$[0°/90°/\theta_i/90°/0°]$

Table 4 Genetic algorithm parameters

parameter	value
population size	50
probability of cross-over	0.97
probability of mutation	0.50

Table 5 Optimization for plate 1

ΔT	method	FE mesh	θ_1	θ_2	θ_3	θ_4	P_1	P_2	P_1^r	P_2^r
0	GA	2 × 2	-41.1	23.2	32.1	-38.1	139.8	249.8	121.5	195.1
°C	Powell	2 × 2	-32.0	32.1	31.6	-31.6	143.6	266.7	125.3	203.4
	Powell	4 × 4	-27.0	25.0	25.5	-26.4	127.6	234.6	126.2	229.0
-25	GA	2 × 2	-30.8	48.1	45.7	-31.4	300.4	323.7	193.1	217.4
°C	Powell	2 × 2	-28.9	45.7	48.4	-25.9	303.3	342.7	204.9	232.6
	Powell	4 × 4	-14.3	53.7	54.6	-13.3	257.7	292.0	251.3	281.1
-50	GA*	4 × 4	4.8	30.8	32.9	3.7	254.6	314.0	243.6	298.5
°C	Powell	6 × 6	4.4	36.0	36.6	4.3	250.2	295.7	247.6	288.6
-75	GA*	4 × 4	-37.2	-6.7	-6.3	-28.5	207.8	231.1	165.7	209.1
°C	Powell	6 × 6	-34.5	-10.8	-10.3	-34.8	222.6	225.2	217.6	221.1
-100	GA*	4 × 4	12.3	36.8	34.7	19.4	197.5	210.0	143.7	158.9
°C	Powell	6 × 6	20.3	33.9	33.3	19.8	207.5	232.0	202.0	219.5

a. (*) GA performed more than once

b. P_i^r are the equivalent forces for a finer mesh

c. θ_i in degrees and P_i in N

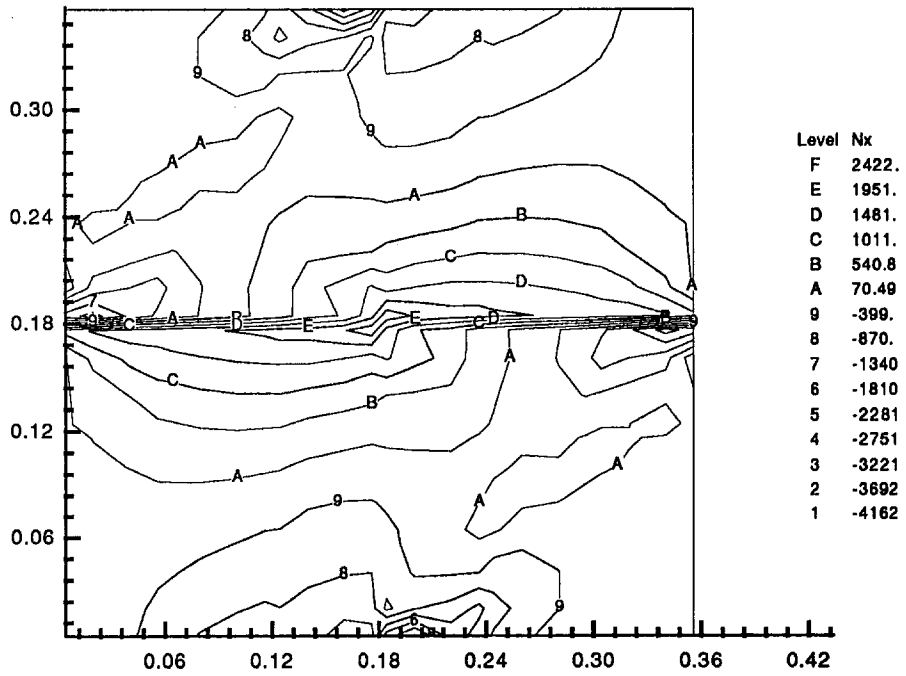

Fig. 4(*a*) Thermal residual stress distribution (N_{xx})

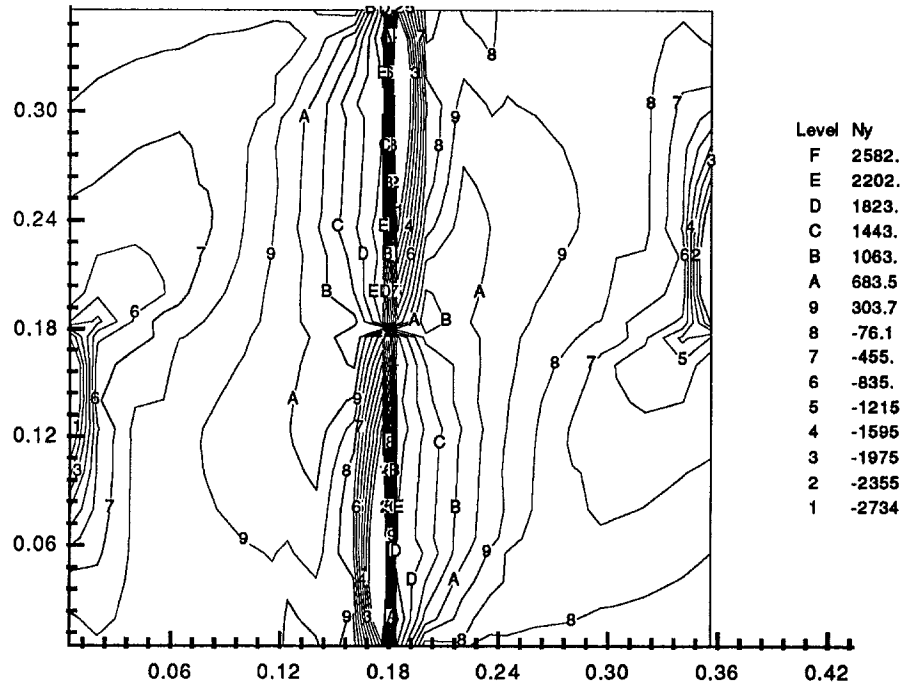

Fig. 4(*b*) Thermal residual stress distribution (N_{yy})

effects of stringers placed in the x and y-directions along the plate center lines.

The thermal residual stresses vary linearly with the temperature decrement but the way they affect the buckling behavior of each plate is different. Therefore, a small temperature decrement can enhance the buckling load more than a large temperature difference. This is why the $\Delta T = -25°C$ case is, among the results shown, of better performance. Moreover, notice that there is a decrease in P_1 as ΔT varies from $-25°C$ to $-100°C$. This means that the thermal residual stresses have an adverse effect on the single-ply laminate which cannot be reversed, even by carefully choosing the subdomain orientations for larger ΔT.

6.2 Case 2—Three-Ply Plate. One concern regarding case 1 is the continuity of the plate. In actual applications, single-ply plates such as the one simulated would exhibit a material failure either as a result of the thermal stresses or from a combination of thermal and prebuckling mechanical stresses at the interface between the subregions. The fragile liaison between the subregions is not capable of resisting large stresses.

The solution proposed here is to simply keep the subregions together by placing external uniform layers of composite material on the plate of case 1. This procedure produces a structure similar to a sandwich plate where the core is composed of subregions and the facings have uniform orientation.

In case two, the total thickness of 0.6 mm is kept but one 0-deg facing layer is attached on the top and bottom of the "core." Thus, each layer is 0.2 mm thick.

Differently from the optimal designs for plate 1, the optimal

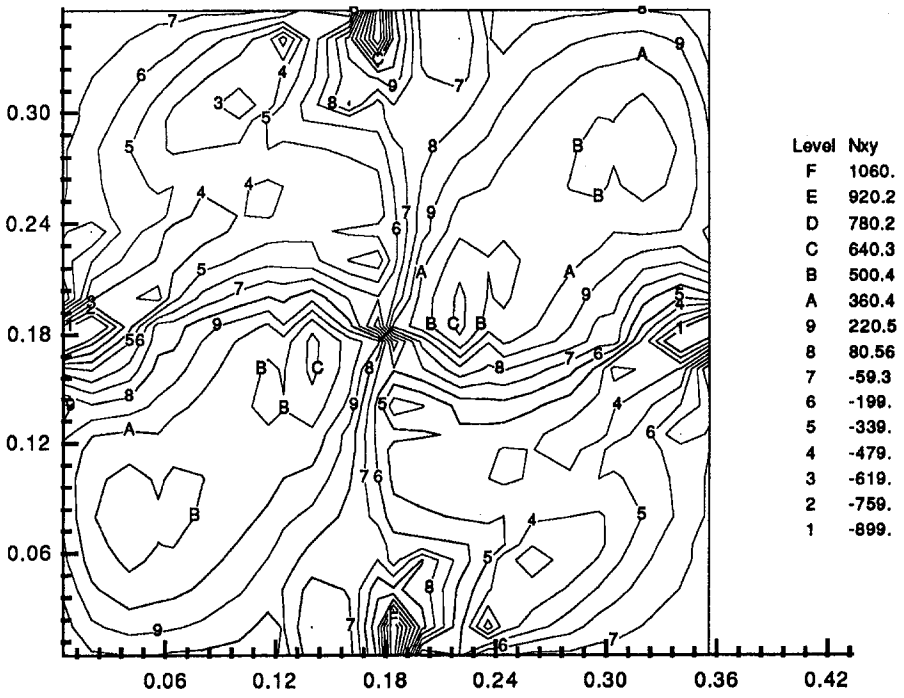

Fig. 4(*c*) Thermal residual stress distribution (N_{xy})

designs for plate 2 possess eigenvectors associated with λ_1 which are symmetric about the center lines of the plate. Moreover, it can be noticed from Table 6 that all the angles have close absolute values. This suggests that the mechanism by which the thermal residual stresses acted to improve the buckling load has changed from plate 1 to 2 in the sense that the optimal eigenvector shape was modified. Furthermore, a comparison between the optimal eigenvalues presented in Tables 5 and 6 shows that higher levels are reached in the latter.

It is noticed that the optimal designs in Table 6 are of the form $\theta_1 = \theta_4 = -\theta$, $\theta_2 = \theta_3 = \theta$. Based on this fact, a test to check the validity of the results found for plate 1 was conducted. For the single-ply plate at $\Delta T = -50$°C and subdomains oriented as $\theta_1 = \theta_4 = -\theta$ and $\theta_2 = \theta_3 = \theta$, the angle $\theta = 16$ deg produces the highest buckling load of $P_1 = 224.2$ N which is lower than the value found (247.6 N) in Table 5. In addition, if Powell's method is started using the optimal design orientations of plate 2 at −50°C to optimize plate 1 at the same temperature difference the resulting configuration is $\theta_1 = -69.3$ deg, $\theta_2 = 68.1$ deg, $\theta_3 = 69.3$ deg, and $\theta_4 = -68.5$ deg with $P_1 = 103.7$ N which is certainly a local optimum.

6.3 Case 3—Five-Ply Plate. In this case, the total thickness is maintained at 0.6 mm but two facing layers are added above and below the "core." Results are shown in Table 7.

A comparison between Tables 6 and 7 shows that the five-ply plate is superior to the three-ply plate; the choice of cross-ply facings yielded a better performance. It suggests that an even more sophisticated optimization, which encompasses the facings orien-

Table 6 Optimization for plate 2

ΔT	method	FE mesh	θ_1	θ_2	θ_3	θ_4	P_1	P_2	P_1^r	P_2^r
0	GA	2 × 2	-6.1	27.9	13.4	-7.8	98.06	226.9	97.33	208.6
°C	Powell	2 × 2	-7.0	7.9	9.3	-9.4	98.26	231.1	97.56	212.3
	Powell	4 × 4	-8.4	8.6	8.1	-8.4	97.57	212.3	97.53	211.7
-25	GA	2 × 2	-77.1	59.1	69.1	-73.6	244.7	333.4	214.2	262.1
°C	Powell	2 × 2	-78.3	72.0	71.5	-73.3	254.1	357.9	227.1	288.7
	Powell	4 × 4	-75.5	73.0	73.8	-75.4	228.7	297.9	225.0	294.3
-50	GA	2 × 2	-85.2	61.6	64.5	-87.6	253.1	364.0	201.2	232.5
°C	Powell	2 × 2	-79.8	80.4	78.3	-79.5	285.6	337.4	241.3	265.5
	Powell	4 × 4	-81.0	82.4	82.4	-80.9	250.0	305.1	245.5	300.6
-75	GA	2 × 2	-77.8	79.8	83.8	-83.8	292.8	300.1	207.8	220.4
°C	Powell	2 × 2	-82.9	80.6	83.1	-83.2	297.1	334.9	245.4	260.8
	Powell	4 × 4	-86.1	83.9	83.1	-83.4	257.2	304.0	252.2	299.1
-100	GA	2 × 2	-87.5	84.0	76.9	-85.6	289.4	256.9	215.4	238.0
°C	Powell	2 × 2	-88.5	82.6	81.9	-83.5	302.0	335.5	247.4	257.1
	Powell	4 × 4	-88.5	87.5	82.6	-83.5	259:9	301.0	254.8	295.5

a. P_i^r are the equivalent forces for a finer mesh

b. θ_i in degrees and P_i in N

Table 7 Optimization for plate 3

ΔT	method	FE mesh	θ_1	θ_2	θ_3	θ_4	P_1	P_2	P_1^r	P_2^r
0	GA	2 × 2	3.9	0.5	-8.5	1.6	96.39	320.2	95.88	269.3
°C	Powell	2 × 2	-1.9	2.1	2.1	-2.2	96.71	320.4	96.11	269.4
	Powell	4 × 4	-1.1	0.9	0.8	-1.2	96.12	269.4	96.09	268.0
-25	GA	2 × 2	-59.2	50.3	53.5	-77.0	222.5	377.3	206.5	319.3
°C	Powell	2 × 2	-48.1	46.0	46.4	-46.0	238.1	385.1	217.5	321.8
	Powell	4 × 4	-47.6	47.4	47.3	-47.7	217.6	322.0	216.0	320.3
-50	GA	2 × 2	-38.4	62.6	60.0	-69.9	309.7	359.4	265.0	293.0
°C	Powell	2 × 2	-51.6	51.3	51.2	-52.0	319.3	345.5	261.0	277.9
	Powell	4 × 4	-63.4	63.5	63.3	-63.4	267.8	300.8	264.7	297.7
-75	GA	2 × 2	-67.8	43.3	61.2	-82.0	342.0	347.6	274.8	277.9
°C	Powell	2 × 2	-66.5	60.8	54.4	-82.0	344.1	351.4	276.5	284.6
	Powell	4 × 4	-73.6	71.8	73.1	-72.0	285.4	304.0	281.6	300.4
-100	GA	2 × 2	-8.0	16.9	44.8	-7.9	347.3	352.7	283.2	285.0
°C	Powell	2 × 2	-17.9	21.5	11.8	-11.5	357.2	357.7	285.7	288.9
	Powell	4 × 4	-11.2	15.0	14.9	-10.8	289.9	310.4	285.6	307.8

a. P_i^r are the equivalent forces for a finer mesh

b. θ_i in degrees and P_i in N

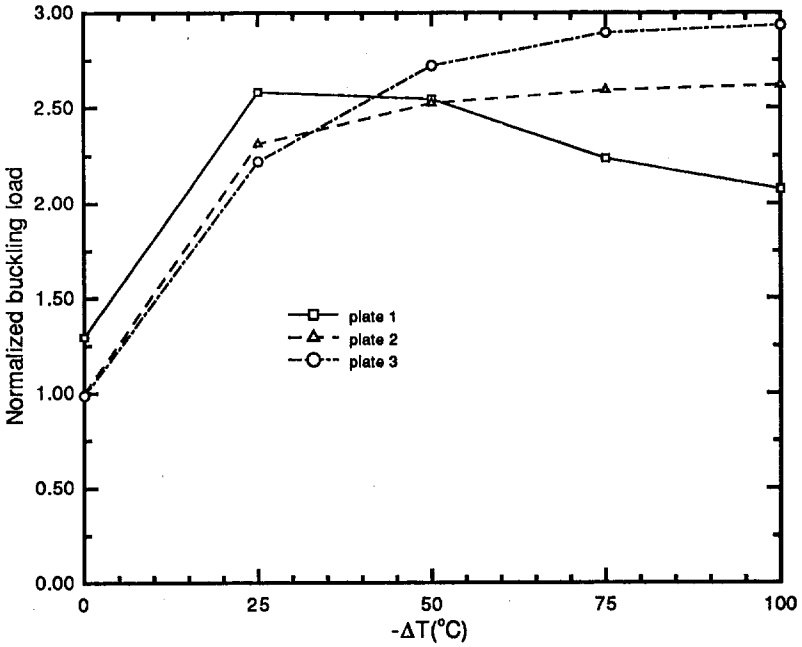

Fig. 5 Comparison between optimized plates

tations, could be implemented. The facings would still be uniform but their orientation would be allowed to vary from ply to ply.

7 Comments

The results achieved undoubtedly indicate that the thermal residual stresses can be effectively tailored in order to enhance the buckling strength of composite plates. In some cases the critical buckling load is up to three times that of the best plate where thermal residual stresses are disregarded ($\Delta T = 0°C$). Figure 5 shows the comparison between the plates optimized in this work. The buckling loads are normalized by the buckling load of a plate of the same thickness composed of a [0 deg] laminate, $P_1 = 97.30$ N.

Bi-cubic Lagrangian elements were used in the finite element analysis although it is often recommended that elements as simple as possible are implemented in optimization procedures. As a matter of fact, bi-quadratic Lagrangian elements were tried but did not revealed themselves of any advantage; the bi-cubics have superior performance.

Convergence analyses were made for both thermal and buckling problems. As a general rule, finer meshes are required for the buckling problem. It suggests that different meshes, coarse and fine for the thermal and buckling problems, respectively, could be used. Nevertheless, since the thermal and prebuckling problems consume only a fraction of time compared to the buckling problem, there is little point in accelerating the numerically inexpensive steps 1 and 2.

In the single-ply plate, the thermal residual stresses, either alone or combined with prebuckling mechanical stresses, could eventually induce failure at the subregion interface or delamination. The proposed remedy to this problem was the placement of uniform facings onto the "core." Nevertheless, large stress levels could still develop leading to plate failure even before the instability is reached. A constrained optimization search would be necessary to avoid this undesirable side effect. The most straightforward technique to take constraints into account is the incorporation of penalty functions to the objective function. This technique has proven successful in optimization using GA (Le Riche and Haftka, 1993) and, along with the choice of a suitable failure criteria, could be implemented here.

A more realistic optimization of plates with thermal residual stresses would consider a continuous range of operating temperature rather than a discrete one. Optimal designs should then be tested within a relatively broad range of temperature before becoming operational. For instance, the single-ply optimal design at 0°C was investigated and, surprisingly, it buckles under the residual thermal effects alone for temperature differences greater than $\Delta T = -73°C$. Similarly, optimal designs may fail at temperatures other than that at which they were conceived to operate. Studies towards optimality criteria that assess the design response at a continuous temperature domain would be of great use.

Acknowledgments

Valuable discussions with Prof. Sérgio F. M. de Almeida are appreciated and gratefully acknowledged. Without his comments this work would not be possible.

This work was partially financed by the Brazilian governmental agency CAPES (Coordenadoria de Aperfeiçoamento de Pessoal de Nível Superior) and by NSERC, Research Grant No. 3663.

References

Adams, D. S., Bowles, D. E., and Herakovich, C. T., 1988, "Thermally Induced Transverse Cracking in Graphite-Epoxy Cross-ply Laminates," *Environmental effects on composite materials,* Vol. 3, Springer, ed., Technomic, Lancaster, PA, pp. 247–274.

Almeida, S. F. M., and Hansen, J. S., 1997, "Enhanced Elastic Buckling Loads of Composite Plates With Tailored Thermal Residual Stresses," ASME JOURNAL OF APPLIED MECHANICS, Vol. 64, pp. 772–780.

Bathe, K.-J., and Wilson, E. L., 1976, *Numerical Methods in Finite Element Analysis,* Prentice-Hall, Englewood Cliffs, NJ, Chapters 11 and 12.

Heppler, G. R., and Hansen, J. S., 1984, "A Mindlin Element for Thick and Deep Shells," *Computer Methods in Applied Mechanics and Engineering,* Vol. 54, No. 1, pp. 21–47.

Holland, J. H., 1975, *Adaptation in Natural and Artificial Systems,* The University of Michigan Press, Ann Arbor, MI.

Jones, R. M., 1975, *Mechanics of Composite Materials,* Hemisphere, Washington, DC, Chapter 4.

Le Riche, R., and Haftka, R. T., 1993, "Optimization of Laminate Stacking Sequence for Buckling Load Maximization by Genetic Algorithm," *AIAA Journal,* Vol. 31, No. 5, pp. 951–956.

Ram, S., and Sinha, P. K., 1992, "Hygrothermal Effects on the Buckling of Composite Laminated Plates," *Composite Structures,* Vol. 21, pp. 233–247.

Strang, G., and George, J. F., 1973, *An Analysis of the Finite Element Method,* Prentice-Hall, Englewood Cliffs, NJ, Chapter 10.

Vanderplaats, G. N., 1984, *Optimization Techniques for Nonlinear Engineering Design with Applications,* McGraw-Hill, New York, Chapter 3.

Nonlinear Vibration of Parametrically Excited Moving Belts, Part I: Dynamic Response

L. Zhang
Graduate Student

J. W. Zu
Assistant Professor

Department of Mechanical and Industrial Engineering,
University of Toronto,
Five King's College Road,
Toronto, ON M5S 3G8, Canada

The dynamic response and stability of parametrically excited viscoelastic belts are investigated in these two consecutive papers. In the first paper, the generalized equation of motion is obtained for a viscoelastic moving belt with geometric nonlinearity. The linear viscoelastic differential constitutive law is employed to characterize the material property of belts. The method of multiple scales is applied directly to the governing equation which is in the form of continuous gyroscopic systems. No assumptions regarding the spatial dependence of the motion are made. Closed-form solutions for the amplitude and the existence conditions of nontrivial limit cycles of the summation resonance are obtained. It is shown that there exists an upper boundary for the existence condition of the summation parametric resonance due to the existence of viscoelasticity. The effects of viscoelastic parameters, excitation frequencies, excitation amplitudes, and axial moving speeds on dynamic responses and existence boundaries are investigated.

1 Introduction

Moving belts used in power transmissions are an example of a class of mechanical systems commonly referred to as axially moving materials. One major problem in this system is the occurrence of large transverse belt vibrations which result from the time-dependent crankshaft-driven belt tension. Such vibrations are termed as parametric vibrations. Dynamic response and stability associated with parametric vibrations are of primary concern in engineering.

The vibration analysis of a parametrically excited, axially moving system has been studied extensively. Mahalingam (1957) was the first one to notice the possibility of parametric resonance due to the tension fluctuation in a translating string. Huang et al. (1995) studied the dynamic response and stability of a moving string undergoing three-dimensional vibration. Mockensturm et al. (1996) obtained analytical expressions for the amplitudes and stability boundaries of nontrivial limit cycles.

In the aforementioned investigations for moving belt systems, the belt material is assumed to be linear elastic and damping is either ignored or introduced simply as linear viscous without reference to any damping mechanism. However, since belts are usually composed of some viscoelastic metallic or ceramic reinforcement materials like glass-cord and viscoelastic polymeric materials such as rubber, viscoelastic constitutive relation should be employed to accurately describe the material property of moving belts.

The literature that is specially related to viscoelastic moving continuum is very limited. However, various methods have been presented for the vibration analysis of viscoelastic material systems. Stevens (1966) considered the stability of a simple viscoelastic column subjected to a harmonically varying axial load. Fung et al. (1996) extended the concept of Stevens to the dynamic stability of a simply supported viscoelastic beam subjected to harmonic and parametric excitations simultaneously. There is only one paper by Fung et al. (1997) so far discussing the numerical method for dynamic response of a viscoelastic moving string.

In this paper, based on the linear viscoelastic differential constitutive law, the equation of motion in the form of gyroscopic system is obtained for a parametrically excited viscoelastic moving belt with geometric nonlinearity. The method of multiple scales is applied directly to the governing equation. Closed-form solutions for the amplitude of nontrivial limit cycles of the summation resonance and the corresponding existence conditions are obtained. Numerical examples show effects of viscoelastic parameter, excitation frequencies, excitation amplitudes and axial moving speeds on dynamic responses, and existence boundaries.

2 Equation of Motion

A prototypical model of a viscoelastic moving belt is shown in Fig. 1, where c is the transport speed of the belt, L is the length of the belt span, and V is the displacement in the transverse direction.

Consider that the viscoelastic string is in a state of uniform initial stress, and only the transverse vibration in the y-direction is taken into consideration. The Lagrangian strain component in the x-direction related to the transverse displacement is $\epsilon(x, t) = V_x^2(x, t)/2$. Thus, the equation of motion in the y-direction can be obtained by Newton's second law as

$$\rho \frac{\partial^2 V}{\partial t^2} + 2\rho c \frac{\partial^2 V}{\partial t \partial x} + \left(\rho c^2 - \frac{T}{A}\right) \frac{\partial^2 V}{\partial x^2} = + E^*(\tfrac{1}{2} V_x^2) V_{xx} + V_x \{E^*(\tfrac{1}{2} V_x^2)\}_x \quad (1)$$

where the subscript notation x denotes partial differentiation with respect to the spatial Cartesian coordinate x, A is the area of cross section of the string, ρ is the mass per unit volume, T is the tension in the belt, and E^* is the linear differential operator determined by the viscoelastic property of belt materials.

It is assumed that the tension T is characterized as a small periodic perturbation $T_1 \cos \Omega t$ on the steady-state tension T_0, i.e.,

$$T = T_0 + T_1 \cos \Omega t \quad (2)$$

where Ω is the frequency of the crankshaft.

The Kelvin viscoelastic model is chosen to describe the viscoelastic property of the belt material. The linear differential operator E^* for the Kelvin viscoelastic model is given below,

Contributed by the Applied Mechanics Division of THE AMERICAN SOCIETY OF MECHANICAL ENGINEERS for publication in the ASME JOURNAL OF APPLIED MECHANICS.
Discussion on the paper should be addressed to the Technical Editor, Professor Lewis T. Wheeler, Department of Mechanical Engineering, University of Houston, Houston, TX 77204-4792, and will be accepted until four months after final publication of the paper itself in the ASME JOURNAL OF APPLIED MECHANICS.
Manuscript received by the ASME Applied Mechanics Division, Apr. 7, 1998; final revision, Dec. 14, 1998. Associate Technical Editor: R. C. Benson.

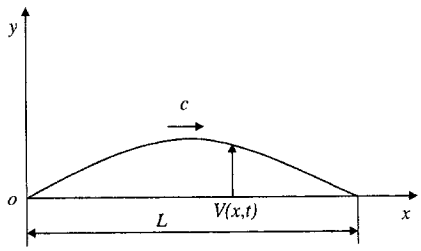

Fig. 1 A prototypical model of a viscoelastic moving belt

$$E^* = E_0 + \eta \frac{\partial}{\partial t}, \tag{3}$$

where E_0 is the stiffness constant of the spring and η is the dynamic viscosity of the dashpot.

Introducing the following nondimensional parameters

$$v = \frac{V}{L} \quad \xi = \frac{x}{L} \quad \tau = t\sqrt{\frac{T_0}{\rho A L^2}} \quad \gamma = c\sqrt{\frac{\rho A}{T_0}}$$

$$a = \frac{T_1}{T_0} \quad \omega = \Omega\sqrt{\frac{\rho A L^2}{T_0}} \quad E_e = \frac{E_0 A}{T_0} \quad E_v = \eta\sqrt{\frac{A}{\rho T_0 L^2}}, \tag{4}$$

the corresponding nondimensional equation of the transverse motion can be obtained as

$$\frac{\partial^2 v}{\partial \tau^2} + 2\gamma\frac{\partial^2 v}{\partial \tau \partial \xi} + (\gamma^2 - 1 - a\cos\omega\tau)\frac{\partial^2 v}{\partial \xi^2} = N(v) \tag{5}$$

where the nonlinear operator $N(v)$ is defined as

$$N(v) = \tfrac{3}{2}E_e v_\xi^2 v_{\xi\xi} + E_v\frac{\partial}{\partial \tau}(\tfrac{1}{2}v_\xi^2)v_{\xi\xi} + v_\xi E_v\frac{\partial}{\partial \tau}(v_\xi v_{\xi\xi}) \tag{6}$$

in which the first term on the right side of Eq. (6) is a term related to elasticity and the last two terms are terms related to viscoelasticity.

Introduce the mass, gyroscopic, and linear stiffness operators as follows:

$$M = I, \quad G = 2\gamma\frac{\partial}{\partial \xi}, \quad K = (\gamma^2 - 1)\frac{\partial^2}{\partial \xi^2} \tag{7}$$

where operators M and K are symmetric and positive definite and G is skew-symmetric for subcritical transport speeds. Employing a small dimensionless parameter ϵ as a bookkeeping device, Eq. (5) can be rewritten in a standard symbolic form

$$Mv_{\tau\tau} + Gv_\tau + Kv = \epsilon N(v) + \epsilon a\cos\omega\tau\frac{\partial^2 v}{\partial \xi^2}. \tag{8}$$

Equation (8) is in the form of a continuous gyroscopic system with weakly nonlinearity and parameter excitation term. The method of multiple scales will be employed to solve Eq. (8) directly.

3 Method of Multiple Scales

For nonlinear vibration analysis of an axially moving elastic material, Wickert and Mote (1990) proposed a complex form of the discretization process which used the travelling eigenfunctions instead of the stationary eigenfunctions. Based on this discretization process and KBM method, Wickert (1992) analyzed the free vibration of a gyroscopic system with weakly nonlinear stiffness. Moon and Wickert (1997) obtained near and exact-resonant response amplitudes of nonlinear vibrations of power transmission belts. In their study, the tension is assumed as a time-independent constant, and internal resonance and multimode responses are not considered.

There exists an alternative direct perturbation method which treats the continuous nonlinear governing partial differential equations directly. Pakdemirli et al. (1995) showed that there are discrepancies between the two approaches for principal, subharmonic, and superharmonic resonance of some nonlinear systems.

In this section, the method of multiple scales is applied directly to the governing partial differential equation, which is in the form of a continuous gyroscopic system. No assumptions regarding the spatial dependence of the motion are made. A first-order uniform approximation is sought in the form

$$v(\xi, \tau, \epsilon) = v_0(\xi, T_0, T_1) + \epsilon v_1(\xi, T_0, T_1) + \ldots \tag{9}$$

where $T_0 = \tau$ is a fast scale characterizing motions occurring at one of the natural frequencies ω_k of the system or ω; $T_1 = \epsilon\tau$ is a slow scale characterizing the modulation of the amplitudes and phases due to the nonlinearity, viscoelasticity, and possible resonance.

Substituting Eq. (9) into (8), using the chain rule of time derivatives and equating coefficients of like powers of ϵ lead to

$$M\frac{\partial^2 v_0}{\partial T_0^2} + G\frac{\partial v_0}{\partial T_0} + Kv_0 = 0 \tag{10}$$

$$M\frac{\partial^2 v_1}{\partial T_0^2} + G\frac{\partial v_1}{\partial T_0} + Kv_1 = -2M\frac{\partial^2 v_0}{\partial T_0 \partial T_1} - G\frac{\partial v_0}{\partial T_1} + N(v_0) + a\cos\omega T_0\frac{\partial^2 v_0}{\partial \xi^2}. \tag{11}$$

When the perturbation frequency ω approaches the sum of any two natural frequencies of the system, summation parametric resonance can occur. As a special case of the summation parametric resonance, the principal parametric resonance will also be presented when ω approaches $2\omega_i$. A detuning parameter μ is introduced to quantify the deviation of ω from $\omega_n + \omega_l$, and is described by

$$\omega = \omega_n + \omega_l + \epsilon\mu \tag{12}$$

in which ω_n and ω_l are the nth and lth natural frequencies of the corresponding linear system.

To investigate the summation parametric response and stability, solution of Eq. (10) can be expressed as

$$v_0 = \psi_n(\xi)A_n(T_1)e^{i\omega_n T_0} + \psi_l(\xi)A_l(T_1)e^{i\omega_l T_0} + cc \tag{13}$$

where $\psi_n(\xi)$ and $\psi_l(\xi)$ are the nth and lth complex eigenfunction of the displacement field, and cc denotes the complex conjugate of all preceding terms on the right side of Eq. (13). Functions A_n and A_l will be determined by eliminating the secular terms from v_1.

Substituting Eqs. (12) and (13) into (11) and expressing the trigonometric functions in exponential form result in

$$\begin{aligned} M\frac{\partial^2 v_1}{\partial T_0^2} + G\frac{\partial v_1}{\partial T_0} + Kv_1 = NST + [&-2i\omega_n A_n' M\psi_n - A_n' G\psi_n \\ &+ \frac{a\bar{A}_l}{2}\frac{\partial^2 \bar{\psi}_l}{\partial \xi^2}e^{i\mu T_1} + M_{2n}(3E_e + 2i\omega_n E_v)A_n^2\bar{A}_n]e^{i\omega_n T_0} \\ &+ [-2i\omega_l A_l' M\psi_l - A_l' G\psi_l + \frac{a\bar{A}_n}{2}\frac{\partial^2 \bar{\psi}_n}{\partial \xi^2}e^{i\mu T_1} \\ &+ M_{2l}(3E_e + 2i\omega_l E_v)A_l^2\bar{A}_l e]^{i\omega_l T_0} + cc \end{aligned} \tag{14}$$

where

$$M_{2k} = \frac{1}{2}\left[\left(\frac{\partial \psi_k}{\partial \xi}\right)^2\frac{\partial^2 \bar{\psi}_k}{\partial \xi^2} + 2\frac{\partial \psi_k}{\partial \xi}\frac{\partial \bar{\psi}_k}{\partial \xi}\frac{\partial^2 \psi_k}{\partial \xi^2}\right] \quad f \text{ or } k = n, 1. \tag{15}$$

NST in Eq. (14) represents all the nonsecular terms and the overbar denotes complex conjugate.

Due to the nonlinearity and viscoelasticity, *NST* involves some complicated spatial distribution functions. Thus, the spatial variations of the first order solution v_1 is different from that of linear solution v_0. The validity of the assumption that the spatial variation can be represented in terms of linear eigenfunctions is therefore, questionable. However, this assumption is commonly used in the nonlinear vibration analysis.

Equation (14) has a solution only if a solvability condition is satisfied. This solvability condition demands that the right side of Eq. (14) be orthogonal to every solution of the homogeneous problem. For general case where internal resonance does not exist, the solvability condition can be determined as

$$-2i\omega_n A_n' m_n - A_n' g_n i + (3E_e + 2i\omega_n E_v)A_n^2 \bar{A}_n m_{2n} + \frac{a\bar{A}_l}{2} m_{ln} e^{i\mu T_1} = 0 \quad (16)$$

$$-2i\omega_l A_l' m_l - A_l' g_l i + (3E_e + 2i\omega_l E_v)A_l^2 \bar{A}_l m_{2l} + \frac{a\bar{A}_n}{2} m_{nl} e^{i\mu T_1} = 0 \quad (17)$$

in which

$$m_k = \langle M\psi_k, \psi_k \rangle \quad g_k = -i\langle G\psi_k, \psi_k \rangle$$
$$m_{2k} = \langle M_{2k}, \psi_k \rangle \quad \text{for} \quad k = n, l \quad (18)$$

$$m_{nl} = \left\langle \frac{\partial^2 \bar{\psi}_n}{\partial \xi^2}, \psi_l \right\rangle \quad m_{ln} = \left\langle \frac{\partial^2 \bar{\psi}_l}{\partial \xi^2}, \psi_n \right\rangle \quad (19)$$

and the notation $\langle \cdot, \cdot \rangle$ represents the standard inner product of two complex functions over $\xi \in (0, 1)$.

Referring to Wickert and Mote (1990), the kth natural frequency and eigenfunction normalized for $m_k = 1$ of linear moving belts are $\omega_k = k\pi(1 - \gamma^2)$ and $\psi_k = \sqrt{2}\sin(k\pi\xi)e^{(ik\pi\gamma\xi)}$, respectively. Substituting these eigenvalues and eigenfunctions into Eqs. (18) and (19) leads to

$$g_k = 2k\pi\gamma^2 \quad m_{2k} = -\tfrac{1}{4}\pi^4 k^4(3 + 2\gamma^2 + 3\gamma^4) \quad (20)$$

$$m_{nl} = m_{ln} = \frac{4\pi n^2 l^2 v[-\sin(n + l)\pi v + I(1 - \cos(n + l)\pi v)]}{(n + l)[(n + l)^2 v^2 - (n - l)^2]}. \quad (21)$$

Note that both g_k and m_{2k} are real and $m_{nl} = m_{ln}$. To solve the nonlinear Eqs. (16) and (17), express A_n and A_l in polar form

$$A_n = \tfrac{1}{2}\alpha_n e^{i\beta_n} \quad A_l = \tfrac{1}{2}\alpha_l e^{i\beta_l}. \quad (22)$$

Note that α_k and β_k $(k = n, l)$ represent the amplitude and the phase angle of the response, respectively. Substituting Eq. (22) into (16) and (17) and separating the resulting equation into real and imaginary parts yield

$$\alpha_n' = \frac{E_v\omega_n m_{2n}}{4n\pi}\alpha_n^3 + \frac{a\alpha_l}{4n\pi}[\cos\theta\,\mathrm{Im}(m_{nl}) + \sin\theta\,\mathrm{Re}(m_{nl})] \quad (23)$$

$$\alpha_l' = \frac{E_v\omega_l m_{2l}}{4l\pi}\alpha_l^3 + \frac{a\alpha_n}{4l\pi}[\cos\theta\,\mathrm{Im}(m_{nl}) + \sin\theta\,\mathrm{Re}(m_{nl})] \quad (24)$$

$$\theta' = \mu + \frac{3E_e m_{2n}\alpha_n^2}{8n\pi} + \frac{3E_e m_{2l}\alpha_l^2}{8l\pi} + (\cos\theta\,\mathrm{Re}(m_{nl}) - \sin\theta\,\mathrm{Im}(m_{nl}))\left(\frac{a\alpha_l}{4n\pi\alpha_n} + \frac{a\alpha_n}{4l\pi\alpha_l}\right) \quad (25)$$

where $\mathrm{Re}(m_{nl})$ and $\mathrm{Im}(m_{nl})$ indicate the real and imaginary components of m_{nl} and

$$\theta = \mu T_1 - \beta_n - \beta_l. \quad (26)$$

4 Dynamic Response and Existence Conditions

For nonlinear systems, limit cycles may exist in the vicinity of a parametric instability region. In this section, the interest is focused on the behavior of limit cycles around the parametric instability regions for elastic and viscoelastic nonlinear systems.

Steady-State Response of Elastic Moving Belts. For the steady-state response of elastic moving belts, the amplitudes α_n, α_l, and the phase angle θ in Eqs. (23) to (25) should be constant. Thus, for elastic systems, setting $\alpha_n' = 0$, $\alpha_l' = 0$, $\theta' = 0$ and $E_v = 0$ in Eqs. (23) to (25) and eliminating the term $\cos\theta\,\mathrm{Im}(m_{nl}) + \sin\theta\,\mathrm{Re}(m_{nl})$ from Eqs. (23) and (24) yield

$$\alpha_l^2 = \frac{n}{l}\alpha_n^2. \quad (27)$$

For steady-state analysis, eliminating θ from Eqs. (23) and (25) with $\alpha_n' = 0$, $\theta' = 0$ and substituting Eq. (27) into the resulting equation, the amplitudes of steady-state response of summation parametric resonance for elastic systems are obtained:

$$\alpha_{n0}^2 = \frac{\mu \pm \frac{a}{2\sqrt{nl}\pi}\sqrt{\mathrm{Re}(m_{nl})^2 + \mathrm{Im}(m_{nl})^2}}{-\left(\frac{3E_e m_{2n}}{8n\pi} + \frac{3E_e m_{2l} n}{8l^2\pi}\right)}$$

$$\alpha_{l0}^2 = \frac{n}{l}\frac{\mu \pm \frac{a}{2\sqrt{nl}\pi}\sqrt{\mathrm{Re}(m_{nl})^2 + \mathrm{Im}(m_{nl})^2}}{-\left(\frac{3E_e m_{2n}}{8n\pi} + \frac{3E_e m_{2l} n}{8l^2\pi}\right)}. \quad (28)$$

From the amplitude expression (28) of elastic problems, it can be seen that the first limit cycle exists if $\mu \geq -((\sqrt{\mathrm{Im}(m_{nl})^2 + \mathrm{Re}(m_{nl})^2})/2\sqrt{nl}\pi)a$ and the second limit cycle exists if $\mu \geq ((\sqrt{\mathrm{Im}(m_{nl})^2 + \mathrm{Re}(m_{nl})^2})/2\sqrt{nl}\pi)a$.

It should be mentioned that existence conditions of limit cycles are the same as the stability conditions of the trivial solution for elastic systems (Zhang and Zu, 1998). Thus, it is concluded that for elastic summation parametric resonance the nontrivial limit cycles bifurcate from the trivial limit cycle at the stability boundary of the trivial limit cycle.

Steady-State Response of Viscoelastic Moving Belts. For the steady-state response of viscoelastic moving belts, setting $\alpha_n' = 0$, $\alpha_l' = 0$, $\theta' = 0$ and eliminating the term $\cos\theta\,\mathrm{Im}(m_{nl}) + \sin\theta\,\mathrm{Re}(m_{nl})$ from Eqs. (23) and (24) lead to the following relationship between α_n and α_l:

$$\alpha_l^2 = \frac{n^2}{l^2}\sqrt{\frac{n}{l}}\alpha_n^2. \quad (29)$$

It is seen that the relation between α_n and α_l of viscoelastic systems is different from that of elastic systems. Eliminating θ from Eqs. (23) and (25) with $\alpha_n' = 0$, $\theta' = 0$ and substituting Eq. (29) into the resulting equation, the following amplitude modulation equation for steady-state response is obtained:

$$c_1\alpha_n^6 + c_2\alpha_n^4 + c_3\alpha_n^2 = 0 \quad (30)$$

where c_1, c_2, and c_3 are time-independent constants determined by the system property.

It is obvious that Eq. (30) possesses a singular point at the origin (trivial periodic solution). In addition, two nontrivial singular points may exist describing limit cycles with amplitudes

$$\alpha_{n0}^2 = \frac{-c_2 \pm \sqrt{c_2^2 - 4c_1c_3}}{2c_1}$$

$$\alpha_{l0}^2 = \frac{n^2}{l^2}\sqrt{\frac{n}{l}}\frac{-c_2 \pm \sqrt{c_2^2 - 4c_1c_3}}{2c_1}. \tag{31}$$

Equation (31) represents the amplitudes of the steady-state response of the summation parametric resonance for viscoelastic systems. As a special case, the response amplitude of principal parametric resonance ($n = l$) for viscoelastic belts is given in the following:

$$\alpha_{n0}^2 = \frac{\frac{3E_e n\pi\mu}{8} \pm \sqrt{\frac{n^2\pi^2a^2\sin^2 n\pi\gamma}{4\gamma^2}\left(\frac{3E_e}{8}\right)^2 - \left(n^2\pi^2\mu^2 - \frac{n^2\pi^2a^2\sin^2 n\pi\gamma}{4\gamma^2}\right)\left(\frac{E_v\omega_n}{4}\right)^2}}{2\left[\left(\frac{3E_e}{8}\right)^2 + \left(\frac{E_v\omega_n}{4}\right)^2\right](-m_{2n}).} \tag{32}$$

From the amplitude Eq. (31) of viscoelastic systems, it can be seen that the two nontrivial steady-state solutions exist only when the following conditions are satisfied:

$$c_2^2 - 4c_1c_3 \geq 0 \quad -c_2 \pm \sqrt{c_2^2 - 4c_1c_3} \geq 0. \tag{33}$$

Substituting the expressions of c_1, c_2, and c_3 into Eq. (33) leads to the following conclusions that the first limit cycle of viscoelastic systems exists if

$$\frac{\left(\frac{1}{l}\sqrt[4]{\frac{n}{l}} + \frac{1}{n}\sqrt[4]{\frac{l}{n}}\right)\sqrt{\mathrm{Im}(m_{nl})^2 + \mathrm{Re}(m_{nl})^2}}{4\pi}a$$

$$\leq \mu \leq \frac{\left(\frac{n}{l^2}\sqrt{\frac{n}{l}} + \frac{1}{l}\right)\sqrt{(\mathrm{Im}(m_{nl})^2 + \mathrm{Re}(m_{nl})^2)c_1}}{-4\pi E_v\omega_n m_{2n}}a \tag{34}$$

and the second limit cycle exists if

$$\frac{\left(\frac{1}{l}\sqrt[4]{\frac{n}{l}} + \frac{1}{n}\sqrt[4]{\frac{l}{n}}\right)\sqrt{\mathrm{Im}(m_{nl})^2 + \mathrm{Re}(m_{nl})^2}}{4\pi}a$$

$$\leq \mu \leq \frac{\left(\frac{n}{l^2}\sqrt{\frac{n}{l}} + \frac{1}{l}\right)\sqrt{(\mathrm{Im}(m_{nl})^2 + \mathrm{Re}(m_{nl})^2)c_1}}{-4\pi E_v\omega_n m_{2n}}a. \tag{35}$$

It can be seen from Eqs. (34) and (35) that the existence conditions of nontrivial limit cycles have an upper boundary for

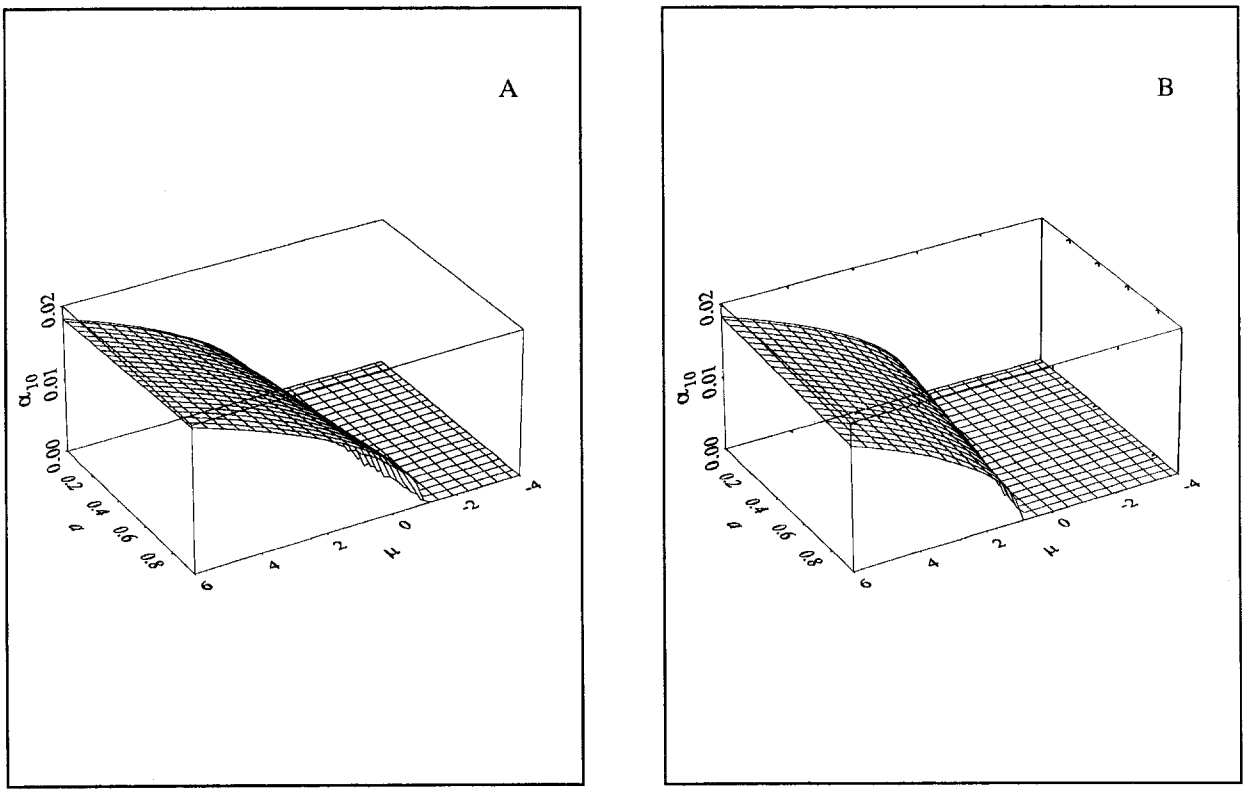

Fig. 2 The response amplitudes of nontrivial limit cycles for the summation parametric resonance of an elastic moving belt ($n = 1$, $l = 2$, $E_e = 400$, $E_v = 0$, $\gamma = 0.2$); (*A*) the first limit cycle, (*B*) the second limit cycle

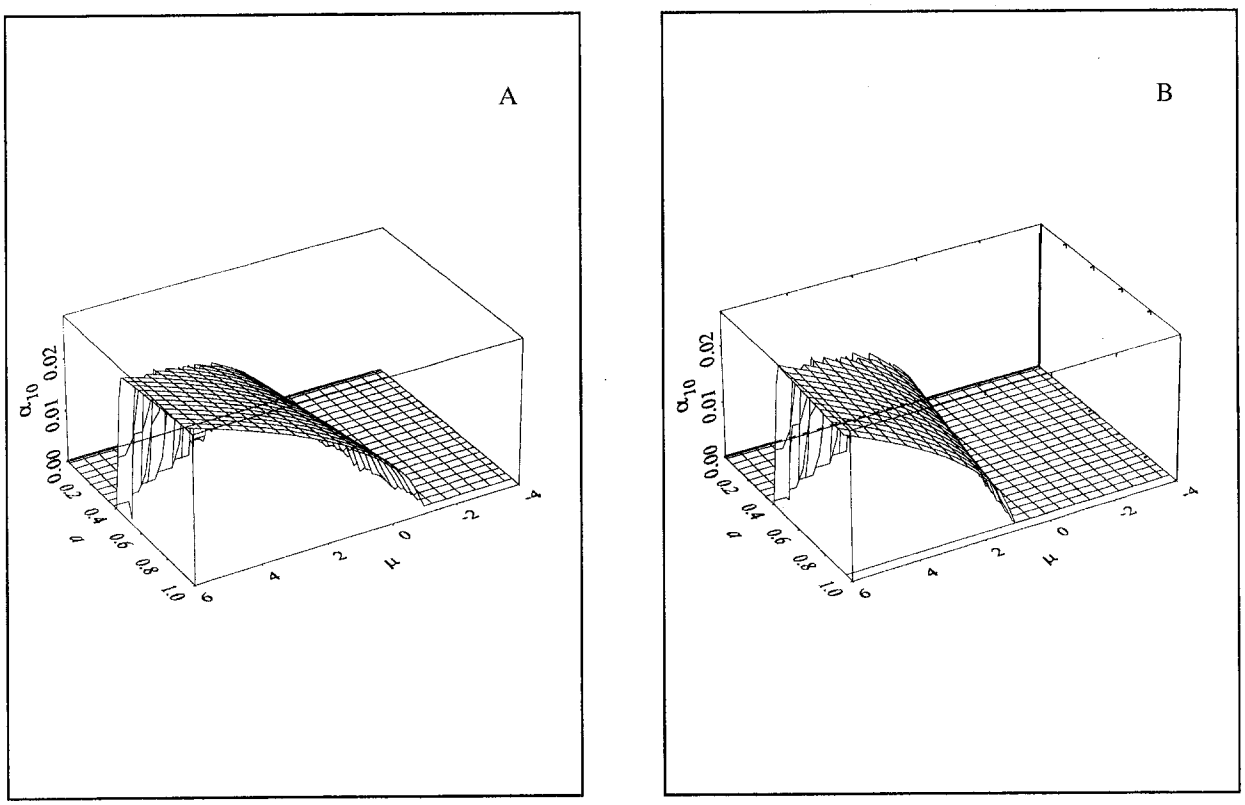

Fig. 3 The response amplitude of nontrivial limit cycles for the summation parametric resonance of a viscoelastic moving belt (n = 1, l = 2, E_e = 400, E_v = 10, γ = 0.2); (*A*) the first limit cycle, (*B*) the second limit cycle

viscoelastic models, which is different from the conclusion of the corresponding elastic systems. The upper boundaries of existence conditions for the first limit cycle and the second limit cycle are identical and are determined by the viscoelastic parameter E_v. The lower boundaries of existence conditions have no relation with the viscoelastic property of the system and are different from those of the corresponding elastic systems. In addition, the boundaries of existence of nontrivial limit cycles have no relation with the nonlinear parameter E_e.

5 Numerical Results and Discussions

In this section, numerical results of steady-state responses and existence boundaries for the summation parametric resonance of moving belts are presented. Effects of the viscoelastic parameter, the amplitude of excitation, the frequency of excitation, and the transport speed on the response of nontrivial limit cycles are investigated.

The response amplitudes of limit cycles of summation parametric resonance (n = 1, l = 2) for an elastic system and a viscoelastic nonlinear system are shown in Fig. 2 and Fig. 3, respectively. The nondimensional transport speed γ is 0.2 and the nonlinear parameter E_e is 400. In Fig. 3, the viscoelastic parameter is 10. From Fig. 2, it can be seen that the amplitude increases without bound as μ increases. When the excitation amplitude grows, the response amplitude increases. Only the trivial solution exists if the existence conditions of nontrivial solutions are not satisfied. It is evident from Fig. 3 that though the amplitude increases with the growth of the excitation amplitude a and frequency μ, there exists an upper bound. The nontrivial limit cycle will vanish when a and μ approach this bound. This phenomenon for viscoelastic moving belts is quite different from the corresponding elastic systems.

The effects of viscoelastic parameter E_v on the amplitude and the existence boundary of nontrivial limit cycles are illustrated in Fig. 4. The system parameters are E_e = 400, a = 0.5, and γ = 0.25. Three different values of E_v are chosen as 0, 25, and 50. It is clear that the amplitude decreases with the increase of E_v for the first limit cycle while the amplitude increases with the growth of E_v for the second limit cycle. The most important phenomenon is that the existence condition has an upper boundary for viscoelastic system.

Translation speeds not only influence the amplitude of the

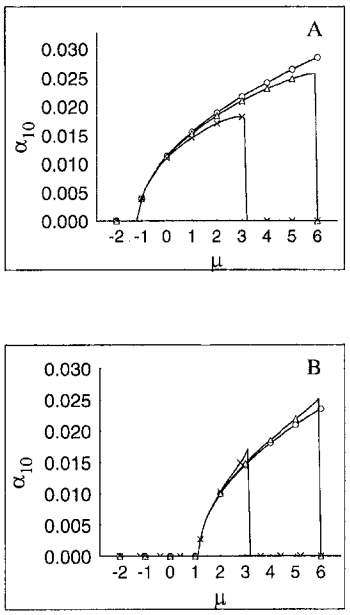

Fig. 4 Effects of E_v on the amplitude of limit cycles of the first mode for summation parametric resonance (n = 1, l = 2, E_e = 400, γ = 0.25, a = 0.5); (*A*) the first limit cycle, (*B*) the second limit cycle, ○ E_v = 0, △E_v = 25, × E_v = 50

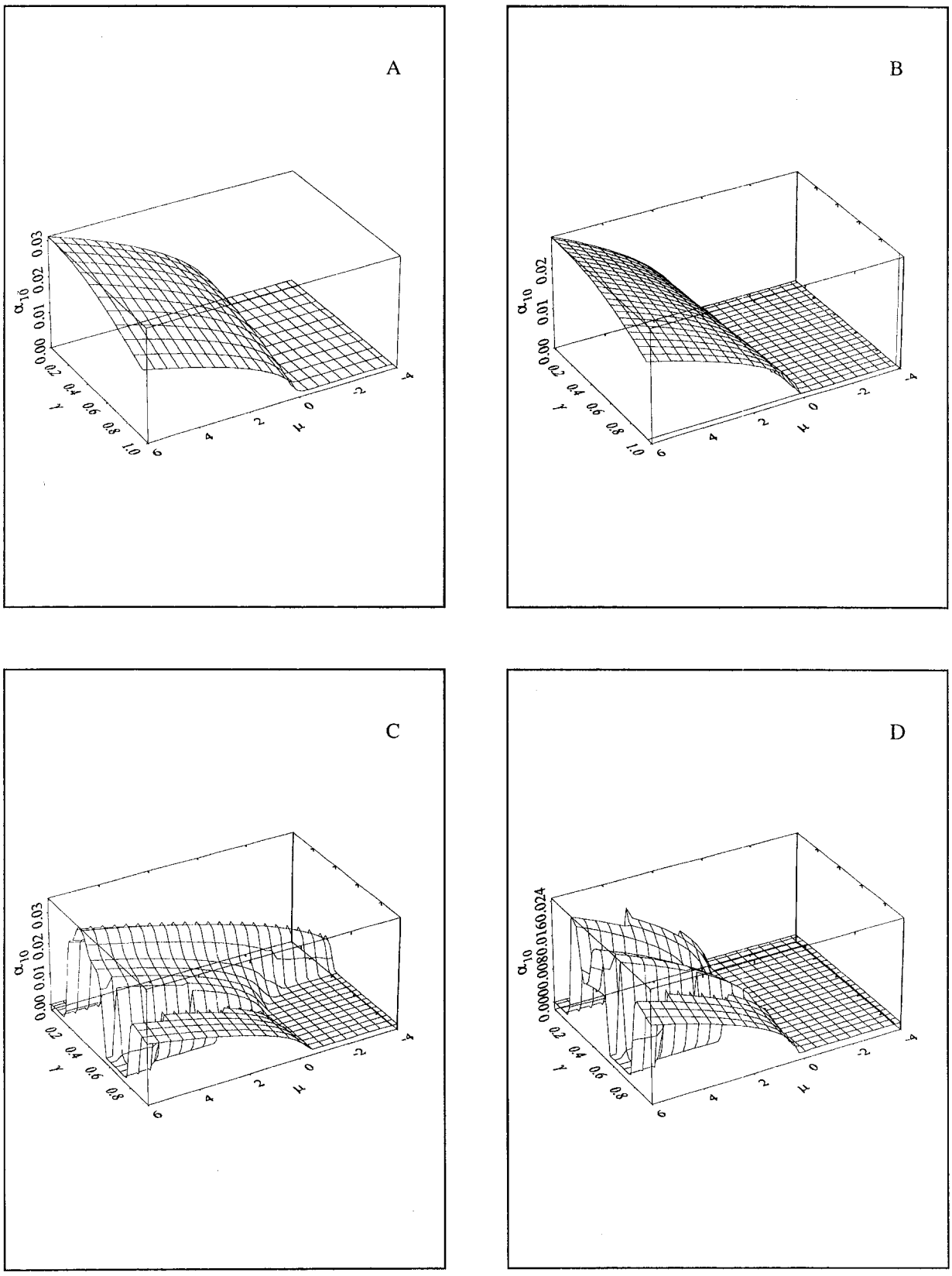

Fig. 5 Effects of the transport speed on the first mode amplitude of nontrivial limit cycles of the parametric resonance (E_e = 400, E_v = 10, a = 0.5); (*A*) the first limit cycle (n = 1, l = 1), (*B*) the second limit cycle (n = 1, l = 1), (*C*) the first limit cycle (n = 1, l = 2), (*D*) the second limit cycle (n = 1, l = 2)

nontrivial limit cycles, but also influence the existence region of limit cycles significantly. Figure 5 illustrates the effect of the translating speed on non-trivial limit cycles of the principal (n = l = 1) and the summation (n = 1, l = 2) parametric resonance. The excitation amplitude a is chosen as 0.5 and the nonlinear parameter E_e is 400. From Fig. 5, for principal parametric reso-

nance, it is seen that the amplitude of limit cycles decreases with the increase of transport speeds. The nontrivial amplitude grows more slowly with μ when translation speeds is larger. Moreover, for the translation speed unsatisfying Eq. (34) and (35), the nontrivial limit cycles no longer exist. These results indicate that by increasing the transport speed while keeping other parameters constant, an unstable belt can be stabilized. For the summation parametric resonance, the relation between the response and the transport speed is much more complicated. There exists a maximum value of response for the first limit cycle and a minimum value of response for the second limit cycle when γ is around 0.2.

The excitation frequency (detuning) μ on the upper boundary of existence is plotted against viscoelastic property E_v in Fig. 6. In this example, $\gamma = 0.25$, $E_e = 400$, and $a = 0.5$. It is much clearer that when E_v increases, μ decreases. Since the lower boundary has no relation with E_v, the region of existence will narrow with the increase of E_v. Especially when E_v approach zero, the upper boundary of μ will approach infinite. This agrees with the conclusion obtained by Mockensturm et al. (1996) that there is no upper boundary of existence for elastic problems.

The relation between the excitation frequency μ and the transport speed on the boundaries of existence condition for the first limit cycles is plotted in Fig. 7. The system parameters are $E_v = 10$, $E_e = 400$, and $a = 0.5$. It is clear that the transport speed has a significant effect on the boundary of existence.

6 Conclusions

In this paper, the dynamic response of parametrically excited viscoelastic moving belts is investigated. The Kelvin viscoelastic model is employed to characterize the property of belt materials. The method of multiple scales is applied directly to the governing equation of motion which is in the form of continuous gyroscopic systems. No assumptions about the spatial dependence of the motion are made in this approach. Closed-form expressions are found for the response and existence conditions of the summation parametric resonance.

The following conclusions can be drawn from the above study:

1 The amplitude of the first limit cycle decreases with the increase of the viscoelastic parameter E_v while the amplitude of the second limit cycle increases with E_v.

2 The amplitude of the limit cycles decreases with increasing transport speeds for principal parametric resonance. There is no such a simple relation for the summation parametric resonance.

3 There exists an upper existence boundary for the viscoelastic model and this upper boundary of existence for limit cycles is determined by the viscoelastic property E_v.

4 The lower boundary of existence for limit cycles of elastic systems is identical to the stability boundary of the trivial solution. This suggests that nontrivial limit cycles of the summation parametric resonance bifurcate from the trivial limit cycle at the boundary of the trivial limit cycle.

5 The boundaries of existence have no relation with the nonlinear parameter E_e.

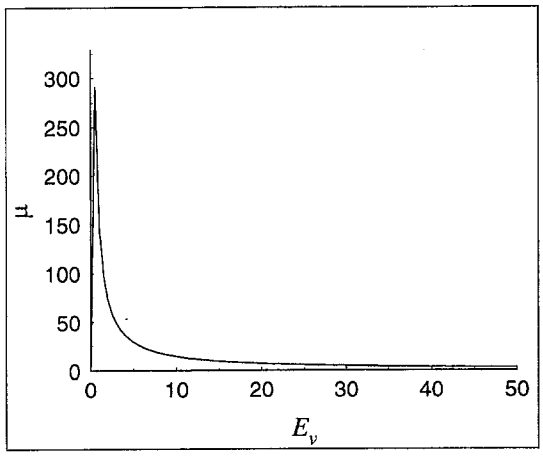

Fig. 6 Relations of μ and E_v on the upper existence boundary of nontrivial limit cycles for summation parametric resonance ($n = 1$, $l = 2$, $E_e = 400$, $\gamma = 0.25$, $a = 0.5$)

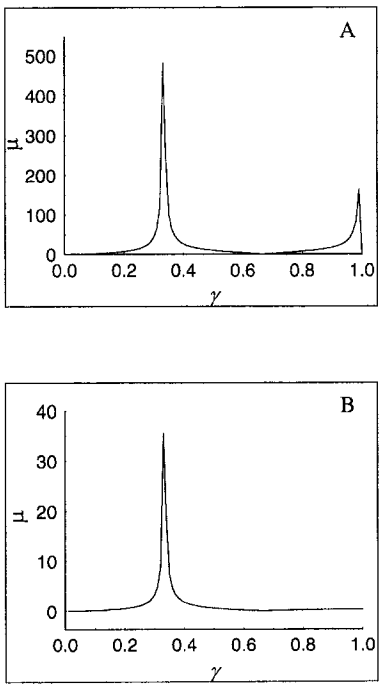

Fig. 7 Effects of the transport speed on the existence boundary of non-trivial limit cycle for summation parametric resonance ($n = 1$, $l = 2$, $E_e = 400$, $a = 0.5$, $E_v = 10$); (*A*) upper boundary, (*B*) lower boundary

Acknowledgment

This research is financially supported by a research grant from the Materials and Manufacturing Ontario in Canada.

References

Fung, R. F., Huang, J. S., and Chen, Y. C., 1996, "Dynamics Stability of a Viscoelastic Beam Subjected to Harmonic and Parametric Excitations Simultaneously," *Journal of Sound and Vibration,* Vol. 198, pp. 1–16.

Fung, R. F., Huang, J. S., and Chen, Y. C., 1997, "The Transient Amplitude of the Viscoelastic Traveling String: an Integral Constitutive Law," *Journal of Sound and Vibration,* Vol. 201, pp. 153–167.

Huang, J. S., Fung, R. F., and Lin, C. H., 1995, "Dynamic Stability of a Moving String Undergoing Three-dimensional Vibration," *International Journal of Mechanics Sciences,* Vol. 37, pp. 145–160.

Mahalingam, S., 1957, "Transverse Vibration of Power Transmission Chains," *British Journal of Applied Physics,* Vol. 8, pp. 145–148.

Mockensturm, E. M., Perkins, N. C., and Ulsoy, A. G., 1996, "Stability and Limit Cycles of Parametrically Excited, Axially Moving Strings," ASME *Journal of Vibration and Acoustics,* Vol. 118, pp. 346–351.

Moon, J., and Wicker, J. A., 1997, "Nonlinear Vibration of Power Transmission Belts," *Journal of Sound and Vibration,* Vol. 200, pp. 419–431.

Pakdemirli, M., Nayfeh, S. A., and Nayfeh, A. H., 1995, "Analysis of One-to-One Autoparametric Resonances in Cables-Discretization vs. Direct Treatment," *Nonlinear Dynamics,* Vol. 8, pp. 65–83.

Stevens, K. K., 1966, "On the Parametric Excitation of a Viscoelastic column," *American Institute of Aeronautics and Astronautics Journal,* Vol. 4, pp. 2111–2116.

Wickert, J. A., and Mote, C. D., Jr., 1990, "Classical Vibration Analysis of Axially Moving Continua," ASME JOURNAL OF APPLIED MECHANICS, Vol. 57, pp. 738–744.

Wickert, J. A., 1992, "Nonlinear Vibration of a Travelling Tensioned Beam," *International Journal of Nonlinear Mechanics,* Vol. 27, pp. 503–517.

Zhang, L., and Zu, J. W., 1998, "Nonlinear Vibration of Parametrically Excited Viscoelastic Moving Belts, Part 2: Stability Analysis," ASME JOURNAL OF APPLIED MECHANICS, Vol. 66, pp.

Nonlinear Vibration of Parametrically Excited Viscoelastic Moving Belts, Part II: Stability Analysis

L. Zhang
Graduate Student

J. W. Zu
Assistant Professor

Department of Mechanical and Industrial Engineering, University of Toronto, Five King's College Road, Toronto, ON M5S 3G8, Canada

The amplitude and existence conditions of nontrivial limit cycles are derived in the companion paper by the use of the method of multiple scales. In this paper, the stability for parametrically excited viscoelastic moving belts is studied. Stability boundaries of the trivial limit cycle for general summation parametric resonance are obtained. The Routh-Hurwitz criterion is used to investigate the stability of nontrivial limit cycles. Closed-form expressions are found for the stability of nontrivial limit cycles of general summation parametric resonance. It is shown that the first limit cycle is always stable while the second limit cycle is always unstable for the viscoelastic moving belts. The effects of viscoelastic parameters, excitation frequencies, excitation amplitudes, and axial moving speeds on stability boundaries are discussed.

1 Introduction

The dynamic stability problem of the parametric vibration of elastic moving materials has been investigated by many researchers (Mahalingam, 1957; Mote, 1968; Ulsoy et al., 1978). More recently, Huang et al. (1995) studied the dynamic stability of a moving string undergoing three-dimensional vibration. Mockensturm et al. (1996) obtained closed-form expressions for stability boundaries of the nth-mode principal and the first summation parametric resonance of linear systems using KBM method. An analytical expression was also given for the stability of nontrivial limit cycles of nonlinear elastic systems. Pakdemirli and Ulsoy (1997) determined the stability boundaries of an axially accelerating linear moving string analytically.

For viscoelastic systems, Stevens (1966) showed that in some cases the stability regions may be broadened significantly as the material becomes more viscoelastic in nature. Fung et al. (1996) extended the concept of Stevens to the dynamic stability of a simply supported viscoelastic beam subjected to harmonic and parametric excitations simultaneously.

In the first paper by Zhang and Zu (1998), a closed-form solution of limit cycles of summation parametric resonance is obtained. It is shown that there exists an upper boundary of existence due to the existence of viscoelasticity. In this paper, the Routh-Hurwitz (Chen, 1971) criterion is employed to investigate the stability of nontrivial limit cycles. It is shown the first limit cycle is always stable while the second limit cycle is always unstable for viscoelastic moving belts. Examples highlight the important effects of viscoelastic parameters, excitation frequencies, excitation amplitudes, and axial moving speeds on stability boundaries.

2 Stability of the Trivial Limit Cycle

It has been shown (Wanda, 1990) that the stability of the trivial limit cycle of nonlinear systems coincides with the stability of the equilibrium point of the corresponding linear systems. Thus, it is convenient to perform the stability analysis of linear systems to obtain the stability boundary of the trivial limit cycle of nonlinear systems. In this section, the stability boundaries of general summation parametric resonance are obtained based on the amplitude modulation equations for linear systems derived by the use of direct multiple scales method (Zhang and Zu, 1998). The amplitude modulation equations are given as

$$-2i\omega_n m_n A_n' - g_n A_n' i + \frac{aA_l}{2} m_{nl} e^{i\mu T_1} = 0$$

$$-2i\omega_l m_l A_l' - g_l A_l' i + \frac{aA_n}{2} m_{nl} e^{i\mu T_1} = 0. \tag{1}$$

Note that the nonlinear terms have been taken out from the original equations. In order to transform Eq. (1) into equations with constant coefficients, introduce the following transformation:

$$A_n = (a_{1r} + ia_{1i}) e^{(i\mu T_1/2)+\beta T_1} \quad A_l = (a_{2r} + ia_{2i}) e^{(i\mu T_1/2)+\beta T_1}. \tag{2}$$

Substituting Eq. (2) into (1) and separating the real and imaginary parts from the resulting equations lead to

$$n\pi\mu a_{1r} + 2n\pi\beta a_{1i} + \frac{a}{2} a_{2r}\,\mathrm{Re}(m_{nl}) + \frac{a}{2} a_{2i}\,\mathrm{Im}(m_{nl}) = 0 \tag{3}$$

$$-2n\pi\beta a_{1r} + n\pi a_{1i} + \frac{a}{2} a_{2r}\,\mathrm{Im}(m_{nl}) - \frac{a}{2} a_{2i}\,\mathrm{Re}(m_{nl}) = 0 \tag{4}$$

$$l\pi\mu a_{2r} + 2l\pi\beta a_{2i} + \frac{a}{2} a_{1r}\,\mathrm{Re}(m_{nl}) + \frac{a}{2} a_{1i}\,\mathrm{Im}(m_{nl}) = 0 \tag{5}$$

$$-2l\pi\beta a_{2r} + l\pi\mu a_{2i} + \frac{a}{2} a_{1r}\,\mathrm{Im}(m_{nl}) - \frac{a}{2} a_{1i}\,\mathrm{Re}(m_{nl}) = 0. \tag{6}$$

Expressing a_{2r} and a_{2i} in terms of a_{1r} and a_{1i} from Eqs. (3) and (4) and substituting the resulting equations into Eqs. (5) and (6) yield

$$\left[\frac{a\,\mathrm{Re}(m_{nl})}{2} - \frac{nl\pi^2\,\mathrm{Re}(m_{nl})(\mu^2+4\beta^2)}{\frac{a}{2}\left(\mathrm{Re}(m_{nl})^2 + \mathrm{Im}(m_{nl})^2\right)}\right] a_{1r} + \left[\frac{a\,\mathrm{Im}(m_{nl})}{2} - \frac{nl\pi^2\,\mathrm{Im}(m_{nl})(\mu^2+4\beta^2)}{\frac{a}{2}\left(\mathrm{Re}(m_{nl})^2 + \mathrm{Im}(m_{nl})^2\right)}\right] a_{1i} = 0 \tag{7}$$

Contributed by the Applied Mechanics Division of THE AMERICAN SOCIETY OF MECHANICAL ENGINEERS for publication in the ASME JOURNAL OF APPLIED MECHANICS.
Discussion on the paper should be addressed to the Technical Editor, Professor Lewis T. Wheeler, Department of Mechanical Engineering, University of Houston, Houston, TX 77204-4792, and will be accepted until four months after final publication of the paper itself in the ASME JOURNAL OF APPLIED MECHANICS.
Manuscript received by the ASME Applied Mechanics Division, Apr. 7, 1998; final revision, Dec. 14, 1998. Associate Technical Editor: R. C. Benson.

$$\left[\frac{a\,\mathrm{Im}(m_{nl})}{2}-\frac{nl\pi^2\,\mathrm{Im}(m_{nl})(\mu^2+4\beta^2)}{\frac{a}{2}\left(\mathrm{Re}(m_{nl})^2+\mathrm{Im}(m_{nl})^2\right)}\right]a_{1r}$$

$$+\left[-\frac{a\,\mathrm{Re}(m_{nl})}{2}+\frac{nl\pi^2\,\mathrm{Re}(m_{nl})(\mu^2+4\beta^2)}{\frac{a}{2}\left(\mathrm{Re}(m_{nl})^2+\mathrm{Im}(m_{nl})^2\right)}\right]a_{1i}=0. \quad (8)$$

For a nontrivial solution, the determinant of the coefficient matrix in Eqs. (7) and (8) must vanish, i.e.,

$$\left[\frac{a\,\mathrm{Re}(m_{nl})}{2}-\frac{nl\pi^2\,\mathrm{Re}(m_{nl})(\mu^2+4\beta^2)}{\frac{a}{2}\left(\mathrm{Re}(m_{nl})^2+\mathrm{Im}(m_{nl})^2\right)}\right]^2$$

$$+\left[\frac{a\,\mathrm{Im}(m_{nl})}{2}-\frac{nl\pi^2\,\mathrm{Im}(m_{nl})(\mu^2+4\beta^2)}{\frac{a}{2}\left(\mathrm{Re}(m_{nl})^2+\mathrm{Im}(m_{nl})^2\right)}\right]^2=0. \quad (9)$$

Since the system is stable only when β has a negative real component, the transition at which $\beta = 0$ is where the stability boundaries are located. Therefore, the stability condition for the general summation resonance of linear moving belts is obtained as

$$\mu^2 > \frac{8n^3l^3\gamma^2(1-\cos((n+l)\pi\gamma))a^2}{(n+l)^2[(n+l)\gamma+n-l][(n+l)\gamma-n+l]}. \quad (10)$$

It is seen that Eq. (10) is the same as the existence condition of nontrivial limit cycles of nonlinear elastic systems in part 1 of the paper. This suggests that the nontrivial limit cycle of summation parametric resonance of elastic systems bifurcates from the instability boundary of trivial solution.

3 Stability of the Nontrivial Limit Cycles

As shown by Zhang and Zu (1998), the equations of amplitudes α_n and α_l for nontrivial limit cycles and the corresponding phase angle θ are derived using the method of multiple scales as

$$\alpha_n' = \frac{E_v\omega_n m_{2n}}{4n\pi}\alpha_n^3+\frac{a\alpha_l}{4n\pi}[\cos\theta\,\mathrm{Im}(m_{nl})+\sin\theta\,\mathrm{Re}(m_{nl})] \quad (11)$$

$$\alpha_l' = \frac{E_v\omega_l m_{2l}}{4l\pi}\alpha_l^3+\frac{a\alpha_n}{4l\pi}[\cos\theta\,\mathrm{Im}(m_{nl})+\sin\theta\,\mathrm{Re}(m_{nl})] \quad (12)$$

$$\theta' = \mu+\frac{3E_e m_{2n}\alpha_n^2}{8n\pi}+\frac{3E_e m_{2l}\alpha_l^2}{8l\pi}$$

$$+(\cos\theta\,\mathrm{Re}(m_{nl})-\sin\theta\,\mathrm{Im}(m_{nl}))\left(\frac{a\alpha_l}{4n\pi\alpha_n}+\frac{a\alpha_n}{4l\pi\alpha_l}\right). \quad (13)$$

In order to analyze the stability of steady-state solutions of α_{n0}, α_{l0}, and θ_0, introduce small variations ϵ_{α_n},ϵ_{α_l}, and ϵ_θ as

$$\alpha_n=\alpha_{n0}+\epsilon_{\alpha_n},\quad \alpha_l=\alpha_{l0}+\epsilon_{\alpha_l},\quad \theta=\theta_0+\epsilon_\theta. \quad (14)$$

Note that $\alpha_{n0}' = 0$, $\alpha_{l0}' = 0$, $\theta_0' = 0$ for steady-state solutions. Substituting expression (14) into Eqs. (11) to (13) and linearizing the resulting equations, the following relations are obtained:

$$\epsilon_{\alpha_n}' = \frac{3E_v\omega_n m_{2n}\alpha_{n0}^2}{4n\pi}\epsilon_{\alpha_n}+\frac{a[\cos\theta_0\,\mathrm{Im}(m_{nl})+\sin\theta_0\,\mathrm{Re}(m_{nl})]}{4n\pi}\epsilon_{\alpha_l}$$

$$+\frac{a\alpha_{l0}[-\sin\theta_0\,\mathrm{Im}(m_{nl})+\cos\theta_0\,\mathrm{Re}(m_{nl})]}{4n\pi}\epsilon_\theta \quad (15)$$

$$\epsilon_{\alpha_l}' = \frac{a[\cos\theta_0\,\mathrm{Im}(m_{nl})+\sin\theta_0\,\mathrm{Re}(m_{nl})]}{4l\pi}\epsilon_{\alpha_n}+\frac{3E_v\omega_l m_{2l}\alpha_{l0}^2}{4l\pi}\epsilon_{\alpha_l}$$

$$+\frac{a\alpha_{n0}[-\sin\theta_0\,\mathrm{Im}(m_{nl})+\cos\theta_0\,\mathrm{Re}(m_{nl})]}{4l\pi}\epsilon_\theta \quad (16)$$

$$\epsilon_\theta' = \left[\frac{3E_e m_{2n}\alpha_{n0}}{4n\pi}+(\cos\theta_0\,\mathrm{Re}(m_{nl})-\sin\theta_0\,\mathrm{Im}(m_{nl}))\left(\frac{a}{4l\pi\alpha_{l0}}-\frac{a\alpha_{l0}}{4n\pi\alpha_{n0}^2}\right)\right]\epsilon_{\alpha_n}$$

$$+\left[\frac{3E_e m_{2l}\alpha_{l0}}{4l\pi}+(\cos\theta_0\,\mathrm{Re}(m_{nl})-\sin\theta_0\,\mathrm{Im}(m_{nl}))\left(\frac{a}{4n\pi\alpha_{n0}}-\frac{a\alpha_{n0}}{4l\pi\alpha_{l0}^2}\right)\right]\epsilon_{\alpha_l}$$

$$-(\sin\theta_0\,\mathrm{Re}(m_{nl})+\cos\theta_0\,\mathrm{Im}(m_{nl}))\times\left(\frac{a\alpha_{l0}}{4n\pi\alpha_{n0}}+\frac{a\alpha_{n0}}{4l\pi\alpha_{l0}}\right)\epsilon_\theta. \quad (17)$$

To avoid the complexity of evaluating θ_0, it is necessary to express those terms relating to θ_0 in terms of α_{n0} and α_{l0}. This can be accomplished by setting $\alpha_{n0}' = 0$, $\alpha_{l0}' = 0$ and $\theta_0' = 0$ in Eqs. (11) to (13) and rearranging the resulting equations as

$$\frac{a[\cos\theta_0\,\mathrm{Im}(m_{nl})+\sin\theta_0\,\mathrm{Re}(m_{nl})]}{4n\pi}=-\frac{E_v\omega_n m_{2n}\alpha_{n0}^3}{4n\pi\alpha_{l0}} \quad (18)$$

$$\frac{a[\cos\theta_0\,\mathrm{Im}(m_{nl})+\sin\theta_0\,\mathrm{Re}(m_{nl})]}{4l\pi}=-\frac{E_v\omega_l m_{2l}\alpha_{l0}^3}{4l\pi\alpha_{n0}} \quad (19)$$

$$g=\cos\theta_0\,\mathrm{Re}(m_{nl})-\sin\theta_0\,\mathrm{Im}(m_{nl})=-\frac{4nl\pi\alpha_{l0}\alpha_{n0}\left(\mu+\frac{3E_e m_{2n}\alpha_{n0}^2}{8n\pi}+\frac{3E_e m_{2l}\alpha_{l0}^2}{8l\pi}\right)}{al\alpha_{l0}^2+an\alpha_{n0}^2}. \quad (20)$$

Substitution of Eqs. (18), (19), and (20) into (15), (16), and (17) results in equations for perturbed motions with coefficients matrix expressed in terms of α_{n0} and α_{l0} as

$$\begin{Bmatrix}\epsilon_{a_n}'\\ \epsilon_{\alpha_l}'\\ \epsilon_\theta'\end{Bmatrix}=H\begin{Bmatrix}\epsilon_{a_n}\\ \epsilon_{\alpha_l}\\ \epsilon_\theta\end{Bmatrix} \quad (21)$$

where

$$\mathbf{H}=\begin{bmatrix}\frac{3E_v\omega_n m_{2n}\alpha_{n0}^2}{4n\pi} & -\frac{E_v\omega_n m_{2n}\alpha_{n0}^3}{4n\pi\alpha_{l0}} & \frac{a\alpha_{l0}g}{4n\pi}\\ -\frac{E_v\omega_l m_{2l}\alpha_{l0}^3}{4l\pi\alpha_{n0}} & \frac{3E_v\omega_l m_{2l}\alpha_{l0}^2}{4l\pi} & \frac{a\alpha_{n0}g}{4l\pi}\\ \frac{3E_e m_{2n}\alpha_{n0}}{4n\pi}+g\left(\frac{a}{4l\pi\alpha_{l0}}-\frac{a\alpha_{l0}}{4n\pi\alpha_{n0}^2}\right) & \frac{3E_e m_{2l}\alpha_{l0}}{4l\pi}+g\left(\frac{a}{4n\pi\alpha_{n0}}-\frac{a\alpha_{n0}}{4l\pi\alpha_{l0}^2}\right) & \frac{E_v\omega_n m_{2n}\alpha_{n0}^2}{4n\pi}+\frac{E_v\omega_l m_{2l}\alpha_{l0}^2}{4l\pi}\end{bmatrix}. \quad (22)$$

Stability of the nontrivial limit cycles is now decided by the nature of the eigenvalues of the matrix **H**. If all the eigenvalues have negative real parts, the steady-state solutions are stable. On the other hand, if the real part of at least one of the eigenvalues is positive, the corresponding steady-state solution is unstable. By the use of Routh-Hurwitz criterion the stability conditions can be determined as

$$h_1 < 0 \quad h_2 > 0 \quad h_3 < 0 \quad h_4 < 0 \tag{23}$$

where

$$h_1 = H(1, 1) + H(2, 2) + H(3, 3) \tag{24}$$

$$h_2 = \begin{vmatrix} H(1,1) & H(1,2) \\ H(2,1) & H(2,2) \end{vmatrix} + \begin{vmatrix} H(1,1) & H(1,3) \\ H(3,1) & H(3,3) \end{vmatrix} + \begin{vmatrix} H(2,2) & H(2,3) \\ H(3,2) & H(3,3) \end{vmatrix} \tag{25}$$

$$h_3 = |\mathbf{H}| \quad h_4 = h_1 h_2 - h_3 \tag{26}$$

and $|\ |$ denotes the determinant of a matrix.

It should be noted that if $h_1 < 0$, $h_3 < 0$ and $h_4 < 0$, h_2 is greater than zero. Thus, $h_1 < 0$, $h_3 < 0$, and $h_4 < 0$ are the sufficient conditions that the system is stable. However, if $h_1 = 0$, $h_2 > 0$ must be considered for the stability analysis.

Substituting the expression of matrix **H** in Eq. (22) into Eqs. (24) to (26), and performing complicate manipulations (the Appendix) result in

$$h_1 = \frac{E_v \omega_n m_{2n} \alpha_{n0}^2}{n\pi} + \frac{E_v \omega_l m_{2l} \alpha_{l0}^2}{l\pi} \tag{27}$$

$$h_2 = \frac{E_v^2 \omega_n \omega_l m_{2n} m_{2l} \alpha_{n0}^2 \alpha_{l0}^2}{2nl\pi^2} + 3\left(\frac{E_v \omega_n m_{2n} \alpha_{n0}^2}{4n\pi} + \frac{E_v \omega_l m_{2l} \alpha_{l0}^2}{4l\pi}\right)^2 + a^2 g^2 \left(\frac{\alpha_{n0}}{4l\pi\alpha_{l0}} - \frac{\alpha_{l0}}{4n\pi\alpha_{n0}}\right)^2 - \frac{3E_e m_{2l} \alpha_{n0} \alpha_{l0} ag}{16l^2\pi^2} - \frac{3E_e m_{2n} \alpha_{n0} \alpha_{l0} ag}{16n^2\pi^2} \tag{28}$$

$$h_3 = \pm \frac{E_v m_{2n} m_{2l} \left(\frac{\alpha_{l0}}{4n\pi\alpha_{n0}} + \frac{\alpha_{n0}}{4l\pi\alpha_{l0}}\right)\left(\frac{\omega_n \alpha_{n0}}{l\alpha_{l0}} + \frac{\omega_l \alpha_{l0}}{n\alpha_{n0}}\right) \alpha_{n0}^2 \alpha_{l0}^2}{4\left(m_{2n} l + m_{2l} \frac{n^3}{l^2} \sqrt{\frac{n}{l}}\right)\pi^2} \times \sqrt{c_2^2 - 4c_1 c_3} \tag{29}$$

where plus sign in h_3 and h_4 is selected for the first limit cycle and minus sign in h_3 and h_4 is selected for the second limit cycle.

Based on Eqs. (27) to (30) and the Routh-Hurwitz criterion, viscoelastic moving belts and elastic moving belts are examined, respectively, in the following.

Parametric Resonance of Viscoelastic Moving Belts: $E_v \neq 0$. Since $m_{2n} < 0$ and $m_{2l} < 0$ (see Zhang and Zu, 1998), it can be seen from Eqs. (27), (29), and (30) that h_1, h_3, and h_4 are always less than zero for the first limit cycle. Thus, the first limit cycle is always stable. It is also evident that h_3 is always greater than zero for the second limit cycle. Thus, the second amplitude limit cycle is always unstable.

Considering the existence condition of limit cycles given in the first paper (Zhang and Zu, 1998), the following conclusions can be drawn for parametric resonance of viscoelastic moving belts:

1 If

$$-\frac{\left(\frac{1}{l}\sqrt[4]{\frac{n}{l}} + \frac{1}{n}\sqrt[4]{\frac{l}{n}}\right)\sqrt{\mathrm{Im}(m_{nl})^2 + \mathrm{Re}(m_{nl})^2}}{4\pi} \leq \mu \leq \frac{\left(\frac{n}{l^2}\sqrt{\frac{n}{l}} + \frac{1}{l}\right)\sqrt{(\mathrm{Im}(m_{nl})^2 + \mathrm{Re}(m_{nl})^2)c_1}}{4\pi E_v \omega_n m_{2n}} a,$$

the first limit cycle exists and it is always stable.

2 If

$$\frac{\left(\frac{1}{l}\sqrt[4]{\frac{n}{l}} + \frac{1}{n}\sqrt[4]{\frac{l}{n}}\right)\sqrt{\mathrm{Im}(m_{nl})^2 + \mathrm{Re}(m_{nl})^2}}{4\pi} \leq \mu \leq \frac{\left(\frac{n}{l^2}\sqrt{\frac{n}{l}} + \frac{1}{l}\right)\sqrt{(\mathrm{Im}(m_{nl})^2 + \mathrm{Re}(m_{nl})^2)c_1}}{4\pi E_v \omega_n m_{2n}} a,$$

the second limit cycle exists and it is always unstable.

It is noted that the lower boundaries of limit cycles do not coincide with the stability boundary of linear systems, which is quite different from the corresponding elastic systems. The reason is that the viscoelastic model introduces material damping which will lead to the vanish of limit cycles in some region. Therefore, for viscoelastic model, there exists an upper boundary and a lower boundary. In other words, viscoelasticity narrows the stable region for the first limit cycle and also narrows the unstable region for the second limit cycle. Since the second limit cycle is always unstable, this corresponds to a saddle point or a motion which is unrealizable in either numerical or laboratory experiments.

$$h_4 = \frac{\frac{l^3 E_v^3 \omega_n^3 m_{2n}^4 \alpha_{n0}^4 \alpha_{l0}^2}{64n^7\pi^4}\left(3 + \sqrt{\frac{n}{l}} + 15\frac{l}{n} + 13\frac{l^2}{n^2}\sqrt{\frac{n}{l}} + 13\frac{l^3}{n^3} + 15\frac{l^3}{n^3}\sqrt{\frac{n}{l}} + \frac{3l^4}{n^4} + \frac{l^5}{n^5}\sqrt{\frac{n}{l}}\right)}{\left(\frac{m_{2n}}{4n\pi} + \frac{m_{2l}}{4l\pi}\frac{n^2}{l^2}\sqrt{\frac{n}{l}}\right)} + \left(\frac{E_v \omega_n m_{2n} \alpha_{n0}^2}{n\pi} + \frac{E_v \omega_l m_{2l} \alpha_{l0}^2}{l\pi}\right) a^2 g^2 \left(\frac{\alpha_{n0}}{4l\pi\alpha_{l0}} - \frac{\alpha_{l0}}{4n\pi\alpha_{n0}}\right)^2 \pm \frac{E_v \alpha_{n0}^2 \alpha_{l0}^2 m_{2n}^2 \omega_n}{16\pi^3\left(\frac{m_{2n}}{4n\pi} + \frac{m_{2l}}{4l\pi}\frac{n^2}{l^2}\sqrt{\frac{n}{l}}\right)}\left(\frac{\alpha_{n0}}{n^3\alpha_{l0}} + \frac{\omega_l m_{2l}^2 \alpha_{l0}}{l^3 \omega_n m_{2n}^2 \alpha_{n0}}\right)\left(\frac{\alpha_{l0}}{4n\pi\alpha_{n0}} + \frac{\alpha_{n0}}{4l\pi\alpha_{l0}}\right)\sqrt{c_2^2 - 4c_1 c_3} \tag{30}$$

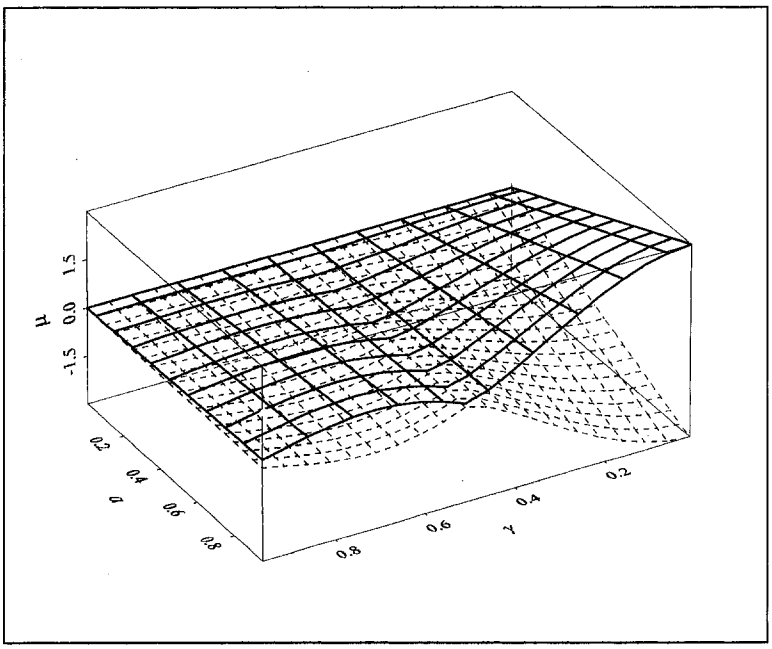

Fig. 1 Stability boundaries of the trivial limit cycle for the second principal parametric resonance ($n = 2$, $l = 2$, $E_e = 400$, $\gamma = 0.2$); the upper boundary, – – – – the lower boundary

Elastic Summation Parametric Resonance: $E_v = 0$. Since $E_v = 0$, h_1, h_3, and h_4 are equal to zero. In this case, the limit cycles are stable if and only if $h_2 > 0$. Setting $E_v = 0$, h_2 can be rewritten as

$$h_2 = a^2 g^2 \left(\frac{\alpha_{n0}}{4l\pi\alpha_{l0}} - \frac{\alpha_{l0}}{4n\pi\alpha_{n0}} \right)^2 - \frac{3E_e m_{2l}\alpha_{n0}\alpha_{l0} ag}{16l^2\pi^2} - \frac{3E_e m_{2n}\alpha_{n0}\alpha_{l0} ag}{16n^2\pi^2}. \quad (31)$$

For elastic parametric resonance, there exist the following relations,

$$\alpha_l^2 = \frac{n}{l}\alpha_n^2 \quad g = \pm\sqrt{\mathrm{Re}(m_{nl})^2 + \mathrm{Im}(m_{nl})^2}, \quad (32)$$

where the plus sign is selected for the first limit cycle and the minus sign is selected for the second limit cycle. Substituting Eq. (32) into (31) yields

$$h_2 = \pm\left(\frac{-3E_e m_{2l}\alpha_{n0}\alpha_{l0} a}{16l^2\pi^2} - \frac{3E_e m_{2n}\alpha_{n0}\alpha_{l0} a}{16n^2\pi^2} \right) \times \sqrt{\mathrm{Re}(m_{nl})^2 + \mathrm{Im}(m_{nl})^2}. \quad (33)$$

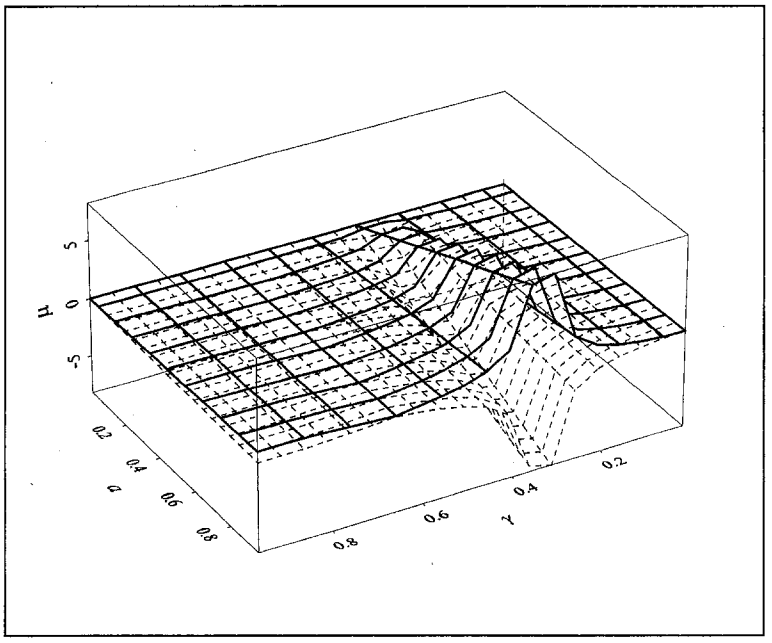

Fig. 2 Stability boundaries of the trivial limit cycle for the first summation parametric resonance ($n = 1$, $l = 2$, $E_e = 400$, $\gamma = 0.2$); the upper boundary, – – – – the lower boundary

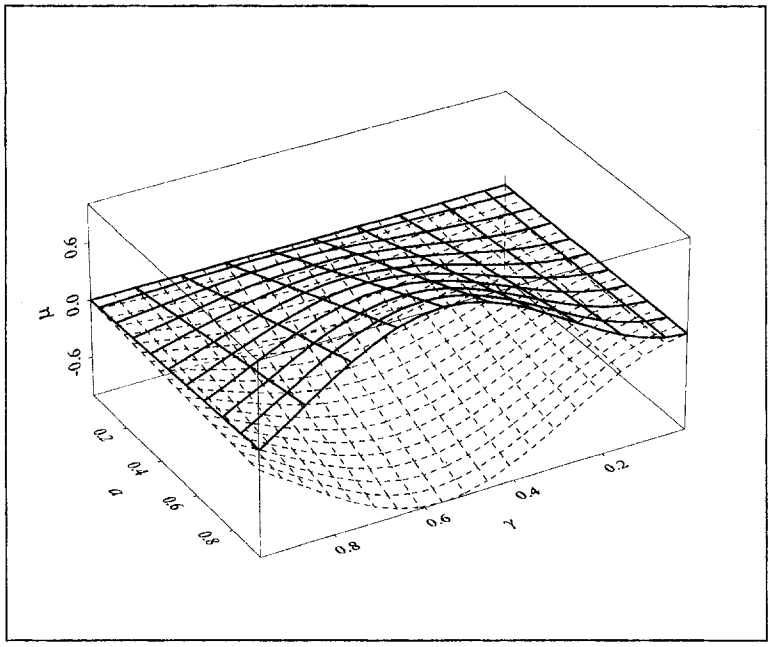

Fig. 3 Stability boundaries of the trivial limit cycle for the summation parametric resonance (n = 1, l = 3, E_o = 400, γ = 0.2); the upper boundary, – – – – the lower boundary

It can be seen that $h_2 > 0$ for the first limit cycle while $h_2 < 0$ for the second limit cycle. This leads to the conclusion that the first limit cycle is always stable and the second limit cycle is always unstable for the parametric resonance of elastic moving belts.

Considering the existence condition of limit cycles, the following conclusions can be drawn for parametric resonance of elastic moving belts:

1 If $\mu \geq -(\sqrt{\mathrm{Im}(m_{nl})^2 + \mathrm{Re}(m_{nl})^2}/2\sqrt{nl}\ \pi)a$, the first limit cycle exists and it is always stable.

2 If $\mu \geq (\sqrt{\mathrm{Im}(m_{nl})^2 + \mathrm{Re}(m_{nl})^2}/2\sqrt{nl}\ \pi)a$, the second limit cycle exists and it is always unstable.

Comparing with Eq. (10), it is suggested that the nontrivial limit cycle of summation parametric resonance of elastic systems bifurcates from the instability boundary of the trivial solution.

4 Numerical Results and Discussion

In this section, numerical results for stability analysis of summation parametric resonance of moving belts are presented. Effects of the viscoelastic parameter, the amplitude of excitation, the frequency of excitation and the transport speed on stability boundaries of nontrivial limit cycles are discussed.

The stability boundary of the trivial solution for the second-mode principal parametric resonance (n = 2, l = 2) and the summation parametric resonance (n = 1, l = 2 and n = 1, l = 3) are plotted in Fig. 1 to Fig. 3 as a function of the transport speed, excitation amplitude, and frequency (detuning). From Fig. 1, it is seen that for the second-mode principal parametric resonance, there are two translating speeds where the slopes are unbounded and the instability region closes altogether. The instability region reaches maximum when the transport speed γ approaches zero. As the translating speed grows, the instability region begins to close. The instability region widens with the increase of the excitation amplitude. From Fig. 2 (n = 1, l = 2) and Fig. 3 (n = 1, l = 3), it is evident that the instability region almost closes when the transport speed is very small. As the transport speed γ increases, the instability becomes wider, reaches a maximum and closes as the translation speed increases to the critical speed.

The stability regions of the first nontrivial limit cycle and the second limit cycle are illustrated in Fig. 4 and Fig. 5 for summation parametric resonance (n = 1, l = 2) of a viscoelastic moving belt. Four different values of E_v, i.e., 1, 10, 25, 50 are chosen to show the effect of the viscoelastic property on the stability and instability regions. Since the first limit cycle is always stable while the second limit cycle is always unstable for viscoelastic materials, the stable (unstable) region of the first (second) limit cycle should be the same as the corresponding region of existence. It can be seen that the lower boundaries for different E_v are identical, while the upper boundaries are different for different E_v. The lower boundaries for the first and the second limit cycle have the same absolute value but opposite sign. The upper boundaries for the first and the second limit cycle with the same E_v are identical.

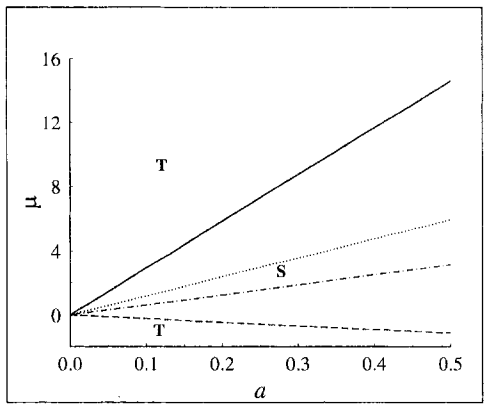

Fig. 4 Effects of E_v on the stability boundary of the first limit cycle of the first mode for the summation parametric resonance (n = 1, l = 2, E_o = 400, γ = 0.25); ——— upper boundary, E_v = 10; · · · · upper boundary, E_v = 25; – · – · – upper boundary, E_v = 50; — — — the lower boundary; S = stable region; T = trivial solution region

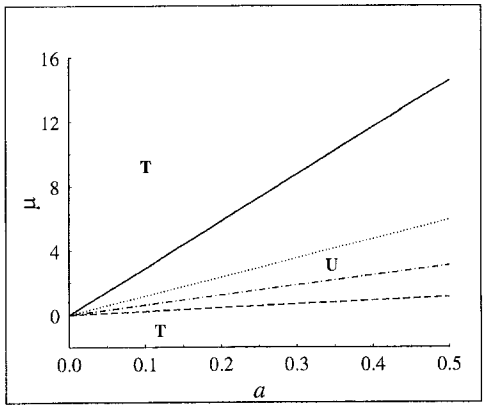

Fig. 5 Effects of E_v on the instability boundary of the second limit cycle of the first mode for the summation parametric resonance ($n = 1$, $l = 2$, $E_e = 400$, $\gamma = 0.25$); ——— upper boundary, $E_v = 10$; · · · · upper boundary, $E_v = 25$; – · – · – upper boundary, $E_v = 50$; — — — the lower boundary; U = unstable region; T = trivial solution region

5 Conclusions

In this paper, the dynamic stability of parametrically excited viscoelastic belts is investigated. The Routh-Hurwitz criterion is employed to investigate the stability of limit cycles. Closed-form expressions are found for the stability of limit cycles of the general summation parametric resonance of viscoelastic moving belts. The following conclusions are drawn in this study:

1 The first limit cycle is always stable for both viscoelastic and elastic parametric resonance.

2 The second limit cycle is unstable for both viscoelastic parametric resonance and for elastic parametric resonance.

3 The existence boundary of nontrivial limit cycles of elastic systems coincides with that of the stability boundary of the trivial limit cycle. For viscoelastic systems, however, the existence boundary of nontrivial limit cycles is different from the stability boundary of the trivial limit cycle.

4 Viscoelasticity leads to the upper boundary of existence for nontrivial limit cycles. This suggests that viscoelasticity narrows the stable region of the first limit cycle and the unstable region of the second limit cycle.

5 The translating speed, excitation frequency, and excitation amplitude have significant influence on the stable and unstable region of limit cycles.

Acknowledgment

This research is financially supported by a research grant from the Materials and Manufacturing Ontario in Canada.

References

Chen, C. F., 1971, "Hurwitz stability criterion and Fuller's aperiodicity criterion in non-linear system analysis," *International Journal of Electronics,* Vol. 31, pp. 609–619.

Fung, R. F., Huang, J. S., and Chen, Y. C., 1996, "Dynamics Stability of a Viscoelastic Beam Subjected to Harmonic and Parametric Excitations Simultaneously," *Journal of Sound and Vibration,* Vol. 198, pp. 1–16.

Huang, J. S., Fung, R. F., and Lin, C. H., 1995, "Dynamic Stability of a Moving String Undergoing Three-dimensional Vibration," *International Journal of Mechanics Sciences,* Vol. 37, pp. 145–160.

Mahalingam, S., 1957, "Transverse Vibration of Power Transmission Chains," *British Journal of Applied Physics,* Vol. 8, pp. 145–148.

Mockensturm, E. M., Perkins, N. C., and Ulsoy, A. G., 1996, "Stability and Limit Cycles of Parametrically Excited, Axially Moving Strings," ASME *Journal of Vibration and Acoustics,* Vol. 118, pp. 346–351.

Mote, C. D., Jr., 1968, "Parametric Excitation of an Axially Moving String," ASME JOURNAL OF APPLIED MECHANICS, Vol. 35, pp. 171–175.

Pakdemirli, M., and Ulsoy, A. G., 1997, "Stability Analysis of an Axially Accelerating String," *Journal of Sound and Vibration,* Vol. 203, pp. 815–832.

Stevens, K. K., 1966, "On the Parametric Excitation of a Viscoelastic Column," *American Institute of Aeronautics and Astronautics Journal,* Vol. 4, pp. 2111–2116.

Ulsoy, A. G., Mote, C. D., Jr., and Szymani, R., 1978, "Principal Developments in Band Saw Vibration and Stability Research," *Holz als Rohund Werkstoff,* Vol. 36, pp. 273–280.

Wanda, S., 1990, *The Behavior of Nonlinear System,* Kluwer Academic Publishers, Amsterdam, The Netherlands.

Zhang, L., and Zu, J. W., 1998, "Nonlinear Vibration of Parametrically Excited Viscoelastic Moving Belts Part 1: Dynamic Response," ASME JOURNAL OF APPLIED MECHANICS, Vol. 66, pp. 396–402.

APPENDIX

The main difficulty in the stability analysis of nontrivial limit cycles lies in how to evaluate h_3 and h_4. In the Appendix, the main procedure in deriving the expressions of h_3 and h_4 is shown.

Substituting Eq. (22) into (26), the determinant h_3 of matrix **H** can be obtained as follows:

$$h_3 = \left(\frac{E_v\omega_n m_{2n}\alpha_{n0}^2}{4n\pi} + \frac{E_v\omega_l m_{2l}\alpha_{l0}^2}{4l\pi}\right)\frac{E_v^2\omega_n\omega_l m_{2n}m_{2l}\alpha_{n0}^2\alpha_{l0}^2}{2nl\pi^2}$$
$$- \frac{a\alpha_{n0}g}{4l\pi}\left\{\frac{3E_v\omega_n m_{2n}\alpha_{n0}^2}{4n\pi}\left[\frac{3E_e m_{2l}\alpha_{l0}}{4l\pi} + g\left(\frac{a}{4n\pi\alpha_{n0}}\right.\right.\right.$$
$$\left.\left.\left. - \frac{a\alpha_{n0}}{4l\pi\alpha_{l0}^2}\right)\right] + \frac{E_v\omega_n m_{2n}\alpha_{n0}^3}{4n\pi\alpha_{l0}}\left[\frac{3E_e m_{2n}\alpha_{n0}}{4n\pi} + g\left(\frac{a}{4l\pi\alpha_{l0}}\right.\right.\right.$$
$$\left.\left.\left. - \frac{a\alpha_{l0}}{4n\pi\alpha_{n0}^2}\right)\right]\right\} + \frac{a\alpha_{l0}g}{4n\pi}\left\{\frac{-E_v\omega_l m_{2l}\alpha_{l0}^3}{4l\pi\alpha_{n0}}\left[\frac{3E_e m_{2l}\alpha_{l0}}{4l\pi}\right.\right.$$
$$\left. + g\left(\frac{a}{4n\pi\alpha_{n0}} - \frac{a\alpha_{n0}}{4l\pi\alpha_{l0}^2}\right)\right] - \frac{3E_v\omega_l m_{2l}\alpha_{l0}^2}{4l\pi}\left[\frac{3E_e m_{2n}\alpha_{n0}}{4n\pi}\right.$$
$$\left.\left. + g\left(\frac{a}{4l\pi\alpha_{l0}} - \frac{a\alpha_{l0}}{4n\pi\alpha_{n0}^2}\right)\right]\right\}. \quad \text{(A1)}$$

Using the relation between α_{n0} and α_{l0}, i.e., $(\omega_n m_{2n}\alpha_{n0}^3/\omega_l m_{2l}\alpha_{l0}^3) = (\alpha_{l0}/\alpha_{n0})$, and performing algebraic manipulations, h_3 can be rewritten as

$$h_3 = \left(\frac{E_v\omega_n m_{2n}\alpha_{n0}^2}{4n\pi} + \frac{E_v\omega_l m_{2l}\alpha_{l0}^2}{4l\pi}\right)\frac{E_v^2\omega_n\omega_l m_{2n}m_{2l}\alpha_{n0}^2\alpha_{l0}^2}{2nl\pi^2}$$
$$- \frac{3agE_eE_v\omega_n m_{2n}m_{2l}\alpha_{n0}^3\alpha_{l0}}{16nl^2\pi^3} - \frac{3agE_eE_v\omega_l m_{2n}m_{2l}\alpha_{l0}^3\alpha_{n0}}{16n^2l\pi^3}. \quad \text{(A2)}$$

It is difficult to determine if h_3 is greater than zero from Eq. (A2) directly. The expression of g in terms of the specific steady solution (the first limit cycle or the second limit cycle) must be obtained first. However, it would be too complicated to evaluate h_3 if substituting the expressions of α_{n0} and α_{l0} directly into the expression of g in Eq. (20) as well as Eq. (A2). This difficulty can be overcome by using the following relation derived from the amplitude expressions of steady-state response,

$$3aE_eg = -\frac{\left(\pm\sqrt{c_2^2 - 4c_1c_3} - 2E_v^2\omega_n^2 m_{2n}^2\alpha_{n0}^2\frac{l^2}{n^2}\sqrt{\frac{l}{n}}\right)\left(\frac{\alpha_{l0}}{4n\pi\alpha_{n0}} + \frac{\alpha_{n0}}{4l\pi\alpha_{l0}}\right)}{\left(\frac{m_{2n}}{4n\pi} + \frac{m_{2l}n^2}{4l^3\pi}\sqrt{\frac{n}{l}}\right)}. \quad \text{(A3)}$$

Note that plus sign is selected for the first limit cycle and the minus sign is selected for the second limit cycle. Substituting Eq. (A3) into Eq. (A2) results in

where

$$h_3 = \pm \frac{E_v m_{2n} m_{2l} \alpha_{n0}^2 \alpha_{l0}^2 \left(\frac{\alpha_{l0}}{4n\pi\alpha_{n0}} + \frac{\alpha_{n0}}{4l\pi\alpha_{l0}} \right) \left(\frac{\omega_n \alpha_{n0}}{l\alpha_{l0}} + \frac{\omega_l \alpha_{l0}}{n\alpha_{n0}} \right)}{4\left(m_{2n} l + m_{2l} \frac{n^3}{l^2} \sqrt{\frac{n}{l}} \right) \pi^2} \times \sqrt{c_2^2 - 4c_1 c_3} + \frac{E_v m_{2n} m_{2l} \alpha_{n0}^2 \alpha_{l0}^2}{4\left(m_{2n} l + m_{2l} \frac{n^3}{l^2} \sqrt{\frac{n}{l}} \right) \pi} (a_1 + a_2) \quad \text{(A4)}$$

$$a_1 = E_v \omega_n \omega_l \left(\frac{E_v \omega_n m_{2n} \alpha_{n0}^2}{4n\pi} + \frac{E_v \omega_l m_{2l} \alpha_{l0}^2}{4l\pi} \right) \times \left(\frac{2m_{2n}}{n} + \frac{2m_{2l} n^2}{l^3} \sqrt{\frac{n}{l}} \right) \quad \text{(A5)}$$

$$a_2 = -2E_v \omega_n^2 m_{2n}^2 \alpha_{n0}^2 \frac{l^2}{n^2} \times \sqrt{\frac{l}{n}} \left(\frac{\alpha_{l0}}{4n\pi\alpha_{n0}} + \frac{\alpha_{n0}}{4l\pi\alpha_{l0}} \right) \left(\frac{\omega_n \alpha_{n0}}{l\alpha_{l0}} + \frac{\omega_l \alpha_{l0}}{n\alpha_{n0}} \right). \quad \text{(A6)}$$

Substituting the relation between α_{n0} and α_{l0} into Eq. (A5) and (A6) and performing complicated algebraic manipulation yields $a_1 + a_2 = 0$. Therefore, the expression of h_3 can be simplified as shown in Eq. (29).

Substituting the expressions of h_1, h_2, and h_3 into Eq. (26), h_4 can be obtained as follows:

$$h_4 = 3\left(\frac{E_v \omega_n m_{2n} \alpha_{n0}^2}{4n\pi} + \frac{E_v \omega_l m_{2l} \alpha_{l0}^2}{4l\pi} \right) \frac{E_v^2 \omega_n \omega_l m_{2n} m_{2l} \alpha_{n0}^2 \alpha_{l0}^2}{2nl\pi^2} + 12\left(\frac{E_v \omega_n m_{2n} \alpha_{n0}^2}{4n\pi} + \frac{E_v \omega_l m_{2l} \alpha_{l0}^2}{4l\pi} \right)^3 + \frac{3agE_e E_v \omega_n m_{2n}^2 \alpha_{n0}^3 \alpha_{l0}}{16n^3\pi^3} + \frac{3agE_e E_v \omega_l m_{2l}^2 \alpha_{l0}^3 \alpha_{n0}}{16l^3\pi^3} + \left(\frac{E_v \omega_n m_{2n} \alpha_{n0}^2}{n\pi} + \frac{E_v \omega_l m_{2l} \alpha_{l0}^2}{l\pi} \right) \times a^2 g^2 \left(\frac{a}{4n\pi\alpha_{n0}} - \frac{a\alpha_{n0}}{4l\pi\alpha_{l0}^2} \right)^2. \quad \text{(A7)}$$

Substituting Eq. (A3) into (A7) results in

$$h_4 = \frac{a_3}{\left(\frac{m_{2n}}{4n\pi} + \frac{m_{2l}}{4l\pi} \frac{n^2}{l^2} \sqrt{\frac{n}{l}} \right)} + \left(\frac{E_v \omega_n m_{2n} \alpha_{n0}^2}{n\pi} + \frac{E_v \omega_l m_{2l} \alpha_{l0}^2}{l\pi} \right) \times a^2 g^2 \left(\frac{\alpha_{n0}}{4l\pi\alpha_{l0}} - \frac{\alpha_{l0}}{4n\pi\alpha_{n0}} \right)^2 \pm \frac{E_v \alpha_{n0}^2 \alpha_{l0}^2 m_{2n}^2 \omega_n}{16\pi^3 \left(\frac{m_{2n}}{4n\pi} + \frac{m_{2l}}{4l\pi} \frac{n^2}{l^2} \sqrt{\frac{n}{l}} \right)} \times \left(\frac{\alpha_{n0}}{n^3\alpha_{l0}} + \frac{\omega_l m_{2l}^2 \alpha_{l0}}{l^3 \omega_n m_{2n}^2 \alpha_{n0}} \right) \left(\frac{\alpha_{l0}}{4n\pi\alpha_{n0}} + \frac{\alpha_{n0}}{4l\pi\alpha_{l0}} \right) \times \sqrt{c_2^2 - 4c_1 c_3} \quad \text{(A8)}$$

where

$$a_3 = 3\left(\frac{m_{2n}}{4n\pi} + \frac{m_{2l}}{4l\pi} \frac{n^2}{l^2} \sqrt{\frac{n}{l}} \right) \times \left(\frac{E_v \omega_n m_{2n} \alpha_{n0}^2}{4n\pi} + \frac{E_v \omega_l m_{2l} \alpha_{l0}^2}{4l\pi} \right) \frac{E_v^2 \omega_n \omega_l m_{2n} m_{2l} \alpha_{n0}^2 \alpha_{l0}^2}{2nl\pi^2} + 12\left(\frac{m_{2n}}{4n\pi} + \frac{m_{2l}}{4l\pi} \frac{n^2}{l^2} \sqrt{\frac{n}{l}} \right) \left(\frac{E_v \omega_n m_{2n} \alpha_{n0}^2}{4n\pi} + \frac{E_v \omega_l m_{2l} \alpha_{l0}^2}{4l\pi} \right)^3 + \frac{E_v^3 \omega_n^3 m_{2n}^4 \alpha_{n0}^4 \alpha_{l0}^2}{32\pi^4} \left(\frac{\alpha_{n0}}{n^3\alpha_{l0}} + \frac{l^6 \alpha_{l0}}{n^9 \alpha_{n0}} \right) \frac{l^2}{n^2} \times \sqrt{\frac{l}{n}} \left(\frac{\alpha_{l0}}{n\alpha_{n0}} + \frac{\alpha_{n0}}{l\alpha_{l0}} \right). \quad \text{(A9)}$$

Using the relation between α_{n0} and α_{l0}, and performing complicate algebraic manipulation, a_3 can be rewritten as

$$a_3 = \frac{l^3 E_v^3 \omega_n^3 m_{2n}^4 \alpha_{n0}^4 \alpha_{l0}^2}{64n^7\pi^4} \left(3 + \sqrt{\frac{n}{l}} + 15\frac{l}{n} + 13\frac{l^2}{n^2}\sqrt{\frac{n}{l}} + 13\frac{l^3}{n^3} + 15\frac{l^3}{n^3}\sqrt{\frac{n}{l}} + \frac{3l^4}{n^4} + \frac{l^5}{n^5}\sqrt{\frac{n}{l}} \right). \quad \text{(A10)}$$

Substituting Eq. (A10) into (A8), the final form of h_4 can be obtained as shown in Eq. (30).

Comparison of the In-Plane Natural Frequencies of Symmetric Cross-Ply Laminated Beams Based on the Bernoulli-Euler and Timoshenko Beam Theories

V. Yıldırım[1]
Associate Professor,
Department of Mechanical Engineering,
University of Çukurova,
01330 Balcalı-Adana, Turkey

E. Sancaktar
Professor,
Department of Polymer Engineering,
The University of Akron,
Akron, OH 44325-0301
Fellow ASME

E. Kıral
Professor
Department of Civil Engineering,
University of Çukurova,
01330 Balcalı-Adana, Turkey

The in-plane free vibration problem of symmetric cross-ply laminated beams is studied based on the transfer matrix method. Distributed parameter model is used in the mathematical formulation. The rotary inertia, the shear and extensional deformation effects, are considered for the Timoshenko's beam analysis. These effects are neglected in the Bernoulli-Euler analysis. The exact overall dynamic transfer matrix of the beam is obtained by making use of the numerical algorithm available in the literature. In order to obtain detailed knowledge about the effects of the rotary inertia, shear and axial deformations on the first six non-dimensional frequencies, the results of Timoshenko and Bernoulli-Euler theories are compared with each other for length-to-thickness ratios from ranging 3 to 20. Fixed-fixed, fixed-simple, and fixed-free boundary conditions are considered for three values of the thickness-to-width ratios of a rectangular section (2, 1, 0.5).

1 Introduction

The dynamic problems of laminated composite beams have not been studied as extensively as plates and shells. Vinson and Sierakowski (1986) obtained the exact solution of a simply supported composite beam based on the classical theory, which neglects the effects of the rotary inertia and shearing deformation. Kapania and Raciti (1989a) presented a survey in the vibration analysis of laminated composite beams. It is evident from the literature survey that the free vibration problem of beams is generally studied considering the out-of-plane uniaxial bending and axial oscillations. Kapania and Raciti (1989b) studied nonlinear vibrations of unsymmetrical laminated beams. Chandrasekhara et al. (1990) derived the equation of motion of composite beams based on the first-order shear deformation theory. Hodges et al. (1991) solved the equations of motion using a mixed finite element and an exact integration method. Abramovich (1992) presented exact solutions based on the Timoshenko-type equations for symmetrically laminated composite beams with ten different boundary conditions. The rotary inertia and shear deformation effects were investigated for simply supported straight beams (Abramovich, 1992). Singh and Abdelnassar (1992) examined the forced vibration response of composite beams considering a third-order shear deformation theory. Chandrasekhara and Bangera (1992) studied the free vibration characteristics of laminated composite beams using a higher-order shear deformation theory. Krishnaswamy et al. (1992) obtained the governing equations of laminated composite beams using the Hamilton's principle and presented analytical solutions. Abramovich and Livshits (1994) studied the in-plane free vibrations of nonsymmetrically laminated cross-ply composite beams based on Timoshenko-type equations. Khedeir and Reddy (1994) investigated the free vibration of cross-ply laminated beams with arbitrary boundary conditions by the state space approach (transfer matrix method) and higher-order shear deformation theory. Nabi and Ganesan (1994) developed a general finite element code based on the first-order shear deformation theory. Eisenberger et al. (1995) used the dynamic stiffness analysis of laminated beams using a first-order shear deformation theory. Abramovich et al. (1995) treated vibration of multispan nonsymmetric composite beams. Rao and Ganesan (1997) worked out the dynamical behavior of tapered composite beams by the third-order shear deformation theory. Zappe and Lesiutre (1997) presented a smeared laminate model based on the first-order shear deformation theory for the dynamic analysis of laminated beams.

As it is well known, the Bernoulli-Euler beam theory omits the rotary, the shear, and the extensional deformation effects. Since the ratio of extensional stiffness to the transverse shear stiffness (E_1/E_2) is high, the effect of shear in laminated beams is more significant than in homogeneous beams. These effects can be considered in the analysis by the Timoshenko beam theory. Khedeir and Reddy's (1994) study showed that the effects of the rotary inertia and shear deformation can be significant even for the fundamental frequencies of laminated beams with boundary conditions such as fixed-free, fixed-simple, and fixed-fixed.

The objective of the present study is to formulate the purely in-plane free vibration problem of symmetric cross-ply laminated beams in an accurate manner and to present a detailed knowledge about the effects of rotary inertia, axial, and shear deformations. These effects are studied considering the length-to-thickness (L/h) ratios, the boundary conditions, E_1/E_2 ratios, and the thickness-to-width (h/b) ratios of a cross section for the first six natural in-plane frequencies.

[1] To whom correspondence should be addressed.

Contributed by the Applied Mechanics Division of THE AMERICAN SOCIETY OF MECHANICAL ENGINEERS for publication in the ASME JOURNAL OF APPLIED MECHANICS.

Discussion on the paper should be addressed to the Technical Editor, Professor Lewis T. Wheeler, Department of Mechanical Engineering, University of Houston, Houston, TX 77204-4792, and will be accepted until four months after final publication of the paper itself in the ASME JOURNAL OF APPLIED MECHANICS.

Manuscript received by the ASME Applied Mechanics Division, July 28, 1998; final revision, Jan. 19, 1999. Associate Technical Editor: W. K. Liu.

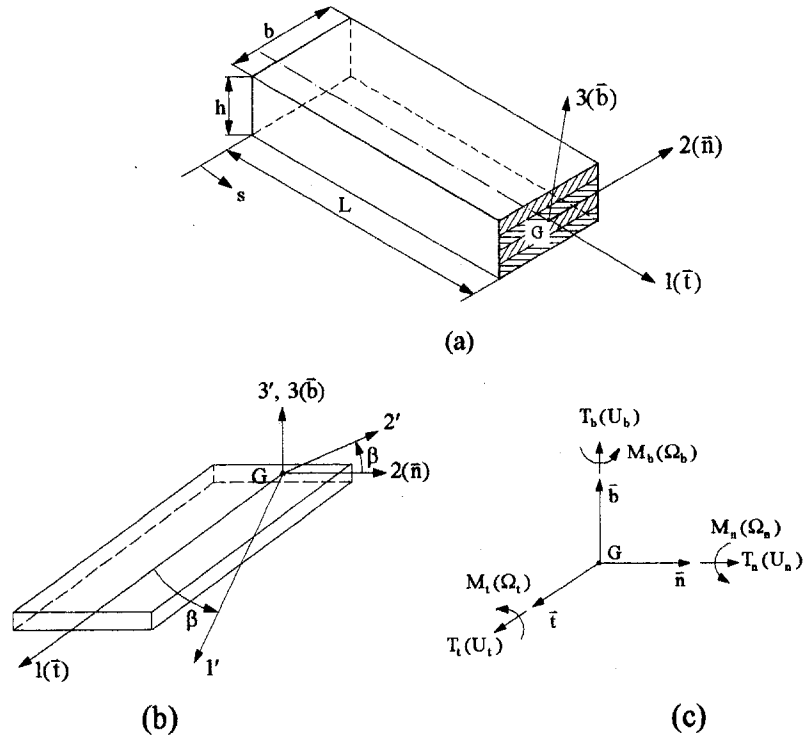

Fig. 1 *(a)* **A laminated composite beam, *(b)* the beam and material symmetry axes, *(c)* stress and displacement resultants in Frenet coordinates**

2 Formulation of the Problem

2.1 Elements of the Reduced and Transformed Stiffness Matrix. The generalized Hooke's law for a linearly elastic material can be written in the conventional contracted notation for engineering stresses ($\sigma_1 = \sigma_{11}$, $\sigma_2 = \sigma_{22}$, $\sigma_3 = \sigma_{33}$, $\sigma_4 = \sigma_{23}$, $\sigma_5 = \sigma_{13}$, $\sigma_6 = \sigma_{12}$), and engineering strains ($e_1 = e_{11}$, $e_2 = e_{22}$, $e_3 = e_{33}$, $e_4 = 2e_{23}$, $e_5 = 2e_{13}$, $e_6 = 2e_{12}$) as follows:

$$\sigma_i = C_{ij}e_j \quad \text{or} \quad e_i = S_{ij}\sigma_j, \quad (i, j = 1, 2, \ldots, 6) \tag{1}$$

where C_{ij} and S_{ij} represent the elements of the stiffness and compliance matrices, respectively. Employing the classical rod theory with $\sigma_2 = \sigma_3 = \sigma_4 = 0$ (Fig. 1(*a*)), the strain components subscripted by 2, 3, and 4 are determined in terms of the other strain components in Eq. (1) as below:

$$e_\beta = S_{\beta j}\alpha_{jk}e_k, \quad (j, k = 1, 5, 6; \beta = 2, 3, 4) \quad \text{and}$$

$$\alpha_{jk} = \alpha_{kj} \tag{2}$$

where

$$\alpha_{11} = \frac{S_{55}S_{66} - S_{56}^2}{d}, \quad \alpha_{55} = \frac{S_{11}S_{66} - S_{16}^2}{d},$$

$$\alpha_{66} = \frac{S_{11}S_{55} - S_{15}^2}{d},$$

$$\alpha_{15} = \frac{S_{16}S_{56} - S_{15}S_{66}}{d}, \quad \alpha_{56} = \frac{S_{15}S_{16} - S_{11}S_{56}}{d},$$

$$\alpha_{16} = \frac{S_{15}S_{56} - S_{16}S_{55}}{d},$$

$$d = \begin{vmatrix} S_{11} & S_{15} & S_{16} \\ S_{15} & S_{55} & S_{56} \\ S_{16} & S_{56} & S_{66} \end{vmatrix}. \tag{3}$$

Substitution of Eq. (2) into Eq. (1) gives the following:

$$\sigma_i = Q_{ij}e_j \quad (i, j = 1, 5, 6) \tag{4}$$

where

$$Q_{ij} = C_{ij} + C_{i\beta}S_{\beta k}\alpha_{kj}, \quad (i, j, k = 1, 5, 6; \beta = 2, 3, 4). \tag{5}$$

Representing the reduced stiffness matrix of a lamina by $\bar{\mathbf{Q}}$ and using the following contractions,

$$\bar{\sigma}_1 = \sigma_1, \quad \bar{\sigma}_2 = \sigma_6, \quad \bar{\sigma}_3 = \sigma_5, \quad \bar{e}_1 = e_1, \quad \bar{e}_2 = e_6, \quad \bar{e}_3 = e_5,$$

$$\bar{Q}_{11} = Q_{11}, \quad \bar{Q}_{12} = Q_{16}, \quad \bar{Q}_{13} = Q_{15}, \quad \bar{Q}_{21} = Q_{61}, \quad \bar{Q}_{23} = Q_{65},$$

$$\bar{Q}_{22} = Q_{66}, \quad \bar{Q}_{31} = Q_{51}, \quad \bar{Q}_{33} = Q_{55}, \quad \bar{Q}_{32} = Q_{56} \tag{6}$$

the generalized Hooke's law for beams may be written as follows:

$$\bar{\sigma}_i = \bar{Q}_{ij}\bar{e}_j, \quad (i, j = 1, 2, 3). \tag{7}$$

Figure 1(*b*) shows the relations between the material axes of elastic symmetry (1′, 2′, 3′) and the beam principal axes (1, 2, 3) for a rotation about the 3-axis. The angle between the fiber direction and the beam axis is denoted by β. Equation (7) is written in the following transformed form (Yıldırım, 1999a):

$$\bar{\sigma}_i = \overline{Q'_{ij}}\bar{e}_j, \quad (i, j = 1, 2, 3) \tag{8}$$

Using Equations (5) and (6) with the transformed stiffness and compliance matrices, $\mathbf{C}'$ and $\mathbf{S}'$, the nonzero terms of $\overline{\mathbf{Q}'}$ for cross-ply laminates are obtained as follows (in Eq. (3) $\alpha_{15} = \alpha_{16} = \alpha_{56} = 0$ and $d = S_{11}S_{55}S_{66}$ for $\beta = 0$ deg and $\beta = 90$ deg):

$$\bar{Q}'_{11} = C'_{11} + (C'_{12}S'_{21} + C'_{13}S'_{31})/S'_{11}, \quad \bar{Q}'_{22} = C'_{66},$$

$$\bar{Q}'_{33} = C'_{55} \tag{9}$$

where

$$m = \cos\beta$$

$$C'_{11} = m^4C_{11} + 2(m^2 - m^4)C_{12} + C_{22}(1 - 2m^2 + m^4) + 4(m^2 - m^4)C_{66}$$

$$C'_{12} = (m^2 - m^4)C_{11} + (m^2 - m^4)C_{22} + C_{12}(1 - 2m^2 + 2m^4) - 4(m^2 - m^4)C_{66}$$

$$C'_{13} = m^2C_{12} + (1 - m^2)C_{23}$$

$$C'_{55} = (1 - m^2)C_{44} + m^2C_{55}$$

$$C'_{66} = (m^2 - m^4)C_{11} - 2(m^2 - m^4)C_{12} + (m^2 - m^4)C_{22} + (1 - 4m^2 + 4m^4)C_{66}$$

$$S'_{11} = m^4S_{11} + 2(m^2 - m^4)S_{12} + S_{22}(1 - 2m^2 + m^4) + (m^2 - m^4)S_{66}$$

$$S'_{12} = (m^2 - m^4)S_{11} + (m^2 - m^4)S_{22} + S_{12}(1 - 2m^2 + 2m^4) + (m^4 - m^2)S_{66}$$

$$S'_{13} = m^2S_{12} + (1 - m^2)S_{23}. \tag{10}$$

In the derivation of Eqs. (10), three-dimensional transformation matrices given by Jones (1975) and Reuter (1971) are used (Yıldırım, 1999a). The elements of $\mathbf{C}'$ and $\mathbf{S}'$ coincide with the elements of elasticity and compliance matrices in the off-axis coordinate system given by Graff and Springer (1991). The Poisson effect can be considered in this way although this effect vanishes for the cross-ply laminates.

2.2 The Governing Equations. Denoting the time by t, the position coordinate by s (Fig. 1(*a*)), the displacement vector of any point on the beam axis by $\mathbf{U}^o(s, t)$, the rotation vector about an axis passing through G by $\mathbf{\Omega}^o(s, t)$, and the relative extension and the relative rotation of the unit length on the beam axis by $\mathbf{e}^o(s, t)$ and $\boldsymbol{\omega}^o(s, t)$ respectively, the geometric compatibility equations are given by the assumption that the relationship between the forces and deformations are small and linear as follows (Yıldırım, 1999a):

$$\mathbf{e}^o = \bar{\mathbf{e}}^o = \frac{\partial \mathbf{U}^o}{\partial s} + \mathbf{t}\mathbf{x}\mathbf{\Omega}^o, \quad \boldsymbol{\omega}^o = \frac{\partial \mathbf{\Omega}^o}{\partial s}. \tag{11}$$

The equation of motion may be written referring to the undeformed configuration as

$$\frac{\partial \mathbf{T}^o}{\partial s} + \mathbf{p}^{ex} = \mathbf{p}^{in}, \quad \frac{\partial \mathbf{M}^o}{\partial s} + \mathbf{t}\mathbf{x}\mathbf{T}^o + \mathbf{m}^{ex} = \mathbf{m}^{in} \tag{12}$$

where $\mathbf{t}$ is the tangential unit vector (Fig. 1). The external distributed load and moment vectors per unit length are denoted by $\mathbf{p}^{ex}(s, t)$ and $\mathbf{m}^{ex}(s, t)$, respectively. These vectors are to be zero for the free vibration analysis. The internal force and moment vectors are represented by $\mathbf{T}^o(s, t)$ and $\mathbf{M}^o(s, t)$. For constant and double symmetric sections, the Frenet ($\mathbf{t}$, $\mathbf{n}$, $\mathbf{b}$) components of the inertia force and moment vectors are given by

$$p_i^{in} = \rho A \frac{\partial^2 U_i^o}{\partial t^2}, \quad m_i^{in} = \rho I_i \frac{\partial^2 \Omega_i^o}{\partial t^2} \quad (i = t, n, b) \tag{13}$$

where ρ is the mass density, A is the cross-sectional area, I_t is the torsional moment of inertia, and I_n and I_b are the inertia moments about the normal, $\mathbf{n}$, and binormal, $\mathbf{b}$, axes.

For a laminated rod with N homogeneous anisotropic layers, the resultant constitutive equations can be obtained as follows (Yıldırım, 1999a):

$$T_i^o = A_{ij}\bar{e}_j^o + B_{ij}\omega_j^o, \quad M_i^o = F_{ij}\bar{e}_j^o + D_{ij}\omega_j^o \quad (i, j = 1, 2, 3) \tag{14}$$

where

$$A_{ij} = \sum_{k=1}^{N} \overline{Q'_{ij}}^{(k)} A^{(k)},$$

$$B_{ij} = F_{ji} = \epsilon_{mjp} \sum_{k=1}^{N} \overline{Q'_{im}}^{(k)} \int_{A^{(k)}} x_p dA,$$

$$D_{ij} = \epsilon_{ihn}\epsilon_{mjp} \sum_{k=1}^{N} \overline{Q'_{nm}}^{(k)} \int_{A^{(k)}} x_p x_h dA \tag{15}$$

and all the indices range from 1 to 3. In Eqs. (15), $x_1 = 0$ for any point of the cross section and

$$\int_A x_2^2 dA = I_b, \quad \int_A x_3^2 dA = I_n. \tag{16}$$

Equations (11), (12), and (14) govern the dynamic behavior of composite space beams. These vectoral equations correspond to 18 scalar equations. However, inverting Eqs. (14) and eliminating $\mathbf{e}^o$ and $\boldsymbol{\omega}^o$ from Eq. (11), the total number of vectoral equations can be reduced to 4. Assuming the harmonic motion, the free vibration equations can be obtained as follows:

$$d\mathbf{U}/ds = \mathbf{A}'\mathbf{T} + \mathbf{B}'\mathbf{M} + \mathbf{\Omega}x\mathbf{t},$$

$$d\mathbf{\Omega}/ds = \mathbf{F}'\mathbf{T} + \mathbf{D}'\mathbf{M},$$

$$d\mathbf{T}/ds = -\rho A\omega^2\mathbf{U},$$

$$d\mathbf{M}/ds + \mathbf{t}x\mathbf{T} = -\rho I_i\omega^2\mathbf{\Omega} \quad (i = t, n, b) \tag{17}$$

where ω (rad/s) is the circular frequency, and

$$\mathbf{A}' = \mathbf{A}^* - \mathbf{B}^*\mathbf{D}^{*-1}\mathbf{F}^*, \quad \mathbf{B}' = \mathbf{B}^*\mathbf{D}^{*-1},$$

$$\mathbf{F}' = -\mathbf{D}^{*-1}\mathbf{F}^*, \quad \mathbf{D}' = \mathbf{D}^{*-1} \tag{18}$$

with

$$\mathbf{A}^* = \mathbf{A}^{-1}, \quad \mathbf{B}^* = -\mathbf{A}^{-1}\mathbf{B},$$

$$\mathbf{F}^* = \mathbf{F}\mathbf{A}^{-1}, \quad \mathbf{D}^* = \mathbf{D} - \mathbf{F}\mathbf{A}^{-1}\mathbf{B}. \tag{19}$$

If the laminates are symmetric then $\mathbf{B}' = \mathbf{F}' = 0$. Referring to Eqs. (17), the following can be obtained in Frenet coordinates for the in-plane free vibration of symmetric laminated composite straight beams (Fig. 1(*c*)).

$$\frac{dU_t}{ds} = A'_{11}T_t = ADE,$$

$$\frac{dU_n}{ds} = \Omega_b + A'_{22}k'T_n = \Omega_b + SDE,$$

$$\frac{d\Omega_b}{ds} = D'_{33}M_b,$$

$$\frac{dT_t}{ds} = -\bar{A}\omega^2U_t,$$

$$\frac{dT_n}{ds} = -\bar{A}\omega^2U_n,$$

$$\frac{dM_b}{ds} = -\bar{I}_3\omega^2\Omega_b - T_n = RIE - T_n \tag{20}$$

Table 1 Comparison of out-of-plane bending and axial natural frequencies $[=\omega L^2(\rho/E_2h^2)^{1/2}]$ of [0°/90°/0°] beams (h/b = 1) (CLT = classical lamination theory, FSDT = first-order shear deformation theory)

	Boundary conditions	L/h	Modes 1	2	3	4
Khedeir and Reddy (1994) (CLT)	Fixed-free	5	6.316	—	—	—
		10	6.310	—	—	—
	Fixed-simple	5	27.142	—	—	—
		10	27.527	—	—	—
	Fixed-fixed	5	39.336	—	—	—
		10	39.931	—	—	—
Khedeir and Reddy (1994) (FSDT)	Fixed-free	5	4.134	—	—	—
		10	5.479	—	—	—
	Fixed-simple	5	9.652	—	—	—
		10	16.335	—	—	—
	Fixed-fixed	5	10.432	—	—	—
		10	19.051	—	—	—
Present (FSDT)	Fixed-free	5	4.133	13.429	25.514	36.429
		10	5.476	22.205	46.095	68.988
	Fixed-simple	5	9.650	20.718	31.748	42.685
		10	16.331	37.811	60.324	82.725
	Fixed-fixed	5	10.431	20.755	31.798	42.687
		10	19.048	38.602	60.740	82.871

where T_t and T_n are the axial and shear forces, M_b is the bending moment respectively. k' is the shear coefficient assumed to be 6/5 for the rectangular section of this study. ADE, SDE, and RIE represent the effects of the axial deformation, shear deformation, and the rotary inertia, respectively. The other terms in Eqs. (20) are as follows:

$$\bar{A} = \sum_{k=1}^{N} \rho^{(k)} A^{(k)}, \quad \bar{I}_3 = \sum_{k=1}^{N} \rho^{(k)} I_b^{(k)},$$

$$A'_{11} = 1/\sum_{k=1}^{N} \bar{Q}'^{(k)}_{11} A^{(k)} = 1/A_{11}$$

$$A'_{22} = 1/\sum_{k=1}^{N} \bar{Q}'^{(k)}_{22} A^{(k)} = 1/A_{22};$$

$$D'_{33} = 1/\sum_{k=1}^{N} (\bar{Q}'^{(k)}_{11} I_b^{(k)}) = 1/D_{33} \tag{21}$$

Equations (17) can be written in matrix form as

$$d\mathbf{Z}/ds = \bar{\mathbf{D}}\mathbf{Z} \tag{22}$$

where $\mathbf{Z}$ is the state vector and $\bar{\mathbf{D}}$ is the dynamic differential matrix. The solution of Eqs. (22) is given by Pestel and Leckie (1963)

$$\mathbf{Z}(s) = \mathbf{F}(s, \omega)\mathbf{Z}(0). \tag{23}$$

Here $\mathbf{F}$ is the overall dynamic transfer matrix. Considering the rotary inertia, axial, and shear deformation effects, it is very difficult to obtain the closed form of $\mathbf{F}$ for dynamic problems of beams. So, it is necessary to use the numerical solution for $\mathbf{F}$. Denoting the unit matrix by $\mathbf{I}$, the standard expression of $\mathbf{F}$ for constant sections is given as (Pestel and Leckie, 1963)

$$\mathbf{F}(s, \omega) = e^{s\bar{\mathbf{D}}} = \mathbf{I} + s\bar{\mathbf{D}} + s^2\bar{\mathbf{D}}^2/2! + s^3\bar{\mathbf{D}}^3/3! + \ldots . \tag{24}$$

The presence of the factorial and power terms in Equation (24) restricts the required number of terms for an accurate solution. In order to able to devise a numerical algorithm which allows the numerious terms in the series, Eq. (24) can be written using the Cayley-Hamilton theorem as follows:

$$\mathbf{F}(s, \omega) = \sum_{k=0}^{p} \Phi_k(s, \omega)\bar{\mathbf{D}}^k. \tag{25}$$

Equation (25) is used to calculate the transfer matrix by the numerical algorithm given by Yıldırım (1996, 1998, 1999b). In Eq. (25), $(p + 1)$ corresponds to the number of equations in canonical form (e.g., p is equal to 5 for this study), and $\Phi_k(s, \omega)$ are functions of scalar infinite series in s and ω. The number of terms considered in the infinite series Φ determines the accuracy of the solution. In this study, 600 terms are taken into account in each Φ series of Eq. (25). Six hundred terms in Eq. (25) correspond to 3600 terms in Eq. (24).

After computation of all Φ functions in an accurate manner, the frequency equation can be obtained from the boundary conditions given at both ends ($s = 0$ and $s = L$) using Eq. (23). The boundary conditions considered in this study are as follows: clamped end: $U_t = U_n = \Omega_b = 0$; hinged end: $U_t = U_n = M_b = 0$; and free end: $T_t = T_n = M_b = 0$. The natural frequency is determined by setting the determinant of the coefficient matrix equal to zero. The frequency equation for fixed-simple ends is as follows:

$$\begin{bmatrix} 0 \\ 0 \\ 0 \end{bmatrix}_{s=L} = \begin{bmatrix} F_{14} & F_{15} & F_{16} \\ F_{24} & F_{25} & F_{26} \\ F_{64} & F_{65} & F_{66} \end{bmatrix}_{s=L} \begin{bmatrix} T_t \\ T_n \\ M_b \end{bmatrix}_{s=0} \tag{26}$$

In this study, all numerical computations are performed using the double-precision arithmetic. The natural frequencies are obtained by the method of searching determinant of the coefficient matrix.

3 Applications

To assess the accuracy of the present results with the reported values an example is solved. Material properties of the beam for this study are: $E_1/E_2 = 40$, $G_{12} = G_{13} = 0.6E_2$, $G_{23} = 0.5E_2$, $\nu_{12} = 0.25$ (Khedeir and Reddy, 1994). Here E_i, G_{ij}, ν_{ij} represent the Young's moduli, shear moduli, and Poisson's ratios for an orthotropic lamina. Table 1 shows the natural frequencies. Khedeir and Reddy's (1994) frequencies in Table 1 are related to the out-of-plane bending and axial oscillations. A good agreement is observed with the literature values. For various thickness/weight (h/b) ratios, purely in-plane (axial + in-plane bending) frequencies of the same beam are obtained and presented in Table 2. As

Table 2 Purely in-plane (in-plane bending and axial) natural frequencies [$=\omega L^2(\rho/E_2h^2)^{1/2}$] of [0°/90°/0°] beams

			Modes			
		L/h	1	2	3	4
h/b = 10	Fixed-free	5	0.52527	3.21119	8.66226	16.1507
		10	0.52684	3.28137	9.09553	17.5699
	Fixed-simple	5	2.25776	7.05205	14.0125	22.6295
		10	2.29924	7.37661	15.1778	25.5016
	Fixed-fixed	5	3.21513	8.45153	15.6689	24.3479
		10	3.31912	9.03105	17.4118	27.2082
h/b = 1	Fixed-free	5	3.85324	13.1300	25.6687	36.9845
		10	4.78485	21.0494	44.9508	68.7084
	Fixed-simple	5	9.57245	20.9267	32.3530	43.6691
		10	15.4562	37.0120	60.1735	83.4215
	Fixed-fixed	5	10.5552	21.0138	32.4296	43.6758
		10	18.5669	38.2898	60.8458	83.7069
h/b = 0.1	Fixed-free	5	5.52498	16.5673	27.7252	38.7042
		10	10.8829	32.6126	55.2156	76.8831
	Fixed-simple	5	11.0747	22.1978	33.3101	41.2747
		10	21.9663	44.2982	66.5530	85.2599
	Fixed-fixed	5	11.1013	22.1980	33.3119	44.4206
		10	22.1676	44.2990	66.5656	88.7913

can be seen from Table 2 that the dimensionless natural frequencies increase with decreasing h/b ratios.

A number of examples are solved to investigate the effects of the rotary inertia, axial, and shear deformations on the natural frequencies of symmetric cross-ply laminated beams. It should be noted that for the Bernoulli-Euler analysis, the effects of the axial deformation has been taken nearly zero instead of exact zero in order to prevent singularity of the characteristic equation's matrix. All layers are assumed to have the same thickness and the beam is assumed to have orthotropic material properties in the material principal axes. The definition of nondimensional frequency is the same as in Tables 1 and 2. The relative error is determined as

$$\text{relative error} = 100(\varpi^T - \varpi^B)/\varpi^T \tag{27}$$

where, ϖ^T and ϖ^B denote Timoshenko's and Bernoulli's frequencies, respectively. Variation of the first six in-plane nondimensional natural frequencies are presented in Figs. 2–4 with varying length/height (L/h) ratios, boundary conditions, and h/b ratios. These figures include the Timoshenko solutions and relative errors for Bernoulli theory. It is observed from the figures that relative errors increase with decreasing L/h ratios, increasing number of modes, decreasing h/b ratios, and with the number of constrains for boundary conditions. The effect of the h/b ratios is more important for the in-plane frequencies. The rotary inertia, shear, and axial deformation effects are also prominent for the L/h = 20 condition. For the fundamental frequencies, while the relative error is −2 percent for the fixed-free beam with L/h = 20 and h/b =

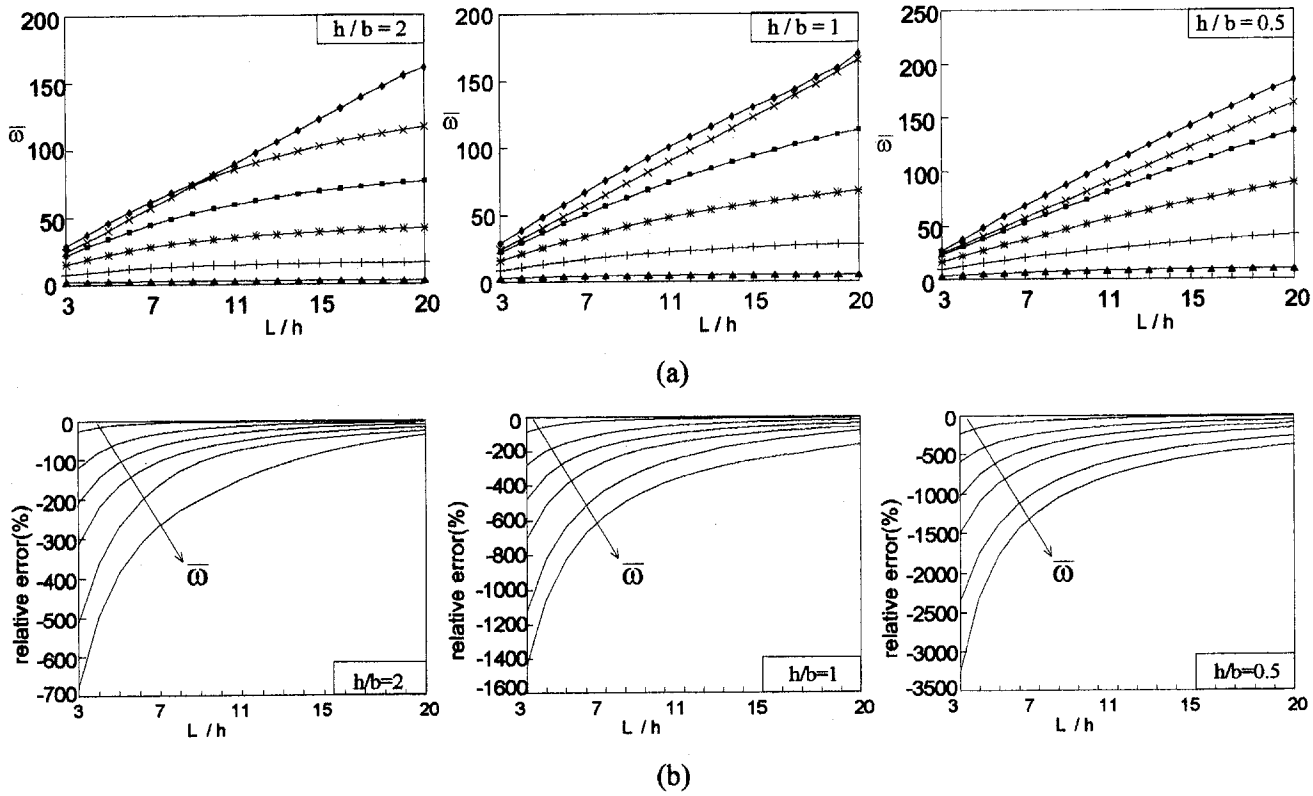

Fig. 2 The first six natural frequencies of (0°/90°0°) fixed-free beam (*a*) Timoshenko's results, (*b*) relative errors for Bernoulli solution

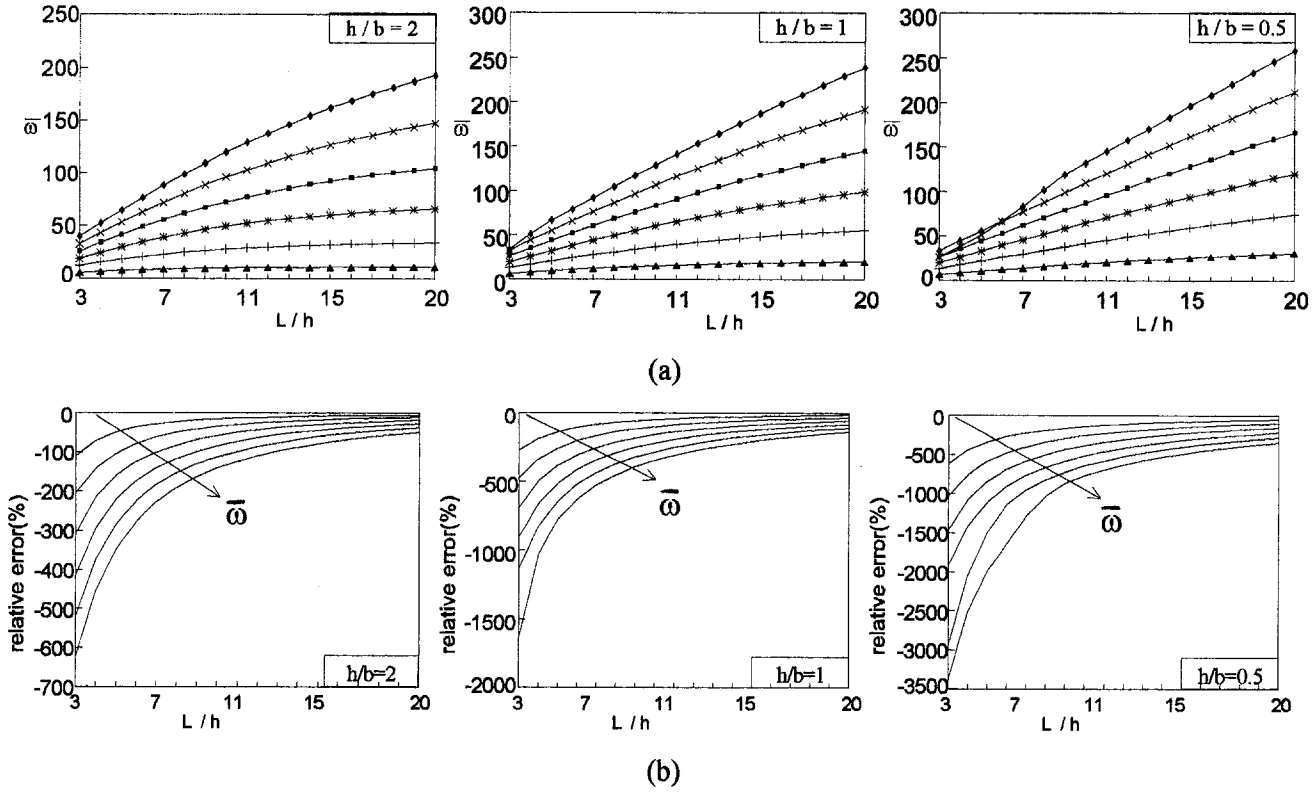

Fig. 3 The first six natural frequencies of (0°/90°0°) fixed-simple beam (*a*) Timoshenko's results, (*b*) relative errors for Bernoulli solution

2, this value reaches −81 percent for the fixed-fixed beam with $L/h = 20$ and $h/b = 0.5$. Figures 2–4 reveal that the dynamic problems of laminated composites must be solved by considering the rotary inertia, axial, and shear deformation effects to obtain realistic solutions.

Table 3 shows the variation of the purely in-plane Timoshenko's

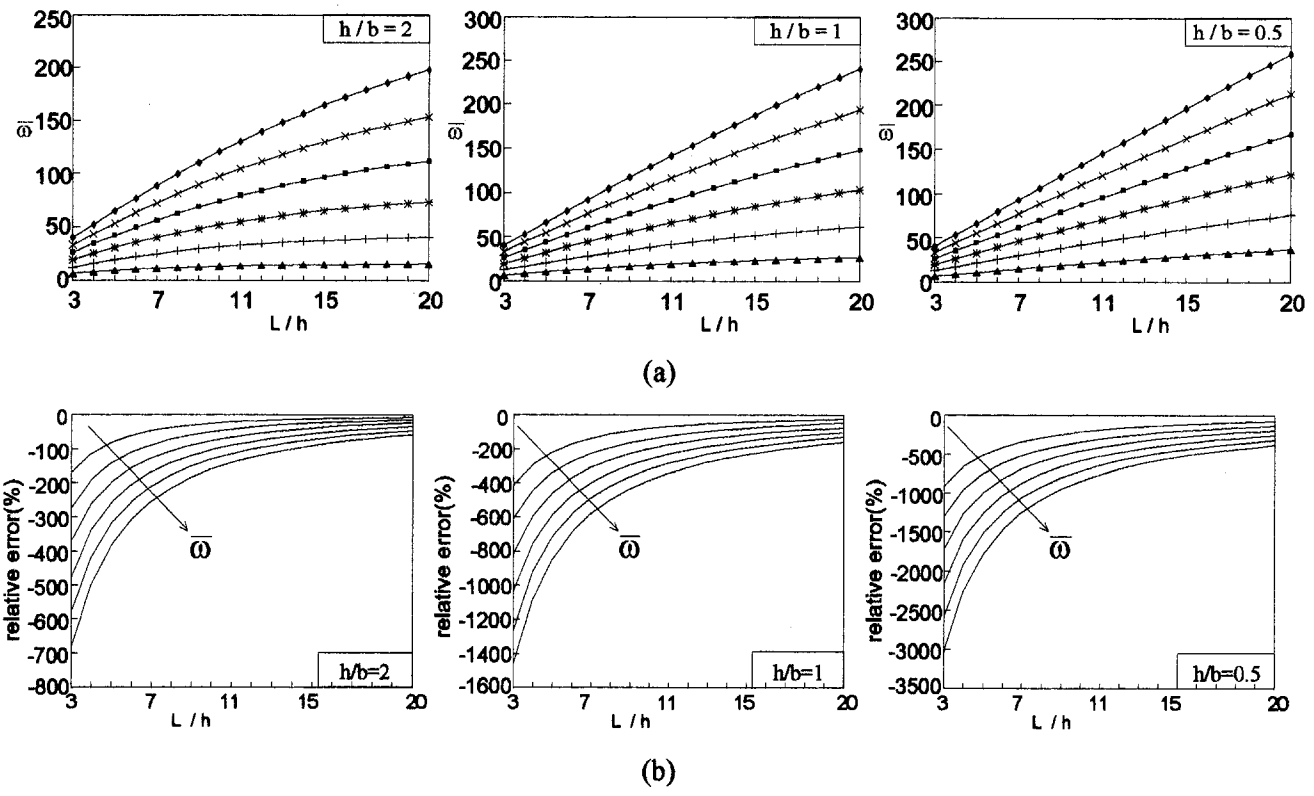

Fig. 4 The first six natural frequencies of (0°/90°0°) fixed-fixed beam (*a*) Timoshenko's results, (*b*) relative errors for Bernoulli solution

Table 3 Variation of the purely in-plane Timoshenko's natural frequencies [$=\omega L^2(\rho/E_2h^2)^{1/2}$] of [0°/90°/0°] beam with the ratio of E_1/E_2 for fixed-fixed ends ($L/h = 5$, $h/b = 1$)

	Modes					
E_1/E_2	1	2	3	4	5	6
1	5.5327	13.117	15.708	22.303	31.416	32.284
	(−17%)*	(−36%)*	(−122%)*	(−159%)*	(−174%)*	(−273%)*
20	10.084	20.222	31.655	42.987	54.348	58.070
	(−137%)*	(−225%)*	(−308%)*	(−396%)*	(−486%)*	(−666%)*
40	10.555	21.014	32.430	43.676	54.933	66.116
	(−218%)*	(−340%)*	(−459%)*	(−586%)*	(−715%)*	(−846%)*

* The relative errors for Bernoulli's results (Eq. (27))

natural frequencies of [0°/90°/0°] beam with the ratio of E_1/E_2 for fixed-fixed ends ($L/h = 5$, $h/b = 1$). As can be expected for anisotropic beams, the relative errors for Bernoulli's solution increases with increasing E_1/E_2 ratios.

Finally, a graphite-epoxy material (AS4/3501-6) ($E_1 = 144.8$ GPa, $E_2 = 9.65$ GPa, $G_{12} = G_{13} = 4.14$ GPa, $G_{23} = 3.45$ GPa, $\rho = 1389.23$ kg/m^3, $\nu_{12} = 0.3$) is chosen to examine the behavior of the beam made of a physical material. Comparison of the first four out-of-plane bending natural frequencies of [0°/90°/90°/0°] graphite-epoxy beam for fixed-fixed ends ($L/h = 10$, $h/b = 1$) with the reported results is given in Table 4. A very good agreement is observed from the table. The purely in-plane and out-of-plane natural frequencies are also presented in Table 5 for Timoshenko and Bernoulli beam theories. The rotary inertia and shear deformation effects are prominent for out-of-plane vibration.

4 Discussions

Resolving Eqs. (17) into Frenet components, the 12 scalar equations can be obtained for the free vibration of symmetric cross-ply laminated beams. For this particular layer sequences and straight beams, these equations can be investigated by dividing them into four groups. This classification can be made as follows referring to the element of the state vector: (1) axial vibration: $\mathbf{Z} = \{U_t, T_t\}^T$, (2) torsional vibration: $\mathbf{Z} = \{\Omega_t, M_t\}^T$, (3) in-plane bending vibration: $\mathbf{Z} = \{U_n, \Omega_b, T_n, M_b\}^T$, (4) out-of-plane bending vibration: $\mathbf{Z} = \{U_b, \Omega_n, T_b, M_n\}^T$. The items (1) and (3) are called as the purely in-plane vibration. The purely out-of-plane vibration is denoted by the items (2) and (4). The axial and torsional free vibration equations can be expressed by an equation with second degree. Similarly, the bending equations can be denoted by a fourth-order equation. For symmetric angle-ply case the classification can be made as the purely in-plane and out-of-plane vibrations. In this case, both $\mathbf{A}'$ and $\mathbf{D}'$ matrices have out-of diagonal elements. For unsymmetric case it is not possible to separate the equations into subgroups.

The transfer matrix method, which reduces the boundary value problem to the initial value problem, is chosen as the solution method in this study. As it is known, this method provides an exact solution to one-dimensional dynamic problems, which can be formulated by distributed or lumped parameter mathematical models, in condition that the overall dynamic transfer matrix, $\mathbf{F}$, is exact. If $\mathbf{F}$ is not computed accurately, some frequencies associated with higher modes can be skipped. The exact solution is obtained by using the distributed parameter model as in this study instead the lumped parameter model as described in Myklestad's method (Pestel and Leckie, 1963). Moreover the method uses minimal computing memory comparing to the other methods such as the finite element procedure for the solution to dynamic problems. A beam supported at two ends can be considered as only one element in the solution. The dimensions of the coefficient matrix is of 6×6 in the case of a space rod supported at its ends. The dynamic problem of beams made of generally orthotropic layers or isotropic material can be solved by the same dimensions. The dimensions of the eigenvalue matrix increase with the number of intermediate supports. The mainly drawback of the transfer matrix method is the determination of the natural frequencies by the method of searching determinant.

The numerical algorithm used in this study allows the exact determination of $\mathbf{F}$ pertaining to symmetric cross-ply laminated beams with constant section. For other cases, the exact overall transfer matrix can be obtained by integration of the equations governing the dynamic behavior of those beams. Computing time for the determination of $\mathbf{F}$ with the present algorithm is considerable less than the integration procedure. This algorithm can also be used for symmetric cross-ply laminated beam supported by elastic foundation.

Table 4 Comparison of the out-of-plane bending natural frequencies [$=\omega L^2(\rho/E_1h^2)^{1/2}$] of [0°/90°/90°/0°] graphite-epoxy beam for fixed-fixed ends ($L/h = 10$, $h/b = 1$)

Modes	Singh and Abdelnaser (1992)	Abramovich and Livshits (1994)	Present
1	3.7751	3.7576	3.6964
2	8.0440	7.8718	7.7529
3	12.998	12.573	12.415
4	18.165	17.373	17.196

Table 5 The purely in-plane and out-of-plane Timoshenko frequencies [$=\omega L^2(\rho/E_1h^2)^{1/2}$] of [0°/90°/90°/0°] graphite-epoxy beam for fixed-fixed ends ($L/h = 10$, $h/b = 1$)

	In-plane		Out-of-plane	
Modes	Timoshenko	Bernoulli	Timoshenko	Bernoulli
1	3.3874	4.7168 (−39%)*	3.6964	6.0703 (−64%)*
2	7.4350	13.002 (−75%)*	7.7529	16.733 (−116%)*
3	12.143	25.489 (−110%)*	12.415	32.803 (−164%)*
4	17.092	42.134 (−147%)*	17.196	54.225 (−215%)*
5	22.140	62.940 (−184%)*	20.326	81.002 (−299%)*
6	22.943	87.909 (−283%)*	22.010	113.135 (−414%)*

* The relative errors for Bernoulli's results (Eq. (27))

5 Conclusions

The in-plane free vibration behavior of symmetric cross-ply laminated composite beams has been studied by the transfer matrix method, which has not been used widely for composite beam analysis. In this formulation, it is possible to isolate the effects of the rotary inertia, transverse shear and axial deformations to study their influence. The overall transfer matrix is obtained by using the effective numerical algorithm, as previously done with isotropic materials. The accuracy of the formulation has been verified with the reported results. It was observed from the comparisons that this formulation offers exact results for the natural frequencies associated with the first and the higher modes. The effects of the rotary inertia, shear, and axial deformations have been investigated by considering L/h, E_1/E_2, and h/b ratios, and different boundary conditions for the first six natural frequencies. It was concluded that these effects must be considered in the free and forced vibration analysis of composite beams.

Acknowledgments

This study was sponsored by the Scientific and Technical Research Council of Turkey (TUBITAK). The first author gratefully acknowledges the TUBITAK.

References

Abramovich, A., 1992, "Shear Deformation and Rotary Inertia Effects of Vibrating Composite Beams," *Composite Structures,* Vol. 20, pp. 165–173.

Abramovich, H., and Livshits, A., 1994, "Free Vibrations of Non-Symmetric Cross-Ply Laminated Composite Beams," *Journal of Sound and Vibration,* Vol. 176, No. 5, pp. 597–612.

Abromovich, H., Eisenberger, M., and Shulepov, O., 1995, "Vibrations of Multispan Non-Symmetrical Composite Beams," *Composites Engineering,* Vol. 5, No. 4, pp. 397–404.

Chandrasekhara, K., Krisnamurthy, K., and Roy, S., 1990, "Free Vibration of Composite Beams Including Rotary Inertia and Shear Deformation," *Composite Structures,* Vol. 14, pp. 269–279.

Chandrashekhara, K., and Bangera, K. M., 1992, "Free Vibration of Composite Beams Using A Refined Shear Flexible Beam Element," *Computers and Structures,* Vol. 43, No. 4, pp. 719–727.

Eisenberger, M., Abramovich, H., and Shulepov, O., 1995, "Dynamic Stiffness Analysis of Laminated Beams Using A First Order Shear Deformation Theory," *Composite Structures,* Vol. 31, pp. 265–271.

Graff, E., and Springer, G. S., 1991, "Stress Analysis of Thick, Curved Composite Laminates," *Computers and Structures,* Vol. 38, No. 1, pp. 41–55.

Hodges, D. H., Atilgan, A. R., Fulton, M. V., and Rehfield, L. W., 1991, "Free-Vibration Analysis of Composite Beams," *Journal of the American Helicopter Society,* Vol. 36, No. 3, pp. 36–47.

Jones, R. M., 1975, *Mechanics of Composite Materials,* Hemisphere, New York.

Kapania, R. K., and Raciti, S., 1989a, "Recent Advances in Analysis of Laminated Beams and Plates, Part II: Vibrations and Wave Propagation," *AIAA Journal,* Vol. 27, pp. 935–946.

Kapania, R. K., and Raciti, S., 1989b, "Non-Linear Vibrations of Unsymmetrically Laminated Beams," *AIAA Journal,* Vol. 27, No. 2, pp. 201–210.

Khedeir, A. A., and Reddy, J. N., 1994, "Free Vibration of Cross-Ply Laminated Beams with Arbitrary Boundary Conditions," *International Journal of Engineering Science,* Vol. 32, No. 12, pp. 1971–1980.

Krishnaswamy, S., Chandrasekhara, K., and Wu, W. Z. B., 1992, "Analytical Solutions to Vibration of Generally Layered Composite Beams," *Journal of Sound and Vibration,* Vol. 159, No. 1, pp. 85–99.

Nabi, M. S., and Ganesan, N., 1994, "Generalized Element for the Free Vibration Analysis of Composite Beams," *Computers and Structures,* Vol. 51, No. 5, pp. 607–610.

Pestel, E. C., and Leckie, F. A., 1963, *Matrix Methods in Elastomechanics,* McGraw-Hill, New York.

Rao, S. M., and Ganesan, N., 1997, "Dynamic Response of Non-Uniform Composite Beams," *Journal of Sound and Vibration,* Vol. 200, No. 5, pp. 563–577.

Reuter, Robert C., Jr., 1971, "Concise Property Transformation Relations for an Anisotropic Lamina," *J. Composite Materials,* Apr., pp. 270–272.

Singh, M. P., and Abdelnaser, A. S., 1992, "Random Response of Symmetric Cross-Ply Composite Beams with Arbitrary Boundary Conditions," *American Institute of Aeronautics and Astronautics Journal,* Vol. 30, No. 4, pp. 1081–1088.

Vinson, J. R., and Sierakowski, R. L., 1986, *Behaviour of Structures Composed of Composite Materials,* Martinus Nijhoff, Dordrecht, The Netherlands.

Yıldırım, V., 1996, "Investigation of Parameters Affecting Free Vibration Frequency of Helical Springs," *International Journal for Numerical Methods in Engineering,* Vol. 39, No. 1, pp. 99–114.

Yıldırım, V., 1998, "A Parametric Study on the Free Vibration of Non-Cylindrical Helical Springs," ASME JOURNAL OF APPLIED MECHANICS, Vol. 65, pp. 157–163.

Yıldırım, V., 1999a, "Governing Equations of Initially Twisted Elastic Space Rods Made of Laminated Composite Materials," *International Journal of Engineering Science,* to be published.

Yıldırım, V., 1999b, "An Efficient Method for Predicting the Natural Frequencies of Cylindrical Helical Springs," *International Journal of Mechanical Sciences,* Vol. 41, pp. 919–939.

Zappe, J. A., and Lesieutre, G. A., 1997, "Vibration Analysis of Laminated Beams Using an Iterative Smeared Laminate Model," *Journal of Sound and Vibration,* Vol. 199, No. 2, pp. 275–284.

On the Initiation and Propagation of Buckles in a Beam on a Nonlinear Foundation

T. A. Netto
Assoc. Mem. ASME

S. Kyriakides
Fellow ASME

X. Ouyang
Assoc. Mem. ASME

Research Center for Mechanics of Solids, Structures & Materials, WRW 110, The University of Texas at Austin, Austin, TX 78712

The model of propagating buckles consisting of a beam on a nonlinear foundation with an up-down-up response developed by Chater et al. (1983) is revisited and used to study the dynamics of propagating buckles. The foundation is altered in order to allow variation of the ratio of the propagation pressure to the collapse pressure within a range that is similar to that seen in typical pipelines. In addition, the pressurizing fluid is modeled as an acoustic fluid. The model is used to study steady-state dynamic propagation of buckles where the fluid properties are shown to play a decisive role on the buckle velocity. The full dynamic problem is also analyzed including the transient dynamic initiation of a buckle in a structure under uniform pressure by a point load. Finally, the critical duration that the point load must have for it to initiate a propagating buckle is studied for a particular example.

1 Introduction

Propagating instabilities is now well established as a class of instabilities which affect certain structures of larger size. Under uniform loading, such structures exhibit instabilities which often start as global but quickly localize to a small section of the structure. At this stage, if the load is reduced below a critical level, the deformation process can be arrested and most of the structure remains intact. If, on the other hand, the load is maintained above this critical level, the local collapse propagates dynamically into the rest of the structure. Kyriakides (1994) reviewed a body of work spanning a period of 15 years on four structures which exhibit such instabilities. Offshore pipelines under external pressure, long circular shell liners of tunnels under external pressure, and long panels under uniform lateral loads all develop localized collapse which can propagate along the length of the structures. The inflation of long rubber-like tubes is similarly affected except that in this case the instability is in the form of a local bulge which tends to spread along the length of the tube. More recently, additional examples of this type behavior have been uncovered in many cases at the micromechanical level of materials such as shape memory metals, cellular materials including honeycombs, some types of wood, and fiber composites in compression.

Although the mechanical details behind each of these instabilities differ from problem to problem, a common underlying feature of all problems in this class is a local *up-down-up* response like the one shown in Fig. 1. In other words, for a range of the pertinent load parameter, the structures have three possible equilibria (Ericksen, 1975). The first ascending brunch represents prebuckling states, the second ascending branch represents buckled states while the negative slope branch joining them represents transitional unstable states. The presence of the limit load in this local response indicates that, if the structure is sufficiently large, following the onset of instability localized deformation will be energetically preferred. The presence of the local minimum in the response indicates that the structure exhibits a mechanism for limiting (arresting) localized deformation.

If the instability is initiated at a constant load, its propagation will be dynamic for all problems in this class. The dynamics of propagating instabilities have received relatively modest attention to date. Chater et al. (1983) developed a nice mechanical model for a propagating instability consisting of an elastic beam on a nonlinear elastic foundation with an up-down-up response. They used the model to study first the quasi-static initiation and propagation of an instability and then the dynamic steady-state propagation. The dynamic version of the problem included the effect of having an incompressible fluid under the foundation which is forced out by the propagating instability. This was an effort to establish the effect of fluid inside a pipeline on the velocity of propagation of buckles. Youn (1991) extended the same model by adding a local zone of higher stiffness to the foundation and used it to mimic the quasi-static engagement of a propagating buckle with a buckle arrestor in an offshore pipeline.

Here we revisit the model and use it to study various aspects of the dynamic initiation and propagation of buckles including the initial transient behavior. Kyriakides and Babcock (1979) showed experimentally that the pressurizing fluid (air or water) outside the pipe plays an important role on the velocity of propagating buckles in empty pipelines (see also Netto and Kyriakides (1999a)). In an effort to capture this effect, the pressurizing fluid is modeled as an acoustic fluid which allows radiation of energy away from the receding beam (this fluid model was used by Song and Tassoulas (1993) to successfully reproduce numerically the steady-state velocities of propagation in Kyriakides and Babcock (1979)).

2 The Quasi-Static Problem

The basic model is the same as in Chater et al. (1983) but with a modified expression for the nonlinear foundation. The model consists of a long, linear elastic beam with a bending rigidity D per unit width. The beam is resting on a nonlinear elastic foundation of stiffness $k(w)$ per unit width and is loaded by a uniform pressure P. The equilibrium equation of the structure is

$$D\frac{d^4w}{dx^4} + k(w)w = P. \tag{1}$$

Contributed by the Applied Mechanics Division of THE AMERICAN SOCIETY OF MECHANICAL ENGINEERS for publication in the ASME JOURNAL OF APPLIED MECHANICS.
Discussion on the paper should be addressed to the Technical Editor, Professor Lewis T. Wheeler, Department of Mechanical Engineering, University of Houston, Houston, TX 77204-4792, and will be accepted until four months after final publication of the paper itself in the ASME JOURNAL OF APPLIED MECHANICS.
Manuscript received by the ASME Applied Mechanics Division, Sept. 9, 1998; final revision, Nov. 20, 1998. Associate Technical Editor: L. T. Wheeler.

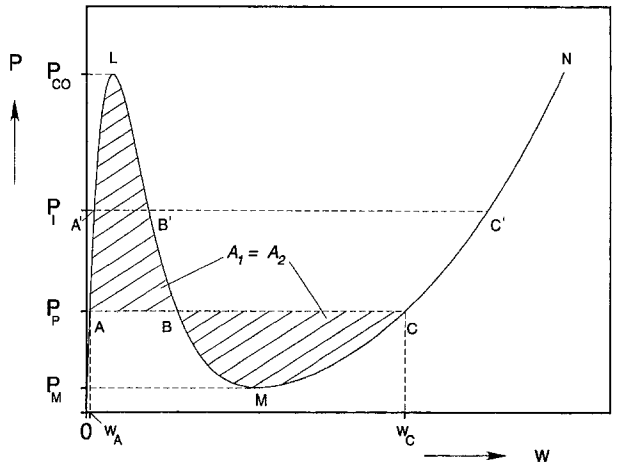

Fig. 1 Pressure-displacement response of foundation and critical pressures (*local* response)

The model's unique characteristics are due to the up-down-up response assigned to the foundation which has the following pressure-displacement relationship:

$$P(w) = k(w)w = k_o[e^{-\bar{a}w} + \bar{b}w^2]w \tag{2a}$$

where k_o, $\bar{a}$, and $\bar{b}$ are constants which will be chosen in ways that introduce some parity between the model and some of the critical parameters of pipelines under external pressure (see Appendix A). It will be convenient to nondimensionalize the displacement by a value of choice w_o; thus, if

$$\omega = \frac{w}{w_o}, \tag{2b}$$

(2*a*) can be written as

$$P(\omega) = k_o w_o \kappa(\omega)\omega = k_o w_o[e^{-a\omega} + b\omega^2]\omega. \tag{2c}$$

The foundation response is shown in Fig. 1. It has the following special characteristics:

(i) $$\left.\frac{dP}{dw}\right|_{w=0} = k_o.$$

(ii) The pressure maximum represents the highest pressure at which small deformation prebuckling states can be sustained and will be called collapse pressure (P_{CO}). For the range of values of the variables a and b that will be used in the calculations that follow, P_{CO} is approximately given by

$$P_{CO} \approx \frac{k_o w_o}{ea}. \tag{4}$$

(iii) The lowest pressure at which "buckled" (w_C) and straight (w_A) configurations can coexist is the equal area pressure of Maxwell (see construction of Fig. 1). This is also the pressure at which a buckle propagates quasi-statically (*propagation pressure* P_p) and is given by

$$P_P = \frac{1}{(w_C - w_A)} \int_{w_A}^{w_C} k(w)w\,dw \tag{5a}$$

or

$$P_P = \frac{k_o w_o}{(\omega_C - \omega_A)a}\left\{-e^{-a\omega_C}\left(\omega_C + \frac{1}{a}\right) + e^{-a\omega_A}\left(\omega_A + \frac{1}{a}\right) + \frac{ab}{4}(\omega_C^4 - \omega_A^4)\right\}. \tag{5b}$$

In the results that follow $a = 40$ while the value of b will be varied in order to generate models with various ratios of the two characteristic pressures (P_P/P_{CO}).

The spatial coordinate x will be nondimensionalized as follows:

$$\xi = \frac{x}{\lambda}, \quad \lambda = \left(\frac{D}{k_o}\right)^{1/4} \tag{6}$$

where λ is proportional to the characteristic wavelength of small amplitude sinusoidal waves that develop in beams on elastic foundations. Using (2*a*) and (6), Eq. (1) can be written as

$$\frac{d^4\omega}{d\xi^4} + \kappa(\omega)\omega = \frac{P}{k_o w_o}. \tag{7}$$

This equation is solved numerically over the domain $0 \le \xi \le l$. $\xi = 0$ is assumed to be a symmetry point and the value of l is chosen large enough for the far end of the beam to remain flat while localized collapse initiates and propagates from the symmetry point. The two-point boundary value problem is expressed in difference form and solved numerically in an incremental fashion using the IMSL package BVPFD routine (see Lentini and Pereyra (1977) and Pereyra (1979)). The pressure is assumed to be one of the unknowns. The solution is characterized by limit load and turning point instabilities thus, initially, the displacement at $\xi = 0$ is prescribed. The resulting boundary conditions are

$$\omega(0) = \omega^*, \quad \omega'(0) = 0, \quad \omega'''(0) = 0,$$
$$\omega'(l) = 0 \quad \text{and} \quad \omega''(l) = 0. \tag{8a}$$

At some stage following the initiation of the instability, $\omega(0)$ stops growing and the volume under the beam becomes the prescribed quantity. Thus, the first of (8*a*) is replaced by

$$v = \int_0^l \omega(\xi)d\xi = v^*. \tag{8b}$$

The pressure-change in volume ($\delta v/v_o$) response for a particular set of problem parameters for which $P_P/P_{CO} = 0.219$ (Case II in Table 1) is shown in Fig. 2(*a*) ($v_o = w_o\lambda l$). A sequence of deformed configurations corresponding to the points marked with solid bullets on the response are shown in Fig. 2(*b*). Initially, as the pressure increases the foundation recedes uniformly and the beam remains flat (configuration ①). The response follows the nonlinearity of the foundation until the pressure maximum is reached. At this stage, with the addition of a small disturbance at $\xi = 0$, the deformation localizes in this neighborhood (② to ⑤). Localization takes place with decreasing pressure and, as a result, away from the localizing zone, the structure unloads. In the present scheme, the foundation is elastic and during unloading its nonlinear response is traced back. For the beam length used (176λ) the volume recovered from the part of the structure that is unloading is much larger than the decrease in volume that takes place in the collapsing part of the structure. The net effect is the formation of a cusp in the response characteristic of problems in this class which are elastic (see Kyriakides and Chang (1991) and Power and Kyriakides (1994)). It should be noted that the details of the cusp are affected by the overall length of the structure while the limit load is sensitive to

Table 1 Model parameters for cases analyzed

Case	$\frac{P_P}{P_{CO}}$	a	b	k_o lbin^{-3} (GNm^{-3})	D lbin (Nm)
I	0.269	40	0.0637	548×10^3 (149)	2500 (282)
II	0.219	40	0.0283	388×10^3 (105)	2500 (282)
III	0.184	40	0.0142	183×10^3 (49.6)	2500 (282)

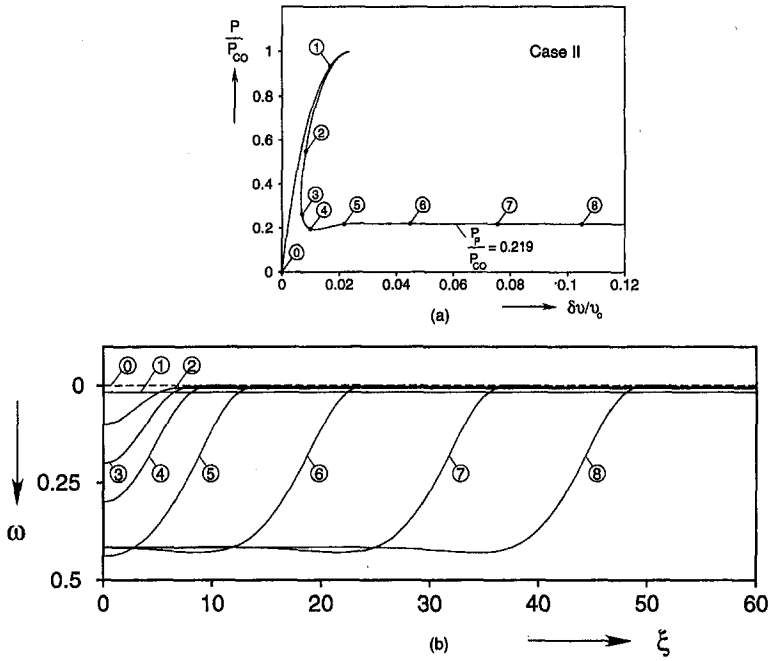

Fig. 2 (*a*) Pressure-displaced volume response during quasi-static buckle initiation and propagation, (*b*) corresponding sequence of beam deformed configurations

small geometric imperfections. The effect of small imperfections on the propagation of the buckle is small and, as a result, we will limit attention to the behavior of the perfect structure.

By configuration ⑤ the local downward displacement of the beam is arrested and the buckle starts to propagate along the length of the beam. Steady state is achieved soon after configuration ⑤ as indicated by the pressure plateau that develops in the response at the level of P_P. Beyond this point, the buckle profile connecting the straight part of the beam with the collapsed section propagates unchanged from left to right as seen in configurations ⑥ to ⑧.

As pointed out above, in this model the two characteristic pressures (P_P and P_{CO}) are strictly determined by the response assigned to the foundation. The beam bending rigidity plays a role in the determination of the length of the profile of the buckle (Chater et al., 1983). In the present example the profile length is approximately 16λ.

Additional calculations were performed for the same beam but for different values of b and k_o listed in Table 1 so that the ratio of P_P/P_{CO} attains values of 0.269 (Case I) and 0.184 (Case III) as shown in Fig. 3(*a*). The pressure change in volume responses calculated for these cases are shown in Fig. 3(*b*). They have the same general characteristics as the response shown above but they terminate into different pressure plateaus.

Figure 4(*a*) shows a comparison of the steady-state buckle profiles for the three cases. For the parameters used the normalized profile lengths are similar: 15λ, 16λ, and 17λ, respectively, for Cases I, II, and III despite the difference in the maximum deflection (w_C) achieved in each case. Indeed, the three profiles become nearly coincident when ω is normalized by ω_C as shown in Fig. 4(*b*).

3 Dynamic Problem

We now consider the dynamic version of the problem. The beam has density ρ and is pressurized by an acoustic fluid with density ρ_f and speed of sound of c_f. The simplest method of incorporating the effect of the local change in pressure due to radiation of energy away from the receding surface of the beam is to assume that a plane wave is emanating from every point on the beam producing a pressure change given by

$$\Delta P = c_f \rho_f v \tag{9}$$

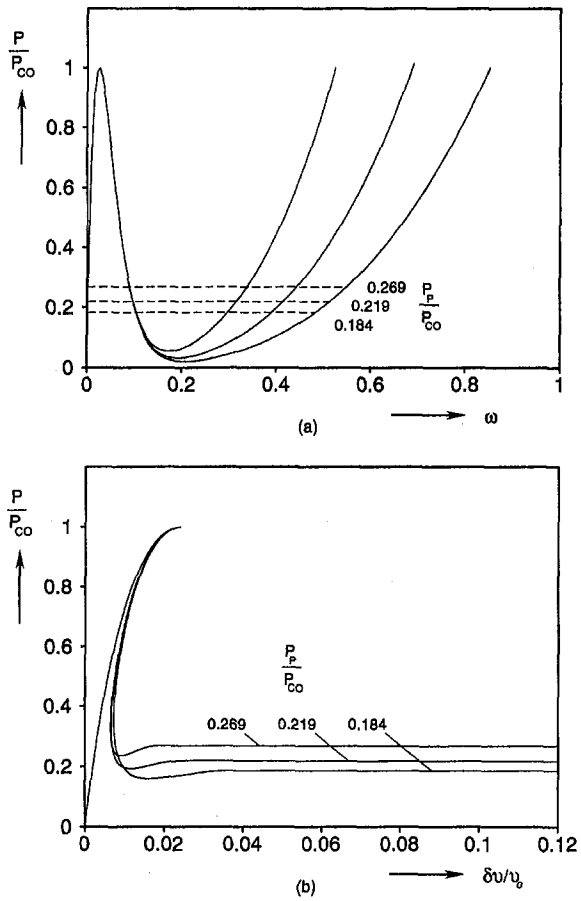

Fig. 3 (*a*) Local pressure-deflection responses for three different foundations, (*b*) corresponding quasi-static pressure-displaced volume responses

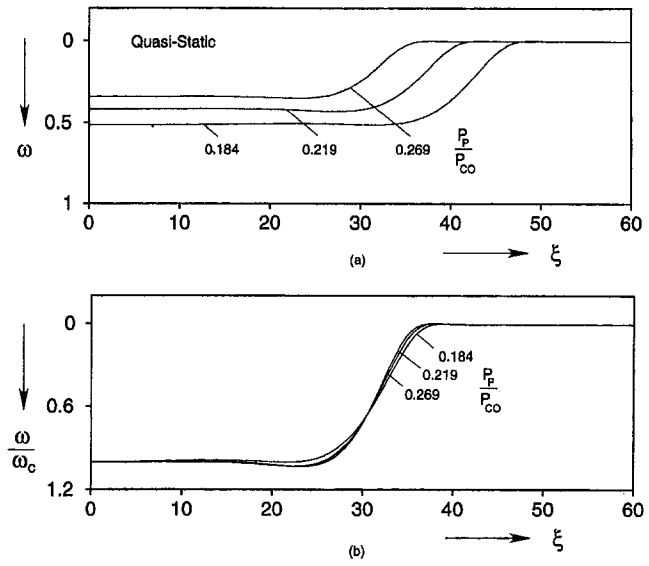

Fig. 4 (*a*) Steady-state quasi-static profiles for Cases I, II, and III and (*b*) normalized counterparts

where v is the outward normal component of the velocity of the beam surface. Incorporating the assumption that the beam slope is small at all times

$$v \approx -\frac{\partial w}{\partial t} \quad \text{and} \quad \Delta P = -c_f \rho_f \frac{\partial w}{\partial t}. \tag{10}$$

Thus, the equation of motion of the beam becomes

$$D\frac{\partial^4 w}{\partial x^4} + k(w)w + \rho h \frac{\partial^2 w}{\partial t^2} = P - \rho_f c_f \frac{\partial w}{\partial t} \tag{11}$$

in which the fluid is seen to play the role of damping to the motion (ρ is the density of the beam and h is its thickness).

(a) Steady-State Buckle Propagation. We first consider a buckle which has been initiated at a pressure $P_I > P_P$, has reached a steady-state condition, and is traveling at a constant velocity U as shown in Fig. 5. This enables the usual transformation of

$$X = x - Ut. \tag{12}$$

If simultaneously we nondimensionalize the variables with λ and w_o, Eq. (11) can be written as follows:

$$\frac{d^4\omega}{d\Xi^4} + \left(\frac{\rho h U^2}{k_o \lambda^2}\right)\frac{d^2\omega}{d\Xi^2} + \left(\frac{\rho_f c_f U}{k_o \lambda}\right)\frac{d\omega}{d\Xi} + \kappa(\omega)\omega = \frac{P}{k_o w_o}, \qquad \Xi = \frac{X}{\lambda}. \tag{13}$$

The fluid parameters are chosen to correspond to those of water ($\rho_f c_f \equiv \rho_w c_w$). The domain is $0 \le \Xi \le l$ and boundary conditions (8) still hold. The two-point boundary value problem is again expressed in difference form and is solved with the BVPFD solver. The velocity is prescribed and the pressure is evaluated from the solution. The solution represents a buckled configuration in steady-state propagation. The buckle profile can occur anywhere in the domain and thus the solution is nonunique. This difficulty is overcome by prescribing the volume displaced by the beam. Initially, the solution yields a fictitious $P - \delta v$ response but after several increments P remains constant as δv is increased further indicating that a steady-state solution has been reached. The value of the buckle velocity is then increased and the process is repeated.

Figure 6(a) shows plots of buckle velocity as a function of the initiation pressure for the three structures analyzed earlier. In each case solutions are obtained for $P_P < P_I < P_{CO}$ (the collapse pressure of each case is indicated on the abscissa). The velocity is normalized by the critical velocity of the structure given by

$$U_C = \left[\frac{4k_o D}{(\rho h)^2}\right]^{1/4} \tag{14}$$

based on the spring stiffness at small deflections. (Kenney (1954) showed that for a point load traveling at a constant velocity U on a beam resting on a foundation with constant stiffness, when $U > U_C$ the deformation downstream of the load gets progressively smaller as the velocity is increased; a phenomenon akin to supersonic events in fluids.) The velocity varies somewhat nonlinearly with pressure although the nonlinearity is different from that exhibited by the velocity of buckles in pipelines (Kyriakides and Babcock, 1979). As expected, the velocity at a given value of P_I/P_{CO} becomes higher as the stiffness of the structure increases.

Figure 6(b) shows a comparison of the buckle profiles for Case II at the propagation pressure and at $P_I/P_P = 3.414$ when the steady-state velocity is $0.0687U_C$. The buckle is deeper due to the higher pressure but the slope of the transition region does not change very much by dynamics. This conclusion was found to hold for all cases examined.

As is obvious from Eq. (11), the fluid as modeled plays the role of damping. This has several consequences. For example, for a beam on a foundation of constant stiffness k, the damping becomes critical when it reaches the level of $2\sqrt{\rho h k}$. In the case of steady-state propagation of a disturbance, this critical damping increases to some degree with the velocity (see Eq. (18) of Kenney (1954)). In the present problem, exact derivation of the critical value of damping is difficult due to the nonlinearity. However, a conservative procedure is to require that

$$\rho_f c_f < 2\sqrt{\rho h k} \tag{15}$$

with k being the slope of the foundation stiffness on the second ascending branch corresponding to the pressure at which the buckle is propagating. In the course of this study, the properties of the fluid, the beam and the foundation were varied and it was confirmed that in some cases where (15) was violated no solution could be found.

The velocity of propagation is strongly dependent on the fluid properties. Figure 7 shows the velocity for the structure with $P_P/P_{CO} = 0.219$ but with fictitious fluids with a $\rho_f c_f = \mu(\rho_w c_w)$ ($\mu = 0.045$, 0.45 and 1). As μ becomes smaller the velocity increases. Kyriakides and Babcock (1979) (see also Netto and Kyriakides (1999a)) reported that pipe buckle velocities in experiments in which air was the pressurizing medium were significantly higher than the buckle velocities measured at the same pressures when water was the pressurizing fluid. However, in that problem other dissipation mechanisms also play a role in the determination of the velocity of the buckle and the difference is not

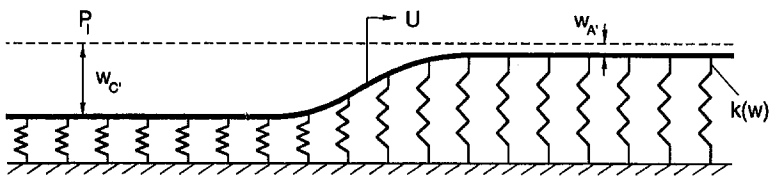

Fig. 5 Schematic of steady-state dynamic buckle propagation

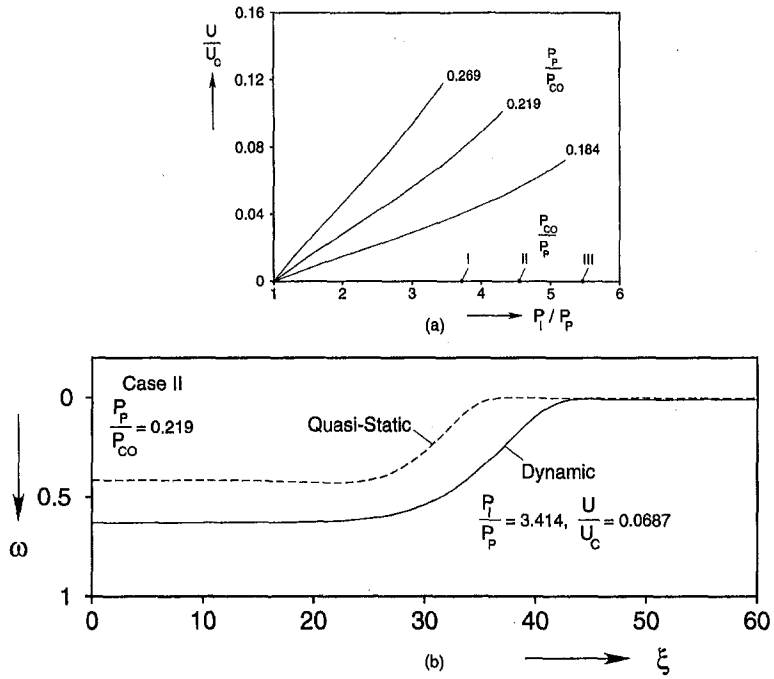

Fig. 6 (*a*) **Buckle velocity as a function of pressure for the three cases,** (*b*) **comparison between steady-state quasi-static and dynamic profiles (Case II)**

as large as in the present problem. It is interesting to note that in the extreme case when the fluid is removed ($\rho_f c_f = 0$) the velocity ceases to depend on the pressure (as observed by Chater et al. (1983)).

(b) The Transient Problem. We now consider the transient initiation and propagation of a buckle in the same structure. Consider the same beam and foundation under a uniform pressure $P > P_P$. The fluid properties used are $\rho_f c_f = \rho_w c_w$. The initiation of propagating buckles is a complex subject deserving special attention. Here, we choose to initiate it with a line force $F(t)$ per unit width applied at $x = 0$ as shown in Fig. 8. Thus, the equation of motion becomes

$$D\frac{\partial^4 w}{\partial x^4} + k(w)w + \rho h\frac{\partial^2 w}{\partial t^2} = P - \rho_f c_f\frac{\partial w}{\partial t}. \tag{16}$$

The line load will have amplitude F and duration T sufficient to initiate the buckle (the sufficiency of these will be discussed further in the next section). Thus,

$$F(t) = \begin{cases} 0, & t < 0 \\ F, & 0 < t < T \\ 0, & t > 0. \end{cases} \tag{17}$$

The variables w_o and x will be normalized as in (2*b*) and (6) while time will be normalized by

$$\tau = \frac{t}{t_o}, \quad t_o = \sqrt{\frac{\rho h}{k_o}} \tag{18}$$

where t_o is proportional to the period of a small deflection wave traveling at the critical velocity defined in (14). Equation (16) can then be written as

$$\frac{\partial^4 \omega}{\partial \xi^4} + \kappa(\omega)\omega + \frac{\partial^2 \omega}{\partial \tau^2} = \frac{P}{k_o w_o} - \frac{\rho_f c_f}{\sqrt{k_o \rho h}}\frac{\partial \omega}{\partial \tau}. \tag{19}$$

The boundary conditions are

$$\omega'(0, \tau) = 0, \quad \omega'(l, \tau) = 0, \quad \omega''(l, \tau) = 0 \quad \forall\, \tau$$

and

$$\omega'''(0, \tau) = \begin{cases} F/\lambda k_o w_o, & 0 < \tau < T/t_o, \\ 0, & \tau > T/t_o \end{cases} \tag{20}$$

where $\omega' \equiv \partial\omega/\partial\xi$.

Equation (19) with boundary conditions (20) are integrated using the implicit integration scheme described in Appendix B. The velocity and acceleration at time $\tau + \Delta\tau$ are evaluated in terms of $\omega(\xi)|_{\tau+\Delta\tau}$ and the solution at τ. The two-point BVP for $\tau + \Delta\tau$

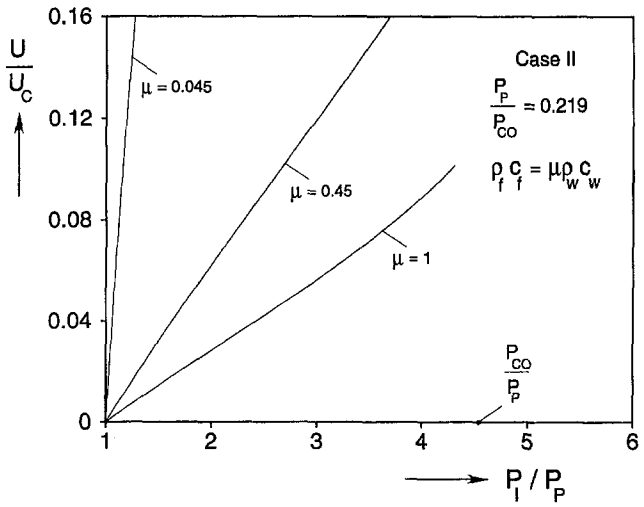

Fig. 7 Influence of the fluid properties on buckle velocity (Case II)

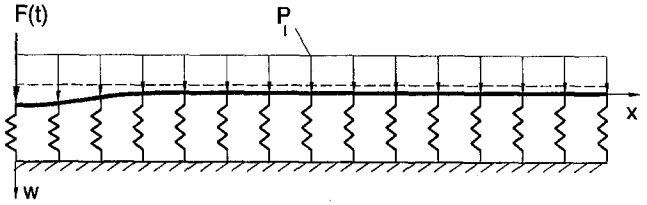

Fig. 8 Schematic of buckle initiation by a point force

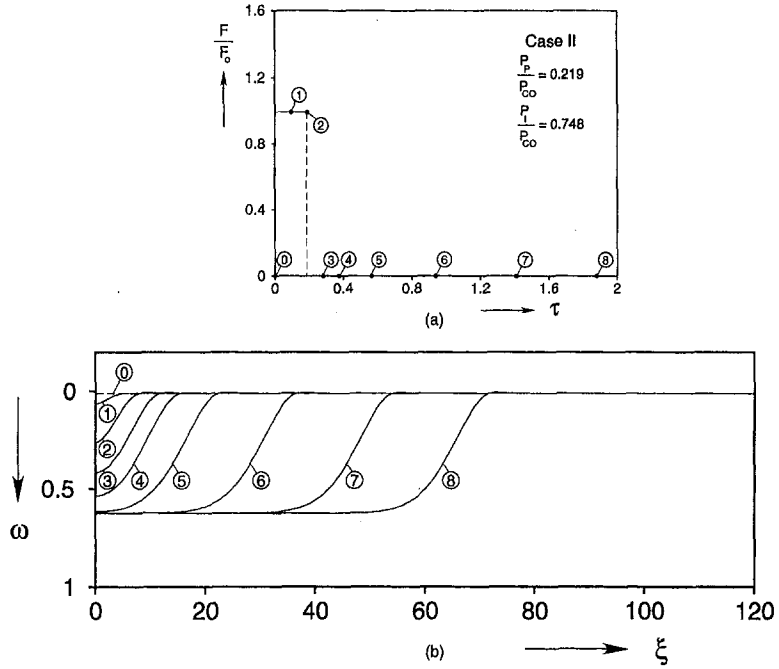

Fig. 9 (*a*) Point force as a function of time, (*b*) beam deformed configurations during the transient initiation of a buckle followed by steady-state dynamic propagation

is then solved using the BVPFD solver. The process is repeated successively producing the solution as a function of time. Time increments of the order of $0.002t_o$ were used at the initiation stage of the calculation but were increased by a factor of 10 as steady-state propagation was reached.

Results from a transient analysis involving Case II are shown in Figs. 9 and 10. The pressure is at a level of $0.748P_{CO}$. The amplitude of the force is $F = 0.99F_o$ per unit width where $F_o = \lambda P_{CO}$ and its duration is $T = 0.188t_o$ (Fig. 9(*a*)). This duration is almost double the minimum duration required (critical value) to initiate the buckle at this amplitude of F. Figure 9(*b*) shows a sequence of calculated deformed configurations. A more dense set of configurations appear in the ξ–τ–ω diagram in Fig. 10. The numbered configurations correspond to the times marked in Fig. 9(*a*).

The pressure is applied first so in configuration ⓪ the beam is straight but uniformly displaced (corresponds to $w_{A'}$ in Fig. 1). On the application of the force at the origin, the beam starts to deflect locally as seen in ①. By the time the load pulse terminates, the beam has deflected sufficiently for the buckle to be initiated. Localized deformation continues to take place driven by the pressure alone. By configuration ⑤, the downward motion at $\xi = 0$ terminates (at $w_{C'}$ in Fig. 1), the buckle profile is fully developed and starts to propagate along the length of the beam in a steady-state manner. The time taken for the buckle to get fully developed is $0.564t_o$. The steady-state nature of the propagation is clearly illustrated in Fig. 10 where the upper ridge of each buckled configuration is seen to fall on a straight line in the ξ–τ plane the slope of which represents the velocity of propagation. The steady-state velocity is $0.0687U_C$ which is the same as the value corre-

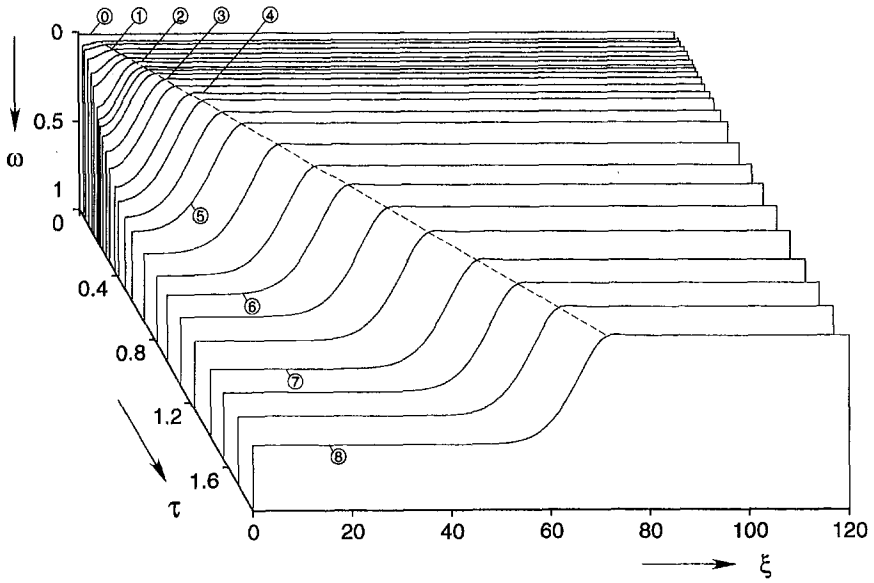

Fig. 10 ξ–τ–ω diagram showing the buckle history

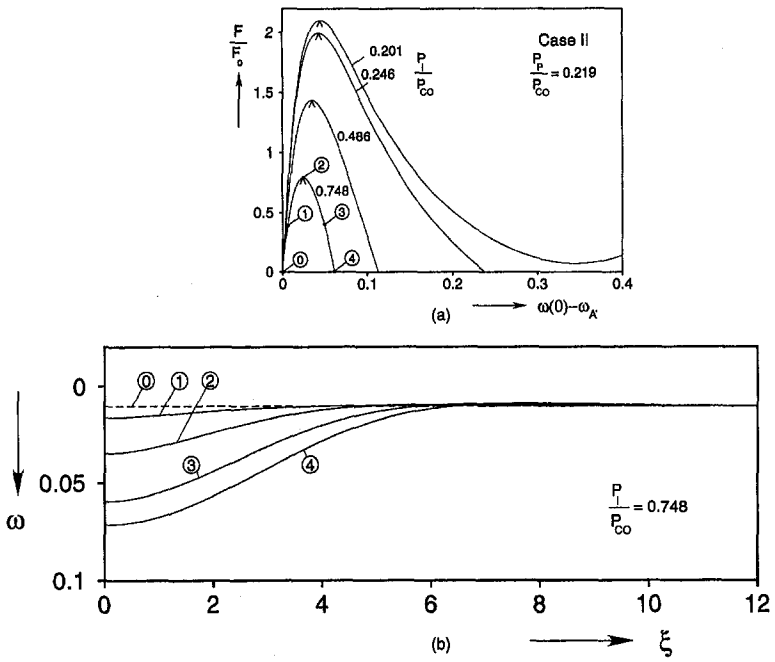

Fig. 11 (*a*) **Force versus displacement at $\xi = 0$ for quasi-static case, (*b*) corresponding beam deformed configurations for $P_l/P_{CO} = 0.748$ (Case II)**

sponding to this pressure in Fig. 6(*a*). The steady-state buckle profile is also the same as that in Fig. 6(*b*).

An interesting feature of the results in Fig. 10 is that the ridge of the deflecting beam is traveling at the steady-state velocity even at the early stages of the deformation history when the buckle is not fully developed. This is different from dynamic propagation of buckles in pipes where during their initiation buckles take time to accelerate to the steady-state velocity. Another difference is that here the buckle profile does not undergo the initial sharpening reported in Netto and Kyriakides (1999b).

(c) Dynamic Initiation of Buckles by a Point Force. The issue of the critical combination of the line force amplitude F and its duration T in order for them to initiate a propagating buckle in the model structure at a given pressure $P > P_P$ is considered next (for a general expose of dynamic buckling see Simitses (1990)). First we examine the quasi-static version of the problem in which we calculate the beam response to the point load at particular pressure levels. Equation (7) is solved with boundary conditions (8*a*) (without $\omega'''(0) = 0$) and ω^* being prescribed incrementally. Figure 11(*a*) shows plots of the force as a function of the displacement at $\xi = 0$ at pressure levels of $P_l/P_{CO} = 0.748$, 0.486, 0.246, and 0.201. In all cases the force-displacement response exhibits a limit load. For the three higher pressures, the force decays down to zero level indicating that the pressure takes over and causes the deformation to grow and propagate. For $P_l/P_{CO} = 0.748$ this is demonstrated in the deformed beam configurations shown in Fig. 11(*b*) (correspond to the force levels marked in Fig. 11(*a*)). The lowest pressure considered ($P_l/P_{CO} = 0.201$) is below the propagation pressure, and so although the beam initially undergoes localized collapse the pressure is not high enough to propagate the buckle and the force is seen to recover after reaching a local minimum. Figure 12 shows the maximum level reached by the line force as a function of the pressure (designated as F_S). Included in the same figure is the displacement at the origin corresponding to F_S. The two quantities monotonically decrease as the pressure increases. As expected, the force drops to zero level when $P_l = P_{CO}$.

We now return to the transient problem and seek to evaluate the shortest duration that a given load amplitude must be applied for it to initiate a propagating buckle at a particular pressure level. This is called critical duration and is designated as

$$\tau_C = T_C/t_o. \tag{21}$$

The sequence of events associated with the initiation of a buckle was demonstrated in Figs. 9 and 10. The line load is applied long enough to destabilize the structure sufficiently so that upon its removal the buckle keeps growing and eventually propagates. For contrast, Fig. 13 shows a similar calculation at the same pressure and force levels in which the duration of the load pulse was not sufficiently long ($T/t_o = 0.094$). Upon the termination of the pulse the beam rebounds (dashed lines in Fig. 13(*b*)) and a buckle is not initiated. The critical pulse duration for $F/F_o = 0.99$ was determined by successive calculations to be $\tau_C = 0.105$.

The critical times of load pulses of various amplitudes were evaluated in this fashion for pressure levels of $P_l/P_{CO} = 0.748$ and 0.486 for Case II. The results are summarized in Fig. 14. For long duration pulses, the force levels are the same as the values calculated in the quasi-static calculations (F_s). As the pulse duration decreases the force amplitude required to initiate a buckle increases significantly. Interestingly, the results for the two pressure levels scale with the static force level.

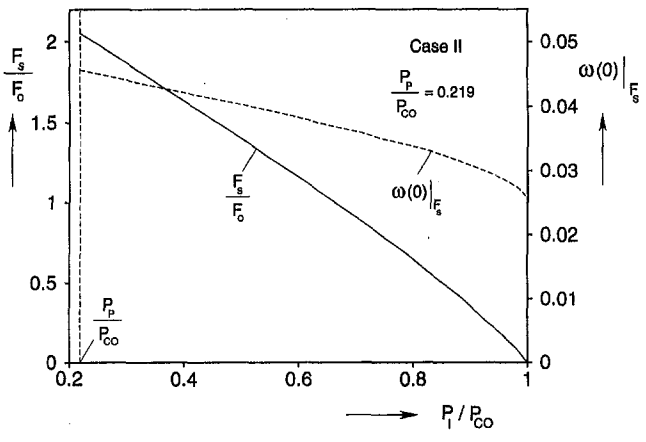

Fig. 12 Maximum concentrated load and corresponding displacement at $\xi = 0$ as a function the applied pressure

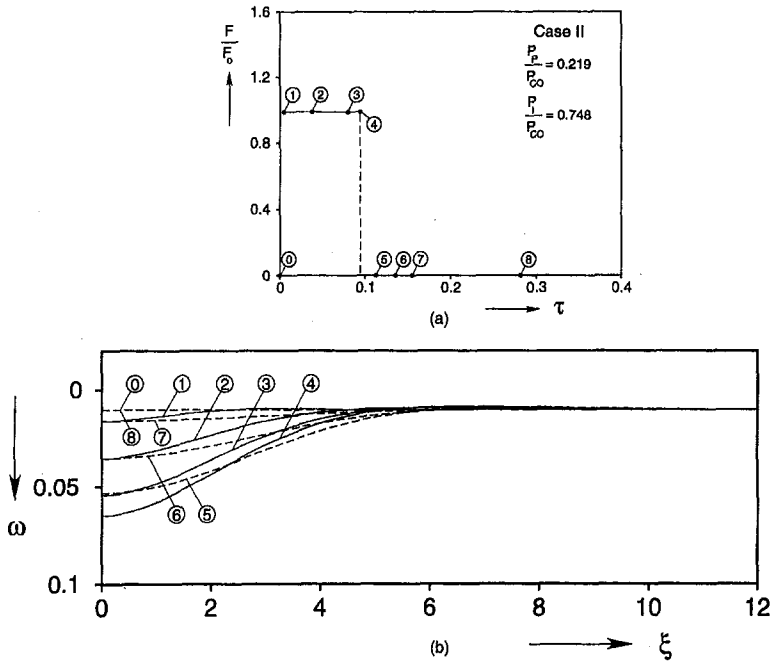

Fig. 13 (*a*) Point force as a function of time, (*b*) beam deformed configurations for case which the applied load failed to initiate a propagating buckle at $P_I/P_{CO} = 0.748$

Conclusions

The beam on a nonlinear foundation model of Chater et al. (1983) has been revisited. The expression for the up-down-up foundation response has been modified somewhat in order to enable calibration of the model to parameters of actual pipes. The effect of the pressurizing fluid has been added by approximating it as an acoustic fluid. The model has been used to establish the steady-state and transient dynamic propagation of the buckle as a function of pressure. The velocity of propagation depends mainly on the fluid properties. This dependence is more extreme than that in pipes because the model does not possess the other energy dissipation mechanisms of the actual structures. In the transient analysis, the buckle was found to start propagating at the steady-state velocity much earlier than in the actual problem. The dynamic initiation of buckles in the model by a point force has been examined and the minimum time that the force must be applied for the buckle to be initiated has been quantified.

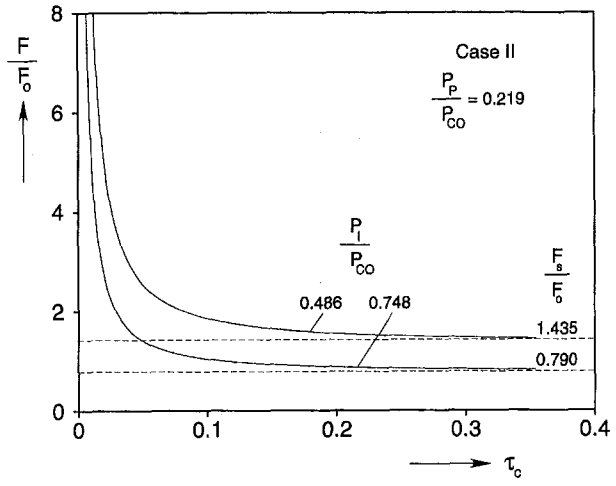

Fig. 14 Point force amplitude as a function of the duration required for buckle to be initiated

Acknowledgments

The work reported here was conducted with support from the University of Texas at Austin. The work of TAN was also sponsored by CNPq-Brazil. Any findings, conclusions and recommendations expressed herein are those of the authors and do not necessarily reflect those of the sponsors.

References

Chater, E., Hutchinson, J. W., and Neale, K. W., 1983, "Buckle propagation on a beam on a nonlinear elastic foundation," *Proc. IUTAM Symposium Collapse: The Buckling of Structures in Theory and Practice,* J. M. T. Thompson and G. W. Hunt, eds, Cambridge University Press, Cambridge, UK, pp. 31–41.

Dyau, J.-Y., and Kyriakides, S., 1993a, "On the localization of collapse in cylindrical shells under external pressure," *Int'l J. Solids & Structures,* Vol. 30, pp. 463–482.

Dyau, J.-Y., and Kyriakides, S., 1993b, "On the propagation pressure of long cylindrical shells under external pressure," *Int'l J. Mechanical Sciences,* Vol. 35, pp. 675–713.

Ericksen, J. L., 1975, "Equilibrium of Bars," *J. Elasticity,* Vol. 5, pp. 191–201.

Kenney, J. T., 1954, "Steady-State Vibration on Beam on Elastic Foundation for Moving Loads," ASME JOURNAL OF APPLIED MECHANICS, Vol. 76, pp. 359–364.

Kyriakides, S., 1994, "Propagating instabilities in structures," *Advances in Applied Mechanics,* Vol. 30, J. W. Hutchinson and T. Y. Wu, eds., Academic Press, Boston, pp. 67–189.

Kyriakides, S., and Babcock, C. D., 1979, "On the dynamics and the arrest of the propagating buckle in offshore pipelines," *Proc. Offshore Technology Conference,* Houston TX, OTC Paper 3479, pp. 1035–1045.

Kyriakides, S., and Chang, Y.-C., 1991, "The initiation and propagation of a localized instability in an inflated elastic tube," *Int'l J. Solids & Structures,* Vol. 27, pp. 1085–1111.

Lentini, M., and Pereyra, V., 1977, "An adaptive finite difference solver for nonlinear two-point boundary value problems with mild boundary conditions," *SIAM J. Numerical Analysis,* Vol. 14, pp. 91–111.

Netto, T. A., and Kyriakides, S., 1999a, "Dynamic performance of integral buckle arrestors for offshore pipelines. Part I Experiments," *Int'l J. Mechanical Sciences,* to appear.

Netto, T. A., and Kyriakides, S., 1999b, "Dynamic performance of integral buckle arrestors for offshore pipelines. Part II Analysis," *Int'l J. Mechanical Sciences,* to appear.

Newmark, N. M., 1959, "A method of computation for structural dynamics," *ASCE J. Eng. Mech. Div.,* Vol. 85, pp. 67–94.

Pereyra, V., 1979, "PASVAC3: An adaptive finite difference FORTRAN program for first order nonlinear ordinary boundary problems," *Codes for Boundary Value Problems in ODEs,* Proc. of a Working Conference, Houston, TX, May 1978, B. Childs, M. Scott, J. W. Daniel, E. Denman and P. Nelson, eds., Springer-Verlag, New York, pp. 67–88.

Power, T. L., and Kyriakides, S., 1994, "Localization and Propagation of Instabilities in Long Shallow Panels Under External Pressure," ASME JOURNAL OF APPLIED MECHANICS, Vol. 61, pp. 755–763.

Simitses, G. J., 1990, *Dynamic Stability of Suddenly Loaded Structures*, Springer-Verlag, New York.

Song, H.-W., and Tassoulas, J. L., 1993, "Finite element analysis of propagating buckles," *Int'l J. Numerical Methods in Engineering*, Vol. 36, pp. 3529–3552.

Youn, S.-K., 1991, "Study of buckle propagation and its arrest on a beam on a nonlinear elastic foundation using finite element method," *Computers & Structures*, Vol. 39, pp. 381–386.

APPENDIX A

Some parity between propagating buckles in pipes and in the present model can be achieved by selecting the model variables so that some of the critical quantities are matched. In Table A1 we list calculated values of collapse and propagation pressures for three representative steel pipes with the material properties of a typical steel (Young's modulus $E = 30$ msi, Poisson's ratio $\nu = 0.3$, yield stress $\sigma_o = 45$ ksi, and hardening exponent $n = 13$; for details on how these are calculated see Dyau and Kyriakides (1993a, b)). The model parameters corresponding to each case (Table 1) were selected as follows. Equation (4) with $w_o = 1$ and $a = 40$ is used to choose k_o so that the values of P_{CO} are matched to those in Table A1. The value of b in Eq. (2*c*) was then selected through an iterative process so that the model propagation pressure (5*b*) matches that of the pipes. The beam thickness was selected to be $h = 0.1$ in (2.54 mm) as this yielded buckle profile lengths (l/ω_C) which were of the same order as those of the pipes (at P_P). The beam density was made equal to that of steel and apart from the cases specified the pressurizing fluid was water.

Table A1 Pipe parameters for three example cases analyzed

Case	$\frac{D}{t}$	P_{CO} psi (bar)	P_P psi (bar)	$\frac{P_P}{P_{CO}}$
I	17.5	5043 (347.8)	1357 (93.6)	0.269
II	21.88	3565 (248.9)	782 (53.9)	0.219
III	31.82	1679 (115.8)	310 (21.4)	0.184

APPENDIX B

The equation of motion of the structure (19) is solved using the implicit integration numerical scheme described below. Assume that the solution $\omega(\xi, \tau)$ is known for $0 \le \xi \le l$. At time $\tau + \Delta\tau$ (19) is

$$\left.\frac{\partial^4 \omega}{\partial \xi^4}\right|_{\tau+\Delta\tau} + k(\omega)\omega|_{\tau+\Delta\tau} + \left.\frac{\partial^2 \omega}{\partial \tau^2}\right|_{\tau+\Delta\tau} = \frac{P}{k_o w_o} - \frac{\rho_f c_f}{\sqrt{k_o \rho h}} \left.\frac{\partial \omega}{\partial \tau}\right|_{\tau+\Delta\tau}. \tag{B1}$$

The time derivatives in (B1) are estimated as follows (Newmark, 1959):

$$\omega|_{\tau+\Delta\tau} = \omega|_\tau + \Delta\tau\dot{\omega}|_\tau + (\Delta\tau)^2[(\tfrac{1}{2} - \beta)\ddot{\omega}|_\tau + \beta\ddot{\omega}|_{\tau+\Delta\tau}], \tag{B2}$$

$$\dot{\omega}|_{\tau+\Delta\tau} = \dot{\omega}|_\tau + \Delta\tau[(1 - \gamma)\ddot{\omega}|_\tau + \gamma\ddot{\omega}|_{\tau+\Delta\tau}] \tag{B3}$$

where,

$$\beta = \tfrac{1}{4}(1 - \alpha)^2 \quad \text{and } \gamma = \tfrac{1}{2} - \alpha \tag{B4}$$

and ($\dot{\bullet}$) denotes differentiation w.r.t. τ.

In this study, the damping parameter α is set to zero, i.e., the trapezoidal rule is employed in the integration of the equations of motion (also known as constant average acceleration method). Thus, Eqs. (B2) and (B3) become

$$\omega|_{\tau+\Delta\tau} = \omega|_\tau + \Delta\tau\dot{\omega}|_\tau + \frac{(\Delta\tau)^2}{4}(\ddot{\omega}|_\tau + \ddot{\omega}|_{\tau+\Delta\tau}) \tag{B5}$$

and

$$\dot{\omega}|_{\tau+\Delta\tau} = \dot{\omega}|_\tau + \frac{\Delta\tau}{2}(\ddot{\omega}|_\tau + \ddot{\omega}|_{\tau+\Delta\tau}). \tag{B6}$$

Using (B5) and (B6), the time derivatives $\dot{\omega}|_{\tau+\Delta\tau}$ and $\ddot{\omega}|_{\tau+\Delta\tau}$ are evaluated in terms of $\omega|_{\tau+\Delta\tau}$ and the variables at time τ. They are substituted in (B1) which then becomes a two-point BVP for $\omega|_{\tau+\Delta\tau}$. The equation is solved using the BVPFD solver. The solution marches on in time by prescribing a new value for $\Delta\tau$.

D. D. Sivan
Defence Science and Technology Organisation
Land Operations Division, Salisbury, South Australia, 5108

Y. M. Ram
Department of Mechanical Engineering, Louisiana State University, Baton Rouge, LA 70803
Mem. ASME

Physical Modifications to Vibratory Systems With Assigned Eigendata

The problem of determining the structural modification needed to prescribe some natural frequencies and mode shapes, in the presence of model uncertainty, is considered. This problem has been previously solved by Ram and Braun (ASME Journal of Applied Mechanics, *Vol. 58, 1991), and a mathematical family of solutions has been derived. It is shown here how to extract from the complete mathematical set some physical solutions that can be realized by actual modifications to the system.*

1 Introduction

Forward problems in structural modification are those concerned with the determination of modal data caused by known modifications to structures. The associated backward problems deal with the determination of the necessary structural modifications which produce prescribed modal data. Various analytical approaches for solving forward problems are reviewed in Baldwin and Hutton (1985). In order to solve these problems it is required to know either the analytical model of the structure or, equivalently, the complete set of its natural frequencies and mode shapes. Note that if the analytical model of the unmodified system and the analytical model of the modification are known explicitly, then the forward problem is trivial. The interesting case is when the data are given in terms of experimental results, measured by modal tests. The obvious advantage of using these data is by virtue of their independence of analytical model assumptions. However, a complete set of eigendata cannot be obtained by experiments (see, e.g., Berman, 1984). Incomplete set of modal data does not describe the model fully. An approximation in a Rayleigh-Ritz sense has been derived for the solution of the forward problem in Ram, Braun, and Blech (1988). The truncation error obtained by this approximation has been bounded in Ram and Braun (1990a-b) and in Ram, Blech, and Braun (1990).

The associated backward problem in which we wish to determine the modification matrices that assign prescribed spectral data, has been analyzed in Ram and Braun (1991) and a mathematical family of solutions for the problem has been obtained. The set of solutions contains all possible mathematical modifications, irrespective of their potential to be realized. It may be that for some particular problems none of the solutions can be implemented by physical changes to the structure. If realizable solutions do exist then it is not clear how to extract such solutions from the general set. In fact, this difficulty has been mentioned in Ram and Braun (1991) and left as an open problem for future study. We address this problem here.

The main results obtained in Ram and Braun (1991) are summarized for completeness in Section 2. They lead to a certain singular Lyapunov-type equations. The necessary and sufficient conditions for the solvability of these equations are derived in Section 3. Using the conditions obtained and certain connectivity assumptions we determine in Section 4 realizable solutions. A numerical example demonstrating the results is given in Section 5, and the paper is summarized in Section 6.

2 Background

We now summarize the main results of Ram and Braun (1991). Consider an n degree-of-freedom vibratory system which is modeled by the symmetric definite generalized eigenvalue problem

$$\mathbf{K}\Phi = \mathbf{M}\Phi\Lambda, \quad \Phi^T\mathbf{M}\Phi = \mathbf{I} \tag{1}$$

where $\mathbf{K} \in R^{n\times n}$ and $\mathbf{M} \in R^{n\times n}$ are symmetric positive definite matrices, $\Lambda = \text{diag}\{\lambda_1, \lambda_2, \ldots, \lambda_n\}$, $\Phi = [\phi_1|\phi_2|\ \ldots\ |\phi_n]$ with $\phi_i \in R^n$, $i = 1, 2, \ldots, n$, and $\mathbf{I}$ is the identity matrix of appropriate dimensions. Partition Φ and Λ in the form

$$\Phi = [\Phi_1|\Phi_2], \quad \Phi_1 \in R^{n\times m}, \tag{2}$$

$$\Lambda = \begin{bmatrix} \Lambda_1 & \\ & \Lambda_2 \end{bmatrix}, \quad \Lambda_1 \in R^{m\times m}. \tag{3}$$

Suppose that Φ_1 and Λ_1 are given (e.g., measured by a modal test), and consider Φ_2 and Λ_2 unknown. Let a new modal set $\tilde{\Lambda}_1 = \text{diag}\{\tilde{\lambda}_1, \tilde{\lambda}_2, \ldots, \tilde{\lambda}_m\}$, $\tilde{\Phi}_1 = [\tilde{\phi}_1|\tilde{\phi}_2|\ \ldots\ |\tilde{\phi}_m]$ be given, and suppose that $\tilde{\Phi}_1 \in \text{span}\{\Phi_1\}$, ie., there exists an invertible $\mathbf{W} \in R^{m\times m}$ such that

$$\tilde{\Phi}_1 = \Phi_1\mathbf{W}. \tag{4}$$

We would like to determine the symmetric modifications $\hat{\mathbf{M}}$ and $\hat{\mathbf{K}}$ such that

$$\tilde{\mathbf{K}}\tilde{\Phi}_1 = \tilde{\mathbf{M}}\tilde{\Phi}_1\tilde{\Lambda}_1, \quad \tilde{\Phi}_1^T\tilde{\mathbf{M}}\tilde{\Phi}_1 = \mathbf{I}, \tag{5}$$

where $\tilde{\mathbf{K}} = \mathbf{K} + \hat{\mathbf{K}}$ and $\tilde{\mathbf{M}} = \mathbf{M} + \hat{\mathbf{M}}$. By achieving this goal a modified system with partial spectrum $\tilde{\Lambda}_1$ and modal matrix $\tilde{\Phi}_1$ may be constructed. Since $\mathbf{M}$ and $\mathbf{K}$ cannot be reconstructed uniquely from Λ_1 and Φ_1, this objective cannot be met. To overcome this difficulty a residual matrix

$$\mathbf{R} = (\tilde{\mathbf{M}})^{-1/2}(\tilde{\mathbf{K}}\tilde{\Phi}_1 - \tilde{\mathbf{M}}\tilde{\Phi}_1\tilde{\Lambda}_1) \tag{6}$$

is defined and the following problem is formulated:

Problem 1: Mathematical Backward Problem

Let Λ_1, Φ_1, $\tilde{\Lambda}_1$ and $\tilde{\Phi}_1$ be given and let $\mathbf{M}$ and $\mathbf{K}$ be unknown. Find $\hat{\mathbf{M}}$ and $\hat{\mathbf{K}}$ which minimize the Frobenius matrix norm $\|\mathbf{R}\|_F$.

If $\|\mathbf{R}\|_F = 0$ then $\hat{\mathbf{M}}$ and $\hat{\mathbf{K}}$ which solve Problem 1 are the exact modifications that solve (5). If $\|\mathbf{R}\|_F$ is small then with $\hat{\mathbf{M}}$ and $\hat{\mathbf{K}}$ which solve Problem 1 Eq. (5) is satisfied approxi-

Contributed by the Applied Mechanics Division of THE AMERICAN SOCIETY OF MECHANICAL ENGINEERS for publication in the ASME JOURNAL OF APPLIED MECHANICS.

Discussion on the paper should be addressed to the Technical Editor, Professor Lewis T. Wheeler, Department of Mechanical Engineering, University of Houston, Houston, TX 77204-4792, and will be accepted until four months after final publication of the paper itself in the ASME JOURNAL OF APPLIED MECHANICS.

Manuscript received by the ASME Applied Mechanics Division, Apr. 14, 1997; final revision, Aug. 10, 1998. Associate Technical Editor: M. Shinozuka.

mately in a Rayleigh-Ritz sense, as shown in Parlett, 1980, pp. 321–322.

Let $\mathbf{A}^+$ be the Moore-Penrose generalized inverse of $\mathbf{A}$ and denote

$$\mathbf{P} = (\mathbf{\Phi}_1^T)^+((\mathbf{W}\mathbf{W}^T)^{-1} - \mathbf{I})\mathbf{\Phi}_1^+ \tag{7}$$

$$\mathbf{T} = (\mathbf{\Phi}_1^T)^+((\mathbf{W}\tilde{\mathbf{\Lambda}}_1^{-1}\mathbf{W}^T)^{-1} - \mathbf{\Lambda}_1)\mathbf{\Phi}_1^+, \tag{8}$$

and

$$\mathbf{H} = \mathbf{\Phi}_1\mathbf{\Phi}_1^+. \tag{9}$$

It has been shown in (Ram and Braun, 1991) that the solution to Problem 1 is given by

$$\hat{\mathbf{M}} = \mathbf{P} + \mathbf{X} - \mathbf{H}^T\mathbf{X}\mathbf{H}, \tag{10}$$

$$\hat{\mathbf{K}} = \mathbf{T} + \mathbf{Y} - \mathbf{H}^T\mathbf{Y}\mathbf{H} \tag{11}$$

where $\mathbf{X} \in \mathrm{R}^{n\times n}$ and $\mathbf{Y} \in \mathrm{R}^{n\times n}$ are arbitrary symmetric matrices. The Lyapunov-type Eqs. (10) and (11) represent a family of mathematical solutions for Problem 1. Note that it follows from (9) that $\mathbf{H}$ is singular whenever $m < n$.

We now focus on the practical problem of determining the solutions from the set (10)–(11) which are realizable, i.e., solutions that can be implemented by a physical change in the structure. The following questions arise: (a) are there solutions in the set (10)–(11) which are realizable? (b) if there are, how can we extract such realizable solutions? and (c) if there are no realizable solutions in (10)–(11), how can we determine one which is close in some sense to a mathematical solution in the set? Before attempting to answer these questions, we need to take a close look at the solvability of the singular Lyapunov equations.

3 The Conditions for Solvability

Let us divert our attention from the problem of determining a realizable solution and consider the following problem. Let $\hat{\mathbf{M}}$, $\mathbf{P}$, and $\mathbf{H}$ be given. Determine the condition which ensures that there exists a matrix $\mathbf{X}$ such that (10) is satisfied.

Theorem 1.

Let

$$\mathbf{H} = \mathbf{U}\mathbf{\Sigma}\mathbf{U}^T, \quad \mathbf{U}\mathbf{U}^T = \mathbf{I}, \tag{12}$$

be the spectral decomposition of $\mathbf{H}$ and partition

$$\mathbf{U} = [\mathbf{U}_1|\mathbf{U}_2], \quad \mathbf{U}_1 \in \mathrm{R}^{n\times m}. \tag{13}$$

Then the system (10), together with the definitions (7) and (9), is a consistent system of equations if and only if

$$\mathbf{U}_1^T\hat{\mathbf{M}}\mathbf{U}_1 = \mathbf{U}_1^T\mathbf{P}\mathbf{U}_1. \tag{14}$$

Proof.

We first show that if (14) is not satisfied then (10) does not hold. Multiplying (10) from right and left by $\mathbf{U}^T$ and $\mathbf{U}$, respectively, gives

$$\mathbf{U}^T\hat{\mathbf{M}}\mathbf{U} = \mathbf{U}^T(\mathbf{P} + \mathbf{X})\mathbf{U} - \mathbf{\Sigma}\mathbf{U}^T\mathbf{X}\mathbf{U}\mathbf{\Sigma} \tag{15}$$

Noting that (9) implies that

$$\mathbf{\Sigma} = \begin{bmatrix} \mathbf{I}_m & \\ & \mathbf{O} \end{bmatrix} \tag{16}$$

we may write (15) in the following block matrix form

$$\begin{bmatrix} \mathbf{U}_1^T\hat{\mathbf{M}}\mathbf{U}_1 & \mathbf{U}_1^T\hat{\mathbf{M}}\mathbf{U}_2 \\ \mathbf{U}_2^T\hat{\mathbf{M}}\mathbf{U}_1 & \mathbf{U}_2^T\hat{\mathbf{M}}\mathbf{U}_2 \end{bmatrix} = \begin{bmatrix} \mathbf{U}_1^T\mathbf{P}\mathbf{U}_1 & \mathbf{U}_1^T(\mathbf{P} + \mathbf{X})\mathbf{U}_2 \\ \mathbf{U}_2^T(\mathbf{P} + \mathbf{X})\mathbf{U}_1 & \mathbf{U}_2^T(\mathbf{P} + \mathbf{X})\mathbf{U}_2 \end{bmatrix}. \tag{17}$$

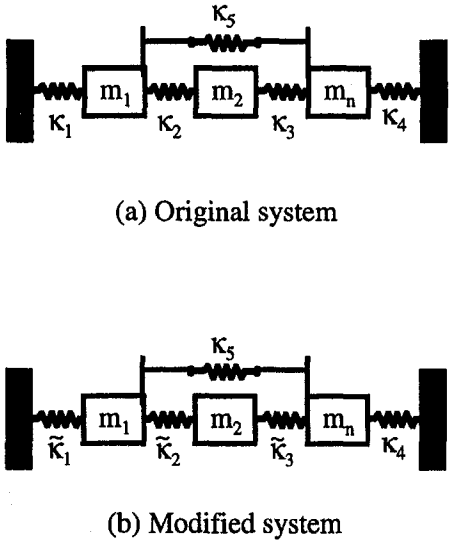

Fig. 1 A three-degree-of-freedom system and its modification. (*a*) Original system, (*b*) Modified system.

Since the leading block in (17) is independent of $\mathbf{X}$ it follows that if (14) is not satisfied then (10) does not hold.

Conversely, if (14) holds then we may always find $\mathbf{X}$ such that (10), or equivalently (17), holds. One such possible obvious choice is

$$\mathbf{X} = \hat{\mathbf{M}} - \mathbf{P}, \tag{18}$$

and the proof of the theorem is completed.

In an analogous manner we may prove that

$$\mathbf{U}_1^T\hat{\mathbf{K}}\mathbf{U}_1 = \mathbf{U}_1^T\mathbf{T}\mathbf{U}_1 \tag{19}$$

is a necessary and sufficient condition for the solvability of (11).

We now show how to use the conditions (14) and (19) in the determination of realizable solutions to Problem 1.

4 Realizable Solutions

It follows from the solvability results of Section 3 that instead of finding $\mathbf{X}$ which determines a realizable $\hat{\mathbf{M}}$ via (10), we may find a realizable $\hat{\mathbf{M}}$ which satisfies the condition (14). Then, by Theorem 1, $\hat{\mathbf{M}}$ belongs to the mathematical family of solutions (10) which solves Problem 1. Similarly, by determining a realizable $\hat{\mathbf{K}}$ which satisfies (19) we have a solution from the family (11).

We now show how to apply this general principle in a particular case. Consider an n-degree-of-freedom mass-spring system, such as that shown in Fig. 1(a) for $n = 3$. Suppose that only $m < n$ eigenvalues $\lambda_1, \lambda_2, \ldots, \lambda_m$ and their corresponding mass-normalized mode shapes $\phi_1, \phi_2, \ldots, \phi_m$ are given. Hence, generally the system cannot be reconstructed from these data. We wish to modify the system with the objective that the eigenvalues $\tilde{\lambda}_1, \tilde{\lambda}_2, \ldots, \tilde{\lambda}_m$ and the associated normalized eigenvectors $\tilde{\phi}_1, \tilde{\phi}_2, \ldots, \tilde{\phi}_m$ of the modified system are prescribed. Suppose that the allowed modifications are restricted to changes in the n existing masses, the $n - 1$ springs connecting neighboring masses and the spring connecting the left system to the ground. Denote the changes in these parameters by $\hat{m}_i$ and $\hat{\kappa}_i$, $i = 1, 2, \ldots, n$, respectively. Such a modification for the three-degree-of-freedom case is illustrated in Fig. 1(b), where $\tilde{m}_i = m_i + \hat{m}_i$ and $\tilde{\kappa}_i = \kappa_i + \hat{\kappa}_i$, $i = 1, 2, 3$.

The connectivity conditions for this problem are (see, e.g., Gladwell, 1986, p. 23)

$$\hat{\mathbf{M}} = \text{diag}\,\{\hat{m}_1, \hat{m}_2, \ldots, \hat{m}_n\} \tag{20}$$

and

$$\hat{\mathbf{K}} = \mathbf{E}\hat{\mathbf{D}}\mathbf{E}^T \tag{21}$$

where

$$\hat{\mathbf{D}} = \text{diag}\,\{\hat{\kappa}_1, \hat{\kappa}_2, \ldots, \hat{\kappa}_n\} \tag{22}$$

and

$$\mathbf{E} = \begin{bmatrix} 1 & -1 & & \\ & 1 & -1 & \\ & & \ddots & \ddots \\ & & & 1 \end{bmatrix} \in R^{n\times n}. \tag{23}$$

Realizable solutions in this case are those which satisfy the connectivity relations (20)–(23), in addition to the requirements that $\tilde{\mathbf{M}}$ has positive diagonal and the diagonal of $\tilde{\mathbf{K}}$ is positive weakly dominant.

We now show how to determine a diagonal $\hat{\mathbf{M}}$ which satisfy (14). For convenience denote

$$\mathbf{B} = \mathbf{U}_1^T\mathbf{P}\mathbf{U}_1, \tag{24}$$

so that (14) can be written as

$$\mathbf{U}_1^T\hat{\mathbf{M}}\mathbf{U}_1 = \mathbf{B}. \tag{25}$$

Partition

$$\mathbf{U}_1 = [\mathbf{u}_1|\mathbf{u}_2|\ \ldots\ |\mathbf{u}_m] \tag{26}$$

and

$$\mathbf{B} = [\mathbf{b}_1|\mathbf{b}_2|\ \ldots\ |\mathbf{b}_m]. \tag{27}$$

Then (25) consists of the following m systems of m equations:

$$\mathbf{U}_1^T\hat{\mathbf{M}}\mathbf{u}_k = \mathbf{b}_k, \quad k = 1, 2, \ldots, m. \tag{28}$$

Note that (28) can be written equivalently as systems of linear equations

$$\mathbf{A}_k\hat{\mathbf{m}} = \mathbf{b}_k, \quad k = 1, 2, \ldots, m \tag{29}$$

where

$$\mathbf{A}_k = [a_{i,j}]_k = [u_{j,i}u_{j,k}]_k \tag{30}$$

$$\hat{\mathbf{m}} = (\hat{m}_1, \hat{m}_2, \ldots, \hat{m}_n)^T \tag{31}$$

and where $u_{i,j}$ is the $i-j$ element of $\mathbf{U}$. Hence, denoting

$$\mathbf{A} = [\mathbf{A}_1^T|\mathbf{A}_2^T|\ \ldots\ |\mathbf{A}_m^T]^T \tag{32}$$

and

$$\mathbf{b} = (\mathbf{b}_1^T|\mathbf{b}_2^T|\ \ldots\ |\mathbf{b}_m^T)^T \tag{33}$$

Eq. (25), and its equivalent systems of Eq. (29), can be written in the linear form

$$\mathbf{A}\hat{\mathbf{m}} = \mathbf{b}. \tag{34}$$

The system (34) consists of m^2 equations with n unknowns. It should be noted, however, that generally only $p = m(m+1)/2$ Eqs. of (34) are linearly independent. (We could eliminate the dependent Eqs. in (34), but for the sake of simplicity we decided not to pursue this issue). Hence, depending whether the ratio n/p is less than, equal to, or greater than unit, the system (34) has no solution, a unique solution, or a family of solutions, respectively. If the system (34) has no solution, we may still solve (34) in a least squares sense and obtain an approximation to $\hat{\mathbf{M}}$. A realizable solution must have the additional property that $\mathbf{M} + \hat{\mathbf{M}}$ is positive definite. When $\mathbf{M}$ is unknown and $\hat{\mathbf{M}}$ contains negative diagonal elements it may be difficult to say whether the solution is really realizable. We may restrict the magnitude of negative values in $\hat{\mathbf{M}}$ by solving the least-squares problem (34) under inequality constraints. A study of this topic is presented in Lawson and Hanson (1974).

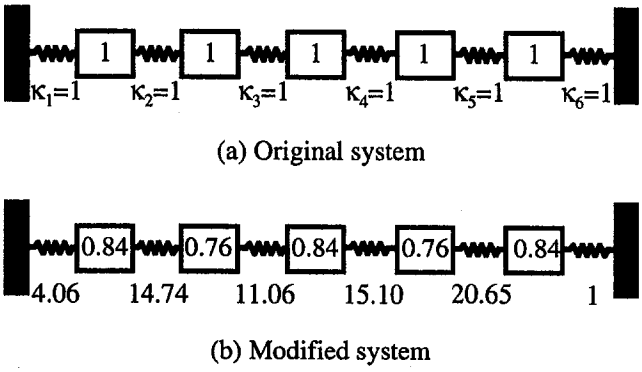

Fig. 2 A five-degree-of-freedom system and its modification. (*a*) Original system, (*b*) Modified system.

The modification of the stiffness matrix may be determined in a similar manner. Denote

$$\mathbf{C} = \mathbf{U}_1^T\mathbf{T}\mathbf{U}_1 \tag{35}$$

and

$$\mathbf{V} = [\nu_{i,j}] = \mathbf{E}^T\mathbf{U}_1. \tag{36}$$

Then the solvability condition (19) and the connectivity condition (21) imply that we need to find a diagonal $\hat{\mathbf{D}}$ which satisfies

$$\mathbf{V}^T\hat{\mathbf{D}}\mathbf{V} = \mathbf{C}. \tag{37}$$

According to (22) the diagonal elements of $\hat{\mathbf{D}}$ determine the modification to the stiffness matrix. This problem can be written in the linear form

$$\mathbf{Z}\hat{\mathbf{k}} = \mathbf{c} \tag{38}$$

where

$$\hat{\mathbf{k}} = (\hat{\kappa}_1, \hat{\kappa}_2, \ldots, \hat{\kappa}_n)^T, \tag{39}$$

$$\mathbf{Z} = [\mathbf{Z}_1^T|\mathbf{Z}_2^T|\ \ldots\ |\mathbf{Z}_m^T]^T, \tag{40}$$

$$\mathbf{c} = (\mathbf{c}_1^T|\mathbf{c}_2^T|\ \ldots\ |\mathbf{c}_m^T)^T \tag{41}$$

and where $\mathbf{Z}_k$ and $\mathbf{c}_k$ are defined by

$$\mathbf{Z}_k = [z_{i,j}]_k = [\nu_{j,i}\nu_{j,k}]_k \tag{42}$$

and

$$\mathbf{C} = [\mathbf{c}_1|\mathbf{c}_2|\ \ldots\ |\mathbf{c}_m]. \tag{43}$$

Here again only $p = m(m+1)/2$ Eqs. in (38) are linearly independent. So, depending on the ratio n/p, (38) may be solved exactly, or in least squares sense, for the unknown $\hat{\mathbf{k}}$. The magnitude of the elements of $\hat{\mathbf{k}}$ may be controlled by solving (38) subject to inequality constraints.

We have demonstrated how to determine a realizable modification for a specific case, namely the mass-spring system, with a particular modification constraint. The principle that the realizable modification may be determined by the solvability conditions (14) and (19), however, is applicable for the more general case. Other problems, e.g., discrete models of beams or plates, involve other connectivity conditions. These conditions together with (14) and (19) may yield a realizable model of modifications.

5 An Example

The system shown in Fig. 2(*a*) has five eigenpairs. Suppose that we know only two of its eigenvalues

Table 1 Modifications to the masses and spring constants

i	$\hat{m}_i$	$\hat{k}_i$
1	−0.1600	3.0653
2	−0.2400	13.7389
3	−0.1600	10.0593
4	−0.2400	14.1000
5	−0.1600	19.6549

$$\lambda_1 = 3,\ \lambda_2 = 3.7321$$

and their two corresponding mass-normalized eigenvectors

$$\phi_1 = (-0.5 \quad 0.5 \quad 0 \quad -0.5 \quad 0.5)^T,$$
$$\phi_2 = (0.2887 \quad -0.5 \quad 0.5774 \quad -0.5 \quad 0.2887)^T,$$

while the actual system is considered unknown. Clearly, a five-degree-of-freedom system which generally consists of 15 springs and 5 masses cannot be reconstructed uniquely from the above 12 pieces of information. In other words, there are many different mass-spring systems with the same two eigenpairs. Although the system is considered unknown we may determine a modification, optimal in a Rayleigh-Ritz sense, which changes the two given eigenpairs to say

$$\check{\lambda}_1 = 50,\ \check{\lambda}_2 = 70,$$
$$\check{\phi}_1 = (-0.6443 \quad 0.75 \quad -0.2887 \quad -0.25 \quad 0.3557)^T,$$
$$\check{\phi}_2 = (0.0387 \quad -0.25 \quad 0.5774 \quad -0.75 \quad 0.5387)^T.$$

This will be done by changing the five masses and the five springs $\kappa_1, \ldots, \kappa_5$, shown in Fig. 1($a$), only. Note that the new eigenvectors are constrained by

$$[\check{\phi}_1 | \check{\phi}_2] = [\phi_1 | \phi_2]\mathbf{W}$$

where

$$\mathbf{W} = \begin{bmatrix} 1 & 0.5 \\ -0.5 & 1 \end{bmatrix}.$$

We note that despite its simplicity, this problem may represent an important engineering application where the analytical model of a vibrating structure is unknown, modal data are available, and the objective is to determine structural modification which assign part of the eigendata. As mentioned above this objective can be achieved only by approximation, optimal in some sense.

Using (7) and (9) we obtain

$$\mathbf{P} = \begin{bmatrix} -0.0667 & 0.0789 & -0.0333 & -0.0211 & 0.0333 \\ 0.0789 & -0.1000 & 0.0577 & 0.0000 & -0.0211 \\ -0.0333 & 0.0577 & -0.0667 & 0.0577 & -0.0333 \\ -0.0211 & 0.0000 & 0.0577 & -0.1000 & 0.0789 \\ 0.0333 & -0.0211 & -0.0333 & 0.0789 & -0.0667 \end{bmatrix},$$

and

$$\mathbf{H} = \begin{bmatrix} 0.3333 & -0.3943 & 0.1667 & 0.1057 & -0.1667 \\ -0.3943 & 0.5000 & -0.2887 & 0.0000 & 0.1057 \\ 0.1667 & -0.2887 & 0.3333 & -0.2887 & 0.1667 \\ 0.1057 & 0.0000 & -0.2887 & 0.5000 & -0.3943 \\ -0.1667 & 0.1057 & 0.1667 & -0.3943 & 0.3333 \end{bmatrix}.$$

The spectral decomposition of $\mathbf{H}$, given by (12), yields

$$\mathbf{U} = \begin{bmatrix} 0.5774 & 0.0000 & -0.6597 & -0.3829 & 0.2912 \\ -0.6830 & -0.1830 & -0.3142 & -0.0068 & 0.6334 \\ 0.2887 & 0.5000 & 0.1324 & 0.6086 & 0.5279 \\ 0.1830 & -0.6830 & -0.2682 & 0.6420 & -0.1261 \\ -0.2887 & 0.5000 & -0.6137 & 0.2659 & -0.4683 \end{bmatrix}$$

and, as expected, $\Sigma = \text{diag}\{1 \quad 1 \quad 0 \quad 0 \quad 0\}$. We thus have by (13)

$$\mathbf{U}_1 = \begin{bmatrix} 0.5774 & 0.0000 \\ -0.6830 & -0.1830 \\ 0.2887 & 0.5000 \\ 0.1830 & -0.6830 \\ -0.2887 & 0.5000 \end{bmatrix}.$$

Invoking (30) and (27) we have

$$\mathbf{A}_1 = \begin{bmatrix} 0.3333 & 0.4665 & 0.0833 & 0.0335 & 0.0833 \\ 0.0000 & 0.1250 & 0.1443 & -0.1250 & -0.1443 \end{bmatrix}$$

$$\mathbf{A}_2 = \begin{bmatrix} 0.0000 & 0.1250 & 0.1443 & -0.1250 & -0.1443 \\ 0.0000 & 0.0335 & 0.2500 & 0.4665 & 0.2500 \end{bmatrix}$$

$$\mathbf{b}_1 = \begin{pmatrix} -0.2000 \\ 0.0000 \end{pmatrix}, \quad \mathbf{b}_2 = \begin{pmatrix} 0.0000 \\ -0.2000 \end{pmatrix}.$$

The linear system of Eqs. (34) is thus

$$\begin{bmatrix} 0.3333 & 0.4665 & 0.0833 & 0.0335 & 0.0833 \\ 0.0000 & 0.1250 & 0.1443 & -0.1250 & -0.1443 \\ 0.0000 & 0.1250 & 0.1443 & -0.1250 & -0.1443 \\ 0.0000 & 0.0335 & 0.2500 & 0.4665 & 0.2500 \end{bmatrix} \times \begin{pmatrix} \hat{m}_1 \\ \hat{m}_2 \\ \hat{m}_3 \\ \hat{m}_4 \\ \hat{m}_5 \end{pmatrix} = \begin{pmatrix} -0.2 \\ 0.0 \\ 0.0 \\ -0.2 \end{pmatrix}.$$

The second and third equations are identical, hence the above system consists of three independent equations with five unknowns. There is thus a continuous family of realizable solutions. We choose arbitrarily the unique solution with the minimal norm by solving

$$\hat{\mathbf{m}} = \mathbf{A}^+\mathbf{b}.$$

This solution has the attractive feature of minimizing the required changes in the mass configuration (see e.g., Golub and Van Loan, 1983, pp. 162–164). This minimal modification is given in Table 1. In a similar manner, using (35)–(43) we find that there exists a continuous family of realizable stiffness modifications which solves Problem 1. The one which requires

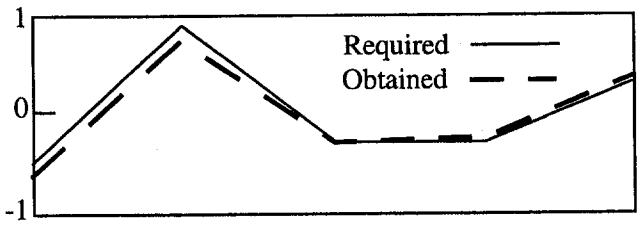

(a) $\tilde{\phi}_1$

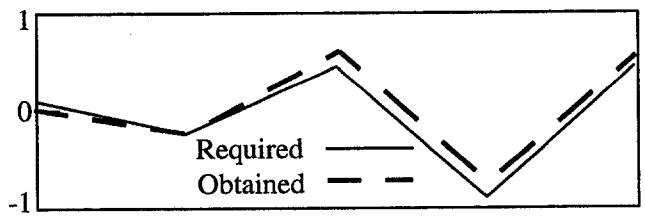

(b) $\tilde{\phi}_2$

Fig. 3 The required mode shapes and their approximations

the minimal spring changes in the Euclidean vector norm sense is shown in Table 1.

To evaluate the results we added the modification matrices obtained to the (so far regarded "unknown") mass and stiffness matrices of the original system, and solved the eigenvalue problem associated with the modified system. The modified system, shown in Fig. 2(*a*), is indeed realizable, and has eigenvalues $\hat{\lambda}_1 = 51.1143$ and $\hat{\lambda}_2 = 71.8761$. The associated mass normalized mode shapes, together with the required modes are shown in Fig. 3. Recalling that only incomplete modal data has been used, the approximation seems satisfactory in this case.

6 Summary

We have considered the problem of approximating realizable mass and stiffness modifications required to assign some eigenvalues and eigenvectors. The analytical model of the system has been considered unknown, and only truncated set of eigenpairs associated with the unmodified system has been used. The families of mathematical solutions for the problem, suggested in (Ram and Braun, 1991), have been replaced by solvability conditions. These conditions, together with the connectivity imposed by the realizable constraints, form sets of equations which define realizable solutions. We have analyzed the mass-spring system model with certain constraints on the permitted modifications. The solvability conditions have been then transformed to a standard linear form and solved in a least-squares sense. A numerical example has provided a satisfactory approximation to the modifications in a particular, specially chosen, case.

References

Baldwin, J. F., and Hutton, S. G., "Natural Modes of Modified Structures," *AIAA Journal,* Vol. 23, No. 11, pp. 1737–1743, 1985.

Berman, A., "System Identification of Structural Dynamic Models—Theoretical and Practical Bounds," *AIAA* paper 84-0929, pp. 123–129, 1984.

Gladwell, G. M. L., *Inverse Problems in Vibration,* Martinus Nijhoff Publishers, Dordrecht, 1986.

Golub, G. H., and Van Loan, C. F., *Matrix Computations,* Johns Hopkins University Press, Maryland, 1983.

Lawson, C. L., and Hanson, R. J., *Solving Least Squares Problems,* Prentice-Hall, 1974.

Parlett, B. N., *The Symmetric Eigenvalue Problem,* Prentice-Hall, 1980.

Ram, Y. M., Braun, S. G., and Blech, J. J., "Structural Modification in Truncated Systems by the Rayleigh-Ritz Method," *Journal of Sound and Vibration,* Vol. 125, No. 2, pp. 203–209, 1988.

Ram, Y. M., Blech, J. J., and Braun, S. G., "Eigenproblem Error Bounds With Application to the Symmetric Dynamic System Modification," *SIAM Journal on Matrix Analysis and Applications,* Vol. 11, pp. 553–564, 1990.

Ram, Y. M., and Braun, S. G., "Upper and Lower Bounds for the Natural Frequencies of Modified Structures Based on Modal Testing Results," *Journal of Sound and Vibration,* Vol. 137, No. 1, pp. 69–81, 1990a.

Ram, Y. M., and Braun, S. G., "Structural Dynamic Modifications Using Truncated Data: Bounds for the Eigenvalues," *Mechanical Systems and Signal Processing,* Vol. 4, No. 1, pp. 39–52, 1990b.

Ram, Y. M., and Braun, S. G., "An Inverse Problem Associated With Modification of Incomplete Dynamic System," ASME JOURNAL OF APPLIED MECHANICS, Vol. 58, No. 1, pp. 233–237, 1991.

Vibration Considerations in Foil-Bearing Design

A. A. Renshaw
Department of Mechanical Engineering,
Columbia University,
New York, NY 10027
Mem. ASME

The semianalytic foil-bearing solution algorithm of Eshel and Elrod (1965) is extended to the solution of the linearized, free vibration problem for one-dimensional self-pressurized foil bearings. The results demonstrate that unwanted variations in the spacing between the moving foil and the stationary bearing surface can be eliminated through proper design. The penetration depth through which vibration of the free span penetrates into the foil bearing is determined by two exponential exponents, one describing inlet penetration, the other describing outlet penetration. When the inlet exponent is large and negative and the outlet exponent is large and positive, there is negligible coupling between the vibration of the free spans and the vibration of the spacing between the foil and the stationary bearing surface. This decoupling is desirable in magnetic recording and web handling applications and can be achieved by properly selecting two dimensionless parameters, one describing the ratio of the viscous forces to the tape tension, the other describing the ratio of the tape transport speed to the wave speed in the tape. The values of these two parameters in current designs of both magnetic tape recording and web-handling devices are consistent with the design goal of minimizing foil vibration over the bearing. The inlet and outlet exponents are the roots of a fourth-order polynomial, and, in most cases, good estimates for these roots can be found without explicitly solving the foil-bearing problem. The effects of the air compressibility, tape bending stiffness, and slip flow are also investigated. Tape bending stiffness is found to play a significant role in vibration coupling. These results provide new insight into the influence of vibration on foil-bearing design.

1 Introduction

Self-pressurized foil bearings are often used in magnetic tape drives to position a flexible magnetic tape over a stationary recording head as the tape is wound from one reel to another. Foil bearings are also found in web-handling devices to assist in transporting, drying, and controlling the web during processing. In both applications, performance is generally enhanced by foil bearing designs that: (1) minimize the spacing between the moving foil and the stationary bearing surface and (2) minimize the temporal variations of this spacing.

The equilibrium spacing between the foil and the stationary bearing surface has been extensively analyzed during the past four decades. A one-dimensional steady-state model of the foil bearing was first proposed and approximately solved by Blok and Van Rossum (1953). His results were subsequently improved and extended by Baumeister (1963), Langlois (1963), and Eshel and Elrod (1965). Since then, numerous efficient and increasingly sophisticated numerical algorithms for solving the one and two-dimensional steady-state foil-bearing problem have been proposed (for example, Stahl et al., 1974; Lacey and Talke, 1990; Moes, 1991; Ono et al., 1991; Wickert, 1993; Sakai et al., 1996).

Vibration of the spacing between the foil and the stationary bearing has only recently attracted research attention. Wickert (1993) and Lakshmikumaran and Wickert (1996) linearized the foil-bearing equations about the steady equilibrium and then determined the eigenvalues associated with free linear vibration about the equilibrium using a finite difference algorithm. Using the real and imaginary parts of those eigenvalues as measures of the system damping and stiffness, they performed several parametric studies aimed at optimizing these quantities. One interesting phenomenon that was demonstrated by their work was the existence of two different types of vibration modes. The first kind of vibration mode possesses significant motion of the foil both before and after the stationary bearing with, presumably, small but nonzero motion across the bearing. The other vibration mode had significant motion only after the bearing. The results shown were not adequate to determine the magnitude of motion across the bearing in either vibration mode or its relevance to foil-bearing design.

In the present paper, we use a simple, one-dimensional model and the semianalytic method of Eshel and Elrod (1965) to show that vibration coupling across the stationary bearing produces unwanted variations in the spacing and that such coupling can be eliminated through proper design. The penetration depth through which vibration of the free spans penetrates into the bearing is determined by two exponential exponents, one describing inlet penetration, the other describing outlet penetration. When the inlet exponent is large and negative and the outlet exponent is large and positive, there is negligible coupling between vibration of the free spans and vibration of the foil bearing film thickness. This situation is desirable in both magnetic recording and web-handling devices and can be achieved by properly selecting two dimensionless parameters, one describing the ratio of the viscous forces to the tape tension, the other describing the ratio of the tape transport speed to the wave speed in the tape. The values of these two parameters in current designs of magnetic tape recording and web-handling devices are consistent with the design goal of minimizing foil vibration over the bearing. The inlet and outlet exponents are the roots of a fourth-order polynomial, and, in most cases, good estimates for these roots can be found without explicitly solving the foil bearing problem. The effects of the air compressibility, tape bending stiffness, and slip flow are also investigated. Tape bending stiffness is found to play a significant role in vibration coupling. These results provide new insight into the influence of vibration on foil bearing design.

Contributed by the Applied Mechanics Division of THE AMERICAN SOCIETY OF MECHANICAL ENGINEERS for publication in the ASME JOURNAL OF APPLIED MECHANICS.
Discussion on the paper should be addressed to the Technical Editor, Professor Lewis T. Wheeler, Department of Mechanical Engineering, University of Houston, Houston, TX 77204-4792, and will be accepted until four months after final publication of the paper itself in the ASME JOURNAL OF APPLIED MECHANICS.
Manuscript received by the ASME Applied Mechanics Division, Apr. 7, 1998; final revision, Dec. 15, 1998. Associate Technical Editor: N. C. Perkins.

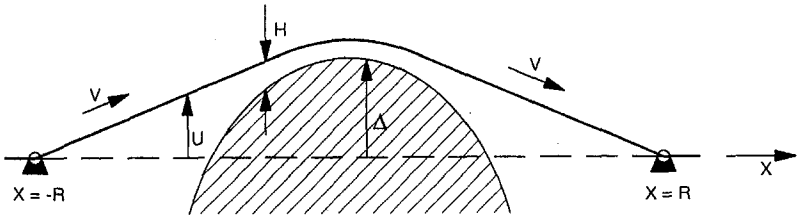

Fig. 1 Schematic of the foil-bearing problem

2 Modeling

A thin flexible tape (or web) of constant linear density ρ, tension σ, and width W travels at constant speed V between two fixed eyelets located at $X = -R$ and $X = R$ as shown in Fig. 1. The transverse displacement of the tape is $U(T, X)$ where T is time. A stationary recording head (or web control bar) with transverse profile

$$\Delta(X) = \Delta_o - X^2/2R \tag{1}$$

lies below the tape, and a thin film of air of viscosity μ supports the tape as it wraps around the recording head so that the tape does not make direct contact with the recording head. The thickness of the air film between the recording head and the tape is

$$H = U - \Delta \tag{2}$$

and P is the pressure difference from ambient within this air film. The tape is modeled as an axially moving string (Wickert and Mote, 1990)

$$\rho(U_{,TT} + 2VU_{,TX} + V^2U_{,XX}) - \sigma U_{,XX} = PW \tag{3}$$

where a comma indicates partial differentiation. The pressure in the air film is modeled by the one-dimensional incompressible isothermal Reynolds equation (Szeri, 1980)

$$(H^3P_{,X})_{,X} = 12\mu H_{,T} + 6\mu VH_{,X}. \tag{4}$$

The tape displacement and pressure satisfy the boundary conditions

$$U = P = 0 \quad \text{at} \quad X = \pm R. \tag{5}$$

Dimensionless variables are defined by

$$u = U/R \quad \delta = \Delta/R \quad h = H/R$$

$$x = X/R \quad t = T\sqrt{\sigma/\rho R^2} \quad p = PRW/(\sigma - \rho V^2) \tag{6}$$

for which Eqs. (1)–(4) become

$$\delta = \delta_o - x^2/2 \tag{7}$$

$$h = u - \delta \tag{8}$$

$$u_{,tt} + 2vu_{,tx} + (v^2 - 1)u_{,xx} = (1 - v^2)p \tag{9}$$

$$v(h^3p_{,x})_{,x} = 2\epsilon^3h_{,t} + v\epsilon^3h_{,x} \tag{10}$$

where

$$v = V\sqrt{\rho/\sigma} \quad \epsilon^3 = 6\mu VW/(\sigma - \rho V^2) \quad \delta_o = \Delta_o/R. \tag{11}$$

Straight lines emanating from each eyelet are tangent to the recording head at the locations

$$x'_L = -1 + \sqrt{1 - 2\delta_o} \quad x'_R = 1 - \sqrt{1 - 2\delta_o} \tag{12}$$

where subscripts L and R indicate the left and right side of the recording head. The span to the left of the recording head is termed the inlet span, while the span to the right of the recording head is termed the outlet span.

The steady-state problem depends on the parameters ϵ and δ_o, while the transient problem depends on v, ϵ, and δ_o. All three parameters are usually small. For magnetic recording applications, consider the commonly used test problem of Stahl, White, and Deckert (1974) (Lacey and Talke, 1990; Wickert, 1993) for which $\Delta_o = 0.63$ cm, $R = 1.97$ cm, $\rho/W = 0.0207$ kg/m^2, $\sigma/W = 277$ N/m, $V = 2.54$ m/s, and $\mu = 1.81 \times 10^{-5}$ kg/m-s. For these values $v = 0.02$, $\epsilon = 0.01$, $\delta_o = 0.3$, and $x' = \pm 0.4$. In a typical web-handling device such as the Heidelberg Harris M 1000 BE, $R = 9.2$ cm, $W = 97$ cm, $\rho = 0.02$ kg/m^3, $\sigma = 500$ N, $V = 11$ m/s, and $\mu = 1.81 \times 10^{-5}$ kg/m-s. For these values, $v = 0.07$, $\epsilon = 0.01$.

In the sequel, we impose the formal restrictions $\epsilon < 1$, $v < 1$ and $\delta_o < \frac{1}{2}$ in order to ensure that the problem is both physically and geometrically well posed.

3 Equilibrium

Under steady-state conditions, Eqs. (7) and (9) give

$$p = 1 - h_{,xx} \tag{13}$$

which, together with (8) and (10), give the classical foil-bearing equation (Blok and Van Rossum, 1953; Baumeister, 1963; Langlois, 1963; Eshel and Elrod, 1965)

$$h_{,xxx} = \epsilon^3(\epsilon^2\bar{h} - h)/h^3 \tag{14}$$

where $\bar{h}$ is an integration constant. ($\bar{h}$ has been scaled by ϵ^2 in order to simplify subsequent manipulations.) The particular solution $h = \epsilon^2\bar{h}$ is a good approximation to the actual solution over most of the recording head, but is inadequate when the tape is far from the recording head and does not satisfy the boundary conditions (5).

Eshel and Elrod (1965) developed a solution algorithm for (14) based on numerical integration. We summarize that solution here in order to improve the clarity of the vibration analysis of the next section. Assume that over some finite region I in the center of the recording head h is given by

$$h = \epsilon^2(\bar{h} + y(x)) \tag{15}$$

where $|y| \ll \bar{h}$. When $|y| \ll \bar{h}$, (14) can be linearized to give

$$\epsilon^3\bar{h}^3y_{,xxx} + y = 0 \tag{16}$$

whose general solution is

$$y = ae^{-x/\epsilon\bar{h}} + e^{x/2\epsilon\bar{h}}[b \sin(\sqrt{3}x/2\epsilon\bar{h}) + c \cos(\sqrt{3}x/2\epsilon\bar{h})]. \tag{17}$$

Since $\epsilon \ll 1$, that part of (17) proportional to a is exponentially large as $\epsilon \to 0$ for any $x = x_o < 0$, while those parts of (17) proportional to b and c are exponentially large as $\epsilon \to 0$ at any $x = x_o > 0$. As a result, $|y| \ll \bar{h}$ is valid only if the contribution of (17) proportional to a is non-negligible only on the left edge of I and the contribution of (17) proportional to b and c is non-negligible only on the right edge of I. Therefore, in the inlet region $x'_L \ll x \ll 0$, h must be well approximated by

$$h = \epsilon^2[\bar{h} + a_oe^{-(x-x_L')/\epsilon\bar{h}}] \tag{18}$$

while in the outlet region $0 \ll x \ll x'_R$, h must be well approximated by

$$h = \epsilon^2\{\bar{h} + e^{(x-x'_R)/2\epsilon\bar{h}}[b_o \sin(\sqrt{3}(x - x'_R)/2\epsilon\bar{h}) + c_o \cos(\sqrt{3}(x - x'_R)/2\epsilon\bar{h})]\}. \quad (19)$$

With the four parameters $\bar{h}$, a_o, b_o, and c_o fixed, (18) and (19) can be differentiated and evaluated to estimate h, $h_{,x}$, and $h_{,xx}$ at any x within the appropriate region. These estimates can then be used as initial values to numerically integrate (14) either from $x = x_o$ to $x = -1$ in the case where $x'_L \ll x_o \ll 0$ and (18) has been used, or from $x = x_o$ to $x = 1$ in the case where $0 \ll x_o \ll x'_R$ and (19) has been used. The errors in the boundary conditions at $x = \pm 1$ can then be used as inputs to a multidimensional nonlinear equation solver to modify initial estimates of $\bar{h}$, a_o, b_o, and c_o until the boundary conditions are satisfied. While the solver could simultaneously determine for all four parameters using the four boundary conditions, it is more efficient to first determine $\bar{h}$ and a_o using the boundary conditions at $x = -1$ since (18) is independent of b_o and c_o and then, with $\bar{h}$ and a_o fixed, determine b_o and c_o using the boundary conditions at $x = 1$.

Because of the large difference in the exponential exponents in (17), (14) is generally too stiff to be numerically integrated from $x = x'_L$ to $x = x'_R$. Judgement is therefore required in choosing x_o, the starting point for the numerical integration, in order to prevent spurious errors related to the numerical stiffness of (14) from creeping into the estimate of the boundary conditions at $x = \pm 1$ and to avoid needless and time consuming numerical integration over regions in which the approximations (18) and (19) are adequate. For the results reported here, we used $x_o = x'_L + \epsilon/2$ for the inlet and $x_o = x'_R - \epsilon/2$ for the outlet. These starting locations gave results that were within 0.1 percent of the results produced using starting locations closer to the center of the bearing.

For $\epsilon = 0.01$ and $\delta_o = 0.3$, the four parameters are $\bar{h} = 0.6430$, $a_o = 0.5292$, $b_o = -0.0712$, and $c_o = -0.1408$. The value of $\bar{h}$ agrees exactly with the value determined by Eshel and Elrod (1965).

4 Free Linear Vibration

We next consider harmonic vibration of (9) and (10) linearized about the equilibrium found in the previous section as first proposed by Wickert (1993). Letting

$$u = u_e + \tilde{u}e^{\lambda t} \quad p = p_e + \tilde{p}e^{\lambda t} \quad h = h_e + \tilde{u}e^{\lambda t} \quad (20)$$

where subscript e denotes the equilibrium solutions and the tildes indicate small, spatially dependent functions, the linear versions of (9) and (10) are

$$\lambda^2\tilde{u} + 2v\lambda\tilde{u}_{,x} + (v^2 - 1)\tilde{u}_{,xx} = (1 - v^2)\tilde{p} \quad (21)$$

$$v(h_e^3\tilde{p}_{,x} + 3h_e^2\tilde{u}p_{e,x})_{,x} = 2\epsilon^3\lambda\tilde{u} + \epsilon^3 v\tilde{u}_{,x}. \quad (22)$$

Equation (21) can be solved for $\tilde{p}$ and substituted into (22) to give a single linear fourth-order ordinary differential equation for $\tilde{u}$

$$v(1 - v^2)h_e^3\tilde{u}_{,xxxx} + vh_e^2[3(1 - v^2)h_{e,x} - 2\lambda v h_e]\tilde{u}_{,xxx} - \lambda v h_e^2(6vh_{e,x} + \lambda h_e)\tilde{u}_{,xx} + v[(1 - v^2)(\epsilon^3 + 3h_e^2h_{e,xxx}) - 3\lambda^2h_e^2h_{e,x}]\tilde{u}_{,x} + (1 - v^2)[2\epsilon^3\lambda + 3vh_e(h_eh_{e,xxxx} + 2h_{e,x}h_{e,xxx})]\tilde{u} = 0. \quad (23)$$

We now extend the solution algorithm of Eshel and Elrod (1965) to numerically solve (23). We seek an approximate, analytic solution to (23) valid over the interval I to provide starting values for $\tilde{u}$ and its derivatives for numerical integration. Over most of I, $h_e = \epsilon^2\bar{h}$ and (23) is well approximated by

$$v(1 - v^2)\epsilon^3\bar{h}^3\tilde{u}_{,xxxx} - 2\lambda v^2\epsilon^3\bar{h}^3\tilde{u}_{,xxx} - \lambda^2 v\epsilon^3\bar{h}^3\tilde{u}_{,xx} + v(1 - v^2)\tilde{u}_{,x} + 2\lambda(1 - v^2)\tilde{u} = 0. \quad (24)$$

Equation (24) is a fourth-order linear ordinary equation with constant (complex) coefficients. Consequently, its solution is

$$\tilde{u} = c_1e^{\omega_1(x-x'_L)} + c_2e^{\omega_2(x-x'_L)} + c_3e^{\omega_3(x-x'_R)} + c_4e^{\omega_4(x-x'_R)} \quad (25)$$

where c_1–c_4 are complex constants and ω_1–ω_4 are the four roots of the polynomial

$$v(1 - v^2)\epsilon^3\bar{h}^3\omega^4 - 2\lambda v^2\epsilon^3\bar{h}^3\omega^3 - \lambda^2 v\epsilon^3\bar{h}^3\omega^2 + v(1 - v^2)\omega + 2\lambda(1 - v^2) = 0 \quad (26)$$

ordered such that

$$\mathrm{Re}[\omega_1] \le \mathrm{Re}[\omega_2] \le \mathrm{Re}[\omega_3] \le \mathrm{Re}[\omega_4]. \quad (27)$$

There are five unknown complex parameters embedded in (25)—λ and c_1–c_4—and only four boundary conditions. However, the magnitude of the eigenfunction is arbitrary, so one nonzero coefficient c_1–c_4 can be arbitrarily set to unity. As a result, there are as many unknown parameters as boundary conditions, and the problem is well posed.

Unfortunately, there is no simple analytic formula for the roots of (26) so it is difficult to know a priori whether only a few of the four independent solutions in (25) are non-negligible in either the inlet or the outlet spans. Just as in the equilibrium problem, such a simplification would enable us to decompose the problem into inlet and outlet problems in which only two unknown parameters are sought at a time. While such a simplification may not always be possible, for physically relevant values of v, ϵ, and δ_o, $\mathrm{Re}[\omega_1] \ll -1$, $1 \ll \mathrm{Re}[\omega_3] \ll \mathrm{Re}[\omega_4]$, and, $\mathrm{Re}[\omega_2] \ll -1$ or $\mathrm{Re}[\omega_2] = O(1)$. This knowledge enables us to decompose the eigenvalue problem into separate inlet and outlet eigensolutions each of which requires at most only two nonlinear solutions for two complex parameters rather than a more difficult single nonlinear solution for four complex parameters.

The Inlet Eigensolution: The inlet eigensolution is found as follows. An initial estimate is made for λ and c_1. At $x = x_o = x'_L + \epsilon/2$, $\tilde{u}$ is approximated by

$$\tilde{u} = c_1e^{\omega_1(x-x'_L)} + e^{\omega_2(x-x'_L)}. \quad (28)$$

Equation (23) is numerically integrated to $x = -1$. The nonlinear equation solver adjusts estimates of λ and c_1 until the boundary conditions at $x = -1$ are satisfied. Then, with λ and c_1 determined, $\tilde{u}$ is approximated by

$$\tilde{u} = c_1e^{\omega_1(x-x'_L)} + e^{\omega_2(x-x'_L)} + c_3e^{\omega_3(x-x'_R)} + c_4e^{\omega_4(x-x'_R)} \quad (29)$$

at $x = x_o = x'_R - \epsilon/2$ and (23) is integrated to $x = 1$. The nonlinear equation solver then determines c_3 and c_4 so that the boundary conditions at $x = 1$ are satisfied. In the case when $\mathrm{Re}[\omega_2] \ll -1$, $\tilde{u}$ is negligible across the bearing (the interval I) so that $c_3 = c_4 = 0$. In this case, the inlet eigensolution decouples from motions of the tape over the bearing and in the outlet span.

The Outlet Eigensolution: For the outlet eigensolution, $\tilde{u}$ is approximated by

$$\tilde{u} = c_3e^{\omega_3(x-x'_R)} + e^{\omega_4(x-x'_R)} \quad (30)$$

Table 1 The first few inlet and outlet eigenvalues for $\epsilon = 0.01$, $v = 0.02$, and $\delta_o = 0.3$

n	Inlet λ_n	Outlet λ_n
1	$-0.134 \pm 5.08i$	$-0.141 \pm 5.10i$
2	$-0.313 \pm 10.3i$	$-0.309 \pm 10.3i$
3	$-0.481 \pm 15.5i$	$-0.467 \pm 15.5i$
4	$-0.632 \pm 20.7i$	$-0.610 \pm 20.8i$
5	$-0.796 \pm 25.9i$	$-0.738 \pm 26.0i$

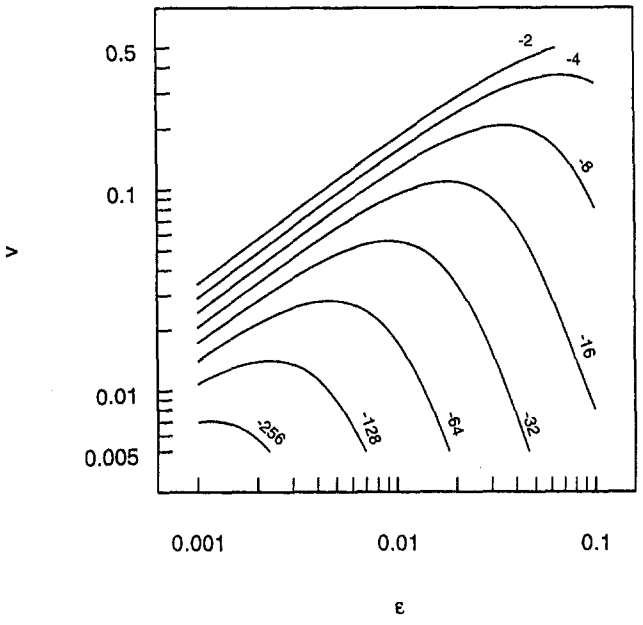

Fig. 2 Contour plot of Re[ω_2] for the inlet eigensolution with minimum |Im[λ]|. $\delta_o = 0.3$.

at $x = x_o = x'_R - \epsilon/2$ and (23) is integrated to $x = 1$. Estimates of λ and c_3 are adjusted until the boundary conditions at $x = 1$ are satisfied. Since $1 \ll \text{Re}[\omega_3] \ll \text{Re}[\omega_4]$, $\tilde{u}$ is negligible across the bearing (the interval I) and throughout the inlet span. Hence the outlet eigensolution decouples from motions in the inlet and over the bearing.

If both $\text{Re}[\omega_3] = O(1)$ and $\text{Re}[\omega_2] = O(1)$, then the inlet and outlet eigensolutions do not decouple and the nonlinear equation solver must find all four unknown parameters simultaneously. This is not the case for the parameter ranges considered here.

The first few inlet and outlet eigenvalues for $\epsilon = 0.01$, $v = 0.02$, and $\delta_o = 0.3$ are shown in Table 1. As noted in previous analyses (Wickert, 1993; Lakshmikumaran and Wickert, 1996), the natural frequencies of these eigensolutions, Im[λ], are close to $n\pi(1 - v^2)/(1 - x'_R)$, $n = 1, 2, 3, \ldots$, the frequencies of an unloaded axially moving string whose span length is $(1 - x'_R)$ (Wickert and Mote, 1990). In addition, these solutions are lightly damped.

Re[λ] and Im[λ] are important foil-bearing vibration characteristics, and previous studies (Wickert, 1993; Lakshmikumaran and Wickert, 1996) have explored variations of system parameters to determine their influence on Re[λ] and Im[λ]. However, while these same studies have identified eigensolutions both with and without coupling between the inlet and outlet spans, the implications of this coupling have not been fully brought to light. Specifically, vibratory motion of decoupled eigensolutions does not affect the film thickness over the recording head and is therefore highly desirable for high fidelity magnetic recording and web handling. Coupled eigensolutions, however, do involve non-negligible variations of the film thickness, which may degrade recording fidelity. *As a result, the magnitudes of* Re[ω_2] *and* Re[ω_3] *may be more important vibration considerations for foil bearing design than* Re[λ] *and* Im[λ].

Figure 2 shows a contour plot of Re[ω_2] for the inlet eigensolution with minimum |Im[ω]| for the parameter ranges $0.001 \leq \epsilon \leq 0.1$ and $0.005 \leq v \leq 0.5$ with $\delta_o = 0.3$. Figure 3 shows contour plots of the inlet Re[λ] and Im[λ] over the same range. The value of Re[ω_2] is most negative, and therefore most decoupled, for small ε and v. For a fixed ε, increases in v increase Re[ω_2]. For example, in the test case $\epsilon = 0.01$ and $v = 0.02$, $\text{Re}[\omega_2] = -62$. Doubling v to 0.04 increases Re[ω_2] to −41, which is more susceptible to span coupling, whereas halving v to 0.01 decreases Re[ω_2] to −82. In the cases explored by Wickert (1993) and Lakshmikumaran and Wickert (1996) $\epsilon = 0.01$ but $v = 0.5$. Here $\text{Re}[\omega_2] = 0.07$, and there is extensive deleterious coupling between the inlet and outlet spans. As shown in Fig. 3, over most of the parameter range explored, $4.5 < \text{Im}[\lambda] < 5.5$, which is close to the unloaded string natural frequency. Damping is improved by increasing ε; however, increases in ε also increase the nominal film thickness across the recording head, which may be detrimental to recording fidelity. Increases in v increase Re[λ] slightly, but Re[λ] < 0 over the full range explored.

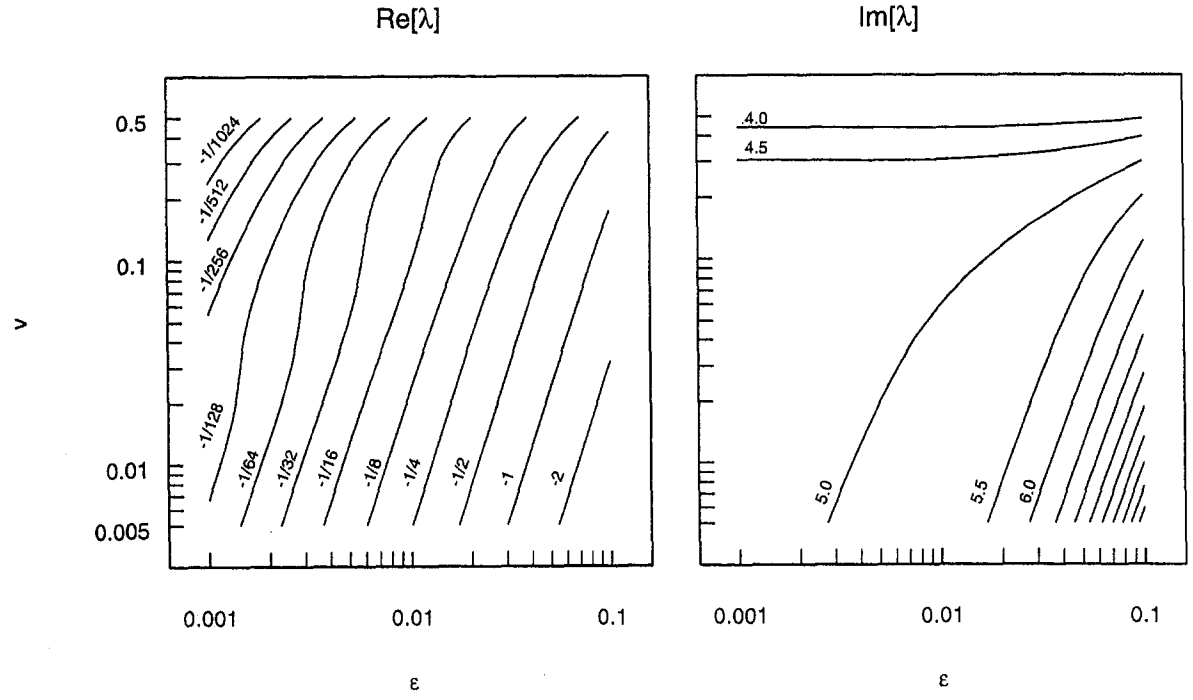

Fig. 3 Contour plots of Re[λ] and Im[λ] for the inlet eigensolution with minimum |Im[λ]|. $\delta_o = 0.3$.

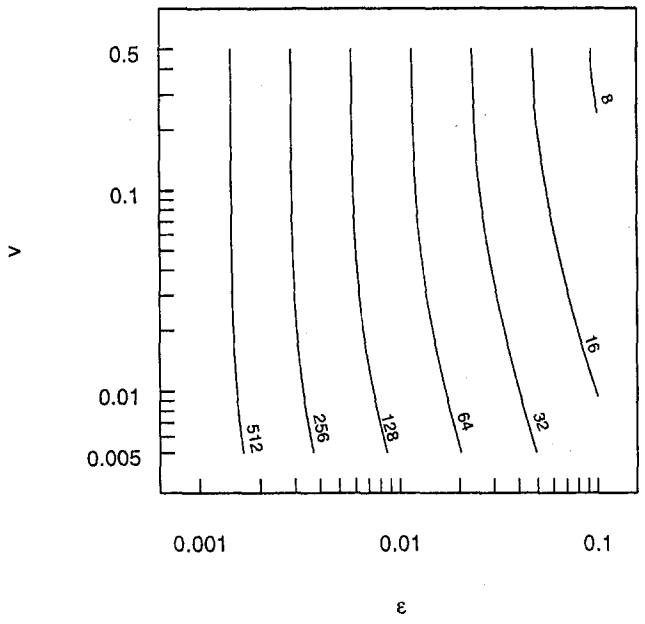

Fig. 4 Contour plot of Re[ω_3] for the outlet eigensolution with minimum |Im[λ]|. $\delta_o = 0.3$.

Figure 4 shows a contour plot of Re[ω_3] and Fig. 5 shows contour plots of Re[λ] and Im[λ] for the outlet eigensolution with the minimum |Im[λ]| over the same ranges as Figs. 3 and 4. Unlike the inlet eigensolution, the value of Re[ω_3] is essentially independent of v, and except for exceptionally large values of ϵ, is always large and positive. Hence the outlet eigensolution is always decoupled in the parameter ranges of interest. Despite this change in coupling, the behavior of the outlet Re[λ] and Im[λ] shown in Fig. 5 is very similar to the behavior of the inlet Re[λ] and Im[λ] shown in Fig. 3.

5 A Possible Design Strategy

The shape of the contour plot in Fig. 2 suggests the following design strategy for foil bearings which is supported by actual values of ϵ and v for existing foil-bearing devices. The first step is to set v by determining the maximum velocity and strength of the foil. Next, with v fixed, ϵ is chosen to minimize the value of Re[ω_2] so as to reducing temporal film thickness variations. For any fixed v, Fig. 2 shows that an optimal ϵ exists that minimizes Re[ω_2]. The only free parameters available at this stage are the foil width and viscosity. Since viscosity is usually difficult to change, this optimization essentially sets the foil width. Finally, with both v and ϵ determined, the radius of curvature of the foil bearing is chosen to achieve the desired film thickness.

This strategy is quite different than that suggested by steady-state analyses that set ϵ and R to achieve a desired film thickness. The fact that existing devices operate at values of ϵ that do, in fact, minimize Re[ω_2] for their specific values of v is only circumstantial support for the strategy. Nevertheless, the strategy proposed will lead to foil bearing designs with well decoupled inlet and outlet vibration responses.

6 Discussion

One of the most compelling features of this analysis is that the decoupling parameters, Re[ω_2] and Re[ω_3], are *exponential* exponents so that the response across the bearing is orders of magnitude smaller than at the tangency points. For design purposes, response amplitude and mode shape can be ignored since their effect will be negligible in a well-decoupled bearing. For example, in the test problem of Stahl, White, and Deckert (1974), Re[ω_2] = −62. This value implies that by a distance of 0.04 into the bearing, the vibratory response is reduced to five percent of its value at the tangency point. By a distance of 0.1, the response is only 0.2 percent.

The roots of the polynomial (26) depend on four parameters: λ, $\bar{h}$, ϵ, and v. However, the results show that λ is well approximated by the unloaded axially moving string eigenvalues, $in\pi(1 - v^2)/(1 - x'_R)$ and $\bar{h} \sim 0.6430$. These approximations enable us to find approximations for ω for different values of ϵ and v without actually solving the eigenvalue problem. For example, the four roots of (26) when $\epsilon = 0.01$, $v = 0.02$, $\bar{h} = 0.6430$, and $\lambda = i\pi(1 - v^2)/(1 - x'_R) = 4.96i$ are compared against the actual roots for both the inlet and outlet eigensolutions in Table 2. The

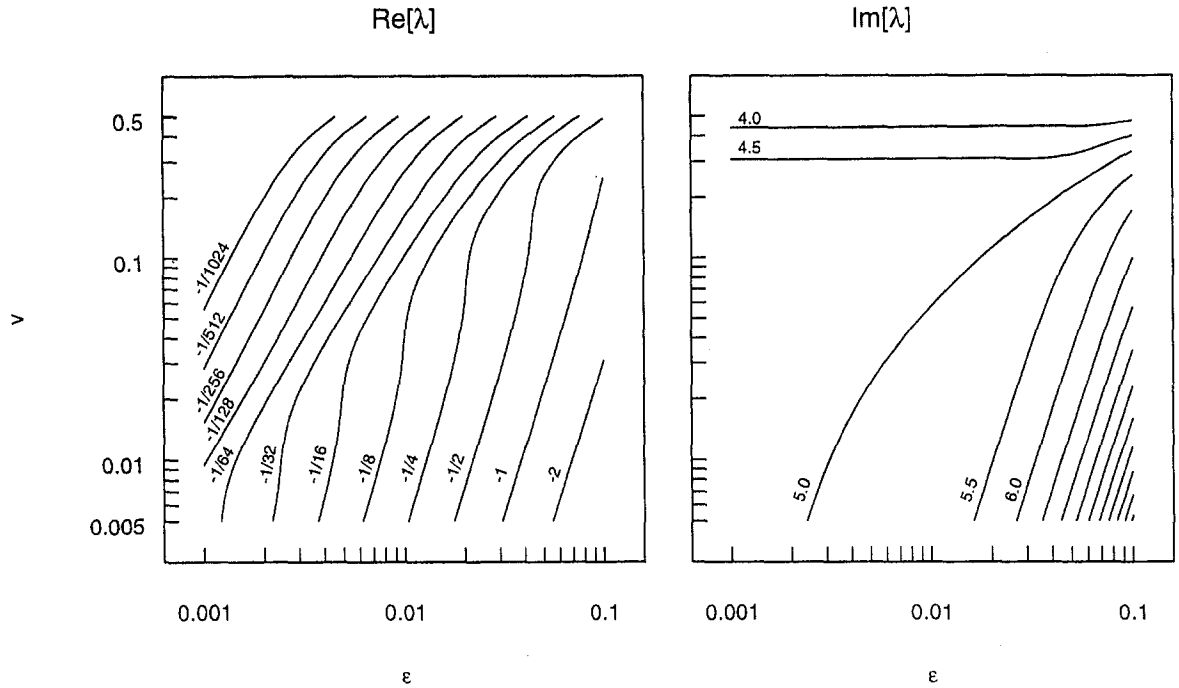

Fig. 5 Contour plots of Re[λ] and Im[λ] for the outlet eigensolution with minimum |Im[λ]|. $\delta_o = 0.3$.

Table 2 Actual inlet and outlet roots ω_n compared with the direct solution of Eq. (26) using $\lambda = 4.96i$ and $\bar{h} = 0.6430$. $\epsilon = 0.01$, $v = 0.02$, $\delta_o = 0.3$.

n	Inlet ω_n	Outlet ω_n	Direct ω_n
1	$-209.4 + 64.8i$	$-209.7 + 64.9i$	$-207.8 + 65.3i$
2	$-62.3 - 178.2i$	$-62.4 - 178.6i$	$-63.1 - 176.2i$
3	$93.1 + 208.3i$	$93.1 + 208.6i$	$93.9 + 207.1i$
4	$178.6 - 94.8i$	$178.9 - 94.8i$	$177.1 - 96.0i$

estimated roots deviate from the actual roots by about one percent in all cases.

In contrast to most current foil bearing studies, we have used the simplest possible model. The effects of air compressibility, tape bending stiffness and slip flow have not been included in order not to divert our attention from the fundamental mechanism of vibration coupling. However, such extensions are straightforward to incorporate. For example, consider the dimensionless axially moving beam model with the compressible Reynolds equation and a slip-flow correction

$$u_{,tt} + 2vu_{,tx} + (v^2 - 1)u_{,xx} + \beta u_{,xxxx} = (1 - v^2)p \quad (31)$$

$$v[h^3(1 + \alpha p)p_{,x}]_{,x} + \epsilon^2\bar{h}\eta v(h^2 p_{,x})_{,x} = 2\epsilon^3[h(1 + \alpha p)]_{,t} + \epsilon^3 v[h(1 + \alpha p)]_{,x} \quad (32)$$

where α, β, and η are dimensionless measures of compressibility, tape bending stiffness, and slip flow, respectively (Wickert, 1993). For this model, the polynomial defining the exponential exponents ω is

$$-\beta v(1 + \alpha + \eta)\epsilon^3\bar{h}^3\omega^6 + v(1 - v^2)(1 + \alpha + \eta)\epsilon^3\bar{h}^3\omega^4 - 2\lambda v^2(1 + \alpha + \eta)\epsilon^3\bar{h}^3\omega^3 - \lambda^2 v(1 + \alpha + \eta)\epsilon^3\bar{h}^3\omega^2 + v(1 - v^2)(1 + \alpha)\omega + 2\lambda(1 - v^2)(1 + \alpha) = 0 \quad (33)$$

which is sixth order because (31) is fourth order instead of second order and there are two boundary conditions on u at $x = \pm 1$. As a result of this increase in order, decoupling occurs when the real parts of three of the roots are large and negative and the real parts of the other three roots are large and positive. For the test problem of Stahl, White, and Deckert (1974), $\alpha = 0.14$, $\beta = 0.00014$, and $\eta = 0.31$. If we let $\bar{h} = 0.6430$ and $\lambda = 4.96i$, we obtain the six roots shown in Table 3. In this case the crucial numbers are $\mathrm{Re}[\omega_3] = -36$ and $\mathrm{Re}[\omega_4] = 43$, which are about half what they are for the simplified model ($\alpha = \beta = \eta = 0$). Hence, in the more complete model, the foil bearing appears to be more susceptible to vibration.

Of the three parameters, α, β, and η, the roots of (33) appear to be most dependent on β. The roots shown in Table 3 are essentially unchanged when $\alpha = \eta = 0$. For $\alpha = \eta = 0$, $\mathrm{Re}[\omega_3] = -19$ for $\beta = 0.01$ and $\mathrm{Re}[\omega_3] = -13$ for $\beta = 0.1$. Consequently, it is anticipated that high tape-bending stiffness may be detrimental to vibration decoupling.

Although comparisons of numerical solution schemes are difficult, the Eshel/Elrod solution algorithm appears to be less computationally expensive in both time and memory than other solutions

Table 3 Direct solution of Eq. (33) using $\lambda = 4.96i$ and $\bar{h} = 0.6430$. $\epsilon = 0.01$, $v = 0.02$, $\alpha = 0.14$, $\beta = 0.00014$, $\eta = 0.31$.

n	ω_n
1	$-147.9 - 42.4i$
2	$-116.9 + 98.8i$
3	$-35.8 - 128.9i$
4	$43.3 + 141.6i$
5	$102.0 - 98.9i$
6	$155.2 + 29.8i$

algorithms. Lakshmikumaran and Wickert (1996) spend considerable effort reducing the number of finite difference nodes required to achieve convergence of their eigenvalue analysis. Such memory considerations are not relevant to the Eshel/Elrod algorithm. The only potential convergence issues in the Eshel/Elrod algorithm are the convergence of the nonlinear equation solver and the accuracy of the numerical integration. For the results presented here, these were not problems. The one serious disadvantage of the Eshel/Elrod algorithm is that it can not be easily extended to two-dimensional problems.

In many modern recording heads there is direct contact between the magnetic tape and the recording head at the asperity level and the recording heads are flat rather than semicircular with negative pressure designs that preload the tape against the head. While the results derived here may be useful for describing the inlet foil bearing dynamics to such a bearing, the simple one-dimensional analysis here cannot account for such two-dimensional effects as cross-tape flow and asperity contact.

7 Conclusions

1 The numerical algorithm first proposed by Eshel and Elrod (1965) for the solution of the one-dimensional equilibrium foil-bearing problem is extended to the solution of the eigenvalue problem describing harmonic linear vibration problem about equilibrium. This solution algorithm appears to be computationally less expensive than previously described algorithms.

2 Analytic analysis of the eigensolutions over the stationary bearing indicates that some eigensolutions describe non-negligible motion of the foil over the bearing as well as in both free spans of the tape, while other eigensolutions describe non-negligible motion only in one free span. The former eigensolutions, herein denoted as coupled eigensolutions, may be undesirable since disturbances in the spans create film thickness variations over the bearing. The later eigensolutions, herein denoted as decoupled eigensolutions, may be desirable since disturbances in the spans do not affect the film.

3 Decoupled vibration modes can be achieved by proper selecting two dimensionless parameters describing the foil-bearing system, herein denoted ϵ and v. A design strategy for selecting these two parameters is described that maximizes decoupling.

4 Excellent approximations for the magnitude of coupling can be made by solving a fourth-order polynomial equation without actually solving the foil bearing problem.

5 The effects of air compressibility, tape bending stiffness, and slip flow can be incorporated into this analysis in a straightforward manner. Of these three effects, tape bending stiffness appears to play the most important role in influencing the magnitude of vibration coupling.

References

Baumeister, H. K., 1963, "Nominal Clearance of the Foil Bearing," *IBM Journal of Research and Development,* Vol. 7, No. 2, Apr., pp. 153–154.

Blok, H., and van Rossum, J. J., 1953, "The Foil Bearing—A New Departure in Hydrodynamic Lubrication," *Lubrication Engineering,* Vol. 9, No. 6, Dec., pp. 316–320.

Eshel, A., and Elrod, Jr., H. G., 1965, "The Theory of the Infinitely Wide, Perfectly Flexible, Self-Acting Foil Bearing," ASME *Journal of Basic Engineering,* Vol. 87, pp. 831–836.

Lacey, C. A., and Talke, F. E., 1990, "A Tightly Coupled Numerical Foil Bearing Solution," *IEEE Transactions on Magnetics,* Vol. 26, pp. 3039–3043.

Lakshmikumaran, A. V., and Wickert, J. A., 1996, "On the Vibration of Coupled Traveling String and Air Bearing Systems," ASME *Journal of Vibration and Acoustics,* Vol. 118, pp. 398–405.

Langlois, W. E., 1963, "The Lightly Loaded Foil Bearing at Zero Angle of Wrap," *IBM Journal of Research and Development,* Vol. 7, No. 2, Apr., pp. 112–116.

Moes, H., 1991, "The Air Gap Between Tape and Drum in a Video Recorder," *Journal of Magnetism and Magnetic Materials,* Vol. 95, pp. 1–13.

Ono, K., Kodama, N., and Michimura, S., 1991, "A New Numerical Analysis

Method for Two-Dimensional Foil Bearing Problems Based on Inverse Analysis Concept," *JSME International,* Series III, Vol. 34, No. 1, pp. 82–90.

Sakai, K., Nagawa, Y., Okuyama, K., Terayama, T., 1996, "Thin Spacing Analysis for Head-Tape Interface," ASME *Journal of Tribology,* Vol. 118, pp. 800–812.

Stahl, K. J., White, J. W., and Deckert, K. L., 1974, "Dynamic Response of Self-Acting Foil Bearings," *IBM Journal of Research and Development,* Vol. 18, pp. 513–520.

Szeri, A. Z., ed., 1980, *Tribology: Friction, Lubrication, and Wear,* McGraw-Hill, New York.

Wickert, J. A., and Mote, Jr., C. D., 1990, "Classical Vibration Analysis of Axially Moving Continua," ASME JOURNAL OF APPLIED MECHANICS, Vol. 57, pp. 738–744.

Wickert, J. A., 1993, "Free Linear Vibration of Self-Pressurized Foil Bearings," *Journal of Vibration and Acoustics,* Vol. 115, pp. 145–151.

Application of the Lie Group Transformations to Nonlinear Dynamical Systems

V. N. Pilipchuk

R. A. Ibrahim
Fellow ASME

Department of Mechanical Engineering,
Wayne State University,
Detroit, MI 48202

This paper describes the theory of Lie group operators in a form suitable for the applied dynamics community. In particular, it is adapted to analyzing the dynamic behavior of nonlinear systems in the presence of different resonance conditions. A key ingredient of the theory is the Hausdorff formula, which is found to be implicitly reproduced in most averaging techniques during the transformation process of the equations of motion. The method is applied to examine the nonlinear modal interaction in a coupled oscillator representing a double pendulum. The system equations of motion are reduced to their simplest (normal) form using operations with the linear differential operators according to Hausdorff's formula. Based on the normal form equations, different types of resonance regimes are considered. It is shown that the energy of the parametrically excited first mode can be regularly (or nonregularly) shared with the other mode due to the internal resonance condition. If the second mode is parametrically excited, its energy is localized and is not transferred to the first mode, even in the presence of internal resonance.

1 Introduction

The quantitative theory of nonlinear vibration has been advanced by new developments in asymptotic expansion techniques originally developed for solving nonlinear differential equations. Most traditional methods are essentially based on perturbation methods or averaging techniques (Giancaglia, 1972; Nayfeh and Mook, 1979). The theory of Poincare normal forms (Nayfeh, 1993), which is similar to averaging techniques, retains resonance terms, since all nonresonance terms are removed from the equations of motion by means of a special coordinate transformation. In this case the Poincare normal forms is qualified as the simplest possible form of the equations of motion. Alternatively, one can use Lie group operators, which can lead to the simplest form of the system equations of motion. The Lie group theory has become a powerful tool for studying differential equations among mathematicians and specialists, and needs to be adapted for dynamicists. Belinfante et al. (1966) presented an overview of the mathematical structure of Lie groups and Lie algebras with applications to nonlinear differential equations. Hori (1966) used Lie series to construct an additional first integral in an autonomous Hamiltonian system. Zhuravlev (1986) developed an algorithm for the asymptotic integration of nonlinear differential equations as monomial Lie group transformations of the phase space into itself.

In this paper we adapt the Lie group operators to transform nonlinear dynamical systems into their simplest form. The method is essentially based on the work of Zhuravlev (1986) and Zhuravlev and Klimov (1988). An essential ingredient of the Lie group operators is the Hausdorff formula, which will be demonstrated in the Appendix. This formula relates the Lie group operators of the original system and the new one, and the operator of coordinate transformation. Zhuravlev (1986) and Zhuravlev and Klimov (1988) made a conjecture that most of averaging techniques reproduce this formula, each time implicitly, during the transformation process. There is no need to do this, since it is reasonable to start the transformation using Hausdorff's relationship.

The theory of Lie groups deals with a set of transformations. In other words, an original dynamical system, $\dot{\mathbf{y}} = \mathbf{f}(\mathbf{y}, \epsilon)$, is transformed into its simplest form, $\dot{\mathbf{z}} = \mathbf{g}(\mathbf{z}, \epsilon)$, by means of a coordinate transformation, $\mathbf{y} \to \mathbf{z}$, which is given as the solution $\mathbf{z} = \mathbf{z}(\mathbf{y}, \epsilon)$ of a third dynamical system, $d\mathbf{z}/d\epsilon = \mathbf{T}(\mathbf{z}, \epsilon)$, $\mathbf{z}|_{\epsilon=0} = \mathbf{y}$, in the same phase space. The selection of the vector-function $\mathbf{T}(\mathbf{z}, \epsilon)$ depends on the desired properties of the transformed system. One of the advantages of the group formulation is that it specifies a general class of near identical transformations. Specifically, one should select the expression $\mathbf{z} = \mathbf{z}(\mathbf{y}, \epsilon)$ among solutions of a dynamical system, but not among all classes of the near identical transformations. Another basic advantage is that all manipulations of the scheme can be done in linear terms, i.e., the monomial Lie group operators. Moreover, the result of transformation in general terms of operators is well known and is given by the Hausdorff formula.

Since the theory of Lie group operators is not well known in the applied dynamics community, in Section 2 we will outline the general scheme of transformations, including normal form coordinates and Lie group operators. The method is demonstrated using a nonlinear system simulating liquid sloshing impact interaction with an elastic support structure (Pilipchuk and Ibrahim, 1997). The example considers different cases of simultaneous parametric and internal resonance conditions.

2 General Scheme of Transformation

2.1 Normal Form Coordinates. In terms of the principal coordinates q_k, a nonlinear dynamical system of n-degrees-of-freedom may be described by a set of $n + 1$ autonomous differential equations written in the standard form

$$\ddot{q}_k + \omega_k^2 q_k = \epsilon F_k(q_1, \ldots, q_{n+1}, \dot{q}_1, \ldots, \dot{q}_{n+1}); \quad k = 1, \ldots, n+1 \quad (1)$$

where a dot denotes differentiation with respect to time t, ϵ is a small parameter, and an external excitation has been replaced by the coordinate q_{n+1}. The functions F_k include all nonlinear terms and possibly parametric excitation terms, and ω_k are the principal mode frequencies.

The Poincare normal form theory deals with sets of first-order

Contributed by the Applied Mechanics Division of THE AMERICAN SOCIETY OF MECHANICAL ENGINEERS for publication in the ASME JOURNAL OF APPLIED MECHANICS.

Discussion on the paper should be addressed to the Technical Editor, Professor Lewis T. Wheeler, Department of Mechanical Engineering, University of Houston, Houston, TX 77204-4792, and will be accepted until four months after final publication of the paper itself in the ASME JOURNAL OF APPLIED MECHANICS.

Manuscript received by the ASME Applied Mechanics Division, Feb. 25, 1998; final revision, Oct. 26, 1998. Associate Technical Editor: A. A. Ferri.

differential equations written in terms of normal form coordinates (Nayfeh, 1993). In this case it is convenient to transform the $(n + 1)$ second-order differential Eqs. (1) into $(n + 1)$ first-order differential equations plus their conjugate set. This can be done by introducing the complex coordinates $y_k(t)$ (Landau and Lifshitz, 1976):

$$y_k = \dot{q}_k + i\omega_k q_k$$

$$q_k = \frac{1}{2i\omega_k}(y_k - \bar{y}_k), \quad \dot{q}_k = \frac{1}{2}(y_k + \bar{y}_k). \tag{2}$$

The physical meaning of these coordinates can be understood by considering the linear case (obtained after setting $\epsilon = 0$). The linear solution of (1) and its first derivative (the velocity) are, respectively,

$$q_k = A_k e^{i\omega_k t} + \bar{A}_k e^{-i\omega_k t}, \quad i^2 = -1$$

$$\dot{q}_k = (A_k e^{i\omega_k t} - \bar{A}_k e^{-i\omega_k t}) i\omega_k$$

where A_k and $\bar{A}_k$ are complex and an overbar denotes conjugate.

The complex coordinates y_k and $\bar{y}_k$ can be viewed as vectors rotating in the complex plane with angular velocities ω_k and $-\omega_k$, respectively,

$$y_k = \dot{q}_k + i\omega_k q_k = 2i\omega_k A_k e^{i\omega_k t}$$

$$\bar{y}_k = -2i\omega_k A_k e^{-i\omega_k t}.$$

Introducing the transformation (2) into the equations of motion (1) gives

$$\ddot{q}_k + \omega_k^2 q_k = \frac{d}{dt}(\dot{q}_k + i\omega_k q_k) - i\omega_k(\dot{q}_k + i\omega_k q_k)$$

$$= \frac{dy_k}{dt} - i\omega_k y_k = \epsilon F_k(y_1, \ldots, y_{n+1}; \bar{y}_1, \ldots, \bar{y}_{n+1})$$

or

$$\dot{y}_k = i\omega_k y_k + \epsilon F_k(y_1, \ldots, y_{n+1}; \bar{y}_1, \ldots, \bar{y}_{n+1}); \quad k = 1, \ldots, n+1 \tag{3}$$

and the corresponding complex conjugate (cc) set of equations

where

$$F_k(y_1, \ldots, y_{n+1}; \bar{y}_1, \ldots, \bar{y}_{n+1}) = F_k(q_1, \ldots, q_{n+1}, \dot{q}_1, \ldots, \dot{q}_{n+1})|_{q_j=(1/2i\omega_j)(y_j-\bar{y}_j), \dot{q}_k=(1/2)(y_k+\bar{y}_k)}. \tag{4}$$

These terms can be represented in the polynomial form

$$F_k = \sum_{|\sigma|=2,3,\ldots} F_k^{\sigma} y_1^{m_1} \ldots y_{n+1}^{m_{n+1}} \bar{y}_1^{l_1} \ldots \bar{y}_{n+1}^{l_{n+1}} \tag{5}$$

where the Taylor coefficients are defined by the partial differentiation of (4) as

$$F_k^{\sigma} = \frac{1}{\sigma!} \frac{\partial^{|\sigma|} F_k}{\partial y_1^{m_1} \ldots \partial y_{n+1}^{m_{n+1}} \partial \bar{y}_1^{l_1} \ldots \partial \bar{y}_{n+1}^{l_{n+1}}} \Bigg|_{y=0}.$$

Here the multi-index notations, $\sigma = \{m_1, \ldots, m_{n+1}, l_1, \ldots, l_{n+1}\}$, $|\sigma| = m_1 + \ldots + m_{n+1} + l_1 + \ldots + l_{n+1}$, $\sigma! = m_1! \ldots m_{n+1}! l_1 \ldots l_{n+1}!$, have been used. Equations (3) correspond to the standard form, which is ready for analysis in terms of Lie group operators.

2.2 Lie Groups Operators. To apply the theory of the Lie groups we rewrite Eqs. (3) in the form

$$\dot{\mathbf{y}} = A\mathbf{y}, \quad A = A_0 + \epsilon A_1 \tag{6}$$

where

$$\mathbf{y} = (y_1, \ldots, y_{n+1}; \bar{y}_1, \ldots, \bar{y}_{n+1})^T$$

and

$$A_0 = \sum_{k=1}^{n+1} i\omega_k y_k \frac{\partial}{\partial y_k} + c.c. \quad \text{and} \quad A_1 = \sum_{k=1}^{n+1} F_k \frac{\partial}{\partial y_k} + c.c. \tag{7}$$

are operators of linear and nonlinear components of the system, respectively.

In order to bring the equations of motion to their simplest form, we introduce the coordinate transformation in the Lie series form

$$\mathbf{y} = e^{-\epsilon U}\mathbf{z} = \mathbf{z} - \epsilon U\mathbf{z} + \frac{\epsilon^2}{2!} U^2\mathbf{z} - \ldots$$

$$\mathbf{y} = (y_1, \ldots, y_{n+1}; \bar{y}_1, \ldots, \bar{y}_{n+1})^T \rightarrow \mathbf{z} = (z_1, \ldots, z_{n+1}; \bar{z}_1, \ldots, \bar{z}_{n+1})^T \tag{8}$$

where the operator of transformation U is represented in the power series form with respect to the small parameter ϵ

$$U = U_0 + \epsilon U_1 + \ldots. \tag{9}$$

The coefficients of this series are

$$U_j = \sum_{k=1}^{n+1} T_{j,k} \frac{\partial}{\partial z_k} + c.c. \tag{10}$$

where

$$T_{j,k} = T_{j,k}(z_1, \ldots, z_{n+1}; \bar{z}_1, \ldots, \bar{z}_{n+1}); \quad j = 0, 1, \ldots; \quad k = 1, \ldots, n+1 \tag{11}$$

are unknown functions to be determined.

One of the advantages of this process is that the inverted coordinate transformation to the form (8) can be easily written as

$$e^{\epsilon U}\mathbf{y} = \mathbf{z} \tag{12}$$

where one simply replaces $\mathbf{z}$ with $\mathbf{y}$ in the operator of transformation, U.

If $\epsilon = 0$, transformation (8) becomes identical, $\mathbf{y} = \exp(0)\mathbf{z} = \mathbf{z}$. In this case Eq. (6) has the simplest linear form and there is no need to transform the system. For $\epsilon \neq 0$ transformation (8) converts the system (6) into the following one:

$$\dot{\mathbf{z}} = B\mathbf{z} \tag{13}$$

where the new operator B is given by the Hausdorff formula (Belinfante, 1966)

$$B = A + \epsilon[A, U] + \frac{\epsilon^2}{2!}[[A, U], U] + \ldots \tag{14}$$

where $[A, U] = AU - UA$ is the commutator of operators A and U.

Substituting the power series expansions for A and U given by relations (6) and (9) into (14) gives

$$B = A_0 + \epsilon(A_1 + [A_0, U_0]) + \epsilon^2\left([A_0, U_1] + [A_1, U_0] + \frac{1}{2!}[[A_0, U_0], U_0]\right) + \ldots. \tag{15}$$

A simple calculation gives

$$B = \sum_{k=1}^{n+1} \{i\omega_k z_k + \epsilon[F_k + (A_0 - i\omega_k)T_{0,k}]\} \frac{\partial}{\partial z_k} + c.c + O(\epsilon^2) \tag{16}$$

where the terms of order ϵ^2 have been ignored, $F_k = F_k|_{y\to z}$, $A_0 = A_0|_{y\to z}$.

The above relationships show that a transformation of the system $\dot{\mathbf{y}} = A\mathbf{y} \to \dot{\mathbf{z}} = B\mathbf{z}$ can be considered in terms of operators $A \to B$. To bring the system into its normal (the simplest) form, one must eliminate as many nonlinear terms as possible from the transformed system such that the system dynamic characteristics are preserved. It follows from (16) that all nonlinear terms of order ϵ would be removed if

$$F_k + (A_0 - i\omega_k)T_{0,k} = 0, \quad \text{and } c.c.$$

Representing the unknown functions in the polynomial form

$$T_{0,k} = \sum_{|\sigma|=2,3,\ldots} T^{\sigma}_{0,k} z_1^{m_1} \ldots z_{n+1}^{m_{n+1}} \bar{z}_1^{l_1} \ldots \bar{z}_{n+1}^{l_{n+1}} \tag{17}$$

and taking into account (5) one obtains the left-hand sides of the above written conditions as

$$F_k + (A_0 - i\omega_k)T_{0,k} = \sum_{|\sigma|=2,3,\ldots} (F^{\sigma}_k + i\Delta^{\sigma}_k T^{\sigma}_{0,k}) z_1^{m_1} \ldots z_{n+1}^{m_{n+1}} \bar{z}_1^{l_1} \ldots \bar{z}_{n+1}^{l_{n+1}}, \quad \text{and } c.c.$$

where

$$\Delta^{\sigma}_k = (m_1 - n_1 - \delta_{1k})\omega_1 + \ldots + (m_{n+1} - l_{n+1} - \delta_{n+1,k})\omega_{n+1}.$$

To reach zeroth coefficient of nonlinear form $z_1^{m_1} \ldots z_{n+1}^{m_{n+1}} \bar{z}_1^{l_1} \ldots \bar{z}_{n+1}^{l_{n+1}}$, one must put

$$T^{\sigma}_{0,k} = i \frac{F^{\sigma}_k}{\Delta^{\sigma}_k}$$

if only $\Delta^{\sigma}_k \neq 0$. If $\Delta^{\sigma}_k = 0$ for definite k and σ then the corresponding nonlinear term cannot be eliminated from the transformed equation since it is qualified as a resonance term.

Finally, the result of transformation is summarized as follows.

The Original Set.

$$\dot{y}_k = i\omega_k y_k + \epsilon \sum_{|\sigma|=2,3,\ldots} F^{\sigma}_k y_1^{m_1} \ldots y_{n+1}^{m_{n+1}} \bar{y}_1^{l_1} \ldots \bar{y}_{n+1}^{l_{n+1}}; \quad k = 1, 2, 3 \tag{18}$$

The Transformation of Coordinates.

$$y_k = z_k - \epsilon \sum_{\substack{|\sigma|=2,3,\ldots \\ \Delta^{\sigma}_k \neq 0}} i \frac{F^{\sigma}_k}{\Delta^{\sigma}_k} z_1^{m_1} \ldots z_{n+1}^{m_{n+1}} \bar{z}_1^{l_1} \ldots \bar{z}_{n+1}^{l_{n+1}} + O(\epsilon^2) \tag{19}$$

The Transformed Set.

$$\dot{z}_k = i\omega_k z_k + \epsilon \sum_{\substack{|\sigma|=2,3,\ldots \\ \Delta^{\sigma}_k = 0}} F^{\sigma}_k z_1^{m_1} \ldots z_{n+1}^{m_{n+1}} \bar{z}_1^{l_1} \ldots \bar{z}_{n+1}^{l_{n+1}} + O(\epsilon^2) \tag{20}$$

This is the normal form of the system, and the summation in this form is much simpler than the one in the original set (18). The summation in (20) contains only those terms that give rise to resonance while the first term on the right-hand side stands for the fast component of the motion. The fast component of the motion can be extracted by introducing the complex amplitudes $a_k(\tau)$ as

$$z_k = a_k(\tau) \exp(i\omega_k \tau). \tag{21}$$

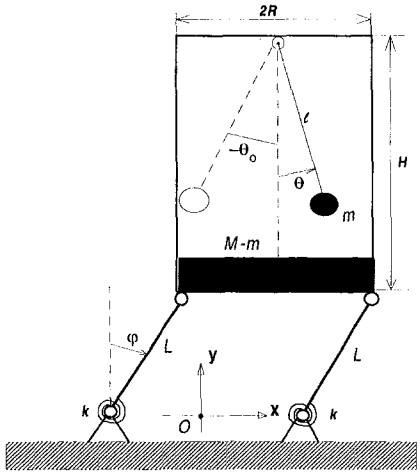

Fig. 1 Schematic diagram of the model

Substituting (21) into (20) and taking into account the resonance condition, $\Delta^{\sigma}_k = 0$, gives

$$\dot{a}_k = \epsilon \sum_{\substack{|\sigma|=2,3,\ldots \\ \Delta^{\sigma}_k = 0}} F^{\sigma}_k a_1^{m_1} \ldots a_{n+1}^{m_{n+1}} \bar{a}_1^{l_1} \ldots \bar{a}_{n+1}^{l_{n+1}} + O(\epsilon^2). \tag{22}$$

Note that relationships (19)–(22) have been obtained under no concrete assumptions regarding the type of resonance. In order to promote our understanding of this method we consider a nonlinear coupled two-degree-of-freedom system under parametric excitation.

3 Application

3.1 System Modeling. In this section we consider a nonlinear system considered previously by Pilipchuk and Ibrahim (1997). The system can be viewed as the simplest model of liquid free surface in a moving container interacting with the dynamics of an elastic support structure. The sloshing part of the liquid free surface can be replaced by an equivalent mechanical model in the form of simple pendulums or mass spring systems (Abramson, 1966). The first asymmetric sloshing mode is the most significant which can be modeled by one simple pendulum. Other modes have less influence on the dynamic characteristics of the system dynamics. The mathematical model can be developed by considering a simple pendulum suspended in a rigid container. The container is supported by four massless rods of length L which are restrained by four torsional springs k at the base, as shown in Fig. 1. The system is subjected to parametric excitation $F_y(t)$. Let M be the total mass of the container, including the liquid, and m be the equivalent sloshing mass of the first asymmetric mode of the liquid free surface. The fluid free surface is modeled as a pendulum of mass m and length l. Following Pilipchuk and Ibrahim (1997), the interaction between the pendulum and the tank walls will be phenomenologically described by a special potential field of interaction, which is very weak in the region $|\theta| < \theta_0$, but grows rapidly in the neighborhood of the points $\theta = \pm\theta_0$. The corresponding force of interaction is

$$F_i = b\left(\frac{\theta}{\theta_0}\right)^3 \tag{23}$$

where b is a positive constant parameter.

For a small magnitude of the angle θ_0, i.e., $\theta_0 = \epsilon \ll \pi/2$, the interaction between the pendulum and the tank will be observed in a small region of the angle coordinate, where $\theta \sim \epsilon$. In this region the relationships $\sin\theta = \theta + O(\epsilon^3)$ and $\cos\theta = 1 + O(\epsilon^2)$ hold. Thus the geometrical nonlinear terms are of orders $O(\epsilon^2)$, $O(\epsilon^3)$,

at the same time the nonlinearity of the pendulum motion is $(\theta/\theta_0)^3 = O(1)$.

It follows that one can keep the nonlinear terms but linearize the rest of the terms in the equations of motion derived by Pilipchuk and Ibrahim (1997). As a result, one obtains

$$l^2 m \frac{d^2\theta}{dt^2} + lLm \frac{d^2\varphi}{dt^2} + lm[g - F_y(t)]\theta + b\left(\frac{\theta}{\theta_0}\right)^3 = 0 \quad (24)$$

$$lLm \frac{d^2\theta}{dt^2} + L^2 M \frac{d^2\varphi}{dt^2} - LM[g - F_y(t)]\varphi + k\varphi = 0. \quad (25)$$

It is convenient to introduce the following dimensionless variables

$$x_1 = \frac{\theta}{\theta_0}, \quad x_2 = \frac{\varphi}{\theta_0}, \quad \tau = \sqrt{\frac{g}{l}}\, t, \quad f_y(\tau) = \frac{F_y(t)}{g} \quad (26)$$

$$\epsilon = \frac{b}{Lmg\theta_0}, \quad \lambda = \frac{l}{L}, \quad \mu = \frac{m}{M}, \quad \nu = \frac{\omega_L}{\omega_l} = \sqrt{\lambda\left(\frac{k}{MLg} - 1\right)}$$

$$\omega_L^2 = \frac{k - LMg}{ML^2}, \quad \omega_l^2 = \frac{g}{l}. \quad (27)$$

The parameter ν is important for future analysis. It denotes the ratio of two local frequencies, i.e., the frequency of the tank ω_L in the absence of the pendulum motion, and the frequency of the pendulum ω_l when the tank is standing still. The frequency ω_l is equivalent to the fluid first antisymmetric sloshing mode and depends on the tank geometry and fluid depth (see, for example, Abramson, 1966).

Taking into account the notations listed in (26) and (27), the equations of motion are written in the matrix form

$$\mathbf{M}\ddot{\mathbf{x}} + [\mathbf{K} + f_y(\tau)\mathbf{Q}]\mathbf{x} + \epsilon\mathbf{N}(\mathbf{x}) = \mathbf{0} \quad (28)$$

where a dot denotes a derivative with respect to the nondimensional time parameter τ, $\mathbf{x} = (x_1\ x_2)^T$, and

$$\mathbf{M} = \begin{pmatrix} \lambda & 1 \\ 1 & 1/(\lambda\mu) \end{pmatrix}, \quad \mathbf{K} = \begin{pmatrix} \lambda & 0 \\ 0 & \nu^2/(\lambda\mu) \end{pmatrix},$$

$$\mathbf{Q} = \begin{pmatrix} -\lambda & 0 \\ 0 & \dfrac{1}{\mu} \end{pmatrix}, \quad \mathbf{N}(\mathbf{x}) = \begin{pmatrix} x_1^3 \\ 0 \end{pmatrix}.$$

It is convenient to analyze the problem in terms of the principal coordinates of the linear system, when $\epsilon = 0$ and $f_y(\tau) \equiv 0$,

$$\mathbf{M}\ddot{\mathbf{x}} + \mathbf{K}\mathbf{x} = \mathbf{0}. \quad (29)$$

The principal coordinates are determined by solving the eigenvalue problem

$$\mathbf{K}\mathbf{H} = \omega^2\mathbf{M}\mathbf{H} \quad (30)$$

where $\mathbf{x} = \mathbf{H}\cos\omega\tau$, $\mathbf{H} = \binom{h1}{h2}$ and the natural frequencies, ω, are given by the solution of the characteristic equation

$$\det(\mathbf{K} - \omega^2\mathbf{M}) = 0 \Rightarrow \omega^4 - \frac{1 + \nu^2}{1 - \mu}\omega^2 + \frac{\nu^2}{1 - \mu} = 0. \quad (31)$$

The two normal mode frequencies and their eigenvectors are

$$\omega_1^2 = \frac{1 + \nu^2 - \sqrt{(1 - \nu^2)^2 + 4\mu\nu^2}}{2(1 - \mu)}, \quad h_2 = \frac{\lambda\mu\omega_1^2}{\nu^2 - \omega_1^2} h_1$$

in-phase mode (32)

$$\omega_2^2 = \frac{1 + \nu^2 + \sqrt{(1 - \nu^2)^2 + 4\mu\nu^2}}{2(1 - \mu)}, \quad h_2 = \frac{\lambda\mu\omega_2^2}{\nu^2 - \omega_2^2} h_1$$

out-of-phase mode. (33)

The principal coordinates q_1, q_2 are introduced as

$$\mathbf{x}(\tau) = \hat{\mathbf{H}}_1 q_1(\tau) + \hat{\mathbf{H}}_2 q_2(\tau)$$

where

$$\hat{\mathbf{H}}_k = \mathbf{H}_k/r_k, \quad r_k = \sqrt{\mathbf{H}_k^T\mathbf{M}\mathbf{H}_k}, \quad \hat{\mathbf{H}}_k = \begin{pmatrix} H_{k1} \\ H_{k2} \end{pmatrix}; \quad k = 1, 2$$

are normalized vectors satisfying the orthogonality conditions

$$\hat{\mathbf{H}}_k^T\mathbf{M}\hat{\mathbf{H}}_j = \delta_{kj} \quad (k = 1, 2; j = 1, 2) \quad (34)$$

where δ_{kj} is the Kronecker's symbol.

Now consider the external excitation to be small and harmonic with respect to time, i.e., $f_y(\tau) = \epsilon q_3(\tau)$, where $q_3(\tau)$ is the solution of the harmonic oscillator with a natural frequency ω_3. In terms of the principal coordinates, the system equations of motion may be written in the standard autonomous form

$$\ddot{q}_1 + \omega_1^2 q_1 = -\epsilon[(Q_{11}q_1 + Q_{12}q_2)q_3 + N_1(q_1, q_2)]$$

$$\ddot{q}_2 + \omega_2^2 q_2 = -\epsilon[(Q_{21}q_1 + Q_{22}q_2)q_3 + N_2(q_1, q_2)]$$

$$\ddot{q}_3 + \omega_3^2 q_3 = 0 \quad (35)$$

where $Q_{kj} = \hat{\mathbf{H}}_k^T\mathbf{Q}\hat{\mathbf{H}}_j$, $N_k = \hat{\mathbf{H}}_k^T\mathbf{N}(\hat{\mathbf{H}}_1 q_1(\tau) + \hat{\mathbf{H}}_2 q_2(\tau))$.

This set of equations corresponds to the standard form (1), with $n = 2$ and it is transformed to (3) with

$$F_1 = -(Q_{11}q_1 + Q_{12}q_2)q_3 - N_1(q_1, q_2)|_{q_j = (1/2i\omega_j)(y_j - \bar{y}_j)}$$

$$F_2 = -(Q_{21}q_1 + Q_{22}q_2)q_3 - N_2(q_1, q_2)|_{q_j = (1/2i\omega_j)(y_j - \bar{y}_j)}$$

$$F_3 = 0. \quad (36)$$

Note that the third Eq. (35) is linear and basically is not transformed during the future transformation. To illustrate the general scheme we consider the model with cubic nonlinearity in the neighborhood of three types of resonance conditions.

4.1 Parametric Excitation of the In-Phase Mode. Consider the case when the natural frequencies of the system and the excitation frequency satisfy the resonance conditions

Internal resonance, $\omega_2 = 3\omega_1$, and

parametric resonance: $\omega_3 = 2\omega_1$. (37)

Substituting the expressions of the natural frequencies (32) and (33) into $\omega_2 = k\omega_1$ gives the resonance condition in terms of the system parameters ν and μ as

$$\nu^2 = \frac{1 + k^4 - \mu(1 + k^2)^2 + \sqrt{[1 + k^4 - \mu(1 + k^2)^2]^2 - 4k^4}}{2k^2},$$

$$0 < \mu \le \left(\frac{1 - k^2}{1 + k^2}\right)^2. \quad (38)$$

Under conditions (37), Eqs. (22) take the form

$$\dot{a}_1 = \frac{\epsilon}{24\omega_1^3}[i(9H_{11}^4|a_1|^2 + 2H_{11}^2H_{21}^2|a_2|^2)a_1 - \underbrace{3Q_{11}\omega_1\bar{a}_1 a_3}_{\text{Parametric}}$$

$$- \underbrace{Q_{12}\omega_1 a_2\bar{a}_3}_{\text{Parametric+Internal}} - \underbrace{3iH_{11}^3H_{21}\bar{a}_1^2 a_2}_{\text{Internal}}] \quad (39)$$

$$\dot{a}_2 = \frac{\epsilon}{72\omega_1^3}[i(18H_{11}^2H_{21}^2|a_1|^2 + H_{21}^4|a_2|^2)a_2$$

$$+ \underbrace{9Q_{21}\omega_1 a_1 a_3}_{\text{Parametric+Internal}} - \underbrace{9iH_{11}^3H_{21}a_1^3}_{\text{Internal}}] \quad (40)$$

$$\dot{a}_3 = 0 \quad (41)$$

where the type resonance is written under those terms which produce the indicated resonance condition. The combined label

"parametric + internal" is the result of cross-coupling due to parametric excitation, such as $Q_{12}q_2q_3$ and $Q_{21}q_1q_3$ in Eqs. (35). In the absence of internal resonance conditions these terms will not appear in Eqs. (39) and (40). Introducing the polar coordinate transformation

$$a_k = \rho_k(\tau)\,\exp[i\varphi_k(\tau)]; \quad k = 1, 2, 3 \tag{42}$$

and substituting these expressions into (39)–(41) gives

$$\dot{\rho}_3 = 0, \quad \dot{\varphi}_3 = 0$$

and, taking $\rho_3(\tau) = \rho_3 = \text{const}$, $\varphi_3 = 0$,

$$\dot{\rho}_1 = -\frac{\epsilon}{24\omega_1^3}[\underbrace{3Q_{11}\omega_1\rho_1\rho_3\cos 2\varphi_1}_{\text{Parametric}} + \underbrace{Q_{12}\omega_1\rho_2\rho_3\cos(\varphi_1-\varphi_2)}_{\text{Parametric+Internal}} + \underbrace{3H_{11}^3H_{21}\rho_1^2\rho_2\sin(3\varphi_1-\varphi_2)}_{\text{Internal}}]$$

$$\dot{\varphi}_1 = \frac{\epsilon}{24\omega_1^3}[9H_{11}^4\rho_1^2 + 2H_{11}^2H_{21}^2\rho_2^2 + \underbrace{3Q_{11}\omega_1\rho_3\sin 2\varphi_1}_{\text{Parametric}} + \underbrace{Q_{12}\omega_1\frac{\rho_2\rho_3}{\rho_1}\sin(\varphi_1-\varphi_2)}_{\text{Parametric+Internal}} - \underbrace{3H_{11}^3H_{21}\rho_1\rho_2\cos(3\varphi_1-\varphi_2)}_{\text{Internal}}]$$

$$\dot{\rho}_2 = \frac{\epsilon}{72\omega_1^3}[\underbrace{9Q_{21}\omega_1\rho_1\rho_3\cos(\varphi_1-\varphi_2)}_{\text{Parametric+Internal}} + \underbrace{9H_{11}^3H_{21}\rho_1^3\sin(3\varphi_1-\varphi_2)}_{\text{Internal}}]$$

$$\dot{\varphi}_2 = \frac{\epsilon}{72\omega_1^3}[18H_{11}^2H_{21}^2\rho_1^2 + H_{21}^4\rho_2^2 + \underbrace{9Q_{21}\omega_1\frac{\rho_1\rho_3}{\rho_2}\sin(\varphi_1-\varphi_2)}_{\text{Parametric+Internal}} - \underbrace{9H_{11}^3H_{21}\frac{\rho_1^3}{\rho_2}\cos(3\varphi_1-\varphi_2)}_{\text{Internal}}]. \tag{43}$$

Taking into account expressions (21), (42), (2) one can write

$$z_k = \rho_k(\tau)\,\exp\{i[\omega_k\tau + \varphi_k(\tau)]\}$$

$$q_k = \frac{1}{2i\omega_k}(y_k - \bar{y}_k) = \frac{1}{2i\omega_k}(z_k - \bar{z}_k) + O(\epsilon)$$

$$= \frac{\rho_k(\tau)}{\omega_k}\sin[\omega_k\tau + \varphi_k(\tau)] + O(\epsilon); \quad k = 1, 2, 3.$$

Recall that the third equation for q_3 plays an auxiliary role and is not transformed during the transformation. The external force is defined now as $f_y(\tau) = \epsilon q_3(\tau) = \epsilon(\rho_3/\omega_3)\sin\omega_3\tau$.

In the neighborhood of the system equilibrium position the nonlinearity plays no significant role. In order to describe the dynamics of the system in close vicinity to the equilibrium, one can drop the system nonlinearities. This can be done in terms of Eqs. (43) by setting all $H_{kj} = 0$. In this case the set of equations admits an analytical family of solutions, if

$$2\varphi_1 = m\pi; \quad m = 0, 1, 2, \ldots \quad \text{and}$$

$$\varphi_1 - \varphi_2 = n\pi; \quad n = 0, 1, 2, \ldots. \tag{44}$$

Substituting these stationary phases into (43) gives the linear set of equations

$$\dot{\rho}_1 = -\frac{\epsilon\rho_3}{24\omega_1^2}[3(-1)^m Q_{11}\rho_1 + (-1)^n Q_{12}\rho_2]$$

$$\dot{\rho}_2 = (-1)^n\frac{\epsilon\rho_3}{8\omega_1^2}Q_{21}\rho_1. \tag{45}$$

The solution can be written as

$$\rho_1 = C_1\exp(r_1\tau) + C_2\exp(r_2\tau)$$

$$\rho_2 = (-1)^n\frac{\epsilon\rho_3}{8\omega_1^2}Q_{21}\left[\frac{C_1}{r_1}\exp(r_1\tau) + \frac{C_2}{r_2}\exp(r_2\tau)\right] \tag{46}$$

where

$$r_{1,2} = -\frac{\epsilon Q_{11}\rho_3}{16\omega_1^2}\left[(-1)^m \pm \sqrt{1 - \frac{4Q_{12}Q_{21}}{3Q_{11}^2}}\right]. \tag{47}$$

Both r_1 and r_2 are real and positive for even integer m and for all $0 < \mu < ((1-k^2)/(1+k^2))^2$, $k = (\omega_2/\omega_1)$ (see (38)). Apparently for odd m, both r_1 and r_2 are real and negative. These two cases correspond to exponentially unstable and stable regimes with stationary phases, respectively. In the presence of nonlinearity, the exponentially growing amplitudes will reach bounded values. Figures 2(*a*) and 2(*b*) give different time-history records of the response amplitudes, as obtained by numerically integrating Eqs. (43) for two different values of parametric excitation amplitude. Both records indicate that the response of the two modes does not achieve any steady state. It is also seen that the first mode which is parametrically excited transfers energy to the second mode through nonlinear coupling. This energy transfer takes place when the two modes are in internal resonance. It is obvious that the simultaneous presence of internal and parametric resonances is the main source of the unsteady state of the system response in the present case. If one of these resonance conditions exists alone in the absence of the other, one may get a steady-state response.

4.2 Parametric Excitation of the Out-of-Phase Mode. This case deals with parametric excitation of the second mode subject to the resonance conditions:

$$\text{Internal resonance: } \omega_2 = 3\omega_1, \qquad \text{parametric resonance: } \omega_3 = 2\omega_2. \tag{48}$$

Under these conditions Eqs. (22) take the form

$$\dot{a}_1 = \frac{i\epsilon}{24\omega_1^3}H_{11}^2[\underbrace{(9H_{11}^2|a_1|^2 + 2H_{21}^2|a_2|^2)a_1 - 3H_{11}H_{21}\bar{a}_1^2a_2}_{\text{Internal}}] \tag{49}$$

$$\dot{a}_2 = \frac{\epsilon}{72\omega_1^3}[i(18H_{11}^2H_{21}^2|a_1|^2 + H_{21}^4|a_2|^2)a_2 - \underbrace{Q_{22}\omega_1\bar{a}_2a_3}_{\text{Parametric}} - \underbrace{9iH_{11}^3H_{21}a_1^3}_{\text{Internal}}] \tag{50}$$

$$\dot{a}_3 = 0. \tag{51}$$

Introducing variables $\{\rho_k(t), \varphi_k(t)\}$ (42) one obtains

$$\dot{\rho}_1 = \frac{\epsilon}{8\omega_1^3}H_{11}^3H_{21}\rho_1^2\rho_2\sin(\varphi_2 - 3\varphi_1)$$

$$\dot{\varphi}_1 = \frac{\epsilon}{24\omega_1^3}H_{11}^2[9H_{11}^2\rho_1^2 + 2H_{21}^2\rho_2^2 - \underbrace{3H_{11}H_{21}\rho_1\rho_2\cos(\varphi_2 - 3\varphi_1)}_{\text{Internal}}]$$

$$\dot{\rho}_2 = \frac{\epsilon}{72\omega_1^3}[\underbrace{9H_{11}^3H_{21}\rho_1^3\sin(3\varphi_1 - \varphi_2)}_{\text{Internal}} - \underbrace{Q_{22}\omega_1\rho_2\rho_3\cos 2\varphi_2}_{\text{Parametric}}]$$

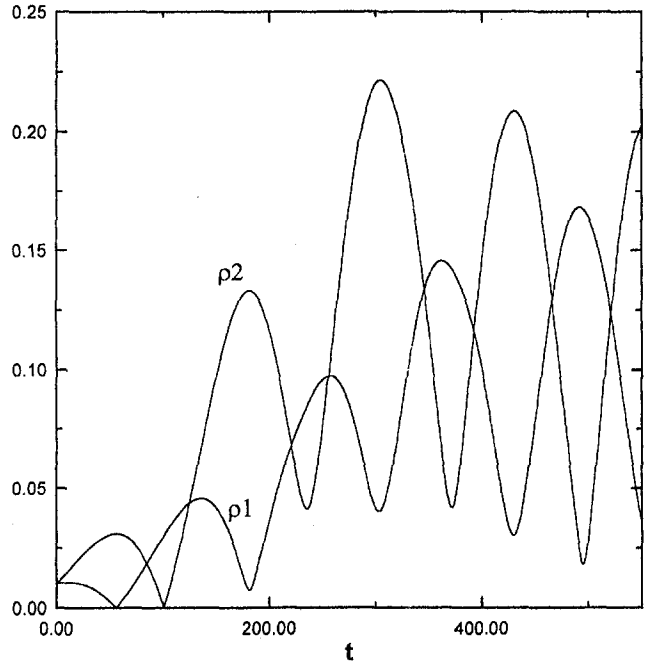

Fig. 2(*a*) Excitation amplitude $\rho_3 = 0.5$, $\varphi_3 = 0$

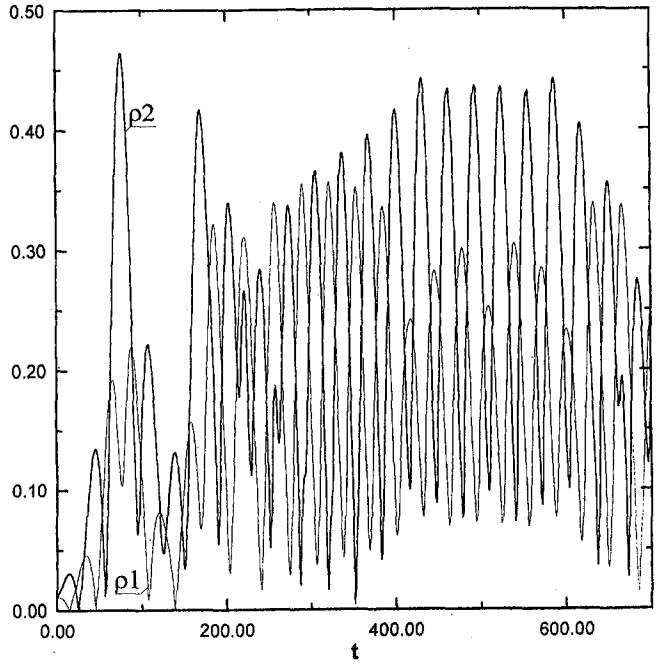

Fig. 2(*b*) Excitation amplitude $\rho_3 = 2.0$, $\varphi_3 = 0$

Fig. 2 Response time-history records under resonance conditions $\omega_2 = 3\omega_1$, and $\omega_3 = 2\omega_1$ for $\omega_1 = 0.81829$, $\omega_2 = 2.63487$, $\epsilon = 0.53$, $\lambda = 0.25$, $\mu = 0.576$, $\nu = 1.50689$, $\rho_3 = 0.5$, $\varphi_3 = 0$. Initial conditions: $\rho_1 = \rho_2 = 0.01$, $\varphi_1 = \varphi_2 = 0.01$.

$$\dot{\varphi}_2 = \frac{\epsilon}{72\omega_1^3}\Bigg[18H_{11}^2H_{21}^2\rho_1^2 + H_{21}^4\rho_2^2 - \underbrace{9H_{11}^3H_{21}\frac{\rho_1^3}{\rho_2}\cos(3\varphi_1 - \varphi_2)}_{\text{Internal}} + \underbrace{Q_{22}\omega_1\rho_3\sin 2\varphi_2}_{\text{Parametric}}\Bigg]$$

$$\dot{\rho}_3 = 0, \quad \dot{\varphi}_3 = 0. \tag{52}$$

If cubic nonlinearities are neglected, these equations are reduced to the following form:

$$\dot{\rho}_1 = 0, \quad \dot{\varphi}_1 = 0$$

$$\dot{\rho}_2 = -\frac{\epsilon Q_{22}}{72\omega_1^2}\rho_2\rho_3\cos 2\varphi_2, \quad \dot{\varphi}_2 = \frac{\epsilon Q_{22}}{72\omega_1^2}\rho_3\sin 2\varphi_2.$$

These equations indicate that the two modes are uncoupled and that the second mode accumulates energy due to parametric resonance. The second-mode amplitude and phase are obtained by separation of variables, and are given by the expressions

$$\rho_2 = \frac{C_1}{\sqrt{\sin 2\varphi_2}}, \quad \tan\varphi_2 = C_2\exp\left(\frac{\epsilon Q_{22}\rho_3}{36\omega_1^2}\tau\right) \tag{53}$$

where C_1 and C_2 are constants. In this case the response is unimodal, governed mainly by the second-mode response, which does not transfer energy to the first mode. Figure 3 shows a sample of the time-history record as obtained by numerical integration of Eqs. (52). It is seen that the solution for the amplitudes is periodic bounded and achieves a steady state. On the other hand the linear solution reveals that the amplitude is unbounded since as $\tau \to \infty$, $\varphi_2 \to \pi/2$, and $\rho_2 \to \infty$.

4.3 "Mixed" Parametric Excitation. This case considers parametric excitation of both modes under internal and combination parametric resonance conditions of the following form:

$$\text{Internal resonance: } \omega_2 = 3\omega_1,$$

$$\text{parametric resonance: } \omega_3 = \omega_1 + \omega_2.$$

The normal form complex equations are obtained as

$$\dot{a}_1 = \frac{\epsilon}{48\omega_1^3}\Big[2ia_1H_{11}^2(9H_{11}^2|a_1|^2 + 2H_{21}^2|a_2|^2) - \underbrace{6iH_{11}^3H_{21}\bar{a}_1^2a_2}_{\text{Internal}} - \underbrace{Q_{12}\omega_1\bar{a}_2a_3}_{\text{Parametric}}\Big]$$

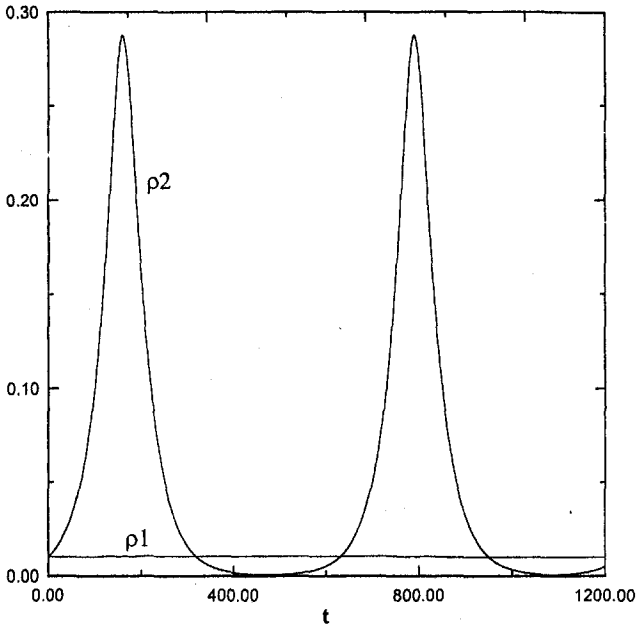

Fig. 3 Response time-history record under resonance conditions $\omega_2 = 3\omega_1$, and $\omega_3 = 2\omega_2$ for $\omega_1 = 0.81829$, $\omega_2 = 2.63487$, $\epsilon = 0.53$, $\lambda = 0.25$, $\mu = 0.576$, $\nu = 1.50689$, $\rho_3 = 2.0$, $\varphi_3 = 0$. Initial conditions: $\rho_1 = \rho_2 = 0.01$, $\varphi_1 = \varphi_2 = 0.01$.

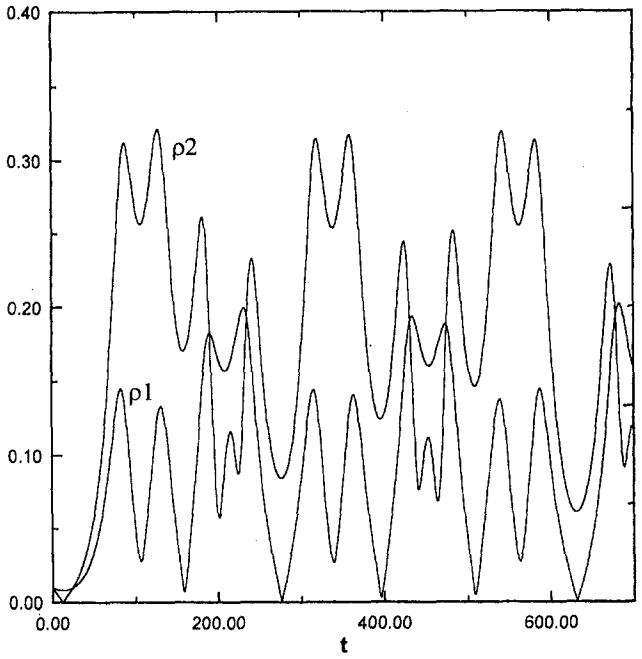

Fig. 4(*a*) Response time-history record under resonance conditions $\omega_2 = 3\omega_1$, and $\omega_3 = \omega_1 + \omega_2$ for $\omega_1 = 0.81829$, $\omega_2 = 2.63487$, $\epsilon = 0.53$, $\lambda = 0.25$, $\mu = 0.576$, $\nu = 1.50689$, $\rho_3 = 2.0$, $\varphi_3 = 0$, and initial conditions: $\rho_1 = \rho_2 = 0.01$, $\varphi_1 = \varphi_2 = 0.01$.

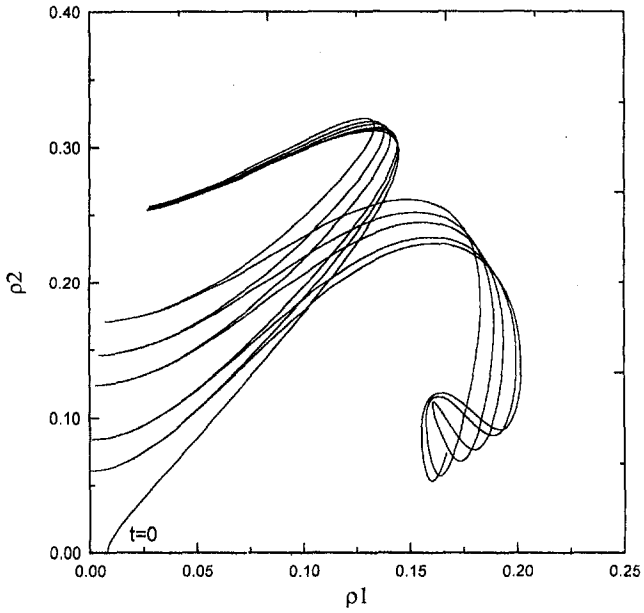

Fig. 4(*b*) Trajectory of the system on the plane of amplitudes

$$\dot{a}_2 = -\frac{\epsilon}{144\omega_1^3}[-2ia_2H_{21}^2(18H_{11}^2|a_1|^2 + H_{21}^2|a_2|^2) + \underset{\text{Internal}}{18iH_{11}^3H_{21}a_1^3} + \underset{\text{Parametric}}{9Q_{21}\omega_1\bar{a}_1a_3}]$$

$$\dot{a}_3 = 0. \tag{54}$$

It is seen that the parametric excitation appears as a cross coupling between the two modes, while the internal resonance is a result of nonlinear coupling. Introducing the polar coordinates $\{\rho_k(t), \varphi_k(t)\}$ (42) gives

$$\dot{\rho}_1 = -\frac{\epsilon\rho_2}{48\omega_1^3}[\underset{\text{Internal}}{6H_{11}^3H_{21}\rho_1^2\sin(3\varphi_1 - \varphi_2)} + \underset{\text{Parametric}}{Q_{12}\omega_1\rho_3\cos(\varphi_1 + \varphi_2)}]$$

$$\dot{\varphi}_1 = \frac{\epsilon}{48\rho_1\omega_1^3}[18H_{11}^4\rho_1^3 + 4H_{11}^2H_{21}^2\rho_1\rho_2^2 - \underset{\text{Internal}}{6H_{11}^3H_{21}\rho_1^2\rho_2\cos(3\varphi_1 - \varphi_2)} + \underset{\text{Parametric}}{Q_{12}\omega_1\rho_2\rho_3\sin(\varphi_1 + \varphi_2)}]$$

$$\dot{\rho}_2 = -\frac{\epsilon\rho_1}{16\omega_1^3}[\underset{\text{Internal}}{-2H_{11}^3H_{21}\rho_1^2\sin(3\varphi_1 - \varphi_2)} + \underset{\text{Parametric}}{Q_{21}\omega_1\rho_3\cos(\varphi_1 + \varphi_2)}]$$

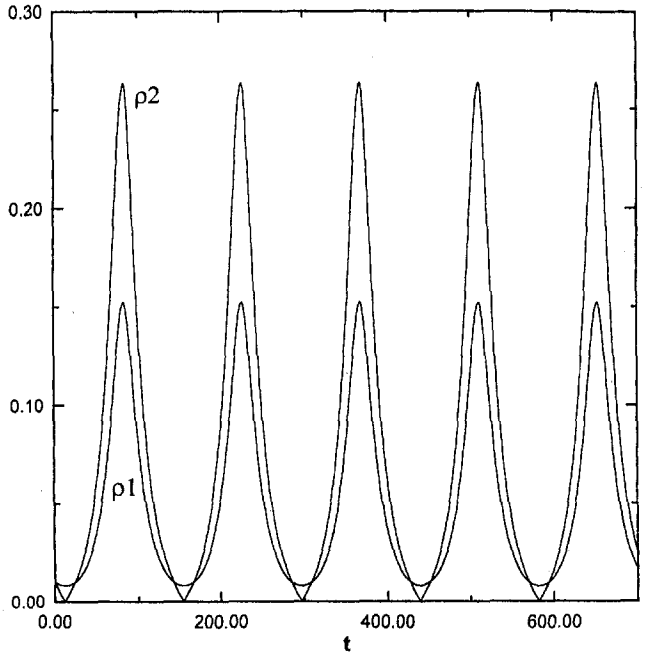

Fig. 5(*a*) Response time-history record for the case of Fig. 4 in the absence of internal resonance

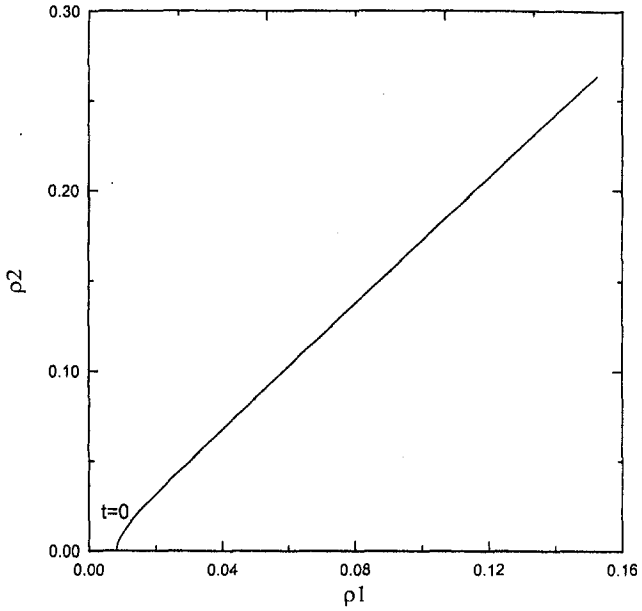

Fig. 5(*b*) Trajectory of the system on the plane of amplitudes

$$\dot{\varphi}_2 = \frac{\epsilon}{144\rho_2\omega_1^3}[36H_{11}^2H_{21}^2\rho_1^2\rho_2 + 2H_{21}^4\rho_2^3 - 18H_{11}^3H_{21}\rho_1^3\cos(3\varphi_1 - \varphi_2) + 9Q_{21}\omega_1\rho_1\rho_3\sin(\varphi_1 + \varphi_2)]$$

Internal — Parametric

$$\dot{\rho}_3 = 0, \quad \dot{\varphi}_3 = 0. \tag{55}$$

In the absence of internal resonance $\omega_2 = 3\omega_1$, all terms marked as "Internal" are dropped. Figure 4(*a*) shows the system response in the time domain in the presence of internal resonance. The response does not achieve a steady state and is nearly quasi-periodic. The corresponding trajectory is shown in Fig. 4(*b*) in the plane of amplitudes. Figures 5(*a*) and 5(*b*) show the system response in the absence of internal resonance in the time and amplitude domains, respectively. It is seen that the response achieves a steady state, as expected. The response in the amplitude domain, Fig. 5(*b*), exhibits a single linear trajectory. It can be seen that in both cases the system accumulates energy due to parametric resonance. The internal resonance is responsible for the exchange of energy between the two modes (compare the amplitude planes shown in Figs. 4(*b*) and 5(*b*)).

5 Conclusions

The method of Lie group operators has been presented in a form suitable for the analysis of the response of nonlinear dynamical systems. The key ingredient of the method is the Hausdorff formula, which is implicitly reproduced in the averaging techniques. The method has been implemented to determine the response of coupled modes of a nonlinear system to parametric excitation in the presence of internal resonance. The system simulates the interaction between the first asymmetric sloshing mode with an elastic support structure. The interaction is modeled based on a phenomenological concept by introducing a power function with a higher exponent. The equations of motion are reduced to their simplest (normal) form by means of single-parameter Lie group operators. Based on the normal form equations, different kinds of resonance regimes are considered under parametric excitation. In the neighborhood of 1:3 internal resonance, it is shown that the energy of the parametrically excited in-phase mode can regularly (or nonregularly) oscillate between the two modes due to internal resonance between the modes. If the out-of-phase mode is parametrically excited, its energy is localized without transfer to the other mode, even under 1:3 internal resonance. The results reported in this paper have also been obtained using the method of multiple scales by Ibrahim and El-Sayad (1998). Furthermore, the analysis can be extended to dynamical systems with other different weak conservative and nonconservative nonlinearities.

Acknowledgment

This research is supported by National Science Foundation under Grant No. CMS-9634223, and by the Institute for Manufacturing Research of Wayne State University.

References

Abramson, H. N., ed., 1966, "The Dynamic Behavior of Liquids in Moving Containers," NASA-SP-106.

Belinfante, J. G., Kolman, B., and Smith, H., 1966, "An introduction to Lie groups algebras, with applications," *SIAM Review,* Vol. 8, No. 1, pp. 11–46.

Giancaglia, G. E. O., 1972, *Perturbation Methods in Nonlinear Systems,* Springer, Berlin.

Hori, G. I., 1966, "Theory of general perturbation with unspecified canonical variables," *Astronautical Society of Japan,* Vol. 18, No. 4.

Ibrahim, R. A., and El-Sayad, M. A., 1998, "Simulataneous Parametric and Internal Resonances in Systems Involving Impact Forces," *Proc. of the IUTAM Symposium on Unilateral Multibody Dynamics,* Munich, Kluwer, Dordrecht, The Netherland.

Landau, L. D., and Lifshitz, E. M., 1976, *Mechanics* (Course of Theoretical Physics, Vol. 1), Pergamon Press, London.

Nayfeh, A. H., 1993, *Method of Normal Forms,* John Wiley and Sons, New York.

Pilipchuk, V. N., and Ibrahim, R. A., 1997, "The Dynamics of a nonlinear System Simulating Liquid Sloshing Impact in Moving Structures," *Journal Sound and Vibration,* Vol. 205, No. 5, pp. 593–615.

Zhuravlev, V. Ph., 1986, "The Application of Monomial Lie Groups to the Problem of Asymptotically integrating Equations of Mechanics," *Pricladnaya Matematika Mekhanika (PMM),* Vol. 50, pp. 346–352.

Zhuravlev, V. Ph., and Klimov, D. M., 1988, *Applied methods in Vibration Theory,* Nauka, Moscow.

APPENDIX

Hausdorff's Formula

The mathematical formulation presented in Section 2 is based on the Hausdorff formula. The derivation of this formula is hard to find in the Western literature. The purpose of this appendix is to present a simple justification of this formula. This justification cannot be considered as a rigorous mathematical proof.

Consider the Caushy problem for the vector-function $\mathbf{y}(t)$: $\dot{\mathbf{y}} = \mathbf{f}(\mathbf{y})$, $\mathbf{y}|_{t=0} = \mathbf{y}^0$. Using the monomial Lie group operator, $A = \mathbf{f}(\mathbf{y})(\partial/\partial\mathbf{y})$, the equation is rewritten as $\dot{\mathbf{y}} = A\mathbf{y}$, and its formal solution can be represented in the exponential form

$$\mathbf{y} = e^{tA}\mathbf{y}^0. \tag{56}$$

Here the operator A must act on $\mathbf{y}^0$ components, i.e., $A = \mathbf{f}(\mathbf{y}^0)(\partial/\partial\mathbf{y}^0)$.

Similarly, one has the exponential form of transformation $\mathbf{y} \mapsto \mathbf{z}$ depending on parameter ϵ:

$$\mathbf{z} = e^{\epsilon U}\mathbf{y}. \tag{57}$$

For the Cauchy problem in the new coordinates $\dot{\mathbf{z}} = B\mathbf{z}$, $\mathbf{z}|_{t=0} = \mathbf{z}^0$ one can write a formal solution as

$$\mathbf{z} = e^{tB}\mathbf{z}^0 \tag{58}$$

Now consider two different ways of transformating $\mathbf{y}^0 \mapsto \mathbf{z}(t)$ as indicated in Fig. 6. Taking into account (56)–(58), these transformations can be written in the form

$$\mathbf{z} = e^{\epsilon U}\mathbf{y} = e^{\epsilon U}e^{tA}\mathbf{y}^0, \quad \text{and} \quad \mathbf{z} = e^{tB}\mathbf{z}^0 = e^{tB}e^{\epsilon U}\mathbf{y}^0.$$

Equating the right-hand sides, and recalling that $\mathbf{y}^0$ is an arbitrary initial point, gives

$$e^{\epsilon U}e^{tA} = e^{tB}e^{\epsilon U} \tag{59}$$

when $\epsilon = 0$ the transformation becomes identical and the operator of transformed system coincides with the original one: $A = B$. For small ϵ one has

$$A = B + \left.\frac{dB}{d\epsilon}\right|_{\epsilon=0}\epsilon + O(\epsilon^2). \tag{60}$$

Now consider expression (59) with the time parameter t equal to ϵ. Expanding the exponents in power series, in leading-order terms with respect to ϵ, one obtains

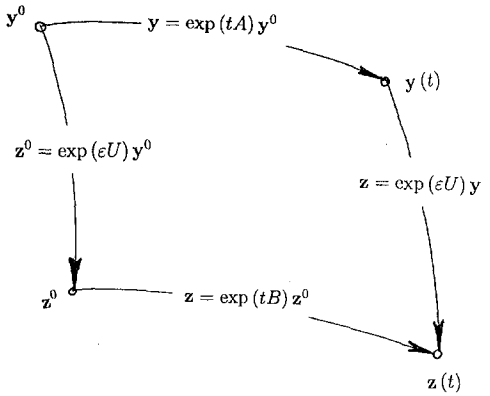

Fig. 6 Two different ways of transformating $\mathbf{y}^0 \mapsto \mathbf{z}(t)$

$$A + \epsilon UA = B + \epsilon BU.$$

Substituting (60) into the last expression gives

$$\frac{dB}{d\epsilon} = [B, U] \tag{61}$$

where $[B, U] = BU - UB$ is the commutator.

This is the Hausdorff equation for the operator of the transformed system. The equation is supposed to be solved under the initial condition $B|_{\epsilon=0} = A$. A solution of the Caushy problem (61) can be found in the power series form

$$B = A + \epsilon[A, U] + \frac{\epsilon^2}{2!}[[A, U], U] + \ldots.$$

This expression is called the Hausdorff formula.

Interaction Between Slow and Fast Oscillations in an Infinite Degree-of-Freedom Linear System Coupled to a Nonlinear Subsystem: Theory and Experiment

I. T. Georgiou[1]
Assoc. Mem. ASME

I. Schwartz

Special Project in Nonlinear Science,
Code 6700.3,
Naval Research Laboratory,
Washington, DC 20375

E. Emaci

A. Vakakis
Assoc. Mem. ASME

Department of Mechanical and
Industrial Engineering,
University of Illinois at
Urbana, Champaign,
Urbana, IL 61801

The interaction dynamics of a cantilever linear beam coupled to a nonlinear pendulum, a prototype for linear/nonlinear coupled structures of infinite degrees-of-freedom, has been studied analytically and experimentally. The spatio-temporal characteristics of the dynamics is analyzed by using tools from geometric singular perturbation theory and proper orthogonal decompositions. Over a wide range of coupling between the linear beam and the nonlinear pendulum, the coupled dynamics is dominated by three proper orthogonal (PO) modes. The first two dominant PO modes stem from those characterizing the reduced slow free dynamics of the stiff/soft (weakly coupled) system. The third mode appears in all interactions and stems from the reduced fast free dynamics. The interaction creates periodic and quasi-periodic motions that reduce dramatically the forced resonant dynamics in the linear substructure. These regular motions are characterized by four PO modes. The irregular interaction dynamics consists of low-dimensional and high-dimensional chaotic motions characterized by three PO modes and six to seven PO modes, respectively. Experimental tests are also carried out and there is satisfactory agreement with theoretical predictions.

1 Introduction

Many mechanical components in naval/marine, aerospace, and automobile engineering consist of linear or weakly nonlinear continuous substructures such as rods and plates coupled to nonlinear oscillators. Examples of such structures are ship and sea cranes, coupled cable structures supporting rigid bodies, and tethered spacecrafts. In applications, the linear substructure is designed to support the nonlinear substructure, or vice versa. A basic issue regarding the dynamics of a linear/nonlinear coupled structure is the stability of the motions of its substructures; in particular, one needs to examine the interaction of the linear and nonlinear motions by reducing the dynamics on appropriate low dimensional invariant manifolds.

The qualitative dynamics of a linear/nonlinear coupled structure depends on the ratio of the nonlinear substructure mass to that of the linear substructure, and on the ratio of the fundamental frequency of the nonlinear substructure to that of the linear one (Georgiou, 1993; Georgiou et al., 1998a). When the coupling between the linear and nonlinear substructures is small, the linear substructure generates high-frequency oscillations (fast dynamics), whereas the nonlinear one low-frequency oscillations (slow dynamics). In this case, one obtains a stiff/soft coupled structure. Such a stiff/soft coupled structure can be viewed (Georgiou, 1993; Georgiou et al., 1998a; Georgiou and Schwartz, 1997a) as a singular perturbation of the soft substructure, and ideas from geometric singular perturbations (Fenichel, 1979; Knobloch and Aulbach, 1984; Nipp, 1985; Jones, 1995) and invariant manifolds (Wiggins, 1990; Scheck, 1990; Boothby, 1985) can be combined to study systematically the dynamics. The pivotal feature of the singular perturbation/invariant manifold approach in solid mechanics (Georgiou, 1993; Georgiou et al., 1996a) is the natural introduction of slow and fast invariant manifolds of motion in the phase space of the dynamics. Physically, for sufficiently weak substructure coupling the existence of a slow (fast) invariant manifold means that there are motions during which the soft (stiff) substructure of the coupled system behaves qualitatively the same as the uncoupled soft (stiff) substructure. In essence, the stiff (soft) substructure is enslaved by the soft (stiff) one. If dissipation is present, the slow manifold is attracting (exponentially stable), and the long-term motions of the coupled system are dominated by motions very close to those of the uncoupled soft substructure. Moreover, one can study the dynamics of a linear/nonlinear coupled structure as the mass and frequency ratios of the corresponding stiff/soft substructures vary (Georgiou et al., 1998a). As substructure coupling increases, instabilities emanating transversely from the invariant manifolds of the stiff/soft system render the dynamics complex, in the sense that many degrees-of-freedom are activated. In this case one obtains interaction between slow and fast waves rather than almost decoupled slow and fast dynamics. This has been observed in previous works where numerical studies of the dynamics of coupled linear/nonlinear systems were carried out (Georgiou et al., 1998a, 1996a; Georgiou and Schwartz, 1999a).

The singular perturbation/invariant manifold approach was combined (Georgiou and Schwartz, 1999a) with ideas form proper orthogonal projections (Sirovich, 1987) to study how the qualita-

[1] Currently Research Engineer, SAIC–Science Applications International Corporation, McLean VA 22102.

Contributed by the Applied Mechanics Division of THE AMERICAN SOCIETY OF MECHANICAL ENGINEERS for publication in the ASME JOURNAL OF APPLIED MECHANICS.

Discussion on the paper should be addressed to the Technical Editor, Professor Lewis T. Wheeler, Department of Mechanical Engineering, University of Houston, Houston, TX 77204-4792, and will be accepted until four months after final publication of the paper itself in the ASME JOURNAL OF APPLIED MECHANICS.

Manuscript received by the ASME Applied Mechanics Division, Dec. 23, 1997; final revision, Oct. 30, 1998. Associate Technical Editor: N. C. Perkins.

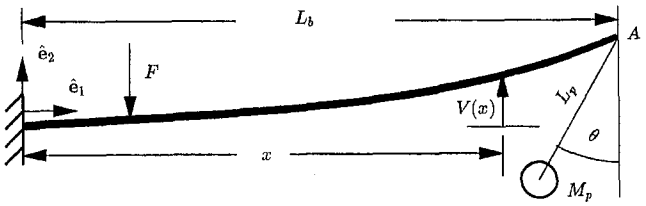

Fig. 1 Schematic of the beam/pendulum configuration

tive dynamics change as the coupling in a soft/stiff structure is increased. The system studied in (Georgiou and Schwartz, 1996a) was a linear viscoelastic rod coupled to a pendulum. The pendulum was the soft substructure, and was directly forced. We found that the proper orthogonal decomposition of spatio/temporal numerical solutions extracted the spatial normal modes of the coupled system. Furthermore, abrupt changes from periodic motions to chaos occurred (Georgiou and Schwartz, 1999a), similar to those found in (Schwartz and Georgiou, 1998). The number of proper orthogonal modes required to study the complicated motion produced by the abrupt transition from periodicity to chaos was larger than the number of degrees-of-freedom supporting the periodic motion (Georgiou and Schwartz, 1999a). Preliminary general results show why singularly perturbed systems which exhibit slaving between degrees-of-freedom have fewer acting PO modes (Schwartz and Georgiou, 1998).

In this paper we apply the singular perturbation/proper orthogonal decomposition methodology (Georgiou and Schwartz, 1999a) to study the interaction of forced fast oscillations and unforced slow oscillations in a coupled structure that consists of a linear viscoelastic beam supporting at its tip a nonlinear pendulum. Our objective is to understand the nature of the interaction of fast/slow dynamics of a system representative of more practical structures. Furthermore, we perform experiments to validate theoretical results, and show that proper orthogonal projections of numerical and experimental data extract correctly the spatial modes of such coupled structures.

2 The Beam/Pendulum System

Figure 1 depicts a coupled linear/nonlinear structure consisting of a cantilever linear viscoelastic beam coupled to a nonlinear pendulum oscillator. The coupled structure is constrained to move only in the plane defined by the unit vectors $\hat{\mathbf{e}}_1$, $\hat{\mathbf{e}}_2$. Let θ and v denote, respectively, the displacement of the pendulum and the displacement field for the beam. The pendulum is free to rotate in the plane defined by $\hat{\mathbf{e}}_1$, and $\hat{\mathbf{e}}_2$. The length, cross section, mass density, modulus of elasticity, and coefficient of viscous damping of the beam are denoted by L_b, A_b, ρ_b, E_b, I_b, δ_b. The length, mass, and coefficient of viscous damping for the pendulum are denoted by L_p, M_p, δ_p. The frequency of the uncoupled pendulum is given by $\omega_p^2 = g/L_p$, whereas the fundamental frequency of the uncoupled beam is given by $\omega_1^2 = \kappa_1^4 E_b I_b / L_b^4 A_b \rho_b$. We introduce the following dimensionless parameters: space $\xi = x/L_b$, time $\tau = \omega_p t$, beam displacement $V = v/L_p$, distributed force $F = f/A\rho g$; mass ratio $\beta = M_p/A_b\rho_b L_b$, frequency ratio $\mu = \omega_p/\omega_1$; and damping factors for the beam and pendulum: $2\zeta_b = \delta_b I_b \kappa_1^4/\omega_1 A\rho L_b^4$, $2\zeta_p = C_p/\omega_p M_p$, respectively.

The stable and unstable equilibrium configurations of the unforced coupled system are given by

$$C: \quad 6\hat{V}(\xi) = \mu^2\beta\kappa_1^4(\xi - 3)\xi^2 \quad \hat{\theta} = 0, \tag{1a}$$

$$S_{\pm 1}: \quad 6\hat{V}(\xi) = \mu^2\beta\kappa_1^4(\xi - 3)\xi^2, \quad \hat{\theta} = \pm\pi. \tag{1b}$$

Let $W = V - \hat{V}$ denote the displacement of the beam with respect to the static stable equilibrium C. Then the motion of the beam/pendulum system is described by the following system of coupled equations:

$$\mu^2\kappa_1^4\ddot{W}(\xi, \tau) + W_{\xi\xi\xi\xi}(\xi, \tau) + 2\zeta_b\mu\dot{W}_{\xi\xi\xi\xi}(\xi, \tau) = \mu^2\kappa_1^4 F(\xi, \tau), \tag{2a}$$

$$\ddot{\theta}(\tau) + [1 + \ddot{W}_A(\tau)] \sin(\theta(\tau)) + 2\zeta_p\dot{\theta}(\tau) = 0, \tag{2b}$$

where the term $\ddot{W}_A(\tau) \equiv W(\xi = 1, \tau)$ denotes the acceleration of the beam tip, and the constant κ_1 is the first root of the well-known equation

$$\cosh(\kappa_1) + \cos(\kappa_1) + 1 = 0 \tag{3}$$

that determines the natural frequencies of the uncoupled cantilever beam. The boundary conditions are

$$W(\xi = 0, \tau) = 0, \quad W_\xi(\xi = 0, \tau) = 0,$$
$$W_{\xi\xi}(\xi = 1, \tau) = 0, \tag{4a}$$

$$W_{\xi\xi\xi}(\xi = 1, \tau) + \mu^2\beta\kappa_1^4[1 - T(\tau)\cos(\theta(\tau))] = 0 \tag{4b}$$

where the term $T(\tau) \equiv \dot{\theta}^2(\tau) + [1 + \ddot{W}_A(\tau)]\cos(\theta(\tau))$ denotes the normalized tension in the pendulum arm.

The coupling between the beam and pendulum is nonlinear parametric and appears in the equations of motion of the pendulum (2*b*) and the natural boundary conditions of the beam (4*b*). Note that the natural frequency of the uncoupled pendulum and the fundamental natural frequency of the uncoupled beam are normalized at $\omega_p = 1$, and $\omega_1 = 1/\mu$, respectively.

We are interested in analyzing the interaction dynamics between the beam and the pendulum substructures for various levels of coupling. Clearly, for fixed mass ratio β, the strength of coupling depends on only the frequency ratio μ.

3 The Reduced Dynamics of the Stiff/Soft System

To understand the mechanisms causing the interaction dynamics, we first need to understand the global geometry of the reduced dynamics of the system with weak coupling. For fixed mass ratio β, the beam/pendulum system is weakly coupled, also referred to as stiff/soft, if the frequency ratio μ is sufficiently small. The beam is the stiff substructure and generates high-frequency oscillations, or fast dynamics, whereas the pendulum is the soft substructure and generates low-frequency oscillations, or slow dynamics. For fixed pendulum parameters, as $\mu \to 0$, the beam becomes increasingly stiff. In fact, at $\mu = 0$, the coupled system reduces to the uncoupled pendulum

$$\ddot{\theta} + \sin(\theta) + 2\zeta_p\dot{\theta} = 0. \tag{5}$$

The limiting process reveals two important properties. First, the degrees-of-freedom drop from infinity to just one; and second, the coupled system, for sufficiently small μ, can be viewed as a *singular* perturbation of the nonlinear soft subsystem. By definition, a dynamical system is singularly perturbed when the perturbation increases its degrees-of-freedom.

The above properties show that increase and reduction of the dimension of dynamics should be central themes in developing techniques to understand basic issues, such as interactions among substructures, in dynamics of coupled systems. A systematic analytic/computational technique based on singular perturbations and invariant manifolds of motion has been developed and applied to mechanical and structural systems to study the reduced dynamics (Georgiou, 1993; Georgiou et al., 1998a). Details for the singular perturbation approach of the beam/pendulum problem are given in the Appendix and in Georgiou and Schwartz (1999a).

For the weakly coupled system, we have the following concrete results: In phase space of the unforced dissipative system, there exists an invariant manifold. The manifold is two-dimensional, global, and attracting. It contains the purely slow free motions of the system. For any motion residing on this manifold, the state of the beam is given by

$$(W(\xi, \tau), \dot{W}(\xi, \tau)) = (\mathcal{H}^1_\mu(\xi, \theta(\tau), \dot{\theta}(\tau)), \mathcal{H}^2_\mu(\xi, \theta(\tau), \dot{\theta}(\tau))) \quad (6)$$

where $\mathcal{H}^i_\mu$, $i = 1, 2$ are $O(\mu^2)$ and derived in the Appendix. According to Eq. (6), the beam slow dynamics are slaved to those of the pendulum. The pendulum slow dynamics, referred to as the master slow dynamics, is governed by an oscillator which is a regular perturbation in μ of the uncoupled pendulum (Georgiou and Schwartz, 1996b).

There exists a stable infinite-dimensional linear manifold passing through the stable equilibrium C. The manifold is given by

$$(\theta, \dot{\theta}) = (0, 0). \quad (7)$$

There exists an unstable infinite-dimensional linear manifold passing through the unstable equilibrium $S_{\pm 1}$. The manifold is given by

$$(\theta, \dot{\theta}) = (\pm\pi, 0). \quad (8)$$

These manifolds are very important since they contain motions which are small perturbations of the motions of the uncoupled substructures. They stem from analogous invariant manifolds of the conservative system. The manifolds become time dependent for the forced system.

We are interested in analyzing the interaction dynamics. To this end, we will determine and analyze the amplitude and shapes of optimum degrees-of-freedom. In particular, we will analyze the acceleration field obtained from the numerical integration of the equations of motion in singular perturbation formulation and experiments with a physical prototype for the beam/pendulum structure. In doing so, we keep in mind the fundamental geometric structure of the reduced dynamics of the stiff/soft system.

4 Proper Orthogonal Decomposition Analysis for Coupled Vector Fields

We will determine optimum degrees-of-freedom for the coupled position and acceleration fields:

$$\mathcal{P}(\xi, \tau) = [W(\xi, \tau), \theta(\tau)], \quad \mathcal{A}(\xi, \tau) = [\ddot{W}(\xi, \tau), \ddot{\theta}(\tau)]. \quad (9)$$

To this end, we defined the following inner products:

$$\langle [g^b(\xi), g^p], [f^b(\xi), f^p] \rangle = \int_0^1 g^b(\xi) f^b(\xi) d\xi + g^p f^p, \quad (10a)$$

$$\langle g^b(\xi), f^b(\xi) \rangle = \int_0^1 g^b(\xi) f^b(\xi) d\xi. \quad (10b)$$

All functions have the required smoothness for all mathematical operations to be well defined.

To determine independent spatio-temporal characteristics of a vector field, say the acceleration field, we expand it as follows:

$$\mathcal{A}(\xi, \tau) = [\ddot{W}(\xi, \tau), \ddot{\theta}(\tau)] = \sum_{k=1}^{K} \alpha_k(\tau) \sqrt{\lambda_k} [\Phi^b_k(\xi), \Phi^p_k]. \quad (11)$$

$$\ddot{W}(\xi, \tau) = \sum_{k=1}^{K} \nu_k(\tau) \sqrt{\gamma_k} \Upsilon^b_k(\xi). \quad (12)$$

The function of time $\alpha_k(\tau)$ and the function of space $\sqrt{\lambda_k}[\Phi^b_k(\xi), \Phi^p_k]$ represent the amplitude dynamics and the shape of the kth PO mode. The scalar $\lambda_k \geq 0$ is the fraction of the energy, defined by Eq. (16), of the vector field contained in this mode. The amplitudes α_k and the scalars λ_k are the eigenfunctions and eigenvalues of the following eigenproblem:

$$\frac{1}{T_2 - T_1} \int_{T_1}^{T_2} C(\tau, s) \alpha_k(s) ds = \lambda_k \alpha_k(\tau), \quad (13)$$

where $C(\tau, s) \equiv \int_0^1 \ddot{W}(\xi, \tau) \ddot{W}(\xi, s) d\xi + \ddot{\theta}(\tau) \ddot{\theta}(s)$ is the temporal autocorrelation operator over the time window $[T_1, T_2]$. We have $0 \leq \lambda_k$ since $C(\tau, s) = C(s, \tau)$.

The spatial distribution, or shape, of the kth mode can be determined by the following projection:

$$\Phi_k(\xi) \equiv \sqrt{\lambda_k}[\Phi^b_k(\xi), \Phi^p_k] = \frac{1}{T_2 - T_1} \int_{T_1}^{T_2} \alpha_k(\tau) \times [\ddot{W}(\xi, \tau), \ddot{\theta}(\tau)] d\tau. \quad (14)$$

The terms $\sqrt{\lambda_k}\, \Phi^b_k(\xi)$ and $\sqrt{\lambda_k}\, \Phi^p_k$ represent, respectively, the beam and pendulum spatial components of the mode. The norms of $\Phi_k(\xi)$ and and $\Phi^b_k(\xi)$ are defined by using the inner products (10a) and (10b), respectively.

The normalized beam component of the mth mode is defined by

$$\hat{\Phi}^b_m(\xi) = \frac{\Phi^b_m(\xi)}{\|\Phi^b_m(\xi)\|}. \quad (15)$$

The "energy" of the acceleration field over the time window $[T_1, T_2]$ is defined by

$$E \equiv \frac{1}{T_2 - T_1} \int_{T_1}^{T_2} C(\tau, \tau) d\tau \quad (16)$$

and should not be confused with mechanical energy, since it is a measure of the second-order fluctuation of the system. It can be shown that $E = \sum_{k=1}^{K} \lambda_k = 1$. Therefore, $0 \leq \lambda_k \leq 1$; Clearly, the eigenvalues are energy fractions; we ordered them as follows: $0 \leq \ldots \leq \lambda_m \leq \lambda_{m-1} \leq \ldots \leq \lambda_2 \leq \lambda_1 \leq 1$. Moreover, we say that mode Φ_n is more energetic than mode Φ_m, if $\lambda_n > \lambda_m$.

A spatio-temporal record of data, numerical or experimental, will be characterized by the sequence $\{\lambda_k, \alpha_k(\tau), \Phi_k(\xi)\}_{k=1}^{k=K}$. The set $\mathcal{S} \equiv \{\lambda_k\}_{k=1}^{k=K}$ will be referred to as the proper orthogonal decomposition (POD) spectrum.

Equation (13) guarantees that the temporal amplitudes as well as the companion spatial modes are orthonormal. Furthermore, the expansion is optimal in the sense that the amount of energy contained in n modes is equal or larger to that contained in the first n modes of any other basis expansion. For this reason, the expansion is called POD, or K-L expansion (Sirovich, 1987). In solid mechanics, it has been applied to study aspects of the dynamics of vibro-impact problems (Cusumano et al., 1994). The POD method has been combined with geometric singular perturbations in (Georgiou and Schwartz, 1999a). Recently the POD method has been applied and developed further to analyze the finite element dynamics of geometrically exact nonlinear continua (Georgiou et al., 1997b; Georgiou and Sansour, 1998b).

We will apply the POD technique to identify the optimum degrees-of-freedom in the dynamics of the beam/pendulum coupled structure. We analyze sets of spatio-temporal data over the space-time domain $[0, 1] \times [T_1, T_2]$. The space-time domain is discretized into N and M points, respectively: $1 = N\Delta\xi$, $T_2 - T_1 = M\Delta\tau$, where $\Delta\xi$ and $\Delta\tau$ are space and time increments, respectively. We integrate the equations of motion in singular perturbation formulation (24) for $N = 32$ beam modes by using the Gear method. The space interval [0, 1] is discretized into 32 equispaced points, and including the pendulum, we have 33 points in space.

5 Experimental Procedure

Now we describe the experimental procedure to obtain spatio-temporal data. A prototype for linear/nonlinear coupled structures was built and tested. Figure 2(a) shows a beam/pendulum exper-

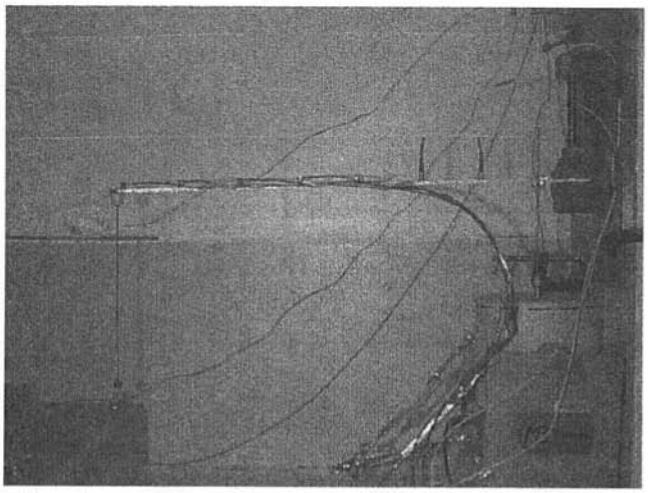

Fig. 2(*a*)

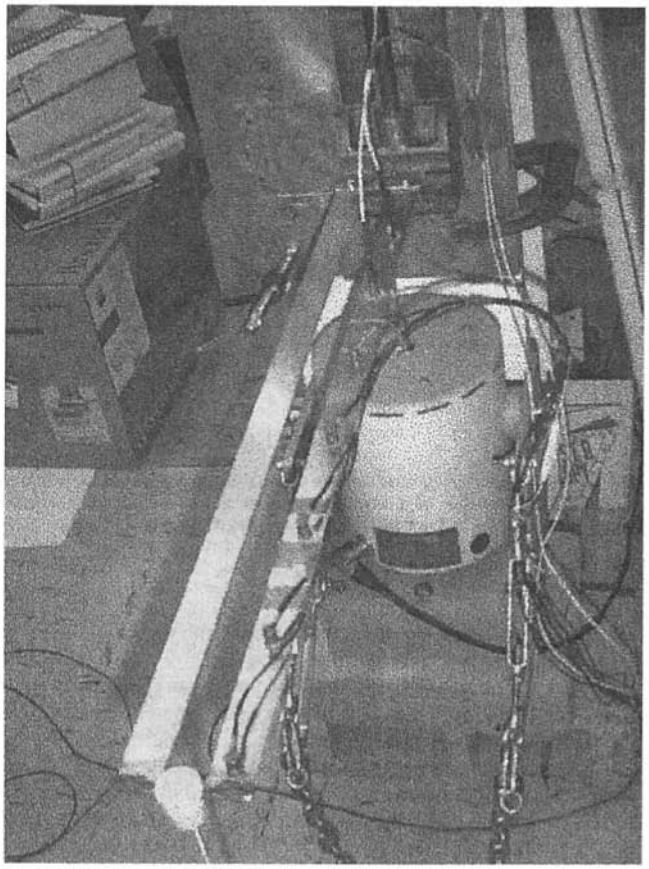

Fig. 2(*b*)

Fig. 2 The beam/pendulum physical system: (*a*) side view, (*b*) top view showing arrangement of the seven accelerometers

imental setup. The beam substructure consists of two identical beams that are coupled at their tips by a rigid bar about which a pendulum can rotate freely. The length, width, and thickness of the beam are $L_b = 660.40$ mm, $D_d = 25.40$ mm, $H_b = 3.175$ mm, respectively. In the experiment, we vary the strength of the coupling between the beam and the pendulum by varying the pendulum length or the pendulum mass. In particular, the length of the pendulum is varied from 50.80 mm to 292.10 mm to cause variation in μ from 0.419 to 0.175, respectively.

For fixed coupling parameters (μ, β), the beam/pendulum coupled system was forced by applying a concentrated harmonic force, $F = P \cos(\hat{\Omega}t)$, generated by a shaker with sensitivity 54.174 mV/(pounds of force) at $x = 25.40$ mm ($\hat{\xi} = 1/26$) away from the clamped end of the beam. The forcing frequency $\hat{\Omega}$ was varied in an interval containing the fundamental frequency of the coupled beam, measured at $\hat{\omega}_1^c = 28.525$ rad/s. Seven accelerometers, see Fig. 2(*b*), were attached at the locations $x_1 = 116.40$ mm, $x_2 = 205.40$ mm, $x_3 = 293.40$ mm, $x_4 = 382.40$ mm, $x_5 = 471.40$ mm, $x_6 = 559.40$ mm, $x_7 = 645.40$ mm, to collect spatio-temporal data for the acceleration field of the beam and derive PO modes similar to those derived from numerical experiments. The corresponding sensitivities, measured in mV/g, of the accelerometers are $s_1 = 9.84$, $s_2 = 9.72$, $s_3 = 96.60$, $s_4 = 98.10$, $s_5 = 9.80$, $s_6 = 10.15$, $s_7 = 10.12$, where g denotes the acceleration of gravity.

Several experiments were performed for the following values of coupling (μ, β): (0.175, 0.1), (0.183, 0.1), (0.4189, 0.1), (0.2324, 0.05), (0.211, 1.0). The acceleration of the beam during transient, periodic, quasi-periodic, and chaotic motions was measured and recorded.

6 On the Nature of the Interaction Dynamics

During pure slow or fast motions, that is, when the dynamics are restricted to the invariant manifolds, there cannot be interaction between the beam and pendulum substructures. To the contrary, during slow motions the beam substructure is slaved to the pendulum substructure. This implies that the motion of the beam does not contain the natural frequency of the beam but frequencies related to the frequency of the pendulum. We expect interactions in the stiff/soft system, where the attracting fast and slow invariant manifolds are global, during motions initiated a finite distance away from the invariant manifolds. Furthermore, we expect interactions during motions initiated in the neighborhood of unstable regions of the invariant manifolds. The mass ratio and the frequency ratio, the coupling parameters, control the energy level of the transverse instabilities of the invariant manifolds.

6.1 The Spatial Signature of the Slow Dynamics. In this section, we determine the PO modes of the acceleration field of free motions of the coupled system with small coupling as predicted by the equations of motion and measured from experiments. We fix the coupling parameters at (μ, β) = (0.175, 0.1). First, we analyze the acceleration field as predicted by the equations of motion for dissipation (ζ_b, ζ_p) = (0.005, 0.01). We analyze global motions initiated near the slow invariant manifold. A global motion with initial conditions (θ, $\dot{\theta}$) = (1.75, 0.0) for the pendulum is initiated near the slow invariant manifold if the initial conditions for the beam are computed from Eq. (6). The POD analysis for the coupled acceleration field for this motion, the transients have been removed, gives a spectrum that consists of three points: $\mathcal{S} = \{\lambda_1, \lambda_2, \lambda_3\}$. The shape of the first mode is characterized by $\sqrt{\lambda_1}\|\Phi_1^b\| = O(\beta\mu^2)$, $\sqrt{\lambda_1}|\Phi_1^p| = O(1)$. Thus, most of the energy of the dominant mode is contained in the pendulum substructure. The shapes of the other two modes are characterized by: $\sqrt{\lambda_m}\|\Phi_m^b\| = O(1)$, $\sqrt{\lambda_m}|\Phi_m^p| = O(\beta\mu^2)$, $m = 2, 3$. Thus, most of the remaining energy is contained in the beam substructure. Since in the experiments with the physical system, we measure only the acceleration of the beam, we exclude the pendulum acceleration dynamics and analyze the acceleration field of the beam only. We find that its POD spectrum consists of two points: $\mathcal{S} = \{\gamma_1, \gamma_2\}$. Now we have the following computational result:

$$\hat{\Phi}_1^b(\xi) = \hat{\Phi}_2^b(\xi) = \sqrt{\gamma_1}\Upsilon_1^b(\xi), \quad \hat{\Phi}_3^b(\xi) = \sqrt{\gamma_2}\Upsilon_2^b(\xi), \quad (17a)$$

$$\nu_1(\tau) = \alpha_2(\tau), \quad \nu_2(\tau) = \alpha_3(\tau). \quad (17b)$$

The above equation reveals that the POD analysis of the beam acceleration field gives all temporal information for the coupled acceleration field but the dynamics related to pendulum substructure. The spatial information is partial. Moreover, the shapes of the beam components of the first two modes of the coupled acceler-

ation not only do coincide but are identical to the scaled dominant PO mode of the beam acceleration field. This is shown in Fig. 3(*a*) depicting the beam components of the three PO modes.

A similar experiment was performed with the physical system with $\mu = 0.175$, achieved by fixing the pendulum length $L_p = 292.10$ mm. Figure 3(*b*) shows the spatio-temporal behavior of the beam acceleration, as recorded by the seven accelerometers for a motion with initial conditions $(\theta, \dot{\theta}) = (1.75, 0.0)$, $(W, \dot{W}) = (0.0, 0.0)$. Compared to the motion of the numerical experiment discussed above, this motion is not initiated near the slow invariant manifold. However, if an attracting slow invariant manifold exists, the motion after an initial time interval will come close to the slow invariant manifold. Physically, the motion will be dominated by an underlining slow motion. Figure 3(*c*) reveals that the shape of the dominant PO mode of this record of experimental data is almost identical to that extracted from a record of numerical data for a motion predicted by the equations of motion.

We have computed the PO modes as a function of the pendulum amplitude, or energy level, for motions initiated near the slow invariant manifold. To keep the motions for a sufficiently long time close to motions of the conservative system, we have set the

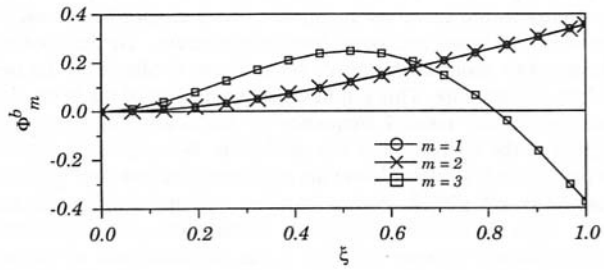

Fig. 3(*a*)

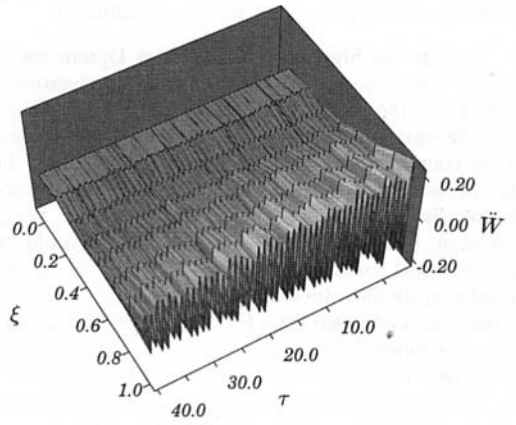

Fig. 3(*b*)

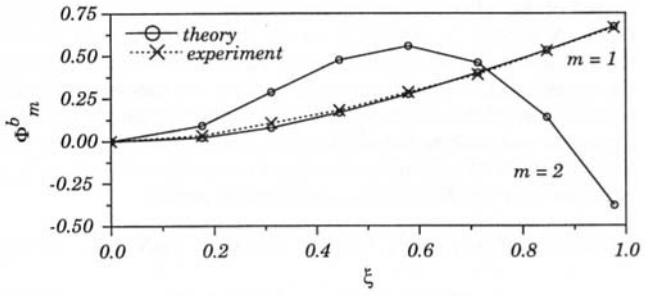

Fig. 3(*c*)

Fig. 3 (*a*) Shapes of the beam components of the PO modes of the coupled acceleration field and the beam acceleration field (theory), (*b*) spatio-temporal measurement of the beam acceleration of the physical system shown in Fig. 2, (*c*) Shapes of PO modes of the beam acceleration field (theory-experiment).

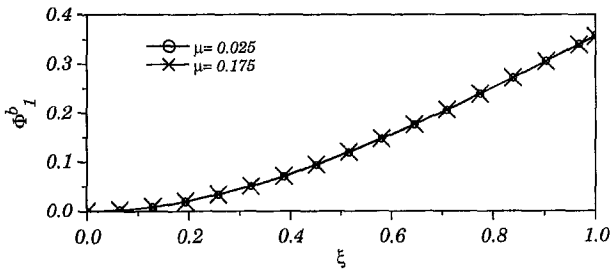

Fig. 4(*a*)

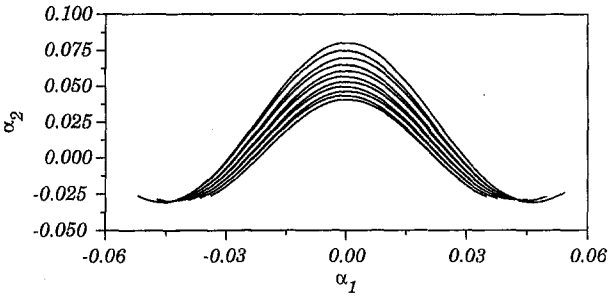

Fig. 4(*b*)

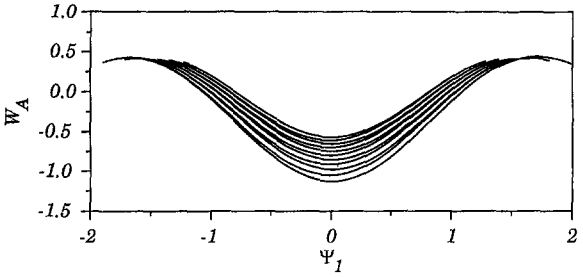

Fig. 4(*c*)

Fig. 4 (*a*) The single PO mode of the beam slow dynamics is identical to the beam PO modes of a coupled motion not residing on the slow invariant manifold, (*b*) projection of the slow dynamics onto the plane $\alpha_1 - \alpha_2$, (*c*) projection of the slow dynamics onto the plane $\Psi_1 - W_A$.

dissipation of the pendulum $\zeta_p = 0$. Since the dependence of the slow dynamics on the beam dissipation ζ_b is $O(\zeta_b \mu^3)$, the slow dynamics are close to the dynamics of the conservative system for a sufficiently long time. The conservative system possesses a global slow invariant manifold (Georgiou and Schwartz, 1999b). The numerical experiment reveals that a generic motion in the neighborhood of the slow manifold is governed by three PO modes if $\theta_l < \theta$ and by two PO modes if $\theta < \theta_l$. For coupling strength $(\mu, \beta) = (0.175, 0.1)$, we have $0.5 < \theta_l < 1.0$. The shapes of the modes do not change with the energy level.

Now for weak coupling, there exists a global slow invariant manifold. For the unforced system, it is two-dimensional and is the geometric realization in phase space of a single degree-of-freedom. We lower the coupling at $\mu = 0.025$, considered to be weak, and initiate a motion on the slow invariant manifold. The POD analysis of the beam acceleration gives a POD spectrum with a single point: $\mathcal{S} = \{\gamma\}$, with $\gamma = 1.0$. Thus, all energy is contained in a single mode. We have the following decomposition:

$$\ddot{W}(\xi, \tau) = \nu(\tau)\Upsilon^b(\xi). \tag{18}$$

Figure 4(*a*) reveals that this single PO mode is identical to the beam components of the first and second PO modes for coupling $\mu = 0.175$. Note that at this level of coupling there is interaction.

The above result seems to agree with the expectation that the dynamics restricted to a two-dimensional invariant manifold should be characterized by a single PO mode. However, the POD

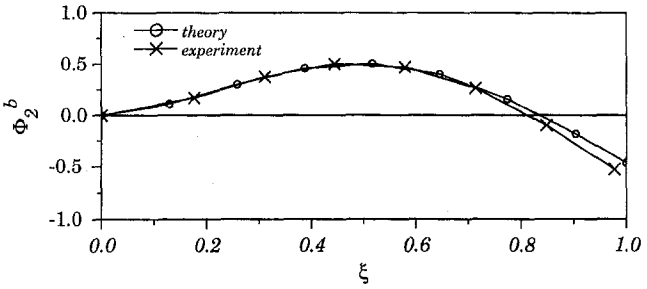

Fig. 5 The beam component of the first fast PO mode

analysis of the coupled acceleration field gives a POD spectrum with two points: $\mathcal{S} = \{\lambda_1, \lambda_2\}$. So we have the following decomposition:

$$[\ddot{W}(\xi, \tau), \ddot{\theta}(\tau)] = \alpha_1(\tau)\sqrt{\lambda_1}[\Phi_1^b(\xi), \Phi_1^p] + \alpha_2(\tau)\sqrt{\lambda_2}[\Phi_2^b(\xi), \Phi_2^p]. \quad (19)$$

Just as in the case of small coupling, we have the following remarkable results: First, the first PO mode is dominated by the pendulum whereas the second one by the beam. Second, the shapes of the beam components of two PO modes not only do coincide but also are identical to the single PO mode, that is, we have the computational result

$$\hat{\Phi}_1^b(\xi) = \hat{\Phi}_2^b(\xi) = \Upsilon^b(\xi), \quad (20a)$$

$$\nu(\tau) = \alpha_2(\tau). \quad (20b)$$

A motion on the two-dimensional manifold is characterized by two PO modes because the slaved beam dynamics have basic frequency twice that of the master slow dynamics of the pendulum: $\omega_b = 2\omega_p$ (Georgiou and Schwartz, 1999b). Numerical experiments reveal that the long-time dynamics of local and global motions initiated near the slow invariant manifold possess two PO modes satisfying relation (20). This verifies the singular perturbation result that, for weak coupling, the slow invariant manifold is global and attracting. Figure 4(*b*) shows the projection of the dynamics on the slow manifold onto the plane spanned by the amplitudes of the two PO modes. Figure 4(*c*) reveals that this trajectory is topologically the same as the trajectory from the projection of the dynamics onto the configuration plane $\Psi_1 - W_A$. Equation (20*a*) will be referred to as the *spatial signature* of the free slow dynamics. It does underline the spatial characteristics of the free interaction dynamics at small coupling.

The fast invariant manifolds are linear. The best way to excite a fast PO mode is to force the beam at one of its natural frequencies. In particular, any motion initiated on the fast manifold and forced with $\Omega = \omega_1$ is characterized by a single PO mode with shape identical to that of $\Upsilon^b(\xi)$. And any motion initiated on the fast manifold and forced at $\Omega = \omega_2$ is characterized by a single PO mode with shape identical to that of $\Phi_3^b(\xi)$, the beam component of the third PO mode supporting free interaction motions in the neighborhood of the slow invariant manifold for small coupling. It turns out that this mode has shape similar to that of the second PO mode computed from acceleration measurements in the physical system. Figure 5 shows good agreement between theory and experiment. Since this mode is identified in the free interaction dynamics, it is called the dominant fast PO mode.

6.2 The Temporal Signature of the Slow Dynamics. We now examine the amplitude of the dominant mode of the acceleration of the beam as predicted by theory and measured in the experiment for the system with coupling $(\mu, \beta) = (0.175, 0.1)$. The time scale of numerical and experimental time series is renormalized such that the beam frequency is $f_b = 1$ and the pendulum frequency is $f_p = \mu$. The frequency spectrum of the amplitude of the dominant mode derived from the spatio-temporal measurements of the beam acceleration is computed to be $\mathcal{F}_1^{\text{exper}} = \{2, 4, 4.9485, 6.1067, 6.9489\} \times f_p^{\text{exper}}$ where $f_p^{\text{exper}} = 0.2090$ whereas that predicted by theory is given by $\mathcal{F}_1^{\text{theor}} = \{2, 4, 5.5, 6, 7.5\} \times f_p^{\text{theor}}$ where $f_p^{\text{theor}} = 0.195265$. We have $f_p^{\text{exper}} \approx f_p^{\text{theor}}$. Furthermore, in both spectra the dominant harmonic is at the fast frequency and lies between $4\omega_p$ and $6\omega_p$. The experiment verifies the existence of the slow invariant manifold predicted by singular perturbation theory. This is so since as we shall see below both spectra $\mathcal{F}_1^{\text{exper}}$ and $\mathcal{F}_1^{\text{theor}}$ bear the frequency or temporal signature of the free slow dynamics. What is important is the fact that this has been accomplished by applying the POD method to experimental and numerical data.

Motivated by the fact that the spectrum of the dominant mode above contains frequencies close to multiples of the slow and fast frequencies, we have computed the frequency spectra of the three PO modes supporting the coupled acceleration field for the system with $(\mu, \beta) = (0.175, 0.1)$ and zero dissipation in the pendulum substructure. We have the following computational result:

$$\mathcal{F}_1 = \{\omega_p, 3\omega_p + a_1, 5\omega_p + a_2, \ldots,\}, \quad (21a)$$

$$\mathcal{F}_2 = \{2\omega_p, 4\omega_p + b_1, 6\omega_p + b_2, \ldots,\}, \quad (21b)$$

$$\mathcal{F}_3 = \{2\omega_p, 4\omega_p + c_1, 6\omega_p + c_2, \ldots,\}. \quad (21c)$$

The numerical experiments reveal the existence of a critical pendulum amplitude, $1.55 < \theta_{cr} < 1.75$, or energy level. When the critical amplitude is crossed, the detuning factors a_m, b_m, c_m above change sign. In particular, near this critical motion, we have $a_1 = a_2 = b_1 = b_2 = c_1 = c_2 = 0$; and the dominant harmonics of the three modes are at ω_p, $6\omega_p$, and $8\omega_p$, respectively. Near the critical energy level, the spectra $\mathcal{F}_1$ and $\mathcal{F}_2$ are characterized by $\omega_1 = 6\omega_p$. Since for any motion on the slow manifold the beam basic frequency ω_b is twice the pendulum basic frequency ω_p, the above relation yields $\omega_1 = 3\omega_b$. *Thus, we have a* 3:1 *internal resonance between the fast dynamics and the slaved slow beam dynamics.* This resonance is global since it involves a global motion.

A motion on the global slow invariant manifold is characterized by two PO modes. For $\mu = 0.025$, we have the following computational and analytic result for a motion on the slow invariant manifold: The amplitude of the dominant PO mode is characterized by the spectrum: $\mathcal{F}_m = \{\omega_p, 3\omega_p, 5\omega_p, \ldots\}$, to be referred to as the *master* slow spectrum, whereas the spectrum of the slaved amplitude is given by $\mathcal{F}_s = \{2\omega_p, 4\omega_p, 6\omega_p, \ldots\}$, to be referred to as the *slaved* slow spectrum. We call the set $\{\mathcal{F}_s, \mathcal{F}_m\}$ the *temporal or frequency* signature of the uncoupled free slow dynamics. From Eq. (21) we see that interaction between slow and fast free dynamics manifests itself as an interweaving of the master and slaved slow spectra. Moreover, additional rational multiples of the slow frequency are generated. Here we see how knowledge of the slow invariant manifold guides us to gain fundamental understanding of the interaction dynamics. In analyzing the PO modes of the interaction dynamics, we will look for the spatial and temporal signatures of the free slow dynamics.

The POD method has identified successfully the spatio-temporal characteristics of the motions restricted to the two-dimensional slow invariant manifold. Moreover, it reveals that a PO mode is not sufficient to describe the coupled dynamics on a two-dimensional invariant manifold. Thus, it is not always true that a PO mode represents completely a degree-of-freedom, that is, an oscillator. Here we add that the position and acceleration fields give most of the time PO modes with identical shapes.

7 Interactions in Regular Motions

Interactions between slow and fast dynamics can occur whenever a motion lies neither on the slow nor on the fast invariant manifolds. A motion escapes from an invariant manifold, when the latter develops transversal instabilities. Interaction mechanisms

will produce regular and chaotic attractors. We will analyze them by computing the spatial and temporal characteristics of the PO modes.

We are interested in the interaction between the resonance fast beam dynamics and the slow pendulum unforced dynamics. We force the beam at its fundamental natural frequency. We perform numerical and physical experiments with initial conditions: $(\theta, \dot{\theta}) \approx (0.01, 0.0)$, $(W, \dot{W}) = (0, 0)$. These conditions initiate a motion slightly off the fast invariant manifold. This experiment will produce attractors for the interaction dynamics due to the transverse instabilities of the fast invariant manifold. Furthermore, we perform other numerical and physical experiments with initial conditions: (1) $(\theta, \dot{\theta}) \approx (\pi/2, 0.0)$, $(W, \dot{W}) = (0, 0)$, and (2) $(\theta, \dot{\theta}) = (\pi, \dot{\theta}_0)$, $(W, \dot{W}) \approx (0, 0)$ where $\dot{\theta}_0 \approx 0.0$. These initial conditions place, respectively, a motion at a finite distance off the slow manifold and another motion on the slow invariant manifold. This experiment will generate attractors for the interaction dynamics due to transverse instabilities of the nonlinear slow invariant manifold.

For weak coupling, such as $(\mu, \beta) = (0.025, 0.1)$, a generic motion initiated near the fast or the slow invariant manifold is attracted by the fast invariant manifold for sufficiently large forcing amplitudes. The long-time dynamics reside on the fast manifold; it is linear and resonant, and supported by a single PO mode with shape identical to that of the single mode supporting the acceleration field of the beam during purely slow free motions. For small coupling, the motion is repelled if the forcing amplitude exceeds a critical value. This motion, depending on the forcing and dissipation, is chaotic or regular, that is, periodic or quasi-periodic. For example, the system with coupling $(\mu, \beta) = (0.175, 0.1)$, considered to be small, dissipation $(\zeta_b, \zeta_p) = (0.005, 0.01)$, undergoes a stable periodic motion when forced at $(\Omega, P) = (\omega_1, 260)$ where $\omega_1 = 4.8293$ is the value of the first natural frequency of the beam with the pendulum mass at its tip. The forced fast dynamics of the beam substructure and the unforced slow dynamics of the pendulum substructure interact in such a way as to produce a stable periodic motion. During this motion, the beam amplitude is very small compared to that of the resonant dynamics, that is, the dynamics restricted to the fast manifold. However, the amplitude of the pendulum is large, reaching a value around $\pi/2$. Thus, the interaction causes a *dramatic decrease in the resonant* linear dynamics.

The POD analysis of the coupled acceleration and beam acceleration fields yields four and three PO modes, respectively. The first two dominant modes satisfy the following result: $\hat{\Phi}_1^b(\xi) \approx \hat{\Phi}_2^b(\xi)$, $\hat{\Phi}_1^b(\xi) = \sqrt{\gamma_1}\, \Upsilon_1^b(\xi) = \Upsilon^b(\xi)$. The beam components of the first two PO modes do not coincide but have similar shapes. This is the spatial signature of the free slow dynamics, although slightly distorted. Moreover, $\sqrt{\lambda_1}\|\Phi_1^b\| = O(1)$, $\sqrt{\lambda_2}|\Phi_2^p| = O(\beta\mu^2)$. The energy of the dominant mode is now contained in the beam substructure whereas the energy of the second mode is contained in the pendulum substructure. The opposite is true for motions on the slow invariant manifold. The other two modes have beam components with shapes similar to the second and third PO modes of the beam with a mass at its tip. They have the spatial characteristics of the fast modes of the pendulum substructure.

All amplitudes of the PO modes but the second one have basic frequency at $2\omega_p$ and additional frequencies at ω_1 and multiples of it. The second mode, where the pendulum substructure dominates, has basic frequency at ω_p and other frequencies close to multiples of ω_1. Just as in the case of free interaction dynamics in the neighborhood of the slow invariant manifold, the interaction causing the periodic motion mixes slow and fast frequencies. The multiples of the pendulum frequency reflect the frequency signature of the free slow dynamics. In particular, we find the relation $\omega_1 = 3\omega_b = 6\omega_b$ in the frequency spectra of the amplitudes of the PO modes. It seems that the interaction mechanism creating the periodic motion manifests itself as a 3:1 internal resonance between the fast dynamics and the slaved slow dynamics. Recall that we have already encountered this internal resonance in the interactions of the slow and fast free dynamics.

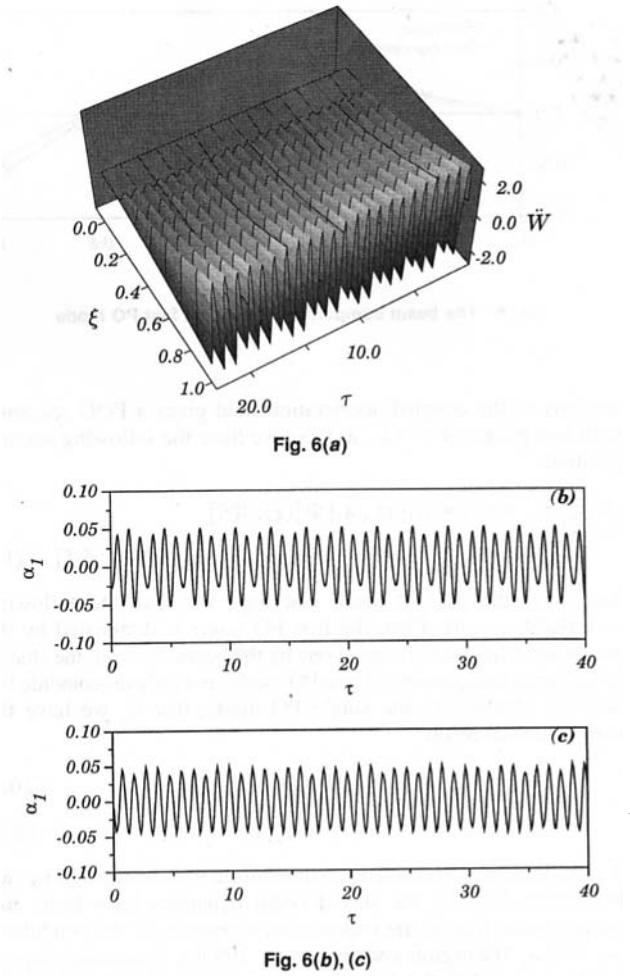

Fig. 6(*a*)

Fig. 6(*b*), (*c*)

Fig. 6 (*a*) Spatio-temporal behavior of the acceleration field as recorded by the accelerometers. The amplitude of the first beam PO mode: (*b*) theory, (*c*) experiment.

Figure 6(*a*) shows the spatio-temporal behavior, as recorded by the accelerometers, of the beam acceleration during a periodic motion of the physical system. This motion has similar characteristics as the one predicted by the equations of motion. The POD analysis reveals that this motion is supported by three PO modes. Figures 6(*b*) and 6(*c*) show good qualitative agreement between the experimental dynamics and those predicted by the equation of motion for the amplitude of the first PO mode.

Depending on the amount of dissipation, the system may respond with a quasi-periodic motion where the pendulum performs large amplitude oscillations whereas the beam oscillations have very small amplitude compared to that of the resonant dynamics. For example, at coupling strength $(\mu, \beta) = (0.4226, 0.1)$, considered to be strong since it creates a 2:1 internal resonance, and dissipation $(\zeta_p, \zeta_b) = (0.01, 0.05)$, the system responds with stable quasi-periodic motion when forced at $(\Omega, P) = (\omega_1, 280)$ where $\omega_1 = 2$ is the natural frequency of the beam. The coupled acceleration field of this motion is supported by four PO modes whereas that of the beam by three PO modes. The first two dominant modes satisfy the following result: $\Phi_1^b(\xi) \approx \Phi_2^b(\xi)$, $\Phi_1^b(\xi) = \sqrt{\gamma_1}\, \Upsilon_1^b(\xi) \approx \Upsilon^b(\xi)$. This is the spatial signature of the free slow dynamics, although distorted quantitatively but not qualitatively. Moreover, $\sqrt{\lambda_1}\|\Phi_1^b\| = O(1)$, $\sqrt{\lambda_2}|\Phi_2^p| = O(\beta\mu^2)$: The energy of the dominant mode is contained in the beam substructure whereas that of the second mode is contained in the pendulum substructure. The spatial characteristics of the first three

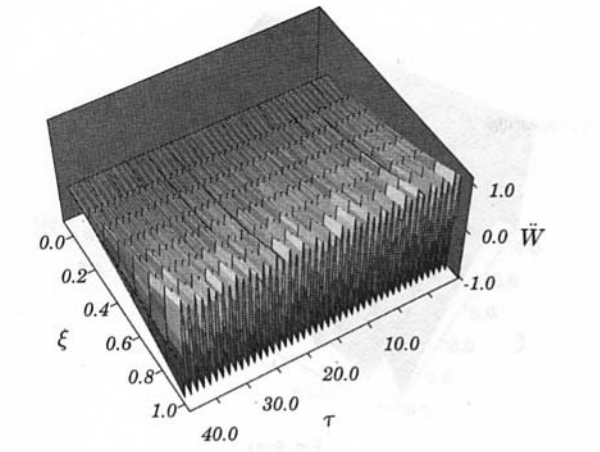

Fig. 7(*a*)

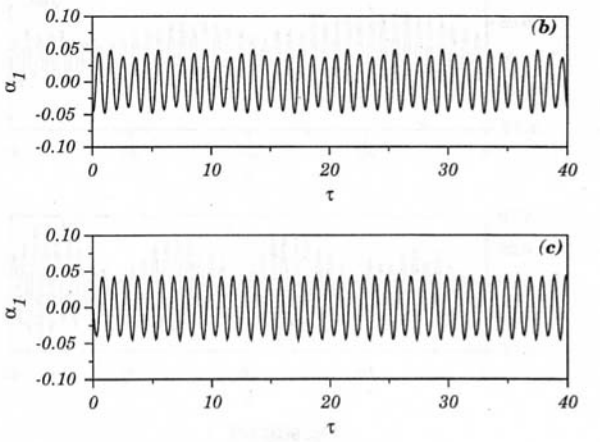

Fig. 7(*b*), (*c*)

Fig. 7 (*a*) Spatio-temporal behavior of the acceleration field as recorded by the accelerometers. The amplitude of the first beam PO mode: (*b*) theory, (*c*) experiment.

PO modes are qualitatively the same as that for the periodic motion at small coupling.

Such a quasi-periodic motion has been observed in experiments with the physical system at 2:1 internal resonance, obtained by fixing the pendulum length at $L_p = 50.80$ mm. Figure 7(*a*) shows the spatio-temporal behavior, as recorded by the accelerometers, of the acceleration of the beam. During this motion, the pendulum executes large amplitude motions whereas the beam motion has been reduced to very small amplitudes. The POD analysis of the beam acceleration data gives three to four modes. Figures 7(*b*) and 7(*c*) reveal qualitative and quantitative agreement between experiment and theory for the amplitude dynamics of the dominant PO mode during such a quasi-periodic motion.

The system at 2:1 internal resonance and dissipation $(\zeta_b, \zeta_p) = (0.005, 0.01)$ responds to small amplitudes of forcing with periodic motions. The coupled acceleration field of this periodic motion is supported by four PO modes whereas that of the beam by three PO modes. The shapes of these PO modes are almost identical to those of the periodic motion at small coupling $\mu = 0.175$. The frequency spectrum of the amplitude of the dominant mode contains $(\omega_p, 3\omega_p)$ whereas that of the second mode contains $(2\omega_p, 4\omega_p)$. Here we do not see a mixing of the master slow spectrum and slaved slow spectrum. However, the interaction leaves its signature as a phase difference between the pendulum and the beam oscillations. Recall that there is no phase difference between the slow master and slaved slow dynamics.

We have found periodic motions and quasi-periodic motions supported by four PO modes for all levels of sufficiently large coupling. All motions have spatial and temporal characteristics dominated by those of the free slow and fast dynamics of the stiff/soft system. Figure 8(*a*) reveals that the regular motions of the physical system are dominated by the same PO modes. Certainly, the consistency is remarkable. Figure 8(*b*) shows the same remarkable consistency for the numerical experiments. Figure 8(*c*) shows the POD spectra for regular motions of the physical system, whose PO modes are shown in Fig. 8(*b*), and regular motions, whose PO modes are shown in Fig. 8(*a*), predicted by the equations of motion in singular perturbation formulation. The plateau in the spectrum of the experimental motions is due to the presense of noise.

8 Interactions in Chaotic Motions

When forced at the first natural frequency of the beam, the beam/pendulum system can respond with irregular motions, that is, chaos. The chaotic attractors do not reside on the underlining slow and fast invariant manifolds. Thus, they must involve interactions between the slow and fast dynamics. Note that the dynamics restricted to the fast invariant manifold are linear and resonant. If the system is forced at a frequency of the same order of the natural frequency of the pendulum, it undergoes under certain conditions

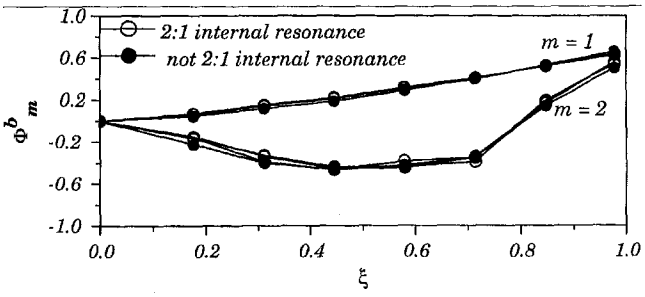

Fig. 8(*a*)

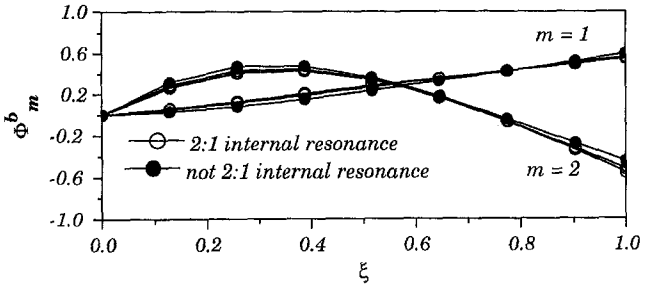

Fig. 8(*b*)

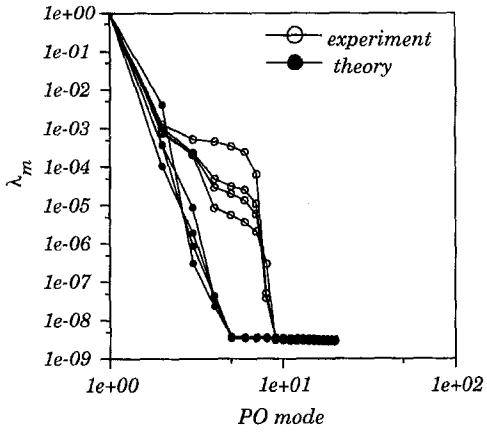

Fig. 8(*c*)

Fig. 8 The first two beam PO modes: (*a*) experiment, (*b*) theory. (*c*) The POD spectrum for various regular motions for experiment and theory.

chaotic motions residing on a slow invariant manifold if the coupling is weak. These chaotic motions involve only pure slow dynamics and do not involve any interaction with the fast dynamics. However, if the coupling is not weak, chaotic motions are not restricted to an invariant slow manifold.

For coupling strength $(\mu, \beta) = (0.175, 0.1)$, dissipation factors $(\zeta_b, \zeta_p) = (0.005, 0.01)$, and forcing frequency $\Omega = \omega_1 \approx 4.8293$, the fast invariant manifold is unstable for $P > 40$. The irregular motions repelled by the unstable regions of the fast and slow invariant manifolds exhibit energy transfer between the pendulum and the continuum. For $40 < P < P_1 \approx 100$, the pendulum librates and experiences complete amplitude modulations whereas the beam experiences small amplitude modulations. A Poincare map reveals that this motion is chaotic and that its projection onto the pendulum phase plane $\Psi_1 - \Psi_2$ is restricted almost to a line. We call this a weak chaotic attractor. The POD analysis of the coupled acceleration field yields three PO modes. The first two modes have identical beam components. Most of the energy of the dominant mode is contained in the beam substructure. Clearly, this is the signature of the underlining slow and fast dynamics. However, the third mode, which is the fast mode, differs in shape from the third mode supporting interactions during regular forced and unforced motions. The frequency spectrum of the amplitude of the first PO mode is centered about the natural frequency of the beam, which turns out to be about $6\omega_p$. The frequency spectrum of the second mode distributed around the frequencies: $3\omega_p$, $9\omega_p$, and $15\omega_p$. The frequency spectrum of the third mode is distributed in narrow continuous bands about the frequencies: $6\omega_p$, $12\omega_p$, and $15\omega_p$.

As we increase the forcing, the modulation of the beam dynamics increases, reflecting the fact that the interaction becomes more intense. For instance, at forcing level $P = 200$, we have a chaotic motion with complete energy transfer between the beam and pendulum. Now the coupled acceleration field of the chaotic attractor is supported by six PO modes. *The number of PO modes increases in going from chaotic motions with weak beam modulations to chaotic motions with complete energy transfer between the beam and pendulum substructures.* The frequency spectrum of the amplitude of the first mode is continuous and centered about the natural frequency of the coupled beam. The frequency spectrum of the amplitude of the second mode is continuous and contains pendulum low frequencies. Here we see that the interaction leaves signs in both the spatial and temporal distributions of the PO modes.

At some critical forcing the chaotic attractor becomes abruptly periodic. This is the periodic attractor we discussed above, characterized by four PO modes. Over a range (P_l, P_r) of forcing amplitude, the response is periodic with dramatic reduction in the beam amplitude. For $P > P_r$, the large-amplitude periodic motion coexists with a chaotic motion. During such a chaotic motion the pendulum rotates and librates irregularly. When the pendulum rotates for a long time, the beam dynamics are reduced dramatically. This attractor is characterized by six PO modes. Again, the first two modes bear the spatial signature of the slow and fast dynamics. Figure 9(*a*) shows the spatio-temporal behavior, as recorded by the accelerometers, of the acceleration of the beam for the system with coupling at $\mu = 0.175$. This motion is chaotic and after 20 minutes of natural time is asymptotically attracted by the periodic motion of large amplitude shown in Figure 6(*a*). Figure 9(*b*) through 9(*e*) shows the time series and spectra of the dominant mode. Clearly, there is good qualitative and quantitative agreement between theory and experiment.

The periodic motion of large-amplitude loses stability abruptly around a critical forcing amplitude P_{cr} for fixed Ω or near a critical frequency Ω_{cr} for fixed P. The resulting motion is chaotic. And the transition from regular to chaotic motions is underlined by hysteresis. The abrupt change from periodicity, or quasi-periodicity, generates a new frequency in the temporal dynamics. The coupled acceleration field of this new chaotic attractor is characterized by seven PO modes. This is called a strong hyperchaotic attractor.

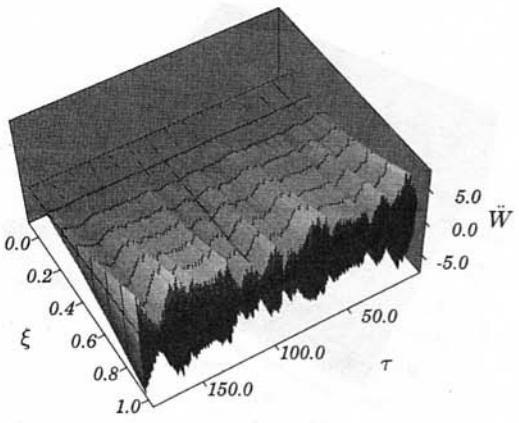

Fig. 9(*a*)

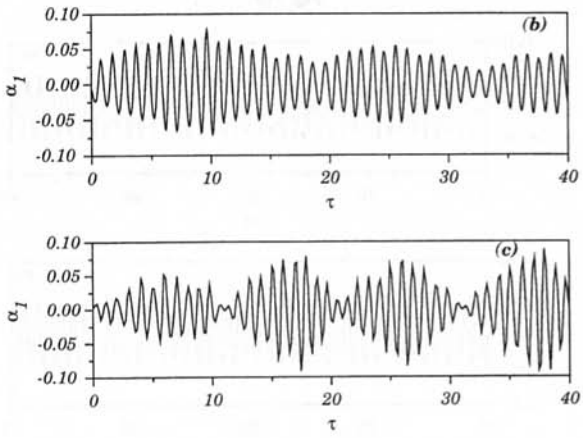

Fig. 9(*b*), (*c*)

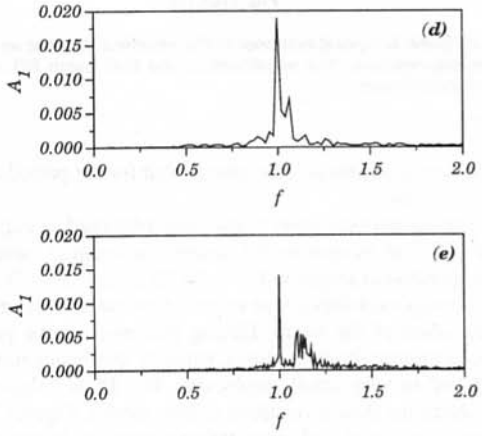

Fig. 9(*d*), (e)

Fig. 9 (*a*) Spatio-temporal behavior of the acceleration field as recorded by the accelerometers. The amplitude α_1: (*b*) experiment, (*c*) theory. The FFT of α_1: (*d*) experiment, (*e*) theory.

Contrary to the chaotic attractors we have encountered so far where the beam components of the first and second modes have similar shapes to the single mode $\Upsilon^b(\xi)$ supporing the acceleration of the beam during free slow motions, now the second and third modes of this new attractor have beam components with shapes similar to the beam component of the fast mode supporting interactions during free motions in the neighborhood of the slow invariant manifold. Now the pendulum substructure dominates the third mode. All other modes are dominated by the beam substructure. So interaction leaves now a new spatial signature in the creation of a new fast mode where the pendulum dominates. The

creation of the new fast mode is due to the disappearance of the slow mode dominated by the pendulum. Furthermore, the high-order PO modes bear considerable spatial modulation. This is a nonlinear phenomenon and a sign of interaction.

We observe the same phenomena, though more intense, in the coupled system at 2:1 internal resonance. The chaotic motions that coexist with regular attractors are characterized by six PO modes. The quasi-periodic motion mentioned above loses stability abruptly and triggers a chaotic motion of large amplitude during which energy is exchanged irregularly between the beam and the pendulum. This have been observed both in numerical and physical experiments. Figure 10(a) shows the spatio-temporal behavior, as recorded with the accelerometers, of the beam acceleration during the chaotic motion generated by the abrupt loss of stability of the quasi-periodic shown in Figure 7(a). Figures 10(b) through 10(e) shows the time history and spectra of the amplitude of the dominant mode. Clearly, there is good qualitative and quantitative agreement between theory and experiment. The chaotic attractor predicted by the equations of motion and the one recorded from the experiment contain the high frequency. This hyper-chaotic attractor is characterized by seven PO modes.

Figure 11(a) shows the shapes of the dominant modes supporting regular and chaotic motions in the physical system. Clearly, the consistency is remarkable. *The chaotic and regular attractors bear the spatial signature of the free slow and fast dynamics of the stiff/soft system.* The same remarkable consistency is found also in the results from the POD analysis of numerical experiments with the equations of motion. Figure 11(b) shows the POD spectrum of chaotic motions predicted by theory and measured in the physical system. The equations of motion predict and the experiment verifies (Georgiou et al., 1997c) that the change from periodicity to chaos is underlined by a strong hysteresis, energy transfer among the PO modes, and shape changes in the PO modes.

9 Conclusions and Discussion

Using tools from geometric singular perturbations, invariant manifolds, and proper orthogonal projections, we studied the interaction of fast/slow dynamics in a coupled linear/nonlinear structure consisting of a cantilever linear beam coupled to a pendulum. The objective of the study was to understand interactions of linear/nonlinear dynamics. For sufficiently small coupling between the linear and nonlinear substructures, large-amplitude unforced slow motions, generated by the slow pendulum, interact with the resonant fast dynamics of the linear beam; the result is a substantial reduction of the fast resonant dynamics. In this case, the interacting dynamics are dominated by the slow and fast PO (proper orthogonal) modes. The slow and fast PO modes are, respectively, nonlinear and linear spatial modes of the coupled structure and stem from the slow and fundamental fast invariant manifolds of the stiff/soft system. The slow invariant manifold is two-dimensional and is the geometric realization of a nonlinear normal mode. It is characterized by two PO modes. For higher values of coupling, the unforced slow dynamics of the pendulum substructure interact with the forced linear dynamics of the beam substructure in such a way as to produce periodic, quasi-periodic, and chaotic motions. There are periodic and quasi-periodic motions characterized by four PO modes, and chaotic motions characterized by three, six, and seven PO modes. The first three dominant modes bear the spatial and temporal signatures of the slow and fast free dynamics of the stiff/soft system. The change from periodicity to chaos and vice versa is characterized by a hysteresis phenomenon, which is clearly a nonlinear dynamical effect. We built a cantilever beam/pendulum system and performed experiments to validate the theoretical findings. The experiment verifies the theoretical findings, especially, the abrupt transition from periodicity to chaos, and the nonlinear hysteresis. Furthermore, the experiment verifies the spatial and temporal characteristics of the slow invariant manifold as predicted by singular perturbation technique in previous works.

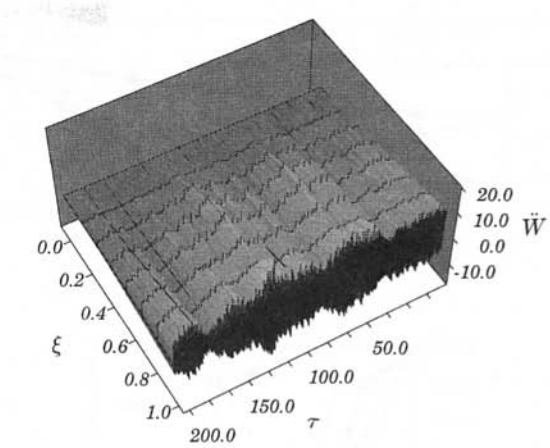

Fig. 10(a)

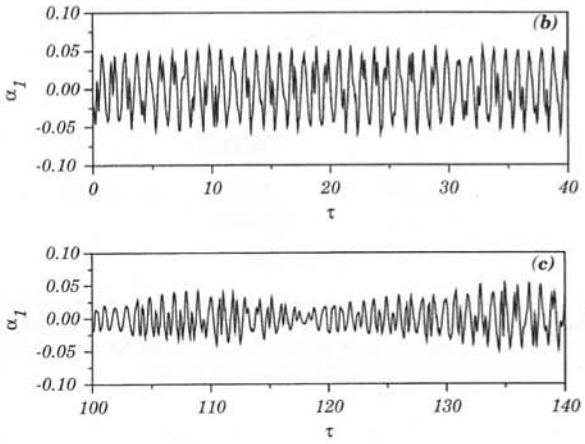

Fig. 10(b), (c)

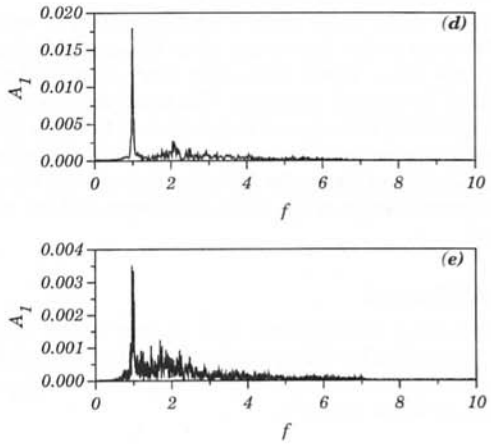

Fig. 10(d), (e)

Fig. 10 (a) Spatio-temporal behavior of the acceleration field as recorded by the accelerometers. The amplitude α_1: (b) experiment, (c) theory. The FFT of α_1: (d) experiment, (e) theory.

The physical system is a perturbation of the ideal system described by the equations of motion. Furthermore, we have to deal with the issue of noise. Since the primary objective is to analyze numerical and experimental data by applying the POD method and relate the dynamics to the dynamics of the soft/stiff system, it is satisfactory to find remarkable consistencies separately in the numerical and separately in the experimental results and reasonable qualitative and quantitative agreement between experiment and theory. Clearly, this is the case here. We verified experimentally the fact that proper orthogonal projections can be used to

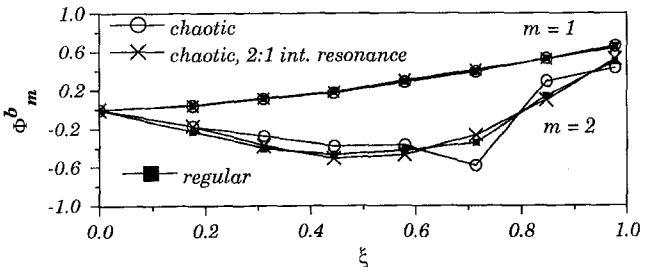

Fig. 11(*a*)

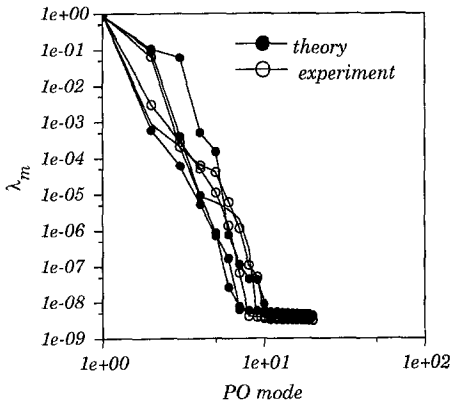

Fig. 11(b)

Fig. 11 (*a*) The first two beam PO modes supporting regular and chaotic motions in the physical system, (*b*) the POD spectrum of chaotic motions predicted by the equations of motion in singular perturbation formulation and from measurements in the physical system

identify the modes of coupled structures from spatio-temporal data, from measurements and numerics.

Finally, we mention that there is a previous body of work where a flexible beam with a large mass at its tip supports a pendulum (Cuvalci and Ertas, 1996). This study deals with the interaction dynamics of 2:1 internal resonance. The heavy mass constrains the coupled system to behave as a two-degree-of-freedom system. In the general case we consider here, we have shown that the interaction dynamics are due to the interplay between the whole spectrum of normal modes of the linear continuum and the nonlinear oscillator.

Acknowledgment

The numerical computations were as part of the DOD HPC project "Dynamical Modeling and Control in Large Scale Coupled Structural and Electronic Systems." Ira Schwartz was supported by the Office of Naval Research.

References

Fenichel, N., 1979, "Geometric singular perturbation theory for ordinary differential equations," *J. of Diff. Equat.*, Vol. 31, pp. 53–98.

Boothby, W. M., 1985, *An Introduction to Differential Manifolds and Riemanian Geometry,* Academic Press, London.

Cusumano, J. P., Sharkady, M. T., and Kimple, B. W., 1994, "Experimental measurements of dimensionality and spatial coherence in the dynamics of a flexible-beam impact oscillator," *Phil. Trans. R. Soc. Lond.*, Vol. A347, pp. 421–438.

Cuvalci, O., and Ertas, A., 1996, "Pendulum as Vibration Absorber for Flexible Structures: Experiments and Theory," *Journal of Vibration and Acoustics,* Vol. 118, pp. 558–566.

Georgiou, I. T., 1993, "Nonlinear dynamics and chaotic motions of a singularly perturbed nonlinear viscoelastic beam," Ph.D. dissertation, Purdue University, West Lafayette, IN.

Georgiou, I. T., Bajaj, A. K., and Corless, M., 1998a, "Slow and fast invariant manifolds, and normal modes in a two-degree-of-freedom structural dynamical system with multiple equilibrium states," *Int. J. of Non-Linear Mech.*, Vol. 33, No. 2, pp. 275–300.

Georgiou, I. T., Corless, M., and Bajaj, A. K., 1996a, "Dynamics of nonlinear structures with multiple equilibria: A singular perturbation-invariant manifold approach," *J. Appl. Math. Phys. (ZAMP),* to appear.

Georgiou, I. T., and Schwartz, I. B., 1999a, "Dynamics of Large Scale Coupled Structural/Mechanical Systems: A Singular Perturbation/Proper Orthogonal Decomposition Approach," *J. Appl. Math. (SIAM),* Vol. 59, No. 4, pp. 1178–1207.

Georgiou, I. T., and Schwartz, I. B., 1997a, "Slaving the In-Plane Motions of a Nonlinear Plate to its Flexural Motions: An Invariant Manifold Approach," ASME JOURNAL OF APPLIED MECHANICS, Vol. 64, pp. 175–182.

Georgiou, I. T., Sansour, J., Sansour, C., and Schwartz, I. B., 1997b, "Nonlinear dynamics of geometrically exact in-plane rods: the finite element/proper orthogonal decomposition approach," *Acta Mechanica,* to appear.

Georgiou, I. T., and Schwartz, I. B., 1999b, "The Slow Nonlinear Normal Mode and Stochasticity in the Dynamics of a Conservative Flexible Rod/Pendulum Configuration," *Journal of Sound and Vibration,* Vol. 220, No. 3, pp. 383–411.

Georgiou, I. T., Schwartz, I. B., Emaci, E., and Vakakis, A. F., 1997c, "Chaos and Hysteresis in Dynamics of Coupled Structures: Experiment and Theory," *Proceedings of the Fourth Experimental Chaos Conference,* M. Ding, W. Ditto, L. Pecora, M. Spano, and S. Vohra, eds., World Scientific, Singapore.

Georgiou, I. T., and Sansour, J., 1998b, "Analyzing the finite element dynamics of nonlinear in-plane rods by the method of proper orthogonal decomposition," *Computational Mechanics, New Trends and Applications,* S. Idelsohn, E. Onate, and E. Dvorkin, eds., CIMNE, Barcelona, Spain.

Jones, C., 1995, *Geometric singular perturbation theory in dynamical systems* (Springer Lecture Notes Math. 1609), pp. 44–120.

Knobloch, H. W., and Aulbach, B., 1984, "Singular perturbations and integral manifolds," *J. Math. Phys. Sci.,* Vol. 18, No. 5, pp. 415–423.

Nipp, K., 1985, "Invariant manifolds of singularly perturbed ordinary differential equations," *J. Appl. Math. Phys. (ZAMP),* Vol. 36, pp. 311–320.

Mira, C., 1997, "Some Historical Aspects of Nonlinear Dynamics-Possible Trends for the Future," *J. Franklin Inst.,* Vol. 334B, No. 5, pp. 1075–1113.

Pontrjagin, L. S., 1957, "Asymptotic behavior of solutions of differential equations when the higher derivatives contain a small parameter as a factor," *Izv. Akad. Nauk (Ser. mat.),* Vol. 21, pp. 605–621 (in Russian).

Scheck, F., 1990, *Mechanics,* Springer-Verlag, New York.

Tikhonov, A. N., 1952, "Systems of differential equations containing a small parameter with higher order derivatives," *Mat. Sbornik,* Vol. 31, No. 73, pp. 575–584 (in Russian).

Sirovich, L., 1987, "Turbulence and the Dynamics of Coherent Structures, Pt. I, Coherent Structures," *Quart. Appl. Math.,* Vol. 45, pp. 561–571.

Schwartz, I. B., and Triandaf, I., 1996, "Chaos and intermittent bursting in a reaction-diffusion process," *Chaos,* Vol. 6, pp. 229–237.

Schwartz, I. B., and Georgiou, I. T., 1998, "Instant chaos and hysteresis in coupled linear-nonlinear oscillators," *Physics Letters, A,* Vol. 242, pp. 307–312.

Wiggins, S., 1990, *Introduction to Applied Nonlinear Dynamical Systems and Chaos,* Springer-Verlag, New York.

APPENDIX

Approaching the Equations of Motion as a Singular Perturbation Problem: A Review

In this section we formulate the equations of motion as a singular perturbation problem. First, we transform the coupled PDE/POD equations of motion (2) and the associated boundary equations (4) into a set of coupled linear/nonlinear oscillators. A method based on modal decomposition to reduce linear PDEs in solid mechanics coupled at their boundaries to nonlinear oscillators to coupled linear-nonlinear oscillators is given in (Georgiou, 1993; Georgiou and Schwartz, 1999a). For the present beam/pendulum system, this procedure gives

$$\ddot{\theta} + \left[1 + \sum_{m=1}^{N} (-1)^{m+1}\ddot{\eta}_m\right] \sin(\theta) + 2\zeta_p\dot{\theta} = 0, \quad (22a)$$

$$\left[\delta_{mk} + (-1)^{m+k+2}4\beta\cos^2(\theta)\right]\ddot{\eta}_k + \frac{\eta_m}{\mu^2\mu_m^2} + 2\zeta_b\frac{\dot{\eta}_m}{\mu\mu_m^2}$$

$$+ (-1)^{m+1}4\beta[\dot{\theta}^2\cos(\theta) - \sin^2(\theta)] = F_m P\cos(\Omega\tau), \quad (22b)$$

where δ_{mk} denotes the Kronocker delta, and F_m are coefficients from the modal projection of a harmonic in time force applied at a point, and $m = 1, 2, \ldots, N \to \infty$. The modal amplitudes and velocities in (22*b*) stem from the expansion

$$W(\xi, \tau) = \sum_{m=1}^{N} \eta_m(\tau)\phi_m(\xi) \quad (23)$$

where $\phi_m(\xi)$ are the spatial natural modes of the uncoupled cantilever beam.

To analyze the global dynamics of the above coupled oscillators, we need to determine invariant manifolds of motion. Invariant manifolds of motion are naturally introduced if the above coupled oscillators are cast as a singular perturbation problem. The frequency ratio μ qualifies as a singular perturbation parameter. Coupled oscillators (22) can be formulated as follows:

$$\dot{\mathbf{\Psi}} = \mathbf{A}(\mathbf{\Psi};\, N)Z + \mathbf{F}(\mathbf{\Psi},\, \Theta;\, N), \tag{24a}$$

$$\dot{\Theta} = \mathbf{R}\Theta, \tag{24b}$$

$$\mu\dot{Z} = \mathbf{B}(\mathbf{\Psi};\, N)Z + \mathbf{G}(\mathbf{\Psi},\, \Theta;\, N) \tag{24c}$$

where the variables $\mathbf{\Psi} \equiv (\mathbf{\Psi}_1, \mathbf{\Psi}_2) = (\theta, \dot{\theta})$, and $\Theta \equiv (\Theta_1, \Theta_2) = (\cos(\Omega\tau), \sin(\Omega\tau))$ denote the pendulum state and the harmonic forcing, respectively. The variable $Z \equiv (\{Z_1, Z_2\}, \ldots, \{Z_{2m-1}, Z_m\})$, $m = 1, \ldots, N \to \infty$, denotes the scaled states of the beam modal oscillators. They are given by

$$\{\eta_m,\, \dot{\eta}_m\} = \{\mu^2\mu_m^2 Z_{2m-1},\, \mu\mu_m^2 Z_{2m}\}. \tag{25}$$

Note that the scaling factors, $\mu_m \equiv \omega_1/\omega_m = \kappa_1^2/\kappa_m^2$ where κ_m is a root of Eq. (3), are the normalized frequencies of the uncoupled cantilever beam. Moreover, the various functions in Eq. (24) are determined from Eq. (22).

For a global analysis of the dynamics in phase space, geometry in the form of invariant manifolds of motion plays a pivotal role. The singular perturbation formulation (24) introduces naturally in phase space two fundamental invariant manifolds of motion: a slow one containing pure slow dynamics, and a fast one containing pure fast dynamics.

For fixed mass ratio β, and sufficiently small μ, the dynamics evolve on a single slow time scale and multiple fast time scales. In particular, whenever $\Omega = O(1)$, Eq. (24*a*) and Eq. (24*b*) form the slow system, and Eq. (24*c*) forms the fast system. In this case, we are forcing the slow pendulum dynamics. The dynamics are nonlinear and reside in a low-dimensional nonlinear subspace, the so called slow invariant manifold $\mathcal{N}_\mu$. The slow manifold is described by the graph of a function

$$\mathcal{N}_\mu = \{(\mathbf{\Psi},\, \Theta,\, Z) | Z = \mathbf{H}_\mu(\mathbf{\Psi},\, \Theta)\}. \tag{26}$$

The vector-valued function $\mathbf{H}_\mu$ is the solution to the so-called slow manifold condition (Georgiou and Schwartz, 1997a, 1999a).

For the unforced system ($P = 0$), the slow invariant manifold is two-dimensional; it contains all static equilibrium states given by

$$C \equiv (\{\hat{\mathbf{\Psi}}_1,\, \hat{\mathbf{\Psi}}_2\}, \ldots, \{\hat{Z}_{2m-1},\, \hat{Z}_{2m}\}) = (\{0,\, 0\}, \ldots, \{0,\, 0\}), \tag{27a}$$

$$S_{\pm 1} \equiv (\{\hat{\mathbf{\Psi}}_1,\, \hat{\mathbf{\Psi}}_2\}, \ldots, \{\hat{Z}_{2m-1},\, \hat{Z}_{2m}\}) = (\{\pm\pi,\, 0\}, \ldots, \{0,\, 0\}). \tag{27b}$$

They are the discrete analogues of the equilibrium configurations (1).

On the other hand, whenever $\Omega = O(1/\mu)$, Eq. (24*b*) becomes part of the fast system, and we are forcing the beam fast dynamics. The pure fast dynamics are linear and reside either on the stable infinite-dimensional linear manifold:

$$\mathcal{L}_\mu^s = \{(\mathbf{\Psi},\, \Theta,\, Z) | \mathbf{\Psi} = (0,\, 0)\}, \tag{28}$$

or the unstable infinite-dimensional linear manifold:

$$\mathcal{L}_\mu^u = \{(\Psi,\, \Theta,\, Z) | \mathbf{\Psi} = (\pm\pi,\, 0)\}. \tag{29}$$

The linear fast manifolds intersect transverserly the slow invariant manifold at the static equilibria (27). Therefore, the slow and fast invariant manifolds span the entire phase space. By definition, there is no interaction between the substructures whenever the dynamics reside on the slow or fast invariant manifolds. Interactions occur as long as the dynamics are not restricted to these particular invariant manifolds.

Regarding the history of development of singular perturbations, Mira (1997) traces it back to the early works of Tikhonov (1952) and Pontrjagin (1957). The modern geometric development has its roots in the works of Fenichel (1979). The latest developments and applications are discussed in Jones (1995).

A Three-Dimensional Frictional Contact Element Whose Stiffness Matrix is Symmetric

S. H. Ju
Associate Professor,
Department of Civil Engineering,
National Cheng-Kung University,
Tainan, Taiwan, R.O.C.

R. E. Rowlands
Professor,
Department of Mechanical Engineering,
University of Wisconsin-Madison,
Madison, WI 53706
Fellow ASME

A three-dimensional contact element based on the penalty function method has been developed for contact frictional problems with sticking, sliding, and separation modes in finite element analysis. A major advantage of this contact element is that its stiffness matrix is symmetric, even for frictional contact problems which have extensive sliding. As with other conventional finite elements, such as beam and continuum elements, this new contact element can be added to an existing finite element program without having to modify the main finite element analysis program. One is therefore able to easily implement the element into existing nonlinear finite element analysis codes for static, dynamic, and inelastic analyses. This element, which contains one contact node and four target nodes, can be used to analyze node-to-surface contact problems including those where the contact node slides along one or several target surfaces.

1 Introduction

Computationally, the analysis of frictional contact problems is extremely difficult, even for static cases involving the simplest constitutive relation. Much of the difficulty lies in the fact that the contact areas and the friction directions of the bodies under consideration are unknown a priori and the contacting surfaces change in size, shape, and mode (sticking, sliding, or separating) as the loading increases. Largely because of the high nonlinearity and notwithstanding appreciable amount of prior effort on the topic (Chaudhary and Bathe, 1986; Hallquist et al., 1985; Kulak, 1989; Laursen and Simo, 1993; Malone and Johnson, 1994; Mottershead et al., 1992; Parishch, 1989; Peric and Owen, 1992; Paradopoulos and Taylor, 1993), development of a reliable and efficient three-dimensional frictional contact algorithm in finite element analysis remains one of the challenging problems in computational solid mechanics. Parishch (1989) and Paradopoulos and Taylor (1993) developed a three-dimensional contact algorithm without friction. Malone and Johnson (1994) and Kulak (1989) established the explicit contact algorithms using a very small time-step length to simulate three-dimensional contact problems. Chaudhary and Bathe (1986) and Hallquist et al. (1985) used the Lagrange multiplier approach to solve the three-dimensional contact problems. Mottershead et al. (1992) developed a three-dimensional contact algorithm, but no three-dimensional example was included in their paper. Laursen and Simo (1993) developed a continuum formulation for the finite deformation frictional contact between deformable bodies. Peric and Owen (1992) established the contact algorithms using the penalty method. Only Chaudhary and Bathe (1986) included a comparison between theoretical and numerical solutions.

Contact element stiffness matrices are symmetric for frictionless contact problems. Unfortunately, problems involving sliding friction result in an unsymmetrical stiffness matrix, and this difficulty is demonstrated in the above references. Analyses having unsymmetrical matrices typically require about twice the amount of storage space and twice the amount of calculation time as do those with symmetric matrices. Although the sliding area sometimes involves only a relatively small part of total contact area, the stiffness matrix is still unsymmetrical. This disadvantage is alleviated here by extending the algorithm of our previous two-dimensional contact element (Ju et al., 1995) into a three-dimensional frictional contact element having a symmetric stiffness matrix. The amount of both computing time and storage needed can be significant concerns when solving engineering problems. Ability to reduce these quantities is a major advantage of the present method. This paper demonstrates the three-dimensional contact element's ability to satisfactorily model frictional static or dynamic contact problems even when the amount of sliding is extensive.

The present three-dimensional contact element is an extension of penalty methods for displacement formulations (Kanto and Yogawa, 1990; Mottershead, 1992; Peric and Owen, 1992; Paradopoulos, 1993; Ju et al., 1995). It can be implemented into an existing nonlinear finite element program without having to modify a main finite element program or solution method. This element, which contains one contact node and four target nodes, enables one to analyze node-to-surface contact problems such as those involving the contact node sliding along one or several target surfaces. This element can be used for static or dynamic (involving impact and collision) analyses and for a variety of constitutive behaviors.

2 Formulating Stiffness Matrix of Five-Node Contact Element

2.1 Governing Matrix Equation of the Penalty Method. With reference to Fig. 1, the governing matrix equation of the penalty method at a certain iteration is (Ju et al., 1995)

$$(\mathbf{K} + \mathbf{K}_s)\mathbf{dx} = \mathbf{F}_{ext} - \mathbf{F}_{int} - \mathbf{FS}_{int} \tag{1}$$

where

- $\mathbf{dx}$ = incremental displacement vector between two successive iterations
- $\mathbf{K}$ = total tangent stiffness matrix of bodies (i.e., contactor and target)
- $\mathbf{K}_s$ = total stiffness matrix of all contact elements
- $\mathbf{F}_{ext}$ = external force vector including the inertia forces of a dynamic problem
- $\mathbf{F}_{int}$ = internal force vector of contactor and target bodies

Contributed by the Applied Mechanics Division of THE AMERICAN SOCIETY OF MECHANICAL ENGINEERS for publication in the ASME JOURNAL OF APPLIED MECHANICS.
Discussion on the paper should be addressed to the Technical Editor, Professor Lewis T. Wheeler, Department of Mechanical Engineering, University of Houston, Houston, TX 77204-4792, and will be accepted until four months after final publication of the paper itself in the ASME JOURNAL OF APPLIED MECHANICS.
Manuscript received by the ASME Applied Mechanics Division, Dec. 5, 1996; final revision, July 3, 1997. Associate Technical Editor: W. K. Liu.

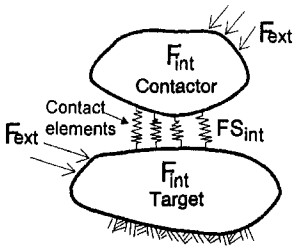

Fig. 1 Contact of two bodies

$\mathbf{FS}_{int}$ = internal normal and frictional force vector of contact elements

Quantities $\mathbf{K}$ and $\mathbf{F}_{int}$ of Eq. (1) are assembled by using typical elements, such as plane-stress, plane-strain, linear, or nonlinear elements. The stiffness matrix $\mathbf{K}_S$ and internal force vector $\mathbf{FS}_{int}$ are discussed below.

2.2 Stiffness Matrix of the Node-to-Node Element. This study uses Coulomb friction:

$$F = f_s - \mu f_n \tag{2}$$

where f_n and f_s are the magnitudes of normal and frictional forces (they are always both positive) and μ is the frictional coefficient. If $F = 0$, the element slides. If $F < 0$, the element sticks rather than slides. For node-to-node contact and providing three degrees-of-freedom in the local directions, the element stiffness matrix at a point can be formulated as

$$\begin{Bmatrix} df_s \\ df_{sl} \\ df_n \end{Bmatrix} = [K_{\text{local}}] \begin{Bmatrix} dU \\ dV \\ dW \end{Bmatrix} \tag{3}$$

where

$$[K_{\text{local}}] = [K_{\text{stick}}] = \begin{bmatrix} k & 0 & 0 \\ 0 & k & 0 \\ 0 & 0 & k \end{bmatrix} \text{ for sticking, and} \tag{4}$$

$$[K_{\text{local}}] = [K_{\text{slide-unsymmetrical}}] = \begin{bmatrix} 0 & 0 & \mu k \\ 0 & k_v & 0 \\ 0 & 0 & k \end{bmatrix} \text{ for sliding.} \tag{5}$$

Quantity f_{sl} is the internal friction force, dU is the relative displacements between two successive iterations in the last tangential direction (direction of the frictional stress at the end of last iteration), dV is the relative displacements due to the change of the tangential direction between the present and last iteration (dU is perpendicular to direction dV), dW is the relative displacement in the normal direction between two successive iterations, k is an input large penalty constant, and k_v is the penalty constant for dV. Since the two triangles of the force and the displacement systems are similar (Fig. 2), the following equation can be obtained:

$$k_v = \frac{df_{sl}}{dV} = \frac{df_s}{dU} = \frac{F_s^n}{U^n}, \tag{6}$$

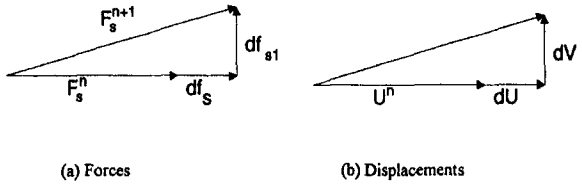

Fig. 2 Forces and displacements

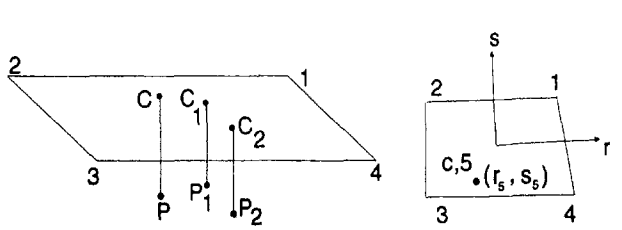

Point P_1 = Contact node at last iteration;
Point P_2 = Contact node at current iteration;
Point C_1 = Contact position at last iteration
Point C_2 = Contact position at current iteration
Point C = Contact position at last time step.

Fig. 3 Contact analysis during two iterations and natural coordinate (r-s)

where F_s^n is the friction force of the last or nth iteration, and U^n is the equivalent displacement of the friction force at this last or nth iteration. One can approximate k_v by the average value of (df_s/dU) of all the iterations during this force or time-step. Matrix $[K_{\text{slide-unsymmetrical}}]$ is unsymmetrical and can be replaced by a symmetric element stiffness matrix K_{slide} as follows:

$$[K_{\text{local}}] = [K_{\text{slide}}] = \begin{bmatrix} \mu^2 k & 0 & \mu k \\ 0 & k_v & 0 \\ \mu k & 0 & k \end{bmatrix}. \tag{7}$$

Equation (7) obeys the Mohr-Coulomb friction theory ($df_S = \mu \mathbf{d}f_n$); however, the incremental normal force df_n contains the term $\mu k dU$. If this term is omitted from the calculation of the total normal force ($F_n = kV$), the contact analyses from Eqs. (5) and (7) will produce a similar result at the convergent state ($dU \cong 0$, $dV \cong 0$, and $dW \cong 0$). Although a symmetric formulation can be obtained by using this algorithm, the convergence might be slow for problems which involve extensive sliding contact. This symmetric solution scheme is often efficient for contact problems having both sticking and sliding modes, since it is as about twice as fast as the unsymmetrical solution scheme. The amount of the computer memory needed can also be significantly reduced.

The stiffness matrices discussed above are expressed in local coordinates. They can be transformed back into the global coordinates as follows:

$$\mathbf{K} = [T]^T [K_{\text{local}}][T] \tag{8}$$

$$\text{where } [T] = \begin{bmatrix} -u_1 & -u_2 & -u_3 \\ v_1 & v_2 & v_3 \\ w_1 & w_2 & w_3 \end{bmatrix} = \begin{bmatrix} -\{u\}^T \\ \{v\}^T \\ \{w\}^T \end{bmatrix}. \tag{9}$$

In this case $\{u\}$, $\{v\}$ and $\{w\}(\{u\} = \{v\} \times \{w\})$ are the unit direction vectors parallel to the displacements U, V, and W, respectively. The $-\{u\}$ in Eq. (9) means that the direction of the frictional force is opposite to that of displacement U.

2.3 Five-Node Node-to-Surface Contact Element. In order to solve node-to-surface contact problems, a linear transformation matrix is used to transform the two-node (node-to-node) stiffness to the five-node (node-to-surface) stiffness (Fig. 3). It can be shown that the two-node stiffness matrix is similar to the truss element as follows:

$$\mathbf{K}_2 = \begin{bmatrix} K & -K \\ -K & K \end{bmatrix} \tag{10}$$

where $\mathbf{K}$ is the global stiffness matrix for sticking, separating, or sliding modes, respectively, and is evaluated from Eq. (4) or (5). From Fig. 3,

$$\begin{Bmatrix} f_1 \\ f_2 \\ f_3 \\ f_4 \\ f_5 \end{Bmatrix} = \begin{bmatrix} N_1 & 0 \\ N_2 & 0 \\ N_3 & 0 \\ N_4 & 0 \\ 0 & 1 \end{bmatrix} \begin{Bmatrix} f_s \\ f_c \end{Bmatrix} \quad \text{or} \quad \mathbf{f} = \mathbf{H}^T \mathbf{f}_c \tag{11}$$

where

$$N_1 = (1 + r_5)(1 + s_5);$$

$$N_2 = (1 - r_5)(1 + s_5);$$

$$N_3 = (1 - r_5)(1 - s_5);$$

$$N_4 = (1 + r_5)(1 - s_5); \text{ and} \tag{12}$$

r_5 and s_5 are the natural coordinates (r-s-t) of point 5.

The nodal forces at nodes 1, 2, 3, 4, 5, and c are given by f_1, f_2, f_3, f_4, f_5 and f_c, respectively. Nodes c and 5 are the same node and it is the contact point in the target surface. One can derive the stiffness for the five-node element from Eqs. (10) and (11). These can be used for the node-to-surface contact problem as follows:

$$\mathbf{K}_5 = \mathbf{H}^T\mathbf{K}_2\mathbf{H} = \mathbf{K}\begin{bmatrix} N_1N_1 & N_1N_2 & N_1N_3 & N_1N_4 & -N_1 \\ N_2N_1 & N_2N_2 & N_2N_3 & N_2N_4 & -N_2 \\ N_3N_1 & N_3N_2 & N_3N_3 & N_3N_4 & -N_3 \\ N_4N_1 & N_4N_2 & N_4N_3 & N_4N_4 & -N_4 \\ -N_1 & -N_2 & -N_3 & -N_4 & 1 \end{bmatrix}. \tag{13}$$

If the current coordinates of Points 1 through 5 (see Fig. 3) and the contact modes (sticking, sliding or separating) are known, Eq. (13) can be used to provide the tangent stiffness matrix of the node-to-surface contact element. The following paragraph will discuss how to generate the internal force of the contact element. Figure 3 shows the node-to-surface contact model during two successive iterations, iteration 1 and iteration 2. All nodes in Fig. 3 have been updated by adding the displacement of the last iteration. The normal direction, **w**, of plane 1234 is approximated as

$$\mathbf{w} = \frac{\overline{13} \times \overline{24}}{|\overline{13} \times \overline{24}|} \tag{14}$$

where $\overline{13}$ means vector 13. The contact positions P_1 and P_2 of last and current iterations are known at the end of the current iteration. If it is not a separation mode, points P_1 and P_2 will be inside the target body according to the penalty method theory. Location of point C_2 can be evaluated by solving the equations of surface 1234 and line $C_2 - P_2$, the latter direction being equal to **w**. Finally, the magnitude (U) and direction (**u**) of the frictional displacement for sticking mode can be found from

$$U\mathbf{u} = \overline{CC_2} - (\overline{CC_2} \cdot \mathbf{w})\mathbf{w}. \tag{15}$$

The direction **u** of the frictional displacement for sliding mode is still calculated from Eq. (15). The normal displacement W is

$$W = \overline{P_2C_2} \cdot \mathbf{w}. \tag{16}$$

A negative value for W means that node 5 has separated from the four-node target surface (Fig. 3) and the situation involves the separation mode. The direction of displacement V, **v**, for all modes is defined as

$$\mathbf{v} = \mathbf{w} \times \mathbf{u}. \tag{17}$$

Knowing the displacements, one can now evaluate the local internal forces, F_n and F_s at node 5 of the contact element. The normal force is

$$F_n = kW. \tag{18}$$

The friction force is

$$F_S = kU + (\mathbf{u}_1 \cdot \mathbf{u})F_{sl} \text{ for sticking, and} \tag{19}$$

$$F_S = \mu F_n \text{ for sliding,} \tag{20}$$

where k is the penalty constant, F_{sl} is the internal frictional force at the end of the previous increment, and $\mathbf{u}_1$ is the unit direction vector parallel to the displacements U of the last iteration.

The local internal forces, F_n and F_s, at node 5 can be found from the above equations. Global internal forces at nodes 1 to 5 can be calculated using the following Eqs. (21) and (22). Adding the element internal forces to the global force vector enables one to obtain $\mathbf{FS}_{\text{int}}$ in Eq. (1), i.e.,

$$\begin{Bmatrix} F_{x5} \\ F_{y5} \\ F_{z5} \end{Bmatrix} = [\mathbf{u}^T \quad -\mathbf{v}^T]\begin{Bmatrix} F_s \\ F_n \end{Bmatrix} \tag{21}$$

$$\begin{Bmatrix} F_{x1} \\ F_{x2} \\ F_{x3} \\ F_{x4} \end{Bmatrix} = -F_{x5}\begin{bmatrix} N_1 \\ N_2 \\ N_3 \\ N_4 \end{bmatrix}, \quad \begin{Bmatrix} F_{y1} \\ F_{y2} \\ F_{y3} \\ F_{y4} \end{Bmatrix} = -F_{y5}\begin{bmatrix} N_1 \\ N_2 \\ N_3 \\ N_4 \end{bmatrix},$$

$$\begin{Bmatrix} F_{z1} \\ F_{z2} \\ F_{z3} \\ F_{z4} \end{Bmatrix} = -F_{z5}\begin{bmatrix} N_1 \\ N_2 \\ N_3 \\ N_4 \end{bmatrix}. \tag{22}$$

2.4 Sticking, Sliding, or Separation Mode Determination. One first uses Eq. (16) to evaluate whether or not there is separation. If W of Eq. (16) is negative, then node 5 has separated from the four-node target surface (Fig. 3). Under such condition, the penalty constant and internal forces of the contact element are both set to zero. If $W \geq 0$, one then checks to see whether sliding or sticking occurs. Sticking is first assumed. Thus, if $F_s < \mu F_n$, sticking occurs; if $F_s \geq \mu F_n$, one has sliding.

From Eqs. (13), (18), (19), and (20), the current tangent stiffness matrix and current contact forces of a node-to-plane contact element can be obtained at each iteration, when all the coordinates are updated to the present coordinates. These equations incorporating the implicit updated Lagrangian method can be used to simulate large sliding motions. However, it should be noted that the use of excessively large incremental steps should be avoided. To do so lead to convergence difficulties in the equilibrium iterations because the predicted intermediate state is too far from the solution. Another convergence difficulty is the frequent change of contact modes, such as sticking to sliding or contact to separation. This condition can be found in the loading-unloading cases.

3 Illustrative Examples

3.1 General Comments. The algorithm of this new three-dimensional contact element was programmed into Ju's (1993) finite element codes. Five examples were thereby conducted to assess the reliability of the current three-dimensional contact model. Since few theoretical solutions are available for contact problems, results of several of the present cases are compared with the previous two-dimensional frictional contact element (Ju et al., 1995). Units are ignored in these illustrative examples. At each force or time-step of these analyses, the convergence ratio is set as detailed below:

- for static analyses

$$\left|\left(\sum_{i=1} \text{REFOR}_i^2\right)/\sum_{i=1} \text{TOFOR}_i^2\right| \leq \text{convergence ratio} = 1/300 \tag{23}$$

- for dynamic analyses

$$\left|\left(\sum_{i=1} dU_i^2\right)/\sum_{i=1} U_i^2\right| \leq \text{convergence ratio} = 1/300 \tag{24}$$

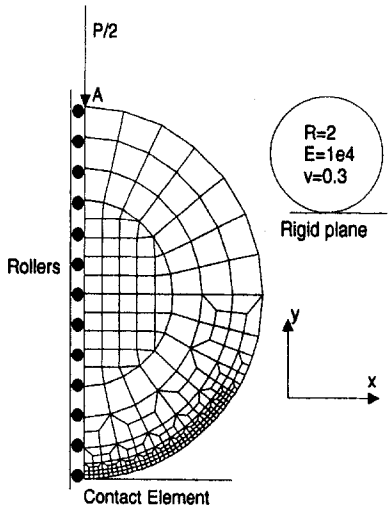

Fig. 4 Hertz contact problem and finite element mesh (264 eight-node brick elements and 30 five-node contact elements; E = 1e4, v = 0.3, radius R = 2, penalty constant = 5000)

where

REFOR$_i$: residual nodal forces;
TODU$_i$: incremental nodal forces between two successive steps. If it is equal to zero, the program sets it to one;
dU: incremental displacement between two successive iterations;
U: total incremental displacement between two success steps;
N: total number of degrees-of-freedom.

3.2 Hertz Contact. The first illustrative example is an infinitely long, solid elastic cylinder resting on a rigid plane. The cylinder is subjected to a downward concentrated load P at point A (Fig. 4). This physical situation was modeled here as one circular disk with one element layer which is fixed in the z-direction (Fig. 4). The half-model of the disk is discretize by 264 eight-node brick elements. The disk radius $R = 2$ and it has $E = 1e4$ and $v = 0.3$. A fine mesh is used in the contact area to obtain reliable results. Friction is ignored between the cylinder and the rigid base in the classical Hertz analytical analysis. Figure 5 shows the contact normal stress between the elastic cylinder and rigid plane at increasing load levels. Results of Fig. 5 using the present

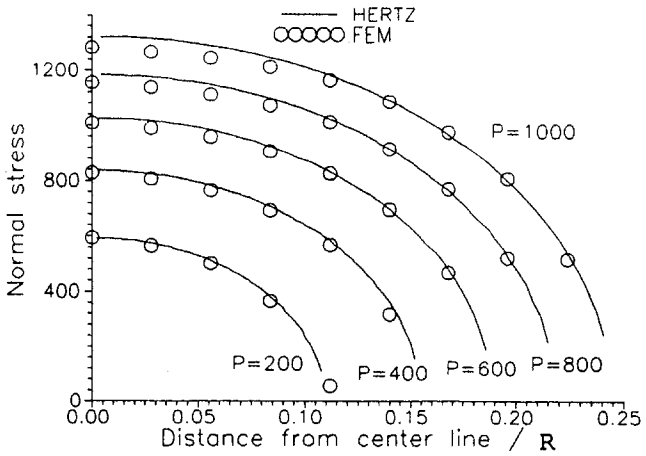

Fig. 5 Comparison of three-dimensional and Hertz results for normal contact stress between elastic cylinder and rigid plate of Fig. 4 (E = 1e4, v = 0.3, μ = 0.3)

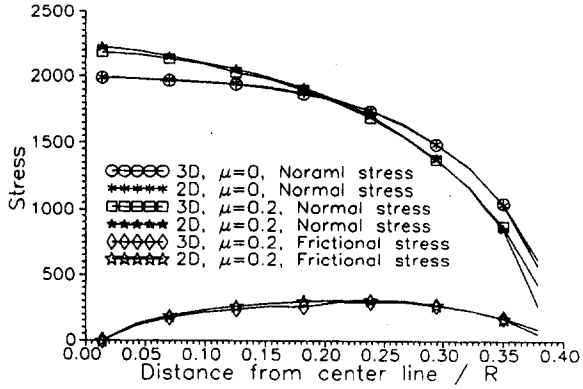

Fig. 6 Comparison of present three-dimensional and previous two-dimensional finite element method results (Ju et al., 1995) for the contact vertical normal and horizontal shear stresses between elastic cylinder and rigid plate of Fig. 4 (E = 1e4, v = 0.3, μ = 0.3)

finite element analysis are in excellent agreement with the classical Hertz theory.

The classical Hertz solution ignores friction. In order to explore the effect of friction on the normal contact stress, a uniform body force of 200 per unit volume was applied to the cylinder of Fig. 4 but with the frictional coefficient (μ) equal to 0.0 and 0.2, respectively. When the contact area (angle) is small, the friction will increase the maximum normal stress and further decrease the contact area. Figure 6 compares the results using the previous two-dimensional contact analysis (Ju et al., 1995) with the present three-dimensional algorithm. The mesh is the same as the three-dimensional mesh in x-y-plane (Fig. 4). The comparisons shown in Fig. 6 again indicate excellent agreement.

Fifty equal force steps were used in the FEA to reach $P = 1000$ of Fig. 5. The uniform body force of 200 of Fig. 6 was achieved in 20 equal increments. On average, 2.4 iterations were used per load increment.

Results of Figs. 5 and 6 illustrate the reliability of the present frictional contact element for elastic frictional case involving moderate amounts of clearance, sliding, and fixation.

3.3 Dynamic Contact With Friction. Consider two elastic bodies $E = 1e4$, $v = 0.3$ and mass density = 1000 on a rigid foundation (Fig. 7) and subjected simultaneously to two dynamic forces: a downward pressure W on surface (ABCD) of the upper body and an in-plane force P applied to the mass center of this upper body (Fig. 8). The coefficient of friction at the interfaces between the two blocks is 0.8 whereas that between the lower block and its foundation is infinite. By assuming no gravity or other forces, the body motion can be calculated theoretically using kinetics. The finite element mesh of Fig. 7 employs the new three-dimensional contact elements between the contacting surfaces ($\mu = 0.8$). Newmark's method was employed in the transient finite element analysis with the time interval of 0.5 s and a total of 200 time-steps. On average, 3.8 iterations were used per load increment.

Figure 9 shows virtually identical displacements by the current finite element analysis method and theory. Figure 10 illustrates the positions of the two blocks at 0, 75 and 100 s after the start of contact. This example demonstrates that the present contact element can also be applied to problems involving large deformation, extensive sliding, and transient events.

3.4 Contacting Cantilever Beams. The two cantilever beams ($E = 1e9$ and $v = 0.2$) of Fig. 11, which are clamped at the left ends, touch each other but do so without any initial contacting force. The frictional coefficient between the beams is $\mu = 0.2$. A downward pressure of $P = 10.74e5$ is then applied to the top surface of the upper cantilever beam, and five equal force steps were used in the finite element analysis to reach this pressure. The

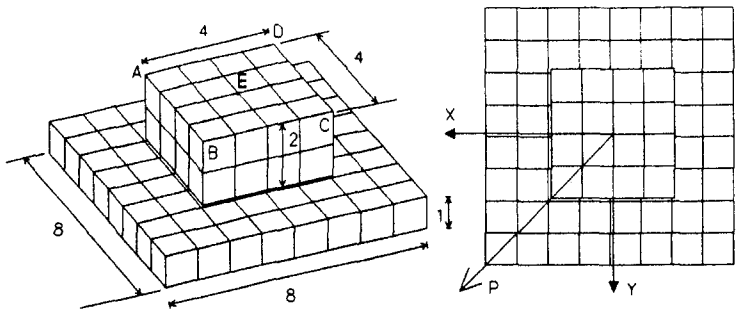

Fig. 7 Model of dynamic contact analysis and finite element mesh (96 eight-node brick elements, 720 five-node contact elements, E = 1e4, v = 0.2, mass density = 1000, μ = 0.8, penalty constant = 7000)

present three-dimensional algorithm is used to analyze this static problem, and 10.2 iterations were used per load increment on average. Since we are unaware of any theoretical solution for this problem, results of the present three-dimensional contact analysis are compared with those using the previous two-dimensional contact analysis (Ju et al., 1995). The two-dimensional and three-dimensional finite element meshes are indicated in Fig. 11. The good agreement of Fig. 12 for the normal and frictional stresses at the contact surface between the three-dimensional and two-dimensional contact analyses further demonstrates the reliability of this three-dimensional frictional contact algorithm. The deformed images of two-dimensional and three-dimensional analyses of Fig. 13 indicate the extensive amount of sliding involved in this problem. The finite element results remain accurate even after the tip of the upper cantilever beam has slid across two elements of the lower beam.

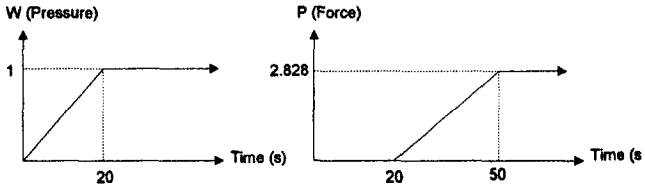

Fig. 8 Force, P, and pressure, W, applied to top block of Fig. 7

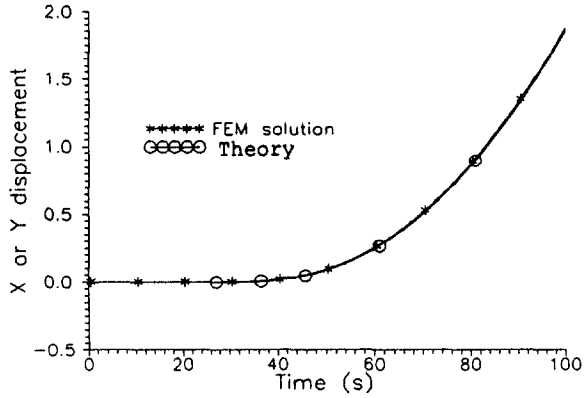

Fig. 9 Time-history displacements of Point E in Fig. 7 by the present three-dimensional frictional contact algorithm and theory (E = 1e4, v = 0.3, mass density = 1000, μ = 0.8)

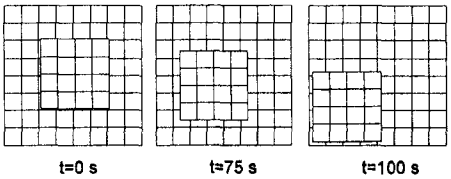

Fig. 10 Top view of blocks of Fig. 7 at t = 0, 75, and 100 s, respectively

3.5 Two Contacting Rings. Two contacting elastic rings of unit width and inner diameters of D = 30 and d = 18, respectively, are supported at their respective centers, Fig. 14(a). The outside of the larger ring and the inside of the smaller ring are modeled by the rigid-body effect with two master nodes at their respective centers, points A and B. The center of the larger ring (point A) can only rotate in three directions, whereas the center of the smaller ring (point B) can move vertically as well as rotate in three directions. The smaller ring is subjected to a dynamic force P and a dynamic moment M, Fig. 14. Material properties, dimen-

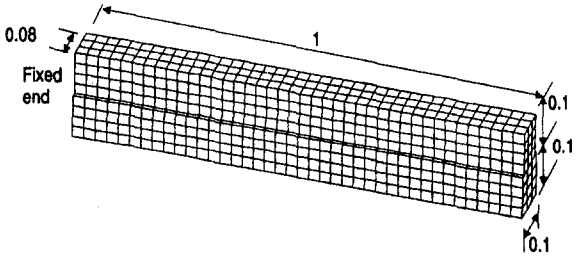

(a) 3-D Finite element mesh

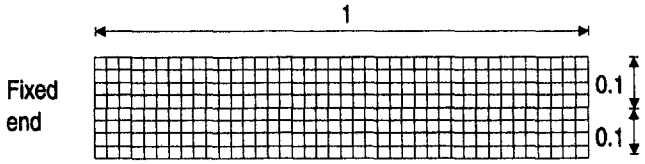

(b) 2-D Finite element mesh

Fig. 11 Discretized model of two contacting cantilever beams (total of 960 eight-node brick elements, and 1234 five-node contact elements, E = 1e9, v = 0.2, μ = 0.2, penalty constant = 3e5)

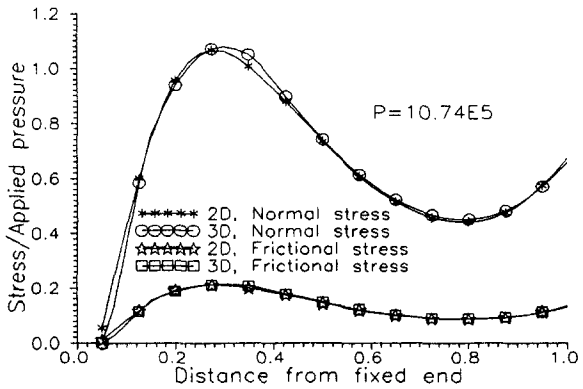

Fig. 12 Normal and frictional shear stresses between cantilever beams of Fig. 11 by present three-dimensional contact algorithm and previous two-dimensional finite element method (Ju et al., 1995)

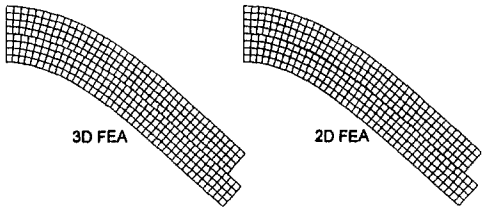

Fig. 13 Deformed cantilever beams of Fig. 11

sions, and mass densities are indicated in Fig. 14(*a*). The coefficient of friction (μ) between the interfaces of the rings is set to 0, 0.1 and 0.4, respectively, for three separate finite element analyses. In the absence of gravity or other forces, the motion of these bodies can be calculated theoretically using kinetics. For $\mu = 0$, frictionless sliding occurs between the contacting rings and the outer ring deforms but does not rotate; for $\mu = 0.1$, both slipping and fixation occurs along the contacting interface between the two rings; and for $\mu = 0.4$ the outer ring is in full rotation.

The finite element mesh of Fig. 14(*b*) was modeled by 504 eight-node elements for the bodies plus 828 five-node three-dimensional frictional contact elements between the contacting surfaces of the rings. The Newmark method was employed in the transient finite element analysis with a time interval of 0.001 s and a total of 800 time-steps. On average, 4.8 iterations were used per load increment.

The rotations in the direction of the applied moment of Figs. 15 and 16 evaluated using the present three-dimensional frictional contact elements are virtually identical to those predicted theoretically, where the theoretical solution was established from the basic theory of kinetics of rigid bodies. The rotations in the other two directions are not shown here since they are approximately zero in the finite element analyses. Since P and M act in the plane of Fig. 14(*a*), the theoretical out-of-plane rotations are exactly zero. Figure 17 shows the deformed contact portions of the rings at six different times after load initiation. A cut in the images of Fig. 17 has been introduced deliberately to show the relative displacements of the two rings. These results demonstrate reliability of the present three-dimensional frictional contact algorithm for fully sliding, partially sliding, and fully sticking conditions between contacting curved surfaces of two elastic bodies subjected to loading and unloading.

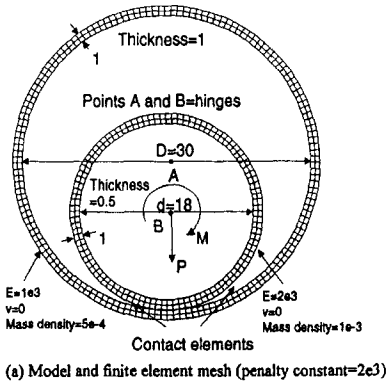

(a) Model and finite element mesh (penalty constant=2e3)

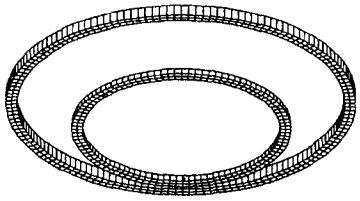

(b) 3-D view of the finite element mesh

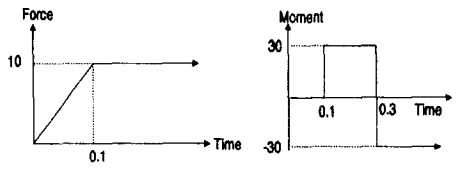

(c) Applied force and moment

Fig. 14 Model, mesh, and loading of two contacting elastic rings (504 eight-node elements, 828 five-node contact elements, penalty constant = 2000)

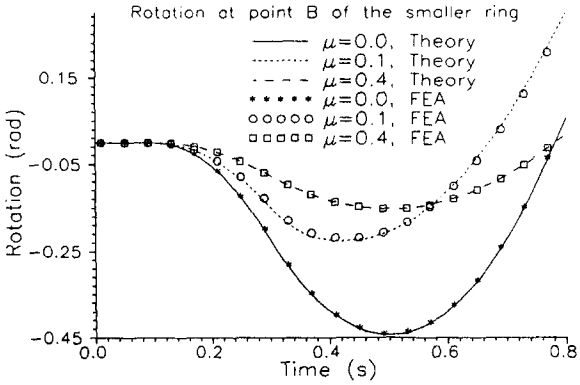

Fig. 15 Comparison of present finite element method and theoretical solutions for resulting rotation at point B of the smaller ring of Fig. 14

3.6 Forming of a Pan. Consider an initially flat plate ($E = 1000$, $v = 0.3$, $\sigma_y = 2$, H = isotropic hardening ratio = 5) which is elastoplastically deep-drawn into a pan by a rigid die. Initial dimensions of the plate are $50 \times 40 \times 1$ and those of the rigid die are $40 \times 30 \times 5$, Fig. 18. The plate is numerically clamped (fixed) along its boundaries (four edges)

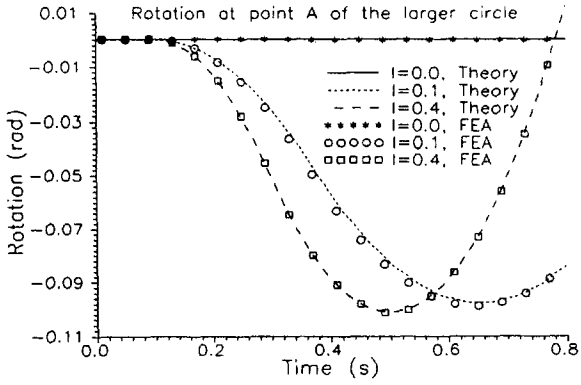

Fig. 16 Comparison of present finite element method and theoretical solutions for resulting rotation at point A of the larger ring of Fig. 14

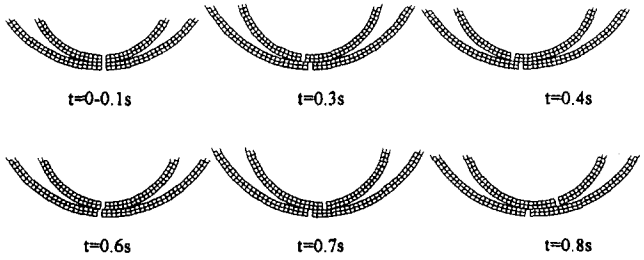

Fig. 17 Rings of Fig. 14 at several different times after load initiation (μ = 0.1). (Only parts of the rings are shown in the figure, where two elements are cut in order to show the relative displacement.)

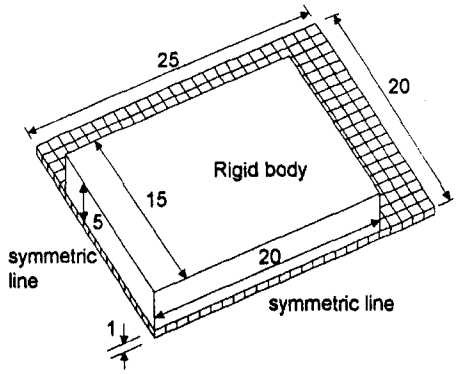

Fig. 18 Finite element model and mesh for elastoplastic forming of a pan (500 eight-node elements, 376 five-node contact elements, $E = 1000$, $v = 0.3$, $F_y = 2$, $H = 5$, penalty constant = 300)

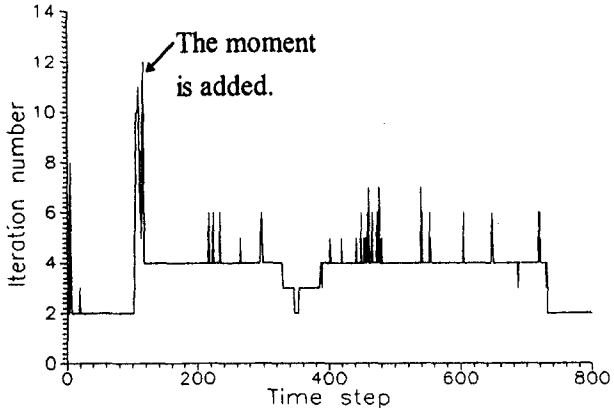

Fig. 21 Iteration number at the various time-steps of the problem of Fig. 14 ($\mu = 0.1$)

but otherwise unsupported. The coefficient of friction $\mu = 0.2$ is assumed for all contacts between the plate and the inserting die. The displacement-controlled analysis was performed using 50 displacement steps, while each step was set to 1 unit of downward displacement. On average, 6.2 iterations were used per displacement increment. Because of symmetry, only one fourth of the structure was meshed with 500 eight-node solid elements and 376 five-node contact elements, Fig. 18. Some successively deformed shapes are contained in Fig. 19, while contours of the effective plastic strain of the fully deformed plate are shown in Fig. 20. This example indicates that this contact element can successfully handle nonlinear material problems.

4 Discussion

The frictional contact element developed herein is versatile for node-to-surface contact problems involving eight-node brick or four-node plate elements. Several target surfaces can be inputted with one contact node; therefore, the contact node can be the target contact at any location within these target surfaces. This is very usefully for situations involving large deformation or clearance. The normal direction of a target surface of this three-dimensional contact element is calculated from the cross product of the two diagonal vectors of the four-node target surface, and only one normal direction is set to a target surface.

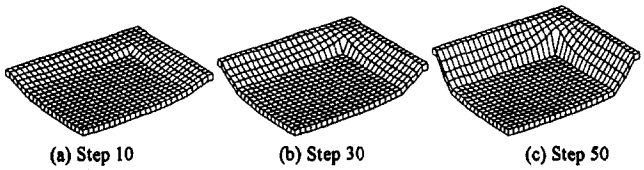

Fig. 19 Successively deformed pan of Fig. 18

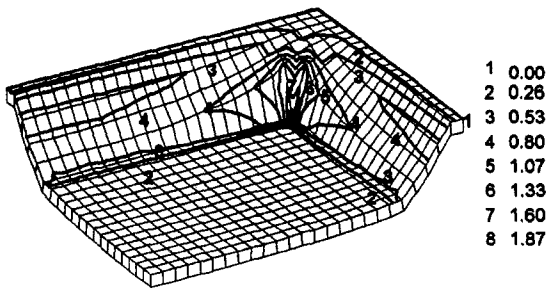

Fig. 20 Contours of the effective plastic strain at final stage of the deep-drawn pan of Figs. 18 and 19

Numerical convergence can be difficult if a contact node slides from one target surface to another target surface with a great change of the normal direction. However, this difficulty can be circumvented by modeling the curved surface with an interpolation function such as three-dimensional cubic spline, or by using a fine mesh such as done here for the contacting rings of Figs. 14 through 17.

For frictional contact, one normally strives to find a large penalty constant which can achieve convergence. A very large penalty constant usually yields an oscillated numerical solution; furthermore, such a solution might converge slowly or sometimes not converge at all. A small penalty constant typically results in easy convergence, but the numerical results might be less reliable. Satisfactory use of the penalty function method is highly dependent therefore upon using an appropriate value for the penalty constant. We previously proposed (Ju et al., 1995) a simple scheme for finding a reasonable penalty constant. That scheme can be used to select an adequate penalty constant at the beginning of contact analyses. For large deformation analyses, a practical way to check the adequacy of the penalty constant is to plot the deformed shape. If the penetration of the contact element is sufficiently small that it cannot be seen, the solution is acceptable.

The present examples required between two to twelve iterations to achieve the convergence during a force or time-step. Figure 21 shows the number of iterations employed during the various time-steps for the problem of Fig. 14 under $\mu = 0.1$. The highest peak of Fig. 21 is associated with the application of the moment.

5 Summary and Conclusion

A three-dimensional contact element having symmetric stiffness matrix has been developed to analyze frictional contact problems. Results demonstrate the element's reliability to analyze sliding contact problems using either static or transient large displacement finite element analyses, including those involving extensive sliding and loading plus unloading. Sticking, sliding, and clearance can be handled, as can linear, nonlinear, and inelastic materials behaviors.

Acknowledgment

S. H. Ju was partially supported by NSF in R.O.C. (project No. NSC-84-2213-E-006-119) and R. E. Rowlands acknowledges partial support from the USDA in USA (project No. 94-37103-1021).

References

Chaudhary, A. B., and Bathe, K. J., 1986, "A Solution Method for Static and Dynamic Analysis of the Three-Dimensional Contact Problems with Friction," *Computers & Structures,* Vol. 24, pp. 855–873.

Hallquist, J. O., Goudreau, G. L., and Benson, D. J., 1985, "Sliding Interfaces with Contact-impact in Large-scale Lagrangian Computations," *Comp. Method Appl. Mech. Eng.*, Vol. 51, pp. 107–137.

Ju, S. H., 1993, "Creep-fatigue Analysis of Solder Joints," Ph.D. thesis, University of Wisconsin-Madison.

Ju, S. H., Stone, J. J., and Rowlands, R. E., 1995, "A New Symmetric Contact Element Stiffness Matrix for Frictional Contact Problems," *Computers & Structures*, Vol. 54, No. 2, pp. 289–301.

Kanto, Y., and Yogawa, G., 1990, "A Dynamic Contact Buckling Analysis by the Penalty Finite Element Method," *International Journal for Numerical Methods in Engineering*, Vol. 29, pp. 755–774.

Kulak, R. F., 1989, "Adaptive Contact Element for Three-dimensional Explicit Transient Analysis," *Comp. Method Appl. Mech. Eng.*, Vol. 72, pp. 125–151.

Laursen, T. A., and Simo, J. C., 1993, "A Continuum-based Finite Element Formulation for the Implicit Solution of Multibody Large Deformation Frictional Contact Problems," *International Journal for Numerical Methods in Engineering*, Vol. 36, pp. 3451–3485.

Malone, J. G., and Johnson, N. L., 1994, "A Parallel Finite Element Contact/Impact Algorithm for Non-linear Explicit Transient Analysis: Part I—the Search Algorithm and Contact Mechanics," *International Journal for Numerical Methods in Engineering*, Vol. 37, pp. 559–590.

Mottershead, J. E., Pascoe, S. K., and English, R. G., 1992, "A General Finite Element Approach for Contact Stress Analysis," *International Journal for Numerical Methods in Engineering*, Vol. 33, pp. 765–779.

Paradopoulos, P., and Taylor, R. L., 1993, "A Simple Algorithm for Three-Dimensional Finite Element Analysis of Contact Problems," *Computers & Structures*, Vol. 46, pp. 1107–1118.

Parishch, H., 1989, "A Consistent Tangent Stiffness Matrix for Three-dimensional Nonlinear Contact Analysis," *International Journal for Numerical Methods in Engineering*, Vol. 28, pp. 1803–1812.

Peric, D., and Owen, D. R. J., 1992, "Computational Model for 3-D Contact Problems with Friction Based on the Penalty Method," *International Journal for Numerical Methods in Engineering*, Vol. 35, pp. 1289–1309.

APPENDIX

From Fig. 3, the equation of surface 1234 is

$$x = N_1x_1 + N_2x_2 + N_3x_3 + N_4x_4$$

$$y = N_1y_1 + N_2y_2 + N_3y_3 + N_4y_4$$

$$z = N_1z_1 + N_2z_2 + N_3z_3 + N_4z_4 \tag{A1}$$

where

$$N_1 = (1 + r)(1 + s);)$$

$$N_2 = (1 - r)(1 + s);$$

$$N_3 = (1 - r)(1 - s);$$

$$N_4 = (1 + r)(1 - s).$$

The equation of line E_2P_2 is

$$\frac{x - x_{p2}}{P_x} = \frac{y - y_{p2}}{P_y} = \frac{z - z_{p2}}{P_z} = E \tag{A2}$$

where $P_x = x_{e2} - x_{p2}$, $P_y = y_{e2} - y_{p2}$, $P_z = z_{e2} - z_{p2}$ and E is a constant. Rearrange Eqs. (A1) and (A2) give

$$\begin{bmatrix} x_1 - x_2 - x_3 + x_4 & x_1 + x_2 - x_3 - x_4 & x_1 - x_2 + x_3 - x_4 & -4P_x \\ y_1 - y_2 - y_3 + y_4 & y_1 + y_2 - y_3 - y_4 & y_1 - y_2 + y_3 - y_4 & -4P_y \\ z_1 - z_2 - z_3 + z_4 & z_1 + z_2 - z_3 - z_4 & z_1 - z_2 + z_3 - z_4 & -4P_z \end{bmatrix} \begin{Bmatrix} r \\ s \\ rs \\ E \end{Bmatrix} = \begin{Bmatrix} 4x_{p2} - (x_1 + x_2 + x_3 + x_4) \\ 4y_{p2} - (y_1 + y_2 + y_3 + y_4) \\ 4z_{p2} - (z_1 + z_2 + z_3 + z_4) \end{Bmatrix}. \tag{A3}$$

The three unknowns, r, s, and E in equation (A3) can be solved directly using the Newton-Rapshon method or a direct method.

H. Liu
Graduate Student

M. Saka
Professor,
Department of Mechanical Engineering

Tohoku University,
Aoba, Armaki, Aoba-Ku,
Sendai 980-8579, Japan

H. Abé
President,
Tohoku University,
2-1-1 Katahira, Aoba-ku,
Sendai 980-8577, Japan
Mem. ASME

I. Komura
Chief Researcher,
Heavy Apparatus Engineering Laboratory,
Toshiba Corporation,
1-9 Suehiro-cho, Tsurumi-ku,
Yokohama 230-0045, Japan

H. Sakamoto
Senior Specialist,
Isogo Nuclear Engineering Center,
Toshiba Corporation,
8 Shinsugita-cho, Isogo-ku,
Yokohama 235-0032, Japan

Analysis of Interaction of Multiple Cracks in a Direct Current Field and Nondestructive Evaluation

A method of analysis is proposed for nondestructive evaluation of multiple cracks by means of the d.c. (direct current) potential drop technique. Two and three-dimensional multiple cracks are treated. A methodology for considering interaction of cracks based on the equation for an isolated crack is given to calculate the potential drop between both sides of a crack in multiple cracking in a plate. The inverse problem to evaluate the crack depth is analyzed by comparing the potential drop calculated in this way with the measurement. It is shown that the evaluated crack depth is in good agreement with the actual one.

1 Introduction

Nondestructive evaluation of cracks is needed for integrity assessment of structures based on fracture mechanics. So far many investigations have been carried out concerning nondestructive evaluation of an isolated crack. Contrary to this, nondestructive evaluation of multiple cracks is a subject less explored.

Multiple cracks are known to initiate by the combined action of stress and aggressive environment such as high temperature, chemical interaction, and oxidation on the surface of structural components. For example, multiple cracks have been observed on the tiebolt-hole segment of a jet-engine turbine disk (Beissner et al., 1981). According to Parkins and Singh (1990) service failures by stress corrosion cracking are almost invariably characterized by multiple cracking. To predict service lives of structures containing multiple cracks and to prevent catastrophic fracture, it is necessary to use suitable methods to evaluate the cracks quantitatively. Ultrasonic testing is not applicable for nondestructive evaluation of multiple cracks, because the distance between cracks is sometimes much smaller than the probe diameter. Even in the case of surface Rayleigh waves, nondestructive evaluation of three-dimensional multiple cracks with semielliptical or semicircular shapes arbitrarily located on the surface of a material is a difficult proposition.

A method for nondestructive evaluation of two-dimensional multiple cracks has been developed (Ghajarieh et al., 1994, 1995), where the distance between cracks has been assumed to be known in advance based on observation from the side of the cracked surface by using the penetrant method, for example. This method was based on the numerical analysis of inverse problem concerned with the d.c. potential drop technique. In the case of multiple cracks, both the crack depth and the distance between cracks affect the potential drop. Namely the electric field perturbations due to the cracks interact. We call this phenomenon interaction of cracks. So one cannot determine the depths of cracks by using evaluation equation for an isolated crack. The interaction of cracks has well been considered by using the finite element method for multiple cracks using the method of Ghajarieh et al. and the depths of cracks have been determined.

However, in order to evaluate multiple cracks through the analysis of inverse problem by using the finite element method, a comparatively powerful computational tool is needed and performing the analysis is time-consuming. In addition, three-dimensional multiple cracks occur more frequently in worksites, compared with the problem of two-dimensional multiple cracks.

It is stated that in order to evaluate an isolated crack in the welding zone using the d.c. potential drop technique, Abé and Kanoh (1990) have proposed a method which has considered the interaction between the crack and the weld being the electrical inhomogeneity. The present paper is based on their method to analyze the interaction in the problem of multiple cracks. In the present paper, the potential drop for multiple cracks is calculated by successively adding the terms of interaction effects of the multiple cracks, where the calculation is based on the evaluation equation for an isolated crack. Then the crack depths are evaluated

Contributed by the Applied Mechanics Division of THE AMERICAN SOCIETY OF MECHANICAL ENGINEERS for publication in the ASME JOURNAL OF APPLIED MECHANICS.
Discussion on the paper should be addressed to the Technical Editor, Professor Lewis T. Wheeler, Department of Mechanical Engineering, University of Houston, Houston, TX 77204-4792, and will be accepted until four months after final publication of the paper itself in the ASME JOURNAL OF APPLIED MECHANICS.
Manuscript received by the ASME Applied Mechanics Division, Apr. 3, 1997; final revision, Aug. 13, 1998. Associate Technical Editor: M. Taya.

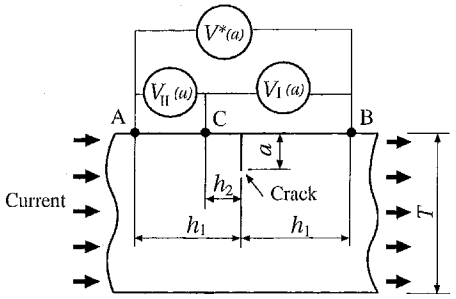

Fig. 1 An isolated two-dimensional crack

by analyzing the inverse problem. This method is verified with the experimental results.

2 Evaluation Equation of d.c. Potential Drop

2.1 Case of a Two-Dimensional Isolated Surface Crack. First, consider the problem of isolated crack as the basis of multiple cracks. For a two-dimensional crack located in the middle of two points A and B measuring potential drop $V^*(a)$ as shown in Fig. 1, Johnson (1965) has obtained the analytical solution given by

$$\frac{V^*(a)}{V^*(a_0)} = \frac{\cosh^{-1}\left(\dfrac{\cosh \pi h_1/2T}{\cos \pi a/2T}\right)}{\cosh^{-1}\left(\dfrac{\cosh \pi h_1/2T}{\cos \pi a_0/2T}\right)} \tag{1}$$

where a is the crack depth, a_0 a reference crack depth, T the thickness of the plate, and h_1 the distance of the crack from A and B. Crack surfaces are assumed to be insulated electrically.

For the crack which is not in the middle of two measuring points, Eq. (1) is not applicable. Ghajarieh et al. (1994) have modified the Johnson's equation to the potential drop $V_I(a)$ between two points B and C where a crack lies at a distance h_1 and h_2 from the points as shown in Fig. 1. It is given by

$$V_I(a) = \frac{2TV_0}{\pi}\left[\cosh^{-1}\left(\frac{\cosh \pi h_1/2T}{\cos \pi a/2T}\right) + \cosh^{-1}\left(\frac{\cosh \pi h_2/2T}{\cos \pi a/2T}\right)\right] \tag{2}$$

where V_0 is the potential drop for a 1-mm distance in the direction of current flow in an uncracked part of the plate.

According to Eqs. (1) and (2), we can get the following evaluation equation of the potential drop $V_{II}(a)$ between two measuring points A and C beside the crack as shown in Fig. 1:

$$V_{II}(a) = \frac{2TV_0}{\pi}\left[\cosh^{-1}\left(\frac{\cosh \pi h_1/2T}{\cos \pi a/2T}\right) - \cosh^{-1}\left(\frac{\cosh \pi h_2/2T}{\cos \pi a/2T}\right)\right]. \tag{3}$$

2.2 Calibration Equation of Potential Drop for a Semielliptical Surface Crack in an Infinite Plate. The problem of current flow in a material is governed by the Laplace equation as

$$\nabla^2 \phi = 0 \tag{4}$$

where ϕ is the electrical potential and ∇^2 is the three-dimensional Laplace operator. Equation (4) can readily be solved by using the finite element method.

Consider a semielliptical surface crack which is perpendicular to the surface of an infinite plate as shown in Fig. 2. As far as we know, there is no literature treated the analytic solution in a closed

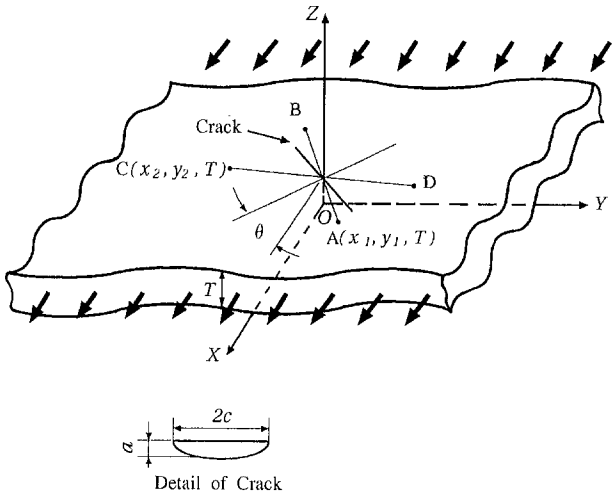

Fig. 2 Infinite plate containing a semielliptical surface crack

form for the problem of Fig. 2. Hence the numerical calculation is carried out. The maximum depth of the crack is $a(<T)$ and its half-length on the surface of the plate is $c(\geq a)$. A constant current is introduced far from the crack. The crack surface is at an angle to the direction of the current far from the crack. A Cartesian coordinates system (X, Y, Z) is introduced as shown in Fig. 2, where the Z-axis is perpendicular to the surface of the plate and the origin O is located on the bottom surface of the plate below the deepest point of the crack. The angle of skew between the normal to the crack surface and the positive direction of the X-axis is denoted by $\theta(|\theta| \leq \pi/2)$ and its positive direction is defined as in a counterwise direction. Consider a point A existing at $X = x_1$ and $Y = y_1$ on the surface of the plate and its symmetric point B about the Z-axis. The potential drop between A and B, $V_{AB}(\theta)$, is found empirically to be approximated by the following equation from the numerical results obtained by the finite element analysis:

$$\frac{V_{AB}(\theta)}{V_{0AB}} = f(x_1)\left[\left[\frac{\cosh^{-1}\left[\dfrac{\cosh(\pi x_1/2T)}{\cos\{\pi a/2T - \pi a/2(T+c)\}}\right]}{\pi|x_1|/2T} \times \cos^2\theta + \sin^2\theta + \frac{\{4\pi aT/(c+T/2)^2\}\cos\theta}{\cosh\left(\dfrac{4\pi x_1}{T}\right)\left\{1 + \dfrac{|x_1|}{(2c-a)}\right\}\exp\left(\dfrac{|x_1|+|y_1|}{c}\right)} - \left\langle \frac{\cosh^{-1}\left[\dfrac{\cosh(\pi x_1/2T)}{\cos\{\pi a/2T - \pi a/2(T+c)\}}\right]}{\pi|x_1|/2T} - 1 \right\rangle \times \cos^2\theta \Big/ \exp\left\{\frac{(c+T)}{2\pi|y_1|}\right\}\right]\right] + \frac{a|\sin\theta|\cos\theta}{|x_1|\exp\left(\dfrac{|x_1 + y_1\tan\theta|}{c}\right)} \tag{5}$$

where V_{0AB} is the potential drop between A and B in the case that no crack exists. The quantity V_{0AB} is given by $2V_0|x_1|$. Moreover

$$f(x) = \begin{cases} 1 & x \neq 0 \quad (6a) \\ 0 & x = 0. \quad (6b) \end{cases}$$

It is noted that Eq. (5) is valid except for on the intersection of the crack surface to the plate surface and covers Eq. (1). An example

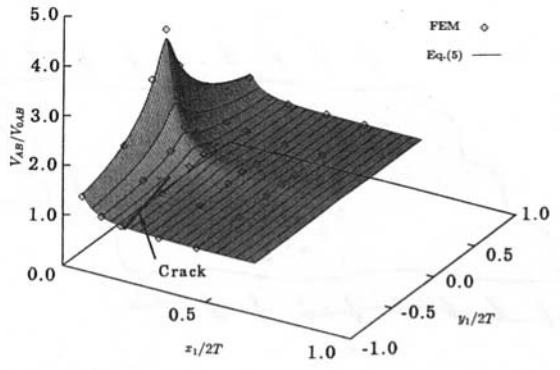

Fig. 3 Comparison of Eq. (5) with the finite element method calculation for an infinite plate containing a semielliptical surface crack, where c = 5 mm, a = 4 mm, T = 7.5 mm, and $\theta = \pi/36$

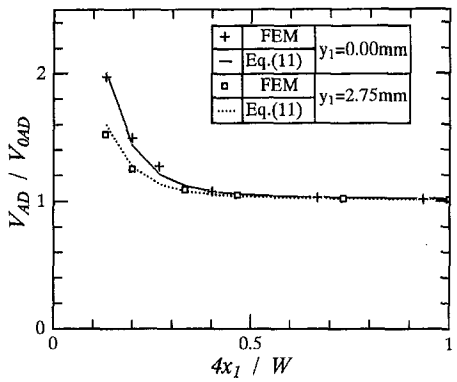

Fig. 5 Comparison of Eq. (11) with the finite element method calculation for a finite plate containing a semielliptical surface crack, where c = 5 mm, a = 2 mm, W = 30 mm, t = 5 mm, T = 7.5 mm, and $\theta = \pi/36$

of the comparison between Eq. (5) and the finite element method calculation results is shown in Fig. 3. Although Fig. 3 shows only an example, the calibration equation has been confirmed for many cases to agree well with the results of the finite element method.

Similarly, by considering a point C existing at $X = x_2$ and $Y = y_2$ and its symmetric point D about the Z-axis, the potential drop between C and D, $V_{CD}(\theta)$, is obtained.

The potential drop between A and D, which are on both sides of the crack, $V_{AD}(\theta)$, and the potential drop between A and C, which are beside the crack, $V_{AC}(\theta)$, are calculated by using $V_{AB}(\theta)$ and $V_{CD}(\theta)$ as

$$V_{AD}(\theta) = \tfrac{1}{2}\{V_{AB}(\theta) + V_{CD}(\theta)\} \tag{7}$$

and

$$V_{AC}(\theta) = \tfrac{1}{2}|V_{AB}(\theta) - V_{CD}(\theta)|. \tag{8}$$

The demonstration of Eqs. (7) and (8) is given in the Appendix. The increment of the potential drop between A and D, $\Delta V_{\mathrm{I}}(\theta)$, and that between A and C, $\Delta V_{\mathrm{II}}(\theta)$, are calculated by

$$\Delta V_{\mathrm{I}}(\theta) = V_{AD}(\theta) - V_{0AD} \tag{9}$$

and

$$\Delta V_{\mathrm{II}}(\theta) = V_{AC}(\theta) - V_{0AC} \tag{10}$$

where V_{0AD} and V_{0AC} are the potential drop in the cases where no crack exists.

2.3 Calibration Equation of Potential Drop for a Semielliptical Surface Crack in a Finite Plate. Next, derive the evaluation equation of the potential drop for an isolated crack in a finite plate. For a semielliptical surface crack, which is perpendicular to the surface of a plate having the width W as shown in Fig. 4, the calibration equations of the potential drop between points A and D, $V_{AD}(\theta)$, and of the potential drop between points A and C, $V_{AC}(\theta)$, are proposed as follows. The potential drop $V_{AD}(\theta)$ is based on the results of the finite element method and expressed empirically by the sum of the potential drop between A and D in the case without a crack, the increment of the potential drop $\Delta V_{\mathrm{I}}(\theta)$ due to a crack which is calculated by Eq. (9), assuming the crack is in an infinite plate, and the effect of side walls and crack interaction, $\Delta V_{w\mathrm{I}}(\theta)$, as

$$\begin{cases} V_{AD}(\theta) = V_{0AD} + \Delta V'_{\mathrm{I}}(\theta) & (11a) \\ \Delta V'_{\mathrm{I}}(\theta) = \Delta V_{\mathrm{I}}(\theta) + \Delta V_{w\mathrm{I}}(\theta) & (11b) \\ \Delta V_{w\mathrm{I}}(\theta) = \dfrac{(aW - S)}{\pi}\left\{\dfrac{h_1}{(W + r_A)^2} + \dfrac{h_2}{(W + r_D)^2}\right\} \times \left(\dfrac{\pi}{2} - \dfrac{W}{W + t}\right) V_0 \cos\theta & (11c) \end{cases}$$

where $\Delta V'_{\mathrm{I}}(\theta)$ represents the increment of the potential drop due to the crack in a finite plate. The area of the crack is denoted by S, and h_1, h_2, r_A, r_D and t are the distances shown in Fig. 4. In the case of a crack passing through the plate width, the effect of the walls is disregarded, because it is small.

An example of the comparison between Eq. (11) and the finite element method calculation results is shown in Fig. 5, where D is symmetric to A about the center of the crack. In the same way as Fig. 5, Eq. (11) has been confirmed for many cases to agree well with the results of the finite element method.

Similarly, the potential drop $V_{AC}(\theta)$ is obtained by

$$\begin{cases} V_{AC}(\theta) = V_{0AC} + \Delta V'_{\mathrm{II}}(\theta) & (12a) \\ \Delta V'_{\mathrm{II}}(\theta) = \Delta V_{\mathrm{II}}(\theta) + \Delta V_{w\mathrm{II}}(\theta) & (12b) \\ \Delta V_{w\mathrm{II}}(\theta) = \dfrac{(aW - S)}{\pi}\left|\dfrac{h_1}{(W + r_A)^2} - \dfrac{h_3}{(W + r_C)^2}\right| \times \left(\dfrac{\pi}{2} - \dfrac{W}{W + t}\right) V_0 \cos\theta & (12c) \end{cases}$$

where $\Delta V'_{\mathrm{II}}(\theta)$, $\Delta V_{\mathrm{II}}(\theta)$, and $\Delta V_{w\mathrm{II}}(\theta)$ are the increment of the potential drop due to the crack in a finite plate; the increment of the potential drop due to the crack which is calculated by Eq. (10), assuming the crack in an infinite plate; and the effect of side walls and crack interaction, respectively. The quantities h_3 and r_C are the distances shown in Fig. 4.

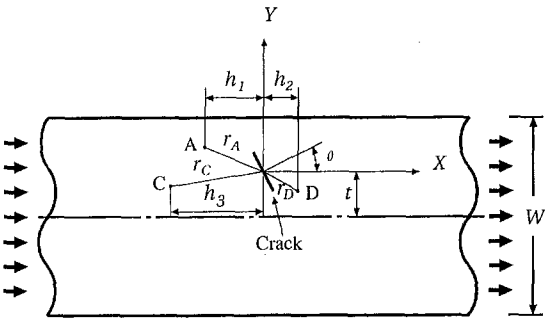

Fig. 4 Finite plate containing a semielliptical surface crack

2.4 Case of a Finite Plate Containing Multiple Cracks. Three-dimensional multiple cracks as shown in Fig. 6, which are semielliptical and perpendicular to the surface of a plate, are treated. A constant current is introduced far from the cracks. The maximum depth of the ith crack ($i = 1, 2, \ldots, n$) and the half-length on the surface of the plate are denoted by a_i and c_i, respectively, where n is the total number of cracks. The normal of the surfaces of the cracks is at an angle to the direction of current

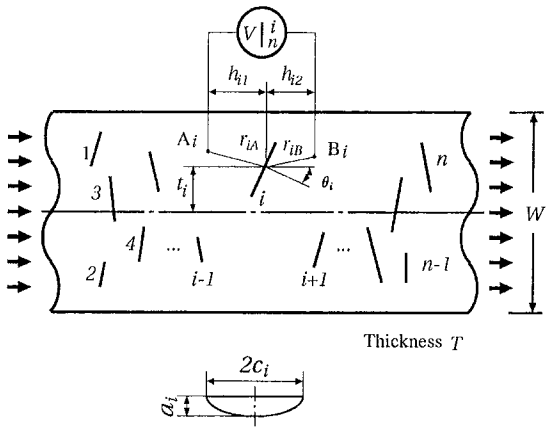

Detail of ith Crack

Fig. 6 Modeling of three-dimensional multiple cracks

flow far from the cracks by angles $\theta_i(|\theta_i| < \pi/2)$. Consider calculating the potential drop $V|_n^i$ between points A_i and B_i, which are on both sides of the ith crack (see Fig. 6). First as the simplest case of multiple cracks, a plate containing two cracks is considered. Then evaluate the potential drop $V|_2^1$ between points A_1 and B_1, which are on the surface of the material, simply by

$$V|_2^1 = V_{01} + \Delta V_{\mathrm{I}}^{(1)} + \Delta V_{w\mathrm{I}}^{(1)} + \Delta V_{\mathrm{II}}^{(2)} + \Delta V_{w\mathrm{II}}^{(2)} + \frac{\{\Delta V_{\mathrm{I}}^{(1)} + \Delta V_{w\mathrm{I}}^{(1)}\}\{\Delta V_{\mathrm{II}}^{(2)} + \Delta V_{w\mathrm{II}}^{(2)}\}}{AV_{01}} \quad (13)$$

where V_{01} is the potential drop between A_1 and B_1 in the case without crack, $\Delta V_{\mathrm{I}}^{(1)}$ is the increment of the potential drop between A_1 and B_1 for an assumed infinite plate only containing the first crack, $\Delta V_{w\mathrm{I}}^{(1)}$ is the effect of interaction between the side walls and the first crack, $\Delta V_{\mathrm{II}}^{(2)}$ is the increment of the potential drop between A_1 and B_1 for an assumed infinite plate only containing the second crack, $\Delta V_{w\mathrm{II}}^{(2)}$ is the effect of interaction between the side walls and the second crack, and A is an unknown coefficient. The sixth term on the right-hand side of Eq. (13) expresses the interaction between the first and second cracks. In the case where no crack exists, Eq. (13) is equal to V_{01}. For an assumed finite plate only containing the first crack, $V|_2^1$ in Eq. (13) is equal to $V_{01} + \Delta V_{\mathrm{I}}^{(1)} + \Delta V_{w\mathrm{I}}^{(1)}$, which is the evaluation equation for a finite plate containing an isolated crack. Also for an assumed finite plate only containing the second crack, $V|_2^1$ is equal to $V_{01} + \Delta V_{\mathrm{II}}^{(2)} + \Delta V_{w\mathrm{II}}^{(2)}$. In this case two measuring points A_1 and B_1 are beside the second crack. For its general case as shown in Fig. 7, $\Delta V_{w\mathrm{II}}^{(j)}$ ($j = 1, 2, \ldots, i-1, i+1, \ldots, n$) is approximated similarly to Eq. (12c) by

$$\Delta V_{w\mathrm{II}}^{(j)} = \frac{(a_j W - S_j)}{\pi}\left|\frac{h_{jA}}{(W + r_{jA})^2} - \frac{h_{jB}}{(W + r_{jB})^2}\right| \times \left(\frac{\pi}{2} - \frac{W}{W + t_j}\right) V_0 \cos\theta_j \quad (14)$$

where S_j ($= \pi a_j c_j/2$) is the area of the jth crack, and h_{jA}, h_{jB}, r_{jA}, r_{jB}, and t_j are the distances shown in Fig. 7.

Next Eq. (13) is extended to the case of a plate containing three cracks. First consider the interaction between the second and third cracks. The increment of the potential drop ΔV_{II}^1 for an assumed finite plate containing the second and third cracks and without the first crack is evaluated by

$$\Delta V_{\mathrm{II}}^1 = \Delta V_{\mathrm{II}}^{(2)} + \Delta V_{w\mathrm{II}}^{(2)} + \Delta V_{\mathrm{II}}^{(3)} + \Delta V_{w\mathrm{II}}^{(3)} + \frac{\{\Delta V_{\mathrm{II}}^{(2)} + \Delta V_{w\mathrm{II}}^{(2)}\}\{\Delta V_{\mathrm{II}}^{(3)} + \Delta V_{w\mathrm{II}}^{(3)}\}}{AV_{01}}. \quad (15)$$

Then consider another interaction of the first crack. The potential drop $V|_3^1$ between points A_1 and B_1 is evaluated by

$$V|_3^1 = V_{01} + \Delta V_{\mathrm{I}}^{(1)} + \Delta V_{w\mathrm{I}}^{(1)} + \Delta V_{\mathrm{II}}^1 + \frac{\{\Delta V_{\mathrm{I}}^{(1)} + \Delta V_{w\mathrm{I}}^{(1)}\}\Delta V_{\mathrm{II}}^1}{AV_{01}}. \quad (16)$$

The methodology is extended successively to calculate the potential drop $V|_n^i$ between points A_i and B_i, which are on both sides of the ith crack (see Fig. 6). It is given by

$$V|_n^i = V_{0i} + \Delta V_{\mathrm{I}}^{(i)} + \Delta V_{w\mathrm{I}}^{(i)} + \Delta V_{\mathrm{II}}^i + \frac{\{\Delta V_{\mathrm{I}}^{(i)} + \Delta V_{w\mathrm{I}}^{(i)}\}\Delta V_{\mathrm{II}}^i}{AV_{0i}}. \quad (17)$$

The potential drop $\Delta V_{w\mathrm{I}}^{(i)}$ is approximated similarly to Eq. (11c) by

$$\Delta V_{w\mathrm{I}}^{(i)} = \frac{(a_i W - S_i)}{\pi}\left\{\frac{h_{i1}}{(W + r_{iA})^2} + \frac{h_{i2}}{(W + r_{iB})^2}\right\} \times \left(\frac{\pi}{2} - \frac{W}{W + t_i}\right) V_0 \cos\theta_i \quad (18)$$

where h_{i1}, h_{i2}, r_{iA}, r_{iB}, and t_i are the distances shown in Fig. 6. The increment of the potential drop ΔV_{II}^i between A_i and B_i obtained for an assumed finite plate without the ith crack as shown in Fig. 7 is calculated by considering successively the interaction of respective cracks.

3 Characteristic of Coefficient A

The unknown coefficients which have appeared in the denominator in the fifth term on the right-hand side of Eq. (17) and been contained in ΔV_{II}^i implicitly, have been expressed by the same symbol A. In order to show that this dealing is appropriate, consider a model with three cracks, and evaluate the potential drop $V|_3^1$ between two points which are on both sides of the first crack.

By paying attention to the first crack, let us consider the interactions of the second and third cracks. First assume a plate only containing the first and second cracks, where A is written as A_1, and the sum of the effects of the first and second cracks, side walls, and the interaction of side walls and cracks, $\Delta V_{\mathrm{I}}^{(1)} + \Delta V_{w\mathrm{I}}^{(1)} + \Delta V_{\mathrm{II}}^{(2)} + \Delta V_{w\mathrm{II}}^{(2)} + \{\Delta V_{\mathrm{I}}^{(1)} + \Delta V_{w\mathrm{I}}^{(1)}\}\{\Delta V_{\mathrm{II}}^{(2)} + \Delta V_{w\mathrm{II}}^{(2)}\}/(A_1 V_{01})$ is calculated. Then if another interaction of the third crack is considered by writing A as A_2, the potential drop $V|_3^1$ is evaluated by

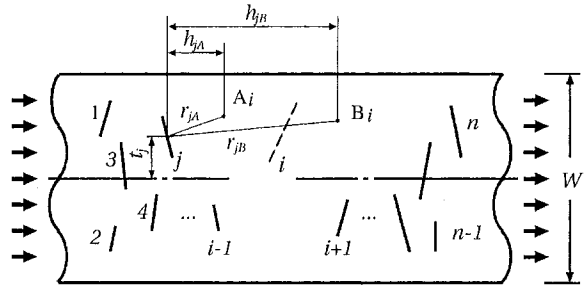

Fig. 7 Plate containing three-dimensional multiple cracks without the ith crack

$$V|_3^1 = V_{01} + \left(\Delta V_{\mathrm{I}}^{(1)} + \Delta V_{w\mathrm{I}}^{(1)} + \Delta V_{\mathrm{II}}^{(2)} + \Delta V_{w\mathrm{II}}^{(2)} + \frac{(\Delta V_{\mathrm{I}}^{(1)} + \Delta V_{w\mathrm{I}}^{(1)})(\Delta V_{\mathrm{II}}^{(2)} + \Delta V_{w\mathrm{II}}^{(2)})}{A_1 V_{01}} \right) + \Delta V_{\mathrm{II}}^{(3)} + \Delta V_{w\mathrm{II}}^{(3)}$$
$$+ \frac{\left(\Delta V_{\mathrm{I}}^{(1)} + \Delta V_{w\mathrm{I}}^{(1)} + \Delta V_{\mathrm{II}}^{(2)} + \Delta V_{w\mathrm{II}}^{(2)} + \frac{(\Delta V_{\mathrm{I}}^{(1)} + \Delta V_{w\mathrm{I}}^{(1)})(\Delta V_{\mathrm{II}}^{(2)} + \Delta V_{w\mathrm{II}}^{(2)})}{A_1 V_{01}} \right)(\Delta V_{\mathrm{II}}^{(3)} + \Delta V_{w\mathrm{II}}^{(3)})}{A_2 V_{01}} = V_{01} + \Delta V_{\mathrm{I}}^{(1)} + \Delta V_{\mathrm{II}}^{(2)}$$
$$+ \Delta V_{\mathrm{II}}^{(3)} + \Delta V_{w\mathrm{I}}^{(1)} + \Delta V_{w\mathrm{II}}^{(2)} + \Delta V_{w\mathrm{II}}^{(3)} + \frac{(\Delta V_{\mathrm{I}}^{(1)} + \Delta V_{w\mathrm{I}}^{(1)})(\Delta V_{\mathrm{II}}^{(2)} + \Delta V_{w\mathrm{II}}^{(2)})}{A_1 V_{01}} + \frac{(\Delta V_{\mathrm{I}}^{(1)} + \Delta V_{w\mathrm{I}}^{(1)})(\Delta V_{\mathrm{II}}^{(3)} + \Delta V_{w\mathrm{II}}^{(3)})}{A_2 V_{01}}$$
$$+ \frac{(\Delta V_{\mathrm{II}}^{(2)} + \Delta V_{w\mathrm{II}}^{(2)})(\Delta V_{\mathrm{II}}^{(3)} + \Delta V_{w\mathrm{II}}^{(3)})}{A_2 V_{01}} + \frac{(\Delta V_{\mathrm{I}}^{(1)} + \Delta V_{w\mathrm{I}}^{(1)})(\Delta V_{\mathrm{II}}^{(2)} + \Delta V_{w\mathrm{II}}^{(2)})(\Delta V_{\mathrm{II}}^{(3)} + \Delta V_{w\mathrm{II}}^{(3)})}{A_1 A_2 V_{01}^2}. \quad (19)$$

Next, change the order of the cracks considered. First assume a plate containing only the second and third cracks, where A is written as A_3, and the sum of the effects of the second and third cracks, side walls, and the interaction of side walls and cracks, $\Delta V_{\mathrm{II}}^{(2)} + \Delta V_{w\mathrm{II}}^{(2)} + \Delta V_{\mathrm{II}}^{(3)} + \Delta V_{w\mathrm{II}}^{(3)} + \{\Delta V_{\mathrm{II}}^{(2)} + \Delta V_{w\mathrm{II}}^{(2)}\}\{\Delta V_{\mathrm{II}}^{(3)} + \Delta V_{w\mathrm{II}}^{(3)}\}/(A_3 V_{01})$, is calculated. Then if another interaction of the first crack is considered by writing A as A_4, the potential drop $V|_3^1$ is evaluated by

$$V|_3^1 = V_{01} + \left(\Delta V_{\mathrm{II}}^{(2)} + \Delta V_{w\mathrm{II}}^{(2)} + \Delta V_{\mathrm{II}}^{(3)} + \Delta V_{w\mathrm{II}}^{(3)} + \frac{(\Delta V_{\mathrm{II}}^{(2)} + \Delta V_{w\mathrm{II}}^{(2)})(\Delta V_{\mathrm{II}}^{(3)} + \Delta V_{w\mathrm{II}}^{(3)})}{A_3 V_{01}} \right) + \Delta V_{\mathrm{I}}^{(1)} + \Delta V_{w\mathrm{I}}^{(1)}$$
$$+ \frac{\left(\Delta V_{\mathrm{II}}^{(2)} + \Delta V_{w\mathrm{II}}^{(2)} + \Delta V_{\mathrm{II}}^{(3)} + \Delta V_{w\mathrm{II}}^{(3)} + \frac{(\Delta V_{\mathrm{II}}^{(2)} + \Delta V_{w\mathrm{II}}^{(2)})(\Delta V_{\mathrm{II}}^{(3)} + \Delta V_{w\mathrm{II}}^{(3)})}{A_3 V_{01}} \right)(\Delta V_{\mathrm{I}}^{(1)} + \Delta V_{w\mathrm{I}}^{(1)})}{A_4 V_{01}} = V_{01} + \Delta V_{\mathrm{I}}^{(1)} + \Delta V_{\mathrm{II}}^{(2)}$$
$$+ \Delta V_{\mathrm{II}}^{(3)} + \Delta V_{w\mathrm{I}}^{(1)} + \Delta V_{w\mathrm{II}}^{(2)} + \Delta V_{w\mathrm{II}}^{(3)} + \frac{(\Delta V_{\mathrm{II}}^{(2)} + \Delta V_{w\mathrm{II}}^{(2)})(\Delta V_{\mathrm{II}}^{(3)} + \Delta V_{w\mathrm{II}}^{(3)})}{A_3 V_{01}} + \frac{(\Delta V_{\mathrm{II}}^{(2)} + \Delta V_{w\mathrm{II}}^{(2)})(\Delta V_{\mathrm{I}}^{(1)} + \Delta V_{w\mathrm{I}}^{(1)})}{A_4 V_{01}}$$
$$+ \frac{(\Delta V_{\mathrm{II}}^{(3)} + \Delta V_{w\mathrm{II}}^{(3)})(\Delta V_{\mathrm{I}}^{(1)} + \Delta V_{w\mathrm{I}}^{(1)})}{A_4 V_{01}} + \frac{(\Delta V_{\mathrm{I}}^{(1)} + \Delta V_{w\mathrm{I}}^{(1)})(\Delta V_{\mathrm{II}}^{(2)} + \Delta V_{w\mathrm{II}}^{(2)})(\Delta V_{\mathrm{II}}^{(3)} + \Delta V_{w\mathrm{II}}^{(3)})}{A_3 A_4 V_{01}^2}. \quad (20)$$

Since Eq. (19) should be equal to Eq. (20), coefficients A_1 to A_4 must satisfy the next conditions.

$$A_1 = A_4, \quad A_2 = A_4, \quad A_2 = A_3, \quad A_1 A_2 = A_3 A_4 \quad (21)$$

According to Eq. (21), it can be found that $A_1 = A_2 = A_3 = A_4$, which means that our dealing concerned with A is appropriate. It can easily be verified in the same way as the above that A takes only one value in the case of arbitrary n cracks.

4 Range of Coefficient A

When the depths of cracks except for the ith crack are assumed to be fixed, $V|_n^i$ increases due to an increase of the depth a_i of the ith crack. Therefore

$$\frac{\partial V|_n^i}{\partial a_i} > 0. \quad (22)$$

According to Eq. (17), we can get

$$\frac{\partial V|_n^i}{\partial a_i} = \frac{\partial \{\Delta V_{\mathrm{I}}^{(i)} + \Delta V_{w\mathrm{I}}^{(i)}\}}{\partial a_i}\left(1 + \frac{\Delta V_{\mathrm{II}}^i}{A V_{0i}}\right) \quad (23)$$

By substituting Eq. (23) into Eq. (22) and considering $\partial\{\Delta V_{\mathrm{I}}^{(i)} + \Delta V_{w\mathrm{I}}^{(i)}\}/\partial a_i > 0$, we can get

$$A > -\frac{\Delta V_{\mathrm{II}}^i}{V_{0i}}. \quad (24)$$

It is noted that ΔV_{II}^i contains A implicitly, and A must satisfy Eq. (24).

5 Simplified Evaluation Method

For both two and three-dimensional multiple cracks, consider a procedure to evaluate the depths of cracks by means of the above-mentioned analysis of crack interactions and by consulting the nondestructive evaluation method for two-dimensional multiple cracks (Ghajarieh et al., 1994). The distances between

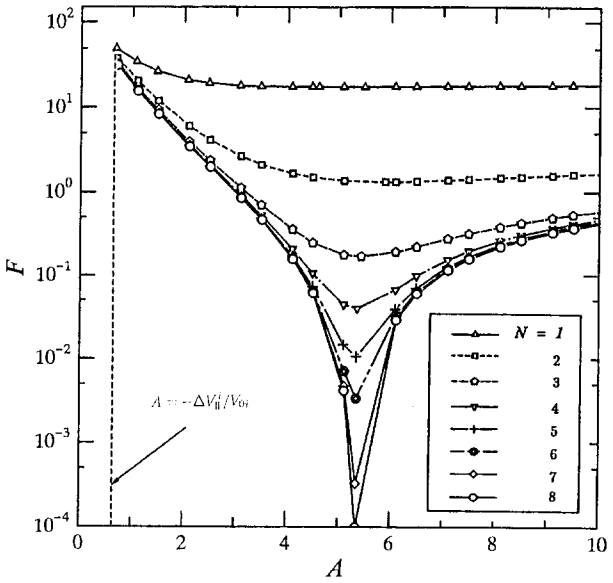

Fig. 8 Relation between function F and coefficient A in the case of the coefficient $\alpha = 0.5$ and $a_{iA}/T = 0.5$ in specimen SP1, where N is the repeated number of calculation, α is defined in Eq. (27), and SP1 is shown in Fig. 9

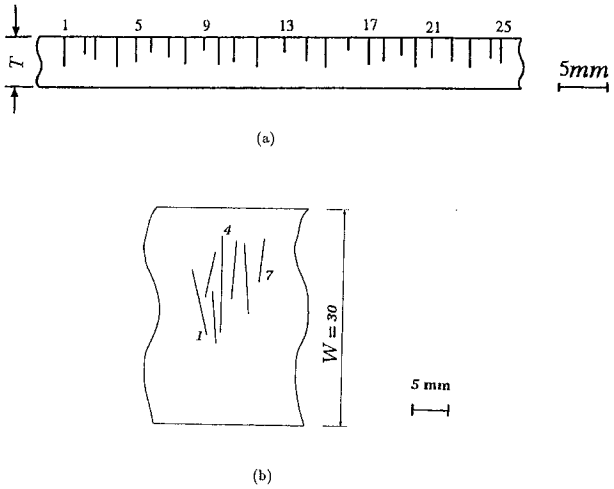

Fig. 9 Specimens used for experiment, (*a*) specimen SP1 containing two-dimensional multiple cracks and (*b*) specimen SP2 containing three-dimensional multiple cracks

cracks and the lengths of cracks on the material surface are assumed to be known in advance based on observation from the side of the cracked surface by using the penetrant method, for example. However, the crack depths are unknown. The procedure to determine the depths is proposed as follows:

1 Introduce a constant d.c. current to the material. Measure the potential drop between two points on the cracked surface, where the points are on both sides of the ith crack, and denote the potential drop by V_i^M and define F by

$$F = \sum_{i=1}^{n} \left(\frac{V_i^M - Vl_n^i}{V_{0i}} \right)^2 . \tag{25}$$

2 Assume any value a_{iA} for the depth of the ith crack.

3 We have confirmed as illustrated in Fig. 8 that in the range of Eq. (24), a value of A, which gives the minimum value of F, can be obtained uniquely. Therefore, give different values for A step by step. Compare the values of F calculated. Then determine the value of A giving the minimum value of F.

4 Based on steps 2 and 3, calculate the value of Vl_n^i by using Eq. (17), then calculate F.

5 If F takes a value less than an infinitesimal value ϵ, the depth of the ith crack is evaluated as a_{iA}. Otherwise the assumption of the crack depth is modified by

$$a'_{iA} = a_{iA} + \Delta a_{iA} \tag{26}$$

where

$$\Delta a_{iA} = \begin{cases} \alpha \dfrac{V_i^M - Vl_n^i}{V_i^M} (T - a_{iA}) & (\text{when} \quad V_i^M > Vl_n^i) \quad (27a) \\ \alpha \dfrac{V_i^M - Vl_n^i}{Vl_n^i} a_{iA} & (\text{when} \quad V_i^M < Vl_n^i) \quad (27b) \end{cases}$$

The coefficient α takes a value in the range $0 < \alpha \leq 1$. Set $a_{iA} = a'_{iA}$ and repeat step 3.

6 Experiment

The specimens made of austenitic stainless steel AISI304 were used and named SP1 and SP2, respectively. The thickness T, the width W, and the length L of SP1 containing two-dimensional multiple cracks were 5, 25, and 300 mm as shown in Fig. 9(*a*), and those values of SP2 containing three-dimensional multiple cracks were 7.5, 30, and 300 mm as shown in Fig. 9(*b*), respectively. Multiple cracks were modeled by electric-discharge machined notches having a width of 0.1 mm for SP1, and 0.15 mm for SP2.

A schematic diagram of the experiment is shown in Fig. 10. A constant d.c. current of 17A was introduced on both sides of the specimen. The left probe was fixed at a distance of 70 mm for SP1, and 80 mm for SP2 from the center of the first crack on the surface while the right probe was moved along the line crossing the center of the crack in the direction of current flow far from cracks. Potential measuring points are shown in Fig. 10. The potential drop between two points on the cracked surface, where the points are on both sides of the ith crack, was measured by using a digital microvoltmeter.

7 Result and Discussion

The comparisons between the final values of the crack depths calculated by the present method and the actual crack depths are shown in Figs. 11 and 12 for specimens SP1 and SP2, respectively. In SP1, the value of ϵ used was 10^{-4}. In SP2, ϵ was 10^{-3}. According to Fig. 11, the final values of calculated crack depths are independent of the initially assumed crack depths. The crack depths evaluated by the present method agree well with the actual depths (see Figs. 11 and 12).

Also, as an example, the comparisons between the crack depths evaluated by using Eq. (7) for an isolated crack without considering the interaction of multiple cracks and the actual crack depths are shown in Fig. 13 for specimen SP2. It can be observed from Fig. 13 that the successive interactions of cracks and side walls must be considered additionally to the evaluation equation for an isolated crack as done in the present paper, because the difference between the evaluated and actual values is quite large.

Finally, it is stated that the present method evaluated the depths of the cracks with a personal computer (i486SX) or a workstation (R4000SC) in a short time. As an example, in the case of $\alpha = 0.5$ and $a_{iA}/T = 0.5$ in SP1, the calculation time was 28 seconds by using a personal computer.

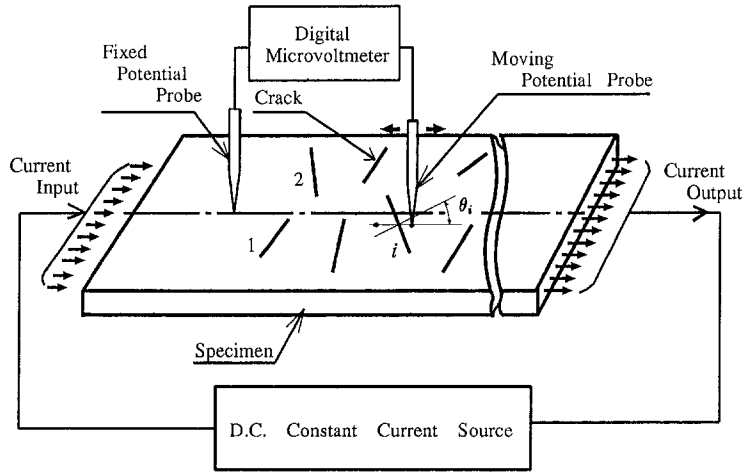

Fig. 10 Schematic diagram of experiment

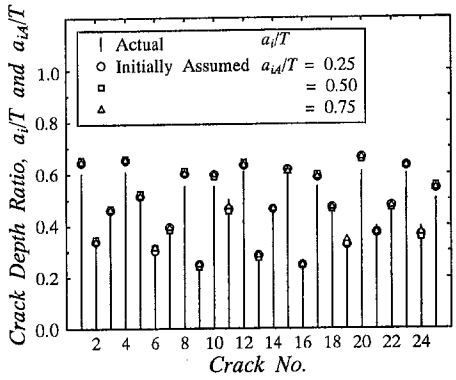

Fig. 11 Comparison between the final values of the calculated crack depths obtained by using 0.25, 0.5, and 0.75T for initially assumed crack depth with α of 0.5 and the actual crack depths in SP1

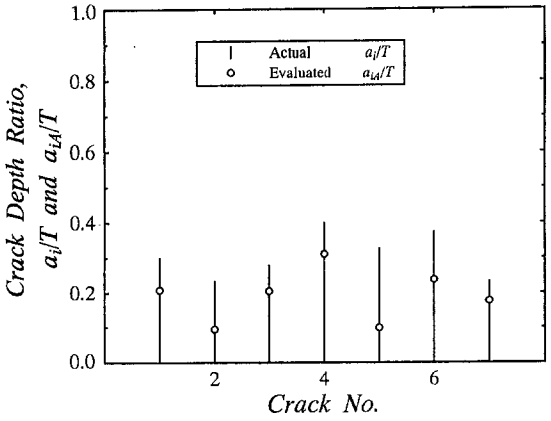

Fig. 13 Comparison between the value of crack depth evaluated by Eq. (7) and the actual crack depth

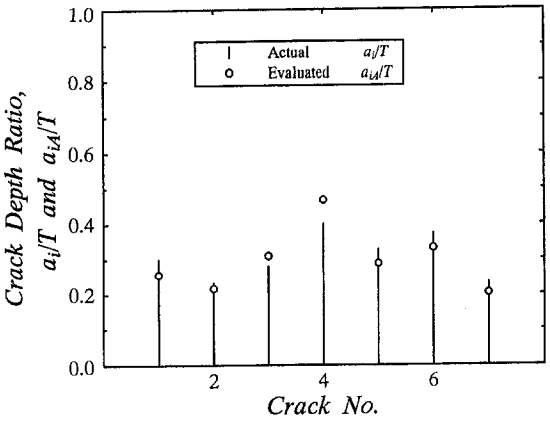

Fig. 12 Comparison between the final values of the calculated crack depths obtained by using 0.15T for initially assumed crack depth with α of 0.15 and the actual crack depths in SP2

8 Conclusion

A method of nondestructive evaluation of two and three-dimensional surface multiple cracks was proposed, which was based on the d.c. potential drop technique and analyzing simply the interaction of multiple cracks. It was shown by the experiment and calculation that the present method is valid.

Acknowledgments

This work was partly supported by The Ministry of Education, Science, Sports and Culture under Grant-in-Aid for Scientific Research (C) (2) 07805010 and Scientific Research (A) (2) 08555021.

References

Abé, H., and Kanoh, Y., 1990, "An Inverse Problem in Nondestructive Inspection of a Crack in a Plate with an Inhomogeneity by Means of the Electrical Potential Method," *Micromechanics and Inhomogeneity,* G. J. Weng, M. Taya, and H. Abé, eds., Springer-Verlag, New York, pp. 1–15.

Beissner, R. E., Teller, C. M., Burkhardt, G. L., Smith, R. T., and Barton, J. R., 1981, "Detection and Analysis of Electric-Current Perturbation Caused by Defects," *Eddy-Current Characterization of Materials and Structures,* ASTM STP 722, G. Birnbaum, and G. Free, eds., ASTM, Philadelphia, PA, pp. 428–446.

Ghajarieh, R., Saka, M., Abé, H., Komura, I., and Sakamoto, H., 1995, "Simplified NDE of Multiple Cracks by Means of the Potential Drop Technique," *NDT & E International,* Vol. 28, No. 1, pp. 23–28.

Ghajarieh, R., Saka, M., Sugawara, T., Abé, H., Komura, I., and Sakamoto, H., 1994, "NDE of Multiple Cracks on the Surface of Materials by Means of the Potential Drop Technique," *NDT & E International,* Vol. 27, No. 3, pp. 143–150.

Johnson, H. H., 1965, "Calibrating the Electric Potential Method for Studying Slow Crack Growth," *Journal of Materials Research & Standards,* Vol. 5, No. 9, pp. 442–445.

Parkins, R. N., and Singh, P. M., 1990, "Stress Corrosion Crack Coalescence," *Journal of Science and Engineering Corrosion,* Vol. 46, No. 6, pp. 485–499.

APPENDIX

Demonstration of the Equation of the Potential Drop Between Measuring Points on the Surface of an Infinite Plate Containing an Isolated Crack

In the text, the equations of the potential drop between two measuring points on the cracked surface were given by Eqs. (7) and (8). Let us derive these equations.

First denote the electrical potential at A, B, C, and D in Fig. 2 by ϕ_A, ϕ_B, ϕ_C, and ϕ_D, respectively, and at the origin O by ϕ_O. Since point A is symmetric about the Z-axis to B and C is to D, respectively, we have

$$\begin{cases} \phi_A - \phi_O = \phi_O - \phi_B & \text{(A1}a\text{)} \\ \phi_C - \phi_O = \phi_O - \phi_D. & \text{(A1}b\text{)} \end{cases}$$

Then

$$\begin{cases} \phi_B = 2\phi_O - \phi_A & \text{(A2}a\text{)} \\ \phi_C = 2\phi_O - \phi_D & \text{(A2}b\text{)} \end{cases}$$

Based on the above, the derivation of Eqs. (7) and (8) is as follows:

For the case of $\phi_A > \phi_C > \phi_O > \phi_D > \phi_B$ as an example,

$$\begin{aligned} V_{AB}(\theta) + V_{CD}(\theta) &= |\phi_A - \phi_B| + |\phi_C - \phi_D| \\ &= \phi_A - \phi_B + \phi_C - \phi_D \\ &= \phi_A - 2\phi_O + \phi_A + 2\phi_O - \phi_D - \phi_D \\ &= 2(\phi_A - \phi_D) \\ &= 2V_{AD}(\theta) \end{aligned} \tag{A3}$$

and

$$\begin{aligned} |V_{AB}(\theta) - V_{CD}(\theta)| &= \|\phi_A - \phi_B| - |\phi_C - \phi_D\| \\ &= |\phi_A - \phi_B - \phi_C + \phi_D| \\ &= |\phi_A - 2\phi_O + \phi_A - \phi_C + 2\phi_O - \phi_C| \\ &= 2(\phi_A - \phi_C) \\ &= 2V_{AC}(\theta). \end{aligned} \tag{A4}$$

In this way, Eqs. (7) and (8) are proven.

Dynamic Buckling and Post-buckling of Imperfect Orthotropic Cylindrical Shells Under Mechanical and Thermal Loads, Based on the Three-Dimensional Theory of Elasticity

M. Shariyat
Ph.D. Student.

M. R. Eslami
Professor,
Mem. ASME.

Mechanical Engineering Department,
Amirkabir University of Technology,
Hafez Avenue No. 24,
Tehran, 15914, Iran

The three-dimensional theory of elasticity in curvilinear coordinates is employed to investigate the dynamic buckling of an imperfect orthotropic circular cylindrical shell under mechanical and thermal loads. Accurate form of the strain expressions of imperfect cylindrical shells is established through employing the general Green's strain tensor for large deformations and the equations of motion are derived in terms of the second Piola-Kirchhoff stress tensor. Then, the governing equations are properly formulated and solved by means of an efficient and relatively accurate solution procedure proposed to solve the highly nonlinear equations resulting from the above analysis. The proposed formulation is very general as it can include the influence of the initial imperfections, temperature distribution, and temperature dependency of the mechanical properties of materials, effect of various end conditions, possibility of large-deformation occurrence and application of any combination of mechanical and thermal loadings. No simplifications are done when solving the resulting equations. Furthermore, in contrast to the displacement-based layer-wise theories and the three-dimensional approaches proposed so far, the stress, force and moment boundary conditions as well as the displacement type ones, can be incorporated accurately in these formulations. Finally, a few examples of mechanical and thermal buckling of some orthotropic cylindrical shells are considered and results of the present three-dimensional elasticity approach are compared with the buckling loads predicated by the Donnell's equations, some single-layer theories, some available results of the layer-wise theory and the recently published three-dimensional approaches and the accuracy of the later methods are discussed based on the exact method presented in this paper.

Introduction

Because of their large strength-to-weight ratio of fiber-reinforced composite materials, they have found many applications in aerospace, aeronautic, marine, automobile, and other industries. Behavior of the composite components differs from that of metallic counterparts in that the former are heterogeneous, anisotropic, and considerably more shear deformable than the latter. In these materials, transverse shear and normal stress effects may be significant, even in thin composite shells. Disregarding such effects can lead to approximately as much as 120 percent or more errors in predication of the critical buckling loads (Kardomateas and Philobos, 1995). Complete analysis of the buckling of composite cylindrical shells requires that the directional properties of the materials, possibility of large-deformation occurrence, end conditions, temperature distribution effects (thermal loading), temperature dependency of the mechanical properties, initial imperfections, and inelastic deformations to be considered. For this reason, even the static buckling phenomenon of a composite cylindrical shell is not clarified well, yet.

The classical shell theory suggested by Donnell (1976) have formed the basis for dynamic stability analysis of many works in the literature. The transverse shear and normal stress and strains are disregarded in this approach. Some of these studies are done by Saigal et al. (1987), Liaw and Yang (1991), Argento and Scott (1993), and Kasagi and Sridharan (1995).

In many references, effect of the transverse normal and shear stresses and strains are accounted for by means of higher-order strain-displacement expressions (Zukas, 1974; Reddy and Liu, 1985; Stein, 1986; Dennis and Palazotto, 1989; Simitses and Anastasiadis, 1992; Barbero et al., 1990). Recently a high-order shear-deformation theory was proposed by Eslami and Shariyat (1998) which is most suitable for incorporation of stress and displacement edge conditions.

To improve the accuracy of the usual two-dimensional formulations, through consideration of the transverse shear and normal stresses, some displacement-based layer-wise theories are proposed by some authors (for example, Reddy and Savoia (1992) and Robbins and Reddy (1993)) which can produce much more accurate results but suffer from the point that the boundary conditions (for example, the simply supported end condition) cannot be exactly incorporated in these formulations. Recently, the authors have proposed a new general layer-wise theory which can overcome this problem (Eslami and Shariyat, 1998).

Contributed by the Applied Mechanics Division of THE AMERICAN SOCIETY OF MECHANICAL ENGINEERS for publication in the ASME JOURNAL OF APPLIED MECHANICS.

Discussion on the paper should be addressed to the Technical Editor, Professor Lewis T. Wheeler, Department of Mechanical Engineering, University of Houston, Houston, TX 77204-4792, and will be accepted until four months after final publication of the paper itself in the ASME JOURNAL OF APPLIED MECHANICS.

Manuscript received by the ASME Applied Mechanics Division, Jan. 8, 1998; final revision, Sept. 14, 1998. Associate Technical Editor: J. N. Reddy.

More recently, efforts for introducing a three-dimensional elasticity solution for the static buckling of perfect, single-layered thick composite cylindrical shells under mechanical loads alone, were done by Kardomateas (1993a, b, 1995b), Kardomateas and Chung (1994), and Radhamohan and Venkataramana (1975). In the formulations of Kardomateas (1993a, b, 1995b), Kardomateas and Chung (1994), and Radhamohan and Venkataramana (1975) the transverse shear deformability and normal stress are automatically incorporated and the dependency on a particular shell theory is eliminated. The proposed formulations are rather simple, linear, static, and disregard the initial imperfections and temperature effects and are suitable for single-layer thick composite shells. Besides, one of the Fourier triple series terms is adopted in the solution (which can justified for thick shells only) and the boundary conditions are only satisfied geometrically. Thus, the problem is reduced to a standard eigenvalue problem that is solved by discretizing the shell thickness and using the finite difference method in this direction.

In contrast to the study of shell buckling under mechanical loads, studies of thermal buckling of composite shells are more restricted. Generally, these investigations are based on static buckling consideration and belong to the equivalent single-layer theories (for example, Radhamohan and Venkataramana (1975) and Thangaratnam et al. (1990)). A paper review by Thornton (1993) summarizes thermal buckling of plates and shells research.

In the present paper, the three-dimensional theory of elasticity in curvilinear coordinates is employed to investigate the dynamic buckling of an imperfect orthotropic circular cylindrical shell under mechanical and thermal loading. Mechanical loads may be composed of axial compression, external pressure, torsion, or a combination of them. For this purpose, instead of employing the conventional infinitesimal displacements or using the Von Karman assumptions, first the Green's strain tensor for large deflections in curvilinear coordinates is used, and the strain expressions of an imperfect circular cylindrical shell are derived. Then, the governing equations are properly formulated and an efficient and relatively accurate solution algorithm for treatment of the highly nonlinear equations resulting from this approach are introduced. This method can be used to assist the dynamic behavior as well as the stability of the cylindrical shells. The proposed formulation is very general and no simplifications are made in solving the resulting equations. To employ the presented procedure for solution, the shell is discretized into a three-dimensional mesh of grid points and the derivative expressions with respect to the spacial coordinates are substituted by a fourth-order finite difference approximation and the resulted equations are solved by means of the fourth-order Runge-Kutta method for time marching. It can be noted that the solution of a cylindrical shell under mechanical loads is boundary conditions driven whereas it is constitutive equation driven in the case of thermal loading. Finally, few examples of cylindrical shells under mechanical and thermal loads of the well-known references that are treated by other theories are reconsidered for comparison purposes and the efficiency and accuracy of the presented formulations are proved.

Formulation

Strain-Displacement and Stress-Strain Expressions. As it will be explained later, the response of the cylindrical shell under a time-varying load is investigated to find the buckling point. Then, this approach requires that behavior of the shell slightly beyond the buckling point (post-buckling) be studied, too. For this reason, in this paper, a general formulation based on considering the possibility of large-deflection occurrence is adopted.

The position vector of a point before deformation is given by

$$\mathbf{R}^{(0)} = \mathbf{R}^{(0)}(\alpha^1, \alpha^2, \alpha^3) \tag{1}$$

where $(\alpha_1, \alpha_2, \alpha_3)$ are the curvilinear coordinates of the point. After deformation, the point moves to a new position, the position vector to which is denoted by

$$\mathbf{R} = \mathbf{R}(\alpha^1, \alpha^2, \alpha^3). \tag{2}$$

If the covariant base vectors associated with the initial configuration and after deformation are denoted by $\mathbf{g}_\lambda$ and $\mathbf{G}_\lambda$, respectively, then we have

$$\mathbf{g}_\lambda = \mathbf{R}^{(0)}_{,\lambda} \quad \mathbf{G}_\lambda = \mathbf{R}_{,\lambda}. \tag{3}$$

Defining the displacement vector, $\mathbf{u}(\alpha^1, \alpha^2, \alpha^3)$ by

$$\mathbf{R} = \mathbf{R}^{(0)} + \mathbf{u}, \tag{4}$$

we have

$$\mathbf{G}_\lambda = \frac{\partial x^k}{\partial \bar{x}^\lambda}\,\mathbf{g}_k = (\delta^k_\lambda + u^k_{;\lambda})\mathbf{g}_k \tag{5}$$

where x and $\bar{x}$ are the coordinate systems corresponding to initial and final configurations, respectively, δ is the Kronecker symbol, and the symbol ";" stands for the covariant derivative. Since the initial dimensions are considered in calculations, Green's strain tensor for large deformations is used in its general form which can be written in curvilinear coordinates as (Washizu, 1982)

$$f_{ij} = \tfrac{1}{2}(G_{ij} - g_{ij}) \tag{6}$$

where g_{ij} and G_{ij} are the Euclidian metric tensors defined as

$$g_{ij} = \mathbf{g}_i \cdot \mathbf{g}_j \quad G_{ij} = \mathbf{G}_i \cdot \mathbf{G}_j. \tag{7}$$

Substituting Eq. (5) into Eq. (6), the following expressions of the strain in terms of the displacement components are obtained. After rearrangement,

$$f_{ij} = \tfrac{1}{2}(u_{i;j} + u_{j;i} + u_{\alpha;i}u^\alpha_{;j}). \tag{8}$$

The tensorial and physical components of the displacements and strains can be related through the following expressions (Flugge, 1972):

$$U_i = \sqrt{g^{ii}}\,u_i = \sqrt{g_{ii}}\,u^i$$

$$\epsilon_{ij} = \frac{f_{ij}}{\sqrt{g_{ii}}\,\sqrt{g_{jj}}} \tag{9}$$

where g^{ij} are the associated metric tensors. Expansion of Eq. (8) leads to the strain-displacement relations of a perfect circular cylindrical shell. These equations, after rearrangement and employing Eq. (9), are

$$\epsilon_{rr} = W_{,r} + \tfrac{1}{2}[(W_{,r})^2 + (V_{,r})^2 + (U_{,r})^2]$$

$$\epsilon_{\theta\theta} = \frac{1}{r}(V_{,\theta} + W) + \frac{1}{2r^2}[(V_{,\theta} + W)^2 + (W_{,\theta} - V)^2 + (U_{,\theta})^2]$$

$$\epsilon_{xx} = U_{,x} + \tfrac{1}{2}[(W_{,x})^2 + (V_{,x})^2 + (U_{,x})^2]$$

$$\epsilon_{r\theta} = \frac{1}{2r}[rV_{,r} + (W_{,\theta} - V)(W_{,r} + 1) + (V_{,\theta} + W)V_{,r} + U_{,r}U_{,\theta}]$$

$$\epsilon_{rx} = \tfrac{1}{2}[W_{,x}(1 + W_{,r}) + U_{,r} + V_{,r}V_{,x} + U_{,r}U_{,x}]$$

$$\epsilon_{x\theta} = \frac{1}{2}\left(V_{,x} + \frac{1}{r}U_{,\theta}\right) + \frac{1}{2r}[V_{,x}(V_{,\theta} + W) + U_{,\theta}U_{,x} + W_{,x}(W_{,\theta} - V)] \tag{10}$$

where U, V, and W are the displacement components in the axial, circumferential and radial directions, respectively. For an imperfect shell, some initial strains exist due to the initial deformations of the shell. These imperfections are practically in the radial direction (considering the presence of initial axial and circumferential imperfections does not alter the generality of the present discussion). So, the initial strains $\epsilon_{ij0} \equiv \epsilon_{ij0}(W_0)$, where W_0 is the

initial radial imperfection. Expressions of these strains can be obtained from Eq. (10) by substituting U, $V = 0$ and $W = W_0$. Thus, strains due to loading are derived by substracting the initial strains from the final strains:

$$\epsilon_{ij} = \tilde{\epsilon}_{ij} - \epsilon_{ij0}. \tag{11}$$

$\tilde{\epsilon}_{ij} \equiv \tilde{\epsilon}_{ij}(U, V, W + W_0)$ are the final strains. Therefore, referring to Eqs. (10) and (11), the strain-displacement relations for imperfect shells become

$$\epsilon_{rr} = W_{,r} + \tfrac{1}{2}[(W_{,r})^2 + 2W_{,r}W_{0,r} + (V_{,r})^2 + (U_{,r})^2]$$

$$\epsilon_{\theta\theta} = \frac{1}{r}(V_{,\theta} + W) + \frac{1}{2r^2}\{(V_{,\theta} + W + W_0)^2 + [(W + W_0)_{,\theta} - V]^2 + (U_{,\theta})^2 - W_0^2 - (W_{0,\theta})^2\}$$

$$\epsilon_{xx} = U_{,x} + \tfrac{1}{2}[(W_{,x})^2 + 2W_{,x}W_{0,x} + (V_{,x})^2 + (U_{,x})^2]$$

$$\epsilon_{r\theta} = \frac{1}{2}V_{,r} + \frac{1}{2r}[(W_{,\theta} - V)(W_{,r} + 1) - VW_{0,r} + W_{,r}W_{0,\theta} + W_{,\theta}W_{0,r} + (V_{,\theta} + W + W_0)V_{,r} + U_{,r}U_{,\theta}]$$

$$\epsilon_{rx} = \tfrac{1}{2}(W_{,x}(1 + W_{,r}) + W_{0,x}W_{,r} + W_{0,r}W_{,x} + U_{,r} + V_{,r}V_{,x} + U_{,r}U_{,x})$$

$$\epsilon_{x\theta} = \frac{1}{2}\left(V_{,x} + \frac{1}{r}U_{,\theta}\right) + \frac{1}{2r}[V_{,x}(V_{,\theta} + W + W_0) + U_{,\theta}U_{,x} + (W + W_0)_{,x}(W_{,\theta} - V) + W_{,x}W_{0,\theta}]. \tag{12}$$

The stress-strain relation of an orthotropic body in the orthotropy axes can be expressed as

$$\{\sigma^*\} = [Q]\{\epsilon_M^*\} \tag{13}$$

where $\{\sigma^*\}$ and $\{\epsilon_M^*\}$ are the stress components and mechanical strain components and $[Q]$ is the stiffness matrix. In the orthotropy axes

$$[Q] = [S]^{-1} \tag{14}$$

and

$$[S] = \begin{pmatrix} \frac{1}{E_1} & \frac{-\nu_{21}}{E_2} & \frac{-\nu_{31}}{E_3} & 0 & 0 & 0 \\ \frac{-\nu_{12}}{E_1} & \frac{1}{E_2} & \frac{-\nu_{32}}{E_3} & 0 & 0 & 0 \\ \frac{-\nu_{13}}{E_1} & \frac{-\nu_{23}}{E_2} & \frac{1}{E_3} & 0 & 0 & 0 \\ 0 & 0 & 0 & \frac{1}{2G_{12}} & 0 & 0 \\ 0 & 0 & 0 & 0 & \frac{1}{2G_{13}} & 0 \\ 0 & 0 & 0 & 0 & 0 & \frac{1}{2G_{23}} \end{pmatrix}. \tag{15}$$

Equations (13) to (15) are valid for all orthogonal coordinate systems, including the cylindrical coordinate system (Vinson and Sierakowski, 1987).

In the general case

$$\{\epsilon_M^*\} = \{\epsilon_{ij}^* - \alpha_{ij}^*\Delta T\} \tag{16}$$

and

$$\{\sigma^*\} = [Q]\{\epsilon_{ij}^* - \alpha_{ij}^*\Delta T\}. \tag{17}$$

In these equations, α_{ij}^* are the coefficients of the thermal expansion tensor in the orthotropy axes. Transformation of the stress and strain tensors from the orthotropy coordinate of the orthotropic shell to the geometrical coordinates yields the relation between the stress and strain components in these coordinates as

$$\{\epsilon\} = [\bar{T}]\{\epsilon^*\} \quad \{\sigma\} = [\bar{T}]\{\sigma^*\} \tag{18}$$

or, regarding Eqs. (13) to (18),

$$\{\sigma\} = [\bar{Q}]\{\epsilon_{ij} - \alpha_{ij}\Delta T\}, \tag{19}$$

where the transformed stiffness and coefficients of thermal expansion matrices in geometrical coordinates, $[\bar{Q}]$ and $\{\alpha_{ij}\}$, are

$$[\bar{Q}] = [\bar{T}][Q][T]^{-1}$$

$$\{\alpha\} = [\bar{T}]\{\alpha^*\}. \tag{20}$$

$[\bar{T}]$ is the transformation matrix which is defined as

$$[\bar{T}] = \begin{pmatrix} 0 & 0 & 1 & 0 & 0 & 0 \\ \sin^2\theta & \cos^2\theta & 0 & \sin 2\theta & 0 & 0 \\ \cos^2\theta & \sin^2\theta & 0 & -\sin 2\theta & 0 & 0 \\ 0 & 0 & 0 & 0 & \sin\theta & \cos\theta \\ 0 & 0 & 0 & 0 & \cos\theta & -\sin\theta \\ 0.5\sin 2\theta & -0.5\sin 2\theta & 0 & \cos 2\theta & 0 & 0 \end{pmatrix}, \tag{21}$$

where θ is the ply angle.

Since fiber orientation varies during the buckling, the stress and strain components correspond to the deformed shape of the element and must be incorporated in the constitutive Eq. (19). For this purpose, strain components of the cylindrical coordinates must be transformed using the following equation:

$$e_{ij}(\bar{x}) = f_{kl}\frac{\partial x^k}{\partial \bar{x}_i}\cdot\frac{\partial x^l}{\partial \bar{x}_j} = f_{kl}\cdot(\delta_i^k + u_{,i}^k)\cdot(\delta_j^l + u_{,j}^l). \tag{22}$$

Equations of Motion

Following the manner described in Washizu (1982), the equations of motion for large deflections are

$$(\sqrt{g}\,\boldsymbol{\tau}^k)_{,k} + \mathbf{P}\sqrt{g} = \rho\frac{d^2\mathbf{R}}{dt^2}. \tag{23}$$

$\mathbf{R}$ is the position vector and $\mathbf{P}$ is the body force vector defined per unit volume of the body before deformation and $g = |g_{ij}|$. The traction vector $\boldsymbol{\tau}$ can be resolved in the direction of the base and lattice vectors $\mathbf{g}_\mu$ and $(\mathbf{G}_\mu)$ to obtain the first and second Piola-Kirchhoff stress tensors $(\hat{\tau}^{k\mu})$ and $(\tau^{k\mu})$, respectively, as

$$\boldsymbol{\tau}^k = \tau^{k\mu}\mathbf{G}_\mu = \hat{\tau}^{k\mu}\mathbf{g}_\mu. \tag{24}$$

Then, from Eqs. (5) and (24) it is immediately concluded that

$$\hat{\tau}^{k\mu} = \tau^{ki}(\delta_i^\mu + u_{;i}^\mu). \tag{25}$$

The following expression holds in the curvilinear coordinates:

$$\mathbf{g}^k\cdot\mathbf{g}_\mu = \begin{Bmatrix} \lambda \\ \mu\nu \end{Bmatrix}\mathbf{g}_\lambda \tag{26}$$

where the notation $\{(\lambda/\mu\nu)\}$ is the Christoffel three-index symbol of the second kind. Therefore, Eq. (23) can be expressed in a scalar form by resolving it in the direction of the base vectors $\mathbf{g}_\lambda$, such as

$$[\sqrt{g}\,\hat{\tau}^{kj}]_{,j} + \sqrt{g}\,\hat{\tau}^{pj}\begin{Bmatrix} k \\ j\rho \end{Bmatrix} + \sqrt{g}\,P_g^k = \rho\frac{d^2R^k}{dt^2} \quad (k = 1, 2, 3) \tag{27}$$

or

$$[\sqrt{g}\,(\delta_i^k + u_{;i}^k)\tau^{ij}]_{,j} + \sqrt{g}\,(\delta_i^\rho + u_{;i}^\rho)\tau^{ij}\left\{ \begin{matrix} k \\ j\rho \end{matrix} \right\} + \sqrt{g}\,P_g^k = \rho \frac{d^2u^k}{dt^2} \quad (k = 1, 2, 3) \quad (28)$$

where the suffix g in P_g^k denotes that the components are taken in the direction of the base vectors. In the absence of body forces, Eq. (28) becomes

$$[\sqrt{g}\,(\delta_i^k + u_{;i}^k)\tau^{ij}]_{,j} + \sqrt{g}(\delta_i^\rho + u_{;i}^\rho)\tau^{ij}\left\{ \begin{matrix} k \\ j\rho \end{matrix} \right\} = \rho \frac{d^2u^k}{dt^2} \quad (k = 1, 2, 3) \quad (29)$$

and its counterpart in infinitesimal deformations is

$$\tau_{;j}^{ij} = \rho \frac{d^2u^i}{dt^2} \quad (i = 1, 2, 3). \quad (30)$$

The above equations can be written in terms of the physical components of the stress through using the following relation:

$$\sigma^{ij} = \tau^{ij} \cdot \sqrt{\frac{g_{jj}}{g^{ii}}}. \quad (31)$$

The boundary conditions are satisfied by means of the following equation:

$$\mathbf{F} = (\mathbf{g}_k \cdot \boldsymbol{\nu})\boldsymbol{\tau}^k \quad (32)$$

where $\mathbf{F}$ is the boundary traction vector and $\boldsymbol{\nu}$ is the unit normal vector on the boundary surface before deformation,

$$\boldsymbol{\nu} = \nu_k \mathbf{g}^k. \quad (33)$$

It can be noted that resolution of $\mathbf{F}$ in the directions of the base vectors reads

$$\mathbf{F} = \tau^{k\mu}\nu_k(\delta_\mu^\lambda + u_{;\mu}^\lambda)\mathbf{g}_\lambda. \quad (34)$$

Numerical Solution and Buckling Criteria

Since in the resulting equations of motion the stress terms and their derivatives are coupled and are nonlinear functions of the displacement components, they are highly nonlinear equations of displacements. Nonlinear problems of mechanics are often solved by adopting an incremental formulation. By the incremental solution procedure, the real time-variant system is approximated in a step-by-step way assuming time-invariance within each time step.

Equation (28), in terms of the physical components, can be rewritten in the following form:

$$f_1(\sigma_{ij}) = \ddot{W}$$
$$f_2(\sigma_{ij}) = \ddot{V}$$
$$f_3(\sigma_{ij}) = \ddot{U} \quad (35)$$

so that the following perturbed equations hold for the time interval Δt (Eslami and Shariyat, 1998a, b; Shariyat et al., 1996):

$$f_1(\tilde{\sigma}^{ij}) = \Delta\ddot{W}$$
$$f_2(\tilde{\sigma}^{ij}) = \Delta\ddot{V}$$
$$f_3(\tilde{\sigma}^{ij}) = \Delta\ddot{U} \quad (36)$$

in which the incremented terms are demonstrated by a tilde symbol. The displacements have to satisfy the initial conditions, for ($x = 0, L$ and $\theta = 0, 2\pi$), during each time step,

$$\Delta u = 0 \quad \Delta v = 0 \quad \Delta w = 0$$
$$\Delta\dot{u} = \dot{u} \quad \Delta\dot{v} = \dot{v} \quad \Delta\dot{w} = \dot{w}, \quad (37)$$

furthermore, the continuity of (σ_r, $\sigma_{r\theta}$, and σ_{rx}) and (ϵ_x, ϵ_θ, and ϵ_{0x}) must be considered in the numerical solution.

The numerical solution procedure is accomplished through the following steps:

1 The numerical solution begins with discretizing the cylindrical shell into $m \times n \times k$ grid points in the axial, circumferential and radial directions, respectively.

2 The initial deviations of the shell at the grid points are defined and the initial values of the displacement components (u, v, w) are set to zero.

3 Time is incremented.

4 Corresponding increments of the mechanical and thermal loads are found.

5 According to the temperature distribution described in the previous step, the mechanical properties in geometrical coordinates of the shell are related through Eqs. (20) and (21) to those in the orthotropy directions of the materials. In this way, the dependency of E_1, E_2, ν_{12}, and α_{ij}^* coefficients on temperature can be expressed as prescribed functions.

6 Derivative terms of u, v, and w, with respect to the spatial coordinates that appeared in Eq. (12), are approximated by a second-order finite difference method (the central difference method) and the strain components along the geometrical coordinates are computed in each grid point.

7 The tensorial strain components are computed from their physical components calculated at the previous step by means of Eq. (9) and are related to those of the lattice coordinates through Eq. (22). The physical components of the latter strains are computed from Eq. (9) by substituting g_{ij} by G_{ij}.

8 Based on the constitutive Eq. (19) the physical components of the second Piola-Kirchhoff stress tensor and, therefore, the corresponding tensorial components at each grid point are calculated.

9 Derivatives of the stress terms of Eq. (28) are approximated by a second-order finite difference method and derivatives involving multiplications of the radial distance of the points in the stresses are substituted by a fourth-order finite difference approximation.

While kinematic and stress boundary conditions may be directly incorporated in the formulations, force and moment boundary conditions are satisfied through relating axial or circumferential stresses of the grid points of the longitudinal edges by means of a numerical integrating method, such as Simpson's method. Thus, in contrast to the governing equations between the force/moment and displacement of the grid points, stresses at the longitudinal edges are related through linear equations to the applied loads. Therefore, even the force/moment boundary conditions are incorporated in a numerically exact procedure.

10 In the process of solution, time-invariance for terms appeared in the first sides of Eq. (36) is assumed during each time step. Thus, a set of second-order differential equations are derived that can be solved by employing the fourth-order Runge-Kutta method subjected to the initial (Eq. (37)) and boundary conditions. To improve the convergence of the proposed procedure, it is advisable to complete steps 6 to 10 for each individual point, before proceeding to the remaining points instead of considering all the points simultaneously.

11 When all equations in each iterative step of the current time interval are solved, the maximum value of the lateral displacements (w_{max}) is determined.

12 In each grid point, the displacement increments (Δu, Δv, and Δw) are added to displacement components obtained at the end of the previous time interval. To improve the results, solution is continued by using more iterations starting from step 6, until difference of the successive values of w_{max} of the same time interval becomes negligible.

13 The corrected values of u, v, w, $\dot{u}$, $\dot{v}$, and $\dot{w}$ obtained in

this manner are considered as initial values for the next time interval.

14 Beginning from step 4, results corresponding to the next time increments are obtained.

15 Possibility of dynamic buckling occurrence is checked. For this purpose, variations of w_{max} versus time or versus applied load (external pressure, axial load, temperature gradient, etc.) are plotted.

16 In the case of no buckling point occurrence, amplitude of the applied loads are increased and calculations are continued starting from step 2.

Buckling load can be determined using one of the two equivalent stability criteria stated below:

1 The generalized concept of dynamic buckling proposed by Budiansky (1974). This concept is associated with dynamic buckling of a structure where small changes in the magnitude of loading lead to large changes in the structure response. According to this criterion, abrupt reduction in slope of the maximum lateral displacement versus load curve (minimum slope) indicates a dynamic buckling state.

2 Large increase of the displacements amplitude with time. Qualitatively, if the time histories of the maximum lateral deformation or other modes of deformation are given for several amplitudes of the applied load, the critical buckling load can simply be defined as the load at which large increase in the amplitude of the deformations is seen to occur (Saigal et al., 1987).

Calculations and Results

Results are presented for pure mechanical or pure thermal loads and the interaction between these loads is not considered here. Dynamic behavior of the shells, except where mentioned, is investigated under step loads. To ensure incorporation of the higher buckling modes effect, the mesh is chosen sufficiently fine and time interval is adopted small enough. Therefore, the improvement in the results due to increasing the mesh density or decreasing time step is negligibly small. For this purpose, in the following results, a mesh composed of approximately 150,000 three-dimensional grid points is chosen. To avoid round-off errors, the calculations are carried out in the double-precision mode. For example, the improvement noticed in the displacement component values by increasing this number of grid points to 200,000 in the first example, is of the order of 10^{-12}. To reduce influence of the solution procedure on the accuracy of the final results, fourth-order approximations with respect to both spatial variables and time is employed, and integrating time interval of the order of 10^{-6} is adopted.

Buckling Under Mechanical Loads. As a first example, static buckling results of the present accurate three-dimensional elasticity formulation are compared with those of the latest three-dimensional analysis proposed by Kardomateas and Philobos (1995a) and the modified Donnell's equations. Formulations of the above reference are suitable for static buckling of thick perfect single-layer circular cylindrical shells under mechanical loads and are based on infinitesimal strains assumption (linear strain-displacement expressions).

Furthermore, in deriving the final results, one of the triple Fourier series is chosen (which means separation of variables in all coordinate directions and neglecting the coupling of the buckling modes which usually occurs), boundary conditions are satisfied in average and the results are obtained using a finite difference method. Therefore, the results are less accurate than the layer-wise theories, especially that proposed previously by the authors (Eslami and Shariyat, 1998) which assumes independency of the variables in the radial direction only. None of the above simplifications are made in the present analysis.

For comparison purposes, boron/epoxy cylindrical shells are considered for two fiber orientations: circumferential reinforcement ($E_2 > E_1, E_3$) and axial reinforcement ($E_3 > E_1, E_2$). The geometric and mechanical properties of the shells (for the axial reinforcement case) are

$$E_1 = E_2 = 18.6159 \text{ (GPa)} \quad E_3 = 206.844 \text{ (GPa)}$$

$$G_{12} = 2.55107 \text{ (GPa)} \quad G_{13} = G_{23} = 4.48162 \text{ (GPa)}$$

$$\nu_{21} = 0.45 \quad \nu_{31} = \nu_{32} = 0.3$$

$$b = 1 \text{ (m)} \quad l/b = 5$$

where b is the external radius of the shells.

The critical loads are defined by normalizing the external pressure and the axial load ($\bar{p}$ and $\bar{P}$) as

$$\bar{p} = \frac{pb^3}{E_2 h^3} \quad \bar{P} = \frac{P \cdot b}{\pi E_3 h(b^2 - a^2)} \tag{38}$$

where a is the internal radius of the shell and the load interaction parameter, S, is defined as

$$\frac{P}{2\pi} = S \cdot p \cdot b^2. \tag{39}$$

Table 1 Comparison of various theories results for cylindrical shells under combined external pressure and axial load. For each case, the first row gives ($\bar{p}$) and the second row gives ($\bar{P}$).

b/a	Donnell	P3D	Present, Static	Present, Dynamic
Load interaction parameter, $S = 1$				
1.03	.4134	.3899	.3927	.3142
	.1880	.1773	.1788	.1432
1.05	.3090	.2834	.2905	.2334
	.2319	.2127	.2180	.1752
1.1	.2793	.2352	.2569	.2046
	.4092	.3446	.3765	.2998
1.15	.2880	.2140	.2346	.1846
	.6183	.4593	.4869	.3872
Load interaction parameter, $S = 5$				
1.03	.2845	.2511	.2617	.2083
	.6467	.5708	.5949	.4739
1.05	.2137	.1826	.1945	.1546
	.8019	.6852	.7297	.5817
1.1	.1519	.1125	.1321	.1046
	1.1125	.8245	.9367	.7478
1.15	.1092	.0754	.0906	.0715
	1.1719	.8089	.9611	.7628

Table 1 shows the static critical loads as predicted by the modified Donnell's equations, preliminary three-dimensional theory approach of Kardomateas and Philobos (1995a) as well as the results of the present accurate approach for static and dynamic buckling (step loading). Results of the preliminary three-dimensional analysis is denoted by (P3D).

Table 2 gives a comparison of the predicted critical loads for a very long shell, under external pressure based on static buckling results of a first-order shear-deformation shell theory (Simitses et al., 1993) (FOSD), a higher-order shear-deformation equivalent-layer theory (Simitses et al., 1993) (HOSD), the preliminary three-dimensional theory approach (Kardomateas and Philobos, 1995a), the general layer-wise theory of the authors (Eslami and Shariyat, 1998) (GLW), and the static and dynamic buckling analysis of the present theory. The critical pressures are normalized with respect to the classical theory (Donnell's shell theory) results.

In the next example, buckling of a four-ply laminated imperfect cylindrical shell under uniform axial compression of Shienman et al. (1983) and Liaw and Yang (1990) is reexamined. The cylinder is considered to be simply supported with radius $R = 19.0$ (cm)

Table 2 Comparison of various theories results for cylindrical shells under external pressure

Geometry	FOSD	HOSD	P3D	GLW	Present, Static	Present, Dynamic
Circumferential reinforcement						
h = 6.35 (mm), h/R = 0.03, L/R = 100	0.9668	0.9637	0.9694	0.9608	0.9613	.7698
h = 12.7 (mm), h/R = 0.07, L/R = 100	0.9050	0.8933	0.9148	0.8892	0.894	.7352
Axial reinforcement						
h = 6.35 (mm), h/R = 0.03, L/R = 100	0.9822	0.9822	0.9817	0.9816	0.9812	.7792
h = 12.7 (mm), h/R = 0.07, L/R = 100	0.9588	0.9556	0.9605	0.9528	0.9534	.7589

and $L/R = 2$. Thickness of each layer is .0135 (cm) and the laminate construction is [0°/30°/60°/90°]. The material of each lamina is assumed as boron/epoxy, AVCO 550 with the following properties:

$$E_x = 207 \text{ (GPa)}, \quad E_\theta = E_x = 18.6 \text{ (GPa)}$$
$$G_{\theta x} = 4.48 \text{ (GPa)} \quad \nu_{x\theta} = \nu_{xz} = \nu_{z\theta} = .21.$$

The initial geometric imperfections of the shell are defined as

$$w_0(x, \theta) = W_0 h \cdot \sin\left(\frac{\pi_x}{L}\right) \cdot \cos(8\theta) \tag{40}$$

where W_0 is the amplitude of imperfection and h is the total thickness of the shell.

Results of static and dynamic buckling analysis performed by Shienman et al. (1983) and Liaw and Yang (1990) as well as the present results are illustrated in Fig. 1. In the earlier results, an equivalent layer approach is adopted and Von Karman-type expressions of strains are chosen. Results of Shienman et al. (1983) are based on Hoff-Simitses criterion (the total potential energy approach) that is explained in detail in Simitses (1990), so that the static and dynamic loads for $W_0 = 0$ are identical. In Liaw and Yang (1990), Love-Kirchhoff assumptions are employed and the nonlinear equations of motion are linearized and solved using an incremental method previously described in Saigal et al. (1987). As seen from this figure, the reduction in buckling loads is diminished as imperfection amplitude increases. In other words, imperfection sensitivity is more noticeable in small-imperfection amplitudes. In comparison with the other results, the present formulation gives smaller critical loads. This is due to incorporation of the exact strain-displacement relations of the imperfect shell in the exact nonlinear three-dimensional elasticity analysis presented here.

In Fig. 2, comparison among the predictions of the more accurate approaches, recently proposed by the authors, namely, a higher-order shear deformation equivalent-layer theory (HOSDEL) (Eslami and Shariyat, 1998a), a general layer-wise theory (GLW) (Eslami and Shariyat, 1998b) and the present approach is presented. As it may be noticed from this figure, the present results are more conservative.

Figure 3 reveals the effect of various impulsive loads (rectangular, triangular, and parabolic impulsive loads) and their time duration on the predicted critical loads. For this purpose, the following nondimensional time is used:

$$t^* = \frac{\bar{\tau}}{\bar{\tau}_0} \tag{41}$$

where $\bar{\tau}$ is the pulse duration and $\bar{\tau}_0$ is the free-vibration period of the shell. In Fig. 3, P_{cr} is the static buckling load. These results indicate that shell stiffness increases for the short duration of loading (especially if the pulse duration is comparable to the hoop breathing mode). For short time durations, the dynamic buckling loads are larger than the static buckling load. It is believed that this phenomenon is due to the inertia wave re-vibration between the

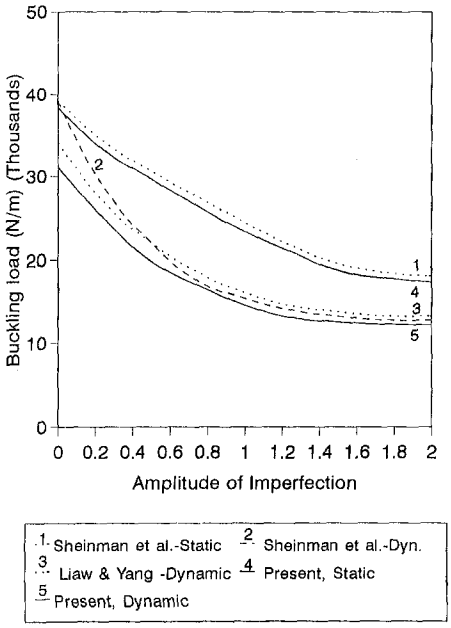

Fig. 1 Effect of imperfection amplitude on the dynamic buckling load

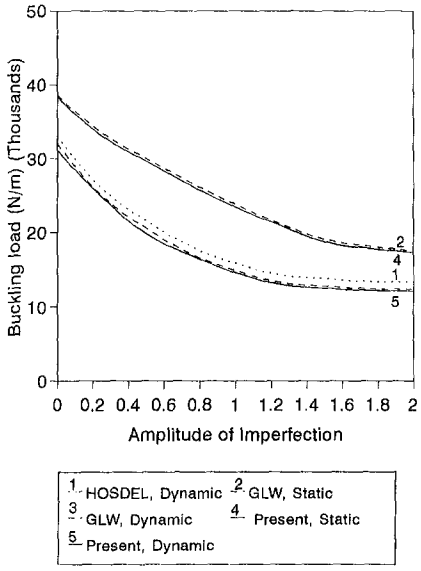

Fig. 2 Comparison of the results of the higher-order shear-deformation equivalent-layer theory, general layer-wise theory, and the present three-dimensional theory of approach

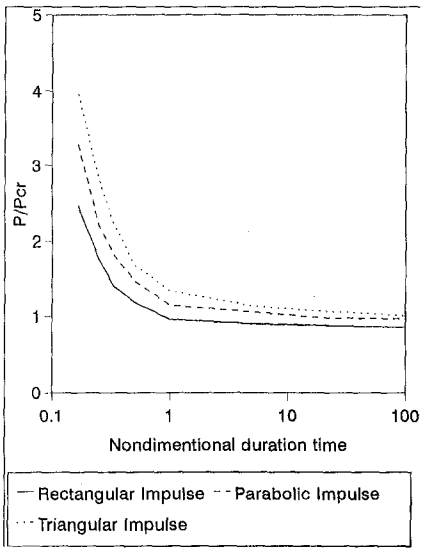

Fig. 3 Effect of different types of impulsive loads and various loading durations on the buckling load of the cylindrical shell

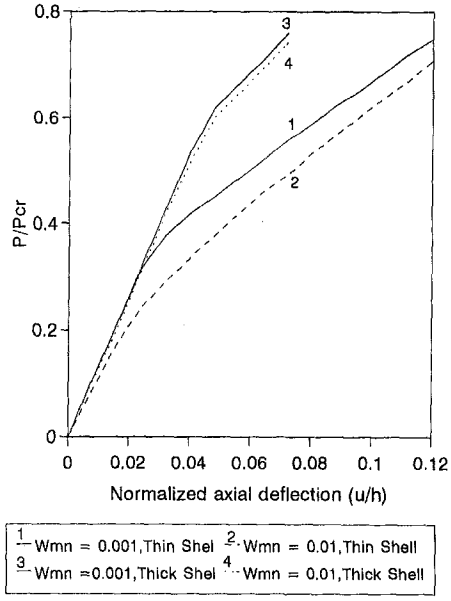

Fig. 4 Comparison of the static post-buckling analysis results of the thin shells. The illustrated results correspond to the internal surface at (x = 1).

impacted and fixed ends of the shell (Lindberg, 1987, 1989; Zimcik and Tennyson, 1980; Ganapathi and Varadan, 1995). For a given amplitude, the step load has a maximum curve area. Thus, as it may be expected, this type of loading has the worst influence on the strength of the shell. The critical loads corresponding to the triangular impulsive loads is the largest.

In order to investigate the large deflection behavior of imperfect multilayered cylindrical shells, a post-buckling analysis is carried out for three-layered cross-ply (0°90°0°) shells with the following properties:

$$E_1 = 209.5 \text{ (GPa)} \quad E_2 = E_3 = 7 \text{ (GPa)}$$

$$G_{12} = G_{13} = 3.5 \text{ (GPa)} \quad G_{23} = 1.4 \text{ (GPa)}$$

$$\nu_{12} = \nu_{13} = \nu_{23} = 0.3$$

$$h_i = h/3 \quad R = 914 \text{ (mm)} \quad L = 2540 \text{ (mm)}.$$

Two sets are considered: thin shells with total thickness of h = 2.54 (mm) and moderately thick shells with h = 25.4 (mm). The initial imperfection is assumed to have the form

$$w_0 = \sum_{m=1}^{M} \sum_{n=0}^{N} W_0^{mn} \sin\left(\frac{m\pi x}{L}\right) \cos(n\theta) \tag{42}$$

where m and n are the numbers of axial and circumferential half-waves, respectively.

Static axial load versus axial deflection curves of the thin and thick shells are shown simultaneously in Fig. 4 for two different amplitude imperfections. As stated before, points where abrupt change in displacement modes (such as axial deflection) due to small increase in the applied loads is noticed, and indicate buckling occurrence. In Fig. 4, the axial load is normalized with respect to the classical static buckling loads. The deformed shape and buckling modes of the thin and thick shells are illustrated in Figs. 5 and 6, respectively. It may be easily seen that the imperfection sensitivity is higher for thinner shells. Comparison of Figs. 5 and 6 reveals that in thick cylindrical shells, in contrast to thin shells, lower buckling modes are dominant, so that very thick shells buckle in an axisymmetric manner. In Fig. 7 the dynamic post-buckling response of the aforementioned cylindrical shells is compared with the static response.

Thermal Buckling. Numerical results for materially orthotropic clamped cylindrical shells of Radhamohan and Venkataramana (1975) are reexamined. Though the material properties are functions of temperature, as a first approximation, the assumed properties are representative in the temperature range under consideration. These properties are

$$E_1 = 13.17 \text{ (GN/m}^2\text{)} \quad E_2 = E_3 = 34.61 \text{ (GN/m}^2\text{)}$$

$$G_{12} = G_{13} = G_{23} = 5.17 \text{ (GN/m}^2\text{)} \quad \nu_{12} = \nu_{13} = \nu_{23} = 0.25.$$

The shell is subjected to uniform temperature rise throughout. Results of static thermal buckling of Radhamohan and Venkataramana (1975), which are based on the parametric differentiation

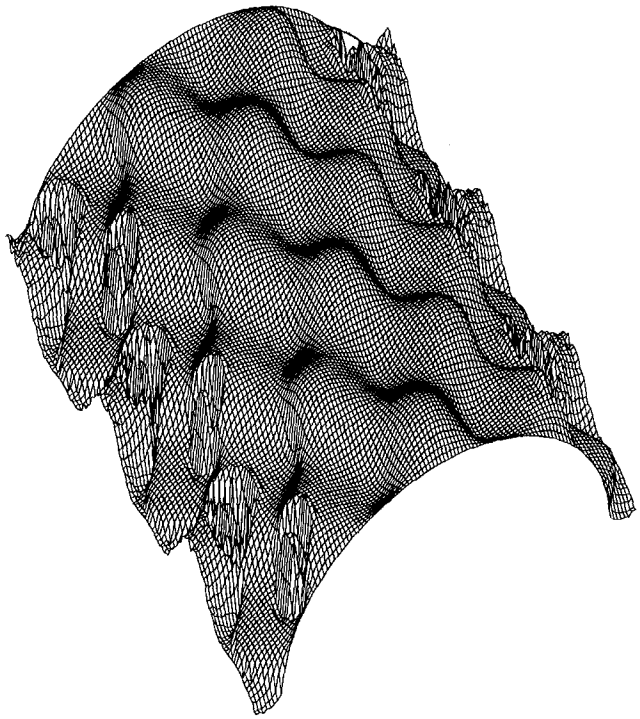

Fig. 5 Buckling modes of a thin laminated cylindrical shell

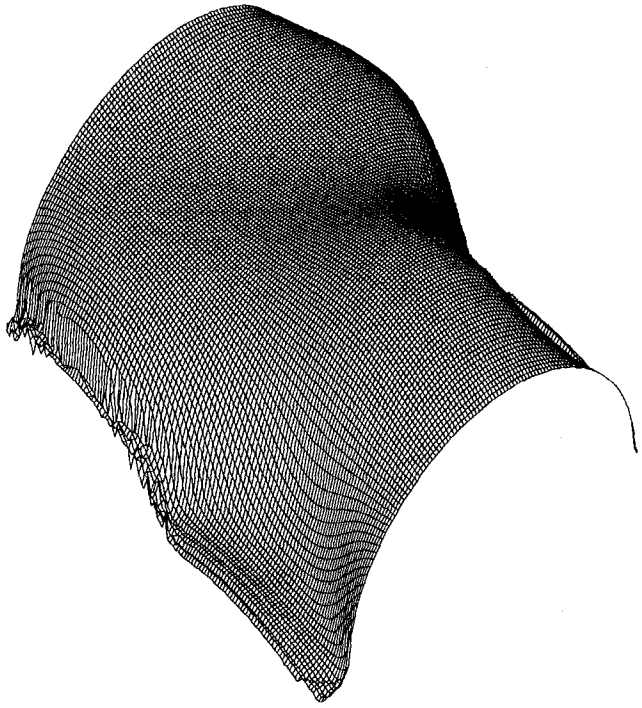

Fig. 6 Buckling modes of a thick laminated cylindrical shell

technique (with temperature as a parameter), is depicted along with the static and dynamic thermal buckling of the present formulation in Fig. 8. In this figure, the thermal buckling parameter $\alpha_2 T_{cr}$ chosen in Radhamohan and Venkataramana (1975) is shown for various curvature parameters $Z = l^2/\{\text{R.h.}\sqrt{1-\nu_1\nu_2}\}$. As it may be expected, the static results of the present study are lower.

As a second example, thermal buckling analysis of shells constructed from materials with the following mechanical and thermal properties are considered:

$$E_{11} = 1.5 \times 10^5 (\text{N/cm}^2) \quad E_{22} = E_{33} = 0.1\, E_{11}$$

$$G_{12} = G_{13} = G_{23} = 0.5\, E_{22} \quad \nu_{12} = \nu_{13} = \nu_{23} = 0.25$$

$$\alpha_1 = \alpha_2 = \alpha_3 = 10^{-6}\ (^\circ\text{C}^{-1}) \quad L^2/Rh = 400.$$

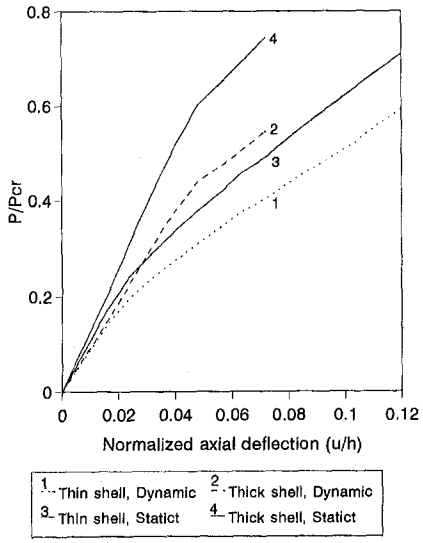

Fig. 7 A comparison between the dynamic and the static buckling results of the thin and the thick shells. The illustrated results correspond to the internal surface at (x = 1) and (W_{mn} = 0.01).

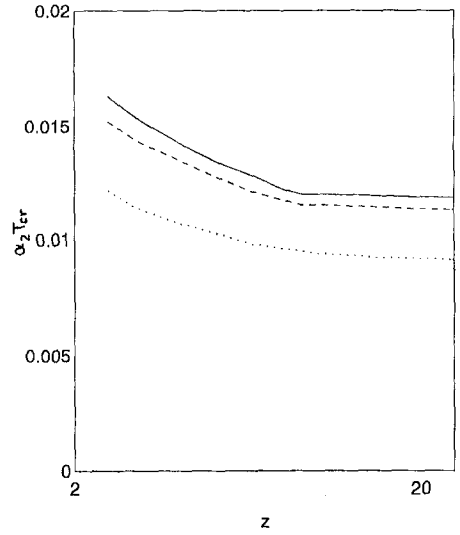

Fig. 8 Variation of critical temperature with curvature as predicted by the present approach and the conventional approaches. — Radhamohan and Venkataramana, (1975); —— present, static; · · · present, dynamic.

In Thangaratnam et al. (1990), static thermal buckling analysis of composite cylindrical shells with the above properties is accomplished through extending the linear Semiloof shell element formulated by Irons, which is based on the classical assumptions and infinitesimal strains. The results were obtained using one term of the double Fourier series. It is proved that a large number of modes are amplified during the buckling, so that this form of solution can cause notable errors. The shells are considered to undergo uniform temperature rise. The predicted static critical temperature (T_{cr}) proposed by Thangaratnam et al. (1990) for angle-ply cylindrical shells undergoing axisymmetric buckling modes, along with the results of the static and dynamic buckling analysis developed in the current paper, are illustrated in Fig. 9. For this purpose, two staking sequences ($[\phi/-\phi/\phi]$ and $[\phi/-\phi/\phi/-\phi/\phi]$) are used. As it can be seen, the critical temperature is considerably dependent on the inclination angle of the fibers (ϕ), which is measured from the cylinder cross section. Its maximum is attained in ϕ = 90 deg, where the least axial strength of the shell is obtained. Indeed, in the

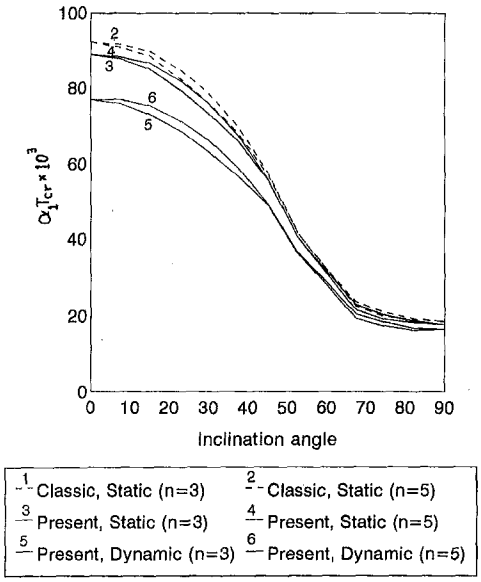

Fig. 9 Comparison of classical and present critical temperatures of symmetric angle-ply cylindrical shells

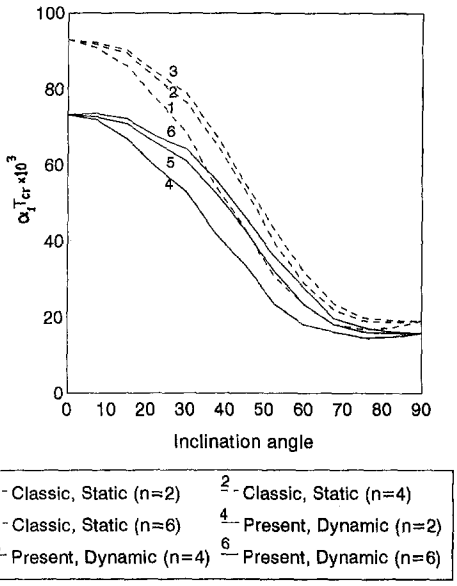

Fig. 10 Comparison of classical and present critical temperatures of antisymmetric angle-ply cylindrical shells

cylindrical shells, the predominant stress is the axial one and circumferential stress is developed mainly in the axial edges. It is shown (for example, in Liaw and Yang (1990) that in the case of mechanical buckling, the critical loads vary symmetrically about $\phi = 45$ deg. As is shown in Fig. 10, effect of the nonlinearity of the strain-displacement relations in critical thermal loads of the antisymmetric shells is larger. Thus, the differences between curves corresponding to these two approaches is larger in this case. In Fig. 10, staking sequences are taken to be $[\phi/-\phi]$, $[\phi/-\phi/\phi/-\phi]$ and $[\phi/-\phi/\phi/-\phi/\phi/-\phi]$. Figures 9 and 10 indicate that increasing number of the layers, while fixing the overall thickness of the shell, leads to a higher strength for the shell. This variation is more pronounced for the two-layer shell. This conclusion is in agreement with the report of Zimcik and Tennyson (1980) for mechanical buckling. Linear analysis done by Eslami et al. (1996) reveals that the critical buckling temperatures for isotropic materials are independent of modulus of elasticity and are inversely proportional to the coefficient of thermal expansion. Whereas in the nonlinear analysis introduced in this paper, all of the mechanical properties are coupled together. Hence, the critical load is a function of all of the mechanical and thermal properties of the materials.

Conclusion

The presented results indicate that as the orthotropy degree G_{ij}/E_1 increases, the discrepancy between results of the classical and the more accurate theories (the equivalent-layer high-order shear-deformation theory, layer-wise theory, and the present approach) increases. Antisymmetric staking sequences amplify this discrepancy.

Comparison of the above numerical examples verify that the predictions of the present approach are more conservative. Regarding the numerical computations, though the accuracy of the three-dimensional approach formulation is higher, convergency of the conventional equivalent single-layer and layer-wise theories, whose equations of motion can be considered as integral equations in term of stress components (in the radial direction), is higher. Thus, the relaxation techniques are recommended for three-dimensional elasticity approaches.

References

Argento, A., and Scott, R. A., 1993, "Dynamic Instability of Layered Anisotropic Circular Cylindrical Shells, Part I: Theoretical Development," *J. Sound and Vibration,* Vol. 162, No. 2, pp. 311–322.

Barbero, E. J., Reddy, J. N., and Teply, J. L., 1990, "General Two-Dimensional Theory of Laminated Cylindrical Shells," *AIAA J.,* Vol. 28, No. 3, pp. 544–553.

Budiansky, B., 1974, "Theory of Buckling and Postbuckling Behavior of Elastic Structures," *Advances in Applied Mechanics,* pp. 1–65.

Dennis, S. T., and Palazotto, A. N., 1989, "Transverse Shear Deformation in Orthotropic Cylindrical Pressure Vessels, Using a Higher-Order Shear Theory," *AIAA J.,* Vol. 27, No. 10, pp. 1441–1447.

Donnell, L. H., 1976, *Beams, Plates, and Shells,* McGraw-Hill, New York.

Eslami, M. R., and Shariyat, M., 1998a, "A High-Order Theory for Dynamic Buckling and Post-buckling Analysis of Imperfect Laminated Cylindrical Shells," ASME *Journal of Pressure Vessel Technology,* accepted for publication.

Eslami, R. R., and Shariyat, M., 1998b, "Layer-wise Theory for Dynamic Buckling and Postbuckling of Laminated Composite Cylindrical Shells," *AIAA J.,* Vol. 36, No. 9.

Eslami, M. R., Ziaii, A. R., and Ghorbanpour, A., 1996, "Thermoelastic Buckling of Thin Cylindrical Shells Based on Improved Stability Equations," *J. Thermal Stresses.*

Flugge, W., 1972, *Tensor Analysis and Continuum Mechanics,* Springer-Verlag, New York.

Ganapathi, M., and Varadan, T. K., 1995, "Dynamic Buckling of Laminated Anisotropic Spherical Caps," ASME JOURNAL OF APPLIED MECHANICS, Vol. 62, pp. 13–19.

Kardomateas, G. A., 1993a, "Buckling of Thick Orthotropic Cylindrical Shells Under External Pressure," ASME JOURNAL OF APPLIED MECHANICS, Vol. 60, pp. 195–202.

Kardomateas, G. A., 1993b, "Stability Loss in Thick Transversely Isotropic Cylindrical Shells Under Axial Compression," ASME JOURNAL OF APPLIED MECHANICS, Vol. 60, pp. 506–513.

Kardomateas, G. A., 1995, "Bifurcation of Equilibrium in Thick Orthotropic Cylindrical Shells Under Axial Compression," ASME JOURNAL OF APPLIED MECHANICS, Vol. 62, pp. 43–52.

Kardomateas, G. A., and Chung, C. B., 1994, "Buckling of Thick Orthotropic Cylindrical Shells Under External Pressure Based on Non-Planar Equilibrium Modes," *Int. J. Solids and Structures,* Vol. 31, No. 16, pp. 2195–2210.

Kardomateas, G. A., and Philobos, M. S., 1995, "Buckling of Thick Orthotropic Cylindrical Shells Under Combined External Pressure and Axial Compression, *AIAA J.,* Vol. 33, No. 10, pp. 1946–1953.

Kasagi, A., and Sridharan, S., 1995, "Imperfection Sensitivity Layered Composite Cylinders," *J. Engineering Mechanics,* Vol. 121, No. 7, pp. 810–818.

Liaw, D. G., and Yang, T. Y., 1990, "Symmetric and Asymmetric Dynamic Buckling of Laminated Thin Shells With the Effect of Imperfection and Damping," *J. Composite Materials,* Vol. 24, pp. 188–207.

Lindberg, H. E., 1987, "Dynamic Buckling of Cylindrical Shells From Oscillating Waves Following Axial Impact," *Int. J. Solids and Structures,* Part I, Vol. 23, No. 6, pp. 669–692.

Lindberg, H. E., 1991, "Dynamic Pulse Buckling of Imperfection Sensitive Shells," ASME JOURNAL OF APPLIED MECHANICS, Vol. 58, pp. 743–748.

Radhamohan, S. K., and Venkataramana, J., 1975, "Thermal Buckling of Orthotropic Cylindrical Shells," *AIAA J.,* Vol. 13, No. 3, pp. 397–399.

Reddy, J. N., and Liu, C. F., 1985, "A Higher-Order Shear Deformation Theory of Laminated Elastic Shells," *Int. J. Engineering Science,* Vol. 23, No. 3, pp. 319–330.

Reddy, J. N., and Savoia, M., 1992, "Layer-Wise Shell Theory for Postbuckling of Laminated Circular Cylindrical Shells," *AIAA J.,* Vol. 30, No. 8, pp. 2148–2154.

Robbins, J. R., and Reddy, J. N., 1993, "Modelling of Thick Composites Using a Layer-wise Laminate Theory," *Int. J. Numerical Methods in Engineering,* Vol. 36, pp. 655–677.

Saigal, S., Yang, T. Y., and Kapania, R. K., 1987, "Dynamic Buckling of Imperfection-Sensitive Shell Structures," *AIAA J.,* Vol. 24, No. 10, pp. 718–724.

Shariyat, M., Eslami, M. R., and Shakeri, M., 1996, "Elastic-Plastic Dynamic Buckling Analysis of Imperfect Cylindrical Shells," *J. Computer Structures,* submitted for publication.

Shienman, I., Shaw, I. D., and Simitses, G. J., 1983, "Nonlinear Analysis of Axially Loaded Laminated Cylindrical Shells," *J. Computer Structures,* Vol. 16, pp. 131–137.

Simitses, G. J., 1990, *Dynamic Stability of Suddenly Loaded Structures,* Springer-Verlag, Berlin.

Simitses, G. A., and Anastasiadis, J. S., 1992, "Shear Deformable Theories for Cylindrical Laminates: Equilibrium and Buckling With Applications," *AIAA J.,* Vol. 30, No. 3, pp. 826–834.

Simitses, G. J., Tabiei, A., and Anastasiadis, J. S., 1993, "Buckling of Moderately Thick, Laminated Cylindrical Shells Under Lateral Pressure," *J. Composite Engineering,* Vol. 3, No. 5, pp. 409–417.

Stein, M., 1986, "Nonlinear Theory for Plates and Shells Including the Effect of Transverse Bending," *AIAA J.,* Vol. 24, No. 9, pp. 1537–1544.

Thangaratnam, R. K., Palaninathan, R., and Ramachandran, J., 1990, "Thermal Buckling of Laminated Composite Shells," *AIAA J.,* Vol. 28, No. 5, pp. 859–860.

Thornton, E. A., 1993, "Thermal Buckling of Plates and Shells," ASME *Applied Mechanics Reviews,* Vol. 46, pp. 485–506.

Vinson, J. R., and Sierakowski, R. L., 1987, *The Behavior of Structures Composed of Composite Materials,* Martinus Nijhoff, Dordrecht, The Netherlands, Chapter 5.

Washizu, K., 1982, *Variational Methods in Elasticity and Plasticity,* Pergamon Press, New York.

Zimcik, D. G., and Tennyson, R. C., 1980, "Stability of Circular Cylindrical Shells Under Transient Axial Impulsive Loading," *AIAA J.,* Vol. 18, No. 6, pp. 691–699.

Zukas, J. A., 1974, "Effect of Transverse and Normal Shear Strains in Orthotropic Shells," *AIAA J.,* Vol. 12, No. 12, pp. 1753–1775.

Response of Finite Cracks in Orthotropic Materials due to Concentrated Impact Shear Loads

C. Rubio-Gonzalez
Research Assistant

J. J. Mason
Assistant Professor

Department of Aerospace and Mechanical Engineering, University of Notre Dame, Notre Dame, IN 46556

The elastodynamic response of an infinite orthotropic material with a finite crack under concentrated in-plane shear loads is examined. A solution for the stress intensity factor history around the crack tips is found. Laplace and Fourier transforms are employed to solve the equations of motion leading to a Fredholm integral equation on the Laplace transform domain. The dynamic stress intensity factor history can be computed by numerical Laplace transform inversion of the solution of the Fredholm equation. Numerical values of the dynamic stress intensity factor history for several example materials are obtained. The results differ from mode I in that there is heavy dependence upon the material constants. This solution can be used as a Green's function to solve dynamic problems involving finite cracks and in-plane shear loading.

1 Introduction

The use of composite materials is becoming more common in many engineering applications. The dynamic behavior of cracked bodies in such materials is a subject of many theoretical and experimental works. Both stationary and propagating cracks under dynamic loads in isotropic materials have been analyzed extensively (Freund, 1990; Parton and Boriskovsky, 1989; Chen and Sih, 1977). However, for orthotropic materials the available solutions are few (Kassir and Bandyopadhyay, 1983; Shindo and Nozaki, 1986; Rubio-Gonzalez and Mason, 1999), this is due in part to the mathematical complexity of such problems. Recently Rubio-Gonzalez and Mason (1999) presented the solution for a finite crack in orthotropic materials subjected to concentrated impact loads in mode I. Their solution was able to predict the singularities and discontinuities in the stress intensity factor history associated with the arrival of shear, dilatational, and Rayleigh stress waves at the crack tips. One conclusion of that work is that crack-face displacements due to the dilatational wave are small and have little effect on the results. Thus the ratio of the Rayleigh wave speed to the shear wave speed, c_R/c_s, determines most of the behavior of $K_I(t)$ including the time of the singularities and jumps in this function. However, as will be seen here, the behavior for in-plane shear loading is very different. The arrival of the dilatational wave at the crack tip causes a jump in $K_{II}(t)$ which is significant in the overall shape of the stress intensity factor history, especially for fiber-reinforced composites with fibers aligned with the plane of the crack.

Shear loading of cracks in composite systems is drawing the attention of investigators as an important factor in dynamic failure of composites and debonding of bimaterials. The theoretical analysis of Liu et al. (1995) predicts that the near-tip deformation field for transonic interfacial crack growth is predominantly of a shear nature. Experimental observations of Lambros and Rosakis (1995) and Shukla et al. (1998) support that prediction. Lambros and Rosakis (1995) were able to measure cracks propagating at 1.5 times the lower Rayleigh wave speed of the constituents in a bimaterial plate. More recent work by Rosakis and co-workers (1998) has demonstrated that shear loaded stationary cracks in unidirectional composites can accelerate to supersonic speeds, speeds above the Rayleigh wave speed for that material and orientation. Finally in quasi-static tests, shear-dominated loading can often lead to unstable crack growth (Shivakumar and Crews, 1998). Consequently, it seems that dynamic shear loading of cracks may be of primary importance in the impact failure of composites.

In the present work, the problem of an infinite orthotropic body with a finite crack subjected to suddenly applied shear line loads on its faces is examined. The crack lies on the principal axes of the material. The Green's function presented here, the solution related to the geometry shown schematically in Fig. 1, has not been reported to date although the quasi-static solution is presented by Isida (1972) as

$$K_I(t=\infty) = \frac{q}{\sqrt{\pi a}}\left(\sqrt{\frac{a+\chi_0}{a-\chi_0}} + \sqrt{\frac{a-\chi_0}{a+\chi_0}}\right) \tag{1}$$

where χ_o, q, and a are defined in the figure. The quasi-static solution for tangent opposite loads on a semi-infinite crack will be used as a normalization parameter in this study, however, and it is given by

$$K_0 = q\sqrt{\frac{2}{\pi(a-\chi_0)}}. \tag{2}$$

It is worth noting that, while the dynamic stress intensity factor for normal opposite line loads on a semi-infinite crack has been published for isotropic materials (Freund, 1974), it appears that the dynamic stress intensity factor for tangent opposite line loads in semi-infinite cracks is not available. However, a solution for tangent line loads pointing *in the same direction* on semi-infinite cracks is given by Abou-Sayed et al. (1980).

Integral transform methods are usually the techniques employed to solve problems involving cracked orthotropic bodies subjected to impact loads (Kassir and Bandyopadhyay, 1983; Shindo and Nozaki, 1986). This approach leads to a Fredholm integral equation on the Laplace transform domain, rather than a Weiner-Hopf equation (Freund, 1990) as is found for isotropic materials. The

Contributed by the Applied Mechanics Division of THE AMERICAN SOCIETY OF MECHANICAL ENGINEERS for publication in the ASME JOURNAL OF APPLIED MECHANICS.

Discussion on the paper should be addressed to the Technical Editor, Professor Lewis T. Wheeler, Department of Mechanical Engineering, University of Houston, Houston, TX 77204-4792, and will be accepted until four months after final publication of the paper itself in the ASME JOURNAL OF APPLIED MECHANICS.

Manuscript received by the ASME Applied Mechanics Division, June 18, 1998; final revision, Jan. 11, 1999. Associate Technical Editor: M. Ortiz.

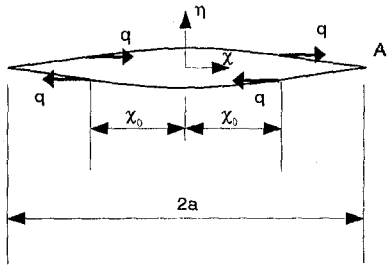

Fig. 1 Schematic of the finite crack geometry with concentrated shear loads

dynamic stress intensity factor on the time domain is recovered, in the most difficult step of the analysis, by numerical inversion of the solution of the Fredholm equation. This process can be numerically challenging and computationally intensive. Rubio-Gonzalez and Mason (1999) have shown that with the appropriate numerical methods to solve the Fredholm integral equation and to perform the Laplace inversion, excellent results may be found in the solution of dynamic crack problems by integral transform methods. In this work the method of Honig and Hirdes (1984) is used for the inversion of the Laplace transform.

2 Governing Equations

Consider the plane problem of an infinite orthotropic medium containing a finite crack (Fig. 1). Let E_i, μ_{ij}, and ν_{ij} $(i, j = 1, 2, 3)$ be the engineering elastic constants of the material where the indices 1, 2, and 3 correspond to the directions (χ, η, z) of a system of Cartesian coordinates chosen to coincide with the axes of material orthotropy. The crack plane is $\eta = 0$ and the origin of the $\chi\eta$-axes is the midpoint of the distance between the crack tips. The normalized coordinates $x = \chi/a$ and $y = \eta/a$ are introduced such that the crack tips are located at $x = \pm 1$ and the loads at $x = \pm x_0$. The normalized time t is introduced in the form $t = c_s\tau/a$ where $c_s = \sqrt{\mu_{12}/\rho}$ with ρ being the mass density. Concentrated shear forces of magnitude q are applied as shown.

The problem under consideration is restricted to two dimensions with wave propagation in the x–y plane only. By setting all the derivatives with respect to z to be zero, it is readily shown that the displacement equations of motion (Nayfeh, 1995) in the normalized coordinates reduce to

$$c_{11}\frac{\partial^2 u}{\partial x^2} + \frac{\partial^2 u}{\partial y^2} + (1 + c_{12})\frac{\partial^2 v}{\partial x \partial y} = \frac{\partial^2 u}{\partial t^2}, \tag{3}$$

$$\frac{\partial^2 v}{\partial x^2} + c_{22}\frac{\partial^2 v}{\partial y^2} + (1 + c_{12})\frac{\partial^2 u}{\partial x \partial y} = \frac{\partial^2 v}{\partial t^2}, \tag{4}$$

where u and v are the x and y components of the normalized displacement vector and c_{11}, c_{12}, and c_{22} are nondimensional parameters related to the elastic constants by the relations

$$c_{11} = \frac{E_1}{\mu_{12}[1 - (E_2/E_1)\nu_{12}^2]},$$

$$c_{22} = (E_2/E_1)c_{11}, \tag{5}$$

$$c_{12} = \nu_{12}c_{22} = \nu_{21}c_{11},$$

for generalized plane stress, and by

$$c_{11} = \frac{E_1}{\mu_{12}\Delta}(1 - \nu_{23}\nu_{32}),$$

$$c_{22} = \frac{E_2}{\mu_{12}\Delta}(1 - \nu_{13}\nu_{31}),$$

$$c_{12} = \frac{E_1}{\mu_{12}\Delta}\left(\nu_{21} + \frac{E_2}{E_1}\nu_{13}\nu_{32}\right),$$

$$\Delta = 1 - \nu_{12}\nu_{21} - \nu_{23}\nu_{32} - \nu_{31}\nu_{13} - \nu_{12}\nu_{23}\nu_{31} - \nu_{13}\nu_{21}\nu_{32}, \tag{6}$$

for plane strain. In the orthotropic solid, c_s represents the velocity of the in-plane shear wave propagating along the principal material axes. The stresses are related to the displacements by the equations

$$\frac{\sigma_x}{\mu_{12}} = c_{11}\frac{\partial u}{\partial x} + c_{12}\frac{\partial v}{\partial y},$$

$$\frac{\sigma_y}{\mu_{12}} = c_{12}\frac{\partial u}{\partial x} + c_{22}\frac{\partial v}{\partial y}, \tag{7}$$

$$\frac{\tau_{xy}}{\mu_{12}} = \frac{\partial u}{\partial y} + \frac{\partial v}{\partial x}.$$

The corresponding boundary conditions are

$$\sigma_y(x, 0, t) = 0 \quad \text{for} \quad |x| < \infty,$$

$$\tau_{xy}(x, 0, t) = -\tau(x)H(t) \quad \text{for} \quad |x| < 1, \tag{8}$$

$$u(x, 0, t) = 0 \quad \text{for} \quad |x| > 1,$$

in addition to the condition of zero displacements at infinity and zero initial conditions. The traction $\tau(x)$ is a known function of x and $H(t)$ is the Heaviside step function.

Equations (3), (4), and (8) constitute a mathematical statement of the problem. For the moment $\tau(x)$ represents a general load on the crack faces, later it will be substituted by a function representing the line loads.

3 Method of Solution

The method of solution of the governing equations presented here follows that of Kassir and Bandyopadhyay (1983) and Sneddon (1966). In Eqs. (3) and (4), the time variable may be removed by application of the Laplace transform

$$f^*(p) = \int_0^\infty f(t)e^{-pt}dt, \quad f(t) = \frac{1}{2\pi i}\int_{\mathrm{Br}} f^*(p)e^{pt}dt, \tag{9}$$

where Br denotes the Bromwich path of integration which is a line parallel to the imaginary axis in the p-plane. Applying relations (9) to Eqs. (3) and (4) and assuming zero initial conditions for the displacements and velocities, the transformed field equations become

$$c_{11}\frac{\partial^2 u^*}{\partial x^2} + \frac{\partial^2 u^*}{\partial y^2} + (1 + c_{12})\frac{\partial^2 v^*}{\partial x \partial y} - p^2 u^* = 0, \tag{10}$$

$$\frac{\partial^2 v^*}{\partial x^2} + c_{22}\frac{\partial^2 v^*}{\partial y^2} + (1 + c_{12})\frac{\partial^2 u^*}{\partial x \partial y} - p^2 v^* = 0, \tag{11}$$

where the transformed displacement components, u^* and v^*, are now functions of the variables x, y, and p. The application of the Laplace transform to the boundary conditions (8) gives

$$\sigma_y^*(x, 0, t) = 0 \quad \text{for} \quad |x| < \infty,$$

$$\tau_{xy}^*(x, 0, t) = -\tau(x)/p \quad \text{for} \quad 0 < |x| < 1, \tag{12}$$

$$u^*(x, 0, t) = 0 \quad \text{for} \quad |x| > 1.$$

To obtain a solution of the differential Eqs. (10) and (11) subject to conditions (12), we exploit the symmetry of the problem by letting

$$u^*(x, y, p) = \int_0^\infty A(s, y, p)\cos(sx)ds, \tag{13}$$

$$v^*(x, y, p) = -\int_0^\infty B(s, y, p) \sin(sx)ds, \quad (14)$$

where A and B are the Fourier cosine and sine transforms of the Laplace transform of the displacements, u^* and v^*, respectively, and are yet to be determined. Substituting these transforms into Eqs. (10) and (11), the functions A and B are found to satisfy the simultaneous ordinary differential equations

$$(c_{11}s^2 + p^2)A - \frac{d^2A}{dy^2} + (1 + c_{12})s\frac{dB}{dy} = 0, \quad (15)$$

$$(s^2 + p^2)B - c_{22}\frac{d^2B}{dy^2} - (1 + c_{12})s\frac{dA}{dy} = 0. \quad (16)$$

The solution of these equations which vanishes for $|y| \to \infty$ is

$$A(s, y, p) = A_1(s, p)e^{-\gamma_1 y} + A_2(s, p)e^{-\gamma_2 y},$$

$$B(s, y, p) = \frac{\alpha_1}{s}A_1(s, p)e^{-\gamma_1 y} + \frac{\alpha_2}{s}A_2(s, p)e^{-\gamma_2 y}, \quad (17)$$

where A_1 and A_2 are arbitrary functions and $\alpha_j(s, p)$ stands for the functions

$$\alpha_j(s, p) = \frac{c_{11}s^2 + p^2 - \gamma_j^2}{(1 + c_{12})\gamma_j}, \quad j = 1, 2 \quad (18)$$

with γ_1^2 and γ_2^2 being two distinct roots of the quadratic equation

$$c_{22}\gamma^4 + [(c_{12}^2 + 2c_{12} - c_{11}c_{22})s^2 - (1 + c_{22})p^2]\gamma^2 + (c_{11}s^2 + p^2)(s^2 + p^2) = 0. \quad (19)$$

It can be shown that for many materials the roots γ_1 and γ_2 are real and positive and the expressions for the displacements in the Laplace transform domain become

$$u^* = \int_0^\infty (A_1e^{-\gamma_1 y} + A_2e^{-\gamma_2 y}) \cos(sx)ds, \quad (20)$$

$$v^* = -\int_0^\infty (\alpha_1A_1e^{-\gamma_1 y} + \alpha_2A_2e^{-\gamma_2 y}) \frac{\sin(sx)}{s} ds, \quad (21)$$

and using (7) the corresponding expression for σ_y^* is given by

$$\sigma_y^* = -\mu_{12}\int_0^\infty [(c_{12}s^2 - \alpha_1\gamma_1c_{22})A_1e^{-\gamma_1 y} + (c_{12}s^2 - \alpha_2\gamma_2c_{22})A_2e^{-\gamma_2 y}] \frac{\sin(sx)}{s} ds. \quad (22)$$

Applying the first condition of (12) to Eq. (22) yields

$$A_2(s, p) = -\beta A_1(s, p),$$

$$\beta = \frac{c_{12}s^2 - c_{22}\alpha_1\gamma_1}{c_{12}s^2 - c_{22}\alpha_2\gamma_2}. \quad (23)$$

Therefore, the expressions for the transformed components of displacement become

$$u^*(x, y, p) = \int_0^\infty (e^{-\gamma_1 y} - \beta e^{-\gamma_2 y})A_1(s, p) \cos(sx)ds, \quad (24)$$

$$v^*(x, y, p) = -\int_0^\infty (\alpha_1e^{-\gamma_1 y} - \beta\alpha_2e^{-\gamma_2 y}) \frac{A_1(s, p)}{s} \sin(sx)ds, \quad (25)$$

and the associated stress components are given by

$$\sigma_x^* = -\mu_{12}\int_0^\infty [(c_{11}s^2 - \alpha_1\gamma_1c_{12})e^{-\gamma_1 y} - (c_{11}s^2 - \alpha_2\gamma_2c_{12})\beta e^{-\gamma_2 y}] \frac{A_1(s, p)}{s} \sin(sx)ds, \quad (26)$$

$$\sigma_y^* = -\mu_{12}\int_0^\infty (c_{12}s^2 - \alpha_1\gamma_1c_{22})(e^{-\gamma_1 y} - e^{-\gamma_2 y}) \times \frac{A_1(s, p)}{s} \sin(sx)ds, \quad (27)$$

$$\tau_{xy}^* = \mu_{12}\int_0^\infty [-(\alpha_1 + \gamma_1)e^{-\gamma_1 y} + \beta(\alpha_2 + \gamma_2)e^{-\gamma_2 y}] \times A_1(s, p) \cos(sx)ds. \quad (28)$$

Introducing the functions

$$S(s, p) = (1 - \beta)A_1(s, p), \quad (29)$$

$$G(s, p) = \frac{-(\alpha_1 + \gamma_1) + \beta(\alpha_2 + \gamma_2)}{s(1 - \beta)\eta}, \quad (30)$$

$$\eta = \frac{1}{c_{22}N_1N_2(1 + c_{12})(N_1 + N_2)} \times \{(c_{12}^2 + c_{12} - c_{11}c_{22})(c_{12}N_1N_2 - c_{11}) - c_{22}[c_{12}N_1^2N_2^2 + c_{11}(N_1^2 + N_1N_2 + N_2^2)]\}, \quad (31)$$

$$N_{1,2}^2 = \frac{1}{2c_{22}}\{c_{11}c_{22} - c_{12}^2 - 2c_{12} \pm [(c_{11}c_{22} - c_{12}^2 - 2c_{12})^2 - 4c_{11}c_{22}]^{1/2}\}, \quad (32)$$

and in view of the second and third boundary conditions in (12), Eqs. (24) and (28) yield the following pair of dual integral equations for the determination of the function $S(s, p)$:

$$\int_0^\infty sG(s, p)S(s, p) \cos(sx)ds = -\frac{\tau(x)}{\mu_{12}\eta p} \quad 0 < x < 1, \quad (33)$$

$$\int_0^\infty S(s, p) \cos(sx)ds = 0 \quad x > 1, \quad (34)$$

where $\tau(x)$ is the distributed load along the crack faces. The constant η in (30) has been chosen such that for large s, the function $G(s, p)$ becomes

$$G(s, p) = 1 + O(1/s).$$

Using $\cos(sx) = \sqrt{sx\pi/2}J_{-1/2}(sx)$ and defining $\bar{S}(s, p) = s^{1/2}S(s, p)$ and $r_1(s, p) = G(s, p) - 1$, these last equations can be written as

$$\int_0^\infty s[r_1(s, p) + 1]\bar{S}(s, p)J_{-1/2}(sx)ds = g(x) \quad 0 < x < 1,$$

$$\int_0^\infty \bar{S}(s, p) J_{-1/2}(sx) ds = 0 \quad x > 1,$$

where

$$g(x) = -\sqrt{\frac{2}{\pi x}} \frac{\tau(x)}{\mu_{12}\eta p}. \tag{35}$$

Following the procedure given by Sneddon (1966), the function $S(s, p)$ of the original integral Eqs. (34) and (33) can be found in terms of another unknown function, $\Theta(r, p)$, in the form

$$S(s, p) = -\frac{q}{\pi a \mu_{12}\eta p} \int_0^1 w^{1/2}\Theta(w, p) J_0(sw) dw \tag{36}$$

where $\Theta(r, p)$ satisfies the following Fredholm integral equation

$$\Theta(r, p) + \int_0^1 \Theta(u, p) K(r, u, p) du = H_2(r), \tag{37}$$

with symmetrical kernel

$$K(r, u, p) = (ru)^{1/2} \int_0^\infty w[G(w, p) - 1] J_0(rw) J_0(uw) dw, \tag{38}$$

and free term

$$H_2(r) = \frac{2a\sqrt{r}}{q} \int_0^r \frac{\tau(w)}{\sqrt{r^2 - w^2}} dw. \tag{39}$$

For the case of concentrated loads as illustrated in Fig. 1, we have $\tau(x) = (q/a)\delta(x - x_0)$ where the denominator appears due to the normalization of x, such that the free term becomes

$$H_2(r) = \begin{cases} \dfrac{2\sqrt{r}}{\sqrt{r^2 - x_0^2}} & \text{for} \quad x_0 < r \\ 0 & \text{for} \quad x_0 > r. \end{cases} \tag{40}$$

Note that the free term is discontinuous in r. Integrating $S(s, p)$ by parts in Eq. (36), gives

$$S(s, p) = -\frac{q}{\pi a \mu_{12}\eta p s} \left\{ \Theta(1, p) J_1(s) - \int_0^1 w J_1(sw) \frac{d}{dw}[w^{-1/2}\Theta(w, p)] dw \right\}. \tag{41}$$

From Eq. (28) we know that in the Laplace transform domain τ^*_{xy} is

$$\tau^*_{xy}(x, 0, p) = \mu_{12}\eta \int_0^\infty sG(s, p) S(s, p) \cos(sx) ds$$

and substituting (41) it is found that

$$\tau^*_{xy}(x, 0, p) = -\frac{q}{\pi a}\left[\frac{\Theta(1, p)}{p} \int_0^\infty G(s, p) J_1(s) \cos(sx) ds\right] - \frac{q}{\pi a p}\left\{\int_0^\infty G(s, p) \cos(sx) ds \times \int_0^1 w J_1(sw) \frac{d}{dw}[w^{-1/2}\Theta(w, p)] dw\right\}. \tag{42}$$

As stated by Kassir and Bandyopadhyay (1983), the stress intensity factor extracted from (42) is

$$K_{II}(t) = \frac{q}{\sqrt{\pi a}} \mathcal{L}^{-1}\left\{\frac{\Theta(1, p)}{p}\right\}, \tag{43}$$

where $\mathcal{L}^{-1}$ denotes the inverse of the Laplace transform.

4 Numerical Results

4.1 Quasi-static Solution. We can show that the dynamic formulation is consistent with the quasi-static solution; that is, we recover Eq. (1) exactly when $t \to \infty$. To do this we invoke the final value theorem for Laplace transforms (Debnath, 1995), which states that if $K_{II}(t)$ is given by (43), then

$$K_{II}(\infty) = \lim_{t\to\infty} K_{II}(t) = \lim_{p\to 0} \frac{q}{\sqrt{\pi a}} \Theta(1, p).$$

Noting that by construction $G(s, p) \to 1$ when $p \to 0$, therefore the kernel, Eq. (38), vanishes and Eq. (37) gives $\Theta(r, p) = H_2(r)$ for $p \to 0$, in particular $\Theta(1, p) = H_2(1)$, and hence

$$K_{II}(\infty) = \frac{q}{\sqrt{\pi a}} \frac{2a}{\sqrt{a^2 - \chi_0^2}},$$

which is exactly the expression (1). In the plots to follow, Figs. 2–5, it can be shown by careful numerical Laplace transform inversion that the results decay to the quasi-static solution as $t \to \infty$. For that reason interest is focused on the early time, transient response.

4.2 Transient Response. The Fredholm integral equation, (37), was solved numerically using the Nystrom method (Atkinson, 1997) to find $\Theta(r, p)$. The values of $\Theta(1, p)$ were then extracted. This method requires the application of an approximate quadrature rule to the Fredholm integral Eq. (37) and then the evaluation of the resulting equation at the quadrature points r_i to get

$$\Theta(r_i, p) + \sum_{j=1}^{N} w_j K(r_i, u_j, p)\Theta(u_i, p) = H_2(r_i), \tag{44}$$

where w_j are the weights of the quadrature rule, while the N points r_i are the abscissas. This is a set of N linear algebraic equations in N unknowns. For this problem $N = 200$ quadrature points were selected in order to get good accuracy and the trapezoidal quadrature rule was chosen because of the complex behavior of Θ and the discontinuous nature of the free term H_2.

Numerical inversion of the Laplace transform was performed using the method of Honig and Hirdes (1985) to find $K_{II}(t)$ according to Eq. (43). In this method the choice of the Bromwich path is made automatically using a straightforward convergence criterion.

The numerical results presented correspond to isotropic and orthotropic cases. Properties of transversely isotropic materials with fibers parallel and perpendicular to the x-axis are considered in the second case. The properties used are taken from Schwartz (1997) and are given in Table 1.

Figure 2 shows the stress intensity factor history for an isotropic material in plane stress with concentrated loads located at $x_o = 0.6$. Note that the isotropic material is a degenerate case of the governing Eqs. (3) and (4). For the isotropic material $c_{11} = c_{22} = 2/(1 - \nu)$ and $c_{12} = 2\nu/(1 - \nu)$. Hence $\gamma_1 = \gamma_2$ for $p = 0$ leading to $\beta = 1$ and $G(s, p)$ not defined. Consequently, the isotropic case presented here was obtained from the orthotropic formulation letting $E_1 = E$, $E_2 = (1 - \epsilon)E$, $\nu_{12} = \nu_{23} = \nu$ and $\mu_{12} = (E_1 + E_2)/(4(1 + \nu))$ where E and ν correspond to the isotropic properties and ϵ is a small quantity with $\epsilon \ll 1$. Note that the stress intensity factor is indeed discontinuous and that the

Table 1 Mechanical properties used for the analysis

	Graphite Epoxy	E-Glass Epoxy	Boron Epoxy	Isotropic material
E_1 (GPa)	156.75	45	207	200
E_2 (GPa)	10.41	12	19	199.8
ν_{12}	0.31	0.19	0.21	0.3
ν_{23}	0.49	0.19	0.21	0.3
μ_{12} (GPa)	7.07	5.5	6.4	76.92
ρ (Kg/m^3)	1580	2100	1990	7840

numerical inversion technique captures the discontinuity quite well. It is worth noting that the presence of the singularity of $K_{II}(t)$ when the Rayleigh wave arrives is also captured in the numerical results. The singularity in $K_{II}(t)$ at $t = 1.08$ (label R_1) is similar to that found in the surface displacements in the calculated solution of Lamb's problem, where a concentrated shear load is applied on a half-space (Chao, 1960).

The stress intensity factor is zero until the arrival at the tip $x = +1$ at the normalized time $t = 0.59$ (label P_1) of the dilatational wave originated by the load at $x = x_0$; at this time a jump in $K_{II}(t)$ is observed. Before this time, a slight increase that is a numerical artifact is seen. Obviously the dilatational wave has an important effect in the dynamic response unlike in mode I loading where that wave had a minimum effect in $K_I(t)$ (Rubio-Gonzalez and Mason, 1999). When the Rayleigh wave arrives, $K_{II}(t)$ experiences a singularity and a jump followed by a stable value given by Eq. (2). This cycle is repeated when a second dilatational wave arrives from the further point load at $t = 2.36$ (label P_2) but with decaying amplitude due to the increased distance between point load and crack tip.

The oscillations observed near the discontinuity in $K_{II}(t)$ are due to the convergence of the method employed to invert the Laplace transform. These oscillations are quite similar to Gibb's phenomenon as seen in the Fourier transform or Fourier series representation of a discontinuous function (Papoulis, 1962).

The results for $x_0 \neq 0.6$ are very similar. However, if x_0 is very close to 1, then numerical difficulties arise in the solution of the Fredholm equation. Due the discontinuity in the free term $H_2(r)$ in (40), the discrete representation $H_2(r_i)$ in Eq. (44) becomes a vector with mostly zero components as $x_0 \to 1^-$. Consequently, more quadrature points are needed.

Figure 3 shows the results for the orthotropic material in plane stress with concentrated shear loads also at $x_0 = 0.6$. Figure 3(a) corresponds to the case of fibers parallel to the x-axis while 3(b) to fibers parallel to the y-axis. Note a clear difference in the behavior, this is due to the fact that c_d has an important effect in $K_{II}(t)$, and in this case the difference is more noticeable since c_d is quite different in each case, see Table 2. Figure 3(b) is more similar to Fig. 2, i.e., two separated cycles are observed, corresponding to the arrival of waves generated by the load at $x = +x_0$ and then the waves generated by the load at $x = -x_0$. This happens because $x_0/c_R < (1 + x_0)/c_d$. That is the Rayleigh wave from $+x_0$ arrives before the dilatational wave from $-x_0$. However, in Fig. 3(a) where $x_0/c_R > (1 + x_0)/c_d$ the dilatational waves caused by both loads arrive at the tip $x = +1$ before any other wave, thus their effects are added and as a result $K_{II}(t)$ reaches the maximum

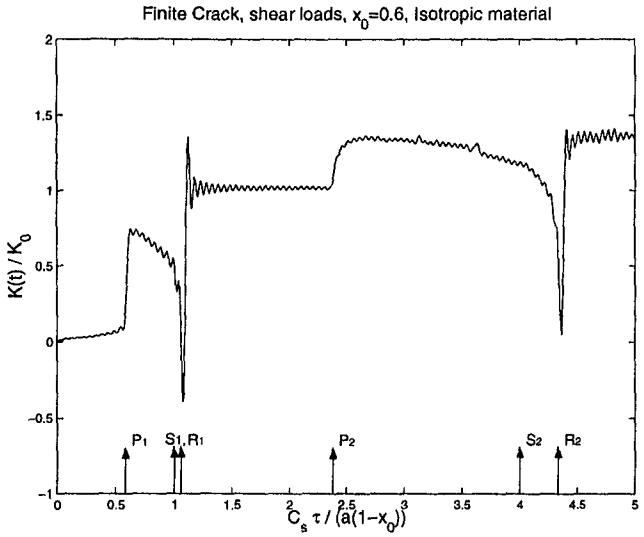

Fig. 2 Stress intensity factor history for a finite crack with concentrated shear loads in an isotropic material. The normalization factor is given by Eq. (2). The labels P_1, S_1, and R_1 correspond to the arrival at the crack tip $x = +1$ of the dilatational, shear, and Rayleigh waves at the crack tip $x = +1$ generated by the load at $x = +x_0$, respectively. Similarly, P_2, S_2, and R_2 correspond to the arrival of the dilatational, shear, and Rayleigh waves at the crack tip $x = +1$ as generated by the load at $x = -x_0$.

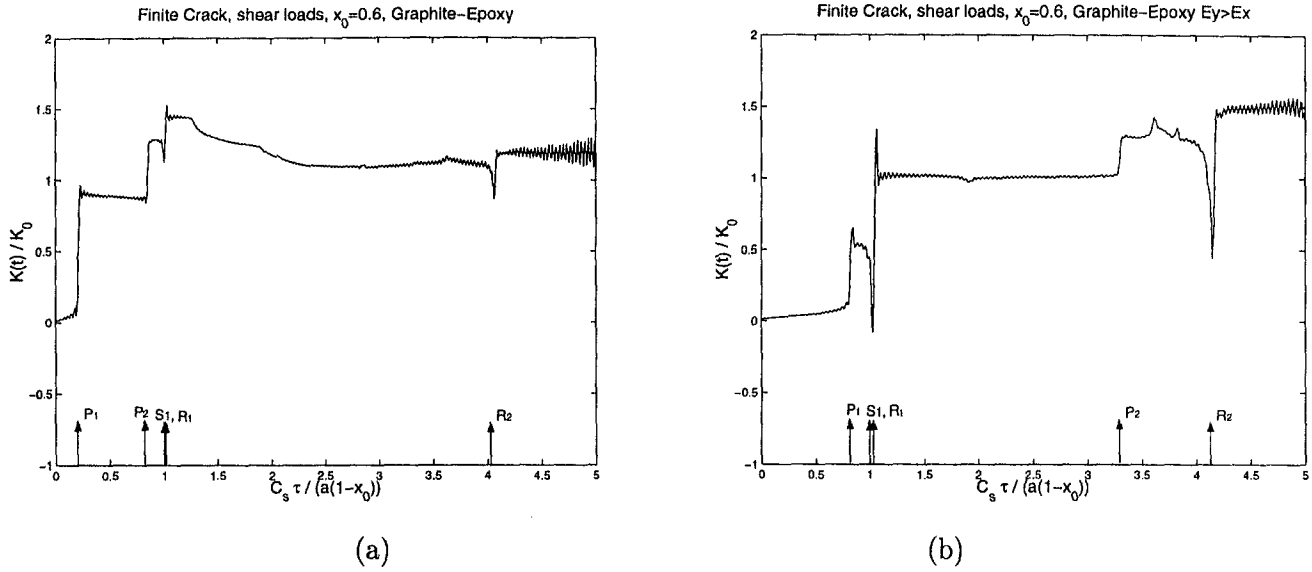

Fig. 3 Stress intensity factor history for a finite crack with concentrated shear loads in an orthotropic material. The normalization factor is given by Eq. (2). The material properties correspond to a graphite-epoxy composite with the fibers (*a*) parallel to the *x*-axis, and (*b*) fibers parallel to *y*-axis. Labels P_i, S_i, and R_i are defined in Fig. 2.

Table 2 Wave speeds for the different materials. The composite materials are considered with fibers and wave propagation parallel to x-axis, except in graphite-epoxy y where wave propagation is considered along the y-axis.

Velocity (m/s)	Graphite Epoxy x	Graphite Epoxy y	Boron Epoxy x	E Glass Epoxy x	Isotropic material
c_d	10086	2974	10251	4685	5860
$c_d^{pl-\sigma}$	9992	2574	10219	4651	5294
c_s	2115	2115	1793	1618	3132
$c_R^{pl-\sigma}$	2083	2037	1783	1572	2869

dynamic overshoot sooner. The three main jumps in Fig. 3(a) occur at $t = 0.21$ (arrival of the dilatational wave from $+x_0$, mark P_1), $t = 0.84$ (arrival of the dilatational wave from $-x_0$, mark P_2) and $t = 1.01$ (arrival of the Rayleigh wave from $+x_0$, mark R_1). Note that in Fig. 3(b) the numerical solution captures quite well the singularities and jumps when the Rayleigh waves arrive at $t = 1.03$ and $t = 4.15$, but for long times the solution shows rapid oscillations, this is due to the insufficient accuracy in the numerical Laplace inversion technique and can be remedied with more computational effort. Looking at Figs. 2 and 3(b) we note that the plateaus are independent of the elastic constants c_{11}, c_{12}, and c_{22} as expected from Eq. (2). A small error is observed in Figs. 2 and 3 since the stress intensity factor should be zero until the dilatational wave arrives, and these figures show a value slightly different from zero. This is due to the approximate numerical methods used to solve the Fredholm integral equation and to invert the Laplace transform.

Figures 4 and 5 show the stress intensity factor $K_{II}(t)$ for boron-epoxy and E glass-epoxy composites, respectively. In both cases the fibers are considered along the x-axis. For fibers along the y-axis the results are quite similar to Figs. 2 and 3(b); two similar cycles of discontinuity at the arrival of the dilatational wave and singularity at the arrival of the Rayleigh wave are observed. We note a similar behavior in Fig. 4 to that illustrated in 3(a) for the graphite-epoxy material. The difference is in the times when the jumps occur, that is, the times of the arrival of the dilatational waves, marks P_1 and P_2. For Fig. 3(a) the jumps occur at $t = 0.2$ and $t = 0.84$, while in Fig. 4 they occur at $t = 0.17$ and $t = 0.70$. For the E glass-epoxy composite, Fig. 5, even though the fibers are along the x-axis, we observe the two cycles

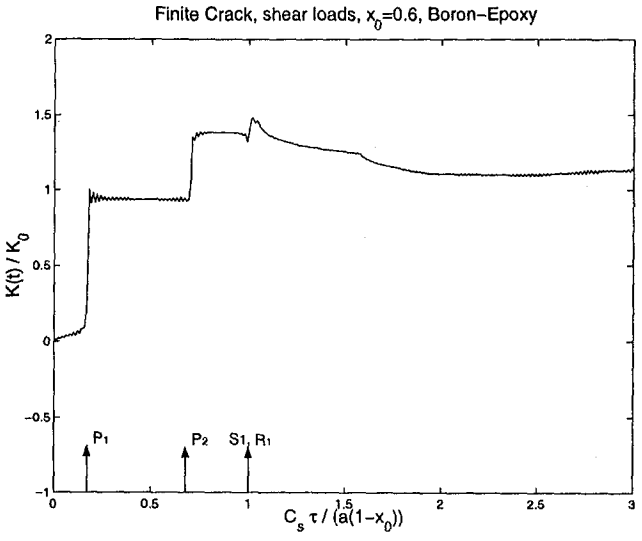

Fig. 4 Stress intensity factor history for a finite crack with concentrated shear loads in an orthotropic material. The normalization factor is given by Eq. (2). The material properties correspond to boron-epoxy composite with the fibers parallel to the x-axis. Labels P_i, S_i, and R_i are defined in Fig. 2.

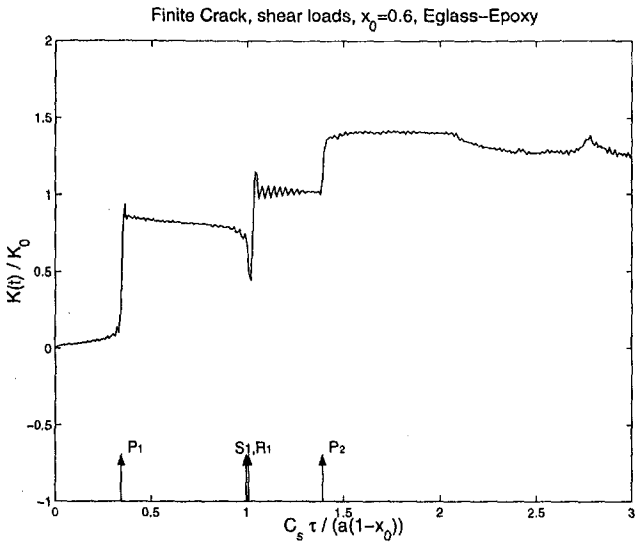

Fig. 5 Stress intensity factor history for a finite crack with concentrated shear loads in orthotropic material. The normalization factor is given by Eq. (2). The material properties correspond to E glass-epoxy composite with the fibers parallel to the x-axis. Labels P_i, S_i, and R_i are defined in Fig. 2.

typical of the case when the fibers are along the y-axis. This is due to the fact that for this material in this orientation $x_0/c_R < (1 + x_0)/c_d$. Clearly, there is a strong dependence of $K_{II}(t)$ on the elastic constants in these figures.

It should be noted that for wave propagation along the material principal axes wave pure modes are obtained (Nayfeh, 1995), i.e., the polarization vector is directed either along or normal to the propagation direction. Hence, we can distinguish dilatational and shear waves without ambiguity for this case of a crack lying on the principal axes of the material. Also, for some materials the singularity when the Rayleigh wave arrives is difficult to capture. This is because the singularity occurs at times between the arrival of the shear wave and the arrival of the Rayleigh wave. As $c_s/c_R \to 1$, the duration of this period approaches 0 making it hard to numerically capture the singularity. (See Figs. 3(a) and 4 where $c_s/c_R = 1.015$ and 1.006, respectively.)

The method outlined here can easily be applied to solve the problem of a finite crack with a single pair of impact concentrated shear loads (Fig. 6(a)). As illustrated in Fig. 6, this problem can be treated by a superposition of the two problems shown, that is, one with a symmetric (Fig. 6(b)) and the other with an antisymmetric (Fig. 6(c)) displacement field. The symmetric part is just the problem solved above with a load of magnitude $q/2$ instead of q. To solve the antisymmetric part we follow a similar procedure, the only difference would be the proposed displacement fields, Eqs. (13) and (14), it would require sine and cosine transforms instead of cosine and sine for u^* and v^*, respectively, due to the new symmetry. Application of Laplace and Fourier transforms leads to a reduction of the governing equations to a system of dual integral equation. The stress intensity factor in the Laplace domain is obtained for each problem, and then they are superimposed in this domain. Finally, the Laplace inversion is performed on the sum to obtain $K_{II}(t)$ for the original problem. This method of superposition was successfully used by Rubio-Gonzalez and Mason (1999) to find $K_I(t)$ for a single pair of normal loads in a finite crack.

5 Conclusions

The dynamic response of a finite crack in orthotropic materials subjected to concentrated in-plane impact shear loads has been presented. The quasi-static solution can be extracted exactly from the dynamic formulation when $t \to \infty$. The transient response

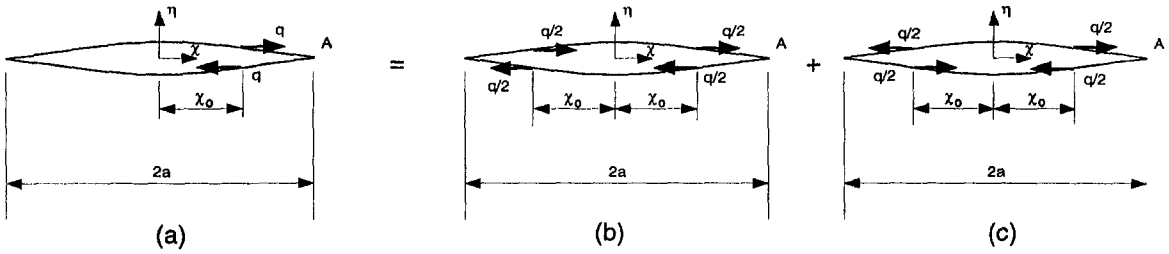

Fig. 6 Schematic of the finite crack geometry with a single pair of concentrated shear loads. (*a*) Original problem which may be solved by a superposition of (*b*) a symmetric problem and (*c*) an antisymmetric problem.

shows a strong dependence on the material properties. Some important points follow from this analysis:

1 The arrival of the dilatational wave at the crack tip makes an important contribution to the dynamic stress intensity factor $K_{II}(t)$, unlike in mode I loading where that wave had a minimum effect in $K_I(t)$.

2 The condition if x_0/c_R is greater or less than $(1 + x_0)/c_d$, where $x_0 = 0.6$ for this analysis, determines the main features of the dynamic stress intensity factor $K_{II}(t)$. When the greater sign holds, the dilatational waves caused by both loads arrive at the tip $x = +1$ before any other waves, thus their effects are added and as a result $K_{II}(t)$ reaches the maximum dynamic overshoot sooner; this behavior is illustrated in Figs. 3(*a*) and 4 corresponding to graphite-epoxy and boron-epoxy composites, respectively, with fibers along the x-axis in both cases. When the lesser sign holds, two separated and similar cycles in $K_{II}(t)$ occur; each one corresponding to the arrival of stress waves at the crack tip generated by the two load pairs. This behavior is illustrated in Figs. 2, 3(*b*), and 5.

3 When $x_0/c_R < (1 + x_0)/c_d$, Figs. 2, 3(*b*), and 5, a plateau is observed between the two cycles (between R_1 and P_2). On this plateau $K_{II}(t)/K_0 = 1$ regardless of the value of the elastic constants.

Acknowledgment

Support of this work by the Office of Naval Research Young Investigator Program under grant N00014-96-1-0774 supervised by Dr. Y. Rajapakse and by the Mexican Government through CONACYT (Consejo Nacional de Ciencia y Tecnologia) are gratefully acknowledged.

References

Abou-Sayed, I. S., Burgers, P., and Freund, L. B., 1980, "Stress Intensity Factor Due to the Parallel Impact Loading of the Faces of the Crack," *Fracture Mechanics,* 12th Conference ASTM-STP-700, pp. 164–173.

Atkinson, K. E., 1997, *The Numerical Solution of Integral Equations of the Second Kind,* Cambridge University Press, New York.

Chen, E. P., and Sih, G. C., 1977, "Transient Response of Cracks to Impact Loads," *Elastodynamic Crack Problems,* G. C. Sih, ed., Noordhoff International Publishing. Leyden, The Netherlands.

Debnath, L., 1995, *Integral Transforms and their Applications,* CRC Press, Boca Raton, FL.

Chao, C. C., 1960, "Dynamical Response of an Elastic Half-Space Surface Loadings," ASME JOURNAL OF APPLIED MECHANICS, Vol. 27, pp. 559–567.

Freund, L. B., 1974, "The Stress Intensity Factor due to Normal Impact Loading on the Faces of a Crack," *Int. J. Engng. Sci.,* Vol. 12, pp. 179–189.

Freund, L. B., 1990, *Dynamic Fracture Mechanics,* Cambridge University Press, New York.

Honig, G., and Hirdes, U., 1984, "A Method for the Numerical Inversion of Laplace Transforms," *J. Comp. Appl. Math.,* Vol. 10, pp. 113–132.

Isida, M., 1972, "Data on Crack Tip Stress Intensity Factors," *JSME,* Vol. 75, No. 642, pp. 1127–1135.

Kassir, M. K., and Bandyopadhyay, K. K., 1983, "Impact Response of a Cracked Orthotropic Medium," ASME JOURNAL OF APPLIED MECHANICS, Vol. 50, pp. 630–636.

Lambros, J., and Rosakis, A., 1995, "Shear Dominated Transonic Interfacial Crack Growth in a Bimaterial-I. Experimental Observations," *J. Mech. Phys. Solids,* Vol. 43, No. 2, pp. 169–188.

Liu, C., Huang, Y., and Rosakis, A., 1995, "Shear Dominated Transonic Interfacial Crack Growth in a Bimaterial-II. Asymptotic Fields and Favorable Velocity Regimes," *J. Mech. Phys. Solids,* Vol. 43, No. 2, pp. 189–206.

Nayfeh, A. H., 1995, *Wave Propagation in Anisotropic Media with Applications to Composites,* North-Holland, Amsterdam.

Papoulis, A., 1962, *The Fourier Integral and Its Applications,* McGraw-Hill, New York.

Parton, V. Z., and Boriskovsky, V. G., 1989, "Dynamic Fracture Mechanics," *Stationary Cracks,* Vol. 1, Hemisphere, New York.

Rubio-Gonzalez, C., and Mason, J. J., 1999, "Green's Functions for the Stress Intensity Factor Evolution in Finite Cracks in Orthotropic Materials," *Int. J. of Fracture,* submitted for publication.

Rosakis, A. J., 1998, Plenary Lecture, The US National Congress in Applied Mechanics, Gainesville, FL, June.

Schwartz, M. M., 1997, *Composite Materials: Properties, Nondestructive Testing and Repair,* Vol. 1, Prentice-Hall, Englewood Cliffs, NJ.

Shindo, Y., and Nozaki, H., 1986, "Impact Response of a Finite Crack in an Orthotropic Strip," *Acta Mechanica,* Vol. 62, pp. 87–104.

Shivakumar, K. N., and Crews, J. H., 1998, "Modified Mixed-Mode Bending Test Apparatus for Measuring Delamination Fracture Toughness of Laminates Composites," *J. Composites Materials,* to appear.

Shukla, A., Singh, R., Lambros, J., and Rosakis, A., 1998, "Investigation of the Mechanics of Intersonic Crack Propagation Along a Bimaterial Interface Using Coherent Gradient Sensing and Photoelasticity," *Proceedings of Royal Society, London,* to appear.

Sneddon, I. N., 1966, *Mixed Boundary Value Problems in Potential Theory,* North-Holland, Amsterdam.

N. I. Shbeeb

W. K. Binienda

Department of Civil Engineering,
The University of Akron,
Akron, OH 44325-3905

K. L. Kreider
Department of Mathematics
and Computer Science,
The University of Akron,
Akron, OH 44325-4002

Analysis of the Driving Forces for Multiple Cracks in an Infinite Nonhomogeneous Plate, Part I: Theoretical Analysis

A general methodology is constructed for the fundamental solution of an arbitrarily oriented crack embedded in an infinite nonhomogeneous plate in which the shear modulus varies exponentially with one coordinate. The stress is evaluated as a summation of two states of stresses; one is associated with a local coordinate system in an infinite plate, while the other is associated with the boundaries of a finite plate defined in a structural coordinate system. The fundamental solution is used to generate stress intensity factors and strain energy release rates for fully interactive multiple crack problems. Part I of this paper focuses on the analytical development of the solution. In Part II, the numerical technique used in solving singular integral equations obtained in Part I is presented, along with a parametric study.

Introduction

One of the disadvantages of composites is the mismatch of the thermal expansion coefficients between its constituents. This mismatch produces residual stresses, which may initiate debonding, delamination, and microcracks. For example, the application of a ceramic layer as a thermal barrier coating for a metal substrate often produces debonding at the interface after a small number of thermomechanical load cycles. In order to minimize the mismatch between the ceramic layer and metal substrate, a new technology was recently developed. This technology allows fully tailored processing of materials and interfacial zones with predetermined continuously varying mechanical properties that are known as functionally graded materials (see Asish et al. (1997) and Holt et al. (1993)).

Functionally graded materials can be described as two-phase particulate composites, wherein the volume fraction of its constituents differs continuously in the thickness direction (see Niino and Maeda, 1990; Hirano and Yamada, 1988; Hirano et al., 1988; Kawasaki and Watanabe R., 1990; Pindera et al., 1994, 1995, 1997; Needleman and Suresh, 1996). This implies that the composition profile can be tailored to give appropriate thermomechanical properties.

A number of authors have investigated cracks in inhomogeneous or functionally graded materials. For instance, Delale and Erdogan (1983) solved the crack problem for the nonhomogeneous plane. The authors considered the plane elasticity problem, in which the material is isotropic, has a constant Poisson's ratio (ν), and the Young's modulus (E) is of an exponential form varying in the x-direction, namely,

$$E(x) = E_0 e^{\beta x} \tag{1}$$

where β is a nonhomogeneity constant and E_0 is the Young modulus of the homogeneous material. They found that Poisson's ratio did not have much effect on the resulting stress intensity factors. They also found that the strain-energy release rate at the crack embedded in the portion of the medium with higher stiffness is lower than that corresponding to the crack tip on the less stiff side of the material. Hence, the crack grows in the direction of the less stiff material.

Also, Delale and Erdogan (1988) solved the collinear crack problem for two dissimilar homogeneous elastic half-planes bonded to a very thin nonhomogeneous layer. The elastic properties of the interfacial material varied continuously between those of the two semi-infinite planes. The Airy stress function was used in their formulation of the solution. They assumed that the stress function is composed of two functions; one is associated with an infinite plane containing the crack on the x-axis, while the second is an uncracked strip. Their results showed that if the crack approaches the less stiff material, the strain energy release rate increases. Crack growth due to fatigue, creep, and corrosion was considered in Erdogan (1995), and crack growth due to thermal stresses was considered in Erdogan and Wu (1996).

However, the problem of multiple oriented cracks embedded in a nonhomogeneous infinite plate has not yet been addressed. Thus, the present paper deals with the general solution to a single and multiple oriented cracks embedded in a nonhomogeneous infinite plate. It is assumed that the functionally graded materials have a constant Poisson's ratio and the shear modulus is of an exponential form. The solution is valid for both plane stress and plane strain.

General Problem Formulation

The solution of the mixed boundary value problem for the stress intensity factors or strain energy release rates at a crack tip is obtained from the perturbation part of the problem (see Fig. 1). Before any particular problem is addressed, the general strategy of solution is discussed in this section.

Assume that there are two states of stresses, $\sigma_{ij}^{(1)}$ and $\sigma_{ij}^{(2)}$. The stress $\sigma_{ij}^{(1)}$ is associated with a local coordinate system (x_1-y_1) in an infinite plate, while the stress $\sigma_{ij}^{(2)}$ is associated with the boundaries of a finite plate defined in a structural coordinate system (x-y). In the case of infinite plate problems, only the first state of stress exists, but for the general problem the total stresses in the local coordinate system are expressed as

$$\sigma_{y_1y_1}^{T}(x_1, y_1) = \sigma_{y_1y_1}^{(1)}(x_1, y_1) + \sigma_{y_1y_1}^{(2)}(x_1, y_1)$$
$$\tau_{y_1y_1}^{T}(x_1, y_1) = \tau_{y_1y_1}^{(1)}(x_1, y_1) + \tau_{y_1y_1}^{(2)}(x_1, y_1) \tag{2}$$

Contributed by the Applied Mechanics Division of THE AMERICAN SOCIETY OF MECHANICAL ENGINEERS for publication in the ASME JOURNAL OF APPLIED MECHANICS.

Discussion on the paper should be addressed to the Technical Editor, Professor Lewis T. Wheeler, Department of Mechanical Engineering, University of Houston, Houston, TX 77204-4792, and will be accepted until four months after final publication of the paper itself in the ASME JOURNAL OF APPLIED MECHANICS.

Manuscript received by the ASME Applied Mechanics Division, June 18; final revision, Nov. 23, 1998. Associate Technical Editor: M.-J. Pindera.

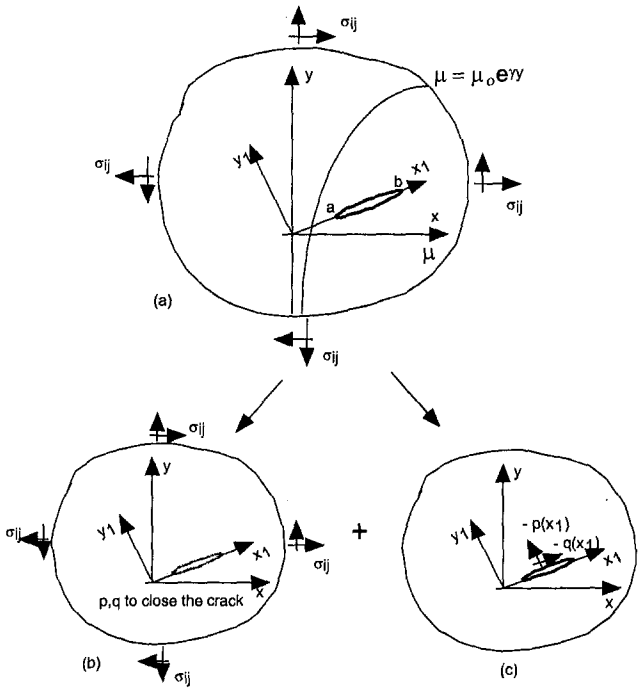

Fig. 1 Methodology of solution for the fundamental problem; (*a*) mixed boundary value problem for the functionally graded materials, (*b*) infinite functionally graded materials plate without crack, (*c*) perturbation problem of a crack loaded by surface tractions

where

$$\sigma^{(1)}_{y_1y_1}(x_1, y_1) = \sin^2(\theta)\sigma_{xx}(x, y) + \cos^2(\theta)\sigma_{yy}(x, y) - 2\sin(\theta)\cos(\theta)\tau_{xy}(x, y)$$

$$\tau^{(1)}_{y_1y_1}(x_1, y_1) = -\sin(\theta)\cos(\theta)\sigma_{xx}(x, y) + \sin(\theta)\cos(\theta)\sigma_{yy}(x, y) + (\cos^2(\theta) - \sin^2(\theta))\tau_{xy}(x, y)$$

$$x = x_1\cos(\theta) - y_1\sin(\theta)$$

$$y = x_1\sin(\theta) + y_1\cos(\theta)$$

and σ_{xx}, σ_{yy}, and τ_{xy} denote global stresses and θ is the angle between the local crack direction x_1 and global x-axis. The stress boundary conditions obtained from the perturbation problem are

$$-p_1(x_1) = \lim_{y_1\to 0}\sigma^T_{y_1y_1}(x_1, y_1)$$

$$-p_2(x_1) = \lim_{y_1\to 0}\tau^T_{x_1y_1}(x_1, y_1) \quad (3)$$

where $p_1(x_1)$ and $p_2(x_1)$ are the normal and shear tractions at the inner crack surfaces.

Upon substitution of Eq. (2) into Eq. (3), the boundary conditions become

$$-p_1(x_1) = \lim_{y_1\to 0}\sigma^{(1)}_{y_1y_1}(x_1, y_1) + \lim_{y_1\to 0}\sigma^{(2)}_{y_1y_1}(x_1, y_1)$$

$$-p_2(x_1) = \lim_{y_1\to 0}\tau^{(1)}_{x_1y_1}(x_1, y_1) + \lim_{y_1\to 0}\tau^{(2)}_{x_1y_1}(x_1, y_1) \quad (4)$$

Notice that the principal part is produced from the first part of Eq. (4). The stresses are expressed in the most general form as follows:

$$\sigma^{(1)}_{y_1y_1}(x_1, y_1) = \frac{1}{2\pi}\int_a^b K^{(1)}_{1j}(x_1, y_1, t)f_j(t)dt$$

$$\tau^{(1)}_{x_1y_1}(x_1, y_1) = \frac{1}{2\pi}\int_a^b K^{(1)}_{2j}(x_1, y_1, t)f_j(t)dt$$

$$\sigma^{(2)}_{y_1y_1}(x_1, y_1) = \frac{1}{2\pi}\int_a^b K^{(2)}_{1j}(x_1, y_1, t)f_j(t)dt$$

$$\tau^{(2)}_{x_1y_1}(x_1, y_1) = \frac{1}{2\pi}\int_a^b K^{(2)}_{2j}(x_1, y_1, t)f_j(t)dt$$

$$\text{for} \quad a < (x_1, t) < b \quad (5)$$

where the f_j are so-called auxiliary functions defined as derivatives with respect to x_1 of the crack-opening displacement along the crack. The kernels are expressed as

$$K^{(1)}_{ij}(x_1, y_1, t) = \int_{-\infty}^{\infty} X^{(1)}_{ij}(\alpha, y_1)e^{\alpha i(x_1-t)}d\alpha$$

$$K^{(2)}_{ij}(x_1, y_1, t) = \int_{-\infty}^{\infty} X^{(2)}_{ij}(\alpha, x_1\cos\theta - y_1\sin\theta)e^{\alpha i(x_1\sin\theta + y_1\cos\theta - t)}d\alpha. \quad (6)$$

The explicit forms of $X^{(1)}_{ij}$ and $X^{(2)}_{ij}$ depend on the stress and displacement continuity of the problem. If $X^{(1)}_{ij}$ does not vanish as $|\alpha|$ approaches infinity, then an asymptotic analysis is performed to separate the singular part from the regular part. Consequently, Eq. (6) can be integrated numerically. To emphasize the behavior as $|\alpha|$ approaches infinity, Eq. (6) can be written in the form

$$K^{(1)}_{ij}(x_1, y_1, t) = \int_{-\infty}^{\infty} X^{(1)}_{ij}(\alpha)e^{-|\alpha|y_1 + \alpha i(x_1-t)}d\alpha$$

$$K^{(2)}_{ij}(x_1, y_1, t) = \int_{-\infty}^{\infty} X^{(2)}_{ij}(\alpha)e^{-|\alpha|(x_1\sin\theta + y_1\cos\theta) + \alpha i(x_1\cos\theta - y_1\sin\theta - t)}d\alpha. \quad (7)$$

Substituting Eq. (7) into (5), the following stress representations are obtained:

$$\sigma^{(1)}_{y_1y_1}(x_1, y_1) = \frac{1}{2\pi}\int_{-\infty}^{\infty} X^{(1)}_{1j}(\alpha)e^{-|\alpha|y_1 + i\alpha(x_1-t)}d\alpha\int_a^b f_j(t)dt$$

$$\tau^{(1)}_{x_1y_1}(x_1, y_1) = \frac{1}{2\pi}\int_{-\infty}^{\infty} X^{(1)}_{2j}(\alpha)e^{-|\alpha|y_1 + i\alpha(x_1-t)}d\alpha\int_a^b f_j(t)dt \quad (8)$$

$$\sigma^{(2)}_{y_1y_1}(x_1, y_1) = \frac{1}{2\pi}\int_{-\infty}^{\infty} X^{(2)}_{1j}(\alpha)e^{-|\alpha|(x_1\sin\theta + y_1\cos\theta) + i\alpha(x_1\cos\theta - y_1\sin\theta - t)}d\alpha\int_a^b f_j(t)dt$$

$$\tau^{(2)}_{x_1y_1}(x_1, y_1) = \frac{1}{2\pi}\int_{-\infty}^{\infty} X^{(2)}_{2j} \times (\alpha)e^{-|\alpha|(x_1\sin\theta + y_1\cos\theta) + i\alpha(x_1\cos\theta - y_1\sin\theta - t)}d\alpha\int_a^b f_j(t)dt. \quad (9)$$

To simplify further, substitute Eq. (8) into the first terms of Eq. (4) to obtain

$$\lim_{y_1 \to 0} \begin{Bmatrix} \sigma^{(1)}_{y_1 y_1} \\ \tau^{(1)}_{x_1 y_1} \end{Bmatrix}$$

$$= \lim_{y_1 \to 0} \left[\frac{1}{2\pi} \int_{-\infty}^{\infty} X_{ij}^{(1)}(\alpha) e^{-|\alpha| y_1 + i\alpha(x_1 - t)} d\alpha \int_a^b f_j(t) dt \right]. \quad (10)$$

Assume that the leading order term of $X_{ij}^{(1)}$ has the asymptotic form

$$X_{ij}^{(1)}(\alpha) \to c_{ij}^{(1)} \pm i d_{ij}^{(1)} \quad \text{as} \quad \alpha \to \pm\infty. \quad (11)$$

Define N as

$$N = \frac{1}{2\pi} \int_{-\infty}^{\infty} X_{ij}^{(1)}(\alpha) e^{-|\alpha| y_1 + i\alpha(x_1 - t)} d\alpha. \quad (12)$$

This integral must be analyzed asymptotically. Splitting N into two parts ($\alpha < 0$ and $\alpha > 0$) and combining them together by letting $\alpha \to -\alpha$ for $\alpha < 0$, we obtain

$$N = \frac{1}{2\pi} \int_0^{\infty} \{[X_{ij}^{(1)}(\alpha) + X_{ijc}^{(1)}(\alpha) - 2c_{ij}^{(1)}] \cos(\alpha(t - x_1)) + [X_{ijc}^{(1)}(\alpha) - X_{ij}^{(1)}(\alpha) + 2id_{ij}^{(1)}] i \sin(\alpha(t - x_1))\} d\alpha + \lim_{y_1 \to 0} \left[\frac{1}{2\pi} \mathrm{SIP}^{(1)} \right] \quad (13)$$

where $X_{ijc}^{(1)}(\alpha)$ is the complex conjugate of $X_{ij}^{(1)}(\alpha)$ and the singular integral part ($\mathrm{SIP}^{(1)}$) of the equation is

$$\mathrm{SIP}^{(1)} = \int_0^{\infty} 2e^{-\alpha y_1} \{c_{ij}^{(1)} \cos(\alpha(t - x_1)) + d_{ij}^{(1)} \sin(\alpha(t - x_1))\} d\alpha. \quad (14)$$

The following integral identities are used to evaluate Eq. (14) (Abramowitz and Stegun, 1964):

$$\int_0^{\infty} e^{-\alpha n} \cos(m\alpha) d\alpha = \frac{n}{n^2 + m^2}$$

$$\int_0^{\infty} e^{-\alpha n} \sin(m\alpha) d\alpha = \frac{m}{n^2 + m^2}. \quad (15)$$

Hence, it can be shown that (14) becomes

$$\mathrm{SIP}^{(1)} = 2 \frac{c_{ij}^{(1)} y_1}{(t - x_1)^2 + y_1^2} + 2 \frac{d_{ij}^{(1)}(t - x_1)}{(t - x_1)^2 + y_1^2}, \quad (16)$$

whereupon letting $y_1 \to 0$ and substituting the result into (13), the following expression is obtained:

$$N = \frac{1}{2\pi} \int_0^{\infty} \{[X_{ij}^{(1)} + X_{ijc}^{(1)} - 2c_{ij}^{(1)}] \cos(\alpha(t - x_1)) + [X_{ijc}^{(1)} - X_{ij}^{(1)} + 2id_{ij}^{(1)}] i \sin(\alpha(t - x_1))\} d\alpha + \frac{1}{\pi} \frac{d_{ij}^{(1)}}{t - x_1}. \quad (17)$$

To compute this integral, the infinite interval and the oscillation in the integrand must be dealt with. To this end, introduce the second-order asymptotic terms:

$$X_{ij}^{(1)} \to (c_{ij}^{(1)} \pm i d_{ij}^{(1)}) + \left(\frac{e_{ij}^{(1)}}{\alpha} \pm i \frac{g_{ij}^{(1)}}{\alpha} \right) \quad \text{as} \quad \alpha \to \pm\infty. \quad (18)$$

Introducing these terms yields

$$N = \frac{1}{2\pi} \int_0^{\infty} \left\{ \left[X_{ij}^{(1)}(\alpha) + X_{ijc}^{(1)}(\alpha) - 2\left(c_{ij}^{(1)} + \frac{e_{ij}^{(1)}}{\alpha} \right) \right] \times \cos(\alpha(t - x_1)) + \left[X_{ijc}^{(1)}(\alpha) - X_{ij}^{(1)}(\alpha) + 2i\left(d_{ij}^{(1)} + \frac{g_{ij}^{(1)}}{\alpha} \right) \right] \times i \sin(\alpha(t - x_1)) d\alpha + \frac{1}{\pi} \frac{d_{ij}^{(1)}}{t - x_1} + \frac{1}{2\pi} \int_0^{\infty} \frac{2e_{ij}^{(1)} \cos(\alpha(t - x_1))}{\alpha} d\alpha - \frac{1}{2\pi} \int_0^{\infty} \frac{2g_{ij}^{(1)} \sin(\alpha(t - x_1))}{\alpha} d\alpha. \quad (19)$$

To evaluate the last two terms of Eq. (19), the following identities are used (Abramowitz and Stegun, 1964):

$$\int_0^{\infty} \frac{1}{\alpha} \sin(\alpha(t - x_1)) d\alpha = \frac{\pi}{2} \frac{(t - x_1)}{|t - x_1|}$$

$$\int_U^{\infty} \frac{1}{\alpha} \cos(\alpha(t - x_1)) d\alpha = -Ci(U(t - x_1))$$

$$\equiv -\left(C_0 + \log|U(t - x_1)| + \int_0^{|U(t - x_1)|} \frac{\cos\beta - 1}{\beta} d\beta \right) \quad (20)$$

where Ci denotes the cosine integral, C_0 is the Euler constant, and U is arbitrary; it is chosen large enough to insure the numerical convergence of the integral. The following expression replaces Eq. (19):

$$N = \frac{1}{2\pi} \int_0^{\infty} \left\{ \left[X_{ijc}^{(1)}(\alpha) - X_{ij}^{(1)}(\alpha) + 2i\left(d_{ij}^{(1)} + \frac{g_{ij}^{(1)}}{\alpha} \right) \right] i \sin(\alpha(t - x_1)) \right\} d\alpha + \frac{1}{2\pi} \int_0^{U} \{[X_{ij}^{(1)}(\alpha) + X_{ijc}^{(1)}(\alpha) - 2c_{ij}^{(1)}] \cos(\alpha(t - x_1))\} d\alpha + \frac{1}{2\pi} \int_U^{\infty} \left\{ \left[X_{ij}^{(1)}(\alpha) + X_{ijc}^{(1)}(\alpha) - 2\left(c_{ij}^{(1)} + \frac{e_{ij}^{(1)}}{\alpha} \right) \right] \cos(\alpha(t - x_1)) \right\} d\alpha + \frac{1}{\pi} \frac{d_{ij}^{(1)}}{t - x_1} - \frac{g_{ij}^{(1)}}{2} \frac{(t - x_1)}{|t - x_1|} - \frac{e_{ij}^{(1)}}{\pi} Ci(U(t - x_1)). \quad (21)$$

Using the above results, the first terms on the right in (4) can be expressed as

$$\lim_{y_1\to 0}\sigma^{(1)}_{y_1y_1}(x_1, y_1) = \frac{1}{\pi}\int_a^b \frac{d^{(1)}_{1j}f_j(t)}{t-x_1}\,dt + \frac{1}{2\pi}\int_a^b k^{(1)}_{1j}(x_1, t)f_j(t)dt$$

$$+ \int_a^b \left[\frac{g^{(1)}_{1j}}{2}\frac{(t-x_1)}{|t-x_1|} - \frac{e^{(1)}_{1j}}{\pi}Ci(U(t-x_1))\right]f_j(t)dt \quad (22)$$

$$\lim_{y_1\to 0}\tau^{(1)}_{x_1y_1}(x_1, y_1) = \frac{1}{\pi}\int_a^b \frac{d^{(1)}_{2j}f_j(t)}{t-x_1}\,dt + \frac{1}{2\pi}\int_a^b k^{(1)}_{2j}(x_1, t)f_j(t)dt$$

$$+ \int_a^b \left[\frac{g^{(1)}_{2j}}{2}\frac{(t-x_1)}{|t-x_1|} - \frac{e^{(1)}_{2j}}{\pi}Ci(U(t-x_1))\right]f_j(t)dt \quad (23)$$

where

$$k^{(1)}_{ij}(x_1, t) = \int_0^\infty \left\{\left[X^{(1)}_{ijc}(\alpha) - X^{(1)}_{ij}(\alpha) + 2i\left(d^{(1)}_{ij} + \frac{g^{(1)}_{ij}}{\alpha}\right)\right] i\sin(\alpha(t-x_1))\right\}d\alpha$$

$$+ \int_0^U \{[X^{(1)}_{ij}(\alpha) + X^{(1)}_{ijc}(\alpha) - 2c^{(1)}_{ij}]\cos(\alpha(t-x_1))\}d\alpha$$

$$+ \int_U^\infty \{[X^{(1)}_{ij}(\alpha) + X^{(1)}_{ijc}(\alpha) - 2\left(c^{(1)}_{ij} + \frac{e^{(1)}_{ij}}{\alpha}\right)\cos(\alpha(t-x_1))d\alpha. \quad (24)$$

A similar procedure is applied to the second terms on the right in Eq. (4), by inserting the asymptotic expansions

$$X^{(2)}_{ij} = (a^{(2)}_{ij} \pm ib^{(2)}_{ij})\alpha + (c^{(2)}_{ij} \pm id^{(2)}_{ij}) \quad \text{as} \quad \alpha \to \pm\infty \quad (25)$$

into Eq. (9). Simplifications can be made with the use of the integral identities (Abramowitz and Stegun, 1964):

$$\int_0^\infty \alpha e^{-\alpha n}\cos(m\alpha)d\alpha = \frac{n^2-m^2}{(n^2+m^2)^2}$$

$$\int_0^\infty \alpha e^{-\alpha n}\sin(m\alpha)d\alpha = \frac{2nm}{(n^2+m^2)^2}. \quad (26)$$

Hence, the second terms on the right in Eq. (4) become

$$\lim_{y_1\to 0}\sigma^{(2)}_{y_1y_1}(x_1, y_1) = \frac{1}{\pi}\int_a^b \left[\frac{a^{(2)}_{1j}(x_1^2\sin^2\theta - \cos^2\theta(t-x_1)^2)}{(x_1^2\sin^2\theta + \cos^2\theta(t-x_1)^2)^2}\right.$$

$$+ \frac{2b^{(2)}_{1j}x_1(t-x_1)\sin\theta\cos\theta}{(x_1^2\sin^2\theta + \cos^2\theta(t-x_1)^2)^2}$$

$$\left. + \frac{c^{(2)}_{1j}x_1\sin\theta + 2d^{(2)}_{1j}\cos\theta(t-x_1)}{(x_1^2\sin^2\theta + \cos^2\theta(t-x_1)^2)^2}\right]f_j(t)dt$$

$$+ \frac{1}{2\pi}\int_a^b k^{(2)}_{1j}(x_1, t)f_j(t)dt \quad (27)$$

$$\lim_{y_1\to 0}\tau^{(2)}_{x_1y_1}(x_1, y_1) = \frac{1}{\pi}\int_a^b \left[\frac{a^{(2)}_{2j}(x_1^2\sin^2\theta - \cos^2\theta(t-x_1)^2)}{(x_1^2\sin^2\theta + \cos^2\theta(t-x_1)^2)^2}\right.$$

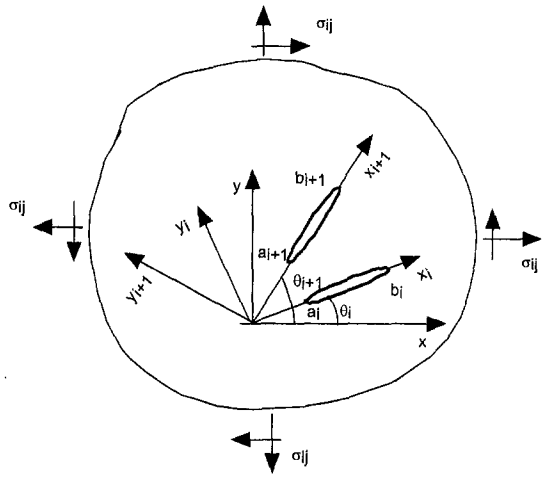

Fig. 2 Radial multiple cracks embedded in the infinite functionally graded materials plate

$$+ \frac{2b^{(2)}_{2j}x_1(t-x_1)\sin\theta\cos\theta}{(x_1^2\sin^2\theta + \cos^2\theta(t-x_1)^2)^2}$$

$$\left. + \frac{c^{(2)}_{2j}x_1\sin\theta + 2d^{(2)}_{2j}\cos\theta(t-x_1)}{(x_1^2\sin^2\theta + \cos^2\theta(t-x_1)^2)^2}\right]f_j(t)dt$$

$$+ \frac{1}{2\pi}\int_a^b k^{(2)}_{2j}(x_1, t)f_j(t)dt \quad (28)$$

where

$$k^{(2)}_{ij}(x_1, t) = \int_0^\infty \{[X^{(2)}_{ijc}(\alpha) - X^{(2)}_{ij}(\alpha) + 2i(\alpha b^{(2)}_{ij} + d^{(2)}_{ij})e^{-\alpha x_1\sin\theta}]i\sin(\alpha(t-x_1))\}d\alpha$$

$$+ \int_0^\infty \{[X^{(2)}_{ij}(\alpha) + X^{(2)}_{ijc}(\alpha) - 2(\alpha a^{(2)}_{ij} + c^{(2)}_{ij})e^{-\alpha x_1\sin\theta}]\cos(\alpha(t-x_1))\}d\alpha. \quad (29)$$

It should be noted that (27) and (28) do not contain any singularities and the asymptotic expansion is applied only for computational efficiency.

Fundamental Solution

The formulation in the previous section is used to solve the problem of radial multiple cracks in an infinite isotropic functionally graded materials. as depicted in Fig. 2. When dealing with an infinite plate, only Eqs. (22), (23), and (24) are used. Before doing so, the fundamental solution for a single crack is required. Konda and Erdogan (1994) solved the single crack problem using the Navier equations. In this work, the same problem is solved using the Airy stress function. The shear modulus μ varies exponentially with y.

The shear modulus is defined as follows:

$$\mu(y) = \mu_0 e^{\gamma y}$$

$$\mu(x_1, y_1) = \mu_0 e^{\beta x_1 + \delta y_1}$$

$$\delta = \gamma\cos(\theta)$$

$$\beta = \gamma\sin(\theta) \quad (30)$$

where γ, δ, and β are real constants and represent the coefficients of nonhomogeneity.

The Airy stress function $U(x_1, y_1)$ is defined by

$$\sigma_{x_1x_1}(x_1, y_1) = \frac{\partial^2 U}{\partial y_1^2}$$

$$\sigma_{y_1y_1}(x_1, y_1) = \frac{\partial^2 U}{\partial x_1^2}$$

$$\tau_{x_1y_1}(x_1, y_1) = -\frac{\partial^2 U}{\partial x_1 \partial y_1}. \tag{31}$$

The stresses and strains are related through

$$\epsilon_{x_1x_1}(x_1, y_1) = \frac{\partial u_1}{\partial x_1} = \frac{1}{8\mu(x_1, y_1)}[(\kappa + 1)\sigma_{x_1x_1} + (\kappa - 3)\sigma_{y_1y_1}]$$

$$\epsilon_{y_1y_1}(x_1, y_1) = \frac{\partial v_1}{\partial y_1} = \frac{1}{8\mu(x_1, y_1)}[(\kappa - 3)\sigma_{x_1x_1} + (\kappa + 1)\sigma_{y_1y_1}]$$

$$\epsilon_{x_1y_1}(x_1, y_1) = \frac{1}{2}\left(\frac{\partial u_1}{\partial y_1} + \frac{\partial v_1}{\partial x_1}\right) = \frac{1}{2\mu(x_1, y_1)}\tau_{x_1y_1} \tag{32}$$

where u_1 and v_1 are horizontal and vertical displacements, and κ is defined as

$$\kappa = 3 - 4\nu \quad \text{for plane strain}$$

$$\kappa = \frac{3 - \nu}{1 + \nu} \quad \text{for plane stress.} \tag{33}$$

Using the above definitions for stresses together with the strain-stress relations in the compatibility equation,

$$\frac{\partial^2 \epsilon_{x_1x_1}}{\partial x_1^2} + \frac{\partial^2 \epsilon_{y_1y_1}}{\partial y_1^2} - 2\frac{\partial^2 \epsilon_{x_1y_1}}{\partial x_1 \partial y_1} = 0. \tag{34}$$

We obtain the fourth-order governing equation for $U(x_1, y_1)$:

$$\nabla^4 U(x_1, y_1) - 2\delta\frac{\partial}{\partial y_1}(\nabla^2 U(x_1, y_1)) - 2\beta\frac{\partial}{\partial x_1}(\nabla^2 U(x_1, y_1)) + \frac{8\beta\delta}{1 + \kappa}\frac{\partial^2 U(x_1, y_1)}{\partial x_1 \partial y_1} + \beta^2\left(\frac{\kappa - 3}{1 + \kappa}\frac{\partial^2 U(x_1, y_1)}{\partial y_1^2} + \frac{\partial^2 U(x_1, y_1)}{\partial x_1^2}\right) + \delta^2\left(\frac{\partial^2 U(x_1, y_1)}{\partial y_1^2} + \frac{\kappa - 3}{1 + \kappa}\frac{\partial^2 U(x_1, y_1)}{\partial x_1^2}\right) = 0 \tag{35}$$

where

$$\nabla = \left(\frac{\partial^2}{\partial x_1^2} + \frac{\partial^2}{\partial y_1^2}\right). \tag{36}$$

Defining the Fourier transform of $U(x_1, y_1)$ as

$$V(\alpha, y_1) = \int_{-\infty}^{\infty} U(x_1, y_1)e^{-i\alpha x_1}dx_1 \tag{37}$$

and applying Eqs. (37) to (35), the following characteristic equation is obtained for the coefficient n in the assumed solution $V(\alpha, y_1) = B(\alpha)e^{ny_1}$:

$$n^4 - 2\delta n^3 + \left(\beta^2\frac{\kappa - 3}{\kappa + 1} + \delta^2 - 2\alpha(i\beta + \alpha)\right)n^2 + \alpha\delta\left(\frac{8\beta}{\kappa + 1}i + 2\alpha\right)n + \alpha^2\left(\alpha^2 + \delta^2\frac{3 - \kappa}{\kappa + 1} + \beta(2i\alpha - \beta)\right) = 0 \tag{38}$$

which has complex roots

$$n_1 = \frac{1}{2}\left(\delta + \beta\sqrt{\frac{3 - \kappa}{\kappa_2 + 1}}\right) - \frac{1}{2}\sqrt{\left(\delta + \beta\sqrt{\frac{3 - \kappa}{\kappa + 1}}\right)^2 + 4\left(\alpha^2 + i\alpha\left(\beta - \delta\sqrt{\frac{3 - \kappa}{\kappa + 1}}\right)\right.}$$

$$n_2 = \frac{1}{2}\left(\delta - \beta\sqrt{\frac{3 - \kappa}{\kappa + 1}}\right) - \frac{1}{2}\sqrt{\left(\delta - \beta\sqrt{\frac{3 - \kappa}{\kappa + 1}}\right)^2 + 4\left(\alpha^2 + i\alpha\left(\beta + \delta\sqrt{\frac{3 - \kappa}{\kappa + 1}}\right)\right.}$$

$$n_3 = \frac{1}{2}\left(\delta + \beta\sqrt{\frac{3 - \kappa}{\kappa + 1}}\right) + \frac{1}{2}\sqrt{\left(\delta + \beta\sqrt{\frac{3 - \kappa}{\kappa + 1}}\right)^2 + 4\left(\alpha^2 + i\alpha\left(\beta - \delta\sqrt{\frac{3 - \kappa}{\kappa + 1}}\right)\right.}$$

$$n_4 = \frac{1}{2}\left(\delta - \beta\sqrt{\frac{3 - \kappa}{\kappa + 1}}\right) + \frac{1}{2}\sqrt{\left(\delta - \beta\sqrt{\frac{3 - \kappa}{\kappa + 1}}\right)^2 + 4\left(\alpha^2 + i\alpha\left(\beta + \delta\sqrt{\frac{3 - \kappa}{\kappa + 1}}\right)\right.}. \tag{39}$$

Therefore, the solution to the Fourier-transformed compatibility Eq. (35) is written as

$$V(\alpha, y_1) = B_1(\alpha)e^{n_1y_1} + B_2(\alpha)e^{n_2y_1} + B_3(\alpha)e^{n_3y_1} + B_4(\alpha)e^{n_4y_1} \tag{40}$$

so that

$$U(x_1, y_1) = \frac{1}{2\pi}\int_{-\infty}^{\infty}[B_1(\alpha)e^{n_1y_1} + B_2(\alpha)e^{n_2y_1} + B_3(\alpha)e^{n_3y_1} + B_4(\alpha)e^{n_4y_1}]e^{ix_1\alpha}d\alpha. \tag{41}$$

A bounded form of Eq. (41) can be obtained upon examination of the roots of the characteristic equations. The real parts of n_1 and n_2 are negative while those of n_3 and n_4 are positive as α approaches infinity. Hence U is defined for positive and negative y_1 as

$$U(x_1, y_1) = \frac{1}{2\pi}\int_{-\infty}^{\infty}(B_1e^{n_1y_1} + B_2e^{n_2y_1})e^{ix_1\alpha}d\alpha \quad \text{for} \quad y_1 > 0$$

$$U(x_1, y_1) = \frac{1}{2\pi}\int_{-\infty}^{\infty}(B_3e^{n_3y_1} + B_4e^{n_4y_1})e^{ix_1\alpha}d\alpha \quad \text{for} \quad y_1 < 0. \tag{42}$$

Normal and shear stresses must be continuous at $y_1 = 0$. The continuity conditions can be represented by Eq. (31) as

$$\frac{\partial U(x_1, 0^+)}{\partial y_1} = \frac{\partial U(x_1, 0^-)}{\partial y_1}$$

$$U(x_1, 0^+) = U(x_1, 0^-) \tag{43}$$

where 0^+ is for $y_1 > 0$ and 0^- is for $y_1 < 0$. Conditions (43) can be used to eliminate B_3 and B_4,

$$B_3 = \frac{n_4 - n_1}{n_4 - n_3} B_1 + \frac{n_4 - n_2}{n_4 - n_3} B_2$$

$$B_4 = \frac{n_1 - n_3}{n_4 - n_3} B_1 + \frac{n_2 - n_3}{n_4 - n_3} B_2. \quad (44)$$

The remaining two unknowns B_1 and B_2 can be expressed in terms of the auxiliary functions

$$f_1(x_1) = \frac{\partial}{\partial x_1} [u_1(x_1, 0^+) - u_1(x_1, 0^-)]$$

$$f_2(x_1) = \frac{\partial}{\partial x_1} [v_1(x_1, 0^+) - v_1(x_1, 0^-)]. \quad (45)$$

The final expressions for the stresses are obtained using (31) and Hooke's law,

$$\sigma_{x_1x_1}(x_1, y_1^+) = \frac{1}{2\pi} \int_{-\infty}^{\infty} \left[n_1^2 \frac{F_1(\alpha)h_{22} - F_2(\alpha)h_{12}}{h_{11}h_{22} - h_{12}h_{21}} e^{n_1y_1} + n_2^2 \frac{-F_1(\alpha)h_{21} + F_2(\alpha)h_{11}}{h_{11}h_{22} - h_{12}h_{21}} e^{n_2y_1} \right] e^{ix_1\alpha} d\alpha \quad (46)$$

$$\sigma_{y_1y_1}(x_1, y_1^+) = -\frac{1}{2\pi} \int_{-\infty}^{\infty} \alpha^2 \left[\frac{F_1(\alpha)h_{22} - F_2(\alpha)h_{12}}{h_{11}h_{22} - h_{12}h_{21}} e^{n_1y_1} + \frac{-F_1(\alpha)h_{21} + F_2(\alpha)h_{11}}{h_{11}h_{22} - h_{12}h_{21}} e^{n_2y_1} \right] e^{ix_1\alpha} d\alpha \quad (47)$$

$$\tau_{x_1y_1}(x_1, y_1^+) = -\frac{i}{2\pi} \int_{-\infty}^{\infty} \alpha \left[n_1 \frac{F_1(\alpha)h_{22} - F_2(\alpha)h_{12}}{h_{11}h_{22} - h_{12}h_{21}} e^{n_1y_1} + n_2 \frac{-F_1(\alpha)h_{21} + F_2(\alpha)h_{11}}{h_{11}h_{22} - h_{12}h_{21}} e^{n_2y_1} \right] e^{ix_1\alpha} d\alpha \quad (48)$$

where

$$h_{11} = \frac{\kappa + 1}{8\mu_0} (n_1 - n_3)(n_1 - n_4)$$

$$h_{12} = \frac{\kappa + 1}{8\mu_0} (n_2 - n_3)(n_2 - n_4)$$

$$h_{21} = \frac{i\alpha - \beta}{8\mu_0} (\alpha^2(1 + \kappa) - \delta^2(\kappa - 3)) \times \left[\frac{(n_1 - n_3)(n_1 - n_4)}{(\delta - n_1)(\delta - n_3)(\delta - n_4)} \right]$$

$$h_{22} = \frac{i\alpha - \beta}{8\mu_0} (\alpha^2(1 + \kappa) - \delta^2(\kappa - 3)) \times \left[\frac{(n_2 - n_3)(n_2 - n_4)}{(\delta - n_2)(\delta - n_3)(\delta - n_4)} \right]$$

$$F_j(\alpha) = \int_a^b f_j(t) e^{(\beta - i\alpha)t} dt \quad \text{for} \quad j = 1, 2. \quad (49)$$

The singular integral equations can be solved for the auxiliary functions using the boundary conditions

$$-p_1(x_1) = \lim_{y_1 \to 0} \sigma_{y_1y_1}(x_1, y_1), \quad a < x_1 < b$$

$$-p_2(x_1) = \lim_{y_1 \to 0} \tau_{x_1y_1}(x_1, y_1), \quad a < x_1 < b. \quad (50)$$

Equations (47) and (48) are rearranged as follows:

$$\sigma_{y_1y_1}(x_1, y_1^+) = -\frac{1}{2\pi} \int_{-\infty}^{\infty} \alpha^2 \left[\frac{h_{22}e^{n_1y_1} - h_{21}e^{n_2y_1}}{h_{11}h_{22} - h_{12}h_{21}} F_1(\alpha) + \frac{h_{11}e^{n_2y_1} - h_{12}e^{n_1y_1}}{h_{11}h_{22} - h_{12}h_{21}} F_2(\alpha) \right] e^{ix_1\alpha} d\alpha \quad (51)$$

$$\tau_{x_1y_1}(x_1, y_1^+) = -\frac{i}{2\pi} \int_{-\infty}^{\infty} \alpha \left[\frac{n_1h_{22}e^{n_1y_1} - n_2h_{21}e^{n_2y_1}}{h_{11}h_{22} - h_{12}h_{21}} F_1(\alpha) + \frac{n_2h_{11}e^{n_2y_1} - n_1h_{12}e^{n_1y_1}}{h_{11}h_{22} - h_{12}h_{21}} F_2(\alpha) \right] e^{ix_1\alpha} d\alpha. \quad (52)$$

As α goes to infinity, $n_1 \cong n_2$, so a comparison of Eqs. (51) and (52) to (8) motivates the following definitions:

$$X_{11} = -\alpha^2 \left[\frac{h_{22} - h_{21}}{h_{11}h_{22} - h_{12}h_{21}} \right] \quad X_{12} = -\alpha^2 \left[\frac{h_{11} - h_{12}}{h_{11}h_{22} - h_{12}h_{21}} \right]$$

$$X_{21} = -i\alpha \left[\frac{n_1h_{22} - n_2h_{21}}{h_{11}h_{22} - h_{12}h_{21}} \right] \quad X_{22} = -i\alpha \left[\frac{n_2h_{11} - n_1h_{12}}{h_{11}h_{22} - h_{12}h_{21}} \right]. \quad (53)$$

The leading order behavior of X_{ij} is determined to be

$$X_{11}(\alpha) \to \frac{\delta}{\pm\alpha(1 + \kappa)} \quad \text{as} \quad \alpha \to \pm\infty$$

$$X_{12}(\alpha) \to \frac{\pm 2i}{(1 + \kappa)} + \frac{\beta}{\pm\alpha(1 + \kappa)} \quad \text{as} \quad \alpha \to \pm\infty$$

$$X_{21}(\alpha) \to \frac{\pm 2i}{(1 + \kappa)} + \frac{\beta}{\pm\alpha(1 + \kappa)} \quad \text{as} \quad \alpha \to \pm\infty$$

$$X_{22}(\alpha) \to \frac{-\delta}{\pm\alpha(1 + \kappa)} \quad \text{as} \quad \alpha \to \pm\infty \quad (54)$$

indicating that the analogues to $d_{ij}^{(1)}$, $e_{ij}^{(1)}$, $c_{ij}^{(1)}$ and $g_{ij}^{(1)}$ described earlier in Eqs. (12) and (18) become

$$d_{12}^1 = d_{21}^1 = \frac{2}{1 + \kappa}$$

$$e_{11}^1 = -e_{22}^1 = \frac{\delta}{1 + \kappa}$$

$$e_{12}^1 = e_{21}^1 = \frac{\beta}{1 + \kappa}$$

$$c_{11}^1 = c_{12}^1 = c_{21}^1 = c_{22}^1 = d_{11}^1 = d_{22}^1 = g_{11}^1 = g_{12}^1 = g_{21}^1 = g_{22}^1 = 0. \quad (55)$$

Now substituting (53) and (55) into (22) and (23), the final singular integral equations are reached:

$$-\frac{\kappa + 1}{2\mu(x_1, 0)} p_1(x_1) = \frac{1}{\pi} \int_a^b \frac{f_2(t)}{t - x_1} dt + \frac{1}{\pi} \int_a^b k_{12}(x_1, t) f_2(t) dt - \frac{1}{\pi} \int_a^b \frac{\beta}{2} Ci(U(t - x_1))] f_2(t) dt + \frac{1}{\pi} \int_a^b k_{11}(x_1, t) f_1(t) dt - \frac{1}{\pi} \int_a^b \frac{\delta}{2} Ci(U(t - x_1))] f_1(t) dt \quad (56)$$

$$-\frac{\kappa+1}{2\mu(x_1,0)}p_2(x_1)=\frac{1}{\pi}\int_a^b\frac{f_1(t)}{t-x_1}dt+\frac{1}{\pi}\int_a^b k_{21}(x_1,t)f_1(t)dt$$
$$-\frac{1}{\pi}\int_a^b\frac{\beta}{2}Ci(U(t-x_1))]f_1(t)dt+\frac{1}{\pi}\int_a^b k_{22}(x_1,t)f_2(t)dt$$
$$+\frac{1}{\pi}\int_a^b\frac{\delta}{2}Ci(U(t-x_1))]f_2(t)dt \quad (57)$$

where

$$k_{11}(x_1,t)=\frac{\kappa+1}{4}\left\{\int_0^\infty\{[X_{11c}-X_{11}]i\sin(\alpha(t-x_1))\}d\alpha\right.$$
$$+\int_0^U\{[X_{11}+X_{11c}]\cos(\alpha(t-x_1))\}d\alpha$$
$$\left.+\int_U^\infty\left\{\left[X_{11}+X_{11c}-2\frac{\delta}{\alpha(1+\kappa)}\right]\times\cos(\alpha(t-x_1))\right\}d\alpha\right\} \quad (58)$$

$$k_{12}(x_1,t)=\frac{\kappa+1}{4}\left\{\int_0^\infty\left\{\left[X_{12c}-X_{12}+\frac{4i}{1+\kappa}\right]\times i\sin(\alpha(t-x_1))d\alpha\right.\right.$$
$$+\int_0^U\{[X_{12}+X_{12c}]\cos(\alpha(t-x_1))\}d\alpha$$
$$\left.\left.+\int_U^\infty\left\{\left[X_{11}+X_{11c}-2\frac{\beta}{\alpha(1+\kappa)}\right]\times\cos(\alpha(t-x_1))d\alpha\right.\right. \quad (59)$$

$$k_{21}(x_1,t)=\frac{\kappa+1}{4}\left\{\int_0^\infty\left\{\left[X_{21c}-X_{21}+\frac{4i}{1+\kappa}\right]\times i\sin(\alpha(t-x_1))d\alpha\right.\right.$$
$$+\int_0^U\{[X_{21}+X_{21c}]\cos(\alpha(t-x_1))\}d\alpha$$
$$\left.\left.+\int_U^\infty\left\{\left[X_{21}+X_{21c}-2\frac{\beta}{\alpha(1+\kappa)}\right]\times\cos(\alpha(t-x_1))\right\}d\alpha\right. \quad (60)$$

$$k_{22}(x_1,t)=\frac{\kappa+1}{4}\left\{\int_0^\infty\{[X_{22c}-X_{22}]i\sin(\alpha(t-x_1))\}d\alpha\right.$$
$$+\int_0^U\{[X_{22}+X_{22c}]\cos(\alpha(t-x_1))\}d\alpha$$
$$\left.+\int_U^\infty\left\{\left[X_{22}+X_{22c}+2\frac{\delta}{\alpha(1+\kappa)}\right]\times\cos(\alpha(t-x_1))\right\}d\alpha\right\}. \quad (61)$$

Since there are no boundaries considered in this problem, the analogues to equations (27) and (28) do not appear here.

The definitions for the stress intensity factors and the strain energy release rate can be found in Part II, along with the numerical technique used in solving the system of singular integral Eqs. (56) and (57).

Multiple Crack Formulation

To formulate the multiple crack problem, the total stresses of the system need to be determined. Each crack is located along its local x_i-axis, oriented at angle θ_i. The cracks are ordered so that $\theta_{i+1} > \theta_i$. The local coordinates are related by

$$x_i=x_{i+1}\cos(\theta_{i+1}-\theta_i)-y_{i+1}\sin(\theta_{i+1}-\theta_i)$$
$$y_i=x_{i+1}\sin(\theta_{i+1}-\theta_i)+y_{i+1}\cos(\theta_{i+1}-\theta_i)$$
$$x_{i+1}=x_i\cos(\theta_{i+1}-\theta_i)+y_i\sin(\theta_{i+1}-\theta_i)$$
$$y_{i+1}=-x_i\sin(\theta_{i+1}-\theta_i)+y_i\cos(\theta_{i+1}-\theta_i) \quad (62)$$

and the stresses are related through the transformation:

$$\begin{Bmatrix}\sigma_{x_ix_i}\\ \sigma_{y_iy_i}\\ \tau_{x_iy_i}\end{Bmatrix}=\begin{bmatrix}m^2 & n^2 & -2mn\\ n^2 & m^2 & 2mn\\ mn & -mn & m^2-n^2\end{bmatrix}\begin{Bmatrix}\sigma_{x_{i+1}x_{i+1}}\\ \sigma_{y_{i+1}y_{i+1}}\\ \tau_{x_{i+1}y_{i+1}}\end{Bmatrix}$$
$$\begin{Bmatrix}\sigma_{x_{i+1}x_{i+1}}\\ \sigma_{y_{i+1}y_{i+1}}\\ \tau_{x_{i+1}y_{i+1}}\end{Bmatrix}=\begin{bmatrix}m^2 & n^2 & 2mn\\ n^2 & m^2 & -2mn\\ -mn & mn & m^2-n^2\end{bmatrix}\begin{Bmatrix}\sigma_{x_ix_i}\\ \sigma_{y_iy_i}\\ \tau_{x_iy_i}\end{Bmatrix}$$
$$m=\cos(\theta_{i+1}-\theta_i);\quad n=\sin(\theta_{i+1}-\theta_i). \quad (63)$$

The material constants are

$$\beta_i=\gamma\sin(\theta_i)$$
$$\delta_i=\gamma\cos(\theta_i). \quad (64)$$

The stresses for each coordinate system are expressed for positive $y_i > 0$ and negative $y_i < 0$, denoted as y_i^+ and y_i^-, respectively:

$$\sigma_{x_ix_i}(x_i,y_i^+)=\frac{1}{2\pi}\int_{-\infty}^\infty\left[\frac{n_1^{(i)2}h_{22}^{(i)(i)}e^{n_{1(i)}^{(i)}y_i}-n_2^{(i)2}h_{21}^{(i)(i)}e^{n_{2(i)}^{(i)}y_i}}{h_{11}^{(i)(i)}h_{22}^{(i)(i)}-h_{12}^{(i)(i)}h_{21}^{(i)(i)}}F_1^{(i)}(\alpha)\right.$$
$$\left.+\frac{n_2^{(i)2}h_{11}^{(i)(i)}e^{n_{2(i)}^{(i)}y_i}-n_1^{(i)2}h_{12}^{(i)(i)}e^{n_{1(i)}^{(i)}y_i}}{h_{11}^{(i)(i)}h_{22}^{(i)(i)}-h_{12}^{(i)(i)}h_{21}^{(i)(i)}}F_2^{(i)}(\alpha)\right]e^{ix_i\alpha}d\alpha \quad (65)$$

$$\sigma_{y_iy_i}(x_i,y_i^+)=-\frac{1}{2\pi}\int_{-\infty}^\infty\alpha^2\left[\frac{h_{22}^{(i)(i)}e^{n_{1(i)}^{(i)}y_i}-h_{21}^{(i)(i)}e^{n_{2(i)}^{(i)}y_i}}{h_{11}^{(i)(i)}h_{22}^{(i)(i)}-h_{12}^{(i)(i)}h_{21}^{(i)(i)}}F_1^{(i)}(\alpha)\right.$$
$$\left.+\frac{h_{11}^{(i)(i)}e^{n_{2(i)}^{(i)}y_i}-h_{12}^{(i)(i)}e^{n_{1(i)}^{(i)}y_i}}{h_{11}^{(i)(i)}h_{22}^{(i)(i)}-h_{12}^{(i)(i)}h_{21}^{(i)(i)}}F_2^{(i)}(\alpha)\right]e^{ix_i\alpha}d\alpha \quad (66)$$

$$\tau_{x_iy_i}(x_i, y_i^+) = -\frac{i}{2\pi}\int_{-\infty}^{\infty}\alpha\left[\frac{n_1 h_{22}^{(i)(i)} e^{n_{1y_i}^{(i)}} - n_2 h_{21}^{(i)(i)} e^{n_{2y_i}^{(i)}}}{h_{11}^{(i)(i)} h_{22}^{(i)(i)} - h_{12}^{(i)(i)} h_{21}^{(i)(i)}} F_1^{(i)}(\alpha) + \frac{n_2 h_{11}^{(i)(i)} e^{n_{2y_i}^{(i)}} - n_1 h_{12}^{(i)(i)} e^{n_{1y_i}^{(i)}}}{h_{11}^{(i)(i)} h_{22}^{(i)(i)} - h_{12}^{(i)(i)} h_{21}^{(i)(i)}} F_2^{(i)}(\alpha)\right] e^{ix_i\alpha} d\alpha \quad (67)$$

$$\sigma_{x_ix_i}(x_i, y_i^-) = \frac{1}{2\pi}\int_{-\infty}^{\infty}\left[\frac{n_3^2 N_{22}^{(i)(i)} e^{n_{3y_i}^{(i)}} - n_4^2 N_{21}^{(i)(i)} e^{n_{4y_i}^{(i)}}}{N_{11}^{(i)(i)} N_{22}^{(i)(i)} - N_{12}^{(i)(i)} N_{21}^{(i)(i)}} F_1^{(i)}(\alpha) + \frac{n_4^2 N_{11}^{(i)(i)} e^{n_{4y_i}^{(i)}} - n_3^2 N_{12}^{(i)(i)} e^{n_{3y_i}^{(i)}}}{N_{11}^{(i)(i)} N_{22}^{(i)(i)} - N_{12}^{(i)(i)} N_{21}^{(i)(i)}} F_2^{(i)}(\alpha)\right] e^{ix_i\alpha} d\alpha \quad (68)$$

$$\sigma_{y_iy_i}(x_i, y_i^-) = -\frac{1}{2\pi}\int_{-\infty}^{\infty}\alpha^2\left[\frac{N_{22}^{(i)(i)} e^{n_{3y_i}^{(i)}} - N_{21}^{(i)(i)} e^{n_{4y_i}^{(i)}}}{N_{11}^{(i)(i)} N_{22}^{(i)(i)} - N_{12}^{(i)(i)} N_{21}^{(i)(i)}} F_1^{(i)}(\alpha) + \frac{N_{11}^{(i)(i)} e^{n_{4y_i}^{(i)}} - N_{12}^{(i)(i)} e^{n_{3y_i}^{(i)}}}{N_{11}^{(i)(i)} N_{22}^{(i)(i)} - N_{12}^{(i)(i)} N_{21}^{(i)(i)}} F_2^{(i)}(\alpha)\right] e^{ix_i\alpha} d\alpha \quad (69)$$

$$\tau_{x_iy_i}(x_i, y_i^-) = -\frac{i}{2\pi}\int_{-\infty}^{\infty}\alpha\left[\frac{n_3 N_{22}^{(i)(i)} e^{n_{3y_i}^{(i)}} - n_4 N_{21}^{(i)(i)} e^{n_{4y_i}^{(i)}}}{N_{11}^{(i)(i)} N_{22}^{(i)(i)} - N_{12}^{(i)(i)} N_{21}^{(i)(i)}} F_1^{(i)}(\alpha) + \frac{n_4 N_{11}^{(i)(i)} e^{n_{4y_i}^{(i)}} - n_3 N_{12}^{(i)(i)} e^{n_{3y_i}^{(i)}}}{N_{11}^{(i)(i)} N_{22}^{(i)(i)} - N_{12}^{(i)(i)} N_{21}^{(i)(i)}} F_2^{(i)}(\alpha)\right] e^{ix_i\alpha} d\alpha \quad (70)$$

where

$$N_{11}^{(i)} = \frac{\kappa + 1}{8\mu_0}(n_1^{(i)} - n_3^{(i)})(n_3^{(i)} - n_2^{(i)})$$

$$N_{12}^{(i)} = \frac{\kappa + 1}{8\mu_0}(n_4^{(i)} - n_2^{(i)})(n_1^{(i)} - n_4^{(i)})$$

$$N_{21}^{(i)} = \frac{i\alpha - \beta}{8\mu_0}(\alpha^2(1 + \kappa_2) - \delta_i^2(\kappa - 3)) \times \left[\frac{(n_1^{(i)} - n_3^{(i)})(n_3^{(i)} - n_2^{(i)})}{(\delta_i - n_1^{(i)})(\delta_i - n_2^{(i)})(\delta_i - n_3^{(i)})}\right]$$

$$N_{22}^{(i)} = \frac{i\alpha - \beta}{8\mu_0}(\alpha^2(1 + \kappa_2) - \delta_i^2(\kappa - 3)) \times \left[\frac{(n_4^{(i)} - n_2^{(i)})(n_1^{(i)} - n_4^{(i)})}{(\delta_i - n_2^{(i)})(\delta_i - n_1^{(i)})(\delta_i - n_4^{(i)})}\right] \quad (71)$$

and h_{ij}'s are defined as in (49) for the ith crack. Assume that there are n cracks present, so the stresses for the ith crack can be expressed as

$${}_i\sigma_{y_iy_i}^T(x_i, y_i) = \sigma_{y_iy_i}^i(x_i, y_i) + \sum_{j=i+1}^{n}\sigma_{y_jy_j}^j[x_j(x_i, y_i), y_j(x_i, y_i)]$$

$${}_i\tau_{y_iy_i}^T(x_i, y_i) = \tau_{y_iy_i}^i(x_i, y_i) + \sum_{j=i+1}^{n}\tau_{y_jy_j}^j[x_j(x_i, y_i), y_j(x_i, y_i)] \quad (72)$$

where $\sigma_{y_iy_i}^{(j)}$, $\tau_{x_iy_i}^{(j)}$ are found using (63); they are evaluated asymptotically as in (9) and (10), respectively. Thus, the final singular integral equation for the ith crack can be expressed as

$$\left({}_i - \frac{\kappa + 1}{2\mu(x_i, 0)} p_1^{(i)}(x_i)\right) = \frac{1}{\pi}\int_{a_i}^{b_i}\frac{f_2^{(i)}(t_i)}{t_i - x_i}dt_i + \frac{1}{\pi}\int_{a_i}^{b_i}k_{12}^{(i)}(x_i, t_i)f_2^{(i)}(t_i)dt_i - \frac{1}{\pi}\int_{a_i}^{b_i}\frac{\beta_i}{2}Ci(U_i(t_i - x_i))\Bigg]f_2^{(i)}(t_i)dt_i + \frac{1}{\pi}\int_{a_i}^{b_i}k_{11}^{(i)}(x_i, t_i)f_1^{(i)}(t_i)dt_i - \frac{1}{\pi}\int_{a_i}^{b_i}\frac{\delta_i}{2}Ci(U(t_i - x_i))\Bigg]f_1^{(i)}(t_i)dt_i + \sum_{j=i+1}^{n}\Bigg\{\frac{1}{\pi}\int_{a_j}^{b_j}\Bigg[\frac{a_{11}^{(j)}(x_i^2\sin^2\Delta\theta_i - (t_j - x_i\cos\Delta\theta_i)^2)}{(x_i^2\sin^2\Delta\theta_i + (t_j - x_i\cos\Delta\theta_i)^2)^2} + \frac{c_{11}^{(j)}x_i\sin\Delta\theta_i((t_j - x_i\cos\Delta\theta_i)^2 + x_i^2\sin^2\Delta\theta_i)}{(x_i^2\sin^2\Delta\theta_i + (t_j - x_i\cos\Delta\theta_i)^2)^2} + \frac{2b_{11}^{(j)}x_i\sin\Delta\theta_i(t_j - x_i\cos\Delta\theta_i)}{(x_i^2\sin^2\Delta\theta_i + \cos^2\Delta\theta_i(t - x_i)^2)^2} + \frac{(t_j - x_i\cos\Delta\theta_i)d_{11}^{(j)}(x_i^2\sin^2\Delta\theta_i + (t_j - x_i\cos\Delta\theta_i)^2)}{(x_i^2\sin^2\Delta\theta_i + (t_j - x_i\cos\Delta\theta_i)^2)^2}\Bigg] \times f_1^{(j)}(t_j)dt_j + \frac{1}{\pi}\int_{a_j}^{b_j}k_{11}^{(j)}(x_i, t_j)f_1^{(j)}(t_j)dt_j + \frac{1}{\pi}\int_{a_j}^{b_j}\Bigg[\frac{a_{12}^{(j)}(x_i^2\sin^2\Delta\theta_i - (t_j - x_i\cos\Delta\theta_i)^2)}{(x_i^2\sin^2\Delta\theta_i + (t_j - x_i\cos\Delta\theta_i)^2)^2} + \frac{c_{12}^{(j)}x_i\sin\Delta\theta_i((t_j - x_i\cos\Delta\theta_i)^2 + x_i^2\sin^2\Delta\theta_i)}{(x_i^2\sin^2\Delta\theta_i + (t_j - x_i\cos\Delta\theta_i)^2)^2} + \frac{2b_{12}^{(j)}x_i\sin\Delta\theta_i(t_j - x_i\cos\Delta\theta_i)}{(x_i^2\sin^2\Delta\theta_i + \cos^2\Delta\theta_i(t - x_i)^2)^2} + \frac{d_{12}^{(j)}(t_j - x_i\cos\Delta\theta_i)(x_i^2\sin^2\Delta\theta_i + (t_j - x_i\cos\Delta\theta_i)^2)}{(x_i^2\sin^2\Delta\theta_i + (t_j - x_i\cos\Delta\theta_i)^2)^2}\Bigg] \times f_2^{(j)}(t_j)dt_j + \frac{1}{\pi}\int_{a_j}^{b_j}k_{12}^{(j)}(x_i, t_j)f_2^{(j)}(t_j)dt_j\Bigg\} \quad (73)$$

$$\left({}_i - \frac{\kappa + 1}{2\mu(x_i, 0)} p_2^{(i)}(x_i)\right) = \frac{1}{\pi}\int_{a_i}^{b_i}\frac{f_1^{(i)}(t_i)}{t_i - x_i}dt_i + \frac{1}{\pi}\int_{a_i}^{b_i}k_{21}^{(i)}(x_i, t_i)f_1^{(i)}(t_i)dt_i$$

$$- \frac{1}{\pi}\int_{a_i}^{b_i} \frac{\beta_i}{2} Ci(U_i(t_i - x_i)) \Big] f_1^{(i)}(t_i)dt_i$$

$$+ \frac{1}{\pi}\int_{a_i}^{b_i} k_{22}^{(i)}(x_i, t_i) f_2^{(i)}(t_i)dt_i$$

$$- \frac{1}{\pi}\int_{a_i}^{b_i} \frac{\delta_i}{2} Ci(U(t_i - x_i)) \Big] f_2^{(i)}(t_i)dt_i$$

$$+ \sum_{j=i+1}^{n} \left\{ \frac{1}{\pi}\int_{a_j}^{b_j} \left[\frac{a_{21}^{(j)}(x_i^2 \sin^2 \Delta\theta_i - (t_j - x_i \cos \Delta\theta_i)^2)}{(x_i^2 \sin^2 \Delta\theta_i + (t_j - x_i \cos \Delta\theta_i)^2)^2} \right.\right.$$

$$+ \frac{c_{21}^{(j)} x_i \sin \Delta\theta_i((t_j - x_i \cos \Delta\theta_i)^2 + x_i^2 \sin^2 \Delta\theta_i)}{(x_i^2 \sin^2 \Delta\theta_i + (t_j - x_i \cos \Delta\theta_i)^2)^2}$$

$$+ \frac{2b_{21}^{(j)} x_i \sin \Delta\theta_i (t_j - x_i \cos \Delta\theta_i)}{(x_i^2 \sin^2 \Delta\theta_i + \cos^2 \Delta\theta_i (t - x_i)^2)^2}$$

$$+ \frac{(t_j - x_i \cos \Delta\theta_i) d_{21}^{(j)}(x_i^2 \sin^2 \Delta\theta_i + (t_j - x_i \cos \Delta\theta_i)^2)}{(x_i^2 \sin^2 \Delta\theta_i + (t_j - x_i \cos \Delta\theta_i)^2)^2}$$

$$\times f_1^{(j)}(t_j)dt_j + \frac{1}{\pi}\int_{a_j}^{b_j} k_{21}^{(j)}(x_i, t_j) f_1^{(j)}(t_j)dt_j$$

$$+ \frac{1}{\pi}\int_{a_j}^{b_j} \left[\frac{a_{22}^{(j)}(x_i^2 \sin^2 \Delta\theta_i - (t_j - x_i \cos \Delta\theta_i)^2)}{(x_i^2 \sin^2 \Delta\theta_i + (t_j - x_i \cos \Delta\theta_i)^2)^2} \right.$$

$$+ \frac{c_{22}^{(j)} x_i \sin \Delta\theta_i((t_j - x_i \cos \Delta\theta_i)^2 + x_i^2 \sin^2 \Delta\theta_i)}{(x_i^2 \sin^2 \Delta\theta_i + (t_j - x_i \cos \Delta\theta_i)^2)^2}$$

$$+ \frac{2b_{22}^{(j)} x_i \sin \Delta\theta_i (t_j - x_i \cos \Delta\theta_i)}{(x_i^2 \sin^2 \Delta\theta_i + \cos^2 \Delta\theta_i (t - x_i)^2)^2}$$

$$+ \frac{d_{22}^{(j)}(t_j - x_i \cos \Delta\theta_i)(x_i^2 \sin^2 \Delta\theta_i + (t_j - x_i \cos \Delta\theta_i)^2)}{(x_i^2 \sin^2 \Delta\theta_i + (t_j - x_i \cos \Delta\theta_i)^2)^2}$$

$$\left.\left. \times f_2^{(j)}(t_j)dt_j + \frac{1}{\pi}\int_{a_j}^{b_j} k_{22}^{(j)}(x_i, t_j) f_2^{(j)}(t_j)dt_j \right\} \quad (74)$$

where the constants $a_{mn}^{(j)}$, $b_{mn}^{(j)}$, $c_{mn}^{(j)}$, $d_{mn}^{(j)}$, and $k_{mn}^{(j)}$ can be found either in Shbeeb (1998) or in Shbeeb, Binienda, and Kreider (1998). The kernels $k_{mn}^{(i)}$ are defined as in Eqs. (58) through (61) using Eq. (62) and $\Delta\theta_i = \theta_{i+1} - \theta_i$.

The companion paper, Part II (Shbeeb et al., 1999), presents numerical technique of solution, validation of the results, and parametric studies. In particular, Eqs. (56) and (57), which include spatially varying material properties, are used to examine the influence of geometrical and material parameters on the magnitudes of the stress intensity factors and strain energy release rates.

Conclusions

The general solution to the mixed boundary value problem for crack analysis in a functionally graded material is obtained by a new semianalytic methodology in Fourier transform space. The stress intensity factors and strain energy release rates are computed. The solution for a single crack is generalized to the case of fully interactive multiple cracks. The analysis reduces to a set of singular integral equations. Asymptotic expansions of the singular terms are converted analytically to real space for numerical efficiency and accuracy. The numerical code can be run on a PC, and produces accurate results that compare favorably with results found in the literature, as demonstrated in Part II of this work.

Acknowledgment

This work was supported in part by NASA Lewis Research Center through grant NAG3-2069 and by The University of Akron. We are grateful to Dr. Gary Halford at NASA for his helpful suggestions and encouragement.

References

Abramowitz, A., and Stegun, I. E., 1964, *Handbook of Mathematical Functions*, National Bureau of Standards.

Asish, G., Yoshinari, M., Ivar, R., and John, J. L., eds., 1997, "Functionally Graded Materials," *Ceramic Trans.*, Vol. 76, The American Ceramic Society, Westerville, OH.

Delale, F., and Erdogan, F., 1983, "The Crack Problem for a Non-Homogeneous Plane," ASME JOURNAL OF APPLIED MECHANICS, Vol. 50, pp. 609–614.

Delale, F., and Erdogan, F., 1988, "On the Mechanical Modeling of the Interfacial Region in Bonded Half-Planes," ASME JOURNAL OF APPLIED MECHANICS, Vol. 55, pp. 317–324.

Erdogan, F., 1995, "Fracture Mechanics of Functionally Graded Materials," *Composites Engineering*, Vol. 5, No. 7, pp. 753–770.

Erdogan, F., and Wu, H. B., 1996, "Crack Problems in FGM Layers under Thermal Stresses," *Journal of Thermal Stresses*, Vol. 19, pp. 237–265.

Hirano, T., Yamada, T., Teraki, J., Niino, M., and Kumakawa, A., 1988, "A Study on Functionally Gradient Material Design System for a Thrust Chamber," *Proc. 16th Int. Symp. On Space Technology and Science*, Sapporo, Japan.

Hirano, T., and Yamada, T., 1988, "Multi-Paradigm Expert System Architecture Based Upon the Inverse Design Concept," Int. Workshop on Artificial Intelligence for Industrial Applications, Hitachi, Japan.

Holt, J. B., Mitsue, K., Toshio, H., and Zuhir, A. M., eds., 1993, "Functionally Graded Materials," *Ceramic Trans.*, Vol. 34, The American Ceramic Society, Westerville, OH.

Kawasaki, A., and Watanabe, R., 1990, "Fabrication of Sintered Functionally Gradient Material by Powder Spray Forming Process," FGM-90, *Proc. of the 1st Int. Symp. on FGM*, Sendai, Japan.

Konda, N., and Erdogan, F., 1994, "The Mixed Mode Crack Problem in a Non-Homogeneous Elastic Medium," *Engineering Fracture Mechanics*, Vol. 47, No. 4, pp. 533–545.

Needleman, A., and Suresh, S., eds., 1996, "Mechanics and Physics of Layered and Graded Materials," *Journal of the Mechanics and Physics of Solids*, Vol. 44, No. 5.

Niino, M., and Maeda, S., 1990, "Recent Development Status of Functionally Gradient Materials," *I. S. I. J. Int.*, Vol. 30, pp. 699–703.

Pindera, M-J., Arnold, S. M., and Hui, D., eds., 1994, "Use of Composites in Functionally Graded Materials," *Composites Engineering*, Vol. 4, No. 1.

Pindera, M-J., Aboudi, J., Arnold, S. M., and Jones, W. F., eds., 1995, "Use of Composites in Multi-Phased and Functionally Graded Materials," *Composites Engineering*, Vol. 5, No. 7.

Pindera, M-J., Aboudi, J., Glaeser, A., and Arnold, S. M., eds., 1997, "Use of Composites in Functionally Graded Materials," *Composites* (Part B: Engineering), Vol. 28B, No. 1–2.

Shbeeb, N. I., 1998, "General Crack Problems in Functionally Graded Materials," Ph.D. dissertation, The University of Akron, Akron, OH.

Shbeeb, N. I., Binienda, W. K., and Kreider, K. L., 1998, "Analysis of Multiple Cracks in an Infinite Functionally Graded Plate," NASA CR208676.

Shbeeb, N. I., Binienda, W. K., and Kreider, K. L., 1999, "Analysis of the Driving Forces for Multiple Cracks in an Infinite Nonhomogeneous Plate, Part II: Numerical Solutions," ASME JOURNAL OF APPLIED MECHANICS, Vol. 66, pp.

N. I. Shbeeb

W. K. Binienda

Department of Civil Engineering,
The University of Akron,
Akron, OH 44325-3905

K. L. Kreider
Department of Mathematics and
Computer Science,
The University of Akron,
Akron, OH 44325-4002

Analysis of the Driving Forces for Multiple Cracks in an Infinite Nonhomogeneous Plate, Part II: Numerical Solutions

In Part I of this work, an analytical model was developed for the fundamental solution for a crack embedded in an infinite nonhomogeneous plate. This fundamental solution is used here to generate the stress intensity factors and strain energy release rates for fully interactive multiple crack problems. Also, a numerical technique used in solving the singular integral equation in Part I is presented, along with a parametric study. The parametric study addresses the influence of crack distance, relative angular orientation, and the coefficient of nonhomogeneity on the crack driving forces. The strain energy release rate is recommended for use as a crack propagation criterion because it depends on the local material properties as well as all the remaining parameters contained in the stress intensity factors.

Introduction

The system of singular integral equations for a crack embedded in an infinite nonhomogeneous material was obtained in Part I (Eqs. (56) and (57)). The singular part and two additional terms were extracted using asymptotic expansions of the kernels at infinity, producing an efficient and accurate method for evaluation of the stress intensity factors and strain energy release rate. Also, the fundamental solution was used to formulate the solution for multiple cracks in an infinite nonhomogeneous plate (see Eqs. (73) and (74) in Part I).

Here in Part II, the numerical technique used in solving the system of integral equations is discussed, using as an example Eqs. (56) and (57) of Part I. Then, a parametric study is conducted to examine the influence of each parameter of the solutions on the stress intensity factor and strain energy release rate.

Numerical Solution Technique

The singular integral Eqs. (56) and (57) in Part I need to be normalized before any numerical integration scheme can be applied. Introduce the following normalized quantities:

$$t = \frac{b-a}{2}s + \frac{b+a}{2}, \quad x_1 = \frac{b-a}{2}r + \frac{b+a}{2},$$

$$k_{ij}^*(r, s) = \frac{b-a}{2}k_{ij}(x_1, t)$$

$$f_i^*(s) = f_i(t), \quad p_i^*(r) = p_i(x), \quad \mu^*(r, 0) = \mu(x_1, 0)$$

$$(i, j) = (1, 2).$$

Then the integral equations can be rewritten as

$$-\frac{\kappa+1}{2\mu^*(r,0)}p_i^*(r) = \frac{1}{\pi}\int_{-1}^{1}\sum_{j=1}^{2}\left[\frac{\chi_{ij}}{s-r} + k_{ij}^*(r, s) - \frac{\chi_{ij}\beta}{2}Ci\left(U\left(\frac{b-a}{2}(s-r)\right)\right) - \frac{\delta_{ij}\delta}{2}Ci\left(U\left(\frac{b-a}{2}(s-r)\right)\right)\right]f_i^*(s)ds, \quad (i = 1, 2) \quad (1)$$

where

$$\chi_{ij} = \begin{pmatrix} 0 & 1 \\ 1 & 0 \end{pmatrix}, \quad \delta_{ij} = \begin{pmatrix} 1 & 0 \\ 0 & 1 \end{pmatrix}. \quad (2)$$

The unknown singular functions $f_i(s)$ consist of a known singular weight $w(s)$ and unknown regular functions $g_i(s)$

$$f_i(s) = g_i(s)w(s) \quad (3)$$

where

$$w(s) = \frac{1}{\sqrt{1-s^2}}. \quad (4)$$

The integration of the Cauchy-type singular integral Eq. (1) is obtained using a numerical collocation technique such as the Lobatto-Chebyshev method, producing a system of algebraic equations in $g(t_i)$:

$$-\frac{\kappa+1}{2\mu^*(r_p,0)}p_i^*(r_p) = \sum_{j=1}^{2}\frac{1}{\pi}\sum_{k=1}^{n}\left[\frac{\chi_{ij}}{s_k-r_p} + k_{ij}^*(r_p, s_k) - \frac{\chi_{ij}\beta}{2}Ci\left(U\left(\frac{b-a}{2}(s_k-r_p)\right)\right) - \frac{\delta_{ij}\delta}{2}Ci\left(U\left(\frac{b-a}{2}(s_k-r_p)\right)\right)\right]g_j^*(s_k)w_k, \quad (i = 1, 2) \quad (5)$$

where $p = 1, \ldots, n-1$ and Ci is the cosine integral. Values for the abscissa s_k, weights w_k, and collocation points r_p, can be found in Binienda and Arnold (1995). In Eq. (5), there are $2n$ unknowns but only $(2n-2)$ linear equations. Consequently, two additional

Contributed by the Applied Mechanics Division of THE AMERICAN SOCIETY OF MECHANICAL ENGINEERS for publication in the ASME JOURNAL OF APPLIED MECHANICS.

Discussion on the paper should be addressed to the Technical Editor, Professor Lewis T. Wheeler, Department of Mechanical Engineering, University of Houston, Houston, TX 77204-4792, and will be accepted until four months after final publication of the paper itself in the ASME JOURNAL OF APPLIED MECHANICS.

Manuscript received by the ASME Applied Mechanics Division, June 16, 1998; final revision, Nov. 23, 1998. Associate Technical Editor: M.-J. Pindera.

Table 1 Validation of the solution

cγ	Konda and Erdogan (1994) $k_1(a)/\sqrt{c}$	Present Study $k_1(a)/\sqrt{c}$	Konda and Erdogan (1994) $k_2(a)/\sqrt{c}$	Present Study $k_2(a)/\sqrt{c}$
0.25	1.036	1.036	0.065	0.062
0.50	1.101	1.101	0.129	0.122
1.0	1.258	1.260	0.263	0.243

Table 2 Two collinear cracks in an isotropic plate

$\frac{r_d}{c}$	From literature				Present Method	
	Horri and Nemat-Nasser (1985)		Erdogan (1962)			
	Inner	Outer	Inner	Outer	Inner	Outer
0.22	---	---	1.45387	1.11741	1.45736	1.11786
0.50	1.2289	1.0811	1.22894	1.08107	1.22894	1.08107
0.857	1.1333	1.0579	1.13326	1.05786	1.13329	1.05787

equations are needed, which are furnished by the discrete single valuedness conditions

$$\sum_{k=1}^{n} g_i(s_k)w_k = 0 \quad i = 1, 2. \tag{6}$$

Equations (5) and (6) can be represented as follows:

$$[A]_{2n\times 2n}\{g\}_{2n} = \{P\}_{2n} \tag{7}$$

so the unknowns are obtained formally by

$$\{g\} = [A]^{-1}\{P\}. \tag{8}$$

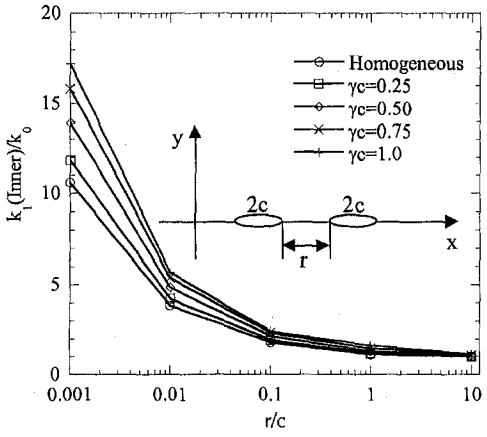

Fig. 1 Mode I normalized stress intensity factor versus normalized inner crack tips distance for two collinear horizontal cracks (σ_{yy} = 1.0, σ_{xx} = τ_{xy})

Finally, the stress intensity factor is written in terms of $g_1(s)$ and $g_2(s)$. Details appear in Shbeeb (1998); the results are

$$k_1(a) = \frac{2\sqrt{2}\mu_0}{(\kappa+1)\sqrt{b-a}} e^{\beta a} g_2(a)$$

$$k_1(b) = \frac{2\sqrt{2}\mu_0}{(\kappa+1)\sqrt{b-a}} e^{\beta b} g_2(b)$$

$$k_2(a) = \frac{2\sqrt{2}\mu_0}{(\kappa+1)\sqrt{b-a}} e^{\beta a} g_1(a)$$

$$k_2(b) = \frac{2\sqrt{2}\mu_0}{(\kappa+1)\sqrt{b-a}} e^{\beta b} g_1(b). \tag{9}$$

Note that the crack tips are represented in Eq. (8) by $a = s_1$, $b = s_n$. The strain energy release rates are defined as

$$G_1(a) = \frac{\pi(\kappa+1)}{8\mu_2(a,0)} k_1^2(a)$$

$$G_1(b) = \frac{\pi(\kappa+1)}{8\mu(b,0)} k_1^2(b)$$

$$G_2(a) = \frac{\pi(\kappa+1)}{8\mu(a,0)} k_2^2(a)$$

$$G_2(b) = \frac{\pi(\kappa+1)}{8\mu(b,0)} k_2^2(b). \tag{10}$$

It should be mentioned that the cosine integral in Eq. (5) contains an integrable singularity at $s = r$. However, the use of the Lobatto-Chebyshev method eliminates the need to do any analytic evaluation as long as care is taken to obtain numerical conver-

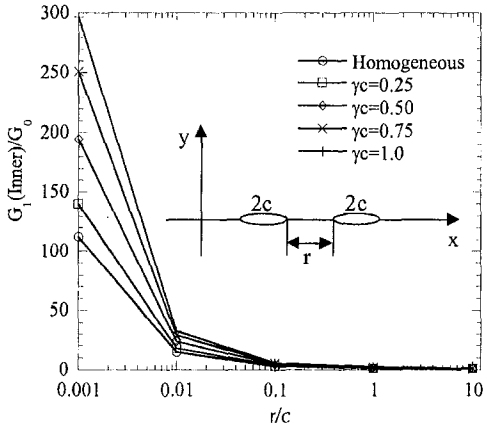

Fig. 2 Mode I normalized strain energy release rate versus normalized inner crack tips distance for two collinear horizontal cracks (σ_{yy} = 1.0, $\sigma_{xx} = \tau_{xy}$)

gence. A similar situation occurs with the step function in Eqs. (22) and (23) in Part I.

For validation, two simulations were run. First, the normalized Mode I stress intensity factor produced by this technique compares favorably to that of Konda and Erdogan (1994) over a range of nonhomogeneity constants γ, as summarized in Table 1. Second, the results for two collinear cracks embedded in an isotropic plate are shown in Table 2 to match results in the literature over a range of distances between crack tips.

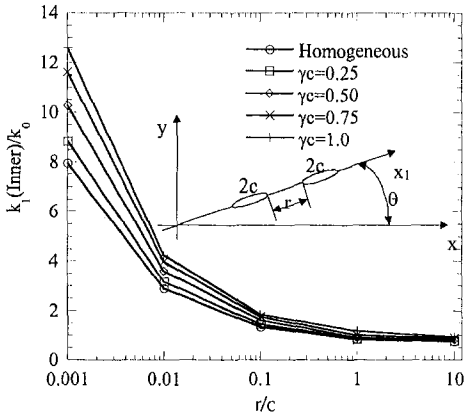

(a)

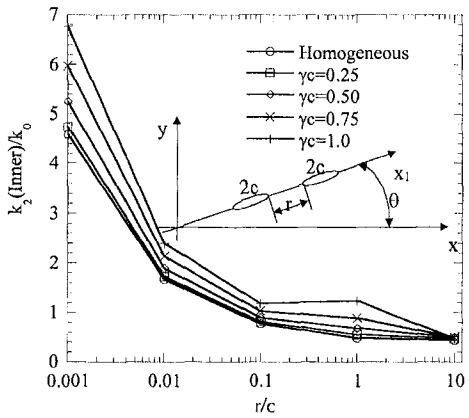

(b)

Fig. 3 Normalized stress intensity factor versus normalized inner crack tips distance for two collinear cracks along the θ = 30 deg (σ_{yy} = 1.0, $\sigma_{xx} = \tau_{xy}$); (*a*) Mode I, (*b*) Mode II

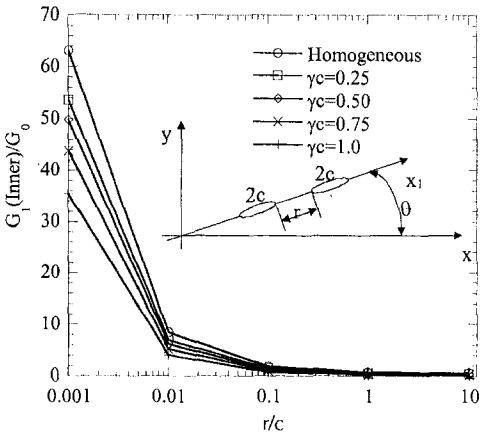

(a)

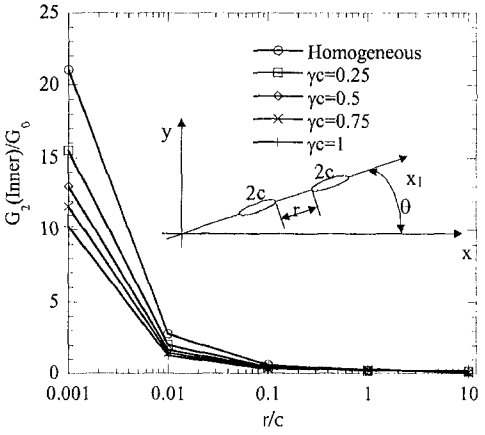

(b)

Fig. 4 Normalized strain energy release rate versus normalized inner crack tips distance for two collinear cracks along the θ = 30 deg (σ_{yy} = 1.0, $\sigma_{xx} = \tau_{xy}$); (*a*) Mode I, (*b*) Mode II

Parametric Studies

In the following studies, the length of each crack is chosen to be $2c = 2$. The infinite plate is subjected to normal stress $\sigma_{yy} = 1$ psi along the y global direction. Each crack is located along its local x_i-axis, oriented at angle θ_i (with respect to the global x-axis). All geometrical dimensions are normalized with respect to c. The parametric studies are presented for the normalized Mode I and Mode II stress intensity factor, i.e., k_1/k_0 and k_2/k_0, and normalized strain energy release rate, i.e., G_1/G_0 and G_2/G_0, where $k_0 = \sigma_{yy}\sqrt{c}$ and $G_0 = k_0\pi(\kappa+1)/8\mu_0$. The nonhomogeneity constant γ is used to define the shear modulus by $\mu_2 = \mu_0 e^{\gamma y}$.

The first study takes into consideration the problem of two collinear horizontal cracks (see insert in Fig. 1 or 2). Figures 1 and 2 show the Mode I normalized stress intensity factor and Mode I normalized strain energy release rate (respective Modes II are zero) versus the logarithm of the normalized crack-tip distance r/c. Notice that as the distance between the cracks decreases, the stress intensity factor and strain energy release rate increase for all positive nonhomogeneity constants γ. The homogeneous case is represented by $\gamma = 0$. Both driving forces increase as γ increases because the material becomes locally stiffer. The increase is especially significant for a crack-tip distance less than 0.01 because of increased crack interaction.

The case of collinear inclined cracks at 30 deg from the horizontal axis is shown in Figs. 3 and 4. Mode I stress intensity factor, shown in Fig. 3(*a*), has larger magnitudes than the corresponding Mode II stress intensity factor (shown in Fig. 3(*b*)) for both homogeneous and nonhomogeneous materials because the normal

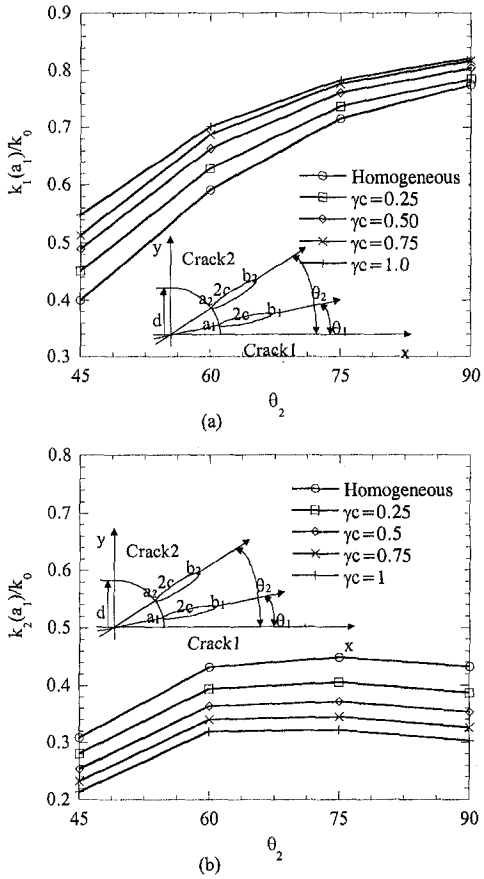

Fig. 5 Normalized stress intensity factor at tip a_1 versus crack (2) orientation angle θ_2 for two inclined cracks ($\sigma_{yy} = 1.0$, $\sigma_{xx} = \tau_{xy} = 0.0$, $d = 1.0$, $\theta_1 = 30$ deg); (*a*) Mode I, (*b*) Mode II

traction components applied at the crack surface are larger than the shear component. As before, both modes show an increase in SIF with decreasing crack-tip distance and with increasing nonhomogeneity γ.

Figures 4(*a*) and 4(*b*) display Mode I and II strain energy release rate. The magnitude of Mode I strain energy release rate is almost three times larger than the corresponding Mode II strain energy release rate. Both modes of strain energy release rate increase with decreasing normalized crack-tip distance r/c (similar to stress intensity factor) and with decreases in nonhomogeneity, γ, (different from stress intensity factor). It should be pointed out that the material stiffness at each crack tip dominates the results for strain energy release rate to the point of reversing the trend in behavior of stress intensity factor with respect to γ. Also, note for $r/c > 1$ no discernable difference in strain energy release rate is observed.

The case of two cracks located along two different local radial axes at distance $d = 1$ from the origin is shown in the remaining figures. The location of the crack 1 is kept constant at 30 deg while orientation of the second crack is changed from 45 to 90 deg. Both stress intensity factor and strain energy release rate are shown for each crack tip versus the orientation angle of the second crack.

Figures 5(*a*) and 5(*b*) display Mode I and II SIF while Figs. 6(*a*) and 6(*b*) represent both modes of strain energy release rate at the left crack tip of crack 1. Notice that when the second crack approaches the first crack, the tip a_1 is shielded and all driving force components are significantly reduced. Mode II stress intensity factor has its maximum at an orientation angle of the second crack of about 70 deg. As before, by increasing local material stiffness (increasing γ), higher magnitudes for Mode I stress intensity factor and lower magnitudes for Mode II stress intensity factor are produced.

Both modes of strain energy release rate depend not only on the square of the stress intensity factor but also on the material stiffness at the crack tip. This influence is especially evident in Figs. 5(*a*) and 6(*a*) where the homogeneous case produces the smallest Mode I strain energy release rate at orientation angle 45 deg, similar to the corresponding stress intensity factor. However, the homogeneous Mode I strain energy release rate curve increases for higher angles, in contrast to the corresponding stress intensity factor, which decreases.

The difference in behavior of stress intensity factor and strain energy release rate is even better shown in Figs. 7 and 8. Here the shielding effect does not exhibit itself. Both modes of stress intensity factor are smallest for a homogeneous material (see Figs. 7(*a*) and 7(*b*) for Mode I and II stress intensity factor), while both components of strain energy release rate are largest (see Figs. 8(*a*) and 8(*b*) for Mode I and II strain energy release rate), because of the influence of the crack-tip material stiffness. Hence, the remaining parametric studies are presented with strain energy release rate only, as it is the more complete driving force parameter.

The results for the left crack tip of the second crack are shown in Figs. 9 and 10. Mode I strain energy release rate monotonically decreases to almost zero at 75 deg, and at approximately 50 deg does not depend on γ, as shown in Fig. 9(*a*). In the 45–50 deg range, the homogeneous case produces the highest Mode I strain energy release rate while the smallest strain energy release rate is found in the 50–90 deg range. Mode II strain energy release rate is higher than Mode I for orientation angle 45–90 due to the dominant shear traction component applied at the crack surface. Both modes decrease with increasing orientation angle, as shown in Fig. 9(*b*).

Mode I strain energy release rate at the b_2 crack tip is shown in Fig. 10(*a*). For all orientation angles, the homogeneous case yields

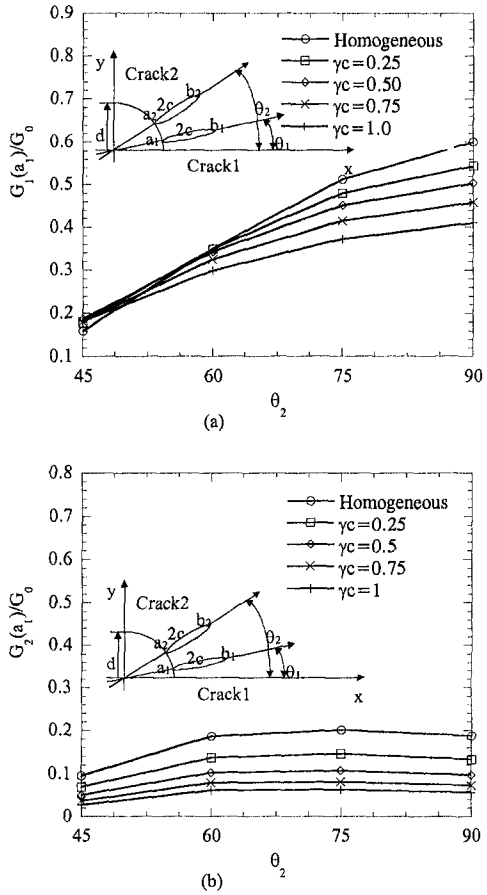

Fig. 6 Normalized strain energy release rate at tip a_1 versus crack (2) orientation angle θ_2 for two inclined cracks ($\sigma_{yy} = 1.0$, $\sigma_{xx} = \tau_{xy} = 0.0$, $d = 1.0$, $\theta_1 = 30$ deg); (*a*) Mode I, (*b*) Mode II

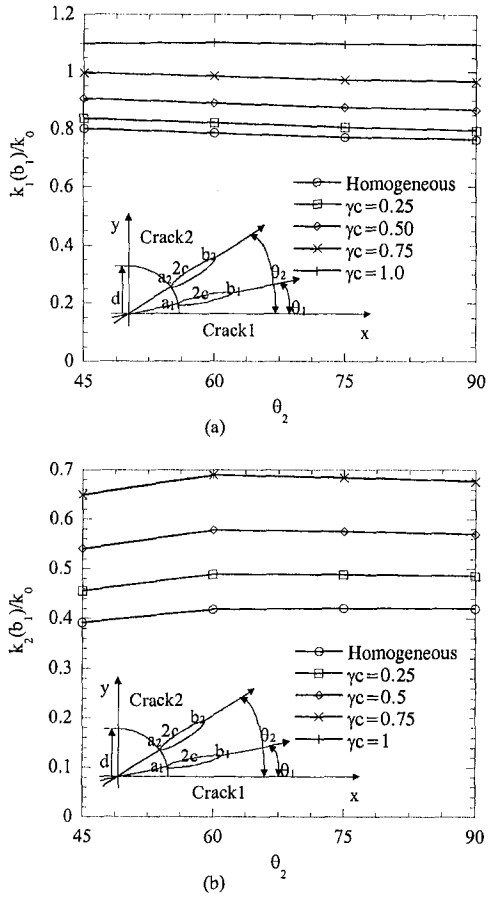

Fig. 7 Normalized stress intensity factor at tip b_1 versus crack (2) orientation angle θ_2 for two inclined cracks ($\sigma_{yy} = 1.0$, $\sigma_{xx} = \tau_{xy} = 0.0$, $d = 1.0$, $\theta_1 = 30$ deg); (*a*) Mode I, (*b*) Mode II

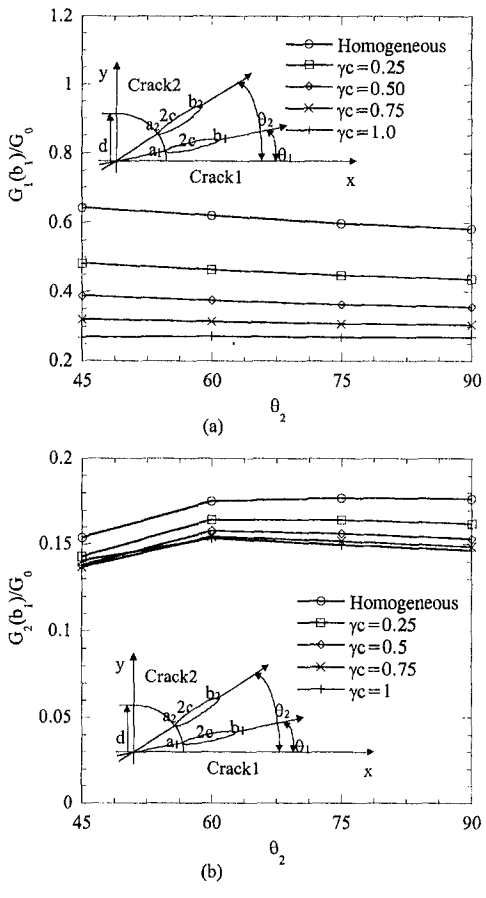

Fig. 8 Normalized strain energy release rate at tip b_1 versus crack (2) orientation angle θ_2 for two inclined cracks ($\sigma_{yy} = 1.0$, $\sigma_{xx} = \tau_{xy} = 0.0$, $d = 1.0$, $\theta_1 = 30$ deg); (*a*) Mode I, (*b*) Mode II

the highest Mode I strain energy release rate. For all nonhomogeneity constants, Mode I strain energy release rate decreases with increasing orientation angles. The nonhomogeneous material with the highest γ also decreases to zero, but does so at a smaller angle because the crack tip remains closed. Mode II strain energy release rate is shown in Fig. 10(*b*). The trend here is not as clear; Mode II strain energy release rate is clearly the highest for large γ, but for smaller γ, the orientation angle plays an important role due to the applied traction forces at the crack surface. However, all the curves attain their maximum values around 55 deg.

All of these parametric studies demonstrate that the effect of the material properties, crack orientation, and location of the additional crack are interdependent and consequently produce behavior different for nonhomogeneous materials than for homogeneous materials. The model developed in this work can be used to study fracture problems in nonhomogeneous materials and can be used to tailor the properties in order to reduce driving force components and effectively increase the life of these materials.

Conclusions

The parametric studies presented here examine the effects of nonhomogeneity constant, crack orientation, and crack-tip distance on stress intensity factors and strain energy release rates for multiple cracks. They reveal that both stress intensity factors and strain energy release rates are highly dependent not only on the crack geometrical parameters (crack orientation, location, and relative distance), but also on the value of the nonhomogeneity constant γ and the local stiffness of the material at each crack tip.

The results demonstrate that the driving forces can be amplified by collinear crack orientation or can be reduced by the shielding effect between cracks above or below. The character of the amplification or shielding remains similar for nonhomogeneous materials, but in most cases, increasing the nonhomogeneity increases the stress intensity factor and reduces the strain energy release rate.

The well-known one-to-one relation between the stress intensity factor and the strain energy release rate curves is not always valid for nonhomogeneous materials, because the strain energy release rate also depends on the material's elastic constants. Hence, the stress intensity factor curves may have a different character than the strain energy release rate curves. Consequently, the appropriate driving forces to be used as a crack propagation criterion need further investigation so as to determine which driving force (stress intensity factor or strain energy release rate) best correlates with appropriate experimental results. However, since the strain energy release rate includes the influence of the stress intensity factor and material stiffness at the tip, it is recommended that total strain energy release rates be used as the driving force parameter for cracks in nonhomogeneous materials.

For practical engineering applications, the effects of boundaries must be included in the singular integral equations, and correlation with experimental studies is required to determine the local toughness of functionally graded materials. Further research on this topic is warranted.

Acknowledgment

This work was supported in part by NASA Lewis Research Center through grant NAG3-2069 and by The University of Akron. We are grateful to Dr. Gary Halford at NASA for his helpful suggestions and encouragement.

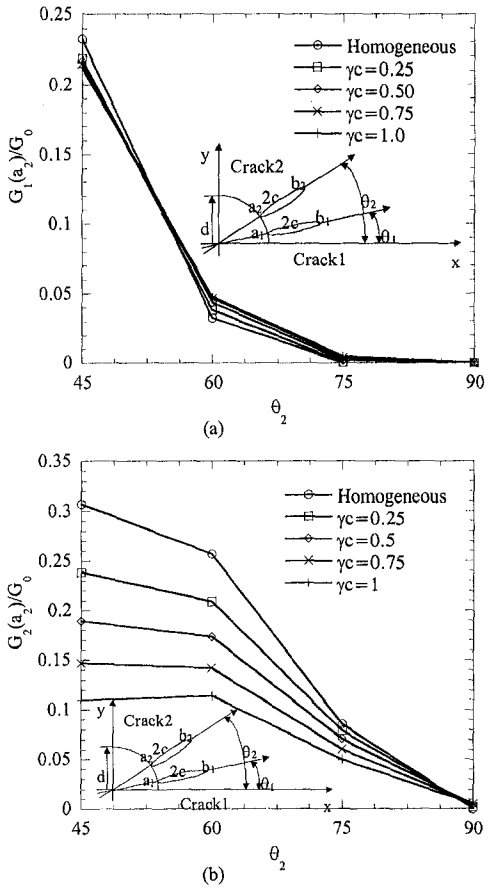

Fig. 9 Normalized strain energy release rate at tip a_2 versus crack (2) orientation angle θ_2 for two inclined cracks ($\sigma_{yy} = 1.0$, $\sigma_{xx} = \tau_{xy} = 0.0$, $d = 1.0$, $\theta_1 = 30$ deg); (*a*) Mode I, (*b*) Mode II

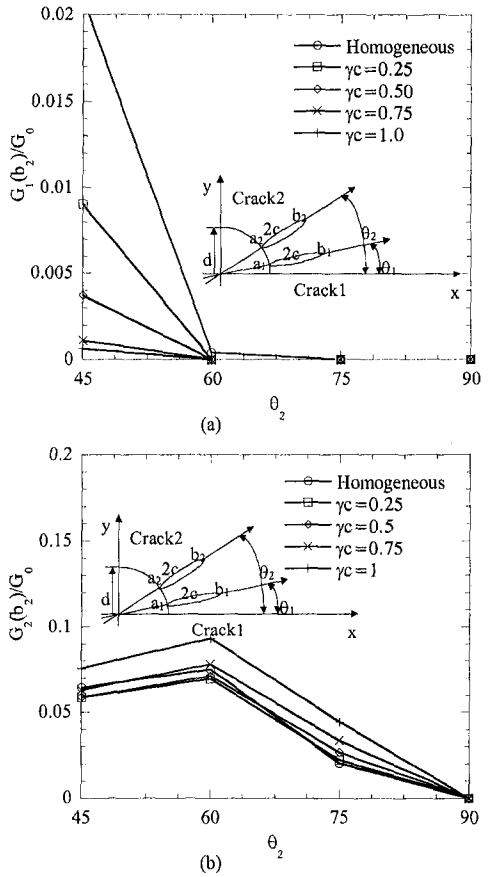

Fig. 10 Normalized strain energy release rate at tip b_2 versus crack (2) orientation angle θ_2 for two inclined cracks ($\sigma_{yy} = 1.0$, $\sigma_{xx} = \tau_{xy} = 0.0$, $d = 1.0$, $\theta_1 = 30$ deg); (*a*) Mode I, (*b*) Mode II

References

Binienda, W. K., and Arnold, S. M., 1995, "Driving Force Analysis in an Infinite Anisotropic Plate with Multiple Crack Interactions," *International Journal of Fracture,* Vol. 71, pp. 213–245.

Erdogan, F., 1962, "On the Stress Distribution in Plates with Collinear Cuts Under Arbitrary Loads," *Proceedings of the Fourth U.S. National Congress of Applied Mechanics,* Vol. 1, ASME, New York, pp. 547–553.

Horii, H., and Nemat-Nasser, S., 1985, "Elastic Fields of Interacting Inhomogeneities," *Int. J. Solids Structure,* Vol. 21, No. 7, pp. 731–745.

Konda, N., and Erdogan, F., 1994, "The Mixed Mode Crack Problem in a Non-Homogeneous Elastic Medium," *Engineering Fracture Mechanics,* Vol. 47, No. 4, pp. 533–545.

Shbeeb, N. I., 1998, "General Crack Problems in Functionally Graded Materials," Ph.D. dissertation, The University of Akron, Akron, OH.

Shbeeb, N. I., Binienda, W. K., and Kreider, K. L., 1999, "Analysis of the Driving Forces for Multiple Cracks in an Infinite Nonhomogeneous Plate, Part I: Theoretical Analysis," ASME JOURNAL OF APPLIED MECHANICS, Vol. 66, pp. 492–500.

Wavelet Analysis of Laser-Generated Surface Waves in a Layered Structure With Unbond Regions

T.-T. Wu[1]
Mem. ASME

Y.-Y. Chen

Institute of Applied Mechanics,
National Taiwan University,
Taipei, Taiwan

This paper presents the results on the utilization of a wavelet transform to study the dispersion of laser-generated surface waves in an epoxy-bonded copper-aluminum layered specimen with and without unbond areas. Laser ultrasonic experiments based on the point-source/point-receiver (PS/PR) technique were undertaken to measure surface wave signals in a layered specimen. The wavelet transform with a Morlet wavelet function was adopted to analyze the group velocity dispersion of the surface wave signals. A novel hybrid formula for group velocity dispersion is proposed for measurements across unbond regions. Results and data obtained are in good agreement with calculated and experimental dispersion curves. The general behavior of the group velocity dispersion for different measurement configurations can be utilized to differentiate the unbond regions in a layered structure.

1 Introduction

The detection of delamination and/or bonding quality in bonded structures is of practical importance in the NDE of composite structures such as layered fiber-reinforced composites, brazed metallic tools, etc. Although ultrasonic methods are available for some on-line monitoring of the manufacturing process, the utilization of liquid couplants prevents some important applications such as on-line monitoring of hot and moving objects. As such, based on this line of thinking, laser ultrasonics provides a useful alternative method for monitoring manufacturing processes. The noncontact feature and the ability of broadband signal generation of laser ultrasonic methods have demonstrated its great potential in NDE applications (Scruby and Drain, 1990). Past applications include using laser ultrasound to investigate the Lamb wave propagation phenomena in thin plates (Hutchins et al., 1989; Dewhurst et al., 1987; Nakano and Nagai, 1991) and to obtain the scan images of thin graphite/epoxy laminates and silicon wafers (Veidt and Sachse, 1994). In past studies (Spicer et al., 1990; Hurley et al., 1997), precise modeling of the laser source and theoretical computations of the elastic waves in thin as well as thick plates were made. Besides, restrictions on using the lowest plate modes to extract the elastic modulus and thickness information of a thin plate using laser-generated ultrasonic waves were noted. In addition, a laser-generated ultrasonic bulk wave (Castagnede et al., 1991) and surface wave (Wu and Chai, 1994; Chai and Wu, 1994) were also applied to the determination of elastic constants of anisotropic materials. In these studies, the deviation of the propagation direction between the energy velocity and phase velocity was considered. The elastic constants for the composite overlays can be measured by employing a line-focused pulsed laser (Doyle and Scala, 1991) in such a way that both the phase velocities and the skew angles between phase and group velocities of the skimming longitudinal waves on the surface are measured to fit the elastic constants. Laser ultrasound has also been applied to the study of Lamb wave propagation in paper (Johnson et al., 1996). The results show that the lowest Lamb wave modes can be identified clearly with minimal damage to the paper. The laser-generated ultrasonic guided waves have recently been applied to layered isotropic (Wu and Chen, 1996) and carbon fiber-reinforced polymer composite laminates (Scudder et al., 1996). Results and data are in good agreement with the calculated and experimental results.

During the last decade, the wavelet transform has been explored and applied to analyze nonstationary transient signals that appear in different physical situations (Ruskai et al., 1992). For example, there are successful applications of the wavelet transform method in the dispersive analysis of elastic waves in structures (Onsay and Haddow, 1994; Kishimoto et al., 1995). In the area of laser ultrasound, Cho et al. (1996) utilized the wavelet transform to measure the group velocity of laser generated surface waves in metallic specimens with subsurface lateral defects. The mathematical theory and the associated advantages of the wavelet transform can be found in the review articles by Rioul and Vetterli (1991) and Hlawatsch and Boudreaux-Bartels (1992).

In this paper, we utilized the wavelet transform to study the dispersion of laser generated surface waves in an epoxy-bonded copper-aluminum layered specimen with and without an unbond area. Laser ultrasonic experiments, based on the point-source/point-receiver (PS/PR) technique, were conducted to measure surface wave signals in the layered specimen. A Nd:YAG laser was utilized as a point source and the elastic wave signals were received through the utilization of a PZT transducer with a small acting area. The received wave signals were then processed using the wavelet transform to obtain the dispersion as related to the fundamental surface wave mode. The influences of the bonding layer thickness and the unbond area on the group velocity dispersion of the fundamental surface wave mode were studied and discussed.

2 Wavelet Transform

The wavelet transform is one of the important linear time-frequency representations of signals, which map a one-dimensional signal of time into a two-dimensional function of time and frequency. In contrast to the short-time Fourier transform, a wavelet transform preserves the feature of automatically scaling

[1] To whom correspondence should be addressed.

Contributed by the Applied Mechanics Division of THE AMERICAN SOCIETY OF MECHANICAL ENGINEERS for publication in the ASME JOURNAL OF APPLIED MECHANICS.

Discussion on the paper should be addressed to the Technical Editor, Professor Lewis T. Wheeler, Department of Mechanical Engineering, University of Houston, Houston, TX 77204-4792, and will be accepted until four months after final publication of the paper itself in the ASME JOURNAL OF APPLIED MECHANICS.

Manuscript received by the ASME Applied Mechanics Division, Oct. 28, 1997; final revision, July 10, 1998. Associate Technical Editor: J. R. Barber.

the time window function to cover both high-frequency and low-frequency signal resolutions.

The mathematical definition of a wavelet transform of a signal $f(t)$ can be written as (Rioul and Vetterli, 1991)

$$W_f^{\psi}(a, b) = \int_{-\infty}^{\infty} f(t)\psi_{a,b}^*(t)dt \quad (1)$$

$$\psi_{a,b}(t) = |a|^{-1/2}\psi\left(\frac{t-b}{a}\right) \quad (2)$$

where the superscript "*" denotes the complex conjugate, $a, b \in \mathbf{R}$ and $a > 0$. The wavelet transform (Eq. (1)) is the inner product of the signal $f(t)$ and the wavelet function, $\psi_{a,b}(t)$ which measures the similarity between the signal and the wavelet functions. The wavelet functions $\psi_{a,b}(t)$ is a scaled and translated version of the basic wavelet $\psi(t)$ in which the parameter "a" determines the time scaling and parameter "b" determines the time shift (translation). From Eq. (2), it is easy to see that as the scale parameter a increases, the wavelet function $\psi_{a,b}(t)$ becomes dilated in time, and the wavelet analysis becomes more concentrated in its long-time behavior (low-frequency) of the signal. On the contrary, as the scale parameter a decreases, the wavelet function $\psi_{a,b}(t)$ becomes compressed in time, and we see that the wavelet analysis works best for high frequency signals. The coefficient of the wavelet transform indicates the similarity between the signal and a particular wavelet function quantitatively. In order to assure the existence of the inverse wavelet transform, the basic wavelet function is assumed to oscillate in time and $\int\psi(t)dt = 0$ (Rioul and Vetterli, 1991).

To analyze a digitized signal, the parameters a and b can be discretized according to $a = a_0^m$, $b = nb_0a_0^m$, where $a_0 > 1$ and m, n are integers. In particular, the choice of $a_0 = 2$ and $b_0 = 1$ has been shown to generate an orthonormal basis and preserve remarkable inversion property (Onsay and Haddow, 1994). With the discrete parameters a and b, the discretized wavelet transform can be written as

$$DW_f^{\psi}(a_0^m, nb_0a_0^m) = \sum_{k=0}^{N-1} \frac{1}{\sqrt{a_0^m}}\psi^*\left(\frac{k\Delta t - nb_0a_0^m}{a_0^m}\right)f(k\Delta t) \quad (3)$$

where Δt is the sampled time interval. The choice of a particular wavelet function depends strongly on the transient characteristics of the signal being analyzed. In this study, the Morlet wavelet is utilized as the wavelet function. The definition of the Morlet wavelet is defined as Onsay and Haddow (1994)

$$\psi(t) = \pi^{-1/4}(e^{-i\omega_c t} - e^{-\omega_c^2/2})e^{-t^2/2} \quad (4)$$

$$\tilde{\psi}(\omega) = \pi^{-1/4}(e^{-(\omega-\omega_c)^2/2} - e^{-(\omega_c^2+\omega^2)/2}) \quad (5)$$

where ω_c is the center frequency of the Morlet wavelet and $\tilde{\psi}(\omega)$ denotes the Fourier transform of $\psi(t)$.

3 Calculations of Surface Wave Dispersion in Layered Media

The propagation of a surface wave in an isotropic layered half-space has been studied by many researchers in the past and relevant references can be found in the book by Ewing et al. (1957). The following calculations of dispersive surface waves in a layered media were calculated by a general-purpose computer program (Chen, 1994). The program was written based on the sextic formalism of Stroh (Stroh, 1962; Braga, 1990) for the calculations of dispersion curves of isotropic as well as anisotropic multilayered media.

4 Laser Ultrasonic Experiments and Wavelet Analysis

4.1 Experimental Setup and Specimen. A 1-mm deep shallow square slot (area 120 × 80 mm^2) was machined from an aluminum block with equal width and length of 200 mm and with a height of 150 mm. A thin copper plate of 1-mm thickness was then bonded carefully on top of the aluminum block with epoxy resin. The top view and side view of the specimen are as shown in Fig. 1. The densities of the aluminum specimen and the copper layer are 2698 kg/m^3 and 8500 kg/m^3, respectively. In Fig. 1(*a*), the travel distance of the wave disturbances in the unbond area and well bond are denoted as l_1 and l_2, respectively. The longitudinal and shear wave velocities of the copper and aluminum specimens were measured by ultrasonic pulse-echo method as follows:

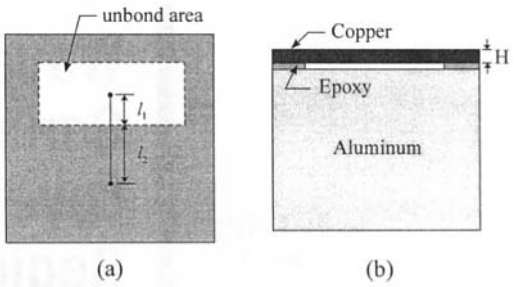

Fig. 1 Top view (*a*) and side view (*b*) of the specimen

aluminum: $C_L = 6389.1$ m/s, $C_T = 3097.8$ m/s

copper: $C_L = 4545.5$ m/s, $C_T = 2222.2$ m/s.

The density and the elastic wave velocities of the epoxy were also measured by the ultrasonic pulse-echo method. A small epoxy specimen was made from the same mixture as that used for bonding the copper thin plate and the aluminum block. The measured results of the epoxy sample are as follows:

$C_L = 2500.0$ m/s, $C_T = 1112.2$ m/s, $\rho = 1157.8$ kg/m^3.

Figure 2 shows the experimental setup utilized in the present study. A Nd:YAG pulsed laser (Quanta-Ray, GCR-130, wavelength 532 nm) was utilized to generate elastic waves in the layered specimen. The duration of the laser pulse utilized was 10 ns and the pulse energy carried was about 100 mJ. As shown in Fig. 2, the layered specimen rested on a precision translation stage to accurately control the distance between the source and the receiver. A NBS conical transducer (Proctor, Jr., 1982) measured the generated elastic wave signals from the laser sources. The received voltage signals from the conical transducer were then amplified by a preamplifier and recorded by a digital oscilloscope (LeCroy 9314L). A trigger signal synchronized with the laser source was utilized to trigger the digital oscilloscope. The recorded signals were then sent to a personal computer for analysis.

To study the dispersion of surface waves in an epoxy-bonded layered specimen, measurements were conducted in a well-bond

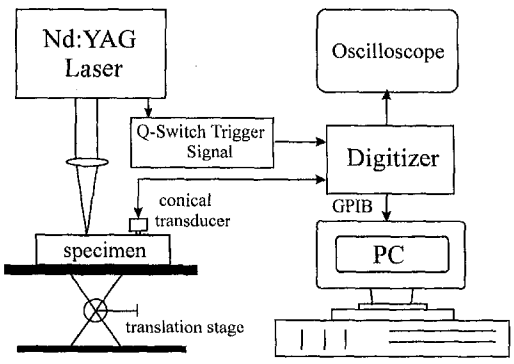

Fig. 2 Experimental setup of the laser ultrasonic experiment

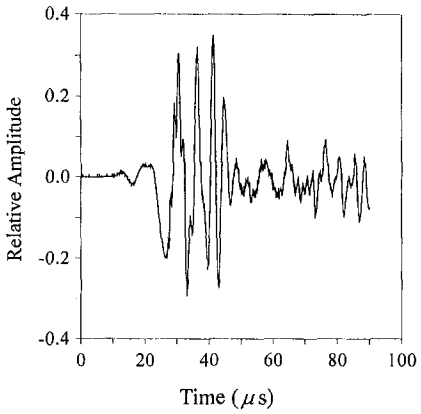

Fig. 3 Wave signal received on the surface of the epoxy-bonded copper-aluminum specimen (source to receiver distance is 60 mm)

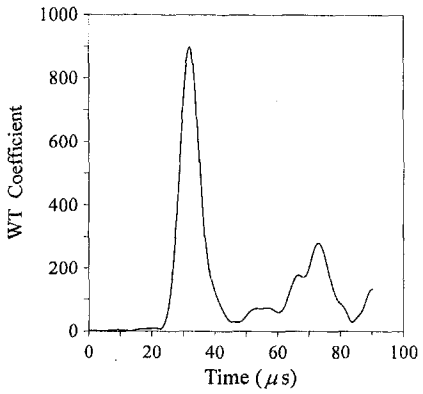

Fig. 5 Time response of a particular frequency equal to 0.59 MHz that is extracted from Fig. 5. The peak of the time response is about 33 μs.

area. Figure 3 shows the typical wave signal (vertical displacement) received on the surface of the copper-aluminum specimen. The distance between the laser point source and receiver was 60 mm and the vertical axis represents the relative amplitude of the displacement signal. The signal shows that the lower frequency disturbances propagate faster than the higher frequency signals. To have quantitative measurements of the arrivals of all the frequency components of the received signal, the wavelet analysis was adopted.

4.2 Wavelet Analysis. The dispersion curve of the fundamental mode of surface waves in a layered medium can be obtained using a conventional spectral analysis method (Wu and Chen, 1996). In this method, Fourier analysis of the wave disturbances at two different locations is required, and therefore, two receivers are needed. As the wavelet transform maps a one-dimensional signal of time into a two-dimensional function of time and frequency, the information of the frequency content of a specific time can be extracted easily from the transform results. Therefore, in the wavelet transform method, once the time origin of the laser point source is known, the group velocity dispersion can be obtained by analyzing the wave disturbance from one location, and this, thus avoiding the use of a second receiver. It is worth noting that the conventional spectral analysis technique is used to obtain the phase velocity dispersion of the surface wave, while the wavelet transform method is employed to obtain the group velocity dispersion.

Figure 4 shows the wavelet transform of the signal shown in Fig. 3. The vertical axis is the coefficient of the wavelet transform and the planar axes are the time and frequency, respectively. From Fig. 4, one can find the frequency content of the wave signal at a specific time or the time domain response of a particular frequency. Since the elastic waves in a layered medium are dispersive, the phase or group velocities are dependent on the frequency of the wave signal. Shown in Fig. 5 is the time response of a particular frequency equal to 0.59 MHz. From the figure, we can see that the arrival time of the wave group around 0.59 MHz is located at the peak of the time response, which is about 33 μs. The second large peak in the figure is due to the reflection from the boundary of the specimen. Since the distance between the laser point source and the receiver is known, the group velocity of the particular frequency can thus be determined by dividing the travel distance with the group delay 33 μs (Kishimoto et al., 1995).

The solid circles in Fig. 6 represent the group velocities calculated from the wavelet transform results (Fig. 4) according to the aforementioned procedures. This experimental result demonstrates clearly the dispersive behavior of the laser generated elastic waves in this layered specimen. The group velocity of the fundamental surface wave mode decreases with the increase of frequency to a minimum, then, increases to a certain value. The solid line in Fig. 6 is the theoretical dispersion relation of the fundamental surface waves in the copper-aluminum half-space not taking into account the thickness of the bonding epoxy layer. As shown in the curve, the phase velocity of the fundamental surface wave mode in the copper-aluminum layered half-space approaches to the Rayleigh

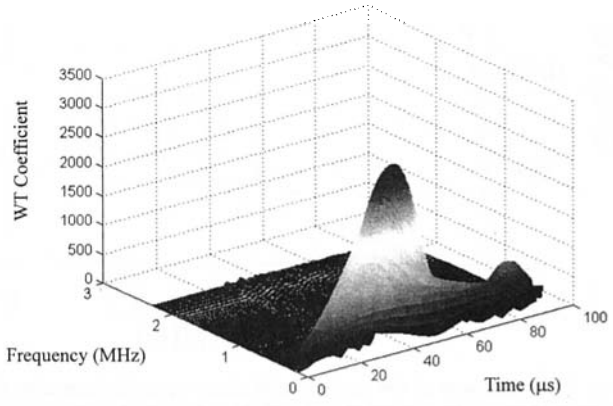

Fig. 4 Wavelet transform of the wave signal as shown in Fig. 3

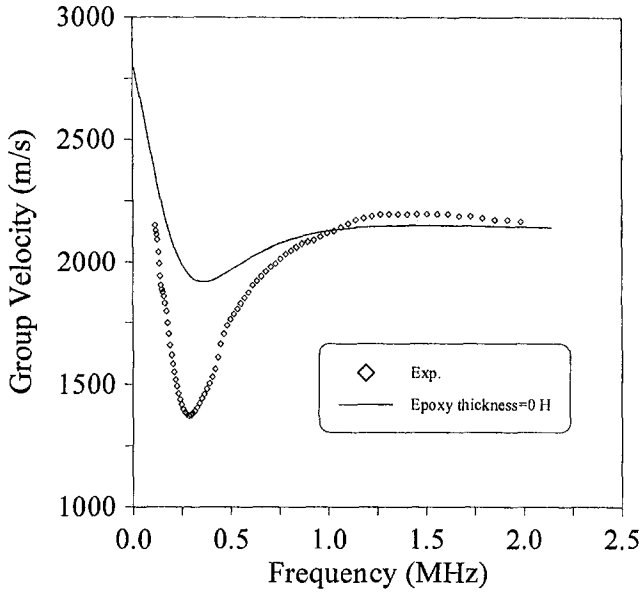

Fig. 6 Theoretical (solid line, without the epoxy layer) and experimental (solid circles) group velocity dispersion of the fundamental surface wave in an epoxy-bonded copper-aluminum specimen

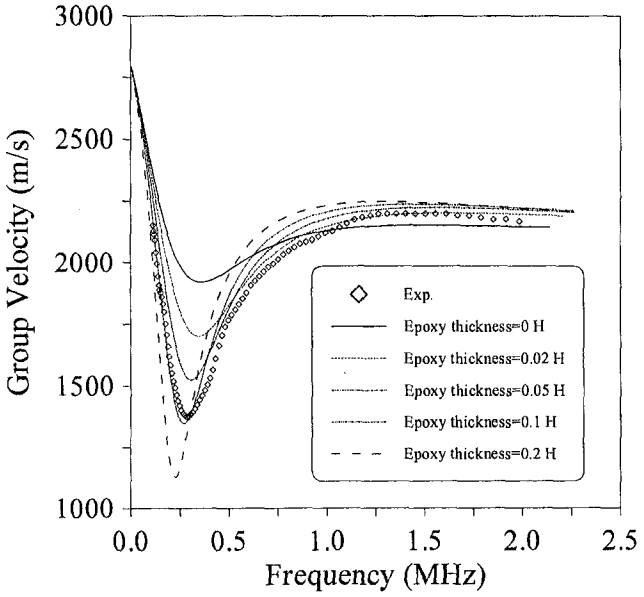

Fig. 7 Theoretical dispersion as related to the fundamental surface wave in a three-layered half-space (copper-epoxy-aluminum half-space) with different epoxy layer thickness

surface wave velocity of aluminum as the wave number approaches zero. On the other hand, the phase velocity of the fundamental surface wave mode approaches to the Rayleigh surface wave velocity of copper as the wave number increases.

Figure 7 shows the calculated dispersion as related to the fundamental surface waves in a three-layered half-space (copper-epoxy-aluminum half-space). The five curves in Fig. 7 represent the dispersion relationship to the thickness of the epoxy layer when varied from 0 to 0.2 H. The calculated results show that the thickness of the epoxy layer plays an important role in the dispersion of the fundamental surface waves in such a bonded layered half space. It is clear that a small change in the epoxy thickness causes a considerable change in the magnitude of the group velocity. We note that a dip in the surface wave dispersion of a bonded layered half space provides a qualitative (and quantitative, if an inversion algorithm is implemented (Wu and Liu, 1999)) indication of the thickness of the bonding layer. When we compare the calculated and the measured dispersion curves shown in Fig. 7, we see that the thickness of the epoxy bonding layer of the specimen is close to 0.1 H which is approximately 0.1 mm.

5 Dispersion of Surface Waves in a Layered Structure With Unbond Areas

In the detection of an unbond area with laser generated surface waves, three different situations regarding the location of the source and the receiver may be involved. The first situation is one where both the source and the receiver are located in the region of a well-bond area and the second situation is where both are located in the unbond region. The third and last situation is one in which either the source or the receiver is located in the unbond region. The first case was studied in a previous section. In the following subsections, the other cases are discussed.

5.1 Measurements on Top of an Unbond Area. For the case where both the source and receiver are located in the unbond area of a layered structure, the surface layer (copper layer in this paper) acts like a thin plate. Figure 8 shows a typical signal that is received at an unbond region, in this case where the distance between the laser source and the receiver is 70 mm. From the time-domain signal, one can find easily the dispersive behavior of the signal which results in higher frequency signals propagating faster than the lower frequency signals. On processing the received

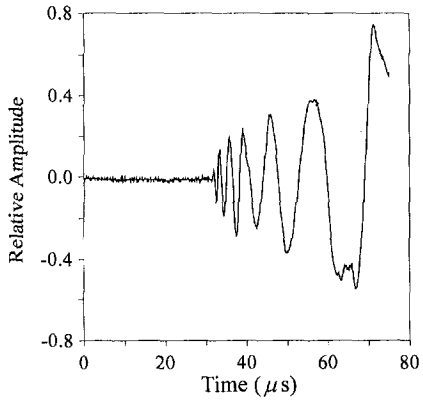

Fig. 8 Wave signal received in the unbond region where the distance between the laser source and the receiver 70 mm

signal as shown in Fig. 8 using the wavelet transform, the group velocity dispersion can be obtained. The solid circles shown in Fig. 9 are the measured group velocities and the solid line is the corresponding theoretical calculation of the Lamb wave dispersion in a copper plate. Although there are some deviations between the measured and the calculated results, the general trend of the lowest antisymmetric Lamb mode is very clear. The results show that when both the source and receiver are located on the unbond area, the wave dispersion characteristics are close to that of a thin plate as expected. In other words, the differences between the surface wave and the Lamb wave dispersion can be utilized to detect the unbond area.

5.2 Measurements Across an Unbond Area. As measurements are made across an unbond area, the laser generated elastic waves propagate through both the well bond and the unbond areas making the wave response become more complicated. The wave propagates in the unbond region with the Lamb mode and then in the well-bond region with the generalized surface mode. In the following measurements, the laser point sources were located in the unbond region and the receivers were located in the well-bond region. The travel distances in the well-bond region were fixed at 70 mm, while those for the unbond region are at 35 mm and 55

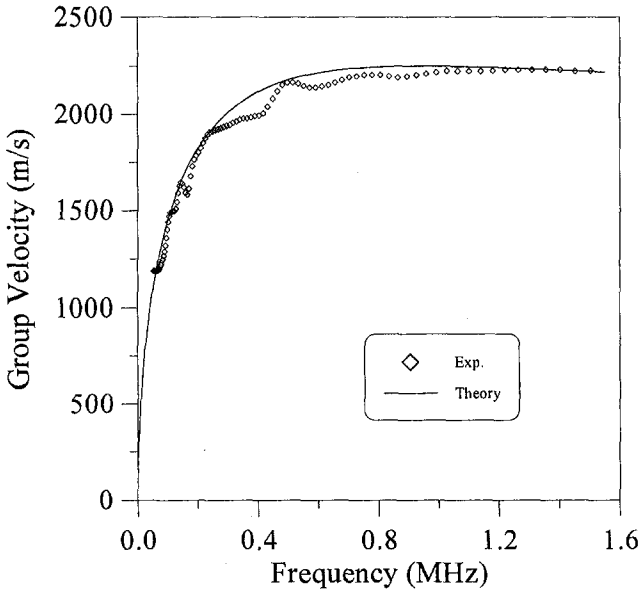

Fig. 9 Comparison of the experimental group velocity dispersion for measurement in the unbond region and the Lamb wave dispersion of a copper plate (solid line)

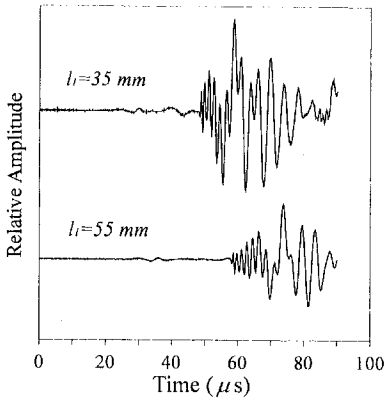

Fig. 10 Wave signals for a propagation of 70 mm in a well-bonded region and 35 mm and 55 mm in the unbond region, respectively

mm, respectively. Figure 10 shows the received wave signals with the upper one representing the case of l_1 = 35 mm and the lower one for the case of l_1 = 55 mm. l_1 represents the propagating distance in the unbond region. Except for the skimming longitudinal bulk waves, the figure shows that the major wave group is initiated by high-frequency disturbances.

The signals shown in Fig. 10 are then processed by the wavelet transform and the obtained group velocity dispersions are shown in Fig. 11 (35 mm) and Fig. 12 (55 mm). The results show that the measured dispersion curves are different from the theoretical dispersion curve of bonding thickness 0.1 H. The measured group velocities shown in Figs. 11 and 12, indicates that the group velocity dispersion is dependent on the travel distance of the laser generated elastic waves in the unbond region. Thus, for measurements across an unbond region, the dispersion relation is neither close to that of the lowest Lamb mode nor to that of the generalized surface wave mode.

5.3 Dispersion Curve for Measurement Across Unbond Areas. In the case of a well-bonded copper-epoxy-aluminum layered medium (Fig. 7), the group velocity of the generalized surface wave decreases from the Rayleigh wave velocity of the aluminum (the substrate) to a minimum value, then increases to the Rayleigh wave velocity of the surface layer (copper thin plate). On

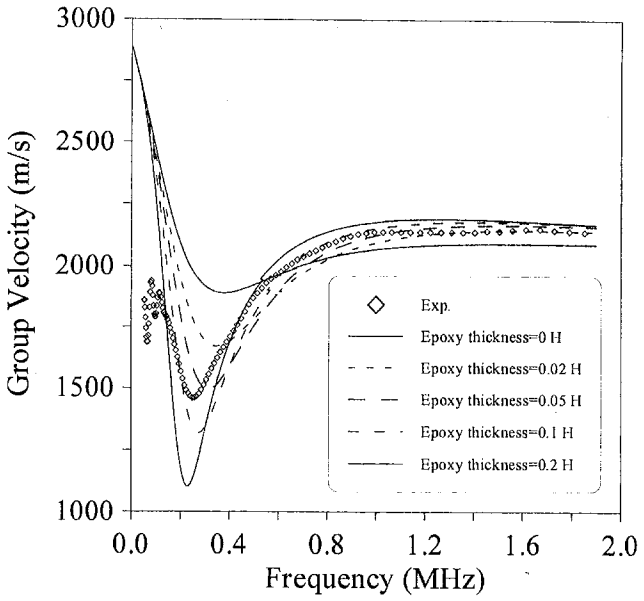

Fig. 11 Group velocity dispersions for surface wave propagating 70 mm in a well-bonded region and 35 mm in an unbond region

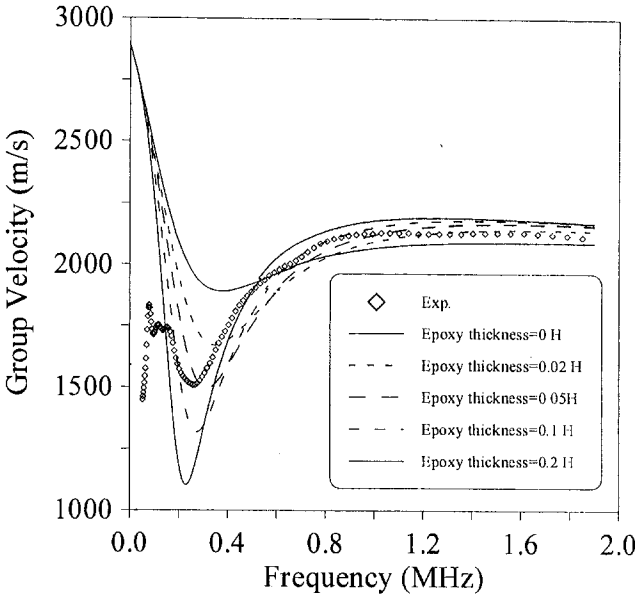

Fig. 12 Group velocity dispersions for surface wave propagating 70 mm in a well-bonded region and 55 mm in an unbond region

the other hand, as shown in Fig. 9, the group velocity of the lowest Lamb mode (antisymmetric) increases rapidly from zero to the Rayleigh wave velocity of the copper plate. In Figs. 11 and 12, results show that for measurements across the well-bond and unbond region, the group velocity dispersion at the very lowest frequency preserves a similar trend as that for the Lamb wave dispersion. In addition, as the travel distance in an unbond region increases, the Lamb mode becomes more pronounced, and therefore, the group velocities at the lower frequencies become smaller.

The aforementioned observations indicate that for elastic wave propagating through both well-bond and unbond regions, the group velocity dispersion can not be predicted from either the Lamb wave analysis or the generalized surface wave analysis. The group velocity dispersion for measurements across a well-bond and unbond region appears to lie somewhere between the Lamb wave and the generalized surface wave dispersion. Generally speaking, most of the energy of an elastic disturbance propagating in an elastic waveguide is carried by the fundamental wave mode. Therefore, it is reasonable to assume that the elastic wave propagation in an unbond region is with the group velocity of a Lamb wave. In the case of a well-bond region, the elastic wave propagation is with the group velocity of the generalized surface wave.

With the aforementioned observations and discussions, the group velocity for the case of measurement across an unbond region is approximated as

$$v(\omega) = \frac{l_1 + l_2}{\dfrac{l_1}{v_1(\omega)} + \dfrac{l_2}{v_2(\omega)}} \tag{6}$$

where l_1, l_2 are the propagation distances in the unbond region and the well-bond region, respectively. v_1, v_2 are the group velocities of the fundamental antisymmetric Lamb mode and the generalized surface wave mode, respectively. The lines in Fig. 13 are the theoretical calculations of the group velocity dispersions for the case where l_1 = 35 mm, l_2 = 70 mm and the bonding thickness are varied from 0 to 0.2 H. The theoretical predictions show that the initial parts of the dispersion curves are dominated by the fundamental mode of the antisymmetric Lamb wave. Furthermore, the minimum group velocities shown in Fig. 11 (the generalized surface wave) are increased due to the adding of the Lamb wave propagation effect. The results shown in Fig. 13 demonstrated that the proposed group velocity dispersion (with bonding thickness 0.1

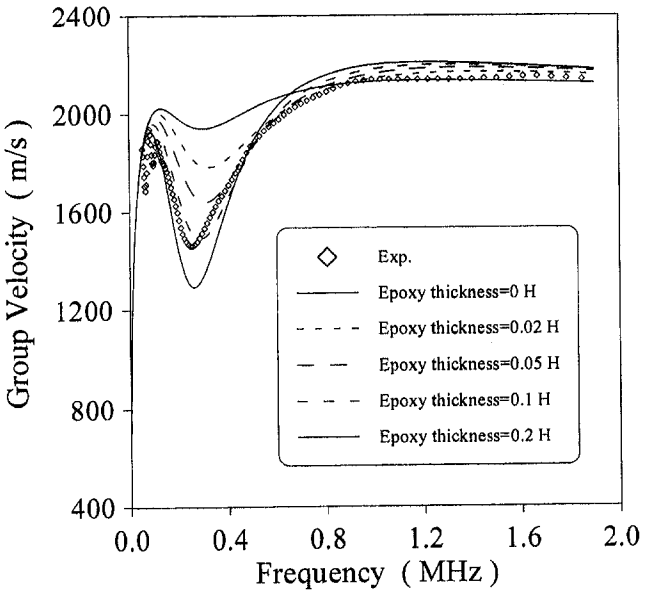

Fig. 13 Synthetic group velocity dispersion for the case where l_1 = 35 mm and l_2 = 70 mm with different bonding thickness ranging from 0 to 0.2 H

H) for measurements across the unbond region agrees well with the measured data (solid circles). Similar results are also found for the case where l_1 = 55 mm, l_2 = 70 mm as is shown in Fig. 14.

The results shown in this section demonstrates that for laser ultrasonic measurements across a well-bond and unbond region, the group velocity dispersion can be approximated by the proposed formula with reasonable accuracy. The results also reveal that the propagation distance in an unbond region could be determined from the hybrid group velocity dispersion if a simple inversion algorithm is adopted.

6 Discussions

Based on the predictions of Eq. (6), as long as the propagation distances in the well-bond and the unbond regions are equal, the group velocity dispersive relationships are equal. It is independent of whether the source or the receiver is on the unbond region or not. Figure 15 shows the measured time domain signals for the receiver (solid line) and the laser source (dashed line) located in the unbond region, respectively. In the measurement mode, the travel distances in both of the well bond and the unbond regions were fixed at 35 mm. In Fig. 15, we find that the time-domain signal for both cases deviate slightly from each other. However, the group velocity dispersions of both cases shown in Fig. 16 (open circles and triangles) coincide with each other. This result shows that the arrival time of the frequency component for both the aforementioned cases have similar propagation speeds. This experimental result demonstrates further the validity of Eq. (6) in the current application.

It is worth noting that as the laser point source or the receiver is very close to the boundary of a well-bond and unbond region, the diffraction induced by the discontinuity is not considered in Eq. (6). In addition, the results of Figs. 11 and 12 show that Eq. (6) can only predict the group velocity dispersion for measurements across the unbond region to a certain degree of accuracy. For a complete description of the group velocity dispersion of the aforementioned problem, a more theoretical investigation needs to be undertaken.

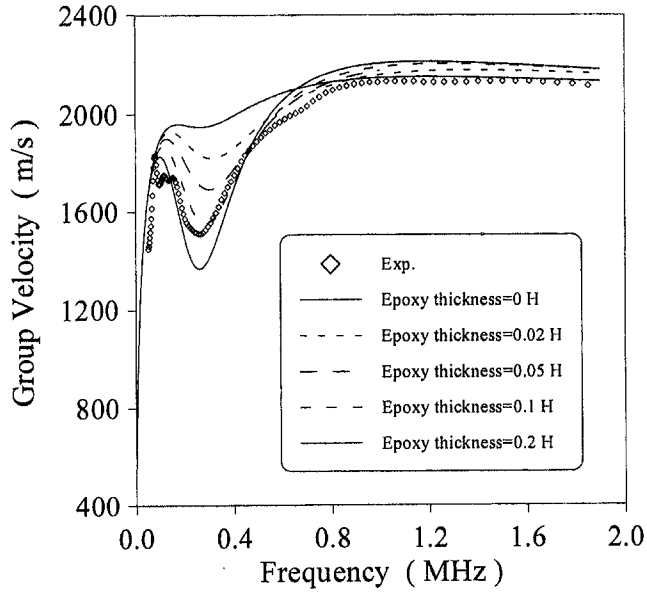

Fig. 14 Synthetic group velocity dispersion for the case where l_1 = 55 mm and l_2 = 70 mm with different bonding thickness, ranging from 0 to 0.2 H

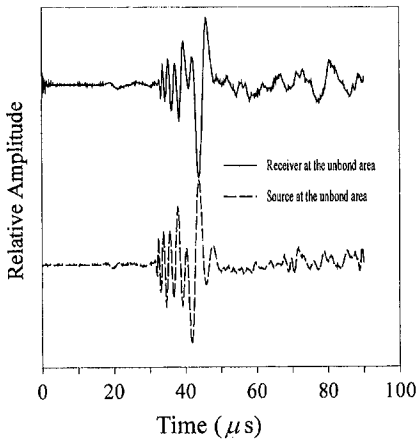

Fig. 15 Measured time domain signals for the receiver (solid line) and laser source (dashed line) located in the unbond region, respectively. The travel distances in both of the well bond and unbond regions are fixed at 35 mm.

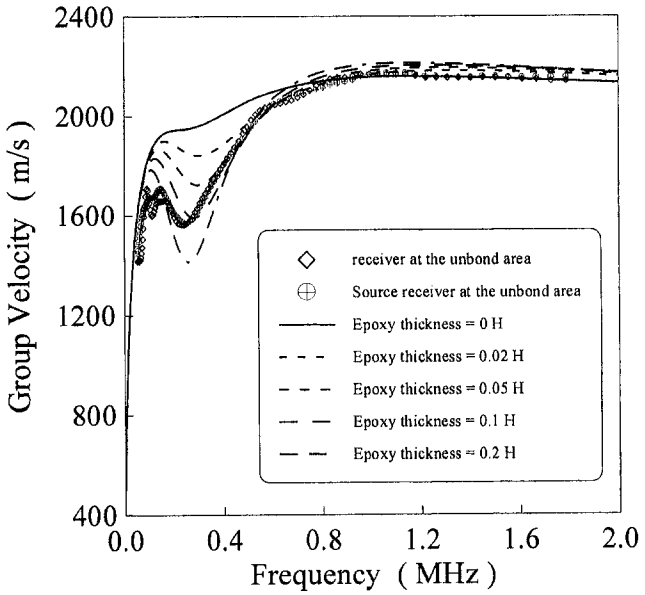

Fig. 16 The group velocity dispersions for the cases as shown in Fig. 15

7 Conclusions

Based on the results of this study, it has been shown that the wavelet transform with a Morlet wavelet function can be adopted to analyze laser-generated dispersive surface waves in a layered medium with or without an unbond area. For the case of an epoxy-bonded layered medium, the bonding thickness strongly affects the dispersive behavior of the surface waves. In laser ultrasonic measurements using a point-source/point-receiver (PS/PR) technique, when both the source and the receiver are in the unbond region, the lowest antisymmetric Lamb mode results. As the line of the source and the receiver are across the well-bond and unbond boundary, the group velocity dispersion cannot be explained by existing theories. An approximated group velocity dispersion formula was proposed and data obtained matches well with the experimental results. The general behavior of the group velocity dispersion for different measurement configurations can be utilized further to differentiate the unbond regions in layered structures in a more precise way.

Acknowledgments

The authors thank the National Science Council (NSC) of R.O.C. for the financial support of this research through grant NSC86-2212-E-002-078.

References

Braga, M. B., 1990, "Wave Propagation in Anisotropic Layered Composites," Ph.D. dissertation, Stanford University, Stanford, CA.

Castagnede, B., Kim, K. Y., Sachse, W., and Thompson, M. O., 1991, "Determination of the Elastic Constants of Anisotropic Materials Using Laser-Generated Ultrasonic Signals," *J. Appl. Phys.*, Vol. 70, No. 1, pp. 150–157.

Chai, J.-F., and Wu, T. T., 1994, "Determinations of Anisotropic Elastic Constants Using Laser Generated Surface Waves," *J. Acoustic Soc. Am.*, Vol. 95, No. 6, pp. 3232–3241.

Chen, Y.-C., 1994, "Dispersion of Surface Waves in an Anisotropic Layered Medium," M.S. thesis, National Taiwan University.

Cho, H., Ogawa, S., and Takamoto, M., 1996, "Noncontact Laser Ultrasonics for Detecting Subsurface Lateral Defects," *NDT&E International*, Vol. 29, No. 5, pp. 301–306.

Dewhurst, R. J., Edwards, C., McKie, A. D. W., and Palmer, S. B., 1987, "Estimation of the Thickness of Thin Metal Sheet Using Laser Generated Ultrasound," *Appl. Phys. Lett.*, Vol. 51, pp. 1066–1068.

Doyle, P. A., and Scala, C. M., 1991, "Ultrasonic Measurement of Elastic Constants for Composite Overlays," *Rev. Prog. in QNDE*, Vol. 10B, pp. 1453–1459.

Ewing, W. M., Jardetzky, W. S., and Press, F., 1957, *Elastic Waves in Layered Media*, McGraw-Hill, New York.

Hlawatsch, F., and Boudreaus-Bartels, G. F., 1992, "Linear and Quadratic Time-Frequency Signal Representations," *IEEE Signal Process Mag.*, Vol. 9, pp. 21–67.

Hurley, D. A., Spicer, J. B., Conant, R. J., and Telschow, K. L., 1997, "Determination of the Optical Absorption Coefficient via Analysis of Laser Generated Plate Waves," *IEEE Ultrasonics, Ferro. Freq. Control*, Vol. 44, No. 4, pp. 902–908.

Hutchins, D. A., Lundgren, K., and Palmer, S. B., 1989, "A Laser Study of the Transient Lamb Waves in Thin Materials," *J. Acoust. Soc. Am.*, Vol. 85, No. 4, pp. 1441–1448.

Johnson, M. A., Berthelot, Y. H., Brodeur, P. H., and Jacobs, L. A., 1996, "Investigation of Laser Generation of Lamb Waves in Copy Paper," *Ultrasonics*, Vol. 34, pp. 703–710.

Kishimoto, K., Inoue, H., Hamada, M., and Shibuya, T., 1995, "Time-Frequency Analysis of a Dispersive Waves by Means of Wavelet Transform," ASME JOURNAL OF APPLIED MECHANICS, Vol. 62, pp. 841–846.

Nakano, H., and Nagai, S., 1991, "Laser Generation of Anti-symmetric Lamb Waves in Thin Plates," *Ultrasonics*, Vol. 29, pp. 230–234.

Onsay, T., and Haddow, A. G., 1994, "Wavelet Transform Analysis of Transient Wave Propagation in a Dispersive Medium," *J. Acoustic Soc. Am.*, Vol. 95, No. 3, pp. 1441–1449.

Proctor, T. M., Jr., 1982, "An Improved Piezoelectric Acoustic Emission Transducer," *J. Acoustic Soc. Am.*, Vol. 71, No. 5, pp. 1163–1168.

Rioul, O., and Vetterli, M., 1991, "Wavelet and Signal Processing," *IEEE Sp. Magazine*, Oct., pp. 14–38.

Ruskai, M. B., Belykin, G., Daubechies, I., Meyer, Y., Coifman, R., Mallat, S., and Ralphel, L., eds., 1992, *Wavelets and Their Applications*, Jones and Bartlett, Boston.

Scruby, C. B., and Drain, L. E., 1990, *Laser Ultrasonics: Techniques and Applications*, IOP Publishing Ltd., Bristol, UK.

Scudder, L. P., Hutchin, D. A., and Guo, N., 1996, "Laser-Generated Ultrasonic Guided Waves in Fiber-Reinforced Plates: Theory and Experiment," *IEEE Trans. Ultra. Ferro. and Freq. Control*, Vol. 43, No. 5, pp. 870–880.

Spicer, J. B., McKie, A. D. W., and Wagner, J. W., 1990, "Quantitative Theory for Laser Ultrasonic Waves in a Thin Plate," *Appl. Phys. Lett.*, Vol. 57, No. 18, pp. 1882–1884.

Stroh, A. N., 1962, "Steady-State Problems in Anisotropic Elasticity," *J. Math. and Phys.*, Vol. 41, pp. 77–103.

Veidt, M., and Sachse, W., 1994, "Ultrasonic Point-Source/Point-Receiver Measurements in Thin Specimens," *J. Acoust. Soc. Am.*, Vol. 96, No. 4, pp. 2318–2326.

Wu, T. T., and Chai, J.-F., 1994, "Propagation of Surface Waves in Anisotropic Solids: Theoretical Calculation and Experiment," *Ultrasonics*, Vol. 32, No. 1, pp. 21–29.

Wu, T.-T., and Chen, Y. C., 1996, "Dispersion of Laser Generated Surface Waves in an Epoxy-Bonded Layered Medium," *Ultrasonics*, Vol. 34, pp. 793–799.

Wu, T.-T., and Liu, Y.-H., 1999, "Inverse Determinations of Thickness and Elastic Properties of a Bonding Layer Using Laser-Generated Surface Waves," *Ultrasonics*, Vol. 37, pp. 23–30.

Macrocrack-Microcrack Interaction in Piezoelectric Materials, Part I: Basic Formulations and *J*-Analysis

Y.-H. Chen
Dean and Professor

J.-J. Han
Doctoral Student

School of Civil Engineering
and Mechanics,
Xi'an Jiaotong University,
Xi'an Shaanxi Province 710049,
P. R. China

The macrocrack-microcrack interaction problem in transversely isotropic piezoelectric materials is studied. The microcracks near a macrocrack tip in the process zone are assumed to be parallel to the latter, while the poling direction of the piezoelectric materials is assumed to be perpendicular to the cracks. Three kinds of elementary solutions with different crack configurations and under different loading conditions are given, from which the interaction problem is reduced to a system of Fredholm integral equations by using the pseudo-traction electric displacement method (abbreviated PTED). After the equations are solved numerically, the traditional mode I and mode II stress intensity factors and the electric displacement intensity factor are evaluated. In order to confirm the proposed method as well as the numerical results, a consistency check is proposed which is based on the J-integral analysis and provides a powerful tool to examine the numerical results. Thus, any mistakes are avoided since they would certainly lead to unsatisfied numerical results contrary to the check. It is concluded also that the disturbance of the near-tip electric field provides another source of shielding.

1 Introduction

Due to the well-known performance of the mechanical-electrical coupling in piezoelectric ceramics, these kinds of materials are found to have widely technological applications such as transducers, sensors, and actuators. Generally speaking, piezoelectric ceramics show brittle nature, from the mechanical point of view, and susceptible to fracture when a macrocrack is formed. The understanding of the fracture behavior of piezoelectric ceramics is of great importance, thereby it received considerable attention in the recent ten years. Sosa and Pak (1990), Sosa (1991, 1992), Pak (1990, 1992), Pak and Sun (1995a, b), and Pak and Carman (1997) studied the two-dimensional problems for an elliptic hole or crack in piezoelectric materials. They defined two kinds of stress intensity factors (SIF's), i.e., the traditional mode I and mode II SIF's and the electric displacement intensity factor (EDIF). Moreover, they found that the mode I and mode II SIF's are independent of the electric loading, while the EDIF is independent of the mechanical loading. This means that the mechanical loading and the electric loading are not coupled in single crack situations when taking SIF's and EDIF to be the crack-tip dominant parameters. It is not clear that the same conclusion could be given in multiple crack problems.

As regards the conservation integrals in piezoelectric materials, Pak (1990) and Suo et al. (1992) proposed the *J*-integral which also has a clear physical significance as the total potential energy release rate (TPERR). However, Pak and Sun (1995a, b) pointed out that neither the stress intensity factors nor the TPERR are suitable for describing the fracture behavior of piezoelectric ceramics. They showed that a new fracture criterion should be proposed, which is based on the mechanical strain energy release rate (MSERR). Under this criterion, they found that the mechanical loading and the electric loading are coupled and that the positive electric fields aid the crack propagation, while the negative electric fields impede the crack propagation.

On the other hand, the fracture toughness of engineering brittle materials is significantly influenced by the microstructure of the materials, such as microcracks, microvoids, and microinclusions. The interaction between a macrocrack tip and the near-tip material microstructure has been studied by a number of researchers (see, e.g., Rose, 1986; Rubinstein, 1986; Horii and Nemat-Nasser, 1985, 1987; Chudnovsky et al., 1987; Gong and Horii, 1989; Gong and Meguid, 1991; Chen and Hasebe, 1994). The so-called shielding problems in such materials have brought a considerable interest in the past ten years (see, e.g., Hutchinson, 1987; Ortitz, 1987, 1988, 1989). It has been shown, from experimental studies as well as analytical estimations, that the existence of microcracks in the near-tip process zone shields a macrocrack tip from the remote loading. Hutchinson (1987) point out that the shielding effect arises from two consequences of microcracking, i.e., the reduction in the effective elastic moduli and the release of the residual stresses. It could be imagined that the fracture toughness of piezoelectric materials would also be influenced by the microstructure of the near-tip process zone. However, the shielding problem in such materials, to the present author's knowledge, has not been studied yet, neither analytically nor experimentally. Specially, how the electric loading influences the shielding effect is not clear and thus worthy of investigation.

The goal of the present study is to supply the lack of analytical estimations for shielding problems in piezoelectric materials. As a first attempt, in Part I of this paper, attention is focused on the macrocrack-microcrack interaction in a transversely isotropic piezoelectric material. The microcracks are assumed to be parallel to the macrocrack, while the poling direction of the material is perpendicular to the cracks. In Section 2, elementary solutions with two kinds of crack configurations and subjected to three kinds of loadings are given, respectively. In Section 3, a pseudo-traction electric displacement (PTED) method is proposed, which is motivated by the well-known pseudo-traction method (Horii and Nemat-Nasser, 1985, 1987). Using the elementary solutions and the PTED method, the interaction problem can be reduced to a

Contributed by the Applied Mechanics Division of THE AMERICAN SOCIETY OF MECHANICAL ENGINEERS for publication in the ASME JOURNAL OF APPLIED MECHANICS.
Discussion on the paper should be addressed to the Technical Editor, Professor Lewis T. Wheeler, Department of Mechanical Engineering, University of Houston, Houston, TX 77204-4792, and will be accepted until four months after final publication of the paper itself in the ASME JOURNAL OF APPLIED MECHANICS.
Manuscript received by the ASME Applied Mechanics Division, May 7, 1998; final revision, Oct. 27, 1998. Associate Technical Editor: M. Ortiz.

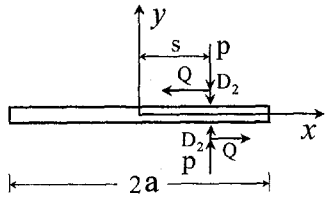

Fig. 1 A finite crack loaded by concentrated tractions and concentrated electric displacement

system of Fredholm integral equations whose solutions could be given numerically with the aid of the Chebyshev numerical integral technique. After doing so, the effect of the microcracks on the mechanical SIF's and the electric displacement intensity factor at the macrocrack tip is evaluated. Nevertheless, the derived numerical results should be examined. However, no previously known results exist for comparisons. A possible way is to make some comparisons with the results in degenerated cases. This might lead to some incorrect and unexpected conclusions when a tiny mistake in manipulations escapes from such comparisons (Chen and Hasebe, 1998). In Section 4, a consistency check is proposed which is based on the conservation nature of the J-integral (Pak, 1990; Suo et al., 1992). It is proved that although the check represents a necessary condition rather than a sufficient condition, it does provide a powerful tool to confirm the present numerical results. Moreover, it is shown that there is a wastage of the J-integral when the remote J-integral, J^{∞}, transmits across the microcracking zone from the infinity to the macrocrack tip (Chen, 1996; Zhao and Chen, 1997; Chen and Ma, 1997). The influence of the electric displacement loading on the wastage is shown in the figures which provides another source of shielding induced from the disturbance of the near-tip electric field due to microcracking.

2 Elementary Solutions

Consider a two-dimensional problem for a transversely isotropic piezoelectric material under plane-strain conditions. Assume that the poling direction of the piezoelectric material is parallel to the y-axis (see Figs. 1 and 2). The constitutive equations can be written as (Sosa, 1992)

$$\begin{Bmatrix} \epsilon_{11} \\ \epsilon_{22} \\ 2\epsilon_{12} \end{Bmatrix} = \begin{bmatrix} a_{11} & a_{12} & 0 \\ a_{12} & a_{22} & 0 \\ 0 & 0 & a_{33} \end{bmatrix} \begin{Bmatrix} \sigma_{11} \\ \sigma_{22} \\ \sigma_{12} \end{Bmatrix} + \begin{bmatrix} 0 & b_{21} \\ 0 & b_{22} \\ b_{13} & 0 \end{bmatrix} \begin{Bmatrix} D_1 \\ D_2 \end{Bmatrix}$$

$$\begin{Bmatrix} E_1 \\ E_2 \end{Bmatrix} = -\begin{bmatrix} 0 & 0 & b_{13} \\ b_{21} & b_{22} & 0 \end{bmatrix} \begin{Bmatrix} \sigma_{11} \\ \sigma_{22} \\ \sigma_{12} \end{Bmatrix} + \begin{bmatrix} \delta_{11} & 0 \\ 0 & \delta_{22} \end{bmatrix} \begin{Bmatrix} D_1 \\ D_2 \end{Bmatrix}, \quad (1)$$

where ϵ_{ij}, σ_{ij}, D_i, and E_i are the strain, the stress, the electric displacement, and the electric field, respectively. And $(i, j) = 1, 2$, a_{ij}, b_{ij}, and δ_{ii} are reduced material constants which were discussed in details by Sosa (1991).

The stress components and the electric displacement components could be expressed by three complex potentials $\Phi_k(Z_k)$ $(k = 1, 2, 3)$ as follows (Sosa, 1992):

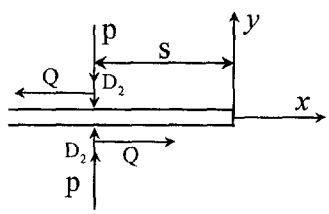

Fig. 2 A semi-infinite crack loaded by concentrated tractions and concentrated electric displacement

$$\sigma_{11} = G_4(\Phi_k(Z_k), Z_k) = \sum_{k=1}^{3} [\mu_k^2 \Phi_k(Z_k) + \overline{\mu_k^2}\,\overline{\Phi_k(Z_k)}]$$

$$\sigma_{22} = G_1(\Phi_k(Z_k), Z_k) = \sum_{k=1}^{3} [\Phi_k(Z_k) + \overline{\Phi_k(Z_k)}]$$

$$\sigma_{12} = G_2(\Phi_k(Z_k), Z_k) = -\sum_{k=1}^{3} [\mu_k \Phi_k(Z_k) + \overline{\mu_k}\,\overline{\Phi_k(Z_k)}]$$

$$D_1 = G_5(\Phi_k(Z_k), Z_k) = \sum_{k=1}^{3} [\lambda_k \mu_k \Phi_k(Z_k) + \overline{\lambda_k \mu_k}\,\overline{\Phi_k(Z_k)}]$$

$$D_2 = G_3(\Phi_k(Z_k), Z_k) = -\sum_{k=1}^{3} [\lambda_k \Phi_k(Z_k) + \overline{\lambda_k}\,\overline{\Phi_k(Z_k)}], \quad (2)$$

where, the overbar denotes the complex conjugation, and

$$Z_k = x + \mu_k y$$

$$\lambda_k = -[(b_{21} + b_{13})\mu_k^2 + b_{22}]/(\delta_{11}\mu_k^2 + \delta_{22}) \quad (k = 1, 2, 3), \quad (3)$$

in which μ_k are three roots with positive imaginary parts of the following governing equation:

$$A\mu^6 + B\mu^4 + C\mu^2 + D = 0, \quad (4)$$

where

$$A = a_{11}\delta_{11}$$

$$B = a_{11}\delta_{22} + 2a_{12}\delta_{11} + a_{33}\delta_{11} + b_{21}^2 + b_{13}^2 + 2b_{21}b_{13}$$

$$C = a_{22}\delta_{11} + 2a_{12}\delta_{22} + a_{33}\delta_{22} + 2b_{21}b_{22} + 2b_{13}b_{22}$$

$$D = a_{22}\delta_{22} + b_{22}^2. \quad (5)$$

2.1 A Finite Crack. As shown in Fig. 1, a finite crack in an infinite piezoelectric material is considered which is loaded by concentrated tractions P and Q as well as the concentrated electric displacement D_2 on both crack faces. From the conditions with superscripts + and − denoting the upper and lower boundary values, respectively,

$$\begin{aligned} &\sigma_{22}^{+}(x) = \sigma_{22}^{-}(x) \\ &\sigma_{12}^{+}(x) = \sigma_{12}^{-}(x) \quad (y = 0^{\pm},\ -\infty < x < \infty) \\ &D_2^{+}(x) = D_2^{-}(x), \end{aligned} \quad (6)$$

the following relations could be obtained:

$$\sum_{k=1}^{3} [\Phi_k(x) - \bar{\Phi}_k(x)]^{+} = \sum_{k=1}^{3} [\Phi_k(x) - \bar{\Phi}_k(x)]^{-}$$

$$\sum_{k=1}^{3} [\mu_k \Phi_k(x) - \overline{\mu_k}\,\overline{\Phi}_k(x)]^{+} = \sum_{k=1}^{3} [\mu_k \Phi_k(x) - \overline{\mu_k}\,\overline{\Phi}_k(x)]^{-}$$

$$\sum_{k=1}^{3} [\lambda_k \Phi_k(x) - \overline{\lambda_k}\,\overline{\Phi}_k(x)]^{+} = \sum_{k=1}^{3} [\lambda_k \Phi_k(x) - \overline{\lambda_k}\,\overline{\Phi}_k(x)]^{-}, \quad (7)$$

which are the simplest Rieman-Hilbert problems whose solutions are holomorphic functions. Considering the remote conditions, the

holomorphic functions should be zero and then the following relations are derived:

$$\sum_{k=1}^{3} \Phi_k(Z_k) = \sum_{k=1}^{3} \bar{\Phi}_k(Z_k)$$

$$\sum_{k=1}^{3} \mu_k \Phi_k(Z_k) = \sum_{k=1}^{3} \overline{\mu_k}\, \overline{\Phi}_k(Z_k)$$

$$\sum_{k=1}^{3} \lambda_k \Phi_k(Z_k) = \sum_{k=1}^{3} \overline{\lambda_k}\, \overline{\Phi}_k(Z_k). \quad (8)$$

The boundary conditions on the crack faces in Fig. 1 are well known as

$$\sigma_{22}^{+}(x) = \sigma_{22}^{-}(x) = P\delta(x - s)$$

$$\sigma_{12}^{+}(x = \sigma_{12}^{-}(x) = Q\delta(x - s) \quad (y = 0^{\pm}, |x| < a) \quad (9)$$

$$D_2^{+}(x) = D_2^{-}(x) = D_2\delta(x - s)$$

where a is the half-length of the crack, s is the distance shown in Fig. 1, and $\delta(x - s)$ is the Derac function which has a different meaning from δ_{11} and δ_{22} in Eq. (1).

Substituting Eq. (2) into Eq. (9), it follows that

$$\sum_{k=1}^{3} [\Phi_k^{+}(x) + \bar{\Phi}_k^{-}(x)] = P\delta(x - s)$$

$$\sum_{k=1}^{3} [\mu_k \Phi_k^{+}(x) + \overline{\mu_k}\, \overline{\Phi}_k^{-}(x)] = -Q\delta(x - s)$$

$$\sum_{k=1}^{3} [\lambda_k \Phi_k^{+}(x) + \overline{\lambda_k}\, \overline{\Phi}_k^{-}(x)] = -D_2\delta(x - s), \quad (10)$$

where the superscripts + and − refer to the upper and lower boundary values of the corresponding complex potentials.

Furthermore, substituting Eq. (8) into (10) leads to the following equations:

$$\Phi_k^{+}(x) + \Phi_k^{-}(x) = (A_{k1}P + A_{k2}Q + A_{k3}D_2)\delta(x - s) \quad (k = 1, 2, 3), \quad (11)$$

where A_{ij} are elements of the following matrix:

$$\mathbf{A} = [A_{ij}] = \frac{1}{\Delta}\begin{bmatrix} \mu_2\lambda_3 - \mu_3\lambda_2 & \lambda_3 - \lambda_2 & \mu_2 - \mu_3 \\ \mu_3\lambda_1 - \mu_1\lambda_3 & \lambda_1 - \lambda_3 & \mu_3 - \mu_1 \\ \mu_1\lambda_2 - \mu_2\lambda_1 & \lambda_2 - \lambda_1 & \mu_1 - \mu_2 \end{bmatrix}, \quad (12)$$

$$\Delta = \mu_1(\lambda_2 - \lambda_3) + \mu_2(\lambda_3 - \lambda_1) + \mu_3(\lambda_1 - \lambda_2). \quad (13)$$

Equation (11) is a typical Rieman-Hilbert problem whose solution is

$$\Phi_k^{a}(Z_k) = \frac{(A_{k1}P + A_{k2}Q + A_{k3}D_2)}{2\pi(s - Z_k)} \left(\frac{a^2 - s^2}{Z_k^2 - a^2}\right)^{1/2} \quad (k = 1, 2, 3) \quad (14)$$

where the superscript a refers to the first elemental solution corresponding to the case of Fig. 1.

The stresses at any point in the xy-plane induced by P, Q, and D_2 could be given by substituting Eq. (14) into (2) which will be discussed below.

2.2 A Semi-Infinite Crack. Consider a semi-infinite crack in an infinite piezoelectric material as shown in Fig. 2, which is loaded by the concentrated tractions P and Q as well as the concentrated electric displacement D_2 on the both faces.

Repeating the same procedure from (6) to (14), the solution of the problem shown in Fig. 2 is given as follows:

$$\Phi_k^{b}(Z_k) = \frac{(A_{k1}P + A_{k2}Q + A_{k3}D_2)\sqrt{|s|}}{2\pi(s - Z_k)Z_k^{1/2}} \quad (k = 1, 2, 3) \quad (15)$$

where the superscript b refers to the second elemental solution shown in Fig. 2 and s refers to the distance from the traction acting point to the origin.

The stresses at any point in the xy-plane induced by P, Q, and D_2 could be given by substituting Eq. (15) into (2) which will be discussed below.

2.3 Remote Loading Conditions. Consider a semi-infinite crack in an infinite piezoelectric material loaded by the remote stress intensity factors K_{I}^{∞} and K_{II}^{∞}, and also by the remote electric displacement intensity factor K_e^{∞}. Without going into detail, the solution is given as

$$\Phi_k^{\infty}(Z_k = f_k(Z_k)Z_k^{-1/2} + P_k(Z_k) \quad (k = 1, 2, 3), \quad (16)$$

where $f_k(Z_k)$ and $P_k(Z_k)$ could be determined by using the remote conditions. After doing so, the following formulation is given:

$$\Phi_k^{\infty}(Z_k) = (A_{k1}K_{\mathrm{I}}^{\infty} + A_{k2}K_{\mathrm{II}}^{\infty} + A_{k3}K_e^{\infty})Z_k^{-1/2} \quad (k = 1, 2, 3) \quad (17)$$

where A_{k1}, A_{K2}, and A_{K3} are the elements of the matrix A_{ij} in (12).

3 Pseudo-Traction Electric Displacement Method (PTED)

Consider a semi-infinite macrocrack interacting with N arbitrarily located parallel microcracks in the near-tip process zone in a transversely isotropic piezoelectric material (see Fig. 3). Here the small scale approach has been adopted. At infinity, the loading conditions are K_{I}^{∞}, K_{II}^{∞}, and K_e^{∞}. The global coordinate system (x, y) and N local coordinate systems (x_i, y_i) ($i = 1, 2, \ldots N$) are preferred with the origins taken to be the macrocrack tip and the microcrack centers, respectively. As mentioned above, the poling direction of the material coincides with the y-direction. The geometric parameters φ_i, d_i, and a_i denote the location angle, the location distance, and the half-length of the ith microcrack. All the crack faces are traction-free and charge-free.

The original interaction problem shown in Fig. 3 has been decomposed into $N + 2$ subproblems as Horii and Nemat-Nasser treated in brittle solids (1985,, 1987) (see Fig. 4).

In the subproblem 1 of Fig. 4, the semi-infinite crack is loaded

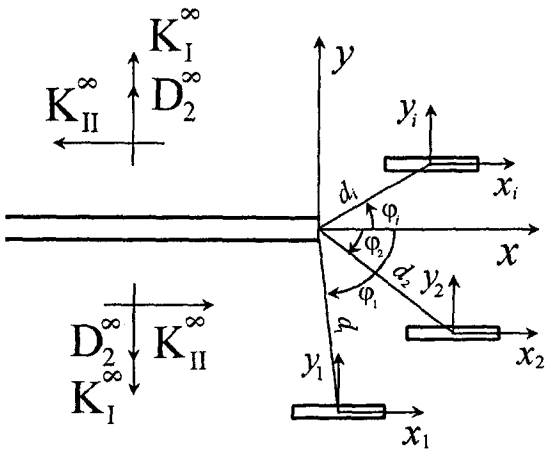

Fig. 3 Macrocrack-microcrack interaction

by remote SIF's K_I^∞ and K_{II}^∞, and the remote EDIF K_e^∞. According to the discussion presented in Section 2.3, the normal stress $f_{ip0}(s)$, the tangential stress $f_{iq0}(s)$, and the electric displacement $f_{iD0}(s)$ induced from the remote intensity factors at any point $(s, 0)$ on the ith microcrack location are given by (2) and (17):

$$f_{ip0}(s) = G_1(\Phi_k^\infty(Z_k), Z_k)$$
$$f_{iq0}(s) = G_2(\Phi_k^\infty(Z_k), Z_k) \quad i = 1, 2, \ldots N, \tag{18}$$
$$f_{iD0}(s) = G_3(\Phi_k^\infty(Z_k), Z_k)$$

where

$$Z_k = \mathrm{Re}(d_i e^{i\varphi_i} + s) + \mu_k \,\mathrm{Im}(d_i e^{i\varphi_i} + s) \tag{19}$$

and G_1, G_2, and G_3 are known functions which are given explicitly in Eq. (2).

In the subproblem 2 of Fig. 4, the macrocrack is subjected to the unknown pseudo-tractions $P^0(x)$ and $Q^0(x)$, and the unknown pseudo-electric displacement $d_2^0(x)$. The solutions can be obtained by using the elementary solution in Section 2.2 and the integration technique. The normal stress $\sigma_{22}^{i0}(s)$, the tangential stress $\sigma_{12}^{i0}(s)$, and the electric displacement $D_2^{i0}(s)$ at any point $(s, 0)$ on the ith microcrack location can be expressed as

$$\sigma_{22}^{i0}(s) = \int_{-\infty}^{0} [f_{ip0p}(t, x, y)P^0(t) + f_{ip0q}(t, x, y)Q^0(t) + f_{ip0d}(t, x, y)d_2^0(t)]dt$$

$$\sigma_{12}^{i0}(s) = \int_{-\infty}^{0} [f_{iq0p}(t, x, y)P^0(t) + f_{iq0q}(t, x, y)Q^0(t) + f_{iq0d}(t, x, y)d_2^0(t)]dt$$

$$D_2^{i0}(s) = \int_{-\infty}^{0} [f_{iD0p}(t, x, y)P^0(t) + f_{iD0q}(t, x, y)Q^0(t) + f_{iD0d}(t, x, y)d_2^0(t)]dt, \tag{20}$$

where $x + iy = d_i e^{i\varphi i} + s$, the nine kernel functions $f_{ip0p}(t, x, y), \ldots, f_{iD0d}(t, x, y)$ are known real functions, which could be expressed by using (2) and (15) without any difficulty. Here the subscripts i, 0, p, q, D, d have definite meanings which refer to the microcrack, the macrocrack, the normal traction, the tangential traction, the poling direction, and the electric displacement, respectively.

In the subproblem $i + 2$ of Fig. 4, the ith microcrack is subjected to the unknown pseudo-tractions $P^i(x_i)$ and $Q^i(x_i)$, and the unknown pseudo-electric displacement $d_2^i(x_i)$. Without going into detail, the normal stress $\sigma_{22}^{0i}(s)$, the tangential stress $\sigma_{12}^{0i}(s)$, and the electric displacement $D_2^{0i}(s)$ at any point $(s, 0)$ on the macrocrack location are obtained as follows:

$$\sigma_{22}^{0i}(s) = \int_{-a_i}^{a_i} [f_{0pip}(t, x_i, y_i)P^i(t) + f_{0piq}(t, x_i, y_i)Q^i(t) + f_{0pid}(t, x_i, y_i)d_2^i(t)]dt$$

$$\sigma_{12}^{0i}(s) = \int_{-a_i}^{a_i} [f_{0qip}(t, x_i, y_i)P^i(t) + f_{0qiq}(t, x_i, y_i)Q^i(t) + f_{0qid}(t, x_i, y_i)d_2^i(t)]dt$$

$$D_2^{0i}(s) = \int_{-a_i}^{a_i} [f_{0Dip}(t, x_i, y_i)P^i(t) + f_{0Diq}(t, x_i, y_i)Q^i(t) + f_{0Did}(t, x_i, y_i)d_2^i(t)]dt, \tag{21}$$

where the nine kernel functions $f_{0pip}(t, x, y), \ldots, f_{0qid}(t, x, y)$ are known real functions, which could be expressed by using (2) and (14), and $x_i + iy_i = -d_i e^{i\varphi i} + s$.

Similarly, the normal stress $\sigma_{22}^{ji}(s)$, the tangential stress $\sigma_{12}^{ji}(s)$, and the electric displacement $D_2^{ji}(s)$ induced from the ith microcrack at any point on the jth ($j \neq i$) microcrack are obtained as follows:

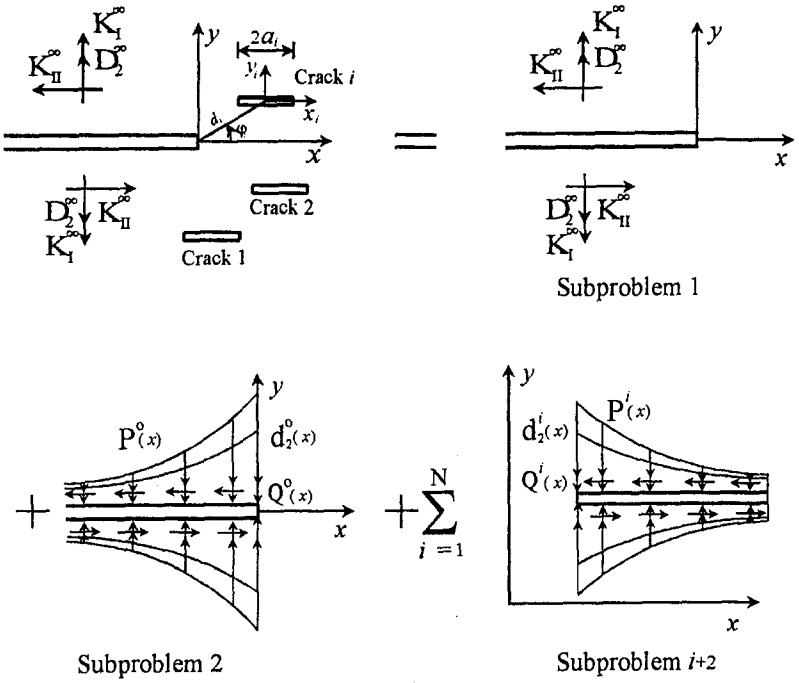

Fig. 4 Decomposition of macrocrack-microcrack interaction problem

$$\sigma_{22}^{jl}(s) = \int_{-a_i}^{a_i} [f_{jpip}(s, x_i, y_i)P^i(t) + f_{jpiq}(s, x_i, y_i)Q^i(t) + f_{jpid}(s, x_i, y_i)d_2^i(t)]dt$$

$$\sigma_{12}^{jl}(s) = \int_{-a_i}^{a_i} [f_{jqip}(s, x_i, y_i)P^i(t) + f_{jqiq}(s, x_i, y_i)Q^i(t) + f_{jqid}(s, x_i, y_i)d_2^i(t)]dt$$

$$D_2^{jl}(s) = \int_{-a_i}^{a_i} [f_{jDip}(s, x_i, y_i)P^i(t) + f_{jDiq}(s, x_i, y_i)Q^i(t) + f_{jDid}(s, x_i, y_i)d_2^i(t)]dt, \quad (22)$$

where the nine kernel functions in (22) are known real ones, which could be expressed by using (2) and (14), and $x_i + iy_i = d_j e^{i\varphi_j} - d_i e^{i\varphi_i} + s$ $(j \neq i)$.

Now, the original problem is reduced to the following integral equations after performing the superimposing technique:

$$P^0(s) + \sum_{l=1}^{N} \sigma_{22}^{0l}(s) = 0$$

$$Q^0(s) + \sum_{l=1}^{N} \sigma_{12}^{0l}(s) = 0 \quad (-\infty < s < 0)$$

$$d_2^0(s) + \sum_{l=1}^{N} D_2^{0l}(s) = 0$$

$$P^i(s) + \sum_{j=0}^{N} \sigma_{22}^{ij}(s) = -f_{ip0}(s) \quad (j \neq i)$$

$$Q^i(s) + \sum_{j=0}^{N} \sigma_{12}^{ij}(s) = -f_{iq0}(s) \quad (j \neq i) \quad (-a_i < s < a_i)$$

$$d_2^i(s) + \sum_{j=0}^{N} D_2^{ij}(s) = -f_{iD0}(s) \quad (j \neq i)$$

$$(i = 1, 2, \ldots N). \quad (23)$$

where σ_{22}^{0l}, σ_{12}^{0l}, D_2^{0l}, σ_{22}^{ij}, σ_{12}^{ij}, and D_2^{ij} have been defined by (20), (21), (22), while f_{ip0}, f_{iq0}, and f_{iD0} are known as expressed by (18).

Using the Chebyshev numerical integration technique, the system of integral Eqs. (23) could be solved numerically for the unknown pseudo-tractions and pseudo-electric displacement $P^i(s)$, $Q^i(s)$, and $d_2^i(s)$ $(i = 0, 1, 2, \ldots N)$. After doing so, the intensity factors of the macrocrack tip and those at the ith microcrack tips are given

$$K_{\mathrm{I}}^t = K_{\mathrm{I}}^\infty - \int_{-\infty}^{0} \sqrt{2}P^0(s) \Big/ \sqrt{-\pi s}\, ds$$

$$K_{\mathrm{II}}^t = K_{\mathrm{II}}^\infty - \int_{-\infty}^{0} \sqrt{2}\, Q^0(s) \Big/ \sqrt{-\pi s}\, ds$$

$$K_e^t = K_e^\infty - \int_{-\infty}^{0} \sqrt{2}\, d_2^0(s) \Big/ \sqrt{-\pi s}\, ds \quad (24)$$

and

$$K_{\mathrm{I}}^{Ri} = -\int_{-a_i}^{a_i} P^i(s)(a_i + s)^{1/2}(a_i - s)^{-1/2} \Big/ \sqrt{\pi a_i}\, ds$$

$$K_{\mathrm{I}}^{Li} = -\int_{-a_i}^{a_i} P^i(s)(a_i - s)^{1/2}(a_i + s)^{-1/2} \Big/ \sqrt{\pi a_i}\, ds$$

$$K_{\mathrm{II}}^{Ri} = -\int_{-a_i}^{a_i} Q^i(s)(a_i + s)^{1/2}(a_i - s)^{-1/2} \Big/ \sqrt{\pi a_i}\, ds$$

$$K_{\mathrm{II}}^{Li} = -\int_{-a_i}^{a_i} Q^i(s)(a_i - s)^{1/2}(a_i + s)^{-1/2} \Big/ \sqrt{\pi a_i}\, ds$$

$$K_e^{Ri} = -\int_{-a_i}^{a_i} d_2^i(s)(a_i + s)^{1/2}(a_i - s)^{-1/2} \Big/ \sqrt{\pi a_i}\, ds$$

$$K_e^{Li} = -\int_{-a_i}^{a_i} d_2^i(s)(a_i - s)^{1/2}(a_i + s)^{-1/2} \Big/ \sqrt{\pi a_i}\, ds$$

$$(i = 1, 2, \ldots N) \quad (25)$$

where the superscripts R and L refer to the right tip and the left tip of the ith microcrack, respectively.

4 Consistency Check

From the above-mentioned manipulations, numerical results for the SIF's and the EDIF at the macrocrack tip and the microcrack tips could be given, which will be discussed in detail in Part II of this series. However, it is not easy to confirm the results surely and steadily since no previously known results could be used for comparisons. A possible way from which the present results could be demonstrated is to make some comparisons in degenerated cases. However, it is not clear, at least not fully clear, from the physical point of view, that if the present results are really correct in general cases, after the above-mentioned comparisons are performed. Specially, if there were a tiny mistake in the above-mentioned manipulations which has no influence on the results in the degenerated cases and does influence the final results in general cases, the conclusions derived could be incorrect or misleading. Such a mistake could not be recognized by making the above-mentioned comparisons. Therefore, a question arises as to what the present authors should do to examine their numerical results more surely and steadily (Chen and Hasebe, 1998).

In this section a consistency check is proposed which starts from the total potential energy release rate (TPERR) in piezoelectric materials. As defined by Pak (1990) and Suo et al. (1992), the J-integral in such materials has a clear physical significance as the TPERR and its formulation is given as

$$J = \int_\Gamma \frac{1}{2}(\sigma_{ij}\epsilon_{ij} - D_i E_i)dy - n_i\sigma_{ip}\frac{\partial u_p}{\partial x_1}ds - n_i D_i \frac{\partial \varphi}{\partial x_1}ds \quad (26)$$

where, u_p $(p = 1, 2)$ is the displacement, φ is the electric potential, and Γ is a closed contour to be chosen. Customarily, in single-crack problems, Γ is generally taken as a smooth curve that starts from one point on the lower face and ends at another point on the upper face of a crack.

For making the consistency check, several closed contours are specially introduced (see Fig. 5) along which the J-integral is evaluated, respectively. In Fig. 5, Γ^∞ is corresponding to the remote mechanical-electric field, Γ^t is corresponding to the macrocrack tip, while Γ^Δ is corresponding to the N microcracks and Γ^i encloses the ith microcrack only. According to the path-independent nature of the J-integral, it is obvious that

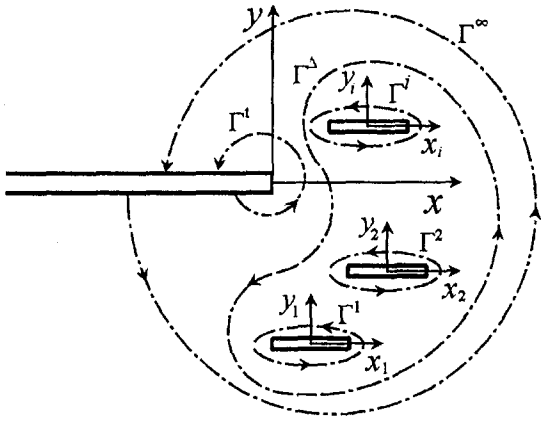

Fig. 5 Special closed contours for evaluating the *J*-integral

$$\Delta J = \sum_{l=1}^{N} J^{(l)} \tag{27}$$

where ΔJ is evaluated along Γ^{Δ} and $J^{(l)}$ is evaluated along Γ^{l}, and

$$J^{\infty} = J^{t} + \Delta J \tag{28}$$

$$J^{t}/J^{\infty} + \Delta J/J^{\infty} = 1 \tag{29}$$

where J^{∞} is evaluated along Γ^{∞} and J^{t} is evaluated along Γ^{t}.

Equation (29) is similar to the author's previous conclusions in brittle solids (Chen, 1996), in bimaterial solids (Zhao and Chen, 1997), and in anisotropic solids (Chen and Ma, 1997), which reveals that the remote TPERR is divided into two parts. One of them is contributed from the macrocrack tip and the other is induced from the existence of the microcracks. The detailed formulations of the two parts are given as follows:

$$J^{t} = \tfrac{1}{4}[\mathbf{K}^{t}]^{T}\mathbf{H}[\mathbf{K}^{t}] \tag{30}$$

$$J^{Rl} = \tfrac{1}{4}[\mathbf{K}^{Rl}]^{T}\mathbf{H}[\mathbf{K}^{Rl}] \quad (l = 1, 2, 3, \ldots, N) \tag{31}$$

$$J^{Ll} = \tfrac{1}{4}[\mathbf{K}^{Ll}]^{T}\mathbf{H}[\mathbf{K}^{Ll}] \quad (l = 1, 2, 3, \ldots, N) \tag{32}$$

$$J^{(l)} = J^{Rl} - J^{Ll} \quad (l = 1, 2, 3, \ldots, N) \tag{33}$$

where

$$[\mathbf{K}^{t}] = [K_{\mathrm{II}}^{t} \quad K_{\mathrm{I}}^{t} \quad K_{e}^{t}]^{T} \tag{34}$$

$$[\mathbf{K}^{Rl}] = [K_{\mathrm{II}}^{Rl} \quad K_{\mathrm{I}}^{Rl} \quad K_{e}^{Rl}]^{T} \quad (l = 1, 2, 3, \ldots, N) \tag{35}$$

$$[\mathbf{K}^{Ll}] = [K_{\mathrm{II}}^{Ll} \quad K_{\mathrm{I}}^{Ll} \quad K_{e}^{Ll}]^{T} \quad (l = 1, 2, 3, \ldots, N) \tag{36}$$

and $\mathbf{H}$ is a 3×3 matrix related to the piezoelectric material constants as

$$\mathbf{H} = 2\,\mathrm{Re}(i\mathbf{A}\mathbf{B}^{-1}) \tag{37}$$

in which

$$[\mathbf{A}] = \begin{bmatrix} p_1 & p_2 & p_3 \\ q_1 & q_2 & q_3 \\ r_1 & r_2 & r_3 \end{bmatrix} \tag{38}$$

$$[\mathbf{B}] = \begin{bmatrix} -\mu_1 & -\mu_2 & -\mu_3 \\ 1 & 1 & 1 \\ -\lambda_1 & -\lambda_2 & -\lambda_3 \end{bmatrix} \tag{39}$$

and

$$p_k = a_{11}\mu_k^2 + a_{12} - b_{21}\lambda_k$$

$$q_k = (a_{12}\mu_k^2 + a_{22} - b_{22}\lambda_k)/\mu_k \quad k = 1, 2, 3$$

$$r_k = -(b_{13} + \delta_{11}\lambda_k)\mu_k. \tag{40}$$

What's more, the relation (29) provides a necessary condition as well as a powerful tool for the consistency check to examine the numerical results derived by the above-mentioned technique PTED. Taking the PZT-4 piezoelectric ceramic as an example whose material constants are presented in Table 1, numerical examinations derived by the PTED method are shown in Table 2 and Fig. 6, respectively. Here, the normalized distance $d_n = (d - a)/a = 0.3$, 0.5, and 1.0, respectively, and the location angle φ is taken to be a variable from 0 deg to 160 deg. Only one microcrack is considered in the near-tip process zone of a macrocrack which is under the combined mechanical-electric loading conditions, i.e., $K_{\mathrm{I}}^{\infty} \neq 0$, $K_{\mathrm{II}}^{\infty} = 0$, and $K_{e}^{\infty} = 10^{-8}K_{\mathrm{I}}^{\infty}CN^{-1}$. It is shown that the consistency check is really satisfied by the present numerical results. The examinations presented in Table 2 and Fig. 6 confirm the results derived without taking any comparisons with some known results in degenerated cases since any mistake in the manipulations mentioned in the above section, if exists, will certainly lead to unsatisfied conclusions contrary to the check (29).

It should be noted that the relation (29) as well as the results shown in Fig. 6 reveals that there is a wastage, i.e., ΔJ, when the remote TPERR, J^{∞} transmits across the microcracking zone from the infinity to the macrocrack tip. The wastage is just due to the redistribution of the near-tip stress field and the near-tip electric field induced from microcracking. The major difference between the present investigation and the author's previous ones is the influence of the disturbed near-tip electric field on the wastage which represents as another consequence induced from microcracking. Thus, there are three kinds of energy dissipative processes due to microcracking in piezoelectric materials which do lead to the phenomenon of shielding effect and material toughness enhancement. As discussed by Hutchinison (1987), the first two ones are well known, i.e., the reduction on the effective moduli and the release of residual stresses at the microcrack location. The last one is the just above-mentioned disturbed near-tip electric field (DNTEF). It will be discussed further in Part II of this series that the disturbance of the near-tip electric field do to microcracking really provides another source of shielding.

5 Conclusions

From the above-mentioned manipulations and computations, the following conclusions are given:

Table 1 The reduced material constants of the PZT-4 piezoelectric ceramic

a_{11}	a_{12}	a_{22}	a_{33}
8.205×10^{-12}	-3.144×10^{-12}	7.495×10^{-12}	19.3×10^{-12} $(\mathrm{m^2N^{-1}})$
b_{21}	b_{22}	b_{13}	
-16.62×10^{-3}	23.96×10^{-3}	39.4×10^{-3}	$(\mathrm{m^2C^{-1}})$
δ_{11}	δ_{22}		
7.66×10^{7}	9.82×10^{7}	$(\mathrm{V^2N^{-1}})$	

Table 2 Numerical examinations by using a consistency check under compound mechanical-electric loading conditions ($K_I^\infty \neq 0$, $K_{II}^\infty = 0$, $K_e^\infty = 10^{-8} K_I^\infty CN^{-1}$)

$\varphi =$ ($d_n = 0.3$)	8°	20°	60°	90°	120°	160°
Microcrack						
K_I^R/K_I^∞	0.5854	0.6233	0.7721	0.8265	0.7447	0.2250
K_{II}^R/K_I^∞	0.0086	0.0371	0.0691	0.0079	-0.0984	-0.1007
$K_e^R/K_I^\infty (\times 10^{-8}\,\mathrm{CN}^{-1})$	0.5735	0.5546	0.4911	0.4546	0.4217	0.3300
K_I^L/K_I^∞	1.0308	1.1659	0.7967	0.4661	0.2116	-0.0004
K_{II}^L/K_I^∞	0.0766	0.1004	-0.1603	-0.1811	-0.1206	-0.0161
$K_e^L/K_I^\infty (\times 10^{-8}\,\mathrm{CN}^{-1})$	0.9154	0.7548	0.4530	0.3345	0.2419	0.1171
$\Delta J/J^\infty$	-0.5033	-0.2458	0.0372	0.0873	0.1107	0.0964
Macrocrack						
K_I^t/K_I^∞	1.3127	1.3877	0.9990	0.7928	0.7589	0.9807
K_{II}^t/K_I^∞	0.0534	0.0290	-0.1928	-0.1323	-0.0109	0.0113
$K_e^t/K_I^\infty (\times 10^{-8}\,\mathrm{CN}^{-1})$	1.2286	1.1240	0.9818	0.9508	0.9378	0.9518
J^t/J^∞	1.5033	1.2458	0.9628	0.9127	0.8892	0.9042
$(J^t + \Delta J)/J^\infty$	1.0000	1.0000	1.0000	1.0000	1.0000	1.0000

1 The pseudo-traction electric displacement method is effective to treat the macrocrack-microcrack interaction problem in piezoelectric materials.

2 The proposed consistency check really provides a powerful tool to examine numerical results for the interaction problem, although it represents a necessary condition rather a sufficient condition.

3 There is a wastage when the remote J-integral transmits across the microcracking zone from infinity to the macrocrack tip since microcracks in the near-tip process zone not only reduce the effective moduli and release the residual stresses, but also disturb the near-tip electric field. The latter provides another source of shielding.

Acknowledgments

This work was supported by the Chinese National Natural Science Foundations.

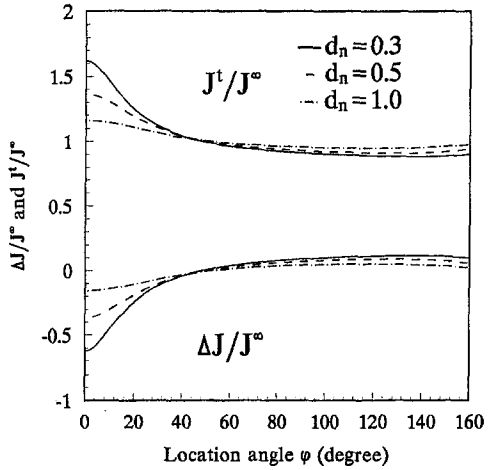

Fig. 6 Numerical examination for the consistency check taking $d_n = (d - a)/a = 0.3$, 0.5, and 1.0, respectively

References

Chen, Y. H., 1996, "On the contribution of microcrack in near-tip stress field to J-integral," *International Journal of Engineering Science,* Vol.34, pp.819–829.

Chen, Y. H., and Hasebe, N., 1998, "A consistency check for strongly interaction interacting multiple crack problem in isotropic, bimaterial and orthotropic bodies," *International Journal of Fracture,* in press.

Chen, Y. H., and Hasebe, N., 1994, "Interaction between a main crack and a parallel microcrack in an orthotropic plane elastic solid," *International Journal of Solids and Structures,* Vol.31, pp.1877–1890.

Chen, Y. H., and Ma, H., 1997, "Explicit formulation of the J_2-integral in anisotropic materials and its application," *Science in China (E),* Vol.40, pp.588–596 (English edition).

Chudnovsky, A., Dolgopolsky, A., and Kachanov, M., 1987, "Elastic Interaction of a Crack with a Microcrack Array—Part I and Part II," *International Journal of Solids and Structures,* Vol.23, pp.1–21.

Gong, S. X., and Horii, H., 1989, "General solution to the problem of microcracks near the tip of a main crack," *Journal of the Mechanics and Physics and Structures,* Vol.37, pp.27–46.

Gong, S. X., and Meguid, S. A., 1991, "On the effect of the release of residual stress duo to near-tip microcracking," *International Journal of Fracture,* Vol.52, pp.257–274.

Horii, H., and Nemat-Nasser, S., 1985, "Elastic fields of interacting inhomogeneities," *International Journal of Solids and Structures,* Vol.21, pp.601–629.

Horii, H., and Nemat-Nasser, S., 1987, "Interacting micro-crack near the tips in the process zone of a macro-crack," *Journal of the Mechanics and Physics in Solids,* Vol.35, pp.601–629.

Hutchinson, J. W., 1987, "Crack tip shielding by microcracking in brittle solids," *Acta Metall.,* Vol.35, pp.1605–1619.

Ortiz, M., 1987, "A continuum theory of crack shielding in ceramics," ASME JOURNAL OF APPLIED MECHANICS, Vol.54, pp.54–58.

Ortiz, M., 1988, "Microcrack coalescence and macroscopic crack growth initiation in brittle solids," *International Journal of Solids and Structures,* Vol.24, pp.231–250.

Ortiz, M., 1989, "Maximal Crack-Tip Shielding by Microcracking," ASME JOURNAL OF APPLIED MECHANICS, Vol.56, pp.279–283.

Pak, S. B., and Carman, G. P., 1997, "Minimizing Stress Levels in Piezoelectric Media Containing Elliptical Voids," ASME JOURNAL OF APPLIED MECHANICS, Vol.64, pp.466–470.

Pak, S. B., and Sun, C. T., 1995a, "Fracture criteria for piezoelectric ceramics," *Journal of the American Ceramic Society,* Vol.78, pp.1475–1480.

Pak, S. B., and Sun, C. T., 1995b, "Effect of electric fields on fracture of piezoelectric ceramics," *International Journal of Fracture,* Vol.70, pp.203–216.

Pak, Y. E., 1990, "Crack Extension Force in a Piezoelectric Material," ASME JOURNAL OF APPLIED MECHANICS, Vol.57, pp.647–653.

Pak, Y. E., 1992, "Linear electric-elastic fracture mechanics of piezoelectric materials," *International Journal of Fracture,* Vol.54, pp.79–100.

Rose, L. R. F., 1986, "Microcrack Interaction with a Main Crack," *International Journal of Fracture,* Vol.31, pp.233–246.

Rubinstein, A. A., 1986, "Macrocrack-Microdefect Interaction," ASME JOURNAL OF APPLIED MECHANICS, Vol.53, pp.505–510.

Sosa, H., 1991, "Plane problems in piezoelectric media with defects," *International Journal of Solids and Structures,* Vol.28, pp.491–505.

Sosa, H., 1992, "On the fracture mechanics of piezoelectric solids," *International Journal of Solids and Structures,* Vol.29, pp.2613–2622.

Sosa, H., and Pak, Y. E., 1990, "Three-dimensional eigenfunction analysis of a crack in a piezoelectric material," *International Journal of Solids and Structures,* Vol.26, pp.1–15.

Suo, Z., Kuo, C. M., Barnett, D. M., and Willis, J. R., 1992, "Fracture mechanics for piezoelectric ceramics," *Journal of Mechanics and Physics of Solids,* Vol.40, pp.739–765.

Zhao, L. G., and Chen, Y. H., 1997, "On the contribution of subinterface microcracks near-tip of an interface crack to the *J*-integral in bimaterial solids," *International Journal of Engineering Science,* Vol.35, pp.387–407.

Macrocrack-Microcrack Interaction in Piezoelectric Materials, Part II: Numerical Results and Discussions

Y.-H. Chen
Dean and Professor

J.-J. Han
Doctoral Student

School of Civil Engineering
and Mechanics,
Xi'an Jiaotong University,
Xi'an Shaanxi Province 710049,
P. O. China

Numerical results are shown in figures and tables. The major features for the traditional stress intensity factors and the electric displacement intensity factor against the microcrack location angle and the distance of the microcrack center from the macrocrack tip are discussed. It is shown that, unlike single-crack problems, the mechanical loading and the electric loading are coupled together since the microcrack not only releases the near-tip stresses, but also disturbs the near-tip electric field. Furthermore, the influence of the electric loading on the mechanical strain energy release rate (MSERR) at the macrocrack tip is discussed in detail. It is found that the variable nature of the MSERR against the normalized electric loading is monotonic and proportional wherever the parallel microcrack is located near the macrocrack tip. However, the slope of the MSERR's curve considering microcracking diverges far from those without considering microcracking. This finding reveals that, besides the two sources of microcrack shielding discussed by Hutchinson (1987) for brittle solids, the disturbance of the near-tip electric field due to microcracking really provides another source of shielding for piezoelectric solids.

1 Introduction

In Part I of this series, the TPERR analysis for the macrocrack-microcrack interaction is studied and the wastage of the TPERR is found when the remote J-integral transmits across the microcracking zone from infinity to the macrocrack tip. However, it is doubt that whether or not the wastage could be used as a criterion to determine the microcrack shielding or amplification effect in piezoelectric materials as it would be in brittle materials. This is due to the conclusion derived by Pak and Sun (1995a, b) that the TPERR, i.e., the J-integral is not suitable for describing the fracture behavior of piezoelectric ceramics. Moreover, they proposed a new criterion, i.e., the mechanical strain energy release rate (MSERR) for this purpose. As defined by them, the MSERR is given as

$$G_{\mathrm{I}}^{M} = \lim_{\delta \to 0} \frac{1}{2\delta} \int_0^{\delta} \sigma_{22}(x) \Delta u_2(\delta - x) dx \quad \text{for the mode I,} \quad (1)$$

and

$$G_{\mathrm{II}}^{M} = \lim_{\delta \to 0} \frac{1}{2\delta} \int_0^{\delta} \sigma_{12}(x) \Delta u_1(\delta - x) dx \quad \text{for the mode II} \quad (2)$$

where the superscript M refers to the MSERR and Δu_1 and Δu_2 are the jumps of the displacement components measured from the lower face to the upper face of a macrocrack.

For the mode I, the MSERR is related with the crack-tip SIF's and the EDIF as follows:

$$G_{\mathrm{I}}^{M} = \tfrac{1}{4}(H_{21} K_{\mathrm{I}} K_{\mathrm{II}} + H_{22} K_{\mathrm{I}}^2 + H_{23} K_{\mathrm{I}} K_e) \quad (3)$$

where H_{ij} $(i, j = 1, 2, 3)$ is the elements of the 3×3 matrix $\mathbf{H}$ which has been given in (37) of Part I.

Although the foregoing formulations presented in Part I are concerned with multiple microcracks and under the combined mode I and mode II and electric loading conditions, numerical results shown in Part II are limited to a single microcrack interacting with a macrocrack tip under the combined mode I and electric loading conditions. For the sake of convenience, a special piezoelectric material—the PZT-4 piezoelectric ceramic— is taken as an example with the reduced material constants listed in Table 1 of Part I. In the forthcoming numerical results, the plane-strain conditions are always assumed and the poling direction of the material is always taken to be perpendicular to both macrocrack and microcrack, i.e., parallel to the y-direction (see Fig. 1 of Part I). All the numerical results have been confirmed by using the consistency check presented in Part I.

In Sections 2 and 3 attention is focused on the variable tendencies of the traditional stress intensity factors and the electric displacement intensity factor at the macrocrack tip influenced by microcracking. In Section 4 the influence of the electric loading on the mechanical strain energy release rate is studied. It is found that, unlike the conclusion derived by Pak and Sun (1995a, b) for single-crack problems, the mechanical loading and the electric loading are coupled in the presented interaction problem since the microcrack not only releases the near-tip residual stresses and reduces the effective elastic moduli in the process zone, but also disturbs the near-tip electric field. The latter presents another source of shielding. It is concluded that the electric loading plays an important role in microcrack shielding problems for piezoelectric materials. The influence of the loading, whenever it is positive or negative on the mechanical strain energy release rate, always leads to decreasing the amplitude of the amplification effect and the neutral shielding angle, and in turn the amplification region near the macrocrack tip.

Contributed by the Applied Mechanics Division of THE AMERICAN SOCIETY OF MECHANICAL ENGINEERS for publication in the ASME JOURNAL OF APPLIED MECHANICS.
Discussion on the paper should be addressed to the Technical Editor, Professor Lewis T. Wheeler, Department of Mechanical Engineering, University of Houston, Houston, TX 77204-4792, and will be accepted until four months after final publication of the paper itself in the ASME JOURNAL OF APPLIED MECHANICS.
Manuscript received by the ASME Applied Mechanics Division, May 7, 1998; final revision, Oct. 27, 1998. Associate Technical Editor: M. Ortiz.

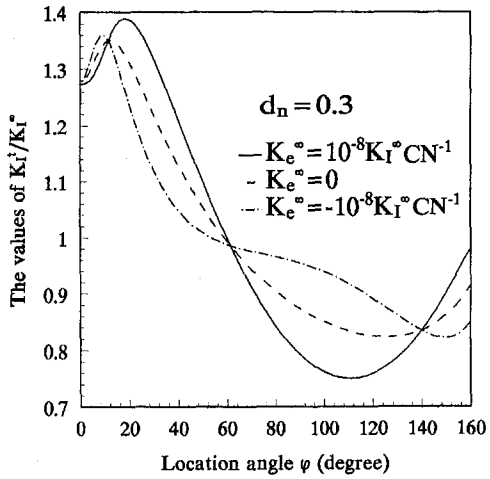

Fig. 1 Normalized mode I stress intensity factor against the location angle φ

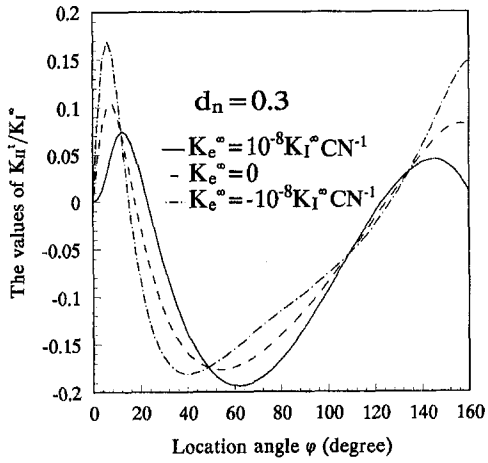

Fig. 2 Normalized mode II stress intensity factor against the location angle φ

2 The Traditional Stress Intensity Factors

In this section the interaction effect between a microcrack and a semi-infinite macrocrack is represented by the traditional stress intensity factors, i.e., the normalized SIF's K_I^i/K_I^∞ and K_{II}^i/K_I^∞. In Fig. 1, K_I^i/K_I^∞ against the microcrack location angle φ is plotted taking the normalized distance $d_n = (d - a)/a = 0.3$ (where d is the distance between the microcrack center and the macrocrack tip and a is the half-length of the microcrack). Three kinds of loading conditions are considered for making comparisons: (i) combined mode I and positive electric loading, i.e., $K_I^\infty \neq 0$, $K_{II}^\infty = 0$, $K_e^\infty = 10^{-8}K_I^\infty CN^{-1}$; (ii) purely mode I loading, i.e., $K_I^\infty \neq 0$, $K_{II}^\infty = 0$, $K_e^\infty = 0$; and (iii) combined mode I and negative electric loading, i.e., $K_I^\infty \neq 0$, $K_{II}^\infty = 0$, $K_e^\infty = -10^{-8}K_I^\infty CN^{-1}$. It is seen that the corresponding three curves show very complicated variable tendencies which are dissimilar to those found by Pak and Sun (1995a, b) in single-crack problems. The mechanical loading and the electric loading are really coupled due to the existence of the microcrack. In other words, the mode I stress intensity factor is no longer independent of the electric loading. For example, in the range of φ between 12 deg and 141 deg, the positive electric loading leads to aiding the interaction effect, while the negative electric loading leads to impeding the effect. However, it is not always the case. In the ranges of φ between 0 deg and 12 deg and between 141 deg and 160 deg, an opposite influence of the electric loading could be seen, i.e., the positive electric loading leads to impeding the effect, while the negative electric loading leads to aiding the effect. What's more, as shown in Fig. 1, there exist three special locations for the considered parallel microcrack in the near-tip process zone at which neither the positive nor the negative electric loading has influence on the K_I^i/K_I^∞. The location angles corresponding to three special locations could be called as neutral electric loading angles (NELA) denoted by φ_{NE}. In the present case (taking the PZT-4 piezoelectric ceramic and setting $d_n = 0.3$) the NELA φ_{NE} equals to about 12 deg, 65 deg, and 141 deg, respectively. It is found also in Fig. 1 that the electric displacement loading plays an important role in the macrocrack-microcrack interaction problem. The electric loading not only leads to shifting the maximum amplification location and amplitude when $K_I^i/K_I^\infty > 1$, but also leads to shifting the maximum shielding location and amplitude when $K_I^i/K_I^\infty < 1$. Table 1 shows the comparisons of the maximum amplification and maximum shielding location angles and the corresponding values of K_I^i/K_I^∞ among the three kinds of loading conditions mentioned above. It is concluded that the positive electric loading leads to increasing the maximum amplification location angle φ_{ma} and to decreasing the maximum shielding location angle φ_{ms} and the negative electric loading just leads to an opposite influence on φ_{ma} and φ_{ms}.

In Fig. 2, the mode II SIF K_{II}^i/K_I^∞ against φ is plotted. It is seen that there are four neutral electric loading angles at which neither the positive nor the negative electric loading has influence on K_{II}^i/K_I^∞. However, the values of the NELA do not coincide with those shown in Fig. 1 for the mode I SIF K_I^i/K_I^∞. It is seen also that the electric loading leads to shifting the maximum amplification and maximum shielding location for K_{II}^i/K_I^∞ too. However, quite the contrary, the positive electric loading increases both φ_{ma} and φ_{ms}, while the negative loading decreases both φ_{ma} and φ_{ms}.

In Figs. 3(*a, b, c, d*), the mode I SIF K_I^i/K_I^∞ against the normalized distance $d_n = (d - a)/a$ is plotted. Four location angles of the parallel microcrack are considered, i.e., $\varphi = 8$ deg, 30 deg, 80 deg, and 160 deg, respectively. It is seen in Fig. 3(*a*) for $\varphi = 8$ deg that there is a transformation distance $d_{nt} = 0.175$ at which neither the positive nor the negative electric loading has influence on the mode I SIF. When the distance d_n is less than d_{nt}, the

Table 1 The maximum amplification angles φ_{Ma} and the SIF's values and the maximum shielding angles φ_{Ms} and the SIF's values

	$K_I^\infty \neq 0, K_{II}^\infty = 0,$ $K_e^\infty = 10^{-8}K_I^\infty CN^{-1}$	$K_I^\infty \neq 0, K_{II}^\infty = 0,$ $K_e^\infty = 0$	$K_I^\infty \neq 0, K_{II}^\infty = 0,$ $K_e^\infty = -10^{-8}K_I^\infty CN^{-1}$
Maximum amplification angles	18.0°	12.0°	9.0°
SIF's values	1.3899	1.3521	1.3613
Maximum shielding angles	110.5°	126.0°	149.5°
SIF's values	0.7504	0.8235	0.8215

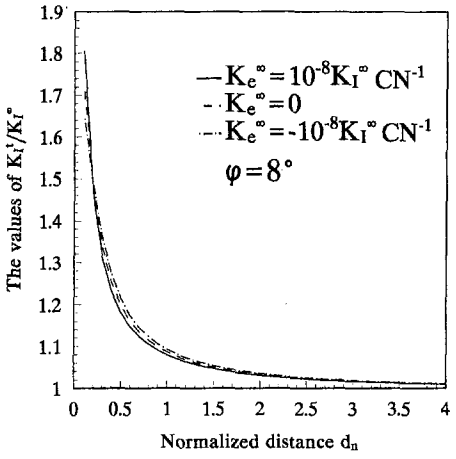

Fig. 3(*a*) φ = 8 deg

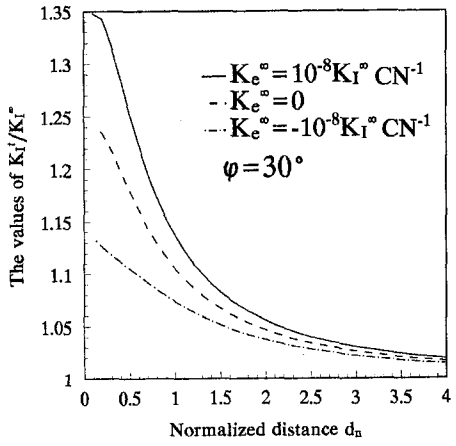

Fig. 3(*b*) φ = 30 deg

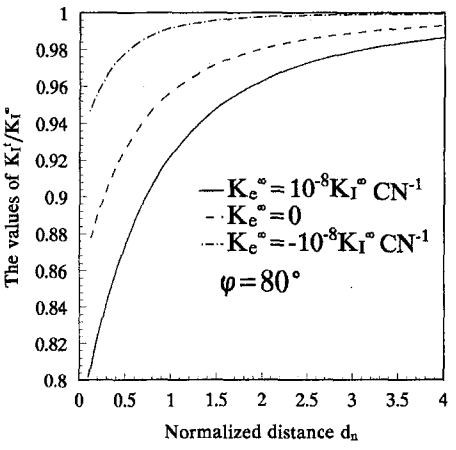

Fig. 3(*c*) φ = 80 deg

positive electric loading leads to increasing K_I^t/K_I^∞ and the negative electric loading leads to decreasing K_I^t/K_I^∞. This nature could be called as regular influence of electric loading (RIEL). On the contrary, when d_n is larger than d_{nt}, the influence of the electric loading just shows an opposite nature. This nature could be called as opposite influence of electric loading (OIEL). However, in Figs. 3(*b, c, d*) there are no such transformation distances at all. It is seen that in Fig. 3(*b*) for φ = 30 deg and in Fig. 3(*d*) for φ = 160 deg the variable tendencies of mode I SIF influenced by the electric loading are always RIEL, while in Fig. 3(*c*) for φ = 80 deg the tendencies are always OIEL. It is concluded that the influence of

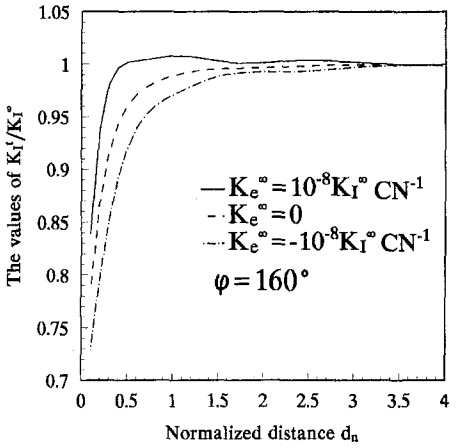

Fig. 3(*d*) φ = 160 deg

Fig. 3 Normalized mode I stress intensity factor against the normalized distance d_n

the electric loading on the mode I SIF is dependent of the location of the microcrack, i.e., dependent of φ and d_n, due to the coupling nature of the mechanical loading and electric loading in the present

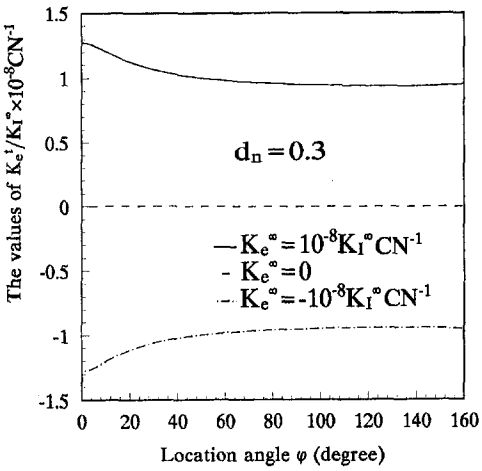

Fig. 4(*a*) d_n = 0.3

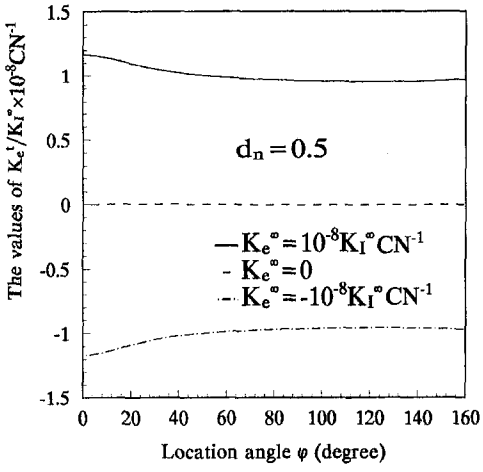

Fig. 4(*b*) d_n = 0.5

Fig. 4 Normalized electric displacement intensity factor against the location angle φ

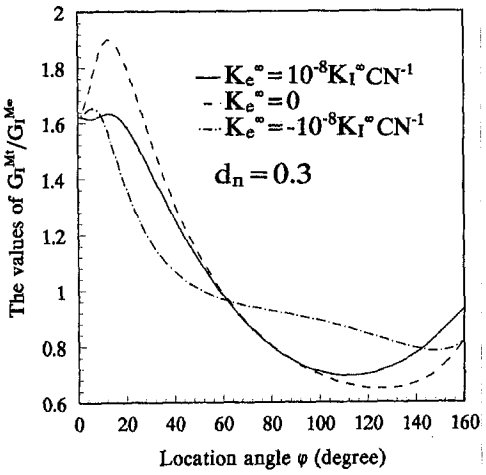

Fig. 5(*a*) $d_n = 0.3$

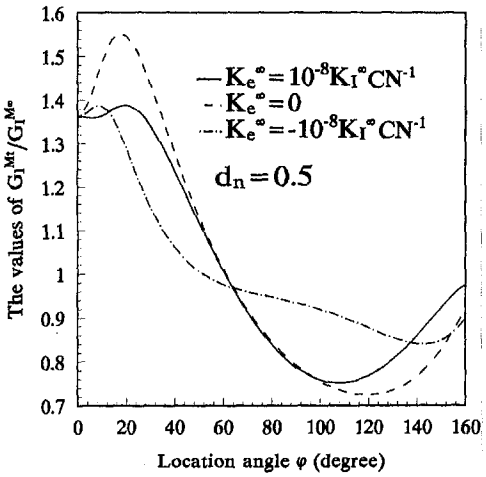

Fig. 5(*b*) $d_n = 0.5$

Fig. 5 Normalized mechanical strain energy release rate against the location angle φ

macrocrack-microcrack interaction problem. This reveals that the disturbance of the near-tip electric field induced from microcracking provides another source of shielding.

3 The Electric Displacement Intensity Factor

Of the great interest are the variable tendencies of the electric displacement intensity factor (EDIF) against the microcrack location angle φ taking $d_n = 0.3$. Here the EDIF has been normalized by $K_I^\infty \times 10^{-8} CN^{-1}$. It is seen in Figs. 4(*a*) and 4(*b*) that no matter how the microcrack location angle φ is, the positive electric loading always leads to increasing the normalized EDIF and the negative electric loading always leads to decreasing the normalized EDIF. Moreover, it is found that the variable nature of $K_e^t/K_I^\infty \times 10^{-8} CN^{-1}$ against $K_e^\infty/K_I^\infty \times 10^{-8} CN^{-1}$ is monotonic and nearly proportional, wherever the parallel microcrack is located in the near-tip process zone. The normalized EDIF at the macrocrack tip $K_e^t/K_I^\infty \times 10^{-8} CN^{-1}$ is approximately equal to the remote EDIF $K_e^\infty/K_I^\infty \times 10^{-8} CN^{-1}$ for large values of the location angle, for example, $\varphi > 40$ deg. However, for smaller values of the angle, the influence of the existence of the microcrack could not be neglected and the maximum influence occurs at the collinear situation, i.e., $\varphi = 0$. This conclusion coincides well with the well-known fact that the disturbance of the microcrack in the collinear case on the near-tip electric field is much larger than those in the other parallel cases corresponding to $\varphi > 0$. This reveals again that the disturbance of the near-tip electric field induced from microcracking really provides another source of shielding.

4 The Mechanical Strain Energy Release Rate (MSERR)

The influence of the electric loading on the mechanical strain energy release rate is studied in this section. The MSERR against the location angle of the microcrack under the three kinds of combined mechanical-electric loading conditions is plotted in Figs. 5(*a*) and 5(*b*) taking the normalized distance $d_n = 0.3$ and 0.5, respectively. Here, the MSERR G_I^{Mt} is normalized by

$$G_I^M = \tfrac{1}{4}(H_{22}K_I^2 + H_{23}K_IK_e) \tag{4}$$

where, as assumed earlier, $K_I^\infty \neq 0$, $K_{II}^\infty = 0$, while $K_e^\infty = 10^{-8}K_I^\infty CN^{-1}$, 0, $-10^{-8}K_I^\infty CN^{-1}$, respectively.

It is seen that as the angle φ increases from zero (corresponding to the collinear cases) the MSERR increases until the maximum value is reached. After the maximum value, the MSERR decreases as the angle φ increases, until the minimum value is reached. It is seen also that the values of the MSERR considering the electric loading diverge significantly from those without considering the electric loading. This provides another evidence of the disturbance of the near-tip electric field due to microcracking. What's more, the variable tendencies of the three curves in Fig. 5(*a*) or Fig. 5(*b*) seem quite different in magnitude from those shown in Fig. 1 for the mode I stress intensity factor. Although the electric loading leads to shifting the maximum amplification location and amplitude when $G_I^{Mt}/G_I^{M\infty} > 1$ and the maximum shielding location and amplitude when $G_I^{Mt}/G_I^{M\infty} < 1$, as contrasted with those for the mode I SIF shown in Fig. 1, the electric loading, whatever it is positive or negative, always leads to impeding the amplitude of the MSERR in the amplification regions corresponding to $G_I^{Mt}/G_I^{M\infty}$

Table 2 The maximum amplification angles and the MSERR's values and the maximum shielding angles and the MSERR's values ($d_n = 0.3$)

	$K_I^\infty \neq 0, K_{II}^\infty = 0,$ $K_e^\infty = 10^{-8}K_I^\infty CN^{-1}$	$K_I^\infty \neq 0, K_{II}^\infty = 0,$ $K_e^\infty = 0$	$K_I^\infty \neq 0, K_{II}^\infty = 0,$ $K_e^\infty = -10^{-8}K_I^\infty CN^{-1}$
Maximum amplification angles	12.5°	13.0°	6.0°
MSERR's values	1.6346	1.9024	1.6559
Maximum shielding angles	112.0°	126.0°	148.5°
MSERR's values	0.6952	0.6489	0.7849

Table 3 The neutral shielding angle φ_{NE}

	$K_I^\infty \neq 0, K_{II}^\infty = 0,$ $K_e^\infty = 10^{-8} K_I^\infty CN^{-1}$	$K_I^\infty \neq 0, K_{II}^\infty = 0,$ $K_e^\infty = 0$	$K_I^\infty \neq 0, K_{II}^\infty = 0,$ $K_e^\infty = -10^{-8} K_I^\infty CN^{-1}$
$d_n = 0.3$	58.0°	59.0°	51.0°
$d_n = 0.5$	60.5°	61.0°	51.5°

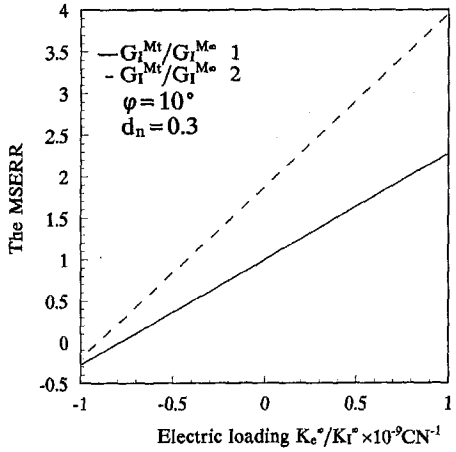

Fig. 6(*a*) d_n = 0.3 and φ = 10 deg

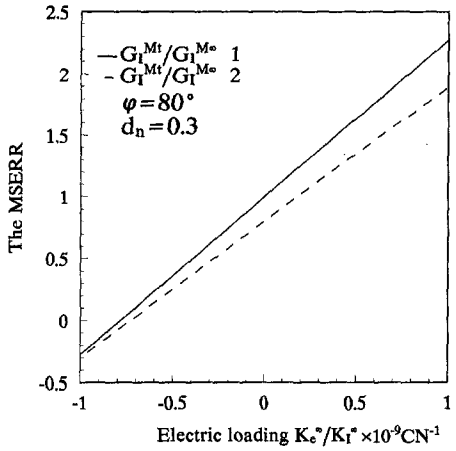

Fig. 6(*b*) d_n = 0.3 and φ = 80 deg

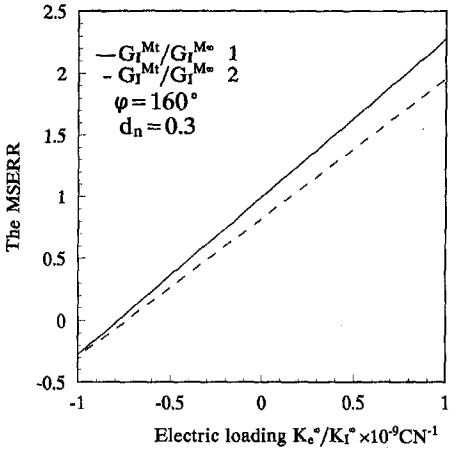

Fig. 6(*c*) d_n = 0.3 and φ = 160 deg

Fig. 6 Normalized mechanical strain energy release rate against the electric loading

> 1 and to decreasing the neutral shielding angle at which a transition from the amplification effect to the shielding effect occurs. Table 2 shows the maximum amplification angles, the corresponding values of the MSERR, and the maximum shielding angles and corresponding values of the MSERR. Table 3 shows the values of the neutral shielding angle under the above-mentioned three kinds of loading conditions. Therefore, the amplification region in the near-tip stress field under combined mechanical-electric loading should always be smaller than that under purely mechanical loading, whatever the electric loading is positive or negative, due to the disturbance of the microcrack in the near-tip electric field. Indeed, this conclusion reveals again that the electric loading plays an important role in microcrack shielding problems in piezoelectric solids. Moreover, it reveals that the mode I SIF and MSERR represent quite different physical natures in the macrocrack-microcrack interaction problem as they would do in single-crack problems (Pak and Sun, 1995a, b).

The MSERR against the electric loading is plotted in Figs. 6(*a*), 6(*b*), 6(*c*) taking d_n = 0.3 and φ = 10 deg, 80 deg, and 160 deg, respectively. Here, all the values of the MSERR are normalized by $G_I^{M\infty} = H_{22}(K_I^\infty)^2/4$ taking the electric loading to be variable. It is seen that the variable tendencies are also quite different from those for the traditional mode I stress intensity factor K_I^t/K_I^∞. In each of the figures from 6(*a*) to 6(*c*) two cases are considered for comparisons, one of which denoted by the label 1 is corresponding to the case without considering the microcrack, while the other denoted by label 2 is corresponding to the case considering the microcrack. It is found that in both cases for every figure the variable tendencies of the MSERR against the electric loading are linear although the slope of the case 2 is different from the slope of case 1. As $K_e^\infty/K_I^\infty 10^{-9} CN^{-1}$ increases from −1 to 1, the $G_I^{Mt}/G_I^{M\infty}$ in both cases for every figure always increases proportionally. Detailed investigations reveal that in Fig. 6(*a*) an amplification effect of the microcrack could be seen since the values of $G_I^{Mt}/G_I^{M\infty}$ in the case 2 (with the microcrack) are always larger than that in the case 1 (without the microcrack), while in Figs. 6(*b*) and 6(*c*) shielding effects could be seen since the values of $G_I^{Mt}/G_I^{M\infty}$ in the case 2 (with the microcrack) are always smaller than those in the case 1 (without microcrack).

Finally, it should be emphasized that the influence of the oriented angle of microcracking corresponding to inclined microcracks on the mode I SIF and the MSERR is poorly understood at present, which will inevitably require further investigation in the sequel.

6 Conclusions

From the above-mentioned discussion, the following conclusions could made.

1 The mechanical loading and the electric loading are coupled in the macrocrack-microcrack interaction problem in piezoelectric materials since the microcracks in the near-tip process zone of a macrocrack not only release the near-tip residual stresses and reduce the effective elastic moduli in the zone, but also disturb the near-tip electric field. The latter presents another source of shielding.

2 The electric loading plays an important role in microcrack shielding problems for piezoelectric materials. Whatever

the loading is positive or negative, the influence of the loading on the mechanical strain energy release rate at the macrocrack tip always leads to decreasing the neutral shielding angle and the amplitude of the amplification effect and in turn the amplification region near the macrocrack tip.

3 For a fixed microcrack location the MSERR against the electric loading shows a linear nature as it could be in single crack problems. As the electric loading increases from a negative value to a positive value the MSERR increase proportionally. However, the slope of the linear relation between the MSERR and the electric loading depends on the location of the microcrack.

Acknowledgment

This work was supported by the Chinese National Science Foundation.

References

Hutchinson, J. W., 1987, "Crack tip shielding by microcracking in brittle solids," *Acta Metall.*, Vol.35, pp.1605–1619.

Pak, S. B., and Sun, C. T., 1995a, "Fracture criteria for piezoelectric ceramics," *Journal of the American Ceramic Society*, Vol.78, pp.1475–1480.

Pak, S. B., and Sun, C. T., 1995b, "Effect of electric fields on fracture of piezoelectric ceramics," *International Journal of Fracture*, Vol.70, pp.203–216.

Biphasic Poroviscoelastic Behavior of Hydrated Biological Soft Tissue

J-K. Suh[1]
e-mail: fsuh@mailhost.tcs.tulane.edu
Assoc. Mem. ASME

M. R. DiSilvestro
Departments of Orthopaedic Surgery, Mechanical Engineering, and Bioengineering, University of Pittsburgh, Pittsburgh, PA 15213

Hydrated biological soft tissue consists of a porous extracellular matrix (ECM) and an interstitial fluid. The poroelastic theory (Biot, 1962), which was originally developed for soil mechanics, has been widely used for mathematical modeling of such hydrated biological tissue. This theory assumes that the ECM is incompressible and purely elastic, and that the interstitial fluid is incompressible and inviscid. The overall viscoelasticity of the tissue is expressed as a result of the frictional interaction between the elastic porous matrix and the interstitial fluid. The poroelastic theory, also known as the biphasic theory (Mow et al., 1980) in the biomechanics field, has served well over the past 20 years as an excellent modeling tool for the interstitial fluid flow-dependent viscoelastic response of hydrated soft tissue. It has been demonstrated that hydrated soft tissue also possesses a significant intrinsic viscoelasticity, independent of the interstitial fluid flow. The biphasic poroviscoelastic (BPVE) theory, which was first introduced by Mak (1986a and 1986b), incorporates a viscoelastic relaxation function into the effective solid stress of the poroelastic theory thus accounting for both intrinsic fluid flow-independent and fluid flow-dependent viscoelasticity. The objective of the present study is to investigate the biphasic poroviscoelastic characteristics of hydrated soft tissue, with an emphasis on the relative contribution of fluid flow-dependent and fluid flow-independent viscoelasticity to the overall viscoelastic behavior of soft tissues.

Introduction

While diverse in morphology and relative composition, all soft connective tissues in the animal body share a basic composition; they consist of cells, extracellular matrix and interstitial water. The extracellular matrix serves as a major building block of tissue type. Although the composition of extracellular matrix varies with the tissue, it generally contains fibers of collagen and elastin embedded in a hydrophilic gel called ground substance. The collagen and elastin fibers are organized in a parallel array of crystalline protein fibers, thus serving as tensile elements. The ground substance is an amorphous polymer made up of mucopolysaccharide (glycosaminoglycans) and other minor glycoproteins. The glycosaminoglycans (GAG) found in most soft connective tissues include chondroitin sulfate, dermatan sulfate, keratan sulfate, and hyarulonic acid. In soft tissues, these GAG molecules are usually present in association with protein, forming large aggregated macromolecule called proteoglycan (PG) (Buckwalter et al., 1989). In a hydrated environment at physiological pH, the GAG molecules aggregated in proteoglycan become negatively charged, and these high negative charges create electrostatic repulsive forces between the molecules. It is electrostatic repulsive force which is responsible for the marked compressive stiffness of soft connective tissue. Interstitial water is the most abundant element in soft connective tissues. It is involved in providing several important biomechanical functions of the tissue not only through binding of water to the hydrophilic GAG molecules, but also through the Donnan osmotic swelling phenomenon and the relative motion between the interstitial water and the porous matrix.

Such hydrated composite structural morphology as described above produces complex mechanical behaviors of soft connective tissues, even under a simple uniaxial loading condition. Many of these complex behaviors of hydrated soft tissues have been approximated with various simplified constitutive, either elastic or viscoelastic, models (Fung, 1994). Within the framework of linear viscoelasticity, finite combinations of springs and dash-pots, such as Kelvin and Voigt models, have been utilized to model the viscoelastic behaviors of soft tissues (Hayes and Mockros, 1971; Parsons and Black, 1977). An integral form of the quasi-linear viscoelasticity theory was also proposed to account for the nonlinear stress-strain characteristics of soft tissues under large deformation (Fung, 1972). More recently, the poroelastic theory (Biot, 1962), which was originally developed for soil mechanics, was first implemented to simulate the viscoelastic behaviors of soft tissue by Mow et al. (1980). This theory, also known as the biphasic theory in the biomechanics field, modeled the soft tissue as a biphasic mixture of an incompressible elastic porous solid matrix saturated with an incompressible inviscid interstitial fluid. This model assumes that the overall viscoelasticity of the tissue is expressed as a result of the frictional interaction between the porous elastic solid matrix and the interstitial fluid. The poroelastic theory has been used extensively to simulate the interstitial fluid *flow-dependent* viscoelastic behavior of various hydrated soft tissues, such as articular cartilage (Mow et al., 1993), intervertebral disk (Laible et al., 1994), arterial wall (Simon et al., 1993), cardiac muscle (Yang et al., 1994), lung (Pitt Ford et al., 1991), and brain (Basser, 1992).

It has been found that hydrated soft tissues such as articular cartilage demonstrate significant viscoelastic behaviors in pure shear (Hayes and Bodine, 1978; Spirt et al., 1989; Zhu et al., 1993). When a soft tissue undergoes a pure shear, or deviatoric deformation, the interstitial fluid flow within the tissue matrix is almost negligible in a volume average sense due to near-incompressible properties of both the solid matrix and the interstitial fluid. Therefore, the viscoelastic phenomenon observed in

[1] To whom correspondence should be addressed: Department of Biomedical Engineering, Lindy Boggs Center, Suite 500, Tulane University, New Orleans, LA 70118.

Contributed by the Applied Mechanics Division of THE AMERICAN SOCIETY OF MECHANICAL ENGINEERS for publication in the ASME JOURNAL OF APPLIED MECHANICS.

Discussion on the paper should be addressed to the Technical Editor, Professor Lewis T. Wheeler, Department of Mechanical Engineering, University of Houston, Houston, TX 77204-4792, and will be accepted until four months after final publication of the paper itself in the ASME JOURNAL OF APPLIED MECHANICS.

Manuscript received by the ASME Applied Mechanics Division, Jan. 13, 1998; final revision, Oct. 1, 1998. Associate Technical Editor: J. T. Jenkins.

the case of pure shear represents an intrinsic (fluid *flow-independent*) viscoelasticity of soft tissue matrix. In fact, PG gel, an aggregate of polyanionic GAG molecules, is intrinsically viscoelastic, independent of an apparent frictional interaction between the solid and the interstitial fluid (Mow et al., 1984; Zhu and Mow, 1990). Collagen fibrils in tendons and ligaments are also known to be intrinsically viscoelastic (Viidik, 1968). Consequently, the extracellular matrix of soft tissue, a mixture of PG and collagen, is expected to demonstrate intrinsic viscoelastic behaviors in the absence of the interstitial fluid flow under shear. In order to account for these intrinsic (fluid *flow-independent*) viscoelastic characteristics along with the biphasic (fluid *flow-dependent*) viscoelasticity of soft tissues, Mak (1986a, b) introduced a biphasic poroviscoelastic (BPVE) theory in which an integral-type linear viscoelasticity was incorporated into the effective solid stress of the biphasic theory. We recently developed a computational model of the BPVE theory for hydrated soft tissues utilizing the penalty Galerkin weighted residual method and a discrete spectrum representation of the relaxation function (Suh and Bai, 1998). The objective of this present study was to investigate the biphasic poroviscoelastic characteristics of hydrated soft tissues using articular cartilage as a model, with an emphasis on the relative contribution of fluid *flow-dependent,* and fluid *flow-independent* viscoelasticity to the overall viscoelastic behavior of soft tissues.

Mathematical Models for Viscoelastic Behaviors of Soft Tissue

Biphasic Poroelastic (BPE) Theory. In the biphasic poroelastic theory, hydrated soft tissue is modeled as a biphasic mixture of porous solid matrix and interstitial fluid. It is assumed that both the porous solid substance and the interstitial fluid are incompressible. The apparent volume of the solid matrix is still compressible through exudation of interstitial fluid. Assuming that the solid phase is linearly elastic with infinitesimal strain and that the interstitial fluid is inviscid, the governing equations of the biphasic poroelastic theory are (Mow et al., 1980):

Continuity equation:

$$\nabla \cdot (\phi^s \mathbf{v}^s + \phi^f \mathbf{v}^f) = \mathbf{0} \tag{1}$$

Momentum equations:

$$\nabla \cdot \boldsymbol{\sigma}^\alpha + \boldsymbol{\pi}^\alpha = \mathbf{0} \quad \alpha = s, f \tag{2}$$

Constitutive equations:

$$\boldsymbol{\sigma}^s = -\phi^s p \mathbf{I} + \tilde{\boldsymbol{\sigma}}^s \tag{3}$$

$$\boldsymbol{\sigma}^f = -\phi^f p \mathbf{I} \tag{4}$$

Here, the superscripts s and f refer to the solid and fluid phases, respectively; ϕ^α is the volume fraction of the α phase; $\mathbf{v}^\alpha$ is the velocity of the α phase; $\boldsymbol{\sigma}^\alpha$ is the total stress tensor of the α phase; and p is the fluid pressure. $\tilde{\boldsymbol{\sigma}}^s$ is the effective solid stress representing the portion of the total solid stress which is in excess of the local fluid pressure (Biot, 1962). With λ^s and μ^s denoting the Lamé elastic constants, the classical Hooke's law leads to the following:

$$\tilde{\boldsymbol{\sigma}}^s = \lambda^s \operatorname{tr}(\boldsymbol{\epsilon}^s)\mathbf{I} + 2\mu^s \boldsymbol{\epsilon}^s \tag{5}$$

where $\boldsymbol{\epsilon}^s$ is the infinitesimal strain tensor of the solid matrix.

$\boldsymbol{\pi}$ is a diffusive momentum exchange between the solid matrix and the interstitial fluid, which can be assumed to be proportional to the interstitial fluid velocity relative to the solid matrix. Assuming a constant diffusive drag coefficient K, it can then be written as

$$\boldsymbol{\pi}^s = -\boldsymbol{\pi}^f = K(\mathbf{v}^f - \mathbf{v}^s). \tag{6}$$

Using Darcy's law, the diffusive drag coefficient K can be expressed in terms of the permeability κ of the solid matrix as follows:

$$K = \frac{\phi^{f\,2}}{\kappa}. \tag{7}$$

While this model assumes that both the solid and the fluid constituents do not possess any intrinsic viscosity, a diffusive interaction occurring at the physical interfaces between the solid and interstitial fluid is incorporated into the continuum model in Eqs. (2) and (6), and thus contributes to the overall viscoelastic behavior of the bulk material.

Biphasic Poroviscoelastic (BPVE) Theory. Based on the intrinsic flow-independent viscoelastic characteristics of the ECM of hydrated soft tissue, the BPVE theory incorporates an integral-type linear viscoelastic representation into the effective solid stress term, as follows (Mak, 1986a and 1986b):

$$\tilde{\boldsymbol{\sigma}}^s = B^s \int_{-\infty}^{t} G_1(t-\tau) \frac{\partial}{\partial \tau} \operatorname{tr}(\boldsymbol{\epsilon}^s) d\tau + 2\mu^s \int_{-\infty}^{t} G_2(t-\tau) \frac{\partial \mathbf{e}^s}{\partial \tau} d\tau. \tag{8}$$

Here, B^s and μ^s represent the intrinsic bulk modulus and the intrinsic shear modulus, respectively, of the solid matrix; $\mathbf{e}^s$ represents the deviatoric strain tensor of the solid matrix, i.e., $\mathbf{e}^s = \boldsymbol{\epsilon}^s - \frac{1}{3} \operatorname{tr}(\boldsymbol{\epsilon}^s)$. $G_1(t)$ and $G_2(t)$ represent the reduced relaxation functions for volumetric and deviatoric terms, respectively.

It has been shown that most hydrated soft tissues demonstrate frequency-insensitive hysteric characteristics over a wide decadic range of frequencies (Fung, 1972). A relaxation function with a continuous spectrum, proposed by Fung (1972), has been widely used to represent such frequency-insensitive viscoelastic behavior of various soft tissues (Myers et al., 1991; Kwan et al., 1993; Fung, 1994). However, an excessive computational burden caused by the convolution integral in Eq. (8) hinders the continuous relaxation spectrum model from being readily used for a practical application. On the other hand, a discrete relaxation spectrum has been proven effective to avoid the repetitive, time-consuming calculation of the convolution integral, thus improving the computational efficiency of the integral-type viscoelastic model description (Suh and Bai, 1998). The present study, therefore, utilized a simplified relaxation function with a discrete spectrum as suggested in our previous study (Suh and Bai, 1998):

$$G(t) = 1 + \bar{G} \sum_{i=1}^{N_d} e^{-t/\tau_i} \tag{9}$$

where τ_i is the discrete relaxation rate, N_d is the number of discrete terms, and $\bar{G}$ is the spectrum magnitude. One disadvantage of this discrete spectrum model is the nonuniqueness of the parametric representation of Eq. (9) (Tschoegl, 1989; Fung, 1994). While the choice of N_d and the interval of τ_i in Eq. (9) are somewhat arbitrary, our preliminary tests demonstrated that $N_d = 3$ and a uniform decadic (10-base logarithmic) interval of τ_i was efficient and comparable to the continuous spectrum model, as shown in Fig. 1 (Suh and Bai, 1998). In this case, τ_1 could be denoted as τ_S, the short-term relaxation rate, and τ_3 as τ_L, the long-term relaxation rate, equivalent to two relaxation rate parameters used in the continuous relaxation spectrum model (Fung, 1972). The intermediate relaxation rate, τ_2, could be defined as follows:

$$\log \tau_2 = (\log \tau_1 + \log \tau_3)/2. \tag{10}$$

In general, $G_1(t) \neq G_2(t)$ in Eq. (8), because it is likely that, in the effective solid stress, the hydrostatic component would relax at

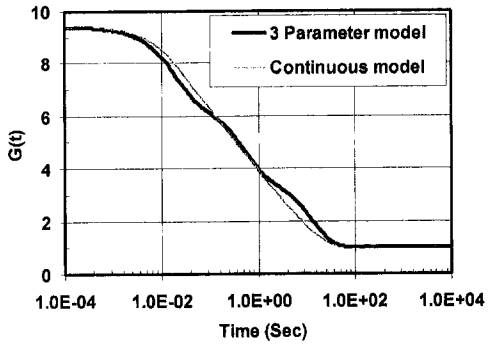

Fig. 1 Reduced stress relaxation functions of the three-parameter discrete model and the continuous spectrum model

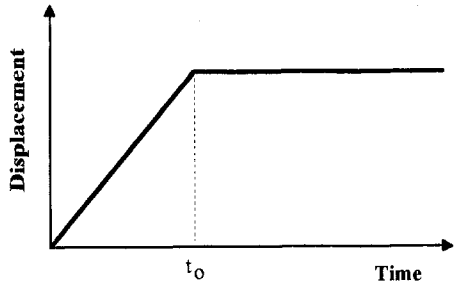

Fig. 3 Diagram of the ramp loading function

a different rate than the deviatoric component. The flow-independent relaxation function for the deviatoric component of the effective solid stress could be experimentally obtained from a dynamic shear test as reported by Hayes and Bodine (1978). However, it is very difficult, or perhaps almost impossible, to experimentally isolate the intrinsic flow-independent relaxation of the hydrostatic component of the effective solid stress, because any volumetric deformation of the solid matrix would induce a concomitant flow of interstitial fluid within the tissue matrix and thereby causes a flow-dependent biphasic relaxation in the stress component. In order to simplify the expression of Eq. (8), therefore, the present study tested two different model assumptions. The first assumption (denoted by "BPVE-1") was that $G_1(t) = 1$ and $G_2(t) = G(t)$, i.e., the hydrostatic component of the effective solid stress is governed simply by a pure elastic law, whereas the deviatoric stress component is governed by a viscoelastic law. The second model assumption (denoted by "BPVE-2") was that both the hydrostatic stress component and the deviatoric stress component are governed by the same relaxation function, i.e., $G_1(t) = G_2(t) = G(t)$.

Finite Element Formulation of the Models. The above governing equations were first transformed into a weak form of the Galerkin weighted residual formulation. The continuity equation, Eq. (1), was then replaced with a penalty form, by which the pressure could be eliminated from the governing equations. As a result, the finite element formulation of the BPVE theory was expressed in terms of the displacement and velocity of the solid and fluid as primary unknown variables as follows:

$$\mathbf{C}\mathbf{v}(t) + \mathbf{K}\boldsymbol{\eta}(t) = \mathbf{F}(t) \tag{11}$$

$$\boldsymbol{\eta}(t) = \int_0^t G(t-\tau)\mathbf{v}(\tau)d\tau \tag{12}$$

Here, **C** and **K** represent the equivalent convective and equivalent stiffness matrices, respectively, and $\mathbf{v}(t)$ represents the nodal velocity vector. $\eta(t)$ is the viscoelastic pseudo-displacement of the solid matrix. Using the discrete relaxation spectrum, Eqs. (10) and (11) could be readily discretized to yield a recursive form in the time domain. A detail of the present finite element formulation can be found in Suh and Bai (1998).

Experiment and Model Simulation

Experiment: Unconfined Ramp Compression. Articular cartilage was harvested from a fresh bovine patella and used in this study. A cylindrical plug uniform in diameter ($d = 3$ mm) and thickness ($h = 1.22 \pm 0.07$ mm) was prepared from the cartilage specimen using a microtome (Vibratome® 1000) and a stainless steel biopsy punch. The specimen was then placed between two loading platens, and mounted on a miniature material testing machine (Vitrodyne® V1000) as shown in Fig. 2. The upper and lower surface of the specimen was glued to the upper and lower loading platens with ethyl cyanoacrylate adhesive. This perfectly adhesive boundary condition was used to eliminate an ambiguous frictional slip between the specimen and the loading platens (Armstrong et al., 1984; Spilker et al., 1990). The specimen was then submerged in a saline bath, and subjected to a protocol of unconfined compression stress relaxation as described below.

After first being equilibrated with an axial tare load of 1 g in a saline bath, the specimen was compressed to an axial strain of ten percent in a ramp function set at a speed of 10 μm/sec (Fig. 3). The axial reaction force exerted by the specimen during the ramp and holding phase was measured using a high precision load cell (maximum capacity 25 lb, Transducer Technology, Inc., CA) connected to the upper loading platen.

Model Simulation: Finite Element Model. Due to symmetry with respect to the center axis, only the upper right quadrant of the tissue domain was considered in the finite element modeling of the unconfined compression experiment (Fig. 2). The finite element mesh was adopted from our previous study (Spilker et al., 1990),

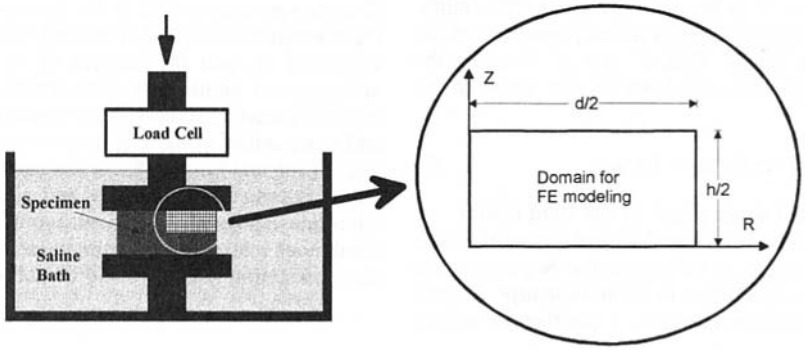

Fig. 2 Schematics of the unconfined compression experiment and its finite element modeling domain

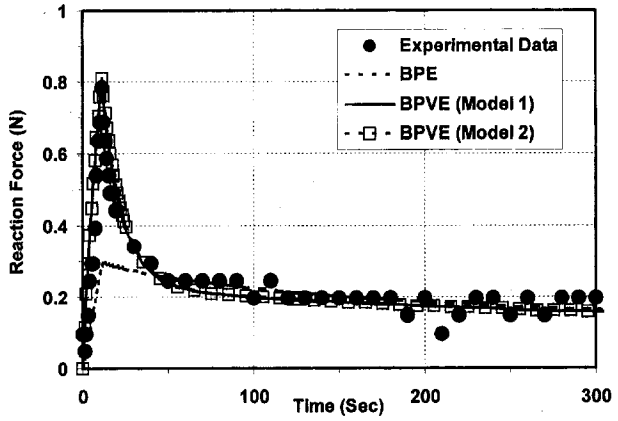

Fig. 4 Comparison of BPE and BPVE models to stress relaxation unconfined compression experimental data

consisting of 140 four-node axisymmetric elements with a total of 165 nodal points. Because of the penalty approximation of the incompressible condition, an axisymmetric mean dilatation formulation suggested by Nagtegaal et al. (1974) was used so that the pressure, strain, and stress variables were evaluated at the centroid of each element, whereas the displacement and velocity variables were evaluated at the nodal points. A perfectly adhesive boundary condition was implemented at the tissue-loading platen interface to account for the interface boundary condition used in the experiment.

Results

During unconfined compression, the tested cartilage specimen exhibited a significant stress relaxation response (Fig. 4); the peak reaction force was 0.78N, and the final equilibrium reaction force was 0.19N. Figure 4 also shows the reaction force mathematically predicted by the BPE model and the BPVE model simulations. It was found that the BPVE model simulations provided an excellent agreement with the experimental data. It was also demonstrated that BPVE-1 and BPVE-2 produced an identical result in predicting the reaction force, suggesting that the effect of the intrinsic, fluid *flow-independent* viscoelastic characteristics of the hydrostatic component of the effective solid stress are almost negligible. The BPVE model parameters which produced a best curve-fit to the experimental reaction force data were: $\lambda^s = 0.01$ MPa and $\mu^s = 0.09$ MPa, $\kappa = 0.5 \times 10^{-14}$ m^4/N · sec, $\bar{G} = 2.8$, $\tau_S = 0.02$ sec, and $\tau_L = 13$ sec. In the unconfined compression stress relaxation protocol, it is possible that the reaction force data alone may not be sufficient to allow a complete parameter identification with the BPVE model. In this study, therefore, the Poisson's ratio of the tissue matrix was thus pre-assumed to be 0.05 based on previous literature (Mow et al., 1989; Athanasiou et al., 1991). The rational of the choice of $\nu = 0.05$ will be discussed in detail later in the paper (see Discussion).

When the corresponding BPE model parameters were used ($\lambda^s = 0.01$ MPa and $\mu^s = 0.09$ MPa, $\kappa = 0.5 \times 10^{-14}$ m^4/N · sec), the BPE model simulation resulted in a noticeably low-peak reaction force and a slow relaxation, especially during the early period ($t < 100$ sec) of unconfined compression (Fig. 4). It was found that the BPE model provided an excellent prediction of the long-term relaxation response ($t > 100$ sec).

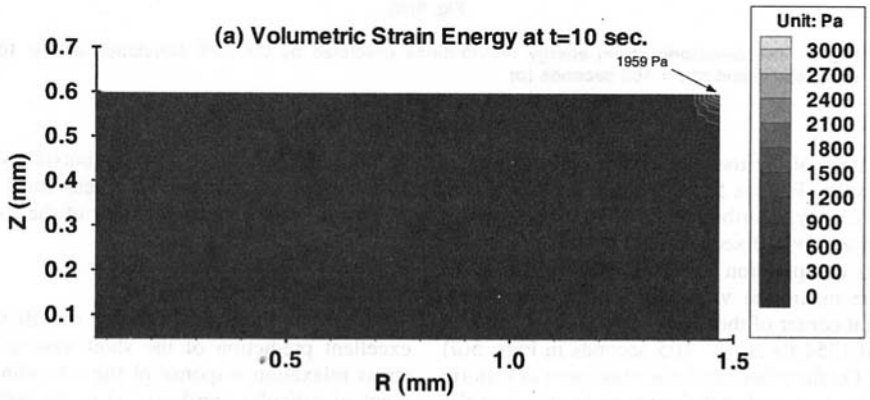

Fig. 5(*a*)

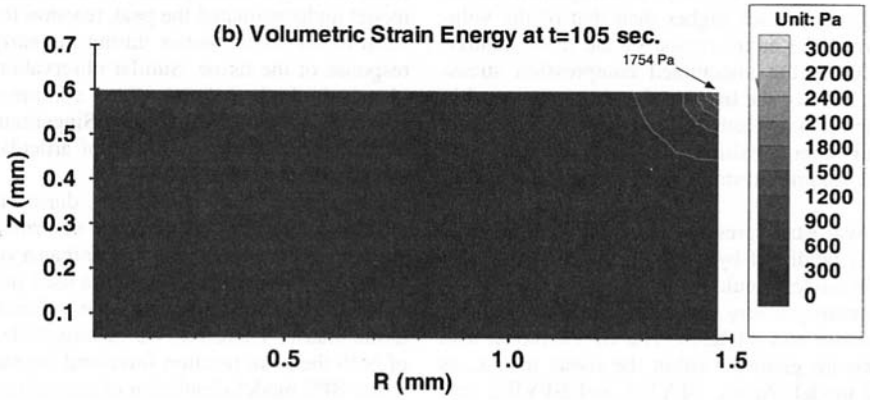

Fig. 5(*b*)

Fig. 5 The volumetric strain energy distributions predicted by the BPE simulation at $t = 10$ seconds (*a*) and at $t = 105$ seconds (*b*)

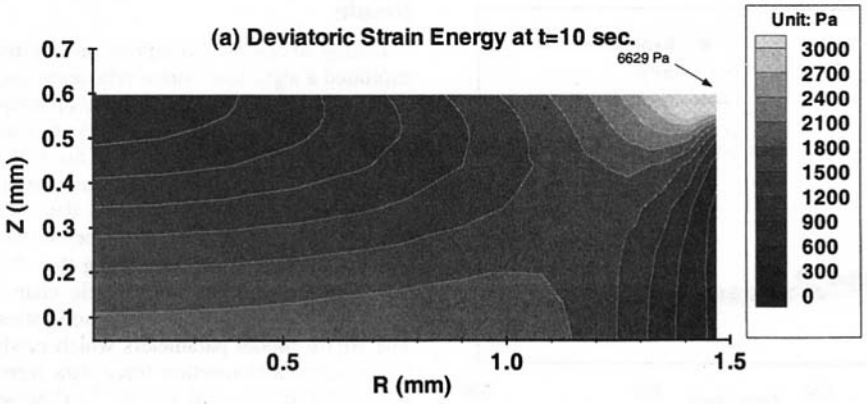

Fig. 6(*a*)

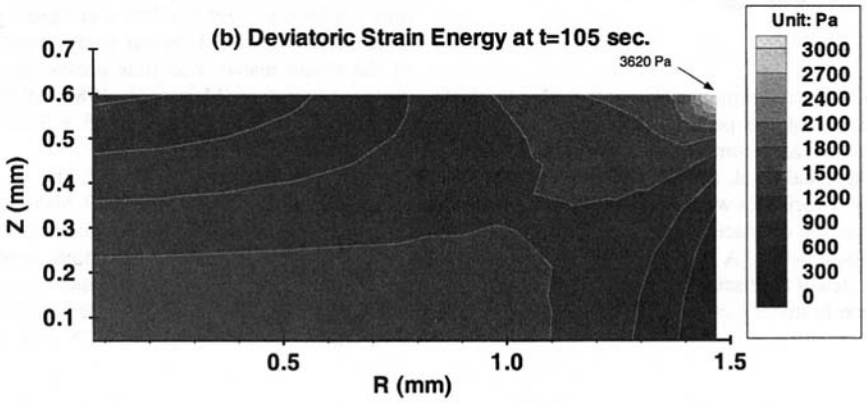

Fig. 6(*b*)

Fig. 6 The deviatoric strain energy distributions predicted by the BPE simulation at t = 10 seconds (*a*) and at t = 105 seconds (*b*)

The deformation pattern of the tissue matrix under unconfined compression is noteworthy. Figures 5 and 6 show the volumetric and deviatoric strain energy distributions in the tissue matrix, respectively, predicted at t = 10 seconds and t = 105 seconds during the unconfined compression experiment using the BPE model simulation. The maximum volumetric strain energy occurred at the upper right corner of the specimen, and was 1960 Pa at t = 10 seconds and 1754 Pa at t = 105 seconds in Figs. 5(*a*) and 5(*b*), respectively. On the other hand, the maximum deviatoric strain energy, which also occurred at the upper right corner of the specimen, was 6629 Pa at t = 10 seconds and 3620 Pa at t = 105 seconds in Figs. 6(*a*) and 6(*b*), respectively. The magnitude of the deviatoric strain energy was much higher than that of the volumetric strain energy over the entire region of the tissue matrix. This indicates that, during the unconfined compression stress-relaxation experiment, most of the tissue deformation occurred in a deviatoric form, rather than a volumetric form. It was also found that the deviatoric strain energy exhibited a significant relaxation with time, whereas the volumetric strain energy underwent only a small relaxation.

Figures 7 show the hydrostatic pressure distributions at the peak time (t = 10 seconds) predicted by the BPE and BPVE model simulations. The BPVE model simulations predicted a larger pressure magnitude (maximum pressure was 122 Kpa) than the BPE model (maximum pressure was 44 KPa). The BPVE model also predicted a larger pressure gradient within the tissue matrix, as compared to the BPE model. Again, BPVE-1 and BPVE-2 predicted a similar pressure pattern.

Figure 8 shows a vector plot of the interstitial fluid velocity at the peak time (t = 10 seconds) predicted by the BPVE model simulation. As the tissue was axially compressed, the interstitial fluid flowed radially toward the outside of the tissue matrix. The maximum fluid velocity at the peak time was predicted to be 3.9 μm/sec at the upper right corner of the tissue.

Discussion and Conclusion

This study demonstrates that the BPVE theory produces an excellent prediction of the short-term as well as the long-term stress relaxation response of the unconfined compression experiment of articular cartilage. Also, the BPE model was found to provide an excellent prediction of the slow relaxation characteristic of the long-term response of the experiment. However, the BPE model underestimated the peak reaction force and the stress relaxation of the tissue matrix during the early period of viscoelastic response of the tissue. Similar observations have been made previously in both the unconfined compression experiment (Armstrong et al., 1984; Brown and Singerman, 1986) and the indentation compression experiment of articular cartilage (Mow et al., 1989; Suh and Bai, 1997).

The present study shows that, during unconfined compression stress relaxation, the majority of deformation in the tissue matrix occurs in a deviatoric form, rather than a volumetric form. Because of the incompressibility condition used in Eq. (1), interstitial fluid flow is created only through the volumetric deformation of the tissue matrix. Therefore, we can conclude that an underestimation of both the peak reaction force and the stress relaxation observed in the BPE model simulation of unconfined compression is caused by its underlying assumption that the viscoelasticity of soft tissue solely depends on the interstitial fluid flow (i.e., the volumetric deformation of the tissue matrix).

It was also found in the present study that the BPE theory was

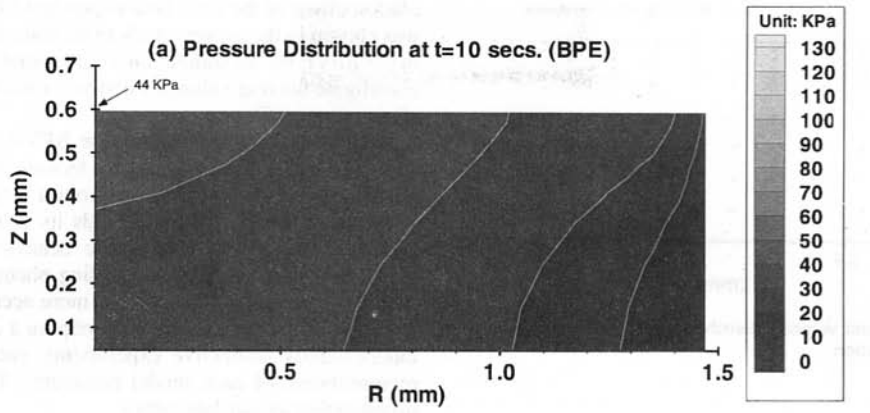

Fig. 7(*a*)

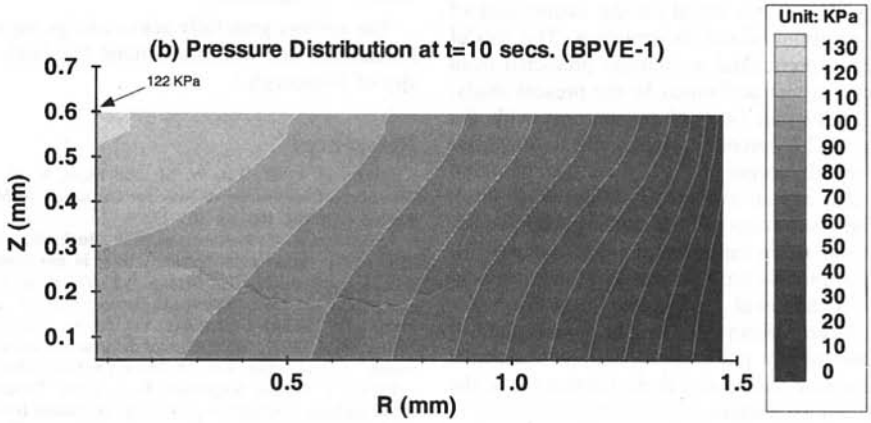

Fig. 7(*b*)

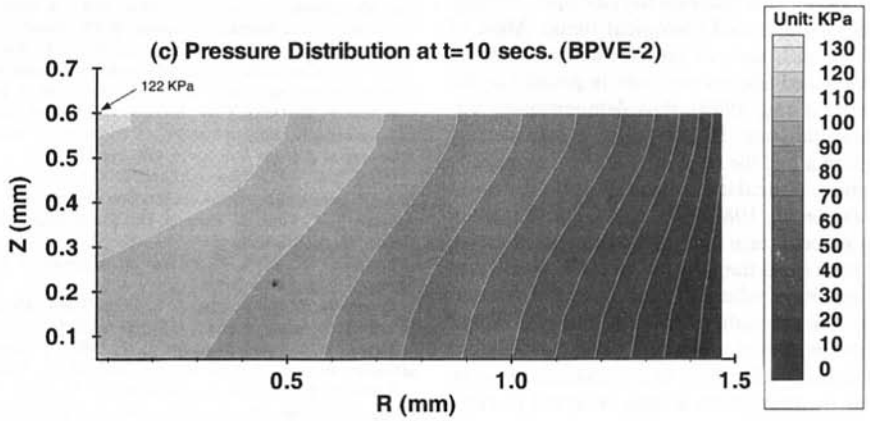

Fig. 7(*c*)

Fig. 7 The hydrostatic pressure distributions at t = 10 seconds predicted by the BPE (*a*), BPVE-1 (*b*), and BPVE-2 (*c*) simulations

able to provide an excellent prediction for the long-term relaxation response of the tissue (Fig. 4). Since most connective soft tissues, such as articular cartilage, are made of very dense extracellular matrix with an extremely low permeability ($\sim 10^{-15}$ m^4/N · sec), the flow velocity of the interstitial fluid is extremely slow ($\sim 10^{-6}$ m/sec), as shown in Fig. 8. Therefore, the fluid *flow-dependent* viscoelastic phenomenon is most likely to occur at a very slow rate. This phenomenon is consistent with the fact that the volumetric strain energy exhibits only a slight relaxation over time (Figs. 5), as compared to the deviatoric strain energy (Fig. 6).

A model, which could accurately simulate the short-term viscoelastic behavior of the tissue, was achieved by implementing the intrinsic, fluid *flow-independent,* viscoelastic representation into the deviatoric component of the effective solid stress. In summary, the present study suggests that, while the long-term viscoelastic response of soft connective tissue is mainly governed by the fluid *flow-dependent* biphasic viscoelasticity, the short-term viscoelastic response is primarily associated with the fluid *flow-independent,* intrinsic viscoelasticity of the tissue matrix. It is also suggested that the fluid *flow-independent* viscoelastic features of the solid matrix need to be taken into consideration, especially when the tissue undergoes a considerable deviatoric deformation.

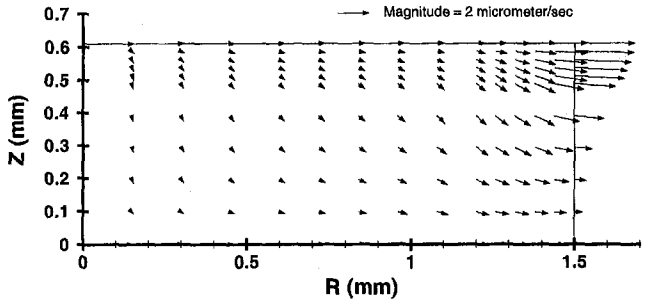

Fig. 8 The interstitial fluid velocity distribution at t = 10 seconds predicted by BPVE-1 simulation

Several limitations associated with the BPVE model assumptions of the present study deserve further discussion. First, the constitutive model, Eqs. (1)–(8), is based on the assumption of linearity in the range of infinitesimal deformation. The model simulation, based on the experimental parameters predicted from the unconfined compression test performed in the present study, produced an average axial-strain (ϵ_{zz}) of ten percent with the maximum axial strain of 27 percent occurring at a localized singular point (the upper right corner of Fig. 2), an average radial strain (ϵ_{rr}) of four percent and an average circumferential strain ($\epsilon_{\theta\theta}$) of four percent. The assumption of linearity has been considered acceptable for similar strain ranges in previous studies, although finite deformation models have shown to improve model simulations in many cases (Suh et al., 1991). Nonlinear viscoelastic modeling including large deformation will be investigated in future studies. Regardless of any potential limitations associated with the simplified assumption of linearity in the present study, the important role of the flow-independent, intrinsic viscoelasticity in the short-term viscoelastic responses of hydrated soft tissues should remain to be valid.

Secondly, the present model also assumes the isotropic, homogenous material properties of hydrated biological tissue. Most of hydrated biological soft tissues, such as muscle, tendon, and ligament, have a highly organized fibrous structure in parallel to the principal loading direction (Fung, 1994), thus demonstrating significant anisotropic characteristics. In this case, a transversely isotropic model assumption along the fiber orientation may need to be taken into consideration. Articular cartilage also has a fibrous microstructure (Buckwalter et al., 1988): The superficial tangential zone (top five to ten percent near the articulating surface of cartilage) and the deep zone (near the junction with the underlying bone) of articular cartilage have relatively well-organized fibrous patterns with a distinctive directionality. However, the majority of the tissue domain is composed of randomly oriented collagen fibers without apparent directionality. Due to this characteristic, an isotropic assumption has therefore been widely accepted in cartilage modeling. Nonetheless, the transversely isotropic or deformation-induced anisotropic models have been proposed to improve the accuracy of mathematical modeling of articular cartilage (Bursac et al., 1997; Soulhat et al., 1997). A combination of the BPVE and the deformation-induced anisotropic characteristics of articular cartilage may be able to provide more accurate model simulations over wide range of loading conditions.

Thirdly, the present study assumed the Poisson's ratio of articular cartilage to be 0.05. It has been shown in the literature (Mow et al., 1989; Athanasiou et al., 1991) that the Poisson's ratio of articular cartilage varies over a wide range between 0 and 0.5. As Poisson's ratio of the tissue approaches 0.5, there would be less change in the apparent volume of the tissue matrix. This would cause less interstitial fluid movement within the tissue matrix, thus reducing the consolidation (or poroelastic) effect of fluid flow-dependent viscoelasticity. In contrast, when the Poisson's ratio approaches zero, there would be more and more change in the apparent volume of the tissue matrix, thus increasing the consolidation effect of the fluid flow-dependent viscoelasticity. $\nu = 0.05$ was chosen in the present study to increase the consolidation effect in the BPVE model simulation. Further studies will be necessary to investigate the true value of Poisson's ratio in the BPVE modeling of articular cartilage.

Finally, the large number of the BPVE model parameters (λ^s, μ^s, κ, $\tilde{G}$, τ_S, and τ_L) can cause a technical difficulty in obtaining unique parameter identification from a single experimental data. While each model parameter holds its distinctive physical interpretation, the overall viscoelastic behavior of soft tissue most likely represents a complex coupling phenomenon of all of these physical parameters. Therefore, a more accurate parameter identification of the BPVE model may require a combination of several independently distinctive experiments, each of which is mostly representative of each model parameter. This is currently under investigation in our laboratory.

Acknowledgment

The authors gratefully acknowledge support from the Whitaker Foundation and Musculoskeletal Research Center of the University of Pittsburgh.

References

Armstrong, C. G., Lai, W. M., and Mow, V. C., 1984, "An Analysis of the Unconfined Compression of Articular Cartilage," ASME *Journal of Biomechanical Engineering,* Vol. 106, pp. 165–173.

Athanasiou, K. A., Rosenwasser, M. P., Buckwalter, J. A., Malinin, T. I., and Mow, V. C., 1991, "Interspecies comparisons of in situ intrinsic mechanical properties of distal femoral cartilage," *J. Orthop. Res.,* Vol. 9, pp. 330–340.

Basser, P. J., 1992, "Interstitial pressure, volume, and flow during infusion into brain tissue," *Microvascular Res.,* Vol. 44, pp. 143–165.

Biot, M. A., 1962, "Mechanics of deformation and acoustic propagation in porous media," *J. Appl. Phys.,* Vol. 33, No. 4, pp. 1482–1498.

Brown, T. D., and Singerman, R. J., 1986, "Experimental determination of the linear biphasic constitutive coefficients of human fetal proximal femoral chondroepiphysis," *J. Biomech.,* Vol. 10, No. 8, pp. 597–605.

Buckwalter, J. A., Hunziker, E., Rosenberg, L., Coutts, R., Adams, M., and Eyre, D., 1988, "Articular cartilage: Composition and Structure," *Injury and repair of the musculoskeletal soft tissues,* Sl.-Y. Woo, and J. A. Buckwalter, Sl.-Y. Woo, and J. As. Buckwalter, eds., American Academy of Orthopaedic Surgeons, pp. 405–425.

Buckwalter, J. A., Smith, K. C., Kazarien, L. E., Rosenberg, L. C., and Ungar, R., 1989, "Articular cartilage and intervertebral disc proteoglycans differ in structure: An electron microscopic study," *J. Orthop. Res.,* Vol. 7, pp. 146–151.

Bursac, P. M., Obitz, T. W., Eisenberg, S. R., and Stamenovic, D., 1997, "Confined and unconfined stress relaxation of cartilage: A transversely isotropic analysis," *Advances in Bioeng.,* Sun River, OR, pp. 157–158.

Fung, Y. C., 1972, "Stress-strain-history relations of soft tissues in simple elongation," *Biomechanics: Its foundations and objectives,* Y. C. Fung, N. Perrone, and M. Anliker, Y. C. Fung, N. Perrone, and Ms. Anliker, eds., Prentice-Hall, Englewood Cliffs, NJ, pp. 181–208.

Fung, Y. C., 1994, *Biomechanics: Mechanical Properties of Living Tissues,* Springer-Verlag, New York.

Hayes, W. C., and Bodine, A. J., 1978, "Flow-independent viscoelastic properties of articular cartilage matrix," *J. Biomech.,* Vol. 11, pp. 407–419.

Hayes, W. C., and Mockros, L. F., 1971, "Viscoelastic properties of human articular cartilage," *J. Appl. Physiol.,* Vol. 31, pp. 562–568.

Kwan, M. K., Lin, TH.-C., and Woo, SL.-Y., 1993, "On the viscoelastic properties of the anteromedial bundle of the anterior cruciate ligament," *J. Biomech.,* Vol. 26, pp. 447–452.

Laible, J. P., Pflaster, D., Simon, B. R., Krag, M. H., Pope, M., and Haugh, L. D., 1994, "A Dynamic Material Parameter Estimation Procedure for Soft Tissue Using a Poroelastic Finite Element Model," ASME *Journal of Biomechanical Engineering,* Vol. 116, pp. 19–29.

Mak, A. F., 1986a, "The Apparent Viscoelastic Behavior of Articular Cartilage: The Contributions From the Intrinsic Matrix Viscoelasticity and Interstitial Fluid Flows," ASME *Journal of Biomechanical Engineering,* Vol. 108, pp. 123–130.

Mak, A. F., 1986b, "Unconfined compression of hydrated viscoelastic tissues: A biphasic poroviscoelastic analysis," *Biorheology,* Vol. 23, pp. 371–383.

Mow, V. C., Ateshian, G. A., and Spilker, R. L., 1993, "Biomechanics of Diarthrodial Joints: A Review of Twenty Years of Progress," ASME *Journal of Biomechanical Engineering,* Vol. 115, pp. 460–467.

Mow, V. C., Gibbs, M. C., Lai, W. M., Zhu, W. B., and Athanasiou, K. A., 1989, "Biphasic indentation of articular cartilage: II. A numerical algorithm and an experimental study," *J. Biomech.,* Vol. 22, pp. 853–861.

Mow, V. C., Kuei, S. C., Lai, W. M., and Armstrong, C. G., 1980, "Biphasic Creep and Stress Relaxation of Articular Cartilage in Compression: Theory and Experiments," ASME *Journal of Biomechanical Engineering,* Vol. 102, pp. 73–83.

Mow, V. C., Mak, A. F., Lai, W. M., Rosenberg, L. C., and Tang, L. H., 1984, "Viscoelastic properties of proteoglycan subunits and aggregates in varying solution concentrations," *J. Biomech.,* Vol. 17, pp. 325–338.

Myers, B. S., McElhaney, J. H., and Doherty, B. J., 1991, "The viscoelastic responses of the human cervical spine in torsion: Experimental limitations of quasi-linear theory, and a method for reducing these effects," *J. Biomech.,* Vol. 24, pp. 811–817.

Nagtegaal, J. C., Parks, D. M., and Rice, J. R., 1974, "On numerically accurate finite element solutions in the fully plastic range," *Comp. Meth. Appl. Mech. Eng.,* Vol. 4, pp. 153–177.

Parsons, J. R., and Black, J., 1977, "The viscoelastic shear behavior of normal rabbit articular cartilage," *J. Biomech.,* Vol. 10, pp. 21–29.

Pitt Ford, T. R., Sachs, J. R., Grotberg, J. B., and Glucksberg, M. R., 1991, "Perialveolar interstitial resistance and compliance in isolated rat lung," *J. Appl. Physiol.,* Vol. 70, pp. 2750–2756.

Simon, B. R., Kaufmann, M. V., McAfee, M. A., and Baldwin, A. L., 1993, "Finite element models for arterial wall mechanics," *J. Biomech. Engrg.,* Vol. 115, pp. 489–496.

Soulhat, J., Buschmann, M. D., and Shirazi-Adl, A., 1997, "A nonhomogeneous composite model of articular cartilage: Development and validation in unconfined compression," *Trans. 43rd ORS,* San Francisco, CA, p. 822.

Spilker, R. L., Suh, J.-K., and Mow, V. C., 1990, "Effects of Friction on the Unconfined Compressive Response of Articular Cartilage: A Finite Element Analysis," ASME *Journal of Biomechanical Engineering,* Vol. 112, pp. 138–146.

Spirt, A. A., Mak, A. F., and Wassell, R. P., 1989, "Nonlinear viscoelastic properties of articular cartilage in shear," *J. Orthop. Res.,* Vol. 7, pp. 43–49.

Suh, J. K., Spilker, R. L., and Holmes, M. H., 1991, "A penalty finite element analysis for nonlinear mechanics of biphasic hydrated soft tissue under large deformation," *Int. J. Num. Meth. Eng.,* Vol. 32, pp. 1411–1439.

Suh, J.-K., and Bai, S., 1997, "Biphasic poroviscoelastic behavior of articular cartilage in creep indentation test," *Trans. 43rd ORS,* San Francisco, CA, p. 823.

Suh, J.-K., and Bai, S., 1998, "Finite Element Formulation of Biphasic Poroviscoelastic Model for Articular Cartilage," ASME *Journal of Biomechanical Engineering,* Vol. 120, pp. 195–201.

Tschoegl, N. W., 1989, *The Phenomenological Theory of Linear Viscoelastic Behavior,* Springer-Verlag, Berlin.

Viidik, A., 1968, "A Rheological Model for Uncalcified Parallel-Fibered Collagenous Tissues," ASME *Journal of Biomechanical Engineering,* Vol. 90, pp. 3–11.

Yang, M., Taber, L. A., and Clark, E. B., 1994, "A Nonlinear Poroelastic Model for the Trabecular Embryonic Heart," ASME *Journal of Biomechanical Engineering,* Vol. 116, pp. 213–223.

Zhu, W., and Mow, V. C., 1990, "Viscometric properties of proteoglycan solutions at physiological concentration," *Biomechanics of Diathrodial Joints,* V. C. Mow, A. Ratcliffe, and SL.-Y. Woo, eds., Springer-Verlag, New York, pp. 313–344.

Zhu, W., Mow, V. C., Koob, T. J., and Eyre, D. R., 1993, "Viscoelastic shear properties of articular cartilage and the effects of glycosidase treatments," *J. Orthop. Res.,* Vol. 11, pp. 771–781.

S. I. Barry

G. N. Mercer

School of Mathematics and Statistics,
University College,
University of New South Wales,
Canberra ACT 2600, Australia

Exact Solutions for Two-Dimensional Time-Dependent Flow and Deformation Within a Poroelastic Medium

Exact analytic solutions are derived for the time-dependent deformation of a poroelastic medium within a two-dimensional finite domain. Solutions are given with a specific set of boundary conditions for the case of a source of fluid at an arbitrary point and for an applied pressure on the boundary. These solutions are ideal for testing numerical schemes for poroelastic flow and deformations due to their relative simplicity.

Introduction

Poroelasticity has wide applications in biology, filtration, and soil science (for example, Gibson et al., 1970; Armstrong et al., 1984; Booker and Carter, 1986; Yang and Taber, 1991; Barry et al., 1995). Many numerical codes have been developed to solve the poroelastic equations for various geometries and applications. However, there are few exact analytic solutions which can be used to test the accuracy of these numerical codes. We present here analytic solutions to the poroelastic equations in a two-dimensional finite domain.

Two situations are considered: a source at some arbitrary position; and an imposed applied pressure on the boundary. Our aim is not to model any particular application of poroelasticity, but to find simple two-dimensional solutions that can be used to test numerical codes.

To date, most analytic solutions in poroelasticity are either one-dimensional or purely cylindrical, both which reduce to diffusion type equations. Numerous solutions to the one-dimensional poroelastic equations, for different applicable boundary conditions, have been given, such as linear solutions by Holmes et al. (1985), Lai and Mow (1980), and Parker et al. (1987) plus nonlinear exact and perturbation solutions by Barry and Aldis (1990, 1991) and Holmes (1983).

For the problem of a pressurized cylindrical shell, exact and perturbation solutions have been given by Kenyon (1976, 1979), Klanchar and Tarbell (1987), and Barry and Aldis (1993). Uniaxial loading of cylinders has also been considered by Armstrong et al. (1984) and Yang and Taber (1991).

Some exact solutions have been found in infinite and semi-infinite regions. Booker and Carter (1986, 1987) used transform techniques to find the steady-state solution of a point sink embedded in a poroelastic half space. Compression of poroelastic layers has also been considered by a number of authors such as Heinrich and Desoyer (1961), Gibson et al. (1970), Mak et al. (1987), and Ateshian et al. (1994). Rudnicki (1987) used infinite Fourier transforms and Laplace transforms on an infinite domain to solve for plain-strain dislocations in an infinite poroelastic medium. The time-dependent relaxation of a linear poroelastic disk after some assumed deformation has been solved by Sachs et al. (1994) and Jensen et al. (1994). Barry et al. (1995, 1997) give steady-state solutions for the deformation of a finite layer by a line source.

The above exact solutions are only marginally useful in testing the accuracy of a two-dimensional numerical scheme. The radial and one-dimensional solutions are unable to test fully two-dimensional deformation effects. Solutions in semi-infinite regions (such as half-spaces or infinite layers) are inappropriate since numerical schemes are restricted to finite domains.

In this paper, we will use Laplace and finite Fourier transforms to solve for the time-dependent displacement, pressure, and flow in a finite linear poroelastic medium. The boundary conditions will be specifically chosen to simplify the resulting solution and to match the appropriate transforms. The difficulty in finding these solutions is putting them in a suitable form so that the inverse Laplace transform can be calculated exactly. Our exact solutions are highly suitable for testing numerical schemes for which there are few analytic solutions for two-dimensional domains.

To obtain analytic solutions we have made the standard linear poroelastic assumptions. The material is initially homogeneous and isotropic with a constant permeability. The stress is assumed to be linearly dependent on the strain and the deformations small. We note that it is a trivial extension to include anisotropic permeability.

Poroelastic Equations

The poroelastic equations were first derived by Biot (1941) studying with the consolidation of soils. These equations were then rederived and extended using mixture theory by Bowen (1980) and applied to the study of soft tissue compression (for example, Lai and Mow, 1980; Mow and Lai, 1980; Armstrong, 1984; Holmes, 1983; Holmes et al., 1985). We have included here a brief overview of the poroelastic equations derived using mixture theory but we refer readers to the above references for a more complete and formal derivation.

The porous material is modeled as a continuous binary mixture of solid and fluid phases (denoted by $\beta = s, f$, respectively) where each point in the mixture is occupied simultaneously by both fluid f and solid s. The porous medium is assumed homogeneous and isotropic with no body forces. Both the solid and fluid phases are assumed to be intrinsically incompressible. Bulk compression of the mixture can arise only by a decrease in the fluid fraction. The density of each phase in the mixture is given by $\rho^\beta = \rho_T^\beta \phi^\beta$ where ρ_T^β is the intrinsic density and ϕ^β the volume fraction of component β. For our binary system $\phi^s + \phi^f = 1$.

The conservation of mass for each phase is

$$\frac{\partial \phi^\beta}{\partial t} + \hat{\nabla} \cdot (\phi^\beta \mathbf{v}^\beta) = q^\beta \tag{1}$$

Contributed by the Applied Mechanics Division of THE AMERICAN SOCIETY OF MECHANICAL ENGINEERS for publication in the ASME JOURNAL OF APPLIED MECHANICS.

Discussion on the paper should be addressed to the Technical Editor, Professor Lewis T. Wheeler, Department of Mechanical Engineering, University of Houston, Houston, TX 77204-4792, and will be accepted until four months after final publication of the paper itself in the ASME JOURNAL OF APPLIED MECHANICS.

Manuscript received by the ASME Applied Mechanics Division, Sept. 1, 1996; final revision, Aug. 10, 1998. Associate Technical Editor: J. T. Jenkins.

where the solid velocity $\mathbf{v}^s = \partial\hat{\mathbf{u}}/\partial\hat{t}$, $\hat{\mathbf{u}}$ is the solid displacement vector, $\hat{\nabla}$ is the gradient operator and $q^s = 0$ and $q^f = q = 0$ except at any sources or sinks in the medium. The overall continuity equation is obtained by adding the equations for both phases so that $\hat{\nabla} \cdot \hat{\mathbf{v}} = q$ where we define $\hat{\mathbf{v}} = \phi^f\mathbf{v}^f + \phi^s\mathbf{v}^s$ as a macroscopic fluid velocity vector.

The momentum equations for each phase can be treated similarly where for small velocities and deformation rates the inertial terms can be assumed negligible. With these assumptions momentum in each phase is $\hat{\nabla} \cdot \mathbf{T}^\beta = -\boldsymbol{\pi}^\beta$, where $\mathbf{T}^\beta$ is the stress tensor for the β phase and $\boldsymbol{\pi}^\beta$ is a drag force between the constituents. The stress tensors can be modeled as

$$\mathbf{T}^\beta = -\phi^\beta\hat{p}\mathbf{I} + \boldsymbol{\sigma}^\beta, \tag{2}$$

$$-\boldsymbol{\pi}^s = \boldsymbol{\pi}^f = K(\mathbf{v}^s - \mathbf{v}^f) - \hat{p}\nabla\phi^s, \tag{3}$$

where $\boldsymbol{\sigma}^s$ represents a solid stress, the "contact stress" (Kenyon 1976), a function of the strain, K is the drag coefficient of relative motion, p is the fluid pressure, and $\mathbf{I}$ the identity tensor. We assume here that the viscous fluid stress is negligible in comparison to the frictional interaction between the fluid and the solid, hence $\boldsymbol{\sigma}^f = \mathbf{0}$ and $\boldsymbol{\sigma}^s \equiv \hat{\boldsymbol{\sigma}}$.

Substituting the interaction term (3) into the momentum equation and using $\phi^s = 1 - \phi^f$ leads to

$$\hat{\nabla} \cdot \hat{\boldsymbol{\sigma}} = \frac{K}{\phi^f}(\mathbf{v}^s - \mathbf{v}^f), \tag{4}$$

or after a little manipulation

$$\hat{\nabla}\hat{p} = \hat{\nabla} \cdot \hat{\boldsymbol{\sigma}} = \frac{1}{\hat{k}}\left(\frac{\partial\hat{\mathbf{u}}}{\partial\hat{t}} - \hat{\mathbf{v}}\right), \tag{5}$$

where $\hat{k} = (\phi^f)^2/K$ is the "permeability" (Lai and Mow, 1980), $\hat{\mathbf{u}}$ is the displacement of the solid, and $\partial\hat{\mathbf{u}}/\partial\hat{t} = \mathbf{v}^s$. The notation we use for the "permeability," $\hat{k}$, conforms to that used in the biological literature and in other derivations of these poroelastic equations (Mow and Lai 1980). The fluid viscosity, which is often written separately in the soil literature, is incorporated into $\hat{k}$.

The solid contact stress is related to the displacements, $\hat{\mathbf{u}} = (\hat{u}, \hat{w})$, by the relationships

$$\hat{\boldsymbol{\sigma}} = \lambda\phi\mathbf{I} + 2\mu\mathbf{e}, \quad \mathbf{e} = \tfrac{1}{2}(\hat{\nabla}\hat{\mathbf{u}} + (\hat{\nabla}\hat{\mathbf{u}})^T), \quad \phi = \hat{\nabla} \cdot \hat{\mathbf{u}} \tag{6}$$

where λ, μ are the Lamé stress constants and $\mathbf{e}$ is the infinitesimal strain tensor.

In Cartesian $(\hat{x}, \hat{z})$ coordinates Eqs. (5) and (6) give

$$\mu\hat{\nabla}^2\hat{u} + (\lambda + \mu)\frac{\partial\phi}{\partial\hat{x}} = \frac{\partial\hat{p}}{\partial\hat{x}}, \tag{7}$$

$$\mu\hat{\nabla}^2\hat{w} + (\lambda + \mu)\frac{\partial\phi}{\partial\hat{z}} = \frac{\partial\hat{p}}{\partial\hat{z}} \tag{8}$$

where

$$\phi = \frac{\partial\hat{u}}{\partial\hat{x}} + \frac{\partial\hat{w}}{\partial\hat{z}} \tag{9}$$

is the dilatation, a measure of the change in porosity of the material. By taking the divergence of Eq. (5) and using conservation of mass we obtain

$$\hat{\nabla} \cdot \left(\hat{k}\frac{\partial\hat{p}}{\partial\hat{x}}, \hat{k}\frac{\partial\hat{p}}{\partial\hat{z}}\right) = \frac{\partial\phi}{\partial\hat{t}} - \hat{\alpha}Q. \tag{10}$$

Nondimensionalisation

We nondimensionalise the poroelastic equations with respect to a typical length of the porous medium h, the Lamé stress constant $\lambda + 2\mu$, a time scale t_0 and the permeability $\hat{k}$ such that

$$p = \frac{\hat{p}}{\lambda + 2\mu}, \quad x = \frac{\hat{x}}{h}, \quad z = \frac{\hat{z}}{h},$$

$$t = \hat{t}\frac{(\lambda + 2\mu)\hat{k}}{h^2}, \quad u = \frac{\hat{u}}{h}, \quad w = \frac{\hat{w}}{h}. \tag{11}$$

Three dimensionless parameters thus occur:

$$m = 1 + \frac{\lambda}{\mu}, \quad P = \frac{\hat{P}}{\lambda + 2\mu}, \quad \alpha = \frac{h^2\hat{\alpha}}{(\lambda + 2\mu)\hat{k}} \tag{12}$$

where m is an elastic parameter, P a scaled applied pressure, and α a scaled source strength. We note that $m = 1/(1 - 2\nu)$ where ν is Poisson's ratio.

Equations (7), (8), and (10) become

$$(m + 1)\frac{\partial^2 u}{\partial x^2} + \frac{\partial^2 u}{\partial z^2} + m\frac{\partial^2 w}{\partial x\partial z} = (m + 1)\frac{\partial p}{\partial x}, \tag{13}$$

$$\frac{\partial^2 w}{\partial x^2} + (m + 1)\frac{\partial^2 w}{\partial z^2} + m\frac{\partial^2 u}{\partial x\partial z} = (m + 1)\frac{\partial p}{\partial z}, \tag{14}$$

$$\frac{\partial^2 p}{\partial x^2} + \frac{\partial^2 p}{\partial z^2} = \frac{\partial\phi}{\partial t} - \alpha Q. \tag{15}$$

Transform Results

The finite sine and cosine transforms (shown here using the x variable) are defined as

$$C_{xn}\{f(x)\} = \int_0^T f(x)\cos\lambda_n x dx = \bar{f}_0(n),$$

$$f(x) = \frac{1}{T}\bar{f}_0(0) + \frac{2}{T}\sum_{n=1}^{\infty}\bar{f}_0(n)\cos\lambda_n x,$$

and

$$S_{xn}\{f(x)\} = \int_0^T f(x)\sin\lambda_n x dx = \bar{f}_1(n),$$

$$f(x) = \frac{2}{T}\sum_{n=1}^{\infty}\bar{f}_1(n)\sin\lambda_n x,$$

where $\lambda_n = n\pi/T$, $n = 0, 1, 2, \ldots$.

Some elemental properties of these transforms are

$$S_{xn}\{f''(x)\} = -\lambda_n^2\bar{f}_1(n) + \lambda_n f(0) - \lambda_n(-1)^n f(T),$$

$$C_{xn}\{f''(x)\} = -\lambda_n^2\bar{f}_0(n) - f'(0) + (-1)^n f'(T),$$

$$S_{xn}\{f'(x)\} = -\lambda_n\bar{f}_0,$$

$$C_{xn}\{f'(x)\} = \lambda_n\bar{f}_1 - f(0) + (-1)^n f(T). \tag{16}$$

The Laplace transform is defined as

$$\mathcal{L}\{f(t)\} = \bar{f}(s) = \int_0^\infty e^{-st}f(t)dt \tag{17}$$

with standard transform properties.

Boundary Conditions

To obtain simple analytic solutions it is important that the boundary conditions and the transforms be chosen with care. Fourier transforms of Eqs. (13)–(15) will be simplified if the

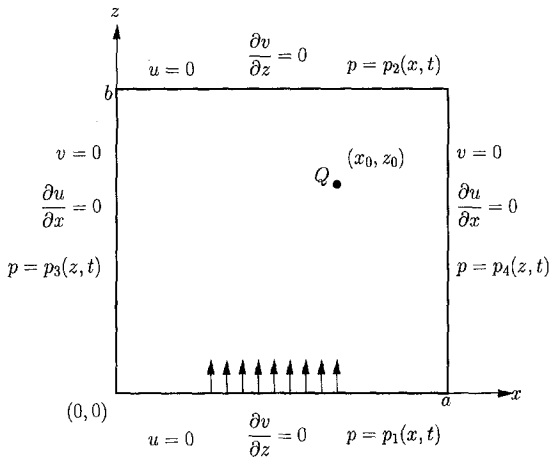

Fig. 1 Schematic diagram of a finite poroelastic medium of nondimensional lengths $x = a$ and $y = b$. Illustrated are an applied pressure, p_1 on the lower boundary and a source Q at some arbitrary position, (x_0, z_0), in the medium. The boundary conditions are also shown.

boundary terms from Eqs. (16), $f(0)$, $f(T)$, $f'(0)$, $f'(T)$, are zero. Because of the cross derivative terms, $(\partial^2 u/\partial x \partial z)$ and $(\partial^2 w/\partial x \partial z)$, in Eqs. (13) and (14), the choice of Fourier transforms for u, w, and p are restricted. One suitable set of boundary conditions that leads to simple solutions is $u = 0$, $\partial w/\partial z = 0$, on $z = 0$ and $z = b$, with $p = p_1(x, t)$ and $p = p_2(x, t)$, respectively. On $x = 0$ and $x = a$ we take $w = 0$, $\partial u/\partial x = 0$, with $p = p_3(z, t)$ and $p = p_4(z, t)$ respectively. These boundary conditions are illustrated in Fig. 1. It should be noted that these boundary conditions are not standard conditions such as zero stress or displacement.

Corresponding to these boundary conditions we define the transformed variables: $\bar{u}(n, q, s) = \mathcal{L}C_{xn}S_{zq}\{u(x, z, t)\}$, $\bar{w}(n, q, s) = \mathcal{L}S_{xn}C_{zq}\{w(x, z, t)\}$, and $\bar{p}(n, q, s) = \mathcal{L}S_{xn}S_{zq}\{p(x, z, t)\}$. For ease of notation the overbar indicates any transformed variable with the independent variables indicating which transform has been used.

Other transforms and boundary conditions are possible, however, these often restrict the choices for the pressure boundary conditions. We found the above system yielded the simplest solutions and, as will be shown in the results, give rise to interesting symmetry properties.

Transformed Equations

The appropriate transforms of the governing equations corresponding to the transform variables are $\mathcal{L}C_{xn}S_{zq}\{(13)\}$, $\mathcal{L}S_{xn}C_{zq}\{(14)\}$, $\mathcal{L}S_{xn}S_{zq}\{(15)\}$. Applying these gives the matrix system

$$\mathbf{A}\begin{bmatrix} \bar{u} \\ \bar{w} \\ \bar{p} \end{bmatrix} = \begin{bmatrix} (m+1)B_1 \\ (m+1)B_2 \\ B_3 \end{bmatrix} \tag{18}$$

where

$$\mathbf{A} = \begin{bmatrix} (1+m)\lambda_n^2 + \lambda_q^2 & m\lambda_n\lambda_q & (m+1)\lambda_n \\ m\lambda_n\lambda_q & \lambda_n^2 + (1+m)\lambda_q^2 & (m+1)\lambda_q \\ \lambda_n & \lambda_q & -(\lambda_n^2 + \lambda_q^2)/s \end{bmatrix}$$

and $\lambda_n = n\pi/a$, $\lambda_q = q\pi/b$. The terms B_1, B_2, B_3 are dependent on the boundary conditions, such that

$$B_1 = \bar{p}_3 - (-1)^n\bar{p}_4, \quad B_2 = \bar{p}_1 - (-1)^q\bar{p}_2,$$

$$B_3 = \frac{-1}{s}(\alpha\bar{Q} + \lambda_n B_1 + \lambda_q B_2),$$

where

$$\bar{p}_1(n, s) = \mathcal{L}S_{xn}\{P_1(x, t)\}, \quad \bar{p}_2(n, s) = \mathcal{L}S_{xn}\{P_2(x, t)\},$$

$$\bar{p}_3(q, s) = \mathcal{L}S_{zq}\{P_3(z, t)\}, \quad \bar{p}_4(q, s) = \mathcal{L}S_{zq}\{P_4(z, t)\},$$

$$\bar{Q}(n, q, s) = \mathcal{L}S_{xn}S_{zq}\{Q(x, z, t)\}.$$

The system of Eqs. (18) can be solved for $\bar{u}$, $\bar{w}$, $\bar{p}$ by simple matrix inversion giving

$$\bar{u}(n, q, s) = B_1\frac{(1+m)\lambda_q^2}{\hat{\lambda}^2} - B_2\frac{(1+m)\lambda_n\lambda_q}{\hat{\lambda}^2} - \alpha\bar{Q}\frac{\lambda_n}{\hat{\lambda}(\hat{\lambda}+s)},$$

$$\bar{w}(n, q, s) = -B_1\frac{(1+m)\lambda_n\lambda_q}{\hat{\lambda}^2} + B_2\frac{(1+m)\lambda_n^2}{\hat{\lambda}^2} - \alpha\bar{Q}\frac{\lambda_q}{\hat{\lambda}(\hat{\lambda}+s)},$$

$$\bar{p}(n, q, s) = B_1\frac{\lambda_n}{\hat{\lambda}} + B_2\frac{\lambda_q}{\hat{\lambda}} + \alpha\bar{Q}\frac{1}{\hat{\lambda}+s}, \tag{19}$$

where $\hat{\lambda} = \lambda_n^2 + \lambda_q^2$.

In the next sections we will consider two different possibilities: first, where the boundary pressure is zero with flow driven by a source and second, where the flow is driven by a pressure on $z = 0$, in the absence of a source.

Source Solution

Here we consider the case of a pulsating point source at (x_0, z_0) with zero pressure on the boundary such that $p_1 = p_2 = p_3 = p_4 = 0$ and

$$Q(x, z, t) = \delta(x - x_0)\delta(z - z_0)\sin\omega t. \tag{20}$$

On transforming this becomes

$$\bar{Q}(n, q, s) = \frac{w \sin\lambda_n x_0 \sin\lambda_q z_0}{s^2 + w^2} \tag{21}$$

with $B_1 = 0$, $B_2 = 0$, $B_3 = -\alpha\bar{Q}/s$. Thus

$$\bar{u}(n, q, s) = -\frac{\alpha\bar{Q}\lambda_n}{\hat{\lambda}(\hat{\lambda}+s)}, \quad \bar{w}(n, q, s) = -\frac{\alpha\bar{Q}\lambda_q}{\hat{\lambda}(\hat{\lambda}+s)},$$

$$\bar{p}(n, q, s) = -\frac{\alpha\bar{Q}}{\hat{\lambda}+s}. \tag{22}$$

The inverse Laplace transform of these are

$$\bar{u}(n, q, t) = \frac{\lambda_n}{\hat{\lambda}}\bar{p}(n, q, t), \quad \bar{w}(n, q, t) = \frac{\lambda_q}{\hat{\lambda}}\bar{p}(n, q, t) \tag{23}$$

where

$$\bar{p}(n, q, t) = -\frac{\alpha \sin\lambda_n x_0 \sin\lambda_q z_0}{\hat{\lambda}^2 + \omega^2} \times (\hat{\lambda}\sin\omega t - \omega\cos\omega t + \omega e^{-\hat{\lambda}t}). \tag{24}$$

The appropriate sine and cosine inverse transforms are

$$u(x, z, t) = \frac{2}{ab}\sum_{q=1}^{\infty}\bar{u}(0, q, t)\sin\lambda_q z + \frac{4}{ab}\sum_{q=1}^{\infty}\sum_{n=1}^{\infty}\bar{u}(n, q, t)\cos\lambda_n x \sin\lambda_q z,$$

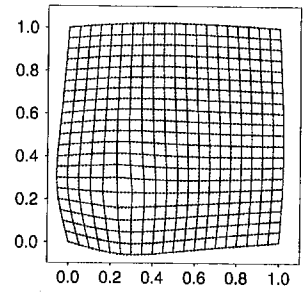

Fig. 2 Deformation of a regular grid due to a source at a position (.25, .25) in the medium. Parameter values are $a = 1$, $b = 1$, $\omega = 1$, $\alpha = 2$ with the displacement shown at time $t = \pi/2$. Solid lines indicate the exact solution while the dashed lines indicate a numerical solution. Note that the solution is independent of the elastic parameter m.

$$w(x, z, t) = \frac{2}{ab} \sum_{n=1}^{\infty} \bar{w}(n, 0, t) \sin \lambda_n x + \frac{4}{ab} \sum_{q=1}^{\infty} \sum_{n=1}^{\infty} \bar{w}(n, q, t) \sin \lambda_n x \cos \lambda_q z,$$

$$p(x, z, t) = \frac{4}{ab} \sum_{q=1}^{\infty} \sum_{n=1}^{\infty} \bar{p}(n, q, t) \sin \lambda_n x \sin \lambda_q z. \quad (25)$$

Pressure Solution

Here we consider the case of $Q = 0$ with a pressure on the lower edge defined by

$$p_1(x, t) = \beta(H(x - x_0) - H(x - x_1))F(t), \quad (26)$$

where H is the Heaviside function, $H(x) = 1$ for $x \geq 0$ and $H(x) = 0$ for $x < 0$, β is the nondimensional pressure magnitude and $F(t)$ is any well-defined function of time. The other pressures are $p_2 = p_3 = p_4 = 0$. Thus

$$\bar{p}_1(n, s) = -\beta(\cos \lambda_n x_1 - \cos \lambda_n x_0)\bar{F}(s), \quad (27)$$

where $\bar{F}(s) = \mathcal{L}\{F(t)\}$. Hence $B_1 = 0$ and $B_2 = \bar{p}_1(n, s)$. Substitution of these into Eq. (19) and calculating the inverse Laplace transform gives

$$\bar{u}(n, q, t) = -\frac{(1 + m)\lambda_n}{\hat{\lambda}} \bar{p}(n, q, t),$$

$$\bar{w}(n, q, t) = \frac{(1 + m)\lambda_n^2}{\hat{\lambda}\lambda_q} \bar{p}(n, q, t) \quad (28)$$

where

$$\bar{p}(n, q, t) = \frac{\lambda_q}{\hat{\lambda}} \beta(\cos \lambda_n x_1 - \cos \lambda_n x_0)F(t), \quad (29)$$

and the sine and cosine inverses can be calculated as in Eq. (25).

Results

The exact solutions were determined by evaluating the relatively simple sums in Eq. (25). The summations converge rapidly without the need for acceleration schemes although convergence does vary with position in the medium (convergence being slower nearer the source and pressure discontinuities). For simplicity the summations were calculated using 40 terms. No discernible difference was found if more terms in the summation were calculated. Indeed, in most cases, substantially fewer terms were necessary to obtain convergent results.

Source Solution. We will first discuss the solution of a source of fluid within the medium, which is unique in being independent of the elastic parameter m. This is apparent from the Eqs. (23)–(24). Figure 2 illustrates the deformation at time, $t = \pi/2$, within the pressure cycle with parameter values $a = 1$, $b = 1$, $\alpha = 2$, $\omega = 1$. The source is positioned at (.25, .25). Solid lines indicate the exact solution while the dashed lines indicate a numerical solution, calculated using a finite difference method we developed with a 21 × 21 grid. Note that the two results are virtually indistinguishable even with such a coarse grid. The numerical solution was also verified to be independent of the parameter m. This unusual independence on the Poisson's ratio is due to the combination of the specific boundary conditions and the interaction of the fluid flow with the solid deformation. This independence provides a good check of any numerical method used and the summation routine.

Pressure Solution. We see a remarkably different behavior with the solution for an applied pressure on the lower surface. Equation (29) shows that the solution has zero time lag and is completely synchronous with the applied pressure. The deformation is thus equivalent to a sequence of steady-state solutions. Unlike the source solution, the deformation is dependent on m. Oddly, the pressure is still independent of the elastic parameter m. Figure 3 illustrates the deformation at time, $t = \pi/2$, where $F(t) = \sin \omega t$ and $a = 1$, $b = 1$, $\beta = 1$, $\omega = 1$, and $m = 1.5$. The solid lines indicate the exact solution while the dashed lines indicate the numerical solution.

Discussion

Other solutions are possible using this transform method. By linearity, the pressure and source solutions can be combined or pressures on other surfaces be applied ($p_2, p_3, p_4 \neq 0$); however, these give no new results. More complicated boundary conditions can also be incorporated using Fourier expansions. For example, by setting $w = \Sigma\, a_i \sin(i\pi y/b)$ on $x = a$ the a_i can be found so the desired boundary condition is obtained. However, this greatly complicates the solution and is not necessary for checking a numerical scheme.

The boundary conditions we impose do not correspond to normal physical boundary conditions. However, our aim is not to find solutions for an applicable problem but to find *simple* exact solutions to test numerical codes. The boundary conditions we assume are natural ones in terms of the governing differential equations, giving simple solutions. Hence the independence of the source solution with m and the pressure solution with time, are due to the natural coupling of the boundary condition and the differential equation. These features provide an excellent mechanism for checking the correct implementation of any numerical scheme.

Solutions can also be found by performing a Fourier transform in only one direction and then solving the resulting system in terms of exponentials as in Barry et al. (1995, 1997). However, this yields solutions in terms of $\sqrt{s}$ making an inverse Laplace trans-

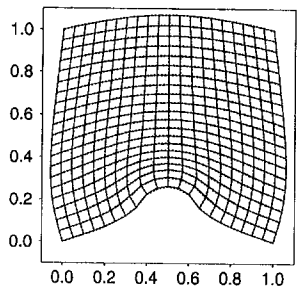

Fig. 3 Deformation of a regular grid due to an applied pressure p_1. Parameter values are $a = 1$, $b = 1$, $m = 1.5$, $\omega = 1$, $\beta = 1$ with the displacement shown at time $t = \pi/2$. Solid lines indicate the exact solution while the dashed lines indicate a numerical solution.

form difficult to find. Our solutions using two finite Fourier transforms has the advantage that the resulting solution is simply expressed and easily inverted. With modern computing power, and the rapid convergence of the summations, inversion of the Fourier transforms given in Eq. (25) is simple to compute.

Although our solutions involve double summations, they are still useful in testing fully numerical codes. The solutions can be calculated to any desired accuracy at any point in the medium. Hence they class as being "exact" analytic solutions.

Conclusion

We have derived a set of exact solutions for the time-dependent two-dimensional flow and deformation of a poroelastic material. Fourier transforms and Laplace transforms were used to formulate the answer in terms of double summations. It was found that a specific set of boundary conditions enabled simple solutions to be found. Two solutions were illustrated: flow from a fluid source and flow from an applied fluid pressure on the boundary. These showed remarkable properties, with the source flow being independent of Poisson's ratio and the second solution being synchronous in time with the applied pressure. The simplicity of these solutions makes them ideal for testing the accuracy of numerical methods.

References

Armstrong, C. G., Lai, W. M., and Mow, V. C., 1984, "An Analysis of the Unconfined Compression of Articular Cartilage," ASME *Journal of Biomechanical Engineering,* Vol. 106, pp. 165–173.

Ateshian, G. A., Lai, W. M., Zhu, W. B., and Mow, V. C., 1994, "An asymptotic solution for the contact of two cartilage layers," *Journal of Biomechanics,* Vol. 27, pp. 1347–1360.

Barry, S. I., and Aldis, G. K., 1990, "Comparison of models for flow induced deformation of soft biological tissues," *Journal of Biomechanics,* Vol. 23, pp. 647–654.

Barry, S. I., and Aldis, G. K., 1991, "Deformation of soft biological tissue due to an unsteady fluid flow," *International Journal of Non-Linear Mechanics,* Vol. 26, pp. 687–699.

Barry, S. I., and Aldis, G. K., 1993, "Radial flow through deformable porous shells," *Journal of the Australian Mathematics Society, Series B,* Vol. 34, pp. 333–354.

Barry, S. I., Aldis, G. K., and Mercer, G. N., 1995, "Injection of fluid into a layer of deformable porous medium," ASME *Applied Mechanics Reviews,* Vol. 48, pp. 722–726.

Barry, S. I., Mercer, G. N., and Zoppou, C., 1997, "Approximate and Analytic Solutions for Deformation of Finite Porous Filters," ASME JOURNAL OF APPLIED MECHANICS, Vol. 64, 929–934.

Biot, M. A., 1941, "General theory of three dimensional consolidation," *Journal of Applied Physics,* Vol. 12, pp. 155–164.

Booker, J. R., and Carter, J. P., 1986, "Long term subsidence due to fluid extraction from a saturated, anisotropic, elastic soil mass," *Quarterly Journal of Mechanics and Applied Mathematics,* Vol. 39, pp. 85–97.

Booker, J. R., and Carter, J. P., 1987, "Withdrawal of a compressible pore fluid from a point sink in an isotropic elastic half space with anisotropic permeability," *International Journal Solids and Structures,* Vol. 23, pp. 369–385.

Bowen, R. M., 1980, "Incompressible porous media models by the theory of mixtures," *International Journal of Engineering Science,* Vol. 18, pp. 1129–1148.

Gibson, R. E., Schiffman, R. L., and Pu, S. L., 1970, "Plane strain and axially symmetric consolidation of a clay layer on a smooth impervious base," *Quarterly Journal of Mechanics and Applied Mathematics,* Vol. 23, pp. 505–520.

Heinrich, G., and Desoyer, K., 1961, "Theorie dreidimensionaler Setzungsvorgaenge in Tonshichten," *Ingenieur-Archiv,* Vol. 30, pp. 225–253.

Holmes, M. H., 1983, "A nonlinear diffusion equation arising in the study of soft tissue," *Quarterly of Applied Mathematics,* Vol. 61, pp. 209–220.

Holmes, M. H., Lai, W. M., and Mow, V. C., 1985, "Singular Perturbation Analysis of the Nonlinear, Flow-dependent Compressive Stress Relaxation Behaviour of Articular Cartilage," ASME *Journal of Biomechanical Engineering,* Vol. 107, pp. 206–218.

Jensen, O. E., Glucksberg, M. R., Sachs, J. R., and Grotberg, J. B., 1994, "Weakly Nonlinear Deformation of a Thin Poroelastic Layer With a Free Surface," ASME JOURNAL OF APPLIED MECHANICS, Vol. 61, pp. 729–731.

Kenyon, D. E., 1976, "Transient Filtration in a Porous Elastic Cylinder," ASME JOURNAL OF APPLIED MECHANICS, Vol. 98, pp. 594–598.

Kenyon, D. E., 1979, "A mathematical model of water flux through aortic tissue," *Bulletin of Mathematical Biology,* Vol. 41, pp. 79–90.

Klanchar, M., and Tarbell, J. M., 1987, "Modeling water flow through arterial tissue," *Bulletin of Mathematical Biology,* Vol. 49, pp. 651–669.

Lai, W. M., and Mow, V. C., 1980, "Drag induced compression of articular cartilage during a permeation experiment," *Biorheology,* Vol. 17, pp. 111–123.

Mak, A. F., Lai, W. M., and Mow, V. C., 1987, "Biphasic indentation of articular cartilage—I. Theoretical analysis," *Journal of Biomechanics,* Vol. 20, pp. 703–714.

Mow, V. C., and Lai, W. M., 1980, "Recent Developments in synovial joint biomechanics," *SIAM Review,* Vol. 22, pp. 275–317.

Parker, K. H., Mehta, R. V., and Caro, C. G., 1987, "Steady flow in porous, elastically deformable materials," ASME JOURNAL OF APPLIED MECHANICS, Vol. 54, pp. 794–800.

Rudnicki, J. W., 1987, "Plane Strain Dislocations in Linear Elastic Diffusive Solids," ASME JOURNAL OF APPLIED MECHANICS, Vol. 54, 545–552.

Sachs, J. R., Glucksberg, M. R., Jensen, O. E., and Grotberg, J. B., 1994, "Linear Flow and Deformation in a Poroelastic Disk With a Free Surface," ASME JOURNAL OF APPLIED MECHANICS, Vol. 61, pp. 726–728.

Yang, M., and Taber, L. A., 1991, "The possible role of poroelasticity in the apparent viscoelastic behaviour of passive cardiac muscle," *Journal of Biomechanics,* Vol. 24, pp. 587–597.

Journal of Applied Mechanics

Brief Notes

A Brief Note is a short paper that presents a specific solution of technical interest in mechanics but which does not necessarily contain new general methods or results. A Brief Note should not exceed 1500 words *or equivalent* (a typical one-column figure or table is equivalent to 250 words; a one line equation to 30 words). Brief Notes will be subject to the usual review procedures prior to publication. After approval such Notes will be published as soon as possible. The Notes should be submitted to the Technical Editor of the JOURNAL OF APPLIED MECHANICS. Discussions on the Brief Notes should be addressed to the Editorial Department, ASME, United Engineering Center, 345 East 47th Street, New York, N. Y. 10017, or to the Technical Editor of the JOURNAL OF APPLIED MECHANICS. Discussions on Brief Notes appearing in this issue will be accepted until two months after publication. Readers who need more time to prepare a Discussion should request an extension of the deadline from the Editorial Department.

Relationships Between Kirchhoff and Mindlin Bending Solutions for Levy Plates

C. M. Wang,[1] G. T. Lim,[2] and K. H. Lee[3]

Introduction

Wang and Alwis (1996) presented an exact deflection relationship between Kirchhoff and Mindlin polygonal plates. All the straight edges of the plates must, however, be simply supported but the transverse loading can be of arbitrary distribution. The derivation of the relationship was based on an analogy approach and the assumption that the moment sum vanishes along the edges including the corner points. When using the relationship, Mindlin solutions obtained for plates with obtuse and reentrant corners are somewhat less accurate due to the moment singularities at such corner points. Nevertheless, the relationship allows easy and exact determination of the more complicated Mindlin plate solutions from the simpler Kirchhoff plate solutions for scalene triangular plates and rectangular plates or near rectangular shaped plates. Such Kirchhoff plate solutions abound in the open literature for use in the relationship.

Wang and Lee (1996) extended the aforementioned work to axisymmetric bending of circular and annular plates. All possible combinations of free, simply supported, and clamped edges were considered and the loading must, however, be rotationally symmetric. In addition to the deflection relationships, they gave the relations for the slope/rotations, moments and transverse shear forces.

The present study continues in this line of investigation by treating the bending problem of Levy plates. In using Levy's method of analysis, the shape of the loading function for Levy plates is restricted to be the same for all sections parallel to the direction of the two simply supported edges. Derived herein are the exact relationships between the bending solutions of Levy plates based on the Kirchhoff plate theory and the Mindlin plate theory. These relationships, hitherto not available, enable engineers to unlock solutions for the Mindlin Levy-plates upon supplying easy available Kirchhoff Levy-solutions without much tedious mathematics. Using the relationships, it was discovered that earlier analytical Mindlin Levy-plate solutions by Cooke and Levinson (1983) were erroneous.

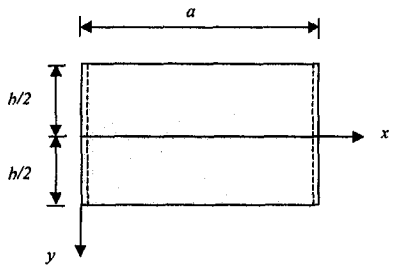

Fig. 1 Levy plate and rectangular coordinate system

Theory

Consider an isotropic Levy plate with uniform thickness h, length a, width b, modulus of elasticity E, Poisson's ratio ν, and shear modulus $G = E/[2(1 + \nu)]$. Adopting the rectangular Cartesian coordinate system as shown in Fig. 1 with its origin at the mid-left side of the plate, the Levy plate is simply supported along the edges $x = 0$ and $x = a$ while the other two edges $y = b/2$ and $y = -b/2$ may be clamped, simply supported, or free. The shape of the transverse loading on the plate is characterized by

$$q(x, y) = \sum_{m=1}^{\infty} q_m(y) \sin \frac{m\pi x}{a}. \quad (1)$$

On the basis of load equivalence from the equilibrium equations for the Kirchhoff and Mindlin plate theories, one can write the following relationships

[1] To whom correspondence should be addressed. Department of Civil Engineering, National University of Singapore, Kent Ridge, Singapore 119260. e-mail: cvewcm@nus.edu.sg

[2] Department of Civil Engineering, National University of Singapore, Kent Ridge, Singapore 119260.

[3] Department of Mechanical and Production Engineering, National University of Singapore, Kent Ridge, Singapore 119260.

Contributed by the Applied Mechanics Division of THE AMERICAN SOCIETY OF MECHANICAL ENGINEERS for publication in the ASME JOURNAL OF APPLIED MECHANICS. Manuscript received by the ASME Applied Mechanics Division, June 2, 1998; final revision, Sept. 17, 1998. Associate Technical Editor: J. N. Reddy.

$$\frac{\partial Q_x^M}{\partial x} + \frac{\partial Q_y^M}{\partial y} = \frac{\partial Q_x^K}{\partial x} + \frac{\partial Q_y^K}{\partial y} \tag{2}$$

$$\frac{\partial^2 M_{xx}^M}{\partial x^2} + 2\frac{\partial^2 M_{xy}^M}{\partial x \partial y} + \frac{\partial^2 M_{yy}^M}{\partial y^2} = \frac{\partial^2 M_{xx}^K}{\partial x^2} + 2\frac{\partial^2 M_{xy}^K}{\partial x \partial y} + \frac{\partial^2 M_{yy}^K}{\partial y^2} \tag{3}$$

where the superscripts K and M denote quantities in the two theories, respectively.

By substituting the usual Levy representations for the stress-resultants, the two load-equivalence relationships may be expressed as

$$\kappa^2 Gh\left(\frac{\mathfrak{M}_m^M}{D} + \mathcal{L}w_m^M\right) = \mathcal{L}\mathfrak{M}_m^K \tag{4}$$

and

$$\mathcal{L}\left(\frac{\mathfrak{M}_m^M}{D}\right) = \mathcal{L}\left(\frac{\mathfrak{M}_m^K}{D}\right) \tag{5}$$

where the moment sums or Marcus moments $\mathfrak{M}$ are given by

$$\mathfrak{M}_m^M = \frac{M_{mxx}^M + M_{myy}^M}{1+\nu} = D\left[\frac{d\psi_{ym}}{dy} - \left(\frac{m\pi}{a}\right)\psi_{xm}\right] \tag{6}$$

$$\mathfrak{M}_m^K = \frac{M_{mxx}^K + M_{myy}^K}{1+\nu} = -D\left[\frac{d^2 w_m^K}{dy^2} - \left(\frac{m\pi}{a}\right)^2 w_m^K\right] = -D\mathcal{L}w_m^K \tag{7}$$

and the Levy operator $\mathcal{L}$ is defined as

$$\mathcal{L}(\cdot) = \frac{d^2(\cdot)}{dy^2} - \left(\frac{m\pi}{a}\right)^2(\cdot). \tag{8}$$

By solving Eq. (5), the relationship between the moment sums of Kirchhoff and Mindlin plates is given by

$$\boxed{\frac{\mathfrak{M}_m^M}{D} = \frac{\mathfrak{M}_m^K}{D} + C_{1m}\sinh\frac{m\pi y}{a} + C_{2m}\cosh\frac{m\pi y}{a}} \tag{9}$$

To solve for w^M in terms of w^K, it is seen that Eq. (4) gives

$$\mathfrak{M}_m^M = -D\mathcal{L}\left(w_m^M - \frac{\mathfrak{M}_m^K}{\kappa^2 Gh}\right). \tag{10}$$

The substitution of Eqs. (7) and (10) into Eq. (9) yields a differential equation, the solution of which leads to the following deflection relationship:

$$w_m^M = w_m^K + \frac{\mathfrak{M}_m^K}{\kappa^2 Gh} + \left(C_{3m} - C_{1m}\frac{ay}{2m\pi}\right)\cosh\frac{m\pi y}{a} + \left(C_{4m} - C_{2m}\frac{ay}{2m\pi}\right)\sinh\frac{m\pi y}{a} \tag{11}$$

where C_{im}, $i = 1, 2, 3, 4$ are constants to be evaluated from the boundary conditions.

It now remains to determine the Mindlin rotation relationships in terms of the Kirchhoff solution. Based on the moment-shear force equilibrium equations and the Levy expressions for the stress resultants, it can be shown that

$$\psi_{xm} + \left(\frac{m\pi}{a}\right)w_m^M = \frac{D}{\kappa^2 Gh}\left[\frac{(1-\nu)}{2}\frac{d^2\psi_{xm}}{dy^2} + \frac{(1+\nu)}{2}\left(\frac{m\pi}{a}\right)\frac{d\psi_{ym}}{dy} - \left(\frac{m\pi}{a}\right)^2\psi_{xm}\right] \tag{12}$$

and

$$\psi_{ym} + \frac{dw_m^M}{dy} = \frac{D}{\kappa^2 Gh}\left[\frac{d^2\psi_{ym}}{dy^2} - \frac{(1-\nu)}{2}\left(\frac{m\pi}{a}\right)^2\psi_{ym} - \frac{(1+\nu)}{2}\left(\frac{m\pi}{a}\right)\frac{d\psi_{xm}}{dy}\right]. \tag{13}$$

The transverse deflection may be eliminated from Eqs. (12) and (13) by first differentiating Eq. (12) with respect to y, and then substituting the expression for the derivative of the deflection into Eq. (13). By doing so, one obtains

$$\frac{d\psi_{xm}}{dy} - \left(\frac{m\pi}{a}\right)\psi_{ym} = \frac{D(1-\nu)}{2\kappa^2 Gh}\left[-\left(\frac{m\pi}{a}\right)\frac{d^2\psi_{ym}}{dy^2} + \left(\frac{m\pi}{a}\right)^3\psi_{ym} + \frac{d^3\psi_{xm}}{dy^3} - \left(\frac{m\pi}{a}\right)^2\frac{d\psi_{xm}}{dy}\right]. \tag{14}$$

By letting

$$\lambda_m^2 = \left(\frac{m\pi}{a}\right)^2 + \frac{2\kappa^2 Gh}{D(1-\nu)} \tag{15}$$

Eq. (14) may be written as

$$\frac{d^3\psi_{xm}}{dy^3} - \lambda_m^2\frac{d\psi_{xm}}{dy} = \frac{m\pi}{a}\left(\frac{d^2\psi_{ym}}{dy^2} - \lambda_m^2\psi_{ym}\right). \tag{16}$$

By solving Eq. (16), one obtains

$$\frac{d\psi_{xm}}{dy} = \frac{m\pi}{a}\psi_{ym} + C_{5m}\sinh\lambda_m y + C_{6m}\cosh\lambda_m y. \tag{17}$$

Before proceeding further, it is noted that the substitution of Eqs. (6) and (7) into Eq. (9) yields

$$\left(\frac{d\psi_{ym}}{dy} - \frac{m\pi}{a}\psi_{xm}\right) = -\left(\frac{d^2 w_m^K}{dy^2} - \frac{m^2\pi^2}{a^2}w_m^K\right) + C_{1m}\sinh\frac{m\pi y}{a} + C_{2m}\cosh\frac{m\pi y}{a}. \tag{18}$$

By differentiating Eq. (17) with respect to y and combining it with Eq. (18), one obtains

$$\frac{d^2\psi_{xm}}{dy^2} - \frac{m^2\pi^2}{a^2}\psi_{xm} = -\frac{m\pi}{a}\left(\frac{d^2 w_m^K}{dy^2} - \frac{m^2\pi^2}{a^2}w_m^K\right) + \lambda_m(C_{5m}\cosh\lambda_m y + C_{6m}\sinh\lambda_m y) + \frac{m\pi}{a}\left(C_{1m}\sinh\frac{m\pi y}{a} + C_{2m}\cosh\frac{m\pi y}{a}\right). \tag{19}$$

By solving Eq. (19), one gets

$$\psi_{xm} = -\frac{m\pi}{a}w_m^K + \lambda_m\frac{D(1-\nu)}{2\kappa^2 Gh}(C_{5m}\cosh\lambda_m y + C_{6m}\sinh\lambda_m y) + \left(C_{7m} + C_{2m}\frac{y}{2}\right)\sinh\frac{m\pi y}{a} + \left(C_{8m} + C_{1m}\frac{y}{2}\right)\cosh\frac{m\pi y}{a}. \tag{20}$$

By substituting Eq. (20) into Eq. (17), one can obtain

$$\psi_{ym} = -\frac{dw_m^K}{dy} + \frac{m\pi}{a}\frac{D(1-\nu)}{2\kappa^2 Gh}(C_{5m}\sinh\lambda_m y + C_{6m}\cosh\lambda_m y) + \left(C_{7m} + C_{2m}\frac{y}{2} + C_{1m}\frac{a}{2m\pi}\right)\cosh\frac{m\pi y}{a} + \left(C_{8m} + C_{1m}\frac{y}{2} + C_{2m}\frac{a}{2m\pi}\right)\sinh\frac{m\pi y}{a}. \quad (21)$$

By substituting Eqs. (11), (20), and (21) into Eq. (12), it is deduced that

$$C_{7m} = \frac{m\pi}{a}\left(\frac{D}{\kappa^2 Gh}C_{1m} - C_{4m}\right) \quad (22)$$

and

$$C_{8m} = \frac{m\pi}{a}\left(\frac{D}{\kappa^2 Gh}C_{2m} - C_{3m}\right). \quad (23)$$

In view of the foregoing deflection and rotation expressions, the relationships between solutions of Mindlin and Kirchhoff plates may be summarized as follows:

- **Deflection Relationship.**

$$w^M = w^K + \frac{\mathfrak{M}^K}{\kappa^2 Gh} + \sum_{m=1}^{\infty}\left[\left(C_{3m} - C_{1m}\frac{ay}{2m\pi}\right)\cosh\frac{m\pi y}{a} + \left(C_{4m} - C_{2m}\frac{ay}{2m\pi}\right)\sinh\frac{m\pi y}{a}\right]\sin\frac{m\pi x}{a} \quad (24)$$

- **Rotation-Slope Relationships.**

$$\psi_x = -\frac{\partial w^k}{\partial x} + \sum_{m=1}^{\infty}\left[\lambda_m\frac{D(1-\nu)}{2\kappa^2 Gh}(C_{5m}\cosh\lambda_m y + C_{6m}\sinh\lambda_m y) + \left(\frac{D}{\kappa^2 Gh}\frac{m\pi}{a}C_{1m} - \frac{m\pi}{a}C_{4m} + C_{2m}\frac{y}{2}\right)\sinh\frac{m\pi y}{a} + \left(\frac{D}{\kappa^2 Gh}\frac{m\pi}{a}C_{2m} - \frac{m\pi}{a}C_{3m} + C_{1m}\frac{y}{2}\right)\cosh\frac{m\pi y}{a}\right]\cos\frac{m\pi x}{a} \quad (25)$$

$$\psi_y = -\frac{\partial w^K}{\partial y} + \sum_{m=1}^{\infty}\left[\frac{m\pi}{a}\frac{D(1-\nu)}{2\kappa^2 Gh}(C_{5m}\sinh\lambda_m y + C_{6m}\cosh\lambda_m y) + \left(\frac{D}{\kappa^2 Gh}\frac{m\pi}{a}C_{1m} - \frac{m\pi}{a}C_{4m} + C_{2m}\frac{y}{2} + C_{1m}\frac{a}{2m\pi}\right)\cosh\frac{m\pi y}{a} + \left(\frac{D}{\kappa^2 Gh}\frac{m\pi}{a}C_{2m} - \frac{m\pi}{a}C_{3m} + C_{1m}\frac{y}{2} + C_{2m}\frac{a}{2m\pi}\right)\sinh\frac{m\pi y}{a}\right]\sin\frac{m\pi x}{a} \quad (26)$$

- **Moment Relationships.**

$$M_{xx}^M = M_{xx}^K + \nu D\sum_{m=1}^{\infty}\left[C_{1m}\sinh\frac{m\pi y}{a} + C_{2m}\cosh\frac{m\pi y}{a}\right]\sin\frac{m\pi x}{a} - D(1-\nu)\sum_{m=1}^{\infty}\left[\lambda_m\frac{D(1-\nu)}{2\kappa^2 Gh}\left(\frac{m\pi}{a}\right)\times(C_{5m}\cosh\lambda_m y + C_{6m}\sinh\lambda_m y) + \left(\frac{m\pi}{a}\right)^2\left(\frac{D}{\kappa^2 Gh}C_{1m} - C_{4m} + C_{2m}\frac{ay}{2m\pi}\right)\sinh\frac{m\pi y}{a} + \left(\frac{m\pi}{a}\right)^2\left(\frac{D}{\kappa^2 Gh}C_{2m} - C_{3m} + C_{1m}\frac{ay}{2m\pi}\right)\cosh\frac{m\pi y}{a}\right]\sin\frac{m\pi x}{a} \quad (27)$$

$$M_{yy}^M = M_{yy}^K + D\sum_{m=1}^{\infty}\left[C_{1m}\sinh\frac{m\pi y}{a} + C_{2m}\cosh\frac{m\pi y}{a}\right]\sin\frac{m\pi x}{a} + D(1-\nu)\sum_{m=1}^{\infty}\left[\lambda_m\frac{D(1-\nu)}{2\kappa^2 Gh}\left(\frac{m\pi}{a}\right)\times(C_{5m}\cosh\lambda_m y + C_{6m}\sinh\lambda_m y) + \left(\frac{m\pi}{a}\right)^2\left(\frac{D}{\kappa^2 Gh}C_{1m} - C_{4m} + C_{2m}\frac{ay}{2m\pi}\right)\sinh\frac{m\pi y}{a} + \left(\frac{m\pi}{a}\right)^2\left(\frac{D}{\kappa^2 Gh}C_{2m} - C_{3m} + C_{1m}\frac{ay}{2m\pi}\right)\cosh\frac{m\pi y}{a}\right]\sin\frac{m\pi x}{a} \quad (28)$$

$$M_{xy}^M = M_{xy}^K + \frac{D(1-\nu)}{2}\sum_{m=1}^{\infty}\left[\left\{\lambda_m^2 + \left(\frac{m\pi}{a}\right)^2\right\}\times\frac{D(1-\nu)}{2\kappa^2 Gh}(C_{5m}\sinh\lambda_m y + C_{6m}\cosh\lambda_m y) + 2\left(\frac{m\pi}{a}\right)^2\left\{\left(\frac{D}{\kappa^2 Gh}C_{1m} - C_{4m} + C_{2m}\frac{ay}{2m\pi}\right)\cosh\frac{m\pi y}{a} + \left(\frac{D}{\kappa^2 Gh}C_{2m} - C_{3m} + C_{1m}\frac{ay}{2m\pi}\right)\sinh\frac{m\pi y}{a}\right\} + C_{1m}\cosh\frac{m\pi y}{a} + C_{2m}\sinh\frac{m\pi y}{a}\right]\cos\frac{m\pi x}{a} \quad (29)$$

- **Shear Force Relationships.**

$$Q_x^M = Q_x^K + \frac{D(1-\nu)}{2}\sum_{m=1}^{\infty}\left[\lambda_m(C_{5m}\cosh\lambda_m y + C_{6m}\sinh\lambda_m y) + \frac{2}{1-\nu}\left(\frac{m\pi}{a}\right)\times\left(C_{1m}\sinh\frac{m\pi y}{a} + C_{2m}\cosh\frac{m\pi y}{a}\right)\right]\cos\frac{m\pi x}{a} \quad (30)$$

$$Q_y^M = Q_y^K + \frac{D(1-\nu)}{2}\sum_{m=1}^{\infty}\left[\left(\frac{m\pi}{a}\right)(C_{5m}\sinh\lambda_m y + C_{6m}\cosh\lambda_m y) + \frac{2}{1-\nu}\left(\frac{m\pi}{a}\right)\times\left(C_{1m}\cosh\frac{m\pi y}{a} + C_{2m}\sinh\frac{m\pi y}{a}\right)\right]\sin\frac{m\pi x}{a} \quad (31)$$

The foregoing relationships contain a total of six unknown constants C_{im}, $i = 1, 2, \ldots, 6$ which are dependent on the six boundary conditions at the two edges $y = -b/2$ and $y = +b/2$, that is, three boundary conditions for each edge. These constants are evaluated for Levy plates with clamped edges at $y = -b/2$ and $y = +b/2$ in the next section.

Illustrative Example: SCSC Levy Plates

For the clamped edges at $y = -b/2$ and $y = +b/2$, the boundary conditions are

$$w^M = w^K = 0, \quad \psi_x = \psi_y = \frac{\partial w^K}{\partial y} = 0. \quad (32)$$

The substitution of the boundary conditions given in Eq. (32) into Eqs. (24) to (26) gives

$$C_{1m} = \frac{\Omega_m^-\left(\coth\frac{m\pi b}{2a}\sinh\frac{\lambda_m b}{2} - \frac{m\pi}{a\lambda_m}\cosh\frac{\lambda_m b}{2}\right)}{\left\{\frac{m\pi}{a\lambda_m}\frac{D}{\kappa^2 Gh}\sinh\frac{m\pi b}{2a}\cosh\frac{\lambda_m b}{2} - \left[\frac{D}{\kappa^2 Gh} + \frac{1}{2}\left(\frac{a}{m\pi}\right)^2\right]\cosh\frac{m\pi b}{2a}\sinh\frac{\lambda_m b}{2} + \frac{ab}{4m\pi}\operatorname{csch}\frac{m\pi b}{2a}\sinh\frac{\lambda_m b}{2}\right\}} \quad (33a)$$

$$C_{2m} = \frac{\Omega_m^+\left(\tanh\frac{m\pi b}{2a}\cosh\frac{\lambda_m b}{2} - \frac{m\pi}{a\lambda_m}\sinh\frac{\lambda_m b}{2}\right)}{\left\{\frac{m\pi}{a\lambda_m}\frac{D}{\kappa^2 Gh}\cosh\frac{m\pi b}{2a}\sinh\frac{\lambda_m b}{2} - \left[\frac{D}{\kappa^2 Gh} + \frac{1}{2}\left(\frac{a}{m\pi}\right)^2\right]\sinh\frac{m\pi b}{2a}\cosh\frac{\lambda_m b}{2} - \frac{ab}{4m\pi}\operatorname{sech}\frac{m\pi b}{2a}\cosh\frac{\lambda_m b}{2}\right\}} \quad (33b)$$

$$C_{3m} = C_{2m}\frac{ab}{4m\pi}\tanh\frac{m\pi b}{2a} - \Omega_m^+\operatorname{sech}\frac{m\pi b}{2a} \quad (33c)$$

$$C_{4m} = C_{1m}\frac{ab}{4m\pi}\coth\frac{m\pi b}{2a} - \Omega_m^-\operatorname{csch}\frac{m\pi b}{2a} \quad (33d)$$

$$C_{5m} = -\frac{2}{1-\nu}\left(\frac{m\pi}{a\lambda_m}\right)\operatorname{sech}\frac{\lambda_m b}{2}\times\left[C_{2m}\cosh\frac{m\pi b}{2a} + \frac{\kappa^2 Gh}{D}\Omega_m^+\right] \quad (33e)$$

$$C_{6m} = -\frac{2}{1-\nu}\left(\frac{m\pi}{a\lambda_m}\right)\operatorname{csch}\frac{\lambda_m b}{2}\times\left[C_{1m}\sinh\frac{m\pi b}{2a} + \frac{\kappa^2 Gh}{D}\Omega_m^-\right] \quad (33f)$$

where

$$\Omega_m^+ = \left(\frac{\mathfrak{M}_m^K(b/2) + \mathfrak{M}_m^K(-b/2)}{2\kappa^2 Gh}\right), \quad \Omega_m^- = \left(\frac{\mathfrak{M}_m^K(b/2) - \mathfrak{M}_m^K(-b/2)}{2\kappa^2 Gh}\right). \quad (34a, b)$$

The above relationships can be used to furnish the deflection, rotations, and stress-resultants of SCSC Levy plates based on the Mindlin plate theory upon supplying the corresponding Kirchhoff plate solutions. This is illustrated below for the Mindlin plate deflection using the example of a uniformly loaded, SCSC Levy plate.

Based on the Kirchhoff plate theory, the transverse deflection for a Levy plate with simply supported and clamped edges under a uniform loading q_0, is given by (Mansfield 1989)

$$w^K(x, y) = \frac{a^4}{D\pi^4}\sum_{m=1}^{\infty}\frac{q_m}{m^4}\times\left(1 + A_m\cosh\frac{m\pi y}{a} + B_m\frac{m\pi y}{a}\sinh\frac{m\pi y}{a}\right)\sin\frac{m\pi x}{a} \quad (35)$$

where

$$q_m = \frac{2q_0}{m\pi}[1 - (-1)^m], \quad (36a)$$

$$A_m = -\frac{1 + \frac{m\pi b}{2a}\coth\frac{m\pi b}{2a}}{\cosh\frac{m\pi b}{2a} + \frac{m\pi b}{2a}\operatorname{csch}\frac{m\pi b}{2a}} \quad (36b)$$

$$B_m = \frac{1}{\cosh\frac{m\pi b}{2a} + \frac{m\pi b}{2a}\operatorname{csch}\frac{m\pi b}{2a}}. \quad (36c)$$

The substitution of Eq. (35) into Eq. (7) yields the moment sum for the Kirchhoff Levy plate, which is

$$\mathfrak{M}^K = \sum_{m=1}^{\infty} q_m\left(\frac{a}{m\pi}\right)^2\left[1 - 2B_m\cosh\frac{m\pi y}{a}\right]\sin\frac{m\pi x}{a}. \quad (37)$$

Under symmetric loading, the Mindlin deflection is symmetrical about the x-axis while the Mindlin rotation ψ_{ym} must take on the

Table 1 Maximum Mindlin deflection parameters $w^M(a/2, 0)D/(q_o a^4)$ of uniformly loaded, square *SCSC* Levy plates

h/a	Cooke and Levinson (1983)	*ABAQUS* (40 × 40 mesh with S8R shell element)	Eq. (39)
0.1	0.00213	0.00221	0.00221
0.2	0.00276	0.00302	0.00302

form of an odd function. Correspondingly, the terms in Eq. (34) become

$$\Omega_m^- = 0, \quad \Omega_m^+ = \frac{\mathfrak{M}_m^K(b/2)}{\kappa^2 Gh}. \tag{38a, b}$$

In view of Eqs. (24), (33), (35) to (38), the deflection of the Mindlin plate is thus given by

$$w^M = \sum_{m=1}^{\infty} \left\{ \frac{q_m}{D} \left(\frac{a}{m\pi} \right)^4 \left[1 + A_m \cosh \frac{m\pi y}{a} + B_m \frac{m\pi y}{a} \sinh \frac{m\pi y}{a} \right] + \frac{q_m}{\kappa^2 Gh} \left(\frac{a}{m\pi} \right)^2 \times \left\{ 1 - 2B_m \cosh \frac{m\pi y}{a} - \left[2B_m \cosh \frac{m\pi b}{2a} - 1 \right] \times \left[\left(\xi_m \frac{ab}{4m\pi} \tanh \frac{m\pi b}{2} - \operatorname{sech} \frac{m\pi b}{2a} \right) \cosh \frac{m\pi y}{a} - \xi_m \frac{ay}{2m\pi} \sinh \frac{m\pi y}{a} \right] \right\} \right\} \sin \frac{m\pi x}{a} \tag{39}$$

where

$$\xi_m = \frac{\tanh \dfrac{m\pi b}{2a} \cosh \dfrac{\lambda_m b}{2} - \dfrac{m\pi}{a\lambda_m} \sinh \dfrac{\lambda_m b}{2}}{\left\{ \dfrac{m\pi}{a\lambda_m} \dfrac{D}{\kappa^2 Gh} \cosh \dfrac{m\pi b}{2a} \sinh \dfrac{\lambda_m b}{2} - \left[\dfrac{D}{\kappa^2 Gh} + \dfrac{1}{2} \left(\dfrac{a}{m\pi} \right)^2 \right] \sinh \dfrac{m\pi b}{2} \cosh \dfrac{\lambda_m b}{2} - \dfrac{ab}{4m\pi} \operatorname{sech} \dfrac{m\pi b}{2a} \cosh \dfrac{\lambda_m b}{2} \right\}}. \tag{40}$$

Table 1 presents the maximum deflection parameters of a square, SCSC Levy plate based on a Poisson's ratio ν of 0.3 and a shear correction factor κ^2 of $\frac{5}{6}$. It can be observed that the deflection values are in agreement with those obtained using ABAQUS (1996), thus confirming the correctness of the derived relationship. The results, however, differ from those determined by Cooke and Levinson (1988). The error made by these researchers will be discussed in a separate paper (Lee et al., 1999).

Concluding Remarks

The exact relationships for the deflection, rotations, and stress resultants of Levy plates between the Mindlin and Kirchhoff solutions have been developed. These relationships allow analysts to readily determine the Mindlin Levy plate solutions from the corresponding well-known Kirchhoff Levy plate solutions. The relationships also help to elucidate the effect of transverse shear deformation on the deflection of Levy plates and serve to provide benchmark solutions for checking numerical solutions.

References

ABAQUS/Standard User's Manual (Version 5.6), 1996, Vols. 1–3. Hibbitt, Karlsson & Sorensen, Inc.

Cooke, D.W., and Levinson, M., 1983, "Thick rectangular plates—II, The generalised Levy solution," *International Journal of Mechanical Sciences,* Vol. 25, pp. 207–215.

Lee, K.H., Lim, G.T., and Wang, C.M., 1999, "Thick Levy plate solutions revisited," manuscript in preparation.

Mansfield, E.H., 1989, *The Bending and Stretching of Plates,* 2nd Ed., Cambridge University Press, Cambridge, UK, pp. 37–40.

Mindlin, R.D., 1951, "Influence of rotary inertia and shear in flexural motion of isotropic elastic plates," ASME JOURNAL OF APPLIED MECHANICS, Vol. 18, pp. 1031–1036.

Wang, C.M., 1997, "Relationships between Mindlin and Kirchhoff bending solutions for tapered circular and annular plates," *Engineering Structures,* Vol. 19, No. 3, pp. 255–258.

Wang, C.M., and Alwis, W.A.M., 1995, "Simply supported Mindlin plate deflections using Kirchhoff plates," *Journal of Engineering Mechanics, ASCE,* Vol. 121, No. 12, pp. 1383–1385.

Wang, C.M., and Lee, K.H., 1996, "Deflection and stress-resultants of axisymmetric Mindlin plates in terms of Kirchhoff solutions," *International Journal of Mechanical Sciences,* Vol. 38, No. 11, pp. 1179–1185.

A Beam Bundle in a Compressible Inviscid Fluid

R. J. Zhang[1]

A three-dimensional homogenization model is developed to predict the overall dynamic behavior of a beam bundle. It is shown that the model is transversely isotropic. This characteristic simplifies the governing equation of the model in the manner that only one scalar parameter appears in it. Transverse isotropy means that any direction in the plane perpendicular to the axis of the beam is the principal direction.

Introduction

A beam bundle is composed of a great number of tubular beams with periodic structure, which are immersed in an acoustic fluid. It can be regarded as a fiber-reinforced composite or a material with microstructure. By means of the asymptotic homogenization method (Bensoussan et al., 1978; Sanchez-Palencia, 1980), a three-dimensional continuum model for the beam bundle has been given by the author (1998a, b). The model is referred to as a unified model, because existing two two-dimensional models, the Schumann-Benner's model (Schumann, 1981a, b) and Brochard-Hammami's model (Hammami, 1990 and Brochard et al., 1991), are its two-dimensional special cases.

In this paper, the fact is revealed that the continuum model is transversely isotropic. This characteristic results in the simplification of the homogenization equation of the model by replacing its tensor parameters by a scalar parameter. It is interesting to point out the fact that the significance of the scalar parameter, D in (13)–(15), is the added fluid area fraction.

For brevity, we will directly begin with the three-dimensional homogenization equations developed by the author (1998a, b, c).

1 Three-Dimensional Homogenization Equations

The three-dimensional homogenized equations for the beam bundle are

$$\left(\frac{\lambda}{c_f^2}+\frac{1-\lambda}{\kappa c_s^2}\right)\ddot{p}-\nabla_\alpha(A_{\alpha\beta}\nabla_\beta p)-\lambda\nabla_3\nabla_3 p+\bar{\rho}_f\nabla_\alpha(B_{\alpha\beta}\ddot{w}_\beta)=0 \quad (1)$$

$$M_{\alpha\beta}\ddot{w}_\beta+B_{\alpha\beta}p+\nabla_3\nabla_3\left(\frac{EI}{|X|}\nabla_3\nabla_3 w_\alpha\right)=0 \quad (2)$$

in which the pressure of fluid p and the deflection of beams w_α are unknown functions to be determined; c_f and c_s are the sound speed in fluid and beams, respectively; $\kappa=\bar{\rho}_s/\bar{\rho}_f$ is the density ratio of beam to fluid; $\bar{\rho}_f$ and $\bar{\rho}_s$ are the mean density of fluid and beams; λ is the fluid volume fraction or porosity of the bundle; EI is the flexural rigidity of beams; $|X|$ is the area of a unit cell composed of the cross section of a beam and surrounding fluid in the plane perpendicular to the beam axis; $\nabla_i=\partial/\partial x_i$ and $x=(x_1, x_2, x_3)$ denote a global coordinate system, with the x_3-axis pointing along the beam; a dot over any quantity denotes its derivative with respect to time t; summation is on repeated subscripts; and Greek subscripts assume the value 1 and 2 while Latin subscripts range from 1 to 3. Tensor parameters in the equations are defined as

$$A_{\alpha\beta}=\lambda\delta_{\alpha\beta}-D_{\alpha\beta} \quad (3)$$

$$B_{\alpha\beta}=(1-\lambda)\delta_{\alpha\beta}+D_{\alpha\beta} \quad (4)$$

$$M_{\alpha\beta}=\bar{\rho}_s(1-\lambda)\delta_{\alpha\beta}+\bar{\rho}_f D_{\alpha\beta}, \quad (5)$$

and

$$D_{\alpha\beta}=\frac{1}{|Y|}\int_{Y_f}\chi_{\beta,\alpha}dy_1dy_2 \quad (6)$$

where $y=(y_1, y_2)$ is a local coordinates defined in a magnified unit cell as

$$y_\alpha=x_\alpha/\epsilon \quad (\alpha=1, 2) \quad (7)$$

with a small nondimensional parameter, $\epsilon \ll 1$, where ϵ is the ratio of the size of the unit cell to the size of the whole structure; a comma represents the derivative to the local coordinates: Y_f is the fluid domain in the magnified unit cell; $|Y|$ is the area of the magnified unit cell; and χ_α is the local function defined in the magnified unit cell and satisfies the following local problem:

$$\begin{cases}\chi_{\alpha,\beta\beta}=0 & \text{on } Y_f\\ \chi_{\alpha,\beta}n_\beta=n_\alpha & \text{at } \Gamma\\ \chi_\alpha=\text{periodic function of } y_1 \text{ and } y_2\\ \displaystyle\int_{Y_f}\chi_\alpha dy_1dy_2=0\end{cases} \quad (8)$$

where Γ is the interface between fluid and beam, n_α is the exterior normal to fluid domain at Γ in the magnified unit cell.

Note that Eqs. (1) and (2) are, in fact, different from those in Zhang (1998a, b) by a factor $|X|$. Similarly, the tensor parameters (3)–(6) are different from their original forms by the same factor. This modification makes the tensor parameters be the nondimensional ones.

2 Isotropic Tensor

First, it is not difficult to show from (8) that

$$\chi_1(y_1, y_2)=\chi_2(-y_2, y_1)=\chi(y_1, y_2). \quad (9)$$

It then follows from (6) that

$$D_{11}=D_{22}=D \quad \text{and} \quad D_{12}=-D_{21}. \quad (10)$$

Further, we can see that tensor $D_{\alpha\beta}$ is symmetric in two subscripts because

$$D_{\alpha\beta}=\frac{1}{|Y|}\int_{Y_f}\chi_{\beta,\alpha}dy=\frac{1}{|Y|}\int_\Gamma\chi_\beta n_\alpha dl\overset{(8b)}{=}\frac{1}{|Y|}\int_\Gamma\chi_\beta\chi_{\alpha,\gamma}n_\gamma dl$$

$$=\frac{1}{|Y|}\int_{Y_f}(\chi_\beta\chi_{\alpha,\gamma})_{,\gamma}dy\overset{(8a)}{=}\frac{1}{|Y|}\int_{Y_f}\chi_{\beta,\gamma}\chi_{\alpha,\gamma}dy. \quad (11)$$

Equation (10) indicates that the symmetric tensor $D_{\alpha\beta}$ is isotropic. Sequentially, due to (3), (4), and (5), all the following tensors are isotropic, too. Thus, we have

$$D_{\alpha\beta}=D\delta_{\alpha\beta}, \quad A_{\alpha\beta}=A\delta_{\alpha\beta},$$

$$B_{\alpha\beta}=B\delta_{\alpha\beta} \quad \text{and} \quad M_{\alpha\beta}=M\delta_{\alpha\beta} \quad (12)$$

[1] Department of Engineering Mechanics, Tongji University, Shanghai 200092, China.

Contributed by the Applied Mechanics Division of THE AMERICAN SOCIETY OF MECHANICAL ENGINEERS for publication in the ASME JOURNAL OF APPLIED MECHANICS. Manuscript received by the ASME Applied Mechanics Division, Jan. 21 1998; final revision, Oct. 15, 1998. Associate Technical Editor: M.-J. Pindera.

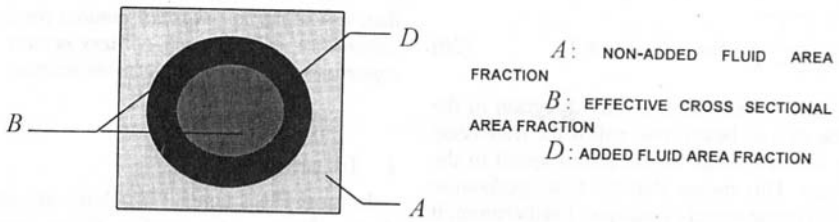

Fig. 1 Significance of *A*, *B*, and *D*

where

$$A = \lambda - D \tag{13}$$

$$B = 1 - \lambda + D \tag{14}$$

and

$$M = \bar{\rho}_s(1 - \lambda) + \bar{\rho}_f D. \tag{15}$$

3 Uniparameter Equations

Substituting (12) into (1) and (2), we obtain the final equations as follows:

$$\left(\frac{\lambda}{c_f^2} + \frac{1-\lambda}{\kappa c_s^2}\right)\ddot{p} - A\nabla_\alpha\nabla_\alpha p - \lambda\nabla_3\nabla_3 p + \bar{\rho}_f B\nabla_\alpha\ddot{w}_\alpha = 0 \tag{16}$$

and

$$M\ddot{w}_\alpha + B\nabla_\alpha p + \nabla_3\nabla_3\left(\frac{EI}{|X|}\nabla_3\nabla_3 w_\alpha\right) = 0. \tag{17}$$

It can be found that all parameters in (16) and (17) are scalar. This indicates that the model is isotropic in the plane perpendicular to the axis of beams. Apparently, there are three scalar parameters A, B, and M in the above equations. However, according to (13)–(15), they are not independent. In fact, for the given geometry (i.e., λ is given), the only parameter in the final equations is D.

4 Added Fluid Area

As can be seen from the definition of M in (15) that the significance of the term $\bar{\rho}_f D$ is the added fluid mass fraction per unit length of beam. Hence, D indicates the cross-sectional area fraction of fluid which is added onto the beam. Then, we can see from (14) that B denotes the total cross-sectional area fraction of the beam and the added fluid. Moreover, (13) indicate that A expresses such an area fraction of the fluid that is not added to the beam. The fact that tensors $A_{\alpha\beta}$, $B_{\alpha\beta}$, and $D_{\alpha\beta}$ are isotropic makes it reasonable that the added fluid has an constant thickness round the beam. A, B, and D are illustrated in Fig. 1.

In the case of the small beam volume fraction, as pointed out by the author (Zhang, 1998b), D has the asymptotic expression

$$D = \frac{\lambda(1-\lambda)}{2-\lambda} \quad \text{for } 1 - \lambda \ll 1. \tag{18}$$

5 Equivalent Sound Speed

In order to find the sound speed in the axial direction, we delete these terms that involve the derivative with respect to x_α in the final Eqs. (16) and (17). In this case, the deflection of beams w_α must be zero, otherwise (17) is not a propagation equation. The propagation equation in the axial direction has the form

$$\ddot{p} - \frac{\lambda}{\dfrac{\lambda}{c_f^2} + \dfrac{1-\lambda}{\kappa c_s^2}}\nabla_3\nabla_3 p = 0. \tag{19}$$

When $\kappa = \bar{\rho}_s/\bar{\rho}_f$ tends to infinity, (19) becomes

$$\ddot{p} - c_f^2\nabla_3\nabla_3 p = 0. \tag{20}$$

Of course, the sound speed in the axial direction is c_f.

Now let us look for the equivalent sound speed in the plane perpendicular to the axis of beams. In this case, the term $-\lambda\nabla_3\nabla_3 p$ in (16) has to be deleted. Only in the following two cases, a propagation equation can be deduced from the Eqs. (16) and (17):

Case 1: Beams are Fixed. In this case, $\ddot{w}_\alpha$ in (16) must be zero and Eq. (17) should be deleted. Then, the propagation equation in any direction x_α ($\alpha = 1$ or 2) is of the form

$$\left(\frac{\lambda}{c_f^2} + \frac{1-\lambda}{\kappa c_s^2}\right)\ddot{p} - A\nabla_\alpha\nabla_\alpha p = 0 \quad (\text{no sum on } \alpha). \tag{21}$$

Correspondingly, the equivalent transverse sound speed (in arbitrary direction) is

$$C_{eq}^{(\text{trans})} = \sqrt{\frac{1}{\dfrac{\lambda}{c_f^2} + \dfrac{1-\lambda}{\kappa c_s^2}}[\lambda - D]}. \tag{22}$$

When $\kappa = \bar{\rho}_s/\bar{\rho}_f$ tends to infinity, (22) reduces to

$$C_{eq}^{(\text{trans})} = c_f\sqrt{1 - \frac{D}{\lambda}}. \tag{23}$$

This is, in fact, similar to what was given by Brochard and Hammami (1991). It reduced to a pure acoustic problem.

Case 2: Beams Move in Phase. The elimination of $\ddot{w}_\alpha$ in the Eqs. (16) and (17) gives an equation in any direction x_α ($\alpha = 1$ or 2) of the form

$$\left(\frac{\lambda}{c_f^2} + \frac{1-\lambda}{\kappa c_s^2}\right)\ddot{p} - \left(A + \bar{\rho}_f\frac{B^2}{M}\right)\nabla_\alpha\nabla_\alpha p = \bar{\rho}_f\frac{B}{M}\nabla_\alpha\left[\nabla_3\nabla_3\frac{EI}{|X|}\nabla_3\nabla_3 w_\alpha\right] \quad (\text{no sum on } \alpha). \tag{24}$$

Obviously, when $\nabla_\alpha[\nabla_3\nabla_3\,(EI/|X|)\nabla_3\nabla_3 w_\alpha] = 0$, which means that all the beams bear the same load or all the beams have the same displacement mode, Eq. (24) becomes a propagation equation. The equivalent transverse sound speed is

$$C_{eq}^{(\text{trans})} = \sqrt{\frac{1}{\dfrac{\lambda}{c_f^2} + \dfrac{1-\lambda}{\kappa c_s^2}}\left[\lambda - D + \frac{(1-\lambda+D)^2}{\kappa(1-\lambda)+D}\right]}. \tag{25}$$

It can be shown that the equivalent transverse sound speed expressed by (25) is similar to what was given by Schumann (1981). In addition, when $\kappa = \bar{\rho}_s/\bar{\rho}_f$ tends to infinity, (25) reduces to (23). This fact can be understood so that $\kappa \to \infty$ means "beams are fixed."

In the case of the small beam volume fraction, see (18), Eq. (23) becomes

$$C_{eq}^{(\text{trans})} = c_f \sqrt{\frac{1}{2-\lambda}} \quad \text{for} \quad 1-\lambda \ll 1. \tag{26}$$

Obviously, there is the same sound speed in any direction in the plane perpendicular to the axis of beams (we call it the transverse sound speed), and there is other value of the sound speed in the axial direction of the beam. This means that the homogenization model of the beam bundle is transversely isotropic. Furthermore, it can be easily seen from (23) that the transverse sound speed is always smaller than the axial one.

Acknowledgment

This work was supported in part by the Research Laboratory of Solid Mechanics of State Education Commission of China, and in part by the Key Discipline of the Shanghai Education Commission.

My research experience at CEA CE/Saclay of FRANCE arouses my interest in the problem and makes it possible to write the paper. I wish to convey my hearty acknowledgment to CEA CE/Saclay and Mme F. Gantenbein for her help, who was my supervisor when I worked there in 1994.

References

Bensoussan, A., Lions, J.-L., and Papanicolaou, G., 1978, *Asymptotic Analysis for Periodic Structures,* North-Holland, Amsterdam.

Brochard, D., and Hammami, L., 1991, "An homogenization method applied to the seismic analysis of LMFBR cores," *SMiRT 11 Transaction,* Vol. E, Aug. Tokyo, Japan, pp. 497–503.

Hammami, L., 1990, "Etude de l'interaction fluide structure dans les faisceaux de tubes par une methode d'homogenisation," these Universite Paris VI.

Sanchez-Palencia, E., 1980, *Non-homogeneous Media and Vibration Theory* (Lecture Notes in Physics), Springer, Berlin.

Schumann, U., 1981a, "Homogenized equations of motion for rod bundles in the fluid with periodic structure," *Ingenieur-Archiv,* Vol. 50, pp. 203–216.

Schumann, U., 1981b, "Virtual density and speed of sound in a fluid-solid mixture with periodic structure," *Int. J. of Multiphase Flow,* Vol. 7, No. 6, pp. 619–633.

Zhang, R.J., 1998a, "A Unified 3-D Homogenization Model of Beam Bundle in Fluid," ASME *Journal of Pressure Vessel Technology,* Vol. 120, pp. 56–61.

Zhang, R.J., 1998b, "Structural homogenized analysis for nuclear reactor core," *Nuclear Engineering and Design,* Vol. 183, pp. 151–156.

Zhang, R.J., 1998c, "Homogenization model for fluid structure interaction in nuclear reactor core," *Flow-induced Vibration and Transient Thermal-Hydraulics—1998,* PVP-Vol. 363, M. K. AuYang, ed., presented at The 1998 ASME/JSME Joint Pressure Vessel and Piping Conference San Diego, CA, July 26–30.

Thermoelastic Contact Between a Flat Punch and an Anisotropic Half-Space

C. K. Chao,[1,3] S. P. Wu,[2,3] and B. Gao[2,3]

The fundamental nature of thermoelastic contact between a flat punch and an anisotropic half-plane solid is studied. Based on Lekhnitskii's stress potentials and anisotropic thermoelasticity theory, the formulation leads to the nonhomogeneous Hilbert problem which can be solved in compact form. The contact traction beneath the punch face is derived in the form of the Cauchy-type integral which is solved numerically. The results show that, depending on the magnitude of the applied force and the total heat flux, either perfect thermal contact throughout the punch face or separation at the punch corners occurs. The contact lengths for separation solutions are also examined.

1 Introduction

In most cases contact problems are accompanied by heat conduction between two bodies. When heat is conducted across an interface between two conducting solids, there will generate some resistance to heat flow across the interface, which is found to be a function of the local contact pressure proposed by Cooper et al. (1969) and Shlykov and Ganin (1964). However, the heat conduction and elasticity problems are coupled through the boundary conditions, which were raised by Clausing (1996) and Barber (1973), since the contact pressure is itself influenced by not only the thermal distortion but also the temperature field in the bodies. For the case of thermoelastic contact between a flat punch and isotropic half-space, Comninou et al. (1981) discussed that, depending on the magnitude and the direction of the total heat flux, one of the possibilities occurs: separation at the punch corners, perfect thermal contact throughout the punch face, or an imperfect contact region at the center with adjacent perfect contact regions. Clements and Toy (1976) used integral transform techniques to solve contact problems for anisotropic media. Recently, Fan and Hwu (1996) studied the punch problems for an anisotropic elastic half-plane by applying Stroh's formalism (Stroh, 1958). To the best of our knowledge, the thermoelastic contact problem associated with anisotropic media is new. In this brief note the two-dimensional thermoelastic problem of an anisotropic elastic half-space indented by a perfectly conducting rigid flat punch is considered. Based on the complex variable representation of two-dimensional elasticity developed by Lekhnitskii (1963) and the method of analytical continuation, the full-field solutions of the temperature field and stress distributions are derived in compact form. Since the Cauchy integral appearing in the expression for contact pressure distribution cannot be evaluated in closed form for anisotropic material, the contact pressure along the punch face and the related contact length are computed numerically which are found to depend on the geometrical parameters, material anisotropy, and the ratio between thermal and mechanical loads. The condition for perfect thermal contact throughout the punch face or separation at the punch corners through these parameters is also discussed in detail and shown in graphic form. The results presented here can be reduced to those for the isotropic case and found to be identical with the solutions given by Comninou et al. (1981).

2 Heat Conduction in the Half-Plane

The heat fluxes in the x_1, x_2 coordinate system of an anisotropic half-plane medium can be expressed as (Ozisik, 1980)

$$h_i = -k_{ij}T_{,j} \quad (i, j = 1, 2) \tag{1}$$

where k_{ij} are the heat conductivity coefficients and T, h_1, h_2 denote temperature and heat fluxes in the x_1, x_2 direction, respectively. A subscript after a comma stands for differentiation with respect to this index and repeat indices imply summation. The steady-state heat conduction equation can be written as

$$h_{i,i} = -k_{ij}T_{,ij} = 0. \tag{2}$$

The general solution to Eq. (2) is given by (Wu, 1984)

$$T = \phi_0(z) + \overline{\phi_0(z)}, \quad z = x_1 + \mu_0 x_2 \tag{3}$$

where the overbar denotes a complex conjugate while the complex function $\phi_0(z)$ is an arbitrary function which can be determined by satisfying the specified boundary conditions and μ_0 is the root of the following characteristic equation with a positive imaginary part:

[1] Professor.

[2] Graduate Student.

[3] Department of Mechanical Engineering, National Taiwan University of Science and Technology, Taipei, Taiwan 106, R.O.C.

Contributed by the Applied Mechanics Division of THE AMERICAN SOCIETY OF MECHANICAL ENGINEERS for publication in the ASME JOURNAL OF APPLIED MECHANICS. Manuscript received by the ASME Applied Mechanics Division, Oct. 2, 1995; final revision, Jan. 10, 1998. Associate Technical Editor: M. Taya.

$$C_{eq}^{(\text{trans})} = c_f \sqrt{\frac{1}{2-\lambda}} \quad \text{for} \quad 1-\lambda \ll 1. \tag{26}$$

Obviously, there is the same sound speed in any direction in the plane perpendicular to the axis of beams (we call it the transverse sound speed), and there is other value of the sound speed in the axial direction of the beam. This means that the homogenization model of the beam bundle is transversely isotropic. Furthermore, it can be easily seen from (23) that the transverse sound speed is always smaller than the axial one.

Acknowledgment

This work was supported in part by the Research Laboratory of Solid Mechanics of State Education Commission of China, and in part by the Key Discipline of the Shanghai Education Commission.

My research experience at CEA CE/Saclay of FRANCE arouses my interest in the problem and makes it possible to write the paper. I wish to convey my hearty acknowledgment to CEA CE/Saclay and Mme F. Gantenbein for her help, who was my supervisor when I worked there in 1994.

References

Bensoussan, A., Lions, J.-L., and Papanicolaou, G., 1978, *Asymptotic Analysis for Periodic Structures,* North-Holland, Amsterdam.

Brochard, D., and Hammami, L., 1991, "An homogenization method applied to the seismic analysis of LMFBR cores," *SMiRT 11 Transaction,* Vol. E, Aug. Tokyo, Japan, pp. 497–503.

Hammami, L., 1990, "Etude de l'interaction fluide structure dans les faisceaux de tubes par une methode d'homogenisation," these Universite Paris VI.

Sanchez-Palencia, E., 1980, *Non-homogeneous Media and Vibration Theory* (Lecture Notes in Physics), Springer, Berlin.

Schumann, U., 1981a, "Homogenized equations of motion for rod bundles in the fluid with periodic structure," *Ingenieur-Archiv,* Vol. 50, pp. 203–216.

Schumann, U., 1981b, "Virtual density and speed of sound in a fluid-solid mixture with periodic structure," *Int. J. of Multiphase Flow,* Vol. 7, No. 6, pp. 619–633.

Zhang, R.J., 1998a, "A Unified 3-D Homogenization Model of Beam Bundle in Fluid," ASME *Journal of Pressure Vessel Technology,* Vol. 120, pp. 56–61.

Zhang, R.J., 1998b, "Structural homogenized analysis for nuclear reactor core," *Nuclear Engineering and Design,* Vol. 183, pp. 151–156.

Zhang, R.J., 1998c, "Homogenization model for fluid structure interaction in nuclear reactor core," *Flow-induced Vibration and Transient Thermal-Hydraulics—1998,* PVP-Vol. 363, M. K. AuYang, ed., presented at The 1998 ASME/JSME Joint Pressure Vessel and Piping Conference San Diego, CA, July 26–30.

Thermoelastic Contact Between a Flat Punch and an Anisotropic Half-Space

C. K. Chao,[1,3] S. P. Wu,[2,3] and B. Gao[2,3]

The fundamental nature of thermoelastic contact between a flat punch and an anisotropic half-plane solid is studied. Based on Lekhnitskii's stress potentials and anisotropic thermoelasticity theory, the formulation leads to the nonhomogeneous Hilbert problem which can be solved in compact form. The contact traction beneath the punch face is derived in the form of the Cauchy-type integral which is solved numerically. The results show that, depending on the magnitude of the applied force and the total heat flux, either perfect thermal contact throughout the punch face or separation at the punch corners occurs. The contact lengths for separation solutions are also examined.

1 Introduction

In most cases contact problems are accompanied by heat conduction between two bodies. When heat is conducted across an interface between two conducting solids, there will generate some resistance to heat flow across the interface, which is found to be a function of the local contact pressure proposed by Cooper et al. (1969) and Shlykov and Ganin (1964). However, the heat conduction and elasticity problems are coupled through the boundary conditions, which were raised by Clausing (1996) and Barber (1973), since the contact pressure is itself influenced by not only the thermal distortion but also the temperature field in the bodies. For the case of thermoelastic contact between a flat punch and isotropic half-space, Comninou et al. (1981) discussed that, depending on the magnitude and the direction of the total heat flux, one of the possibilities occurs: separation at the punch corners, perfect thermal contact throughout the punch face, or an imperfect contact region at the center with adjacent perfect contact regions. Clements and Toy (1976) used integral transform techniques to solve contact problems for anisotropic media. Recently, Fan and Hwu (1996) studied the punch problems for an anisotropic elastic half-plane by applying Stroh's formalism (Stroh, 1958). To the best of our knowledge, the thermoelastic contact problem associated with anisotropic media is new. In this brief note the two-dimensional thermoelastic problem of an anisotropic elastic half-space indented by a perfectly conducting rigid flat punch is considered. Based on the complex variable representation of two-dimensional elasticity developed by Lekhnitskii (1963) and the method of analytical continuation, the full-field solutions of the temperature field and stress distributions are derived in compact form. Since the Cauchy integral appearing in the expression for contact pressure distribution cannot be evaluated in closed form for anisotropic material, the contact pressure along the punch face and the related contact length are computed numerically which are found to depend on the geometrical parameters, material anisotropy, and the ratio between thermal and mechanical loads. The condition for perfect thermal contact throughout the punch face or separation at the punch corners through these parameters is also discussed in detail and shown in graphic form. The results presented here can be reduced to those for the isotropic case and found to be identical with the solutions given by Comninou et al. (1981).

2 Heat Conduction in the Half-Plane

The heat fluxes in the x_1, x_2 coordinate system of an anisotropic half-plane medium can be expressed as (Ozisik, 1980)

$$h_i = -k_{ij}T_{,j} \quad (i, j = 1, 2) \tag{1}$$

where k_{ij} are the heat conductivity coefficients and T, h_1, h_2 denote temperature and heat fluxes in the x_1, x_2 direction, respectively. A subscript after a comma stands for differentiation with respect to this index and repeat indices imply summation. The steady-state heat conduction equation can be written as

$$h_{i,i} = -k_{ij}T_{,ij} = 0. \tag{2}$$

The general solution to Eq. (2) is given by (Wu, 1984)

$$T = \phi_0(z) + \overline{\phi_0(z)}, \quad z = x_1 + \mu_0 x_2 \tag{3}$$

where the overbar denotes a complex conjugate while the complex function $\phi_0(z)$ is an arbitrary function which can be determined by satisfying the specified boundary conditions and μ_0 is the root of the following characteristic equation with a positive imaginary part:

[1] Professor.

[2] Graduate Student.

[3] Department of Mechanical Engineering, National Taiwan University of Science and Technology, Taipei, Taiwan 106, R.O.C.

Contributed by the Applied Mechanics Division of THE AMERICAN SOCIETY OF MECHANICAL ENGINEERS for publication in the ASME JOURNAL OF APPLIED MECHANICS. Manuscript received by the ASME Applied Mechanics Division, Oct. 2, 1995; final revision, Jan. 10, 1998. Associate Technical Editor: M. Taya.

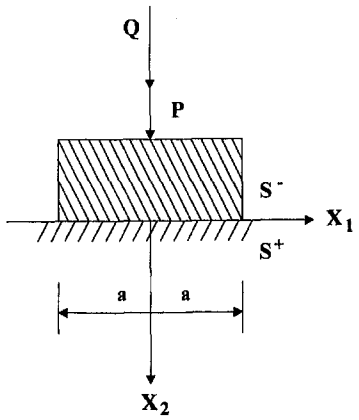

Fig. 1 Geometry of the flat punch

$$k_{22}\mu_0^2 + (k_{12} + k_{21})\mu_0 + k_{11} = 0. \tag{4}$$

Since k_{ij} are positive definite and symmetric, the characteristic value μ_0 in Eq. (4) must be a complex. For isotropic or orthotropic material, the conductivity coefficients k_{12}, k_{21} are zero and the characteristic value μ_0 becomes purely imaginary. Putting $\Phi_0(z) = \phi_0'(z)$ and using Eq. (3), the expression of the heat fluxes in Eq. (1) can be written in the form

$$-h_i = (k_{i1} + \mu_0 k_{i2})\Phi_0(z) + (k_{i1} + \overline{\mu_0} k_{i2})\overline{\Phi_0(z)}. \tag{5}$$

The rigid punch of width $2a$ is pressed into the half-plane $x_2 > 0$ by a compressive force P and the total heat flux Q from the punch to the half-plane as indicated in Fig. 1. If there is perfect thermal contact throughout the given contact region $-a < -c_2 < x_1 < c_1 < a$ pressed by the punch and the remaining part of the half-plane surface is assumed to be insulated (Fig. 2), the conditions give

$$\frac{dT(x_1, 0)}{dx_1} = 0, \quad -c_2 < x_1 < c_1 \tag{6}$$

and

$$h_2 = 0, \quad x_1 > c_1 \quad \text{or} \quad x_1 < -c_2, \quad x_2 = 0. \tag{7}$$

Using Eqs. (6) and (7), Eq. (5) leads to the following Hilbert problem:

$$\Phi_0^+(x_1) + \Phi_0^-(x_1) = 0, \quad -c_2 < x_1 < c_1 \tag{8}$$

where the superscript + (or −) is used to denote the field quantities approached from the medium $x_2 > 0$ (or $x_2 < 0$). The solution to the Hilbert problem can be obtained as (Muskhelishvili, 1953)

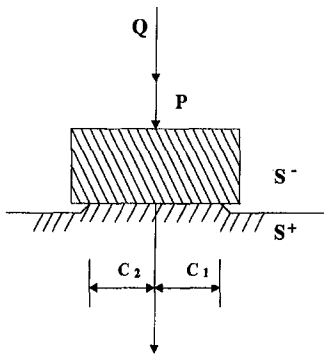

Fig. 2 Geometry for perfect contact and separation

$$\Phi_0(z) = \frac{b_1 z + b_2}{\sqrt{(z - c_1)(z + c_2)}}, \quad z \in S^+. \tag{9}$$

The contant b_1 vanishes in the present study since the heat flux tends to zero at infinity and the remaining contant b_2 can be determined from the condition

$$\int_{-c_2}^{c_1} h_2 dx_1 = Q. \tag{10}$$

It yields

$$b_2 = \frac{-Q}{2\pi d_0} \tag{11}$$

where

$$d_0 = -id_1 = \sqrt{k_{11}k_{22} - k_{12}^2}.$$

Therefore, the final result for $\Phi_0(z)$ in Eq. (9) becomes

$$\Phi_0(z) = \frac{-Q}{2\pi d_0 \sqrt{(z - c_1)(z + c_2)}}, \quad z \in S^+. \tag{12}$$

3 Thermal Stresses

The generalized Hook's law of an anisotropic material can be expressed in contracted notation as (Nowacki, 1962)

$$\epsilon_i = \sum_{j=1}^{6} a_{ij}\sigma_j + \alpha_i T \tag{13}$$

where a_{ij}, α_i denote the compliance tensor and thermal expansion coefficients, respectively. The standard correspondence is adopted as

$$\{\epsilon_i\} = [\epsilon_{11}, \epsilon_{22}, \epsilon_{33}, 2\epsilon_{23}, 2\epsilon_{31}, 2\epsilon_{12}]^T$$
$$\{\sigma_i\} = [\sigma_{11}, \sigma_{22}, \sigma_{33}, \sigma_{23}, \sigma_{31}, \sigma_{12}]^T$$
$$\{\alpha_i\} = [\alpha_{11}, \alpha_{22}, \alpha_{33}, 2\alpha_{23}, 2\alpha_{31}, 2\alpha_{12}]^T \tag{14}$$

where the superscript T denotes the transpose. For two-dimensional anisotropic thermoelasticity, the representation for stresses σ_{ij}, and the derivatives of displacement, u_i', can be expressed in terms of two stress functions $\Phi_1(z_1)$, $\Phi_2(z_2)$ and a temperature function $\phi_0(z_0)$ as follows:

$$\sigma_{11} = 2\,\mathrm{Re}[\mu_1^2\Phi_1(z_1) + \mu_2^2\Phi_2(z_2) + \mu_0^2 P_t\phi_0(z_0)] \tag{15}$$

$$\sigma_{22} = 2\,\mathrm{Re}[\Phi_1(z_1) + \Phi_2(z_2) + P_t\phi_0(z_0)] \tag{16}$$

$$\sigma_{12} = -2\,\mathrm{Re}[\mu_1\Phi_1(z_1) + \mu_2\Phi_2(z_2) + \mu_0 P_t\phi_0(z_0)] \tag{17}$$

$$u_1' = 2\,\mathrm{Re}[p_1\Phi_1(z_1) + p_2\Phi_2(z_2) + p_0\phi_0(z_0)] \tag{18}$$

$$u_2' = 2\,\mathrm{Re}[q_1\Phi_1(z_1) + q_2\Phi_2(z_2) + q_0\phi_0(z_0)] \tag{19}$$

where $u_i' = \partial u_i/\partial x_1$ and Re denotes the real part of the complex function. The arguments $z_j = x_1 + \mu_j x_2$ $(j = 0, 1, 2)$ are used and the characteristic values μ_i $(i = 1, 2)$ are the roots of the fourth-order characteristic equation with positive imaginary part

$$a_{11}\mu^4 - 2a_{16}\mu^3 + (2a_{12} + a_{66})\mu^2 - 2a_{26}\mu + a_{22} = 0. \tag{20}$$

The elastic coefficients p_i, q_i $(i = 1, 2)$ in Eqs. (18) and (19) have been defined by Lekhnitskii (1963), and the thermal coefficients p_0, q_0, and P_t have been defined by Chao and Chang (1994). Now, a complete solution to the half-plane problem has been reduced to the evaluation of two complex functions $\Phi_1(z_1)$, $\Phi_2(z_2)$ which must satisfy the prescribed boundary conditions along the half-plane surface.

Consider a rigid frictionless flat punch normally indenting the half-plane S^+ under the action of a resultant force P. The boundary conditions for this problem are

$$u_2' = 0, \quad \sigma_{12} = 0, \quad -c_2 < x_1 < c_1, \quad x_2 = 0 \tag{21}$$

$$\sigma_{22} = \sigma_{12} = 0, \quad x_1 > c_1 \quad \text{or} \quad x_1 < -c_2, \quad x_2 = 0. \tag{22}$$

Since the shear stress vanishes along the whole half-plane surface, we have from Eq. (17)

$$\mu_1\Phi_1(x_1) + \mu_2\Phi_2(x_1) + P_t\mu_0\phi_0(x_1) + \overline{\mu_1}\overline{\Phi_1(x_1)} + \overline{\mu_2}\overline{\Phi_2(x_1)} + \overline{P_t\mu_0\phi_0(x_1)} = 0. \tag{23}$$

It is easy to verify that Eq. (23) satisfied the following relation:

$$\Phi_2(z_2) = -\frac{\mu_1}{\mu_2}\Phi_1(z_1) - \frac{P_t\mu_0}{\mu_2}\phi_0(z_0). \tag{24}$$

Moreover, the portion of the half-plane surface on the interval $x_1 > c_1$ or $x_1 < -c_2$ is unstressed, which gives

$$\Phi_1^+(x_1) + \Phi_2^+(x_1) + P_t\phi_0^+(x_1) + \overline{\Phi_1^+(x_1)} + \overline{\Phi_2^+(x_1)} + \overline{P_t\phi_0^+(x_1)} = 0. \tag{25}$$

Based on the continuation theorem and using Eq. (24), Eq. (25) allows us to extend the definition of $\Phi_1(z_1)$ from S^+ into S^- by putting

$$\Phi_1(z_1) = \Phi_1(z_1), \quad z_1 \in S^+ \tag{26}$$

$$\Phi_1(z_1) = \frac{-\mu_2}{\mu_2 - \mu_1}\left[\frac{\overline{\mu_2} - \overline{\mu_1}}{\overline{\mu_2}}\overline{\Phi_1(\overline{z_1})} + \frac{\overline{\mu_2} - \overline{\mu_0}}{\overline{\mu_2}}\overline{P_t\phi_0(\overline{z_0})} + \frac{\mu_2 - \mu_0}{\mu_2}P_t\phi_0(z_0)\right], \quad z_1 \in S^-. \tag{27}$$

Furthermore, with the aid of Eqs. (24), (26), and (27), Eqs. (18) and (19) can be combined to yield the following relation:

$$2iu_2' = A\Phi_1(z_1) + B\Phi_1(\overline{z_1}) + C\phi_0(z_0) + D\phi_0(\overline{z_0}) + E\overline{\phi_0}(\overline{z_0}) \tag{28}$$

where

$$A = 2i\left(\frac{\mu_1 - \mu_2}{\mu_2}\right)\left[-\frac{\mu_1 + \mu_2}{\mu_1\mu_2}a_{22} + a_{26}\right] \tag{29}$$

$$B = 2i\left(\frac{\mu_1 - \mu_2}{\mu_2}\right)\left[\frac{\overline{\mu_1} + \overline{\mu_2}}{\overline{\mu_1}\,\overline{\mu_2}}a_{22} - a_{26}\right] \tag{30}$$

$$C = 2i\{P_t[(1/\mu_0 - \mu_0/\mu_2^2)a_{22} + (\mu_0/\mu_2 - 1)a_{26}] + \alpha_2/\mu_0\} \tag{31}$$

$$D = 2i\left(\frac{\mu_0 - \mu_2}{\mu_2}P_t\right)\left[\frac{\overline{\mu_1} + \overline{\mu_2}}{\overline{\mu_1}\,\overline{\mu_2}}a_{22} - a_{26}\right] \tag{32}$$

$$E = 2i\{\overline{P_t}(1 - \overline{\mu_0}/\overline{\mu_2})(1/\overline{\mu_0} - 1/\overline{\mu_1})a_{22} + \alpha_2/\overline{\mu_0}\}. \tag{33}$$

In view of Eq. (28) and knowing that $\phi_0(\overline{z_0}) = \overline{\phi_0(\overline{z_0})}$, $\phi_0^+(x_1) = -\phi_0^-(x_1)$, the boundary condition $u_2' = 0$ on $x_2 = 0$, $-c_2 < x_1 < c_1$ implies

$$A\Phi_1^+(x_1) + B\Phi_1^-(x_1) + (C - D - E)\phi_0^+(x_1) = 0. \tag{34}$$

After some algebraic manipulations, it can be shown that

$$A = B \tag{35}$$

and

$$C - D - E = H = 4\left\{\alpha_2\left(\frac{\sqrt{k_{22}k_{11} - k_{12}^2}}{k_{11}}\right) - a_{22}\,\mathrm{Im}[P_t(1/\mu_0 + \mu_0/(\mu_1\mu_2) - 1/\mu_1 - 1/\mu_2)]\right\} \tag{36}$$

where Im denotes the imaginary part of the complex function.

Now, a general solution to the Hilbert problem, Eq. (34), becomes

$$\Phi_1(z) = \frac{-HX(z)}{2\pi iA}\int_{-c_2}^{c_1}\frac{\phi_0^+(t)}{X^+(t)(t - z)}\,dt + X(z)F \tag{37}$$

where

$$\phi_0^+(t) = \frac{-Q}{2\pi d_1}\sin^{-1}\left(\frac{2t - c_1 + c_2}{c_1 + c_2}\right)$$

$$X(z) = (z - c_1)^{-1/2}(z + c_2)^{-1/2}.$$

Finally, the contant F appearing in Eq. (37) can be determined from the condition

$$-P = \int_{-c_2}^{c_1}\sigma_{22}dt. \tag{38}$$

Substituting Eq. (37) into Eq. (16) and using Eq. (38) we find

$$F = \frac{-i\mu_2 P}{2\pi(\mu_2 - \mu_1)} + M \tag{39}$$

where

$$M = \frac{HQ}{4\pi^3 d_1 A}\int_{-c_2}^{c_1}\frac{1}{\sqrt{(c_1 - t)(t + c_2)}} \times \int_{-c_2}^{c_1}\frac{\sqrt{(c_1 - \xi)(\xi + c_2)}\,\sin^{-1}\left(\frac{2\xi - c_1 + c_2}{c_1 + c_2}\right)}{\xi - t}\,d\xi dt - \left[\frac{iQ(\mu_2 - \mu_0)P_t}{2\pi^2 d_1(\mu_2 - \mu_1)} + \frac{iHQ}{4\pi^2 d_1 A}\right] \times \int_{-c_2}^{c_1}\sin^{-1}\left(\frac{2t - c_1 + c_2}{c_1 + c_2}\right)dt. \tag{40}$$

If one defines

$$a_1 = \frac{c_1 + c_2}{2}, \quad a_2 = \frac{c_1 - c_2}{2}, \quad t = s + a_2, \quad \xi = \eta + a_2$$

Eq. (40) can be put in the form

$$M = \frac{HQ}{4\pi^3 d_1 A}\int_{-a_1}^{a_1}\sqrt{a_1^2 - \eta^2}\,\sin^{-1}\left(\frac{\eta}{a_1}\right) \times \left[\int_{-a_1}^{a_1}\frac{ds}{\sqrt{a_1^2 - s^2}(\eta - s)}\right]d\eta - \left[\frac{iQ(\mu_2 - \mu_0)P_t}{2\pi^2 d_1(\mu_2 - \mu_1)} + \frac{iHQ}{4\pi^2 d_1 A}\right] \times \int_{-a_1}^{a_1}\sin^{-1}\left(\frac{s}{a_1}\right)ds. \tag{41}$$

Table 1 Thermoelastic coefficient (graphite/epoxy $\alpha_6 = k_{12} = 0$)

E_1 (10^9 Nm^{-2})	144.8
E_2 (10^9 Nm^{-2})	9.7
G_{12} (10^9 Nm^{-2})	4.1
ν_{12}	0.3
ν_{23}	0.3
α_1 (10^{-6} K^{-1})	−0.3
α_2 (10^{-6} K^{-1})	28.1
k_{11} (Wm^{-1} K^{-1})	4.62
k_{22} (Wm^{-1} K^{-1})	0.72

Due to the property of symmetry, the integrals appeared in Eq. (41) are found to be zero, and thus we have the result of $M = 0$.

The distribution of normal traction at the interface can be obtained as

$$\sigma_{22}(x_1) = 2\,\mathrm{Re}\left\{\frac{1}{\sqrt{a_1^2-(x_1-a_2)^2}}\times\left[-\frac{P}{2\pi}+\frac{\mu_2-\mu_1}{\mu_2}\frac{HQ}{4\pi^2 iAd_1}\times\int_{-a_1}^{a_1}\frac{\sqrt{a_1^2-\eta^2}}{\eta-(x_1-a_2)}\sin^{-1}\frac{\eta}{a_1}\,d\eta\right]-\frac{\mu_2-\mu_0}{\mu_2}\frac{P_tQ}{2\pi d_1}\sin^{-1}\frac{x_1-a_2}{a_1}\right\}. \quad (42)$$

In view of Eq. (42), the normal traction beneath the punch due to the external force P and total heat flux Q is not symmetric in x_1 for anisotropic material. Note that the normal traction must be a negative value throughout the contact region and the related contact length c_1 and c_2 can be determined from the continuity condition at the transition such that the function, Eq. (42), must be bounded at $x_1 = c_1$ and $x_1 = -c_2$, respectively. Consider the special case $\mu_0 = \mu_1 = \mu_2 = i$ and $c_1 = c_2 = c$ for isotropic material, the final result for the contact length is found to be

$$c = \frac{kP\pi}{Q\alpha E} \quad (43)$$

which is identical to the result given by Comninou et al. (1981) if one replaces α and E by $(1+\nu)\alpha$ and $E/(1-\nu^2)$, respectively, in Eq. (43) for a plane-strain condition. As to anisotropic material ($\mu_0 \neq \mu_1 \neq \mu_2$), the conditions required for a compressive contact stress and separation solutions are more complicated and cannot be evaluated in closed form which must be called for in the numerical technique.

4 Results and Discussion

Since the Cauchy integral appearing in Eq. (42) cannot be evaluated in closed form for general values of x_1, the numerical integration will be evaluated using Gupta and Erdogan (1979). In the calculation, the nondimensional parameter λ^* for anisotropic material defined as

$$\lambda^* = \frac{\alpha_2 Q E_2 a}{k_{11} P} \quad (44)$$

is used which will be properly chosen such that the condition of a negative (compressive) contact stress must be satisfied. An numerical example of orthotropic material as displayed in Table 1 is given to illustrate the use of the present study.

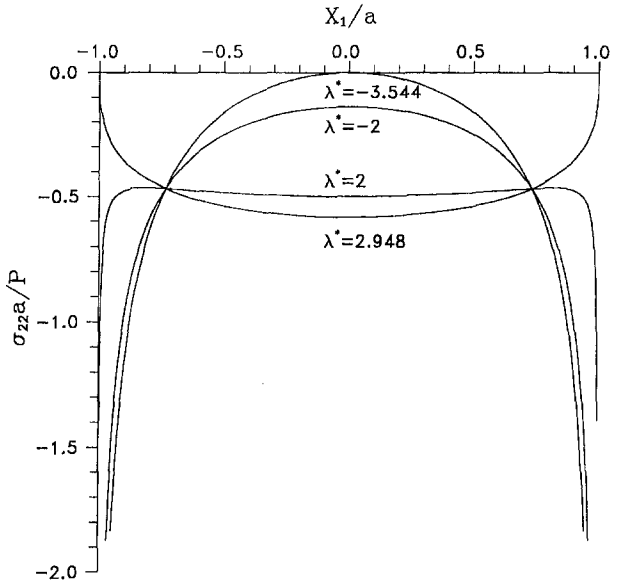

Fig. 3 Contact pressure distribution for perfect contact for Graphite/epoxy

Referring to Fig. 3, perfect contact is maintained throughout the punch face as λ^* ranges from −3.544 to 2.948 for graphite/epoxy composite. Notice that the contact pressure preserves a square-root singularity at the sharp edges of the punch at the expense of the center until the central presure is zero at $\lambda^* = -3.544$. For $\lambda^* > 2.948$, separation begins to occur at the punch corners and leaves a contact width $c_1 + c_2$ which varies inversely with λ^* as indicated in Table 2. It seems to be reasonable that either a smaller force pressing the rigid flat or a large amount of heat flow approaching downward the elastic half-space would result in decreasing of the contact length. Typical contact pressure distributions over the contact region are shown nondimensionally in Fig. 4 for different values of λ^* where the contact pressure tends to vanish at the edge of the contact region as in the isothermal Hertzian problem. Note that the smooth transition from perfect thermal contact to separation is impossible as $\lambda^* < -3.544$ for graphite/epoxy composite. In this case, a region of imperfect contact will be developed around the central part of the punch which may make the solutions rather complicated. We would not further discuss this case in the present study.

5 Conclusions

Based on the developments in the previous sections, the following conclusions are summarized:

1 Using Lekhnitskii's stress formulation and the method of analytical continuation, the thermoelastic contact problem for an anisotropic half-space medium is derived in detail and both the temperature and thermal stress fields are obtained in compact form.

2 The normal traction beneath the punch face is found to be symmetric with respect to the symmetric line of applied force for orthotropic material.

3 The possibility for perfect thermal contact throughout the

Table 2 Contact lengths for graphite/epoxy

λ^*	c_1/a	c_2/a
2.948	0.999	0.999
4.712	0.628	0.628
6.283	0.471	0.471
7.854	0.377	0.377

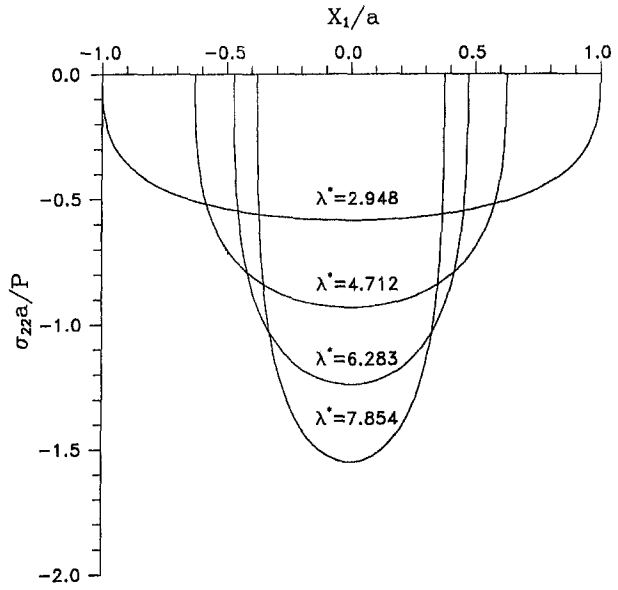

Fig. 4 Contact pressure distribution for perfect contact and separation for Graphite/epoxy

punch face or separation at the punch corners, depending on the mangitude of the applied force and the total heat flux, is discussed in detail. The contact lengths for separation solutions are also computed numerically in terms of the nondimensional parameter λ^* as defined in Eq. (44).

4 Comparison of the contact length with the isotropic case given by Comninou et al. (1981) shows that the results presented here are exact.

Acknowledgment

The authors would like to thank the reviewers who gave valuable comments and suggestions about this article.

References

Barber, J. R., 1973, "Indentation of the Semi-infinite Elastic Solid by a Hot Sphere," *International Journal of Mechanical Science,* Vol. 15, pp. 813–819.

Chao, C. K., and Chang, R. C., 1994, "Thermoelastic Problem of Dissimilar Anisotropic Solids With a Rigid Line Inclusion," ASME JOURNAL OF APPLIED MECHANICS, Vol. 61, pp. 978–980.

Clausing, A. M., 1966, "Heat Transfer at the Interface between Dissimilar Metals-the Influence of Thermal Strain," *International Journal of Heat and Mass Transfer,* Vol. 9, pp. 791–801.

Clements, D. L., and Toy, G. D., 1976, "Two Contact Problems in Anisotropic Elasticity," *Journal of Elasticity,* Vol. 6, pp. 137–147.

Comninou, et al., 1981, "Heat Conduction Through a Flat Punch," ASME JOURNAL OF APPLIED MECHANICS, Vol. 48, pp. 871–875.

Cooper, M. G., Mikic, B. B., and Yovanovich, M. M., 1969, "Thermal Contact Conductance," *International Journal of Heat and Mass Transfer,* Vol. 12, p. 279.

Gupta, G., and Erdogan, F., 1979, "On the Numerical Solution of Singular Integral Equations," *Quarterly of Applied Mathematics,* Vol. 29, 1979, pp. 525–529.

Lekhnitskii, S. G., 1963, *Theory of Elasticity of an Anisotropic Elastic Body,* Holden-day, San Francisco, CA.

Muskhelishvili, N. I., 1953, *Singular Integral Equations,* P. Noordhoff Ltd., Groningen, The Netherlands.

Nowacki, W., 1962, *Thermoelasticity,* Pergamon Press, Oxford, UK.

Ozisik, M. N., 1980, *Heat Conduction,* John Wiley and Sons, New York.

Shlykov, Yu. P., and Ganin, Ye. A., 1964, "Thermal Resistance of Metallic Contacts," *International Journal of Heat and Mass Transfer,* Vol. 7, pp. 921–929.

Wu, C. H., 1984, "Plane Anisotropic Thermoelasticity," ASME JOURNAL OF APPLIED MECHANICS, Vol. 51, pp. 724–726.

Fan, C. W., and Hwu, C., 1996, "Punch Problems for an Anisotropic Elastic Half-Plane," ASME JOURNAL OF APPLIED MECHANICS, Vol. 63, pp. 69–76.

Stroh, A. N., 1958, "Dislocations and Cracks in Anisotropic Elasticity," *Philosophical Magazine,* Vol. 7, pp. 625–646.

Gyroscopic Coupling in Holonomic Lagrangian Dynamical Systems

R. Mukherjee[1,3] and R. C. Rosenberg[2,3]

1 Introduction

Vectorial mechanics and analytical mechanics differ on a number of fundamental issues. The most noteworthy among them relates to the choice of coordinates. The vectorial approach is suited to the rectangular frame of reference and proves to be cumbersome for any other choice. Analytical mechanics, on the other hand, provides complete freedom in the choice of coordinates. This freedom helps in the formulation and solution of the differential equations of motion. The existence of cyclic coordinates, for example, leads to partial integration of the equations of motion, and to conserved quantities (Greenwood, 1988). The freedom of choice in coordinates can also provide useful insight into dynamical interactions between them. For example, there often exists gyroscopic coupling between certain coordinate pairs. Such coupling establishes, in essence, an interaction where energy flows back and forth between the two coordinates, without dissipation. In this paper we take a closer look at gyroscopic coupling in Lagrangian dynamical systems, and specifically holonomic systems.

Few recent papers in the literature discuss gyroscopic coupling in general dynamical systems. Most of the results on the subject are considered well known, and are referenced in advanced textbooks on dynamics (for example, Greenwood, 1988; Meirovitch, 1988). In many readers these results often create the impression that gyroscopic forces appear only in rheonomic systems, and they always appear linear in the generalized velocities. It is, however, well known that scleronomic systems such as the spinning top exhibit gyroscopic coupling. In this note we formally establish the conditions under which gyroscopic coupling exist in scleronomic systems. We show that these gyroscopic forces, when they exist, are quadratic in the generalized velocities and are comprised of a centrifugal force and a Coriolis force, or a pair of Coriolis forces in the coupled coordinates. From a kinematic standpoint, both centrifugal and Coriolis forces have separate physical interpretations. This has perhaps masked the role such force pairs may play in gyroscopic coupling.

In this paper we use the Lagrangian formulation of mechanics to derive a necessary and sufficient condition for existence of gyroscopic coupling in scleronomic systems. The condition is derived from the functional relationships between local-inertial[4] velocities and generalized velocities and apply to both particles and rigid bodies. The condition, derived for systems described by independent generalized coordinates, also applies to systems with holonomic constraints. In the event of coupling, the gyroscopic modulus can be easily obtained from our approach and can be used to identify the gyroscopic force pair and the extent of coupling determined by the flow of energy. Such an analysis provides useful insight since the mechanics of energy flow is nonlinear and not obvious, except in the simplest of systems where a single pair of coordinates, at most, are gyroscopically coupled. The insight provided by our results is appealing and testifies to the elegance of the Lagrangian approach. The simplicity of deduction gives the impression that the results were anticipated by the Lagrangian formulation.

[1] Associate Professor. Assoc. Mem. ASME.

[2] Professor. Mem. ASME.

[3] Department of Mechanical Engineering, Michigan State University, 2555 Engineering Building, East Lansing, MI 48824-1226.

[4] Local-inertial velocities will be precisely defined in Section 3.1.

Contributed by the Applied Mechanics Division of THE AMERICAN SOCIETY OF MECHANICAL ENGINEERS for publication in the ASME JOURNAL OF APPLIED MECHANICS. Manuscript received by the ASME Applied Mechanics Division, Apr. 7, 1998; final revision, Jan. 17, 1999. Associate Technical Editor: A. A. Ferri.

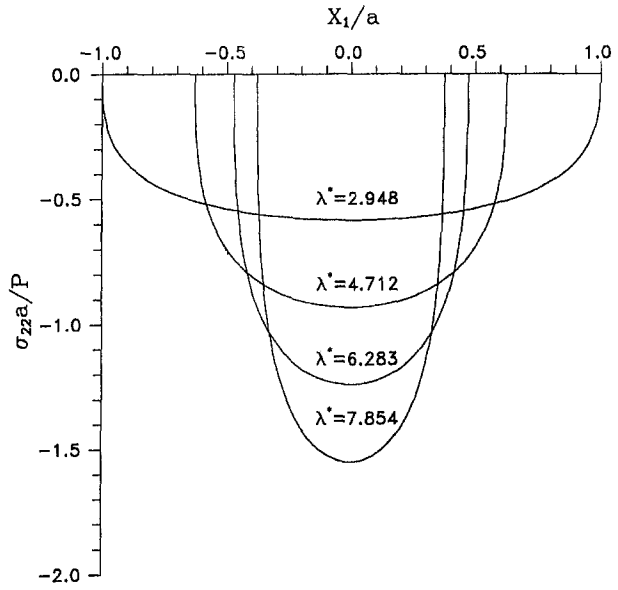

Fig. 4 Contact pressure distribution for perfect contact and separation for Graphite/epoxy

punch face or separation at the punch corners, depending on the mangitude of the applied force and the total heat flux, is discussed in detail. The contact lengths for separation solutions are also computed numerically in terms of the nondimensional parameter λ^* as defined in Eq. (44).

4 Comparison of the contact length with the isotropic case given by Comninou et al. (1981) shows that the results presented here are exact.

Acknowledgment

The authors would like to thank the reviewers who gave valuable comments and suggestions about this article.

References

Barber, J. R., 1973, "Indentation of the Semi-infinite Elastic Solid by a Hot Sphere," *International Journal of Mechanical Science,* Vol. 15, pp. 813–819.

Chao, C. K., and Chang, R. C., 1994, "Thermoelastic Problem of Dissimilar Anisotropic Solids With a Rigid Line Inclusion," ASME JOURNAL OF APPLIED MECHANICS, Vol. 61, pp. 978–980.

Clausing, A. M., 1966, "Heat Transfer at the Interface between Dissimilar Metals-the Influence of Thermal Strain," *International Journal of Heat and Mass Transfer,* Vol. 9, pp. 791–801.

Clements, D. L., and Toy, G. D., 1976, "Two Contact Problems in Anisotropic Elasticity," *Journal of Elasticity,* Vol. 6, pp. 137–147.

Comninou, et al., 1981, "Heat Conduction Through a Flat Punch," ASME JOURNAL OF APPLIED MECHANICS, Vol. 48, pp. 871–875.

Cooper, M. G., Mikic, B. B., and Yovanovich, M. M., 1969, "Thermal Contact Conductance," *International Journal of Heat and Mass Transfer,* Vol. 12, p. 279.

Gupta, G., and Erdogan, F., 1979, "On the Numerical Solution of Singular Integral Equations," *Quarterly of Applied Mathematics,* Vol. 29, 1979, pp. 525–529.

Lekhnitskii, S. G., 1963, *Theory of Elasticity of an Anisotropic Elastic Body,* Holden-day, San Francisco, CA.

Muskhelishvili, N. I., 1953, *Singular Integral Equations,* P. Noordhoff Ltd., Groningen, The Netherlands.

Nowacki, W., 1962, *Thermoelasticity,* Pergamon Press, Oxford, UK.

Ozisik, M. N., 1980, *Heat Conduction,* John Wiley and Sons, New York.

Shlykov, Yu. P., and Ganin, Ye. A., 1964, "Thermal Resistance of Metallic Contacts," *International Journal of Heat and Mass Transfer,* Vol. 7, pp. 921–929.

Wu, C. H., 1984, "Plane Anisotropic Thermoelasticity," ASME JOURNAL OF APPLIED MECHANICS, Vol. 51, pp. 724–726.

Fan, C. W., and Hwu, C., 1996, "Punch Problems for an Anisotropic Elastic Half-Plane," ASME JOURNAL OF APPLIED MECHANICS, Vol. 63, pp. 69–76.

Stroh, A. N., 1958, "Dislocations and Cracks in Anisotropic Elasticity," *Philosophical Magazine,* Vol. 7, pp. 625–646.

Gyroscopic Coupling in Holonomic Lagrangian Dynamical Systems

R. Mukherjee[1,3] and R. C. Rosenberg[2,3]

1 Introduction

Vectorial mechanics and analytical mechanics differ on a number of fundamental issues. The most noteworthy among them relates to the choice of coordinates. The vectorial approach is suited to the rectangular frame of reference and proves to be cumbersome for any other choice. Analytical mechanics, on the other hand, provides complete freedom in the choice of coordinates. This freedom helps in the formulation and solution of the differential equations of motion. The existence of cyclic coordinates, for example, leads to partial integration of the equations of motion, and to conserved quantities (Greenwood, 1988). The freedom of choice in coordinates can also provide useful insight into dynamical interactions between them. For example, there often exists gyroscopic coupling between certain coordinate pairs. Such coupling establishes, in essence, an interaction where energy flows back and forth between the two coordinates, without dissipation. In this paper we take a closer look at gyroscopic coupling in Lagrangian dynamical systems, and specifically holonomic systems.

Few recent papers in the literature discuss gyroscopic coupling in general dynamical systems. Most of the results on the subject are considered well known, and are referenced in advanced textbooks on dynamics (for example, Greenwood, 1988; Meirovitch, 1988). In many readers these results often create the impression that gyroscopic forces appear only in rheonomic systems, and they always appear linear in the generalized velocities. It is, however, well known that scleronomic systems such as the spinning top exhibit gyroscopic coupling. In this note we formally establish the conditions under which gyroscopic coupling exist in scleronomic systems. We show that these gyroscopic forces, when they exist, are quadratic in the generalized velocities and are comprised of a centrifugal force and a Coriolis force, or a pair of Coriolis forces in the coupled coordinates. From a kinematic standpoint, both centrifugal and Coriolis forces have separate physical interpretations. This has perhaps masked the role such force pairs may play in gyroscopic coupling.

In this paper we use the Lagrangian formulation of mechanics to derive a necessary and sufficient condition for existence of gyroscopic coupling in scleronomic systems. The condition is derived from the functional relationships between local-inertial[4] velocities and generalized velocities and apply to both particles and rigid bodies. The condition, derived for systems described by independent generalized coordinates, also applies to systems with holonomic constraints. In the event of coupling, the gyroscopic modulus can be easily obtained from our approach and can be used to identify the gyroscopic force pair and the extent of coupling determined by the flow of energy. Such an analysis provides useful insight since the mechanics of energy flow is nonlinear and not obvious, except in the simplest of systems where a single pair of coordinates, at most, are gyroscopically coupled. The insight provided by our results is appealing and testifies to the elegance of the Lagrangian approach. The simplicity of deduction gives the impression that the results were anticipated by the Lagrangian formulation.

[1] Associate Professor. Assoc. Mem. ASME.

[2] Professor. Mem. ASME.

[3] Department of Mechanical Engineering, Michigan State University, 2555 Engineering Building, East Lansing, MI 48824-1226.

[4] Local-inertial velocities will be precisely defined in Section 3.1.

Contributed by the Applied Mechanics Division of THE AMERICAN SOCIETY OF MECHANICAL ENGINEERS for publication in the ASME JOURNAL OF APPLIED MECHANICS. Manuscript received by the ASME Applied Mechanics Division, Apr. 7, 1998; final revision, Jan. 17, 1999. Associate Technical Editor: A. A. Ferri.

This note is organized as follows. In Section 2 we discuss gyroscopic coupling in dynamical systems, as known in the literature. In Section 3 we derive a necessary and sufficient condition for the existence of gyroscopic coupling between arbitrary generalized coordinates. The condition is derived for a scleronomic system of particles described by independent generalized coordinates, but can be extended easily to constrained holonomic systems and rigid bodies. The physical significance of the gyroscopic modulus is interpreted in Section 4. Two examples are presented in Section 5. In the first example we consider a simple system with two independent generalized coordinates that are gyroscopically coupled. The second example is an extension of the first. It involves three generalized coordinates with gyroscopic coupling between each pair of coordinates. The usefulness of our results become clear from the simplicity of deduction of the complex interaction in the second example, which is not obvious. The imposition of a holonomic constraint renders the second example equivalent to the first. This exercise demonstrates the applicability of our results to constrained systems. Section 6 presents concluding remarks.

2 Gyroscopic Coupling in Generalized Coordinates

Consider a dynamical system described by n generalized coordinates: $q_1, q_2, \ldots, q_n$. A pair of these coordinates, (q_i, q_j) for example, is gyroscopically coupled if there exist generalized forces in these coordinates that have the form $\gamma_{ij}\dot{q}_j$ and $\gamma_{ji}\dot{q}_i$, with $\gamma_{ij} = -\gamma_{ji}$. The gyroscopic forces in the coordinates q_i and q_j are proportional to $\dot{q}_j$ and $\dot{q}_i$, respectively, and their magnitudes depend on the gyroscopic modulus, γ_{ij}. The gyroscopic forces do not make up an action-reaction pair, but are conservative in nature—this can be concluded from the sum of the generalized powers expended by the two gyroscopic forces.

Most of the results on gyroscopic coupling are considered well known and can be referenced in textbooks on dynamics. These results create the notion that gyroscopic forces appear in rheonomic systems and are linear in the generalized velocities. The gyroscopic modulus is a function of the generalized coordinates but not of the generalized velocities. Such a notion is supported by the following analysis, that can be found in (Greenwood, 1988):

Consider a system of N particles whose positions are specified by the Cartesian coordinates $x_1, x_2, \ldots, x_{3N}$. The total kinetic co-energy of the system is

$$T^* = \tfrac{1}{2}\sum_{j=1}^{3N} m_j \dot{x}_j^2. \tag{1}$$

The expression above assumes that the mass of a given particle appears in three separate terms. To express the kinetic co-energy in terms of generalized coordinates, a new set of n coordinates, $q_1, q_2, \ldots, q_n$, is chosen to represent the same system. Using the kinematic relationships

$$x_i = x_i(q_1, q_2, \ldots, q_n, t), \quad i = 1, 2, \ldots, 3N, \tag{2}$$

the kinetic co-energy, for the general case of a rheonomic system, can be written in the form

$$T^* = T_0^* + \sum_{i=1}^{n} a_i \dot{q}_i + \tfrac{1}{2}\sum_{i=1}^{n}\sum_{j=1}^{n} m_{ij}\dot{q}_i\dot{q}_j \tag{3}$$

where

$$T_0^* \triangleq \frac{1}{2}\sum_{k=1}^{3N} m_k\left(\frac{\partial x_k}{\partial t}\right)^2, \quad a_i \triangleq \sum_{k=1}^{3N} m_k \frac{\partial x_k}{\partial q_i}\frac{\partial x_k}{\partial t},$$

$$m_{ij} = m_{ji} \triangleq \sum_{k=1}^{3N} m_k \frac{\partial x_k}{\partial q_i}\frac{\partial x_k}{\partial q_j}. \tag{4}$$

By defining the nonconservative generalized forces as Q_i, $i = 1, 2, \ldots, n$, and the potential energy as V, Lagrange's equations can be written as

$$\sum_{j=1}^{n} m_{ij}\ddot{q}_j + \frac{1}{2}\sum_{j=1}^{n}\sum_{k=1}^{n}\left(\frac{\partial m_{ij}}{\partial q_k} + \frac{\partial m_{ik}}{\partial q_j} - \frac{\partial m_{jk}}{\partial q_i}\right)\dot{q}_j\dot{q}_k + \sum_{j=1}^{n}\gamma_{ij}\dot{q}_j$$

$$+ \sum_{j=1}^{n}\frac{\partial m_{ij}}{\partial t}\dot{q}_j + \frac{\partial a_i}{\partial t} - \frac{\partial T_0^*}{\partial q_i} + \frac{\partial V}{\partial q_i} = Q_i \quad i = 1, 2, \ldots, n. \tag{5}$$

The third term in the left-hand side of Eq. (5) represents the gyroscopic forces. The gyroscopic modulus, γ_{ij} is defined as

$$\gamma_{ij} = \frac{\partial a_i}{\partial q_j} - \frac{\partial a_j}{\partial q_i}. \tag{6}$$

From Eq. (6) and the definition of a_i in Eq. (4), it is clear that the gyroscopic force terms in Eq. (5) are linear in the generalized velocities and vanish if the Cartesian coordinates in Eq. (2) are not explicit functions of time.

The conservative nature of the gyroscopic forces can be ascertained from the zero power expended by these forces in their respective generalized coordinates. Using Eq. (6), it can be easily shown that the power expended by these forces is equal to

$$P^G = \sum_{i=1}^{n} P_i^G = \sum_{i=1}^{n}\dot{q}_i\sum_{j=1}^{n}\gamma_{ij}\dot{q}_j = \sum_{i=1}^{n}\sum_{j=1}^{n}\gamma_{ij}\dot{q}_i\dot{q}_j = 0$$

3 Further Insight Into Gyroscopic Coupling

3.1 The Case of Independent Generalized Coordinates. Supplementary to the analysis in the previous section, we show that gyroscopic coupling can exist in scleronomic systems where the coordinates are not explicit functions of time. Consider a set of inertia elements comprised of particles and rigid bodies. The motion of the particles can be expressed by a set of three translational velocities and the motion of the rigid bodies by a set of three translational velocities and three angular velocities about the principal axes. We will denote the set of all such velocities as v_i, $i = 1, 2, \ldots, M$, and refer to them as local-inertial velocities. We will denote the inertia properties associated with the local-inertial velocities as m_i, $i = 1, 2, \ldots, M$. The (m_i, v_i) pair commonly satisfy the following properties:

$$v_i = \sum_{r=1}^{n} c_{ir}\dot{q}_r, \quad i = 1, 2, \ldots, M \tag{7a}$$

$$T^* = \tfrac{1}{2}\sum_{i=1}^{M} m_i v_i^2 = \tfrac{1}{2}\sum_{i=1}^{M}\sum_{j=1}^{n}\sum_{k=1}^{n} m_i c_{ij}c_{ik}\dot{q}_j\dot{q}_k \tag{7b}$$

where q_r, $r = 1, 2, \ldots, n$, are the generalized coordinates, and the c_{ir}'s are functions of q_r's, in general. Equations (7*a*) and (7*b*) are more general than Eqs. (2) and (1), respectively. This is true since it is often convenient to choose a set of local-inertial velocities that are not integrable[5]. Also, the kinetic energy expression in Eq. (7*b*) allows us to extend the ensuing results to rigid bodies. When rigid bodies are included, then m_i terms refer to the principal mass moments of inertia and the corresponding v_i terms are angular velocities about the principal axes.

[5] The holonomic nature of the system stems from the integrable nature of the constraints acting on the generalized coordinates; it is independent of the integrability or nonintegrability of the local-inertial velocities used to express the kinetic co-energy.

Now consider Lagrange's equation for an arbitrary pair of generalized coordinates q_α, q_β

$$\left(\frac{\partial T^*}{\partial \dot{q}_\alpha}\right)' - \left(\frac{\partial T^*}{\partial q_\alpha}\right) + \left(\frac{\partial V}{\partial q_\alpha}\right) = Q_\alpha \tag{8a}$$

$$\left(\frac{\partial T^*}{\partial \dot{q}_\beta}\right)' - \left(\frac{\partial T^*}{\partial q_\beta}\right) + \left(\frac{\partial V}{\partial q_\beta}\right) = Q_\beta \tag{8b}$$

where $(\cdot)'$ denotes time derivative of $(\cdot)$, and Q_α, Q_β are the nonconservative forces in the α, β coordinates. Using Eq. (7), Eq. (8) can be rewritten as follows:

$$\sum_{i=1}^{M}\sum_{j=1}^{n} m_i c_{ij} c_{i\alpha}\ddot{q}_j + \sum_{i=1}^{M}\sum_{j=1}^{n}\sum_{k=1}^{n} m_i\left[c_{i\alpha}\left(\frac{\partial c_{ij}}{\partial q_k}\right) + c_{ij}\left(\frac{\partial c_{i\alpha}}{\partial q_k}\right) - \frac{c_{ik}}{2}\left(\frac{\partial c_{ij}}{\partial q_\alpha}\right) - \frac{c_{ij}}{2}\left(\frac{\partial c_{ik}}{\partial q_\alpha}\right)\right]\dot{q}_j\dot{q}_k + \left(\frac{\partial V}{\partial q_\alpha}\right) = Q_\alpha \tag{9a}$$

$$\sum_{i=1}^{M}\sum_{j=1}^{n} m_i c_{ij} c_{i\beta}\ddot{q}_j + \sum_{i=1}^{M}\sum_{j=1}^{n}\sum_{k=1}^{n} m_i\left[c_{i\beta}\left(\frac{\partial c_{ij}}{\partial q_k}\right) + c_{ij}\left(\frac{\partial c_{i\beta}}{\partial q_k}\right) - \frac{c_{ik}}{2}\left(\frac{\partial c_{ij}}{\partial q_\beta}\right) - \frac{c_{ij}}{2}\left(\frac{\partial c_{ik}}{\partial q_\beta}\right)\right]\dot{q}_j\dot{q}_k + \left(\frac{\partial V}{\partial q_\beta}\right) = Q_\beta. \tag{9b}$$

We have assumed that the potential energy V is independent of the generalized velocities; hence gyroscopic coupling cannot originate from these terms. The first term in the right-hand side of Eqs. (9*a*) and (9*b*) do not contribute to gyroscopic coupling since they are not functions of the generalized velocities. Similarly, terms in Eq. (9*a*) that do not contain $\dot{q}_\beta$ and terms in Eq. (9*b*) that do not contain $\dot{q}_\alpha$ do not contribute to coupling. Grouping all such terms as "Other Terms Not Of Interest" (OTNOI), we rewrite Eq. (9) as

$$\sum_{i=1}^{M}\sum_{j=1}^{n} m_i\left[c_{i\alpha}\left(\frac{\partial c_{ij}}{\partial q_\beta}\right) + c_{i\alpha}\left(\frac{\partial c_{i\beta}}{\partial q_j}\right) + c_{ij}\left(\frac{\partial c_{i\alpha}}{\partial q_\beta}\right) + c_{i\beta}\left(\frac{\partial c_{i\alpha}}{\partial q_j}\right) - c_{ij}\left(\frac{\partial c_{i\beta}}{\partial q_\alpha}\right) - c_{i\beta}\left(\frac{\partial c_{ij}}{\partial q_\alpha}\right)\right]\dot{q}_j\dot{q}_\beta + \text{OTNOI} = Q_\alpha \tag{10a}$$

$$\sum_{i=1}^{M}\sum_{j=1}^{n} m_i\left[c_{i\beta}\left(\frac{\partial c_{ij}}{\partial q_\alpha}\right) + c_{i\beta}\left(\frac{\partial c_{i\alpha}}{\partial q_j}\right) + c_{ij}\left(\frac{\partial c_{i\beta}}{\partial q_\alpha}\right) + c_{i\alpha}\left(\frac{\partial c_{i\beta}}{\partial q_j}\right) - c_{ij}\left(\frac{\partial c_{i\alpha}}{\partial q_\beta}\right) - c_{i\alpha}\left(\frac{\partial c_{ij}}{\partial q_\beta}\right)\right]\dot{q}_j\dot{q}_\alpha + \text{OTNOI} = Q_\beta \tag{10b}$$

The fourth and sixth term inside the summation of Eq. (10*a*) can be simplified as follows:

$$\sum_{i=1}^{M}\sum_{j=1}^{n} m_i\left[c_{i\beta}\left(\frac{\partial c_{i\alpha}}{\partial q_j}\right) - c_{i\beta}\left(\frac{\partial c_{ij}}{\partial q_\alpha}\right)\right]\dot{q}_j\dot{q}_\beta = \sum_{i=1}^{M} m_i c_{i\beta}\dot{q}_\beta \sum_{j=1}^{n}\left[\left(\frac{\partial c_{i\alpha}}{\partial q_j}\right) - \left(\frac{\partial c_{ij}}{\partial q_\alpha}\right)\right]\dot{q}_j = \sum_{i=1}^{M} m_i c_{i\beta}\dot{q}_\beta\left[\dot{c}_{i\alpha} - \frac{\partial}{\partial q_\alpha}(v_i)\right] = 0.$$

In the simplification above it was assumed that the system is holonomic and therefore generalized velocities are independent of the generalized coordinates. Also, the identity $\dot{c}_{i\alpha} = (\partial v_i/\partial q_\alpha)$, which was obtained by differentiating Eq. (7*a*), was substituted. By eliminating the fourth and sixth terms inside the summation of Eq. (10*b*) in a similar manner, we can rewrite Eq. (10) as follows:

$$\sum_{i=1}^{M}\sum_{j=1}^{n} m_i\left[c_{i\alpha}\left(\frac{\partial c_{ij}}{\partial q_\beta}\right) + c_{i\alpha}\left(\frac{\partial c_{i\beta}}{\partial q_j}\right) + c_{ij}\left(\frac{\partial c_{i\alpha}}{\partial q_\beta}\right) - c_{ij}\left(\frac{\partial c_{i\beta}}{\partial q_\alpha}\right)\right]\dot{q}_j\dot{q}_\beta + \text{OTNOI} = Q_\alpha \tag{11a}$$

$$\sum_{i=1}^{M}\sum_{j=1}^{n} m_i\left[c_{i\beta}\left(\frac{\partial c_{ij}}{\partial q_\alpha}\right) + c_{i\beta}\left(\frac{\partial c_{i\alpha}}{\partial q_j}\right) + c_{ij}\left(\frac{\partial c_{i\beta}}{\partial q_\alpha}\right) - c_{ij}\left(\frac{\partial c_{i\alpha}}{\partial q_\beta}\right)\right]\dot{q}_j\dot{q}_\alpha + \text{OTNOI} = Q_\beta \tag{11b}$$

Comparing Eqs. (11*a*) and (11*b*), it can be seen that gyroscopic coupling manifests itself via the modulus Λ, which is of the form

$$\Lambda_{\alpha\beta} = \sum_{i=1}^{M}\sum_{j=1}^{n} m_i c_{ij}\left[\left(\frac{\partial c_{i\alpha}}{\partial q_\beta}\right) - \left(\frac{\partial c_{i\beta}}{\partial q_\alpha}\right)\right]\dot{q}_j. \tag{12}$$

Accordingly, the gyroscopic forces in the α, β coordinates are

$$\alpha: +\sum_{i=1}^{M}\sum_{j=1}^{n} m_i c_{ij}\left[\left(\frac{\partial c_{i\alpha}}{\partial q_\beta}\right) - \left(\frac{\partial c_{i\beta}}{\partial q_\alpha}\right)\right]\dot{q}_j\dot{q}_\beta$$

$$\beta: -\sum_{i=1}^{M}\sum_{j=1}^{n} m_i c_{ij}\left[\left(\frac{\partial c_{i\alpha}}{\partial q_\beta}\right) - \left(\frac{\partial c_{i\beta}}{\partial q_\alpha}\right)\right]\dot{q}_j\dot{q}_\alpha. \tag{13}$$

From Eq. (13), it becomes evident that the gyroscopic forces are comprised of a centrifugal force and a Coriolis force, and/or both Coriolis forces in the coupled coordinates.

In light of the above facts, we now summarize the main results of this section. Consider a scleronomic system of M inertia elements described by n independent generalized coordinates q_1, q_2, . . . , q_n ($2 \le n \le M$). Let Eq. (7*a*) define the mapping between the local-inertial velocities and the generalized velocities. Then, gyroscopic coupling between an arbitrary pair of coordinates, q_α, q_β, will exist if and only if

$$\Lambda_{\alpha\beta} \triangleq \sum_{i=1}^{M}\sum_{j=1}^{n} m_i c_{ij}\left[\left(\frac{\partial c_{i\alpha}}{\partial q_\beta}\right) - \left(\frac{\partial c_{i\beta}}{\partial q_\alpha}\right)\right]\dot{q}_j \neq 0. \tag{14}$$

The necessity and sufficiency of the condition above can be directly ascertained from Eqs. (11*a*) and (11*b*). In addition to establishing coupling, the condition enables us to identify the pair of gyroscopic forces, namely those given in Eq. (13).

3.2 The Case of Constrained Generalized Coordinates. The Lagrangian formulation for constrained systems is quite similar to that for systems with independent generalized coordinates. For constrained systems, the structure of the differential equations remain unaltered; only the right-hand side is modified to include constraint forces. These forces are referred to as Lagrange multipliers. Since gyroscopic coupling depends on the structure of the differential equations and not on their right-hand side, the results in the previous section are applicable to constrained systems.

4 Some Observations About the Gyroscopic Modulus

4.1 Physical Significance. In the case where both generalized coordinates are rotational displacements, the generalized gyroscopic forces are both moments. For the coordinate pair (q_α, q_β), these moments are

$$\begin{pmatrix} M_\alpha \\ M_\beta \end{pmatrix} = \begin{pmatrix} 0 & \Lambda_{\alpha\beta} \\ -\Lambda_{\alpha\beta} & 0 \end{pmatrix} \begin{pmatrix} \dot{q}_\alpha \\ \dot{q}_\beta \end{pmatrix}.$$

The gyroscopic modulus in this case is the ratio of a moment to an angular velocity and has the units of angular momentum.

In the case where the coordinates are comprised of a linear and an angular displacement, the gyroscopic forces are comprised of a moment and a force, respectively. If we assume q_α and q_β to be the linear and angular displacements, respectively, the generalized forces are

$$\begin{pmatrix} F_\alpha \\ M_\beta \end{pmatrix} = \begin{pmatrix} 0 & \Lambda_{\alpha\beta} \\ -\Lambda_{\alpha\beta} & 0 \end{pmatrix} \begin{pmatrix} \dot{q}_\alpha \\ \dot{q}_\beta \end{pmatrix}.$$

In such cases, the gyroscopic modulus is the ratio of a force to an angular velocity. It can also be considered as the ratio of a moment to a linear velocity. Clearly, the modulus has the units of linear momentum. For the sake of completeness, one may like to explore the coupling between two translational coordinates. Such a coupling is characterized by a gyroscopic modulus, which, being the ratio of a force to a linear velocity, has no clear physical significance. Incidentally, we have not come across a single physical system with this type of coupling.

4.2 Integrability of Local-Inertial Velocities. For the sake of completeness, we would like to point out that gyroscopic coupling is absent in systems where the local-inertial velocities are integrable to expressions involving local-inertial coordinates and generalized coordinates only. This can be explained as follows. Suppose that the local-inertial velocities are integrable to the form in Eq. (2), with the x_i's now denoting local-inertial coordinates. Then the c_{ij}'s can be expressed as $c_{ij} = (\partial x_i/\partial q_j)$. From the expression for the gyroscopic modulus in Eq. (12), it simply follows that

$$\Lambda_{\alpha\beta} = \sum_{i=1}^{M}\sum_{j=1}^{n} m_i c_{ij}\left[\left(\frac{\partial c_{i\alpha}}{\partial q_\beta}\right) - \left(\frac{\partial c_{i\beta}}{\partial q_\alpha}\right)\right]\dot{q}_j$$

$$= \sum_{i=1}^{M}\sum_{j=1}^{n} m_i c_{ij}\left[\frac{\partial}{\partial q_\beta}\left(\frac{\partial x_i}{\partial q_\alpha}\right) - \frac{\partial}{\partial q_\alpha}\left(\frac{\partial x_i}{\partial q_\beta}\right)\right]\dot{q}_j = 0. \quad (15)$$

Clearly, gyroscopic coupling may or may not exist in dynamical systems and this depends largely on the choice of the generalized coordinates.

5 Illustrative Examples

5.1 A Simple Illustrative Example. Consider the spherical pendulum in Fig. 1, where point mass M is suspended by a chord of fixed length L. Two reference frames are used for coordinate description, namely, instantaneous Cartesian coordinates x', y', z' fixed to the body of the pendulum, and independent generalized coordinates q_1 and q_2. The relation between the Cartesian velocities v'_x, v'_y, v'_z, and the generalized velocities $\dot{q}_1$, $\dot{q}_2$ in Eq. (7*a*) can be explicitly written as

$$\begin{pmatrix} v'_x \\ v'_y \\ v'_z \end{pmatrix} = \begin{pmatrix} c_{11} & c_{12} \\ c_{21} & c_{22} \\ c_{31} & c_{32} \end{pmatrix} \begin{pmatrix} \dot{q}_1 \\ \dot{q}_2 \end{pmatrix},$$

$$\begin{pmatrix} c_{11} & c_{12} \\ c_{21} & c_{22} \\ c_{31} & c_{32} \end{pmatrix} \triangleq \begin{pmatrix} L\sin q_2 & 0 \\ 0 & L \\ 0 & 0 \end{pmatrix}. \quad (16)$$

The condition in Eq. (14) involves derivatives of the matrix entries with respect to the generalized coordinates. It is clear from Eq. (16) that all such terms are zero except for the term $(\partial c_{11}/\partial q_2)$, which has a value of $L\cos q_2$. Using this result for $q_\alpha = q_1$ and $q_\beta = q_2$, the gyroscopic modulus in Eq. (12) is found to be $\Lambda = (ML^2 \sin q_2 \cos q_2)\dot{q}_1$. Accordingly, from Eq. (13) the gyroscopic force pair can be identified as

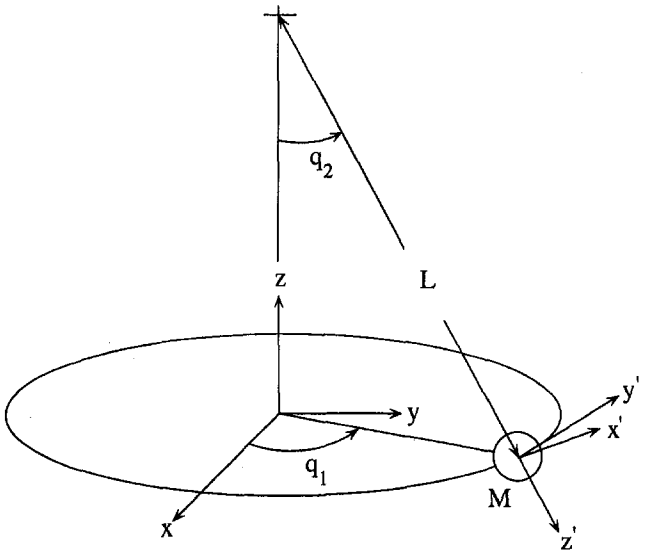

Fig. 1 A spherical pendulum described by two generalized coordinates

$$q_\alpha = q_1\text{: } +[(ML^2 \sin q_2 \cos q_2)\dot{q}_1]\dot{q}_2$$

$$q_\beta = q_2\text{: } -[(ML^2 \sin q_2 \cos q_2)\dot{q}_1]\dot{q}_1. \quad (17)$$

These terms can be identified in Lagrange's equations for the coordinates q_1, q_2, derived below:

$$ML^2 \sin^2 q_2 \ddot{q}_1 + 2ML^2 \sin q_2 \cos q_2 \dot{q}_1\dot{q}_2 = Q_1 \quad (18a)$$

$$ML^2\ddot{q}_2 - ML^2 \sin q_2 \cos q_2 \dot{q}_1^2 + MgL \sin q_2 = Q_2 \quad (18b)$$

where Q_1, Q_2 represent the nonconservative generalized forces in the coordinates q_1, q_2.

5.2 An Extended Example. Consider the spherical pendulum in Fig. 2, which differs from the pendulum in Fig. 1 because the length of the chord is variable. As in the previous example, we use two reference frames for coordinate description. These include the instantaneous Cartesian coordinates x', y', z' and the inde-

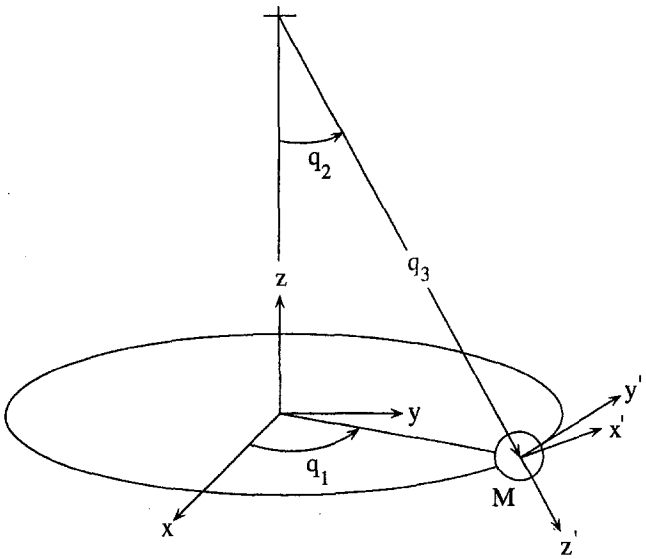

Fig. 2 A spherical pendulum described by three generalized coordinates

pendent generalized coordinates q_1, q_2, and q_3. The relation between the Cartesian velocities v'_x, v'_y, v'_z and the generalized velocities $\dot{q}_1$, $\dot{q}_2$, $\dot{q}_3$ in Eq. (7*a*) can be written as

$$\begin{pmatrix} v'_x \\ v'_y \\ v'_z \end{pmatrix} = \begin{pmatrix} c_{11} & c_{12} & c_{13} \\ c_{21} & c_{22} & c_{23} \\ c_{31} & c_{32} & c_{33} \end{pmatrix} \begin{pmatrix} \dot{q}_1 \\ \dot{q}_2 \\ \dot{q}_3 \end{pmatrix},$$

$$\begin{pmatrix} c_{11} & c_{12} & c_{13} \\ c_{21} & c_{22} & c_{23} \\ c_{31} & c_{32} & c_{33} \end{pmatrix} \triangleq \begin{pmatrix} q_3 \sin q_2 & 0 & 0 \\ 0 & q_3 & 0 \\ 0 & 0 & 1 \end{pmatrix}. \quad (19)$$

Since gyroscopic coupling may exist between the coordinate pairs (q_1, q_2), (q_2, q_3), and (q_3, q_1), we evaluate the modulus in Eq. (12) for each of the cases, namely, $(q_\alpha, q_\beta) = (q_1, q_2)$, $(q_\alpha, q_\beta) = (q_2, q_3)$, and $(q_\alpha, q_\beta) = (q_3, q_1)$. Using Eq. (19) these moduli can be shown to be

$$q_\alpha = q_1, \quad q_\beta = q_2, \quad \Lambda = +(Mq_3^2 \sin q_2 \cos q_2)\dot{q}_1 \quad (20a)$$

$$q_\alpha = q_2, \quad q_\beta = q_3, \quad \Lambda = +(Mq_3)\dot{q}_2 \quad (20b)$$

$$q_\alpha = q_3, \quad q_\beta = q_1, \quad \Lambda = -(Mq_3 \sin^2 q_2)\dot{q}_1. \quad (20c)$$

The gyroscopic moduli in Eqs. (20*a*) and (20*c*) denote coupling between two angular displacement coordinates while the modulus in Eq. (20*b*) denotes coupling between a linear and an angular displacement. In agreement with the discussion in Section 4, the moduli in Eqs. (20*a*) and (20*c*) have the units of angular momentum and the modulus in Eq. (20*b*) has the units of linear momentum.

The condition in Eq. (14) guarantees the existence of gyroscopic forces of the form given in Eq. (13). The gyroscopic force pairs corresponding to Eqs. (20*a*), (20*b*), and (20*c*) are

$$\begin{aligned} q_\alpha = q_1&: +[(Mq_3^2 \sin q_2 \cos q_2)\dot{q}_1]\dot{q}_1 \\ q_\beta = q_2&: -[(Mq_3^2 \sin q_2 \cos q_2)\dot{q}_1]\dot{q}_2 \quad \ldots \quad \ldots \end{aligned} \quad (21a)$$

$$\begin{aligned} q_\alpha = q_2&: +[(Mq_3)\dot{q}_2]\dot{q}_2 \\ q_\beta = q_3&: -[(Mq_3)\dot{q}_2]\dot{q}_3 \quad \ldots \quad \ldots \end{aligned} \quad (21b)$$

$$\begin{aligned} q_\alpha = q_3&: -[(Mq_3 \sin^2 q_2)\dot{q}_1]\dot{q}_1 \\ q_\beta = q_1&: +[(Mq_3 \sin^2 q_2)\dot{q}_1]\dot{q}_3 \quad \ldots \quad \ldots \end{aligned} \quad (21c)$$

The coupling terms above can be seen in Lagrange's equations, derived as follows:

$$Mq_3^2 \sin^2 q_2 \ddot{q}_1 + 2Mq_3^2 \sin q_2 \cos q_2 \dot{q}_1 \dot{q}_2 + 2Mq_3 \sin^2 q_2 \dot{q}_1 \dot{q}_3 = Q_1 \quad (22a)$$

$$Mq_3^2 \ddot{q}_2 - Mq_3^2 \sin q_2 \cos q_2 \dot{q}_1^2 + 2Mq_3 \dot{q}_2 \dot{q}_3 + Mgq_3 \sin q_2 = Q_2 \quad (22b)$$

$$M\ddot{q}_3 - Mq_3 \sin^2 q_2 \dot{q}_1^2 - Mq_3 \dot{q}_2^2 - Mg \cos q_2 = Q_3 \quad (22c)$$

where Q_1, Q_2, Q_3 are the nonconservative forces in the coordinates q_1, q_2, q_3.

To consider a problem with constrained generalized coordinates, we introduce the holonomic constraint

$$\dot{q}_3 = 0 \quad (23)$$

in the example above. This modifies Eq. (22) to the form

$$Mq_3^2 \sin^2 q_2 \ddot{q}_1 + 2Mq_3^2 \sin q_2 \cos q_2 \dot{q}_1 \dot{q}_2 = Q_1 \quad (24a)$$

$$Mq_3^2 \ddot{q}_2 - Mq_3^2 \sin q_2 \cos q_2 \dot{q}_1^2 + Mgq_3 \sin q_2 = Q_2 \quad (24b)$$

$$-Mq_3 \sin^2 q_2 \dot{q}_1^2 - Mq_3 \dot{q}_2^2 - Mg \cos q_2 = Q_3 + \lambda \quad (24c)$$

where λ is a Lagrange multiplier. Clearly, Eqs. (24*a*) and (24*b*) are exactly the same as Eqs. (18*a*) and (18*b*). When $\dot{q}_3 = 0$, the gyroscopic couplings described by Eqs. (21*b*) and (21*c*) also vanish, reducing the coupling to the one in Eq. (21*a*). The forces in Eq. (21*a*) are the same as those in Eq. (17). Clearly, the constraint in Eq. (23) converts the example in this section to the one discussed in the previous section. The third differential equation, namely Eq. (24*c*), gives us an expression for the constraint force, λ, which measures the tension in the chord.

6 Conclusion

Gyroscopic coupling between coordinate pairs of dynamical systems represents a conservative form of interaction where energy flows back and forth between them. The knowledge of such coupling provides insight into the system behavior which is useful for analysis and control system design. While gyroscopic coupling has been known to exist in both scleronomic and rheonomic systems, the mathematical development in the literature conveys the notion that such couplings arise in rheonomic systems only. In this paper we presented an efficient method for identifying gyroscopic coupling in scleronomic dynamical systems. Based on the kinematic relationship between the generalized velocities and local-inertial velocities, we arrived at necessary and sufficient conditions that identify the modulus of coupling and the gyroscopic force pair. The conditions apply to systems with independent generalized coordinates as well as systems with holonomic constraints. In the event that the coupled coordinates are angular displacements, the gyroscopic modulus has the units of angular momentum. When a linear and an angular displacement are gyroscopically coupled, the modulus of coupling has the units of linear momentum. Two examples are presented in the note to illustrate our approach.

References

Greenwood, D. T., 1988, *Principles of Dynamics,* Prentice-Hall, Englewood Cliffs, NJ.
Meirovitch, L., 1988, *Methods of Analytical Dynamics,* McGraw-Hill, New York.

Logarithmic Stress Singularities Resulting From Various Boundary Conditions in Angular Corners of Plates in Extension

G. B. Sinclair[1]

This note considers the in-plane loading of wedge-shaped plates comprised of a single, homogeneous and isotropic, linear elastic material. Several instances of logarithmic stress singularities occurring at the vertices of such plates are provided in the literature. Here considerably more configurations with logarithmic singularities are identified.

1 Introduction

Elastic stress singularities are not of the real world. However, their presence in a stress analysis can be a real fact. Then it is

[1] Department of Mechanical Engineering, Carnegie Mellon University, Pittsburgh, PA 15213-3890.

Contributed by the Applied Mechanics Division of THE AMERICAN SOCIETY OF MECHANICAL ENGINEERS for publication in the ASME JOURNAL OF APPLIED MECHANICS. Manuscript received by the ASME Applied Mechanics Division, Nov. 18, 1997; final revision, Aug. 12, 1998. Associate Technical Editor: J. N. Reddy.

pendent generalized coordinates q_1, q_2, and q_3. The relation between the Cartesian velocities v'_x, v'_y, v'_z and the generalized velocities $\dot{q}_1$, $\dot{q}_2$, $\dot{q}_3$ in Eq. (7*a*) can be written as

$$\begin{pmatrix} v'_x \\ v'_y \\ v'_z \end{pmatrix} = \begin{pmatrix} c_{11} & c_{12} & c_{13} \\ c_{21} & c_{22} & c_{23} \\ c_{31} & c_{32} & c_{33} \end{pmatrix} \begin{pmatrix} \dot{q}_1 \\ \dot{q}_2 \\ \dot{q}_3 \end{pmatrix},$$

$$\begin{pmatrix} c_{11} & c_{12} & c_{13} \\ c_{21} & c_{22} & c_{23} \\ c_{31} & c_{32} & c_{33} \end{pmatrix} \triangleq \begin{pmatrix} q_3 \sin q_2 & 0 & 0 \\ 0 & q_3 & 0 \\ 0 & 0 & 1 \end{pmatrix}. \quad (19)$$

Since gyroscopic coupling may exist between the coordinate pairs (q_1, q_2), (q_2, q_3), and (q_3, q_1), we evaluate the modulus in Eq. (12) for each of the cases, namely, $(q_\alpha, q_\beta) = (q_1, q_2)$, $(q_\alpha, q_\beta) = (q_2, q_3)$, and $(q_\alpha, q_\beta) = (q_3, q_1)$. Using Eq. (19) these moduli can be shown to be

$$q_\alpha = q_1, \quad q_\beta = q_2, \quad \Lambda = +(Mq_3^2 \sin q_2 \cos q_2)\dot{q}_1 \quad (20a)$$

$$q_\alpha = q_2, \quad q_\beta = q_3, \quad \Lambda = +(Mq_3)\dot{q}_2 \quad (20b)$$

$$q_\alpha = q_3, \quad q_\beta = q_1, \quad \Lambda = -(Mq_3 \sin^2 q_2)\dot{q}_1. \quad (20c)$$

The gyroscopic moduli in Eqs. (20*a*) and (20*c*) denote coupling between two angular displacement coordinates while the modulus in Eq. (20*b*) denotes coupling between a linear and an angular displacement. In agreement with the discussion in Section 4, the moduli in Eqs. (20*a*) and (20*c*) have the units of angular momentum and the modulus in Eq. (20*b*) has the units of linear momentum.

The condition in Eq. (14) guarantees the existence of gyroscopic forces of the form given in Eq. (13). The gyroscopic force pairs corresponding to Eqs. (20*a*), (20*b*), and (20*c*) are

$$\begin{aligned} q_\alpha = q_1&: +[(Mq_3^2 \sin q_2 \cos q_2)\dot{q}_1]\dot{q}_1 \\ q_\beta = q_2&: -[(Mq_3^2 \sin q_2 \cos q_2)\dot{q}_1]\dot{q}_2 \quad \ldots \quad \ldots \end{aligned} \quad (21a)$$

$$\begin{aligned} q_\alpha = q_2&: +[(Mq_3)\dot{q}_2]\dot{q}_2 \\ q_\beta = q_3&: -[(Mq_3)\dot{q}_2]\dot{q}_3 \quad \ldots \quad \ldots \end{aligned} \quad (21b)$$

$$\begin{aligned} q_\alpha = q_3&: -[(Mq_3 \sin^2 q_2)\dot{q}_1]\dot{q}_1 \\ q_\beta = q_1&: +[(Mq_3 \sin^2 q_2)\dot{q}_1]\dot{q}_3 \quad \ldots \quad \ldots \end{aligned} \quad (21c)$$

The coupling terms above can be seen in Lagrange's equations, derived as follows:

$$Mq_3^2 \sin^2 q_2 \ddot{q}_1 + 2Mq_3^2 \sin q_2 \cos q_2 \dot{q}_1 \dot{q}_2 + 2Mq_3 \sin^2 q_2 \dot{q}_1 \dot{q}_3 = Q_1 \quad (22a)$$

$$Mq_3^2 \ddot{q}_2 - Mq_3^2 \sin q_2 \cos q_2 \dot{q}_1^2 + 2Mq_3 \dot{q}_2 \dot{q}_3 + Mgq_3 \sin q_2 = Q_2 \quad (22b)$$

$$M\ddot{q}_3 - Mq_3 \sin^2 q_2 \dot{q}_1^2 - Mq_3 \dot{q}_2^2 - Mg \cos q_2 = Q_3 \quad (22c)$$

where Q_1, Q_2, Q_3 are the nonconservative forces in the coordinates q_1, q_2, q_3.

To consider a problem with constrained generalized coordinates, we introduce the holonomic constraint

$$\dot{q}_3 = 0 \quad (23)$$

in the example above. This modifies Eq. (22) to the form

$$Mq_3^2 \sin^2 q_2 \ddot{q}_1 + 2Mq_3^2 \sin q_2 \cos q_2 \dot{q}_1 \dot{q}_2 = Q_1 \quad (24a)$$

$$Mq_3^2 \ddot{q}_2 - Mq_3^2 \sin q_2 \cos q_2 \dot{q}_1^2 + Mgq_3 \sin q_2 = Q_2 \quad (24b)$$

$$-Mq_3 \sin^2 q_2 \dot{q}_1^2 - Mq_3 \dot{q}_2^2 - Mg \cos q_2 = Q_3 + \lambda \quad (24c)$$

where λ is a Lagrange multiplier. Clearly, Eqs. (24*a*) and (24*b*) are exactly the same as Eqs. (18*a*) and (18*b*). When $\dot{q}_3 = 0$, the gyroscopic couplings described by Eqs. (21*b*) and (21*c*) also vanish, reducing the coupling to the one in Eq. (21*a*). The forces in Eq. (21*a*) are the same as those in Eq. (17). Clearly, the constraint in Eq. (23) converts the example in this section to the one discussed in the previous section. The third differential equation, namely Eq. (24*c*), gives us an expression for the constraint force, λ, which measures the tension in the chord.

6 Conclusion

Gyroscopic coupling between coordinate pairs of dynamical systems represents a conservative form of interaction where energy flows back and forth between them. The knowledge of such coupling provides insight into the system behavior which is useful for analysis and control system design. While gyroscopic coupling has been known to exist in both scleronomic and rheonomic systems, the mathematical development in the literature conveys the notion that such couplings arise in rheonomic systems only. In this paper we presented an efficient method for identifying gyroscopic coupling in scleronomic dynamical systems. Based on the kinematic relationship between the generalized velocities and local-inertial velocities, we arrived at necessary and sufficient conditions that identify the modulus of coupling and the gyroscopic force pair. The conditions apply to systems with independent generalized coordinates as well as systems with holonomic constraints. In the event that the coupled coordinates are angular displacements, the gyroscopic modulus has the units of angular momentum. When a linear and an angular displacement are gyroscopically coupled, the modulus of coupling has the units of linear momentum. Two examples are presented in the note to illustrate our approach.

References

Greenwood, D. T., 1988, *Principles of Dynamics,* Prentice-Hall, Englewood Cliffs, NJ.
Meirovitch, L., 1988, *Methods of Analytical Dynamics,* McGraw-Hill, New York.

Logarithmic Stress Singularities Resulting From Various Boundary Conditions in Angular Corners of Plates in Extension

G. B. Sinclair[1]

This note considers the in-plane loading of wedge-shaped plates comprised of a single, homogeneous and isotropic, linear elastic material. Several instances of logarithmic stress singularities occurring at the vertices of such plates are provided in the literature. Here considerably more configurations with logarithmic singularities are identified.

1 Introduction

Elastic stress singularities are not of the real world. However, their presence in a stress analysis can be a real fact. Then it is

[1] Department of Mechanical Engineering, Carnegie Mellon University, Pittsburgh, PA 15213-3890.

Contributed by the Applied Mechanics Division of THE AMERICAN SOCIETY OF MECHANICAL ENGINEERS for publication in the ASME JOURNAL OF APPLIED MECHANICS. Manuscript received by the ASME Applied Mechanics Division, Nov. 18, 1997; final revision, Aug. 12, 1998. Associate Technical Editor: J. N. Reddy.

essential that their participation be recognized if any real use is to be made of the analysis. The objective of this note is to assist in achieving such recognition.

In particular, we are concerned with identifying configurations which can have pure logarithmic stress singularities. That is, stresses which behave like $O(\ln r)$ as $r \to 0$. These are the weakest singularities that occur in elasticity. As a result, they can be the most difficult to detect with numerical methods such as finite element analysis. Asymptotic identification is thus especially useful in avoiding having them pass undetected.

For angular elastic plates under in-plane loading, conditions for logarithmic stress singularities have been available for some time. When the boundary conditions are homogeneous, these conditions are given in Dempsey and Sinclair (1979). When the boundary conditions are inhomogeneous, they can be drawn from Dempsey (1981). Somewhat surprisingly at this time, the number of configurations identified as actually having logarithmic stress singularities is quite small.

Probably the most well-known example of a logarithmic stress singularity is that attending a step shear on a half-plane. The corresponding stress field is given in Kolossoff (1914). Also well known is the logarithmic stress singularity accompanying indentation by a frictionless rigid wedge. A stress field of this type may be found in Sneddon (1951), Section 48.4. There is a further logarithmic singularity in Levy's problem when the plate vertex angle takes on a critical value ϕ_* ($\phi_* = 257.5$ deg). The corresponding stress field is given in Dempsey (1981). There are two more logarithmic singularities when one edge of the plate is subjected to a constant shear traction while the other is free. These occur for vertex angles of ϕ_* or 2π and the accompanying stresses are also given in Dempsey (1981).[2] And there are four more when one edge of the plate is subjected to uniform pressure/shear while the other is clamped. These last are given in Sinclair (1998a). All told to date, there are nine different configurations wherein logarithmic stress singularities are identified as occurring with inhomogeneous boundary conditions. Here we seek to identify other such configurations.

There are even fewer configurations identified in the literature as having logarithmic stress singularities when the boundary conditions are completely homogeneous. One is found for a plate with a vertex angle of $\phi_*/2$ when one edge is subjected to frictionless contact conditions while the other is clamped. The stress field in this instance is given in Dempsey (1978). A second occurs under clamped-free conditions. This may be inferred from Dempsey (1995).[3] Here we seek to add to this number significantly.

We begin, in Section 2, by formulating the class of asymptotic problems of interest, admitting a fairly broad set of boundary conditions. Thereafter, in Section 3, we summarize the requirements for logarithmic stress singularities. We include in these requirements those needed for log-squared stress singularities because these arise naturally. We close, in Section 4, with a list of all configurations that can have logarithmic stress singularities, including, for completeness, specifics of those found in prior work. We also note any instances of log-squared singularities.

2 Formulation

We consider an angular elastic plate subjected to various boundary conditions along its radial edges. We denote the angle subtended at the plate vertex by ϕ, and introduce cylindrical polar coordinates (r, θ) with origin O at the vertex (Fig. 1). Thus the

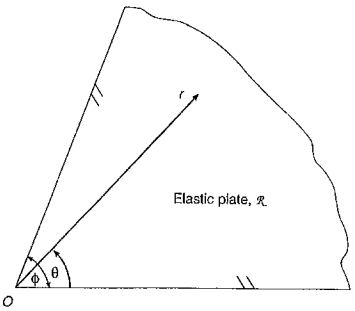

Fig. 1 Geometry and coordinates for the angular elastic plate

open region $\Re$ of interest in our asymptotic treatment is

$$\Re = \{(r, \theta) | 0 < r < \infty, 0 < \theta < \phi\}.$$

With these geometric preliminaries in place, we can formally state the class of problems for analysis as next.

We seek the planar stress components σ_r, σ_θ, $\tau_{r\theta}$, together with their displacements u_r, u_θ, as functions of r, θ throughout $\Re$, satisfying: the stress equations of equilibrium in the absence of body forces,

$$\frac{\partial \sigma_r}{\partial r} + \frac{1}{r}\frac{\partial \tau_{r\theta}}{\partial \theta} + \frac{\sigma_r - \sigma_\theta}{r} = 0,$$

$$\frac{1}{r}\frac{\partial \sigma_\theta}{\partial \theta} + \frac{\partial \tau_{r\theta}}{\partial r} + \frac{2\tau_{r\theta}}{r} = 0, \tag{1}$$

on $\Re$; the stress-displacement relations for a linear elastic plate which is both homogeneous and isotropic,

$$\sigma_r = \frac{\mu}{\kappa - 1}\left[(\kappa + 1)\frac{\partial u_r}{\partial r} + (3 - \kappa)\left(\frac{1}{r}\frac{\partial u_\theta}{\partial \theta} + \frac{u_r}{r}\right)\right],$$

$$\sigma_\theta = \frac{\mu}{\kappa - 1}\left[(\kappa + 1)\left(\frac{1}{r}\frac{\partial u_\theta}{\partial \theta} + \frac{u_r}{r}\right) + (3 - \kappa)\frac{\partial u_r}{\partial r}\right],$$

$$\tau_{r\theta} = \mu\left[\frac{1}{r}\frac{\partial u_r}{\partial \theta} + \frac{\partial u_\theta}{\partial r} - \frac{u_\theta}{r}\right], \tag{2}$$

on $\Re$, wherein μ is the shear modulus and κ is $3 - 4\nu$ for plane strain, $(3 - \nu)/(1 + \nu)$ for plane stress, ν being Poisson's ratio; the singularity conditions at the plate vertex,

$$\sigma = O(\ln r) \quad \text{as } r \to 0, \tag{3}$$

on $\Re$, where σ is any stress component; and any one of the admissible sets of boundary conditions listed in Table 1 on the plate edge at $\theta = 0$ as well as a further such set on the edge at $\theta = \phi$.

Several comments on the foregoing formulation are in order. First, re the stress-displacement relations (2): these hold for $1 < \kappa \leq 3$. For plane strain with an incompressible solid, $\nu = \frac{1}{2}$ yielding $\kappa = 1$. On occasion, such solids are investigated in this work. In these circumstances the first two of (2) are exchanged for

Table 1 Boundary conditions

Assigned Roman numeral	Physical description	Prescribed quantities
I	Stress free	$\sigma_\theta = 0$, $\tau_{r\theta} = 0$
II	Clamped	$u_r = 0$, $u_\theta = 0$
III	Contact with friction	$\tau_{r\theta} = f\sigma_\theta$, $u_\theta = 0$
IV	Cohesive laws	$\sigma_\theta = ku_\theta$, $\tau_{r\theta} = k'u_r$
I′	Uniform tractions	$\sigma_\theta = -p$, $\tau_{r\theta} = q$
II′	Pinching without slip	$u_r = 0$, $u_\theta = r\delta\phi$
III′	Pinching with friction	$\tau_{r\theta} = f\sigma_\theta$, $u_\theta = r\delta\phi$

[2] All of the logarithmic stress fields given in Kolossoff (1914) and Dempsey (1981) are derived by an alternative means in Ting (1984). This alternative derivation has the added attribute of effecting a reasonable transition of stress responses as the plate vertex angle passes through the value with a log singularity.

[3] Dempsey (1995) is concerned with logarithmic amplification of power singularities rather than pure log singularities as here: hence the identification of the latter is not that explicit. These sort of singularities are stronger than just power singularities rather than weaker, and consequently not of as great a concern re passing undetected as pure log singularities.

$$\sigma_r = 2\mu \frac{\partial u_r}{\partial r}, \quad \sigma_\theta = 2\mu\left(\frac{1}{r}\frac{\partial u_\theta}{\partial \theta} + \frac{u_r}{r}\right),$$

$$\frac{\partial u_r}{\partial r} + \frac{1}{r}\frac{\partial u_\theta}{\partial \theta} + \frac{u_r}{r} = 0, \tag{2'}$$

on $\mathfrak{R}$.

Second, re the singularity requirement (3): we also briefly consider log-squared singularities, in which case (3) becomes

$$\sigma = O(\ln^2 r) \quad \text{as } r \to 0,$$

on $\mathfrak{R}$.

Third, re the boundary conditions of Table 3: conditions I and II are the classical conditions used in in-plane singularity analysis. Conditions III are a version of Amonton's law. In these conditions, f is the coefficient of friction. Conditions IV reflect the action of cohesive/adhesive stress-separation laws on elastic response. In these conditions, k and k' are the stiffnesses associated with relative displacement across a boundary in the normal and transverse directions, respectively. And conditions I′, II′, and III′ are inhomogeneous counterparts of conditions I, II, and III. In these conditions, p is a uniform pressure, q a constant shear, and $\delta\phi$ is the angle by which the vertex angle of the plate is reduced due to pinching (pinching implies that $\delta\phi$ is negative on a positive θ-edge). Of course, any logarithmic singularity determined as possible for I, II, or III can also be present with I′, II′ or III′, respectively: We distinguish homogeneous conditions from inhomogeneous here because they receive distinct analysis in the next section.

3 Analysis

The development of requirements for logarithmic stress singularities is based on an extension of the classical analysis of Williams (1952) for power singularities. We outline this development next.

In Williams (1952), the appropriate choice of a separable Airy stress function leads to fields containing four constants which share a common power of r. For example, the normal stress σ_θ is

$$\sigma_\theta = \lambda r^{\lambda-1}[a\cos(\lambda+1)\theta + b\sin(\lambda+1)\theta + (\lambda+1) \times (c\cos(\lambda-1)\theta + d\sin(\lambda-1)\theta)], \tag{4}$$

where a, b, c, and d are the four constants, and λ is the separation-of-variables parameter. The other stresses and the displacements for these basic fields are given in Williams (1952). Substituting these fields into a set of four homogeneous boundary conditions then leads to

$$\mathbf{Aa} = \mathbf{0}, \tag{5}$$

where the vector $\mathbf{a} = (a, b, c, d)$, and $\mathbf{A}$ is a matrix whose elements are in general functions of λ. A nontrivial solution to (5) requires that the determinant D of $\mathbf{A}$ satisfy

$$D = 0. \tag{6}$$

This requirement generates an eigenvalue equation for λ. Determining λ satisfying (6) with $0 < \mathrm{Re}\lambda < 1$ then characterizes the power singularities possible in a particular configuration with homogeneous boundary conditions.

To extend the preceding to consider logarithmic stress singularities, we need stress components containing ln r terms. To this end, we differentiate the basic fields of Williams (1952) throughout with respect to λ: This operation produces fields which continue to satisfy the governing Eqs. (1) and (2), and which contain ln r terms. By way of example, under it σ_θ of (4) becomes

$$\sigma_\theta = r^{\lambda-1}[(\lambda\ln r + 1)(\bar{a}\cos(\lambda+1)\theta + \bar{b}\sin(\lambda+1)\theta + (\lambda+1)(\bar{c}\cos(\lambda-1)\theta + \bar{d}\sin(\lambda-1)\theta)) - \lambda\theta(\bar{a}\sin(\lambda+1)\theta - \bar{b}\cos(\lambda+1)\theta + (\lambda+1)(\bar{c}\sin(\lambda-1)\theta - \bar{d}\cos(\lambda-1)\theta)) + \lambda\bar{c}\cos(\lambda-1)\theta + \lambda\bar{d}\sin(\lambda-1)\theta], \tag{7}$$

where the bars atop constants serve to indicate that they no longer need be the same as their antecedents, a, b, c, and d. Now substituting these fields together with the original basic ones into a set of four homogeneous boundary conditions leads to a system of the form

$$\mathbf{A}\bar{\mathbf{a}}\ln r + \frac{d\mathbf{A}}{d\lambda}\bar{\mathbf{a}} + \mathbf{Aa} = \mathbf{0}, \tag{8}$$

wherein $d\mathbf{A}/d\lambda$ is formed from $\mathbf{A}$ by differentiating each element with respect to λ. General requirements for a nontrivial solution for $\bar{\mathbf{a}}$ in (8) are established in Dempsey and Sinclair (1979). These accommodate the possibilities of multiple materials comprising the plate as well as logarithmic amplification of power singularities. Here we are concerned with a single material and logarithmic singularities by themselves. This leads to a slightly simpler set of requirements. Specifically we have, as our *requirements for logarithmic stress singularities with homogeneous boundary conditions,*

$$\lambda = 1, \quad D = \frac{dD}{d\lambda} = 0, \tag{9a}$$

$$(r_A - 3)\frac{d^2D}{d\lambda^2} = 0, \tag{9b}$$

$$\bar{a}^2 + \bar{b}^2 + \bar{c}^2 \neq 0, \tag{9c}$$

where r_A is the rank of $\mathbf{A}$ when $\lambda = 1$. The first requirements in (9a), (9b) ensure a nontrivial $\bar{\mathbf{a}}$. However, for $\bar{a} = \bar{b} = \bar{c} = 0$, $\bar{d} \neq 0$, no ln r terms participate in the stresses (see, e.g., (7) with $\lambda = 1$). The last requirement (9c) guards against this possibility.

Turning to the inhomogeneous boundary conditions of Table 1, using the basic fields leads to a system of the form

$$\mathbf{Aa} = \mathbf{p}, \tag{10}$$

for $\lambda = 1$, where $\mathbf{p}$ is a vector whose components involve one or more of p, q, and $\delta\phi$. For $\mathbf{p} \neq \mathbf{0}$, we have a problem in (10) if $D = 0$ for $\lambda = 1$, unless the rank of the augmented matrix, $(\mathbf{A}') = (\mathbf{A}:\mathbf{p})$, is also reduced. If this rank reduction does not occur, we can overcome the difficulty by again supplementing the basic fields with auxiliary ones. This leads to the new system

$$\mathbf{A}\bar{\mathbf{a}}\ln r + \frac{d\mathbf{A}}{d\lambda}\bar{\mathbf{a}} + \mathbf{Aa} = \mathbf{p}, \tag{11}$$

for $\lambda = 1$. The system in (11) can be solved to yield fields containing ln r provided that all the requirements in (9a), (9b) are *not* met. Thus our first set of *requirements for logarithmic stress singularities with inhomogeneous boundary conditions* has

$$\lambda = 1, \quad D = 0, \quad r_{A'} \neq r_A, \tag{12a}$$

$$\left(\frac{dD}{d\lambda}\right)^2 + (r_A - 3)^2\left(\frac{d^2D}{d\lambda^2}\right)^2 \neq 0, \tag{12b}$$

$$\bar{a}^2 + \bar{b}^2 + \bar{c}^2 \neq 0, \tag{12c}$$

where $r_{A'}$ is the rank of $\mathbf{A}'$ when $\lambda = 1$. The last requirement (12c) continues to ensure the participation of ln r terms in the stresses of the auxiliary fields.

There remains the possibility that we have inhomogeneous boundary conditions yet (9a) and (9b) do hold. Then merely supplementing the basic fields with auxiliary ones does not in general suffice. We need further auxiliary fields. These are gener-

ated by a further differentiation with respect to λ. By way of example, under this operation σ_θ of (7) becomes

$$\sigma_\theta = \lambda r^{\lambda-1} \ln^2 r[\hat{a} \cos(\lambda+1)\theta + \hat{b} \sin(\lambda+1)\theta + (\lambda+1) \times (\hat{c} \cos(\lambda-1)\theta + \hat{d} \sin(\lambda-1)\theta)] + O(\ln r) + O(1), \quad (13)$$

as $r \to 0$, where the hats atop constants serve to indicate that they can be distinct from earlier constants. With these added fields, it is possible to comply with inhomogeneous boundary conditions. Typically such compliance results in log-squared stress singularities. There is an exception, however. This occurs when $\hat{a} = \hat{b} = \hat{c} = 0$, $\hat{d} \neq 0$. Then the further auxiliary stresses do not have $\ln^2 r$ terms (see, e.g., (13) with $\lambda = 1$). They do, though, have $\ln r$ terms. Hence our second set of *requirements for logarithmic stress singularities with inhomogeneous boundary conditions* has

$$\lambda = 1, \quad D = 0, \quad r_{A'} \neq r_A, \quad (14a)$$

$$\frac{dD}{d\lambda} = (r_A - 3)\frac{d^2D}{d\lambda^2} = 0, \quad (14b)$$

$$\hat{a} = \hat{d} = \hat{c} = 0. \quad (14c)$$

Log-squared stress singularities occur if (14*a*) and (14*b*) are met but not (14*c*): These stresses also include logarithmic terms.

Equations (9), (12), and (14) constitute our requirements for logarithmic stress singularities. We observe that just the first of (9), (9*a*), continues to be put forward in the literature as supposedly containing the requirements for logarithmic stress singularities (see, e.g., Murakami, 1992). While (9*a*) appeals in its relative simplicity, in general it is neither necessary nor sufficient for the existence of log singularities. We amplify this point at the end of the next section.

With the requirements for logarithmic stress singularities at hand, analysis proceeds routinely. We first derive eigenvalue equations of the form of (6) for all possible combinations of homogeneous boundary conditions that can be drawn from Table 1: We tabulate these eigenvalue equations in the section which follows. Then we check (9), (12), and (14) in turn. When potential new configurations with log singularities are revealed, the last requirement in each of (9), (12), and (14) requires the assembling of associated new fields. The algebra involved is straightforward but lengthy: Details are furnished in Sinclair (1998b). Stresses with log singularities and companion displacements are set out ibid: All of these fields are verified directly by substituting them into the governing Eqs. (1), (2) (or (2′) where appropriate), and checking the singularity requirement (3) and the pertinent boundary conditions. In the interests of brevity we omit these fields here, and simply provide the configurations that engender them in the next section.

4 Results

Eigenvalue equations for various combinations of homogeneous boundary conditions are set out in Table 2. For the most part, these are available in the literature. The first, second, and fourth equations, when associated with clamped/free conditions, I/II, can be obtained from Williams (1952). The equation for I–III can be obtained from Gdoutos and Theocaris (1975), while that for II–III is essentially given in Dempsey (1978). The equivalence of stress-free conditions I with those for cohesive laws IV, as far as these eigenvalue equations are concerned, is basically argued in Sinclair (1996).

Configurations which can have logarithmic stress singularities when boundary conditions are homogeneous are listed in Table 3(*a*). Herein ϕ_* satisfies

$$\tan\phi_* = \phi_*, \quad (15)$$

Table 2 Eigenvalue equations

Boundary conditions on $\theta = 0, \phi$	Eigenvalue equation
I or IV–I or IV	$\lambda \sin\phi = \pm\sin\lambda\phi$
II–II	$\lambda \sin\phi = \pm\kappa \sin\lambda\phi$
III–III	$f[(1-\kappa)\sin\lambda\phi \pm (1+\kappa+2\lambda)\sin\phi] = (1+\kappa)(\cos\lambda\phi \mp \cos\phi)$
I or IV–II	$4[\kappa \sin^2\lambda\phi + \lambda^2 \sin^2\phi] = (1+\kappa)^2$
I or IV–III	$2f[(1-\kappa)\sin^2\lambda\phi - \lambda(1+\kappa+2\lambda)\sin^2\phi] = (1+\kappa)(\sin 2\lambda\phi + \lambda \sin 2\phi)$
II–III	$2f[\kappa(1-\kappa)\sin^2\lambda\phi + \lambda(1+\kappa+2\lambda)\sin^2\phi] = (1+\kappa)(\kappa \sin 2\lambda\phi - \lambda \sin 2\phi)$

for $0 < \phi_* < 2\pi$. To one decimal place this gives $\phi_* = 257.5$ deg, as noted in the Introduction. Also,

$$\phi_\kappa = \sin^{-1}\frac{\sqrt{\kappa+1}}{2}, \quad (16)$$

for $0 < \phi_\kappa \leq \pi/2$, and $\bar{\phi}_\kappa$ is such that

Table 3(*a*) Logarithmically singular configurations with homogeneous boundary conditions

Boundary conditions on $\theta = 0, \phi$	Configuration specifications
II–II	$\kappa = 1, \phi = \phi_*$
III–III	$\phi = \pi, 2\pi, \kappa = 1, f \neq 0$
	$\kappa = \cos 2\phi - \frac{\sin 2\phi}{\phi}, f = -\cot\phi, \phi \neq \pi, 2\pi$
I or IV–II	$\phi = \pi - \phi_\kappa, 2\pi - \phi_\kappa, \kappa = -\frac{\tan\phi}{\phi}$
I or IV–III	$\kappa = 1 + 2\cos 2\phi - \frac{2\sin 2\phi}{\phi}, f = -\cot\phi$
II–III	$\phi = \frac{\pi}{2}, \frac{3\pi}{2}, \kappa = 3, f = -\frac{3\phi}{2}$
	$\phi = \bar{\phi}_\kappa, f = \frac{\kappa-1}{3-\kappa}\cot\phi, \kappa \neq 3$

Table 3(*b*) Logarithmically singular configurations with inhomogeneous boundary conditions

Boundary conditions on $\theta = 0, \phi$	Configuration specifications
I′ or IV–I or IV	$\phi = \pi, 2\pi, q \neq 0$
	$\phi = \phi_*, q \neq 0$ or $p \neq 0$
II′–II	$\phi = \pi, 2\pi, \delta\phi \neq 0$
	$\kappa = 1, \delta\phi \neq 0, \phi \neq \phi_*$
III′–III	$\phi = \pi, 2\pi, \delta\phi \neq 0, \kappa \neq 1, f \neq 0$
	$f = 0, \delta\phi \neq 0$
I′ or IV–II	$\phi = \phi_\kappa, \pi \pm \phi_\kappa, 2\pi - \phi_\kappa, p \neq 0$ or $q \neq 0$, and $\kappa \neq -\frac{\tan\phi}{\phi}$
I′ or IV–III	$\phi = \pi, 2\pi, q \neq 0$ or $fp \neq 0$
	$f = -\cot\phi, q \neq 0$ or $fp \neq 0$, and $\kappa \neq 1 + 2\cos 2\phi - \frac{2\sin 2\phi}{\phi}$
II′–III	$\phi = \pi, 2\pi, \delta\phi \neq 0$
	$f = 0, \kappa = 1, \delta\phi \neq 0, \tan 2\phi \neq 2\phi$
	$\phi = \frac{\pi}{2}, \frac{3\pi}{2}, \kappa = 3, \delta\phi \neq 0, f \neq -\frac{3\phi}{2}$
	$f = \frac{\kappa-1}{3-\kappa}\cot\phi, \delta\phi \neq 0, \phi \neq \pi, 2\pi, \bar{\phi}_\kappa, \kappa \neq 3$

$$\kappa(\kappa - 1)^2 + 4\kappa \cos 2\bar{\phi}_\kappa = (3\kappa - 1)\frac{\sin 2\bar{\phi}_\kappa}{\bar{\phi}_\kappa}. \quad (17)$$

It is understood in Table 3(*a*) that κ is constrained to lie within the physically applicable range, $1 \leq \kappa \leq 3$, in addition to any other constraints placed upon it. Some actual values of ϕ, κ, and f are: for III–III, $\phi = 170$ deg, $\kappa = 1.055, f = 5.67$ and $\phi = 355$ deg, $\kappa = 1.013, f = 11.43$; for I or IV–II, $\phi = 101.2$ deg, $\kappa = 2.848$ and $\phi = 274.0$ deg, $\kappa = 2.980$; for I or IV–III and $\kappa = 2$, $\phi =$ 137.4 deg, 202.7 deg, 324.7 deg with $f = 1.09, -2.39, 1.41$, respectively; and for II–III and $\kappa = 2$, $\phi = 119.7$ deg, 227.7 deg, 304.5 deg with $f = -0.57, 0.91, -0.69$, respectively.

Local fields containing logarithmic stress singularities for all the configurations listed in Table 3 can be obtained from Sinclair (1998b). For II–III when $\kappa = 1$ and $f = 0$, fields are also available from Dempsey (1978).

In the analysis of all of the configurations in Table 3(*a*), the ranks of the coefficient matrices involved never drop below two. Dempsey and Sinclair (1979) then has that (9*a*), (9*b*) are necessary requirements.[4] Indeed, all of the requirements in (9) are complied with by all of the log-singular configurations identified in Table 3. Moreover, when situations arose during analysis in which some of the requirements in (9) were complied with but others not, no logarithmic stress singularities were found.

Configurations which have logarithmic stress singularities when boundary conditions are inhomogeneous are listed in Table 3(*b*). Herein ϕ_*, ϕ_κ, $\bar{\phi}_\kappa$ remain as in (15), (16), (17), respectively, and κ continues to be constrained to the physical range. For the representative value of $\kappa = 2$, actual vertex angles for I′ or IV–II are $\phi = 60$ deg, 120 deg, 240 deg, 300 deg.

For I′, II′, and III′, only one plate edge needs to have these inhomogeneous conditions in order to realize configurations which can be superimposed to produce any inhomogeneous loading on both edges (on occasion this requires adding a rigid body rotation). Furthermore, the homogeneous cohesive-law conditions IV share the same logarithmically singular configurations as the inhomogeneous uniform-traction conditions I′. This is because IV can admit rigid-body translations which in turn produce uniform tractions.

Sources for the logarithmic stress fields for the configurations of Table 3(*b*) are: for I′ or IV–I or IV and $\phi = \pi$, Kolossoff (1914); for I′ or IV–I or IV and $\phi = \phi_*, 2\pi$, Dempsey (1981); for II′–II, Sinclair (1998b); for III′–III and $\phi = \pi, f = 0$, Sneddon (1951); for all other III′–III, Sinclair (1998b); for I′ or IV–II, Sinclair (1998a); and for both I′ or IV–III and II′–III, Sinclair (1998b).

The requirements in (12) and (14) are not established as necessary and sufficient for logarithmic stress singularities with inhomogeneous boundary conditions. However, for all of the configurations identified as having logarithmic singularities in Table 3(*b*), one or other of (12) or (14) is complied within its entirety. Moreover, no configurations were encountered during the course of analysis for which (12) or (14) was complied with and there was no logarithmic singularity.

With the exception of the second configuration for III–III, all of the configurations of Table 3(*a*) under the *inhomogeneous* boundary conditions of Table 1 give rise to log-squared stress singularities. Fields in these instances may be obtained from Sinclair (1998a, b).

Finally, re (9*a*) alone as requirements for logarithmic stress singularities: requirements (9*a*) are not necessary. With one exception for I′ or IV–I or IV, all of the configurations with logarithmic singularities under inhomogeneous boundary conditions in Table 3(*b*) do not comply with (9*a*). Nor are requirements (9*a*) sufficient: There are instances for I or IV–I or IV and III–III where (9*a*) is complied with but there are no logarithmic stress fields.

[4] It is difficult to see how the rank could be less than 2 in any further problems but, if this did occur, necessary and sufficient requirements are given in Dempsey and Sinclair (1979).

References

Dempsey, J. P., 1978, "On the Stress Singularities in the Plane Elasticity of the Composite Wedge," Doctoral Dissertation, University of Auckland, Auckland, New Zealand.

Dempsey, J. P., 1981, "The Wedge Subjected to Tractions: a Paradox Resolved," *Journal of Elasticity,* Vol. 11, pp. 1–10.

Dempsey, J. P., 1995, "Power-Logarithmic Stress Singularities at Bi-Material Corners and Interface Cracks," *Journal of Adhesion Science and Technology,* Vol. 9, pp. 253–265.

Dempsey, J. P., and Sinclair, G. B., 1979, "On the Stress Singularities in the Plane Elasticity of the Composite Wedge," *Journal of Elasticity,* Vol. 9, pp. 373–391.

Gdoutos, E. E., and Theocaris, P. S., 1975, "Stress Concentrations at the Apex of a Plane Indentor Acting on an Elastic Half Plane," ASME JOURNAL OF APPLIED MECHANICS, Vol. 42, pp. 688–692.

Kolossoff, G., 1914, "On Some Properties of the Plane Problem of Elasticity Theory," *Zeitschrift für Matematik und Physik,* Vol. 62, pp. 384–409 (in German).

Murakami, Y., 1992, "Stress Singularity for Notch at Bimaterial Interface," *Stress Intensity Factors Handbook,* Vol. 3, Pergamon Press, Oxford, UK, Chapter 18.

Sinclair, G. B., 1996, "On the Influence of Cohesive Stress-Separation Laws on Elastic Stress Singularities," *Journal of Elasticity,* Vol. 44, pp. 203–221.

Sinclair, G. B., 1998a, "Further Paradoxes in Generalized Levy Problems," *Journal of Elasticity,* Vol. 50, pp. 253–259.

Sinclair, G. B., 1998b, "Analysis of Logarithmic Stress Singularities Resulting from Various Boundary Conditions in Angular Elastic Plates in Extension," Report SM 98-3, Department of Mechanical Engineering, Carnegie Mellon University, Pittsburgh, PA.

Sneddon, I. N., 1951, *Fourier Transforms,* McGraw-Hill, New York.

Ting, T. C. T., 1984, "The Wedge Subjected to Tractions: A Paradox Reexamined," *Journal of Elasticity,* Vol. 14, pp. 235–247.

Williams, M. L., 1952, "Stress Singularities Resulting from Various Boundary Conditions in Angular Corners of Plates in Extension," ASME JOURNAL OF APPLIED MECHANICS, Vol. 19, pp. 526–528.

The Elastic and Electric Fields for Elliptical Hertzian Contact for Transversely Isotropic Piezoelectric Bodies

H. J. Ding,[1] P. F. Hou,[1] and F. L. Guo[1]

1 Introduction

The elliptical contact is extremely important since it often arises in engineering applications. The stress field generated by elliptical contact for isotropic elastic materials has been thoroughly investigated. Haines and Ollerton (1963) studied elliptical contact stress under radial and tangential load. The evaluation of the elastic field throughout the contacting bodies for elliptical Hertzian contact has been obtained by Bryant and Keer (1982), and their solutions included slip and stick zones. Sackfield and Hills (1983a, b) also evaluated the stress field for elliptical Hertzian contact under normal loading and shear loading, and more concise formulas for the stress field are given by Sackfield et al. (1993).

Concerning the elliptical Hertzian contact for anisotropic materials, Willis (1966, 1967) reduced the problem to the evaluation of contour integrals using Fourier transforms and presented some explicit formulae on the surface of half-space for transversely isotropic media. Hanson and Puja (1997) obtained the full elastic field resulting from elliptical Hertzian contact of transversely isotropic bodies under normal and shear loading. Gladwell (1980) and

[1] Department of Engineering, Zhejiang University, Hangzhou 310027, P. R. China.

Contributed by the Applied Mechanics Division of THE AMERICAN SOCIETY OF MECHANICAL ENGINEERS for publication in the ASME JOURNAL OF APPLIED MECHANICS. Manuscript received by the ASME Applied Mechanics Division, June 28, 1998; final revision, Jan. 20, 1999. Associate Technical Editor: M.-J. Pindera.

$$\kappa(\kappa - 1)^2 + 4\kappa \cos 2\bar{\phi}_\kappa = (3\kappa - 1)\frac{\sin 2\bar{\phi}_\kappa}{\bar{\phi}_\kappa}. \quad (17)$$

It is understood in Table 3(*a*) that κ is constrained to lie within the physically applicable range, $1 \leq \kappa \leq 3$, in addition to any other constraints placed upon it. Some actual values of ϕ, κ, and f are: for III–III, $\phi = 170$ deg, $\kappa = 1.055, f = 5.67$ and $\phi = 355$ deg, $\kappa = 1.013, f = 11.43$; for I or IV–II, $\phi = 101.2$ deg, $\kappa = 2.848$ and $\phi = 274.0$ deg, $\kappa = 2.980$; for I or IV–III and $\kappa = 2$, $\phi =$ 137.4 deg, 202.7 deg, 324.7 deg with $f = 1.09, -2.39, 1.41$, respectively; and for II–III and $\kappa = 2$, $\phi = 119.7$ deg, 227.7 deg, 304.5 deg with $f = -0.57, 0.91, -0.69$, respectively.

Local fields containing logarithmic stress singularities for all the configurations listed in Table 3 can be obtained from Sinclair (1998b). For II–III when $\kappa = 1$ and $f = 0$, fields are also available from Dempsey (1978).

In the analysis of all of the configurations in Table 3(*a*), the ranks of the coefficient matrices involved never drop below two. Dempsey and Sinclair (1979) then has that (9*a*), (9*b*) are necessary requirements.[4] Indeed, all of the requirements in (9) are complied with by all of the log-singular configurations identified in Table 3. Moreover, when situations arose during analysis in which some of the requirements in (9) were complied with but others not, no logarithmic stress singularities were found.

Configurations which have logarithmic stress singularities when boundary conditions are inhomogeneous are listed in Table 3(*b*). Herein ϕ_*, ϕ_κ, $\bar{\phi}_\kappa$ remain as in (15), (16), (17), respectively, and κ continues to be constrained to the physical range. For the representative value of $\kappa = 2$, actual vertex angles for I′ or IV–II are $\phi = 60$ deg, 120 deg, 240 deg, 300 deg.

For I′, II′, and III′, only one plate edge needs to have these inhomogeneous conditions in order to realize configurations which can be superimposed to produce any inhomogeneous loading on both edges (on occasion this requires adding a rigid body rotation). Furthermore, the homogeneous cohesive-law conditions IV share the same logarithmically singular configurations as the inhomogeneous uniform-traction conditions I′. This is because IV can admit rigid-body translations which in turn produce uniform tractions.

Sources for the logarithmic stress fields for the configurations of Table 3(*b*) are: for I′ or IV–I or IV and $\phi = \pi$, Kolossoff (1914); for I′ or IV–I or IV and $\phi = \phi_*, 2\pi$, Dempsey (1981); for II′–II, Sinclair (1998b); for III′–III and $\phi = \pi, f = 0$, Sneddon (1951); for all other III′–III, Sinclair (1998b); for I′ or IV–II, Sinclair (1998a); and for both I′ or IV–III and II′–III, Sinclair (1998b).

The requirements in (12) and (14) are not established as necessary and sufficient for logarithmic stress singularities with inhomogeneous boundary conditions. However, for all of the configurations identified as having logarithmic singularities in Table 3(*b*), one or other of (12) or (14) is complied within its entirety. Moreover, no configurations were encountered during the course of analysis for which (12) or (14) was complied with and there was no logarithmic singularity.

With the exception of the second configuration for III–III, all of the configurations of Table 3(*a*) under the *inhomogeneous* boundary conditions of Table 1 give rise to log-squared stress singularities. Fields in these instances may be obtained from Sinclair (1998a, b).

Finally, re (9*a*) alone as requirements for logarithmic stress singularities: requirements (9*a*) are not necessary. With one exception for I′ or IV–I or IV, all of the configurations with logarithmic singularities under inhomogeneous boundary conditions in Table 3(*b*) do not comply with (9*a*). Nor are requirements (9*a*) sufficient: There are instances for I or IV–I or IV and III–III where (9*a*) is complied with but there are no logarithmic stress fields.

[4] It is difficult to see how the rank could be less than 2 in any further problems but, if this did occur, necessary and sufficient requirements are given in Dempsey and Sinclair (1979).

References

Dempsey, J. P., 1978, "On the Stress Singularities in the Plane Elasticity of the Composite Wedge," Doctoral Dissertation, University of Auckland, Auckland, New Zealand.

Dempsey, J. P., 1981, "The Wedge Subjected to Tractions: a Paradox Resolved," *Journal of Elasticity,* Vol. 11, pp. 1–10.

Dempsey, J. P., 1995, "Power-Logarithmic Stress Singularities at Bi-Material Corners and Interface Cracks," *Journal of Adhesion Science and Technology,* Vol. 9, pp. 253–265.

Dempsey, J. P., and Sinclair, G. B., 1979, "On the Stress Singularities in the Plane Elasticity of the Composite Wedge," *Journal of Elasticity,* Vol. 9, pp. 373–391.

Gdoutos, E. E., and Theocaris, P. S., 1975, "Stress Concentrations at the Apex of a Plane Indentor Acting on an Elastic Half Plane," ASME JOURNAL OF APPLIED MECHANICS, Vol. 42, pp. 688–692.

Kolossoff, G., 1914, "On Some Properties of the Plane Problem of Elasticity Theory," *Zeitschrift für Matematik und Physik,* Vol. 62, pp. 384–409 (in German).

Murakami, Y., 1992, "Stress Singularity for Notch at Bimaterial Interface," *Stress Intensity Factors Handbook,* Vol. 3, Pergamon Press, Oxford, UK, Chapter 18.

Sinclair, G. B., 1996, "On the Influence of Cohesive Stress-Separation Laws on Elastic Stress Singularities," *Journal of Elasticity,* Vol. 44, pp. 203–221.

Sinclair, G. B., 1998a, "Further Paradoxes in Generalized Levy Problems," *Journal of Elasticity,* Vol. 50, pp. 253–259.

Sinclair, G. B., 1998b, "Analysis of Logarithmic Stress Singularities Resulting from Various Boundary Conditions in Angular Elastic Plates in Extension," Report SM 98-3, Department of Mechanical Engineering, Carnegie Mellon University, Pittsburgh, PA.

Sneddon, I. N., 1951, *Fourier Transforms,* McGraw-Hill, New York.

Ting, T. C. T., 1984, "The Wedge Subjected to Tractions: A Paradox Reexamined," *Journal of Elasticity,* Vol. 14, pp. 235–247.

Williams, M. L., 1952, "Stress Singularities Resulting from Various Boundary Conditions in Angular Corners of Plates in Extension," ASME JOURNAL OF APPLIED MECHANICS, Vol. 19, pp. 526–528.

The Elastic and Electric Fields for Elliptical Hertzian Contact for Transversely Isotropic Piezoelectric Bodies

H. J. Ding,[1] P. F. Hou,[1] and F. L. Guo[1]

1 Introduction

The elliptical contact is extremely important since it often arises in engineering applications. The stress field generated by elliptical contact for isotropic elastic materials has been thoroughly investigated. Haines and Ollerton (1963) studied elliptical contact stress under radial and tangential load. The evaluation of the elastic field throughout the contacting bodies for elliptical Hertzian contact has been obtained by Bryant and Keer (1982), and their solutions included slip and stick zones. Sackfield and Hills (1983a, b) also evaluated the stress field for elliptical Hertzian contact under normal loading and shear loading, and more concise formulas for the stress field are given by Sackfield et al. (1993).

Concerning the elliptical Hertzian contact for anisotropic materials, Willis (1966, 1967) reduced the problem to the evaluation of contour integrals using Fourier transforms and presented some explicit formulae on the surface of half-space for transversely isotropic media. Hanson and Puja (1997) obtained the full elastic field resulting from elliptical Hertzian contact of transversely isotropic bodies under normal and shear loading. Gladwell (1980) and

[1] Department of Engineering, Zhejiang University, Hangzhou 310027, P. R. China.

Contributed by the Applied Mechanics Division of THE AMERICAN SOCIETY OF MECHANICAL ENGINEERS for publication in the ASME JOURNAL OF APPLIED MECHANICS. Manuscript received by the ASME Applied Mechanics Division, June 28, 1998; final revision, Jan. 20, 1999. Associate Technical Editor: M.-J. Pindera.

Johnson (1985) systematically reviewed the history and literatures of the contact problems of isotropic and anisotropic elastic media.

Piezoelectric ceramics of 6-mm crystal symmetry are transversely isotropic piezoelectric materials which have found widespread applications because of their excellent piezoelectric properties. Sosa and Castro (1994) obtained analytic solutions for point force and point charge acting on an orthotropic piezoelectric half-plane through a state-space methodology in conjunction with the Fourier transform technique. Wang and Zheng (1995) gave analytic solutions for a concentrated lateral shear force acting on a transversely isotropic piezoelectric half-space using Hankel transforms. Ding et al. (1996) gave solutions for point force and point charge acting on a transversely isotropic piezoelectric half-space, called extended Boussinesq and Cerruti solutions by the authors, using Fourier transforms. All of the above solutions are derived by transform methods and their final expressions are relatively tedious and complex. Therefore, Ding et al. (1998) obtained the extended Boussinesq and Cerruti solutions in terms of elementary functions. In addition, Fan et al. (1996) studied the two-dimensional contact on a piezoelectric half-plane using Stroh's formalism, and gave the solutions for loads acting on the boundary of anisotropic piezoelectric half-plane.

The potential theory method has been developed by Fabrikant (1989, 1991) as an efficient method to analyze various mixed boundary value problems in elasticity. In this paper, we further generalize the potential theory method to analyze corresponding mixed boundary value problems in piezoelectricity, and obtain the full elastic and electric fields for elliptical Hertzian contact of transversely isotropic piezoelectric bodies in smooth and frictional cases by employing a methodology similar to that of Hanson and Puja (1997), i.e., first evaluating the displacement functions and then differentiating. The displacement functions can be obtained by integrating the extended Boussinesq and Cerruti solutions in transversely isotropic piezoelectric half-space (Ding et al., 1998) in the contact region.

2 General Solution for the Transversely Isotropic Piezoelectric Media

Introduce Cartesian coordinate $Oxyz$ where the z-axis is perpendicular to the isotropic plane. For convenience, the following notations are introduced:

$$U = u + iv, \quad w_1 = w, \; w_2 = \Phi, \quad \sigma_1 = \sigma_x + \sigma_y,$$

$$\sigma_2 = \sigma_x - \sigma_y + 2i\tau_{xy}, \quad \sigma_{z1} = \sigma_z, \; \sigma_{z2} = D_z,$$

$$\tau_{z1} = \tau_{xz} + i\tau_{yz}, \quad \tau_{z2} = D_x + iD_y \tag{1}$$

where u, v, w are displacement components, Φ is the electric potential, σ_x, σ_y, σ_z, τ_{xy}, τ_{xz}, and τ_{yz} are stress components, and D_x, D_y, and D_z are electric displacement components.

In the case of distinct characteristic roots, $s_1 \neq s_2 \neq s_3 \neq s_1$, Ding et al. (1998) gave a concise general solution in terms of four displacement functions F_j ($j = 0, 1, 2, 3$) for transversely isotropic piezoelectric media as follows:

$$U = \Lambda(iF_0 + \sum_{j=1}^{3} F_j), \quad w_m = \sum_{j=1}^{3} s_j k_{mj} \frac{\partial F_j}{\partial z_j},$$

$$\sigma_1 = 2\sum_{j=1}^{3} (m_j - c_{66}) \frac{\partial^2 F_j}{\partial z_j^2}, \quad \sigma_2 = 2c_{66}\Lambda^2(iF_0 + \sum_{j=1}^{3} F_j),$$

$$\sigma_{zm} = \sum_{j=1}^{3} \omega_{mj} \frac{\partial^2 F_j}{\partial z_j^2}, \quad \tau_{zm} = \Lambda\left(s_0\rho_m i \frac{\partial F_0}{\partial z_0} + \sum_{j=1}^{3} s_j\omega_{mj} \frac{\partial F_j}{\partial z_j}\right),$$

$$(m = 1, 2) \tag{2}$$

where $z_j = s_j z$ ($j = 0, 1, 2, 3$), $s_0 = \sqrt{c_{66}/c_{44}}$ and s_j ($j = 1, 2, 3$) are the three characteristic roots of a sixth-order equation defined in Ding et al. (1996) which satisfy the condition $\mathrm{Re}(s_j) > 0$. k_{1j} and k_{2j} are constants dependent on material constants and characteristic roots, and the displacement functions F_j ($j = 0, 1, 2, 3$) satisfy the following equation:

$$\left(\frac{\partial^2}{\partial x^2} + \frac{\partial^2}{\partial y^2} + \frac{\partial^2}{\partial z_j^2}\right) F_j = 0, \quad (j = 0, 1, 2, 3). \tag{3}$$

In addition,

$$\omega_{1j} = c_{44}(1 + k_{1j}) + e_{15}k_{2j}, \quad \omega_{2j} = e_{15}(1 + k_{1j}) - \epsilon_{11}k_{2j},$$

$$m_j = 2c_{66} - \omega_{1j}s_j^2, \; \rho_1 = c_{44}, \; \rho_2 = e_{15}, \; \Lambda = \partial/\partial x + i\partial/\partial y$$

$$(j = 1, 2, 3) \tag{4}$$

and all the above c_{ij}, e_{ij}, and ϵ_{ij} are the elastic, piezoelectric, and dielectric constants, respectively.

3 Extended Boussinesq and Cerruti Solutions in Transversely Isotropic Piezoelectric Half-Space

Cylindrical coordinates (ρ, ϕ, z) are adopted with the z-axis perpendicular to the isotropic plane. The point charge Q_0 and three point forces P_x, P_y, and P_0 with their positive directions the same as the x, y, and z-axes act at an arbitrary point $M(\rho_0, \phi_0, 0)$ on the surface of a transversely isotropic piezoelectric half-space ($z \geq 0$). Ding et al. (1998) obtained the displacement functions as follows:

$$F_0 = iG_0(P\bar{\Lambda} - \bar{P}\Lambda)\chi(z_0)$$

$$F_j = G_j(P\bar{\Lambda} + \bar{P}\Lambda)\chi(z_j) + (P_0\delta_j + Q_0\lambda_j)R_j^*$$

$$(j = 1, 2, 3) \tag{5}$$

where

$$R_j^* = R_j + z_j, \; R_j = \sqrt{\rho^2 + \rho_0^2 - 2\rho\rho_0\cos(\phi - \phi_0) + z_j^2}$$

$$\chi(z_j) = z_j \ln R_j^* - R_j, \quad P = P_x + iP_y \tag{6}$$

and δ_j, λ_j ($j = 1, 2, 3$) and G_j ($j = 0, 1, 2, 3$) are defined in Ding et al. (1998: Section 3). $\bar{P}$ and $\bar{\Lambda}$ are the complex conjugates of P and Λ, respectively.

4 The Elastic and Electric Fields for Elliptical Contact

Consider that a body ① (which may or may not be piezoelectric body) and a piezoelectric body ② are in contact at the point O before forces and charges are applied. Regarding O as the origin, we introduce Cartesian coordinates (x, y, z) as shown in Fig. 1 in Hanson and Puja (1997), in addition to the cylinder coordinates (ρ, ϕ, z). We further consider that there are a pair of forces P_z and a pair of charges $+Q$ and $-Q$ acting on the common normal line in body ① and body ②, respectively. The forces and charges are distant enough from the contact point O. Because of deformation, a contact region S forms around the initial contact point O.

Assume that

(1) the shape of contact region S is ellipse $x^2/a^2 + y^2/b^2 \leq 1$ where $a \geq b$, and its dimensions are sufficiently small compared with those of the bodies ① and ②, so we can regard them as two half-spaces.

(2) there are no free charges in the contact region; if there is also no friction in the contact region, we call such contact "smooth".

(3) the normal electric displacement on the surface of bodies ① and ② is nonzero only inside the contact region S. The contact pressure $p(\rho, \phi)$ and electric displacement $d(\rho, \phi)$ inside the contact region are distributed as follows:

$$p(\rho, \phi) = \frac{3P_z}{2\pi ab}\sqrt{1 - \frac{\rho^2\cos^2\phi}{a^2} - \frac{\rho^2\sin^2\phi}{b^2}},$$

$$d(\rho, \phi) = \frac{3Q}{2\pi ab}\sqrt{1 - \frac{\rho^2\cos^2\phi}{a^2} - \frac{\rho^2\sin^2\phi}{b^2}},$$
$$0 \le \rho \le C(\phi), \quad 0 \le \phi < 2\pi, \tag{7}$$

where $C(\phi)$ is the boundary of the contact region. For the elliptical contact region, $C(\phi)$ has the following form:

$$C(\phi) = ab/\sqrt{a^2\sin^2\phi + b^2\cos^2\phi}. \tag{8}$$

The determination of contact parameters such as a and b, etc., are showed in Ding et al. (1998: Section 4).

4.1 Analytic Solutions for Smooth Contact. Substituting $P_0 = p(\rho_0, \phi_0)\rho_0 d\rho_0 d\phi_0$ and $Q_0 = d(\rho_0, \phi_0)\rho_0 d\rho_0 d\phi_0$ into Eq. (5) and integrating the result over $0 \le \rho_0 \le C(\phi_0)$, $0 \le \phi_0 \le 2\pi$, the displacement functions become

$$F_0(\rho, \phi, z) = 0,$$
$$F_j(\rho, \phi, z) = \frac{3(P_z\delta_j + Q\lambda_j)}{2\pi ab}\psi(\rho, \phi, z_j), \quad (j = 1, 2, 3) \tag{9}$$

where

$$\psi(\rho, \phi, z_j) = \int_0^{2\pi}\int_0^{C(\phi_0)}\sqrt{1 - \frac{\rho_0^2\cos^2\phi_0}{a^2} - \frac{\rho_0^2\sin^2\phi_0}{b^2}} \times \ln R_j^*\rho_0 d\rho_0 d\phi_0, \tag{10}$$

where R_j^* is defined in Eq. (6).

Substituting Eq. (9) into Eq. (2) and using the partial derivatives of $\psi(r, \theta, z_j)$ given by Hanson and Puja (1997), we obtain the elastic and electric fields as follows:

$$U = -\frac{3}{a^3}\sum_{j=1}^{3}(P_z\delta_j + Q\lambda_j) \times \{x[z_j\psi_1(\xi_j) - aI_{11}] + iy[z_j\psi_2(\xi_j) - aI_{12}]\},$$

$$w_m = \frac{3}{2a^3}\sum_{j=1}^{3}(P_z\delta_j + Q\lambda_j)s_j k_{mj} \times \{a^2F(\varphi_j, e) - x^2\psi_1(\xi_j) - y^2\psi_2(\xi_j) - z_j^2\psi_3(\xi_j)\},$$

$$\sigma_1 = -\frac{6}{a^3}\sum_{j=1}^{3}(P_z\delta_j + Q\lambda_j)(m_j - c_{66})z_j\psi_3(\xi_j),$$

$$\sigma_2 = -\frac{6c_{66}}{a^4}\sum_{j=1}^{3}(P_z\delta_j + Q\lambda_j)\{az_j[\psi_1(\xi_j) - \psi_2(\xi_j)] + x^2I_8 - y^2I_3 + a^2(I_{12} - I_{11}) + i2xyI_4\},$$

$$\sigma_{zm} = -\frac{3}{a^3}\sum_{j=1}^{3}(P_z\delta_j + Q\lambda_j)\omega_{mj}z_j\psi_3(\xi_j),$$

$$\tau_{zm} = -\frac{3}{a^3}\sum_{j=1}^{3}(P_z\delta_j + Q\lambda_j)s_j\omega_{mj}[x\psi_1(\xi_j) + iy\psi_2(\xi_j)] \tag{11}$$

where $e = \sqrt{1 - b^2/a^2}$ is the eccentricity of elliptical contact region; ξ_j $(j = 1, 2, 3)$ are the complex elliptical coordinates which can be obtained by replacing z with z_j in Eq. (2) in Hanson and Puja (1997) and which satisfy the condition $1 \le \mathrm{Re}(\xi_j^2) < \infty$; $F(\varphi_j, e)$, $(j = 1, 2, 3)$ are the incomplete elliptic integrals of the first kind; φ_j $(j = 1, 2, 3)$, ψ_k $(k = 1, 2, 3)$, and I_{11}, I_{12}, I_3, I_4, I_8 are given in Appendix A in Hanson and Puja (1997).

4.2 Analytic Solutions for Friction. When bodies ① and ② are also subjected to the tangential loading $T = T_x + iT_y$, which causes slip at the contacting surfaces, we assume that the sliding friction within the contact region can be determined by Coulomb friction law. Consequently, substituting the following equation into Eq. (5)

$$P = \frac{3P_z f}{2\pi ab}\sqrt{1 - \frac{\rho_0^2\cos^2\phi_0}{a^2} - \frac{\rho_0^2\sin^2\phi_0}{b^2}}\,\rho_0 d\rho_0 d\phi_0, \qquad f = f_x + if_y \tag{12}$$

and integrating the result over $0 \le \rho_0 \le C(\phi_0)$, $0 \le \phi_0 \le 2\pi$, the displacement functions become

$$F_0(\rho, \phi, z) = i\frac{3P_z G_0}{2\pi ab}(f\bar{\Lambda} - \bar{f}\Lambda)[z_0\psi(\rho, \phi, z_0) - \Psi(\rho, \phi, z_0)],$$

$$F_j(\rho, \phi, z) = \frac{3P_z G_j}{2\pi ab}(f\bar{\Lambda} + \bar{f}\Lambda)[z_j\psi(\rho, \phi, z_j) - \Psi(\rho, \phi, z_j)] \tag{13}$$

where $\psi(\rho, \phi, z_j)$ is expressed in Eq. (10) and $\Psi(\rho, \phi, z_j)$ is defined as

$$\Psi(\rho, \phi, z_j) = \int_0^{2\pi}\int_0^{C(\phi_0)}\sqrt{1 - \frac{\rho_0^2\cos^2\phi_0}{a^2} - \frac{\rho_0^2\sin^2\phi_0}{b^2}} \times R_j\rho_0 d\rho_0 d\phi_0 \tag{14}$$

where R_j are expressed in Eq. (6). Substituting Eq. (13) into Eq. (2) and using the partial derivatives of $\psi(r, \theta, z_j)$ and $\Psi(\rho, \phi, z_j)$ given by Hanson and Puja (1997), we obtain the elastic and electric fields as follows:

$$U = \frac{3P_z}{2a^4}\sum_{j=1}^{3}G_j \times \{-fa[a^2F(\varphi_j, e) - x^2\psi_1(\xi_j) - y^2\psi_2(\xi_j) - z_j^2\psi_3(\xi_j)] + \bar{f}[a(a^2 - z_j^2)\psi_1(\xi_j) + a[z_j^2 - a^2(1 - e^2)]\psi_2(\xi_j) - 3ay^2I_1 + a(y^2 - x^2)I_2 + 2y^2z_jI_3 - 2x^2z_jI_8 + 3ax^2I_9 + 2a^2z_j(I_{11} - I_{12}) + i4xy(aI_2 - z_jI_4)]\} - \frac{3P_z}{2a^4}G_0 \times \{-fa[a^2F(\varphi_0, e) - x^2\psi_1(\xi_0) - y^2\psi_2(\xi_0) - z_0^2\psi_3(\xi_0)] - \bar{f}[a(a^2 - z_0^2)\psi_1(\xi_0) + a[z_0^2 - a^2(1 - e^2)]\psi_2(\xi_0) - 3ay^2I_1 + a(y^2 - x^2)I_2 + 2y^2z_0I_3 - 2x^2z_0I_8 + 3ax^2I_9 + 2a^2z_0(I_{11} - I_{12}) + i4xy(aI_2 - z_0I_4)]\},$$

$$w_m = -\frac{6P_z}{a^3}\sum_{j=1}^{3}G_j s_j k_{mj} \times \{xf_x[z_j\psi_1(\xi_j) - aI_{11}] + yf_y[z_j\psi_2(\xi_j) - aI_{12}]\},$$

$$\sigma_1 = \frac{12P_z}{a^3}\sum_{j=1}^{3}G_j(m_j - c_{66})[xf_x\psi_1(\xi_j) + yf_y\psi_2(\xi_j)],$$

$$\sigma_2 = \frac{6c_{66}P_z}{a^4}\sum_{j=1}^{3}G_j\Big\{fa[x\psi_1(\xi_j) + iy\psi_2(\xi_j)] + \bar{f}\Big[\frac{x}{a}\{3a^2(I_9 - I_2) + 3az_j(I_4 - I_8) - x^2I_{10}$$

$$+ 3y^2I_6\} + i\frac{y}{a}\{3a^2(I_2 - I_1) + 3az_j(I_3 - I_4) - 3x^2I_7 + y^2I_5\}\Big]\Big\} - \frac{6c_{66}P_z}{a^4}G_0\Big\{fa[x\psi_1(\xi_0) + iy\psi_2(\xi_0)] - \bar{f}\Big[\frac{x}{a}\{3a^2(I_9 - I_2) + 3az_0(I_4 - I_8) - x^2I_{10} + 3y^2I_6\} + i\frac{y}{a}\{3a^2(I_2 - I_1) + 3az_0(I_3 - I_4) - 3x^2I_7 + y^2I_5\}\Big]\Big\},$$

$$\sigma_{zm} = \frac{6P_z}{a^3}\sum_{j=1}^{3} G_j\omega_{mj}[xf_x\psi_1(\xi_j) + yf_y\psi_2(\xi_j)],$$

$$\tau_{zm} = \frac{3P_z}{a^4}\sum_{j=1}^{3} G_js_j\omega_{mj}\{faz_j\psi_3(\xi_j) - \bar{f}[az_j\{\psi_1(\xi_j) - \psi_2(\xi_j)\} - a^2(I_{11} - I_{12}) + x^2I_8 - y^2I_3 + i2xyI_4]\} - \frac{3P_z}{a^4}G_0s_0\rho_m\{faz_0\psi_3(\xi_0) + \bar{f}[az_0\{\psi_1(\xi_0) - \psi_2(\xi_0)\} - a^2(I_{11} - I_{12}) + x^2I_8 - y^2I_3 + i2xyI_4]\} \quad (15)$$

where e, ξ_j ($j = 0, 1, 2, 3$) and $F(\varphi_j, e)$ ($j = 0, 1, 2, 3$) are the same as those in Eq. (11); ψ_k ($k = 1, 2, 3$), I_{11}, I_{12}, and I_l ($l = 1, 2, 3, \ldots 12$) are listed in Appendices A and B in Hanson and Puja (1997).

Acknowledgment

This work is supported by the National Natural Science Foundation of China (19872060) and the Research Laboratory of Failure Mechanics (FML) of the State Education Commission of China.

References

Bryant, M. D., and Keer, L. M., 1982, "Rough Contact Between Elastically and Geometrically Identical Curved Bodies," ASME JOURNAL OF APPLIED MECHANICS, Vol. 49, pp. 345–352.

Ding, H. J., Chen, B., and Liang, J., 1996, "General Solution for Coupled Equations for Piezoelectric Media," *Int. J. Solids Structures,* Vol. 33, pp. 2283–2298.

Ding, H. J., Hou, P. F., and Guo, F. L., 1998, "The Elastic and Electric Fields for Three-Dimensional Contact for Transversely Isotropic Piezoelectric Materials," *Int. J. Solids Structures,* accepted for publication.

Fabrikant, V. I., 1989, *Applications of Potential Theory in Mechanics, Selection of New Results,* Kluwer Academic Publishers, Dordrecht, The Netherlands.

Fabrikant, V. I., 1991, *Mixed Boundary Value Problems of Potential Theory and Their Applications in Engineering,* Kluwer Academic Publishers, Dordrecht, The Netherlands.

Fan, H., Sze, K. Y., and Yang, W., 1996, "Two-Dimensional Contact on a Piezoelectric Half-Space," *Int. J. Solids Structures,* Vol. 33, pp. 1305–1315.

Gladwell, G. M. L., 1980, *Contact Problems in the Classical Theory of Elasticity,* Sijthoff & Noordhoff, Alpen aan den Rijn, The Netherlands.

Haines, D. J., and Ollerton, E., 1963, "Contact Stress Distributions on Elliptical Contact Surfaces Subjected to Radial and Tangential Forces," *Proc. Instn. Mech. Engrs.,* Vol. 177, pp. 95–114.

Hanson, M. T., and Puja, I. W., 1997, "The Elastic Field Resulting From Elliptical Hertzian Contact of Transversely Isotropic Bodies: Closed-Form Solutions for Normal and Shear Loading," ASME JOURNAL OF APPLIED MECHANICS, Vol. 64, pp. 457–465.

Johnson, K. L., 1985, *Contact Mechanics,* Cambridge University Press, Cambridge, UK.

Sackfield, A., and Hills, D. A., 1983a, "Some useful Results in the Classical Hertz Contact Problem," *Journal of Strain Analysis,* Vol. 18, pp. 101–105.

Sackfield, A., and Hills, D. A., 1983b, "Some useful Results in Tangentially Loaded Hertzian Contact Problem," *Journal of Strain Analysis,* Vol. 18, pp. 107–110.

Sackfield, A., Hills, D. A., and Nowell, D., 1993, "The Stress Field Induced by a General Elliptical Hertzian Contact," ASME *Journal of Tribology,* Vol. 115, pp. 705–706.

Sosa, H. A., and Castro, M. A., 1994, "On Concentrated Loads at the Boundary of a Piezoelectric Half-Plane," *J. Mech. Phys. Solids,* Vol. 42, pp. 1105–1122.

Wang, Z., and Zheng, B., 1995, "The General Solution of Three-Dimensional Problems in Piezoelectric Media," *Int. J. Solids Structures,* Vol. 32, pp. 105–115.

Willis, J. R., 1966, "Hertzian Contact of Anisotropic Bodies," *J. Mechanics and Physics Solids,* Vol. 14, pp. 163–176.

Willis, J. R., 1967, "Boussinesq Problem for an Anisotropic Half-space," *J. Mechanics and Physics Solids,* Vol. 15, pp. 331–339.

Exact Eshelby Tensor for a Dynamic Circular Cylindrical Inclusion

Z.-Q. Cheng[1] and R. C. Batra[2]

1 Introduction

This work is motivated by Mikata and Nemat-Nasser's (1990) study of dynamic transformation toughening of ceramics in which a typical dynamic problem of a spherical inclusion was solved. Mikata and Nemat-Nasser (1990, 1991), Mikata (1993), and Cheng and He (1996) have obtained exact analytic solutions for a dynamic spherical inclusion embedded in an infinite linear elastic and isotropic medium. However, the corresponding dynamic problem of a circular cylindrical inclusion has not been studied. Mura (1988) and Mura et al. (1996) have reviewed the literature on inclusion problems.

The time-harmonic elastic field caused by an infinitely long circular cylindrical inclusion is obtained in this paper, and a closed-form expression is derived for the dynamic Eshelby tensor. Unlike the static case, the Eshelby tensor for the dynamic problem is not uniform even at interior points within the circular cylinder. In the limit of quasi-static deformations the present solution reduces to Eshelby's results.

2 Analysis

Following Eshelby (1957, 1959) and Mura (1982), an inclusion is referred to a subset of a matrix that has a prescribed eigenstrain (or transformation strain) and has the same elastic properties as the matrix.

Consider the following time-harmonic eigenstrain

$$e^*_{kl}(\mathbf{x}, t) = e^{\Omega}_{kl}(\mathbf{x})\Lambda(\Omega)e^{-i\omega t},$$

$$\Lambda(\Omega) = \begin{cases} 1, & \mathbf{x} \in \Omega \\ 0, & \mathbf{x} \in R^3 - \Omega \end{cases} \quad (1)$$

where Ω is the region occupied by an inclusion that is embedded in an infinite (i.e., R^3) isotropic, linear elastic medium, and ω denotes an angular frequency. It is assumed that a time-harmonic eigenstrain will induce time-harmonic displacement, strain, and stress fields. Henceforth we omit the factor $\exp(-i\omega t)$. Also, a comma followed by a subscript i denotes a partial derivative with respect to the rectangular Cartesian coordinate x_i, a repeated index implies summation over the range of the index, Latin subscripts range over 1, 2, 3 and Greek subscripts over 1 and 2.

Equations for determining the displacement field in steady-state deformations of a linear elastic isotropic body are

$$\sigma_{ij,j} + \rho\omega^2u_i = 0, \quad \sigma_{ij} = C_{ijkl}[e_{kl} - e^{\Omega}_{kl}\Lambda(\Omega)],$$

[1] Associate Professor, Department of Modern Mechanics, University of Science and Technology of China, Hefei, Anhui 230026, P. R. China. Currently Visiting Research Associate, Virginia Polytechnic Institute and State University, Blacksburg, VA 24061.

[2] Clifton C. Garvin Professor, Department of Engineering Science and Mechanics, Virginia Polytechnic Institute and State University, Blacksburg, VA 24061. Fellow ASME.

Contributed by the Applied Mechanics Division of THE AMERICAN SOCIETY OF MECHANICAL ENGINEERS for publication in the ASME JOURNAL OF APPLIED MECHANICS. Manuscript received by the ASME Applied Mechanics Division, July 28, 1998; final revision, Feb. 2, 1999. Associate Technical Editor: V. K. Kinra.

$$+ 3y^2I_6\} + i\frac{y}{a}\{3a^2(I_2 - I_1) + 3az_j(I_3 - I_4) - 3x^2I_7 + y^2I_5\}\Big]\Big\} - \frac{6c_{66}P_z}{a^4}G_0\Big\{fa[x\psi_1(\xi_0) + iy\psi_2(\xi_0)] - \bar{f}\Big[\frac{x}{a}\{3a^2(I_9 - I_2) + 3az_0(I_4 - I_8) - x^2I_{10} + 3y^2I_6\} + i\frac{y}{a}\{3a^2(I_2 - I_1) + 3az_0(I_3 - I_4) - 3x^2I_7 + y^2I_5\}\Big]\Big\},$$

$$\sigma_{zm} = \frac{6P_z}{a^3}\sum_{j=1}^{3} G_j\omega_{mj}[xf_x\psi_1(\xi_j) + yf_y\psi_2(\xi_j)],$$

$$\tau_{zm} = \frac{3P_z}{a^4}\sum_{j=1}^{3} G_js_j\omega_{mj}\{faz_j\psi_3(\xi_j) - \bar{f}[az_j\{\psi_1(\xi_j) - \psi_2(\xi_j)\} - a^2(I_{11} - I_{12}) + x^2I_8 - y^2I_3 + i2xyI_4]\} - \frac{3P_z}{a^4}G_0s_0\rho_m\{faz_0\psi_3(\xi_0) + \bar{f}[az_0\{\psi_1(\xi_0) - \psi_2(\xi_0)\} - a^2(I_{11} - I_{12}) + x^2I_8 - y^2I_3 + i2xyI_4]\} \quad (15)$$

where e, ξ_j ($j = 0, 1, 2, 3$) and $F(\varphi_j, e)$ ($j = 0, 1, 2, 3$) are the same as those in Eq. (11); ψ_k ($k = 1, 2, 3$), I_{11}, I_{12}, and I_l ($l = 1, 2, 3, \ldots 12$) are listed in Appendices A and B in Hanson and Puja (1997).

Acknowledgment

This work is supported by the National Natural Science Foundation of China (19872060) and the Research Laboratory of Failure Mechanics (FML) of the State Education Commission of China.

References

Bryant, M. D., and Keer, L. M., 1982, "Rough Contact Between Elastically and Geometrically Identical Curved Bodies," ASME JOURNAL OF APPLIED MECHANICS, Vol. 49, pp. 345–352.

Ding, H. J., Chen, B., and Liang, J., 1996, "General Solution for Coupled Equations for Piezoelectric Media," *Int. J. Solids Structures,* Vol. 33, pp. 2283–2298.

Ding, H. J., Hou, P. F., and Guo, F. L., 1998, "The Elastic and Electric Fields for Three-Dimensional Contact for Transversely Isotropic Piezoelectric Materials," *Int. J. Solids Structures,* accepted for publication.

Fabrikant, V. I., 1989, *Applications of Potential Theory in Mechanics, Selection of New Results,* Kluwer Academic Publishers, Dordrecht, The Netherlands.

Fabrikant, V. I., 1991, *Mixed Boundary Value Problems of Potential Theory and Their Applications in Engineering,* Kluwer Academic Publishers, Dordrecht, The Netherlands.

Fan, H., Sze, K. Y., and Yang, W., 1996, "Two-Dimensional Contact on a Piezoelectric Half-Space," *Int. J. Solids Structures,* Vol. 33, pp. 1305–1315.

Gladwell, G. M. L., 1980, *Contact Problems in the Classical Theory of Elasticity,* Sijthoff & Noordhoff, Alpen aan den Rijn, The Netherlands.

Haines, D. J., and Ollerton, E., 1963, "Contact Stress Distributions on Elliptical Contact Surfaces Subjected to Radial and Tangential Forces," *Proc. Instn. Mech. Engrs.,* Vol. 177, pp. 95–114.

Hanson, M. T., and Puja, I. W., 1997, "The Elastic Field Resulting From Elliptical Hertzian Contact of Transversely Isotropic Bodies: Closed-Form Solutions for Normal and Shear Loading," ASME JOURNAL OF APPLIED MECHANICS, Vol. 64, pp. 457–465.

Johnson, K. L., 1985, *Contact Mechanics,* Cambridge University Press, Cambridge, UK.

Sackfield, A., and Hills, D. A., 1983a, "Some useful Results in the Classical Hertz Contact Problem," *Journal of Strain Analysis,* Vol. 18, pp. 101–105.

Sackfield, A., and Hills, D. A., 1983b, "Some useful Results in Tangentially Loaded Hertzian Contact Problem," *Journal of Strain Analysis,* Vol. 18, pp. 107–110.

Sackfield, A., Hills, D. A., and Nowell, D., 1993, "The Stress Field Induced by a General Elliptical Hertzian Contact," ASME *Journal of Tribology,* Vol. 115, pp. 705–706.

Sosa, H. A., and Castro, M. A., 1994, "On Concentrated Loads at the Boundary of a Piezoelectric Half-Plane," *J. Mech. Phys. Solids,* Vol. 42, pp. 1105–1122.

Wang, Z., and Zheng, B., 1995, "The General Solution of Three-Dimensional Problems in Piezoelectric Media," *Int. J. Solids Structures,* Vol. 32, pp. 105–115.

Willis, J. R., 1966, "Hertzian Contact of Anisotropic Bodies," *J. Mechanics and Physics Solids,* Vol. 14, pp. 163–176.

Willis, J. R., 1967, "Boussinesq Problem for an Anisotropic Half-space," *J. Mechanics and Physics Solids,* Vol. 15, pp. 331–339.

Exact Eshelby Tensor for a Dynamic Circular Cylindrical Inclusion

Z.-Q. Cheng[1] and R. C. Batra[2]

1 Introduction

This work is motivated by Mikata and Nemat-Nasser's (1990) study of dynamic transformation toughening of ceramics in which a typical dynamic problem of a spherical inclusion was solved. Mikata and Nemat-Nasser (1990, 1991), Mikata (1993), and Cheng and He (1996) have obtained exact analytic solutions for a dynamic spherical inclusion embedded in an infinite linear elastic and isotropic medium. However, the corresponding dynamic problem of a circular cylindrical inclusion has not been studied. Mura (1988) and Mura et al. (1996) have reviewed the literature on inclusion problems.

The time-harmonic elastic field caused by an infinitely long circular cylindrical inclusion is obtained in this paper, and a closed-form expression is derived for the dynamic Eshelby tensor. Unlike the static case, the Eshelby tensor for the dynamic problem is not uniform even at interior points within the circular cylinder. In the limit of quasi-static deformations the present solution reduces to Eshelby's results.

2 Analysis

Following Eshelby (1957, 1959) and Mura (1982), an inclusion is referred to a subset of a matrix that has a prescribed eigenstrain (or transformation strain) and has the same elastic properties as the matrix.

Consider the following time-harmonic eigenstrain

$$e^*_{kl}(\mathbf{x}, t) = e^{\Omega}_{kl}(\mathbf{x})\Lambda(\Omega)e^{-i\omega t},$$

$$\Lambda(\Omega) = \begin{cases} 1, & \mathbf{x} \in \Omega \\ 0, & \mathbf{x} \in R^3 - \Omega \end{cases} \quad (1)$$

where Ω is the region occupied by an inclusion that is embedded in an infinite (i.e., R^3) isotropic, linear elastic medium, and ω denotes an angular frequency. It is assumed that a time-harmonic eigenstrain will induce time-harmonic displacement, strain, and stress fields. Henceforth we omit the factor $\exp(-i\omega t)$. Also, a comma followed by a subscript i denotes a partial derivative with respect to the rectangular Cartesian coordinate x_i, a repeated index implies summation over the range of the index, Latin subscripts range over 1, 2, 3 and Greek subscripts over 1 and 2.

Equations for determining the displacement field in steady-state deformations of a linear elastic isotropic body are

$$\sigma_{ij,j} + \rho\omega^2u_i = 0, \quad \sigma_{ij} = C_{ijkl}[e_{kl} - e^{\Omega}_{kl}\Lambda(\Omega)],$$

[1] Associate Professor, Department of Modern Mechanics, University of Science and Technology of China, Hefei, Anhui 230026, P. R. China. Currently Visiting Research Associate, Virginia Polytechnic Institute and State University, Blacksburg, VA 24061.

[2] Clifton C. Garvin Professor, Department of Engineering Science and Mechanics, Virginia Polytechnic Institute and State University, Blacksburg, VA 24061. Fellow ASME.

Contributed by the Applied Mechanics Division of THE AMERICAN SOCIETY OF MECHANICAL ENGINEERS for publication in the ASME JOURNAL OF APPLIED MECHANICS. Manuscript received by the ASME Applied Mechanics Division, July 28, 1998; final revision, Feb. 2, 1999. Associate Technical Editor: V. K. Kinra.

$$e_{kl} = \tfrac{1}{2}(u_{k,l} + u_{l,k}), \tag{2}$$

where ρ is the mass density,

$$C_{ijkl} = \lambda\delta_{ij}\delta_{kl} + \mu(\delta_{ik}\delta_{jl} + \delta_{il}\delta_{jk}), \tag{3}$$

λ and μ the Lamé constants and δ_{ij} the Kronecker delta. The corresponding displacement field can be expressed as (Mura, 1982)

$$u_i(\mathbf{x}) = -\int_\Omega C_{jlmn} e^{\Omega}_{mn}(\mathbf{x}') g_{ij,l}(\mathbf{x} - \mathbf{x}')d\mathbf{x}', \tag{4}$$

where g_{ij} is the Green function defined by

$$g_{lm}(\mathbf{x} - \mathbf{x}') = \frac{1}{4\pi\rho\omega^2} \times \left[\beta^2\delta_{lm}\frac{e^{i\beta r}}{r} - \frac{\partial^2}{\partial x_l \partial x_m}\left(\frac{e^{i\alpha r}}{r} - \frac{e^{i\beta r}}{r}\right)\right], \tag{5}$$

$$r^2 = (x_k - x_k')(x_k - x_k'), \quad \alpha^2 = \frac{\rho\omega^2}{\lambda + 2\mu}, \quad \beta^2 = \frac{\rho\omega^2}{\mu}. \tag{6}$$

If $e^{\Omega}_{mn}(\mathbf{x})$ in Eq. (1) is constant over Ω, then the displacement and strain can be expressed as (Mikata and Nemat-Nasser, 1990)

$$u_i(\mathbf{x}) = J_{ikl}(\mathbf{x})e^{\Omega}_{kl}, \quad e_{ij}(\mathbf{x}) = M_{ijkl}(\mathbf{x})e^{\Omega}_{kl}, \tag{7}$$

for both inside and outside of the inclusion, where

$$M_{ijkl}(\mathbf{x}) = \tfrac{1}{2}[J_{ikl,j}(\mathbf{x}) + J_{jkl,i}(\mathbf{x})], \tag{8}$$

$$J_{ikl}(\mathbf{x}) = \frac{1}{4\pi\rho\omega^2}\{\lambda\delta_{kl}f_{,imm}(\mathbf{x}, \alpha) + 2\mu[f_{,ikl}(\mathbf{x}, \alpha) - f_{,ikl}(\mathbf{x}, \beta)] - \mu\beta^2[\delta_{ik}f_{,l}(\mathbf{x}, \beta) + \delta_{il}f_{,k}(\mathbf{x}, \beta)]\}, \tag{9}$$

$$f(\mathbf{x}, k) = \int_\Omega \frac{e^{ikr}}{r}d\mathbf{x}'. \tag{10}$$

Mikata and Nemat-Nasser (1990) called $M_{ijkl}(\mathbf{x})$ in Eq. (8) the dynamic Eshelby tensor. The expression in Eq. (9) slightly differs from that given by Mikata and Nemat-Nasser (1990) since we have used

$$f_{,imm}(\mathbf{x}, \beta) + \beta^2 f_{,i}(\mathbf{x}, \beta) = 0 \tag{11}$$

to simplify (9). For a spherical inclusion, Mikata and Nemat-Nasser (1990) evaluated the integral (10) in closed form and hence computed the exact dynamic Eshelby tensor. Here we evaluate this integral for an infinitely long circular cylindrical inclusion Ω: $x_1^2 + x_2^2 < a^2$ and $-\infty < x_3 < \infty$, and then find the corresponding Eshelby tensor. To do this, we recall the following formulas (Gradshteyn and Ryzhik, 1965).

(a) Integral formula.

$$\int_{-\infty}^{\infty}\frac{e^{ikr}}{r}dx_3' = i\pi H_0^{(1)}(kR), \tag{12}$$

$$R^2 = (x_\alpha - x_\alpha')(x_\alpha - x_\alpha') = z^2 + z'^2 - 2zz'\cos\theta, \tag{13}$$

$$z^2 = x_\alpha x_\alpha, \quad z'^2 = x_\alpha' x_\alpha', \quad \cos\theta = \frac{x_\alpha x_\alpha'}{zz'}. \tag{14}$$

(b) Addition theorem.

$H_0^{(1)}(kR)$

$$= \begin{cases} J_0(kz)H_0^{(1)}(kz') + 2\sum_{M=1}^{\infty} J_M(kz)H_M^{(1)}(kz')\cos M\theta, & (z < z') \\ J_0(kz')H_0^{(1)}(kz) + 2\sum_{M=1}^{\infty} J_M(kz')H_M^{(1)}(kz)\cos M\theta, & (z > z') \end{cases} \tag{15}$$

(c) Recurrence relations

$$\frac{d}{dz}[zJ_1(z)] = zJ_0(z), \quad \frac{d}{dz}[zH_1^{(1)}(z)] = zH_0^{(1)}(z). \tag{16}$$

Here $J_M(z)$ is the Bessel function of order M and $H_M^{(1)}(z)$ is the Hankel function of the first kind of order M.

Based on the formulas (12), (15), and (16), the integral (10) can now be calculated for a circular cylindrical inclusion.

$f(\mathbf{x}, k)$

$$= \begin{cases} \left(\int_0^z z'dz' + \int_z^a z'dz'\right)\int_0^{2\pi}d\theta\int_{-\infty}^{\infty}dx_3'\frac{e^{ikr}}{r}, & \mathbf{x} \in \Omega \\ \int_0^a z'dz'\int_0^{2\pi}d\theta\int_{-\infty}^{\infty}dx_3'\frac{e^{ikr}}{r}, & \mathbf{x} \in R^3 - \Omega \end{cases}$$

$$= \frac{2\pi^2 i}{k}\begin{cases} zJ_1(kz)H_0^{(1)}(kz) + aJ_0(kz)H_1^{(1)}(ka) - zJ_0(kz)H_1^{(1)}(kz), & \mathbf{x} \in \Omega \\ aJ_1(ka)H_0^{(1)}(kz), & \mathbf{x} \in R^3 - \Omega \end{cases} \tag{17}$$

Furthermore, by using

$$J_0(kz)H_1^{(1)}(kz) - J_1(kz)H_0^{(1)}(kz) = -\frac{2i}{\pi kz}, \tag{18}$$

(17) can be simplified to

$$f(\mathbf{x}, k) \equiv N(z, k) = -4\pi\left[\frac{1}{k^2}\Lambda(\Omega) + \Phi(k)\Psi_0(kz)\right], \tag{19}$$

where

$$\Phi(k) = \begin{cases} -\frac{i\pi a}{2k}H_1^{(1)}(ka), & \mathbf{x} \in \Omega \\ -\frac{i\pi a}{2k}J_1(ka), & \mathbf{x} \in R^3 - \Omega \end{cases},$$

$$\Psi_0(kz) = \begin{cases} J_0(kz), & \mathbf{x} \in \Omega \\ H_0^{(1)}(kz), & \mathbf{x} \in R^3 - \Omega \end{cases}. \tag{20}$$

Thus, the exact steady-state Eshelby tensor for an infinite circular cylindrical inclusion is readily obtained from Eqs. (8), (9), and (19). As can be seen from these equations, unlike for the quasi-static problem (Eshelby, 1957), the dynamic Eshelby tensor varies even within the inclusion. The calculation of the dynamic Eshelby tensor (8) requires the following expressions for the derivatives of the potential function $f(\mathbf{x}, k)$.

$$f_{,3}(\mathbf{x}, k) = 0, \quad f_{,\alpha}(\mathbf{x}, k) = x_\alpha DN,$$

$$f_{,\alpha\beta}(\mathbf{x}, k) = \delta_{\alpha\beta}DN + x_\alpha x_\beta D^2 N,$$

$$f_{,\alpha\beta\omega}(\mathbf{x}, k) = (x_\alpha\delta_{\beta\omega} + x_\beta\delta_{\omega\alpha} + x_\omega\delta_{\alpha\beta})D^2N + x_\alpha x_\beta x_\omega D^3 N,$$

$$f_{,\alpha\beta\omega\rho}(\mathbf{x}, k) = (\delta_{\alpha\beta}\delta_{\omega\rho} + \delta_{\alpha\omega}\delta_{\beta\rho} + \delta_{\alpha\rho}\delta_{\beta\omega})D^2N$$

$$+ (x_\alpha x_\beta \delta_{\omega\rho} + x_\alpha x_\omega \delta_{\beta\rho} + x_\alpha x_\rho \delta_{\beta\omega} + x_\beta x_\omega \delta_{\alpha\rho} + x_\beta x_\rho \delta_{\alpha\omega} + x_\omega x_\rho \delta_{\alpha\beta}) D^3 N + x_\alpha x_\beta x_\omega x_\rho D^4 N, \quad (21)$$

where $D = d/(zdz)$ and

$$D^l N = -4\pi \left(-\frac{k}{z}\right)^l \Phi(k)\Psi_l(kz), \ (l \geq 1),$$

$$\Psi_l(kz) = \left(-\frac{z}{k}\right)^l D^l \Psi_0(kz), \ (l \geq 1),$$

$$\Psi_l(kz) = \begin{cases} J_l(kz), & \mathbf{x} \in \Omega \\ H_l^{(1)}(kz), & \mathbf{x} \in R^3 - \Omega \end{cases},$$

$$(l = 0, 1, 2, \ldots), \text{ no sum on } l. \quad (22)$$

3 Quasi-static Deformations

The classical Eshelby tensor S_{ijkl} for quasi-static deformations can be recovered from the present dynamic Eshelby tensor (8) by taking the limit $\omega \to 0$, i.e.,

$$S_{ijkl}(\mathbf{x}) = \lim_{\omega \to 0} M_{ijkl}(\mathbf{x}) = \tfrac{1}{2}[J^S_{ikl,j}(\mathbf{x}) + J^S_{jkl,i}(\mathbf{x})], \quad (23)$$

where

$$J^S_{ikl}(\mathbf{x}) = \lim_{\omega \to 0} J_{ikl}(\mathbf{x}) = \frac{\lambda + \mu}{\lambda + 2\mu} \psi_{,ikl}(\mathbf{x}) - \frac{\lambda}{\lambda + 2\mu} \delta_{kl}\phi_{,i}(\mathbf{x}) - \delta_{ik}\phi_{,l}(\mathbf{x}) - \delta_{il}\phi_{,k}(\mathbf{x}), \quad (24)$$

$$\psi(\mathbf{x}) = \frac{1}{4\pi} \int_\Omega r d\mathbf{x}', \ \phi(\mathbf{x}) = \frac{1}{4\pi} \int_\Omega \frac{1}{r} d\mathbf{x}'. \quad (25)$$

Note that the two integrals (25) over an infinite circular cylinder diverge. However, the derivatives of the potential functions $\psi(\mathbf{x})$ and $\phi(\mathbf{x})$ appearing in (24) converge. The derivatives of $\psi(\mathbf{x})$ and $\phi(\mathbf{x})$ can be calculated in the same form as the derivatives of f in (21). Since a detailed discussion on $\psi(\mathbf{x})$ and $\phi(\mathbf{x})$ for a general ellipsoidal inclusion has been given by Mura (1982), only the relevant results for an infinite circular cylindrical inclusion are given below.

$$D^2\psi = \begin{cases} -\frac{1}{4}, & \mathbf{x} \in \Omega \\ -\frac{a^2}{2z^2} + \frac{a^4}{4z^4}, & \mathbf{x} \in R^3 - \Omega \end{cases},$$

$$D\phi = \begin{cases} -\frac{1}{2}, & \mathbf{x} \in \Omega \\ -\frac{a^2}{2z^2}, & \mathbf{x} \in R^3 - \Omega \end{cases} \quad (26)$$

By using (26), and recalling $S_{ijkl} = S_{jikl} = S_{ijlk}$, the nonzero components of the classical Eshelby tensor can be expressed as

$$S_{\omega\rho\alpha\beta} = \frac{4\nu - 1}{8(1 - \nu)} \delta_{\alpha\beta}\delta_{\omega\rho} + \frac{3 - 4\nu}{8(1 - \nu)} (\delta_{\alpha\omega}\delta_{\beta\rho} + \delta_{\alpha\rho}\delta_{\beta\omega}),$$

$$S_{3\rho 3\beta} = \frac{1}{4} \delta_{\beta\rho}, \quad S_{\omega\rho 33} = \frac{\nu}{2(1 - \nu)} \delta_{\omega\rho}, \quad (27)$$

for the inside of the circular cylinder, and

$$S_{\omega\rho\alpha\beta} = \frac{a^2}{4} \left\{ D_{\omega\rho\alpha\beta} - \frac{1}{1 - \nu} \left[A_{\omega\rho\alpha\beta} \left(\frac{1}{z^2} - \frac{a^2}{2z^4} \right) - 2B_{\omega\rho\alpha\beta} \left(\frac{1}{z^4} - \frac{a^2}{z^6} \right) + 4C_{\omega\rho\alpha\beta} \left(\frac{2}{z^6} - \frac{3a^2}{z^8} \right) \right] \right\},$$

$$S_{3\rho 3\beta} = \frac{a^2}{4z^2} \delta_{\beta\rho} - \frac{a^2}{2z^4} x_\beta x_\rho,$$

$$S_{\omega\rho 33} = \frac{\nu a^2}{2(1 - \nu)} \left(\frac{1}{z^2} \delta_{\omega\rho} - \frac{2}{z^4} x_\omega x_\rho \right), \quad (28)$$

for the outside of the circular cylinder, where ν is the Poisson ratio and

$$A_{\omega\rho\alpha\beta} = \delta_{\alpha\beta}\delta_{\omega\rho} + \delta_{\alpha\omega}\delta_{\beta\rho} + \delta_{\alpha\rho}\delta_{\beta\omega},$$

$$B_{\omega\rho\alpha\beta} = x_\alpha x_\beta \delta_{\omega\rho} + x_\alpha x_\omega \delta_{\beta\rho} + x_\alpha x_\rho \delta_{\beta\omega} + x_\beta x_\omega \delta_{\alpha\rho} + x_\beta x_\rho \delta_{\alpha\omega} + x_\omega x_\rho \delta_{\alpha\beta},$$

$$C_{\omega\rho\alpha\beta} = x_\alpha x_\beta x_\omega x_\rho,$$

$$D_{\omega\rho\alpha\beta} = \frac{2}{z^2} \left(\frac{\nu}{1 - \nu} \delta_{\alpha\beta}\delta_{\omega\rho} + \delta_{\alpha\omega}\delta_{\beta\rho} + \delta_{\alpha\rho}\delta_{\beta\omega} \right) - \frac{2}{z^4} \left(\frac{2\nu}{1 - \nu} x_\omega x_\rho \delta_{\alpha\beta} + x_\alpha x_\omega \delta_{\beta\rho} + x_\alpha x_\rho \delta_{\beta\omega} + x_\beta x_\omega \delta_{\alpha\rho} + x_\beta x_\rho \delta_{\alpha\omega} \right). \quad (29)$$

These expressions for the classical Eshelby tensor agree with those given in Mura (1982).

References

Cheng, Z. Q., and He, L. H., 1996, "Steady-State Response of a Cosserat Medium with a Spherical Inclusion," *Acta Mechanica*, Vol. 116, pp. 97–110.

Eshelby, J. D., 1957, "The Determination of the Elastic Field of an Ellipsoidal Inclusion, and Related Problems," *Proceedings of Royal Society*, Vol. A241, pp. 376–396.

Eshelby, J. D., 1959, "The Elastic Field Outside an Ellipsoidal Inclusion," *Proceedings of Royal Society*, Vol. A252, pp. 561–569.

Gradshteyn, I. S., and Ryzhik, I. M., 1965, *Table of Integrals, Series, and Products*, Academic Press, New York.

Mikata, Y., 1993, "Transient Elastic Field due to a Spherical Dynamic Inclusion with an Arbitrary Time Profile," *Quarterly Journal of Mechanics and Applied Mathematics*, Vol. 46, pp. 275–297.

Mikata, Y., and Nemat-Nasser, S., 1990, "Elastic Field due to a Dynamically Transforming Spherical Inclusion," ASME Journal of Applied Mechanics, Vol. 57, pp. 845–849.

Mikata, Y., and Nemat-Nasser, S., 1991, "Interaction of a Harmonic Wave with a Dynamically Transforming Inhomogeneity," *Journal of Applied Physics*, Vol. 70, pp. 2071–2078.

Mura, T., 1982, *Micromechanics of Defects in Solids*, Martinus Nijhoff Publishers, Dordrecht, Netherlands.

Mura, T., 1988, "Inclusion Problems," ASME *Applied Mechanics Reviews*, Vol. 41, pp. 15–20.

Mura, T., Shodja, H. M., and Hirose, Y., 1996, "Inclusion Problems," ASME *Applied Mechanics Reviews*, Vol. 49, pp. S118–S127.

Torsional Impact Response of a Functionally Graded Material With a Penny-Shaped Crack

C. Li[1] and Z. Zou[1]

1 Introduction

Structural components made of functionally graded materials (FGMs) will be inevitably subjected to time-dependent loadings. The nonhomogeneous properties in addition to the presence of mechanical imperfections such as cracks can have a strong influence on the dynamic response of these components. A knowledge of the dynamic response of this kind of components is essential to achieving an in-depth understanding of the failure mechanisms of FGMs. In this paper, we present the torsional impact response of an unbounded FGM with a penny-shaped crack. By using integral transform techniques, the problem is reduced to solving a Fredholm integral equation of the second kind, which is transformed from a pair of dual integral equations. Subsequently the local dynamic stress fields around the crack tip are obtained. The influence of material nonhomogeneity on the dynamic stress intensity factors is illustrated graphically.

2 Material Property Model

Several models for describing the nonhomogeneity of material properties have been proposed and extensively used, such as the power function (Kassir and Sih, 1975), the exponential form (Ozturk and Erdogan, 1993) and the generalized interlayer model (Wang et al., 1996). However, it is difficult to apply these models to obtain the dynamic response of nonhomogeneous FGMs with cracks. After thorough consideration, we find that the application of the following model

$$\mu(z) = \mu_0(1 + \alpha|z|)^2, \quad \alpha > 0, \tag{1}$$

makes the dynamic response problems of FGMs with cracks tractable. The nonhomogeneity parameter α may be adjusted to approximate the actual material property distribution of FGMs.

3 Formulation of the Problem

Consider a penny-shaped crack of diameter $2a$ embedded in an unbounded functionally graded material and lying in the $z = 0$ plane. For the problem of torsional impact, we have

$$u_\theta = u_\theta(r, z, t), \tag{2}$$

$$\tau_{\theta z} = \mu(z)\frac{\partial u_\theta}{\partial z}, \quad \tau_{r\theta} = \mu(z)\left(\frac{\partial u_\theta}{\partial r} - \frac{u_\theta}{r}\right), \tag{3}$$

$$\frac{\partial^2 u_\theta}{\partial r^2} + \frac{1}{r}\frac{\partial u_\theta}{\partial r} - \frac{u_\theta}{r^2} + \frac{\partial^2 u_\theta}{\partial z^2} + \frac{\mu'(z)}{\mu(z)}\frac{\partial u_\theta}{\partial z} = \frac{\rho}{\mu(z)}\frac{\partial^2 u_\theta}{\partial t^2}, \tag{4}$$

$$u_\theta(r, 0, t) = 0, \quad r \geq a;\ t > 0, \tag{5}$$

$$\tau_{\theta z}(r, 0, t) = -\tau_0 H(t) r/a, \quad 0 \leq r < a;\ t > 0, \tag{6}$$

where t is time, $\mu'(z)$ is the derivative of $\mu(z)$, $H(t)$ is the Heaviside unit step function, and ρ is the mass density of the FGM. Here it is assumed that ρ = constant.

Applying the Laplace transform to Eq. (4) results in

$$\frac{\partial^2 u_\theta^*}{\partial r^2} + \frac{1}{r}\frac{\partial u_\theta^*}{\partial r} - \frac{u_\theta^*}{r^2} + \frac{\partial^2 u_\theta^*}{\partial z^2} + \frac{\mu'(z)}{\mu(z)}\frac{\partial u_\theta^*}{\partial z} = \frac{\rho p^2}{\mu(z)} u_\theta^*, \tag{7}$$

where

$$u_\theta^*(r, z, p) = \int_0^\infty u_\theta(r, z, t)e^{-pt}dt. \tag{8}$$

Considering the symmetry of the problem about the $z = 0$ plane, introducing Hankel transforms of the first order, and accounting for the regularity condition at $z \to \infty$, we obtain the solution of (7) as follows:

$$u_\theta^*(r, z, p) = \int_0^\infty A(s, p)(1 + \alpha z)^{-1/2} K_\beta\left[(1 + \alpha z)\frac{s}{\alpha}\right] \times J_1(sr)sds, \tag{9}$$

where $J_1(\,)$ is the Bessel function of the first kind, $K_\beta(\,)$ is the modified Bessel function of the second kind, and $\beta = \sqrt{1/4 + \rho p^2/\mu_0\alpha^2}$.

In the Laplace transform domain, the boundary conditions on the plane $z = 0$ become

$$u_\theta^*(r, 0, p) = 0, \quad r \geq a, \tag{10}$$

$$\tau_{\theta z}^*(r, 0, p) = -\frac{\tau_0 r}{pa}, \quad 0 \leq r < a. \tag{11}$$

Substituting (9) into (3) and then from (10) and (11), we obtain a pair of dual integral equations

$$\int_0^\infty B(s, p)J_1(sr)ds = 0, \quad r \geq a, \tag{12a}$$

$$\int_0^\infty sB(s, p)G(s, p)J_1(sr)ds = \frac{\tau_0 r}{\mu_0 pa}, \quad 0 \leq r < a, \tag{12b}$$

where

$$B(s, p) = sA(s, p)K_\beta\left(\frac{s}{\alpha}\right), \tag{13}$$

$$G(s, p) = \frac{\frac{\alpha}{2}K_\beta\left(\frac{s}{\alpha}\right) - sK_\beta'\left(\frac{s}{\alpha}\right)}{sK_\beta\left(\frac{s}{\alpha}\right)}. \tag{14}$$

The dual integral Eqs. (12) can be solved by applying the method of Copson (1961). The solution is found as follows:

$$B(s, p) = \frac{4\tau_0 a^{5/2}}{3\mu_0 p\sqrt{2\pi}}\sqrt{s}\int_0^1 \sqrt{\xi}\Phi^*(\xi, p)J_{3/2}(sa\xi)d\xi, \tag{15}$$

where $\Phi^*(\xi, p)$ should satisfy the Fredholm integral equation of the second kind:

$$\Phi^*(\xi, p) + \int_0^1 \Phi^*(\xi, p)M(\xi, \eta, p)d\eta = \xi^2. \tag{16}$$

The kernel function $M(\xi, \eta, p)$ in (16) is computed from

[1] Department of Architectural Engineering, Shijiazhuang Railway Institute, Shijiazhuang City 050043, P. R. China.

Contributed by the Applied Mechanics Division of THE AMERICAN SOCIETY OF MECHANICAL ENGINEERS for publication in the ASME JOURNAL OF APPLIED MECHANICS. Manuscript received by the ASME Applied Mechanics Division, July 7, 1998; final revision, Feb. 12, 1999. Associate Technical Editor: M.-J. Pindera.

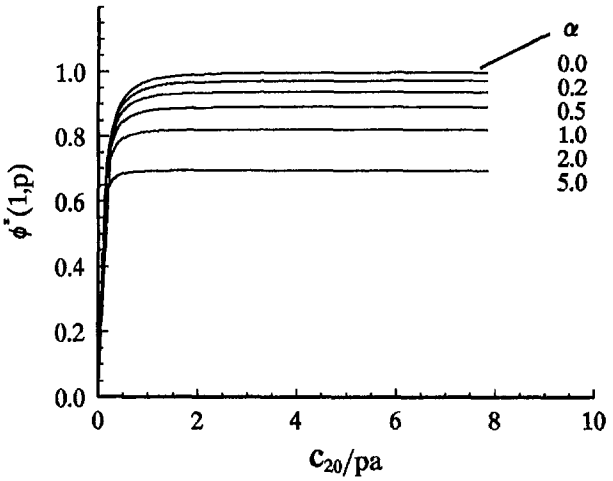

Fig. 1 Variations of $\phi^*(1, p)$ with c_{20}/pa

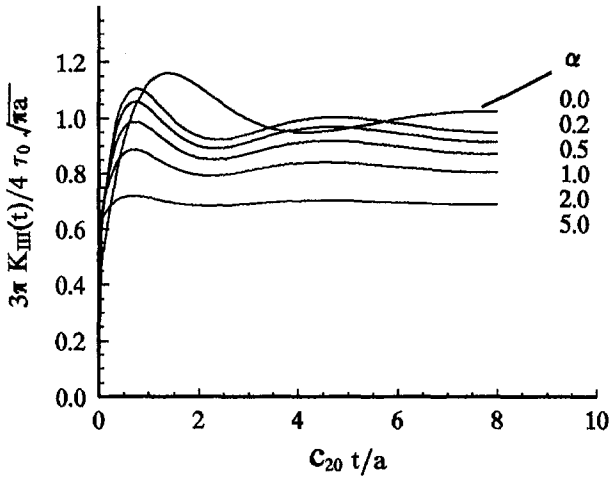

Fig. 2 Dynamic stress intensity factor $K_{III}(t)$ versus time

$$M(\xi, \eta, p) = \sqrt{\xi\eta}\int_0^\infty s\left[G\left(\frac{s}{a}, p\right) - 1\right]J_{3/2}(s\xi)J_{3/2}(s\eta)ds. \quad (17)$$

4 Dynamic Stress Intensity Factor

Integrating $B(s, p)$ in (15) by parts and considering the asymptotic behavior of $K_\beta(x)$ and $K'_\beta(x)$ when $x \to \infty$, we obtain the local stress fields around the crack tip in the Laplace transform domain

$$\tau^*_{\theta z}(r_1, \theta_1, p) = \frac{K^*_{III}(p)}{\sqrt{2\pi r_1}}\cos\left(\frac{\theta_1}{2}\right) + O(r_1^0), \quad (18a)$$

$$\tau^*_{r\theta}(r_1, \theta_1, p) = -\frac{K^*_{III}(p)}{\sqrt{2\pi r_1}}\sin\left(\frac{\theta_1}{2}\right) + O(r_1^0), \quad (18b)$$

where r_1 and θ_1 are the local coordinates at the crack tip. The Laplace transform of the dynamic stress intensity factor $K^*_{III}(p)$ in Eq. (18) is

$$K^*_{III}(p) = \frac{4}{3\pi}\tau_0\sqrt{\pi a}\,\frac{\Phi^*(1, p)}{p}, \quad (19)$$

in which $\Phi^*(1, p)$ is the value of $\Phi^*(\xi, p)$ evaluated at the crack tip corresponding to $\xi = 1$.

The dynamic stress intensity factor in time domain can be obtained by

$$K_{III}(t) = \frac{4}{3\pi}\tau_0\sqrt{\pi a}\,\frac{1}{2\pi i}\int_{Br}\frac{\Phi^*(1, p)}{p}e^{pt}dp, \quad (20)$$

where Br denotes the Bromwich path of integration.

5 Results and Discussion

The functional dependence of the stresses on r_1 and θ_1 as shown in Eqs. (18) reveals that the dynamic stresses in functionally graded materials with cracks also possess the inverse square root singularity in terms of r_1 and that the angular distribution in θ_1 is the same as that in homogeneous solids with cracks. Equation (20) shows that the form of the dynamic stress intensity factor for functionally graded materials is identical to that for homogeneous materials.

Figure 1 shows the numerical results of $\Phi^*(1, p)$ as a function of the dimensionless Laplace transform wave number c_{20}/pa for several different values of α. Here $c_{20} = \sqrt{\mu_0/\rho}$. It is observed that the magnitude of $\Phi^*(1, p)$ decreases with increasing values of the nonhomogeneity parameter α.

By using the numerical Laplace transform inversion techniques, the dynamic stress intensity factor given by Eq. (20) can be evaluated. Figure 2 displays the normalized stress intensity factor $3\pi K_{III}(t)/4\tau_0\sqrt{\pi a}$ as a function of $c_{20}t/a$. It is observed that all the curves reach a peak and then oscillate about static values (Li and Zou, 1998) in a decaying manner. The peak values of the dynamic stress intensity factors for FGMs are smaller than that for homogeneous materials and decrease with increasing values of α. The physical interpretation may be that the larger the material property gradient of the FGM, the higher the restraint of the material to deformation. This suggests that the crack driving force may be reduced by using FGMs to replace homogenous materials in engineering structures. This result encourages our application of FGMs in a wide range of engineering disciplines.

Acknowledgment

This study was supported by the national natural science fund under key project No. 19704100.

References

Copson, E. T., 1961, "On certain dual integral equations," *Proceedings Glasgow Mathematical Association,* Vol. 5, pp. 19–24.

Kassir, M. K., and Sih, G. C., 1975, *Three Dimensional Crack Problems, Volume II in Series on Mechanics of Fracture,* G. C. Sih, ed., Noordhoff International Publishing, Leyden.

Li, Chunyu, and Zou, Zhenzhu, 1998, "Local stress field for the torsion of a functionally graded material with a penny-shaped crack," *International Journal of Fracture,* in press.

Ozturk, M., and Erdogan, F., 1993, "The Axisymmetric Crack Problem in a Nonhomogeneous Medium," ASME JOURNAL OF APPLIED MECHANICS, Vol. 60, pp. 406–413.

Wang, Xuyue, Zou, Zhenzhu, and Wang, Duo, 1996, "On the penny-shaped crack in a nonhomogeneous interlayer under torsion," *International Journal of Fracture,* Vol. 82, pp. 335–343.

Unified Plastic Limit Analyses of Circular Plates Under Arbitrary Load

G. Ma,[1] H. Hao,[1] and S. Iwasaki[2]

1 Introduction

Correct prediction of the load-carrying capacity of circular plates is crucial for achieving an optimal structural design. Hopkins and Prager (1953) and Hodge (1963) investigated the load-carrying capacities of circular plates with limit analysis theorems. The plastic limit solutions for circular plates subjected to an arbitrary rotationally symmetric load were presented by Ghorashi (1994). However, the above studies were performed by using either the square yield criterion or the Tresca criterion. Solutions based on the above two yield criteria have obvious shortcomings in describing the realistic characteristics of a circular plate in the plastic limit state. Hopkins and Wang (1954) investigated the load-carrying capacities of a circular plate under uniformly distributed load with the Mises criterion and a parabolic criterion by an iterative method. Unfortunately, an analytical plastic limit solution based on the Mises criterion for a circular plate under various load conditions is not readily derived because of its nonlinear feature. The unified yield criterion (UYC) (Yu and He, 1991) used in the present paper is based on the assumption that plastic flow is controlled by the combination of the two larger principal shear stresses. Its yield surfaces vary between the lower bound and the upper bound of plastic yielding of a material by changing a weighting coefficient. In the present study, plastic limit load factors, total limit loads, moment fields, and velocity fields of circular plates under arbitrary loads are derived in terms of the UYC. Comparisons and discussions of its three particular solutions corresponding to the Tresca criterion, the Mises criterion (closed form), and the twin shear stress criterion are made.

2 Basic Equations

The fundamental assumptions of the present study are: (i) the entire plate is in the fully plastic state; (ii) the plate is thin ($h \ll a$). When a circular plate of radius a and thickness h is subjected to an arbitrarily distributed axisymmetrical transverse pressure $\mu P(r)$, where μ is a load factor and $P(r)$ is a load distribution function, the equilibrium equation of a circular plate is

$$d(rm_r)/dr - m_\theta = -\int \mu p(r) r dr \tag{1}$$

in which r, m_r, m_θ, and $p(r)$ are dimensionless variables and $r = R/a$, $m_r = M_r/M_0$, $m_\theta = M_\theta/M_0$, and $p(r) = P(r)a^2/M_0$, where R is radial distance, M_r, M_θ, and M_0 are radial, tangential, and ultimate (fully plastic) bending moments, respectively.

The relations between the curvature rate and the rate of deflection are

$$\dot{k}_r = -d^2\dot{w}/dr^2 \quad \text{and} \quad \dot{k}_\theta = -d\dot{w}/(rdr) \tag{2}$$

where $\dot{w}$, $\dot{k}_r$, and $\dot{k}_\theta$ are the dimensionless deflection rate, the dimensionless curvature rates in the radial and circumferential directions, respectively; the dimensionless deflection is defined as $w = W/a$ and W is the actual deflection. According to the associated flow rule,

$$\dot{k}_r = \dot{\lambda}\partial\psi/\partial m_r, \quad \dot{k}_\theta = \dot{\lambda}\partial\psi/\partial m_\theta \tag{3}$$

where $\dot{\lambda}$ is a plastic flow factor and ψ is the plastic potential.

Based on the orthogonal octahedron of twin shear element model, the unified yield criterion specifies that material fails when a certain function of the two larger principal shear stresses reaches the limit value (Yu, 1983). Figure 1 shows the limit trajectory of the UYC expressed by m_r and m_θ. The UYC has obviously piecewise linear forms

$$m_\theta = a_i m_r + b_i \quad (i = 1 \sim 12). \tag{4}$$

The constants a_i and b_i in Eq. (4) for the five lines L_i ($i = 1 \sim 5$) of AB, BC, CD, DE, and EF in Fig. 1 are listed in Table 1. Table 2 gives the radial moments d_i ($i = 0 \sim 5$) corresponding to the yield points A, B, C, D, E, and F, respectively. When b varies from 0 to 1, a family of convex yield criteria which are suitable for different kinds of materials are deduced. In particular, it becomes the Tresca criterion when $b = 0$ and the maximum principal deviatoric stress criterion or the twin shear stress criterion when $b = 1$. The Mises criterion can be approximated by the UYC when $b = 0.5$.

The plastic potential ψ is then expressed as

$$\psi = m_\theta - a_i m_r - b_i \quad (i = 1 \sim 12). \tag{5}$$

Assuming the load function $p(r) = \sum_{j=1}^{\infty} p_j r^{j-1}$, m_r located on the segments L_i are obtained by substituting Eq. (4) into (1) and then integrating Eq. (1),

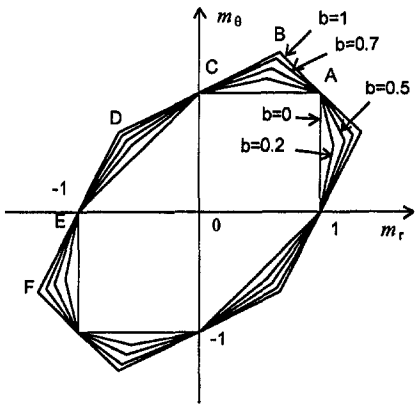

Fig. 1 UYC for generalized plane stress

Table 1 Constants a_i and b_i in the unified yield criterion

	AB (i=1)	BC (i=2)	CD (i=3)	DE (i=4)	EF (i=5)
a_i	-b	b/(1+b)	1/(1+b)	1+b	(1+b)/b
b_i	1+b	1	1	1+b	(1+b)/b

Table 2 Constants d_i

points	A (i=0)	B (i=1)	C (i=2)	D (i=3)	E (i=4)	EF (i=5)
d_i	1	(1+b)/(2+b)	0	-(1+b)/(2+b)	-1	-2(1+b)/(2+b)

[1] School of Civil & Structural Engineering, Nanyang Technological University, Singapore 639798.
[2] Department of Civil and Environmental Engineering, Iwate University, 020 Morioka, Japan.

Contributed by the Applied Mechanics Division of THE AMERICAN SOCIETY OF MECHANICAL ENGINEERS for publication in the ASME JOURNAL OF APPLIED MECHANICS. Manuscript received by the ASME Applied Mechanics Division, Sept. 9, 1998; final revision, Nov. 25, 1998. Associate Technical Editor: W. J. Drugan.

$$m_r = \frac{b_i}{1-a_i} - \mu \sum_{j=1}^{\infty} p_j \frac{r^{j+1}}{(j+1)(j+2-a_i)} + c_i r^{-1+a_i} \quad (i = 1 \sim 5), \quad (6)$$

where c_i ($i = 1 \sim 5$) are integral constants which can be determined from continuity and boundary conditions.

The field of velocity corresponding to the five sides L_i is obtained by substituting Eq. (2) into Eq. (3) and then integrating (3) with the aid of Eq. (5),

$$\dot{w} = \dot{w}_0(c_{1i} r^{1-a_i} + c_{2i}) \quad (i = 1 \sim 5), \quad (7)$$

in which c_{1i}, c_{2i} ($i = 1 \sim 5$) are integral constants, and $\dot{w}_0$ is the velocity at the plate center.

The dimensionless total limit load on the plate is obtained as follows:

$$P_T = 2\pi \int_0^1 \mu p(r) r dr \quad \text{or} \quad P_T = 2\pi\mu \sum_{j=1}^{\infty} \frac{p_j}{j+1}. \quad (8)$$

3 Simply Supported Plate

In the plastic limit state, bending moments of a simply supported circular plate are located on the lines AB and BC from the normality requirement of plasticity. Assuming r_1 is a nondimensional radius of a ring where the moments exactly correspond to point B in Fig. 1, the boundary and continuity conditions are: (1) m_r ($r = 0$) = 1; (2) m_r ($r = r_1$) is continuous and equal to d_1; (3) m_r ($r = 1$) = 0; (4) $\dot{w}$ ($r = 0$) = $\dot{w}_0$; (5) $\dot{w}$ ($r = r_1$) and $d\dot{w}/dr$ ($r = r_1$) are continuous and (6) $\dot{w}$ ($r = 1$) = 0. Then the integral coefficients c_1, c_2, c_{11}, c_{12}, c_{21}, and c_{22} in Eq. (6) and Eq. (7) are determined as

$$c_1 = 0, \quad c_2 = -\frac{b_2}{1-a_2} + \mu \sum_{j=1}^{\infty} \frac{p_j}{(j+1)(j+2-a_2)} \quad (9)$$

$$c_{11} = -\frac{r_1^{-b(2+b)/(1+b)}}{(1+b)^2 - (2b+b^2) r_1^{1/(1+b)}}, \quad c_{21} = 1,$$

$$c_{12} = -c_{22} = -\frac{(1+b)^2}{(1+b)^2 - (2b+b^2) r_1^{1/(1+b)}}. \quad (10)$$

The load factor μ is deduced as

$$\mu = \frac{-d_1 + \dfrac{b_1}{1-a_1}}{\displaystyle\sum_{j=1}^{\infty} \frac{p_j r_1^{j+1}}{(j+1)(j+2-a_1)}} \quad (11)$$

where r_1 satisfies the following equation:

$$d_1 = \frac{b_2}{1-a_2} - \mu \sum_{j=1}^{\infty} \frac{p_j r_1^{j+1}}{(j+1)(j+2-a_2)} + c_2 r_1^{-1+a_2}. \quad (12)$$

The above equation is solved by interval halving for r_1 in the interval (0, 1) for a given value of b between 0 and 1. Substituting the convergent value of r_1 into Eqs. (9)~(11), the moments and velocity distributions in Eq. (6) and Eq. (7) are then obtained. As a special case, when $b = 0$, the plastic solution is the same as that given by Ghorashi (1994) based on the maximum principal stress criterion and the Tresca criterion. If uniformly distributed load is applied, it is identical to the results by using the Tresca criterion (Hodge, 1963).

4 Clamped Circular Plate

Based on the kinematically admissible requirement, the moment fields of the entire clamped plate lie on the five sides corresponding to AB, BC, CD, DE, and EF in Fig. 1. The points A, B, C, D, and E in Fig. 1 correspond to five dividing dimensionless radii on the plate, which divide the plate into five parts. The five radii are denoted by r_0, r_1, r_2, r_3, and r_4, respectively, satisfying $0 = r_0 \le r_1 \le r_2 \le r_3 \le r_4 \le 1$. On the outer edge ($r = r_5 = 1$), the moments m_r and m_θ are assumed to correspond to the yield point F exactly. The continuity and boundary conditions of the clamped plate are (1) m_r ($r = 0$) = 1, (2) m_r ($r = r_i$) = d_i, $i = 1 \sim 4$, and are continuous and (3) m_r ($r = 1$) = d_5. Using the above continuity and boundary conditions, c_i ($i = 1 \sim 5$) in Eq. (6) are determined as

$$c_1 = 0,$$

$$c_i = \left[d_{i-1} - \frac{b_i}{1-a_i} + \mu \sum_{j=1}^{\infty} \frac{p_j r_{i-1}^{j+1}}{(j+1)(j+2-a_i)} \right] r_{i-1}^{1-a_i}, \quad i = 2 \sim 5. \quad (13)$$

The load factor is derived as

$$\mu = \frac{-d_1 + \dfrac{b_1}{1-a_1}}{\displaystyle\sum_{j=1}^{\infty} \frac{p_j r_1^{j+1}}{(j+1)(j+2-a_1)}} \quad (14)$$

in which the dividing radii r_i ($i = 2 \sim 5$) are calculated by the following equations:

$$\frac{b_i}{1-a_i} + \left[d_{i-1} - \frac{b_i}{1-a_i} + \mu \sum_{j=1}^{\infty} \frac{p_j r_{i-1}^{j+1}}{(j+1)(j+2-a_i)} \right] \times r_{i-1}^{1-a_i} r_i^{-1+a_i} - \mu \sum_{j=1}^{\infty} \frac{p_j r_i^{j+1}}{(j+1)(j+2-a_i)} = d_i, \quad i = 2 \sim 5. \quad (15)$$

Thus, the plastic collapse load of the clamped plate is expressed as $\mu \sum_{j=1}^{\infty} p_j r^{j-1}$. Once the load distribution function $p(r)$ that is expressed as a Taylor series is specified, the plastic collapse load is calculated by Eqs. (13)~(15).

Equation (15) has to be solved by an iterative method. As an initial value of r_1 is specified, r_i ($i = 2 \sim 5$) in Eq. (15) are searched subsequently. The condition that r_5 is exactly equal to 1 is used as the convergence criterion. Substituting the obtained values of c_i and r_i into Eqs. (6) and (14), the moment fields as well as the plastic limit load factor of the clamped circular plate are then determined.

The continuity and boundary conditions of velocity on the plate are (4) $\dot{w}$ ($r = 0$) = $\dot{w}_0$, (5) $\dot{w}$ and $d\dot{w}/dr$ ($r = r_i$, $i = 1 \sim 4$) are continuous, and (6) $\dot{w}$ ($r = 1$) = 0. Considering these conditions, the constants c_{1i} and c_{2i} in Eq. (7) can be derived as

$$c_{11} = -\frac{\dot{w}_0}{(d_{14}+d_{24}) d_{13} d_{12} d_{11} + d_{23} d_{12} d_{11} + d_{22} d_{11} + d_{21}},$$

$$c_{21} = \dot{w}_0 \quad (16)$$

and

$$\begin{bmatrix} c_{1(i+1)} \\ c_{2(i+1)} \end{bmatrix} = \begin{bmatrix} d_{1i} & 0 \\ d_{2i} & 1 \end{bmatrix} \begin{bmatrix} c_{1i} \\ c_{2i} \end{bmatrix} \quad (i = 1 \sim 4) \quad (17)$$

Table 3 Plastic limit loads for a simply supported circular plate

$p(r)$	r		$1+r$		1		$2-r$		$1-r$	
	μ	P_r	μ	P_r	μ	P_r	μ	P_r	μ	P_r
b=0	12.00	25.13	4.00	20.94	6.00	18.85	4.00	16.76	12.01	12.57
b=0.5	12.78	26.78	4.31	22.56	6.49	20.38	4.34	18.17	13.02	13.64
b=1	13.36	27.98	4.53	23.73	6.84	21.49	4.58	19.17	13.75	14.40

in which d_{1i} and d_{2i} ($i = 1 \sim 5$) are constants related to the continuity conditions, and they are

$$d_{1i} = \frac{1 - a_i}{1 - a_{i+1}} r_i^{a_{i+1} - a_i}, \quad d_{2i} = -\frac{a_{i+1} - a_i}{1 - a_{i+1}} r_i^{1 - a_i} \quad (i = 1 \sim 4). \quad (18)$$

Substituting these integral constants into (7), the velocity field of the clamped circular plate is obtained.

5 Discussion and Conclusion

Tables 3 and 4 list the plastic limit load factors and the total limit loads of simply supported and clamped plates for five linearly distributed load functions in terms of the three particular yield criteria, namely the Tresca criterion, the Mises criterion (approximated by $b = 0.5$ of the UYC), and the twin shear stress criterion. It can be noticed that the plastic limit load factor as well as the total limit load by the Mises criterion are about 6.5 percent to 8.5 percent larger than those by the Tresca criterion for the simply supported plate and about 12.4 percent to 12.8 percent for the clamped plate. While those by the twin shear stress criterion are about 10.5 percent to 14.5 percent, for the simply supported plate, and 20.9 percent to 21.5 percent, for the clamped plate larger than those by the Tresca criterion. Increasing the load distribution along the plate radius leads to smaller changes between those by different yield criteria, but a larger total limit load, implying that increasing the load distribution might improve the load-carrying capacity of a plate. For a uniformly distributed load, the present results are in good agreement with previous results from different yield criteria (Hopkins and Wang, 1954; Hodge, 1954; Ma et al., 1998) as indicated in Table 5. For a simply supported plate, the circumferential moment is no longer constant if $b \neq 0$ is applied in UYC. Using the Tresca criterion, it was proved in an earlier paper (Hodge, 1954) that the equilibrium equation for a clamped circular plate is invalid if the $m_\theta \sim m_r$ trajectory is on line EF. If UYC is used, however, it is straightforward to extend the trajectory to EF to obtain a nonsingular solution. The solution based on the Tresca criterion is approximated by using a small b value, e.g., $b = 0.001$. The velocity fields corresponding to any criterion ($b \neq 0$ in UYC) other than the Tresca criterion distribute nonlinearly along the plate, which avoids a single linear variation and a singularity at the plate center as given by the Tresca criterion ($b = 0$ in UYC).

The solutions obtained satisfy both the static admissibility of the moment fields and the kinematical admissibility of the velocity field, thus they are the exact solutions of the plates in the plastic limit state. It has been shown that the limit analysis by using the unified yield criterion can give the plastic limit solutions of various yield conditions in a uniform manner. Upper and lower bounds of the plastic load factor and the total limit load are deduced by the two bound criteria corresponding to $b = 0$ and $b = 1$ in the unified yield criterion. The solutions based on different criteria might differ by more than ten percent for a simply supported circular plate, and more than 20 percent for a clamped circular plate.

The effect of shear stress on the collapse load depends on the ratio (h/a) and the load type. The shear stress in a thin plate ($h \ll a$) in the plastic limit state is much smaller than the normal stress σ_s except in a very small area near a concentrated load. However, when the plate is subjected to an intensive implosive pressure, punch failure should be included even for a very thin plate and the influence of shear stress can no longer be ignored.

Table 4 Plastic limit loads for a clamped circular plate

$p(r)$	r		$1+r$		1		$2-r$		$1-r$	
	μ	P_r	μ	P_r	μ	P_r	μ	P_r	μ	P_r
b=0	22.98	48.13	7.57	39.66	11.26	35.37	7.45	31.26	21.87	22.90
b=0.5	25.83	54.09	8.54	44.72	12.72	39.96	8.40	35.19	24.60	25.76
b=1	27.78	58.19	9.20	48.19	13.71	43.06	9.05	37.91	26.46	27.71

Table 5 Comparison of the limit loads with previous results (M_0/a^2)

criteria		Simply supported	Clamped
Tresca	Hopkins & Wang	6.00	11.26
	Present (b=0)	6.00	11.26
Mises	Hopkins & Wang	6.50	12.50
	Present (b=0.5)	6.49	12.72
Yu	Ma, *et al*	6.84	13.71
	Present (b=1)	6.84	13.71

References

Ghorashi, M., 1994, "Limit Analysis of Circular Plates Subjected to Arbitrary Rotational Symmetric Loading," *Int. J. Mech. Sci.*, Vol. 36, No. 2, pp. 87–94.

Hodge, P. G., 1963, *Limit Analysis of Rotationally Symmetric Plates and Shells*, Prentice-Hall, Englewood Cliffs, NJ.

Hopkins, H. G., and Prager, W., 1953, "The Load Carrying Capacities of Circular Plates," *J. Mech. Phys. Solids*, Vol. 2, pp. 1–13.

Hopkins, H. G., and Wang, A. J., 1954, "Load Carrying Capacities for Circular Plates of Perfectly-plastic Material with Arbitrary Yield Condition," *J. Mech. Phys. Solids*, Vol. 3, pp. 117–129.

Ma, Guowei, Iwasaki, S., Miyamoto, Y., and Deto, H., 1998, "Plastic limit analysis of circular plates with respect to the unified yield criterion," *Int. J. Mech. Sci.*, Vol. 40, No. 10, pp. 963–976.

Yu, M. H.,1983, "Twin Shear Stress Yield Criterion," *Int. J. Mech. Sci.*, Vol. 25, No. 1, pp. 71–74.

Yu, M. H., and He, L. N., 1991, "A New Model and Theory on Yield and Failure of Materials under Complex Stress State," *Mechanical Behavior of Materials-6*, Vol. 3, Pergamon Press, Tarrytown, NY, pp. 841–846.

A Novel Formulation for the Exterior-Point Eshelby's Tensor of an Ellipsoidal Inclusion

J. W. Ju[1,3] and L. Z. Sun[2,3]

1 Introduction

Micromechanics of heterogeneous materials is of great interest to researchers in many science and engineering disciplines. It is not only the tool for determining the local stress and strain fields in materials, but also the basis for homogenization to obtain effective mechanical properties of composites. Although the concept of

[1] To whom correspondence should be addressed. Professor. Fellow ASME.

[2] Postdoctoral Research Fellow and Lecturer. Assoc. Mem. ASME.

[3] Department of Civil and Environmental Engineering, University of California, Los Angeles, CA 90095-1593.

Contributed by the Applied Mechanics Division of THE AMERICAN SOCIETY OF MECHANICAL ENGINEERS for publication in the ASME JOURNAL OF APPLIED MECHANICS. Manuscript received by the ASME Applied Mechanics Division, Jan. 27, 1999; final revision, Feb. 15, 1999. Associate Technical Editor: L. T. Wheeler.

Table 3 Plastic limit loads for a simply supported circular plate

$p(r)$	r		$1+r$		1		$2-r$		$1-r$	
	μ	P_r	μ	P_r	μ	P_r	μ	P_r	μ	P_r
b=0	12.00	25.13	4.00	20.94	6.00	18.85	4.00	16.76	12.01	12.57
b=0.5	12.78	26.78	4.31	22.56	6.49	20.38	4.34	18.17	13.02	13.64
b=1	13.36	27.98	4.53	23.73	6.84	21.49	4.58	19.17	13.75	14.40

in which d_{1i} and d_{2i} ($i = 1 \sim 5$) are constants related to the continuity conditions, and they are

$$d_{1i} = \frac{1 - a_i}{1 - a_{i+1}} r_i^{a_{i+1} - a_i}, \quad d_{2i} = -\frac{a_{i+1} - a_i}{1 - a_{i+1}} r_i^{1 - a_i} \quad (i = 1 \sim 4). \quad (18)$$

Substituting these integral constants into (7), the velocity field of the clamped circular plate is obtained.

5 Discussion and Conclusion

Tables 3 and 4 list the plastic limit load factors and the total limit loads of simply supported and clamped plates for five linearly distributed load functions in terms of the three particular yield criteria, namely the Tresca criterion, the Mises criterion (approximated by $b = 0.5$ of the UYC), and the twin shear stress criterion. It can be noticed that the plastic limit load factor as well as the total limit load by the Mises criterion are about 6.5 percent to 8.5 percent larger than those by the Tresca criterion for the simply supported plate and about 12.4 percent to 12.8 percent for the clamped plate. While those by the twin shear stress criterion are about 10.5 percent to 14.5 percent, for the simply supported plate, and 20.9 percent to 21.5 percent, for the clamped plate larger than those by the Tresca criterion. Increasing the load distribution along the plate radius leads to smaller changes between those by different yield criteria, but a larger total limit load, implying that increasing the load distribution might improve the load-carrying capacity of a plate. For a uniformly distributed load, the present results are in good agreement with previous results from different yield criteria (Hopkins and Wang, 1954; Hodge, 1954; Ma et al., 1998) as indicated in Table 5. For a simply supported plate, the circumferential moment is no longer constant if $b \neq 0$ is applied in UYC. Using the Tresca criterion, it was proved in an earlier paper (Hodge, 1954) that the equilibrium equation for a clamped circular plate is invalid if the $m_\theta \sim m_r$ trajectory is on line EF. If UYC is used, however, it is straightforward to extend the trajectory to EF to obtain a nonsingular solution. The solution based on the Tresca criterion is approximated by using a small b value, e.g., $b = 0.001$. The velocity fields corresponding to any criterion ($b \neq 0$ in UYC) other than the Tresca criterion distribute nonlinearly along the plate, which avoids a single linear variation and a singularity at the plate center as given by the Tresca criterion ($b = 0$ in UYC).

The solutions obtained satisfy both the static admissibility of the moment fields and the kinematical admissibility of the velocity field, thus they are the exact solutions of the plates in the plastic limit state. It has been shown that the limit analysis by using the unified yield criterion can give the plastic limit solutions of various yield conditions in a uniform manner. Upper and lower bounds of the plastic load factor and the total limit load are deduced by the two bound criteria corresponding to $b = 0$ and $b = 1$ in the unified yield criterion. The solutions based on different criteria might differ by more than ten percent for a simply supported circular plate, and more than 20 percent for a clamped circular plate.

The effect of shear stress on the collapse load depends on the ratio (h/a) and the load type. The shear stress in a thin plate ($h \ll a$) in the plastic limit state is much smaller than the normal stress σ_s except in a very small area near a concentrated load. However, when the plate is subjected to an intensive implosive pressure, punch failure should be included even for a very thin plate and the influence of shear stress can no longer be ignored.

Table 4 Plastic limit loads for a clamped circular plate

$p(r)$	r		$1+r$		1		$2-r$		$1-r$	
	μ	P_r	μ	P_r	μ	P_r	μ	P_r	μ	P_r
b=0	22.98	48.13	7.57	39.66	11.26	35.37	7.45	31.26	21.87	22.90
b=0.5	25.83	54.09	8.54	44.72	12.72	39.96	8.40	35.19	24.60	25.76
b=1	27.78	58.19	9.20	48.19	13.71	43.06	9.05	37.91	26.46	27.71

Table 5 Comparison of the limit loads with previous results (M_0/a^2)

criteria		Simply supported	Clamped
Tresca	Hopkins & Wang	6.00	11.26
	Present (b=0)	6.00	11.26
Mises	Hopkins & Wang	6.50	12.50
	Present (b=0.5)	6.49	12.72
Yu	Ma, *et al*	6.84	13.71
	Present (b=1)	6.84	13.71

References

Ghorashi, M., 1994, "Limit Analysis of Circular Plates Subjected to Arbitrary Rotational Symmetric Loading," *Int. J. Mech. Sci.*, Vol. 36, No. 2, pp. 87–94.

Hodge, P. G., 1963, *Limit Analysis of Rotationally Symmetric Plates and Shells*, Prentice-Hall, Englewood Cliffs, NJ.

Hopkins, H. G., and Prager, W., 1953, "The Load Carrying Capacities of Circular Plates," *J. Mech. Phys. Solids*, Vol. 2, pp. 1–13.

Hopkins, H. G., and Wang, A. J., 1954, "Load Carrying Capacities for Circular Plates of Perfectly-plastic Material with Arbitrary Yield Condition," *J. Mech. Phys. Solids*, Vol. 3, pp. 117–129.

Ma, Guowei, Iwasaki, S., Miyamoto, Y., and Deto, H., 1998, "Plastic limit analysis of circular plates with respect to the unified yield criterion," *Int. J. Mech. Sci.*, Vol. 40, No. 10, pp. 963–976.

Yu, M. H.,1983, "Twin Shear Stress Yield Criterion," *Int. J. Mech. Sci.*, Vol. 25, No. 1, pp. 71–74.

Yu, M. H., and He, L. N., 1991, "A New Model and Theory on Yield and Failure of Materials under Complex Stress State," *Mechanical Behavior of Materials-6*, Vol. 3, Pergamon Press, Tarrytown, NY, pp. 841–846.

A Novel Formulation for the Exterior-Point Eshelby's Tensor of an Ellipsoidal Inclusion

J. W. Ju[1,3] and L. Z. Sun[2,3]

1 Introduction

Micromechanics of heterogeneous materials is of great interest to researchers in many science and engineering disciplines. It is not only the tool for determining the local stress and strain fields in materials, but also the basis for homogenization to obtain effective mechanical properties of composites. Although the concept of

[1] To whom correspondence should be addressed. Professor. Fellow ASME.

[2] Postdoctoral Research Fellow and Lecturer. Assoc. Mem. ASME.

[3] Department of Civil and Environmental Engineering, University of California, Los Angeles, CA 90095-1593.

Contributed by the Applied Mechanics Division of THE AMERICAN SOCIETY OF MECHANICAL ENGINEERS for publication in the ASME JOURNAL OF APPLIED MECHANICS. Manuscript received by the ASME Applied Mechanics Division, Jan. 27, 1999; final revision, Feb. 15, 1999. Associate Technical Editor: L. T. Wheeler.

micromechanics can be traced back to many decades ago (e.g., Goodier, 1937; Edwards, 1951), Eshelby (1957, 1959) outlined a general method to derive the local strain and stress fields. These fields may be due to the stress-free transformation strains which act in a homogeneous ellipsoidal inclusion embedded in an infinite elastic medium. The local stress and strain fields can also be induced by the applied far-field loading on an infinite medium containing an ellipsoidal inhomogeneity. Subsequently, micromechanics of solids has been widely developed. See, for example, the comprehensive reviews by Mura (1987) and Nemat-Nasser and Hori (1993). The term "eigenstrain" was given by Mura to replace the term "stress-free transformation strain" because eigenstrains can be referred to as such inelastic strains as thermal expansion, phase transformation, initial strains, plastic strains, misfit strains, fictitious inelastic strains, and so on.

In the present work, the Eshelby's tensors for an ellipsoidal inhomogeneous inclusion in an infinite matrix are revisited. We first define the outward unit normal vector for an imaginary ellipsoid. Subsequently, we propose a new formulation for the exterior-point Eshelby's tensor which represents the strain and stress influences of an ellipsoidal inclusion upon a local matrix material point. In particular, explicit tensorial components are given for the exterior-point Eshelby's tensor for a spheroidal inclusion. Finally, we discuss the interfacial discontinuities of Eshelby's tensors and strain/stress tensors across the boundary between the matrix and inclusion.

2 Eshelby's Tensors for an Ellipsoidal Inhomogeneous Inclusion

Let us begin by considering an elastic ellipsoidal inhomogeneous inclusion Ω (phase 1) embedded in a distinct elastic infinite medium $\mathcal{D}$. It is assumed that the subdomain Ω and the matrix $[\mathcal{D} - \Omega]$ (phase 0) are perfectly bonded at the interface.

2.1 Strain/Stress Distributions and Eigenstrains. The constitutive equation of stress $\boldsymbol{\sigma}(\mathbf{x})$ and strain $\boldsymbol{\epsilon}(\mathbf{x})$ at a local point $\mathbf{x}$ in the β-phase ($\beta = 0$ or 1) reads

$$\boldsymbol{\sigma}(\mathbf{x}) = \mathbf{C}^{(\beta)} : \boldsymbol{\epsilon}(\mathbf{x}) \qquad (1)$$

where the symbol ":" denotes the tensor contraction. The elasticity tensors $\mathbf{C}^{(1)}$ of the inclusion and $\mathbf{C}^{(0)}$ of the matrix are isotropic and can be expressed as

$$\mathbf{C}^{(\beta)} = \lambda_\beta \mathbf{1} \otimes \mathbf{1} + 2\mu_\beta \mathbf{I}, \quad (\beta = 0, 1) \qquad (2)$$

where the symbol $\otimes$ denotes the tensor product, and λ_β and μ_β are the Lamé constants of the β-phase. Moreover, $\mathbf{1}$ and $\mathbf{I}$ signify the second-rank and fourth-rank identity tensors, respectively.

Assume that the uniform eigenstrain tensor $\boldsymbol{\epsilon}^t$ is prescribed in the inhomogeneous inclusion Ω and, at the same time, the entire medium is subjected to the far-field applied loading. Eshelby (1957, 1959) proposed a fourth-rank tensor $\mathbf{S}$ which is commonly referred to as the *Eshelby's tensor* to describe the strain and stress fields in the inclusion domain. The Eshelby's tensor is defined as

$$\mathbf{S}(\mathbf{x}) \equiv \int_\Omega \mathbf{G}(\mathbf{x} - \mathbf{x}')d\mathbf{x}' \qquad (3)$$

in which $\mathbf{x}$ is the local point inside the inclusion domain Ω. In addition, the integrand $\mathbf{G}(\mathbf{x} - \mathbf{x}')$ is the fourth-rank Green's function tensor with the following indicial expression (cf. Ju and Chen, 1994):

$$G_{ijkl}(\mathbf{x} - \mathbf{x}') = \frac{1}{8\pi(1 - \nu_0)\|\mathbf{x} - \mathbf{x}'\|^3} \times [(1 - 2\nu_0)(\delta_{ik}\delta_{jl} + \delta_{il}\delta_{jk} - \delta_{ij}\delta_{kl}) + 3\nu_0(\delta_{ik}n_jn_l + \delta_{il}n_jn_k + \delta_{jk}n_in_l + \delta_{jl}n_in_k) + 3\delta_{ij}n_kn_l + 3(1 - 2\nu_0)\delta_{kl}n_in_j - 15n_in_jn_kn_l] \qquad (4)$$

where ν_0 is the Poisson's ratio of the matrix material and $\mathbf{n}$ is the unit vector which is defined as $\mathbf{n} \equiv (\mathbf{x} - \mathbf{x}')/\|\mathbf{x} - \mathbf{x}'\|$. Further, the symbol $\|.\|$ denotes the L_2-norm of a vector, and δ_{ij} is the Kronecker delta.

Eshelby (1957) showed that, after carrying out the volume integration on the inclusion domain, the Eshelby's tensor $\mathbf{S}$ does not depend on the local point $\mathbf{x}$ in an ellipsoidal domain. Thus, the total strain field $\boldsymbol{\epsilon}$ and the total stress field $\boldsymbol{\sigma}$ inside an ellipsoidal domain are also uniform, and can be expressed as

$$\boldsymbol{\epsilon} = \boldsymbol{\epsilon}^0 + \mathbf{S} : \boldsymbol{\epsilon}^{**}, \quad \mathbf{x} \in \Omega \qquad (5)$$

$$\boldsymbol{\sigma} = \boldsymbol{\sigma}^0 + \mathbf{C}^{(0)} \cdot (\mathbf{S} - \mathbf{I}) : \boldsymbol{\epsilon}^{**}, \quad \mathbf{x} \in \Omega \qquad (6)$$

where " $\cdot$ " denotes the tensor multiplication operation. Moreover, we have $\boldsymbol{\sigma}^0 = \mathbf{C}^{(0)} : \boldsymbol{\epsilon}^0$. If the entire medium is loaded by the specified far-field applied stress tensor $\boldsymbol{\sigma}^0$, then the corresponding strain $\boldsymbol{\epsilon}^0$ is derived (not specified) by this relation. On the other hand, if the entire medium is loaded by the specified far-field applied strain tensor $\boldsymbol{\epsilon}^0$, then the corresponding stress $\boldsymbol{\sigma}^0$ is also derived (not specified) by the above relation.

In Eqs. (5) and (6), the total eigenstrain $\boldsymbol{\epsilon}^{**}$ can be shown to be (cf. Sun, 1998)

$$\boldsymbol{\epsilon}^{**} = (\mathbf{S} + \mathbf{A})^{-1} : (\mathbf{B} : \boldsymbol{\epsilon}^t - \boldsymbol{\epsilon}^0) \qquad (7)$$

where the fourth-rank elastic-phase "mismatch tensors" $\mathbf{A}$ and $\mathbf{B}$ are defined as

$$\mathbf{A} = [\mathbf{C}^{(1)} - \mathbf{C}^{(0)}]^{-1} \cdot \mathbf{C}^{(0)}; \quad \mathbf{B} = [\mathbf{C}^{(1)} - \mathbf{C}^{(0)}]^{-1} \cdot \mathbf{C}^{(1)}. \qquad (8)$$

In fact, the total eigenstrain $\boldsymbol{\epsilon}^{**}$ is the sum of the prescribed eigenstrain $\boldsymbol{\epsilon}^t$ and the far-field load-induced eigenstrain $\boldsymbol{\epsilon}^*$ (the "equivalent eigenstrain") of the inhomogeneous inclusion, where $\boldsymbol{\epsilon}^*$ takes the form

$$\boldsymbol{\epsilon}^* = (\mathbf{S} + \mathbf{A})^{-1} : [(\mathbf{I} - \mathbf{S}) : \boldsymbol{\epsilon}^t - \boldsymbol{\epsilon}^0]. \qquad (9)$$

It is noted that the equivalent eigenstrain $\boldsymbol{\epsilon}^*$ is not equal to $[-(\mathbf{S} + \mathbf{A})^{-1} : \boldsymbol{\epsilon}^0]$, except where $\boldsymbol{\epsilon}^t = 0$. That is, when $\boldsymbol{\epsilon}^t = 0$, $\boldsymbol{\epsilon}^*$ reduces to the "noninteracting eigenstrain" (inhomogeneity-induced) $\boldsymbol{\epsilon}^{*0}$ previously defined by Ju and Chen (1994).

If one desires to obtain the strain and stress fields at a material point $\mathbf{x}$ which is outside the ellipsoidal inclusion (i.e., in the matrix), then one needs to introduce another fourth-rank tensor $\bar{\mathbf{G}}(\mathbf{x})$ as follows (Eshelby, 1959, and Mura, 1987):

$$\bar{\mathbf{G}}(\mathbf{x}) \equiv \int_\Omega \mathbf{G}(\mathbf{x} - \mathbf{x}')d\mathbf{x}'. \qquad (10)$$

It is observed that the only difference between the right-hand sides of Eqs. (10) and (3) is that $\mathbf{x}$ is in the matrix in Eq. (10) whereas $\mathbf{x}$ is inside the inclusion in Eq. (3). To avoid confusion, we shall refer to the Eshelby's tensor $\mathbf{S}$ as the *interior-point Eshelby's tensor,* and $\bar{\mathbf{G}}(\mathbf{x})$ as the *exterior-point Eshelby's tensor* in what follows.

Once the exterior-point Eshelby's tensor $\bar{\mathbf{G}}(\mathbf{x})$ is obtained, the total strain field $\boldsymbol{\epsilon}$ and total stress field $\boldsymbol{\sigma}$ in the matrix domain can be derived as (Eshelby, 1959; Mura and Cheng, 1977; and Mura, 1987)

$$\boldsymbol{\epsilon}(\mathbf{x}) = \boldsymbol{\epsilon}^0 + \bar{\mathbf{G}}(\mathbf{x}) : \boldsymbol{\epsilon}^{**}, \quad \mathbf{x} \in \mathcal{D} - \Omega \qquad (11)$$

$$\boldsymbol{\sigma}(\mathbf{x}) = \boldsymbol{\sigma}^0 + \mathbf{C}^{(0)} \cdot \bar{\mathbf{G}}(\mathbf{x}) : \boldsymbol{\epsilon}^{**}, \quad \mathbf{x} \in \mathcal{D} - \Omega \qquad (12)$$

where the details for computing $\boldsymbol{\epsilon}^{**}$ can be found in Sun (1998).

2.2 Derivation of the Exterior-Point Eshelby's Tensor. In this section, we will derive the exterior-point Eshelby's tensor in

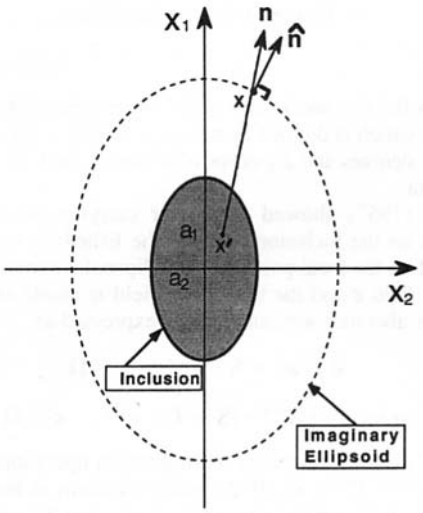

Fig. 1 A schematic representation of an enlarged imaginary ellipsoid and its outward unit normal vector $\hat{n}$

detail. Let the center of an ellipsoidal inhomogeneous inclusion be the origin of the Cartesian coordinate system (x_1, x_2, x_3). Accordingly, the inclusion domain can be expressed as

$$\frac{x_i x_i}{a_I^2} \leq 1, \quad \text{or} \quad \frac{x_1^2}{a_1^2}+\frac{x_2^2}{a_2^2}+\frac{x_3^2}{a_3^2} \leq 1 \tag{13}$$

where a_I $(I = 1, 2, 3)$ is one of the three semi-axes of an ellipsoid. In addition, Eq. (13) follows Mura's (1987) tensorial indicial notation; i.e., repeated lowercase indices are summed up from 1 to 3 while uppercase indices always take on the same numbers as the corresponding lowercase ones but are not summed up.

For any point $\mathbf{x}$ within the matrix phase, similar to Mura (1987), an *imaginary* ellipsoid based on the real inclusion (Eq. (13)) can be constructed as

$$\frac{x_i x_i}{a_I^2+\lambda} = 1 \tag{14}$$

where λ is taken as positive $(\lambda \geq 0)$ and can be uniquely determined in terms of the local point $\mathbf{x}$ of the matrix and a_I from Eq. (14). Further, let us introduce the new outward unit normal vector $\hat{\mathbf{n}}$ at a matrix point $\mathbf{x}$ on the imaginary ellipsoid surface as (see Fig. 1)

$$\hat{n}_i = \frac{x_i}{(a_I^2+\lambda)\sqrt{\Theta(\lambda)}} \tag{15}$$

in which

$$\Theta(\lambda) = \Theta_i(\lambda)\Theta_i(\lambda) \quad \text{and} \quad \Theta_i(\lambda) = \frac{x_i}{a_I^2+\lambda}. \tag{16}$$

With the help of the above definitions and after lengthy derivations, the exterior-point Eshelby's tensor $\bar{\mathbf{G}}(\mathbf{x})$ can be finally expressed in terms of $\hat{\mathbf{n}}$:

$$\begin{aligned}\bar{G}_{ijkl}(\mathbf{x}) = {} & S_{IK}^{(1)}(\lambda)\delta_{ij}\delta_{kl} + S_{IJ}^{(2)}(\lambda)(\delta_{ik}\delta_{jl}+\delta_{il}\delta_{jk}) + S_I^{(3)}(\lambda)\delta_{ij}\hat{n}_k\hat{n}_l \\ & + S_K^{(4)}(\lambda)\delta_{kl}\hat{n}_i\hat{n}_j + S_I^{(5)}(\lambda)(\delta_{ik}\hat{n}_j\hat{n}_l+\delta_{il}\hat{n}_j\hat{n}_k) \\ & + S_J^{(6)}(\lambda)(\delta_{jk}\hat{n}_i\hat{n}_l+\delta_{jl}\hat{n}_i\hat{n}_k) + S_{IJKL}^{(7)}(\lambda)\hat{n}_i\hat{n}_j\hat{n}_k\hat{n}_l \end{aligned} \tag{17}$$

where all the components of $\bar{\mathbf{G}}(\mathbf{x})$ are given by

$$\begin{aligned} S_{IK}^{(1)}(\lambda) = {} & -\frac{\nu_0}{2(1-\nu_0)} J_I(\lambda) \\ & + \frac{1}{4(1-\nu_0)}\left[\frac{a_I^2}{a_I^2-a_K^2} J_I(\lambda) + \frac{a_K^2}{a_K^2-a_I^2} J_K(\lambda)\right] \end{aligned} \tag{18}$$

$$\begin{aligned} S_{IJ}^{(2)}(\lambda) = {} & -\frac{1}{4}[J_I(\lambda)+J_J(\lambda)] \\ & + \frac{1}{4(1-\nu_0)}\left[\frac{a_I^2}{a_I^2-a_J^2} J_I(\lambda) + \frac{a_J^2}{a_J^2-a_I^2} J_J(\lambda)\right] \end{aligned} \tag{19}$$

$$S_I^{(3)}(\lambda) = \frac{\rho^3(\lambda)}{2(1-\nu_0)}[1-\rho_I^2(\lambda)] \tag{20}$$

$$S_K^{(4)}(\lambda) = \frac{\rho^3(\lambda)}{2(1-\nu_0)}[1-2\nu_0-\rho_K^2(\lambda)] \tag{21}$$

$$S_I^{(5)}(\lambda) = \frac{\rho^3(\lambda)}{2(1-\nu_0)}[\nu_0-\rho_I^2(\lambda)] \tag{22}$$

$$S_J^{(6)}(\lambda) = \frac{\rho^3(\lambda)}{2(1-\nu_0)}[\nu_0-\rho_J^2(\lambda)] \tag{23}$$

$$\begin{aligned} S_{IJKL}^{(7)}(\lambda) = {} & \frac{\rho^3(\lambda)}{2(1-\nu_0)}\left[2[\rho_I^2(\lambda)+\rho_J^2(\lambda)+\rho_K^2(\lambda)+\rho_L^2(\lambda)]\right. \\ & \left. + \rho_m(\lambda)\rho_m(\lambda) - \frac{4\rho_M^2(\lambda)\Theta_m(\lambda)\Theta_m(\lambda)}{\Theta(\lambda)} - 5\right] \end{aligned} \tag{24}$$

and $\rho_I(\lambda)$, $\rho(\lambda)$, and $J_I(\lambda)$ are defined as

$$\rho_I(\lambda) = \frac{a_I}{\sqrt{a_I^2+\lambda}}, \quad \rho(\lambda) = [\rho_1(\lambda)\rho_2(\lambda)\rho_3(\lambda)]^{1/3},$$

$$J_I(\lambda) = \int \frac{\rho^3(\lambda)}{a_I^2+\lambda}\, d\lambda. \tag{25}$$

It is noted that the integral $J_I(\lambda)$ cannot be integrated explicitly but can be expressed by the standard elliptic integrals. However, if the inclusion is spheroidal $(a_2 = a_3 \neq a_1)$, we can then integrate $J_I(\lambda)$ explicitly and obtain the components of exterior-point Eshelby's tensor. See Section 3 for details.

The expressions and coherent tensorial structures in Eqs. (17)–(24) for the exterior-point Eshelby's tensor are new and proposed for the first time in the literature. It can also be shown that Eq. (17) is equivalent to Eq. (11.41) in Mura (1987). However, compared with our new formulation, Mura's expression is unfinished, not final, and not explicit. This is, in part, due to the fact that one would have to derive the complicated first and second derivatives of the first and second elliptic integrals in Mura's expression. More importantly, our formulation is geometrically meaningful (in terms of the new outward normal vector $\hat{\mathbf{n}}$) and features a common indicial structure in comparison with that of Mura (1987). Therefore, our treatment is finished, final, explicit, and compact.

Similarly, the interior-point Eshelby's tensor $\mathbf{S}$ takes the form

$$S_{ijkl} = S_{IK}^{(1)}(0)\delta_{ij}\delta_{kl} + S_{IJ}^{(2)}(0)(\delta_{ik}\delta_{jl}+\delta_{il}\delta_{jk}) \tag{26}$$

where

$$\begin{aligned} S_{IK}^{(1)}(0) = {} & -\frac{\nu_0}{2(1-\nu_0)} J_I(0) \\ & + \frac{1}{4(1-\nu_0)}\left[\frac{a_I^2}{a_I^2-a_K^2} J_I(0) + \frac{a_K^2}{a_K^2-a_I^2} J_K(0)\right] \end{aligned} \tag{27}$$

$$\begin{aligned} S_{IJ}^{(2)}(0) = {} & -\frac{1}{4}[J_I(0)+J_J(0)] \\ & + \frac{1}{4(1-\nu_0)}\left[\frac{a_I^2}{a_I^2-a_J^2} J_I(0) + \frac{a_J^2}{a_J^2-a_I^2} J_J(0)\right] \end{aligned} \tag{28}$$

with

$$J_I(0) = J_I(\lambda)|_{\lambda=0}. \tag{29}$$

Here, $S_{IK}^{(1)}(0)$ and $S_{IJ}^{(2)}(0)$ in Eqs. (27) and (28) are the special cases of $S_{IK}^{(1)}(\lambda)$ and $S_{IJ}^{(2)}(\lambda)$ in Eqs. (18) and (19) by setting $\lambda = 0$. It is

also observed that the interior-point Eshelby's tensor depends only on the Poisson's ratio of the matrix and the three semi-axes of the ellipsoidal inclusion.

In general, $S_{IJ}^{(2)}$ is a symmetric tensor while $S_{IJ}^{(1)}$ is not. Therefore, the interior-point Eshelby's tensor is of minor symmetry but not of major symmetry; i.e., $S_{ijkl} = S_{jikl} = S_{ijlk} \neq S_{klij}$. The only exception for the major symmetry is that the Poisson's ratio of the matrix is equal to zero or the inclusion becomes spherical.

3 Explicit Components of the Exterior-Point Eshelby's Tensor for a Spheroid

Let us assume that $a_1 \neq a_2 = a_3$; i.e., the spheroidal inclusion is aligned with the longitudinal x_1-axis. The spheroidal aspect ratio α is defined as $\alpha \equiv a_1/a_2$. The explicit formulas for the first two components $\mathbf{S}^{(1)}(\lambda)$ and $\mathbf{S}^{(2)}(\lambda)$ of the exterior-point Eshelby's tensor in Eqs. (18)–(19) can be shown to be

$$S_{11}^{(1)}(\lambda) = \left[-4\nu_0 - \frac{2}{\alpha^2-1}\right] g(\lambda) - \frac{2}{3(\alpha^2-1)}\rho_1^3(\lambda) + \left[4\nu_0 + \frac{2}{\alpha^2-1}\right]\rho_1(\lambda)\rho_2^2(\lambda) \quad (30)$$

$$S_{12}^{(1)}(\lambda) = S_{13}^{(1)}(\lambda) = \left[-4\nu_0 + \frac{2\alpha^2+1}{\alpha^2-1}\right] g(\lambda) + \left[4\nu_0 - \frac{2\alpha^2}{\alpha^2-1}\right]\rho_1(\lambda)\rho_2^2(\lambda) \quad (31)$$

$$S_{21}^{(1)}(\lambda) = S_{31}^{(1)}(\lambda) = \left[-2\nu_0 - \frac{2\alpha^2+1}{\alpha^2-1}\right] g(\lambda) - \frac{2\alpha^2}{\alpha^2-1}\rho_1(\lambda)\rho_2^2(\lambda) \quad (32)$$

$$S_{22}^{(1)}(\lambda) = S_{23}^{(1)}(\lambda) = S_{32}^{(1)}(\lambda) = S_{33}^{(1)}(\lambda) = \left[-2\nu_0 + \frac{4\alpha^2-1}{4(\alpha^2-1)}\right] g(\lambda) + \frac{\alpha^2}{2(\alpha^2-1)}\frac{\rho_2^4(\lambda)}{\rho_1(\lambda)} \quad (33)$$

and

$$S_{11}^{(2)}(\lambda) = \left[-4\nu_0 + \frac{4\alpha^2-2}{\alpha^2-1}\right] g(\lambda) - \frac{2}{3(\alpha^2-1)}\rho_1^3(\lambda) - \left[4\nu_0 - \frac{4\alpha^2-2}{\alpha^2-1}\right]\rho_1(\lambda)\rho_2^2(\lambda) \quad (34)$$

$$S_{12}^{(2)}(\lambda) = S_{13}^{(2)}(\lambda) = S_{21}^{(2)}(\lambda) = S_{31}^{(2)}(\lambda) = \left[-\nu_0 - \frac{\alpha^2+2}{\alpha^2-1}\right] g(\lambda) - \left[2\nu_0 + \frac{2}{\alpha^2-1}\right]\rho_1(\lambda)\rho_2^2(\lambda) \quad (35)$$

$$S_{22}^{(2)}(\lambda) = S_{23}^{(2)}(\lambda) = S_{32}^{(2)}(\lambda) = S_{33}^{(2)}(\lambda) = \left[2\nu_0 - \frac{4\alpha^2-7}{4(\alpha^2-1)}\right] g(\lambda) + \frac{\alpha^2}{2(\alpha^2-1)}\frac{\rho_2^4(\lambda)}{\rho_1(\lambda)} \quad (36)$$

where

$$g(\lambda) = \begin{cases} -\dfrac{\alpha^2}{\alpha^2-1}\dfrac{\rho_2^2(\lambda)}{\rho_1(\lambda)} + \dfrac{\alpha}{(\alpha^2-1)^{3/2}}\ln\left[(\alpha^2-1)^{1/2}\rho_2(\lambda) + \dfrac{\alpha\rho_2(\lambda)}{\rho_1(\lambda)}\right], & \text{for } \alpha > 1; \\ -\dfrac{\alpha^2}{\alpha^2-1}\dfrac{\rho_2^2(\lambda)}{\rho_1(\lambda)} + \dfrac{\alpha}{(1-\alpha^2)^{3/2}}\tan^{-1}\dfrac{\alpha}{(1-\alpha^2)^{1/2}\rho_1(\lambda)}, & \text{for } \alpha < 1. \end{cases} \quad (37)$$

Furthermore, λ can be solved as

$$\lambda = \frac{r^2 - a_1^2 - a_2^2 + \sqrt{(r^2 + a_1^2 - a_2^2)^2 - 4(a_1^2 - a_2^2)x_1^2}}{2} \quad (38)$$

in which r is the distance between the local point $\mathbf{x}$ in the matrix and the origin of the coordinate system.

All other components of the exterior-point Eshelby's tensor have previously been derived in Eqs. (20) to (24).

4 Discontinuities in Eshelby's Tensors and Strain/Stress Over Interface

From Section 2, it is clear that the exterior-point Eshelby's tensor $\bar{\mathbf{G}}(\mathbf{x})$ and the interior-point Eshelby's tensor $\mathbf{S}$ represent the total eigenstrain contributions to the strain/stress fields of the matrix and inclusion, respectively. An interesting question is whether or not the exterior-point Eshelby's tensor will reduce to the interior-point Eshelby's tensor when the local point $\mathbf{x}$ in the matrix moves to the matrix/inclusion interface as a limiting case. From our explicit formulation of the exterior-point Eshelby's tensor $\bar{\mathbf{G}}(\mathbf{x})$ in Eq. (17), when $\mathbf{x}$ is on the interface ($\lambda = 0$ or $\rho_i = 1$, with $i = 1, 2, 3$), $\bar{\mathbf{G}}(\mathbf{x})$ reduces to

$$\bar{G}_{ijkl}(\mathbf{x}) = S_{IK}^{(1)}(0)\delta_{ij}\delta_{kl} + S_{IJ}^{(2)}(0)(\delta_{ik}\delta_{jl} + \delta_{il}\delta_{jk}) - \frac{\nu_0}{1-\nu_0}\delta_{kl}\hat{n}_i\hat{n}_j - \frac{1}{2}(\delta_{ik}\hat{n}_j\hat{n}_l + \delta_{il}\hat{n}_j\hat{n}_k + \delta_{jk}\hat{n}_i\hat{n}_l + \delta_{jl}\hat{n}_i\hat{n}_k) + \frac{1}{1-\nu_0}\hat{n}_i\hat{n}_j\hat{n}_k\hat{n}_l \quad (39)$$

where $\hat{\mathbf{n}}$ recovers the outward unit normal vector to an ellipsoidal inclusion. Clearly, $\bar{\mathbf{G}}(\mathbf{x})$ generally does not reduce to $\mathbf{S}$. The discontinuity (difference) in the two Eshelby's tensors at the interface can be written as

$$\bar{G}_{ijkl}(\mathbf{x}) - S_{ijkl} = \frac{1}{1-\nu_0}\hat{n}_i\hat{n}_j\hat{n}_k\hat{n}_l - \frac{\nu_0}{1-\nu_0}\delta_{kl}\hat{n}_i\hat{n}_j - \frac{1}{2}(\delta_{ik}\hat{n}_j\hat{n}_l + \delta_{il}\hat{n}_j\hat{n}_k + \delta_{jk}\hat{n}_i\hat{n}_l + \delta_{jl}\hat{n}_i\hat{n}_k). \quad (40)$$

Physically, the total eigenstrain tensor $\boldsymbol{\epsilon}^{**}$ is zero in the matrix and nonzero (Eq. (7)) in the inclusion according to the Eshelby's equivalent inclusion principle. Therefore, the total strain and total stress tensors can be discontinuous on the boundary (Hill, 1961; Mura and Cheng, 1977; Mura, 1987). By subtracting Eq. (5) from (11), we obtain

$$[\boldsymbol{\epsilon}] \equiv \boldsymbol{\epsilon}^{(\text{out})} - \boldsymbol{\epsilon}^{(\text{in})} = (\bar{\mathbf{G}} - \mathbf{S}) : \boldsymbol{\epsilon}^{**} \quad (41)$$

where $[\cdot]$ denotes the jump in the quantity under consideration at the boundary between the inclusion and the surrounding matrix material, and the preceding superscripts (out) and (in) denote quantities just outside and just inside the inclusion, respectively.

Clearly, the exterior-point Eshelby's tensor does *not* coincide with the interior-point Eshelby's tensor even when the local point $\mathbf{x}$ in the matrix moves to the interface.

In the present case, the jump in the total strain tensor across the interface can be derived as

$$[\boldsymbol{\epsilon}] = \tfrac{1}{2}(\hat{\boldsymbol{\lambda}} \otimes \hat{\mathbf{n}} + \hat{\mathbf{n}} \otimes \hat{\boldsymbol{\lambda}}) \tag{42}$$

where $\hat{\mathbf{n}}$ reduces to the outward unit normal vector to the ellipsoidal inclusion. Furthermore, $\hat{\boldsymbol{\lambda}}$ defines the vector of proportionality constant (the magnitude of the jump) determined explicitly by

$$\hat{\boldsymbol{\lambda}} = \frac{1}{1-\nu_0}[\hat{\mathbf{n}} : \boldsymbol{\epsilon}^{**} : \hat{\mathbf{n}} - \nu_0 \operatorname{tr} \boldsymbol{\epsilon}^{**}]\hat{\mathbf{n}} - 2\boldsymbol{\epsilon}^{**} : \hat{\mathbf{n}} \tag{43}$$

where tr $\boldsymbol{\epsilon}^{**}$ is the trace of $\boldsymbol{\epsilon}^{**}$. It can be shown that our above expression for the proportionality constant $\hat{\boldsymbol{\lambda}}$ is equivalent to Eq. (6.8) of Mura (1987, p. 39) for an isotropic inclusion and matrix after some lengthy derivations. However, the present formulation is more explicit and easier to use.

On the other hand, the interfacial jump in the stress tensor becomes (cf. Mura and Cheng, 1977; and Mura, 1987)

$$[\boldsymbol{\sigma}] \equiv \boldsymbol{\sigma}^{(\text{out})} - \boldsymbol{\sigma}^{(\text{in})} = \mathbf{C}^{(0)} : ([\boldsymbol{\epsilon}] + \boldsymbol{\epsilon}^{**}). \tag{44}$$

The above equation is useful for evaluating the stress just outside the inclusion when the stress just inside the inclusion is known.

5 Conclusions

The Eshelby's inclusion problem for an ellipsoidal inhomogeneous inclusion in an infinite matrix is revisited. By introducing the new outward unit normal vector of an enlarged imaginary ellipsoid, a novel formulation is derived for the exterior-point Eshelby's tensor which represents the strain and stress influences of an ellipsoidal inclusion upon a local material point within the matrix (not inclusion). The proposed expression for the exterior-point Eshelby's tensor is simpler, more explicit, compact, geometrically meaningful, and with a common indicial structure, compared with that of Mura (1987). As a special case, we present the explicit tensorial components of the exterior-point Eshelby's tensor for a spheroidal inclusion. Finally, it is demonstrated that the exterior-point Eshelby's tensor does not become the interior-point Eshelby's tensor when the matrix material point moves onto the boundary between the matrix and inclusion. Interfacial discontinuities are obtained for Eshelby's tensors and strain/stress tensors.

Acknowledgment

This work was sponsored by the National Science Foundation, Mechanics and Materials Program, under PYI Grant MSS-9157238. This support is gratefully acknowledged.

References

Edwards, R. H., 1951, "Stress Concentrations Around Spheroidal Inclusions and Cavities," ASME JOURNAL OF APPLIED MECHANICS, Vol. 18, pp. 19–30.

Eshelby, J. D., 1957, "The determination of the elastic field of an ellipsoidal inclusion, and related problems," *Proc. R. Soc. Lond.*, Vol. A241, pp. 376–396.

Eshelby, J. D., 1959, "The elastic field outside an ellipsoidal inclusion," *Proc. R. Soc. Lond.*, Vol. A252, pp. 561–569.

Goodier, J. N., 1937, "On the integration of the thermo-elastic equations," *Phil. Mag.*, Vol. 23, pp. 1017–1032.

Hill, R., 1961, "Discontinuity relations in mechanics of solids," *Progress in Solid Mechanics, II,* edited by I. N. Sneddon and R. Hill, eds., North-Holland Publishing Company, Amsterdam, pp. 245–276.

Ju, J. W., and Chen, T. M., 1994, "Micromechanics and effective moduli of elastic composites containing randomly dispersed ellipsoidal inhomogeneities," *Acta Mechanica,* Vol. 103, pp. 103–121.

Mura, T., 1987, *Micromechanics of Defects in Solids,* 2nd Ed. Martinus Nijhoff, Dordrecht, The Netherlands.

Mura, T., and Cheng, P. C., 1977, "The Elastic Field Outside an Ellipsoidal Inclusion," ASME JOURNAL OF APPLIED MECHANICS, Vol. 44, pp. 591–594.

Nemat-Nasser, S., and Hori, M., 1993, *Micromechanics: Overall Properties of Heterogeneous Materials,* North-Holland, Amsterdam.

Sun, L. Z., 1998, "Micromechanics and Overall Mechanical Behavior of Discontinuously Reinforced Metal Matrix Composites," Ph.D. thesis, University of California, Los Angeles, CA.

Journal of Applied Mechanics

Discussion

The Elastodynamic Green's Function for a Torsional Ring Load[1]

M. Rahman.[2] In the above article, Dr. Lu derived the time-harmonic displacement response of a homogeneous, elastic isotropic medium under a point force of magnitude 2π uniformly distributed along a circular ring in the tangential direction. Solutions for ring loads are useful, especially in the context of axisymmetric boundary value problems of the elasticity theory, since they can be used as Green's functions for deriving the governing integral equations for axisymmetric mixed boundary value problems. However, the author's claim that the corresponding solutions for elastodynamics had not existed in the literature before he derived the present one is incorrect and misleading. In the article by Rahman (1995), elastodynamic solutions for axial, radial shear, and torsional ring loads have been derived for both time-harmonic and transient cases. In particular, the following solution has been derived in Rahman (1995) for a time-harmonic torsional ring source acting on the plane $z = z_0$ (the time dependence is taken in the form $e^{i\omega t}$):

$$u_0^*(r, z) = \frac{1}{\pi}\int_0^{\pi} \cos\phi \, \frac{e^{-ik_2R}}{R}\, d\phi, \qquad (1)$$

where $k_2 = \omega/c_2$ (ω is the circular frequency of vibration and c_2 is the velocity of shear wave propagation) and $R = \sqrt{r^2 + r_0^2 + (z - z_0)^2 - 2rr_0\cos\phi}$ (r_0 is the radius of the circular ring). Some examples illustrating the use of the Green's function (1) have been given in Rahman (1995, 1994). Of course, expression (1) can be written in the form of an infinite series by expanding e^{-ik_2R}. However, the resulting series would converge well for smaller values of k_2 only. Therefore, the integral form of the Green's function (1) is most suitable for numerical purposes. The issues concerning effective numerical evaluation of the integrals of the form (1) are discussed at greater length in the relevant literature, for instance, by Mittra (1973) in the context of mathematically similar problems in electromagnetic scattering theory. In this regard, it is noteworthy that Dr. Lu's double-series solution for the torsional ring load is the least effective. He did not provide any result regarding how well his double series converges, nor did he present any example illustrating the use of the Green's function he derived.

Finally, Dr. Lu attempted to represent the elastodynamic Green's function as the sum of a singular part (the corresponding static solution for the ring load (Kermanidis (1975)) and a regular part—a procedure often exercised in boundary value problems of elastodynamics for writing the corresponding governing integral equations as the sum of a singular part involving the elastostatic ring solution as the Green's function, and a regular elastodynamic part and then inverting the singular part using well-known methods for the corresponding elastostatic problems. It is interesting that although Dr. Lu also agrees that the singular part should be the corresponding elastostatic solution, a close inspection of his expression (22) and (22*a*), however, has revealed that the singular part of his solution is by no means the corresponding elastostatic solution, it being still dependent on the wave parameter k_T!

References

Kermanidis, T., 1975, "A numerical solution for axially symmetrical elasticity problems," *International Journal of Solids & Structures,* Vol. 11, pp. 493–500.

Mittra, R., ed., 1973, *Computer techniques for electromagnetics,* Pergamon Press, New York, 1973.

Rahman, M., 1994, "A penny-shaped crack under time-harmonic torsional body forces," *Engineering Fracture Mechanics,* Vol. 46, No. 4, pp. 599–610.

Rahman, M., 1995, "Some fundamental axisymmetric singular solutions of elastodynamics," *Quarterly Journal of Mechanics and Applied Mathematics,* Vol. 48, Pt. 3, pp. 329–342.

Author's Closure[3]

This author has carefully read Dr. Rahman's papers (Rahman, 1994, 1995), and reached conclusion that in these two papers Dr. Rahman had not derived the solution to the integral in Eq. (1) of the discussion. Rather, Dr. Rahman gave solutions for $\omega = 0$, (or equivalently, $k_{1,2} = 0$). Here, solutions are defined as mathematical expressions without the integral sign. Dr. Rahman should, in this author's opinion, evaluate integrals (i.e., get rid of the integral signs) in Eq. (18), (Rahman, 1994), and Eqs. (13) and (31), (Rahman, 1995), without imposing the condition $\omega = 0$.

While the major task of this author's paper (Lu, 1998) was to derive the elastodynamic Green's function for a time-harmonic torsional ring source, Dr. Rahman's discussion of the paper does provide this author an opportunity to discuss the converging rate of the Green's function. The two-dimensional Green's function for a time-harmonic line source can be expressed in terms of Hankel's function, $H_0(z)$, (Achenbach, Gautesen, and McMaken, 1982). If the expression of the regular term of the Green's function for a torsional ring source, Eq. (22*b*), (Lu, 1998), is compared to the ascending series expansion of $H_0(z)$ (Abramowitz and Stegun, 1964), it is seen that the Green's function converges at least at the same rate as $H_0(z)$ for any given source location and observation point. This is expected since both functions are responses to line sources. The use of the words "least effective" by Dr. Rahman is therefore inappropriate.

As for the statement that Dr. Rahman made in the last paragraph of the discussion, this author simply points out a well-known fact that for a static problem $k_T = k_L = 0$, which is equivalent to $\omega = 0$.

[1] by Y. Lu and published in the Sept. 1998 issue of the ASME JOURNAL OF APPLIED MECHANICS, Vol. 65, pp. 566–568.

[2] 3019 W. 13 Mile Road, Apt. 214, Royal Oak, MI 48073.

[3] Y. Lu, Southwest Research Institute, P.O. Box 28510, San Antonio, TX 78228-0510.

References

Abramowitz, M., and Stegun, I. A., eds., 1964, *Handbook of Mathematical Functions,* National Bureau of Standards, Washington, DC.

Achenbach, J. D., Gautesen, A. K., and McMaken, H., 1982, *Ray Methods for Waves in Elastic Solids: With Applications to Scattering by Cracks,* Pitman Advanced Publishing Program, Boston, MA.

Lu, Y., 1998, "The Elastodynamic Green's Function for a Torsional Ring Source," ASME JOURNAL OF APPLIED MECHANICS, Vol. 65, pp. 566–568.

Rahman, M., 1994, "A Penny-shaped Crack under Time-harmonic Torsional Body Forces," *Engineering Fracture Mechanics,* Vol. 49, No. 4, pp. 599–610.

Rahman, M., 1995, "Some Fundamental Axisymmetric Singular Solutions of Elastodynamics," *Quarterly Journal of Mechanics and Applied Mathematics,* Vol. 48, Pt. 3, pp. 329–342.

Bernoulli Numbers and Rotational Kinematics[1]

W. Pietraszkiewicz.[2]

The kinematic differential Eqs. (21) and (22) of Pfister (1998) are expressed through unconventional tensor power series coe $(\cdot)$ and Ber $(\cdot)$, and the proposed proof is indirect and confusing indeed. Perhaps it may be of some interest to readers of this Journal to note that equivalent equations follow directly as a result of simple transformations, which are analogous to those used by Pietraszkiewicz and Badur (1983) in discussion of spatial changes of the rotation field in continuum mechanics.

With notation used by Pfister (1998), the standard representation of the rotation tensor $\mathbf{R} \in SO(3)$ given already by Gibbs (1884) reads

$$\mathbf{R} = \cos\Psi\mathbf{1} + \sin\Psi\mathbf{n}\times\mathbf{1} + (1-\cos\Psi)\mathbf{n}\otimes\mathbf{n}, \quad (1)$$

where $\otimes$ denotes the tensor product. For a time-dependent $\mathbf{R} = \mathbf{R}(t)$ it follows from (1) that

$$\dot{\mathbf{R}} = (-\sin\Psi\mathbf{1} + \cos\Psi\mathbf{n}\times\mathbf{1} + \sin\Psi\mathbf{n}\otimes\mathbf{n})\dot{\Psi} + \sin\Psi\dot{\mathbf{n}}\times\mathbf{1} + (1-\cos\Psi)(\dot{\mathbf{n}}\otimes\mathbf{n} + \mathbf{n}\otimes\dot{\mathbf{n}}). \quad (2)$$

With $\mathbf{R}^T$ denoting the transposed rotation tensor $(= \mathbf{R}^{-1})$, the angular velocity vector $\boldsymbol{\Omega}$ is an axial vector of the skew-symmetric tensor $\dot{\mathbf{R}}\mathbf{R}^T$, that is $\dot{\mathbf{R}}\mathbf{R}^T = \boldsymbol{\Omega}\times\mathbf{1}$. Introducing (1) and (2) into the left-hand side of this relation, after some algebra we obtain

$$\boldsymbol{\Omega} = \sin\Psi\dot{\mathbf{n}} + (1-\cos\Psi)\mathbf{n}\times\dot{\mathbf{n}} + \dot{\Psi}\mathbf{n}. \quad (3)$$

The Eq. (3) can be solved for $\dot{\mathbf{n}}$ leading to

$$\dot{\mathbf{n}} = \frac{1}{2\ \mathrm{tg}\ \Psi/2}(\boldsymbol{\Omega} - \dot{\Psi}\mathbf{n}) - \frac{1}{2}\mathbf{n}\times\boldsymbol{\Omega}. \quad (4)$$

The simple vector Eqs. (3) and (4) are just the canonical forms of the kinematic differential equations equivalent to (21) and (22) of Pfister (1998). Indeed, introducing the finite rotation vector $\boldsymbol{\Psi} = \Psi\mathbf{n}$ and taking into account that

$$\dot{\boldsymbol{\Psi}} = \dot{\Psi}\mathbf{n} + \Psi\dot{\mathbf{n}}, \quad \boldsymbol{\Psi}\cdot\dot{\boldsymbol{\Psi}} = \boldsymbol{\Psi}\cdot\boldsymbol{\Omega} = \Psi\dot{\Psi},$$

$$\boldsymbol{\Psi}\times(\boldsymbol{\Psi}\times\dot{\boldsymbol{\Psi}}) = (\boldsymbol{\Psi}\cdot\dot{\boldsymbol{\Psi}})\boldsymbol{\Psi} - \Psi^2\dot{\boldsymbol{\Psi}}, \quad (5)$$

the relations (3) and (4) can be transformed into the forms

$$\boldsymbol{\Omega} = \mathbf{A}\cdot\dot{\boldsymbol{\Psi}}, \quad \dot{\boldsymbol{\Psi}} = \mathbf{A}^{-1}\cdot\boldsymbol{\Omega}, \quad (6)$$

where

$$\mathbf{A} = \mathbf{1} + \frac{1-\cos\Psi}{\Psi^2}\boldsymbol{\Psi}\times\mathbf{1} + \frac{\Psi-\sin\Psi}{\Psi^3}\boldsymbol{\Psi}\times(\boldsymbol{\Psi}\times\mathbf{1}),$$

$$\mathbf{A}^{-1} = \frac{1}{\Psi^2}(\boldsymbol{\Psi}\otimes\boldsymbol{\Psi}) - \frac{1}{2}\boldsymbol{\Psi}\times\mathbf{1} - \frac{1}{2\Psi\ \mathrm{tg}\ \Psi/2}\boldsymbol{\Psi}\times(\boldsymbol{\Psi}\times\mathbf{1}). \quad (7)$$

The Eqs. (6) with (7) coincide with (21) and (22) of Pfister (1998), if trigonometric functions in (7) are replaced by Gibbs' functions $\mathrm{gib}_i(\cdot)$. However, in the Eq. (22) of Pfister (1998) two obvious misprints should be corrected: 1 should be replaced by **1**, and the closing parenthesis should be inserted after Ber $(-\hat{\boldsymbol{\Psi}})$.

For other definitions of the finite rotation vector used in the literature, such as tg $\Psi/2\mathbf{n}$, 2 tg $\Psi/2\mathbf{n}$, sin Ψ **n**, or tg $\Psi/4\mathbf{n}$, for example, appropriate equivalent forms of the kinematic differential equations can easily be derived by analogous transformations of (3) and (4).

References

Gibbs, J. W., 1884, *Elements of vector analysis,* New Haven, CT, privately printed, pp. 1–36, 1881; pp. 37–83, 1884 (reprint in The Collected Works of J. Willard Gibbs, Vol. 2, Part 2. Longmans, Green and Co., New York, 1928).

Pietraszkiewicz, W., and Badur, J., 1983, "Finite rotations in the description of continuum deformation," *International Journal of Engineering Science,* Vol. 21, No. 9, pp. 1097–1115.

Pfister, F., 1998, "Bernoulli Numbers and Rotational Kinematics," ASME JOURNAL OF APPLIED MECHANICS, Vol. 65, pp. 758–763.

Author's Closure[3]

I'm happy to note Professor Pietraszkiewicz' interest in kinematic differential equations (KDEs) and in my paper "Bernoulli Numbers and Rotational Kinematics." Some of the points brought up in his discussion can readily be clarified in the following paragraphs.

1 I could not agree that the "proposed proof is indirect and confusing." To set the record straight: Prof. P.'s proof is clearly less efficient than the one given in my paper. I would like to suggest that Prof. P. writes out the details of what leads "after some algebra" to his Eq. (3). The calculations are much more complex than shown in his discussion. The fact that his "run-of-the-mill-proof" leads to a jungle of never-ending equations is certainly one of the reasons that the KDE of the Rotation-vector $\boldsymbol{\Psi}$ has not found adequate attention in kinematics textbooks.

Considering that I obtained the same result within a few lines (without leaving out "some algebra"), I feel that calling my proof "indirect and confusing" should be a rather unfair assessment.

2 Prof. P.'s criticism that the KDEs are expressed "through unconventional tensor power series" could lead to a misinterpretation of my paper.

In fact, *it is actually one of the main points of my paper (and was clearly stated in the Introduction),* to extend Gibbs' *tensor*-power series formulation of the rotation operator, $\mathbf{R} = \exp(\hat{\boldsymbol{\Psi}})$, to the KDEs of $\boldsymbol{\Psi}$. Such a result is missing in Prof. P.'s work. Prof. P.'s arguments and formulations are similar to those found elsewhere in the literature (see, e.g., Shuster, 1993). Instead, my paper was written to achieve a more general goal, i.e., to advance the understanding and to highlight the structure of KDEs through the introduction of meaningful tensor power series:

- The importance of $\exp(t\mathbf{A})$ is well documented in the theory of differential equations. Lesser known is the differential equation of $\exp(\hat{\boldsymbol{\Psi}})$, where the skew $\hat{\boldsymbol{\Psi}}$ is an *arbitrary* function of the scalar t:

$$\frac{d}{dt}\exp(\hat{\boldsymbol{\Psi}}) = \hat{\boldsymbol{\Omega}}\cdot\exp(\hat{\boldsymbol{\Psi}}), \quad (1)$$

[1] By F. Pfister, and published in the Sept. 1998 issue of the ASME JOURNAL OF APPLIED MECHANICS, Vol. 65, pp. 758–763.

[2] Polish Academy of Sciences, Institute of Fluid-Flow Machinery, 80-952 Gdańsk, Poland.

[3] F. Pfister, IPG Automotive Engineering Software + Consulting GmbH, P.O. Box 210522, D-76155 Karlsruhe, Germany.

$$\boldsymbol{\Omega} = \text{coe}\,(\hat{\boldsymbol{\Psi}}) \cdot \dot{\boldsymbol{\Psi}}. \tag{2}$$

I feel that this result in itself justifies the introduction of the *co-exponential series:*

$$\text{coe}\,(z) := (\exp(z) - 1)/z, \quad z \in \mathbb{C}. \tag{3}$$

- In most textbooks the Bernoulli numbers $B_1 = \frac{1}{6}$, $B_2 = \frac{1}{30}$, $B_3 = \frac{1}{42}$, $B_4 = \frac{1}{30}$ . . . are *defined* by

$$\frac{z}{\exp(z) - 1} = 1 - \frac{1}{2}z + \sum_{\nu=1}^{\infty} (-1)^{\nu} \frac{B_{\nu}}{2\nu!} z^{2\nu}. \tag{4}$$

Now, introducing the abriged notation $\text{Ber}\,(z) := \sum_{\nu=1}^{\infty} (B_{\nu}/2\nu!) z^{\nu}$ (Bernoulli series), one has $\text{coe}\,(z)(1 - \frac{1}{2}z + \text{Ber}\,(-(z)^2)) = 1$.

- Using this result (+ some mild mathematical conditions) we find the inverse of coe (**T**) (**T**: arbitrary tensor): $1 - \frac{1}{2}\mathbf{T} + \text{Ber}\,(-\mathbf{T}^2)$. The special case $\mathbf{T} = \hat{\boldsymbol{\Psi}}$ gives

$$(\text{coe}\,(\hat{\boldsymbol{\Psi}}))^{-1} = 1 - \tfrac{1}{2}\hat{\boldsymbol{\Psi}} + \text{Ber}\,(-\hat{\boldsymbol{\Psi}}^2). \tag{5}$$

It is not clear to me how Prof. P. found his Eq. (7). I would like to suggest that he further substantiates his arguments.

- From a purely rigorous mathematical point of view, the choice of "primitive" (sin (·), tan (·), . . .) or "unorthodox" (Ber (·), $\text{gib}_i(\cdot)$, . . .) power series is immaterial. However, there exist good motivations in favor of choosing "unorthodox" series. First, as shown clearly in my paper, this choice results in strictly simpler expressions. Further, and computationally more important, is the fact that by adopting these series the problem can be solved without the need to calculate the norm of $\boldsymbol{\Psi}$, because $\boldsymbol{\Psi}$ only appears quadratically. These facts render the arguments of Prof. P. tenuous at best.

3 An alternative (and perhaps simpler) derivation of Eq. (24) was pointed out to me by Prof. Wohlhart (Wohlhart, 1998):

$\boldsymbol{\Psi}$ is an eigenvector of the orthonormal tensor **R**, $\mathbf{R} \cdot \boldsymbol{\Psi} = \boldsymbol{\Psi}$. Time derivation gives

$$\dot{\mathbf{R}} \cdot \boldsymbol{\Psi} + \mathbf{R} \cdot \dot{\boldsymbol{\Psi}} = \dot{\boldsymbol{\Psi}}. \tag{6}$$

With $\dot{\mathbf{R}} \cdot \mathbf{R}^T = \hat{\boldsymbol{\Omega}} \rightarrow \dot{\mathbf{R}} = \hat{\boldsymbol{\Omega}} \cdot \mathbf{R}$ and $\mathbf{R} \cdot \boldsymbol{\Psi} = \boldsymbol{\Psi}$ one has

$$\boldsymbol{\Psi} \cdot \hat{\boldsymbol{\Omega}} = (\mathbf{R} - \mathbf{1}) \cdot \dot{\boldsymbol{\Psi}}, \tag{7}$$

$$\hat{\boldsymbol{\Psi}} \cdot \boldsymbol{\Omega} = (\mathbf{R} - \mathbf{1}) \cdot \dot{\boldsymbol{\Psi}}. \tag{8}$$

4 Prof. P. correctly indicates two obvious misprints. Unfortunately, three more need to be corrected. (i) p. 759, 1.18: $\sum_{\nu=0}^{\infty} (-1)^{\nu}[(\frac{1}{2}x)^{4\nu})/((2\nu)!)^2]$. (ii) Eq. (30): $\mathbf{R} \equiv \mathbf{1} + \text{gib}_1(\Psi^2)\hat{\boldsymbol{\Psi}} + \text{gib}_2(\Psi^2)\hat{\boldsymbol{\Psi}}^2$. (iii) Eq. (31): $\text{gib}_i(\cdot) := \sum_{\nu=0}^{\infty} [(-1)^{\nu}(\cdot)^{\nu}/(2\nu + i)!]$, $i = 0, 1, 2, 3 \ldots$.

References

Shuster, M. D., 1993, "The Kinematic Equation for the Rotation Vector," *IEEE Transactions on Aerospace and Electronic Systems,* Vol. 29, No. 1, pp. 263–267.

Wohlhart, K., 1998, private communication, Oct.

A Note on the Effective Lamé Constants of a Polycrystalline Aggregate of Cubic Crystals[1]

J. C. Nadeau.[2]

Given the publication of the note by Lubarda (1998), we would like to take this opportunity to generalize and extend the result presented therein.

For an effectively isotropic material let bounds on the bulk κ and shear μ moduli be given, respectively, by

$$0 < \kappa^- \le \kappa \le \kappa^+ \tag{1}$$

$$0 < \mu^- \le \mu \le \mu^+ \tag{2}$$

where a superscript + and − denote an upper and lower bound, respectively. As examples, these upper and lower bounds may, in the case of effectively isotropic composites, take the form of zeroth-order bounds (Nadeau and Ferrari, 1998), the Voigt/Reuss bounds (Hill, 1952; Paul, 1960), or the Hashin-Shtrikman bounds (Hashin and Shtrikman, 1963; Nadeau and Ferrari, 1998). The remaining three isotropic parameters: E, ν, and λ, (i.e., Young's modulus, Poisson's ratio, and a Lamé constant, respectively) expressed in terms of κ and μ are given by the familiar expressions

$$E \equiv E(\kappa, \mu) = \frac{9\kappa\mu}{3\kappa + \mu}$$

$$\nu \equiv \nu(\kappa, \mu) = \frac{3\kappa - 2\mu}{2(3\kappa + \mu)}$$

$$\lambda \equiv \lambda(\kappa, \mu) = \tfrac{1}{3}(3\kappa - 2\mu).$$

The corresponding bounds on these three parameters, in terms of the given bounds on κ and μ, are

$$0 < E^- := E(\kappa^-, \mu^-) \le E \le E(\kappa^+, \mu^+) =: E^+ \tag{3}$$

$$-1 < \nu^- := \nu(\kappa^-, \mu^+) \le \nu \le \nu(\kappa^+, \mu^-) =: \nu^+ < \tfrac{1}{2} \tag{4}$$

$$\lambda^- := \lambda(\kappa^-, \mu^+) \le \lambda \le \lambda(\kappa^+, \mu^-) =: \lambda^+. \tag{5}$$

Note that the lower bounds ν^- and λ^- are functions of the lower bulk modulus bound κ^- and the upper shear modulus bound μ^+, while the upper bounds ν^+ and λ^+ are functions of the upper bulk modulus bound κ^+ and the lower shear modulus bound μ^-.

When the upper and lower bounds for Eqs. (1) and (2) are taken to be the Voigt/Reuss bounds for a polycrystalline aggregate of cubic crystals then Eq. (5) yields the result of Lubarda (1998). When the upper and lower bounds for Eqs. (1) and (2) are taken to be the Hashin-Shtrikman bounds then Eqs. (3) and (4) correspond to the results obtained by Zimmerman (1992).

References

Hashin, Z., and Shtrikman, S., 1963, "A variational approach to the theory of the elastic behaviour of multiphase materials," *Journal of the Mechanics and Physics of Solids,* Vol. 11, pp. 127–140.

Hill, R., 1952, "The elastic behavior of a crystalline aggregate," *Proceedings of the Physical Society, Section A,* Vol. 65, No. 5, pp. 349–354.

Lubarda, V. A., 1998, "A note on the Effective Lamé Constants of a Polycrystalline Aggregates of Cubic Crystals," ASME JOURNAL OF APPLIED MECHANICS, Vol. 65, pp. 769–770.

Nadeau, J. C., and Ferrari, M., 1998, "On optimal zeroth-order bounds with application to Hashin-Shtrikman bounds and anisotropy parameters," *International Journal of Solids and Structures,* submitted for publication.

Paul, B., 1960, "Prediction of elastic constants of multiphase materials," *Transactions of the Metallurgical Society of AIME,* Vol. 218, Feb., pp. 36–41.

Zimmerman, R. W., 1992, "Hashin-Shtrikman bounds on the Poisson ratio of a composite material," *Mechanics Research Communications,* Vol. 19, No. 6, pp. 563–569.

[1] by V. A. Lubarda, and published in the Sept. 1998 issue of the ASME JOURNAL OF APPLIED MECHANICS, Vol. 65, pp. 769–770.

[2] Department of Civil and Environmental Engineering, Duke University, Durham, NC 27708-0287. e-mail: nadeau@duke.edu.

$$\boldsymbol{\Omega} = \text{coe}\,(\hat{\boldsymbol{\Psi}}) \cdot \dot{\boldsymbol{\Psi}}. \tag{2}$$

I feel that this result in itself justifies the introduction of the *co-exponential series:*

$$\text{coe}\,(z) := (\exp(z) - 1)/z, \quad z \in \mathbb{C}. \tag{3}$$

- In most textbooks the Bernoulli numbers $B_1 = \frac{1}{6}$, $B_2 = \frac{1}{30}$, $B_3 = \frac{1}{42}$, $B_4 = \frac{1}{30}$ . . . are *defined* by

$$\frac{z}{\exp(z) - 1} = 1 - \frac{1}{2}z + \sum_{\nu=1}^{\infty} (-1)^{\nu} \frac{B_{\nu}}{2\nu!} z^{2\nu}. \tag{4}$$

Now, introducing the abriged notation $\text{Ber}\,(z) := \sum_{\nu=1}^{\infty} (B_{\nu}/2\nu!) z^{\nu}$ (Bernoulli series), one has $\text{coe}\,(z)(1 - \frac{1}{2}z + \text{Ber}\,(-(z)^2)) = 1$.

- Using this result (+ some mild mathematical conditions) we find the inverse of coe (**T**) (**T**: arbitrary tensor): $1 - \frac{1}{2}\mathbf{T} + \text{Ber}\,(-\mathbf{T}^2)$. The special case $\mathbf{T} = \hat{\boldsymbol{\Psi}}$ gives

$$(\text{coe}\,(\hat{\boldsymbol{\Psi}}))^{-1} = 1 - \tfrac{1}{2}\hat{\boldsymbol{\Psi}} + \text{Ber}\,(-\hat{\boldsymbol{\Psi}}^2). \tag{5}$$

It is not clear to me how Prof. P. found his Eq. (7). I would like to suggest that he further substantiates his arguments.

- From a purely rigorous mathematical point of view, the choice of "primitive" (sin (·), tan (·), . . .) or "unorthodox" (Ber (·), $\text{gib}_i(\cdot)$, . . .) power series is immaterial. However, there exist good motivations in favor of choosing "unorthodox" series. First, as shown clearly in my paper, this choice results in strictly simpler expressions. Further, and computationally more important, is the fact that by adopting these series the problem can be solved without the need to calculate the norm of $\boldsymbol{\Psi}$, because $\boldsymbol{\Psi}$ only appears quadratically. These facts render the arguments of Prof. P. tenuous at best.

3 An alternative (and perhaps simpler) derivation of Eq. (24) was pointed out to me by Prof. Wohlhart (Wohlhart, 1998):

$\boldsymbol{\Psi}$ is an eigenvector of the orthonormal tensor **R**, $\mathbf{R} \cdot \boldsymbol{\Psi} = \boldsymbol{\Psi}$. Time derivation gives

$$\dot{\mathbf{R}} \cdot \boldsymbol{\Psi} + \mathbf{R} \cdot \dot{\boldsymbol{\Psi}} = \dot{\boldsymbol{\Psi}}. \tag{6}$$

With $\dot{\mathbf{R}} \cdot \mathbf{R}^T = \hat{\boldsymbol{\Omega}} \rightarrow \dot{\mathbf{R}} = \hat{\boldsymbol{\Omega}} \cdot \mathbf{R}$ and $\mathbf{R} \cdot \boldsymbol{\Psi} = \boldsymbol{\Psi}$ one has

$$\boldsymbol{\Psi} \cdot \hat{\boldsymbol{\Omega}} = (\mathbf{R} - \mathbf{1}) \cdot \dot{\boldsymbol{\Psi}}, \tag{7}$$

$$\hat{\boldsymbol{\Psi}} \cdot \boldsymbol{\Omega} = (\mathbf{R} - \mathbf{1}) \cdot \dot{\boldsymbol{\Psi}}. \tag{8}$$

4 Prof. P. correctly indicates two obvious misprints. Unfortunately, three more need to be corrected. (i) p. 759, 1.18: $\sum_{\nu=0}^{\infty} (-1)^{\nu}[(\frac{1}{2}x)^{4\nu})/((2\nu)!)^2]$. (ii) Eq. (30): $\mathbf{R} \equiv \mathbf{1} + \text{gib}_1(\Psi^2)\hat{\boldsymbol{\Psi}} + \text{gib}_2(\Psi^2)\hat{\boldsymbol{\Psi}}^2$. (iii) Eq. (31): $\text{gib}_i(\cdot) := \sum_{\nu=0}^{\infty} [(-1)^{\nu}(\cdot)^{\nu}/(2\nu + i)!]$, $i = 0, 1, 2, 3 \ldots$.

References

Shuster, M. D., 1993, "The Kinematic Equation for the Rotation Vector," *IEEE Transactions on Aerospace and Electronic Systems,* Vol. 29, No. 1, pp. 263–267.

Wohlhart, K., 1998, private communication, Oct.

A Note on the Effective Lamé Constants of a Polycrystalline Aggregate of Cubic Crystals[1]

J. C. Nadeau.[2]

Given the publication of the note by Lubarda (1998), we would like to take this opportunity to generalize and extend the result presented therein.

For an effectively isotropic material let bounds on the bulk κ and shear μ moduli be given, respectively, by

$$0 < \kappa^- \le \kappa \le \kappa^+ \tag{1}$$

$$0 < \mu^- \le \mu \le \mu^+ \tag{2}$$

where a superscript + and − denote an upper and lower bound, respectively. As examples, these upper and lower bounds may, in the case of effectively isotropic composites, take the form of zeroth-order bounds (Nadeau and Ferrari, 1998), the Voigt/Reuss bounds (Hill, 1952; Paul, 1960), or the Hashin-Shtrikman bounds (Hashin and Shtrikman, 1963; Nadeau and Ferrari, 1998). The remaining three isotropic parameters: E, ν, and λ, (i.e., Young's modulus, Poisson's ratio, and a Lamé constant, respectively) expressed in terms of κ and μ are given by the familiar expressions

$$E \equiv E(\kappa, \mu) = \frac{9\kappa\mu}{3\kappa + \mu}$$

$$\nu \equiv \nu(\kappa, \mu) = \frac{3\kappa - 2\mu}{2(3\kappa + \mu)}$$

$$\lambda \equiv \lambda(\kappa, \mu) = \tfrac{1}{3}(3\kappa - 2\mu).$$

The corresponding bounds on these three parameters, in terms of the given bounds on κ and μ, are

$$0 < E^- := E(\kappa^-, \mu^-) \le E \le E(\kappa^+, \mu^+) =: E^+ \tag{3}$$

$$-1 < \nu^- := \nu(\kappa^-, \mu^+) \le \nu \le \nu(\kappa^+, \mu^-) =: \nu^+ < \tfrac{1}{2} \tag{4}$$

$$\lambda^- := \lambda(\kappa^-, \mu^+) \le \lambda \le \lambda(\kappa^+, \mu^-) =: \lambda^+. \tag{5}$$

Note that the lower bounds ν^- and λ^- are functions of the lower bulk modulus bound κ^- and the upper shear modulus bound μ^+, while the upper bounds ν^+ and λ^+ are functions of the upper bulk modulus bound κ^+ and the lower shear modulus bound μ^-.

When the upper and lower bounds for Eqs. (1) and (2) are taken to be the Voigt/Reuss bounds for a polycrystalline aggregate of cubic crystals then Eq. (5) yields the result of Lubarda (1998). When the upper and lower bounds for Eqs. (1) and (2) are taken to be the Hashin-Shtrikman bounds then Eqs. (3) and (4) correspond to the results obtained by Zimmerman (1992).

References

Hashin, Z., and Shtrikman, S., 1963, "A variational approach to the theory of the elastic behaviour of multiphase materials," *Journal of the Mechanics and Physics of Solids,* Vol. 11, pp. 127–140.

Hill, R., 1952, "The elastic behavior of a crystalline aggregate," *Proceedings of the Physical Society, Section A,* Vol. 65, No. 5, pp. 349–354.

Lubarda, V. A., 1998, "A note on the Effective Lamé Constants of a Polycrystalline Aggregates of Cubic Crystals," ASME JOURNAL OF APPLIED MECHANICS, Vol. 65, pp. 769–770.

Nadeau, J. C., and Ferrari, M., 1998, "On optimal zeroth-order bounds with application to Hashin-Shtrikman bounds and anisotropy parameters," *International Journal of Solids and Structures,* submitted for publication.

Paul, B., 1960, "Prediction of elastic constants of multiphase materials," *Transactions of the Metallurgical Society of AIME,* Vol. 218, Feb., pp. 36–41.

Zimmerman, R. W., 1992, "Hashin-Shtrikman bounds on the Poisson ratio of a composite material," *Mechanics Research Communications,* Vol. 19, No. 6, pp. 563–569.

[1] by V. A. Lubarda, and published in the Sept. 1998 issue of the ASME JOURNAL OF APPLIED MECHANICS, Vol. 65, pp. 769–770.

[2] Department of Civil and Environmental Engineering, Duke University, Durham, NC 27708-0287. e-mail: nadeau@duke.edu.

Journal of Applied Mechanics

Book Review

Vibrations of Elasto-Plastic Bodies (Springer Series on Foundations of Engineering Mechanics), by V. A. Palmov. Springer-Verlag, New York, 1998. 311 pages.

REVIEWED BY F. ZIEGLER[1]

This book, translated by A. Belyaev, is actually a revised and carefully updated version of the Russian original, published in 1976. It covers fundamental microplasticity, proper constitutive relations, and practical tools for the analysis of dynamic plasticity. By successfully developing such a uniform and applicable approach to various important problems of energy-absorbing media and structures, the author has filled a major gap in the existing literature. Considering steady-state vibrations in elastoplastic bodies, the focus is on important applications in low-cycle fatigue of metals and to the applied theory of amplitude-dependent internal damping, also transient and random vibrations are well covered. The scientific community certainly looks forward to the author's sectional lecture to be delivered at the 20th ICTAM at Chicago in the year 2000.

The controversy on decomposition of large strain, which has strongly influenced computational mechanics in the recent past, is resolved with elegance, based solely on thermodynamic considerations. These theorems appear as part of the fundamentals, which comprise the first two chapters, may (hopefully) alter the common and standardized routines which quite often lead to unreliable numerical results.

The first chapter presents a brief overview of the basic concepts and methods of nonlinear continuum mechanics. Considerable attention is paid to thermodynamic principles, the general theory of rheological modeling (series and/or parallel connections of springs, dashpots, and St. Venant bodies) and the construction of microplasticity theories. Since rheology utilizes an additive decomposition of the strain rate tensor of finite viscoelasticity, elastoplasticity and viscoelastoplasticity into elastic, viscous, and viscoplastic parts, one section is devoted entirely to the applicability of decomposition methods. Three methods are compared, namely the additive decomposition of the strain applied to elastic and viscoplastic or plastic components, the additive decomposition of a strain tensor and the multiplicative decomposition of the deformation gradient. It is shown that only the first method is thermodynamically consistent. The thermodynamic inconsistency of the other methods is explicitly demonstrated.

The second chapter is devoted mainly to the derivation of general amplitude-dependent internal damping in terms of plasticity theory. An analysis of a one-dimensional variant of a simple microplasticity theory in the cases of loading, unloading and cyclic deformation is carried out. It is shown that (i) superimposing a static load does not influence the energy dissipation in the ductile material under cyclic deformation, (ii) energy dissipation in ductile materials under cyclic deformation does not depend on frequency, (iii) energy dissipation is nonlinear in general, linear dissipation is not feasible.

Constitutive equations for elastoplastic materials in three dimensions are studied in the third chapter. Properties of the stress-strain curves of loading and unloading, as well as the properties of cyclic deformation diagrams are investigated. The method of harmonic linearization allows the author to introduce a complex shear modulus which is shown to be independent of the frequency but depends upon the amplitude of the shear stress.

The fourth chapter deals with assigned single-frequency vibrations of elastoplastic bodies of arbitrary shape. Closed-form expressions for the coefficients of the equation for the amplitude-frequency characteristics and for the decay of vibration amplitude are derived by Galerkin's method. The formulae obtained are of a general character and are applicable to the analysis of vibrations in homogeneous and heterogeneous bodies. It is shown that the vibration decrement depends upon the stress state and the amplitude of the shear stress. The vibration decrements due to the derived equations are compared with those obtained in experimental tests, and satisfactory agreement between the theory and test data is ascertained for the energy dissipation.

The fifth chapter outlines the analysis of random deformations of elastoplastic materials. An analysis performed by means of the method of statistical linearization shows that the problem reduces to one within reach of the concept of the complex shear modulus. A few calculations for the complex shear modulus in the cases of polyharmonic deformations and for a simple type of broadband random deformation are given.

Random vibrations of elastoplastic bodies are studied in the sixth chapter. An approximate solution of the boundary value problem is obtained with the aid of Galerkin's method by utilizing a series expansion in terms of normal modes of the elastic body. Closed-form expressions for the decrement of free vibration are derived for the case of asymptotically small plastic strains. Vibration of an infinite plate subject to broadband loading is shown to depend essentially on the character of the energy dissipation over the whole frequency range, and not nearly on near-resonance domains as is the case for finite bodies. The spectral theory of homogeneous random fields is used to construct the solution. By modeling the energy dissipation with the aid of plasticity theory, the problem reduces to an implicit nonlinear integral equation, whose solution is rather easily obtained by the method of successive approximations for any particular spectral density. The approach applied to the analysis of plate vibrations is generalized to the vibration of shallow shells.

The next chapter is devoted to the problem of vibration propagation in nonlinear dissipative media with various rheological constitutive equations. It is found that, for example, vibration propagates down a rod for a finite distance in the case of a rigid-plastic material with linear hardening. In the case of so-called amplitude-dependent "internal friction," vibration occupies the entire rod and possesses a saturation property. This property implies that there exists a limit on the attainable level of vibration

[1] Department of Civil Engineering, Tech-University, Vienna A1040, Austria. Fellow ASME.

which depends on the material properties, the distance from the vibration source and the frequency, but does not depend on the loading intensity.

Vibrations in media with complex structure are analyzed in the eighth and final chapter. The medium is postulated to consist of a carrier medium and an infinite set of noninteracting oscillators with a continuous spectrum of eigenfrequencies attached to the carrier structure. The one-dimensional theory is analyzed in detail. The solution of the problem of vibration propagation indicates that the character of the vibration decay depends weakly on the oscillators' damping and is determined mainly by the spectral properties of the set of oscillators. This implies the resonant character of vibration absorption, i.e., the oscillators act as dynamic absorbers. Applicability of the medium with complex structure for a phenomenological description of complex dynamic structures is discussed. Another theory related to the problem of high-frequency vibrations in complex structures is the theory of vibroconductivity, which leads to an equation identical to that of thermal conductivity with a distributed heat sink, the latter modeling the vibration absorption by the secondary systems of the complex structures.

Well written, well organized, with well-balanced references, and clear illustrations, *Vibrations of Elasto-Plastic Bodies* satisfies a long-standing need for a book providing models and analytical tools for real world problems in dynamic plasticity. It contains many ideas, approaches, and practical methods of solution, as well as comparisons with test results. This book is unique since it contains a systematic analysis of all aspects of vibrations in energy-absorbing media. Practitioners and researchers in the field of dynamic plasticity, and graduate students as well, will all profit from the study of this monograph.